Proceedings of:

The Nineteenth Annual Meeting

The American Society for Precision Engineering

October 24-29, 2004
Wyndham Palace Resort & Spa at Walt Disney World
Orlando, Florida

The American Society for Precision Engineering (ASPE) is a multidisciplinary professional and technical society concerned with research and development, design, manufacture and measurement of high accuracy components and systems. ASPE activities encompass relevant aspects of mechanical, electronic, optical and production engineering, physics, chemistry, and computer and materials science. Membership is open to anyone interested in any aspect of precision engineering.

Founded in 1986, ASPE provides a new focus for a diverse but important community. Other professional organizations have covered aspects of precision engineering, always as a sideline to their principal goals. ASPE is based on the core of generic concepts necessary to achieve precision in any application; independent of discipline, ASPE intends to be the focus for precision technology — and to represent all facets from research to application.

ASPE — The American Society for Precision Engineering
301 Glenwood Avenue, Suite 205, Raleigh, NC 27603
P.O. Box 10826, Raleigh, NC 27605
Telephone: (919) 839-8444 Fax (919) 839-8039

Preface

This book comprises the proceedings of the 2004 Annual Meeting. The contributions reflect the authors' opinions and are published as presented to ASPE, without change. Their inclusion in this publication does not necessarily constitute endorsement by the ASPE, or its editorial staff.

Individual readers of this book and nonprofit libraries acting for them are permitted to make fair use of the material contained in this book to be used in teaching or research; provided they copy said paper in total, as written by the author. Permission is granted to quote excerpts from the scientific or technical works in this book with proper acknowledgment of the source to include: The author's name, the book name, and the ASPE tag line. Reproduction of figures and tables is likewise permitted from the contents of this book, provided that the same acknowledgment of the same source and content is permitted.

Any other type reproduction, systematic copying or multiple reproduction of any material in this book is expressly prohibited except with the written permission of the ASPE editorial staff, addressed to the Society's headquarters.

ISBN 1-887706-36-4

2004

American Society for Precision Engineering
301 Glenwood Avenue, Suite 205
Raleigh, NC 27603

Printed in the United States of America

Welcome Note

Welcome to Orlando for the Nineteenth Annual Meeting of The American Society for Precision Engineering, co-sponsored by the Japan Society for Precision Engineering. The growth and success of the Society reflects the increasing importance of precision engineering in a wide variety of fields of endeavor, from manufacturing to microelectronics to basic science. The Society serves as a focus for precision engineers across all of these fields. The Annual Meeting has evolved into a premier international forum for the exchange of ideas and presentation of research results relating to precision engineering, metrology, controls, and system integration. Precision engineers and scientists from private industry, government laboratories, and universities meet to learn about the latest developments and to exchange ideas about the future directions of these technologies.

This year's meeting continues the tradition of offering two full days of tutorials presented by some of the foremost precision engineers and scientists in the world. The technical sessions and poster presentations offer the latest research results in the areas of ultraprecision machining, metrology, controls, precision grinding, micro-positioning, material processing, design, precision transducers, surface profilometry, machine tool metrology, and error compensation. The commercial exhibit will provide attendees with the opportunity to view and discuss the latest precision engineering equipment, products, and services that are commercially available.

The conference organizing committee is proud to present the program for the Nineteenth Annual Meeting of the ASPE. We welcome your participation and your feedback on how to make next year's meeting even better.

2004 Organizing & Technical Program Committee

Andrew J. Hazelton, Chair
Nikon Research Corporation of America

Georg Aigeldinger, Sandia National Laboratories
Hisayuki Aoyama, University of Electro-Communications
Vivek G. Badami, Corning Tropel Corporation
Keith Carlisle, Lawrence Livermore National Lab.
Martin L. Culpepper, Massachusetts Inst. of Technology
Bradley N. Damazo, Nat'l Inst. of Standards and Technology
Thomas A. Dow, North Carolina State University
Kenneth P. Garrard, North Carolina State University
David D. Gill, Sandia National Laboratories
Hiroshi Hashimoto, Kanagawa University of Technology
Ken'ichiro Horio, Saitama University
Bradley H. Jared, 3M Precision Optics
Byron R. Knapp, Olympic Laser, Inc.
Don A. Lucca, Oklahoma State University
Stephen J. Ludwick, Aerotech, Inc.
Eric R. Marsh, The Pennsylvania State University
Michele H. Miller, Michigan Technological University
Tony L. Schmitz, University of Florida
Alex Sohn, North Carolina State University
Pradeep Subrahmanyan, Electro Scientific Industries, Inc.
Allen Y. Yi, Ohio State University
John C. Ziegert, University of Florida

2004 Scholarship Recipients

Mr. Eric S. Buice, University of North Carolina at Charlotte
R.V. Jones Memorial Scholarship

Mr. Jerald Lee Overcash, University of North Carolina at Charlotte

2004 Annual Meeting
Contents

Preface . . . . . *ii*

Welcome Note . . . . . *iii*

Organizing Committee — 2004 Scholarship Recipient . . . . . *iv*

Sponsor Members . . . . . *vi-vii*

Cooperating Sponsors—Technical Exhibitors . . . . . *viii*

Program . . . . . *ix*

Keynote Address . . . . . *x*

Commercial Session . . . . . *x*

2004 ASPE Lifetime Achievement Awards . . . . . *xi-xii*

Technical Paper Index *1-11*

Technical Papers *15-740*

Authors Index *741-745*

ASPE 2004 Sustaining Corporate Sponsors

ADCOLE Corporation
669 Forest Street
P.O. Box 39
Marlborough, MA
Phone: (508) 485-9100
Fax: (508) 481-6142
www.adcole.com

Aerotech, Inc.
101 Zeta Drive
Pittsburgh, PA 15238-2897
Phone: (412) 967-6845
www.aerotech.com

Corning Tropel Corporation
60 O'Connor Road
Fairport, NY 14450
Phone: (585) 388-3500
Toll-free: (888) 4-TROPEL
www.tropel.com

Fabreeka International, Inc.
P.O. Box 210
1023 Turnpike Street
Stoughton, MA 02072
Phone: (781) 341-3655
Toll-free: (800)-322-7352
www.fabreeka.com

Fisba Optik, L. L. C.
3495 Winton Place
Building E, Suite 120
Rochester, NY 14623
Phone: (585) 427-9155
www.fisbaoptik.com

Lion Precision
563 Shoreview Park Road
St. Paul, MN 55126-7014
(651) 484-6544
(651) 484-6824
www.lionprecision.com

Moore Tool Company, Inc.
800 Union Avenue
Bridgeport, CT 06607-0088
Phone: (203) 366-3224
Fax: (20) 366-5694
www.mooretool.com

AIR BEARINGS FOR INDUSTRY
New Way Machine Components, Inc.
4009-I Market Street
Aston, PA 19014
Phone: (610) 494-6700
Fax: (610) 494-0911
Toll-Free: (800) 394-1046
www.newwaybearings.com

Olympic Precision, Inc.
410 Ida Street West
Bremerton, WA 98312
Phone: (360) 917-0047
Fax: (360) 917-0046

Philips, CFT
Sunnyvale Campus
1140 Ringwood Court
MS SV16
San Jose, CA 95131-1706
Phone: (408) 991-2261
www.cft.philips.com

Professional Instruments Company
7800 Powell Road
Hopkins, MN 55343
Phone: (952) 933-1222
Fax: (952) 933-3315
www.airbearings.com

Queensgate Instruments, Ltd.
Woodland Road
Torquay Devon TQ2 7AY
United Kingdom
Phone: 44-1803-407710
Fax: 44-1803-4076
www.nanopositioning.com

Reflexite Precision Technology Ctr.
200 Park Centre Drive
West Henrietta, NY 14586
Phone: (585) 272-0309
www.reflexite.com

Zygo Corporation
Laurel Brook Road
Middlefield, CT 06455-0448
Phone: (860) 347-8506
Fax: (860) 347-8372
Toll-free: (800) ZYGO-NOW
www.zygo.com

Sponsor Members of the ASPE

Corporate Sponsors

3M Company
St. Paul, MN 55144-1000
Contact: William J. Bryan
(651) 575-1465

Center for Precision Metrology - University of North Carolina at Charlotte
Charlotte, NC 28223-0001
Contact: Gregory W. Caskey
(704) 687-3937

Chardon Tool & Supply Company, Inc.
Chardon, OH 44024
Contact: Weldon Bennett
(216) 286-6440

Contour Fine Tooling, Inc.
Marlborough, NH 03455
Contact: Jeffrey Tomlin
(603) 876-4908

Corning Inc.
Corning, NY 14831
Contact: John Thomas
(607) 974-3842

Cranfield Precision, Div. of Landis Lund
A Western Atlas Corporation
Cranfield, Bedford MK43 OAL, England
Contact: Edric M. E. Brown
011-44-1234-754222

MicroE Systems, Inc.
Natick, MA 01760-1313
Contact: Donald K. Mitchell
(508) 903-5000

Nano Corporation
Tokyo 146-0085, Japan
Contact: Akira Hayashi
011-81-3-3751-3311

Precitech, Inc.
Keene, NH 03431
Contact: Jason Wyman
(603) 357-2511

Taylor Hobson, Ltd.
Leicester LE4 9JQ, UK
Contact: Daniel I. Mansfield
+44-116-2763771, Ext. 2126

Veeco Instruments, Inc.
Tucson, AZ 85706
Contact: Chip Ragan
(520) 741-1044

Cooperating Sponsors

Elsevier Science, Inc.

Japan Society for Precision Engineering

Technical Exhibitors

Accura Technics, L.L.C.

Aerotech, Inc.

ADE Phase Shift

A.L.M.T. Corporation

Bal-Tec Division of Micro Surface Engineering, Inc.

Center for Precision Metrology — University of N. C. at Charlotte

Chardon Tool

Contour Fine Tooling, Inc.

CoorsTek, Inc.

Corning Tropel Corporation

Fabreeka International, Inc.

FRT of America, LLC

G^2 Engineering

Heidenhain Corporation

K & Y Diamond Ltd.

Kriterion, LLC

Lion Precision

Machine Dynamics Research Lab. — Pennsylvania State University

Moore Nanotechnology Systems, LLC

New Way Precision, Inc.

Nikon Instrument, Inc.

Olympic Precision, Inc.

Philips CFT

PI (Physik Instrumente) LP

Precision Engineering Center — N.C. State University

Precision Machining Lab. — University of N.C. at Charlotte

Precision MicroDynmics, Inc.

Precision Systems Lab. — The George Washington University

Precitech, Inc.

Professional Instruments Company, Inc.

Technodiamant, Inc.

Veeco Instruments

Program

2004 ASPE Annual Meeting

Time	Sun., Oct. 24	Mon., Oct. 25	Tues., Oct. 26	Wed., Oct. 27	Thurs., Oct. 28	Fri., Oct. 29
8:00	Registration	Registration	Registration			
9:00	Tutorials	Tutorials	Technical Session I	Technical Session III	Technical Session VI	Technical Tours
10:00			Break	Break	Break	
11:00			Technical Session II	Technical Session IV	Technical Session VII	
12:00			Lunch and Committee Meetings	Awards Lunch and Business Meeting	Lunch and Roundtable Discussions	
1:00			Commercial Session	Technical Session V	Technical Session VIII	
2:00	Tutorials	Tutorials	Break and Poster Session I	Break and Poster Session II		
3:00			Hospitality Hour	Hospitality Hour		
4:00						
5:00		Keynote Address	Science Center Dinner Banquet			
6:00		Welcome Reception				
7:00						
8:00						
9:00						

Keynote Address

E. Clayton Teague

Monday, October 25, 2004 – 6:30 p.m.

Session Chair: Vivek G. Badami (Corning Tropel Corporation)

E. Clayton Teague

Clayton Teague is Director of the Federal National Nanotechnology Coordination Office (NNCO), being appointed in April 2003. As Director of the NNCO, he is the agency representative to the National Science and Technology Council from his position as Chief of the Manufacturing Metrology Division of the National Institute of Standards and Technology (NIST). Beginning with his quantum mechanical tunneling work, since 1967 he has been working in some of the fields now known as nanotechnology. His work has included designing, constructing, and using STMs, AFMs, and interferometers for ultra-high accuracy dimensional metrology of surfaces and micrometer to nanometer-scale features.

Dr. Teague is a member of the American Society for Precision Engineering, has served twice as the Society's president, and is a fellow of the UK Institute of Physics. He served as Editor-in-Chief of the international journal Nanotechnology for ten years and is currently a member of the Editorial Board of the journal. He holds a B.S. and M.S. in physics from the Georgia Institute of Technology and a Ph.D. in physics from the University of North Texas. He has been active in the metrology and standards communities for most of his career and has been privileged to receive a number of honors and awards from the government as well as industrial and private organizations for his work.

Nanotechnology: Hype or the Next Big Thing?

"Now nanotechnology had made nearly anything possible, ..." This quote from an almost ten-year old science fiction novel is indicative of the hype now surrounding nanotechnology. It is being featured in local newspapers as the cure for cancer, in alumni magazines as producing Superman soldiers, in the AARP Bulletin as leading to lifetimes averaging 120 years, and in a large number of investment newsletters being touted as a great investment opportunity. On the other hand, there is an increasing flood of scientific and engineering papers and patents in this field of science, engineering, and technology collectively known as nanotechnology that portend realization of modest progress toward fulfilling the hype. The long-term promise lies in exciting research discoveries and innovations based on new nanoscale processes, phenomena, materials, devices, and systems. Dr. Teague will share his perspectives on the historical development of the field, give an assessment of its current state, argue why he thinks it is the next big thing, and present examples of research, business, and professional opportunities posed by the revolutionary advances in the fundamental understanding and control of matter at the nanometer to atomic level.*

** The Diamond Age, Neal Stephenson, p.37*

Commercial Session

Tuesday, October 26, 1:45 - 3:30 p.m.

Session Co-Chairs: Michele H. Miller (Michigan Technological University) and David D. Gill (Sandia National Laboratories)

The Commercial Session will take place early in the week on Tuesday afternoon. This is a special session where companies and participants are free to open discussions on a less-formal basis and to promote interaction on a variety of topics. In the first part of this session, company representatives are invited to make brief presentations (five minutes) on new products associated with precision engineering. This provides participants with the opportunity to receive timely information on new technologies that have been commercialized into products and services, as well as information on advances that can be expected in the near future.

2004 ASPE Lifetime Achievement Award

John H. Bruning

The 2004 ASPE Lifetime Achievement Award is presented to Dr. John H. Bruning in recognition of his many contributions to the art and science of precision engineering. John Bruning has been involved in advancing the state-of the-art of photolithography and has contributed significantly to many of the key events in the history of this key technology.

John Bruning received a bachelor's degree from Penn State University and a master's and doctorate from the University of Illinois, all in electrical engineering. His doctoral work, completed in 1969 dealt with multiple scattering of electromagnetic and acoustic waves by spheres. Upon graduation, John started at Bell Laboratories in Murray Hill as a member of the technical staff in the optical group. Early work involved the development of high accuracy interferometry for testing precision optical surfaces and lenses. Out of this work came a fundamentally new approach to interferometry known as phase measuring interferometry (PMI), which is the basis of most modern digital interferometers. This development has enabled 10-100 times greater accuracy in manufactured lens components for optical lithography and other precision optics applications.

From 1973-1979 he supervised several groups involved in developing mask inspection systems for photolithography and the exploration of new packaging techniques for integrated circuits and reliability testing methods for these new packaging systems. From 1979 to 1984, he directed several activities within the New Lithographic Systems Group including the mechanical design of EBES-IV, an advanced e-beam mask pattern generator. He initiated and managed the Bell Labs Deep-UV Photolithography Program working with Tropel as optics supplier and authored the fundamental patent for line-narrowed excimer laser photolithography. During this period, he was also involved in optical thin-film filter design, design of uniformers and diffusers, alignment systems and optical design.

In 1984, Bruning left Bell Laboratories to become vice president and general manager of Tropel, a division of GCA Corporation. In 1986, he assumed the additional responsibilities as executive vice president and chief technical officer of GCA. In 1994, Bruning led a management buyout of Tropel. Tropel was acquired by Corning Inc. in March 2001. John is currently the President and CEO of Corning Tropel where he remains involved in developing technical strategy.

John has published extensively and holds 12 patents. He is a recipient of the Distinguished Alumnus Awards from both his alma maters. He is a Fellow of the IEEE and the OSA and in 1993 received the OSA Richardson Medal. In 1996 he received the SEMI Award for developments in Deep-UV photolithography and was elected to the National Academy of Engineering in 1998. John has served as President of the American Society for Precision Engineering and was responsible for starting the Business Forum at the Annual Meeting. He has served as an editor for the Precision Pointers section of the Precision Engineering journal and is also a recipient of the Society's Distinguished Service Award. John continues to be a strong supporter of the Society and is currently a Sustaining Member.

2004 ASPE Lifetime Achievement Award

Ted Arneson

Ted is best known as the founder of Professional Instruments Company and as a pioneer in the development of air bearing spindles. Besides his support of ASPE, Ted has also found time for leadership roles in many volunteer activities, concentrating in the areas of mental health, workplace safety, and watching out for the interests of small manufacturers.

Both sides of Ted's family contained inventive, intuitive individuals with gifts for music, mathematics, and mechanics. His boyhood home was a place where knowledge was valued, points were argued, and books and tools were ever-present. At age 12, his innate mechanical skills led him to open a bicycle shop in his parents' basement. Later he was heavily involved in the family business of building vision-training instruments invented by his father.

Ted worked for General Mills in 1942 and 1943; this major precision-manufacturing plant produced analog-computer torpedo directors, three-dimensional cams, precision gears, and 8" gun sights. He was mentored by several brilliant engineering and manufacturing people, and was given wide exposure to ultra-precision manufacturing processes at a very high level.

After the war, Ted and his brother Harold started a small shop, adopting the "Professional Instruments Company" name. When the Korean War put the economy on a war footing, Ted and Harold decided to subcontract for the defense industries. They bought used machinery, fixed it up, and started to make rather difficult precision parts. They were good enough at it to attract the attention of some executives at Honeywell, who admired them for their pluck and their ability to get really excellent work out of miscellaneous machinery.

Ted and Harold worked 70 hours a week and came up with one fantastic development after another for projects varying from bag-making machines, to magnetic printing of checks, to spherical electrostatic gyroscopes, to 17-inch spherical air bearings for Apollo program space simulators. The P. I. crew was built from scratch, using a training program devised by Ted, featuring on-the-job mentoring, class work, and after-hours self-education. Ted created the culture of hands-on precision and attention to detail that enabled the success of air bearing work at P.I. by creating world-class experts in the fields of metallurgy, dimensional stability, bolted interfaces, metrology and quality control. Ted's vision, guidance, and support enabled advances in navigational devices, ultra-precision grinding, microlithography, diamond-turned optics, computer memory disks, spindle metrology, and measurement of the gravitational constant.

Technical and Poster Sessions Index

The technical program of the 2004 ASPE Annual Meeting contains 186 papers on precision engineering advances. Papers that lent themselves to significant verbal interaction, concise but important discoveries, or strongly visual or tactile subjects have been selected for the poster presentation. Authors will be in attendance to discuss their work on Tuesday, October 26, and Wednesday, October 27, from 3:30 to 5:15 p.m.

Session I
Metrology

Tuesday, October 26, 2004, 8:15 AM - 10:00 AM

Session Chair: Vivek G. Badami (Corning Tropel Corporation), and Eric R. Marsh (The Pennsylvania State University)

1. ***Optical Engineering for Biomedical Optics (Invited Paper)*****
   Zavislan, J. (University of Rochester) . . . . . *page 15*
2. ***Realizing and Disseminating the SI Micronewton with the Next Generation NIST Electrostatic Force Balance***
   Pratt, J. R.; Newell, D.; Kramar, J. A.; Seugling, R. M. (National Institute of Standards and Technology). . . . . *page 16*
3. ***High-resolution Retinal Microscopy Using MEMS-based Adaptive Optics***
   Zhou, Y.; Bifano, T. G. (Boston University) . . . . . *page 20*
4. ***Fiber Deflection Probe for Small Hole Measurements***
   Muralikrishnan, B. (University of North Carolina at Charlotte); Stone, J. A.; Stoup, J. R. (National Institute of Standards and Technology); and Vemuri, S. C.; Sahay, C.; Potluri, A. (University of Hartford). . . . . *page 24*
5. ***Design, Manufacture and Performance Evaluation of a Rapid Probing Machine***
   Bauza, M.; Smith, S. T.; Hocken, R. J. (University of North Carolina at Charlotte) and Woody, S. C.; Jain, P. (InstituTec Inc.) . . . . . *page 28*

Session II
Machine Tools

Tuesday, October 26, 2004, 10:30 AM - 12:15 PM

Session Chair: Kenneth P. Garrard (North Carolina State University), and Byron R. Knapp (Olympic Precision, Inc.)

1. ***Agile Assembly Architecture: A Platform Technology for Microassembly (Invited Paper)***
   Hollis, R. L.; Rizzi, A. A. (Carnegie Mellon Unversity) . . . . . *page 32*
2. ***Active Vibration Isolation of an Unbalanced Machine Tool Spindle***
   Hopkins, D. J.; Geraghty, P. (Lawrence Livermore National Laboratory) . . . . . *page 36*
3. ***The Effects of Asymmetrical Radial Stiffness in Precision Rotating Machines: The Duality of Fixed and Rotating Sensitive Directions***
   Dalrymple, T. M. (University of Florida) . . . . . *page 40*

** *Extended abstract unavailable at press time*

4. **A 10 kHz Short-stroke Rotary Fast Tool Servo**
Montesanti, R. C. (Lawrence Livermore National Laboratory); and Trumper, D. L. (Massachusetts Institute of Technology). . . . page 44

5. **Two-axis Force-feedback Deflection Compensation of Miniature Ball End Mills**
Freitag, K.; Dow, T. A. (North Carolina State University). . . . page 48

Session III

Nano Positioning

Wednesday, October 27, 2004, 8:15 AM - 10:00 AM

Session Chair: Hisayuki Aoyama (University of Electro-Communications), and Georg Aigeldinger (Sandia National Laboratories)

1. **Manufacturing Technologies for Polymer Microsystem (Invited Paper)**
Saile, V. (Karlsruhe University) . . . page 52

2. **Design of a Passive Micro-mechanism Chuck to Minimize the Effect of Backside Particles on Semiconductor Wafer Planarity**
Nimmakayala, P. K.; Sreenivasan, S. V. (The University of Texas at Austin). . . . page 56

3. **Design of a Next Generation 6 DoF Stage for Scanning Application in Vacuum with Nanometer Accuracy and mGauss Magnetic Stray Field**
de Klerk, A. C. P.; Angelis, G. Z. ; van Eijk, J. (Philips, CFT) . . . page 60

4. **A Planar Nano-positioning Table System for Advanced Machine Tools**
Yoshioka, H.; Komatsu, K.; Hashizume, H.; Shinno, H.; Shinshi, T.; Sato, K. (Tokyo Institute of Technology) . . . page 64

5. **Design of a Scanning Stage System with Nanometer Resolution for a X-ray Nanoprobe Instrument**
Shu, D.; Maser, J.; Lai, B.; Vogt, S.; Han, Y.; Tieman, B.; Winarski, R.; Roehrig, C.; Smolyanitskiy, A.; Stephenson, G. B. (Argonne National Laboratory) . . . page 68

Session IV

Precision Machining I

Wednesday, October 27, 2004, 10:30 AM - 12:15 PM

Session Chair: Hiroshi Hashimoto (Kanagawa Institute of Technology), and Tony L. Schmitz (University of Florida)

1. **Ultra-Precision Float Polishing of Optical Materials (Invited Paper)**
Namba, Y. (Chubu University) . . . page 72

2. **Tunable Ultrasonic Vibration-assisted Diamond Turning of Steel**
Overcash, J. L.; Cuttino, J. F. (University of North Carolina at Charlotte) . . . page 76

3. **Micro-machining Using Elliptical Vibration Assisted Machining**
Brocato, B. C.; Dow, T. A.; Sohn, A. (North Carolina State University) . . . page 80

4. **Force Analysis for Segmental Grinding**
Fan, X.; Miller, M. H. (Michigan Technological University) . . . page 84

5. **Ball-end Milling of Free-form Surfaces for Optical Mold Inserts**
Brinksmeier, E.; Autschbach, L. (Bremen University) . . . page 88

Session V

Interferometry

Wednesday, October 27, 2004, 1:45 PM - 3:30 PM

Session Chair: Daniel E. Thompson (Olympic Precision, Inc.), and John C. Ziegert (University of Florida)

1. **Block Regression Phase Digitizing with application to Nonlinearity Measurement and Correction (Invited Paper)****
Chu, D. (Agilent Technologies) . . . page 92

2. **Recent Developments in Homodyne Interferometry**
Lee, W. (Renishaw plc) . . . page 93

** Extended abstract unavailable at press time

3. **Challenges in Interferometric Measurements of MEMS and Semiconductor Devices**
Schmit, J.; Novak, E. L. (Veeco Instruments, Inc.) . . . . . page 97

4. **The Effect of Phase Change on Reflection on Optical Measurements**
Medicus, K. M.; Fricke, L. R.; Brodziak, J. E.; Carnevale, S.; Chaney, M. A.; Wolff, R.; Davies, A. D. (University of North Carolina at Charlotte) . . . . . page 101

Session VI

Novel Systems

Thursday, October 28, 2004, 8:15 AM - 10:00 AM

Session Chair: Alex Sohn (North Carolina State University), and Keith Carlisle (Lawrence Livermore National Laboratory)

1. **A Comparison of Force and Acoustic Emission Sensors in Monitoring Precision Cylindrical Grinding**
Couey, J. A.; Marsh, E. R. (The Pennsylvania State University); Knapp, B. R. (Olympic Precision, Inc.); and Vallance, R. R. (The George Washington University) . . . . . page 105

2. **Indoor GPS Metrology System with 3D Probe for Precision Applications**
Kang, S.; Tesar, D. (University of Texas at Austin) . . . . . page 109

3. **Active Compliant Fixtures for Nanomanufacturing**
Varadarajan, K. M.; Culpepper, M. L. (Massachusetts Institute of Technology) . . . . . page 113

4. **Manufacture of a 150x150 Reflective Spatial Light Modulator Integrated Directly onto CMOS Electronics**
Kim, J.-H.; Bifano, T. G. (Boston University) . . . . . page 117

5. **Fabrication of Atom Trap Chip for Quantum Information Processing**
Nagato, K.; Ohsige, K.; Ooi, T.; Tsuchiya, K.; Hamaguchi, T.; Nakao, M. (The University of Tokyo) . . . . . page 121

Session VII

Precision Machining II

Thursday, October 28, 2004, 10:30 AM - 12:15 PM

Session Chair: Thomas A. Dow (North Carolina State University), and Bradley N. Damazo (National Institute of Standards and Technology)

1. **IR Telescope (Invited Paper)***
Eikenberry, S. (University of Florida)

2. **Shape Control in Ultra-precision Finishing for the Femoral Head of the Artificial Hip Joint by Means of Abrasive Waterjet**
Sawano, H.; Warisawa, S.; Mitsuishi, M. (The University of Tokyo); and Kuramoto, K. (Nakashima Propeller Co., Ltd.) . . . . . page 125

3. **Grinding Simulation with Diamond Pellets and Optimization of its Grinding Conditions**
Uneda, M.; Suwabe, H.; Ishikawa, K. (Kanazawa Institute of Technology) . . . . . page 129

4. **Viscoelastic Stress Analysis of Precision Aspherical Glass Lens Forming Process Using Finite Element Method**
Jain, A.; Yi, A. Y. (Ohio State University) . . . . . page 133

5. **In-Situ Infrared (IR) Detection of the High Pressure Phase Transformation of Silicon During Scratching Test**
Dong, L.; Miller, J. A. (University of North Carolina at Charlotte); and Patten, J. A. (Western Michigan University) . . . . page 137

Session VIII

Micro/Nano Devices

Thursday, October 28, 2004, 1:45 PM - 3:30 PM

Session Chair: Martin L. Culpepper (Massachusetts Institute of Technology), and Stephen J. Ludwick (Aerotech, Inc.)

1. **The Nanostructured Origami™ 3D Fabrication and Assembly Process (Invited Paper)**
Barbastathis, G.; In, H. J.; Arora, W.; Buchner, T.; Smith, H. I. (Massachusetts Institute of Technology) . . . . . page 141

* *Abstract unavailable at press time*

2. ***Optical Fibre Coupled Miniature Interferometers Designed for Application in Micro and Nano Devices***
Jäger, G.; Manske, E.; Hausotte, T.; Füßl, R.; Grünwald, R.; Büchner, H.-J. (Technical University of Ilmenau); and Schott, W. (SIOS Meßtechnik GmbH) . . . . . *page 145*

3. ***Study of Nano-Stereolithography Using Evanescent Light***
Kajihara, Y.; Inazuki, Y.; Takahashi, S.; Takamasu, K. (The University of Tokyo) . . . . . *page 149*

4. ***An Experiment Towards Establishing the Tolerance of Micro-scale Interference Fits***
Jones, J. F.; Aigeldinger, G. (Sandia National Laboratories) . . . . . *page 153*

5. ***Micro-Turbo Charger for A Palmtop Gas Turbine Generator***
Tanaka, S.; Esashi, M. (Tohoku University); Isomura, K. (Ishikawajima-Harima Heavy Industries); and Togo, S.; Hikichi, K.; Goto, S. (Tohoku Gakuin University) . . . . . *page 157*

Poster Session I

Tuesday, October 26, 2004, 3:30 PM - 5:15 PM

Session Chair: Bradley H. Jared (3M Precision Optics)

BIOMEDICAL

Biomedical

1. ***Phase Plate Correction of Ocular Aberrations***
Raasch, T. W.; Yi, A. Y. (Ohio State University); and Roblee, J. W. (Precitech, Inc.) . . . . . *page 161*

EQUIPMENT, MACHINES & INSTRUMENTS

Analysis & Modeling

1. ***Analysis of an Electron Beam Heating of a Silicon Wafer***
Kato, S.; Nakamura, H. (Nippon Institute of Technology); Ono, M. (Tokyo Metropolitan College of Technology); and Saito, N. (Hitachi High-Technologies Corp.) . . . . . *page 165*

2. ***Stiffness Analysis and Kinematic Modeling of Stewart Platform for Machining Applications***
Kumar, S. G.; Bikshapathi, M.; Nagarajan, T; Srinivasa, Y. G. (Indian Institute of Technology - Madras) . . . . . *page 169*

3. ***Compensation for Distortion of Dynamic Sensor Data Using Receptance Coupling***
Schmitz, T. L. (University of Florida) . . . . . *page 173*

4. ***A Precision Active Aerostatic Spindle with an Axial Positioning Actuator***
Shinshi, T.; Hayashi, T.; Inami, Y.; Hashizume, H.; Sato, K.; Shimokohbe, A. (Tokyo Institute of Technology) . . . . . *page 177*

5. ***Design of an Efficient Active Cooled Meso-scale Heat Exchanger Using Functionally Gradient Materials***
Subramanian, R.; Kwon, P.Y. (Michigan State University) . . . . . *page 181*

Controls

1. ***Configuration and Control Aspects of High-Precision Planar Multi-Coordinate Drive Systems***
Kallenbach, E. K.; Kireev, V.; Volkert, R.; Zentner, J.; Bertram, T. (Technical University of Ilmenau) . . . . . *page 185*

2. ***Identification of Friction Elements Through Limit Cycle Analysis***
Kim, M.-S.; Kim, M.-Z.; Chung, S.-C. (Hanyang University) . . . . . *page 189*

3. ***Verification of Precision-limit Positioning of a Direct Drive System with the Existence of Friction***
Liu, B.-Y.; Hsieh, C. (National Cheng Kung University) . . . . . *page 193*

4. ***The Development of the NC Method of Eliminating Machining Point Errors Caused by Machining Centers - First Report (Theory) -***
Nakayabu, T. (Industrial Research Institute of Ishikawa); Hirao, M. (Kanazawa University); Inamura, T. (Nagoya Institute of Technology); Yasui, T. (Industrial Exchange Institute of Kanazawa); Imai, H.; Okaji, M. (National Institute of Advanced Science and Technology); and Kawara, H. (Tsudakoma Corporation) . . . . . *page 197*

5. ***Error Compensation via Command Signal Deconvolution***
Panusittikorn, W.; Garrard, K. P.; Dow, T. A. (North Carolina State University) . . . . . *page 201*

Design & Testing

1. ***Low Cost Flexure Alignment Features***
Abu Ibrahim, F.; Awtar, S.; Sutin, J.; Slocum, A. H. (Massachusetts Institute of Technology) . . . . . *page 205*

2. ***Thin Optic Constraint***
Akilian, M.; Forest, C. R.; Slocum, A. H.; Trumper, D. L.; Schattenburg, M. L. (Massachusetts Institute of Technology) . . . . . *page 209*

3. ***Live Axis Turning***
Buescher, N. P.; Dow, T. A.; Sohn, A. (North Carolina State University); and Norlund, B. K.; Roblee, J. W. (Precitech, Inc.) . . . . page 213

4. ***Assessment of Thin Film UHMWPE Bearings for Precision Slideways***
Buice, E. S.; Yang, H.; Smith, S. T.; Hocken, R. J. (University of North Carolina at Charlotte); and Seugling, R. M. (National Institute of Standards and Technology) . . . . page 217

5. ***High Frequency, Low Force Dynamometer for Micro-Milling Force Measurement***
Burton, D.; Duncan, G. S.; Ziegert, J. C.; Schmitz, T. L. (University of Florida) . . . . page 221

6. ***Development of a Precise Positioning Stage Traveling on Micro-pitch Racks***
Iwata, T.; Honda, S. (Tokyo Metropolitan Institute of Technology) . . . . page 225

7. ***Precision Product Design — From University Labs to Company Catalog***
Kane, N. R. (MicroChips, Inc.); Sihler, J. (Schlumberger-Doll Research); Roblee, J. W.; Walter, M. M.; Blair, R.; Koning, R. J. (Precitech, Inc.); and Slocum, A. H. (Massachusetts Institute of Technology) . . . . page 229

8. ***Development of a Miniature Adjusting Device Sculpted into a Parallel Linkage***
Masuya, Y.; Honda, S. (Tokyo Metropolitan Institute of Technology) . . . . page 233

9. ***A Study on Optimization of Miniature Machine Tool Design***
Mishima, N. (National Institute of Advanced Industrial Science & Technology) . . . . page 237

10. ***Performance of Water Energy Drive Spindle Supported by Water Hydrostatic Bearing***
Nakao, Y.; Kobayashi, F.; Sagesaka, Y. (Kanagawa University) . . . . page 241

11. ***Design Principles for Highest Precision Applications***
Theska, R.; Frank, T.; Hackel, T.; Höhne, G.; Lotz, M. (Technical University of Ilmenau) . . . . page 245

12. ***Development of Force and Moment Control Mechanism for Rotating Parts Using Electromagnetic Force (Application of CMP Head)***
Uda, Y.; Soma, T.; Fujiwara, T.; Sugaya, I. (Nikon Corporation); and Novak, W. T.; Watson, D. C.; Yuan, B.; Hsin, Y. (Nikon Research Corporation of America) . . . . page 249

Mechatronics

1. ***Improvement of Visual Based Motion Error Compensation for Precise Versatile Micro Robot***
Fuchiwaki, O.; Aoyama, H. (University of Electro-Communications); and Misaki, D. (Shizuoka Institute of Technology) . . . . page 253

2. ***Development of Inchworm Type Mobile Robot Movable in Pipes with T-junction***
Kato, S.; Kato, M.; Ogawa, S. (Nippon Institute of Technology); and Ono, M. (Tokyo Metropolitan College of Technology) . . . . page 257

3. ***Fabrication of an Inch-Worm Type Mobile Microrobot Movable in Different Diameter Pipes***
Kato, S.; Aizawa, Y.; Osada, T. (Nippon Institute of Technology); and Ono, M. (Tokyo Metropolitan College of Technology) . . . . page 261

4. ***A Hybrid Stereo Algorithm with 3D Disparity Space for Reconstruction of Surface Morphology with Depth Discontinuity***
Kim, G.-B. (Chungju National University) . . . . page 265

5. ***Electromagnetically Driven UltraFast Tool Servo***
Lu, X.; Trumper, D. L. (Massachusetts Institute of Technology) . . . . page 269

6. ***3D Micro Image Recognition for in Bio-Cell Operation by Micro Robots***
Misaki, D.; Chiba, N.; Usuda, T.; Fuchiwaki, O.; Aoyama, H. (University of Electro-Communications) . . . . page 273

7. ***Desktop Ultra-high-speed Milling Machine with 300krpm Spindle and Linear Motor Stages***
Okazaki, Y. (National Institute of Advanced Industrial Science & Technology) . . . . page 277

8. ***A Microrobot Movable in Flexible Pipes Like the Large Intestine***
Ono, M. (Tokyo Metropolitan College of Technology); and Sasazaki, T.; Otsuki, M.; Kato, N.; Kato, S. (Nippon Institute of Technology) . . . . page 281

9. ***Fabrication of an Artificial Earthworm Type In-pipe Mobile Robot Movable in Primary Cooling-water Pipe of an Atomic Power Plant***
Ono, M. (Tokyo Metropolitan College of Technology); and Naito, T.; Kato, S. (Nippon Institute of Technology) . . . . page 285

10. ***Wear Measurement of Valve Assemblies by Using the Machine Vision***
Park, C.-W.; Chung, S.-C. (Hanyang University) and Chun, K.-J. (Korea Institute of Industrial Technology (KITECH)) . . . . page 289

MEMS, LIGA & Nanotechnology

1. **Compliant Mechanisms for Micro-scale Spatial Manipulators: Applications in Nanomanipulation**
   Chen, S.-C.; Culpepper, M. L. (Massachusetts Institute of Technology) . . . . . page 293
2. **Small-scale Micro/Nano-Manipulators in Precision Alignment and Positioning**
   Golda, D.; Culpepper, M. L. (Massachusetts Institute of Technology) . . . . . page 297
3. **Development of a Micro Screw Thread and a Micro Gear Coiled Extra Fine Wires**
   Honda, S. (Tokyo Metropolitan Institute of Technology) . . . . . page 301
4. **Nano Structure Patterning Using a Scanning Nanopipette Probe Microscope**
   Iwata, F.; Sumiya, Y.; Nagami, S.; Sasaki, A. (Shizuoka University) . . . . . page 305
5. **Micro Tube Manufacturing Method of Tube-shaped Dilatation Micromanipulator Made of Shape Memory Polymer**
   Kamiya, D.; Gamo, Y.; Horie, M. (Tokyo Institute of Technology) . . . . . page 309
6. **Control Method for Pushpull Type Piezo-driven Linear Motion Stage With Smooth Motion, Long Travel Range and High Resolution**
   Lim, K.-S.; Lee, S.-K. (Kwang-Ju Institute of Science & Technology (K-JIST)); Abiko, D.; Aketagawa, M. (Nagaoka University of Technology); Takada, K. (Nagaoka National College of Technology); Munakata, Y.; Lee, J.; Terao, K.; Muraki, T.; Magara, K.; Ono, M. (Chuo Precision Industrial Co., Ltd.) . . . . . page 313
7. **Control of Wettability with Surface Texturing and Its Application**
   Moronuki, N.; Ryu, K.; Kaneko, A. (Tokyo Metropolitan University) . . . . . page 317
8. **Shape of Microtweezers Fabricated for Gripping Micro Objects**
   Nakazato, Y.; Ooide, T.; Miyazawa, H.; Ariga, Y.; Takeuchi, S.; Murakawa, M. (Nippon Institute of Technology) . . . . . page 321
9. **Self-alignment of Microparts Using Liquid Surface Tension – Extension of Function by Vibration Force: Self-alignment of a Group of Microparts and Self-standing**
   Sato, K.; Hoshino, S.; Kobayashi, S. (Tokyo Institute of Technology) . . . . . page 325

Novel Systems

1. **A Six Degree-of-Freedom Tri-layer Chevron Beam Thermal Actuator**
   Chen, S.-C.; Culpepper, M. L. (Massachusetts Institute of Technology) . . . . . page 329
2. **Design and Manufacture of Monolithic, 3D Compliant Mechanisms for Nanomanipulation Equipment**
   Culpepper, M. L.; Chen, S.-C.; Korb, S. (Massachusetts Institute of Technology) . . . . . page 333
3. **Precision Engineering Education at MIT Via Hands-on Design Projects: The MIT Nano-etch-a-sketch Course Project**
   Culpepper, M. L.; Chen, S.-C.; Kartik M. V. (Massachusetts Institute of Technology) . . . . . page 337
4. **Making Wooden Reconstruction Models from the Codex Written by Leonardo da Vinci**
   Kamiya, K.; Kamiya, N.; Nomura, T. (Toyama Prefectural University); and Tashiro, H. (Toyama University) . . . . . page 341
5. **Stability and Accuracy of Thin, Precision Flexure Amplification Mechanisms**
   Landsiedel, N.; Culpepper, M. L. (Massachusetts Institute of Technology) . . . . . page 345
6. **Structured Surfaces Damping Enhancements at Mechanical Interfaces**
   Larsen, E. R.; Davies, M. A.; Smith, K. S.; Nuttall, M. M. (University of North Carolina at Charlotte) . . . . . page 349
7. **Real-time Collaborative Design and Dimension Verification Over the Internet**
   Song, I.-H.; Yeon, K.-H.; Chung, S.-C. (Hanyang University) . . . . . page 352
8. **Implementation of Kinematic Web Handling**
   Sprunt, A. D.; Slocum, A. H. (Massachusetts Institute of Technology) . . . . . page 356
9. **Precision Connector Assembly using Elastic Averaging**
   Willoughby, P. J.; Slocum, A. H. (Massachusetts Institute of Technology) . . . . . page 359
10. **Fluid Film Bearings Requiring No Precision Machining Processes, Formed by Wrapping of 2D Sheets**
    Winter, A. G.; Culpepper, M. L. (Massachusetts Institute of Technology) . . . . . page 362

METROLOGY

Analysis & Modeling

1. **In-Situ Metrology of Swelling Effects on Critical Dimensions in LIGA PMMA Molds**
   Aigeldinger, G.; Ceremuga, J. T.; Krenz, K. D. (Sandia National Laboratories) . . . . . page 366
2. **Non-Stationary Systematic Error Detection with Experimental Verification on an Optical Profiler**
   Gao, Y.; Tse, S. F.; Lo, C. (Hong Kong University of Science & Technology) . . . . . page 370

3. **A Study of CMM Measurement Variation in Precise, Thin-wall Iron Castings**
Gopal, K.; Morse, E. P.; Cuttino, J. F. (University of North Carolina at Charlotte) . . . . . page 374

4. **Surface Roughness Evaluation of a LIGA Micro Component**
Krenz, K. D.; Aigeldinger, G.; Ceremuga, J. T. (Sandia National Laboratories) . . . . . page 378

5. **Measuring Two-axis Stage Mirror Non-flatness Using Linear/Angular Interferometers**
Montoya, J.; Heilmann, R. K.; Schattenburg, M. L. (Massachusetts Institute of Technology) . . . . . page 382

Form & Geometry

1. **Dimensional Analysis of Cross Sectioned High Aspect Ratio Microstructures**
Ceremuga, J. T.; Aigeldinger, G.; Krenz, K. D. (Sandia National Laboratories) . . . . . page 386

2. **Wear Measurement of Engine Valve and Seat Insert Using a Confocal Laser Microscope**
Chun, K. J.; Hong, J. S. (Korea Institute of Industrial Technology (KITECH)) . . . . . page 390

3. **A Multi-purpose Linear Measuring System with Laser Interferometer**
Eom, T. B.; Han, J. W. (Korea Research Institute of Standards and Science) . . . . . page 394

4. **Alternative Artifacts for Evaluating Scanning CMM Performance**
Farooqui, S. A.; Morse, E. P. (University of North Carolina at Charlotte) . . . . . page 398

5. **Three-dimensional Measurement of the Surface Geometries of Grinding Wheel by Using a Laser Displacement Sensor**
Lee, H.-S.; Kawaguchi, K.; Yamada, T. (Nihon University) . . . . . page 402

6. **Six Sigma Comparison of Precision Typological Equipment for the Production of Gas Bearings**
Moore, R. (The Charles Stark Draper Laboratory, Inc.) . . . . . page 406

7. **A Practical Method of Determining Orthogonal Sampling Distances for Flatness Deviation Measurement Using an Electric Capacitance Displacement Sensor**
Saito, T.; Yanagi, K. (Nagaoka University of Technology) . . . . . page 410

Instrumentation, Design & Testing

1. **Long Scan Stage for the Metrological Atomic Force Microscope**
Eom, T. B.; Lee, J. Y.; Kim, J.-A. (Korea Research Institute of Standards and Science) . . . . . page 414

2. **Optimum Clearances for Shearing Work of Sheet Metals**
Okada, Y.; Yoshida, S.; Mitsui, K. (Keio University) . . . . . page 418

3. **Development of Ultra Precise Gear Measuring Instrument. Second Report: Evaluation on the Measuring Accuracy**
Ogasawara, H.; Maeda, N.; Ogasawara, M.; Hayashi, T. (Ogasawara Precision Laboratory Ltd.) . . . . . page 422

4. **Development of Micro-CMM Probe Detecting Contact Angle**
Ogura, I.; Okazaki, Y. (National Institute of Advanced Industrial Science and Technology) . . . . . page 426

5. **Traceable Force Metrology for Micronewton Level Calibration**
Seugling, R. M.; Pratt, J. R. (National Institute of Standards and Technology) . . . . . page 430

6. **A Coarse/fine Motion Control Stage: Preliminary Studies**
Yang, H.; Buice, E. S.; Fagan, T. J.; Smith, S. T.; Hocken, R. J. (University of North Carolina at Charlotte); Otten, D.; Trumper, D. L. (Massachusetts Institute of Technology); and Seugling, R. M. (National Institute of Standards and Technolology) . . . . . page 434

7. **Precision Differential Capacitor**
Van Niekerk, J. B.; Ambekar, P. P.; Nichol, J. G.; Lauben, D. (Stanford University) . . . . . page 438

8. **Programmable Ring Gage**
Warsi, F. M.; Huntsinger, C.; Hocken, R. J. (University of North Carolina at Charlotte) . . . . . page 442

Machine Tool Metrology

1. **The Analysis and Compensation of Position Error in Scanning Type XY Stage from Motion Error Measurement**
Hwang, J.; Park, C.-H.; Lee, C.-H. (Korea Institute of Machinery and Materials); and Kim, S.-W. (Korea Advanced Institute of Science and Technology) . . . . . page 446

2. **Kite Square**
Miller, J. A.; Morse, E. P.; Nettles, J. A.; Turner, J. S. (University of North Carolina at Charlotte) . . . . . page 450

3. **Effects of Targeting Spherical Surfaces with Capacitive Displacement Sensors**
Vallance, R. R. (The George Washington University); Marsh, E. R. (The Pennsylvania State University); and Smith, P. T. (University of Kentucky) . . . . . page 454

Measurement Uncertainty

1. ***Performance Testing of Multisensor CMMs Based on Single Artifact Measurement***
   Bhamidi, K. P.; Morse, E. P. (University of North Carolina at Charlotte) . . . . . *page 458*
2. ***Metrology Artifact Design***
   Folkert, K. F.; Dow, T. A.; Garrard, K. P. (North Carolina State University) . . . . . *page 462*
3. ***Web Based Gage Management System for Quality Assurance***
   Mohamed Ali, A. M.; Raja, J. (University of North Carolina at Charlotte) . . . . . *page 466*
4. ***Highly Stable Measurements of Springs on an OCMM***
   Ren, D.; Lawton, K. M. (University of North Carolina at Charlotte); and Patterson, S. R. (Lawrence Livermore National Laboratory) . . . . . *page 470*

Surface & Subsurface

1. ***Virtual Surface Calibration and Computational Uncertainty***
   Bui, S. H.; Renegar, T. B.; Vorburger, T. V. (National Institute of Standards and Technology) . . . . . *page 474*
2. ***Determination of Aperture Correction Factor of Interference Microscope by Double-Tilt Imaging Method***
   Chen, Y.-L.; Chen, C.-J.; Wang, C.-Y. (Center for Measurement Standards/Industrial Technology Research Institute) . . . . . *page 478*
3. ***Wavelet Analysis of Different Silicon Wafer Surfaces***
   Orji, N. G.; Raja, J. (University of North Carolina at Charlotte) . . . . . *page 482*
4. ***Standard Deviation or Standard Deviation of the Mean - How to Report the Statistical Variation in Surface Calibrations?***
   Song, J. F.; Vorburger, T. V. (National Institute of Standards & Technology) . . . . . *page 486*
5. ***Shape Measurement by the Grating Projection Technique in a Microscope***
   Tashiro, H.; Kurioka, K. (Toyama University); and Nomura, T.; Kamiya, K. (Toyama Prefectural University) . . . . . *page 490*

Poster Session II

Wednesday, October 27, 2004, 3:30 PM - 5:00 PM

Session Chair: Pradeep K. Subrahmanyan (Electro Scientific Industries, Inc.)

OPTICS

Optical Fabrication

1. ***Fabrication of X-ray Microscope Mirrors***
   Chon, K. S.; Namba, Y. (Chubu University) . . . . . *page 494*
2. ***Improve Figure and Finish of Diamond Turned Surfaces with Magneto-Rheological Finishing (MRF)***
   Dumas, P. R.; Golini, D.; Tricard, M. (QED Technologies) . . . . . *page 498*
3. ***Predicting Surface Figure in Diamond Turned Calcium Fluoride Using In-Process Force Measurement***
   Marsh, E. R.; John, B. P.; Couey, J. A. (The Pennsylvania State University); and Vallance, R. R. (The George Washington University) . . . . . *page 502*
4. ***Optical Waveguide Fabricating on Lithium Niobate with UV Laser***
   Nakanishi, A.; Warisawa, S.; Mitsuishi, M. (The University of Tokyo) . . . . . *page 506*
5. ***Fabrication and Microstructure Analysis of Pt/C Multilayers for Hard X-Ray Optics***
   Nonomura, Y.; Ohnishi, N.; Namba, Y. (Chubu University); Yamashita, K. (Nagoya University) . . . . . *page 510*

Optics / Interferometry

1. ***Point Diffraction Interferometer Using an Optical Saturable Absorber***
   Furuhashi, H.; Shibata, A.; Uchida, Y. (Aichi Institute of Technology); Matsuda, K. (National Institute of Advanced Industrial Science and Technology); and Grover, C. P. (National Research Council Canada) . . . . . *page 514*
2. ***Imaging by a Phase Grating Used in Displacement Measurement***
   Ohmura, Y.; Oka, T.; Nakashima, T. (Mitsubishi Electric Corporation); and Hane, K. (Tohoku University) . . . . . *page 518*
3. ***Nonlinearity in Fiber-optic Coupled Heterodyne Interferometer***
   Zhang, L. (University of Florida) . . . . . *page 522*

Optoelectronics

1. ***High-precision Angle Measuring Technology and High-precision Angle Sensor***
   Kojima, T.; Kikuchi, Y.; Seki, S. (Tamagawa-Seiki Co., Ltd.); and Wakiwaka, H. (Shinshu University) . . . . . *page 526*

PROCESSES

Grinding

1. ***Laser Dressing of Metal-Bonded Diamond Wheel***
   Hosokawa, A.; Yunoki, T.; Yamada, K.; Ueda, T. (Kanazawa University) . . . . . *page 530*
2. ***Research on Feed Velocity Control Model of Axisymmetric Aspheric Machining***
   Huang, H.; Guo, Y.; Zhang, Y.; Zheng, L. (Xiamen University) . . . . . *page 534*
3. ***Sizing Method Based on Grinding Ratio in Heavy Grinding***
   Izumi, M.; Ochi, A. (Hiroshima Institute of Technology) . . . . . *page 538*
4. ***Study on the Round-off Truing Method Using Circular Motion - Truing of a Superabrasive Wheel with a Homogeneous Truing Wheel***
   Kitajima, T.; Okuyama, S.; Yamashita, K.; Yui, A. (The National Defense Academy) . . . . . *page 542*
5. ***Ultra-precision Grinding Wheels Based on the Structure of Natural Whetstones***
   Saito, N. (Japan Society for the Promotion of Machine Industry); Takemura, T. (National Institute of Advanced Industrial Science and Technology); and Ikeno, J. (Saitama University) . . . . . *page 546*
6. ***New Diamond Grinding Wheels with Electrically Conductive Cutting Edges***
   Suzuki, K.; Sharma, A. (Nippon Institute of Technology); Iwai, M.; Uematsu, T. (Toyama Prefectural University); and Tanaka, K. (Toshiba Machine Co., Ltd.) . . . . . *page 550*
7. ***Study on Elastic Deformations of Grinding Wheels due to Centrifugal Forces***
   Yamada, T.; Lee, H.-S. (Nihon University) . . . . . *page 554*
8. ***Ultra Precision Grinding of Micro Aspherical Surface -- Development of a Three-axes Controlled Single Point Inclined Grinding Method***
   Yamamoto, Y.; Suzuki, H.; Okino, T.; Hijikata, Y.; Moriwaki, T. (Kobe University); and Fukuta, M.; Nishioka, M.; Kojima, Y. (Toshiba Machine Co., Ltd.) . . . . . *page 558*
9. ***Quantitative Investigation of Relation Between CBN Wheel Life and Loading Using Automatic Image Processing System for Wheel Surface***
   Yasui, H.; Kamiya, T.; Maruo, K. (Kumamoto University) . . . . . *page 562*
10. ***Influence of Fluid Supply on Ultra-smoothness Grinding of Silicon Nitride Ceramic with #140 Metal Bond Diamond Wheel***
    Yasui, H.; Sawa, T.; Yamamoto, Y. (Kumamoto University) . . . . . *page 566*
11. ***Investigation of Wheel Loading Based on Adhesion Theories and Temperature***
    Zhang, P.; Miller, M. H. (Michigan Technological University) . . . . . *page 570*

Machining

1. ***Cutting Force Prediction Using a Molecular Dynamic Assisted Finite Element Simulation Model***
   Aly, M. F.; Ng, E.; Veldhuis, S. C. (McMaster University) . . . . . *page 574*
2. ***Fabrication and Metrology of Micro-scale Sinusoidal Surfaces in Polymer Workpiece Materials***
   Bono, M. J.; Hibbard, R. L. (Lawrence Livermore National Labs) . . . . . *page 578*
3. ***Design and Manufacture of Aspheric Lenses for Novel High Efficient Photovoltaic Concentrator Modules***
   Brinksmeier, E.; Gessenharter, A. (Bremen University); Pérez, D.; Blen, J.; Benítez, P. (Universidad Politécnica de Madrid); and Díaz, V.; Alonso, J. (ISOFOTON S.A.) . . . . . *page 582*
4. ***A Framework of a Model-based Simulation System for Predicting Surface Generation in Ultra-precision Raster Milling of Freeform Surfaces***
   Cheung, C.-F.; Lee, W.-B.; To, S. (Hong Kong Polytechnic University) . . . . . *page 586*
5. ***Machining Characteristics with Nanometer-cutting Machine Equipped Parallel Mechanism***
   Furutani, K.; Suzuki, M. (Toyota Technological Institute) . . . . . *page 590*
6. ***Mechanical Machining of Thin Polycrystalline Diamond Films***
   Gatzen, H. H.; Kourouklis, C. (Hanover University) . . . . . *page 594*
7. ***High-efficient Wire Sawing of GaAs-Wafers by Utilization of Crack Nucleation Mechanisms***
   Hammer, R.; Jurisch, M.; Kleinwechter, A.; Bergner, F. (Freiberger Compound Materials GmbH); and Schaper, M. (Technische Universität Dresden) . . . . . *page 598*

8. **Fabrication of Microcylinder Parts: A Study on Micromanufacturing**
Jin, M.; Hiraga, Y.; Murakawa, M. (Nippon Institute of Technology) . . . . . page 602

9. **Near Dry Machining Utilizing Lubricant Applying Effect - Required Minimal Quantity of Oil Mist -**
Kaneeda, T.; Okada, Y. (Okayama University of Science); Yokomizo, S. (Industrial Technology Center of Okayama Prefecture); Shimada, S. (Osaka Electro-Communication University); and Higuchi, M. (Kansai University) . . . . . page 605

10. **High Precision and High Efficiency Machining of Polybenzimidazole Using the Fine Crystalline Diamond Coated Tool with the Sharp Edge**
Kato, H.; Shintani, K.; Miyahara, K. (Kanazawa Institute of Technology); and Hanyu, H. (OSG Corporation) . . . . . page 609

11. **Development of Surface Texturing System by Mechanical Machining**
Kobayashi, Y.; Shirai, K.; Masaaki, S. (Nihon University); and Tozawa, K. (Nissan Motor Co., Ltd.) . . . . . page 613

12. **Simultaneous Optimization of Removal Rate and Part Accuracy in High-Speed Milling**
Kurdi, M. H.; Schmitz, T. L.; Haftka, R. T.; Mann, B. P. (University of Florida) . . . . . page 617

13. **Ultraprecision Cutting of Molybdenum by Ultrasonic Elliptical Vibration Cutting**
Moriwaki, T.; Suzuki, H.; Mizugaki, J.; Maeyasu, Y. (Kobe University); Higashi, Y. (KEK); and Shamoto, E. (Nagoya University) . . . . . page 621

14. **Fluctuations in Chip Flow Velocity with Time**
Nomura, M. (Kobe University) . . . . . page 625

15. **Experimental Observations of Tool Wear in Multilayer Coated Inserts**
Olortegui-Yume, J. A.; Kwon, P. Y. (Michigan State University) . . . . . page 629

16. **Assessing the Sharpness of Hand Plane Cutter Blades****
Rhorer, R. L. (Gaitherburg, MD) . . . . . page 633

17. **Development of Precision Coated-Cemented-Carbide Tools for Ultra-Precision Cutting of Titanium and Titanium Alloys**
Sakamoto, S.; Yasui, H.; Shinozaki, A.; Shingai, T.; Furuno, T. (Kumamoto University) . . . . . page 634

18. **Work Affected Layer of Machined Surface in Ultra-Precision Cutting of Austenitic Stainless Steel**
Sakamoto, S.; Yasui, H.; Hanaoka, S.; Hayashi, H. (Kumamoto University) . . . . . page 638

19. **High Pressure Phase Transformation and Ductility in Diamond Turned Single Crystal Silicon**
Randall, T.; Walter, J. J. H.; Scattergood, R. O.; Nemanich, R. J. (North Carolina State University) . . . . . page 642

20. **An Improved RCSA Model for Tool Point Frequency Response Prediction**
Schmitz, T. L.; Duncan, G. S.; Tummond, M. F. (University of Florida) . . . . . page 646

21. **Mechanism of Cutting Edge Chipping and its Suppression in Diamond Turning of Copper**
Shimada, S.; Tanaka, H. (Osaka Electro-Communication University); Higuchi, M.; Yamaguchi, T. (Kansai University); Kaneeda, T. (Okayama University of Science); and Yokomizo, S. (Industrial Technology Center of Okayama) . . . . . page 650

22. **Analysis and Improvement of Machining Stability in Noncircular Turning**
Wu, D.; Wang, X.; Chen, K.; Yi, W. (Tsinghua University) . . . . . page 654

Manufacturing

1. **Bonding Quartz Glass at Room Temperature**
Hamaguchi, T.; Yamamoto, N.; Ooi, T.; Tsuchiya, K.; Nakao, M. (The University of Tokyo) . . . . . page 658

2. **Effects of Diffusion Brazing Parameters on Dimensional Variation of Nickel Aluminide Microchannels**
Kanlayasiri, K. (King Mongkut's Institute of Technology) . . . . . page 662

3. **Development of Automated Machining of Precision Inertial Instrument Components**
Kondoleon, A. S.; Faiz, R.; Walker, R. (The Charles Stark Draper Laboratory, Inc.) . . . . . page 666

4. **Pushing The Precision Level of Mechanical Alignment System Into The Nano Meter Region**
Lee, N. K. S.; Li, Z. Q. (Hong Kong University of Science and Technology) . . . . . page 670

5. **Effect of Securing Processes on Precision Assembly**
Lee, N. K. S.; Li, Z. Q. (Hong Kong University of Science and Technology) . . . . . page 674

6. **Multilayered Metal Micro-reactor Integrated for Chemical Synthesis Processes**
Tsuchiya, K.; Yamazaki, J.; Ooi, T.; Hamaguchi, T.; Nakao, M. (The University of Tokyo) . . . . . page 678

Non-conventional

1. **Influence of the Electrical Conductivity of Dielectric Fluid on WEDM Machinability**
Kim, C.H. (Dong-Eui University) . . . . . page 682

** *Extended abstract unavailable at press time*

2. ***Manufacture of a Spatial Light Modulator Integrated Directly on CMOS: Development of a Planarized CMOS-MEMS Interface***
Kim, J. H.; Bifano, T. G. (Boston University) ..... *page 686*

3. ***A Study on the Material Removal Mechanism in EDM -- Single Discharge Experiments with Low Melting Temperature Alloy --***
Kokubo, H.; Horio, K.; Yamazaki, T. (Saitama University); Takezawa, H. (Kogakuin University); and Mohri, N. (The University of Tokyo) ..... *page 690*

4. ***Monitoring of Ultrasonic Vibration Micromachining Process***
Moronuki, N.; Saneshima, S.; Saito, Y. (Tokyo Metropolitan University) ..... *page 694*

5. ***Design and Fabrication of Three Dimensional MEMS Actuators Using Diamond Turning and Electroplating Processes***
Reimann, G.; Bifano, T. G. (Boston University) ..... *page 698*

6. ***Performance of Electrically Conductive CVD Diamond as an Electrode for EDM***
Sharma, A.; Suzuki, K. (Nippon Institute of Technology); Iwai, M.; Uematsu, T. (Toyama Prefectural University); and Sano, S. (Sodick Co., Ltd.) ..... *page 701*

7. ***Laser Planarization Process Assisted by Chemical Mechanical Polishing for Copper Surface***
Takaya, Y.; Miyoshi, T.; Miyamoto, T. (Osaka University); Kimura, K. (Kyushu Institute of Technology); and Suzuki, K. (Rodel Nitta Company) ..... *page 705*

8. ***Characterizing Form, Waviness and Roughness of Micro EDM Electrodes***
Vallance, R. R. (The George Washington University); Morgan, C. J.; Shreve, S. M. (University of Kentucky); and Marsh, E. R. (The Pennsylvania State University) ..... *page 709*

9. ***Investigating Different Methods of Bonding Glass Substrates***
Werkmeister, J. B.; Slocum, A. H. (Massachusetts Institute of Technology) ..... *page 713*

10. ***Fabrication of High Aspect Ratio Metal Shadow Mask for OTFTs***
Yi, S. M.; Jin, S. H.; Lee, H. S.; Lee, J. D.; Chu, C. N. (Seoul National University) ..... *page 717*

11. ***A New Internal Magnetic Assisted Machining Process for Non-ferromagnetic Thick Tubing Using Magnetic Machining Jig***
Zou, Y.; Shinmura, T. (Utsunomiya University) ..... *page 721*

Polishing, Lapping & ECM

1. ***The Method of Finishing the Inside of a Minute Hole***
Mitsuhashi, M.; Horio, K.; Yamazaki, T. (Saitama University) ..... *page 725*

2. ***Flexible Super Finishing Process for Intricate Shapes***
Narayanasamy, K.; Srinivasa, Y. G.; Krishnamurthy, R. (Indian Institute of Technology - Madras); and Raju, H. P. (P.E.S. College of Engineering) ..... *page 729*

3. ***Atomic Structure of Float Polished Surfaces of Calcium Fluoride Single Crystals for Ultra Violet Applications***
Ohnishi, N.; Namba, Y.; Yoshida, S.; Yoshida, T.; Kanda, Y. (Chubu University); Yoshida, K. (Osaka Institute of Technology) ..... *page 733*

4. ***Polisher Life in High Speed Ultra-Smoothness Polishing of NiP Plated Aluminum Magnetic Disk Substrate***
Yasui, H.; Kuribayashi, S.; Matsukawa, S.; Yamasaki, Y.; Yamaguchi, K. (Kumamoto University) ..... *page 737*

Technical Papers

Optical Engineering for Biomedical Optics

James M. Zavislan
The Institute of Optics, University of Rochester, Rochester, NY

The optical engineering of biomedical instruments must consider the optical and mechanical properties of tissues. I will review optical design and analysis practices when tissues or biological materials are part of the optical system. I will present a case study of a clinical reflectance confocal microscopy. I will describe the validation of the instrument and give example images from in-vivo tissue and unprepared ex-vivo tissue.

Realizing and disseminating the SI micronewton with the next generation NIST electrostatic force balance

Jon R. Pratt, David B. Newell, John A. Kramar, and Richard M. Seugling
National Institute of Standards and Technology, Gaithersburg, MD 20899

Introduction

The NIST Electrostatic Force Balance (EFB) compares deadweight and mechanical probe forces to an SI realization of force derived from measurements of the capacitance gradient and voltage in an electronic null balance. In the following abstract, we briefly review recent upgrades to this device and present initial results of inter-comparisons between deadweight and electrical forces at levels of 20 μN and 200 μN in a 10^{-4} Pa vacuum environment. The SI calibration of a secondary microforce standard at NIST is revisited; a topic that was described for the first time in the proceedings of the ASPE Winter Topical meeting of January of 2003[1]. Here, we update the status of that work, focusing on the use of this standard in a calibration experiment recently completed in the Physics Department at Worcester Polytechnic Institute (WPI) [2]. This represents our first experience with disseminating SI force at the micronewton level to a user outside of NIST. Certain commercial equipment, instruments, or materials are identified in this article in order to specify the experimental procedure adequately. Such identification is not intended to imply recommendation or endorsement by the National Institute of Standards and Technology, nor is it intended to imply that the materials or equipment identified are necessarily the best available for the purpose.

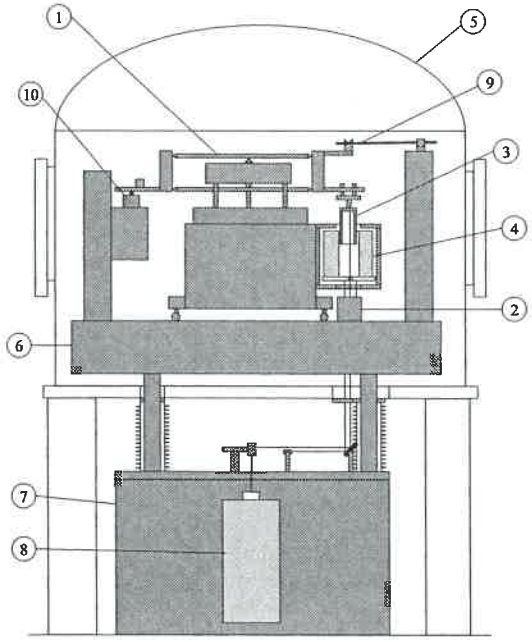

Figure 1. Schematic of balance components:
1) Parallelogram balance 2) Differential plane mirror interferometer 3) Main inner electrode (cross-section) 4) Main outer electrode (cross-section) 5) Vacuum chamber 6) Optical table 7) Granite foundation block 8) Heterodyne laser light source 9) Mass lift 10) Counterweight electrodes

Updates to the EFB

The EFB has four major components that have been updated from the original system [e.g., 3-5]. Briefly, these major components are the suspension, the electrostatic force generator, the displacement measuring interferometer, and the vacuum enclosure, as shown schematically in Figure 1.

The rectilinear spring of the original balance suspension has been replaced by a counterbalanced parallelogram linkage that employs a series of cross-flexure pivots as described in [6]. This new mechanism addresses two perceived shortcomings of the original balance. First, it produces a well-constrained motion axis, easily aligned to gravity that is far less susceptible to off-axis forces. Second, it achieves an on-axis stiffness that can be varied to as small as 0.01 N/m through the use of a novel tensioning spring. With on-axis stiffness less than 1 N/m, sub-nanonewton force resolution is possible given realistic null position resolution on the order of nanometers.

A new interferometer [7] replaces the original column-referenced arrangement, removing a potential source of Abbe′ measurement error in the determination of the capacitance gradient. This displacement metrology helps ensure determination of the gradient at a relative uncertainty below parts in 10^5. In order to accommodate the beam pattern of this new interferometer, however, the electrodes that comprise the electrostatic force generator required modification. The nominal diameter of the cylindrical capacitor has been increased from approximately 15 mm to 20 mm, with the overall geometry redesigned to preserve the nominal 1 pF/mm vertical gradient. The inner electrode now also includes a tip/tilt mount between it and the suspension. Previously, a correction was required to account for a cosine error between the interferometer axis and gravity. Now, the interferometer, suspension, force generator, and gravitational axes can all be adjusted into precise alignment with no need for correction.

Finally, the entire experiment has been reassembled on a custom optical table in a specially designed free standing vacuum chamber. The chamber consists of a collar approximately 1 m in diameter and 0.5 m in depth with

a bell jar approximately 0.5 m in height. The optical table on which the EFB is mounted sits on three legs that protrude from the chamber floor through flexible bellows that terminate in blank flanges. These table legs are supported from below the chamber by a large granite block that forms a raised foundation in the space between the chamber legs, as indicated schematically in Figure 1. Thus, the only contact between the vacuum chamber and the experiment is through the relatively compliant bellows. The move to vacuum removes convective air currents that tend to perturb the now large and compliant balance suspension. Also, operation in vacuum eliminates the need to correct for variations in the index of refraction and the permittivity of free space, both of which are a function of the ambient pressure, temperature, and humidity when making measurements in air.

Operating principles

The EFB generates electrical forces in response to loads along the balance axis that may be calculated from

$$F = \frac{1}{2}\frac{dC}{dz}\left(U_1^2 - U_2^2\right) \qquad (1)$$

where, F is the force in nN, dC/dz is the capacitance gradient in pF/mm, and U_1 is the voltage applied to the outer electrode in V before loading and U_2 is the voltage applied to the outer electrode in V after loading. The balance has two modes of operation, namely a gradient calibration mode and a weighing or force comparison mode.

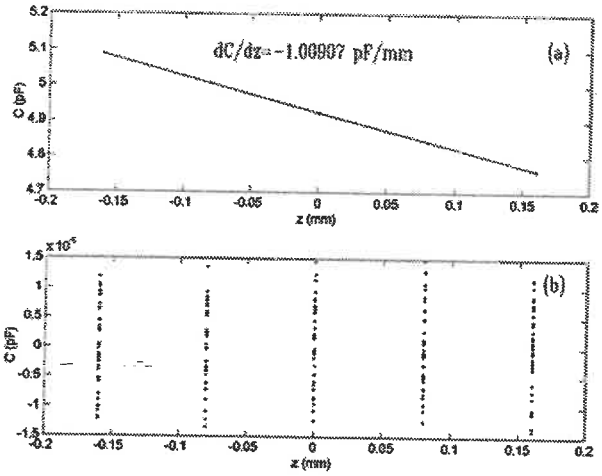

Figure 2. Capacitance gradient data: (a) C(z) and (b) residuals after removal of linear curve fit

Gradient calibration is accomplished by moving the balance suspension through a small range of motion (typically < ± 0.2 mm) about the null position. A second electrode pair on the counterweight side of the balance is used to drive the balance arm, moving the main inner electrode with respect to the fixed main outer electrode. The capacitance and displacement between the fixed and moving electrodes are recorded, so that the general function $C(z)$ is mapped at discrete locations along the balance motion axis. The function $C(z)$ is plotted, and then fit with a straight line from which the gradient, or local slope is determined.

Weighings and force comparisons are accomplished by controlling the voltage on the main electrodes to maintain the null position of the balance. A mechanical imbalance is first introduced on the counterweight side, tipping the balance from its rest position and causing the balance feedback control to apply a bias voltage to restore null. Loads can then be measured on the weighing side of the balance, provided they do not exceed the initial bias. Typically, loads are applied and removed and a force calculated from the change in controlled voltage necessary to maintain null.

Table 1. Gradient and weighing results (one standard deviation uncertainties in parantheses)

Date	T(°C)	dC/dz (pF/mm)	# in set	F_{ef} (μN)*	# in set	F_{mf} (μN)	$\left(\frac{F_{ef}}{F_{mf}}-1\right)\times 10^{-4}$
6/25/04		1.009089(13)	5				
6/25/04				$20.0088(8)^{+}$	300	20.0222(15)	-6.7
6/27/04	22.84(3)	1.009084(15)	180				
6/27/04	22.80(4)			$20.0205(7)^{ac}$	380	-	-0.85
6/28/04	22.74(2)			$20.0096(7)^{+}$	100	-	-6.2
6/28/04	22.73(2)	1.009069(14)	18				
6/28/04	22.3(1)			$20.0205(7)^{ac}$	290	-	-0.83
6/29/04	22.18(4)	1.009072(19)	130				
7/2/04	21.68(2)			$196.063(3)^{-}$	12	196.0125(8)	2.6
7/2/04	21.70(2)			$195.947(4)^{+}$	12	-	-3.3

*Superscripts indicate dc voltage polarity or that amplitude modulated ac voltage was used

Gradient data and force comparison experiments

A typical measurement of the capacitance in vacuum as a function of displacement from null is shown in Figure 2, along with a plot of the residuals as a function of displacement after removal of a straight-line fit to the data. The data consist of eighteen complete scans of the inner electrode from z = 0.16 mm to z = +0.16 mm and back again using four equal increments of displacement. The counterweight electrodes drive the balance arm, using the interferometer for position feedback control, performing a move and hold that fixes the relative displacement at each point to within a few nanometers. A precision capacitance bridge then measures the capacitance between the main inner and outer electrode (on the weighing side) while the counterweight electrodes hold the balance still. The averaging time required by the capacitance bridge in order to achieve six significant figures is approximately 40 seconds and sets the speed at which data is collected. Typically, a single scan was completed within 8 minutes. Each of the eighteen scans was fit with a straight line in a least squares fashion from which a slope was determined. The average value of the slopes was 1.009069 pF/mm, with a standard deviation of 1.4 x 10^{-5} pF/mm. The temperature throughout this experiment was 22.73 °C and deviated by less than 0.02 °C over the entire run.

Deadweight artifacts of nominally 20 μN and 200 μN were fashioned from stainless steel wire for the weighings. Values for the deadweight masses were determined using the average of ten mass readings taken by placing the deadweight on and off a precision mass microbalance ten times. The deadweight load was computed from the product of this mass and a value for gravity of 9.80103 m/s^2 that was derived from knowledge of the laboratory elevation with respect to a local gravity reference point elsewhere on campus. Load values were 20.0222 μN ± 0.0015 μN and 196.0125 μN ± 0.0008 μN respectively, where the stated uncertainty is merely one standard deviation of the ten determinations. These measurements remain to be confirmed by the NIST mass group, though the absolute accuracy is expected to be within 5 parts in 10^4 for the small mass and 5 parts in 10^5 for the larger, based on the microbalance specifications. Separate weighing series for each artifact were performed at vacuum using the EFB. Each artifact was lifted on and off the EFB using an automated lift. The force required to maintain the null position of the balance was computed based on equation one. Results from a variety of weighing series are listed in Table 1. Voltage polarity was swapped in some experiments, and an amplitude-modulated, 1 kHz control voltage was used in others, as identified by the superscripts on the electrical force values reported in Table 1.

Discussion of weighing discrepancies

Electrical forces resulting from the application of positive polarity dc control voltages were consistently less than mechanically determined values; whereas negative polarity voltage resulted in an electrical force value that was greater than expected. Interestingly, the amplitude modulated ac data obtained during 20 μN weighings produced agreement within experimental uncertainty. An explanation of these observations is that the inner and outer electrodes themselves generate a potential due to variations in the work functions at the respective electrode surfaces, for instance due to differences in the polycrystalline structure of the two conductors, or differences in the adsorbed elements and compounds on the two surfaces [8]. In this case, the electrostatic force between the electrodes must be characterized as

$$F = \frac{1}{2}\frac{dC}{dz}\left(U_1^2 - U_2^2 + 2V_s\left(U_1 - U_2\right)\right) \qquad (2)$$

where V_s is the potential difference between the electrodes resulting from the hypothesized surface field effects.

The influence of such a potential can be easily detected by reversing the polarity of the applied voltage, as evidenced by the 200 μN data of Table 1: where for a positive polarity, the electrostatic force was 195.947 μN while for a negative polarity it was 196.063 μN. Clearly, taking $U_1 \approx 800$ V and $U_2 \approx 500$ V in equation (2), a bias voltage on the order of 0.19 V is present, though its origin cannot conclusively be linked to the hypothesized surface potential effects. Adopting a technique traditionally used to identify surface potentials and patch fields [8], we have oscillated the main inner electrode as if it were a Kelvin probe. We observed a very small current $i = V_s\, dC/dt = V_s\, dC/dz\, dz/dt \approx 0.2$ pA as the counterweight electrodes were used to drive the balance through a 0.7 mm p-p sinusoidal oscillation of frequency ν= 0.4 Hz. Knowing dC/dz, and approximating dz/dt by $2\pi\nu$ (0.7) $\sin 2\pi\nu t$ mm/s, this far coarser measurement yielded $V_s \approx 0.12$ V—confirming the presence of a surface potential.

Secondary artifact calibration and dissemination

Two piezoresistive cantilever force sensors were calibrated using the new EFB with the vacuum chamber sealed, but not evacuated. The procedure was similar to that described in [9]; here, a vertical scan stage replaced the lifting fork of Figure 1 and was employed to press the cantilevers against a 1 mm diameter polished ruby sphere that was affixed to the EFB weighing pan. The cantilever force sensitivities were computed using slopes taken from straight-line, least squares approximations to a set of force versus resistance response curves (e.g., as in [1] and [9]). The

sensitivities were 197.7 nN/Ω ± 1 nN/Ω and 260.7 nN/Ω ± 2 nN/Ω, where the uncertainties are simply one standard deviation of the respective calibration sets.

These transfer standards were packaged and transported to WPI, where they were employed as reference artifacts in a series of experiments described in detail in [2]. Briefly, the work described in [2] compares three methods that are available for determining AFM cantilever stiffness: namely thermal, geometric, and loading. Of concern here was the loading method, where a transfer standard was placed on the sample stage of an AFM at WPI, and an uncalibrated cantilever was brought into contact with it. The resistance change of the force transfer standard was measured while the AFM scanner was being ramped with the photodiode voltage change being monitored. The WPI researchers were interested in calibrating the unknown cantilever stiffness, rather than its force sensitivity, as suggested in [9], so the photodiode voltage was converted into a deflection rather than directly into force, by probing the unknown against a stiff sample, immediately before or after contact with the transfer standard. The calibrated displacement of the scanner provided the transfer mechanism to convert the photodiode voltage signal into appropriate units of length. Having characterized both displacement and contact force, the unknown stiffness was computed. Agreement among the different stiffness calibration methods was impressive, with all techniques yielding values for the unknown cantilever stiffness well within 10% of each other [2].

Conclusions

The NIST EFB has been successfully updated and operated in vacuum. Previously unexplained discrepancies between gravitational force and electrostatic force, observed using an earlier version of the balance [3-5], persist with the new balance, but this time a source of the error has been identified along with a corrective experimental procedure. These breakthroughs were possible because of the enhanced stability and precision of the new balance. Convincing evidence that a bias potential exists between the EFB electrodes was drawn from two weighings differing only in voltage polarity, but producing a swing in force of 90 nN. Further investigation is required, but the hypothesized surface field effects seem a very likely source of this discrepancy. The mean value of the two electrical forces agrees well with the redundant cross check provided by the mechanical load, and it suggests that accurate electrical forces can be measured by simply employing a reversal technique to remove the bias.

Acknowledgements

We thank Dr. Nancy Burnham and her student Eric Thorsen for their participation in this work. Thanks also to various reviewers, colleagues, and visitors for suggesting the amplitude modulated, ac control voltage.

References

1. Jon R. Pratt, David Newell, John Kramar, Jonathan Mulholland, and Eric Whitenton, 2003, "Probe-force calibration experiments using the NIST electrostatic force balance," *Proceedings of the American Society for Precision Engineering 2003 Winter Topical Meeting*, University of Florida, pp. 64-69.
2. G.A. Matei, E.J. Thorsen, J.R. Pratt, D.B. Newell, and N.A. Burnham, "Thermal Method of Cantilever Calibration over a 200 kHz Bandwidth", submitted to *Nanotechnology*, August, 2004.
3. D. B. Newell, J. A. Kramar, J.R. Pratt, D. T. Smith, and E. R. Williams, 2003, "The NIST Microforce Realization and Measurement Project," *IEEE Transactions on Instrumentation and Measurement*, Special issue on CPEM 2002, **52**(2), 2003, pp. 508-511.
4. J. A. Kramar, D. B. Newell, J. R. Pratt, 2002, "NIST Electrostatic Force Balance Experiment," *Proceedings of the joint international conference IMEKO TC3/TC5/TC20*, VDI-Berichte 1685, pp. 71-76.
5. Newell, D.B., Pratt, J.R., Kramar, J.A., Smith, D.T., Feeney, L.A., and Williams, E.R., "SI Traceability of Force at the Nanonewton Level," *Proc. Natl. Conf. of Stds Labs. Intl. 2001 Workshop and Symp.*, Washington, D.C., 2001.
6. Jon R. Pratt, David B. Newell, and John A. Kramar, 2002, "A Flexure Balance with Adjustable Restoring Torque for Nanonewton Force Measurement," *Proceedings of the joint international conference IMEKO TC3/TC5/TC20*, VDI-Berichte 1685, pp. 77-82.
7. Differential Plane Mirror Interferometer, Zygo Model 7015, ZMI Optics guide, p. 2-11, Zygo Corp., Connecticut.
8. J.B. Camp, T.W. Darling, and R. E. Brown, 1991, "Macroscopic variations of surface potentials of conductors," *J. Appl. Phys.,*. **69**(10), pp. 7126-7129.
9. J. R. Pratt, D.T. Smith, D.B. Newell, J.A. Kramar, and E. Whitenton, 2004, "Progress towards Systeme International d'Unites traceable force metrology for nanomechanics", *Journal of Materials Research,***19**(1), pp. 366-379.

High-resolution retinal microscopy using MEMS-based adaptive optics

Yaopeng Zhou and Thomas Bifano (tgb@bu.edu)
College of Engineering, Boston University

The availability of precisely controllable micromachined deformable mirrors (μDMs) made using microelectromechanical (MEMS) systems technology has enabled rapid development of adaptive optics in several new applications. In this paper, the design and testing of a retinal imaging system is detailed, with an emphasis on the adaptive optical components and their performance. Retinal imaging is a major diagnostic modality for retinal disease, and can play a critical role for diagnosing systemic diseases such as diabetes and eye-specific diseases such as macular degeneration and diabetic retinopathy, the leading causes of blindness. It is demonstrated in this work that the μDM can enable diffraction-limited imaging of microscale features on and below the surface of the retina, through real-time compensation of aberrations introduced by the eye's cornea and lens.

The scanning laser ophthalmoscope, invented in 1980 by Rob Webb, allows high-contrast, high resolution imaging of the retina. Its confocal detector greatly improves contrast and allows sub-surface imaging, permitting detailed study of the vasculature that supplies capillary blood flow to the retina. A conventional scanning laser ophthalmoscope is limited to resolution of ~8-20 μm laterally and 250-300 μm axially. This resolution is about a factor of five worse than the theoretical resolution of the instrument imposed by its diffraction limited performance. The difference between 10μm resolution (typical SLO performance) and 2μm resolution (diffraction-limited SLO performance) is important because it distinguishes between an instrument that can resolve capillary blood flow and one that can not. Both major causes of blindness worldwide are directly related to physiological defects in capillary blood flow. An instrument that could achieve diffraction limited resolution (particularly on animal subjects) might enable significant progress in the study, diagnosis, and treatment of these diseases. Moreover, direct observation of capillary blood flow in the retina would provide a valuable tool for the study of systemic diseases related to vascular failure – especially diabetes.

To achieve diffraction-limited performance in an SLO, it is necessary to compensate for aberrations of the eye, which account for nearly all degradation in retinal image quality. It is a direct result of the eye's poor performance as an objective lens that the resolution of an SLO is inadequate for resolving micrometer-scale cellular details. Adaptive optics (AO) scanning confocal microscopy systems, by using a deformable mirror and real time control system to correct the aberrations of the eye, can improve resolution in retinal imaging. In the project reported in this paper, an adaptive optics scanning laser ophthalmoscope for imaging of mouse retinas is described.

Figure 1 is a block diagram of the optical system. The μDM is used as a wavefront correction element for AO system. The wavefront is measured using a Shark-Hartmann wavefront sensor. This sensor provides 244 discrete measurements of wavefront slope, distributed uniformly across the aperture (at each of 121 points in an 11 x 11 grid, slope

is measured in two orthogonal directions). The deformable mirror is located at an optical plane conjugate to the Shack-Hartmann lenslet array, and provides 140 degrees of freedom for adjusting wavefront shape (actuators are oriented in a 12 x 12 grid pattern, without the four corner elements). The relay optics are designed to locate the Shack Hartman lenslet centers interstitially with respect to the μDM actuator centers, although this alignment is not critical.

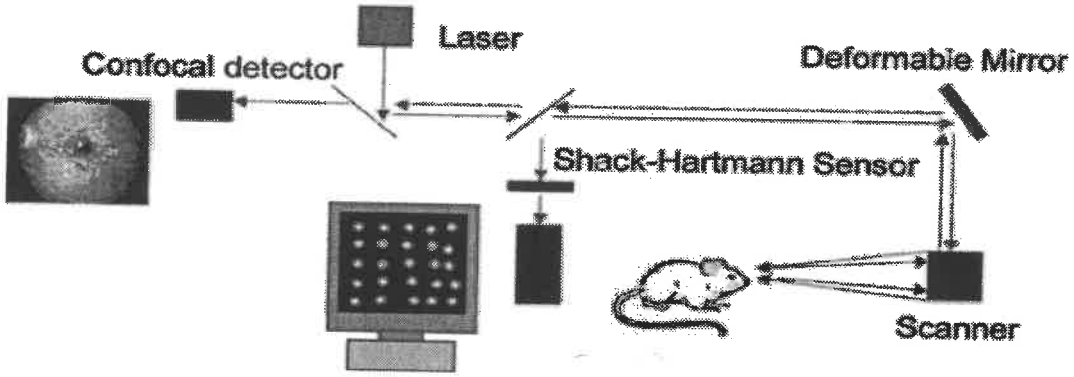

Figure 1: Adaptive optics scanning laser ophthalmoscope test bed schematic. A collimated laser beam is focused by the mouse eye to a spot on the retina. A scanning subsystem forces the spot to raster across a small area at or below the retinal surface. Light scattered from the spot passes back through the scanner (e.g. is de-scanned), and then reflects from the μDM, which is located at a plane conjugate to the mouse pupil. The wavefront is relayed to a Shack-Hartmann wavefront sensor that measures the effects of aberrations on the wavefront. Feedback from this sensor is used in closed loop control to adjust the shape of the μDM to compensate for aberrations of the eye. The corrected beam is relayed to a confocal detector consisting of a precisely aligned aperture and a fast photodetector. The output of the photodetector, when synchronized with the scanner, produces a diffraction-limited video image of the scanned area of the retina.

Because the Shack-Hartmann sensor measures 244 distributed slopes and the deformable mirror provides 140 distributed displacements, a multi-input multi-output control scheme is needed. We elected to implement a reconstructor based on modal control. Each actuator was perturbed independently, and the effect on the wavefront sensor was observed. Using this data and assuming system linearity, a reconstructor matrix was built to map any matrix of actuator deflections to a unique sensor matrix. This reconstructor was inverted using a singular value decomposition to provide a map from any sensor matrix to a best fit actuator deflection matrix. This constitutes a calibration step that is necessary only once, before beginning closed-loop control. Subsequently, control is achieved by multiplying measured sensor data by the inverted reconstructor matrix to estimate wavefront error, and then using this error signal in an integral control loop to adjust the μDM.

Frequently, optical wavefront data is represented by Zernike decomposition, in which the surface is represented by a series of ortho-normal polynomials defined on a unit circle. Coefficients of Zernike polynomials provide a widely recognized basis for evaluating

wavefront aberrations. The first three Zernike terms correspond to piston and tip and tilt of the wavefront: the only three terms that do not affect image resolution. The next three terms correspond to familiar optical aberrations (astigmatism and defocus). Higher order aberrations correspond to less familiar aberrations, including coma, trefoil, spherical aberration, and many more that are unnamed.

A model eye without aberrations was introduced into the optical system described in Figure 1, and the closed-loop controller was commanded to produce, sequentially, wavefront shapes corresponding to each of the first twenty one Zernike polynomials (exclusive of piston, tip, and tilt). The amplitude of the desired shape was fixed at 1.0μm. Figure 2 shows the result, which confirms the capability of the μDM to control wavefront shape.

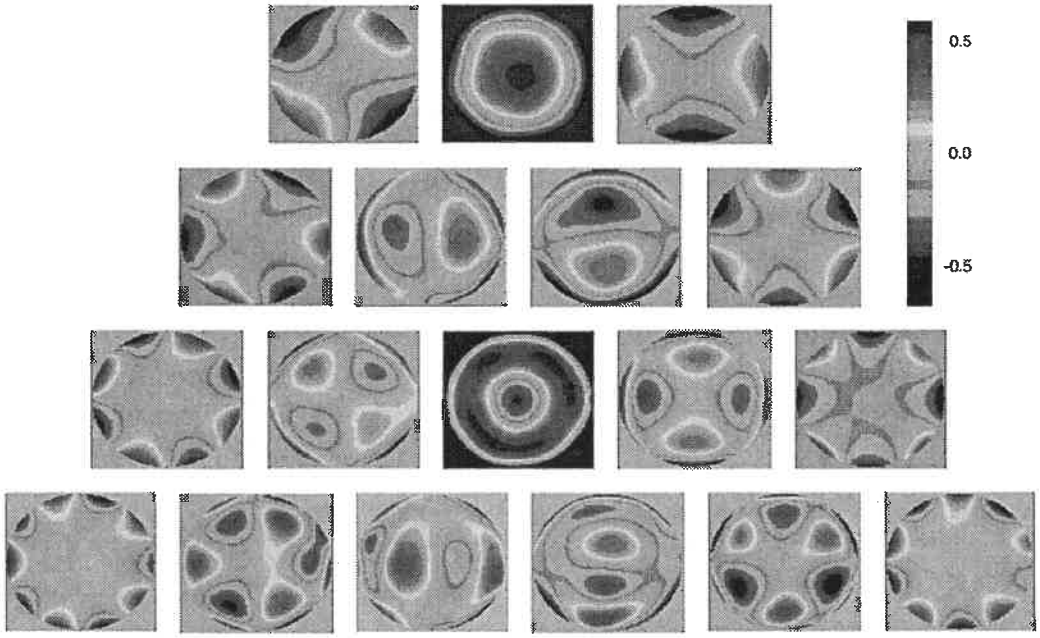

Figure 2: Measured wavefront for Zernike modes 4-21, as obtained by closed-loop control with the μDM in the adaptive optics scanning laser ophthalmoscope.

Subsequently a reticle grid was positioned at the retinal plane of the model eye, and the eye was adjusted to introduce aberration through defocus. The confocal scanned image was recorded before and after adaptive optical compensation using the closed-loop controller, along with the measured wavefront data. Results are shown in Figure 3.

Finally, a mouse was introduced into the apparatus. Biological imaging was significantly more challenging than model-eye imaging, due in part to anesthesia-related cataracts forming in the mouse, tear-film reflections, and excessive scattering from anterior retinal surfaces. Nevertheless, images were obtained and an example is shown in Figure 4, along with a wavefront map. These images were obtained without AO.

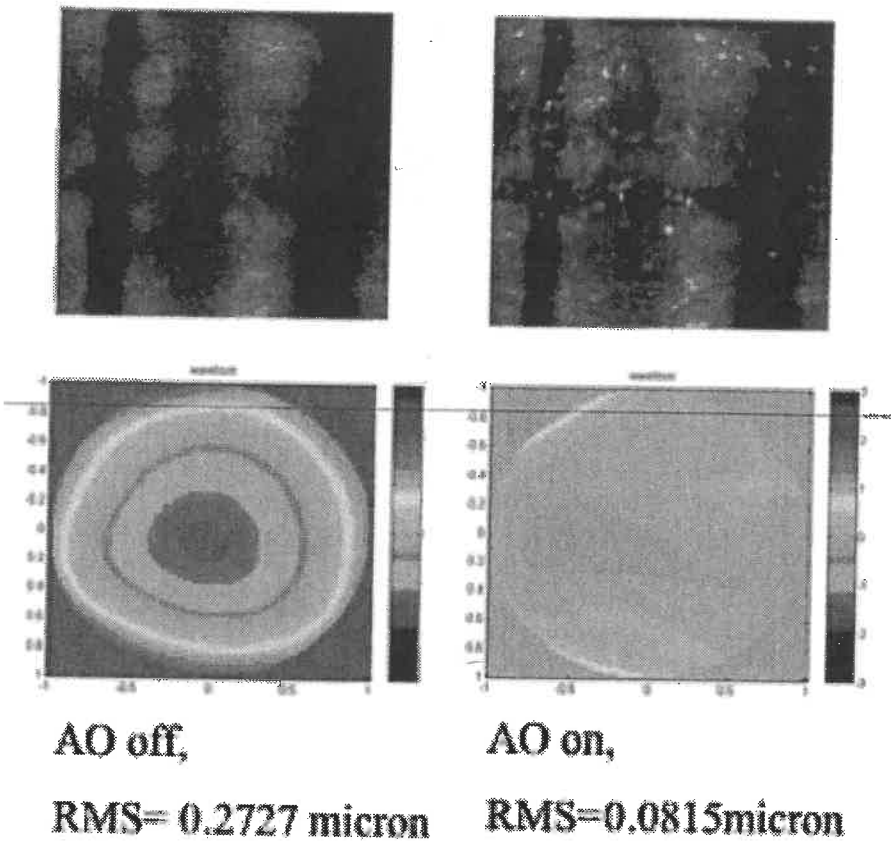

Figure 3: Control of aberrations in a "model" eye consisting of a reticle target and an aberrated imaging lens. With the AO system off, the image was blurred, and the sensor measured 0.2727nm (rms) of aberration. With the AO system on and controlling in a closed feedback loop, the aberration was reduced to 0.0815μm (rms) and the image quality improved significantly. Quantitative tests with an Air Force Resolution Reference Target confirmed diffraction-limited system resolution while under AO control.

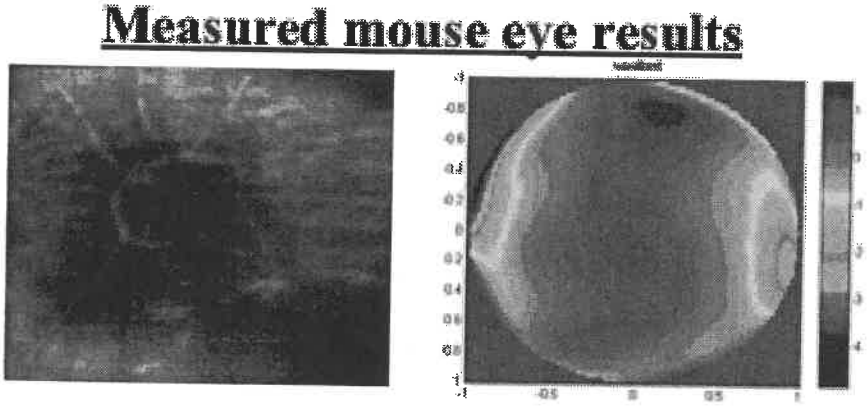

Figure 5: Mouse eye imaged using the AOLSO. At left is the image, including clearly discernable blood vessels measuring 10-20μm. At right is the mouse eye's measured wavefront error, indicating the presence of significant aberrations.

Fiber Deflection Probe for Small Hole Measurements

B. Muralikrishnan[1], J. A. Stone[2], S. C. Vemuri[3], C. Sahay[3], A. Potluri[3], J. R. Stoup[2]

[1]Department of Mechanical Engineering & Engineering Science, UNC Charlotte, Charlotte NC
[2]Precision Engineering Division, National Institute of Standards and Technology, Gaithersburg, MD
[3]Mechanical Engineering Department, University of Hartford, West Hartford, CT

1. Introduction

Measurement of diameter and form of small holes is of great importance in applications such as fuel injector nozzles, fiber optic ferrules, wire drawing dies, holes in printed circuit boards and medical apparatus such as syringes, etc. A variety of technologies that address the problem of small hole measurement are reported in the literature [1-4]. In this paper we describe a probing method, referred to as Fiber Deflection Probing (FDP), for use on Coordinate Measuring Machines (CMM). The technique is simple and yields expanded uncertainty on diameter of 0.11 μm (k = 2). The principle of this technique, characterization and measurement results are presented here.

2. Measurement principle

A thin glass fiber (20 mm long, 50 μm in diameter), fixed at one end and with a ball (85 μm diameter) mounted on the other serves as the probe. A small segment of this fiber is illuminated by a light emitting diode 5 mm below the ball as shown in Fig. 1. The shadow of the fiber is magnified and imaged using a camera. When the probe contacts a surface, it is deflected by a small amount. The magnitude of this deflection is determined by recording the position of the shadow in free state and in deflected state. The deflection of the fiber in pixels can be related to the deflection of the probe tip in micrometers using a calibration procedure that is described later. The deflection of the probe tip is then added to the machine scale reading to obtain coordinates on the surface.

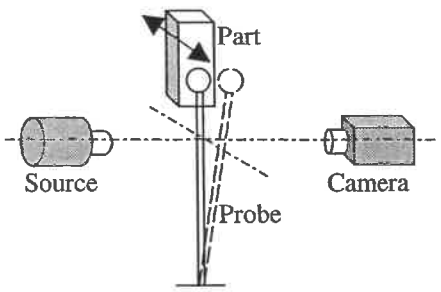

Fig. 1 Measurement principle

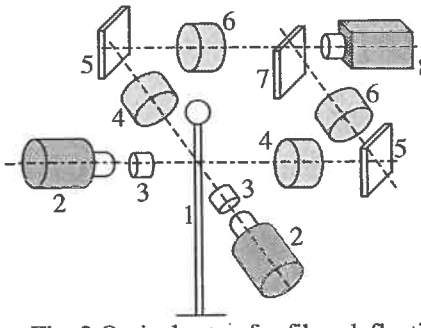

Fig. 2 Optical setup for fiber deflection measurement

In order to obtain deflections in both X and Y, two orthogonal sources are used. The shadows of the stem are magnified using 7X objectives placed 12 mm from the fiber. The resulting images are further magnified using 5X eyepieces and imaged using a CCD camera. Overall magnification is about 35. The optical setup is illustrated in Fig. 2. The mirror in front of the camera (7) extends half way across the pixel array, so that light from one axis illuminates half of the array and light from the second axis falls on the other half of the array.

The shadows of the fiber stem, as projected onto the camera, appear as a dark region with a bright band down the center. As shown in Fig 3(a), two bright bands are seen, one for each direction X and Y. An automatically determined threshold is applied to this image to convert it to a binary image. This is followed by a software routine for particle removal to suppress the influence of any dirt particles. The resulting image is shown in Fig. 3(b). Subsequently, the leading and trailing edge coordinates for both bright bands are determined for each horizontal pixel row. This information is used (through least squares fitting and averaging) to determine the center pixel of each of the bands at the center row.

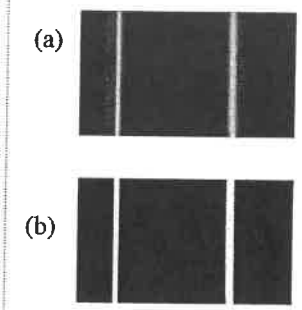

Fig 3 (a) Image as recorded by the camera (b) Binary image after processing

3. Probe characterization in 1D

Before the system is mounted on a CMM for rigorous testing, 1D performance is evaluated using a piezo stage. A long arm is mounted on the piezo stage and is aligned parallel to one optical axis of the deflection system. A retro reflector is held at the end of this arm and a 5 mm steel ball is glued to the backside of the retro reflector. The ball serves the function of a test surface and is centered on the retro to essentially measure at zero Abbe offset. The ball is brought in contact with the fiber, which is deflected by moving the piezo stage. The actual distance traveled by the stage is monitored using a laser interferometer. A schematic of the setup is shown in Fig. 4.

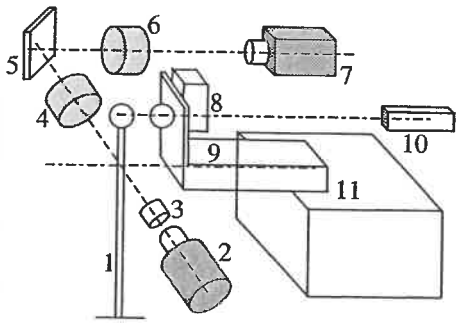

Fig. 4 1D Characterization Setup

1. Fiber
2. Source
3. Collimating lens
4. Objective
5. Fold Mirror
6. Eyepiece
7. Camera
8. Retro reflector with ball mounted behind
9. Long arm
10. Laser
11. Piezo stage

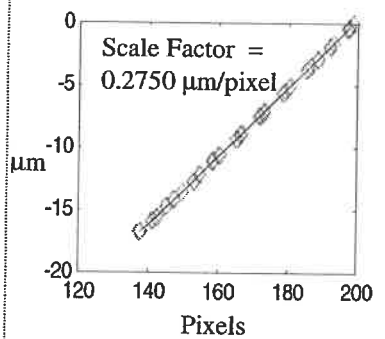

Fig 5. Calibration factor in µm/pixel

This setup is used for calibration (determining a scale factor that relates displacement of the probe stem in pixels to displacement of the tip in micrometers) in one axis (active axis) and also to evaluate linearity in that axis. A typical calibration run produces a plot shown in Fig. 5 and a scale factor in µm/pixel. Fig. 6 shows a linearity plot with 12 runs that was acquired over a 40 min period. In each run, the laser is zeroed (to correct for zero drift) at the start (zero displacement position) and the corresponding pixel reading is noted. For all subsequent deflections (from 1.5 µm to 15 µm in steps of 1.5 µm), the corrected laser position is computed (current laser reading – fiber deviation in pixels × scale factor in µm/pixels). This value should theoretically be identical to the laser reading at the start position, which in this case is zero. One standard deviation error in the graphs (arising from nonlinearity or noise) is between 10 nm and 25 nm for each run in this test. One standard deviation linearity/noise error is of the order of 17 nm over the entire

duration, while it is much smaller for most runs individually. From Fig. 6, it is seen that there are no clear systematic effects in the linearity plot. The deviations shown in the diagram do not repeat well from one run to the next, indicating that the deviations arise primarily from random noise. The solid black line in Fig. 6, an average of the 12 runs, indicates that systematic deviations from linearity averaged over this period do not exceed 4 nm (one standard deviation).

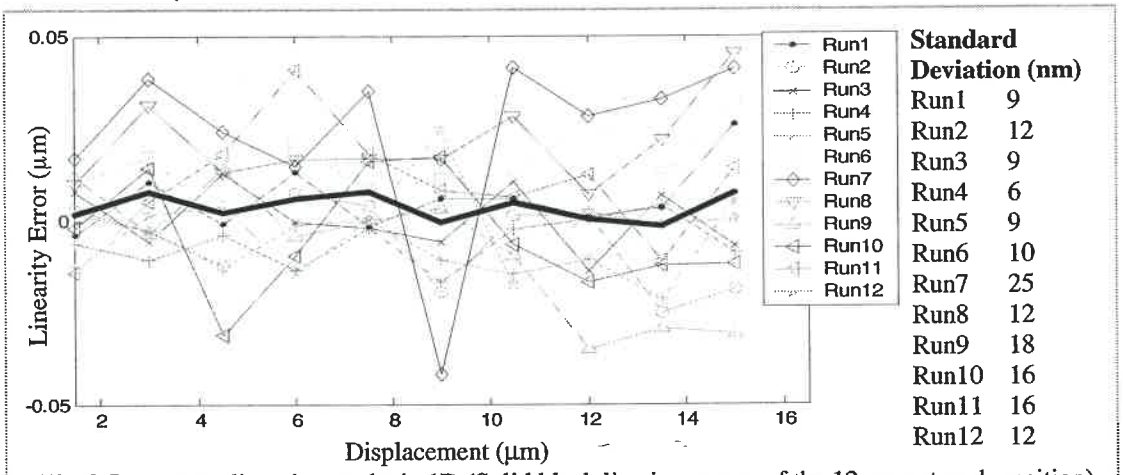

Standard Deviation (nm)	
Run1	9
Run2	12
Run3	9
Run4	6
Run5	9
Run6	10
Run7	25
Run8	12
Run9	18
Run10	16
Run11	16
Run12	12

Fig 6. Long-term linearity results in 1D (Solid black line is average of the 12 runs at each position)

4. Probe characterization in 2D

After the probe is characterized in 1D, the system is moved from the piezo test bed to the CMM. Because the probing system with the camera and optics is heavy, it is mounted on the CMM table with the probe pointing upward. Test artifacts are mounted on the ram. The probe is calibrated in both X and Y directions. In general, it is observed that the scale factor is different in each direction because (1) the magnifications are not identical in both directions and (2) the point of observation on the fiber is not at exactly the same height for the two directions. After obtaining the scale factors, linearity tests are conducted to assess performance. Typically, a standard deviation of 35 nm in linearity error is observed in X and Y. The marginally better performance in the piezo test bed is probably due to better environmental control around the probe as the entire assembly can be shielded from air currents, a situation not feasible on the CMM. Also, a portion of the 35 nm linearity error on the CMM can be attributed to the machine's positioning repeatability (≈ 25 nm) itself.

5. Probing system validation and results

Three artifacts of known diameter and form are measured using FDP to validate the probing system. Prior to each of these measurements, the fiber probe diameter and form are calibrated by measuring a 3 mm ruby sphere of known diameter and form. The diameter of the 3 mm sphere is calibrated using the Universal Measuring Machine (Table 1) and the expanded uncertainty is 0.09 μm (k = 2). The master ball diameter uncertainty is thus a major contributor in the overall uncertainty budget, although a more careful measurement arrangement is expected to lower this significantly. Table 1 shows a comparison of diameters obtained using FDP and other techniques. The agreement in diameters is to within 60 nm, although the uncertainty in the difference is large because of large master ball diameter uncertainty.

Table 1 Comparison of diameters obtained using FDP and other sources

Artifact	Dia from other sources (μm)	Dia from FDP (μm)
5 mm Sphere 1	4999.98 (UMM[1]) ± 0.09	4999.92 ± 0.11
5 mm Sphere 2	5000.19 (UMM[1]) ± 0.09	5000.15 ± 0.11
1 mm Hole	999.53 (M48 CMM[2]) ± 0.15	999.48 ± 0.11

[1]UMM – Universal Measuring Machine at NIST. Two point diameters are measured at 10 locations and averaged. [2]Moore M48 [5] CMM at NIST is used to measure the hole. The number following the symbol ± is the expanded uncertainty (k = 2).

The FDP is then used to measure a 129 μm nominal diameter fiber optic ferrule. The hole is located by simply centering the fiber using the outer surface of the ferrule. Because the hole is concentric with the outer surface to within 2 μm, no special optics are needed to locate the hole. The fiber is inserted 80 μm inside the hole and a measurement is made. The diameter obtained is 129.58 μm. and the residual form error on the hole after removing fiber ball form is 1.04 μm radial out-of-roundness. These are shown in Fig. 7. These values have not yet been verfied using other techniques.

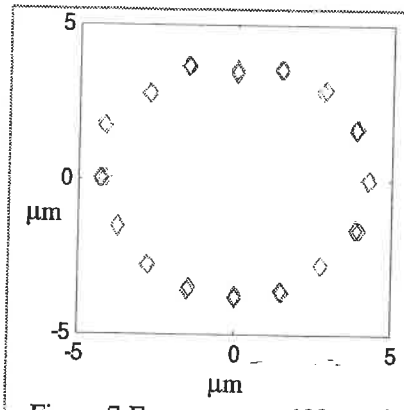

Probe calibration on 3mm Ball:
LS fit mean ϕ = 3088.12 μm
1σ on ϕ over 3 runs = 0.01 μm
Sphere ϕ from UMM = 3000.79 μm
⇒ Fiber Probe Ball ϕ = 87.33 ± 0.10 μm
Test Measurement on ferrule:
LS fit mean ϕ = 42.25 μm
1σ over 3 runs = 0.01 μm
Test Hole ϕ = 42.25+87.33 = **129.58 ± 0.11 μm**
Test Hole OOR = 1.04± 0.11 μm

Figure 7 Form error on 129 μm fiber ferrule hole (radius suppressed). The number following ± is the expanded uncertainty (k = 2).

6. Conclusions

A novel technique for measurement of diameter and form of small holes is presented. The probe is first characterized in 1D using a piezo test-bed setup and linearity errors are of the order of 15 nm to 20 nm. Subsequently, when mounted on a CMM, it is observed that linearity errors are of the order of 35 nm or smaller. A number of test artifacts are measured using the FDP and diameter results agree to within 60 nm with those obtained using other techniques. And finally, the diameter of a 129 μm nominal diameter ferrule is measured. Although an uncertainty budget has not been presented here, analysis indicates expanded uncertainty of 0.11 μm on diameter (k = 2). Contributors include master ball diameter uncertainty, machine positioning repeatability, imaging uncertainty and axis out-of-squareness.

1. G. X. Zhang and S. M. Yang, Annals of the CIRP, 44/1/1995, 461-464
2. Masuzawa T., Hamasaki Y. and Fujino M., Annals of the CIRP, 42/1/1993, 589-592
3. T. Hashimoto, Y. Takaya, T. Miyoshi, R. Nakajima, Proc. of the ASPE, 2003, 83-86
4. H. Schwenke, F. Waldele, C. Weiskirch, H. Kunzmann, Annals of the CIRP 50/1/ 2001, 361-364
5. Commercial equipment and materials are identified in order to adequately specify certain procedures. In no case does such identification imply recommendation or endorsement by the National Institute of Standards and Technology, nor does it imply that the materials or equipment identified are necessarily the best available for the purpose.

Design, manufacture and performance evaluation of a rapid probing machine

Marcin Bauza[1], Shane C. Woody[2], Pavan Jain[2]
Stuart T. Smith[1], Bob Hocken[1]

[1]Center for Precision Metrology, UNC Charlotte, Charlotte, NC, USA 28223

[2]InsituTec Inc., Charlotte, North Carolina, USA, 28213

Abstract

This summary presents the development of a real-time probing system for rapidly (less than a second) and accurately (better than 0.5 micrometer) scanning a circular feature (holes, pins etc.) on the shop floor for 100% inspection. This uses a closed-loop control method employing a sensor probe that can be dynamically translated in a radial direction and that is mounted on a precision spindle. Measurement of the displacement of the stylus tip relative to the probe base as it is maintained against the specimen surface at constant applied force is then used to represent deviation of the surface profile from a circle.

Introduction

In general, profilometry or profiling instruments, including stylus-based and scanning CMM's, represent a robust method for extracting precision measurement of surface parameters. In particular, profilometry is used to measure a workpiece's profile or surface finish and, therefore, is a tool to maintain quality of parts produced within the manufacturing process. In automation processes, because of fast measurement times, optical vision systems emerged as a viable candidate to real-time measurement cycles. However, the tradeoff is accuracies of 5-8 micrometers are produced and form error below the top surface of an OD or ID component is challenging to measure, particularly with burrs or other poorly defined edge features. Although adequate for many processes, optical vision systems can not produce the necessary accuracy for many precision components such as hydraulic spool valves, roller bearings and i,c, engine cylinder liners where accuracies of better than 5 micrometer are essential for 100-300 mm diameter components. For smaller components these accuracy requirements become progressively tighter. Current shop-floor contact-based roundness gauging technologies provide better accuracies (i.e. typically 0.5-1.0 micrometer measurement accuracies) but are unable to provide fast measurement times for 100% inspection on high production cycles, often have no or slow data connectivity to a computer, and are not easily embeddable into a process. One significant issue with some roundness gauges is the need for the component to be rotated while the scanning head measures about a null position to obtain form error. It is challenging to integrate such a system on an automation line where the component must be rotated as well as being aligned with respect to the roundness gauge. Because of the long measurement cycle, presently, it is more common (universal) that sampled components are measured and statistical process control (SPC) methods applied. In the absence of 100% inspection the manufacturing process cannot ensure 100% defect free parts.

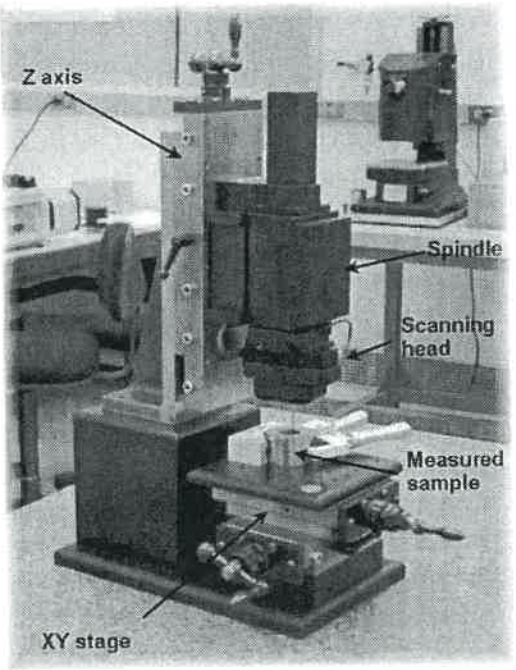

Fig.1 Table top version of Real Time Rapid Probing System configured to conventional slideways

Fixturing is another crucial component for rapid inspection tools. A rapid scanning system cannot be exploited if the setup time is lengthy. The roundness gage is configured to rotate the scanning head rather than rotating the work piece. The low mass scanning head design of this device is compact and mounted to a spindle that is capable of rotating at 60-120 rpm. This generally is more desirable for the measurement of large components such as engine blocks that are difficult to move and, in particular, to rapidly rotate. The

next logical step is to provide fixturing for the process line to center the feature with respect to the roundness gauge as well as level and clamp the component. One of the large uncertainty contributors for roundness gauges is the misalignment of the part, which produces a relatively large uncertainty in 2 UPR. Generally, this may be less of an issue as long as the roundness gage is mounted and measured perpendicular to the workpiece datum surface. The centering of the part is less critical as long as the roundness gauge stays within operating range.

Principle of operation

The roundness measuring system consists of a probe head for measurement of force at a nominally spherical stylus tip in a single linear direction. This force probe is mounted onto a piezoelectrically actuated translator capable of dynamically moving the probe assembly in a direction aligned with the sensitive axis of the probe. This probe head assembly is then mounted onto a spindle through a dovetail slideway again with its axis co-linear to that of the force probe and translator. The three coincident axes of the assembly are radial to the axis of the spindle. Consequently, as the spindle is rotated, the probe tip will follow a circular path the diameter of which is dependent upon the offset of the slideway and the motion of the translator. In operation, the probe tip is positioned on the slideway to be at a specified diameter for the holes (or pins) to be measured. The probe tip is then positioned into the holes (or pins) to be measured and the translator is used to move the tip into contact with the surface at a user defined force. The spindle is then rotated while the translator is used to maintain the probe tip at constant force thereby following surface variations from a circular path. These variations are then used as a measure of the deviation of the holes from the desired value. This can be repeated at different heights to obtain roundness, diameter variation and cylindricity data.

A block diagram indicating the control systems for this instrument is shown in figure 2. There are four major components to this system. The probe sensor comprises a flexure hinge to which the probe tip is mounted. Deflections of this hinge as the probe tip is contacted with the specimen surface are monitored using a capacitance based displacement sensor (cap gage 1 in the figure). This probe sensor assembly is mounted onto the translation stage that comprises a flexure guideway driven by a relaxor based piezoelectric actuator. Again, displacements are monitored using a capacitance sensor (cap gage 2). Both capacitance sensors are monitored using a TI 6713 DSP with demodulation and non-linear curve fitting used to convert from electrical signals to the desired measured value based on calibration curves. The spindle uses custom designed solid bearings and incorporates in-house developed slip rings for transmitting power and electrical signal to the head. Data is synchronized with the spindle rotation using an encoder. All measurement and control is supervised by the DSP with measured data being transferred to a host computer over a real time data exchange software kernel.

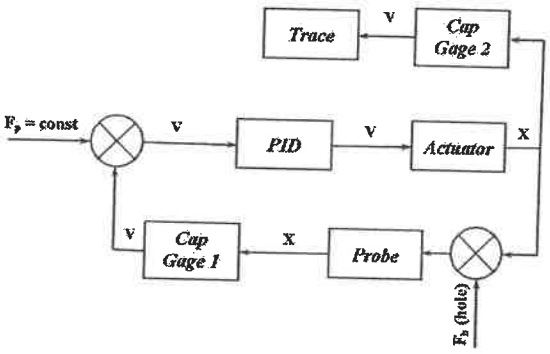

Fig.2: Block diagram indicating the basic control system for the measuring instrument

Probing system specifications

The probing system that we have developed can be assembled in many configurations, for example as a table-top version with manual adjustment to center the measured hole with the spindle axis (shown in fig.1) or automated slideways within a highly automated fixture to be used in a production line. The developed system has the following attributes:

- This is a robust instrument that can measure a part or component within the manufacturing process so that data will be available to the process controller so that it may continuously adapt to remove evolving errors such as out of roundness, eccentricity or cylindricity (with automated *Z* slide)
- High speed scans (less than one second to scan a round shape future)
- Low uncertainties during the high-speed scan (better than 0.1 micrometer when tracking roundness deviations as large as 200 micrometers).
- The short scan times reduce susceptibility to temperature changes and gradients

- Constant low force applied between the probe tip and surface of the measured specimen.
- For some processes this may be fast enough for 100% inspection without interruption of the process.

To get to this current level of performance, it has been necessary to undertake a number of developments. These include

- Force sensors for monitoring probe tip forces and providing a feedback signal for maintaining constant force.
- Translation stages of high bandwidth and precision for the servo control of probe tip.
- Miniature probe sensors for the measurement of microscale features.
- A compact spindle with nanometer systematic repeatability constructed from passive mechanical components.
- Low cost slip rings for transmitting power and electrical signals to the rotating probe assembly.

Results illustrating the performance of the above components are presented in the following section.

System performance results

In the process of characterizing performance of systems components, a number of tests are required to both optimize dynamic response and to assess uncertainties through calibration. Key results of these measurements will be briefly outlined.

To determined the deviations from an ideal hole geometry, it is necessary to measure the radial displacement of the probe translation stage during a scan. In practice, the DSP system provides a value of the capacitance of the sensor that must then be converted to displacement. Calibration of this sensor is achieved using an HP 5528A laser interferometer while translating the stage across full range. From this measured characteristic it is possible to fit a polynomial to the capacitance gage response to convert the measured signal to displacement. A Similar procedure is used to calibrate the force sensor of the probe see figure 3.

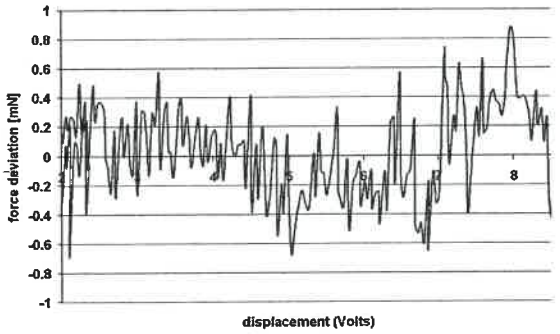

Fig.3: Residual force errors represented as a deviation between a polynomial curve fit and measured data

For maximum productivity, it is necessary to optimize the dynamic response of the radial translation system. To do this, the translation stage is programmed to respond to a step change in contact force (i.e. it is set to a constant force and this is then changed so that the radial stage moves to a new equilibrium position). Typically, the force change would be selected to correspond to the stage displacement of around 10 micrometers. The PID controller was then tuned to produce an optimal step response with a 4 ms settling time.

In combination with optimal control settings, the limit on data collection speed is primarily determined by the fundamental mode frequency of the probe translation stage. A frequency response measurement of the second generation stage on which was mounted a force sensor probe with a 4 mm diameter probe tip on a one inch long shaft and contacting with a steel specimen surface is shown in figure 4.

Accuracy of the complete instrument is fundamentally limited by spindle performance. We have developed a novel spindle design that has shown in preliminary testing to produce systematic errors of better than 50 nm peak to valley. This deviation was also comparable to the uncertainties of the spindle error analyzer system used in these studies. Work is ongoing to improve the accuracy of this measurement and it is expected that results from these tests will be presented.

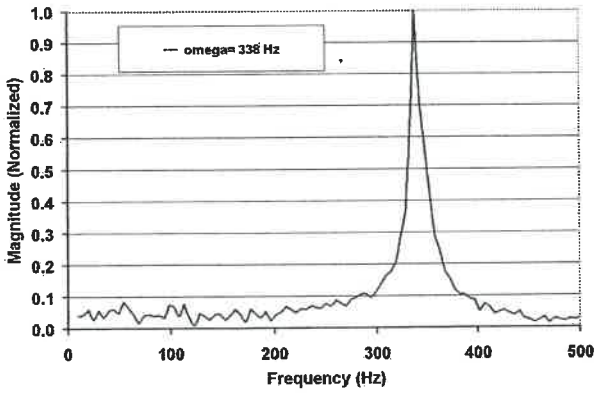

Fig.4: Frequency response of a complete system

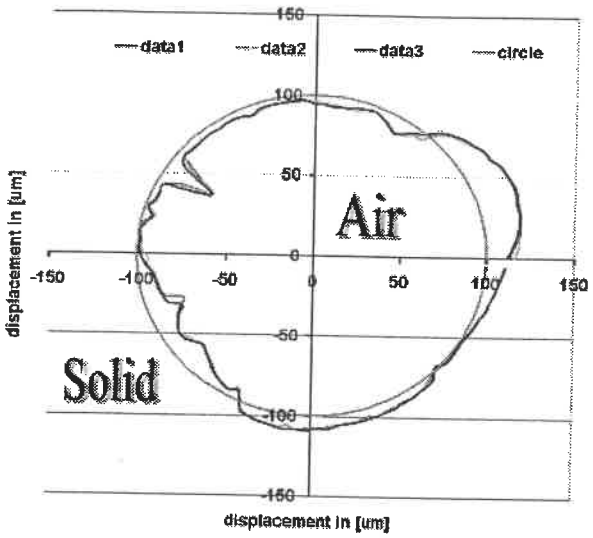

Fig.5: Measurement of drilled hole – 3 traces

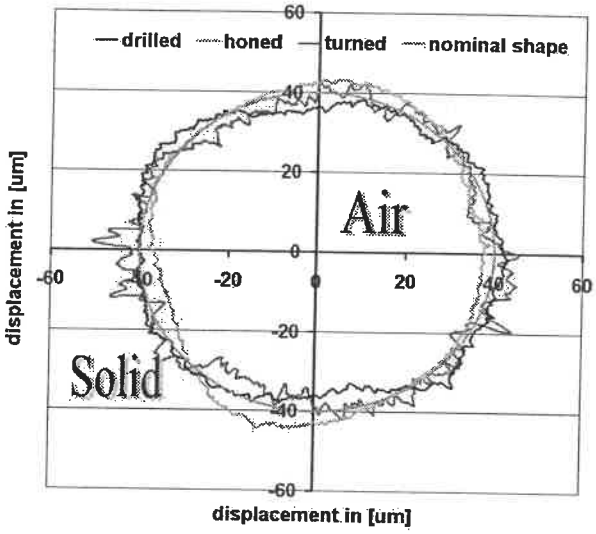

Fig.6: Measurement of 3 holes after different manufacturing process such as drilling, honing and turning

Preliminary experimental data of measured holes

Over the last two years, the complete roundness instrument has undergone a number of prototype developments. These have been used to measure holes and pins with a wide variety of features. For example, to illustrate repeatability and the ability to measure large deviation from an ideal hole, figure 5 shows a series of three repeat profiles from the measurement of a drilled hole in an aluminum/CFRP composite multilayer material.

For more typical hole geometries, figure 6 shows a series of profiles of nominally similar holes that have been produced using drilling, turning and honing. Even using a 4 mm diameter spherical probe tip, it is apparent that the shorter wavelength features are removed by the honing process with turning producing a hole of intermediate surface quality. The overall low UPR shape is comparable for all three holes.

Future directions

One particular challenge of relevance to both fuel injector and microelectronic/MEMS manufacturers is that of metrology of holes of diameters less than 300 micrometers. To satisfy the performance requirements for these measurements, miniature force sensing probes have been developed. Typically, these have a nominal tip diameter of around 5 micrometers with a support shaft of about 3 mm length and can operate at contact forces in the micro Newton range. An image of the current probe inside a fuel injector is shown in figure 7.

Fig.7: Measurement of 100 um fuel injector hole

References

Woody S.C. and Smith S.T., 2004, Performance comparison and modeling of PZN, PMN and PZT stacked actuators in a levered flexure mechanism, *Rev. Sci. Instrum.*, **75**(4), 842 – 848

S.C. Woody and S.T. Smith, 2003, A vector touch sensor probe: An experimental study, *Precision Engineering*, **27**(3), 221 - 233

AGILE ASSEMBLY ARCHITECTURE: A PLATFORM TECHNOLOGY FOR MICROASSEMBLY

Ralph L. Hollis and **Alfred A. Rizzi**
The Robotics Institute, Carnegie Mellon University
Pittsburgh, Pennsylvania, USA

Abstract

It is proposed that fundamental changes will be required for automated assembly of precision micro-scale products. We suggest that the time has come to develop a scalable platform technology *for microassembly and describe initial steps taken in this direction.*

WHAT IS A "PLATFORM TECHNOLOGY"?

Technologies that are so pervasive that they serve as springboards for other technologies and regarded as essential for progress in multiple fields are often referred to as "platform technologies." A platform technology has several characteristics; among them are:

- a common substrate upon which to build,
- a uniform set of services upon which to draw,
- a set of abstractions insulating the user from implementation details,
- standard methods, philosophy, and semantics usable by a broad community, and
- a system architecture comprising modularity, extensibility, and scalability supporting rapid design and efficient implementation.

Precedents in the world of software are computer operating systems. Programmers used to be concerned with the computer hardware directly, spending a great deal of time and effort dealing with registers, memory allocation, and hundreds of atomic operations. Writing a complex "bug-free" computer program was a Herculean effort. Modern operating systems are true platform technologies which are substrates for realizing a wide variety of important applications. They provide an abstraction to the underlying hardware, insulating the user from obscure details; a common and consistent environment for user programs, enabling portability; and transparent allocation and management of hardware resources.

Another precedent can be found in Very Large Scale Integrated (VLSI) circuit design methodology. In the early days, chip designers layed out individual transistors, passive components, and wiring from "scratch." Very dense, efficient, and fast designs were possible, however they took years to create and were extremely difficult to debug. In the 1970s, Mead and Conway [1] observed that *"ICs are so complex and dense that human designers cannot deal with individual devices, instead, they must be handled at a higher level of integrated system architecture."* They decided on a hierarchical, modular approach that combined replicated functional blocks to form larger subsystems. Using this methodology, designers no longer worked at the lowest level, instead they merely combined pre-defined and pre-debugged circuit modules in new ways to create the needed functionality. The results were VLSI circuit designs that were neither optimized in speed nor in silicon area, but could be very rapidly designed, and through the MOSIS foundry service, fabricated in weeks. Nowadays, all circuit design is done using these principles.

One can think of many other kinds of platform technologies serving as foundations for diverse applications.

HOW MICROSYSTEMS ARE ASSEMBLED TODAY

Most small, complex products are assembled manually. When there are very high volumes, very small parts, high precision required, or extreme cleanliness needed, robot assembly lines or robot work cells are used. There remain significant issues concerning robot precision, high integration costs, and lengthy deployment times. In some cases these problems can be avoided with micro-products based on MEMS.

MEMS have the extraordinarily useful property that mechanical and electronic functions can be integrated on the same chip. Moreover, the mechanical structures emerge from the batch fabrication process in fully assembled and operational form. In fact, the avoidance of costly and tedious serial assembly steps is one of MEMS' most remarkable aspects. Micromechanical systems of impressive complexity can be made without assembly of any kind [2]. That said, there is a growing recognition that more complex and more useful microsystems comprised of different materials such as Si, GaAs, metals [*e.g.*, formed by LIGA (Lithographie Galvanoformung Abformungglass)], and plastics will require some form of assembly [2]. Without assembly, MEMS will be forever limited in the impact it can have. Figure 1 illustrates the tremendously difficult problem of correctly and automatically joining together disparate components and materials (perhaps from different vendors around the world) to form a working microassembly. Whatever automation methods are employed, they must be precise, economical, and deployable in finite time.

In recognition of these issues, a number of parallel and sequential methods have been devised for MEMS assembly, including wafer bonding, flip up and folding of planar structures, fluidic self-assembly, and precision robotic assembly [2]. Few of the methods use automation to an appreciable degree.

Wafer-level assembly and packaging: Several wafer bonding techniques have been developed for batch assembly of MEMS components. These include eutectic

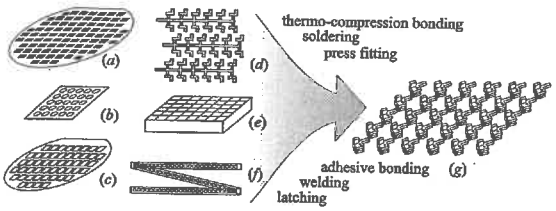

Fig. 1. Hybrid Microassembly (Example): (*a*) CMOS device wafer, (*b*) LIGA parts, (*c*) MEMS device wafer, (*d*) precision molded plastic parts, (*e*) micro-EDM metal parts in trays, (*f*) ribbon of micro-stamped metal parts, (*g*) array of assembled products whose parts are fastened together by various means (after [2]).

bonding between Si and Au-covered Si, Si fusion (atomic) bonding, low temperature glass bonding, and Si-to-Si anodic bonding, among others. After bonding two or more wafers together, the assembly is diced to form multiple assembled MEMS devices, commonly used for packaging MEMS accelerometers and pressure sensors. Batch assembly and packaging by wafer bonding will continue to be an important method for MEMS device assembly.

"Self-assembly" of quasi-3D structures by flip up from the plane: As early as 1992, it became possible to create hinge structures in MEMS permitting planar structures to be fabricated, released, and then folded up out of the plane by hand under a microscope to form lockable quasi-3D structures [3]. Recently, there has been a great deal of interest in "powered" or "assisted" flip-up assembly to produce quasi-3D structures. For example, the surface tension of solder melting in a reflow process can be used to raise up planar structures from the wafer and lock them in place [4]. The flip-up self-assembly approaches to MEMS assembly are extremely important and rapid progress is being made.

Fluidic self-assembly: Whereas the flip-up self-assembly techniques are largely limited to quasi-3D silicon-based structures, related techniques using surface tension for planar alignment has demonstrated the capability of assembling discrete micro parts of different materials to binding sites on a substrate with high efficiency and high accuracy. For example, GaAs diodes have been assembled on Si wafers [5], and cylindrical displays have been created [6]. Fluidic self-assembly results to date have been impressive and appear to be most suitable for creating assemblies with large arrays of identical parts.

Sequential assembly using robotics: Robotic assembly of macro-scale products dates back to the late 1970's. Many issues of "design for assembly," assembly planning, part transfer and feeding, part grasping and details of part-assembly interaction forces have been intensively studied. In the past decade, attention has focused on two important areas: assembly automation that *i*) can be rapidly deployed, with important economic benefits; and that *ii*) can deal effectively with very small parts and precise dimensional features.

With few exceptions, most of the reported work in robotic microassembly has dealt with precision and parts-handling aspects and has taken place in Europe and and to a lesser degree in Asia. Sysmelec, in Switzerland, produces several robotic assembly workstations for MEMS and Microoptoelectromechanical systems (MOEMS) [7]. Assemblies of four layers of microlenses and eight micromachined chips have been produced automatically at CSEM SA (Centre Suisse d'Electronique et de Microtechnique), Microsystems Manufacturing [8]. A flexible microrobot-based microassembly work cell was developed in Germany [9]. In the U.S., work has progressed at Sandia National Laboratories to produce automated microassembly systems [10]. Zyvex has produced small semi-automated robotic systems for microscopic and nanoscopic assembly [11]. Impressive precision microassembly results have been obtained through robotic approaches.

Why a Microassembly Platform Technology is Needed

Despite excellent efforts, there is currently no viable platform for microassembly. Almost everything has to be done by hand, or else by cobbling together an eclectic collection of microscopes, precision stages, and micromanipulators. There is no way to integrate promising parallel or sequential assembly techniques into an automated system without a huge and costly effort, notwithstanding some "point" solutions such as fiber pigtailing.

There are significant drawbacks associated with the assembly methods previously described that offer a real set of opportunities for architectural and system-level advances. For the foreseeable future, micro-scale devices will require packaging into macroscopic "products" to be useful. Moreover, these products are likely to be customized in many different ways and have relatively volatile lifetimes. These considerations point to the need for highly flexible and rapidly deployable *information-intensive* production systems.

Fundamentally, the novel batch assembly technologies listed above suffer from a lack of scalability in three separate directions *i*) product size, *ii*) product heterogeneity, and *iii*) process variety. These dimensions of scalability are critical aspects of delivering assembly technologies capable of effectively bringing complex microstructures from the laboratory setting to the real world. The ability to reliably manipulate and assemble components of vastly different scales allows seamless integration of micro-devices into macroscopic products, making them readily available in a familiar form factor. The ability to integrate components having drastically different material properties enables the effective and efficient integration of function-specific components—*e.g.*, CMOS electronics coupled to MEMS sensors monitoring LIGA mechanisms—as well as the integration of non-MEMS micro-components such as photonics. Finally the ability to incorporate a broad range of processing functions directly into the assembly environment facilitates integration of function-specific and heterogeneous material bonding technologies.

Future hybrid microsystems will greatly benefit from the fusion of heterogeneous technologies. For example, an autonomous wristwatch-sized total chemical analysis system might integrate digital electronics instantiated in

(a) (b) (c)

Fig. 2. Virtual factory views of small microphone assembly processes from the AAA Interface Tool: (*a*) manipulator agent placing micropart on a product held by courier agent, (*b*) dispensing agent, (*c*) microwelding (gap welding) agent.

CMOS, micromechanical structures made from polysilicon, microfluidics formed from plastics, optical interconnects routed in glass fibers and laser light emitted by III-V semiconductor diodes. To succeed in the marketplace, these systems must meet performance goals at low cost and thus be made from known good components using best-of-breed technology. Microsystem-based products are driven by a wide variety of market segments with huge numbers of small to medium volume applications. This desire for many different products combining multiple technologies drives the opportunity for highly flexible production systems that can be rapidly reconfigured to meet these demands.

No coherent microassembly methodology exists today for achieving these levels of integration. Advances in the specific batch assembly processes listed above are impressive and are expected to continue. As a result, micro-components in select areas will gradually increase in sophistication. However, these batch methods currently have inherent material, process and geometric restrictions that inhibit their range of applicability. Wafer bonded assemblies are essentially 2.5D; flip-up self-assembled microstructures are constrained to specific 3D structures and imperfect yields; fluidic self-assembly has future challenges of generating general 3D assemblies with suitable yield. Precision robotic systems have the potential to assemble complex hybrid products from heterogeneous micro-components but they are limited by high equipment complexity and cost, lengthy deployment times, and more fundamentally by their serial one-by-one nature which restricts throughput for many applications.

AGILE ASSEMBLY ARCHITECTURE

At Carnegie Mellon University, we have been developing a flexible architecture for precision assembly over the past several years. Unlike other microassembly approaches, whether wafer-level assembly, self assembly, or serial robotic assembly under a microscope, we visualize a highly modular robotic pipelined approach with a much higher level of *scalability*. This scalability is manifest in four different ways: *i*) the ability to assemble products from MEMS chip size up to products whose size is 100 mm or more, *ii*) the ability to integrate diverse fastening technologies and non-MEMS microscale parts, *iii*) the ability to introduce parallel assembly steps to increase throughput, and *iv*) the ability to assemble complex products requiring an arbitrarily large number of process steps. Achieving this will require solving fundamental problems associated with composable distributed computational/physical systems.

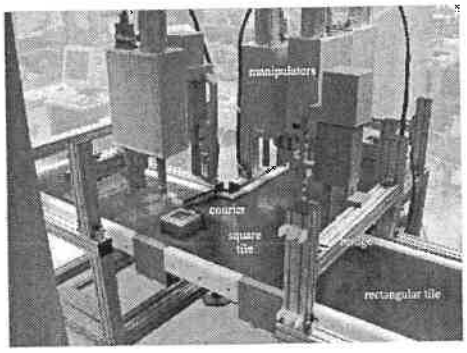

Fig. 3. Photograph of a section of our laboratory minifactory (under development).

We have begun to tackle these issues with a framework and technology for rapid design, programming, and deployment of precision automated assembly systems, called "Agile Assembly Architecture," (AAA), first discussed in [12]. AAA has two components: *i*) a distributed system of tightly integrated mechanical/computational agents (collection of highly modular and intelligent robots, feeders, and fastening equipment), and *ii*) a unified Interface Tool that allows a user to select and order agents over the Internet and to assemble, program, and monitor them both in a simulated (virtual) factory environment and in the real factory. To instantiate these ideas, we have been developing a small, modular assembly system called "minifactory" in our laboratory over the past several years.*

Using our Interface Tool, we have created several virtual factories for assembling small transducers and optoelectronic products. For example, Fig. 2 shows several virtual agents operating in a 29-agent virtual minifactory which assembles small microphone devices. The virtual minifactory was rapidly configured using the AAA Interface Tool. Whereas the assembly operations depicted in the figure are small but still macroscopic, we project that the architecture will be suitable for MEMS-scale operations with integration of appropriate sensing, gripping, and manipulation techniques.

Figure 3 shows part of the modular minifactory system under development in our laboratory. Active components include *courier agents* responsible for transporting products through the factory and participating in assembly and fastening operations, and *manipulator agents* for picking and placing parts. The agents, acting cooperatively, perform 4-DOF assembly operations in an order of magnitude less space and with two orders of magnitude more precision than current state-of-the-art industrial assembly systems. Courier agents move about on an ensemble of platen tiles forming the factory floor, and are based on novel closed-loop planar motors [13] that can move at 1.5 m/s with a position resolution of 0.2 μm (1σ). The manipulator agents have two degrees of freedom (DOF)

*Carnegie Mellon University Microdynamic Systems Laboratory `http://www.cs.cmu.edu/~msl`.

for precise vertical (z) motion and rotary (θ) motion [14]. Many other kinds of agents are possible (*cf.* Fig 2). Agents are designed to be highly generic and therefore widely applicable across broad spectrums of product and process types, so only small items, *e.g.*, part-specific end effectors need to be customized.

Agents are physically and computationally modular, self-describing, and self-representing [15]. Control is distributed during factory execution, and there are built-in mechanisms for synchronizing and registering virtual and real minifactories [16]. The collection of robotic agents in a minifactory is supported by a service infrastructure comprised of modular base units, platen tiles, and bridges. The system is designed from the outset to enable rapid deployment.

In our first-generation minifactory (now retired) we demonstrated cooperative visual servoing between manipulator agents and courier agents and vision-guided parts placement [17]. We also demonstrated cooperative force servoing between a manipulator agent and courier agent at several-mN force levels [18].

For the past several years our effort has focused on completion of the second-generation minifactory shown in Fig. 3. The new minifactory incorporates numerous enhancements over the prototype but is not yet fully operational. All of our work on the project to date has been of a fundamental and generic nature which has served us well. At this stage of development, we are beginning to explore relationships with industry to select strategic areas of application to real product microassembly.

Discussion

We have argued that a platform technology will be necessary (or at least highly desirable) for developing future automated microassembly systems. Like all platform technologies, there must first be an overwhelming need to set the stage for their introduction. We are perhaps not quite at that point yet, but we see it coming in the near future.

Agile Assembly Architecture and minifactory serve as our initial foray into automated hybrid microassembly. As the work proceeds, there is no doubt that some of its concepts will need to be augmented, modified, and perhaps eliminated. A principal attribute is that of *scalability* in product sizes, kinds of fastening processes, parallel processing, and in number of assembly process steps.

Figure 4 schematically illustrates the kind of hybrid microassembly that we believe can someday be performed in minifactory. An automation system based on a microassembly technology platform that could reliably and quickly produce this example product in quantity would serve to illustrate the capability to assemble three-dimensional microproducts from heterogeneous materials.

Acknowledgements

The authors thank the more than 30 persons who have so far contributed to AAA and minifactory. This work was supported in part by NSF grants CDA9503992, DMI9523156, and DMI9527190.

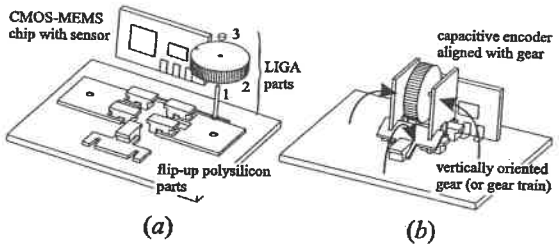

Fig. 4. Exemplary Hybrid Microassembly Test Vehicle: (a) collection of polysilicon MEMS, CMOS-MEMS, and LIGA parts to be assembled, (b) final configuration of the assembly.

References

[1] Carver Mead and Lynn Conway. *Introduction to VLSI Systems.* Addison-Wesley, December 1 1979.

[2] M. B. Cohn, K. F. Böhringer, J. M. Noworolski, A. Singh, C. H. Keller, K. Y. Goldberg, and R. T. Howe. Microassembly technologies for MEMS. In *SPIE Conf. on Micromachining and Microfabrication Process Technology IV*, pages 2–16, Santa Clara, CA, September 21-22 1998.

[3] K. S. J. Pister, M. W. Judy, S. R. Burgett, and R. S. Fearing. Microfabricated hinges. *Sens. Actuators: Phys. A*, A33(3):249–256, 1992.

[4] R. R. A. Syms. Equilibrium of hinged and hingeless structures rotated using surface tension forces. *J. Microelectromechanical Systems*, 4:177–184, 1995.

[5] H. J. Yeh and J. S. Smith. Fluidic assembly for the integration of GaAs light-emitting diodes on Si substrates. *IEEE Photon. Technol. Lett.*, 46:706–709, 1994.

[6] H. O. Jacobs, A. R. Tao, A. Schwartz, D. H. Gracias, and G. M. Whitesides. Fabrication of a cylindrical display by patterned assembly. *Science*, 296:323–325, 2002.

[7] M. Odiet. Micro assembly systems for high volume production. In *2nd Int'l. Workshop on Microfactories*, pages 55–58, Fribourg, Switzerland, October 9-10 2000. FSRM, Neuchatel, Switzerland.

[8] Y. Dupraz and H. de Lambilly. Automatic precise assembly of MEMS for small and medium production volumes. In *2nd Int'l. Workshop on Microfactories*, pages 195–199, Fribourg, Switzerland, October 9-10 2000. FSRM, Neuchatel, Switzerland.

[9] S. Fatikow, J. Seyfried, St. Fahlbusch, A. Buerkle, and F. Schmoeckel. A flexible microrobot-based microassembly station. In *Proc. 7th Int'l. Conf. on Emerging Technologies and Factory Automation*, volume 1, pages 397–406, October 18-21 1999.

[10] J. T. Feddema and R. W. Simon. Visual servoing and CAD-driven microassembly. *IEEE Robotics and Automation Magazine*, pages 18–24, December 1998.

[11] G. D. Skidmore, M. Ellis, E. Parker, N. Sarkar, and R. Merkle. Micro-assembly for top-down nanotechnology. In *Int'l. Symp. on Micromecatronics and Human Science*, pages 3–9, 2000.

[12] R. L. Hollis and A. E. Quaid. An architecture for agile assembly. In *Proc. Am. Soc. of Precision Engineering, 10th Annual Mtg.*, Austin, TX, October 15-19 1995.

[13] Z. J. Butler, R. L. Hollis, A. A. Rizzi, and A. E. Quaid. Closed-loop planar linear motor with integral monolithic three-degree-of-freedom ac-magnetic position/orientation sensor. U. S. Patent #6,175,169, January 16 2000.

[14] H. B. Brown, P. M. Muir, A. A. Rizzi, M. C. Sensi, and R. L. Hollis. A precision manipulator module for assembly in a minifactory environment. In *Int'l Conf. on Intelligent Robots and Systems, IROS '01*, Maui, Hawaii, Oct. 29–Nov. 3 2001.

[15] A. A. Rizzi, J. Gowdy, and R. L. Hollis. Agile assembly architecture: An agent-based approach to modular precision assembly systems. In *IEEE Int'l. Conf. on Robotics and Automation*, pages 1511–1516, Albuquerque, April 1997.

[16] Z. J. Butler. Contact sensor-based coverage of rectilinear environments. In *Int'l Symp. on Intelligent Control*, Boston, October 1999.

[17] Michael L. Chen, Shinji Kume, Alfred A. Rizzi, and Ralph L. Hollis. Visually guided coordination for distributed precision assembly. In *IEEE Int'l. Conf. on Robotics and Automation*, pages 1651–1656, San Francisco, April 2000.

[18] R. DeLuca, A. A. Rizzi, and R. L. Hollis. Force-based interaction for distributed precision assembly. In *Proc. Int'l Symp. on Experimental Robotics*, Honolulu, Hawaii, December 10-13 2000.

Active Vibration Isolation of an Unbalanced Machine Tool Spindle

David. J. Hopkins, Paul Geraghty
Lawrence Livermore National Laboratory, 7000 East Ave, MS/L-792, Livermore, CA. 94550

Abstract
Proper configurations of controls, sensors, and metrology technologies have enabled precision turning machines to achieve nanometer positioning. However, at this level of resolution, vibration sources can become a limiting factor. One of the largest sources of vibration in a turning machine may be an unbalanced rotating spindle. In this paper, a system is implemented to actively cancel spindle unbalance forces. Specifically, to attenuate the spindle housing vibration using an active vibration control system to prevent the unbalance force from disturbing the rest of the machine systems e.g., the slide servo system or the machine metrology frame. The system controls three degrees of motion.

An unbalanced spindle creates a rotating force vector with a once per revolution period. The cause and size of this force is a function of the spindle, the part, the part fixturing, the part setup and the spindle speed. In addition, certain spindle speeds coupled with the size of the unbalance force may contain other harmonics that can excite machine structural resonances. The magnitude of the unbalance force increases as the square of the spindle speed.

The control algorithm of this system is fully implemented on a commercially available machine tool controller and is sensitive only to unbalance induced motion. The paper describes in detail the control algorithm and how it is implemented. The system has demonstrated the ability to adapt in real time to remove the fundamental component of the unbalance force to nanometer levels. However, higher-order structural resonance components of the test bed have been observed when the system is active. The control system is stable and the voice coil (VC) excitation is harmonically clean but the high Q of the mechanical test system is apparently excited by energy leakage. Our results indicate the need to carefully examine the dynamics of any spindle system that would take advantage of this active system.

Introduction
Spindle unbalance forces in a precision machine can impart energy into the machine base and provide a forcing function to the machine slides and the machine metrology frame and may cause undesirable slide motion. This motion can be rejected to some extent by the control system loop gain but the loop gain decreases with increasing frequency. This is exactly opposite of what is desired as the unbalance spindle forces increase with spindle speed (frequency) further compounding the problem. Force disturbance of the metrology frame can cause non-ridge body motion of the frame and distort the measured tool position. Eliminating or canceling the spindle unbalance force reduces these error sources.

The ideal solution is to cancel the unbalance force at the source or rotor of the spindle. This is difficult since the spindle must hold the part and any apparatus that would be used to cancel the rotor unbalance. Our approach is to cancel the vibration forces that radiate from the spindle housing so that these forces do not induce motion into sensitive machine systems.

The basic concept of the system is to measure the force-induced spindle-housing motion and exactly cancel this motion with a controlled moving inertial mass. Essentially, the spindle housing motion is measured with a displacement sensor referenced to the machine base. The measured displacement is sinusoidal and corresponds to the motion profile required of the VC motor creating the opposing force. The displacement measurement, along with the spindle angle (measured with an encoder), is fed to a controller running a specific algorithm. The algorithm computes the required signal and the controller actuates a voice-coil (VC) motor, canceling the original force-induced motion. The amount of force required to cancel the unbalance is a function of frequency (spindle speed), the amount of mass the VC is moving, and the range of VC travel. The equation that relates these variables and describe the motion profile is; $F = (W/g) [-A\_^2 \sin(\_t)]$. Where F is the force, W is the weight the voice coil is moving, g is acceleration due to gravity so W/g is the moving mass. The term $[-A\_^2 \sin(\_t)]$ is the acceleration due to the motion profile and is derived from the second derivative of the VC displacement profile. A represents the maximum peak amplitude of the measured displacement and _ is $2\pi f$ where f is the spindle RPM divided by 60.

The System
The test bed and a simple block diagram of the control system are shown in Figure 1. The test bed structure is designed to be compliant and vertically holds a four inch air-bearing spindle. A bolt can be screwed into the spindle face-plate to unbalance the spindle. The control algorithm is fully implemented on a commercially available controller and is sensitive only to unbalance force induced motion. (The controller performs synchronous demodulation of the

capacitance gauge signal so only signals synchronous to the once per revolution of the spindle are processed and used by the controller.) The VC motors are mounted on the opposite side of the spindle housing directly in-line with the corresponding displacement sensor. The voice coil motors are moving an inertia mass and do not act against a reference structure. We have addressed three degrees of freedom of spindle housing motion of the test bed system, the X direction, (the single VC motor) the Y direction, (the two Y VC motors acting together) and rotationally, the yaw motion (the two Y VC motors acting oppositely).

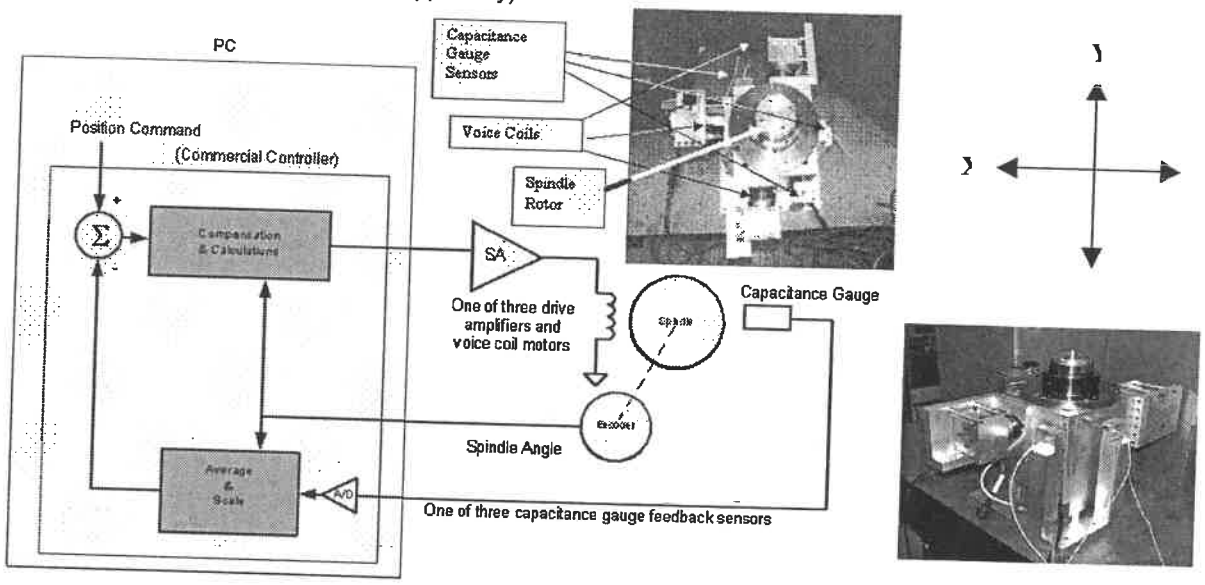

Figure 1: Simple control system block diagram and top and side view of the physical test bed system.

Control Algorithm

When a machine tool controller commutates a brushless motor, it uses a sensor (typically an encoder) to sense the location of the motor rotor and modulates the servo output signals delivered to the torque amplifier (motor current command) for each motor phase. The signals of the two output phases (the PID output or 2nd order filter output– Actuator Excitation - see Figure 2) are modulated (commutated) in many modern day machine tool controllers with a sinusoid, the value of which depends on the angular position of the encoder. The two outputs typically have a commutation angle offset of either 90 degrees or 120 degrees (as in Figure 2) depending on whether the motor is a two phase or three phase device respectively. (In the case of a three phase motor, the torque amplifier typically generates the third phase internal to the amplifier.) If ninety degrees is chosen as the phase offset, e.g., for a two phase brushless motor, the torque command is modulated by the sine and the cosine of the motor rotor angle.

Figure 2 is the typical configuration of a single axis of the 32 possible axes available in the machine tool controller used in this paper. The controller allows configuring a typical servo axis in several ways. The interpolated position command can be set to zero. The PID terms are all adjustable as are the coefficients of the second order filter allowing the filter to be set to a gain of one. The commutation function can be enabled or disabled if the motor is self commutating. The sensor feedback input, normally an encoder, can be used to commutate a motor and also interpolated to create higher resolution position information for the servo axis feedback (Processed Position Feedback). This is the usual case for many applications; however, it is possible to have the commutation feedback for a particular axis be derived from the feedback input of another axis, i.e. the commutation feedback and the processed position feedback do not have to come from the same sensor. Also, the sensor feedback can be derived from any type of device. It is these last two key features that provide a very powerful capability and when coupled with the other capabilities listed, the controller requires no additional components to provide the adaptation algorithm discussed in this paper.

In this system, the sensor feedback for one of the axes is an analog signal derived from a capacitance gauge sensor measuring the displacement of the spindle housing caused by the rotational force of an unbalance spindle. When commutation is enabled for this axis and the axis is commutated from the spindle rotary encoder derived from another axis and the terms of the servo axis are set to a gain of one, the analog displacement signal will be synchronously demodulated at the two outputs of the axis with respect to the angular location of the encoder. This provides a harmonically clean measurement of displacement caused by the unbalance occurring at once per revolution of the spindle. If the sensor signal was not processed in this way, it could be contaminated with other synchronous and non-synchronous displacement noise. By picking 90 degrees as the phase offset between the two output phases of

commutation, the output signals (Actuator Excitation) will be the Fourier transform of the measured displacement signal. (Sine of the encoder angle times the sensor input signal is available at the first output and the cosine of the encoder angle times the sensor input signal is available at the other output.) Once these signals are low pass filtered (integrated), a coefficient for each of these two outputs is available that represents only the synchronous value of the sensor signal. Because of the Fourier transform, any input signal not related to the once per revolution of the rotor are rejected by the transform (It is a selective filter.) The process can be thought of as a two phase synchronous demodulator. When these signals are used as part of a control system that adjust the reference phase (relative to the zero point of the encoder), the sine modulated output represents the magnitude of the input signal and the cosine modulated output represent the amount of phase adjustment needed to obtain the maximum signal gain for the sine output at the maximum location of the unbalance. This is the key to the adaptation aspects of this system. The control system tries to adjust the cosine signal term to a minimum or zero and when this occurs, the sine signal term should be at a maximum or gain of one.

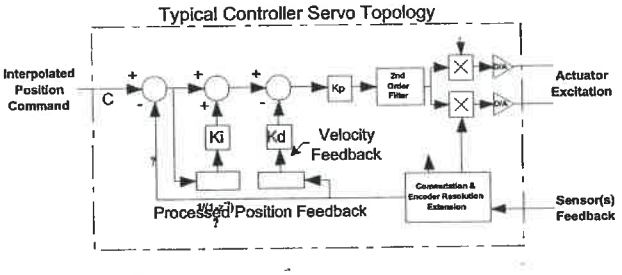

Figure 2: Typical configuration of an axis of the machine tool controller set for a three phase brushless motor.

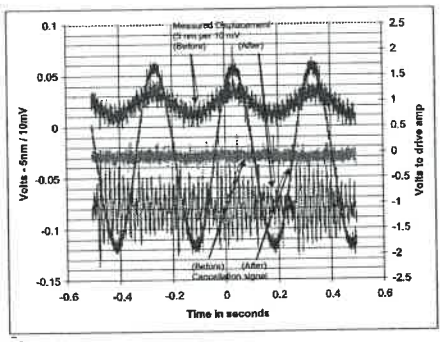

Figure 4: Data Plots (Some plots are offset for easy viewing.)

To be more specific, assume a displacement sensor is observing motion caused by an unbalance force acting on the structure as the spindle rotates. Initially, the maximum amplitude of the displacement signal may not necessarily correlate to the peak of the sine and or the zero of the cosine of the commutation cycle due to the angular position of the encoder versus the angular position of the unbalance. Because of the dual synchronous demodulation, it is possible to find the maximum unbalance signal and the location of this signal relative to the encoder zero. When there is an offset between the encoder commutation angle and the peak of the unbalance signal the sine modulated output will have less than a signal gain of one and the cosine modulated output will have more than a zero or minimum output. If the cosine term is used in a control system loop to adjust a simulated encoder reference or virtual encoder, the adjustment continues until the cosine signal magnitude is zero. At this point, the maximum synchronously demodulated signal is obtained at the first output or sine modulated output. Once this signal is low passed filtered, a DC value is obtained representing the peak of the displacement signal at the maximum unbalanced location. This signal can now be used as an amplitude command to actuate a second motor axis that is also commutating in sync with the virtual encoder. This signal is a sine wave that is used to drive the VC motor actuator canceling the synchronous motion detected by the displacement sensor.

The complete control algorithm is shown in Figure 3. Each dotted outline represents a Block or axis of the machine controller as shown in Figure 2. Blocks 1 and 4 have commutation enabled. Blocks 2, 3 and 5 have commutation disabled. The capacitance gauge sensor input signal is an analog signal representing displacement. Block 1 does the dual synchronous demodulation of this signal as previously described. The mXX register in Blocks 1 and 4 is the phase angle offset between the two commutation outputs and is set to 90 degrees to provide the sine and cosine multiplying values for the commutation (synchronous demodulation) of the displacement signal. The two outputs of Block 1 are filtered (not shown) by a controller filter function built into Block 2 and 3 (The sensor input is filtered before becoming the processed feedback input – See figure 2.). Blocks 2 and 3 respectively provide the servo compensation for the two control loops. The JOG input of Block 2 and 3 are normally set to zero and can be thought of as a DC offset to the filtered signals. If the following error is zero for the cosine path, the phase of the imbalance has been properly determined. If the following error of the sine path is zero, the imbalance has been effectively canceled by the voice coil forcer shown at the output of Block 5. The D/As near Block 2 and Block 3 are available as output analog signals which can be viewed with an oscilloscope or passed through external low pass filters to verify the correct values of the demodulation process. Block 4 uses the sine output to generate a sinusoidal command signal to Block 5 based on the amplitude of the error correction output of Block 2. Block 1 and 4 uses the virtual encoder (offset register label m399) developed from the sum of the actual encoder count and a count value derived from the output magnitude of Block 3. This is part of a feedback loop that adjusts the offset phase register m399. This adjustment continues until the following error at Block 3 reaches zero. When this occurs, the virtual encoder phase is

lined up with the maximum angular location of the unbalance. The filtered sine output is now at a maximum and through feedback, the value of this signal is now used by Block 4 to generate a harmonically clean sine signal whose amplitude will force the VC motor motion to produce zero at the filtered sine path input of Block 2. When this happens, the unbalanced displacement is exactly canceled by the voice coil actuator.

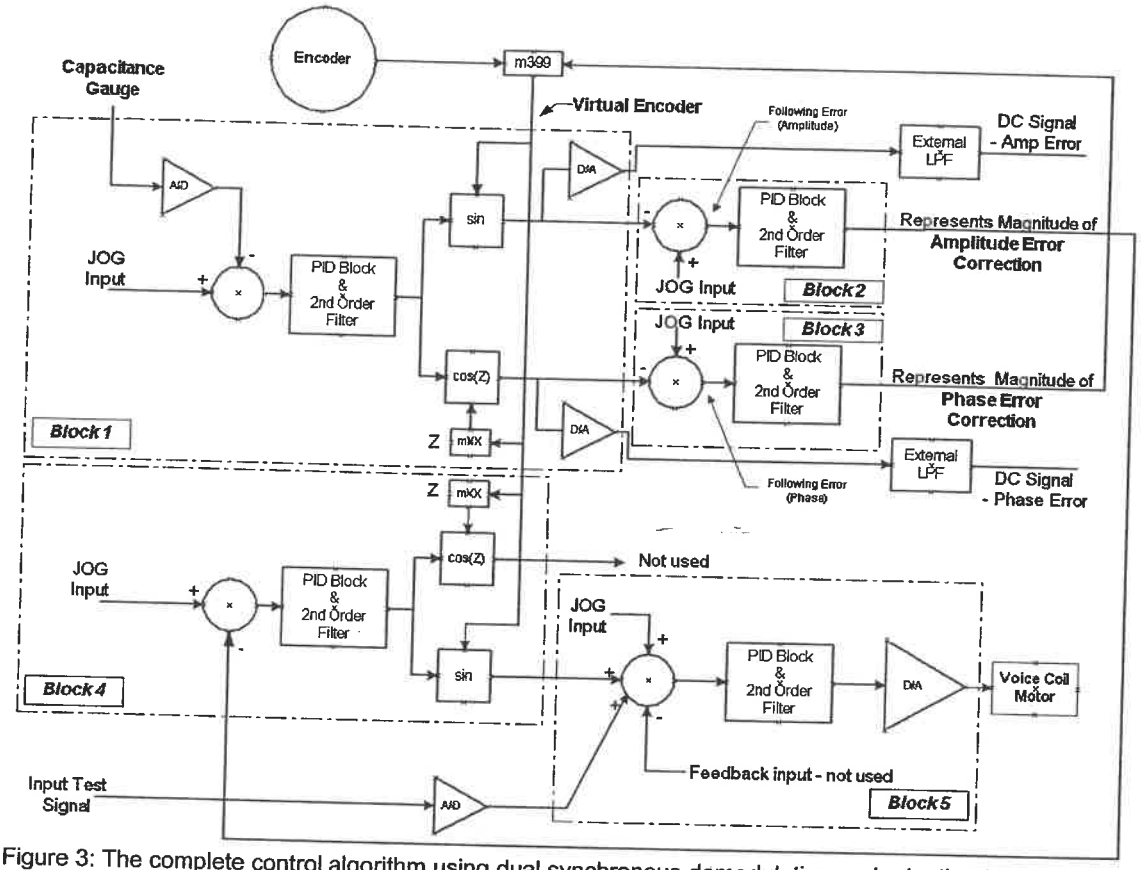

Figure 3: The complete control algorithm using dual synchronous demodulation and adaptive feedback control

Results

Figure 4 shows data plots of the displacement signals before and after activation of the control algorithm. It also shows the voice coil excitation command required to achieve the cancellation. The unbalance spindle produces approximately 50 nm of peak to peak motion at 200RPM. It can be seen that the fundamental component of unbalance is very well suppressed; however, higher frequency displacement signals now dominate the response.

Conclusion

The control algorithm of this test system has demonstrated the ability to adapt in real time to remove the fundamental component of the unbalance rotational force vector to nanometer levels caused by an unbalanced spindle. However, higher order structural resonance components of the test bed have been observed when the system is active. The control system is stable and the voice coil excitation is harmonically clean but the high Q (measured) of the mechanical system is apparently excited by energy leakage. The test bed was purposely designed to be mechanically compliant and potential resonances were not modeled. The test bed does not represent a well designed machine spindle; however, the results indicate the need to carefully examine the dynamics of any spindle system that would take advantage of this active system. Future work would concentrate on testing the control system on a real machine tool spindle or developing a more damped and better modeled mechanical test bed.

Reference

David J. Hopkins, Timm A. Wulff, George F. Weinert, "A Machine Tool Controller using Cascaded Servo Loops and Multiple Feedback Sensors per Axis", Proceedings ASPE Spring Topical Meeting Control of Precision Systems, April 2004.

This work was performed under the auspices of the U.S. Department of Energy by University of California, Lawrence Livermore National Laboratory under Contract W-7405-Eng-4.

The Effects of Asymmetrical Radial Stiffness in Precision Rotating Machines: The Duality of Fixed and Rotating Sensitive Directions

Timothy M. Dalrymple

Dalrymple, Inc., 1039 NE 3rd Street, Gainesville, FL 32601

University of Florida, Gainesville, FL 36205

Abstract

When radial forces act on the structural loop of a machine tool or gauge, errors arise due to finite, asymmetrical structural loop stiffness. For all fixed and rotating sensitive direction applications, the possible errors are as follows: size, nonconcentricity, and form (two—lobe). The type of the error depends on the state of the radial force and the state of the asymmetrically stiff structural loop element. The state of the force or the structural loop element may be either fixed or rotating relative to the fixed coordinate frame of the machine base.

Several authors and standards describe these errors for specific examples of fixed and rotating sensitive direction machine tools and gauges. This article extends this analysis and attempts to show the duality that exists between the fixed and rotating sensitive directions for machine tools and gauges. The purpose of this effort is to provide a systematic accounting of these errors in the uncertainty analysis as well as to provide a useful troubleshooting guide. The results are presented in the form of a structured table which covers all cases. Additionally, simple mathematical descriptions of the errors are presented in matrix and traditional form. Due to space considerations in this abstract, these results are presented separately as indicated.

The analysis presented here distinguishes between the following machine states: fixed or rotating sensitive direction; fixed or rotating asymmetrically stiff structural loop element; and fixed or rotating radial force. For each combination of sensitive direction, force, and structural loop element, the errors are categorized. Superposition may be used to combine individual states in order to analyze real machines with multiple forces and structural loop elements.

Experimental verification is presented for the two most interesting cases. Specifically, the effect of rotating unbalance and asymmetrical stiffness in the support structure for an air-bearing diamond boring machine is presented. Additionally, the effect of a radial gauge force on rotating asymmetrically stiff workpiece is shown for a roundness measurement. Both of these experiments show excellent agreement with the analysis presented.

Finally, the duality that exists between rotating and fixed sensitive direction applications for applied radial loads and asymmetrical stiffness. Through this duality, it is possible to show that the rotating and fixed sensitive direction states indicate a change in the location of an observer and thus the analysis of error is the same in both cases. Again, experimental results are presented to illustrate the duality of the fixed and rotations sensitive directions.

Keywords: asymmetrical stiffness, compliance, sensitive direction, axis of rotation, structural loop, precision machine design, dynamic stiffness.

Nomenclature:

Principal stiffnesses of rotating element k_{1_R}, k_{2_R} and of fixed element k_{1_F}, k_{2_F}

Components of fixed force in fixed frame W_{X_F} W_{Y_F}

Components of rotating force in rotating frame W_{X_R} W_{Y_R}

Phone 352-846-1212. email tmd@ufl.edu

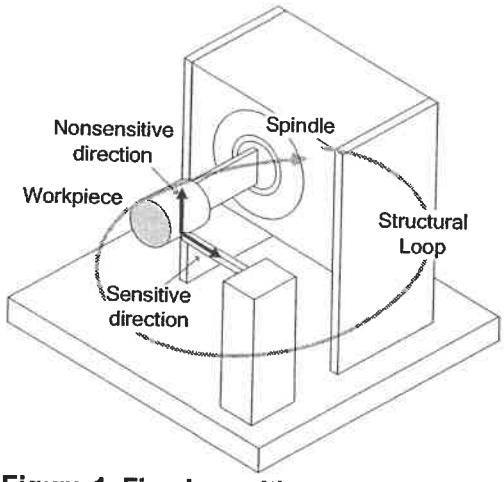

Figure 1 Fixed sensitive direction

Fixed sensitive direction

An example of a fixed sensitive direction application is shown Figure 1. This figure shows a lathe schematically and conceptually illustrates the possibilities for asymmetrical stiffness in elements in the structural loop. Specifically, the workpiece is shown to be attached to the spindle rotor by an element with a rectangular cross-section. For the angle of rotation shown, the rotating structural loop is stiffer vertically than horizontally. As the workpiece rotates, the orientations of the elements rotate. It can be shown that any linear structural loop element, such as the workpiece, chuck, or rotor, can be modeled as in this way regardless of the actual cross section of the material.

Additionally, this figure shows the possibility of asymmetrical stiffness in the spindle support. This is illustrated by a flexure where the vertical stiffness is higher than the horizontal stiffness. These orientations remain fixed as the spindle rotates.

The errors for all four possible cases are summarized graphically in Table 1. These cases are described in detail in the oral presentation and the forthcoming paper [1] where experimental confirmation of results for a precision roundness gauge.

[1] Dalrymple, T. M. The Effects of Asymmetrical Radial Stiffness in Precision Rotating Machines: Part 1 The Fixed Sensitive Direction, to be submitted to Precision Engineering at 2004 ASPE annual Meeting

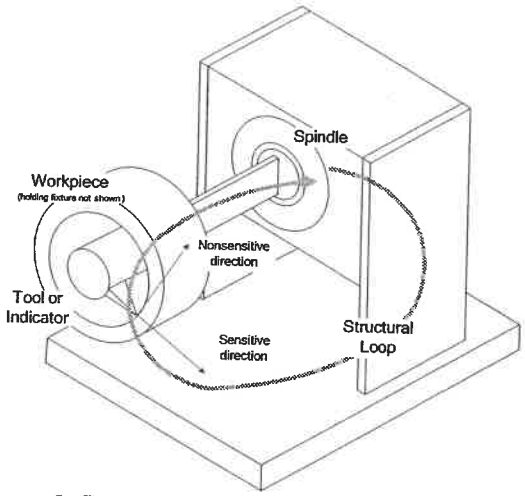

Figure 2 Rotating sensitive direction (work holder is removed

Rotating Sensitive Direction

Figure 2 shows a schematic example of a rotating sensitive direction machines such as a boring machine (or bore roundness gauge). This figure conceptually illustrates asymmetrically stiff in elements—both rotating and fixed—in the structural loop. Specifically, the tool or indicator is shown to be attached to the spindle rotor by a shaft with a rectangular cross-section. For the angle of rotation shown, the rotating structural loop is stiffer vertically than horizontally. As the tool or indicator rotates, the orientation of this element rotates.

Additionally, this figure shows the possibility of asymmetrical stiffness in the spindle support. This is illustrated by a flexure where the vertical stiffness is higher than the horizontal stiffness. These orientations remain fixed as the spindle rotates.

The results for all four possible cases are summarized graphically in Table 2. These cases are described in detail in the oral presentation and the forthcoming paper [2] where experimental results are presented for a diamond boring machine.

[2] Dalrymple, T. M. The Effects of Asymmetrical Radial Stiffness in Precision Rotating Machines: Part 2 The Rotating Sensitive Direction, to be submitted to Precision Engineering at 2004 ASPE annual meeting

Table 1 Fixed sensitive direction first order effects. Principal axes align with respective coordinate systems

Schematic illustration States of the Force(W)--Structural loop	Errors due to indicated applied forces	Machine Tool Example (negative sign on force applies)	Metrology Examples (positive sign on force applies)
Fixed-Fixed 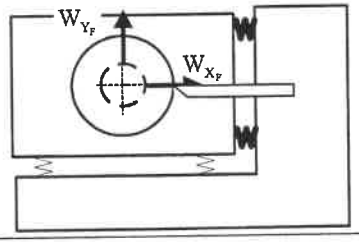	$k_{1_F} = k_{2_F}$ or $k_{1_F} \neq k_{2_F}$ $\mp W_{X_F}$: size $\mp W_{Y_F}$: none	Lathe with symmetrical or asymmetrical spindle support • W_{X_F} Normal cutting force • W_{Y_F} Tangential cutting force	Roundness gauge with symmetrical or asymmetrical spindle support • W_{X_F} Normal gauge force • W_{Y_F} Frictional gauge force
Fixed-Rotating 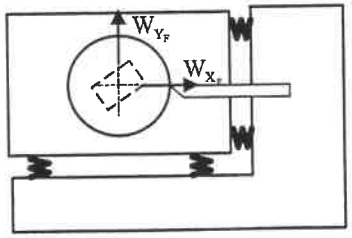	$k_{1_R} = k_{2_R}$ $\mp W_{X_F}$: size $\mp W_{Y_F}$: none	Lathe with symmetrical rotating elements • W_{X_F} Normal cutting force • W_{Y_F} Tangential cutting force	Roundness gauge no rotating asymmetries • W_{X_F} Normal gauge force • W_{Y_F} Frictional gauge force
	$k_{1_R} \neq k_{2_R}$ e.g. $k_{1_R} > k_{2_R}$ size & form / form	Lathe with asymmetrical spindle rotor or workpiece • W_{X_F} Normal cutting force • W_{Y_F} Tangential cutting force	Roundness gauge with asymmetrical spindle rotor or workpiece • W_{X_F} Normal gauge force • W_{Y_F} Frictional gauge force
Rotating-Fixed 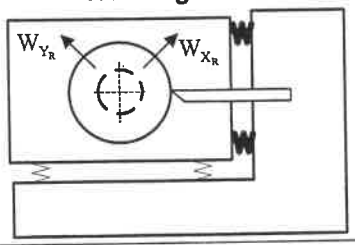	$k_{1_F} = k_{2_F}$ or $k_{1_F} \neq k_{2_F}$ $\mp W_{X_R}$: non-concentric $\mp W_{Y_R}$: non-concentric	Lathe with symmetrical or asymmetrical spindle support • W_{X_R} Rotating unbalance • W_{Y_R} Rotating unbalance	Cylindricity gauge with symmetrical or asymmetrical spindle support • W_{X_R} Rotating unbalance • W_{Y_R} Rotating unbalance
Rotating-Rotating 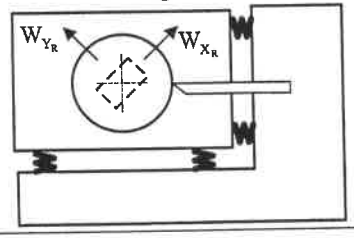	$k_{1_R} = k_{2_R}$ or $k_{1_R} \neq k_{2_R}$ $\mp W_{X_R}$: non-concentric $\mp W_{Y_R}$: non-concentric	Lathe with symmetrical or asymmetrical spindle rotor or workpiece • W_{X_R} Rotating unbalance • W_{Y_R} Rotating unbalance	Cylindricity gauge with symmetrical or asymmetrical rotor or workpiece • W_{X_R} Rotating unbalance • W_{Y_R} Rotating unbalance

Table 2 Rotating sensitive direction first order effects. Assume principal axes align with respective coordinate systems

Schematic illustration States of the Force(W)--Structural loop	Errors due to indicated applied forces	Machine Tool Example (positive sign on force applies	Metrology Examples (negative sign on force applies
Rotating-Rotating 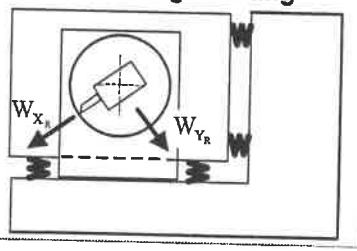 	$k_{1_R} = k_{2_R}$ or $k_{1_R} \neq k_{2_R}$ $\pm W_{X_R}$ | $\pm W_{Y_R}$ 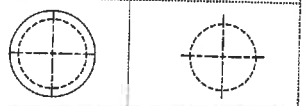 Size | none	Boring Machine with symmetrical or asymmetrical boring bar • W_{X_R} unbalance or normal gauge force • W_{Y_R} unbalance or tangential gauge force (friction)	Roundness bore gauge with symmetrical or asymmetrical probe extension • W_{X_R} unbalance or normal gauge force • W_{Y_R} unbalance or tangential gauge force (friction)
Rotating- Fixed 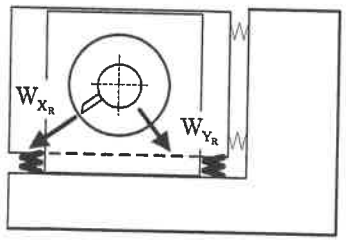 	$k_{1_F} = k_{2_F}$ $\pm W_{X_R}$ | $\pm W_{Y_R}$ 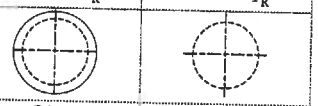 Size | none	Boring machine with symmetrical spindle support • W_{X_R} unbalance or normal cutting force • W_{Y_R} unbalance or tangential cutting force	Roundness bore gauge with symmetrical workhead support • W_{X_R} unbalance or normal gauge force • W_{Y_R} unbalance or tangential gauge force (friction)
	$k_{1_F} \neq k_{2_F}$ e.g. $k_{1_F} > k_{2_F}$ $\pm W_{X_R}$ | $\pm W_{Y_R}$ 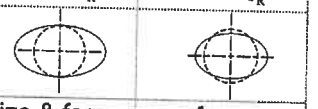 size & form | form	Boring machine with asymmetrical spindle support • W_{X_R} unbalance or normal cutting force • W_{Y_R} unbalance or tangential cutting force	Roundness bore gauge with asymmetrical workhead support • W_{X_R} unbalance or normal gauge force • W_{Y_R} unbalance or tangential gauge force (friction)
Fixed-Rotating 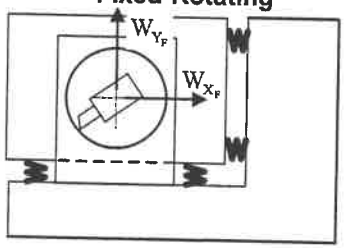 	$k_{1_R} = k_{2_R}$ or $k_{1_R} \neq k_{2_R}$ $\pm W_{X_F}$ | $\pm W_{Y_F}$ non-concentric | non-concentric	Horizontal boring machine with symmetrical or asymmetrical boring bar • W_{X_F} none • W_{Y_F} gravity	Horizontal bore gauge with symmetrical or asymmetrical probe extension • W_{X_F} • W_{Y_F} gravity
Fixed-Fixed 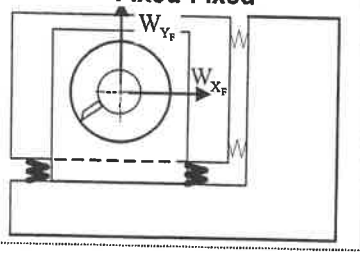 	$k_{1_F} = k_{2_F}$ or $k_{1_F} \neq k_{2_F}$ $\pm W_{X_F}$ | $\pm W_{Y_F}$	Horizontal boring machine with symmetrical or asymmetrical spindle support • W_{X_F} • W_{Y_F} gravity	Horizontal roundness bore gauge with symmetrical or asymmetrical spindle support • W_{X_F} • W_{Y_F} gravity

A 10 kHz Short-Stroke Rotary Fast Tool Servo

Richard C. Montesanti [a,b], David L. Trumper [b]
[a] Lawrence Livermore National Laboratory, Livermore, CA
[b] Massachusetts Institute of Technology, Cambridge, MA

Keywords: fast tool servo, variable reluctance actuator, diamond turning, textured surface

Introduction

This paper presents an overview of the design of our 10 kHz rotary fast tool servo (FTS) with an emphasis on the trade-offs made in this design. The heart of the design is a normal-stress variable reluctance actuator which allows the 1000 g tool tip acceleration required to follow a 5 micron PP sinusoidal trajectory at 10 kHz. At the time that this paper is written (August 2004) the design is complete, and the mechanical, magnetic, and electrical components for a 500 g version of the FTS are being fabricated.

The use of a fast tool servo with a diamond turning machine for producing non-axisymmetric or textured surfaces on a workpiece is well known. A rotary fast tool servo produces an in-and-out motion of the tool relative to a workpiece by swinging the tool along an arc having a fixed radius. Achieving this motion by applying a pure torque to the moving mass of the FTS leads to a reaction torque that is imparted to the machine supporting the FTS. In certain machining applications, for instance, producing a textured surface on a spherical workpiece, a reaction torque on the machine is preferable over the reaction force that a linear type FTS produces. The undesired lateral motion of a tool travelling along an arc can be made negligibly small by choosing an appropriate combination of tool travel and swing radius, and by setting the geometry of the tool arm so that the tangent plane on the workpiece containing the tool tip passes through the axis of rotation of the FTS.

Being able to control a fast tool servo at 10 kHz requires that the mechanical resonant modes be well above that frequency. Achieving a 1000 g tool tip acceleration requires a rotor and payload combination having a high torque-to-inertia ratio. A typical servo system usually has an actuator with its own moving mass connected to a payload through a coupling. In that case, the finite stiffness of the coupling results in an uncoupled resonant mode for the two lumped masses. We have merged the moving masses of our actuator and the payload into a single moving mass by attaching the tool arm directly to the rotating element of the actuator. By getting rid of the uncoupled mode, the first mechanical resonance is at a relatively higher frequency non-rigid body mode of the moving mass structure. Additionally, the merged mass approach results in a lower overall moving mass and a higher torque-to-inertia ratio. Placing the feedback sensor directly behind the tool and careful design of the support structure allows hiding certain flexible modes of the system to further improve high frequency performance.

Following the flexure design used in our earlier 2 kHz rotary fast tool servo [1], the 10 kHz rotary FTS uses an over-constrained flexure suspension for guiding the rotary motion and providing the stiffness needed for diamond turning a workpiece. The power amplifier and control system designed for the new actuator is also similar to the one used in our 2 kHz system [2], and will not be discussed further in this paper.

Normal-Stress Variable Reluctance Actuator

Our normal-stress variable reluctance actuator is designed to produce a magnetic force density an order of magnitude higher than the force density of a typical Lorentz-force actuator or shear-stress variable reluctance actuator. Figure 1 shows a model of the magnetic circuit for this actuator.

The rotor core is a rectangular prism suspended between two opposing C-shaped stator cores with nominal air gaps of 50 μm at the four pole faces. The rotor and stator cores are made of laminated soft magnetic material to reduce the hysteretic and eddy current losses associated with the AC flux. The DC coil provides a biasing magnetic flux in the four air gaps. Each stator core with its two AC coils forms a magnetic circuit with the rotor core. Considering one of the stator cores, energizing its AC coils in a manner that produces flux in a common direction creates a steering flux that circulates around that stator core and the rotor core via the two air gaps between the two. The bias and steering fluxes add at one of those gaps and subtract at the other. The same thing occurs between the other stator core and the rotor core. With proper phasing of the AC fluxes in the two stator cores and balanced magnitudes of DC and AC fluxes, the fluxes can be made to add in diagonally opposed air gaps and subtract in the opposite diagonally opposed air gaps, resulting in a net torque on the rotor with nominally no net force on it. One benefit of the DC magnetic bias is that it linearizes the torque versus current relationship for the actuator. Another benefit is that it reduces the reactive electrical power needed to drive AC flux in the air gaps by a factor of four compared to a non-biased magnetic circuit. The use of a DC magnetic bias can be found in other actuator designs, for instance, in certain electric engraver designs dating back to at least 1937.

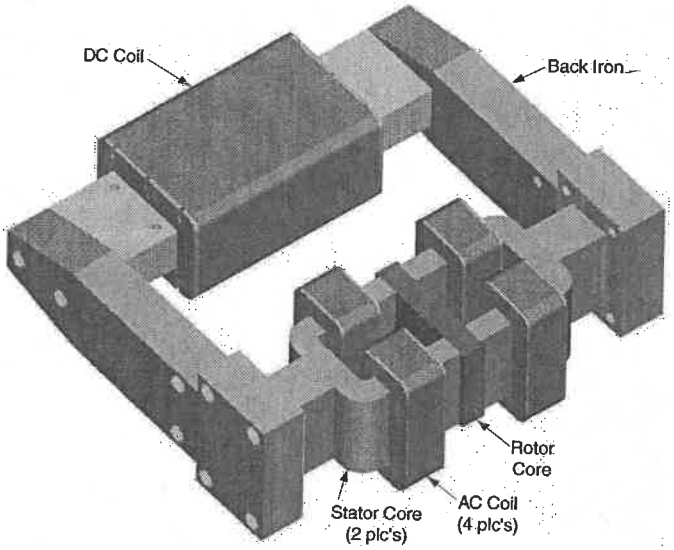

Figure 1: Model of the magnetic circuit for the normal-stress variable reluctance rotary actuator.

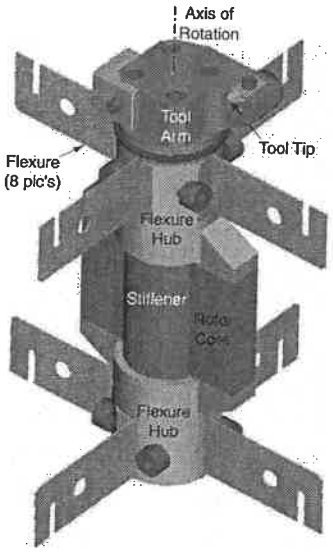

Figure 2: Model of the rotor with a tool arm and flexure suspension.

Figure 2 shows a model of the rotor with an attached tool arm and flexure suspension. The rotor core lamination layers are perpendicular to the axis of rotation. The rotor core is supported by stiffeners on its front and back, and by the flexure hubs at its top and bottom. The flexures are constrained at their inner ends by the flexure hubs and at the outer ends by a stationary support structure, and establish the axis of rotation for the rotor. Referring to Figure 3, the two stiffeners and the two flexure hubs encircle the rotor core. Making the stiffeners from a ceramic material provides high stiffness and avoids having a conducting loop that would produce eddy current power loss by linking the AC magnetic flux in the rotor core. The rotor core, stiffeners, and flexure hubs are joined together with an adhesive. The adhesive joints are designed so that the volumetric shrinkage of the adhesive upon curing causes the stiffeners to be preloaded in tension and the rotor core to be preloaded in compression. This is particularly important for the rotor core because tensile stress in the axial direction, and especially cleavage stresses, could lead to delamination of the core.

Figure 3: Model of a cross-section of the rotor.

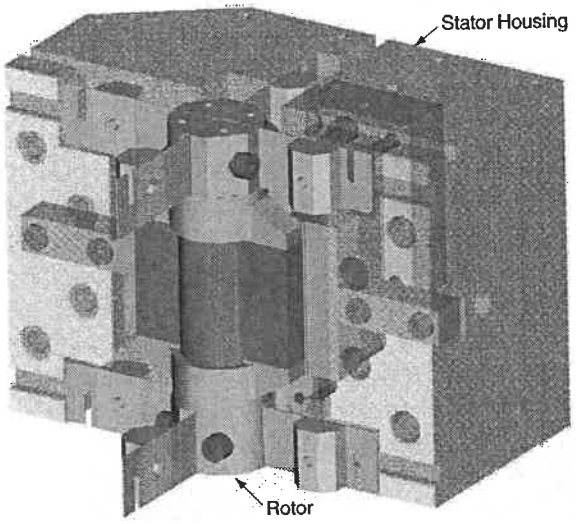

Figure 4: Model of the rotor mounted to one of two stator halves with flexures.

Overview of the Design

Figure 4 shows a model of the rotor mounted to one of the stator housings via the outer ends of four of the eight flexures. In a previous assembly step the stator pole faces are machined relative to the flexure mating surfaces on the stator housing to allow establishing the 50 μm air gaps between the stator and rotor cores. Shims are provided to accommodate any stack-up of manufacturing and assembly errors. The other stator half is added to what is shown in Figure 4 to complete the magnetic circuit and provide a stiff support structure for the rotor, which is essentially encased in a solid block of metal with openings provided for the stator cores, AC coils, flexures, and the flow of cooling fluid.

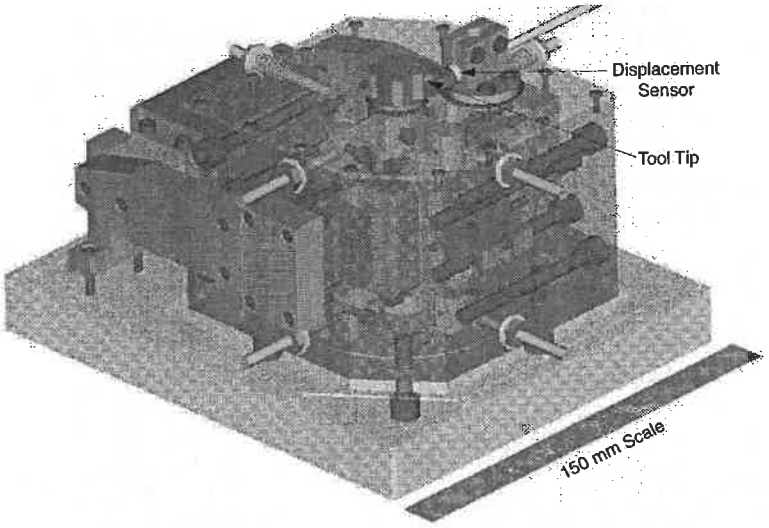

Figure 5: Model of the 10 kHz rotary fast tool servo.

Figure 5 shows a built-up model of the 10 kHz rotary fast tool servo. A capacitance gauge measures the displacement of the tool arm at a location just behind the tool. The FTS is designed for a

maximum stroke of 10 μm peak-to-peak (PP) at low frequencies and was initially designed for a 5 μm PP stroke at 10 kHz (1000 g). The maximum stroke was made smaller than the 50 μm peak-to-peak (PP) stroke of our 2 kHz rotary FTS to allow tailoring the flexure suspension stiffness and fatigue stress level for 10 kHz operation. The designed stroke at 10 kHz was reduced to 2.5 μm PP (500 g) during a trade-off between having a more mechanically robust system versus the more fragile light-weighted rotor needed for 1000 g. We felt it more important to have a proof of principle that was more likely to survive anticipated tests for this first prototype, and expect to adjust design parameters in future versions to achieve 1000 g and beyond.

Referring back to Figures 3 and 4, the dimensions of the rotor core are determined by a trade-off analysis driven by closed-form equations relating those dimensions and the matching dimensions of the stiffeners and flexure hubs to the power losses in the rotor and stator cores, reactive electrical power required to drive the AC flux in the air gaps, current density and cooling requirements for the AC coils, rigid body and non-rigid body first modes of the rotor, and tool acceleration for a 1.5 Tesla peak flux density. Finite element analysis is used to determine the frequency of the first non-rigid body modes of a selection of rotor geometries to provide a bounding analysis for the design space, and agreed with the closed-form equations. Also folded into the trade-off was the attractiveness of using the same design for the flexure mounting hardware that proved successful in our earlier 2 kHz rotary FTS.

For the 500 g version of the FTS that we are currently building, the first non-rigid body mode of the rotor is a torsional mode at 22 kHz that drops to 18 kHz when the tool arm is added. This makes our planned operation at 10 kHz challenging, but with provisions in the design for adding squeeze-film damping and in the spirit of keeping the control system challenging enough for this PhD research work we decided it was acceptable.

Summary

This paper presents an overview of the design of our 10 kHz rotary fast tool servo (FTS) as well as some of the trade-offs made in that design. The novel normal-stress variable reluctance actuator is presented in detail to provide insight into the highly integrated electromagnetic and mechanical designs needed for achieving 1000 g tool tip acceleration and to operate at frequencies up to 10 kHz.

As this work progresses, we will assemble the mechanical, magnetic, and electrical hardware; develop and integrate the control system; characterize the FTS performance with bench tests; and integrate the FTS with a diamond turning machine to perform cutting tests on a workpiece.

Acknowledgments

This work was supported by the Lawrence Livermore National Laboratory through a Laboratory Directed Research and Development project. In accomplishing this work, we would like to acknowledge helpful discussions with MIT Professors James L. Kirtley Jr., Samir A. Nayfeh, and James K. Roberge, and our colleagues in the Precision Motion Control Laboratory at MIT.

References

[1] Richard C. Montesanti and David L. Trumper. *High Bandwidth Short Stroke Rotary Fast Tool Servo.* Proceedings of the American Society for Precision Engineering 2003 Annual Meeting, Volume 30, pages 115–118.

[2] Richard C. Montesanti and David L. Trumper. *Design and Implementation of the Control System for a 2 kHz Rotary Fast Tool Servo.* Proceedings of the American Society for Precision Engineering Spring Topical Meeting on Control of Precision Systems, April 2004, pages 28–33.

TWO-AXIS FORCE-FEEDBACK DELFECTION COMPENSATION OF MINIATURE BALL END MILLS

Karl Freitag, Thomas Dow
Precision Engineering Center, North Carolina State University

INTRODUCTION

The fabrication of injection molding dies is an application of interest for this research. These dies are machined from hard steels (Heat treated to ~ 60 Rockwell C) to provide durable, wear resistant dies. Manufacture of these dies containing small features or precision surfaces require the use of tools with small radii. The tools required for such machining (Diameters < 1.0 mm) termed miniature tools are the focus of this research. These tools are available in several different shank lengths to accommodate various applications and die geometries. Figure 1 contains a photograph of the 0.8 mm diameter miniature ball end mills used. The tools are made of tungsten carbide with a titanium aluminum carbide coating. Although the tool material is very strong, the thin geometry of these tools results in low tool stiffness (0.2 N/μm and less) which becomes a significant factor machining heat treated steels. Deflections of these tools under low (10N) cutting forces can produce part errors of 50 μm with a 4.0 mm long shank. The goal of this research is to reduce tool deflection errors through the use of force-feedback machining. In previous research at the PEC, Hood [1] used the machine axes to compensate deflection of the tool normal to the part. In this compensation technique, the inertia of the machine axes becomes a limiting factor to the response speed of the system. To achieve higher bandwidth, Clayton [2] designed a single-axis tool actuator on the spindle with a force transducer for measuring cutting forces. The present work continues this focus by describing the performance of a two-axis force feedback spindle that measures and compensates for tool deflections in two orthogonal directions.

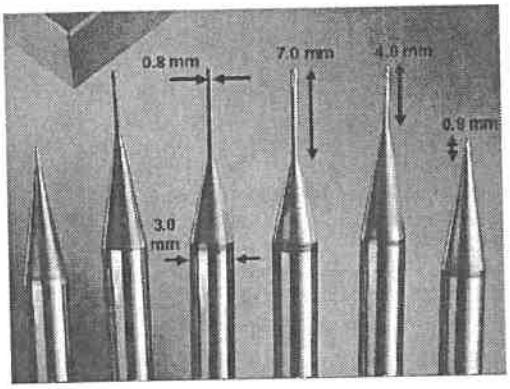

Figure 1. Miniature Ball End Mills

DESCRIPTION OF APPARATUS

The two-axis force feedback actuator uses piezo electric actuators to produce the tool displacement, flexures to guide the displacements, and capacitance gages to provide closed loop position feedback. The spindle actuator assembly contains two 3-axis piezoelectric load cell (Kistler Model 9251) mounted beneath an air-bearing machining spindle and above the actuation platform (See Figure 2). The load cell location was moved from the previous single transducers designs to better measure the real time cutting forces. The load cell was located such that the actuation forces could affect its reading reading. Separation of this force loop in the new design allows more accurate measurement of the cutting forces with minimal interference from the actuation forces.

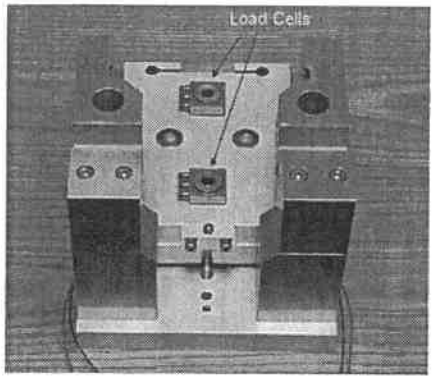

Figure 2. Force Measurement Platform

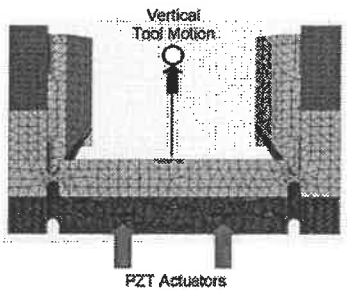

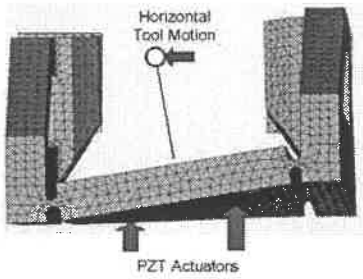

Figure 3. Horizontal and Vertical Tool Actuation

The two load cells are spaced evenly about the spindle's center of gravity to reduce the effects of in-phase or out-of-phase spindle vibration in processing of the force signal. Beneath the force measurement platform are two piezoelectric actuators used to produce the horizontal and vertical tool motion. The two actuators are driven differentially to produce horizontal motion and driven in parallel to produce vertical motion (See Figure 3). The structure contains two different flexure axes for the horizontal and vertical actuation to eliminate undesired tool displacement in the axial direction of the tool. The vertical axis is located in line with the tool center to prevent axial displacement while the horizontal axis is offset from the tool centerline to allow the horizontal actuation (See Figure 4). A photograph of the actuator assembly is shown in Figure 5.

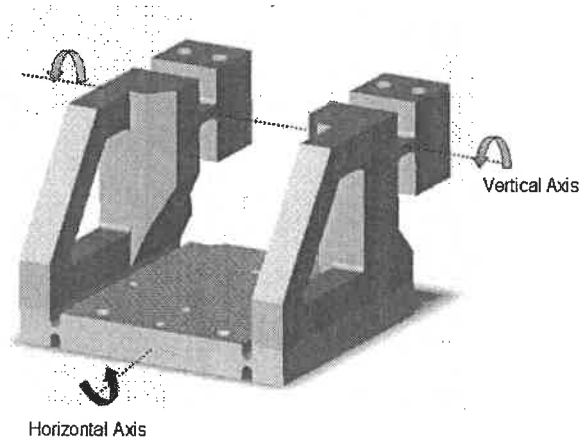

Figure 4. Horizontal and Vertical Flexure Axes

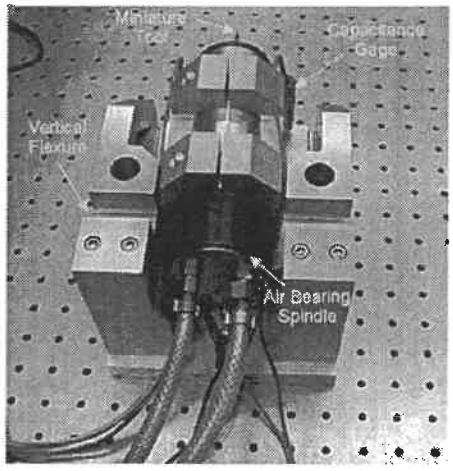

Figure 5. Spindle Actuator Assembly

The acutation system is a two-input two-output system where the displacement at each piezo stack affects both the horizontal and vertical tool position. Control of the actuator is achieved through decoupling of the horizontal and vertical dynamics. Proportional Integral (PI) control is used to control the horizontal and vertical systems separately and then recombined to solve for the individual voltage to each actuator. The horizontal controller produces the differential voltage between the two piezoelectric stacks while the vertical controller produces a sum. The command following of the two-axis actuator was evaluated with an 8 μm square profile. The square motion profile in Figure 6 was carried out in a total time of 500 ms. The entire force

feedback control algorithm is shown below in Figure 7 where the horizontal and vertical tool forces are first measured to produce a desired horizontal and vertical tool position. The two axis controller then positions the tool to the desired position using capacitance gage closed loop feedback.

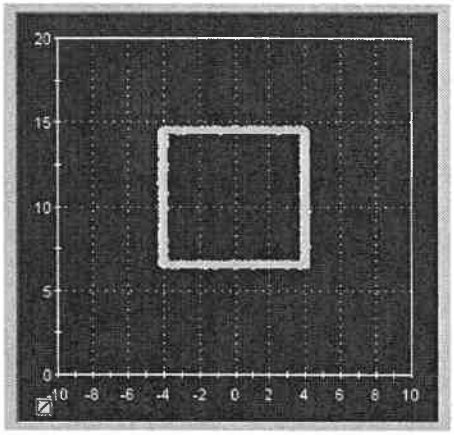

Figure 6. Command Following 8μm Square, 500ms

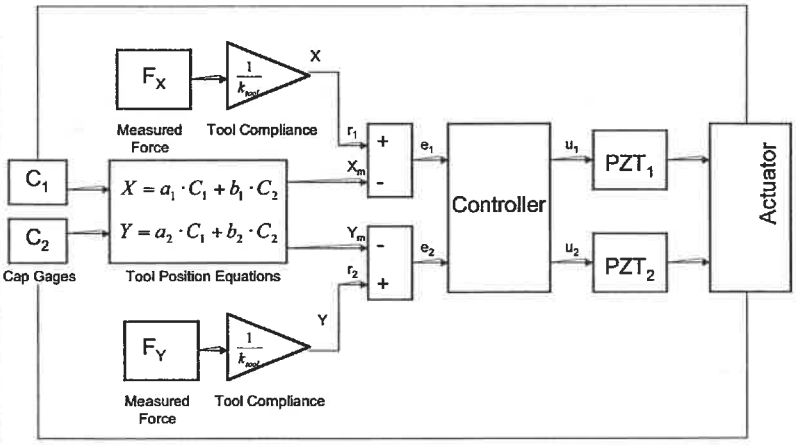

Figure 7. Force Feedback Control Algorithm

EXPERIMENTAL VERIFICATION

To exercise the two-axis force feedback actuator, two 3-dimensional surfaces were raster cut using the force feedback spindle actuator and a fixed spindle for comparison. The two axis spindle actuator was mounted on the Y (Vertical) axis of a Nanoform 600 DTM (Figure 8). The parts were raster cut feeding left to right along the X-axis and using the Y-Axis to provide the cross feed. A 5 mm diameter hemisphere was cut using both the force feedback spindle and a fixed spindle for comparison. A photograph of the raster cut hemisphere is shown in Figure 9. Probe interference when using the Talysurf profilometer near the walls of the hemisphere made it difficulty to obtain accurate measurements of this shape. A four-sided frustum was selected to improve measurement capability. The dimensions of four sided frustum are a 5mm square with a 1mm square located 1.5mm deep (Figure 10). The finished feature was measured by scanning across it with the profilometer. The machining forces for this geometry result in deflection of the tool in both of the active directions of the system as shown in Figure 11. A comparison of the surfaces produced by the force feedback spindle and the fixed spindle are shown in Figure 12.

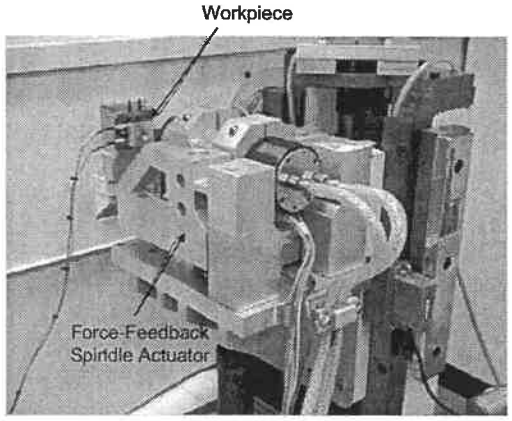

Figure 8. Experimental Apparatus

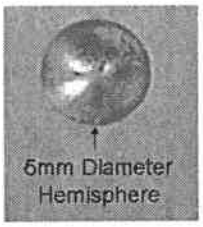

Figure 9. 5mm Hemisphere

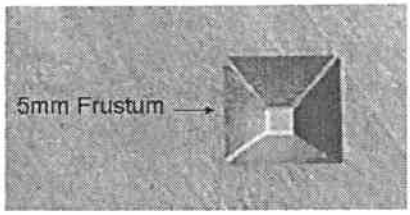

Figure 10. 5mm 4-Sided Frustum

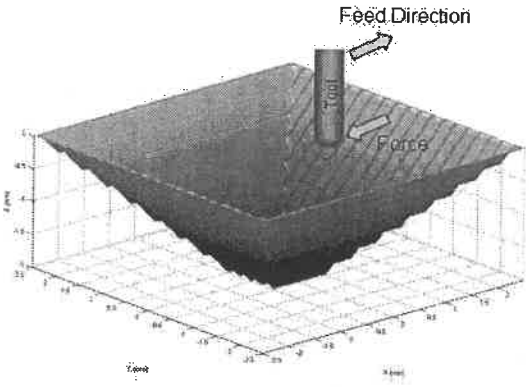

Figure 11. Feed Direction and Tool Force Direction

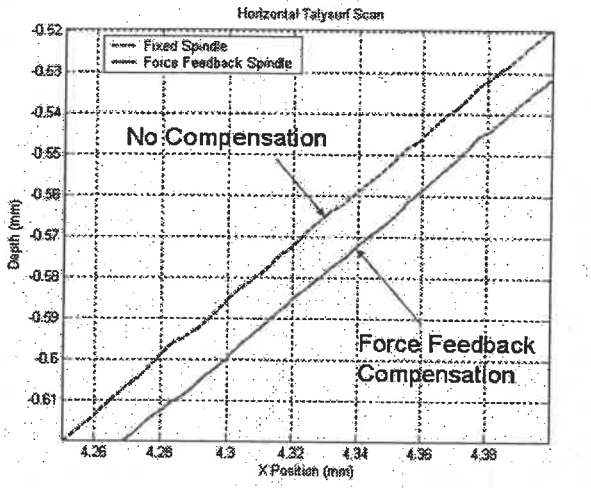

Figure 12. Part Measurement Comparison

Here the error for tool deflection is corrected by moving the tool into the part by approximately 15μm over the uncompensated profiles.

The machining parameters of the four-sided frustum were first a rough cut using a cross feed (ΔY) of 250μm and increasing depth (ΔZ) of 200μm until the rough cut depth of 1.2mm was achieved. A federate of 50mm/min was used for both the rough cut and final pass. The final pass was a 300μm depth of cut with 100μm cross feed (ΔY) to obtain the final part geometry.

CONCLUSIONS

The mechanical design of the 2-axis system allows the machining force in each direction to be independently measured and the tool end positioned to compensate for the resulting deflection. Two 3-axis load cells are used to measure the force and the correction is made with two piezoelectric actuators that use capacitance gages for position feedback. Techniques for capturing the peak force, using that force along with the tool compliance to create a positioning error, comparing that error with the cap gage readings and sending the filtered commands to the actuators have been developed and demonstrated. Two machined features are described: a 5 mm radius hemisphere and a 5 mm wide 4-sided frustrum. Each surface was machined using a raster scan technique and the magnitude and direction of the machining forces were measured and tool deflection compensated. Error in final part geometry due to tool deflection was reduced by 15μm through the implementation of force feedback compensation.

REFERENCES

1. Hood, D., Clayton, S., Buckner, G., Dow, T., Garrard, K., "Closed Loop Control of Milling Tool Deflection", ASPE Proceedings, Vol. 27, pg 623.
2. Clayton, S. Freitag, K , Dow, T.A., "Closed Loop Control of Tool Deflection", ASPE Proceedings, Vol. 30, 2003, pg 459.

Manufacturing Technologies for Polymer Microsystem

Volker Saile
Universität Karlsruhe and Forschungszentrum Karlsruhe, Institut für Mikrostrukturtechnik
Hermann-von-Helmholtz-Platz 1, 76344 Eggenstein-Leopoldshafen, GERMANY

Silicon-based micro-machining technologies have been highly successful in the marketplace, in particular, with systems for automotive and digital display applications. However, other materials such as polymers, metals and ceramics offer additional properties – e.g., electrical, magnetic, temperature -, and can provide superior performance and lower cost for many micro- and nano-system applications, e.g., in life sciences and optics, or for actuators.

Research and development efforts of the Institute for Microstructure Technology (IMT) at Forschungszentrum Karlsruhe (FZK) are focused on fabricating polymer and metal micro-components and -systems. Two process lines have been established for manufacturing such devices in compliance with an ISO 9001:2000 quality management system. The customers of the fabrication-lines include in-house researchers, external academic users, and industrial companies. The first technology, LIGA – a German acronym for deep X-ray lithography with synchrotron radiation, electroplating, and replication by hot-embossing or injection molding, allows for patterning X-ray sensitive resist with structural heights of up to several mm, very high aspect ratios, sub-micron feature details, and optically smooth sidewalls. Applications of the LIGA technology are predominantly in micro-optics and in mechanical components. The second technology, named AMANDA, uses replications processes such as injection molding and hot embossing for batch fabrication of precise housings. Lithographically patterned polymer or glass membranes bonded between two housing components provide specific functions, e.g. as strain gauges or actuators. Typical applications include miniaturized pumps, valves, pressure and flow sensors as well as biochip systems.

LIGA Technology

The LIGA technology (LIGA is a German acronym for Lithographie, Galvanoformung, Abformung, which stands for Lithography, Electroforming, and Replication) was invented in Germany in the 80's [1], originally for the production of fluidic devices with micron-sized lateral features and high aspect ratios. The basic processing sequence is as follows (see Fig.1): A pattern on a X-ray mask is transferred with synchrotron radiation to a thick PMMA (or SU-8) resist layer bonded to or cast onto a conductive substrate (deep X-ray lithography step). After development, the resist relief serves as a template for an electroforming step leading to an inverse metal pattern with a solid base plate generated by over-plating. The metal structure is separated from the substrate and the resist and can now be employed as a super-high precision mold for mass production in injection molding or hot-embossing (replication step). Several varieties of modified LIGA-processes have been developed over the years such as replacing the synchrotron X-ray lithography step by UV-lithography with EPON SU-8 resist ("low-cost LIGA" or "UV-LIGA") or by by-passing the replication process by "Direct-LIGA", where components are fabricated directly with X-rays similar to semiconductor component production. Direct-LIGA offers attractive features such as high yield and highest precision. However, it suffers from long X-ray exposure time for each component with associated high cost and low throughput. Therefore, this technology has been limited to fabrication of prototypes and small volume production for niche markets such as mechanical components with extreme requirements on dimensional precision, sidewall verticality and roughness (see Fig.2). Currently efforts are made towards reducing cost and increasing throughput by using higher sensitivity resists such as SU-8 and/or developing X-ray scanner tools for large area exposures. Such a novel LIGA fabrication line has been proposed by an industrial consortium and will be constructed within the next three years at the ANKA synchrotron facility of Forschungszentrum Karlsruhe.

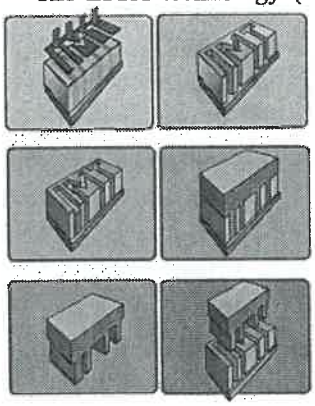

Fig.1: LIGA process sequence. From left to right and top to bottom: X-ray exposure and development; electroplating; metal mold and replication process.

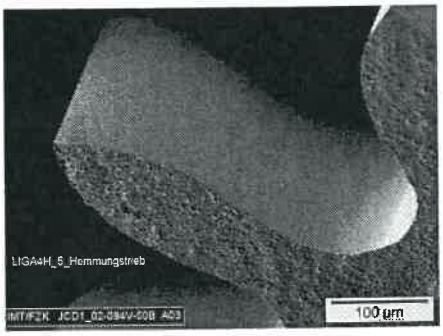

Fig.2: High-precision Ni micro-gear with some 10 nm rms roughness for the sidewalls.

Micro-Optics Applications

For applications in micro-optics, LIGA provides highly attractive features [2]: Typical LIGA components are made of polymers offering a broad range of materials that can be tailored to specific requirements. State-of-art LIGA allows for features with lateral dimensions in the μm range, feature details down to 200 nm, and heights of typically several hundred μm, if required even several mm. The sidewalls of LIGA components are inherently optically flat with surface roughness of the order of some 10 nm. The lateral pattern is determined by the mask layout and in the vertical direction straight sidewalls with inclinations in the mrad range are obtained. Non-vertical walls and more complex, true 3-D structures can be realized by tilting and/or rotating mask and substrate during exposure. Two principle concepts have emerged for micro-optical devices: In the first one, LIGA precision in patterning of polymers, either directly with X-rays or in a replication process with a LIGA mold, is exploited for fabricating complex optical wave-guides, with sidewalls providing optical functions such as those of gratings or mirrors.

In the second concept [3], the high aspect ratio capabilities of LIGA combined with excellent spatial resolution and patterning accuracy over large field sizes are utilized for producing optical benches, base plates and high precision mechanical holders and fixtures. The accuracy of patterning such structures, even in multiple levels, is ideally suited for assembly and packaging of hybrid optical systems at micron or sub-micron precision without the need for active alignment [3]. Fig. 3 shows an example for such a micro-optical system, a Fourier transform infrared spectrometer 4. It is essentially a Michelson interferometer that consists of an optical bench for the passive alignment of the optical components, and an integrated actuator. The optical bench and the actuator are made of Permalloy with a height of 380 μm. The dimensions of the complete system are 11.5x9.4 mm^2.

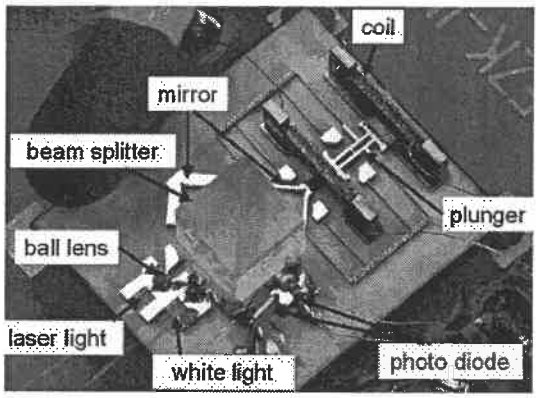

Fig.3a: Spectrometer with optical bench and optical components. The electro-magnetic actuator is on the right hand side (see coils).

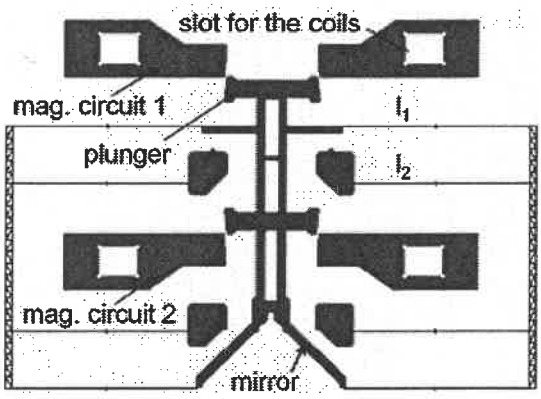

Fig.3b: Schematic view of the actuator with magnetic circuits. The coils are inserted into the slots as indicated.

The light that shall be analyzed is delivered to the system via an optical fiber. It is collimated with a fused silica ball lens with a diameter of 650 μm. At the beam splitter the light is separated into two rays, one reflects off the fixed mirror, the other travels towards the movable mirror. Both rays are reflected and travel back to the beam splitter, where they interfere with each other. The interference signal is recorded with an InGaAs PIN photodiode, which is sensitive in the wavelength range of 850-1700 nm. For the recording of the signal the position of the movable mirror has to be determined very precisely. For this purpose monochromatic laser light is used. The laser light is also delivered to the spectrometer through an optical fiber and propagates in a second optical channel parallel to the "white light" to be analyzed. The actuator is a variable reluctance motor. Fig.3b shows the movable plunger which is attached to a set of four folded cantilever beams and which is surrounded by stationary core structures thus forming two magnetic circuits that are driven by two coils. Since variable reluctance motors only deliver pulling forces the displacement length was increased by using two coils, one for pulling the plunger towards the beamsplitter, the other to pull it to the opposite direction. The mechanically wound coils are inserted into slots patterned in the stationary part of the magnetic circuit. For spectral analysis the optical components, beamsplitter and lenses (see Fig.3a), are assembled on the optical bench. In first tests laser light with a wavelength of 1540 nm was delivered to the spectrometer through a monomode fiber that ensures a good collimation of the beam. With only one coil activated and a displacement of the actuator of 54 μm a spectral resolution of 25 nm was obtained.

LIGA-based replication processes enable medium and high-volume production of polymer optical components and devices at low-cost and high-performance. The technical viability of the LIGA-approach for fabricating micro-optics components, devices and systems has been demonstrated for a variety of application cases such as micro-spectrometers for different wavelength ranges, wave-guides for splitters or star couplers, optical cross connects, optical matrix switches, and others. However, the final goal is transfer of the technology to industries. In this respect, IMT's most successful product is the micro-spectrometer which was originally invented and developed at IMT and which is now produced by the German company Steag microParts and distributed to customers worldwide [5].

In addition to application driven R&D, novel ideas with LIGA are currently pursued by scientists, e.g., investigating three dimensional photonic band gap structures by extending the lithographic process to inclined geometries and multiple exposures [6]. X-ray lenses may serve as an example for science-driven new LIGA applications. Such lenses exploit the tiny difference in refractive indices between matter and vacuum (or air) for focusing X-rays; that of vacuum or air is slightly higher and, therefore, holes in a material serve as lenses. For useful focal lengths many lenses have to be assembled in a long chain along the optical axis. Recently, such lens systems were produced with LIGA techniques and tested with excellent results 7. The lithographic process allows for producing, in parallel, several different lens systems on one substrate, e.g., for different wavelength ranges and/or focal lengths. Furthermore, after making the X-ray mask, many lens systems can be printed with that mask. The lateral geometries can be chosen absolutely free for optimization of optical properties and correction of aberrations. Two materials have been employed for the matrix in which the air lenses are embedded: SU-8 Epoxy for lower photon energies 5–50 keV and electroplated Ni for higher energies >40 keV. A major breakthrough for X-ray lenses was the use of the negative tone SU-8 resist that can be patterned to high accuracy with deep X-ray lithography. When exposed to X-rays, the polymer chains cross-link and the unexposed volume is removed in the development process. The cross-linked areas, however, are rather stable upon further irradiation. They can be directly used for X-ray lenses even when exposed to high intensity X-ray beams. A large variety of different lens designs (Fig.4), for linear as well as double focusing, have been tested recently at various synchrotron radiation facilities and the results have been compared to theoretical calculations. For an X-ray beam from the ESRF facility in Grenoble dimensions for the focal spot size as small as 300-900 nm were obtained limited only by the de-magnified X-ray source size, by diffraction and by fabrication inaccuracies.

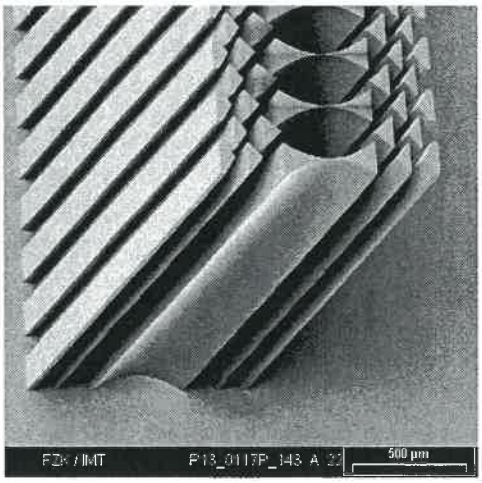

Fig.4: Section of a "mosaic" lens system for 15 to 20 keV photon energy. Height of the structures is 1000µm. The lenses are tilted with respect to the substrate surface. A second lens system following this one is tilted to the other side. By such an arrangement a point focus can be achieved rather than a line focus.

AMANDA Technology

AMANDA is an acronym for Surface micromachining, molding, and diaphragm transfer (in German: *Abformung, Oberflächenmikromechanik und Membranübertragung*) [9]. Fig.5 shows the principle of the technology in fabrication of a pressure sensor as an example.The housing parts of a micro-fluidic component are manufactured by polymer molding from a thermoplastic material, which is selected for complying with the requirements of the specific application. A membrane (diaphragm), typically polyimide, is separately fabricated on a substrate employing thin film processes. Metallic sensor or actuator elements are patterned by lithographic methods onto the membrane. The housing parts and the patterned membranes are bonded together by adhesives or other techniques, followed by integration of fluidic and as electrical connections.

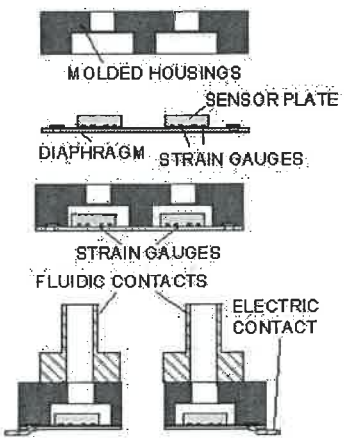

Fig.5: Principle of the AMANDA technology

Applications in micro-fluidics

The first micro-fluidic product developed at IMT several years ago was a micro-pump [10]. In the meantime an entire family of AMANDA devices has been developed including a flow sensors [11], valves [12], and pressure sensors [13] (see Fig.6). All these micro-modules are fabricated in batch with the same processing steps. They can be combined to larger fluidic systems following to some extend the LEGO concept. More recently, special process steps of the AMANDA technology, especially plastic molding and packaging techniques, have been exploited for microfabrication of "Bio-Chips" [14], which can be used in medical, pharmaceutical or chemical analysis. Further, the extension of hot embossing of thermoforming allows for patterning thin polymer foils with microstructures, even on large areas. First applications include chips for the cultivation of living cells in a project towards building artificial organs.

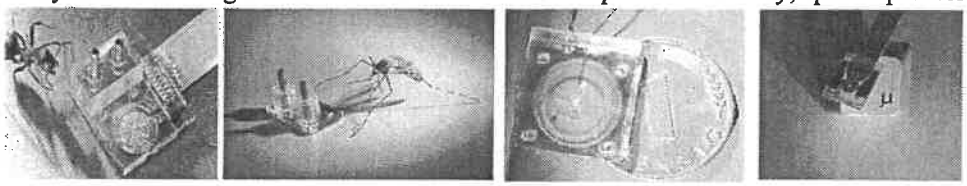

Fig.6: Fluidic devices fabricated with the AMANDA technology. From left to right: micro-pump, micro-flow-sensor, micro-valve, and micro-pressure-sensor.

References

1. E. W. Becker, W. Ehrfeld, P. Hagmann, A. Maner, and D. Münchmeyer, *Fabrication of microstructures with high aspect ratios and great structural heights by synchrotron radiation lithography, galvanoforming, and plastic molding*, Microelectron. Eng. **4** (1986) 35-56.
2. D. Münchmeyer and W. Ehrfeld, *Accuracy limits and potential applications of the LIGA technique in integrated optics*, SPIE Proc. **803** (1987) 72-79; J. Mohr, LIGA – A Technology for Fabricating Microstructures and Microsystems, Sensors and Materials **10** (1998) 363-373.
3. A. Gerlach, P. Ziegler, and J. Mohr, *Assembly of hybrid integrated micro-optical modules using passive alignment with LIGA mounting elements and adhesive bonding techniques*, Microsystem Technol. 7 (2001) 27-31.
4. U. Wallrabe, J. Mohr, and C. Solf, *Miniaturized FTIR Spectrometer with Large Travel Electromagnetic Linear Actuator Consuming Low Power,* ACTUATOR 2004, 9th International Conference on New Actuators, Bremen, Germany (2004) 321-324
5. www.microparts.de
6. G. Feiertag, W. Ehrfeld, H. Lehr, and M. Schmidt, *Sloped irradiation techniques in deep X-ray lithography for 3-D shaping of microstructures*, SPIE Proc. **3048** (1997) 136-143.
7. V. Nazmov, E. Reznikova, J. Mohr, V. Saile, A. Snigirev, I. Snigireva, M. DiMichiel, M. Drakopoulos, R. Simon, and M. Grigoriev, *Refractive lenses fabricated by deep SR lithography and LIGA technology for X-ray energies from 1 keV to 1 MeV*, AIP Conference Proceedings, 705 (2004) 752-755; V. Nazmov,E. Reznikova, A. Somogyi, J. Mohr, and V. Saile, *Planar sets of cross X-ray refractive lenses from SU-8 polymer,* Proc. SPIE Annual Meeting 2004, Denver CO, Aug. 2-6, 2004 (submitted).
8. W.K. Schomburg, R. Ahrens, W. Bacher, J. Martin, and V. Saile, *AMANDA – Surface Machining, Molding, and Diaphragm Transfer*, Sensors and Actuators **76** (1999) 343-348.
9. W.K. Schomburg, J. Vollmer, B. Buestgens, J. Fahrenberg, H. Hein, and W. Menz, *Microfluidic Components in LIGA Technique*, Journal of Micromechanics and Microengineering, **4** (1994) 186-191.
10. D. Dittmann, R. Ahrens, Z. Rummler, K. Schlote-Holubek, and W.K. Schomburg, *Low-Cost Flow Transducer Fabricated with the AMANDA-Process*, The 11th Int. Conf. on Solid-State Sensors and Actuators, Transducers'01, München, Germany, June 10-14, 2001, paper 4B2.10PD.
11. T. Rogge, Z. Rummler, and W.K. Schomburg, *Piezo-Driven Polymer Microvalve Manufactured by the AMANDA Process*, Proc. Eurosensors XVI, Prague, Czech Rep., Sep. 15–18, 2002, 214–217.
12. K. Wulff, Z. Rummler, W.K. Schomburg, *Hybride Drucksensoren aus Kunststoff und Glas nach dem AMANDA-Verfahren*, Wissenschaftliche Berichte FZKA **6682** (2001).
13. M. Heckele, A. Gerlach, A. Guber, and T. Schaller, *Large Area Polymer Replication for Micro-fluidic Devices*, SPIE Proc. **4408** (2001) 469-477.

Design of a passive micro-mechanism chuck to minimize the effect of backside particles on semiconductor wafer planarity

Pawan Kumar Nimmakayala and S.V Sreenivasan
Mechanical Engineering Department
The University of Texas at Austin
Austin, TX 78712

Abstract

There are a number of factors affecting semiconductor wafer planarity, namely intrinsic factors such as warp, bow and non-linear thickness variation [2]; and extrinsic factors such as backside particles [3,4] and chuck flatness [5]. Of these non-planarity causing factors, backside particles are the most detrimental as they affect a large portion of the wafer real estate by causing out-of-plane distortion when they get lodged between the wafer and the wafer chuck [2]. Conventional pin type and groove type chucks correct for the non-planarity causing intrinsic factors sufficiently well but do not adequately address the extrinsic factors, especially that of backside particles. Previously [7], we introduced a chuck called the compliant pin chuck that can minimize the effect of backside particles. This chuck has micro-mechanism pins that react to the presence of particles in ways that eliminate the non-planarity introduced otherwise. In this paper, we discuss some key features related to the design of the compliant pin chuck.

1. Introduction

The increasing demand on lithography systems to transfer sub 100 nm features on semiconductor wafers to allow the production of faster and cheaper chips, has forced these systems to operate under extremely tight process tolerances. One such process parameter that is becoming crucial going forward to next generation pattern transfer (sub 100 nm) is substrate flatness. For example, in the case of optical lithography, an increase in resolution results in a decrease in depth of focus thus requiring an extremely flat substrate for distortion free pattern transfer [1].

There are a number of factors affecting semiconductor wafer planarity, namely intrinsic factors such as warp, bow and non-linear thickness variation [2]; and extrinsic factors such as backside particles [3,4] and chuck flatness [5]. Of these non-planarity causing factors backside particles are the most detrimental as they affect a large portion of the wafer real estate by causing out-of-plane distortion when they get lodged between the wafer and the wafer chuck [2]. Conventional pin type chucks provide only partial relief from the detrimental effects of backside particles by reducing the contact area between the chuck and the wafer. By doing so, they only reduce the probability of lodging particles. However, if particles get lodged between the pins and the wafer they result in producing the same detrimental effects. Moreover, further reducing the contact area is not an adequate solution as it results in weaker pins increasing the chances of pin failure. Also, reducing contact area between the wafer chuck and the wafer results in poor heat transfer by conduction through the chuck which is undesirable in most lithography systems.

Previously [7], we introduced a chuck called the compliant pin chuck (CPC) that can correct for the effects of backside particles on wafer planarity. Unlike the pin type chuck, which has microstructures to support the wafer, the CPC has three-dimensional micro-mechanisms that support the wafer and in the presence of a particle these passive micro-mechanisms react in a way that minimizes the non-planarity introduced otherwise. The present paper explains some key features related to the design and fabrication of the CPC. For further information one may refer [6].

2. The compliant pin - structure

The primary distinguishing feature of the CPC is in the design of its pins. The pins of the CPC are micro-mechanisms which in their most simplistic form can be thought of as a 'T' structure with two raised areas called contact lands (see Figure 1 for illustration). Contact lands serve two purposes: 1.) They are the equivalent to a single pin of a conventional pin type chuck and reduce the contact area between the chuck and the wafer. 2.) They ensure that a bending moment is always applied about the stem of the 'T' structure, which is the flexure element of the mechanism and is referred to as the 'flexure stem'.

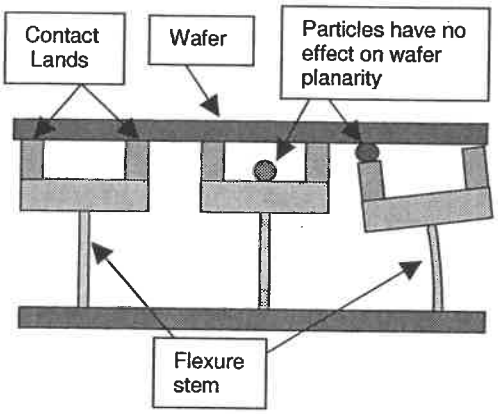

Figure 1. Compliant pins and their principle of operation

3. Design features of the CPC

Some key design features of the CPC are explained in the following section.

3.1 Dual stiffness character of the compliant pin

In order for the CPC to be effective in correcting both the intrinsic and extrinsic non-planarity causing factors, the pins have to exhibit 'dual stiffness character'. By this we mean that when no particles are present, the compliant pins have to be stiff to support the forces (produced by applying vacuum or static load to the wafer) required to correct the warp and bow in the wafer; conversely, in the presence of backside particles the compliant pins should exhibit low stiffness to accommodate the particle. This dual stiffness character is achieved by the proposed compliant pin chuck concept shown in Figure 1. When a wafer is placed on the compliant pins and no particles are present between the wafer and the wafer chuck, both the contact lands of each pin are equally loaded. This produces equal and opposite bending moments about the flexure stem that cancel each other and the compliant pin system is stable and supports the vertical load. In this case, the vertical stiffness of the compliant pin is defined by the bending stiffness of the flexure head and the vertical stiffness of the flexure stem. In case a particle gets lodged between the wafer and the contact land of a compliant pin, the force acting through the particle on a single contact land causes a bending moment to be produced about the flexure stem thereby causing the compliant pin to bend thus allowing the pin to accommodate the particle size. In this latter case, the vertical stiffness of the compliant pin is defined by the bending stiffness of the flexure stem (which is much lower than the vertical stiffness of the flexure stem).

3.2 Lateral stiffness of the pins

It was observed through finite element analysis (FEA) of the compliant pins that with the 'T' structure design the lateral stiffness of the pins was very poor and there was a danger of the pins breaking at the flexure stem and hence a different design was developed that is shown in Figure 2.

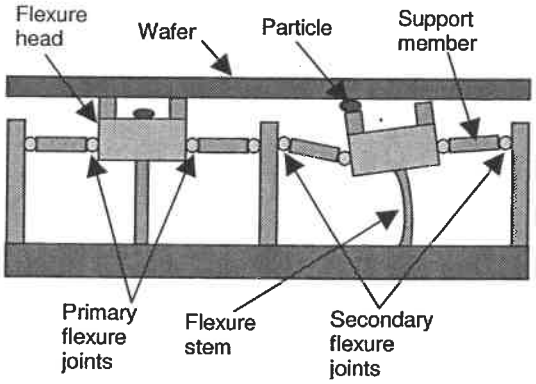

Figure 2. Compliant pin concept with improved lateral stiffness

In this concept, side support members were connected to the 'T' structure by means of two flexure sets. The set of

flexure joints (the primary flexure joints) connect the support members to the flexure head. A second set of flexure joints (the secondary flexure joints) connects the support members to the bulk of the wafer chuck. This increases the lateral stiffness of the pins and still allows the bending behavior of the compliant pin.

3.3 Remote axis of rotation of the compliant pin

The location of the rotation axis of the pin is important as an improperly located rotation axis can cause the reaction end (i.e. the contact land opposite the contact land on which the particle is present) of the compliant pin to introduce non-planarity in the wafer. Figure 3 illustrates this concept.

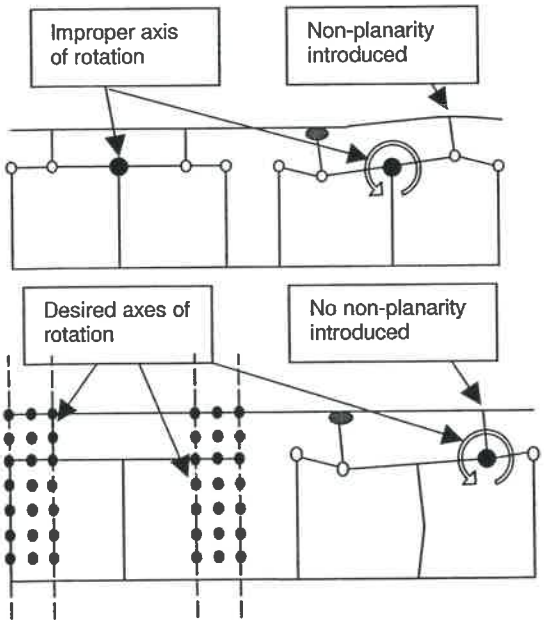

Figure 3. Importance of the location of the rotation axis

It is desired that the compliant pin rotates about a remote axis lying between the primary and the secondary flexure joints to ensure that no non-planarity is introduced in the wafer due to the parasitic motion of the reaction end of the compliant pin. This behavior was confirmed through FEA. Figure 4 shows the finite element simulation model of a single compliant pin in the un-deformed and deformed configurations.

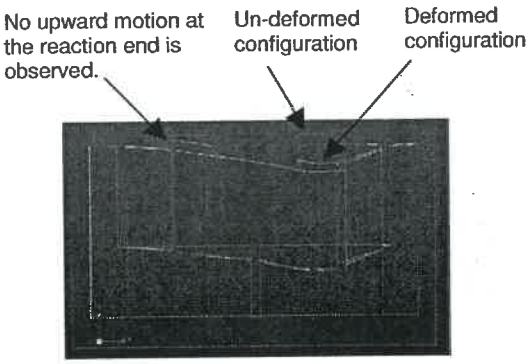

Figure 4. FEA simulation showing a single compliant pin in the un-deformed and deformed configurations

3.4 Multi-layer design of the CPC

To simplify fabrication of the CPC, the critical components of the chuck were distributed into multiple layers. Each layer was then fabricated using 2D lithography processing.

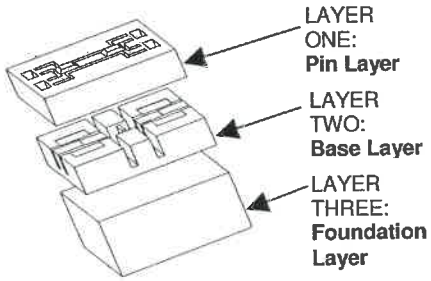

Figure 5. Tri-layer unit cell - single compliant pin model

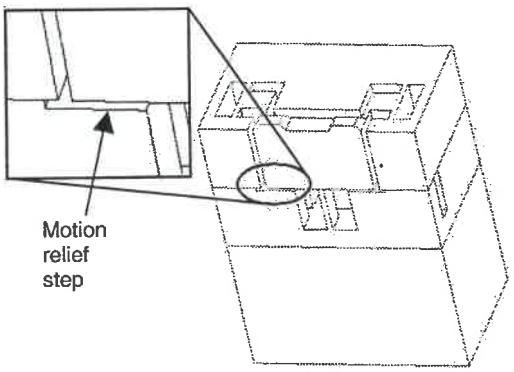

Figure 6. Cross sectional view of the tri-layer stack of a single compliant pin

Once the layers were fabricated they were then aligned and bonded together to yield functional 3D micro-mechanisms. Figure 5 shows a schematic of the layers of

a single repeating unit cell of the CPC and Figure 6 shows the cross sectional view of a compliant pin. The pin layer consists of the contact lands and the primary and secondary flexure joints. The base layer consists of the flexure stem, vacuum channels and motion relief steps (see Figures 6). Motion relief steps are recesses of a defined depth (equal to the design limit of the compliant pin) in the top surface of the base layer that lie under the flexure head and the support members. They are an important feature of the compliant pin design and serve two functions: 1.) They provide the required clearance to allow the flexure head to move to accommodate particles (of sizes within the design limit). 2.) They act as a mechanical stop preventing catastrophic failure of the pins due to the presence of particles that are beyond the design limit of the compliant pin. Should a particle that is larger than the design limit of the compliant pin get lodged between the pin and the wafer the compliant pin would 'ground out' and will then behave like a rigid microstructure similar to a pin of a conventional pin type chuck.

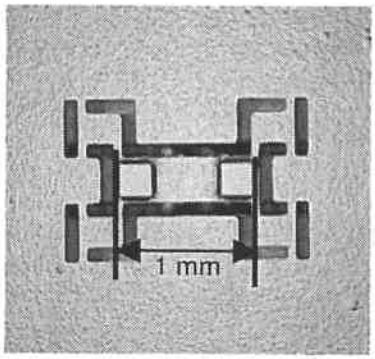

Figure 7. Photograph of a single pin of the fabricated CPC prototype

The bottom-most layer is the foundation layer and its purpose is to provide bulk rigidity to the compliant pin chuck. The only feature it consists of is the vacuum supply hole in the case of a vacuum compliant pin chuck. A 4" CPC prototype was fabricated and showed to have a flatness of 120 nm (3 sigma standard deviation) over an area of 30 mm x 30 mm and demonstrated to be less sensitive to backside particles than a conventional wafer chuck [6,7]. Figure 7 shows a single pin of the fabricated CPC.

4. Summary

Previously [7], a novel chuck called the compliant pin chuck was introduced that can correct for non-planarity introduced by backside particles. In this paper, some key design features of the CPC are explained. The dual stiffness character of the compliant pins that allows the compliant pins to correct both the intrinsic and the extrinsic factors of non-planarity is explained. The modified design of the compliant pins is shown with the side members that increase the lateral stiffness of the compliant pins. Furthermore, the importance of the location of the rotation axis of the compliant pin is described and it is shown that the compliant pins do not introduce any non-planarity in the wafer during operation. Lastly, the multi-layer design of the chuck that simplifies fabrication is explained.

References

[1] Marc J. Madou, 2000 Fundamentals of Micro Fabrication, The science of miniaturization, 2nd edition, CRC Press, New York

[2] Firtion et al. 1980, Apparatus and method for holding and planarizing thin work pieces, US. Patent – 4213698

[3] Micheal West, 1999, Wafer backsides: The key to Future Technologies, Solid state technology supplement

[4] R. Tejeda, R Engelstad and E Lovell, 2002, Particle-induced distortion in EUVL reticles during exposure chucking, Journal of Vacuum Science and Technology B.

[5] H Stauch, K simson, H. U Scheunemann, HL Huber, 1994, Impact of chuck flatness on wafer distortion and stepper overlay – comparison of Experimental and FEM results, Microelectronic engineering 23, pp. 197-201.

[6] Pawan Kumar Nimmakayala, 2004, Development of a compliant pin chuck for minimizing the effect of backside particle on wafer planarity, Master's thesis, The university of Texas at Austin.

[7] Pawan K Nimmakayala, S.V Sreenivasan, 2004, Compliant pin chuck for minimizing the effect of backside particles on wafer planarity, Proceedings of EIPBN conference.

Design of a next generation 6 DoF stage for scanning application in vacuum with nanometer accuracy and mGauss magnetic stray field

Angelo C.P. de Klerk†, Georgo Z. Angelis†, Jan van Eijk†‡

Abstract—[1] **Next generation charged particle lithography and microscopy require scanning stages with extremely high accuracy's, which have to operate in high vacuum and of which the produced stray magnetic field is very small. Philips CFT started a research project to find a solution to these challenges and developed a demonstrator that addresses all the above-mentioned demands.**

A solution has been found in using a combination of electro-magnetic actuators, magnetic bearings and magnetic shields. Electro-magnetic actuators and bearings have excellent properties to achieve nanometer accuracy in closed loop control. However, the demands with respect to the magnetic stray field seem totally in conflict with this concept. A main point in the project was to find an effective and practical shielding to overcome that problem.

The developed demonstrator showed peak servo errors during scan of 3 [nm], while the servo errors for stage rotations were no more than 0.1 [μrad]. Three dimensional magnetic finite element calculations have indicated that it is possible to shield the actuators in such a way that the requirement of 1 [mGauss] at wafer level can be reached. Tests have proven that these calculations are reliable. Though the prototype system is not designed for vacuum compatibility, the concept is such that vacuum compatibility can be achieved comparably easy. The paper will elaborate on the different components of this system.

I. Introduction

For advanced performance in equipment in Semiconductor manufacturing increasing requirements are put in precision positioning modules. For advanced Lithography and for Inspection systems a very smooth scanning motion is required where non-repeatable errors must be smaller than 10 [nm] in amplitude. Also it is required that systems operate in a high vacuum environment. To develop motion devices it is important to design suitable bearing solutions. The application of electro-magnetic bearing solutions gives a big promise for extreme accuracy in vacuum environment. However the combination of magnetic levitation and E-beam instruments appears to be contradictory. E-beam instruments are very sensitive to stray magnetic fields, especially for variations of such stray fields. Philips CFT has developed a demonstrator that addresses all the above-mentioned demands.

The developed stage is guided in the vertical (z, Rx, Ry) direction by four hybrid electromagnets, which at the same time serve as short stroke actuators, enabling stage excursions up to 1 [mm] and 0.1 [mrad]. Total power dissipation for levitation of this 3 [kg] stage amounts no more than 0.1 [W] due to the fact that the hybrid electromagnets also facilitate passive magnetic gravity compensation. In the horizontal direction (x, y, Rz), the stage is actuated and guided using DC moving coil actuators, enabling stage excursions of 120 [mm] in the scan (x) direction and a rotation of 1 [mrad]. Interferometers have been used as 6 DoF position measurement device. The attained resolution is 0.625 [nm]. The magnetically levitated stage is given in Figure 1.

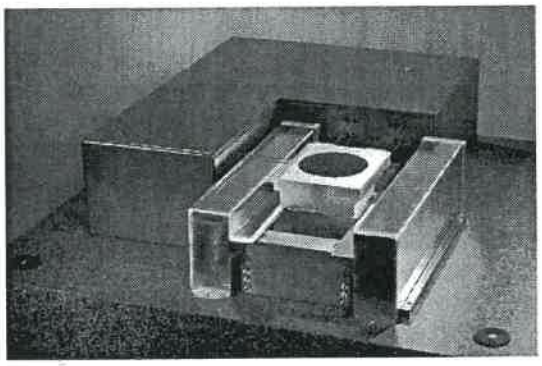

Fig. 1. Realised X-manipulator with nanometer accuracy and milliGauss magnetic stray field.

II. Mechatronic Design Challenges

The stage has to meet the specifications for ultra precision next generation 4 [inch] wafer inspection applications. The stroke and accuracy specifications are given in Table I. The long stroke, i.e. the scanning direction x, has to meet the following scanning specifications, stroke: 120 mm, velocity: 20 mm/s and acceleration: 0.1 mm/s^2.

TABLE I
Stroke Specifications

direction	stroke	[.]	accuracy	[.]
x	$+/-60$	mm	1-10	nm
y	$+/-0.1$	mm	1-10	nm
z	$+/-0.1$	mm	100	nm
Rx	$+/-0.1$	mrad	0.1	μrad
Ry	$+/-0.1$	mrad	0.1	μrad
Rz	$+/-1$	mrad	0.1	μrad

Besides these servo specifications the stage has to be designed to fulfill also the functional and performance specifications as given in Table II.

TABLE II
Additional Specifications

vacuum compatible	$\leq 10^{-7}$	mBar
power dissipation actuator system	≤ 100	mWatt
magnetic field gradient over wafer surface	≤ 1	mGauss
absolute magnetic field over wafer surface	≤ 5	mGauss

‡ Delft University of Technology, Faculty of Mechanical Engineering, Mechatronics Group, Delft, The Netherlands

† Philips CFT, Mechatronics Technologies, P.O. Box 218, SAQ-2121, 5600 MD Eindhoven, The Netherlands, Email:{a.c.p.de.klerk, georgo.angelis, j.van.eijk}@philips.com

[1]Extended version of the paper can be found on the CD-rom

III. Mechanical and Dynamical design

A feasibility study showed that the aforementioned functional requirements can be met with a stage design as shown in Figure 1. To achieve the dynamic specifications as given in Table I under "wafer fab" operating conditions, the open-loop bandwidth (BW) of the system has to be around 150 [Hz]. This bandwidth can be achieved robustly since the first BW limiting resonances of the mechanical design are designed above 800 [Hz]. Furthermore, by using contactless magnetic bearing elements instead of classical roller bearings, intrinsic disturbances by mechanical contact are absent. High scanning accuracy demands are achievable through its dynamic isolation with respect to the environment and no contamination issues due to mechanical wear or lubricants are expected. Both cleanliness and lifetime of the system is improved in this way.

IV. Actuator Design

This MIMO system has 8 actuators, i.e. 4 hybrid electromagnets and 2 times 2 DoF Lorentz actuators which generate the forces to control the 6 DoF. The hybrid electromagnets, are used to levitate the stage and to drive the stage in the z, Rx and Ry direction. The combined Lorentz actuators are used for the actuation in x, y and Rz direction. The choice has been made to use DC moving coil direct drive motors, because these motors have proven themselves in applications with nanometer accuracy. Their design is based on proven in house technology and knowhow at Phlips CFT. A detailed design description and the derivation of all needed formula's for the analytical analysis of such motors can be found in [1].

A. Combined Lorentz Actuator

The combined Lorentz actuator consists of 2 coils which uses the same magnetic circuit. The magnetic circuit consists of, see Figure 2, an iron yoke, a permanent magnet and a flux return guidance. The flux return guidance is made of a stainless steel grade with a low electrical conductivity, the iron yoke is made of normal ferromagnetic steel and the permanent magnet is made of a high grade NeFeB. The thin permanent magnet generates a constant field in the area where the coils are located. This constant field is present over the full stroke.

The x-motor is formed by the magnetic circuit and the x-coil, see the right side of Figure 2. With a given current Ix and the given magnetic field B a force Fx in x-direction is generated, see Figure 2. Only the upper part of the x-coil is present in the magnetic field and therefore this part will only generate a force. The y-motor uses the same magnetic circuit, but uses a different coil, namely the y-coil. With a given current Iy and the given magnetic field B a force Fy in y-direction is generated. Only a small part of the y-coil generates a force in the y-direction, this is allowed because small forces are needed in y-direction. From a mechatronic point of view, the combination of the x- and y-coil in one magnetic circuit is the best solution, it gives a relative simple mechanical design of the stage and only one magnetic circuit is necessary.

This construction of the combined Lorentz actuator can be found on both sides of the stage, so there are two y-motors and two x-motors. Both y-coils work together as one y-actuator and generate a force in y-direction. The two x-coils are used for force in x-direction and torque in Rz-direction.

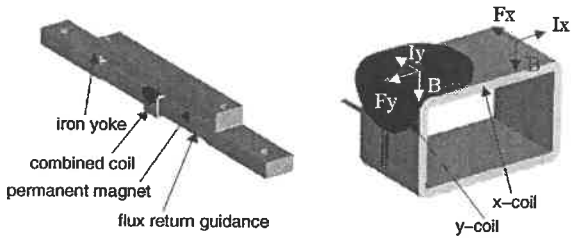

Fig. 2. Combined Lorentz actuator.

B. Hybrid Electromagnet

For levitation of the stage and to drive the stage in the z, Rx and Ry direction four hybrid electromagnets are used. Hybrid means that there is a magnet present in this actuator. This magnet generates a DC-force, which compensates more than 90 % of the weight of the stage. A result of this is that only a small current is necessary to obtain full levitation and therefore a small amount of dissipation in the coil. The hybrid electromagnet generates a force between the surface of the electromagnet and the flux return guidance of the combined Lorentz actuator. This generated force is related to the current I and the airgap z as follows:

$$F \approx g.\frac{a.I^2 + b.I + c}{d.z^2 + e.z + f} \tag{1}$$

with F[N] the actuator force , I[A] the coil current, z[mm] the airgap and $\{a, b, ..., g\}$ unknown parameters to be determined by measurements or simulations.

What can be seen is that this represents non-linear behaviour. In this case position linearization is used and the aim is to create a linear Lorentz like behaviour of the hybrid electromagnet to facilitate linear controller design.

Equation 1 shows that when the current is controlled the force is controlled. When the unknowns of Equation 1 are determined and the actual position is known, the current can be calculated. The parameters are determined by measuring the force as function of the airgap at different currents.

The linearization algorithm is determined at a nominal air gap of 0.5 [mm]. This algorithm is implemented in a digital control system and the effect of the linearization is measured. A force set point F^* is generated and the force F generated by the hybrid electromagnet is measured. What can be concluded is that the force generated by the hybrid electromagnet is almost independent of the airgap and therefore a linear Lorentz like behaviour has been achieved.

C. Dissipation

In order to minimize power dissipation, the permanent magnet of the hybrid electromagnet is dimensioned such that at nominal airgap the set of four actuators generates a force that equals almost the gravity force associated with the moving part of the stage. This means that in principle no current is needed for the levitation of the payload at the nominal air-gap. Current is only needed for initial lift and for compensation of imperfections of the actual system. For driving the combined Lorentz actuator only very small currents are necessary and subsequently these actuator pairs will also not have a large absolute contribution to the total dissipation of the stage. The total dissipated power at the mentioned specifications is less than 100 [mW].

V. Shielding Design

A. Design

The ideal shielding is a closed box of metal with a very large value of the relative permeability. Within this box all the magnetic sources should be present, which are in this case the magnetic circuit of the combined Lorentz actuator and the hybrid electromagnets. The coils of the combined Lorentz actuator and the hybrid electromagnets are connected to the stage and this makes it impossible to have a totally closed box.

During the design phase a 2D FEM package is used which resulted in an initial design which met the specification. This design was the start of the 3D FEM analyses, to investigate the 3D effects. The result of the 3D FEM analyses is a shielding design with a number of layers that is constructed from different materials. This resulted in an absolute magnetic field strength smaller than 5 [mGauss] and a gradient of the magnetic field strength of 1 [mGauss] over the wafer surface.

In order to validate the simulation model, measurements are carried out at a test set-up within Philips. This set-up has a Hall probe which contains 3 active elements. The probe is placed in 3 pairs of Helmholz coils; the coils are rectangular of shape with a side length of approximately 2.5 [m]. With these coils it is possible to create an almost zero magnetic field inside the coils. The probe can be positioned at a x, y and z position. Then the system "pulls" the probe in z-direction to a predefined end position with predefined steps. During this "pull" the magnetic field in x, y and z direction is logged.

During the measurements it became clear that the test setup was not able to measure magnetic field strength up to the milliGauss level. Therefore measurements are performed when the shielding has been removed. These measurements are compared with the simulation results. Figure 3 displays the results of the measurement and the simulations in one graph, this graph is at a certain point in the xy-plane of the stage and the magnetic field strength has been plotted as function of the z-coordinate, where $z = 0$ [mm] is equal to 5 [mm] above the wafer surface.

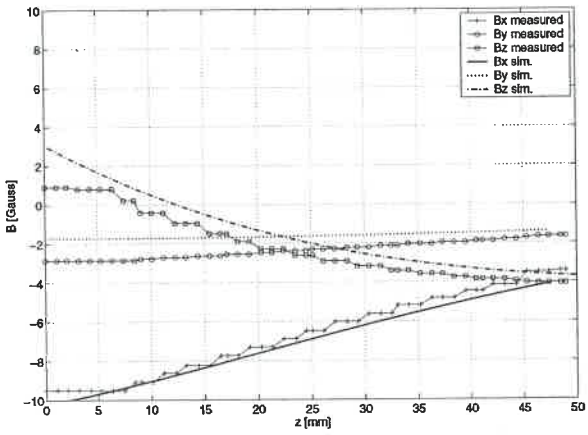

Fig. 3. Stage in shielding validation test set-up.

What can be seen is that the simulation model is a good approximation of the measured magnetic field strength. The simulation model without the shielding has the same layout as the model with the shielding, only the shielding material has a magnetic property that is equal to air. This means that the distribution of the FEM elements is the same in both cases. Therefore can be concluded that the model is valid and that with the right magnetic properties of the shielding the results of the simulations give a good approximation of the magnetic field strength at wafer level, that is an absolute magnetic field strength smaller than 5 [mGauss] and a gradient of the magnetic field strength of 1 [mGauss] over the wafer surface.

VI. Controller Design

In common industrial motion control problems, kinematic relations are used to decouple the motion system in rigid body modes to facilitate decentralised controller design. Decoupling in this approach often works satisfactory if in the frequency region of interest, i.e. around the desired open-loop bandwidth (BW), the rigid body system behavior is not affected by low frequency resonances or high frequency internal flexibilities of the mechatronic structure.

A. Control Configuration

The basic control scheme is displayed in Figure 4. A detailed description can be found in [3]. ST is the sensor transformation from

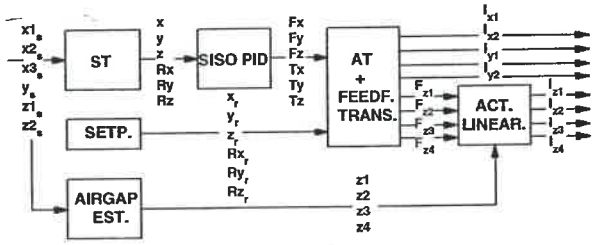

Fig. 4. Basic control scheme: PID feedback and feedforward with setpoint generator, geometric decoupling matrices ST and AT and actuator linearization algorithm including airgap estimation.

'physical' sensor coordinate frame to 'logical' Cartesian coordinate frame, a so-called sensor transformation. This is used to map the six sensor readings to an estimated six degree of freedom (DoF) motion of the point to be controlled. In the present setup the point to be controlled was selected to be the center of gravity (CoG) of the stage. AT is the actuator transformation from 'logical' coordinate frame to 'physical' actuator coordinate frame, a so-called actuator transformation. AT is selected such that the 6-DoF plant dynamics becomes decoupled to enable subsequent multi-loop decentralised feedback controller design. In the derivation of AT it is generally assumed that the plant behaves as a rigid body (at least for low frequencies) so as to achieve decoupling of the dynamics for the frequency range of interest (somewhat beyond the intended bandwidth). Under the assumption that only small angles (Rx, Ry and Rz) are relevant the transformation matrix becomes constant except for the long stroke x.

The controllers have a 'PID + Low Pass' structure. The controller has a parallel structure so as to include a separate saturation level on the integral action. Additional second-order notch filters are implemented to overcome stability problems. Initial controller design is based on estimates of the rigid body gains of the diagonal entries of the plant.

B. Closed-loop Plant Identification and Analysis

The identification experiment is illustrated in Figure 5. Noise v is

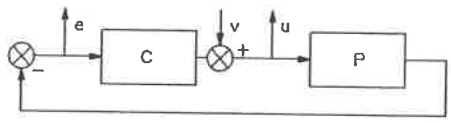

Fig. 5. The basic indirect identification experiment.

injected before the plant P using a random signal generator and the plant input u and the servo error e are traced together with the injected noise. Frequency Response Functions (FRF's) of the plant can be determined by so-called indirect identification. The FRF's of the decoupled multi-input multi-output (MIMO) plant are computed and shown in Figure 6. The following observations can be made regarding the dynamics. Above 850 [Hz] the first BW limiting resonances are observed. Which indicates that a BW of about 150 [Hz] is indeed achievable. Some one sided cross-coupling is present as can be seen by comparing column entries of Figure 6, i.e. each output for one input. By comparing the row entries of Figure 6, i.e. one output for each input, diagonal dominance is observed. The decoupling matrices, AT and/or ST will be calibrated based on the measured FRF data to achieve maximal diagonal dominance thereby assuring tracking performance.

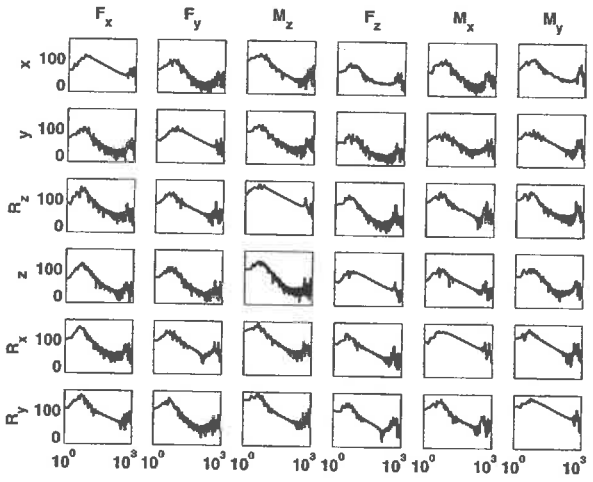

Fig. 6. MIMO FRF of the identified plant, x-axis in [Hz], y-axis in [dB].

C. Feedback and Feedforward Controller Tuning

Based on the measured FRF's, controllers were designed. It is common practice to increase the BW's gradually as more accurate measurements of the dynamics become available. Two iterations in the control design were made to eventually achieve BW's of approximately 150 [Hz] in all directions.

To increase tracking performance in x-direction at the constant velocity phase, a feedforward signal is generated that is proportional to the desired acceleration profile of a third order setpoint, i.e. mass times acceleration equals feed forward force. The feedforward term (mass term) is fine tuned by monitoring servo errors at the acceleration phase and changing the mass term such that errors are minimized at the acceleration phase. Also the feed forward signal is shifted a fraction of a sample in time to minimize servo errors during acceleration phase. Besides this, also the actuator transformation AT is fine tuned to minimize crosstalk between the long stroke actuation (scanning direction x) and all other directions that have to remain zero. The parameter that defines the interaction between x and Ry in the actuator transformation AT is fine tuned by monitoring the Ry error during the acceleration phase of the scanning direction x.

D. Robustness and Performance

Robustness of a feedback controlled system is addressed by showing an open-loop transfer. It reveals the stability margins (gain and phase margins) and the BW that is achieved, see [4]. The BW is limited by resonance frequencies of the structure around 1000 $[Hz]$.

In constant velocity phase the absolute error in x is less than 3.2 $[nm]$ and in the acceleration phase less than 18 $[nm]$. Settling due to acceleration is within 20 $[ms]$. The errors in all the six directions are within specification.

VII. Conclusions and Future Developments

A 1D ultra-precision scanning device, designed to meet next generation wafer fab inspection equipment requirements was designed and build within six months time. It will be compatible with high vacuum and very low magnetic stray field conditions. To achieve this, the stage is equipped with active magnetic bearing elements. The highly modular stage can be adapted to customer requirements.

At Philips CFT a planar version (2D) of the 1D ultra-precision stage is being developed that solves the 130 [nm] (and beyond) wafer fab equipment demand for high precision scanning and point to point motion of 300 [mm] wafers.

The specifications of this prototype are customer specific and in the field of e-beam lithography, wafer inspection but also ion-beam milling and laser-cutting, see [5].

VIII. Acknowledgements

The work presented here, is the result of a team effort of several specialists of the Mechatronics Technology Department at Philips CFT. The team members' contribution and their close co-operation is gratefully acknowledged and highly appreciated.

References

[1] F.M. Roes, 'Requirements and Design document for the High Accuracy Test Bench motors',*internal report Philips CFT, CTB595-98-5394*, 1998.
[2] E.A.L.M. Aerts et. al., Elektronica Vademecum,' ',*ISBN 90 201 1098 8*, Kluwer Technische Boeken, 1980.
[3] G.Z. Angelis, F.M. Roes, 'Hacker control test report v2final',*internal report Philips CFT, CTB595-03-1640*, 2003.
[4] J. Maciejowski, 'Multivariable feedback design', Addison-Wesley, 1989.
[5] M. van Lent, 'Nano MagLev Stage', *brochure Philips CFT, Code 8122 968 9840.1*, 2004.

A PLANAR NANO-POSITIONING TABLE SYSTEM FOR ADVANCED MACHINE TOOLS

Hayato Yoshioka, Kou Komatsu, Hitoshi Hashizume, Hidenori Shinno, Tadahiko Shinshi and Kaiji Sato
Precision and Intelligence Laboratory, Tokyo Institute of Technology
4259, Nagatsuta, Midori-ku, Yokohama, 226-8503, Japan

1. Introduction

Manufacturing environments will require advanced machine tools equipped with an ultraprecision machining function. In order to materialize such a machine tool, it is necessary and indispensable to develop the basic components, i.e., a spindle system, a table system, a frame, a base, etc. In particular, the table system is one of the most important components in an overall machine tool structure and the performance has a great influence on the machining accuracy and productivity of the machine tool. Therefore, specifications of such a table system include high rigidity, compactness, nano-positioning capability and a multiple degree-of-freedom (DOF) motion control function.

Previous research works have been carried out to minimize the error factors by using a linear motor of a noncontact type [1][2][3].

This paper describes a newly developed 3DOF (XYθ) planar nano-positioning table system. The developed system was designed to minimize the structural and kinetic errors of the table. The evaluated performance showed that the developed table system is suitable for advanced machine tools.

2. Concept and structural configuration of the developed planar nano-positioning table system

2.1 Requirements for the table structure

Most of the conventional multiple DOF table systems are realized by stacking one DOF table structure or by applying a parallel link mechanism. However, these structures have some defects, i.e., large-sized structure, accumulated geometric errors, necessity of complicated control, etc.

Requirements for an advanced table system are as follows; (a) compact, lightweight and stable structure, (b) lowered centroid of the table, (c) multiple constrainable structure, (d) Thermal deformation-minimized structure, (e) drive at the centroid of the table, (f) perfect noncontact drive and support functions, (g) use of actuators with linear characteristic, and (h) high performance positioning controller with high resolution sensors.

2.2 Structural configuration of the developed table system

Figures 1 and 2 show the structural configuration of a planar nano-positioning table system based on a new concept. Basic specifications of the system are given in Table 1. As can be seen in Fig.1, the table has a simple square shape and the overall system is designed symmetrically with respect to the driving axes. Applying a multiple constrainable structure, we can materialize the compact structure and lower the centroid of the table. In order to achieve lightweight structure, high stiffness and low thermal deformation, both the table body and the flat base are made of alumina ceramics.

The table is levitated by high stiff aerostatic bearings with porous material and is simultaneously attracted by a vacuum pump from the bottom of the table for pre-loading. Consequently, high stiffness non-contact support of the table can be achieved. Eight voice coil motors (VCM) with linear characteristics are arranged symmetrically around the table body, consequently the driving axes are set to the position of the table's centroid. By using a coil of each VCM as a stator, relative position between the centroid of table and the

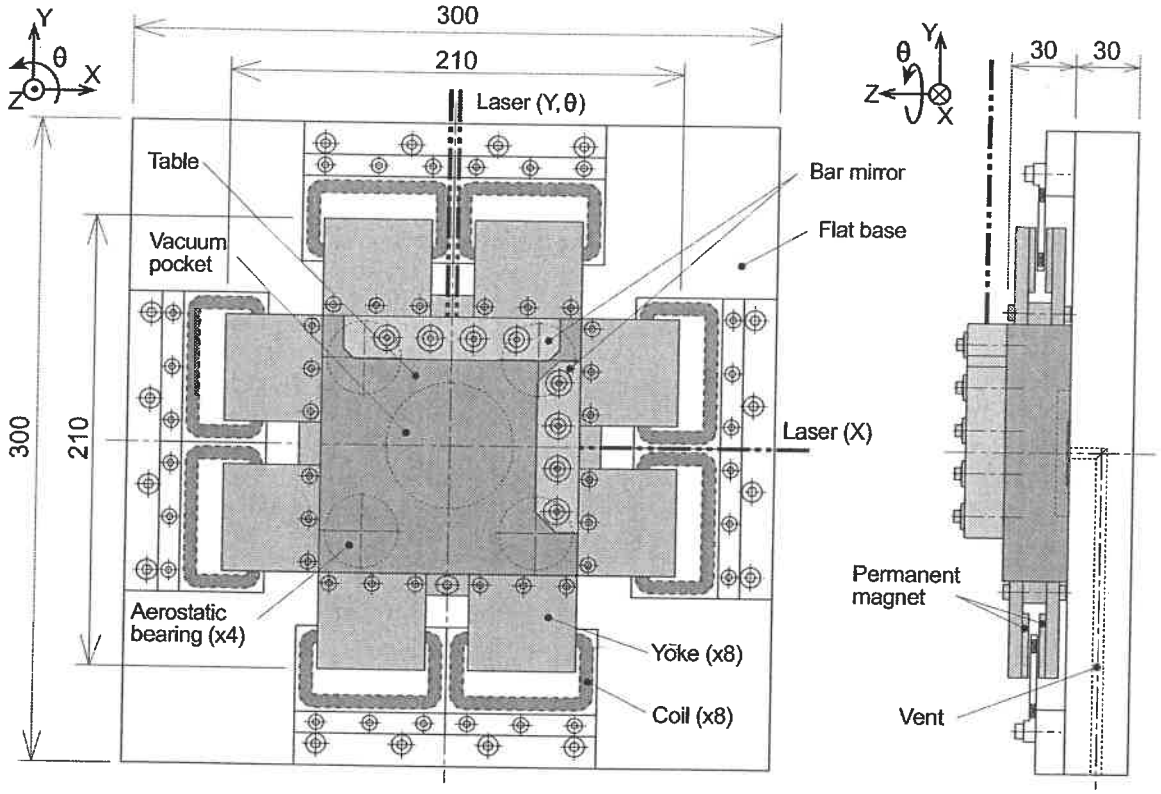

Figure 1 Structural configuration of the developed table system

Table 1 Specifications of the developed table system

Table	Dimensions	120x120x30 mm
	Stroke (X,Y)	± 9mm
	Mass	4.1 kg
	Material	Alumina ceramics
	Stiffness (Z)	83.7 N/μm
Interferometer resolution	X,Y	0.3 nm
	θ	24 nrad
VCM	Thrust constant	0.67 N/A
Controller	Sampling frequency	10 kHz

driving points remains constant in the table stroke area. Consequently, the driving characteristic of the table rotation (θ) is independent of the table position.

The driving principle of the developed table is shown in Fig. 3. Any two of the VCMs that are diametrically opposed on the table can act as one actuator, and the table can be driven using four couples (X1, X2, Y1, Y2). For the movement in X direction, both X1 and X2 equally generate one half of the driving force F_X. On the other hand, Y1 and Y2 control the movements of Y and θ axes, therefore they can generate the resultant driving forces for Y and θ axes.

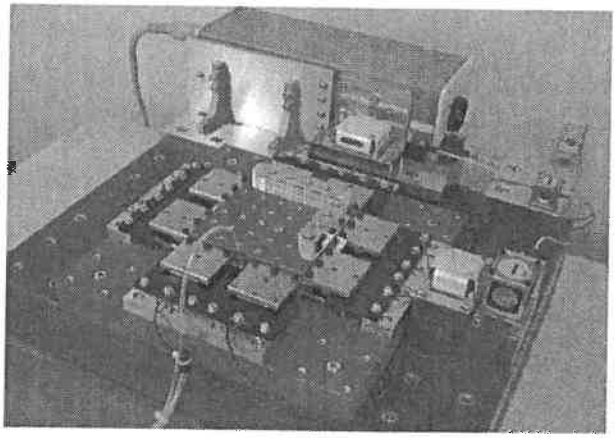

Figure 2 Appearance of the developed table system

The control system consists of PID compensators, acceleration feed forward compensators, high speed current amplifiers, VCMs and laser heterodyne interferometers. Two bar mirrors on the table in Fig.1 are used for measuring the table position as the references. Having no mechanical interdependence of the developed table system, its control system can be simple.

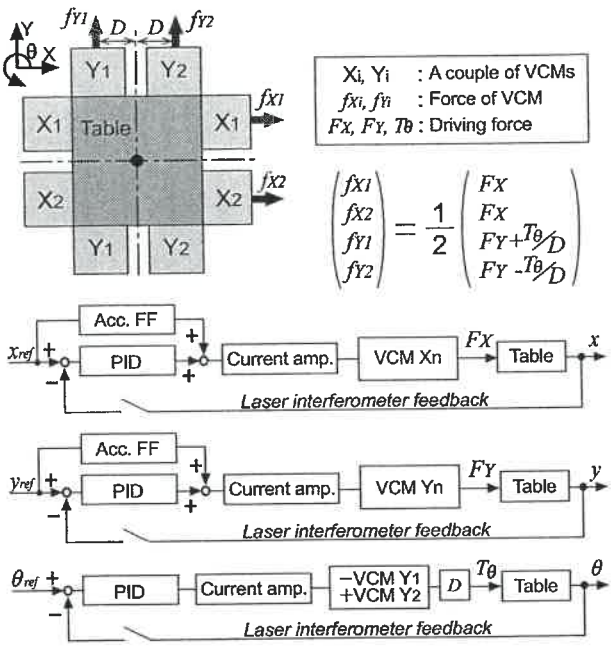

Figure 3 Driving principle of 3DOF driving

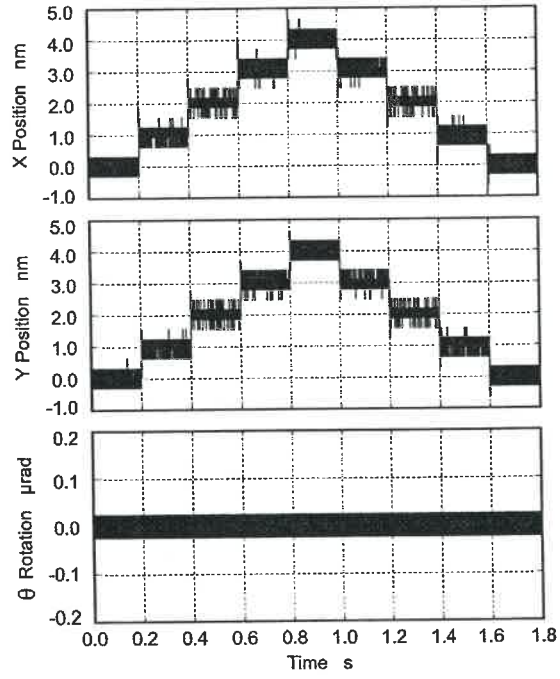

Figure 4 1nm stepwise response

3. Experimental performance evaluations of the developed table system

The performance of the developed table system was evaluated through a series of nano-positioning experiments.

Figure 4 shows the simultaneous stepwise responses of the table on both the X and Y axes. Since the non-contact driving and supporting functions eliminate error factors such as stick-slip phenomenon, a clear 1nm stepwise positioning can be observed in this figure.

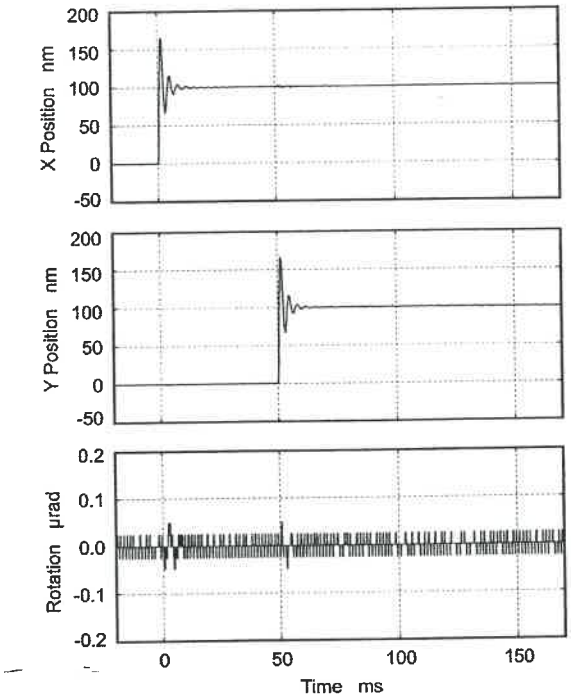

Figure 5 100nm step response

Figure 5 shows the responses in applying 100 nm step reference to the X and Y axes respectively. As shown in the figure, the responses in the X and Y directions are almost identical, hence the system has the same characteristics on the X and Y axes due to its symmetrical structure. Furthermore, this figure proves that the developed system has little interference among driving axes even when the table moves rapidly on the X or Y axis.

Figure 6 shows the error motion of a Point-to-Point positioning using jerk continuous references. Although slight increases in the tracking error can be observed during acceleration periods, the tracking errors are less than ±1nm on the XY axes and ±0.1 μrad on the θ axis during the table driving.

Figure 7 demonstrates the circular trajectory that has a 5mm radius and a 1Hz period in the X-Y plane. Since the developed table system is in a perfect non-contact condition and has linear characteristics, the acceleration feed-forward compensator acts effectually. Thus, nano-motion control can be achieved at the boundary between quadrants.

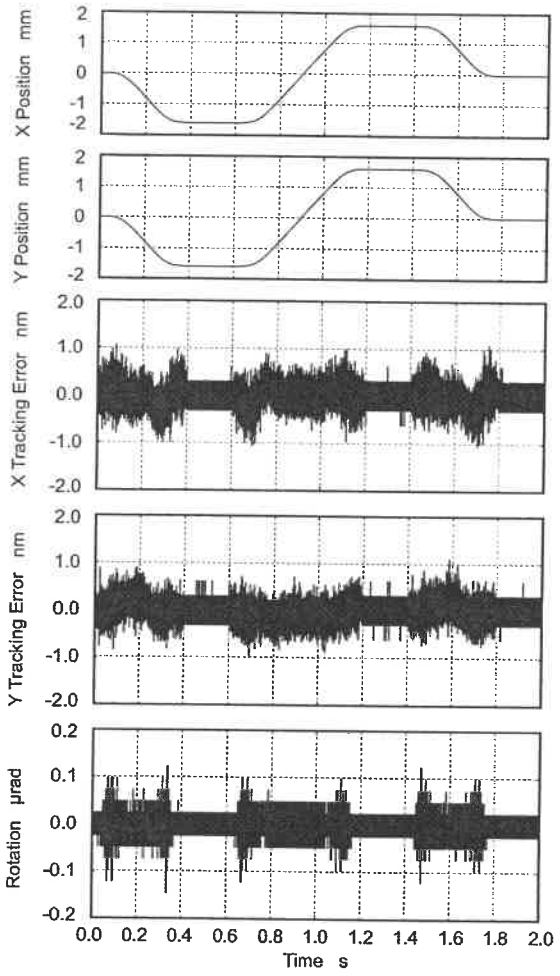

Figure 6 Point-to-Point positioning result

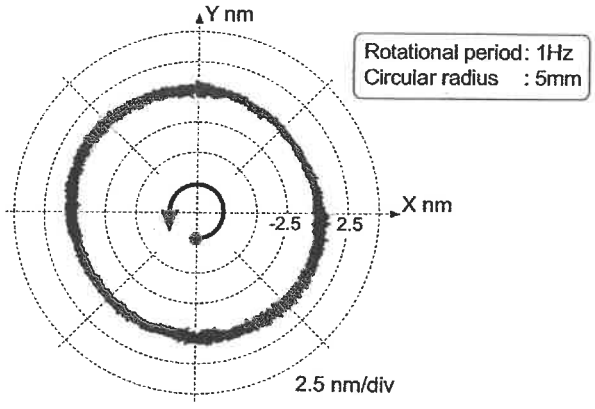

(a) Trajectory error

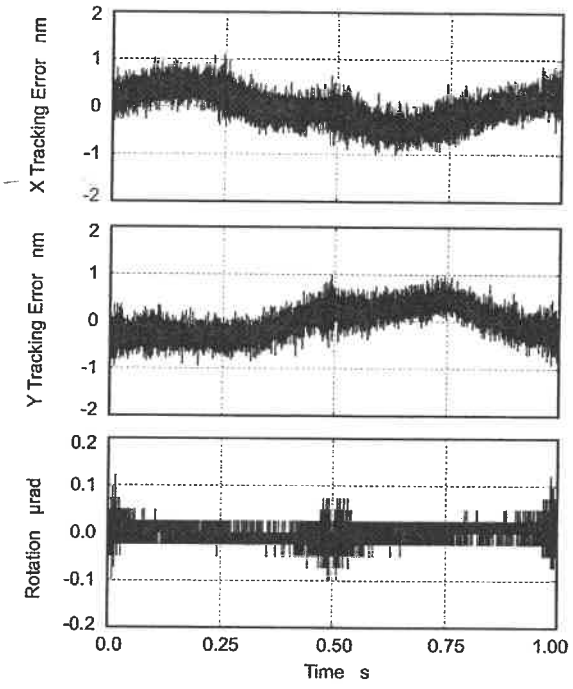

(b) Tracking error in each direction

Figure 7 Circular motion

4. Conclusions

This paper presented the developed planar nano-positioning table system based on a new design concept. The developed system was designed to minimize the structural and kinetic errors. The performance was verified through actual driving experiments. The evaluated results showed that the developed table system has superior fundamental characteristics for nano-positioning capability. The developed table system can be applied to advanced machine tools, such as ultraprecision milling machines, micro EDM machines, etc.

Acknowledgements

This study was funded by JSPS Grants-in-Aid for Scientific Research (S) No.14102015 and NEDO Industrial Technology Research Grant Program in '02.

References

[1]Tomita,Y., Makino,K. and Sugimine,M., High-response XY stage system driven by in-parallel linear motors, Annals of the CIRP, 45/1, 1996, 359-362.

[2]Shinno,H., and Hashizume,H., Nanometer positioning of a linear motor-driven ultraprecision aerostatic table system with electrorheological fluid dampers, Annals of the CIRP, 48/1, 1999, 289-292.

[3]Shinno,H., Hashizume,H., Yoshioka,H., Komatsu,K., Shinshi,T. and Sato,K., X-Y-θ nano-positioning table system for a mother machine, Annals of the CIRP, 53/1, 2004, 337-340

Design of a Scanning Stage System with Nanometer Resolution for a X-ray Nanoprobe Instrument

D. Shu[2], J. Maser[1,2], B. Lai[2], S. Vogt[2], Y. Han[2], B. Tieman[2], R. Winarski[2], C. Roehrig[2], A. Smolyanitskiy[2], and G. B. Stephenson[1,3]

[1]Center for Nanoscale Materials, Argonne National Laboratory, Argonne, IL 60439, U.S.A.
[2]Experimental Facilities Division, Argonne National Laboratory, Argonne, IL 60439, U.S.A.
[3]Materials Sciences Division, Argonne National Laboratory, Argonne, IL 60439, U.S.A.

1. Introduction

A hard x-ray nanoprobe beamline is being developed at the Advanced Photon Source (APS) [1]. The beamline will house a hard x-ray nanoprobe instrument, one of the centerpieces of the x-ray characterization facilities of the Center for Nanoscale Materials (CNM), which is under construction at Argonne National Laboratory (ANL). The instrument will operate with photon energies between 3 keV and 30 keV. The focal length of the nanofocusing optics will typically be in the range of 10-30 mm.

We have developed a prototype instrument with a novel interferometrically controlled scanning stage system [2]. The system consists of nine DC-motor-driven stages, four picomotor-driven stages [3], and two PZT-driven stages. An APS-designed, custom-built laser Doppler displacement meter system provides two-dimensional differential displacement measurement with subnanometer resolution between the zone-plate x-ray optics and the sample holder. The entire scanning system was designed with high stiffness, high repeatability, low drift, flexible scanning schemes, and possibility of fast feedback for differential motion. Designs of the scanning stage system, as well as preliminary mechanical test results, are presented in this paper.

2. Laser Doppler encoder with multiple-reflection optics

Since 1998 a prototype laser Doppler linear encoder (LDLE) with multiple reflections has been under development at the APS [4,5]. With a customized commercial laser Doppler displacement meter (LDDM) [6], this novel linear encoder achieved subangstrom sensitivity in a 300 mm measuring range. The LDDM is based on the principles of radar, the Doppler effect, and optical heterodyning. We have chosen a LDDM as our basic system, not only because of its high resolution (2 nm typically) and fast object speed (2 m/s) but also because of its unique performance independent of polarization, which provides the convenience to create a novel multiple-reflection-based optical design to attain subangstrom linear resolution.

In the self-aligning multiple-reflection optical design for the LDDM system, the heterodyning detector is housed coaxially inside the frequency-stabilized laser source. Instead of a typical single reflection on the moving target, the laser beam is reflected back and forth twelve times between the fixed base and the moving target as shown in Fig. 1 [7]. The laser beam, which is reflected back to the heterodyning detector, is frequency-shifted by the movement of the moving target relative to the fixed base. With same LDDM laser source and detector electronics, this optical path provides twelve times greater resolution for the linear displacement measurement and encoding. A 0.03 nm resolution was reached by the prototype LDLE system recently [8].

3. High-stiffness weak-link for a linear-motion-reduction mechanism

We have developed a novel weak-link linear-motion-reduction mechanism to perform linear motion closed-loop control at the subangstrom level with a travel range in microns. The structure consists of four groups of overconstrained weak-link parallelogram mechanisms [9,10] as shown in Fig. 2. The precision of the modern photochemical machining process using lithography techniques makes it possible to construct a strain-free (or strain-limited) overconstrained mechanism on a thin metal sheet. By stacking these thin metal weak-link sheets with alignment pins, we can construct a solid complex weak-link structure for a reasonable cost.

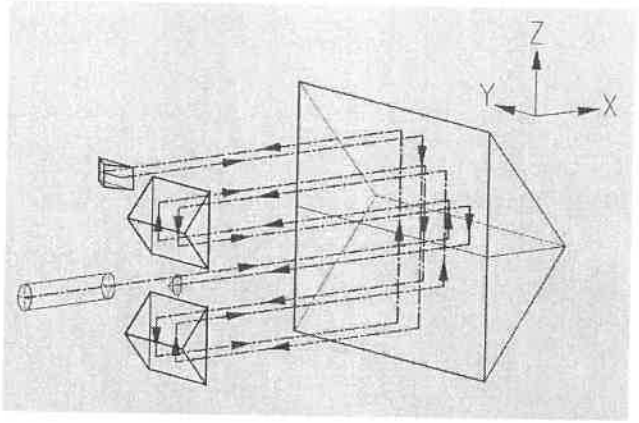

Fig.1. Schematic of the the self-aligning multiple-reflection optical design. With same LDDM laser source and detector electronics, this optical path provides twelve times greater resolution for the linear displacement measurement and encoding.

We have tested the sensitivity of the weak-link linear-motion-reduction mechanism with a laser Doppler linear encoder. During the test, a Physik Instrumente PI-841 PZT actuator with E-501.10 amplifier [11] was used for input motion control. Driving sensitivity better than 0.03 nm was demonstrated with this weak-link linear-motion-reduction mechanism with a 1 micron travel range.

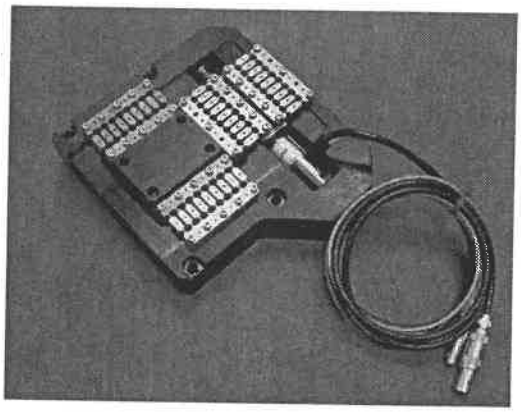

Fig. 2. Photogragh of the high-stiffness weak-link linear-motion-reduction mechanism.

4. Scanning Stage System Design

Besides the detector system, the prototype probe consists of three major component groups: a supporting base with a two-dimensional differential laser Doppler displacement encoder system, a stage group for the zone plate optics, and a stage group for sample holders.

Ideally, the base structure should be made from materials with good thermal stability, such as invar or Zerodur. Here, aluminum alloy was used for prototype purposes. A total of four sets of laser head and sixteen-reflection optics for the LDDM were mounted on the base structure to perform a two-dimensional differential measurement between the x-ray zone plate optics holder and the sample holder. A set of thermal and acoustic shield has been designed to reduce the influence of heat from the laser heads and insure the LDDM stability.

The stages for the zone-plate optics provide a three-dimensional positioning capability with 0.125 nm measuring resolution in 12 mm x 12 mm x 12 mm range. It includes three commercial DC-motor-driven translation stages and two Argonne developed PZT-driven high-stiffness stages using overconstrained weak-link parallelogram mechanisms for ultraprecision motion control. A zone plate holder was mounted on the top of the stage group, which consists of two sets of mini-stages: a pair of x-y commercial DC-motor stage for optical order-sorting-

aperture (OSA) alignment, and a set of Argonne-developed picomotor-driven weak-link x-y-z stages for multiple zone-plate optics alignment.

The stage group for the sample holder is composed of three commercial DC-motor-driven x-y-z scanning stages and a DC-motor-driven rotary stage for x-ray tomography applications. To improve the sample positioning accuracy, two pairs of capacitance sensors were used to dynamically measure the angular and displacement shifts of the rotation axis. The sample position will be determined by the combination of the LDDM system and the capacitance sensor system [2].

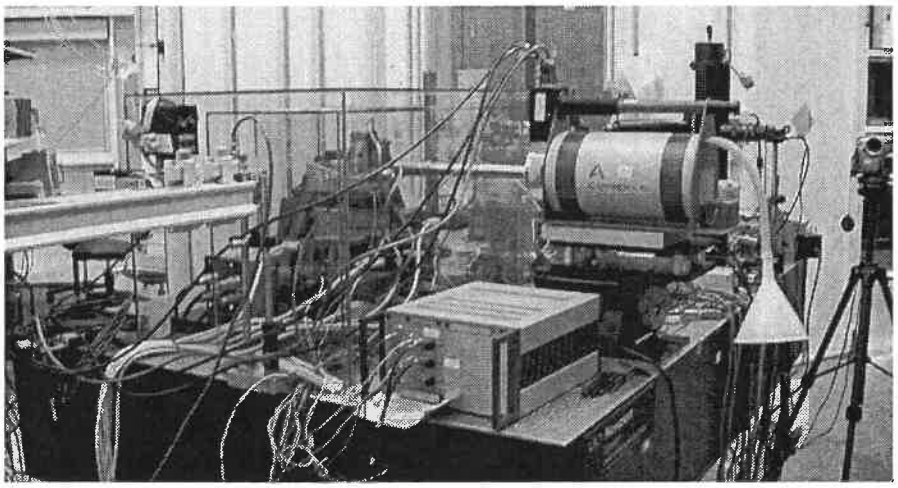

Fig. 3. Photograph of the x-ray nanoprobe prototype at the APS 8-ID-E experimental station.

5. Preliminary Test Results

The controls and feedback system for the nanoprobe is based on a one-dimensional laser linear actuator system used in an atomic force microscope [8]. In this configuration, it has demonstrated an 80 pm displacement resolution in closed-loop control.

We started the x-ray nanoprobe prototype online commissioning in August 2003. Figure 3 shows a photograph of the prototype at the APS 8-ID-E experiment station. Figure 4a and 4b show an active vibration-control test with the prototype system. During this test, the closed-loop control system performed a damping action to a single external mechanical disturbance (an 80 kg mass dropped to the floor from 0.2 m height at three meters away). A series of 1 nm and 3 nm differential vertical and horizontal displacement steps (between zoneplate holder and sample holder) have been demonstrated with closed-loop control as shown in Fig. 4c and 4d.

6. Summary

We have developed a prototype instrument with a novel interferometrically controlled scanning stage system. The system consists of nine DC-motor-driven stages, four picomotor-driven stages, and two PZT-driven stages. An APS-designed, custom-built laser Doppler displacement meter system provides two-dimensional differential displacement measurement between the zone-plate x-ray optics and the sample holder. One nm and 3 nm differential vertical and horizontal displacement steps (between the zone-plate holder and sample holder) have been demonstrated with closed-loop control. We are continuing to work on optimization of the prototype system's dynamic performance.

Acknowledgments

The authors would like to thank D. Nocher, M. Holt, C. Preissner, M. Muscia, and A. Nyman from the Argonne National Laboratory for their help in the prototype development and test. This work was supported by the U.S. Department of Energy, Office of Science, under Contract No. W-31-109-Eng-38.

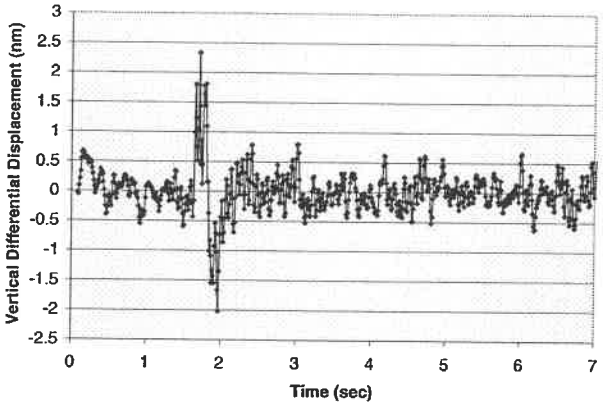

Fig. 4a. Vertical active vibration control test.

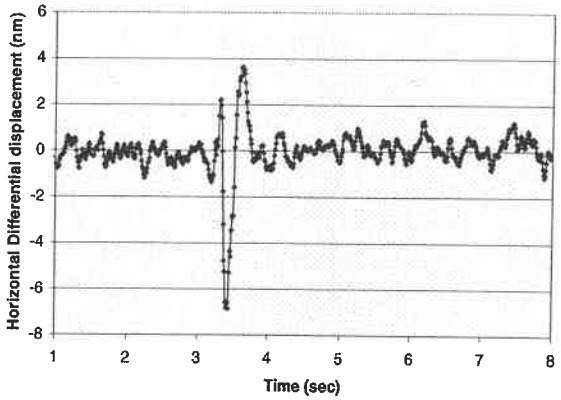

Fig. 4b. Horizontal active vibration control test.

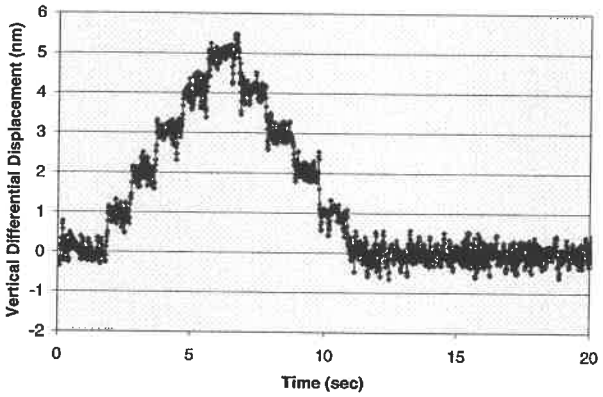

Fig. 4c. Vertical differential displacement test.

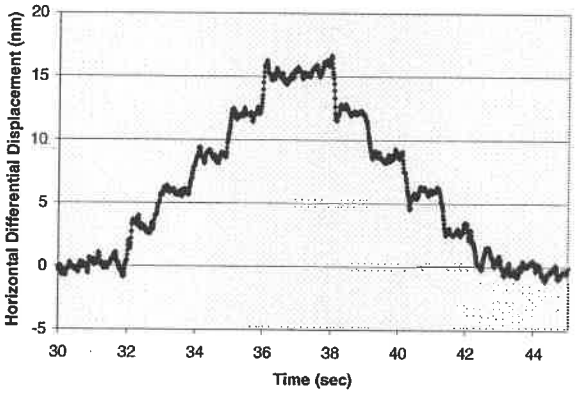

Fig. 4d. Horizontal differential displacement test.

References

1. J. Maser, G. B. Stephenson, D. Shu, B. Lai, S. Vogt, A. Khounsary, Y. Li, C. Benson, G. Schneider, SRI 2003 Conf. Proc., 705, AIP (2004) 470-473.
2. D. Shu, J. Maser, B. Lai, and S. Vogt, SRI 2003 Conf. Proc., 705, AIP (2004) 1287-1290.
3. Picomotor is a trademark of Newfocus Co. California.
4. D. Shu, E. E. Alp, J. Barraza, T. M. Kuzay, and T. Mooney, Proc. SPIE Vol. 3429 (1998) pp. 284-292.
5. U.S. Patent granted No. 5,896,200, Optical design for laser encoder resolution extension and angular measurement, D. Shu, 1999.
6. LDDM is a trademark of the Optodyne Inc., 1180 Mahalo Place, Compton, CA 90220, U.S.A.
7. D. Shu (2001) Patent application in progress.
8. D. Shu, Y. Han, T. S. Toellner, and E. E. Alp, Proc. SPIE Vol. 4771 (2002) pp.78-90.
9. U.S. Patent granted No. 6,607,840, Redundantly constrained laminar structure as weak-link mechanisms, D. Shu, T. S. Toellner, and E. E. Alp, 2003.
10. D. Shu, T. S. Toellner, and E. E. Alp, Nucl. Instrum. Methods A 467-468, 771-774 (2001).
11. Physik Instrumente (PI) is a trademark of the Physik Instrumente GmbH & Co. Germany.

Key words: scanning stage, differential measurement, high precision positioning

The submitted manuscript has been created by the University of Chicago as Operator of Argonne National Laboratory ("Argonne") under Contract No. W-31-109-ENG-38 with the U.S. Department of Energy. The U.S. Government retains for itself, and others acting on its behalf, a paid-up, nonexclusive, irrevocable worldwide license in said article to reproduce, prepare derivative works, distribute copies to the public, and perform publicly and display publicly, by or on behalf of the Government.

ULTRA-PRECISION FLOAT POLISHING OF OPTICAL MATERIALS

Yoshiharu Namba

Chubu University, 1200 Matsumotocho, Kasugai, Aichi 487-8501, Japan

1. Introduction

The float polishing process has been originally developed for making ultra-smooth sapphire surfaces[1] in order to develop the silicon-on-sapphire (SOS) devices. In this application, the substrates have to be dislocation- and contamination-free surfaces, however, the demand for flatness was not serious because of its application as a wafer. The next application was for making VCR magnetic heads of Mn-Zn ferrite single crystals[2-3]. In this application, the requirements of finished surfaces are higher flatness of $\lambda/10$ at 633nm wavelength, small surface roughness of less than 1nm Ry, sharp edges of 10nm radius at corners, dislocation- and elastic stress-free, though the samples were small. The residual elastic stress causes a change of magnetic property on Mn-Zn ferrite single crystal, and dislocation due to machining causes the broadening of the magnetic gap length. The magnetic heads for VHS high density recording were produced tens of millions in a year by using this float polishing technology, because this method can produce the ultra-precision parts in very high yield rate without skilled opticians.

Then, the float polishing has been used for making both ring laser gyroscopes and optics for high power lasers[4] in industries and research institutes. This polishing method can make atomically flat surfaces on single crystals[5-7] and optical glasses[8-11] without subsurface damage. This technology can be also used for making flat on polycrystalline materials[12-13], though there appear steps at the grain boundary due to the difference of removal rate on different crystallographic surfaces.

This paper deals with the method and some results on float polishing of optical materials for obtaining higher optical performance.

2. Polishing Procedure

The key technology of making flat surfaces by polishing is how to obtain and how to maintain a flat lap or polisher, so that opticians suffer troubles in flatness on pitch laps. The single point diamond turning of a tin lap is essential for float polishing. An ultra-precision float polishing machine[8] like a double-column vertical lathe has a hydrostatic oil bearing of high rigidity and accuracy, and a rail head having a tool post. The tin lap of 460mm in outer-diameter and 120mm in inner diameter is set on the horizontal faceplate of the main spindle. The tin lap was fixed on a stainless steel plate by epoxy resin. At first, the tin lap was cut into flat by a sintered diamond tool and cut for making grooves of 1mm depth and width with a pitch of 2mm by a cut-off tool of high speed steel. Then the tin lap was cut flat by a sharp diamond tool of single crystal without any burrs, as shown in Fig. 1. The cutting conditions were 300rpm in revolution of the main spindle, 5μm in depth of cut and 0.3mm/rev in feed rate without lubricant. The lap was cleaned with pure water.

Pre-polished or ultra-precisely ground samples were fixed on a sample holder by low-melting point wax or by a

double sticky tape. The polishing fluid was a mixture of pure water and 3wt% SiO_2 powder, and was controlled within a temperature range of 0.01K. Polishing pressure was only applied by the weight of the sample and sample holder. The rotational speeds of the lap and sample holder were 78rpm and Fig. 2 shows the state of float polishing of Si sample of 100mm in diameter.

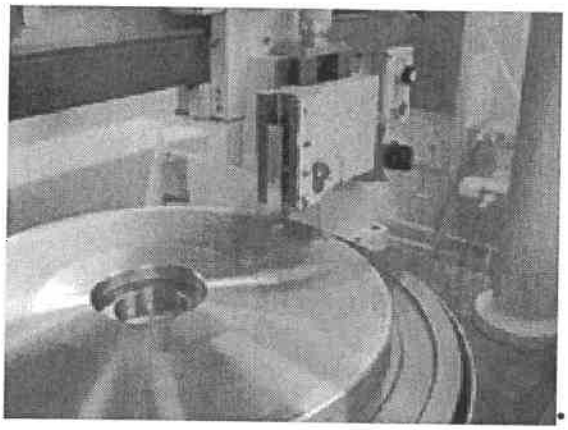

Fig. 1. Single point diamond turning of a tin lap.

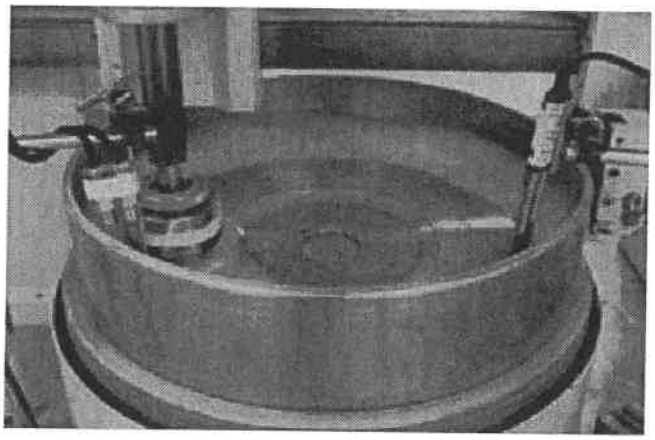

Fig. 2. The state of float polishing.

3. Optical Surface and Optical Properties

Figure 3 shows the flatness of a 100-mm-diameter, 20-mm-thick float-polished Si (001) sample, measured with ZYGO GPI-XP. The flatness was 28.4nm p-v, corresponding to $\lambda/22$ at λ =633nm wavelength, and 4.43nm rms. We also measured the surface roughness using a special scanning probe microscope (SPM) for large samples. The surface roughness values are 0.079nm rms, 0.063nm Ra and 0.59nm Ry, as shown in Fig. 4. Such surface roughness was obtained on various materials[5-7, 9].

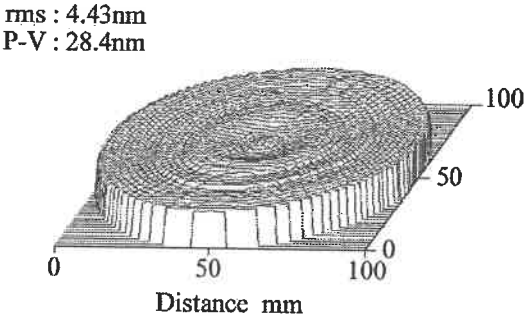

Fig. 3. Flatness of float-polished Si single crystal.

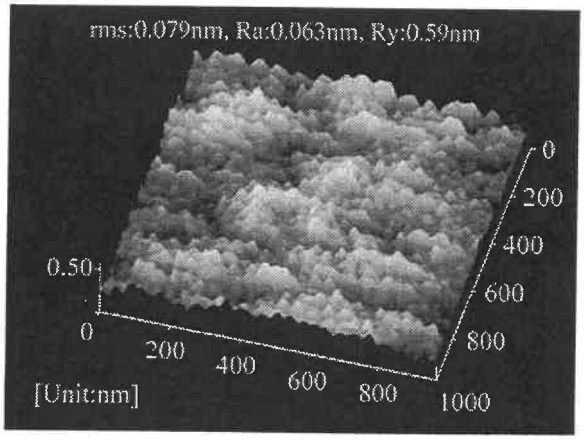

Fig. 4. Surface roughness of float-polished Si single crystal, measured with an SPM.

Figure 5 shows the relation between the specular reflectivity at the wavelength of 0.834nm on polished Si substrates and surface roughness at the grazing incident angle of 0.7 degree. In this figure the solid line shows the

theoretical curve between the specular reflectivity and rms surface roughness on Si substrates. The specular reflectivity increases with the decrease of surface roughness even in the range of less than 0.5nm rms. The maximum sepecular reflectivity is calculated at 93.1% on the zero surface roughness Si. The measured specular reflectivity on the float-polished Si surface shows 91.2%, which is 98% compared with that on the ideal surface.

Figure 6 shows the relation between the laser-induced damage threshold on LHG-8 laser glass and surface roughness for several machining processes and laser irradiating directions. It is clear that the laser-induced damage threshold is a function of surface roughness. Float polished surfaces show the highest laser damage threshold of 31.9J/cm^2 as shown in Fig. 6, though the surface roughness variation is not so different among all the samples in the surface roughness range of less than 0.5nm rms. The reason of those differences is concluded that the float-polished surface is contamination free and also damage free.

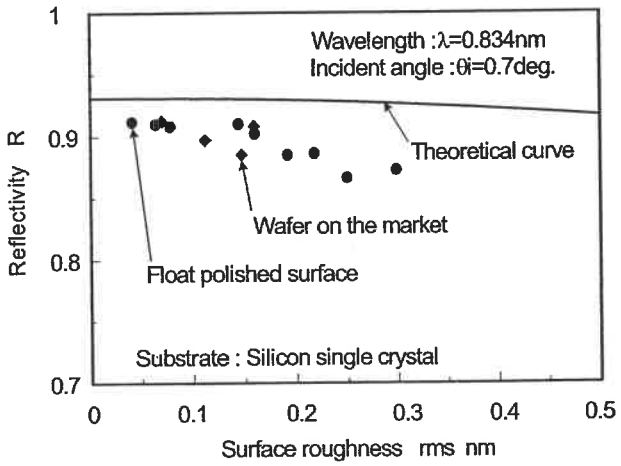

Fig. 5. The relation between the X-ray reflectivity and surface roughness on Si single crystal substrate at the wavelength of 0.834nm at the grazing incidence angle of 0.7degree[5].

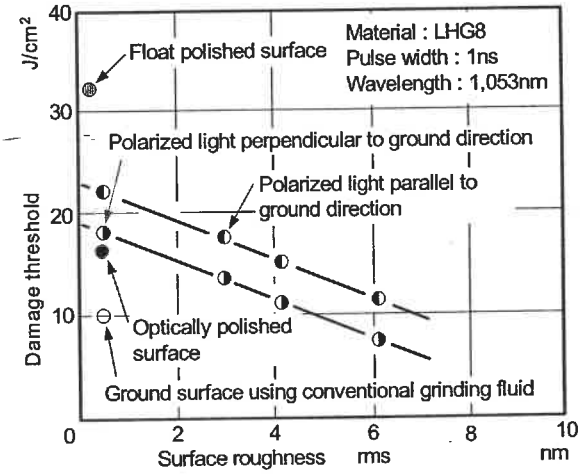

Fig. 6. The laser-induced damage thresholds of ground and polished laser-glass surfaces at the wavelength of 1053nm and pulse width of 1ns as a function of surface roughness[4].

The fracture strength of optical components is very important in space application as well as on the earth. The float-polished Zerodur glass-ceramics sample shows 4.7 times higher facture strength compared with the standard ground and polished samples[10]. In the case of quartz crystals, the float-polished samples showed 10 times higher fracture strength rather than conventionally prepared samples[6].

From the various surface analyses such as reflection electron diffraction, ion microprobe mass spectroscopy, Auger spectroscopy, etch-pit method and cross-section transmission electron microscopy, it was proved that the float-polished surface has no subsurface damage and no contamination.

4. Conclusions

The float polishing has succeeded in making extremely-smooth, damage- and contamination-free flat surfaces on

single crystals and optical glasses. In some case, polished surface roughness shows almost same as ideal surface roughness. The problems to be solved in near future are float polishing of spherical or aspherical shape as well as polycrystalline and composite materials.

Acknowledgements

This study was supported in part by the Grants-in-Aid for Scientific Research (B) Nos. 14350077 and 15360075 from the Japan Society for the Promotion of Science, and also the Grants-in-Aid for Scientific Research on Specially Promoted Research No. 15001002 from the Ministry of Education, Science, Sports and Culture, Japan. In particular, I wish to thank many graduated students who worked in my laboratory for their assistance.

References

[1] Namba Y, Tsuwa H. Ultra-Fine Finishing of Sapphire Single Crystal. Ann CIRP 1977;26(1):325-329.

[2] Namba Y, Tsuwa H. Mechanisms and Some Applications of Ultra-Fine Finishing. Ann CIRP 1978;27(1):511-516.

[3] Namba Y, Tsuwa H. Float Polishing of Mn-Zn Ferrites and Characteristics of Finished Surfaces. In: Proceedings of the Fourth International Conference on Precision Engineering, Tokyo, 1980. p.1017-1022.

[4] Namba Y, Yoshida K, Yoshida H, Nakai S. Ultraprecision grinding of optical materials for high power lasers, Proc. SPIE 1998;3244:320-330.

[5] Namba Y, Zushi K, Tanaka T, Yamashita K, Tawara Y, Okajima T. Effect of surface roughness of Si substrate and Pt-C multilayer coated film on X-ray reflectivity. Initiatives of Precision Engineering at the Beginning of a Millennium, Kluwer Academic Publishers 2001:659-663.

[6] Soares SF, Namba Y. Experimental Quantization of Surface and Sub-Surface Structure in Float Polished Crystalline Quartz. JSME Int'l Journal, Series C, 2004;47(1):93-97.

[7] Namba Y, Ohnishi N, Yoshida S, Harada K, Yoshida K. Ultra-Precision Float Polishing of Calcium Fluoride Single Crystals for Deep Ultra Violet Applications. Ann CIRP, 2004;53(1):459-462.

[8] Namba Y, Tsuwa H, Wada R. Ultra-Precision Float Polishing Machine. Ann CIRP 1987;36(1):211-214.

[9] Bennett JM, Shaffer JJ, Shibano Y, Namba Y. Float Polishing of Optical Materials. Appl Opt 1987;26(4):696-703.

[10] Namba Y, Takehara H, Nagano Y. Fracture Strength of Zero-Thermal Expansion Glass-Ceramics for Ultra-Precision Components. Ann CIRP 2001;50(1):239-242.

[11] Lodha GS, Yamashita K, Kunieda H, Tawara Y, Yu J, Namba Y, Bennett JM. Effect of Surface Roughness and Subsurface Damage on Grazing-Incidence X-Ray Scattering and Specular Reflectance. Appl Opt 1998;37(22):5239-5252.

[12] Namba Y, Tsuwa H. A Chemo-Mechanical Ultrafine Finishing of Polycrystalline Materials. Ann CIRP 1979;28(1):425-429.

[13] Namba Y, Tsuwa H. Surface Properties of Polished Stainless Steel. Ann CIRP 1980;29(1):409-412.

TUNABLE ULTRASONIC VIBRATION-ASSISTED DIAMOND TURNING OF STEEL

Jerald L. Overcash, James F. Cuttino
Center for Precision Metrology
University of North Carolina at Charlotte, Charlotte, North Carolina 28223

Abstract
Vibration-assisted machining (VAM) has significant advantages over conventional machining with regard to tool wear and surface finish. Applying this machining technique to diamond turning applications has broadened the material selection to include hard and brittle materials. The mechanisms describing this ultra-precision machining process are yet to be explained. This paper outlines a new direct drive system that allows variability in the frequency and amplitude of a vibrating tool, which can lead to the analysis of material removal mechanisms. The preliminary results are presented.

Device
A new device has been designed for VAM that allows for variation in the vibration parameters to facilitate in the identification of the empirical relationships describing the means for material removal employing this process. Existing VAM systems extensively exploit resonant behavior to excite the tool tip. The limitations of these systems include fixed operating frequencies and amplitudes. Some VAM systems have utilized direct drive methods that are limited to low operating frequencies due to actuator heating. An ultrasonic vibration-assisted diamond turning (UVADT) device has been constructed that allows for variation of vibration frequency and amplitude to conduct the necessary experiments.[1] A novel driving method has been implemented to induce high frequency vibrations on the tool in the cutting direction only. The motion is realized through piezoelectric actuators acting on a flexure based tool system. Numerous actuators are employed to amplify the frequency output and reduce the actuator temperature. The driving signal is in the form of impulses delivered to each actuator with a phase shift proportional to the number of actuators.

The actuation force is realized by the piezoelectric actuators and opposes the cutting force. Frequencies as high as forty kilohertz and amplitudes above seven micrometers have been achieved at the tool tip during cutting.

Preliminary Surface Results
An initial test part was turned in mild steel to further investigate tool wear and surface finish using the UVADT device. The class of steel was chosen as a free-machining grade, 12L14, with an increased lead content. The significance of applying the technique of vibration-assisted machining to turning steel with a diamond tool lies in the issue of carbon affinity and the resulting acceleration in tool wear from this chemical reaction.

Figure 1: Diamond Turned Steel Ring Part

The test part was manufactured with nine rings in the face of the steel part, eight vibration machined rings and one ring turned conventionally. Mineral oil was the coolant for all cuts in the preliminary part. The tool used was a single crystal diamond with a tool nose radius of 0.020 inches. The ring width was 3 mm and the spindle speed was set at 300 rpm for all cuts in the initial part. The depth of cut was chosen to be 20 micrometers and the frequency of vibration for the vibration cuts was fixed at 40 kHz. A Precitech Nanoform 350 precision diamond turning machine was used as the base for the experiments. The remaining process parameters as well as the resulting surface data are listed in Table 1. The surface data was retrieved using a Wyko Mirau Interferometer with a 20X magnification.

According to the data, ring 1 (no vibration) proves to have the lowest surface roughness (*Ra*) value but ring 9 has the lowest *Rt* value. Notice that the surface roughness values are larger than typical diamond turned surfaces but the depth of cut was also large at 20 micrometers. Generally, the depth of cut for precision diamond turning is less than 10 micrometers, even for soft materials. The depth of cut was chosen for a tool

wear study and not necessarily surface roughness evaluation. Rings 2 through 9 were turned at a single point on the cutting edge. The tool was then removed for measurement and ring 1 was turned using a different location on the tool nose. In all 773.7 meters were cut using vibration-assisted diamond turning and 274.6 meters were cut using conventional diamond turning.

#	Outer Radius (mm)	Inner Radius (mm)	Amp. (um)	Feed (um/ rev)	Ra (nm)	Rt (um)
1	50	47	0	3	45.8	1.5
2	45	42	7	10	342.8	4.0
3	40	37	7	10	144.0	2.7
4	35	32	7	7	121.3	3.0
5	30	27	5	3	66.1	1.5
6	25	22	5	3	68.9	2.5
7	20	17	3	3	51.5	1.7
8	15	12	3	3	58.3	1.8
9	10	7	7	3	57.0	1.1

Table 1: Turning Parameters and Surface Data

Figure 2 shows an optical micrograph of the diamond tool nose after turning both cases. The upper wear region is the result of vibration-assisted machining while the larger wear region in the lower portion of the figure is the consequence of conventional machining. One can see that the damage from conventional diamond turning is significantly more than that due to the UVADT process. Quantitatively, the penetration of the damage from the tool nose for UVADT is approximately 4.9 μm but for conventional diamond turning the damage depth reaches roughly 12.5 μm.

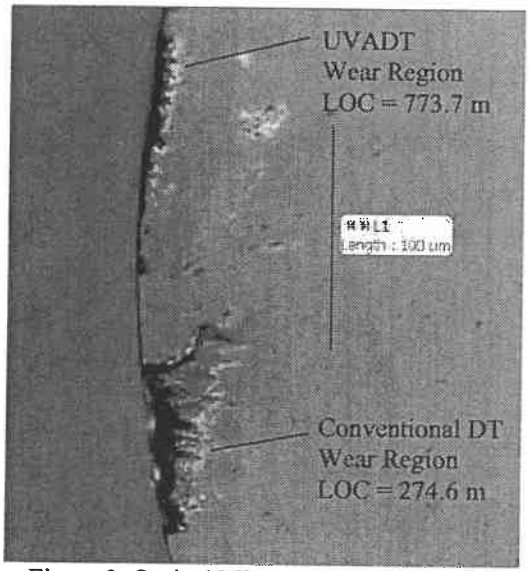

Figure 2: Optical Micrograph of Tool Wear

The chips from these turning experiments were collected and evaluated using the scanning electron microscope (SEM). The resulting chips are shown in Figure 3 and Figure 5 for conventional diamond turning and UVADT, respectively. The carbon content was found to vary with vibration using spectroscopy in-situ with the SEM. The respective element content is presented in Figure 4 and Figure 6.

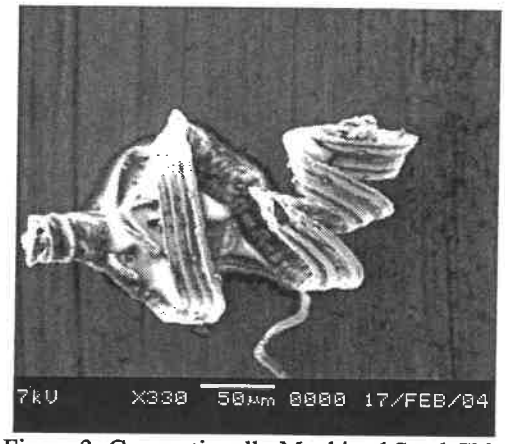

Figure 3: Conventionally Machined Steel Chip

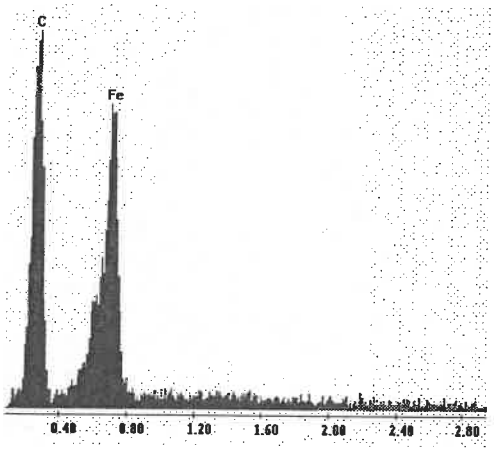

Figure 4: Conventionally Machined Spectrograph

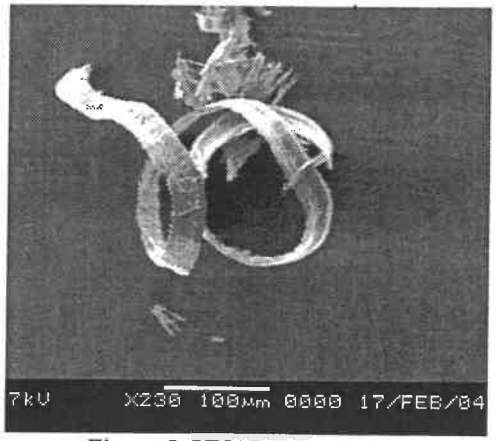

Figure 5: UVADT Steel Chip

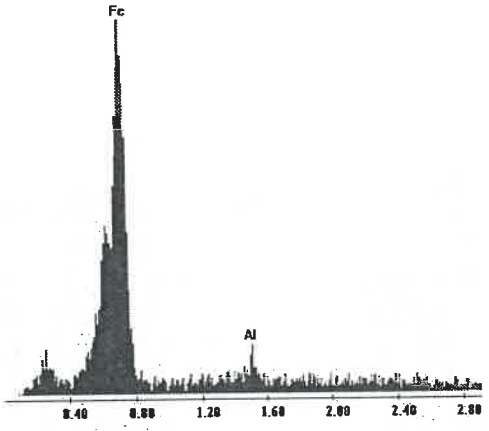

Figure 6: UVADT Spectrograph

Clearly, from Figure 4 and Figure 6, the carbon content varies drastically as determined by the vibration process. The vertical scale is normalized and the element content is represented in percent. Numerous chips have been analyzed showing comparable results with regard to element content.

Further Experimental Results

Additional experiments were carried out with diamond turning 12L14 steel. Efforts were taken to reduce that process variables in a series of ring cuts on the face of the workpiece. For these experiments the cutting velocity was fixed at 10.5 m/min at the center of each ring. Each ring resulted in a length of cut of 12 m at a constant feed of 5 μm/rev. No coolant was used during these cuts and the depth of cut was again 20 μm. The cutting parameters are documented in Table 2 where the mean velocity ratio is the ratio of the vibration velocity to the cutting velocity at the center of the ring. A Kistler 9256A1 dynamometer was used to collect the force data during cutting. The thrust forces are shown in Figure 7 and the cutting forces in Figure 8 as a function of the vibration frequency for varying amplitudes of vibration. The data indicates a trend in force reduction with increasing frequency with some deviations.

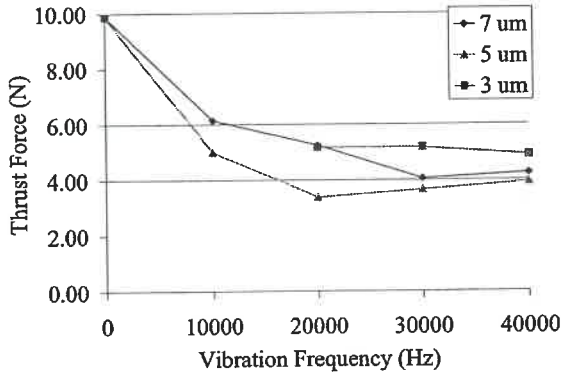

Figure 7: Thrust Force versus Vibration Frequency

#	Inner Radius (mm)	Outer Radius (mm)	Vib. Amp. (um)	Vib. Freq. (Hz)	Mean Velocity Ratio
1	1.79	4.72	7	40000	10.05
2	5.22	6.80	7	30000	7.54
3	7.30	8.50	7	20000	5.03
4	9.00	10.00	7	10000	2.51
5	1.79	4.72	5	40000	7.18
6	5.22	6.80	5	30000	5.39
7	7.30	8.50	5	20000	3.59
8	9.00	10.00	5	10000	1.80
9	1.79	4.72	3	40000	4.31
10	5.22	6.80	3	30000	3.23
11	7.30	8.50	3	20000	2.15
12	9.00	10.00	3	10000	1.08
13	5.22	6.80	0	0	0.00
14	1.79	4.72	0	0	0.00
15	7.30	8.50	0	0	0.00
16	9.00	10.00	0	0	0.00

Table 2: Experimental Parameters

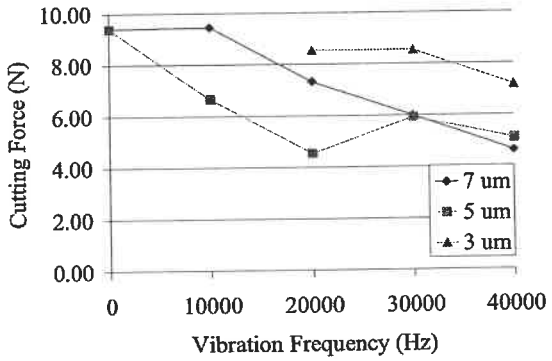

Figure 8: Cutting Force versus Vibration Frequency

Also, the tool forces were found to vary with the vibration amplitude. Figure 9 and Figure 10 show the thrust force and the cutting force as a function of vibration amplitude for varying frequencies, respectively. From the data, the forces are generally higher for lower amplitudes and lower frequencies of tool vibration.

The surface data is given as a function of the vibration frequency in Figure 11. Comparable surface finish values were found between conventional diamond turning and the results when the vibration frequency reached 40 kHz, indicating the higher operating frequencies reduce the surface roughness under these test conditions.

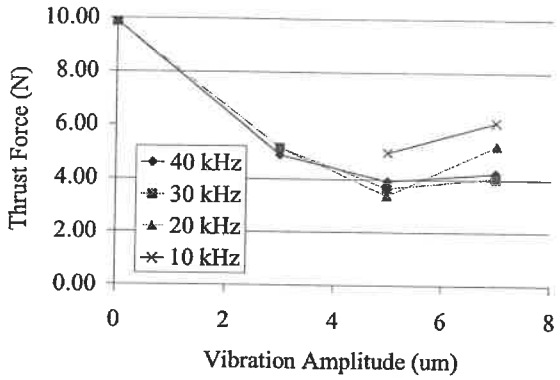

Figure 9: Thrust Force versus Vibration Amplitude

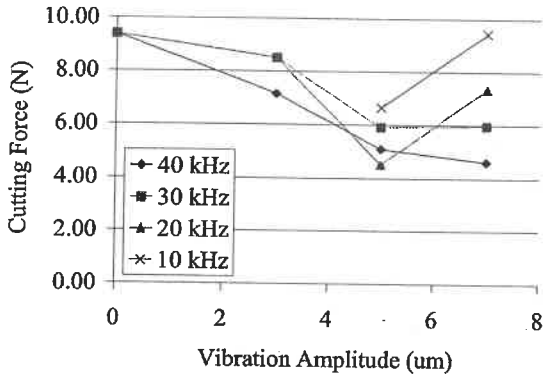

Figure 10: Cutting Force versus Vibration Amplitude

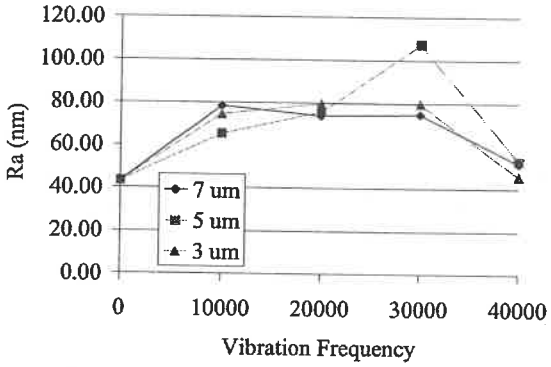

Figure 11: Surface Roughness versus Frequency

The tool wear was documented using an optical microscope and the resulting image is presented in Figure 12. The left wear region is due to 144 meters of cutting using vibration assisted diamond turning and the right wear region is the result of only 48 meters of cutting using conventional diamond turning. Again, the tool wear is reduced by applying the vibration assisted technique even under dry cutting conditions.

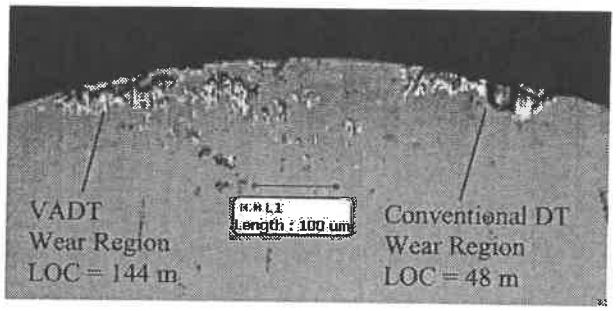

Figure 12: Optical Micrograph of Tool Wear

Summary

A device has been constructed to induce ultrasonic vibrations on the tip of a diamond tool that has the ability to vary the amplitude and frequency. The preliminary workpiece material was chosen to be 12L14 steel and a part was manufactured. The tool wear mechanisms were found to be different for the two cases based on the tool wear and chip data.

The experimental approach to refining the process variables has found that tool wear and workpiece carbon content is reduced by the VAM process. The advantage is 40% less tool wear over nearly three times the length of cut for UVADT as compared with conventional diamond turning of 12L14 steel. As expected, the carbon from the diamond tool charges the workpiece material because of the chemical affinity between the tool and the workpiece. The carbon content in a steel chip produced from conventional diamond turning has substantial carbon content as measured using spectroscopy in-situ with an SEM. Conversely the steel chip produced from UVADT has little or no measurable carbon present. This data is consistent with the theory that the advantages due to the UVADT technique are thermal in nature since the diffusion process is known to be rapidly accelerated with slight temperature increases. Further work must be done to verify these theories.

This work was supported by the industrial affiliates of the Center for Precision Metrology, a National Science Foundation Industry / University Cooperative Research Center supported under grants #EEC9811556 and #EEC0331950. Any opinions, findings, and conclusions or recommendations expressed in this material are those of the author(s) and do not necessarily reflect the views of the National Science Foundation.

[1] J. Overcash and J. Cuttino, "Development of a Tunable Ultrasonic Vibration-Assisted Diamond Turning Instrument", ASPE Proceedings 2003 Annual Meeting, 2003.

MICRO-MACHINING USING ELLIPTICAL VIBRATION ASSISTED MACHINING

B. Brocato, T. Dow and A. Sohn
Precision Engineering Center, North Carolina State University

INTRODUCTION

This paper demonstrates the effectiveness of a new machining process[1] that can be used to create three-dimensional micro-mechanical, micro-optical and micro-fluidic devices. Current MEMS manufacturing techniques, such as like semiconductor lithography and LIGA, suffer from high costs and long lead time for prototyping or short production runs. While micromachining is not what most people think of for creating microstructures, it has the potential for low-cost and fast manufacture of microstructures especially for molding tools [1]. Mechanical milling has been used for making micro-scale 3-D structures, but tool runout relative to feature size becomes worse as tool diameter decreases to produce smaller features. Also, tool deflection increases as tool diameter decreases because of the lack of tool stiffness. The non-rotating tool described will reduced the minimum feature size possible while producing optical quality surface finish.

EXPERIMENTAL APPARATUS

A Diamond Turning Machine (DTM) (NanoForm 600) and a piezoelectric tool servo (UltraMill) are married into a fabrication system that significantly improves the feature resolution of micromachined components. The UltraMill is mounted on a vertical axis that was added to the Z-axis of a 2-axis DTM machine as shown in Figure 1. Also mounted on the Z-axis is a telescope used to find the surface during the UltraMill touch-off process. To create the 3D MEMS devices, the tool is raster scanned over the face of the part using X axis as the scan axis, the Y as the cross-feed axis and the Z to change the depth of cut. An alternate orientation is mounting the UltraMill on the spindle and the part on the Y-axis. The spindle can then be rotated to hold the cutting tool tangent to the cutting direction as the three axes move the part. The X and Z slides of the DTM have hydrostatic oil bearing slides and are driven by DC motors with ball screws. Position feedback is provided by differential laser interferometers with 1.25 nm positioning resolution. The vertical slide (Y) that supports the UltraMill (or the workpiece) is supported by hydrostatic air bearing, driven by a DC motor and ball screw with a high resolution (1 nm) linear encoder for positioning feedback. A Delta-Tau UMAC controller drives the positioning system.

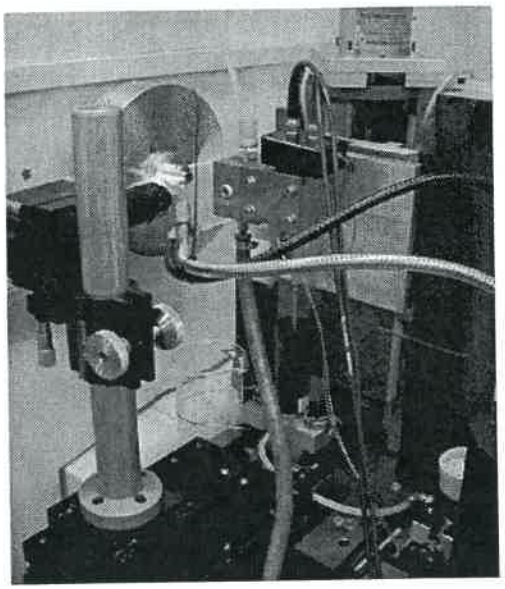

Figure 1. UltraMill mounted on the DTM

Vibrating Tool Holder - UltraMill To create the tool motion, a high-speed piezoelectric actuator called the UltraMill is used. The concept behind this design was to create an adjustable design where the size, shape and frequency of the tool motion could be easily changed. A tool holder is preloaded against a pair of high-voltage piezoelectric stacks as shown in Figure 2. By driving the two stacks with sine and cosine waveforms, an elliptical tool path is created with the

[1] Project funded in part by NSF under contract # DMI-0115175 monitored by G. Hazelrigg

size of the major and minor axes depending on the spacing between stacks, the distance from the tool to the top of the stacks and the amplitude of the actuators. By changing the amplitude and phase of the drive signals, a range of tool paths from nearly linear to circular can be created. A photograph of two generations of the vibrating tool design is also shown in Figure 2. The UltraMill is shown in the foreground with an earlier slower speed design in the background. The UltraMill uses triangular cross-section stacks and a hollow alumina tool holder (weight < 3 gm). A circular titanium diaphragm is mounted at the end of the housing that both seals the housing around the ceramic tool holder and preloads the stacks. The diamond tool[2] is glued to the end of the ceramic holder. The structure was designed to be light and stiff and lowest natural frequency is on the order of 10 KHz. The actuators have a length of 24 mm and a maximum stroke of 22 μm. The maximum excursion for the elliptical motion was a major axis of 52 μm, a minor axis of 8.5 μm and a total size of 104x17 μm measured at 600 v and 4 KHz. While the UltraMill can operate in a frequency range from 1-5 Khz, one of the challenges is cooling the stacks. The cooling system uses a temperature-controlled dielectric fluid pumped into the housing as shown in the cutaway in Figure 2. This system allows the UltraMill to operate continuously at 4000 Hz.

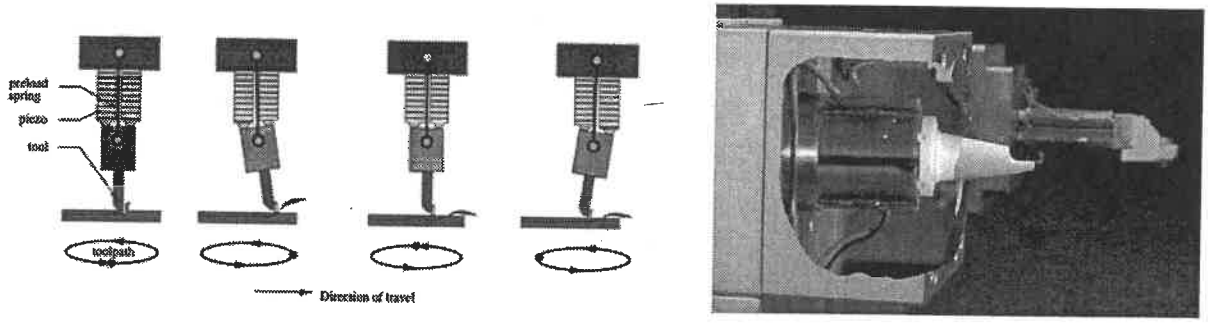

Figure 2. Concept of the Ultramill (left) and photograph of the two prototypes developed (right)

Tool Motion The relationship between the process variables (vibration frequency, amplitude, workpiece speed, depth of cut) are defined in Figure 3. In the case of elliptical tool motion coupled with the linear motion of the workpiece, the dynamic location of the tool edge (x,y) is:

$$x(t) = V_w\ t + a\cos(\omega\ t)$$
$$y(t) = b\ (1 + \sin(\omega\ t)) - d$$

where V_w is the workpiece speed, a and b are the major and minor axes of the ellipse, ω is the frequency of vibration, d is the depth-of-cut and t is time. Figure 3 can be used to illustrate the important parameters of the process [2]; two cycles of the tool are shown and the emphasis will be on the second cycle - a dotted line. This cycle defines the steady-state motion that removes material from the workpiece. Earlier publications on this technique have emphasized the parameters that control the material removal process but the emphasis here is the geometric features produced.

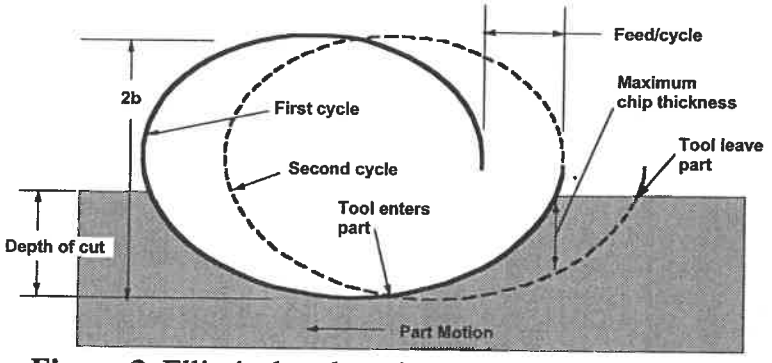

Figure 3. Elliptical tool motion superimposed on part

[2] The diamond tool is 1x1x5 mm in size and was supplied, polished and mounted by Chardon Tool

Surface Features The motion of the diamond tool in the UltraMill produces a series of scalloped features that are elliptical (UltraMill motion) in the cutting direction and circular (tool nose radius) perpendicular to that direction. Thus each scallop has a "characteristic" shape that is a function of the depth of cut and the feed rate in both the cutting direction and the cross feed direction. By choosing the tool nose radius and the depth of cut, different characteristic features can be created and become the building blocks for the surface features created. For example, a 1 mm radius diamond tool operating at the depth of cut of 500 nm with the UltraMill parameters a = 20 μm and b = 4 μm, will produce a characteristic feature with a length of 19 μm and a width of 63 μm for a L/W ratio of 3.25. If the tool nose radius is changed to 50 μm, the length remains unchanged and the width changes to 7 μm for a L/W of 0.75. The surface finish is controlled by the up-feed rate (part speed/UltraMill frequency) and by the cross-feed rate (spacing of scan lines). Surfaces finish better than 20 nm RMS have been created.

Operating Procedure The UltraMill is mounted on the vertical Y-axis as shown in Figure 4 which in turn is mounted to the Z-axis that moves in the direction of depth of cut. The part is mounted on the spindle whose slide moves in the X-direction. An auxiliary diamond tool is mounted next to the UltraMill on the Y-slide as shown in the inset in Figure 4. It is used to face off the test part to make its face in an X-Y plane and guarantee uniform depth of cut over the part. Once the part is faced, the spindle is locked and the UltraMill is touched off to start the machining process. The touch off process is done with the UltraMill operating at equilibrium temperature to deal with the thermal effects of the actuator operation. A long-range zoom microscope (20-130 X) is used to observe the generation of chips from the UltraMill when the surface is reached. The touch off procedure can find the surface to less than 0.5 μm. The features were machined using the X-axis to move the part under the vibrating tool with the Z-axis setting the depth of cut. The structures were raster scanned by cutting in the X-direction, retracting in the Z-direction, indexing in the Y-direction and returning to the start of the X scan.

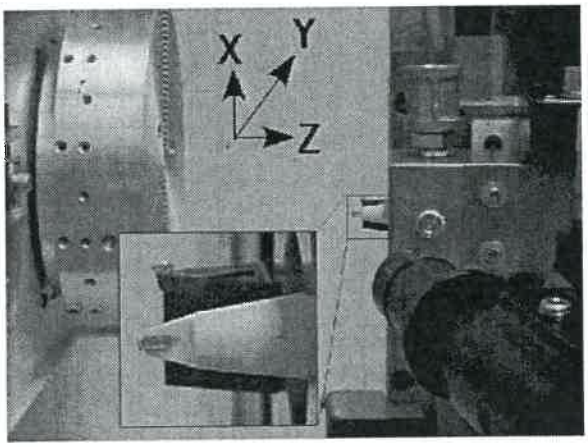

Figure 4. Closeup of the tools on Y axis

PROGRAMMING MEMS FEATURES

The surfaces to be created can be grooved features or 3D shapes. Different programming techniques have been investigated including mathematical description of specific part features, automatic tool path generation from scanned images and CAM software. One complication is the size of the "characteristic" feature created by the UltraMill as discussed above. As the tool depth is increased, the width of the feature also increases. This is normal for round nosed tools and tool radius correction is typically invoked for generating motion programs.

EXPERIMENTAL RESULTS

Grooves Figure 5 shows the results of a series of grooves machined with the UltraMill on a aluminum substrate. The difference in the two micrographs is the depth of cut. When the depth is less than the minor axis of the tool motion ellipse, the chips are discontinuous and if larger, they stay attached. However, the circular nose radius and the tool path combine to make the depth of cut approach zero at the edges of the groove. Notice that in Figure 5(b), the chip are

transparent to the SEM beam indicating a thickness less than 20 nm. As a result of the small chip size and the motion of the tool, a remarkable lack of burring occurs when using the UltraMill. This is a profound advantage compared to other micromachining techniques.

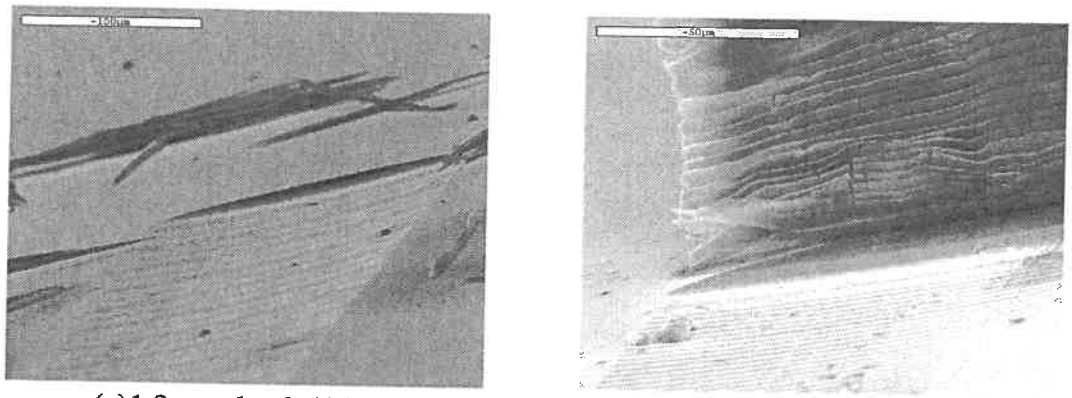

(a)1.3 μm depth (450x) (b) 8 μm depth (1000x)

Figure 5. SEM micrographs of groove and chip geometry (ellipse $a = 20$ μm, $b = 4$ μm)

3D Features Sub-millimeter features were machined to demonstrate the capabilities of the UltraMill fabrication process. The shape chosen was the angstrom symbol used in the PEC logo. The tool had a 1 mm nose radius and the desired feature height was 500 nm. The feature was machined on a copper substrate as shown in Figure 6 and the size of the image is 0.9 mm wide by 0.6 mm high. The height of the features is approximately 350 nm, slightly less than desired. It is also very uniform over the area, which is a testament to the excellent temperature control of the UltmaMill. The part was programmed with 137 scans and the fabrication time was less than 15 minutes. The surface finish on the top of the A surface was 16 nm RMS. Smaller tool radii will permit smaller areal features to be generated.

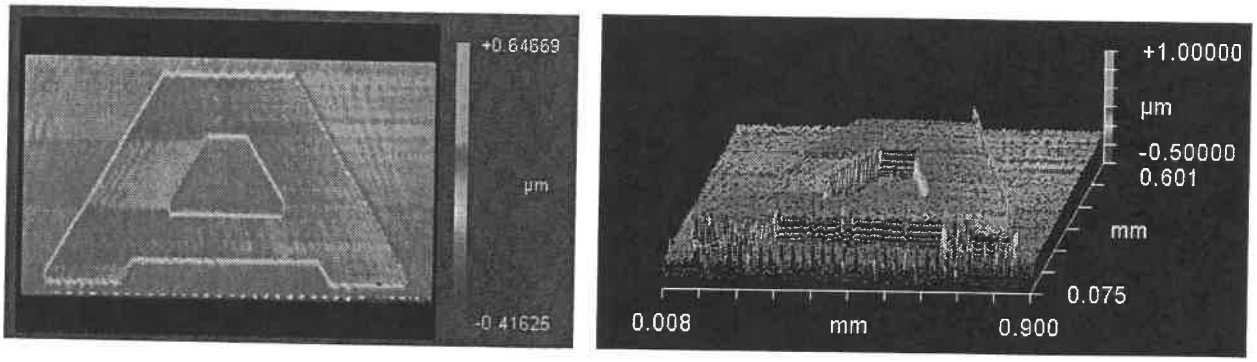

Figure 6. White light interferometer image of machined shape

REFERENCES

1. Schaller, T, Heckele, M, Ruprecht, R, "Mechanical Micromachining for Mold Insert Fabrication and Replication", ASPE Proceedings, Vol.19, Pg 3-8, 1999.
2. Negishi, N, "Elliptical Vibration Assisted Machining with Single Crystal Diamond Tools", MS Thesis, NC State University, 2003.

FORCE ANALYSIS FOR SEGMENTAL GRINDING

Xiaorui Fan, Michele Miller
Michigan Technological University, Houghton, MI

Introduction

Due to the large variety of chemical, electrical, biological, and mechanical properties that ceramics presently exhibit, there are many social and industrial applications with ceramics. On the other hand, some of the desirable properties of ceramics also cause difficulties in machining them to a precise size and shape. Grinding is an enabling technology in the manufacture of ceramic components because it can produce accurate shapes deterministically.

Compared to other machining processes, grinding requires large energy per unit volume of material removed. In other words, for the same amount of material removed, grinding takes much more energy and force. High grinding forces mean higher temperatures that lead to more coolant usage. Both forces and temperatures influence the workpiece accuracy. High grinding forces also make the machining tools wear faster. Methods to reduce grinding forces are, therefore, desirable. For example, high speed grinding has been used to decrease grinding forces [1,2]. The threshold is about 80-180 m/s depending on grinding conditions and workpiece material. Also, in-process dressing sharpens the grinding wheel thus reducing grinding forces.

A number of researchers have demonstrated that segmental grinding is a promising approach to reduce grinding forces. Using a segmental wheel is a convenient way to accomplish intermittent grinding since the spacers of the wheel do not contact the workpiece. Lee et al. [3] explored the cutting force for ceramic face grinding using slotted diamond wheels and built a temperature model for face grinding. Brecker et al. [4] developed a segmental cup wheel to improve grinding performance when work traverse speed is low. He found that the interrupted cutting surface permitted improved cutting fluid effectiveness resulting in significantly lower friction forces, less power, and better surface finish. A.V. Gordeev [5] found that metal bonded segmental wheels wore more slowly than wheels with a continuous working surface.

This paper focuses on developing a force model for segmental wheel grinding. Based on the modeling analysis, optimal segmental wheel geometry will be identified.

Grinding Force Modeling

The grinding force can be divided into normal and tangential components (F_z and F_x respectively). Each of these can be further subdivided into two parts: a cutting component and a rubbing component. The cutting component increases with material removal rate *(MRR)* and the rubbing component is independent of *MRR*:

$$F_z = k_z \cdot MRR^{m_z} + F_{z0}$$
$$F_x = k_x \cdot MRR^{m_x} + F_{x0} \qquad (1)$$

k_z, k_x, m_z, m_x, F_{z0} and F_{x0} are constants that depend on the workpiece material and grinding wheel. F_{z0} and F_{x0} are the rubbing components in the normal and tangential directions, respectively.

MRR Analysis for Segmental Wheel Grinding

Segmental wheel grinding changes the contact pattern between the wheel and workpiece so that the instantaneous material removal rate is different from regular grinding. Based on it, the grinding forces for segmental wheel grinding can be predicted based on the instantaneous MRR change.

The cutting cycle of each segment can be divided into four stages: the previous segment leaving grinding zone, the current segment approaching grinding zone, the current segment entering grinding zone, and the current segment fully contacting the workpiece. The geometry of these four stages was analyzed, and equations for instantaneous MRR were derived based on wheel radius, wheel speed, table speed, depth of cut, and segment size and spacing. Figure 1 shows instantaneous MRR under a set of specific conditions for two segments of grinding, in which 1, 2, 3, and 4 correspond to the four stages respectively. In this plot the contact time between

the wheel and workpiece is a little more than a half cycle (56.8%), and the highest MRR happens in stage 3 when the segment enters to the grinding zone grind zone when the instantaneous depth of cut is highest too).

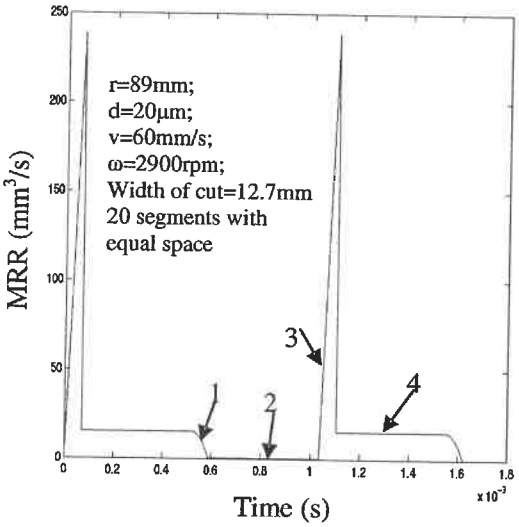

Figure 1: Instantaneous MRR for two segment cycles

Model Calibration Tests

To find the k's, m's and F_0's in Equation 1, a series of surface grinding tests were done with a regular wheel. The experiment setup is shown in Figure 2, and the grinding conditions are shown in Table 1. The wheel was trued with multiple passes to minimize the roundness error. Both normal force F_z and tangential force F_x were measured by a Kistler tri-axial force dynamometer. Then they were amplified and collected by a computer.

Workpiece Material	4140 Steel (50 x 5 x 10 mm)
Grinding Wheel	Aluminum oxide 32AR46-JV40 162 mm dia. x 6.4 mm
Wheel Speed	29.4 m/s
Feed Rate	45, 82, 114, 150 mm/s
Depth of Cut	5, 25, 50, 75, 100 μm
Coolant	No

Table 1: Regular grinding test conditions

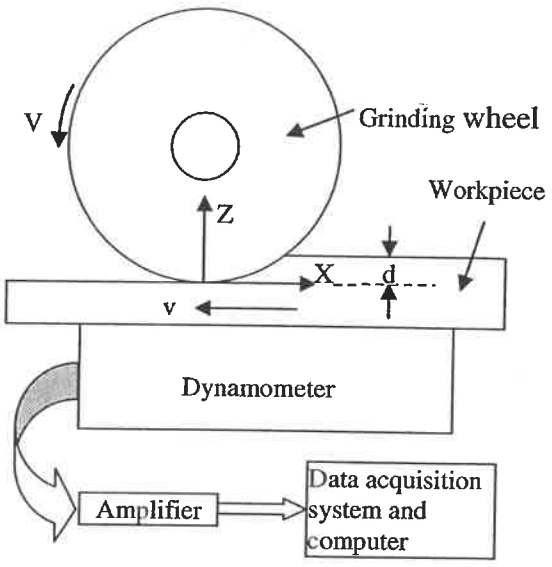

Figure 2: Grinding tests setup

The grinding forces change with depth of cut and table speed as shown in Figure 3 and 4. Every point in these figures is the average of three measurements.

The rubbing components F_{z0} and F_{x0} were measured at sparkout when no new material is removed.

Rubbing component measurements were taken for all the grinding conditions in Table 1. The rubbing components in both directions proved to be independent of table speed or depth of cut of previous passes. In this experiment, F_{z0} and F_{x0} were 0.74 and 0.43 newtons respectively.

Tests were done at five depths of cut and four table speeds for a total of twenty material removal rates.

The curves in Figure 5 are power trend lines fit to twenty points. When MRR is small, it takes more energy to grind material. From this figure, we can find k_z, k_x, m_z, and m_x in Equation (1). In this experiment, they are 4.13, 2.51, 0.77, and 0.81 respectively. So under these grinding conditions, the force model equation is:

$$F_z = 4.13(MRR)^{0.77} + 0.74$$
$$F_x = 2.51(MRR)^{0.81} + 0.43 \qquad (2)$$

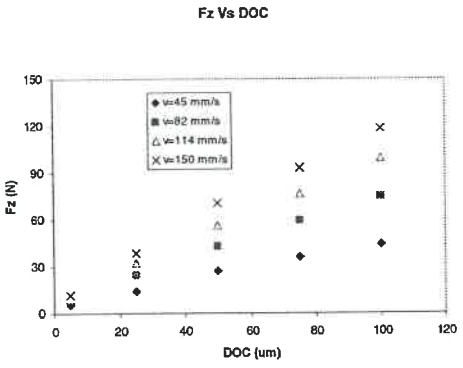

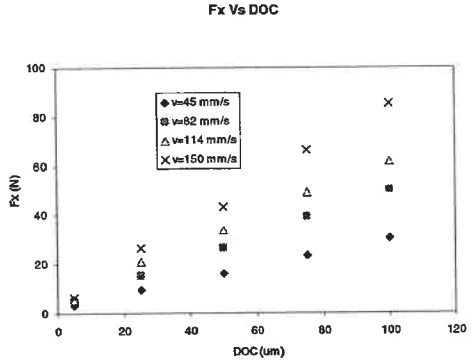

Figure 3: F_z and F_x Vs depth of cut

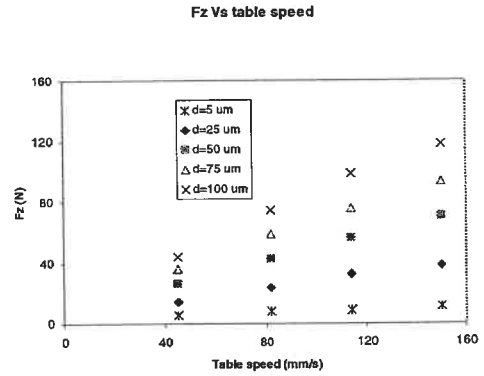

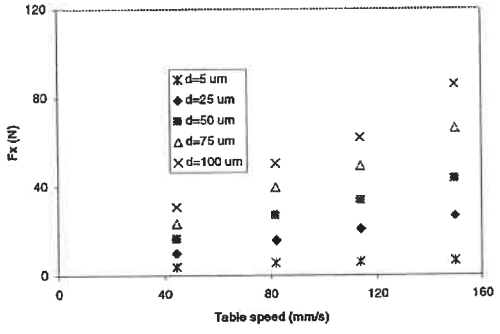

Figure 4: F_z and F_x Vs table speed

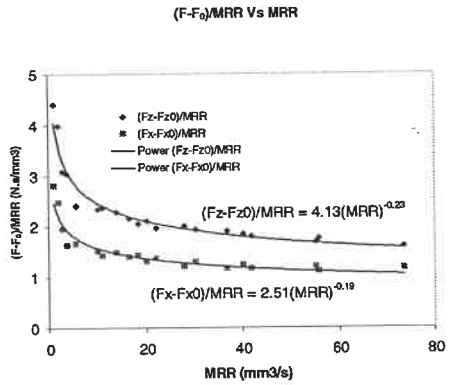

Figure 5: Cutting components Vs MRR

Segmental Grinding Tests

With the instantaneous MRR (as illustrated in Figure 1), Equation 2 can be used to predict segmental grinding forces. Figure 6 depicts the segmental wheels used in experiments for validating the model. They were cut from regular aluminum oxide wheels. Segmental wheel No. 1 has forty teeth and its proportion of segment length to notch length is 1:1. Segmental wheels No. 2 and 3 have twenty segments while No. 4 has ten segments. Wheels No. 3 and 4 have segment to notch length of 3:1.

The experiments were done with these four segmental wheels according to Table 2.

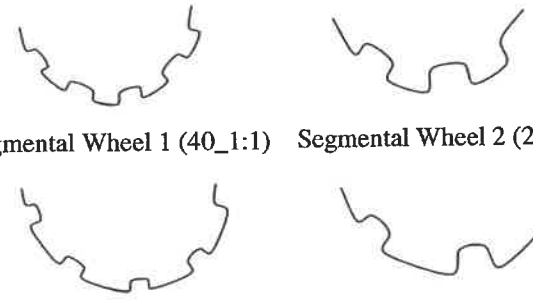

Segmental Wheel 1 (40_1:1) Segmental Wheel 2 (20_1:1)

Segmental Wheel 3 (20_3:1) Segmental Wheel 4 (10_3:1)

Figure 6: Segmental grinding wheels

Workpiece Material	4140 Steel (50 x 5 x 10 mm)
Segmental Wheels	Cut from aluminum oxide 32AR46-JV40 162 mm dia. x 6.4 mm
Wheel Speed	29.4 m/s
Feed Rate	40-150 mm/s
Depth of Cut	25 μm
Coolant	No

Table 2: Segmental wheel grinding conditions

Results and Discussion

Figure 7 compares model prediction from Equation 2 (continuous lines) and average (of three) measured forces (individual points). The error bar corresponds to the 95% confidence interval. For comparison, the modeled and measured forces for regular (no segments) grinding are shown.

The experiment results and model predictions match very well. These plots show that grinding forces reduce when using segmental wheels. Also, fewer segments lead to lower forces and larger segment spacing results in less force. According to MRR analysis, larger segment spaces and fewer segments increase material removed in Stage 3 and decrease that in Stage 1 and 4. Since MRR in Stage 3 is higher than the rest and specific energy is lower with larger MRR, this size effect will result in lower average forces.

Conclusion and Future Work

Segmental wheels are an effective way to reduce grinding forces. However, there are still some concerns. As number of segments decreases, the finished surface roughness increases and the peak forces increase. Meanwhile, the segment is weakened if the space between them is too large.

Future work will focus on the optimal design of segment geometry that can balance following aspects: surface finish, average forces, peak force, subsurface damage and wheel wear.

Reference

[1] Yin, L. and Huang, H., "Ceramic response to high speed grinding," *Machining Science and Technology*, v 8, n 1, 2004, pp. 21-37.

[2] Klocke, F. and Muckli, J., "Grinding at its limits - high-speed grinding," *Technical Paper - Society of Manufacturing Engineers. MR*, n MR99-232, 1999, pp. 1-23.

[3] Lee, K.W., Wong, P.K., and Zhang, J.H., "Study on the grinding of advanced ceramics with slotted diamond wheels," *Journal of Materials Processing Technology*, v 100, n 1, 2000, pp. 230-235.

[4] Brecker, James N. and Shaw, Milton C., "Segmental Cup Grinding Wheel," *Avtomaticheskaya Svarka*, 1975, pp. 441-452.

[5] Gordeev, A. V., "Wear Resistance of Segmental Diamond Wheels," *Machines & Tooling (English translation of Stanki i Instrument)*, v 48, n 2, 1977, pp. 21-22.

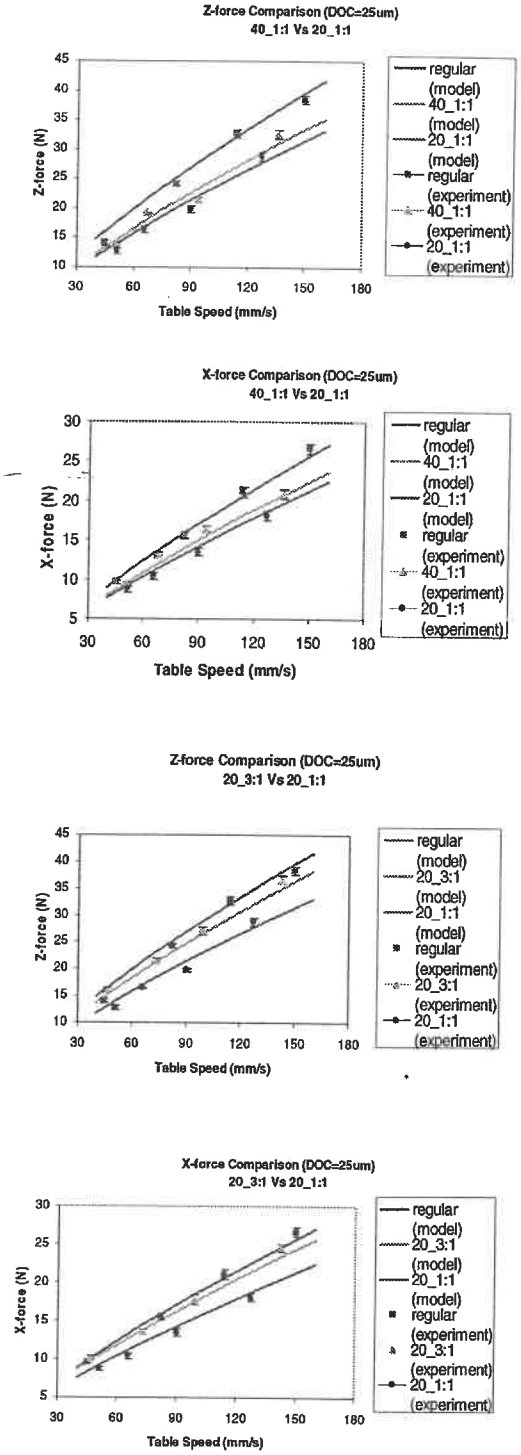

Figure 7: Forces Comparison with Segmental Wheels

Ball-end Milling of Free-form Surfaces for Optical Mold Inserts

Ekkard Brinksmeier, Lutz Autschbach

Laboratory for Precision Machining LFM, University of Bremen, Germany

Abstract
One of the objectives of the Transregional Collaborative Research Center SFB/TR4 of the Universities of Aachen and Bremen, Germany, and Stillwater, Oklahoma is the development of diamond machining processes for metal molds integrated in the process chain for economic mass production of complex optical elements.
In this paper we will discuss the application of diamond ball-end milling for machining of free-form surfaces with small radii of curvature, the generation of NC-programs, requirements on tool alignment and a new high-resolution method for measuring surface slopes, local radii of curvature and figure error of free-form surfaces based on fringe reflection. Surface definition by NURBS is used throughout the process chain from the design stage to mold manufacture, injection molding and testing. The aim of the work presented in this paper is to minimize the number of iteration loops needed for achieving the required surface quality.

Keywords: Diamond ball-end milling, complex surfaces, NURBS, fringe reflection

Introduction

Typical process chains for economic mass production of complex optical components like aspheres, free-form surfaces and structured surfaces include optical design, mold fabrication and replication. If the replication process (e.g. injection molding of plastic lenses or compression molding of glass lenses) does not yield perfect, but repeatable results with constant figure errors, these can be compensated by adapted molding (1). Such surface deviations, caused by inhomogeneous shrinkage and / or other subtle and difficult to control effects, often introduce local radius of curvature errors, whose compensation affords an adequate and flexible machining technique for modifying the mold surface. The most universal technique, also capable of coping with small positive and negative radii of curvature, is diamond ball-end milling (2).

Ball-end milling

The smallest radius of curvature that can be machined by ball-end milling is the radius of the diamond tool. However, machining time is proportional to the inverse of the tool radius, if surface roughness is to be maintained.
Ball-end milling is usually performed with half-arc single crystal diamond tools mounted on a steel shank (Fig. 1a). The achievable figure accuracy of the milled cavities strongly depends on tool alignment. The vertex of the cutting edge must be aligned to coincide with the spindle axis, which was realized with a newly developed adjustable ultra-precision tool holder. Centering of the tool was performed with the help of an optical microscope. Tilt alignment can be done by milling of test cavities and evaluating the created contour with a white-light interferometer (WLI). The setup for tool alignment with an optical microscope is shown in Fig. 1b, while a view on the rake face of a half-arc diamond tool is shown in Fig. 1c. The vertex of the tool could be aligned within 1 µm with respect to the rotational axis and the tilt angles χ and ψ could be set < 0.01°.

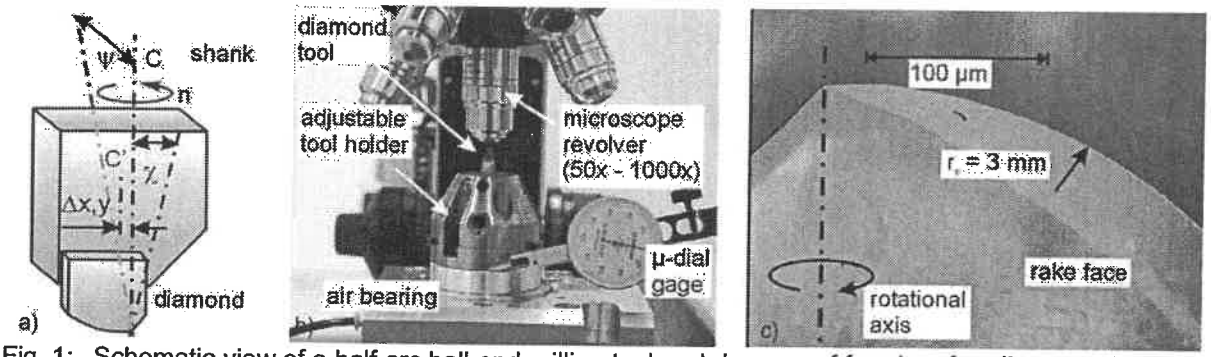

Fig. 1: Schematic view of a half-arc ball-end milling tool and degrees of freedom for alignment (a), setup for alignment with an optical microscope (b), view on the rake face of a half-arc diamond ball-end milling tool (c).

For first milling experiments specimens with ∅ 80 mm were used made of OFHC-Cu, AlMg3 and electroless nickel (NiP). As can be seen in fig. 2, the specimens were designed as inserts for subsequent injection molding of test plates. 6 x 6 matrices were machined by ball-end milling with different diamond tools with nose radius varying between r_ε = 2.5 mm and 5 mm, and with different feed velocities and rotational speeds varying between v_f = 30 mm/min and 200 mm/min and n = 1,000 rpm to 6,000 rpm, resp. The angle between the normal vector of the surface and the axis of rotation was varied between γ_{tilt} = 0° and 40°. The achieved surface roughness, measured with a WLI (cf. Fig. 2b) over an area of 500 μm x 500 μm, was between Ra = 5 nm and 25 nm for NiP and Ra = 15 nm and 40 nm for OFHC-Cu and AlMg3.

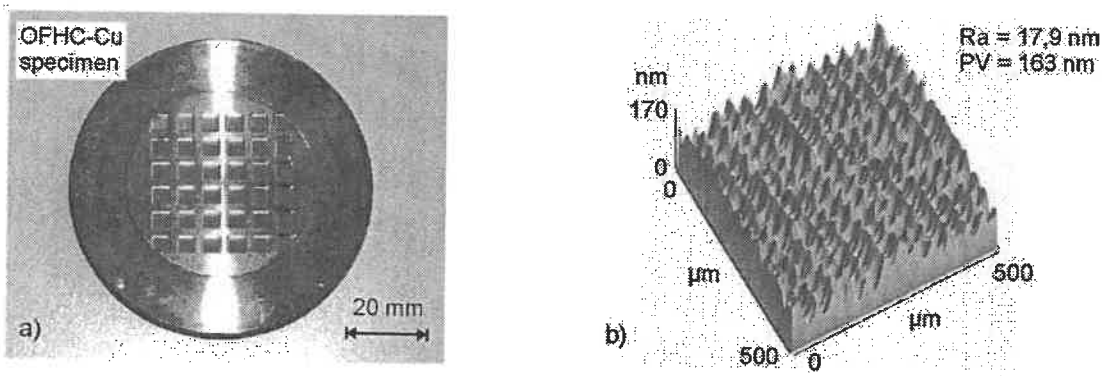

Fig. 2: a) 6 x 6 matrix machined by ball-end milling in OFHC-Cu with different machining parameters.
b) WLI-image of typical ball-end milled OFHC-Cu surface.

Test machining of a free-form surface

Within this work, the NURBS (non-uniform rational B-splines) concept was used as an universal tool for progamming the tool path for ball-end milling operations of free-form surfaces as well as for figure testing and retrofitting of measurement results (cf. Fig. 3) (3).

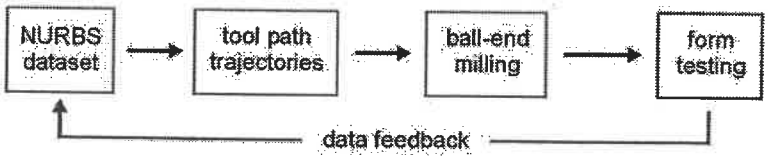

Fig. 3: Basic approach for retrofitting of surface data.

As an example, a free-form mirror surface described by NURBS was machined by ball-end milling which was tailored for projecting the light from a point source onto a screen yielding the logo of the SFB/TR4 (Fig. 4). The mirror surface and the generated tool path for spiral ball-end milling (including tool radius compensation) is shown in Fig. 5. The maximum departure from a plano surface was 1.4 mm. The total cutting distance was 140 m.

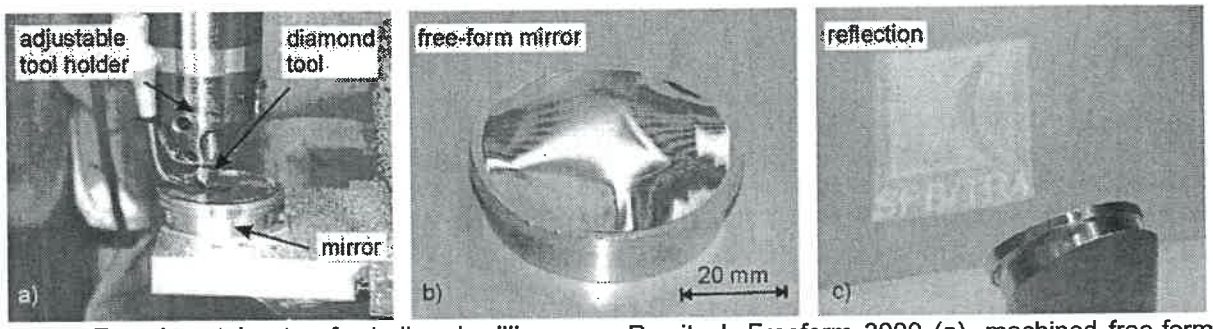

Fig. 4: Experimental setup for ball-end milling on a Precitech Freeform 3000 (a), machined free-form mirror (b) and projection of the SFB/TR4 logo (c).

Ball-end milling was performed on a Precitech Freeform 3000 multi-axis ultra-precision machine using a carbide tool for pre-machining and a half-arc diamond tool with a nose radius of 3 mm for finishing. The increment of the spiral trajectory was 15 µm. Milling was performed at a rotational speed of n = 4,500 rpm with a feed v_f = 125 mm/min. The surface roughness of the milled aluminum mirror was < 20 nm Ra.

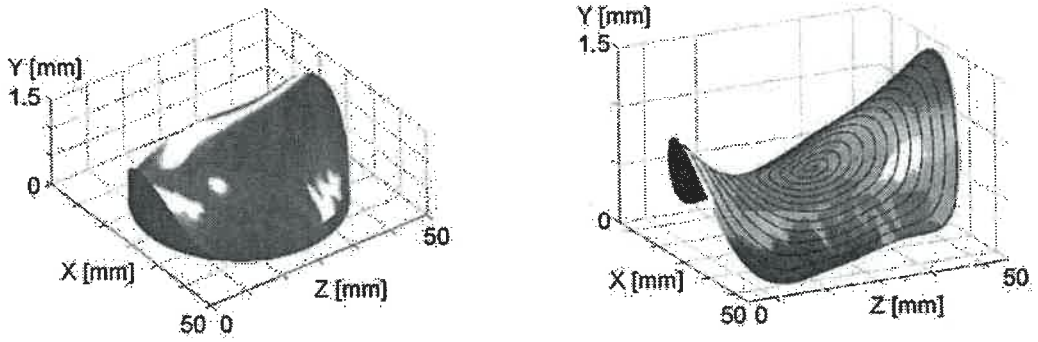

Fig. 5: Free-form mirror surface (CAD simulation) and tool path with spiral infeed for ball-end milling.

Surface inspection by fringe reflection

Easy and fast assessment of the form accuracy of the machined free-form mirror surfaces was achieved by a newly developed fringe reflection method, whereby a TFT monitor projects black and white fringes onto the specimen. The reflected fringe pattern is viewed by a video camera and analysed by a propriatory software routine. Thus, the reflection angles can be determined for every camera pixel and the local gradients can be calculated with high lateral resolution. The surface data are obtained by integration. The vertical resolution is much better than in fringe projection and is in the range of 1 nm. A setup for fringe reflection measurement is shown in Fig. 6a. The reflected fringes and measured slopes in the x- and y-direction are shown in Fig. 6b and 6c, resp.

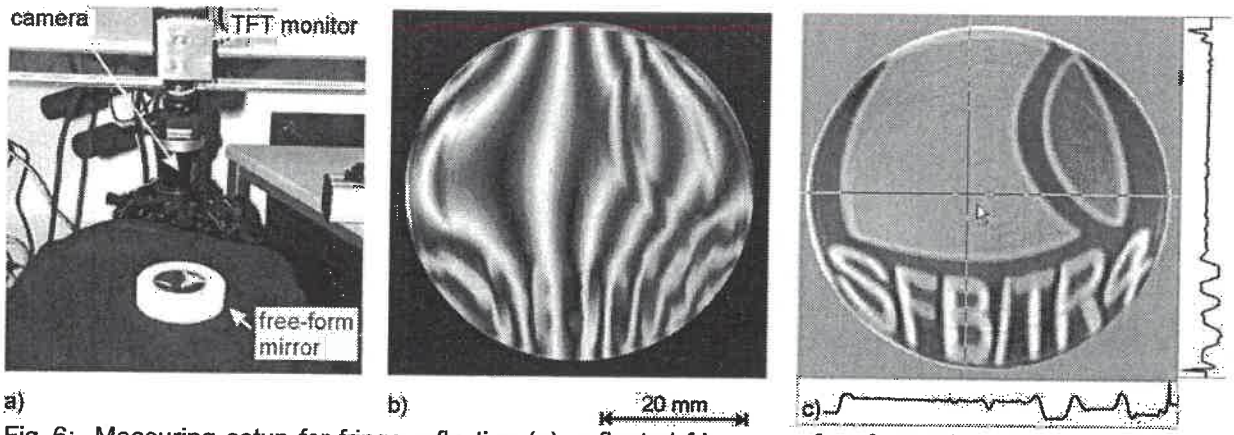

Fig. 6: Measuring setup for fringe reflection (a), reflected fringes on free-form mirror (b) and calculated surface slopes (c).

Summary

In this paper we have presented first results of diamond ball-end milling of free-form surfaces based on NURBS which will form an integral part of the production chain for producing high quality complex optical surfaces developed within the Transregional Cooperative Research Center SFB/TR4. Moreover, we have introduced a new powerful method for the assessment of surface slopes on free-form surfaces by fringe reflection. Both methods will be used in future work providing a basis for economic mass production of aspheres and free-form surfaces by mold fabrication and replication.

Acknowledgement

The research work presented in this paper is part of the SFB/TR4 "Process Chains for the Replication of Complex Optical Elements", funded by the DFG German Science Foundation. The free-form mirror was designed by OEC AG, Munich, Germany. The figure testing of the free-form surface producing the SFB/TR4 logo by fringe reflection was performed in cooperation with BIAS, University of Bremen.

References

1 Masuzawa, T.: State-of-the-art on Micromachining. Annals of the CIRP, Vol. 49/2/2000: pp. 473-488.

2 Brinksmeier, E.: Ultraprecision Maching and Measuring Technology. Proc. 10th International Machine Tool Engineers Conference IMEC, Tokio, Japan, 31.10.-01.11.2002: S. 152-161.

3 Weck, M.; Winterschladen, M.; Pfeifer, T.; Dörner, D.; Brinksmeier, E.; Autschbach, L.; Riemer, O.: Manufacturing of Optical Molds Using an Integrated Simulation and Measurement Interface; Proceedings of SPIE, Vol. 5252, 2003.

Block Regression Phase Digitizing with application to Nonlinearity Measurement and Correction

David Chu, Ph.D.
Precision Motion and Time, AGILENT TECHNOLOGIES, Inc.
MS 52U29 Santa Clara, CA 95052-8059
408-553-2165, e-mail: david_chu@agilent.com

Short Abstract:

Statistical regression (curve-fit) is a viable alternative technique to spectral analysis based DSP. In many cases, it has a clear advantage over DSP in speed, accuracy, and implementation simplicity. The paper gives examples of phase digitizing, nonlinearity measurement and correction for signals from a heterodyne interferometer, using "block regression". This simplified version of the traditional min-squared error regression lends itself to easy implementation with ordinary digital logic components.

RECENT DEVELOPMENTS IN HOMODYNE INTERFEROMETRY

William Lee
Renishaw plc
Wotton-under-Edge, Gloucestershire, UK
william.lee@renishaw.com

Abstract

Continuing developments in homodyne laser interferometer systems [1] are improving both their measurement performance capability and their ease of installation. This paper gives an overview of such a system and explains several of the key design features. Firstly, an overview of the optical detection scheme is given. Secondly, a novel method for improving the Sub Divisional Error (SDE) in a Column Reference (CR) interferometer is described. Finally a technique for improving the frequency stability of fibre optic coupled laser sources is explained.

1. Introduction

Applications where the highest levels of laser interferometer measurement performance are required typically involve positioning within vacuum chambers where the effect of air turbulence on measurement stability is removed. This paper describes an interferometer system suitable for these applications which has the benefits of a fibre optic coupled laser source to simplify installation. The interferometer system consists of a fibre optic coupled laser source and one or two detector heads.

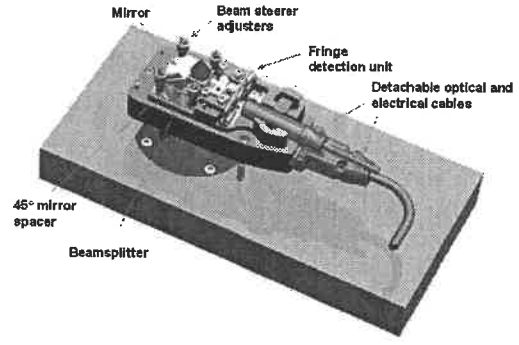

Figure 1 CR detector head with cover removed

The detector heads mount onto the outside wall of a vacuum chamber and contain a CR interferometer, integrated beam steering optics for both pitch and yaw adjustment and an integrated fringe detection unit. Common mode errors, like for example the vibration of the vacuum chamber sidewall, are minimised because the interferometer measures the differential position of two objects inside the chamber. The laser source is situated remotely from the chamber and a fibre optic cable is used to route the laser beam to the detector heads. The detector head is shown in figure1.

2. Integrated fringe detection unit overview

The laser interferometer system contains an integrated fringe detection unit. The detection scheme is shown in figure 2.

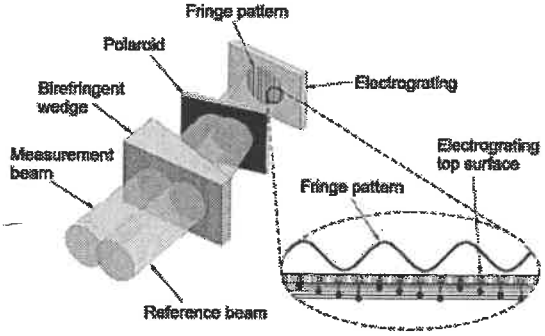

Figure 2 Fringe detection scheme

When the orthogonally polarised measurement and reference beams enter the signal detection unit they pass through a birefringent wedge that creates an angular deviation between the beams. The beams then pass through a Polaroid aligned at 45° to make them interfere. The resultant interference pattern is a linear array of fringes. These fringes are aligned with an integrated linear photodiode array, called an electrograting. The electrograting produces four electrical signals of relative phase 0°, 90°, 180° and 270°. Sine and cosine output signals are produced by differencing the 0° and 180° signals and the 90° and 270° signals. Because of the excellent gain matching of the electrograting, the differential amplifier removes common mode intensity changes on the signals due, for example, to an intensity change of the laser.

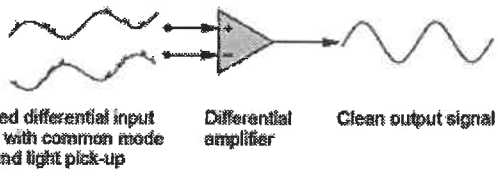
Balanced differential input signals with common mode noise and light pick-up
Differential amplifier
Clean output signal

Figure 3 Common mode rejection

3. *Sub Divisional Error (SDE) performance*

A significant degradation to the SDE performance occurs in CR interferometers when the measurement and reference mirrors are well aligned. A solution to this problem has been developed and the test results are shown.

3.1 *SDE in retro reflector interferometers*

Imperfections in polarising beamsplitter and retro reflector performance typically cause a degradation in the SDE performance of an interferometer [2].

The magnitude of the effect is typically quite small. This is because the leaked beams which cause the degradation are attenuated twice by the polarising coating before they enter the detector optics. This is illustrated in figure 4. Only one of the two leaked beams is shown for clarity.

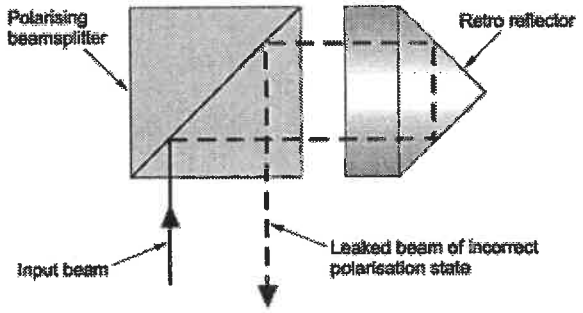

Figure 4 Leaked beam in retro reflector interferometer (only the leaked beam is shown for clarity)

If α is the extinction ratio of the beamsplitter and β is the polarisation cross coupling of the retro reflector then the equation for the intensity of the interference signal of a leaked beam and a measurement beam as a ratio of the measurement signal is:

$$\text{Iratio} = (\alpha^2 + \alpha\beta)^{0.5} \quad (1)$$

With a typical performance polarising beamsplitter (extinction ratio ~ 0.5%) and retro reflector (polarisation cross coupling ~ 1.5%) the SDE contribution is around +/- 0.5 nm (assuming a laser wavelength of 633 nm and a single pass interferometer). In many systems this is negligible.

3.2 *SDE in column reference interferometers*

In a CR interferometer light which has passed once around one arm of the interferometer may leak into the other arm and then return to the detection unit as shown in figure 5. Only one of the two leaked beams is shown for clarity. The leaked beams in the CR interferometer are produced mainly due to imperfections in the beamsplitter polarisation performance.

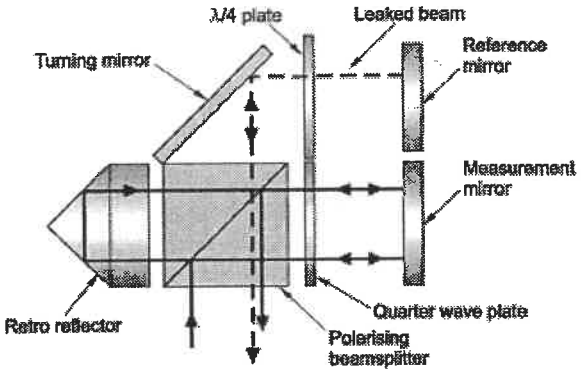

Figure 5 Leaked beam in CR interferometer

To align the system the reference and measurement beams are adjusted so that they return into the detection unit. This is required so that good signal strength is achieved. This means that the beams will be nominally normal to the reference and measurement mirrors.

Because the mirrors are aligned, the leaked beams will also return into the detection unit parallel with the measurement and reference beams. This will cause a significant degradation in the SDE performance of both homodyne and heterodyne interferometers.

The intensity of the signal from the interference of a leaked beam and a measurement beam as a ratio of the measurement signal is described by equation 2. Second order terms have been ignored.

$$\text{Iratio} = \alpha^{0.5} \quad (2)$$

With a typical performance polarising beamsplitter (extinction ratio ~ 0.5%) the SDE contribution of a single leaked beam is around +/- 2.5 nm for both homodyne and heterodyne interferometers (assuming a laser wavelength of 633 nm and a double pass interferometer). In a typical CR application the reference mirror is nominally stationary and therefore a leaked beam, which is incident on the measurement mirror once, is a single pass signal and therefore has half the frequency of the main signal.

In a homodyne interferometer this creates a 'double lissajous' as shown in figure 6.

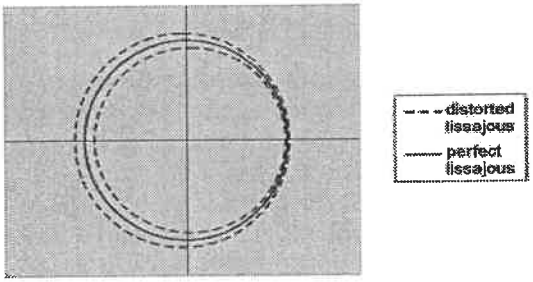

Figure 6 Lissajous distortion from CR interferometer

In a heterodyne interferometer system the phase of the interference signal between the measurement and reference arm will be variably shifted by the 'leaked beam'. Figure 7 shows the shift in the zero crossing point between a perfect heterodyne signal and a distorted heterodyne signal.

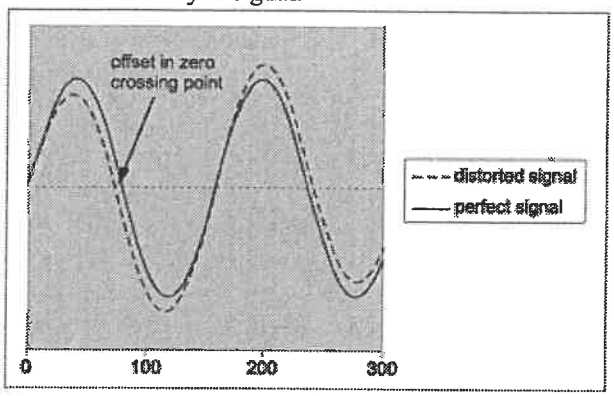

Figure 7 Phase shifting of heterodyne signal

3.3 *Solution in homodyne systems*

A solution to this problem is to generate an angular offset between the leaked beams and the main beams before they enter the detection unit. This means that the interference pattern generated does not match the electrograting. The resultant signal from the electrograting is therefore common on all four of the output channels and has no effect on the measurement.

This may be implemented by angularly offsetting either the measurement mirror or the reference mirror. However, over even relatively short axis lengths, this can create a significant drop in signal strength. Also, especially on a heterodyne system, the user typically has no easy way of detecting if the mirror is sufficiently offset to reduce the SDE. A better way of angularly offsetting the beams is to insert a glass wedge into the first pass of the reference beam of the interferometer as shown in figure 8.

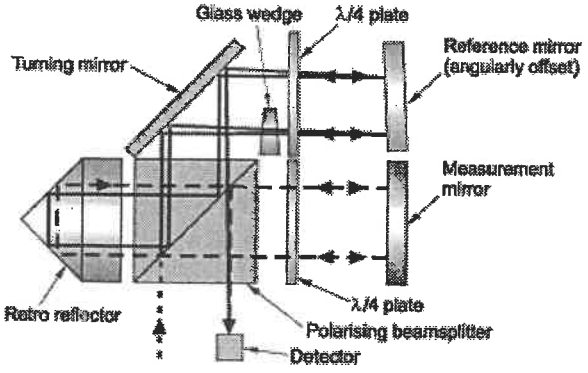

Figure 8. CR interferometer setup with glass wedge.

This will cause the reference beam to be angularly offset from the measurement beam when it enters the detector optics which will alter the fringe pattern generated. If the glass wedge is aligned correctly then the electrograting may simply be rotated to match the fringe pattern again. See figure 9.

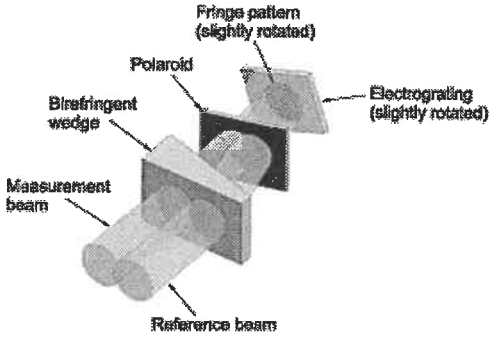

Figure 9 Electrograting rotated to match fringe pattern

Now, when the plane mirrors are aligned to optimise the signal strength, the reference mirror will not be quite normal to the reference beam. The leaked beam returns into the detector optics with an angular offset as shown in figure 10. As it is aligned at a different angle to the other beams, the interference pattern generated does not match the electrograting and therefore does not cause a measurement error.

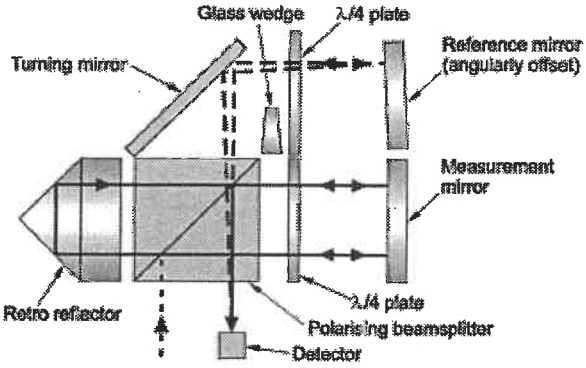

Figure 10 Angularly offset leaked beam – the main reference beam is not shown for clarity

The SDE performance of a batch of CR interferometers with the glass wedge modification was tested. The SDE of all the units were found to be less than +/- 0.5 nm.

3.4 *Solution in Heterodyne systems*

The SDE degradation in heterodyne systems can also be solved with a similar method to the technique described in section 3.3. However, a birefringent wedge is required after the measurement and reference beams have been recombined in order to make the wavefronts parallel again.

4. *Laser frequency stability improvement*

A He-Ne gas laser may be frequency stabilised by controlling the laser tube length. This may be done by controlling the temperature of the tube. The feedback signal for the temperature control comes from the difference in the intensity of the two laser output modes. The intensity of the modes may be measured by separating the modes with a polarising material before shining them onto separate photodiodes [3].

However, the output frequency stability of a laser may be degraded by back-scattered light returning into the laser tube. There are a number of sources of back-scattered light in any interferometer system. With a fibre coupled laser source, a significant source of back-scattered light is the fibre optic itself.

4.1 Degradation of laser frequency stability

When back-scattered light returns into the laser tube, it interferes with the light inside the tube. As the phase of the back-scattered light changes, the interference with the light inside the tube varies between constructive and destructive interference. This causes a variation in the intensity of the laser beam emitted from the tube. The intensity and phase of the back-reflected light in each of the two polarisation states is typically different. Therefore, the intensity variation will occur in the two orthogonal laser modes independently. This causes a difference between the signals from the stabilisation photodiodes. The control algorithm cannot distinguish this intensity difference from a genuine laser frequency change and therefore tries to compensate for it by changing the temperature of the tube to balance the photodiode signals. An overview of the system is shown in figure 11.

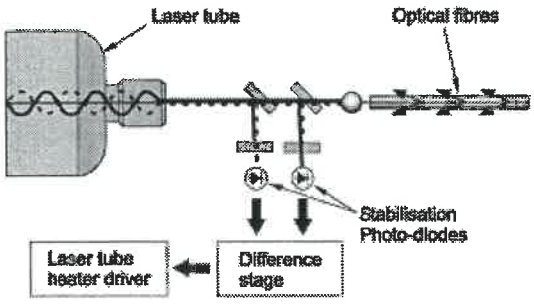

Figure 11 Frequency stabilisation of laser

4.2 Solution

The effect of the back-scattered light on the laser frequency stability may be dramatically reduced if an optical path length modulator is inserted into the optical path between the laser tube and the source of back reflected light. The modulator changes the relative phase of the back-scattered light relative to the laser light inside the tube. If a heater is used to control the length of the tube, then the bandwdith response of the frequency control is fairly slow. If the frequency of the phase modulation is significantly higher than this then the effect of the backreflections on the frequency stability is greatly reduced. The frequency stability of a fibre coupled laser source with and without a phase modulator is shown in figure 12.

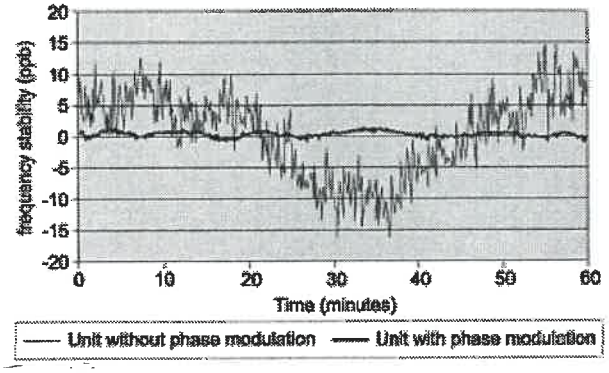

Figure 12 Comparison of frequency stability of laser sources

The phase modulation is also of benefit in CR and plane mirror applications where, due to imperfections in the performance and alignment of optical components, light may leak back into the laser tube when the plane mirrors are aligned normal to the beam. This can degrade the frequency stability of the laser. The effect of this is also minimised by the phase modulation technique.

5. *Conclusions*

Recent developments in homodyne interferometers have improved both their measurement performance capability and their ease of installation. An improvement to the SDE of CR interferometers has been demonstrated. A technique for reducing the sensitivity of laser tubes to back-scattered light has also been shown.

References

[1] Chapman M., Attwood L: Heterodyne and homodyne interferometry, SEMI Technical Symposium: Innovations in Semiconductor Manufacturing 2003.

[2] Bobroff. N: Recent advances in displacement measuring interferometry, Meas. Sci. Technol. 4 (sept 1993) 907-926

[3] Bennet S. J.,Ward R. E.,Wilson D.C.: Frequency stabilzation of Internal mirror He-Ne Lasers. Applied optics vol.12 No.7 (July 1973).

CHALLENGES IN INTERFEROMETRIC MEASUREMENTS OF MEMS AND SEMICONDUCTOR DEVICES

Joanna Schmit and Erik Novak

Veeco Instruments Inc., Tucson, AZ

Introduction

Measuring MEMS and structures of semiconductor devices poses unique challenges to interferometry because these devices are very complex with multiple planes having different roughnesses, their surfaces are often protected by transparent layers like polysilicon, and whole devices are frequently protected by cover glass. The structures of these devices also often have many narrow and deep gaps called trenches that are difficult to measure precisely, thus usually necessitating a destructive method to determine the depth of the trenches, such as cross sectioning and measuring via scanning electron microscope.

However, interference microscopes are ideally suited for these kinds of measurements since they have nanometer to subnanometer vertical resolution with up to 8 millimeters maximum vertical range. Standard objectives allow up to 100X magnification while long-working-distance objectives, including ones compensated for measurements through glass, provide measurement capability at up to 40X magnification even parts are mounted beneath a protective cover glass or in an environmental chamber. Lateral resolution ranges from a few microns to about 500 nanometers, depending on the objective, with fields of view from 10mm to about 50um. Measurements typically take under a few seconds since they are based on full field measurement rather than point-by-point surface scanning.

Trenches measurement

White light interferometry[1] (WLI) provides a common tool in interference microscopy for micro-roughness and profile measurements of surfaces with discontinuities larger than 160nm. The analysis of fringes is based on the principle of low coherence peak sensing where the peak is created at the position of the object's surface. While well known is the fact that light incident on surfaces with sub-wavelength structure undergoes strong diffraction, little attention is paid to the fact that strong diffraction effects are also present when light is incident on objects with structures on the order of microns. These diffraction effects create additional coherence peaks that do not correspond to the surface topology; these additional coherence levels must be properly interpreted by WLI algorithms.

These additional coherence peaks were observed for a silicon surface with etched trenches not only 1.2 microns wide but also 5 and 10 microns wide – dimensions larger than in sub-wavelength structures but not large enough for fringes to represent geometrical structure of the object. The depth of the analyzed trenches was on the order 20 – 40 microns. The experimental data obtained with the Veeco optical profiler NT 8000 was compared with simulated results obtained from rigorous coupled-wave analysis[2] (RCWA) and Hopkins image-formation theory. We have found very good agreement between experimental and simulation results for a trench 5 microns wide and about 23 microns deep[3], and the experimental and simulated fringes are shown in Figure 1. In both cases the fringes in the void area of the trench at its top surface level are visible and are called induced coherence levels. They can significantly limit the range of measurements if interpreted as fringes corresponding to geometrical surface.

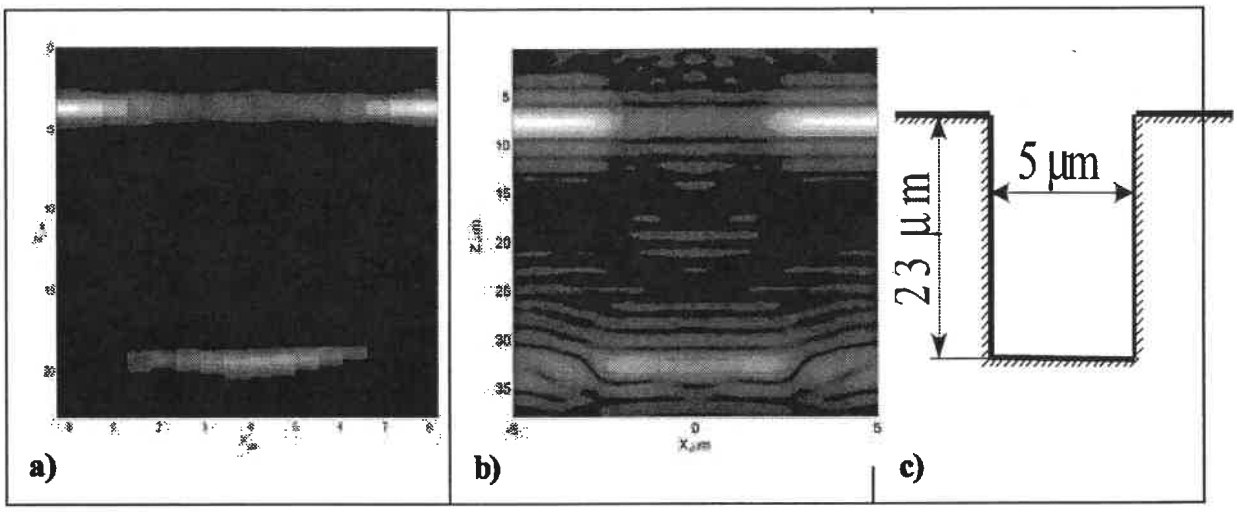

Figure 1. Fringe contrast images from experimental (a) and simulated (b) data for trench 5 microns wide and about 23 microns deep (c). For this structure an additional coherence level is observed above the bottom of the trench in the form of an extension of the coherence level representing incorrectly the top surface of the trench.

The amplitude of the coherence peaks varies the trench width and depth and is influenced by changes in the optical system such as the numerical aperture (NA), magnification, polarization and wavelength spectra. For example, for an objective with a given numerical aperture the amplitude of the additional coherence level increases with the decreasing trench width. The amplitude of the fringes at the bottom of trench decreases making the amplitude of the fringes representing the real surface much weaker than the additional coherence levels created from strong complex diffraction effects. The additional coherence levels can be a problem in i.e. MEMS measurement if not interpreted correctly. With special software we can measure the depth of a 1.2 micron wide and 40 micron deep trench.

Film thickness measurement

There is another group of objects for which white light fringes are not a straightforward representation of object's profile or rather interface. This is the case when an object is covered with a transparent film and the object's surface profile is of interest and not necessarily the top surface of film. For transparent coatings with thicknesses above several microns, two sets of white light fringes are created due to the top and bottom coating interfaces. The maximum of the second set of fringes is created at the distance corresponding to the optical coating thickness for white light. For this, the effective group index of refraction of the coating must be determined experimentally for each of the profiler's objectives to include the effects of the illuminating and imaging numerical apertures and the spectral properties of the source and system. The dispersion of the material, especially when using large NA objectives, quickly reduces the visibility of second set of fringes. Thus, the range of measurable thicknesses can be extended if a narrower bandwidth filter and/or a lower numerical objective is used, up to a maximum of several hundred micrometers thickness. The shift of fringe sets due to reflection of different interfaces can be also accounted for in high precision measurements.

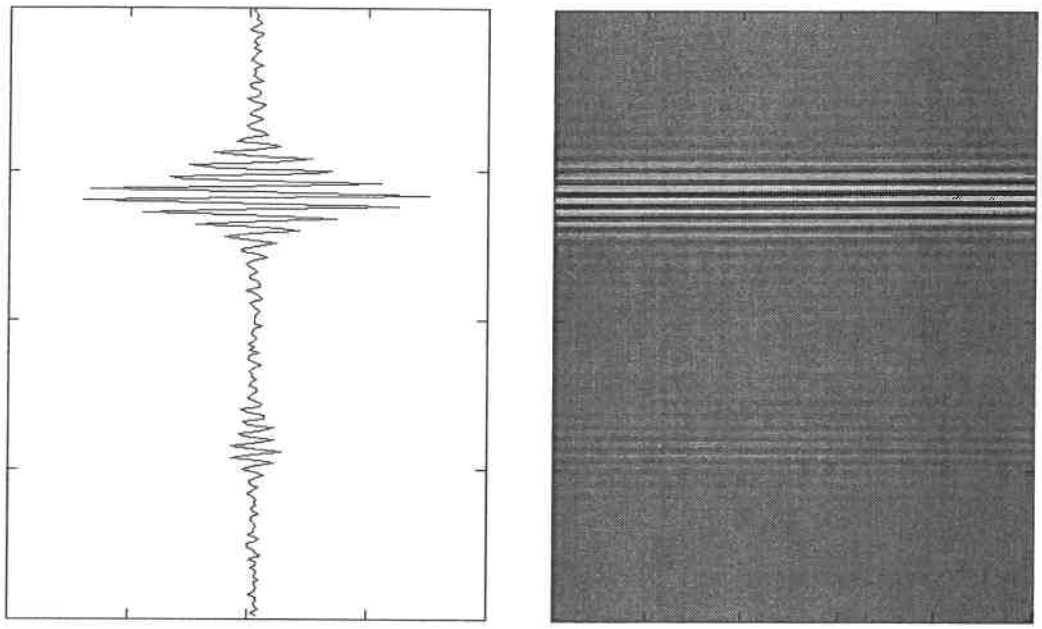

Figure 2. Two sets of white light fringes as seen by a single pixel (a) and the row of pixels (b) for a transparent film. The second set of fringes is created below the true interface between substrate and film due to group index of refraction of film larger than one.

Calibrating effective group index of refraction directly on the system accounts both for the film's group index of refraction and also for the fact that the film is illuminated by multiple beams at a wide range of angles determined by the numerical aperture of the objective. One method of calibration uses a known film thickness sample manufactured from the same material as the test object. Since the thickness of the sample is known, the program determines the proper value for the effective group index of refraction so as to achieve the correct film thickness value.

A different calibration method uses a specially prepared sample or part of the sample under test; this method is often used when the film creates a step to a bare substrate. If it can be assumed that the substrate is a flat surface on each side of the step, the value of the effective group index of refraction can be obtained in one vertical scan. In this case, the film step height, calculated from the top surface of the film to the bare surface (fringes from the film/substrate interface are disregarded), is equalized to the optical thickness of the film determined by the positions of two sets of fringes at the air/film and film/substrate interfaces. The effective group index of refraction can then be calculated.

Using these techniques we have measured many samples like photoresist thickness on MEMS, epoxy-acrylic thickness on flex circuits, polymers, Lithium Tantalate (LiTaO3) films of 5-25 micron thickness on silicon and quartz wafers. The repeatability of an average film thickness measurement is on the order of single nanometers. The typical range of measurable film thicknesses is from 3 to 150 microns depending on the objective and the dispersion of the film. This measurement allows for detection of flows on the surface and interface of the film.

6. Special analysis of samplstructure

In the semiconductor and MEMS industries, film thickness varies over different structures on the substrate; thus, often a single technique for film thickness measurement cannot be applied to the whole field of view. In this case a special software approach[4], through which ideal surface templates are generated for each structure from the design files or prior measurements, can be applied in different regions. These templates may contain multiple sub-regions, or data islands, each of which can be characterized in a different manner. Surface measurements from a white light interference microscope are matched with the ideal object template using a variety of techniques and threshold criteria. The template-based technique is tolerant of errors from both rotation and translation and allows for accurate characterization of each data island and its relative positions.

The software has also a capability of presenting data consisting of any combination of sets of fringes (only first, only second, distance between first and second, first only but second if two sets of fringes exist with extension to multiple sets of fringes) allowing for flexibility in the object's structure display without the necessity of using a template-based technique. Thus, for example a surface profile can be easily displayed if any unwanted fringes due to local or locally varying thickness coatings are present or unwanted fringes are created due to the surface microstructure.

Software can store, display and analyze not only the measured height map but also the intensity map as seen through the conventional microscope; thus, the discoloration effect on paints and coatings can also be documented.

Summary:
Transparent layers and trenches often add to measurement challenges. Interference fringes formed by the unique characteristics of these objects require special analysis to obtain the correct profile of the object's surfaces and sub-surfaces. With developed special software and calibration routines, we can measure the topography of the top surface of a transparent layer, the thickness of the layer up to 150 micrometers and the topography of the sub-surface – the interface between substrate and layer in one measurement scan. With special software we also can measure the depth of trenches with very high depth to width aspect ratio. The ratio can be as large as 15:1 and trenches as narrow as 1.2 microns in width. The measurement of narrow trenches (10 microns and less) is especially challenging since additional fringes induced by diffraction may appear in the gap of the trenches and require a special interpretation.

1. M. Fleischer, R. Windecker, H. J. Tiziani, "Theoretical limits of scanning white-light interferometry signal evaluation algorithms," Applied Optics, **40**, 2815 (2001). .
2. A..Tavrov, M. Totzeck, N. Kerwien, H.J. Tiziani, "Rigorous coupled-wave analysis calculus of sub micrometer interference pattern and resolving edge position versus signal-to-noise ratio," Opt. Eng. **41**(8) 1886-1892 (2002).
3. A. Tavrov, J. Schmit, W. Osten, N. Kerwien, H.J. Tiziani "Induced coherence effects" submitted to Applied Optics.
4. E. Novak, M. Krell, T. Browne, „Templete based software for accurate MEMS characterization," SPIE Proceedings 4980, 75-80 (2003).

The Effect of Phase Change on Reflection on Optical Measurements

Kate M. Medicus[1], Liesel R. Fricke[2], John E. Brodziak Jr[1], Sharon Carnevale[1],
Marcus Chaney[1], Rachel Wolff[2], Angela D. Davies[2]

[1]Department of Mechanical Engineering
[2]Department of Physics and Optical Science
UNC Charlotte, Charlotte, NC

Abstract

Phase change on reflection affects many precision dimensional measurements. The phase change can result in erroneous height measurements. The phase change on reflection was investigated at a glass-metal interface using samples with evaporated metal strips on the back surface of a wedged glass substrate. The samples were measured on a phase shifting interferometer and the phase change was calculated from the apparent measured step heights from the internal reflection at the back glass-metal interface. The background subtraction process was the largest contributor to the phase change uncertainty. The measured phase change for gold, copper, and aluminum is 131.4° ±3.8°, 173.73° ±3.8°, and 200.7 ±3.8°, respectively.

1.0 Introduction and Background

Many precision dimensional measurements are based on interferometry which inherently relies on the reflection of light from a target. Upon reflection, light undergoes a phase change. This phase change on reflection depends on the material properties and can introduce a bias in the measurement. The phase change on reflection varies with incident angle, material properties, wavelength, and material depth. This variation affects measurements ranging from precision radius of curvature (by changing the cat's eye position), center thickness, gage block calibration, to scanning white light interferometry (SWLI) [1]. The goal of this research is to measure the phase change on reflection as a function of incident angle, material, and material depth as well as to determine its resultant effect on measurements such as the radius of curvature.

The phase change on reflection depends on the index of refraction of the material on both sides of the interface. The index is complex for metals and in some precision applications the small imaginary component of nominally transparent materials cannot be ignored. Refractive index values are published for many materials [2-4], however these values are often contradictory, presumably due to variations in material composition and/or film thickness. Furthermore, the optical properties of many alloys are not well known. Thin films, like those used in MEMS devices (which are commonly measured with SWLI), often do not have the same material properties as the bulk material. Interferometry is well suited to measure phase changes, but a difference measurement must be made where the phase change is compared between two materials. A typical configuration is to deposit a region of material A on a substrate of material B and then measure the apparent step height of material A. However, the physical step height must be known to determine phase change on reflection differences [5]. The physical step height contribution can be intrinsically removed by depositing regions of the metal on the back side of a glass substrate and measuring the phase profile of light reflected internally from the back surface. Such investigations have been carried out with SWLI [6], but the angle of incidence and wavelength dependence cannot be easily investigated with this method. In an early experiment [7], fringes of equal chromatic order were used to investigate the phase change on reflection over a range of wavelengths. In this experiment, the phase was not directly measured, but calculated through fringe counting.

We have investigated the phase change on reflection by using a combination of methods discussed in the literature. We are using phase shifting interferometry (PSI) and a sample geometry where an internal reflection is exploited to intrinsically remove the step height from the measurement. Our initial studies focus on normal incidence reflection for a range of metals with 632.8 nm wavelength light. Future work will investigate film thickness, angle of incidence, and wavelength dependence. In this work, we describe the theory behind the measurement, the experimental configuration, and present examples of experimental results.

2.0 Theoretical Calculations

The phase change was measured when light reflects from a non-absorbing media (glass) and an absorbing media (metal) interface, as indicated in Figure 1. The glass has an index of refraction of n_1, and the metal has a complex index of refraction, $n_2 - ik_2$. We first consider the case of normal incident light, $\theta_1=0°$ where, the state of polarization is inconsequential. The phase change for both the s- and p-polarization states are equal [8]. For normal incidence, the Fresnel amplitude reflection coefficient, r is given by

$$r = \frac{n_1 - n_2 + ik_2}{n_1 + n_2 - ik_2} \qquad \text{Eqn. 1 [8].}$$

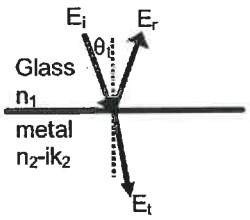

Figure 1: An electric field, E_i, from glass is incident from a glass substrate on bulk metal at an angle of θ_1. The electric field is reflected (E_r) and transmitted in part (E_t).

The angle between the incident field, E_i, and the reflected field, E_r, is the absolute phase change on reflection, ϕ. The tangent of the phase change is the ratio of the imaginary component of r to the real component,

$$\tan\phi = \frac{2n_1 k_2}{n_1^2 - n_2^2 - k_2^2} \qquad \text{Eqn. 2 [8].}$$

While the phase change on reflection is a function of the thickness of the metal, we first consider the case of a bulk material. Published values of n and k [2-4] vary, even within the same source. Using the complex index of refraction for copper, gold, and aluminum from Palik [2] and Eqn. 2, the phase change on reflection was calculated, as shown in Table 1. The values of n and k were interpolated for the He-Ne wavelength which introduced an uncertainty due the choice of fit parameters, as indicated in the ϕ column. The glass substrate used was fused silica with has an index of refraction of 1.457 [9]. The Range column in Table 1 also shows the range of calculated phase change values using various published values [2-4].

Table 1: The complex index of refraction and the calculated phase change values at θ_1=0°, for glass to metal using reference Palik [2].

	n	k	ϕ °	Range, ϕ_s°
Cu	0.41	3.40	134.1 ±0.0	1.1
Au	0.15	3.25	131.7 ±3.2	0.8
Al	1.40	7.60	159.0 ±1.9	3.2

3.0 Experimental Plan: Sample Preparation

The samples were 12.7 mm diameter glass substrates with 3.0 mm wide strips of evaporated metal as shown in Figure 2. The metal was deposited using a Varian 3125 Vacuum Thin Film System. The metal strips have a nominal height of 500 nm. The height was determined by a quartz crystal thickness monitor in the evaporator and confirmed using a calibrated profilometer. The original mask used in the evaporator is shown in Figure 3.

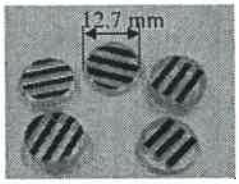

Figure 2: The samples with Au, Al, or Cu.

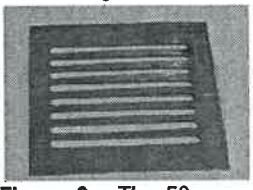

Figure 3: The 50 mm square metal mask.

A redesigned mask and fixture was manufactured (see Figure 4) to reduce shadowing effects and to allow one mask to be scanned during evaporation. This will allow us to create metal films with a ramp profile for future studies.

Figure 4: The redesigned fixture: motor, the location for the ramp profile, and the location for the uniform profile.

3.1 Experimental Plan: Measurements

A Veeco/Wyco PSI was used to measure the phase change. The sample was configured for a back measurement as shown in Figure 5. By measuring through the sample, we are directly measuring the phase change difference between a glass-air interface compared to a glass-metal interface. A front configuration would measure the phase change plus the step height. A Claphamdue flat was used as the transmission flat. This provides a reasonable fringe contrast between the glass and metal regions of the sample and greatly improves measurement quality. A picture of the measurement is shown in Figure 6.

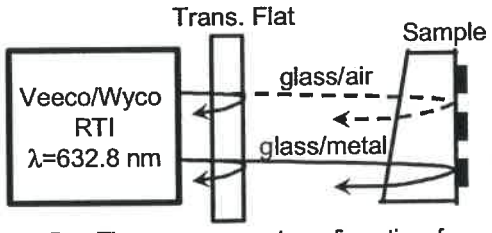

Figure 5: The measurement configuration for normal incidence. The substrate is wedged to prevent interference from the front surface.

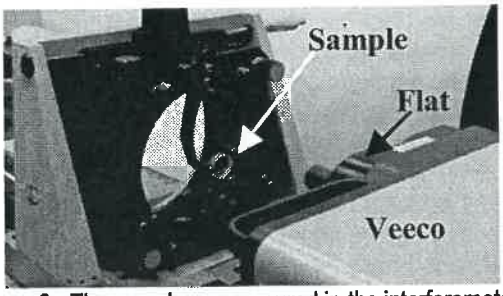

Figure 6: The sample as measured in the interferometer.

The apparent step height observed in the data is the phase change at the glass/metal interface relative to a glass/air interface. The absorption of fused silica is very low, consequently the phase change on reflection is

approximately zero (for an internal reflection). This assumption leads to a negligibly small contribution to the final uncertainty.

4.0 Analysis and Results

Because the measurements were conducted through the glass substrate, the inhomogeneities and surface figure error of the glass are included in the phase change measurement. To correct for this, the back of the substrate was measured in the same configuration and nominally the same position before the metal was deposited. This background measurement was then subtracted from all subsequent measurements. This was done for each substrate. The subtraction process leads to a significant contribution to the uncertainty and is discussed in more detail below.

An example measurement after background subtraction is shown in Figure 7. It is essential to note that the apparent height shown in Figure 7 is not a physical height, but an artifact of the phase change on reflection. All of the light is reflected from the nominally flat back of the glass substrate. The apparent height, h, is converted to phase, ϕ, using in the wavelength of the laser, 632.8 nm, and

$$\phi = \frac{4\pi h}{\lambda} \qquad \text{Eqn. 3.}$$

The additional factor of 2 in Eqn. 3 is because the phase change measurement is double pass for height features but single pass for phase change measurements.

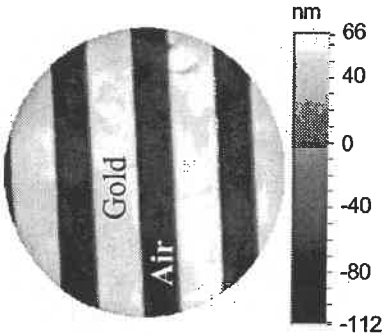

Figure 7: A measurement post background subtraction.

We used the multiple region analysis tool in the Vision software to separate the metal and air regions and to calculate the *RMS*, the number of points, and the mean value of each region. The difference between the mean value for the air and metal regions is the phase change on reflection for the glass/metal interface. The number of points and *RMS* are used to calculate the uncertainty in the mean value.

4.1 Uncertainty

We have investigated the primary sources of uncertainty and estimated their contribution to the measured phase change using a gold measurement as an example for all of the following cases. Variations in the evaporation process create a level of uncertainty not studied here, but will be investigated in the future.

The RMS of each area (metal and air), when divided by the square root of the number of points indicates the uncertainty in the mean value (phase). Without subtraction, the uncertainty in the phase of the metal and air regions are both 0.09°, with subtraction, they are 0.07° and 0.06°, respectively. This reduction demonstrates importance of the background subtraction.

A major source of uncertainty is the background subtraction. The pre- and post-deposition samples can not be repositioned exactly in the same orientation in the interferometer. Rotation, translation, and zoom differences occur between the two measurements. The trimming of the edge pixels also contributes to uncertainty. Shadowing effects require that the edge of each strip be trimmed. This trimming is subjective.

A simplified Monte Carlo simulation was performed to determine the uncertainty associated with repositioning and trimming. In software, we manipulated the data, performed the normal subtraction process, and calculated the resultant phase change. The manipulation was done such that it would be comparable to our best effort at repositioning in the lab: translating ±20 pixels in both x and y, rotating ±10°, zooming ±5%, and trimming 0 to 5 pixels. The phase change for each of the above manipulations was calculated. The worst case for each situation is shown in Table 2. The difference from the non-manipulated case is indicated in the Difference column. These differences were then combined in a root sum square method to calculate the uncertainty associated with repositioning and trimming, 3.8°.

Table 2: Calculated phase change for the worst case for each case for an example measurement of gold.

Without Subtraction	140.5°	
With Subtraction	132.1°	
With Subtraction and Manipulation		Difference
Trim	133.8°	1.7°
Rotate	132.5°	0.4°
Zoom	135.5°	3.3°
Translate	132.2°	0.1°
Subtraction Uncertainty: 3.8°		

Repeatability and reproducibility studies helped to determine the environmental effects of our measurement. Reproducibility was measured by removing the sample from the interferometer, waiting a day, and repeating the measurement. The repeatability of the measurement is 0.26° and reproducibly 0.50°. The final uncertainty is then

calculated by combining all the above uncertainties in a root sum square method. The final combined uncertainty for phase change is on reflection for this experimental method is 3.8°.

4.2 Measured Phase Change

The gold sample was measured on three days, twenty times each, for a total of 60 measurements, where each measurement was an average of eight. The calculated average phase change for gold was 131.4° ±3.8°, corresponding to a height change of 115 nm ±3.8 nm. This compares well to numbers shown in Table 1 from the literature.

The results for the copper and aluminum samples are only preliminary because we were unable to take measurements of the substrate before the metal was deposited. A modified background subtraction was done, though. In software, the metal region of the measurement was masked out. A Zernike analysis was performed on the remaining glass region. Using these Zernike coefficients, a simulated substrate was generated, which was used for subtracting the blank substrate.

The aluminum and copper samples were measured 20 times each, where each measurement was an average of eight. The calculated phase change for copper is 173.73° ±3.8°, and aluminum 200.7° ±3.8°. These numbers do not agree well with the values from Table 1. For comparison, the phase change for gold using the same method is 137°. Future measurements will determine if this variation is due to the modified subtraction process or another variable.

5.0 Continuing Work

Thus far, we have studied the phase change on reflection for different metals. In the future, we will investigate the dependence of the phase change on film thickness and incident angle, and compare measurements at 632.8 nm and 1550 nm.

The capability now exists to manufacture samples with varying film thickness by moving the mask relative to the substrate during the evaporation process. The metal strips will range in thickness from zero to several times the skin depth [3]. The measurement procedure will be the same. However, the analysis will result in a line plot of phase change versus film thickness instead of one number for phase change. This will be compared to theoretical calculations [3].

By using PSI and a skip flat geometry [10] we will directly measure phase change on reflection as a function of angle of incidence. With this geometry we will investigate the angle dependence from 0° to approximately 25°. These results are necessary to determine the effect of phase change on reflection on the radius of curvature measurement.

6.0 Conclusions

The measured phase change for gold, copper, and aluminum is 131.4° ±3.8°, 173.73° ±3.8°, and 200.7 ±3.8°, respectively. By far, the largest contributor to the uncertainty of the phase change is the subtraction process. In the subtraction process, the zoom factor had the greatest effect. Future work could reduce this uncertainty by repositioning the sample to better than ±5% zoom.

Acknowledgments

The authors would like to thank Research Corporation, the National Institute of Standards and Technology, the Center for Precision Metrology, and the National Science Foundation (grants #EEC9811556 and #EEC0331950) for their support of this work. Any opinions, findings, conclusions and/or recommendations expressed in this material are those of the authors and do not necessarily reflect the views of the above named institutions. The authors would also like to thank John Hudak at UNC Charlotte for his assistance with the evaporator.

References

[1] M. Park and S Kim, "Compensation of phase change on reflection in white-light interferometry for step height measurement," Optics Letters, **26**, 7, 2001.

[2] E. Palik, Handbook of Optical Constants of Solids, Academic, San Deigo, CA, 1985

[3] D.E. Gray, Ed, American Institute of Physics Handbook. McGraw-Hill, New York, 3rd Edition, 1982.

[4] D.R. Lide, Ed., CRC Handbook of Chemistry and Physics. CRC Press, Boca Raton, 84th Edition, 2003

[5] T. McWaid, T. Vorburger, J.F. Song, D. Chandler-Horowitz, "The effects of thin films on interferometric step height measurements," SPIE Interferometry: Surface Characterization and Testing, **1776**, 2-13, 1992.

[6] T. Doi, K. Toyoda, and Y. Tanimura, "Effects of phase changes on reflection and their wavelength dependence in optical profilometry," Applied Optics, **36**, 28, 7157-7161, 1997.

[7] J. M. Bennett, "Precise Method for Measuring the Absolute Phase Change on Reflection," JOSA, **54**, 5, 1964

[8] L. Ward, The Optical Constants of Bulk Materials and Films, Adam Hilger, Bristol, 1988.

[9] Melles Griot, www.mellesgriot.com/

[10] C. Evans and R. Parks, personal communications, May 2003.

A Comparison of Force and Acoustic Emission Sensors in Monitoring Precision Cylindrical Grinding

Jeremiah A. Couey, Eric R. Marsh
Penn State University, University Park, PA

Byron R. Knapp
Olympic Laser, Bremerton, WA

R. Ryan Vallance
George Washington University, Washington, DC

Abstract

Aerostatic spindles are used in precision grinding applications requiring high stiffness and very low error motions (5 to 25 nm). Forces generated during precision grinding are small and present challenges for accurate and reliable process monitoring. These challenges are met by incorporating non-contact displacement sensors into an aerostatic spindle that are calibrated to measure grinding forces from rotor motion. Four experiments compare this force-sensing approach to acoustic emission (AE) in detecting workpiece contact, process monitoring with small depths of cut, detecting workpiece defects, and evaluating abrasive wheel wear/loading. Results indicate that force measurements are preferable to acoustic emission in precision grinding since the force sensor offers improved contact sensitivity, higher resolution, and is capable of detecting events occurring within a single revolution of the grinding wheel.

Introduction

AE measurement has been the most popular approach used to monitor grinding processes for the last two decades. AE sensors offer advantages such as low cost and easy installation, with no reduction in machine tool stiffness. Dornfeld and Gomes de Oliveira's 2001 AE review paper showed that acoustic emission sensors may be used to monitor the following grinding processes: contact and collision detection, workpiece runout, defect detection, grinding burn/damage, radial wheel wear, wheel runout and profile measurements, wheel sharpness, chatter/vibration, dressing tool wear, and workpiece thermal deformation [1]. Despite the promising demonstrations for detecting grinding phenomena with acoustic emission sensors, industrial applications are mostly limited to contact detection [2].

Force-measuring instrumentation is generally more expensive than acoustic emission sensor systems, so it is most often used in research applications. For cylindrical grinding operations, researchers historically built custom force measurement systems, although commercial rotating dynamometers are now available [3]. In this work, we use non-contact, high sensitivity capacitive displacement sensors to measure relative displacements between the rotor and stator of the workpiece spindle. This approach is stable, robust, accurate, and offers excellent resolution for the low forces encountered in precision grinding. The instrumented spindle built for this work provides real-time force measurement with 25-mN resolution and 300 Hz bandwidth.

Experimental Setup

Figure 1 shows the instrumented spindle designed specifically for measuring radial forces in the normal and tangential directions during cylindrical grinding. The design features an aerostatic spindle (Professional Instruments 4R Twin-Mount) with a frameless, brushless, DC motor and a 1024 count rotary encoder (Heidenhain) for synchronized data acquisition. Two stator-mounted, high-resolution capacitive displacement sensors (2 mV/nm Lion Precision C1-C) target the rotor in orthogonal directions. Figure 1 also shows the mounting location of the acoustic emission sensor (Kistler 8152B2), which is located as close to the workpiece as possible.

It is important to note that AE sensors are most effective when located near the point of grinding. In conventional grinding, this means that the AE sensor is located on the housing of the work or wheel spindle. In precision and ultra-precision grinding, which usually use aerostatic spindles, a thin film of high-pressure air supports the spindle rotor. As a result, the AE signals are significantly attenuated due to lack of mechanical contact between the stator and rotor.

All experiments were carried out on a two-axis grinding machine (Moore 450) with a programmable resolution of 0.1 micrometers. During experiments, the grinding area is generously flooded with an emulsion coolant. Both the acoustic emission sensor and the capacitance probes are protected from the flood coolant by a shield that is not shown.

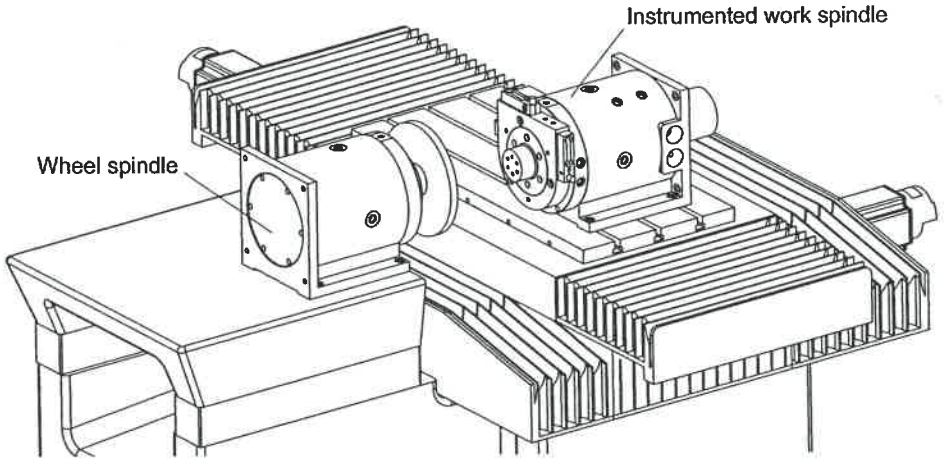

Figure 1: CNC grinding machine with wheel and work aerostatic spindles.

The grinding experiments conducted for this research are on the outer diameter of cylindrical workpieces. The results and approach are also applicable to inner diameter grinding, which is notoriously difficult to monitor because of the low force levels. The cylindrical workpieces are Ø25 mm by 18 mm long and made of 416 or hardened 440C stainless steel. The work spindle rotates at 500 RPM. The abrasive wheel is a 7-inch diameter, ½-inch wide aluminum oxide wheel (Norton 38A46-H8VBE) rotating at 3300 RPM. The wheel is dressed with a single-point diamond tool at 375 mm/min and only 3 mm of the wheel width is used. The feed rates and radial depths of cut vary and are reported individually for each experiment.

Experimental Results

The first experiment explores the resolution and sensitivity of the instrumented spindle. In this experiment, successive low-force grinding passes were made on the outer diameter of a cylindrical 416 stainless steel workpiece as the radial depth of cut is increased. In the first pass the grinding wheel is actually retracted from the workpiece by one micrometer so that the only interaction between the workpiece and wheel is through the grinding coolant. The traverse speed is 375 mm/min.

Several trends are observed in this experiment. First, the signal from the AE sensor erroneously detects contact since its signal is affected by the machine noise and/or workpiece-coolant interaction as shown by the non-grinding (-1.0 micrometer) pass. In contrast, the force measurement is not sensitive to this interaction and achieves more accurate contact detection. Second, the RMS AE signal does not correlate well to depth of cut, especially below 0.4 micrometers where the RMS value only increased above the noise floor by 1 mV. Third, the section view of the 1.6 micrometer pass displays the intra-revolution characteristics of each signal for fifteen workpiece revolutions. The force signal clearly shows a repeatable, cyclical wheel-workpiece interaction synchronous with the rotation of the grinding wheel. This same wheel-synchronous fluctuation is commonly seen in surface grinding force measurements taken with three-component dynamometers. In contrast, it is difficult to correlate the AE signal with the grinding process for a single revolution of the workpiece or grinding wheel. The final observation is that notable spikes are observed in the AE signal of Figure 2 for the three heaviest depths of cut. The source of the spikes is unknown, but they could result from abrasive grain fracture.

The second experiment examines the ability of the sensors to detect workpiece defects. The defect is a small flat milled into the outer diameter of the 416 stainless steel workpiece. The initial depth is 0.18 mm, which corresponds to a 3 mm flat width w. The total part length is 19 mm and the flat length is 8 mm. The outer diameter of the workpiece is ground at a traverse rate of 150 mm/min with five-micrometer radial depths of cut until the flat is completely removed (36 passes).

Figure 3 shows 3D plots of the normal grinding force superimposed (wrapped) around the cylindrical geometry of the workpiece. A slice from the 3D plot gives a polar plot showing the normal force as a function of the angular orientation of the workpiece. The flat is clearly detectable since the normal force drops to zero as the wheel passes over the flat. The sequence of 3D plots demonstrates the elimination of the defect as the flat is removed by successive grinding passes. The higher frequency (helical) undulations are caused by repeatable variations in the grinding wheel and are synchronous with the wheel spindle (which does not rotate at an integer multiple of the work spindle).

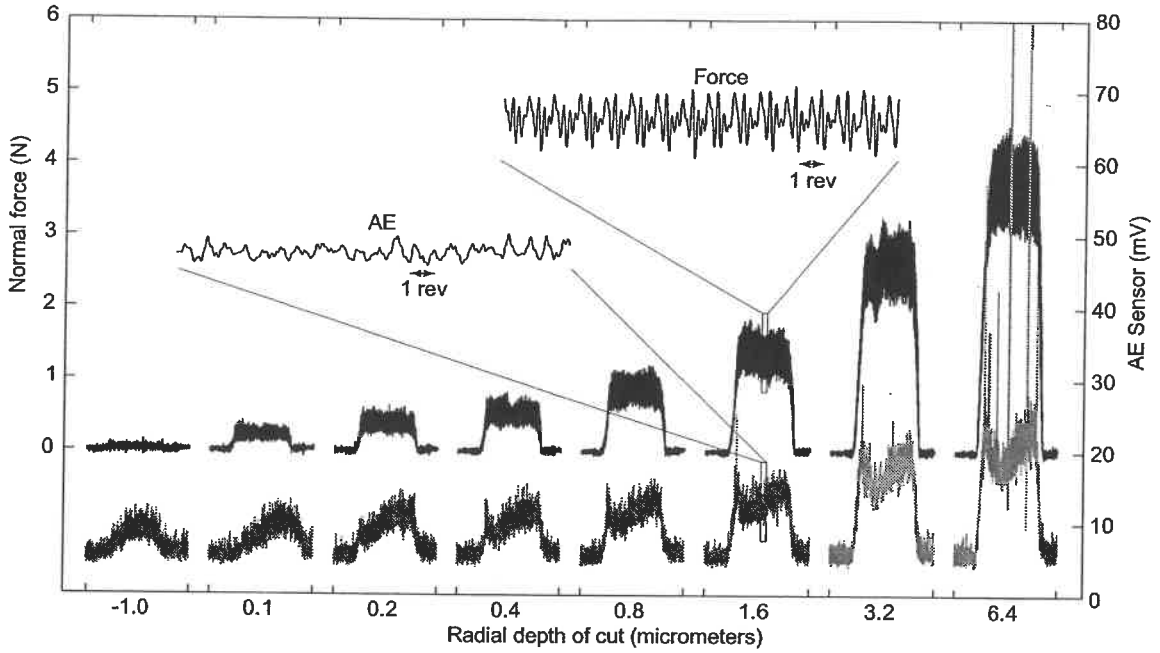

Figure 2: Force and AE output from eight consecutive grinding passes at increasing radial depth of cut.

Figure 4 shows the unwrapped force data for a single grind (w = 1.7 mm) on the workpiece. The figure shows that the workpiece defect is plainly visible in the normal force data, but almost completely absent from the AE sensor. The defect is easily detected in the force data where the abrasive wheel loses contact and the force goes to zero. The defect is more difficult to see within the AE data and the signal does not show the full loss of wheel contact seen in the force signal. This characteristic is best examined in the section view of the graph.

The third experiment compares the ability of the sensors to detect changes in the condition of the grinding wheel that loads and wears over time. The experiment is performed with a hardened 440C stainless steel workpiece, which wears the wheel much more rapidly than 416 stainless steel. For this experiment, the abrasive wheel is freshly dressed, and the workpiece is ground while simultaneously recording the force and RMS AE signal over 45 consecutive passes. The radial depth of cut is three micrometers and the axial feed rate is 225 mm/min. Figure 5 shows the low-pass filtered normal force, tangential force, and AE signals for each of the 45 passes. Both the AE and the force sensors can detect changes in the wheel condition during the grinding process, but the AE sensor consistently shows an unexplained drop off in the middle of the workpiece.

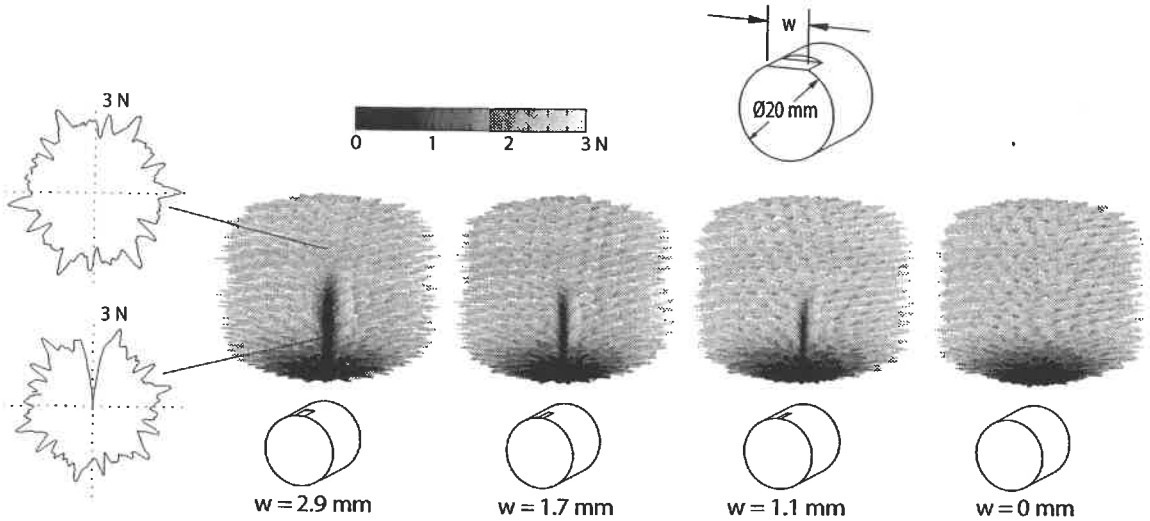

Figure 3: 3D force maps of the normal force when a defect is present in the workpiece.

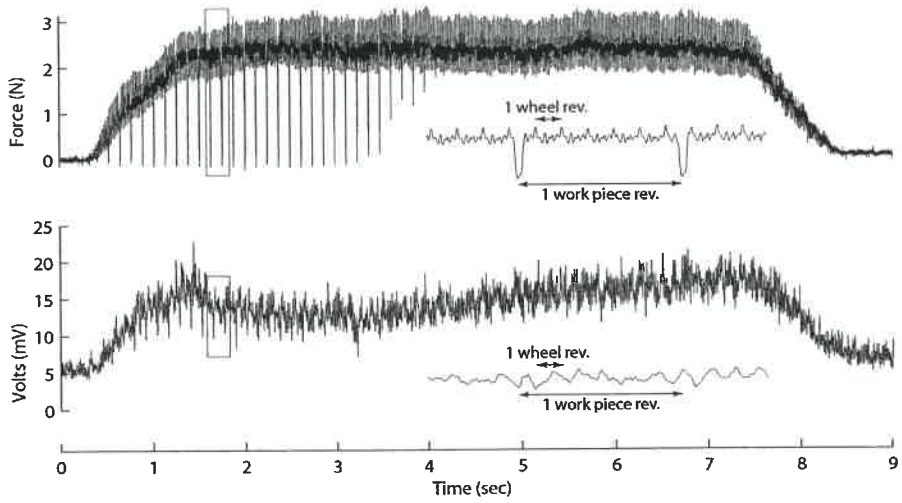

Figure 4: Comparison of the AE and force measurements for defect detection of a workpiece.

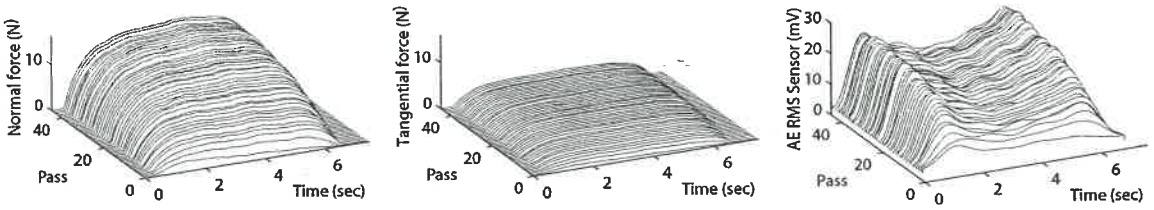

Figure 5: Low-pass filtered normal force, tangential force and RMS AE for 45 consecutive passes on hardened 440C stainless steel.

Conclusion

Monitoring cylindrical grinding is advantageous in optimizing process conditions, improving process control, and producing high quality parts. This is challenging in several precision applications where aerostatic spindles and small depths of cut are common. Detecting small forces with a conventional force sensor requires a compliant element in the machine's force loop, which reduces machine stiffness and degrades precision. AE sensors, which do not degrade machine stiffness, are therefore more common in industry, but they are less sensitive when grinding with aerostatic spindles, where rotor vibrations are not transferred to the spindle housing via mechanical contact. For precision cylindrical grinding of inner or outer diameters, feedback from a force-sensing spindle provides higher measurement sensitivity than acoustic emission, and the measurements correlate with physical aspects during the grinding process.

References

1. Gomes de Oliveira JF, Dornfeld DA. Application of AE contact sensing in reliable grinding monitoring. Annals of the CIRP. 2001;50;1;217-220.

2. Toenshoff HK, Karpuschewski B, Mandrysch T, Inasaki I. Grinding process achievements and their consequences on machine tools challenges and opportunities. CIRP Annals - Manufacturing Technology. 1998;47;2;651-668.

3 Kistler Instrument Company, Winterthur, Switzerland.

Indoor GPS Metrology System with 3D Probe for Precision Applications

Seong-Ho Kang, Delbert Tesar
The University of Texas at Austin, Austin, TX

Abstract

There is an increasing demand from industry for intelligent reverse engineering solutions. The requirement is to be able to perform reverse engineering, to create CAD models, or to compare prototypes with CAD models. A reverse engineering solution that can be used for 6 degrees of freedom pose measurement in a large area is desired. With this application in mind, we have developed a '3D Probe' solution. The 3D Probe is a portable measurement tool equipped with three receivers in optimum locations and a ball probe tip. The operator holds the 3D Probe in his hand and moves the probe tip over an object surface. Then, the X, Y and Z coordinates of the probe tip are measured in real time with high accuracy. Different probe tips of all sizes and shapes can be used on the probe to have access to all areas of the objects. The buttons on the probe allow the operator to start and stop the scanning process. The indicators on the probe give information concerning visibility and scanning mode.

The 3D Probe is specifically designed for intelligent scanning using recently available indoor Global Positioning System (GPS) technology. A battery-operated transmitter uses laser and infrared light to create one-way position information, the relative azimuth and elevation from the transmitter to the receiver. The receiver contains photodiodes and senses the transmitted laser and infrared light signals. With the addition of a second transmitter of known location and orientation, users can calculate the position of the receiver in the base coordinate system. Adding more transmitters increases the accuracy of the system. The signal is transferred through a wireless network connection providing mobility to the operator.

This paper describes the indoor GPS metrology system and the 3D Probe designed for reverse engineering and calibration. The concept of the 3D Probe is presented with the description of its design, components, and calibration process. The general concept and kinematics of the metrology system are described. The metrology system is applied to various engineering problems such as reverse engineering of standardized interface connection, actuator metrology, and robot metrology. Experimental results of standardized interface tests are presented along with procedures for actuator and robot metrology.

Keywords: Metrology; Indoor GPS; Modular robotics

1. Introduction

Open Architecture Systems (OAS) are automated systems built by actuator joint and link modules connected with standardized interfaces. They can be assembled on demand into different geometries ranging from 6 degrees of freedom (DOF) manipulator to 40 DOF manufacturing workcells (Fig. 1) [1]. Such systems allow flexible manufacturing, rapid repair, and upgrade, but these benefits have yet to be realized. A significant barrier is the presence of error between the actual and desired frames. While the accuracy error of a typical robot may be 20 times larger than its repeatability due to assembly, compliance, and tolerance errors [2]. Currently, teaching a robot, an essential process for high precision operations and Off-line Programming (OLP), is a time-consuming operation required for repair, upgrade, reconfiguration, and task change. This fact trumps other modular technology benefits.

The successful application of OAS on high precision operations depends on three research areas [1]. First, high performance standardized interface connections, which guarantee the needed level of connection exchangeability, repeatability, and rigidity, are required. This will make it possible to exchange or reconfigure OAS without decreasing the overall accuracy. Secondly, both geometric and compliance metrology procedures must be developed to model, measure, identify, and compensate for the errors of modular structures. The final step is to develop an advanced metrology system which is accurate, flexible, and easy to use for OAS metrology. The completion of these areas of research will make it possible to correctly predict and maintain the accuracy of the OAS. In the following sections, an advanced metrology system and its applications to actuator, and robot metrologies will be described.

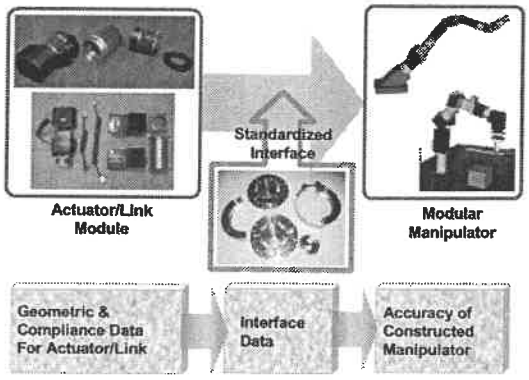

Fig. 1. Open Architecture Systems

2. Indoor GPS Metrology System

Metrology research for robotics involves the development of new technologies and techniques to measure robot poses accurately. Many measurement systems have been developed with large variations in complexity, cost, and required operator skill. State-of-the-art accuracy is on the order of 4/10,000 – 2/1,000 of an inch (0.01 – 0.05 mm) over the robot workspace [1, 2]. Commonly used sensors are: theodolites, laser trackers, cable potentiometers, Coordinate Measurement Machines, acoustic sensors, ball bars, articulated arms, and vision systems.

Recently, Robotics Research Group at the University of Texas at Austin (UTRRG) has been researching advanced metrology systems which can continuously measure both static and dynamic 6 DOF poses and motions accurately. They should be able to measure up to 50 feet even when their lines of sight are interrupted occasionally. This is an important requirement for manufacturing workcell calibration since multiple robots coordinate together in a small area. Multiple laser heads need to be positioned in distributed locations. Metrology systems satisfying these requirements are laser trackers and indoor GPS [3]. As target points increase, however, indoor GPS has a cost advantage over laser trackers due to its measuring capability of an unlimited number of targets [4]. Fig. 2 shows the UTRRG laboratory environment for an indoor GPS, a 6 DOF robot, and a 1 DOF elbow actuator. Four transmitters installed on top of steel posts using tribrachs are rigidly connected to 6 foot deep steel columns. A C-shaped transmitter arrangement is used for reverse engineering.

The concept of a 3D Probe is shown in Figures 3 and 4. A prototype which can be used not only as a hand-held probing tool but also as a tracking device once attached to an object such as a robot or a mobile platform has been built. It has a hardwired connection to a carrying case containing detector batteries, wireless electronics and power supply. Wireless communication has been chosen to transmit data to the control center. A calibration block has also been built for 3D Probe calibration.

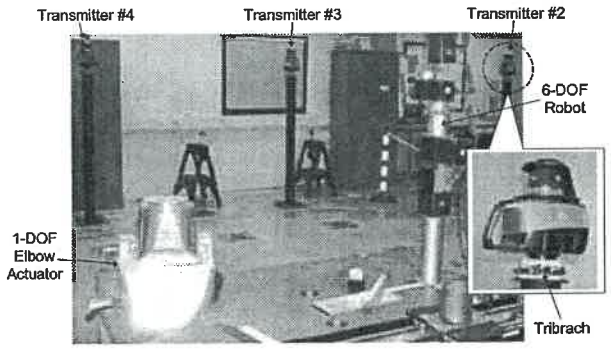

Fig. 2. Laboratory environment [3]

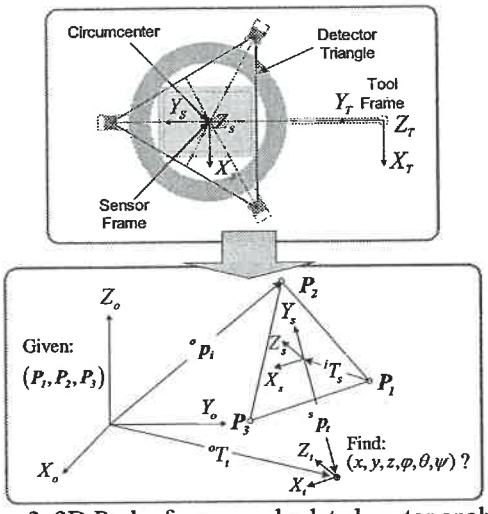

Fig. 3. 3D Probe frames and related vector analysis

3. Implementation

The development of kinematic solution involves three frames. The first is associated with the circumcenter of a triangle formed by three detector positions, the second is attached to the stylus ball probe tip, and the last is the global coordinate system to which all other frames are referenced. Fig. 3 illustrates the 3D Probe with its sensor and tool frames, a vector triangle, and a triangle circumcenter. The pose of the tool frame relative to the global frame can be represented by a homogeneous transformation matrix ${}^{o}T_{t}$ as follows

$$ {}^{o}T_{t} = {}^{o}T_{s}\,{}^{s}p_{t} \qquad (1) $$

where ${}^{o}T_{s}$ is the transformation matrix from the global frame to the sensor frame and ${}^{s}p_{t}$ is the position vector from the sensor frame to the styli ball center. This position vector is unknown, but it can be determined by the calibration process of the 3D Probe once it is assembled or every time a different stylus ball probe is installed. The Eq. (1) can be rewritten as

$$ {}^{o}T_{t} = {}^{o}p_{i}\,{}^{i}T_{s}\,{}^{s}p_{t} \qquad (2) $$

where i $(i=1,2,3)$ represents sensor numbers.

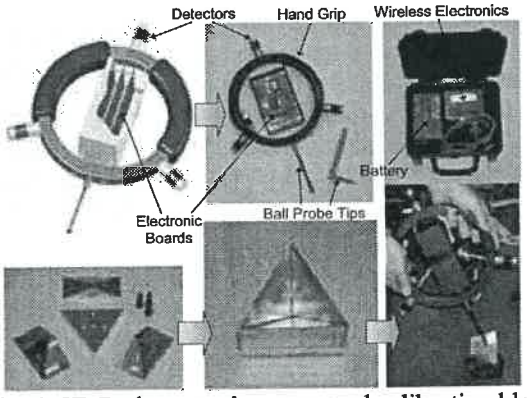

Fig. 4. 3D Probe, carrying case, and calibration block

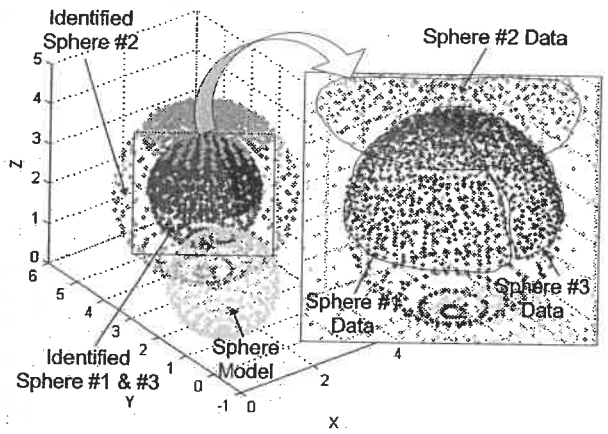

Fig. 5. Simulated sphere data and identification

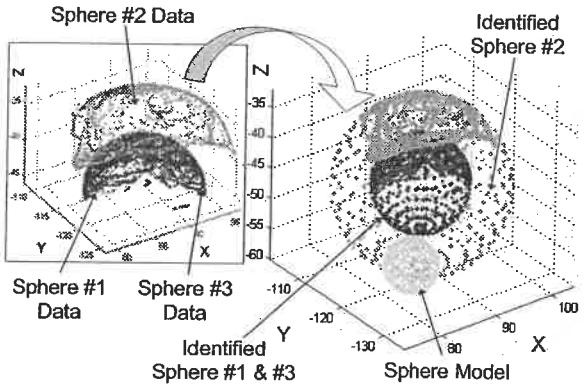

Fig. 6. Measured sphere data and identification

Now an important step is to obtain the vector ${}^{s}\boldsymbol{p}_{t}$ from the sensor frame to the tool frame to eliminate inevitable machining tolerance and assembly errors. The vector has been determined using efficient nonlinear optimization and least squares fitting algorithms [5]. As shown in Figures 5 and 6, the 3D Probe is first placed at the calibration block center. As the probe is rotated about the stylus, three partial spherical data sets are obtained from the sensor measurements. Then, unconstrained nonlinear minimization and least square fitting algorithms are applied to the recorded data which calculate the radii of three spheres and their center locations. The calculated radii are 7.1911, 13.2879, and 7.2723 inches. The x, y, and z coordinates of its center are 88.6076, -118.1211, and -45.8123 inches respectively. Finally, the vector from the center frame to the styli ball center ${}^{s}\boldsymbol{p}_{t}$ is determined. Fig. 6 shows experimentally measured data from the three detectors and the complete spheres created by this technique.

In addition, a distance accuracy test has been performed to investigate the accuracy degradation across the measurement volume. The room floor is divided into several subsections and a scale bar with a known length is used for accuracy tests. Results are shown in Fig. 7. The accuracy error is shown with respect to both vertical and horizontal distance from the transmitters. The 3D Probe prototype tested satisfies the accuracy and operation requirements for robot metrology and workcell calibrations.

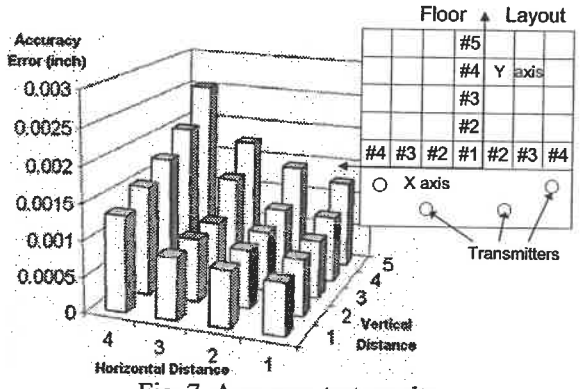

Fig. 7. Accuracy test results

4. Application on OAS Metrology

The developed metrology system has been used for OAS metrology. This includes interface connection performance testing, actuator, and robot metrologies. The 3D Probe has been used for intelligent scanning of these components. Fig. 8 shows how an operator can hold the probe and start scanning. The styli ball center pose is wirelessly transferred to the control center automatically during the scanning. The recorded point cloud data, then, can be used to determine standard geometries such as lines, planes, circles, spheres, and cylinders with the nonlinear optimization and least squares fitting algorithms.

Fig. 9 shows how an interface pair might be tested based on its geometry and what we can learn from this. Both the input and output frames are identified by scanning the surfaces of the female and male interfaces. First, the female top surface is scanned followed by its circular outer surface. After the plane determination, scanned circle point cloud is projected on to the plane resulting in a circle fitting process. The z axis is the normal vector of the plane on the circle center. Either the x or y axis direction is then fixed by a reference

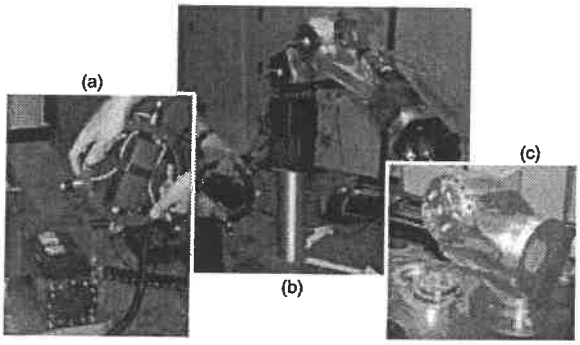

Fig. 8. Application of 3D Probe on actuator (a), robot (b), and interface (c) metrology

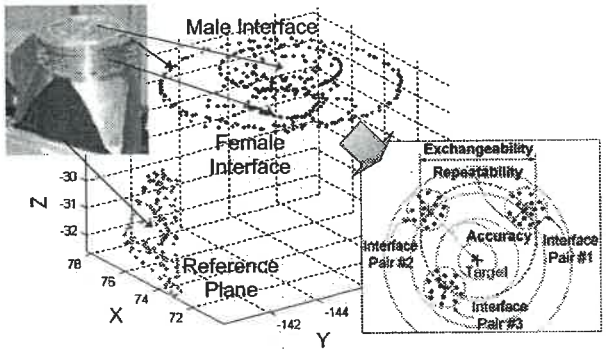

Fig. 9. Scanned point cloud for interface testing

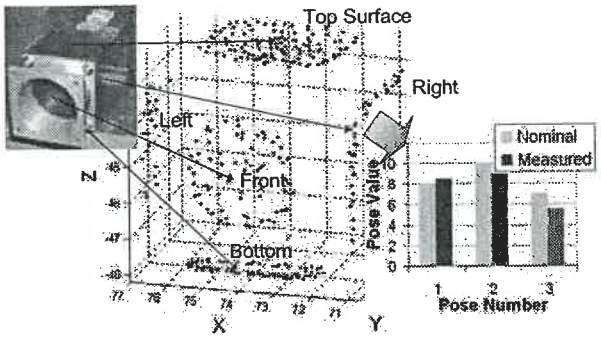

Fig. 10. Scanned point cloud for actuator metrology

plane. The other frame is determined using the same procedure on the male side. By repeatedly measuring these two frames, the distribution of differences between the two frames provides the connection accuracy, repeatability, and exchangeability. This information can be used to predict the overall accuracy of an assembled modular structure with error mapping. The pre-measured data of the interface connections could be written to a serial number on the interface serving as a database key to the calibration data.

Similarly, the 3D Probe could also be used for metrology of actuator joint/link modules and assembled modular robots. Figures 10 and 11 show experimentally measured point clouds needed to determine input/output or base/end-effector frames. A robot's accuracy and repeatability could then be determined based on the ISO and ANSI standard procedures as shown in Fig. 12 [6,7].

5. Conclusion

The 3D Probe prototype presented here is the first model. Thus, a simple design has been chosen for ease of manufacturing. An extensive optimization and analysis will be performed on the next prototype with control buttons and visibility/scanning mode indicators for easy operation. The second prototype will solve the problems found on the first model. Nonetheless, it turned out to be a convenient hand-held device that an operator can carry and use for OAS metrology. The 3D Probe has been successfully used and will continue to be used for interface, actuator, robot, and manufacturing workcell performance tests. This will help us understand the nonlinear phenomena of accuracy error sources and deal with them more effectively.

Acknowledgement

This work was funded by National Science Foundation. Seong-Ho Kang was supported in part by a University of Texas at Austin graduate research fellowship. The authors thank Daniel Poole for his assistance in prototype manufacturing and robot testing.

Reference

[1] S. Kang, "Kinematic Model and Metrology System for Modular Robot Calibration," IEEE ICRA, 2004

[2] Bernhardt, R. and Albright, S.L., Robot Calibration, Chapman & Hall, London, UK, 1993.

[3] ARC Second, Inc., 2004, Product Literature, Company Web Site URL: www.arcsecond.com.

[4] Sharke, Paul, "Measuring Across Space and Time: Large-scale Metrology Moves GPS In Out of the Rain," Mechanical Engineering, Jan, 2003

[5] Craig Shakarji, "Least-Squares Fitting Algorithm," J. Res. Natl. Inst. Stand. Technol. 103, 633, 1998.

[6] ISO, ISO 9283 Robot Testing Standard, 1998.

[7] ANSI, ANSI/RIA R15.05-1-1990, 1990.

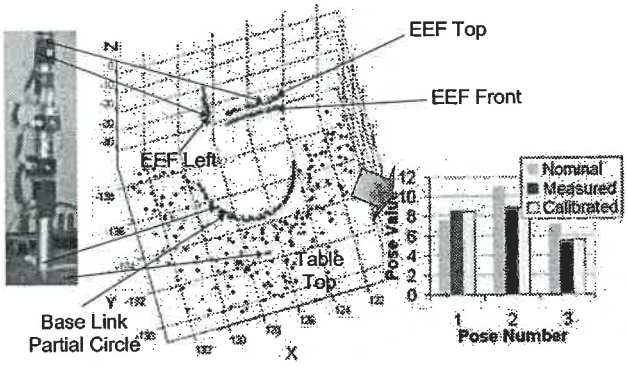

Fig. 11. Scanned point cloud for robot metrology

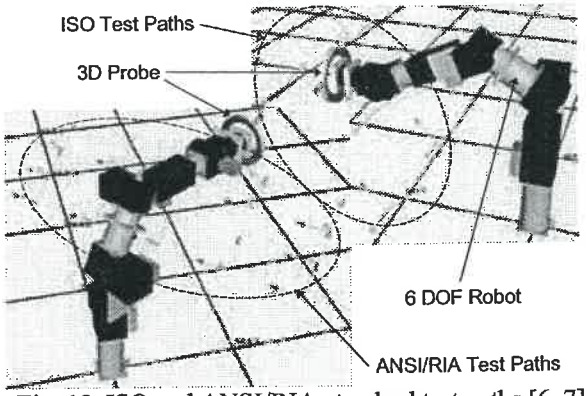

Fig. 12. ISO and ANSI/RIA standard test paths [6, 7]

ACTIVE COMPLIANT FIXTURES FOR NANOMANUFACTURING

Kartik Mangudi Varadarajan
Massachusetts Institute of Technology
Department of Mechanical Engineering
77 Massachusetts Avenue, Room 3-446
Cambridge, MA 02139
Tel: 617-452-4957, mvkartik@mit.edu

Martin L. Culpepper
Massachusetts Institute of Technology
Department of Mechanical Engineering
77 Massachusetts Avenue, Room 3-449b
Cambridge, MA 02139
Tel: 617-452-2359, culpepper@mit.edu

Keywords: Nanomanufacturing, accuracy, repeatability, kinematic coupling, compliant mechanism

1 Introduction

1.1 Summary

The positioning accuracy of kinematic couplings (KCs) is closely linked to manufacturing and assembly tolerances of the balls and grooves. Passive kinematic couplings achieve sub-micron repeatability, yet at best they provide practical accuracy of 10 microns [1]. The contrast between kinematic coupling accuracy and repeatability is shown qualitatively in Fig. 1A. This level of performance is not acceptable for emerging applications in nano-scale research and Nanomanufacturing. We have developed a mechanized kinematic fixture design, Compliant Nano Fixturing, which incorporates precision mechanisms, fixture constraints and actuators/sensors to enable active control of fixtured position to better than 60 nm alignment under closed-loop control. Flexures are used to improve repeatability and active elements are used to enable the fixture to shift the positions/orientations about which it mates, thereby improving alignment accuracy. This is seen in the shift of the CNF's distribution in Fig. 1A.

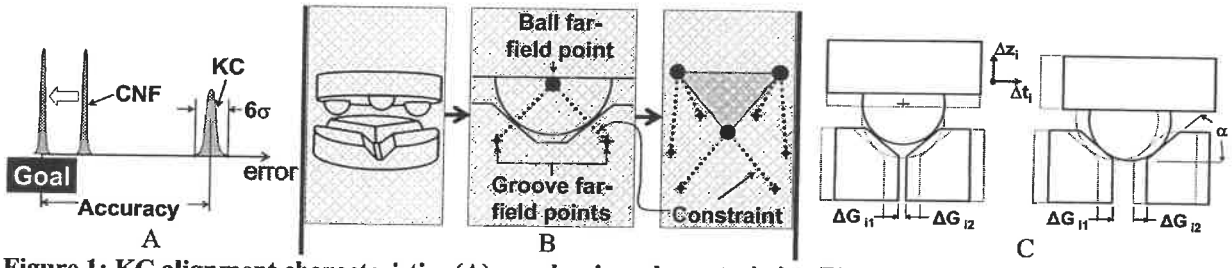

Figure 1: KC alignment characteristics (A), mechanism characteristics (B) and actuated groove design (C)

1.2 Analogy linking kinematic couplings and precision mechanisms

One can think of the constraints between KC balls and grooves as "legs" of a Stewart platform (see Fig. 1B). We see this through a constraint analogy in which the kinematic coupling's ball-groove joints form two constraints. The right side of Fig. 1B shows how the 6 constraints of a KC (2 per ball groove joint x 3 joints per KC) form the constraint profile of a Stewart-Gough platform. From this analogy we can then equate the changing of KC constraints with actuation of a 6 DOF manipulator. Although examples of 2 [2] and 3 [3] axes corrective fixtures exist, we must be able to correct alignment in six axes to achieve tens of nanometer or better positioning. The only existing, 6 axis adjustable coupling, an eccentric ball-shaft design, is limited to micron-level repeatability and accuracy [1] as a consequence of using rolling element bearings. In this paper, we choose to investigate the moving groove design shown in Fig. 1C. The groove surfaces rest upon independent flexure bearings. Through independent actuation of the groove faces, we aim to adjust the fixture in one to six axes with 60 nm resolution.

2 CNF fixture design

2.1 Design concept which uses flexures to guide groove displacement

Figure 2 shows how the grooves, groove flexures and groove plates (to be covered in subsequent sections) are rigidly attached to a monolithic compliant mechanism which contains the six sets of flexure bearings that guide the grooves. Piezo-electric actuators are integrated in the plane of the compliant mechanism such that they are structurally in parallel with their corresponding flexure bearing. The piezo-actuators actuate the flexure-groove-groove plate components in a direction parallel to the plane of coupling. The flexures have been designed so that the overall stiffness (23.7 N/micron in the plane of coupling) is sufficient for most small-scale alignment processes. The KC's balls are pressed into collars which are then pressed into the pallet. It is this pallet which may be use to align parts (attached to the pallet) to many different, grounded mechanized groove components.

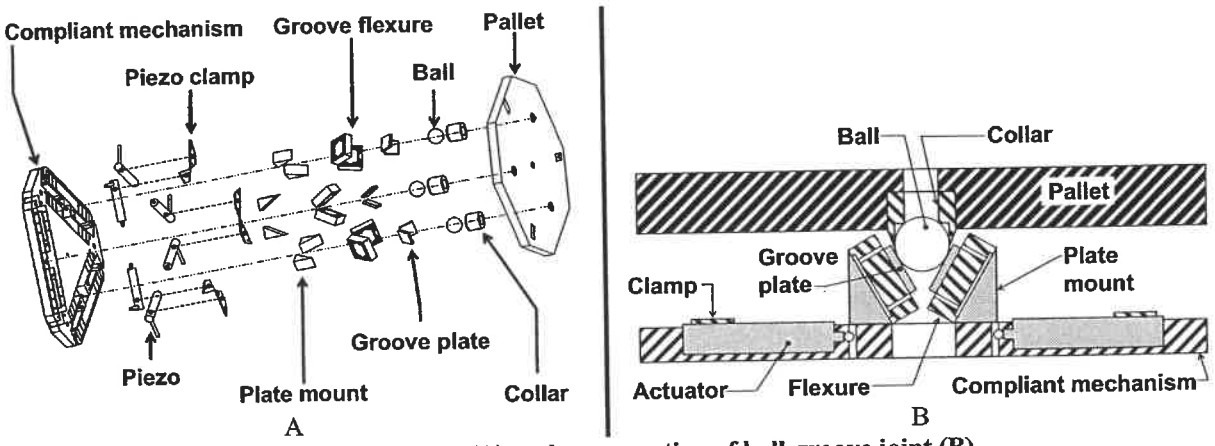

Figure 2: Exploded CNF prototype design (A) and cross-section of ball-groove joint (B)

2.2 Use of flexures in the grooves to limit friction-induced errors and enable mated position adjustments

The performance of kinematic ball-groove fixtures is limited in-part by frictional hysteresis or stick-slip between balls and grooves that slide relative to each other. Flexures can be used to minimize friction-induced errors. In the context of a ball-grove joint, the sliding occurs in two directions:

(1) Into the groove (In the plane of Fig. 2B and parallel to the groove surface): As the coupling engages, the balls slide down into the groove until seated with two points of contact. The friction-induced errors due to this mode of sliding have been addressed by flexures which are placed in grooves such that the ball-groove make contact and then the flexure complies to allow the ball to flex, rather than slide, into a seated position [4].

(2) Along the groove (Into the plane of Fig. 2B): As the balls engage the grooves surfaces, there will be some sliding of the balls along the grooves until the final ball is seated in its groove. The order and amount of ball-groove contact sliding depends on order of ball-groove flat engagement. As a result, variation in order of engagement is a source of coupling error [5]. The CNF design features a groove design which allows engaged or mated ball-groove pairs to move along the groove. This (a) reduces repeatability dependence on order of engagement and (b) enables us to actuate the coupling by changing the groove pattern as shown in Fig. 1C. When this is done, the ball centers must be able to move along the groove to maintain geometric compatibility with the new groove pattern.

The groove flexure shown in Fig. 2 and Fig. 3A was designed to provide stiff constraint in directions (34 N/micron) normal to the ball-groove contacts, and acceptable stiffness (2.13 N/micron) in directions parallel to the groove surface. The flexures were made from 6061 Aluminum and hardened, stainless steel 'groove plates" were bonded to the flexure to provide a contact interface for the hardened stainless steel balls. A parametric stiffness model was formulated for the flexure and then design variables were tailored to achieve a ratio of tangential stiffness to normal stiffness of less than 0.1. The average stiffness of the CNF coupling, in the plane of coupling, was 23.7 N/micron.

2.3 Accuracy/active correction capability

Each groove flexure is mounted upon a corresponding flexure bearing which each consist of six parallel, compliant beams. These guiding flexures can be seen in Fig. 3B adjacent to the flexure grooves (indicated by arrows) and encompassing the piezo-actuators (50μm range, stiffness 20 N/μm). The guiding flexure's stiffness and stress characteristics have been parametrically modeled and optimized to provide an acceptably low stiffness in the actuation direction (1.9 N/μm) and high stiffness in the other directions (440 N/μm normal to actuation direction).

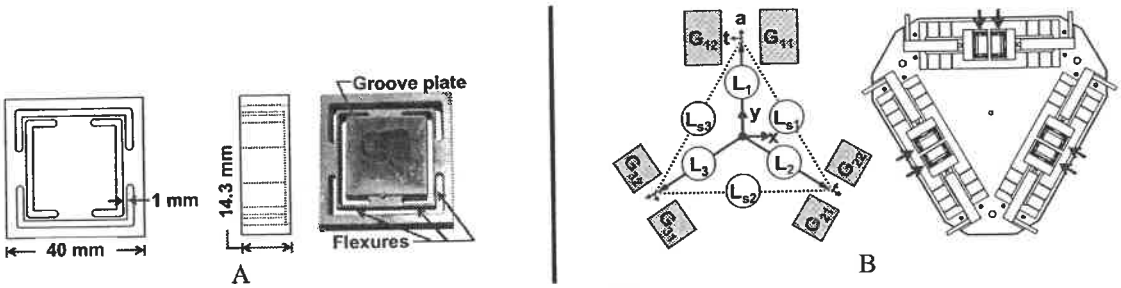

Figure 3: CNF groove flexure design (A) and groove layout (B)

2.4 Kinematic modeling

Figure 3B shows how the grooves are orientated and located with respect to each other by vectors of length L_i. Figure 1C provides examples which illustrate how v-groove i and groove flexure j, may be actuated by an amount ΔG_{ij} to achieve in or out-of-plane motion at a ball-groove joint. Simultaneous in and out-of-plane motion may be achieved by superimposing the in and out-of-plane actuation inputs with different magnitudes. Given the motion of each ball as a function of actuator input, we may then use kinematic solutions for adjustable kinematic couplings [6] to derive equations which describe the fixture's kinematic behavior for the i^{th} groove joint actuation inputs:

$$\Delta g_{i1} = \left(\frac{Z_c - L_i.(\theta_y.c[\theta_i] - \theta_x.s[\theta_i])}{\tan\alpha} \right) + \left(-(X_c - L_i.s[\theta_i].\theta_z).s[\theta_i] + (Y_c + L_i.c[\theta_i].\theta_z).c[\theta_i] \right) \quad (1)$$

$$\Delta g_{i2} = \left(\frac{Z_c - L_i.(\theta_y.c[\theta_i] - \theta_x.s[\theta_i])}{\tan\alpha} \right) - \left(-(X_c - L_i.s[\theta_i].\theta_z).s[\theta_i] + (Y_c + L_i.c[\theta_i].\theta_z).c[\theta_i] \right) \quad (2)$$

3 Experiment

Figure 4A and Fig. B show respectively the grooved and ball-equipped components of the prototype fixture. The majority of the components were waterjet cut from 6061 T6 Aluminum and then machined to add other features. Tests were performed on a thermally isolated, automated test rig, with an air piston applying a 275 N nesting preload through the decoupling flexure shown in Fig. 4C. A dSpace™ data acquisition program controlled the preload engagement for each mating cycle, recorded displacement measurements from six capacitance probes and delivered actuation commands to the piezo-actuators which are then able to drive the coupling with 60 nm resolution.

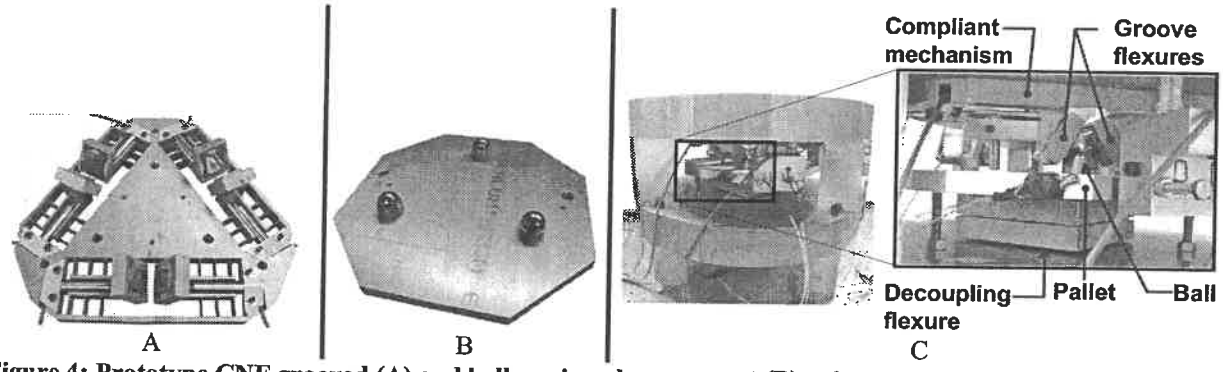

Figure 4: Prototype CNF grooved (A) and ball-equipped component (B) prior to assembly within test rig (C)

4 Discussion of results

Due to page limitations, we may only provide test results which characterize performance in three axes. The plots represent examples of best (y axis) and worst-case (z axis) open loop performance which were measured during the tests. Several test were run in which the fixture was commanded to move in one axis only. The top plots in Fig. 5 show the commanded vs. measured displacement and the middle plots show the off-axis errors. The bottom plots show data from repeated coupling engagement with the piezo-electric actuators receiving a voltage controlled, constant position command.

The worst case, open-loop deviations from desired location were less than 1μm / 20 μradians. This was further reduced through closed loop control to attain better than 60 nm / 2μradians positioning accuracy. This limit is set by the capability of the electronics used to drive the piezo-actuators. If we may depend upon the linearity of the flexure bearings, the mated displacement resolution may be improved to better than 5 nm with improved electronics. The linearity of the plots (no stick slip is evident) indicates that the flexure design allows the ball centers to move along the grooves. Within the parasitic error plots several linear relationships are observable. These are systematic errors that can potentially be reduced through mapping and active adjustment. The waterjet machine which cut the flexures for the fixture was capable of cutting flexure beams with a tolerance of ~ 10% of the flexure beam thickness. As such it is probable that some of these repeatable errors may be due to difference in stiffness between the flexure bearings and differences between the groove flexures. Even so, these are repeatable errors which are a topic of current research aimed at improving the coupling performance through calibration and closed-loop control.

One thousand cycles of engagement and disengagement were performed to characterize the fixture's repeatability characteristics. The ball-groove joints were lubricated with high-pressure grease. The coupling was allowed to settle for 30 seconds before measurements were taken. The test was run over 14 hours. The actuators were supplied with a constant voltage of 2 V. As expected we observe that piezo creep imparts a near-constant rate of transient positioning errors in the Z axis position. The lack of a corresponding, consistent transient trend in the other axes indicates the piezo creep is nearly equal for each piezo-actuator. The difference between the initial (001 – 100 cycles) and settled 1 σ data points (700 – 1000 cycles) of the Y test show less than 50 nm point-to-point difference. This is a strong indicator that little wear or relative sliding motion occurs at the ball-groove interface.

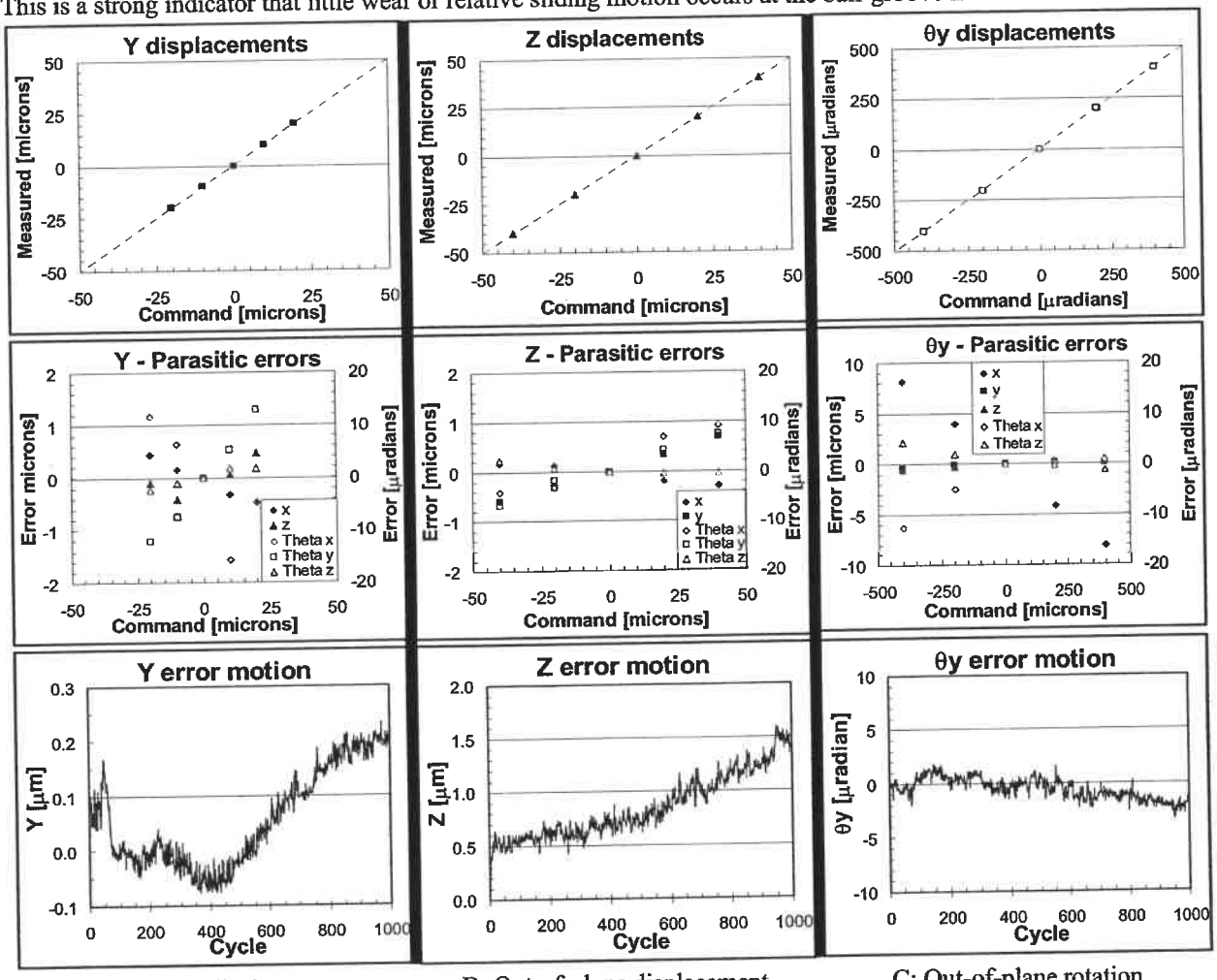

A: In-plane displacement B: Out-of-plane displacement C: Out-of-plane rotation

Figure 5: Open loop experimental results

5 References

[1] Culpepper, ML Mangudi KV, Dibiaso, M, Modeling and design of exact constraint fixtures for micron-level repeatability and accuracy, Accepted for publication in Prec Eng, 2003.

[2] Taylor, JB, and Tu, JF Precision X-Y Microstage with maneuverable kinematic coupling mechanism, Prec Eng, April, 1996, vol. 18, No. 2, p.85 – 94.

[3] Chui, MA, Roadmap of mechanical systems design for the semiconductor automatic test equipment industry, MIT Ph.D. thesis, 1998.

[4] Schouten CH, Rosielle PCJN, Schellekens PHJ. Design of a kinematic coupling for precision applications. Prec Eng;20;46-52.

[5] Hale, LC. and Slocum, AH., Optimal design techniques for kinematic couplings, Prec Eng, April 2001, vol. 25, No. 2, 114-27.

[6] Culpepper, ML, Araque, C, and Rodriguez, M, Design of accurate and repeatable kinematic couplings, Proc of the 2002 Annual Meeting of the American Society for Precision Engineering, October, 2002, pp. 279-84.

Manufacture of a 150×150 reflective spatial light Modulator integrated directly onto CMOS electronics

Jin-hong Kim and Thomas G. Bifano
Boston University, College of Engineering, Boston, MA

Abstract

This paper presents a micromachined Spatial Light Modulator (uSLM) made by integrating metal MEMS directly on top of planarized foundry-prefabricated complementary metal-oxide semiconductor (CMOS) electronics. Our uSLM consists of both 32×32 (i.e. 1024 segments) and 150×150 (i.e. 22500 segments) array sizes of electrostatically actuated, piston-motion, aluminum surface micromachined mirror pixels. Each mirror segment is addressed through directly integrated CMOS electronics having capable of 4-bit resolution phase control. Technical achievements on manufacturing uSLM such as chemical mechanical planarization, metal-polymer surface micromachining process are discussed.

Introduction

A large-scale SLM has been used for high-speed optical correlation and laser communication applications. Such SLMs can rapidly modulate incident coherent light's wavefront properties such as phase and amplitude. In comparison to classical relatively large and expensive SLMs such as liquid crystal phase devices, MEMS based SLMs have dimension comparable with the wavelength of light, and can be inexpensively fabricated in mass arrays of elements. They also have much faster response times, and higher fill factor, and are not subject to optical problems associated with absorption, diffusion, and polarization effects, which are inherent in liquid crystal devices [1].

Our SLMs function by actuating mirror segments in a surface normal direction over a stroke of up to 1/2 wavelength with a position resolution of one part in 16. To achieve better system performance and packaging advantages, MEMS mirror structure is directly integrated with foundry-prefabricated CMOS driver electronics.

Major technical challenges in this work included: the development of planarization processes for prefabricated CMOS electronics, the development of uniform low stress aluminum sputtering deposition processes and the control of print-through on the mirror segments. The manufacturing process was developed and optimized using a fractional factorial experimentation approach.

System description

Our uSLM consists of seven 32 × 32 and one 150×150 array sizes mirror segments in one prototype chip. Each mirror segment has a stroke of 775nm, which enables to alter the phase of the incident light (λ= 1550nm) by up to one wavelength. The device is designed to achieve kilohertz frame rates in a 15mm square aperture. To minimize beam loss, the mirror segment, which is made in aluminum, has optically flat and more than 90% reflective surface. 98um × 98um size mirror segments are placed on 100um × 100um pitch, yield a 98% fill factor. Since fabrication uses batch surface-micromachining process, the technology is readily scalable to megapixel arrays with aperture sizes of up to 20cm.

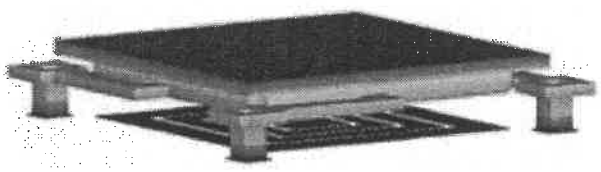

Figure 1. Schematic of a single uSLM segment

Figure 1 illustrates schematic of a single mirror segment. Each mirror pixel is made up of three main components; mirror segment, actuator and electrodes. Mirror sheet is attached into the actuator, which has four folded flexures. The total area of charged electrodes determines the actuator's surface normal positions. The CMOS driver,

which is directly connected to electrodes through small vias, controls the actuator's position by varying the combination of the number of charged electrodes (4-bit, 50nm resolution).

Planarization of CMOS electronics

CMOS driver electronics is custom fabricated by commercial foundry (Austrian Micro Sensors, AMS). Due to existence of multi-layer repetitive deposition and etching processes during CMOS electronics fabrication, the surface of the CMOS electronics shows severely leveled vertical topography. Since further fabrication is performed directly onto the CMOS electronics surface, resulting product will have same surface topography, which is not suitable for our micro mirror applications. To meet the requirements of uSLM, the array should have a RMS figure accuracy and flatness of each segment area of $\lambda/50$ (31nm) and 1nm respectively.

Lee et. al. reported planarization method with additional dielectric layer deposition using RF sputtering followed by subsequent chemical mechanical polishing (CMP) [2]. Further study on planarization process has been done to improve optical quality of the device and better process yields. Additional thick dielectric layer (Si_3N_4) is deposited by Plasma Enhanced Chemical Vapor Deposition (PECVD), since CVD coated film shows lower pinhole densities than RF sputtered film. Up to 4um thick Si_3N_4 film is coated using PECVD. Process temperature is less than 100°C, and thickness variation over the individual chip is measured ±10%.

Nitride-coated CMOS electronics is subsequently planarized with conventional CMP technique. Pressure Sensitive Adhesive (PSA) tapes are used for mounting die. Double sided adhesive carbon tape (SPI supplies, Product #5083) is inserted between PSA layer and glass plates to minimize tilt-error during die attach process. The glass substrate holding CMOS electronics and force-balancing pieces is polished with 30nm grain size colloidal silica slurries until the desired surface topography is achieved.

Figure 2 (top) shows the surface profile of foundry-delivered CMOS electronics. Interferometric contour mapping microscope (Veeco, WYKO NT2000) is used for the measurement. Measured data show that RMS flatness is 523.93nm, peak to valley height difference is 2262.92nm. Figure 2 (bottom) shows the surface profile of the planarized CMOS electronics after polishing. As shown in the picture, initial flatness of 523.93nm RMS before planarization (500um scan length) is reduced to 17.65nm RMS. Peak to valley height difference is reduced from 2262.92nm to 112.43nm.

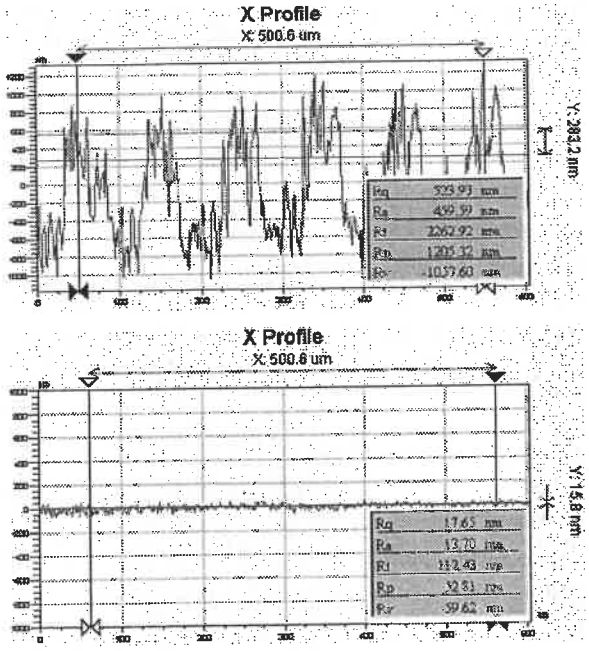

Figure 2. Surface profile of the prefabricated foundry CMOS electronics (top) and planarized CMOS electronics (bottom).

Metal-polymer MEMS fabrication process

Bifano et.al. reported manufacturing process of the 1024 segment large-scale metal MEMS mirror arrays with integrated electronics [3]. Polyimide has been replaced as a sacrificial material rather than photoresist, since photoresist starts to reflow at over 90°C and shows excessive print-through from underlying patterns. Polyimide allows several advantages; such as (1) allows high temperature metal deposition, (2) reduces print-through, (3) allows dry release process rather than wet release which causes possible stiction.

Aluminum is chosen as a structure material, since it allows low cost, uniform film deposition in low temperature and lower voltage activation than the device made of silicon. Also aluminum is a naturally reflective material (more than 90% reflectivity) that meets our

application's requirement. The uniform low stress aluminum sputtering deposition processes are developed by customized deposition chamber and tightly controlled environmental parameters, such as pressure, temperature and RF power.

Integrating MEMS structures on planarized CMOS electronics consists of seven major sub-processes: via cuts/filling, electrode, anchor, actuator, mirror thickener, mirror segment and sacrificial release. Since any topography in structure layers will affect the top mirror layer, maintaining a flat surface in each process step is critical. Also it will prevent the print-through during following fabrication process.

(a) Planarized CMOS electronics

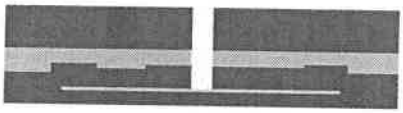

(b) Pattern photoresist and anisotropically etch Si_3N_4

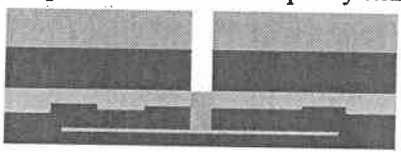

(c) Deposit aluminum to fill vias

(d) Lift-off photoresist mask and metal

(e) Electrode fabrication using pattern/wet-etch

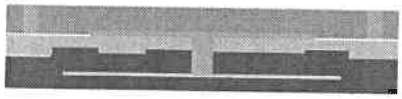

(f) Anchor fabrication (1st sacrificial layer)

Figure 3. Illustration of via etch/fill, electrode, anchor fabrication process

Vias are anisotropically etched by Reactive Ion Etching and filled through planarized Si_3N_4 layer to create interconnections between electrodes and CMOS driver. Subsequent electrode fabrication is followed by thin metal layer deposition/pattern photoresist mask/wet-etch/cleaning processes.

Actuator anchor is fabricated with similar schemes. To form the surface normal gap between electrode and actuator, the 1st sacrificial layer, polyimide (PI2555) is spun on and cured to yield a normal thickness of 2.5um. Metal mask for the anchor is formed by thin metal deposition/pattern photoresist/wet-etch mask metal. The polyimide layer is then anisotropically etched using oxygen plasma. Thick metal deposition is followed to fill the anchor. The bulk of the aluminum and photoresist are then removed by lift-off process (Figure 3).

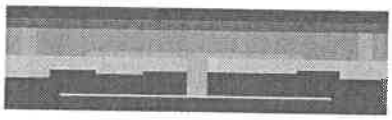

(a) Spin and partially cure 2nd sacrificial layer followed by photoresist

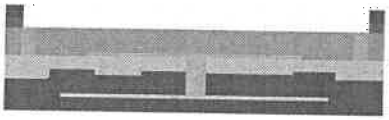

(b) Pattern phtoresist and 2nd sacrificial layer

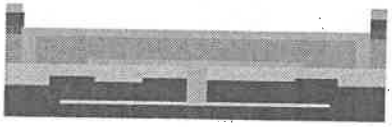

(c) Deposit metal layer

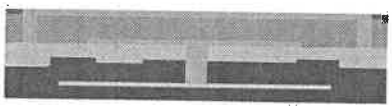

(d) Lift-off metal and fully cure 2nd sacrificial layer

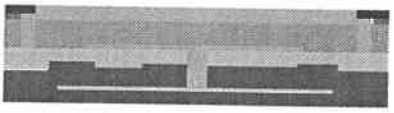

(e) Mirror thickener fabrication (3rd sacrificial layer)

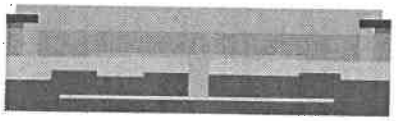

(f) Mirror segment fabrication

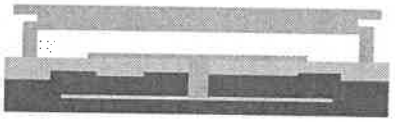

(g) Final release using oxygen plasma

Figure 4. Illustration of actuator, mirror thickener, mirror segment fabrication

The 2nd sacrificial layer, polyimide (PI2556) is spun on to 0.85um thick, then partially cured, allowing the material to be etched by photoresist developer. Photoresist is spun on and patterns the actuator with polyimide using developer. Aluminum is then sputtered to fill the etched actuator pattern. The 2nd sacrificial layer is fully cured after lifting-off the metal and photoresist.

The 0.85um thick actuator thickener as well as the 3rd sacrificial layer (PI2556) is fabricated using the same process used for the actuator. The mirror segment is then fabricated following the 1um thick metal deposition, patterning and wet-etch. After removal of photorsist, the device is fully released by oxygen plasma (Figure 4).

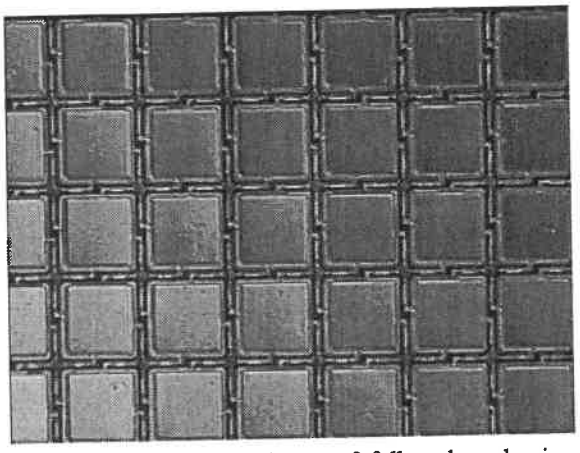

Figure 5. Microscope picture of fully released mirror segments

Figure 5 shows mirror segments after the device is fully released by oxygen plasma. For the evaluation purpose, MEMS structures are fabricated onto the bare silicon substrate, which has the same size as our CMOS electronics die. Figure 5 clearly shows our new process reduces print-through to a great extent. Measurement shows that the print-through in actuator fabrication process is reduced to 50nm from 850nm.

Since the work on via cuts/fill process is still in development at the time of this project, MEMS devices were fabricated on non-planarized CMOS electronics. Electromechanical testing of the fabricated device was performed under a WYKO surface mapping interferometer. As shown in the Figure 6, an individual mirror segment was addressed and deflected with no cross talk or other influence on its neighboring actuators.

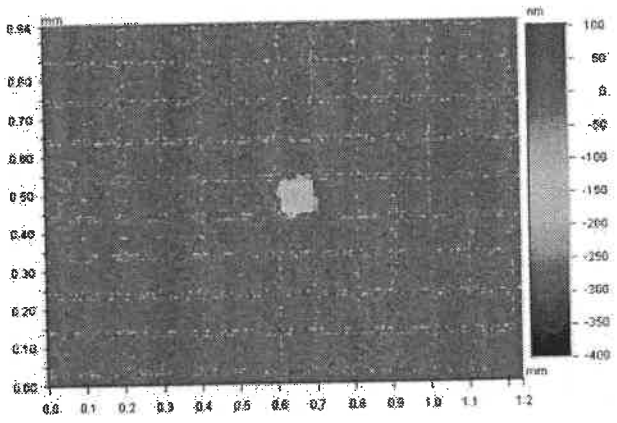

Figure 6. Single pixel addressed with no influence on its neighboring actuators

Conclusion

Technical achievements and challenges associated with manufacturing a large scale uSLM directly integrated on top of the planarized CMOS electronics are described. CMOS electronics is planarized by our chip-scale planarization process using low temperature dielectric material deposition and CMP. A new metal-polymer surface micromachining process to reduce print-through has been developed and we demonstrated an individual pixel actuation by far. The future effort will combine these two successes to produce a large array of uSLM onto the planarized CMOS electronics.

References

[1] R. K. Mali, T. G. Bifano, N. Vandelli, and M. Horenstein, "Development of micromechanical deformable mirrors for phase modulation of light", *Opt. Eng.* 36(2), 1997, pp 542-543

[2] Lee, H., Miller, M. H., and Bifano, T. G., "CMOS chip planarization by chemical mechanical polishing for a vertically stacked metal MEMS integration." J. Micromech. Microeng., [14] 1, pp. 108-115, 2004

[3] Bifano, T., Bierden, P., Cornelissen, S., Dimas, C., Hocheol, L., Miller, M., Perrault, J., "Large-scale metal MEMS mirror arrays with integrated electronics" Proceedings of the SPIE 4755, pp. 467-476, 2002

Fabrication of Atom Trap Chip for Quantum Information Processing

Keisuke NAGATO, Kouhei OHSIGE, Takeshi OOI, Kensuke TSUCHIYA, Tetsuya HAMAGUCHI, and Masayuki NAKAO
Dep. of Mech. Eng., School of Eng., The University of Tokyo, 7-3-1 Hongo, Bunkyo-ku, Tokyo, Japan

KEYWORDS: atom trap chip, quantum information processing, electro-dynamic trap, micro electrodes structure, focused ion beam, etching from a tilted angle

1. Introduction

Recently, laser-cooling technology with neutral atoms has progressed rapidly in the field of ultra-cold atomic physics [1]. Prof. Katori and his colleagues at the University of Tokyo are interested in the demonstration of "quantum information processing (QIP)"[2] with these cold atoms. They have proposed a new method that enables one to manipulate neutral atoms with electric fields where the fields can be produced by micron-sized electrodes on an atom chip [3]. After the atoms are trapped they are planning to use those atoms as qubits (qunatum-bits) for the QIP. As a first step, they have trapped strontium(Sr) atoms [3]. As collaboration, we have fabricated this "atom trap chip" with our micro fabrication technology. This paper reports the design and the process of the fabrication to satisfy the required functions for the structure of the atom chip. Though a special technique of nano-micro fabrication was needed, we overcame with unique methods. We will also show the chip that was actually fabricated. The experiment of trapping Sr atoms on this chip has been demonstrated by the Katori group [4].

2. Electro-dynamic Trapping of Atoms (Proposed by Katori Group)

2.1. Principle

Here we will mention the principle of the electric trapping of atoms and the basic structure of the electrodes. The static voltage on the 4 symmetrical electrodes shown in figure.1 forms a saddle-type Stark potential. Neutral atoms usually experience a quadratic Stark effect, $U=-(1/2)\alpha E^2$, where α is the dipole polarizability of the atom. For atoms in a stable state α is positive, therefore they will be attracted toward field maximum in an inhomogeneous field. By rotating the configuration of the voltages applied on the electrodes by 90 degrees, it forms another saddle-type potential which is spatially rotated 90 degrees in the electrode plane. As discussed in detail in reference [3], by switching mutually these two potentials, the atoms are trapped in the center of the potential. (Figure.1)

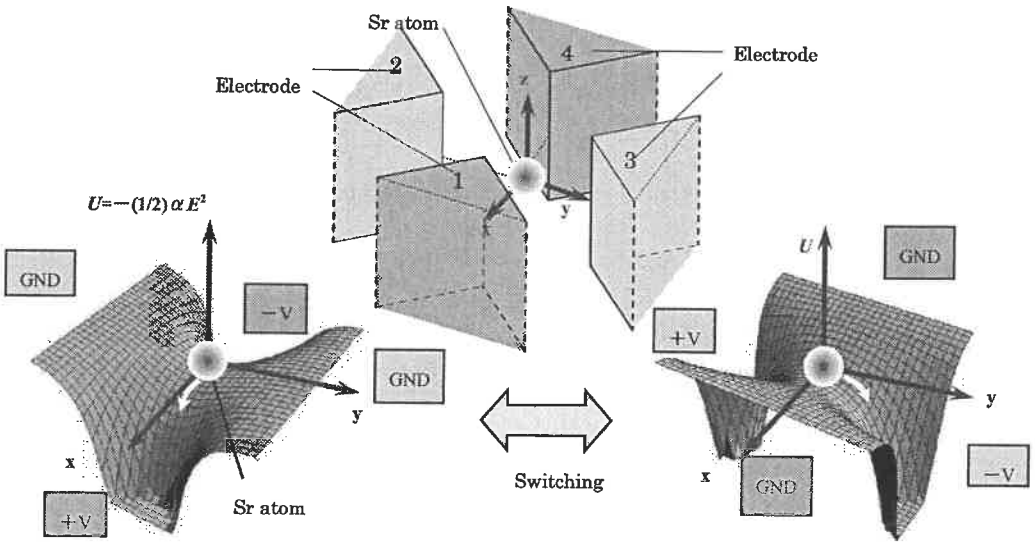

Figure.1. Structure and Stark potential for electro-dynamic trapping of Sr atoms.

2.2. Experiment Procedure (Proposed by Katori Group)

The electro-dynamic trapping of ultra-cold atoms was carried out as the following procedure. (1) Cool and pre-trap Sr atoms above the electrodes. For this experiment, the atoms were cooled and collected by magneto-optically trapping them near a mirror surface ("Mirror MOT"). (2) Switch on and load the collected atoms into a standing-wave confining potential which is produced by counter-propagating far off resonance lasers. Then the loaded atoms are transferred to the center of the electrodes by modulating one of the frequencies of the standing-wave lasers. (3) Apply the switching electric fields and perform the electro-dynamic trapping. (4) Transfer back above the electrodes by the moving standing-wave potential, and then observe the atoms that have been trapped by the electric fields from the micron-sized electrodes. The experiment is performed in an ultrahigh vacuum of ~10^{-10}Torr. (Figure.2)

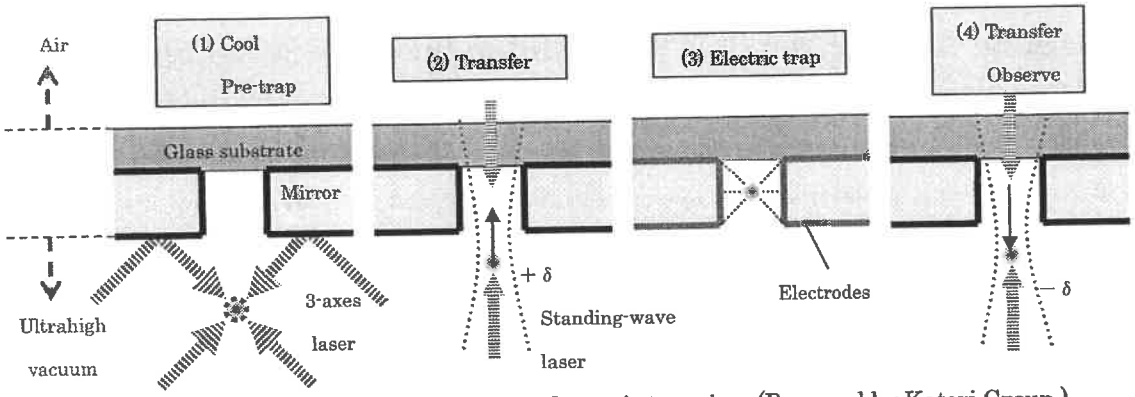

Figure.2. Experiment procedure of electro-dynamic trapping. (Proposed by Katori Group.)

3. Requirements of the Atom Trap Chip

The atom trap chip needs to satisfy the following requirements. FR(1): High reflectivity(R>95%) for 45degrees incident beam at wavelength of 460nm and 689nm, which are used for the "Mirror MOT". (Laser beam diameter: 12mm). FR(3): The basic structure is explained in section 2.1. FR(2),(4): Optical transmission (T>90%) of the laser for the standing-wave laser at wavelength of 800nm (Laser beam diameter: 50μm) (figure.3). In addition, the requirement that the chip will be introduced into ultrahigh vacuum has to be considered.

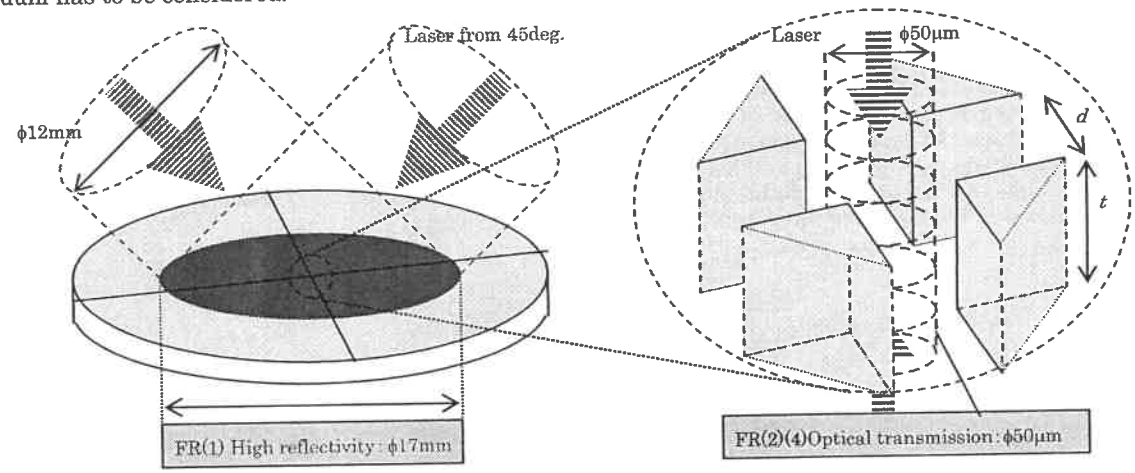

Figure.3. Requirements of the atom trap chip.

4. Design and Fabrication Process

First, the gap-size d and the voltage V of the electrodes are estimated from the requirements mentioned in section 3. Since the confinement potential scale as V/d^2, the smaller the structure is, a lower voltage will be needed for a given potential depth that the atoms can be trapped[3]. However, the ϕ50 μm lasers for the standing-wave potential(FR(2)) have to be transmitted through the center of the electrodes, so the gap-size of the electrodes is determined as d=50μm. Therefore, thickness t of the electrode is determined as t=100μm[4].The voltage is set to ±200V and with these conditions, a stable trap is expected when the switching frequency is about 10kHz[4].

Next the structure and the materials are discussed for each required functions. FR(1)(High reflectivity): To obtain low surface roughness and high surface flatness, metallic thin film on a thick glass substrate(t=100μm), which have high Young's modulus and can be ground easily, was used. We took advantage of the metallic surface of the electrodes and used it also as a mirror for collecting atoms in the MOT. The mirror area needs to be more than ϕ17mm, since the MOT lasers(ϕ12mm) are irradiated from 45 degrees. Therefore, a ϕ25mm glass substrate was used. This includes the wiring pads which has a width of 5mm. FR(2),(4)(Optical transmission): To make a clear space for trapping, we fabricated a through-hole in the center of the electrodes of the thin glass substrate. The 100μm thickness substrate is fragile so it was glued at the rim on a thicker(t=1mm) glass, which was also used as a window that separates air and vacuum and has an AR(Anti-Reflection)-coating on it to have good transmission for the standing-wave lasers. FR(3)(Electrodes): The same electric field can be obtained in between the electrodes whether they are made from metallic thin film on a glass substrate or just fabricated directly from a metallic bulk. To minimize the fabrication time, we took the process of fabricating the glass substrate with metallic thin films.

The details of the fabrication process are mentioned in the following. (1)Fabricate the cross through-hole at the center of the glass substrate (ϕ25mm, t100μm) with high flatness by FIB. (2)Make the silver thin film on the entire surface (topside, inside, backside) except the outer rim of the substrate by sputtering. (3)Etch the thin films to make 4 electrodes. FIB is used for etching in an angle, such as the surface inside the cross through-hole. The details about the FIB are discussed in section 5. (4)Further etch the thin film to the rim by YAG(Yttrium-Aluminum-Garnet) FHG(Forth Harmonic Generation) laser, whose fabrication rate is high, and insulate the 4 electrodes. The area far from the center (about 500μm square) is etched by laser, since the effective trapping potential are not sensitive to the electrode roughness far from the center region. Further fabrications for insulating the electrodes are done in this process. (5)Mount the fabricated substrate on an AR-coated glass window substrate. (6)Glue this chip on to the vacuum chamber port and wire the electrodes to the electrical feedthroughs, which are capable of introducing high-voltage into vacuum. The chamber port and the chip are sealed by Torr-Seal which has very low outgas rate in vacuum.
Figure.5 shows a SIM(Scanning Ion Microscope)view and a SEM(Scanning Electron Microscope)view of the atom trap chip. On the SIM view, surface of glass is shown dark.

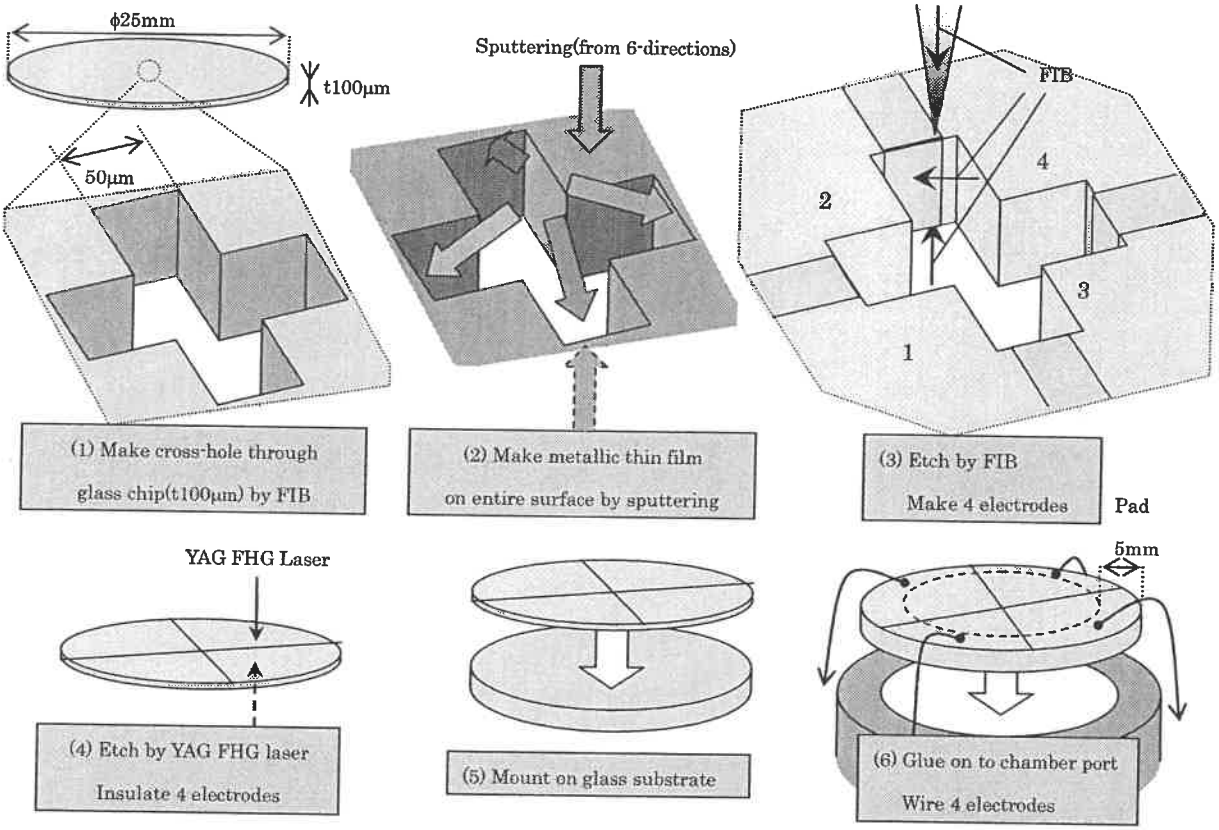

Figure.4. Fabrication process of atom trap chip.

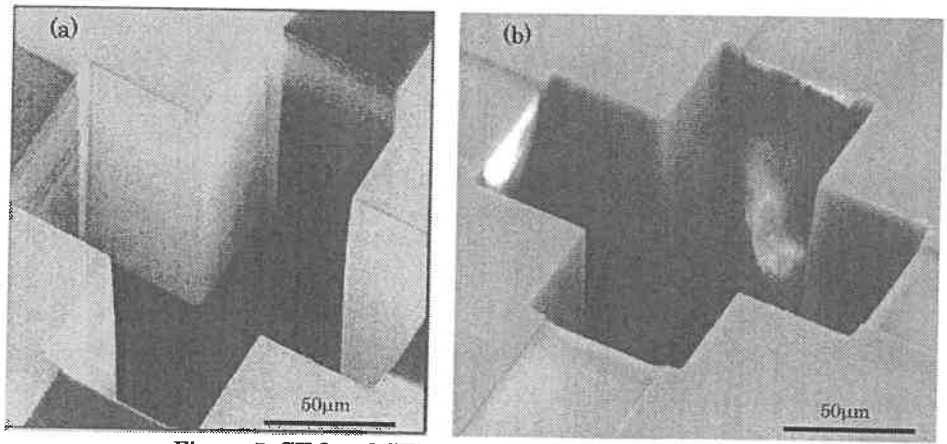

Figure.5. SIM and SEM view of fabricated electrodes.
(a) SIM view. (angle of 30deg.) (b) SEM view. (angle of 45deg.)

5. FIB (Focused Ion Beam) System

The feature of the FIB system we used is mentioned in the following. This FIB is an ion beam accelerated and focused down to 50-500 nanometers by electric fields. It can etch nano-micro scale structure without any masks. Therefore there are some features, such as, positioning directly by observing with the FIB, fabricating various depths and any shape continuously, easy additional fabrication, fabricating with an angle (refer to figure.5.(b)SIM view). These are very suitable for fabrication of atom trap chip. Especially, no other beam except FIB can fabricate obliquely with accuracy of less than 1μm.(Figure.6)

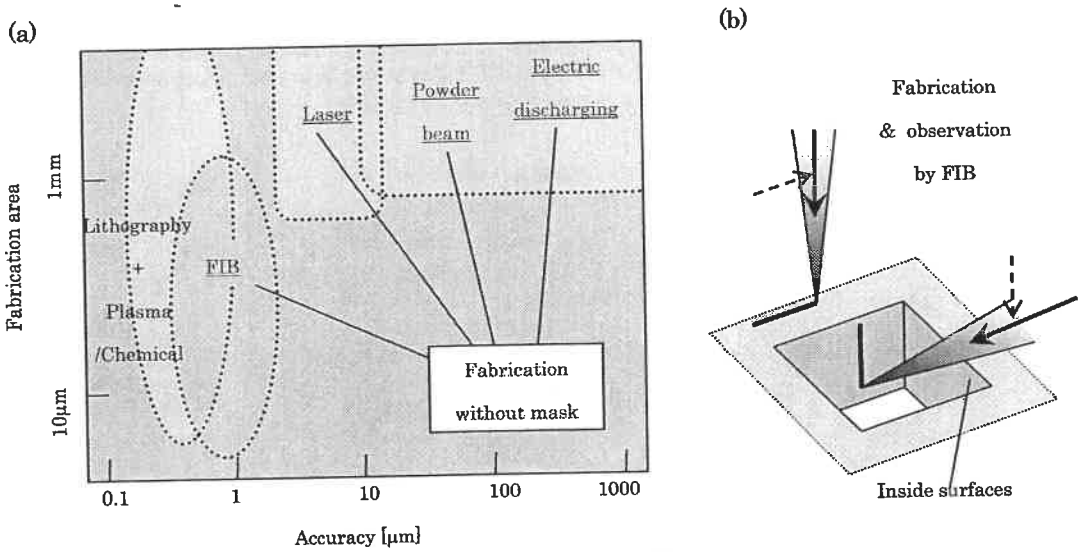

Figure.6. Feature of FIB.
(a) Outline of micro etching. (b) Etching from a tilted angle.

7. Conclusion

The atom trap chip that satisfies the requirement by the experimental process was designed and was fabricated by using FIB for micro etching on the side surfaces. Furthermore, the electric trapping of Sr atoms on this chip was demonstrated by Katori group recently.

8. Acknowledgement

We would like to thank H.Katori, T.Kishimoto, H.Hachisu, and J.Fujiki for providing unpublished data on the atom chip experiment.

References

[1] W. D. Phillips, *Rev. Mod. Phys.*, 70, 721 (1998).
[2] A. M. Stane, *Rep. Prog. Phys.* 61, 117 (1998).
[3] H. Katori and T. Akatsuka, *Jpn. J. Appl. Phys.*, 43, 358 (2004).
[4] T. Kishimoto et al., *ICAP Poster* (Rio de Janeiro, Brazil, 2004).

Shape Control in Ultra-precision Finishing for the Femoral Head of the Artificial Hip Joint by Means of Abrasive Waterjet

Hiroshi SAWANO[*1], Shin'ichi WARISAWA[*1], Mamoru MITSUISHI[*1] and Kouichi KURAMOTO[*2]

[*1]Department of Engineering Synthesis, School of Engineering, The University of Tokyo
7-3-1, Hongo, Bunkyo-ku, Tokyo 113-8656, Japan

[*2]Nakashima Propeller Co., Ltd., 688-1, Joto-kitagata, Okayama-city, Okayama 700-8691, Japan

1. Introduction

A hip joint replacement is provided to a patient with difficulty in walking caused by articular rheumatism or coxarthrosis, which is very important in social rehabilitation. Since the life of an artificial hip joint is restricted to about 20 years, it is necessary to replace it again. The main factor in which the life is restricted is wear destruction of a socket made from ultra high molecular weight polyethylene (UHMWPE) which plays the role of a cartilage. It is known that wear destruction of a socket not only brings about functional deterioration as a joint, but the wear powder discharged further stimulates an osteoclast [1]. In order to extend the life of an artificial hip joint, it is necessary to reduce wear on the sliding surface of an artificial hip joint.

One of the remedy to reduce the wear is to improve surface roughness and roundness of a femoral head, a sphere shape made of metal such as Co-Cr-Mo alloy. It is said that less than 10 nm Ra of surface roughness and 100 nm of roundness are required. In the last paper, a novel machining method of a sphere-shaped femoral head of an artificial hip joint by means of abrasive waterjet was proposed [2]. The proposed method can realize up to 7 nm Ra of surface roughness, however its roundness got worse.

In this paper, in order to improve roundness of a femoral head, a machining model is analyzed. Machined workpiece shape can be calculated by means of a discrete machining model. Furthermore, a nozzle feed speed planning method to improve the roundness is proposed. The feed speed planning can be conducted by feed-forward calculation of machining volume according to the machining model.

2. Finishing method for a femoral head

In the last paper, the machining system which immerses a workpiece into slurry and irradiates a waterjet to the workpiece under the slurry was proposed [2]. In the proposed method, abrasive particles in the slurry involved and accelerated in a waterjet collide with a workpiece. The proposed method is advantageous from the viewpoints of nozzle wear and abrasive reuse as well as ultra fine particle use.

A waterjet technology is applied to finish processing of an artificial hip joint femoral head as shown in Fig.1. The proposed finishing method is as follows: First, abrasive particles are mixed in the water of the machining chamber beforehand. Then, high pressured waterjet shoots out under the water to the workpiece in a tangential manner. Abrasive particles gather around the machining point. The workpiece rotates under the abrasive mixed water. The abrasive nozzle is controlled to circulate around the workpiece.

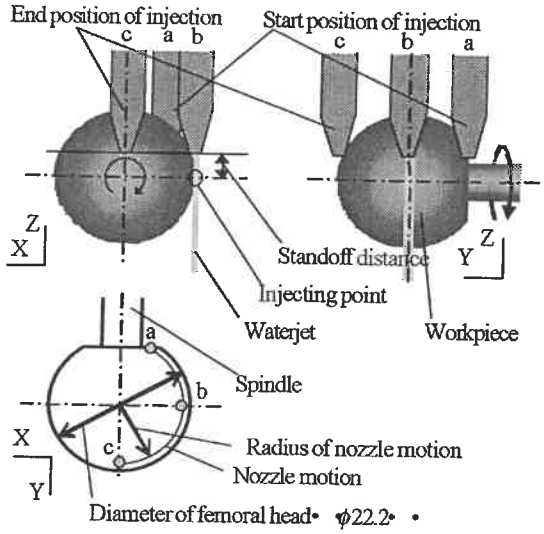

Fig.1 Finishing for the femoral head of an artificial hip joint

3. Analysis of machining volume

3.1 Machining model

Fig.2 explains a machining model. When a point on a workpiece comes near the outer of a waterjet (point A), some abrasives erode the point on a workpiece with the stand-off distance of s_A, the impact angle of α_A and the distance from center of jet of r_A. Then, as the workpiece rotates, the stand-off distance, the impact angle and the distance from center of jet are varied. Until the point reaches point B where the impact angle decreases to 0 degree, the point on the workpiece is eroded by abrasives. The volume of erosion during a rotation is equal to the volume of erosion during the period mentioned above.

By the way, the density of abrasive is reduced during machining. Therefore, for the analysis of a machining volume, it is necessary to analyze the relationship of the volume of erosion with the stand-off distance s, the impact angle α, the

distance from center of jet r and the density of abrasive d.

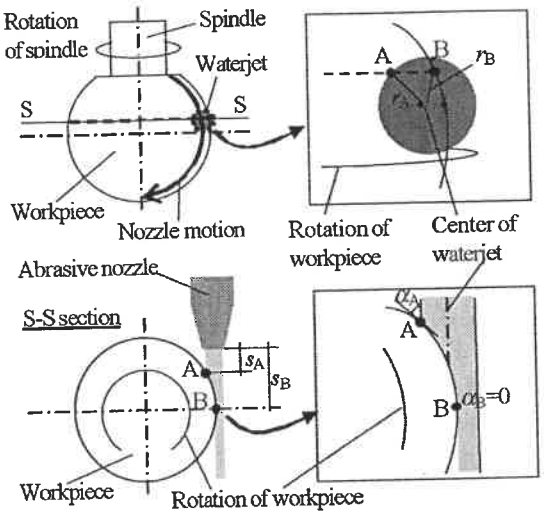

Fig.2 Machining model of finishing for a femoral head

3.2 Machining ability distribution within a waterjet

Machining ability distribution within a waterjet can be calculated from the property of abrasives and a workpiece, the velocity and mass distribution of abrasives. However, it is difficult to measure the velocity and mass distribution of abrasives. Therefore, in this paper, machining ability distribution is experimentally determined. $W(\alpha, r)$ is defined as the erosion ratio per unit time and area, at impact angle α and distance from center of jet r. Based on Bitter's equation, the erosion ratio is described as follows:

in case of $\alpha < \alpha_0$

$$W(\alpha,r)=\frac{J(r)\cos^2\alpha\sin n\alpha}{\beta}+\frac{J(r)\sin^2(\alpha)}{\varepsilon} \quad (1)$$

in case of $\alpha > \alpha_0$

$$W(\alpha,r)=\frac{J(r)\cos^2\alpha}{\beta}+\frac{J(r)\sin^2(\alpha)}{\varepsilon} \quad (2)$$

where $J(r)$ is the kinetic energy of abrasives per unit time, β is the coefficient of cutting wear, ε is the coefficient of deformation wear and $n = \pi/2\alpha_0$. α_0 is called as a critical angle which represents a reflection angle of an abrasive when the vertical velocity of an abrasive is zero.

When $\alpha=\pi/2$, from Equation (2), the coefficient of deformation wear is obtained by the following equation.

$$\varepsilon=\frac{J(r)}{W(\pi/2,r)} \quad (3)$$

When the waterjet shoots out to a workpiece with the impact angle of θ, from Equations (1) and (3), the coefficient of cutting wear is obtained by the following equation.

$$\beta=\frac{J(r)\cos^2\theta\cdot\sin n\theta}{W(\theta,r)-W(\pi/2,r)\sin^2\theta} \quad (4)$$

Then, from Equations (3) and (4), Equations (1) and (2) can be transformed as follows:

in case of $\alpha < \alpha_0$

$$W(\alpha,r)=\frac{(W(\theta,r)-W(\pi/2,r)\sin^2\theta)\cos^2\alpha\cdot\sin n\alpha}{\cos^2\theta\cdot\sin n\theta}+W(\pi/2,r)\cdot\sin^2\alpha \quad (5)$$

in case of $\alpha > \alpha_0$

$$W(\alpha,r)=\frac{(W(\theta,r)-W(\pi/2,r)\sin^2\theta)\cos^2\alpha}{\cos^2\theta\cdot\sin n\theta}+W(\pi/2,r)\cdot\sin^2\alpha \quad (6)$$

Therefore, if $W(\pi/2, r)$, $W(\theta, r)$ and α_0 are obtained, the volume of erosion with any the impact angles can be calculated using equation (5) and (6). The erosion ratio with the impact angle of $\pi/2$ and $\pi/4$ are obtained experimentally as shown in Fig.3. Furthermore, α_0 is determined as 80 degrees experimentally.

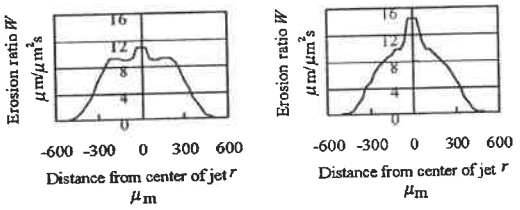

(a) $\alpha=\pi/2$ (b) $\alpha=\pi/4$

Fig.3 Erosion ratio of waterjet

3.3 Relationship of stand-off distance and density of abrasive with erosion ratio

Taking into consideration an effect of stand-off distance s, the erosion ratio is described as $f(s)W(\alpha, r)$, where $f(s)$ is the coefficient of reduction. Furthermore, the erosion ratio is directly proportional to the density of abrasive d. Therefore the erosion ratio with stand-off distance s and density of abrasive d is obtained by

$$W(\alpha,r)\cdot f(s)\cdot k_d d \quad (7)$$

where k_d is the coefficient of proportion. The erosion ratio is estimated by the depth of groove. Relationships of stand-off distance and density of abrasive with the depth of a groove are obtained by experiments as shown in Figs. 4 and 5 respectively. From these experimental results, $f(s)$ and k_d are obtained as

$$f(s)=-0.0352(s-8.5)+1 \quad (8)$$

$$k_d=0.667 \quad (9)$$

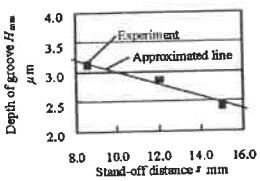

Fig.4 Relationship between the stand-off distance and the depth of groove

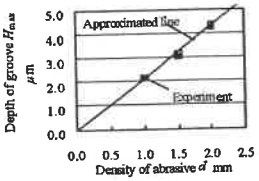

Fig.5 Relationship between the density of abrasive and the depth of groove

4. Simulation method

In this chapter, simulation method to estimate the shape of a workpiece after injection is proposed. The surface of a femoral head is divided into minute elements with the width of δ as shown in Fig.6. Then the machining volume of each element is calculated. Furthermore, the range of waterjet is divided into minute concentric circular elements. Elements on the inner side are defined as from $\mathbf{B}_1$ to $\mathbf{B}_N$. Elements on the outer side are defined as from $\mathbf{B}_1$ to $\mathbf{B}_N$.

Machining volume h_j in minute elements during a rotation is obtained by

$$h_j = \frac{60}{p}\cdot\frac{1}{2\pi R_j\delta}\left(\sum_{i=9N}^{-j} f(s_{ij})\cdot k_d d\cdot W(\alpha_{ij},n)\cdot S_{ij} + \sum_{i=j}^{N} f(s_{ij})\cdot k_d d\cdot W(\alpha_{ij},n)\cdot S_{ij}\right) \quad (10)$$

where p is the rotational speed of a workpiece, R_j is the radius of the minute element $\mathbf{A}_j$ and S_{ij} is the size of the area where the minute element of workpiece $\mathbf{A}_j$ and the minute element of waterjet $\mathbf{B}_i$ intersect each other.

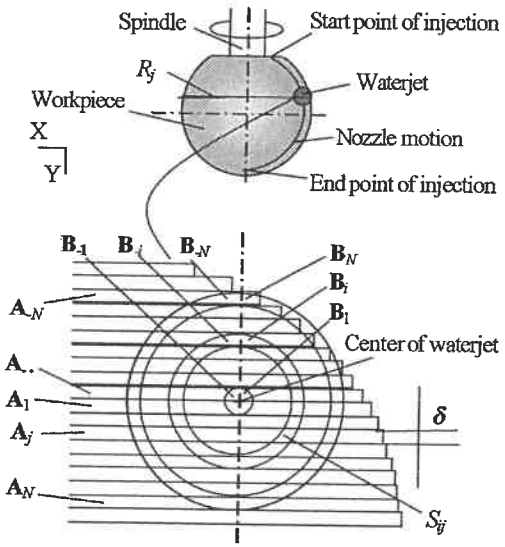

Fig.6 Machining model for simulation

5. Shape control method

5.1 Nozzle feed speed planning method

Relationship between the reciprocal of feed speed of a nozzle and the depth of cut is obtained by simulation as shown in Fig.7, assuming that the density of abrasive is constant during machining, where the width of each minute element is 30 μm. Therefore, the relationship between the feed speed of nozzle and the depth of cut at the angle of β is described as

$$h(\beta) = \frac{1}{v(\beta)}k_v(\beta) \quad (11)$$

where $k_v(\beta)$ is the coefficient of proportion.

The nozzle feed speed planning method is as follows: First, $k_v(\beta)$ in Equation (11) is calculated by the simulation. Then, by using $k_v(\beta)$, the feed speed to achieve the desired depth of cut is obtained by

$$v(\beta) = k_v(\beta)\frac{1}{h_d(\beta)} \quad (12)$$

The feed speed of a nozzle is planned as shown in Fig.9.

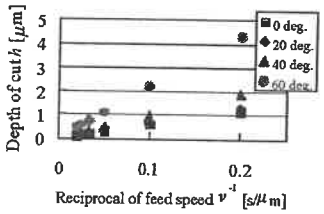

Fig.7 Relationship between the feed speed and the depth of cut

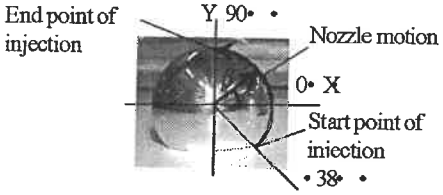

Fig.8 Definition of the angle of a femoral head

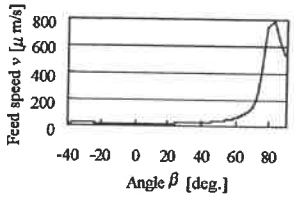

Fig.9 Feed speed to achieve the desired depth of cut

5.2 Compensation of density of abrasive

It is necessary to consider the abrasive density change, because the density of abrasive decreases during machining. In section 3.3, it is clarified that the erosion ratio is proportional to the density of abrasive d. Therefore, it is possible to compensate for the machining volume error caused by the density change of abrasive, by multiplying the feed speed in Equation (12) by $k_d d$.

6. Simulations and experiments

6.1 Conditions of experiments and simulations

In the simulations and experiments, the femoral head of an artificial hip joint with the diameter of 22.2mm made from Co-Cr-Mo alloy was used as a workpiece. The femoral head is in the condition after grinding and before giving hand lapping. Its roundness before the experiments is about 300 nm. Table 1 shows conditions of the experiments and simulations. The following three cases are investigated by the experiments and simulations.

(1) In case of constant feed speed of 0.01mm/s.
(2) In case of variable controlled feed speed without abrasive density compensation.
(3) In case of variable controlled feed speed with abrasive density compensation.

Table 1 Conditions of experiments and simulations

Feed speed of nozzle [mm/s]	0.01, Controlled
Offset distance [mm]	-0.1
Particle size of abrasive [μm]	1.0
Density of abrasive [wt%]	3.2
Standoff distance [mm]	8.5
Water pressure [MPa]	200
Rotational speed of workpiece [rpm]	3000

6.2 Investigation of roundness

The geometry error of a workpiece after injection with the constant feed speed of 0.01mm/s is shown in Fig.10. The geometry error of a workpiece after injection with the variable controlled feed speed without abrasive density compensation is shown in Fig.11. The geometry error of a workpiece after injection with the variable controlled feed speed with abrasive density compensation is shown in Fig.12, respectively.

In the case of injection with the constant feed speed, the depression was formed around 90 degrees of a workpiece. It is because around 90 degrees, the time of shooting waterjet per unit length of a circumference increases as the circular velocity by the rotation of a workpiece decreases. For the reason, the roundness of a workpiece after injection got worse to 576 nm.

By using the feed speed planning method, the roundness of a workpiece after injection was improved to 304 nm. However, the radius of a workpiece after injection increases around 90 degrees because of the reduction in the density of abrasive.

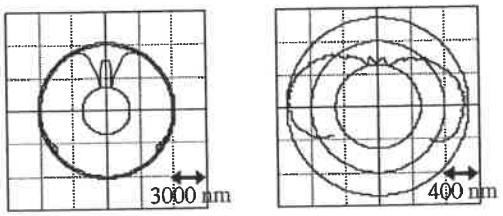

(a) Simulation (b) Experiment

Fig.10 Geometry error (with the constant feed speed)

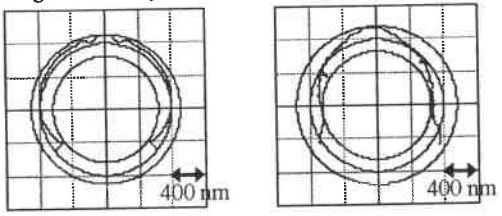

(a) Simulation (b) Experiment

Fig.11 Geometry error (with the feed speed planning method)

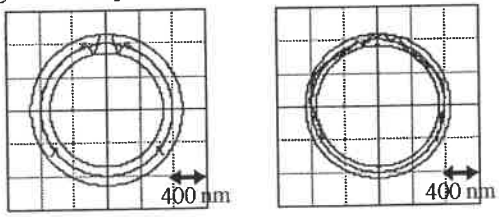

(a) Simulation (b) Experiment

Fig.12 Geometry error (with the correcting method)

By using the compensation method, the roundness of a workpiece after injection was successfully improved to 136 nm. It means that the compensation method can reduce the influence of the reduction in the density of abrasive, and thus the machining volume can be constant on the whole surface of a workpiece.

Furthermore, it was verified that the experimental and simulation results of the machined workpiece shape have good correspondence qualitatively. Therefore, the proposed simulation method is verified to be feasible to estimate the shape of workpiece after injection.

6.3 Discussions

By using the compensation method, the roundness of a workpiece after injection was successfully improved to 136 nm. However, the required roundness of 100 nm was not achieved. By detail observation, there is found the uneven shape around 90 degrees as shown in Fig.12 (b), and thus the roundness of a workpiece gets worse. The cause of this uneven shape is considered that the mesh is divided along Y axis. For the reason, the mesh along the angle is larger around 90 degrees. Therefore, it is necessary to change the width of mesh according to the angle of a workpiece.

7. Conclusions

In this paper, a new machining method for the femoral head of an artificial hip joint by means of abrasive waterjet is presented. Especially, in order to estimate the shape of a workpiece after injection, simulation method was proposed. Furthermore, in order to improve the roundness of a femoral head, the shape control method was proposed. By using the proposed method in finishing for the femoral head of an artificial hip joint, the roundness of a workpiece could be successfully improved to 136 nm.

Acknowledgements

This research was supported by the Grant-in-Aid for Project Costs Associated with Innovation Creation with the Collaboration of Industry, Government and Universities (No.15406) from the Ministry of Education, Culture, Sports, Science and Technology of Japan.

References

[1] P. Eyerer, M. Kurth, HA. Mckellup and T. Mittlemeier, "Characterization of UHMWPE Hip Cups Run on Joint Simulators", J. Biomed. Mater. Res., 21, p.275 (1987).

[2] S. Warisawa, H. Sawano, M. Mitsuishi, K. Kuramoto, "Ultra-precision finishing for the femoral head of the artificial hip joint by means of abrasive waterjet", Journal of Japan Society of Abrasive Technology, 48-2, pp.90-95 (2004). (Japanese)

[3] J. G. A. Bitter, "A Study of Erosion Phenomena part I", Wear, Vol.6, pp.5-21 (1963).

Grinding Simulation with Diamond Pellets and Optimization of Its Grinding Conditions

Michio Uneda*, Hitoshi Suwabe*, and Ken-ichi Ishikawa**

*Department of Mechanical Engineering, Kanazawa Institute of Technology
**Kanazawa Institute of Technology
7-1 Ohgigaoka, Nonoichi, Ishikawa 921-8501 Japan
*uneda@neptune.kanazawa-it.ac.jp

Keywords: Diamond pellets grinding, Thinning layout method, Optimized grinding conditions, Grinding distance

1. Introduction

A lapping processing used free abrasive slurry is one method of the abrasive precision processing. The lapping processing has been used frequently for making silicon wafers and optical glass to high precision surface. However, the abrasive precision processing has a tendency to change the method using from free abrasive slurry to the fixed abrasive grains because of the problems such as low processing efficiency, deterioration of the working environment, and disposal of waste slurry having free abrasive processing. According to these problems, the fixed abrasive grain grinding (lapping) using the diamond pellets has advantage high efficient and the clean processing in the surface machining techniques. Therefore, the applied areas of a diamond pellets grinding (DPG) have increased[1)2)].

The DPG is a surface-machining method of using a DPG plate adhered the many diamond pellets with regularity as shown in Fig.1. In the generality of designing a layout of the many pellets by the DPG plate, the diamond pellets make a figure of circles with the center of the DPG plate for its center.

DPG efficiency depends on a grinding distance between the DPG plate and the work-piece. This is expressed by Preston's equation[3)]. The push for high processing efficiency suggests increasing the grinding distance, and the drive for greater surface accuracy requires decreasing the deviation of that grinding distance. This grinding distance makes a change caused by the layout of the many pellets by the DPG plate. Therefore, we have to examine the grinding conditions from the viewpoint of the grinding distance when we design the layout of the many diamond pellets by the DPG plate. However, in the DPG, there are a few studies on the theoretical and optimized examination in which relates to the optimization problem, though the experimental studies related to the processing characteristics are done[2)].

This study aims to find the optimum conditions in the DPG. This paper presents the calculation method of the grinding distance. Moreover, this paper discusses the results of processing efficiency and accuracy. Especially, a genetic algorithm is used as the optimization method for decreasing the deviation of the grinding distance at the ground work-piece. This optimized results show that the genetic algorithm can design the layout of the many diamond pellets by the DPG plate for which the deviation of the grinding distance is remarkably small.

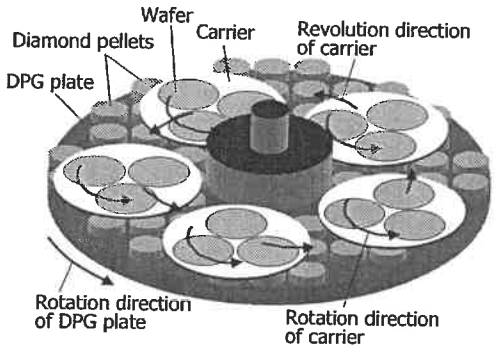

Fig.1 Model of diamond pellets grinding in case of 4-way DPG system

2. Simulation model and method

We use the schematic model as shown in Fig.2 for calculating the grinding distance at the ground work-piece in the 4-way DPG system. This model makes a design for calculating the relative lapping distance between the wafer and the lapping plate at the 4-way wafer lapping system[4)]. This paper describes the simulation method for calculating the grinding distance modified the previous method[4)]. Here, we assume that the grinding quantities are strongly dependent on the grinding distance and the diamond pellets are always flat, and are not worn down in order to simplify our analysis.

In this simulation, R_{lapi}, R_{lapo} and R_{wafer} are the inner and outer radius of DPG plate, and work-piece (wafer) radius, respectively. Moreover, ω_{lap}, ω_{car} and ω_{wafer} are the rotating angular velocity of DPG plate, carrier and work-piece, respectively. The directions of each angular velocity define the counter clockwise from the X-axis at the positive value. Therefore, the central angle $\theta_{car}(r,\theta_0,t)$ and $\theta_{wafer}(r,\theta_0,t)$ are values in the counter clockwise from the X-axis. x_o is the eccentricity of the center $O_{wafer}(t)$ of work-piece from the center O_{lap_t} of the carrier.

Consider the point $N(r,\theta_0,t)$, which locates in radius r of the ground work-piece at time t in Fig.2, where r changes from 0 to R_{wafer}. For time t from 0 to T, the relative grinding distance $L_{relative}(r,\theta_0)$ at radius r can be expressed as follows,

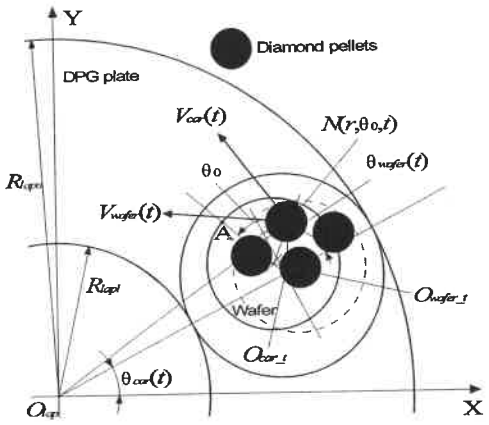

Fig.2 Schematic illustration of DPG for calculating grinding distance

Table 1 Main simulation conditions

Inner radius of DPG plate R_{lapi}: 211.67／2mm
Outer radius of DPG plate R_{lapo}: 668.87／2mm
Radius of wafer R_{wafer}: 50 mm, $(R_o - R_i)/2$
Eccentricity of wafer x_o: 60 mm
Radius of diamond pellet R_p: 6, 7.5, 20mm
Rotation angular velocity of DPG plate ω_{lap}: -3.33rpm
Revolution angular velocity of carrier ω_{car}: 3.3rpm
Rotation angular velocity of carrier ω_{wafer}: 2.5rpm
Calculated time T: $2*(2\pi/\omega_{wafer})$

$$L_{relative}(r,\theta_0) = \int_0^T V_{relative}(r,\theta_0,t)dt \qquad (1)$$

where $V_{relative}(r,\theta_0,t)$ is the relative grinding velocity at time t, and T is processing time. In this simulation, T was given in $2*(2\pi/\omega_{wafer})$ which means the work-piece two rotating time at all calculated conditions. Here, Eq.(1) can be applied in case of used the lapping plate without grooves.

However, in the DPG, the relative grinding velocity at the ground work-piece passing in time t has to been considered on these two patterns. Hence, the pattern (a) is the case that the point $N(r,\theta_0,t)$ contacts with any pellets each other, and the the pattern (b) is the case that the point $N(r,\theta_0,t)$ does not contact with any pellets each other. In the case of pattern (a), the relative grinding velocity is the equal of the lapping velocity calculated

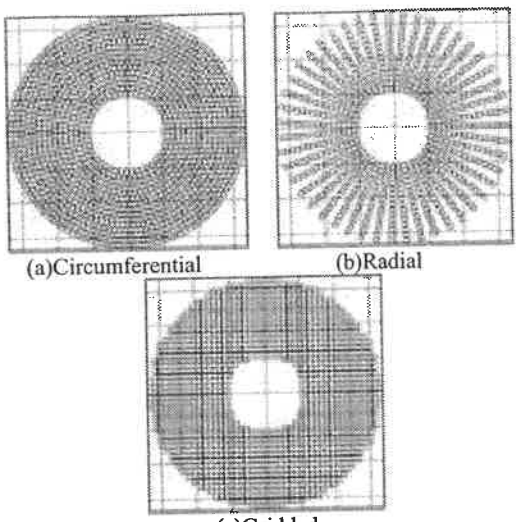

Fig.3 Layout model of diamond pellets at pellets radius R_p of 7.5mm

the 4-way wafer lapping system. In the case of pattern (b), the relative grinding velocity is the equal of zero. Therefore, if Eq.(2) at the work-piece passing in time t establishes, this case means pattern (a).

$$\min\left|\sqrt{(X_w(t)-X_{pm})^2+(Y_w(t)-Y_{pm})^2}\right|_{m=1\sim M} \le R_p \qquad (2)$$

where, (X_{pm},Y_{pm}) is the center coordinates of each pellets and $(X_w(t),Y_w(t))$ is the coordinates of the point $N(r,\theta_0,t)$. R_p stands for the radius of pellets. m is the natural number from 1 to M, and M is the number of pellets.

Figure 3 shows the general layout methods of pellets. Figs.3-(a), (b) and (c) show circumferential, radial and gridded, respectively. This paper discusses effect of the layout method and the pellets radius on the grinding distance characteristics. The main experimental conditions are as shown in Table 1.

3. Computer simulation and consideration

Figure 4 shows the non-dimensional grinding distance for specific cases at pellets radius R_p of 7.5 mm. Figs. 4-(a), (b) and (c) are the results of circumferential, radial and gridded respectively. The ratio of the grinding distance compares the maximum grinding distance at

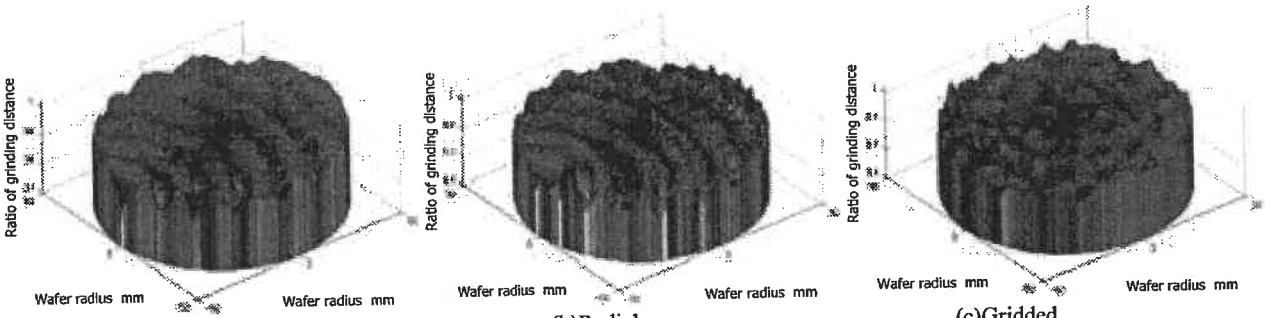

(a)Circumferential (b)Radial (c)Gridded

Fig.4 Calculated results of ratio of relative grinding distance in work-piece surface at pellets radius R_p of 7.5mm

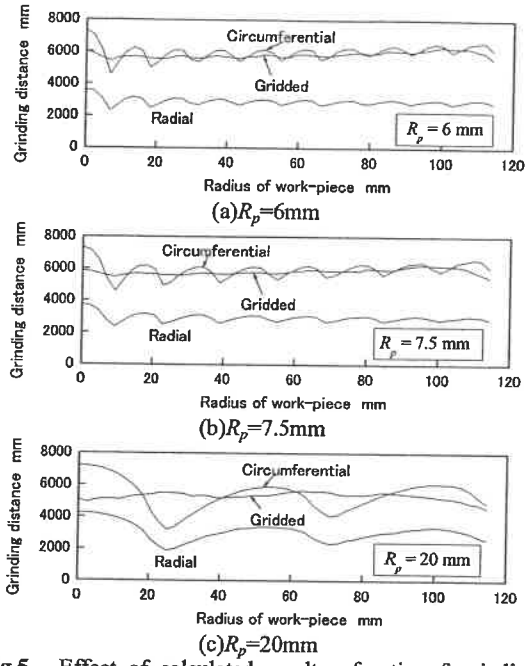

Fig.5 Effect of calculated results of ratio of grinding distance in work-piece radius direction on pellets radius and layout methods

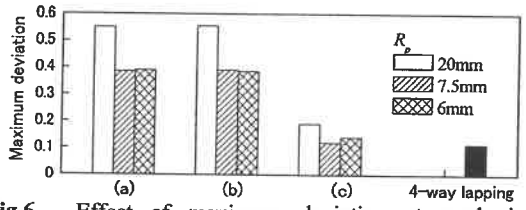

Fig.6 Effect of maximum deviation at work-piece grinding distance on pellets radius and layout methods ((a)Circumferential, (b)Radial, (c)Gridded)

work-piece surface. The figures show the results of circumferential and radial have the regular ruggedness, and the result of gridded does not have that ruggedness.

Figure 5 shows the dimensional grinding distance at the radius direction of work-piece surface when the work-piece diameter is the equals of the width of DPG plate given by subtracting R_{lapi} from R_{lapo}. Figs. 5-(a), (b) and (c) are the results of circumferential, radial and gridded respectively. The figures (a), (b) show the regular ruggedness, and also the width of ruggedness is almost equal to the pellets diameter. On the other hand, the figure (c) does not show such as ruggedness.

Figure 6 shows the result of the maximum deviations when the layout method and pellets radius R_p are changed. This figure shows the maximum deviation in case with the gridded layout method is the smallest, and the maximum deviations decrease as the decreasing pellets radius. Moreover, compared decreasing effect of the maximum deviation with the layout method and pellets radius, effect of the layout method is greater than that of the pellets radius. In addition, the maximum deviation in case with the gridded is almost equal to that in case with the 4-way lapping used ungrooved

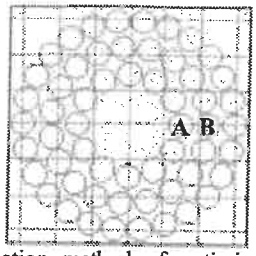

Fig.7 Examination method of optimization of pellets layout method (Example of circumferential layout method of R_p at 35mm)

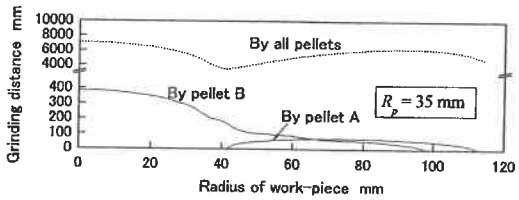

Fig.8 Calculated results of grinding distance at layout method of Fig.7 and effect of grinding distance on pellets A and B

lapping plate as shown black rod.

Summarizing, it should be desirable to adopt the gridded layout method. However, it is difficult to perfectly satisfy the demands for the maximum deviation approaches to zero. Therefore, thinning layout method in the DPG plate will be considered to obtain the high accuracy while decreasing the maximum deviation of the grinding distance. In this paper, the thinning layout method in the DPG plate will be especially optimized using a genetic algorithm.

4. Optimization of thinning layout method using genetic algorithm

4.1 Examination of the application method

The goal of a genetic algorithm[5)6)] is to find a set of parameters that minimizes the output of a fitness function using the latent ability of realizing the solution in which mutation and natural selection are optimum in the evolution theory of the organism.

Consider N chromosomes having M genes in one generation, which iteratively change with selection, crossover, and mutation. In the following discussion p_c and p_m will be used for the crossover probability and the mutation probability, respectively. M is the number of pellets in each generally layout method.

It is necessary to calculate the grinding distance in each pellet because of comparing with the total grinding distance. For example, considered the DPG plate at the pellets radius of 35mm and at the layout method of circumferential as shown in Fig.7. Figure 8 shows the results of the grinding distance by each pellet A and B in Fig.7. The total grinding distance as shown the dotted line is given by adding grinding distance by use of each pellet. Therefore, the generally genetic algorithm can apply this optimized problem with binary code. Thus, one binary digit represents the pellet state as "on" = 1 or "off" = 0 in DPG plate.

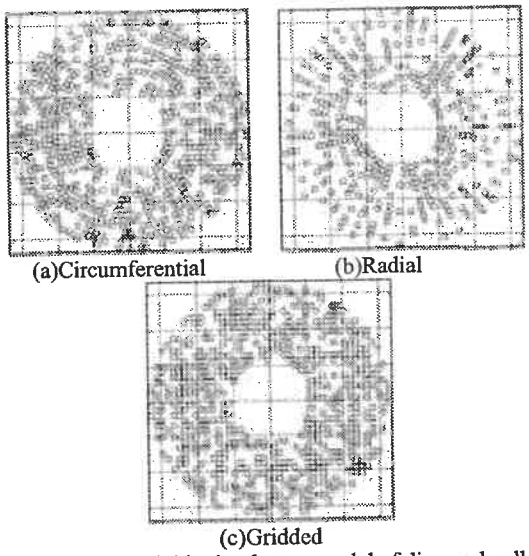

Fig.9 Optimized thinning layout model of diamond pellets at R_p of 7.5mm by GA

4.2 Optimum results

The previous section gave an overview of the optimized method for making thinning layout method in DPG plate using the genetic algorithm. This section describes the application results.

Figure 9 shows the designed result of thinning layout method of each generally layout method when the genetic algorithm applies in this optimized problem. In this paper, N, p_c and p_m are 50, 0.6, and 0.1 respectively. The genetic operation is carried out to 100 generations.

Figure 10 shows the results of the dimensional grinding distance at the radius direction of work-piece surface with/without genetic algorithm. Figure 11 shows the result of maximum deviation for the thinning layout method and pellets radius with genetic algorithm compared with Fig.6. These results show that the genetic algorithm can design thinning layout method for which the maximum deviation of grinding distance is remarkably small.

5. Conclusions

This paper describes effect of the pellets layout method on the grinding distance between DPG plate and work-piece at the 4-way DPG system. And also, this paper especially introduced the use of a genetic algorithm for optimizing the selection thinning layout method in a DPG plate to make the deviation of grinding distance small.

As a result, the following areas are clarified.

(1) The deviation of grinding distance in case with gridded layout method is smaller than that in cases with circumferential and radial layout methods.
(2) The genetic algorithm can design the optimized thinning layout method.
(3) Effect of the genetic algorithm in case with gridded layout method is greater than that in cases with circumferential and radial layout methods.

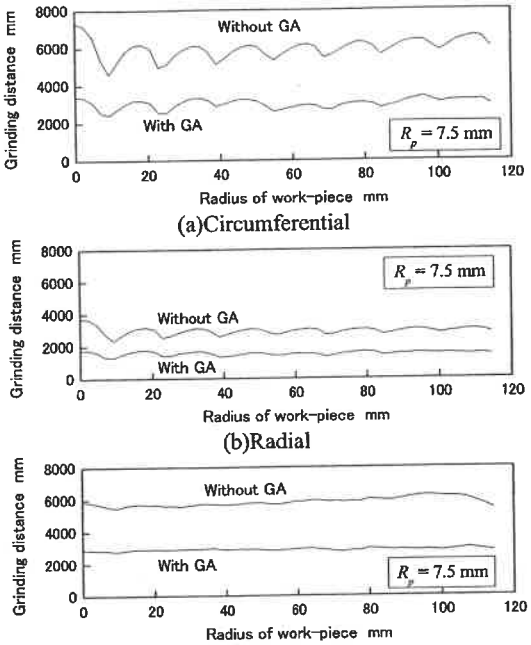

Fig.10 Calculated results of ratio of grinding distance in wafer radius direction on optimized layout methods at R_p of 7.5mm

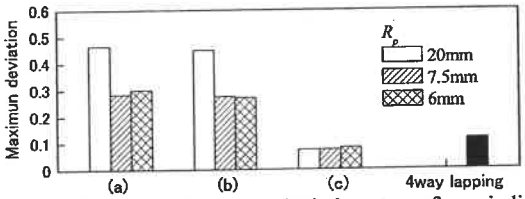

Fig.11 Effect of maximum deviation at wafer grinding distance on pellets radius and optimized layout methods by GA ((a)Circumferential, (b)Radial, (c)Gridded)

6. References

1) M.Jennings: Machining Optical Glass with Rigid and Flexible Diamond Tools, Industrial Diamond Review, 3 (2000) 202.
2) T.Takeuchi: Grinding Performance of Fixed-Abrasive Diamond Wheel for Lapping Machine, Journal of the Japan Society for Abrasive Technology, 48, 6 (2004) 307. (in Japanese)
3) F.W.Preston: The Theory and Design of Plate Glass Polishing Machines, Journal of Glass Technology, 11, 44 (1927) 214.
4) M.Uneda, Y.Nishimoto, K.Ishikawa, and K.Ichikawa: Optimization of Lapping Plate/ Polishing Cloth Groove Rates in Radius Direction Using Genetic Algorithm for 4-Way Wafer System, Journal of the Japan Society of Precision Engineering, 70, 5 (2004) 651. (in Japanese)
5) R.Ishida, H.Murase, and S.Koyama: Fundamental Theories and Application Programs for Genetic Algorithms by Personal Computer, Morikita-Syuppan, (1997). (in Japanese)
6) R.L.Haupt: Thinned Arrays Using Genetic Algorithms, IEEE trans. Antennas and Propagation, 42, 7 (1994) 993.

Viscoelastic Stress Analysis of Precision Aspherical Glass Lens Forming Process using Finite Element Method

Anurag Jain, Allen Y. Yi
Department of Industrial, Welding and Systems Engineering, The Ohio State University
1971 Neil Avenue, Columbus, OH 43210, USA

1. Introduction

The conventional production of lenses is a rather complicated process. Glass raw material which has been pressed to a rough form has to be processed on both sides in order to obtain a finished precision optical component. There have been recent advances in the optical fabrication techniques such as magnetorheological polishing (MRF), ion beam polishing and single point diamond turning (SPDT), but the overall complexity and cost involved in these processes are very high for medium to high volume production of aspherical glass optics. The conventional fabrication methods are more suitable for manufacturing spherical glass lenses. Aspherical lenses on the other hand have one or both surfaces that do not conform to a sphere and provide greater advantage over spherical lenses due to reduced light losses and aberrations, better image quality, and compact lens assemblies. In order to fulfill the high demands on refractive and reflective optical components, it is necessary to develop accurate fabrication techniques that generate aspherical optical surfaces in glass with a figure accuracy of $\lambda/10$ (λ = 633 nm), and a surface roughness of 1-5 nm rms.

For over 30 years, work has been done on developing a process for precision molding of aspherical glass lenses [1, 2]. In a lens molding process (see Figure 1) glass blank or gob is initially heated to a temperature between its transition and softening temperature (heating stage), and subsequently pressed between the two mold halves into a lens shape (forming/molding stage). Controlled cooling of the formed lens is then carried out with the molds in the closed position to remove forming stresses and avoid heat sink marks on the lens surface (annealing stage). Lens is eventually released at a temperature close to room temperature and finally allowed to cool to the ambient temperature. This is a net shape and an environment friendly process and if designed correctly can be suitably adapted for high volume production of precision aspherical glass lenses. Some of the challenges associated with this process include precise mold fabrication, careful temperature control, lens shrinkage, curve conformance and other process issues such as mold wear, mold life and sticking of glass to molds at high temperatures.

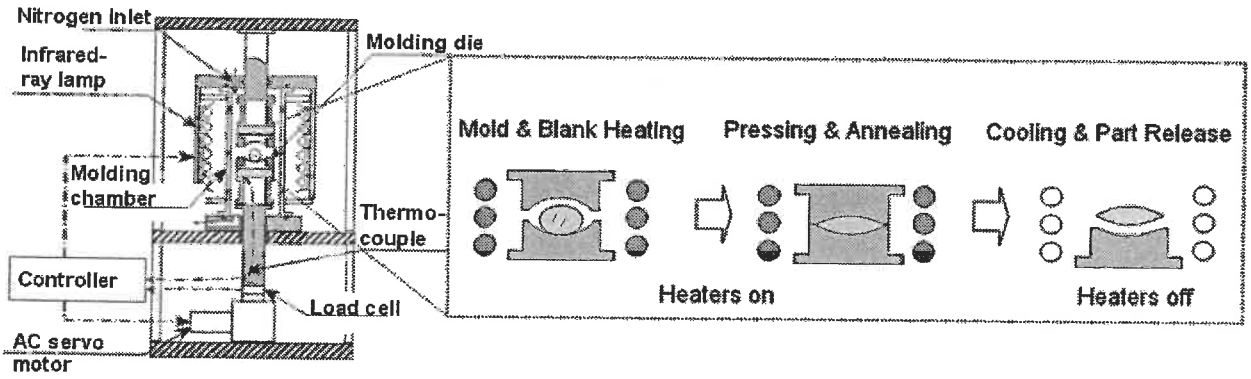

Figure 1: Schematic illustration of a lens molding process

The primary objective of our research is to gain a fundamental understanding of the lens molding process by developing a finite element method (FEM) based simulation model of the process. Specifically in this work it is aimed to incorporate the viscoelastic response of glass, into the numerical calculation and observe its influence on the resultant stress distribution inside a molded lens at the end of the molding stage by independently varying the forming velocity and temperatures. The knowledge of stress distribution at the end of the molding stage is important to design the subsequent annealing step in order to obtain a stress free lens with a homogenous refractive index.

2. Previous Work

Most of the research done in the area of glass forming has been performed in the field related to container forming, television and automobile windscreen screen manufacture etc. All these processes involve bulk glass forming in which demands for precision, irregularity and surface finish are not as stringent as in case of lens molding. A limited amount of work has been done in the past to apply FEM to a glass molding process in general, and in most of these works glass was modeled as a Newtonian fluid and viscoelastic effects were neglected. In the past, the authors have investigated the performance of a lens molding process by conducting actual aspherical lens forming experiments [3]. FEM simulations were also performed by modeling glass as an elastic-plastic [3] and a viscoelastic material [4]. The authors had concluded from the experimental studies that precision aspherical lenses can be molded with a surface variation less than 5 fringes and irregularity less than $\lambda/10$. Qualitative and semi-quantitative agreement between the experimental and the predicted results for curve conformance and stress distribution were obtained. The authors had demonstrated a need for a sophisticated numerical model incorporating accurate high temperature glass properties for more reliable results.

3. Theory of Viscoelasticity as Applied to Glass Forming

Viscoelasticity [5] describes a time dependent response of liquids and solids to either mechanical stress or strain. In the class of viscoelastic materials such as glass, the application of a constant load is followed by a deformation, which can be made up of instantaneous deformation (elastic effect) followed by continual deformation with time (viscous effect), that results in the decay of the applied load and is termed as relaxation. This can best be illustrated with the help of mechanical models – combinations of springs and dashpots, where the spring represents the elastic behavior and dashpot represents the viscous behavior. A single Maxwell model consisting of a spring and a dashpot in series or a generalized Maxwell model (several Maxwell models placed in parallel), shown in Figure 2, can be used to represent a real viscoelastic material behavior. The stress relaxation modulus and the stress relaxation function for this model can be represented by Equations (1) and (2) respectively:

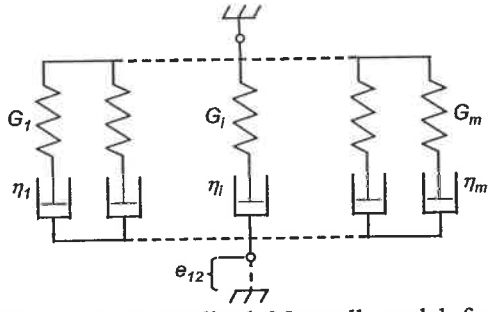

Figure 2: Generalized Maxwell model for modeling viscoelastic stress relaxation

$$G_1(t) = 2G\sum_{i=1}^{n} w_i e^{-t/\tau_i} \qquad (1)$$

$$\psi_1(t) = \frac{G_1(t)}{G_1(0)} = \sum_{i=1}^{n} w_i e^{-t/\tau_i} \qquad (2)$$

where, $G_1(t)$ is the shear stress relaxation modulus, a time dependent analog of its elastic counterpart G (shear modulus), τ_i is the shear stress relaxation time (sec) given by η_i/G_i, (η_i is the viscosity of the dashpot and G_i is the shear modulus of the spring) and w_i is the weighing factor such that $\sum w_i = 1$. In an FEM calculation, the change in stress due to relaxation during forming at high temperature between increments t-Δt and t is calculated and converted to nodal forces and subtracted from external forces [6].

4. Numerical Modeling

2D-Axisymmetric simulations of the lens molding process were conducted using a commercial general purpose, non-linear FEM program MARC, which is suitable for viscoelastic modeling of materials. Figure 3 shows the FEM model of a lens molding process that was used to study the effect of viscoelasticity on residual stress distribution. Only the forming stage of the lens molding process was simulated to observe the effect of process conditions on residual stress distribution inside a molded lens. It should be noted that the simulation conditions were chosen corresponding to the experimental conditions used by the authors in [3].

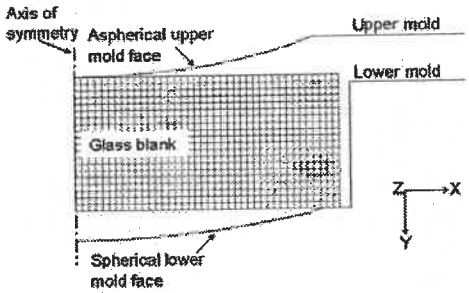

Figure 3: FEM model of lens molding

Four-node axisymmetric, quadrilateral elements were used to model the glass disk blank shown in Figure 3. Upper and lower molds were modeled as rigid bodies. Friction and heat transfer at the glass-mold interface was neglected. The simulations were carried out at three different molding velocities: *(i)* 0.05 mm/sec *(ii)* 0.01 mm/sec and *(iii)* 0.005 mm/sec for a constant glass forming temperature of 685 °C; and also at three different temperatures: *(i)* 670 °C *(ii)* 685 °C and *(iii)* 690 °C for a constant forming velocity of 0.01 mm/sec. Schott grade BK-7 optical glass was used in this study. The diameter of the glass blank used in the simulations was 12 mm and height was 6 mm. Elastic and viscous properties input to the simulation at different temperatures are shown in Table 1 [7-9]. Viscosity measurements at different temperatures for BK 7 glass were performed by the authors using the parallel plate viscometer technique [10].

	Temperature = 670 °C	Temperature = 685 °C	Temperature = 690 °C
Elastic modulus, [MPa]	27737	23626	19515
Shear modulus, [MPa]	10668	9086	7505
Poisson's ratio	0.3	0.3	0.3
Viscosity, [MPa-sec]	158	37	25
Relaxation time, [sec]	0.0148	0.0040	0.0033

Table 1: High temperature glass properties used for the viscoelastic forming analysis

5. Results and Discussion

Figure 4 shows the predicted residual Von Mises stress distribution inside a molded lens for three different forming velocities at the end of the molding stage. It can be observed from the Figure that stresses continue to rise as the molding velocity is increased. The stresses inside the formed lens almost increase by a factor of five as the velocity is increased ten times. This is primarily because at higher velocities the stresses inside the lens do not have enough time to relax causing the building up stress by the end of the molding stage. At lower velocities however, the stresses continue to relax as the glass is being formed resulting in lower stress. The magnitude of the overall stress is not only important for carefully designing the subsequent annealing stage but also from the point of view of lens shrinkage during the cooling stage. Higher stresses result in greater elastic deflection of the glass lens as it cools down to room temperature.

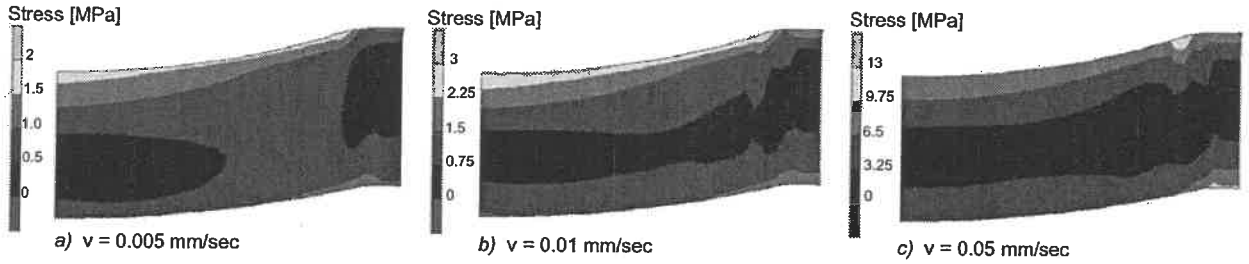

Figure 4: Predicted residual Von Mises stress distribution inside a formed lens for different molding velocities *a)* 0.005 mm/sec *b)* 0.01 mm/sec and *c)* 0.05mm/sec at a constant molding temperature of 685 °C

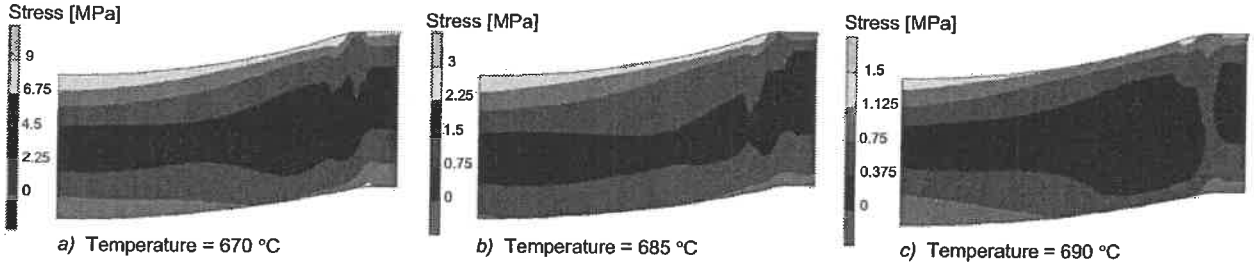

Figure 5: Predicted residual Von Mises stress distribution inside a formed lens for different molding temperatures *a)* 670 °C *b)* 685 °C and *c)* 690 °C at a constant molding velocity of 0.01 mm/sec

Figure 5 shows the predicted residual Von Mises stress distribution inside a molded lens for three different molding temperatures of glass. As the temperature is increased the stresses inside the molded lens continue to decrease. Viscosity has a strong dependence on temperature and as the temperature is increased beyond the transition temperature of glass, its viscosity continues to fall exponentially making the material more fluid and easier to deform resulting in lower stresses. The other reason for lower molding stresses at elevated temperature is as explained above, the lower relaxation time, because of which stresses relax faster at higher temperature (see Table 1 for relaxation times at different temperatures).

Figure 6 shows the predicted load time plot for a glass lens molding simulation at a forming temperature of 690 °C and velocity of 0.01 mm/sec. The predicted results are in qualitative agreement with the experimental results in Reference [3]. Due to the unavailability of experimental data for these simulation conditions the authors were unable to compare the predicted and experimental observations, but the results validate the viscoelastic methodology implemented in the simulation. Minimal loads are required to form glass blank during most part of the molding stage. During the later part as the molds are approaching the closed position the load begins to rise rapidly. This is because the flow of glass is constrained by the upper and lower molds (see Figure 3) that adds resistance to material flow and thus requiring higher force to further deform glass into a lens shape.

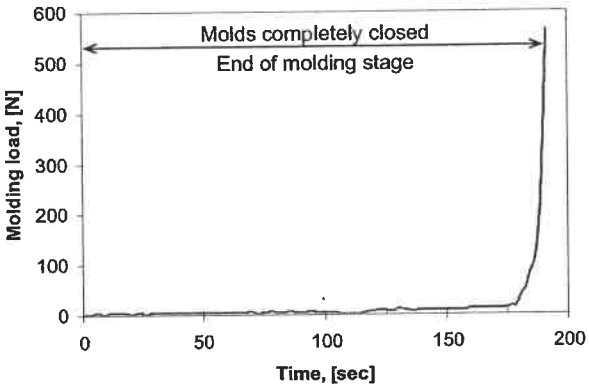

Figure 6: Predicted load time plot during glass lens molding at a forming temperature of 690 °C and velocity of 0.01 mm/sec

6. Conclusions

A numerical FEM model of an aspherical lens molding process incorporating the viscoelastic characteristic of glass has been presented. The molding stage has been simulated for different process conditions. The predicted results of load and stress distribution are in qualitative agreement with the viscoelastic theory and the experimental trends. Precise information of high temperature glass properties and description of heat transfer and friction mechanism at the glass-mold interface would be needed to make accurate numerical predictions.

7. References

1 R. O. Maschmeyer, C. A. Andrysick, T. W. Geyer, H. E. Meissner, C. J. Parker and L. M. Sanford; "Precision Molded Glass Optics," *Applied Optics*, **22**, pp. 2413-2415, (1983).

2 G. A. A. Menden-Piesslinger and J. H. P. Van de Heuvel, "Precision Pressed Optical Components Made of Glass and Glass Suitable Therefore"; US Patent 4391915, (1983).

3 A. Y. Yi and A. Jain, "Compression Molding of Aspherical Glass Lenses - A Combined Experimental and Numerical Analysis," Accepted for publication in *Journal of the American Ceramic Society*, July (2003).

4 A. Jain and A. Y. Yi, "Numerical Modeling of Viscoelastic Stress Relaxation during Glass Lens Forming Process," Submitted to *Journal of the American Ceramic Society*, May (2004).

5 S. Rekhson, "Viscoelasticity of Glass"; pp. 1-115 in *Glass Science and Technology*. Edited by D. R. Uhlmann and N. J. Kreidl, Academic Press Inc, Florida, USA, (1986).

6 T. F. Soules, R. F. Busbey, S. M. Rekhson, A. Markovsky and M. A. Burke, "Finite Element Calculation of Stresses in Glass Parts Undergoing Viscous Relaxation," *Journal of the American Ceramic Society*, **70 (2)**, pp. 90-95, (1983).

7 S. Spinner, "Elastic Moduli of Glasses at Elevated Temperatures by a Dynamic Method," *Journal of the American Ceramic Society*, **39 (3)**, pp. 113-118, (1956).

8 H. Scholze, "Properties of Glass"; pp. 156-319 in *Glass: Nature Structure and Properties*. Edited by H. Scholze, Springer-Verlag, New York, USA, (1991).

9 Internal communication with SCHOTT North America, Inc; Pennsylvania, USA.

10 A. N. Gent, "Theory of the Parallel Plate Viscometer," *British Journal of Applied Physics*, **11**, pp. 85-87, (1960)

In-Situ Infrared (IR) Detection of the High Pressure Phase Transformation of Silicon during Scratching Test

Lei Dong, Jimmie A Miller, University of North Carolina at Charlotte, Charlotte, NC 28223

John A Patten, Western Michigan University, Manufacturing Research Center, Kalamazoo, MI 49008

In this paper a new method of in-situ detection of the high pressure phase transformation of semiconductor materials during dead-load scratching is described. This method is based on the simple fact that single crystal silicon is transparent to IR light while metallic materials are not transparent to IR radiation. The sample material used here is silicon, but the same approach can be applied to germanium and other materials, such as ceramics (SiC), which have appropriate optical properties.

It has been established that silicon goes through a Si-I to Si-II (covalent diamond cubic to metallic) phase transformation under a pressure around 12Gpa, i.e. approximately the hardness of silicon. This Si-II phase is metallic, which is presumed to result in reduced transmission of radiation at IR wavelengths, i.e. metals are not transparent to IR radiation. In this paper experiments are described in which an IR laser-detector system is used in conjunction with a pre-loaded (dead weight) scratching device to detect the metallic high pressure phase of Si in-situ. Loads used are 10, 20, 30 and 40 mN. The apparatus is designed such that IR light passes through a diamond tip (diamond is transparent to the IR laser used), which is a 90 degree conical tip with nominal radius of 5μm, onto the interface/junction between the diamond tip and the silicon as the diamond tip is translated on the silicon wafer. The IR diode laser used in these experiments is an 8mw Infrared laser with a wavelength of 1330 nm. An Infrared detector is placed below the silicon wafer to sense the transmitted IR light. Results show a decreasing trend of IR transmittance after each scratch (multiple scratches are made at each load condition) and an average of ~10% decrease after 4 scratching cycles in the same groove. This indicates, in conjunction with previously reported results (Patten, 2003), that a metallic phase has been generated during scratching and the metallic phase has preferentially blocked the IR laser light. AFM and SEM have been used to measure the groove shape and to study the material generated in the pile-up (displaced) area. These images show that ductile deformation, for the loads investigated, correlate with the generation of the metallic silicon during simulated machining.

Key words: Metallic high pressure phase transformation Infrared Silicon Semiconductor

1. Introduction

High pressure phase transformations during machining of brittle materials have recently attracted the attention of a number of researchers [1]. Significant amounts of work and papers in this area and related fields (diamond anvil cell and nanoindentation) have been published especially in the last twenty years [8]. Much of this previous effort has been focused on investigating the series of phase transformations that occur during the processing of ceramic materials and semiconductors. In the case of silicon, the sample material in this paper, over 12 different phases generated upon loading and unloading in indentation tests of silicon have been identified [2]. Nanoindentation tests are by far the most widely used experiments in this field [3]. Papers on nanoindentation mainly evaluate the effect of different loading and unloading situations (load and depth, and rate effects), indenter geometric shape, stress-strain effects, and thermal effects under pressure. Direct detection of these high pressure phases is generally not available except for diamond anvil cell experiments [4] .Most published work, to our knowledge, suggesting a high pressure metallic phase transformation rely on post process evaluation techniques such as Raman spectroscopy [5]. Direct evidence of a metallic phase transformation, the authors of this paper believe, has much more practical value from an industrial manufacturing point of view. Due to the nature of high pressure phase transformation in brittle materials, in-situ study of this phenomenon has been very difficult, primarily due to the small size scale (micrometers) and high pressures (GPa). Developing a new instrument or modifying a current instrument to make such an in-situ measurement would take considerable time and effort. In this paper a new in-situ approach to detect the metallic phase in silicon during scratching is described. The

apparatus (a modified stylus profilometer) is an extension of previous work on in-situ electrical resistance heating of Si during scratching [6]. Results give direct evidence of the existence of the high pressure metallic phase of silicon during scratching and this correlates well with previous reported and related work utilizing electrical detection [7].

2. Infrared in-situ detection of metallic high pressure phase transformation in Silicon

The previously developed nanoscratching setup is augmented with a laser source and detection system[2]. The laser beam is coupled to a fiber optic cable and then passes through a diamond tip, which is attached to the diode laser's fiber ferrule. The whole system can be easily built but the phenomenon behind this simple experiment might inspire some new thoughts and novel applications.

2.1 Experimental design

The experimental setup is shown in Fig-1. The main part of the system is a profilometer with precision tracing driver (Surfcom110B). The scribing length and speed are controlled by the tracing driver. A dead weight-load is added onto the stylus that holds the ferrule. The load direction is perpendicular to the wafer's surface. The silicon wafer is a p type (100) 4 inch diameter wafer with a thickness of 475~575 micrometer. A 90 degree cone diamond tip (5μm nominal radius) mounted on the ferrule end is used as the scratching tool, see Fig-2. A low power laser (1310 nm wavelength, 8mW power) and corresponding detector (INGAAS DETECTOR 3000MICRON DIA, 900-1700nm) are used as the illumination and detection devices respectively. The diamond tip is gold coated to minimize stray radiation from being emitted from the ferrule end and diamond stylus. Fig-3 and 4 are the SEM images of the gold coated diamond tip before and after scratching test. The area which has the gold removed is about 4 um in diameter. This small area represents the aperture of the illumination system; i.e. the IR radiation mostly emerges from this small area. The small hole ~ 4 micrometer in diameter is visible at the tip of the diamond; i.e. on the radius of the diamond tip. This small hole also represents the area of contact between the diamond tip and the silicon wafer, i.e. the gold coating is removed due to the contact between the diamond tip and the silicon wafer.

2.2 Test of laser signal

The laser output power was calibrated using an IQ-1200 power meter. The diamond tip is attached to the fiber ferrule using epoxy. A thin layer of gold, 2000 Angstrom thick, is vacuum coated on the diamond tip, which is used to converge or concentrate (guide) the laser beam to the contact area between the tip and the wafer. The coating, and small aperture size, brings the laser power down to several micro watts (from the peak of 8mW). The epoxy may also attenuate some of the power of the laser beam. The beam size of the laser, from the fiber, is about 10 μm. The detector reading versus laser power measured on the power meter has been calibrated and shown in Chart-1. The laser runs at 18mA driving current during scratching.

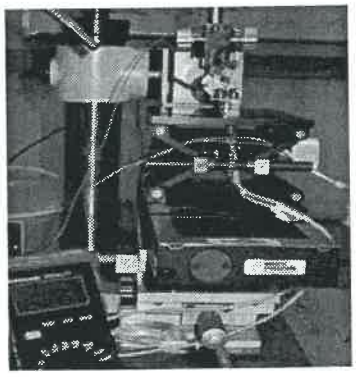

Fig-1 Experimental setup

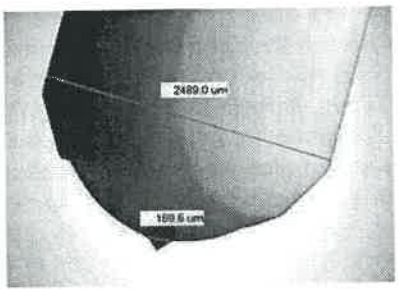

Fig-2 Diamond tip attached on the ferrule

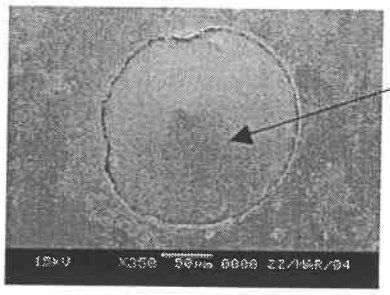

Fig-3 Gold coated tip before scratching test

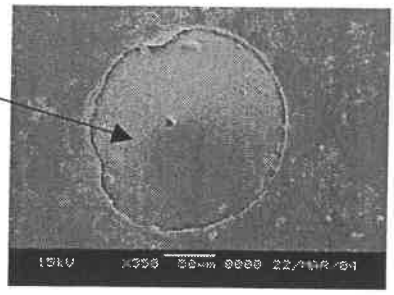

Fig-4 Gold coated tip after scratching test

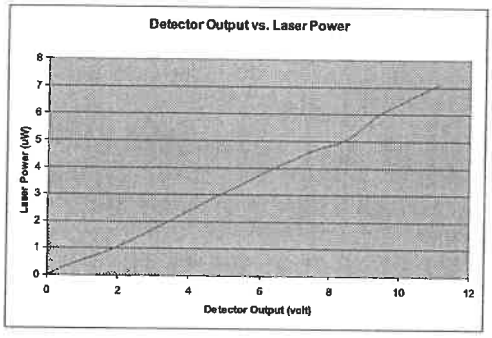

Chart-1 Detector Output vs. Laser Power

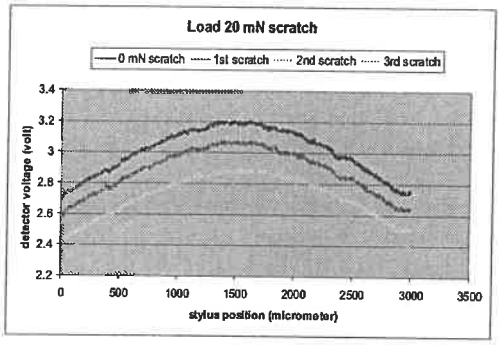

Chart-2 Load 20mN Scratch

2.3 Experimental procedures and results

The Infrared detection experiment is carried out as shown in Fig-5. A pre-determined length of scratch (~4mm) is made across the silicon wafer. This scratch coincides with the diameter of the IR detector beneath the wafer. The sensing area of the detector is 3000 Micrometers in diameter. The diamond tip starts scratching from one side of the detector, going across the full range of the detector and stops on the other end of the detector. The detector, which is fixed below the wafer, measures the Infrared laser signal coming through (transmitted) the silicon wafer. This signal is collected using Labview software. Different weights from 20 mN to 50mN have been tried. Scratching direction is [110].

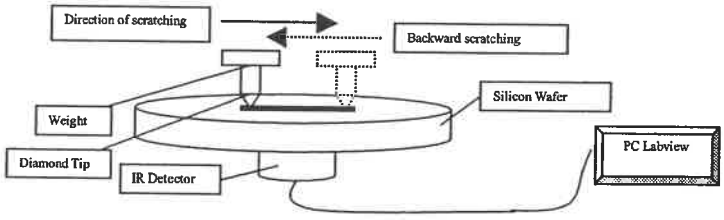

Fig-5 Schematic of scratching procedure

Chart-2 shows a series of 4 scratches at 20mN load; the top curve represents zero weight scratching. This scratch is made when the tip touches the silicon wafer and transverses across, just as one would do in a surface roughness test. The zero weight represents the nominal preload of the surface profilometer or about 0.7 mN. The following three curves represent scratches that are done in the same track on top of the zero weight scratch. For the various loads of 20mN, 30mN, 40mN, 50mN (only the results for the 20mN scratch are presented), the voltage (IR transmitted signal) decreases after each scratch and overall there is about 10% to 15% signal decrease after the 3rd scratch, compared to the zero weight scratch.

3 Discussion and conclusion

The experimental results agree with our premise that a layer of metallic silicon phase, which is generated under high pressure (12~16GPa), blocks some of the infrared light. If there is no metallic phase, then the infrared light would pass through the crystal structure of silicon (covalent or semiconducting silicon) and there should be no signal change detected. This (detector) voltage decrease is direct evidence of the existence of high pressure phase transition (semiconductor to metal) in silicon. This also agrees with earlier work on electrical heating of the transformed metallic phase [4] .

As the loaded diamond tip scratches the silicon wafer, a layer of the high pressure metallic phase, about the thickness of the groove depth, is generated underneath the diamond tip. This metallic phase only exists during the contact, i.e. as long as the high pressure is present. As soon as the tip moves on, the material behind the diamond tip back transforms to an amorphous structure. When the next scratch occurs, the high pressure phase is reformed under the diamond tip. As the groove gets deeper and wider, the metallic zone also grows in extent (scaling with the groove size) resulting in greater attenuation of the IR laser beam. The decreasing detector signal voltage, with subsequent scratches, matches this theory. If this were not the case, the IR laser transmitted signal would actually increase with subsequent scratches as more of the gold coating would be removed (corresponding to the larger groove dimensions). This larger aperture would allow corresponding more of the IR laser to emerge from the diamond tip. The fact that the IR signal decreases, in light of the above, clearly demonstrates the existence of the increasing size of the metallic high pressure phase of silicon under the diamond stylus tip. One of the potential applications of this experimental result is to develop a new concept of semiconductor material machining, which involves preferentially heating and softening (with an IR laser) the high pressure metallic zone to achieve tool wear reduction as well as enhanced ductile machining. It has been shown experimentally that at temperature above 0.3 to 0.4 T_{mi}, the microhardness drops abruptly with increasing temperature[5]. Temperatures in the range of 400 to 600 degrees C would substantially soften silicon and promote augmented ductile machining with potentially drastically reduced cutting forces and less tool wear.

Acknowledgement:
The authors acknowledge the support from National Science Foundation Research Focus Group program, DMR #0203552, Lynnette Madsen Program Director. The authors would also like to thank Jay Mathews (Digital Optics Corporation,Charlotte,NC,28262) for technical help and Scott Williams, M. Yasin Akhtar Raja (Optical Center, UNCC, Charlotte,NC,28223) for laser equipment.

References

1. V.Domnich and Y. Gigots, Rev. Adv. Mater. Sci. 3(2002) 1-36
2. I. Zarudi, L.C. Zhang, J. Mater.Res., Vol.19, No.1, Jan.2004 332-337
3. Yury Gogotsi, Guohui Zhou, Sang-Song Ku, Semicond. Sci.Technol.16 (2001)345- 352
4. John A. Patten, L. Dong, Jimmie A. Miller, ASPE 2003 Annual Meeting Proceedings Oct.26- 31, Vol. 30, (2003) 507-510
5. Gridneda, I.V., Yu.V.Milman, V.I. Trefilov, Phys. Stat .Sol (a) 14, (1972)177-182
6. Nobukastu Hirata, Daniel Abbott, John A. Patten, Robert J. Hocken, Measurements of the electrical conductivity of Silicon during scratching, http://www.micro.physics.ncsu.edu
7. W.C.Oliver and G.M.Pharr, J. Mater. Res. 7, 1564(1992)
8. V.Gogotsi and V. Domnich (eds), High Pressure Surface and Engineering, Institute of Optics, Oct. 2004

The Nanostructured Origami™ 3D Fabrication and Assembly Process

George Barbastathis,[a,(1)] Hyun Jin In,[a] Will Arora,[b]
Tilman Buchner,[a] and Henry I. Smith,[b]

Massachusetts Institute of Technology, Cambridge, MA 02139, USA
[a]Department of Mechanical Engineering,
[b]Department of Electrical Engineering and Computer Science

ABSTRACT — **Nanostructured Origami™ 3D Fabrication and Assembly Process is a method of manufacturing 3D nanosystems using exclusively 2D litho tools. The 3D structure is obtained by folding a nanopatterned 2D substrate. We report on the materials, actuation, and modeling aspects of the manufacturing process, and present experimental results from fabricated structures.**

I. INTRODUCTION

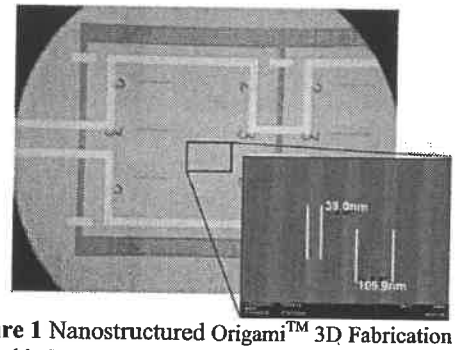

Figure 1 Nanostructured Origami™ 3D Fabrication and Assembly Process

The increasingly frequent use of nanoscale features in system manufacturing provides new tools, and also new challenges for precision engineering. For example, methods such as scanning tunneling microscopy and atomic force microscopy enable patterning of features at atomic scales in two dimensions in serial fashion (one feature at a time). Parallel methods such as electron beam and x-ray lithography, nanoimprinting and dip-pen lithography reliably produce features in the range of 10-40nm. These methods are well suited to planar nanoelectronics and other applications where 2D feature layouts are sufficient. In this paper we report on nanomanufacturing in the 3rd dimension via the Nanostructured Origami™ 3D fabrication and assembly process [1].

The 3rd dimension often provides maximum flexibility in the design and manufacturing of nanosystems. 3D nanopatterning may enable new functions as is the case, for example, in photonic crystals [2] and other nanophotonic devices, as well as electro-chemical energy conversion or storage devices [3]. The 3rd dimension is even more critical in hybrid systems, where the energy storage and mechanical, electrical, optical and other components must be assembled. However, 3D nano- fabrication and assembly remain challenging because of the lack of parallel (in-line) manipulation tools that would allow the placing of components in their proper places. The 3rd dimension also helps overcome the related challenge of bridging the gap between the nanoscale features of a system and the macroscale.

The Nanostructured Origami™ process assembles 3D systems with component features ranging from the nanoscale to the mm scale by using exclusively 2D litho tools. The process starts by patterning a large 2D membrane on a silicon substrate. This can be done via any of the commercial or research-grade methods. The 3rd dimension is achieved by folding the 2D membrane along well- defined creases. For rigid membranes such as silicon, the patterning step includes the definition of hinges. By proper design of the 2D feature layout and proper timing of the folding process, one can achieve almost arbitrary 3D layout.

Figure 1 shows an example of Nanostructured Origami, before the folding step. The surfaces of the three folding segments (only one is shown in the figure) were patterned with gratings of feature size 39nm using electron beam lithography. The lateral size of the segments was 0.5mm×0.5mm and their thickness was 5μm. Upon folding, the hinge curvature would lead to vertical spacing of approximately 10μm between the folded surfaces.

In this paper, we report on our progress in various aspects of realizing practical nanomanufacturing systems based on Nanostructured Origami. In Section II, we describe a new fabrication process in which the segments are made out of SU-8, a robust, epoxy-type photoresist. Because SU-8 is a dielectric, it is ideal for use in optical applications or in other instances where electrical isolation between the segments is desired. This is the case, for example, in energy storage devices [2]. In Section III, we report on a new method of origami folding using residual stress-induced strain mismatch to rotate segments around the hinges. In Section IV, we describe a new algorithm for modeling the kinematics of certain origami folding schemes. We conclude in Section V and briefly reference some applications of Nanostructured Origami that we are pursuing.

II. SU-8 Fabrication Process

The Nanostructured Origami prototypes of Figure 1 were fabricated on a silicon-on-insulator (SOI) wafer. The origami segments were made out of silicon released from the 5μm thick device layer. The segments were connected via gold hinges, which also served as conductors for the current used to actuate the device via Lorentz force.

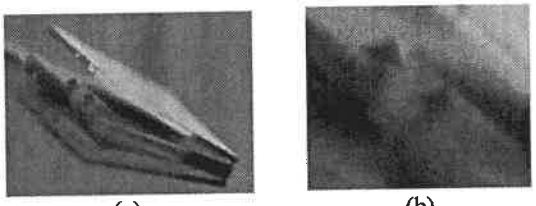

(a) (b)

Figure 2 (a) Origami using the SU-8 process. (b) Close-up view of the alignment pyramids.

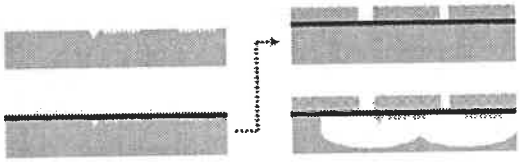

Figure 3 SU-8 process flow (gray=silicon; black=gold; striped=SU-8).

Figure 2 shows a new device fabricated using a similar process except the origami segments were made out of octafunctional epoxidized novalac (SU-8). This is a robust, epoxy-type photoresist commonly used as structural material for micro-electromechanical systems. For Nanostructured Origami, the advantages of the SU-8 process are optical transparency, reduction in process complexity, high aspect ratio, wide range of achievable thicknesses (from 1μm to several millimeters), and the ability to be patterned on both sides.

The basic process flow is shown in Figure 3. Starting with a (100) silicon wafer, a KOH etch step defined patterns into the substrate. A layer of gold was then deposited and patterned to define the hinges. Subsequently, SU-8 was coated and patterned to serve as the structural layer for the origami segments. The patterns defined in the previous KOH etch step acted as a mold for patterning the bottom side of the SU-8. In the final release step, XeF_2 gas was used to etch away the underlying silicon thereby releasing the entire structure.

While the design of the hinges alone was sufficient to align the folded segments to <10μm [1], we exploited the possibility of double sided patterning mentioned earlier to provide an additional alignment mechanism in this design. The mechanism consists of pyramidal spacers and corresponding square openings that fit the spacers tightly. A close-up view of the pyramids is shown in Figure 2(b). With this scheme, alignment is limited exclusively by the available lithographic accuracy. In our case, this was estimated to be better than 3μm.

III. Strain Induced Folding

The Lorentz actuation method is effective for a number of applications but requires the definition of surface-consuming actuation wires on the folded substrate. Moreover, the folding process can be time-consuming for multi-segment origami structures. A promising alternative is to deliberately introduce residual stress in selected areas of an original flexible substrate. The resulting stress can then fold the segment upon release.

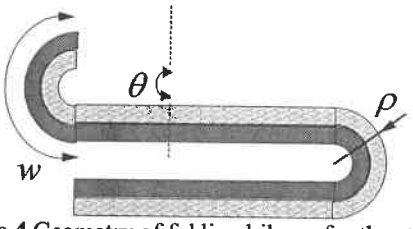

Figure 4 Geometry of folding bilayer for the stress-induced actuation method.

The stress actuation method is implemented by forming a thin film bilayer strip of width w in the region where folding is to take place. If one material is under compressive stress (e.g. silicon nitride) and the other under tensile stress (e.g. chromium) then the bilayer curls in order to relieve the strain mismatch as shown in Figure 4. The curling must result in radius of curvature ρ sufficiently small to produce the desired folding angle θ. In the case of complete folding (θ=180°) ρ also specifies the spacing between the folded segments. The design parameters are the ratio n of Young's moduli and ratio of thicknesses m of the two bilayer materials. Then

$$\rho = \left[\frac{d_2}{6\varepsilon}\right] \cdot \left[\frac{n^2m^4 + 4nm^3 + 6nm^2 + 4nm + 1}{nm(1+m)}\right] \quad (1)$$

where d_2 is the thickness of the bottom layer and ε is the stress-induced strain [4]. The folding angle is $\theta = w/\rho$.

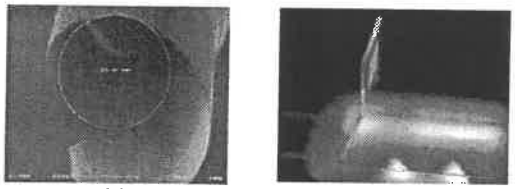

(a) (b)

Figure 5 Stress induced actuation. (a) Chromium on silicon nitride. (b) Chromium on gold, attached to rigid segments made out of SU-8.

Figure 5(a) shows a bilayer fabricated by evaporating chromium over LPCVD stoichiometric silicon nitride (n=1.93) deposited on single crystal silicon. The layer thicknesses were 100nm and 200nm, respectively. For the calibrated value ε=0.026 of our LPCVD machine, the theoretical radius of curvature predicted by (1) is $\rho \approx 20\mu m$. In the experiment, the bilayer curled into a complete loop with $\rho \approx 18\mu m$ upon release from the substrate.

Figure 5(b) shows the result of folding a different bilayer, made out of evaporated chrome on gold using the process described in Section II. In this case, the bilayer was attached to two patterned rigid SU-8 segments.

IV. Kinematic Modeling

Modeling the kinematics of origami structures is necessary to verify two desirable properties: (i) integrity, *i.e.* ensure that the structure is not torn at its hinges during folding; and (ii) compatibility, *i.e.* avoidance of collisions between segments during folding. Note that the integrity concern does not arise in robotic manipulators, for example; in origami, it is essential because of the 2D nature of the segments. Prior works have used affine transformations [5] and pseudo-triangulations [6] to model folding and unfolding. We used screw calculus [7] because it is computationally convenient. Its dual twist calculus permits the straightforward derivation of the dynamical model as well.

Our model begins by attaching a closed "skeleton" structure to the origami segments. The skeleton is then broken into two parts and forward kinematics are performed in the part that contains the actuation mechanism. The second part is constrained by the integrity condition, and so its motion is estimated via inverse kinematics. Singularity in the inverse kinematics of the second part indicates that kinematic integrity is violated in the given structure. Kinematic compatibility is ensured by tracking the segment edges (this function has not yet been implemented in our software tool).

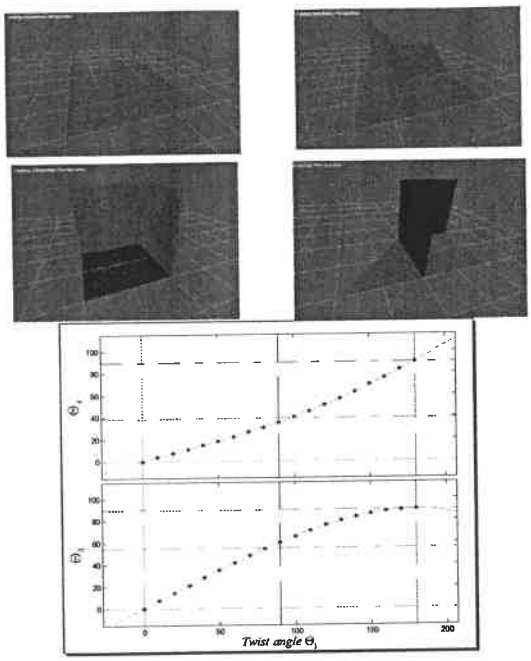

Figure 6 Five-segment origami mechanism (actuation sequence shown clockwise on top) and the folding angles of two of the segments in response to actuation of the diagonal joint.

Figure 6 shows an example of a five-segment origami structure, and the folding angle progression as the diagonal joint is actuated. Our approach is presently limited to similar single-vertex structures [5,6].

VI. CONCLUSION

The preliminary results from the material, actuation, and modeling work presented herein show great promise for the use of Nanostructured Origami in 3D nano-manufacturing. Possible applications with immediate value are miniature 3D electrochemical storage devices [2] embedded in general-purpose microsystems (e.g., distributed sensors), multi-layer diffractive optics, etc.

ACKNOWLEDGEMENTS

We are grateful to Yang Shao-Horn, Ileana Streinu, Jim Daley and the staff at the Microsystems Technology Laboratories. This research was funded by the Army Research Office through MIT's Institute for Soldier Nanotechnologies, DARPA and Sematech through the Interconnects Focus Center, and the National Science Foundation through an SGER grant and MIT's Materials Research Science & Engineering Center.

(1)E-mail gbarb@mit.edu

REFERENCES

[1] S. M. Jurga et al., "Nanostructured Origami," *Proc. 3rd Int. Conf. on Nanotechnology*, vol. 2, pp. 220-223, 2003.
[2] Photonic crystal book.
[3] Y. Shao-Horn et al., "Origami fabrication of electrochemical device on the micrometer scale," 204th Meeting of the Electrochemical Society, Orlando, FL, October 2003 (abstract 1279).
[4] P. O. Vaccaro, K. Kubota, and T. Aida, "Strain-driven self-positioning of micromachined structures," *Appl. Phys. Lett.*, vol. 78, no. 19, pp. 2852-2854, 2001.
[5] s.-m. belcastro, and T. C. Hull, "Modelling the folding of paper in three dimensions using affine transformations," *J. Lin. Alg. and its Apps.*, vol. 348, pp. 273-282, 2002.
[6] R. Hass, et al., "Planar Minimally Rigid Graphs and Pseudo-triangulations," *Proc. ACM Symp. Comp. Geometry (SoCG)* San Diego, CA, pp. 154-163, 2003.
[7] R. W. Brockett, "Robotic manipulators and the product of exponentials formula," *Int. Symp. Math. Theory of Networks and Systems*, Beer Sheba, Israel, pp. 120-129, 1983.

Optical fibre coupled miniature interferometers designed for application in micro and nano devices

Gerd Jäger[a], Eberhard Manske[a], Tino Hausotte[a], Roland Füßl[a], Rainer Grünwald[a], Hans-Joachim Büchner[a], Walter Schott[b]
[a]Technische Universität Ilmenau, Institute of Process Measurement and Sensor Technology, P.O. Box 100 565, 98684 Ilmenau, Germany
[b]SIOS Meßtechnik GmbH, Am Vogelherd 46, 98693 Ilmenau, Germany

Abstract
This paper describes the structure and the mode of operation of one-, two- and three beam miniature interferometers with plane mirror reflector and their application to micro and nano devices. The application is demonstrated by means of a metrological scanning force microscope, a nanopositioning and nanomeasuring machine having a positioning and measuring range 25 mm x 25 mm x 5 mm, a resolution of 0,1 nm and a uncertainty of 5 nm – 10 nm and a laserinterferometric vibrometer having frequency range 0 – 500 kHz and a resolution of 0,3 nm. Particularly results of measurements of the nanopositioning and the nanomeasuring machine and of the laserinterferometric vibrometer are introduced.

Keywords
Nanometer-scale miniature interferometers, optical fibres, metrological AFM, nanopositioning and nanomeasuring machine, laserinterferometric vibrometer

1 Introduction
Laser-interferometric methods are employed in precision measurements and positioning tasks, since they provide means for attaining high metric resolutions and precisions, even over large measurement ranges. The versatility and broad applicability of laserinterferometric methods are unattainable using any other metrological method [1]. Laser interferometers suitable for employment in advanced areas of microtechnology and nanotechnology must have small measuring heads that are insensitive to environmental effects [2]. Such miniature interferometers have been developed at the Institute of Process Measurement and Sensor Technology of the Technische Universität Ilmenau and are manufactured by SIOS Meßtechnik GmbH [3, 4]. Their metrological benefits are due to their employment of cost-effecitve optical technologies, their compact dimensions, and their employment of fiberoptic lightguides for coupling their laser light source, measurement head, and electronic signal-processing unit.

This article deals with the structure, the mode of operation and specifications of one-, two and three beam miniature interferometers with plane mirror reflector and their application to micro and nano devices. Finally, their broad applicability to microtechnology and nanotechnology will be covered, based on the examples of their use on a metrological scanning force microscope, a nanopositioning nanomeasuring machine and a laser interferometric vibrometer.

2 Miniature interferometers
Miniature interferometer systems that we have developed, have the following features:
- modularly designed interferometers and signal-processing electronics,
- ready adaptation to suit various types of measurement tasks,
- highly compact interferometric sensor heads,
- all-fiberoptic optical couplings, and
- nanometer resolutions and precisions over measurement ranges of up to 5 m.

We have developed both interferometers with corner cube prism and with plane mirror.

Fig. 1 shows the difference between a plane mirror interferometer of the state of the art (left) and the interferometer developed by our institute. The most advantage of our plane mirror interferometer is that it has only one measuring beam. The interferometer (left) needs two beams for having tilt invariance in a small angle range of the moving plane mirror.

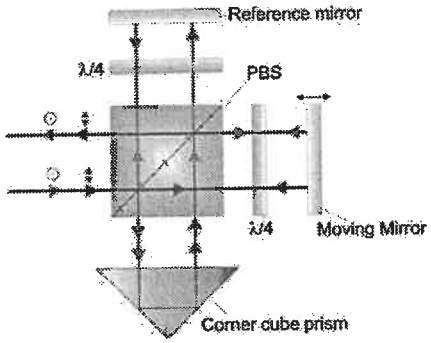

Plane mirror interferometer of the state of the art

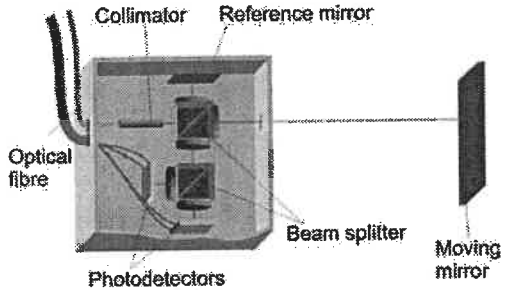

Plane mirror interferometer developed by the Institute of Process Measurement and Sensor Technology

Fig. 1: Plane mirror interferometers

3 Application of miniature interferometers with plane mirror reflector to precision measurements in micro and nano devices

3.1 Metrological scanning force microscope

In order to yield a metrological scanning force microscope whose measurement results may be traced to national standards, a miniature plane-mirror interferometer is incorporated into the microscope such that compliance with the Abbe comparator principle will be maintained on all measurement axes [5, 6]. Our conversion of a "VERITEKT" scanning force microscope to a metrological scanning force microscope was accomplished under subcontract, and working in collaboration with the Physikalisch-Technisches Bundesanstalt (PTB), Braunschweig, Germany. An improvement in expanded uncertainty of measurement to just 0.2 nm (K = 2) along a structural normal was obtained at the PTB using the converted scanning force microscope.

3.2 Nanopositioning and nanomeasuring machine (NPM-Machine)

At the Institute of Process Measurement and Sensor Technology of the Technische Universität Ilmenau a nanopositioning and nanomeasuring machine (see Fig. 2) has been developed and successfully tested and in the last few years continually improved [7, 8, 9].

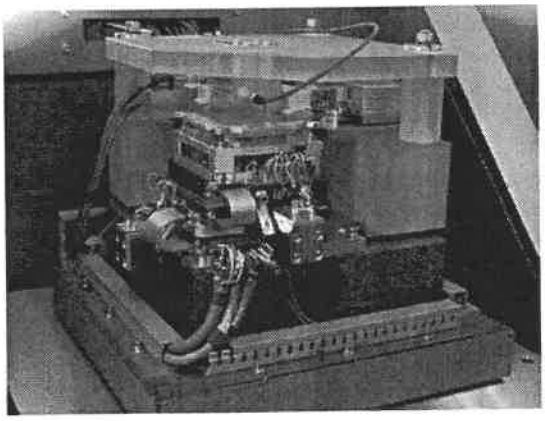

Fig. 2: Nanopositioning and nanomeasuring machine (NPM-Machine) with an optical probe system

The current parameters of the device are as follows: positioning and measuring range of 25 mm x 25 mm x 5 mm, resolution of less then 0,1 nm, expanded uncertainty of less than 10 nm for each axis. The outstanding precision has been obtained because of the compliance with the Abbe comparator principle on all three measurement axes and applying a new concept for compensating systematic errors resulting from mechanical guide systems. These machines are now manufactured by the company SIOS Meßtechnik GmbH Ilmenau. Up to now, eight machines have been built. They are operating successfully in several German and foreign research institutes, including the Physikalisch-Technische Bundesanstalt (PTB).

A series of measurements using the NPM-Machine have been performed. A special focus sensor with subnanometer resolution was developed for installing in the NPM-Machine. In the following, some measurement results obtained with the NPM-Machine and the focus sensor will be described. Fig. 3 shows the measurement results of the PTB nanometer film thickness standard C19R26. The expanded uncertainty with k = 2 is only 1,1 nm. The uncertainty of 1,1 nm includes both the uncertainty of the NPM-Machine and of the focus sensor. The uncertainties in x and y measurements depend on the quality of the object to be measured. Uncertainties of few nanometers can be achieved.

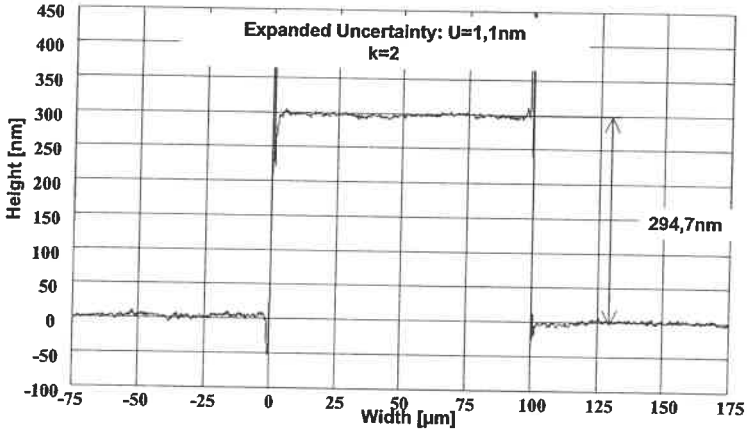

Fig. 3: Measurement result of the PTB film thickness standard C19R26

The NPM-Machine is capable of covering the whole range of 25 mm x 25 mm x 5 mm with nanometer accuracy. Fig. 4 represents the measurement result of a micro lens array as a relatively large object.

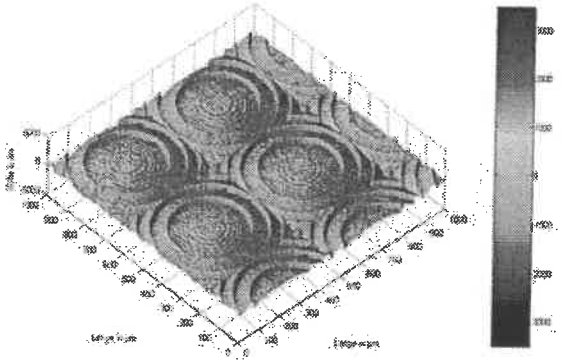

Fig. 4: Micro lens array measured with NPM-Machine and the focus sensor

In the near future it is planed to integrate e.g. STM, AFM, Indenter systems, tactile 3D-Nanoprobes and Nanoprofilometer into the NPM-Machine.

3.3 Laserinterferometric vibrometer

The operation of miniature interferometers equipped with plane-mirror retroreflectors is based on the principle of homodyne interferometry. Employment of plane mirrors with high reflectances is essential if the full benefits of their performance capabilities (measurement ranges of 5 m, resolutions of 0,1 nm, and relative metric accuracies of 10^{-7}) are to be obtained. In order to allow measuring vibrations of rough surfaces, we have developed and successfully tested a new type of vibrometer based on the principle of homodyne interferometry [10]. The vibrometer is shown in Fig. 5. This particular vibrometer allows recording the amplitude-frequency spectra of arbitrarily rough surfaces having specular reflectances of 5×10^{-4} or more over the range 0 - 500 kHz at a resolution of 0,3 nm.

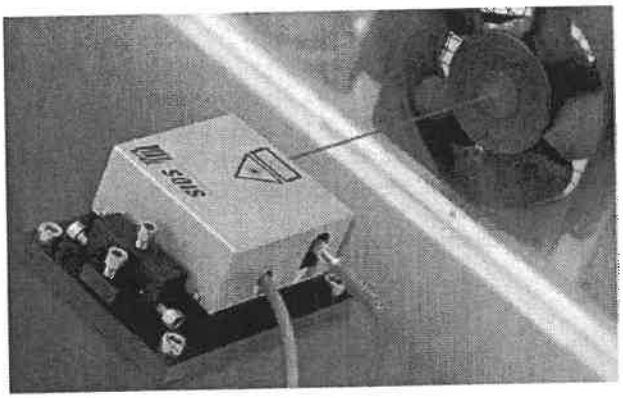

Fig. 5: Laserinterferometric vibrometer

4 Acknowledgements

The authors wish to thank all those colleagues from the TU Ilmenau and from the SIOS Meßtechnik GmbH Ilmenau who have contributed to the developments presented here. Our special thanks are due to the Thuringian Ministry of Science, Research and Arts for promoting the nanocoordinate metrology in the framework of joint projects.

References

[1] G. Jäger: Lasernanomesstechnik – Möglichkeiten, Grenzen und Anwendungen in der modernen Gerätetechnik; Proceedings of the 44th International Scientific Colloquium; Technische Universität Ilmenau, Germany; September 1999, S. 43 – 44

[2] G. Jäger: Precision distance measurement by means of miniaturized interferometers; Proceedings of the XIIIth IMEKO World Congress, Vol. 3, Turin, Italy, September 1994, S. 1712 – 1716

[3] G. Jäger, R. Grünwald; E. Manske: Lichtwellenleitergekoppelte interferenzoptische Sensoren; Technisches Messen 57, 9 (1990), S. 319 – 322

[4] W. Schott, G. Jäger: Miniature interferometers for precise distance measurements (Invited paper), Proceedings of the ASPE, St. Louis, 2002, 17th Annual Meeting, Proceedings, S. 67 – 72

[5] H. Büchner, G. Jäger, E. Manske: Laserinterferometrically assisted 3D-nanometrology on the atomic force microscope type VERITEKT, Proceedings of the 1st euspen International conference, Mai 1999

[6] G. Jäger, E. Manske, T. Hausotte, H. Büchner, R. Grünwald, W. Schott: Nanomeasuring technology – nanomeasuring machines, Proceedings of the 16th Annual Meeting of the ASPE, Crystal City, Arlington, Virginia, USA, Nov. 2001, S. 23 - 27

[7] G. Jäger, E. Manske, T. Hausotte, W. Schott: Operation and analysis of a nanopositioning and nanomeasuring machine, Proceedings of the 17th Annual Meeting of the ASPE, St. Louis, Missouri, USA, 2002, S. 299 – 304

[8] G. Jäger, E. Manske, T. Hausotte, H. Büchner, R. Grünwald, R. Füßl: Application of miniature interferometers to nanomeasuring and nanopositioning devices, Proceedings of the Conference Scanning Probe Microscopy, Sensors and Nanostructures (TEDA), Beijing, China, Mai 2004, S. 23 – 24

[9] G. Jäger, E. Manske, T. Hausotte, R. Füßl, R. Grünwald, H. Büchner, W. Schott, D. Dontsov: Miniature interferometers developed for applications in nano-devices, Proceedings of the 7th International Conference on Mechatronic Technology, ICMT 2003 Taipei, Taiwan, Dezember 2003, S. 41 – 45

[10] D. Dontsov, G. Jäger, U. Gerhardt: Homodyne fibre coupled laser vibrometer, Proceedings of the euspen 2003, Aachen, Germany

Study of Nano-Stereolithography Using Evanescent Light

Yusuke Kajihara, Yuichi Inazuki, Satoru Takahashi, and Kiyoshi Takamasu
The University of Tokyo

Abstract

We proposed a novel stereolithography method using evanescent light instead of propagating light to realize a 100-nanometer resolution. We carried out theoretical and experimental analyses to verify the method. The analyses show that evanescent light energy is sufficient for curing resin and that it is possible to fabricate micro three-dimensional objects with a 100-nanometer resolution.

Keyword: nano-stereolithography, photosensitive resin, propagating light, evanescent light

Introduction

Micro-fabrication technologies have recently developed dramatically and have become required by which devices on the order of micrometer can be fabricated precisely. In particular, methods of fabricating Micro Electro Mechanical System (MEMS) and microscopic optical devices as typified by photonic crystal are in huge demand. The micro-stereolithography, one of Micro-fabrication technologies, have attracted more attention because micro devices can be fabricated rapidly and flexibly [1]. However, the conventional micro-stereolithography method has a critical problem. Since the conventional method uses propagating light for exposure energy, the resolution of fabrication sizes is restricted by the diffraction limit. It means that it is almost impossible to fabricate micro objects with a resolution of sub-micrometer. Then, many kinds of approaches [2][3][4][5] have been demonstrated to overcome this problem.

In this study, we propose a novel stereolithography method using evanescent light instead of propagating light. In this method, we consider an application of the near-field optics and apply evanescent light to exposure energy for curing photosensitive resin. Since evanescent light does not propagate but localizes within the near-field region, its resolution is independent of the diffraction limit. It means that it is possible to fabricate micro three-dimensional objects with a resolution of sub-micrometer. By applying this method, we intend to establish the nano-stereolithography with higher accuracy and flexibility. This paper describes theoretical and experimental analyses we performed to confirm the validity of the proposed concept.

Concept of Nano-Stereolithography Using Evanescent Light

Figure 1 shows one of the stereolithography processes on which the proposed method is based. First, incident light exposes and cures liquid resin (Figure 1(a)). Next, the cured resin layer adhering on the base rod is lifted by the raising unit (Figure 1(b)). Then light beam, which is modulated by a variable mask such as an LCD layer by layer, exposes and cures a next layer (Figure 1(b)). Doing this loop repeatedly (Figure 1(c)), desired object can be fabricated (Figure 1(d)).

In this process, we propose to use evanescent light as the incident light for exposure energy, while propagating light is generally used. Figure 2 shows the characteristic of our proposed evanescent light exposure (Figure 2(b)) to compare it with the conventional propagating light exposure (Figure 2(a)). In the conventional method, since propagating light transmits through the photosensitive resin, the cure depth depends on the absorption coefficient of the resin. This means the thickness of the cured resin layer is over one micrometer and fabricating an overhang structure is very difficult. Therefore the method of conventional micro-stereolithography currently cannot realize a resolution below one micrometer.

In our method, an incident angle of the exposure light beam is set over the critical angle. Under this optical condition, there is no longer propagating light transmitting through the photosensitive resin and the light energy is localized only the near-field area of the interface of the glass plate. This light energy is evanescent light, which is independent of the diffraction limit. Since evanescent light energy is localized within the range of the wavelength, the thickness of the cured resin layer is expected to be less than one micrometer. In addition, there occurs no optical transmission, which makes it possible to fabricate overhang structure. Consequently, it is expected that we can realize a flexible fabrication with a resolution of sub-micrometer.

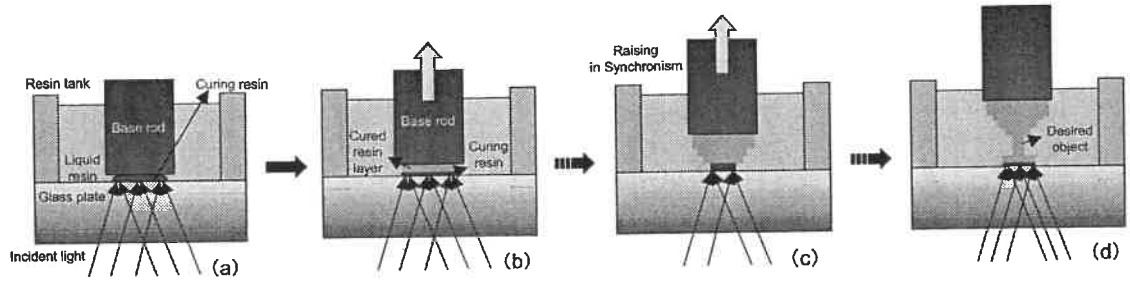

Figure 1. Micro-Stereolithography

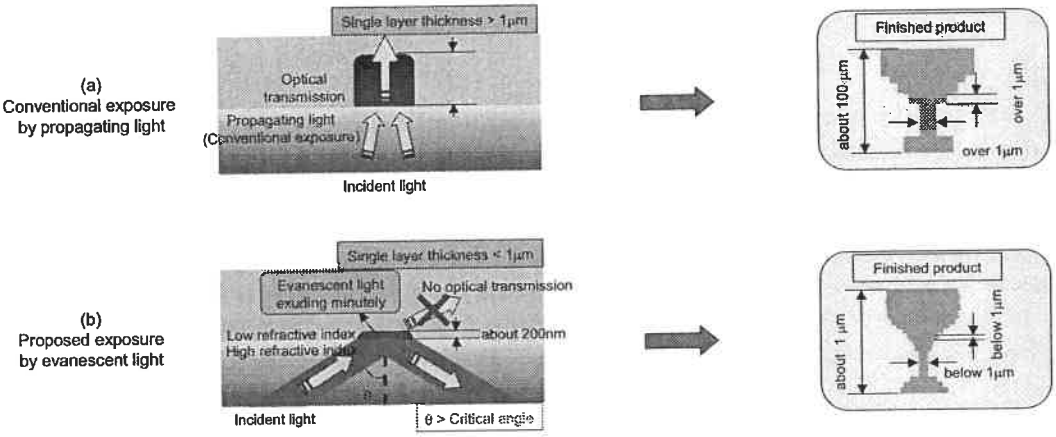

Figure 2. Characteristic of Evanescent Light

Theoretical Analysis

In this section, we theoretically analyze the vertical resolution of fabricated objects, which is one of the most important factors to verify the validity of the proposed method. Parameters are set as shown in Figure 3. The parameter n_1 and n_2 ($n_1 > n_2$) are the refractive indexes of the resin and the glass plate respectively. The wavelength of the incident light is λ_0, the incident angle is θ, the angular frequency is ω, and wavenumber in the resin is k_2. Then electric field E_2 of evanescent light can be expressed as follows by applying Maxwell's equations and Snell's law.

$$\mathbf{E}_2 = \mathrm{A}\exp(i\omega t)\cdot\exp(-\frac{z}{Z_{ev}})\cdot\exp(-ik_2 x\frac{n_1}{n_2}\sin\theta) \qquad (Z_{ev} = \lambda_0 / 2\pi n_2\sqrt{(n_1/n_2)^2\sin^2\theta - 1}) \qquad (1)$$

The distance h, where electric field decays into 1/e of the incidence value, can be calculated as follows by equation (1).

$$h = Z_{ev} = \lambda_0 / 2\pi n_2\sqrt{(n_1/n_2)^2\sin^2\theta - 1} \qquad (2)$$

For example, when n_1=1.78, n_2=1.49 and λ_0=488 nm, the relation of the incident angle θ and the distance h is represented as figure 4. Assuming that the thickness of the cured resin layer depends on the distance where electric field decays into 1/e of the incidence value, it can be flexibly adjusted from 100 to 700nm by changing the incident angle θ.

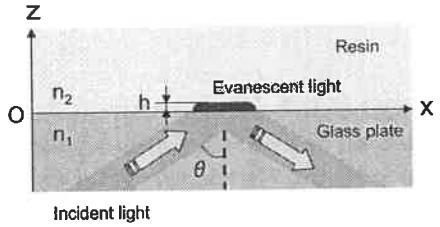

Figure 3. Parameter Definition

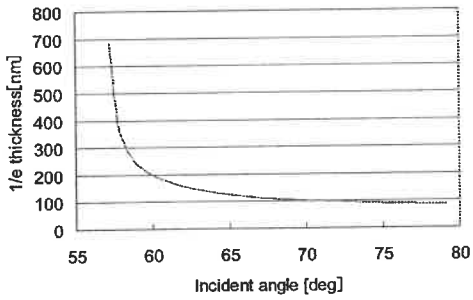

Figure 4. Relation of the incident angle θ and 1/e thickness h

Experimental Analysis

To verify the theoretical analyses mentioned above, we developed an experimental apparatus and carried out some experiments. The apparatus appears in Figure 5. It mainly consists of a semiconductor laser as a light source, a titaniferous prism on which a resin tank is set, and a base rod for lifting fabricated micro-objects. The laser beam, the wavelength of which is 488 nm, is split into the beam A and B by the beam splitter. The beam A and B are for the propagating light exposure and for the evanescent light exposure respectively.

The refractive index of the prism is 1.78, which can easily generate evanescent light on the cover glass located on the prism. The prism and the cover glass are sealed by immersion oil. The refractive indexes of the cover glass and the immersion oil are same as the prism. Urethane acrylate resin (KC1042, JSR corp, nd=1.491) is employed as the photosensitive resin. By installing a glass scale on a single axis stage, the base rod can be precisely positioned with a resolution of ten nanometers.

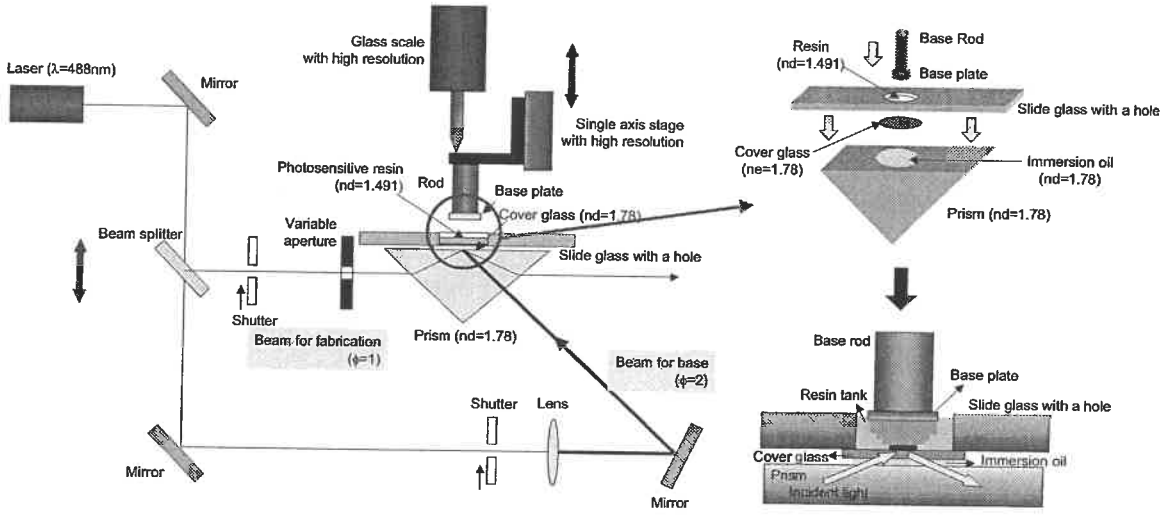

Figure 5. Experimental Apparatus

By using the developed apparatus, we carried out basic experiments to analyze the vertical resolution. In this experiment, the laser power, the incident angle and the exposure time are set at 3 mW, 68 degrees and 120 seconds respectively. We firstly checked whether evanescent light energy was sufficient for curing resin. Figure 6 shows the procedure of the evanescent light exposure experiment. Before the evanescent light exposure, the propagating light exposure was performed to fabricate a cured resin substrate. Then we tried to fabricate a single resin layer on the substrate by the evanescent light.

Figure 7 shows an optical microscope image of a fabricated object. A cured resin layer by evanescent light can be seen. It means that evanescent light energy is sufficient for curing resin. Next, by using an atomic force microscopy (AFM), we measured the thickness of the cured resin layer corresponding to the vertical resolution.

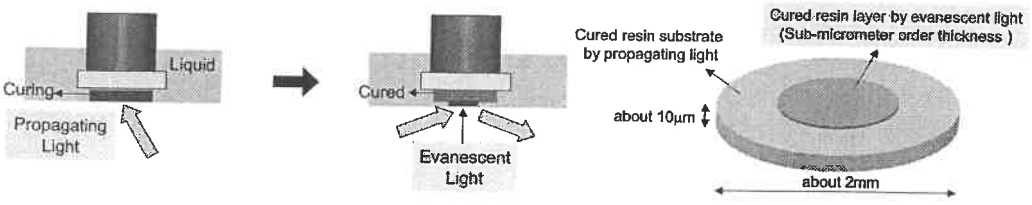

Figure 6. Experimental Procedure

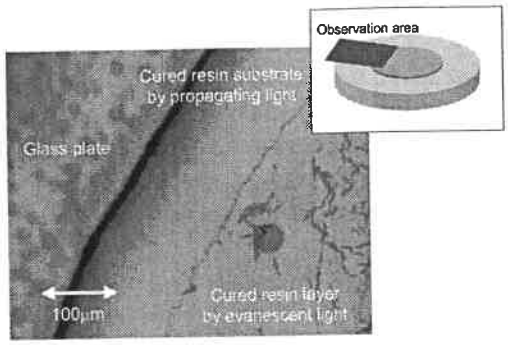

Figure 7. Optical Microscope Image of the Cured Resin Layer

Figure 8 shows an AFM image and a cross-section profile of the cured resin layer by evanescent light. The thickness of the cured resin layer is evaluated at about 300 nanometers and this fact indicates that micro-objects can be fabricated with sub-micrometer vertical resolution.

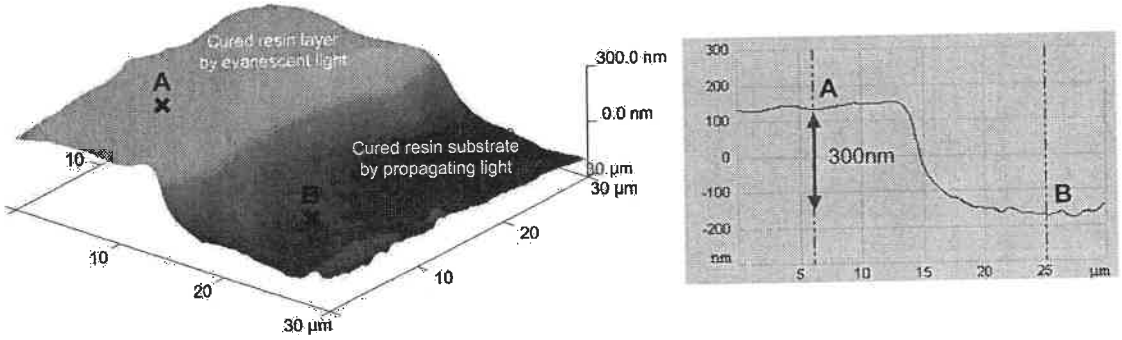

Figure 8. AFM image and Cross-Section Profile of Cured Resin

Conclusion

We proposed a novel stereolithography method using evanescent light. We carried out several theoretical and experimental analyses to verify this method. The theoretical analyses suggested that we could fabricate micro-objects with sub-micrometer resolution. Then we developed the nano-stereolithography system, in which photosensitive resin could be exposed by evanescent light as well as propagating light, and carried out basic experiments. The experimental results showed that evanescent light energy was sufficient for curing resin and that a 300-nanometer thickness layer can be fabricated. These results indicate the feasibility of stereolithography with 100-nanometer resolution, which could not be realized by conventional stereolithography methods.

Acknowledgement

The partial financial support from the Scientific Research Fund of the Japanese Ministry of Education, Culture, Sports, Science, and Technology and Mitsutoyo Association for Science and Technology are gratefully acknowledged.

References

1. P. F. Jacobs et. al., Rapid Prototyping & Manufacturing, Society of Manufacturing Engineers, (1992)
2. T. Hayashi et. al., Proc. Euspen '00, pp98-106, (2000)
3. Shoji Maruo, Koji Ikuta: Submicron Stereolithography for the production of freely movable mechanisms by using single-photon polymerization, Sensors and Actuators A, 100 (2002) 70-76
4. A. Bertsch et al: Rapid prototyping of small size objects, Rapid Prototyping Journal, 6, 4, (2000), 259
5. M. Farsari et al: A novel high-accuracy microstereolithography method employing an adaptive electro-optic mask, Journal of Materials Processing Technology, 107, (2000), 167

An Experiment Towards Establishing the Tolerance of Micro-Scale Interference Fits

James F. (Red) Jones[1] and Georg Aigeldinger[2]
[1]Sandia National Laboratory, Albuquerque, NM
[2]Sandia National Laboratory Livermore, CA

LIGA technology is capable of producing high aspect ratio parts with sub-micron feature sizes out of a variety of metal alloys, ceramics, and thermoplastics. LIGA was invented in Germany, and the German acronym stands for lithography (Lithographie), electroforming (Galvanoformung) and molding (Abformung). LIGA fabricated parts have many unique properties. The lithographic process permits cost effective production of intricate components. High aspect ratios with smooth and straight sidewalls are hallmarks of LIGA fabricated parts while a wide variety of materials enable numerous applications[1,2].

A challenge with LIGA fabricated micromechanical parts is that they generally require some level of assembly to achieve functional mechanisms or devices. In order to assemble these devices, individual parts must be permanently attached to one another. One attachment method that has recently been demonstrated is forcing pins into holes in which the nominal diameter of the hole is smaller than that of the pin[3]. These interference fit assemblies are able to withstand harsh environmental conditions that would destroy adhesively bonded parts. A critical aspect relating to the performance of interference fit assemblies is the tolerances of the mating parts. Unfortunately, no standard for the tolerance of sub-millimeter nominal diameter interference fits currently exists. The applicable standard, ISO286 specifically excludes nominal diameters under 1 mm. Further, this standard evolved through the consensus of experts based on practical experience – not on theory[4], thus no experimental and little theoretical work appears in the literature.

Evolving sufficient practical experience to determine appropriate tolerances for micro-scale interference fits would be a daunting task. Thus, it would be more expedient to develop a scientific basis for establishing the tolerance of micro-scale interference fits. The work reported in this paper describes the classical analytical mathematical model to predict the performance of cylindrical interference fits. The classical model indicates that the geometry and material properties of the parts are the dominant parameters affecting the performance of the assembly. The material properties of LIGA materials are of significant interest and have been published for a handful of alloys[5]. The dimensional metrology of micro-scale parts used in the experiments poses unique challenges[6] and is described in this paper. To assess the performance of the interference fit, the axial insertion force can be measured during assembly and an apparatus to do so is presented. Finally, the experimental results are reviewed in relation to the theoretical model.

Theory

The force required to insert (or extract) the pin from the hole is a good performance metric for an inference fit. To determine the insertion force, Vallance and Doughtie assume a Coulomb friction model to obtain[7],

$$F = f \pi p_c d_c L. \tag{1}$$

Where F is the insertion force, f is the coefficient of friction, p_c is the contact pressure, d_c is the contact diameter, and L is the length of engagement between the pin and the hole. Equation (1) states that the contact pressure times the contact area gives the normal force, which is then multiplied by the coefficient of friction to obtain the axial insertion force. Vallance and Doughtie use thick walled cylinder stress theory to determine the contact pressure,

$$p_c = \frac{AE(d_c^2 - d_i^2)(d_o^2 - d_c^2)}{2d_c^3(d_o^2 - d_i^2)}. \tag{2}$$

Where A is the total shrinkage, E is the modulus, d_i inside diameter of the inner member, and d_o is the outside diameter of the outer member. Assuming that the inner member is a solid pin, the outer member is an infinite plate, substituting the difference between the pin and hole diameters for the total shrinkage, and the average of the pin and hole diameters for the contact diameter, equation (2) reduces to,

$$p_c = \frac{E(d_p - d_h)}{(d_p + d_h)}. \tag{3}$$

Where d_p is the diameter of the pin and d_h is the diameter of the hole. Note that this derivation assumes that the modulus (and Poisson's ratio which was previously reduced to obtain equation (2)) is the same for both the inner and outer members. In fact, this is a reasonable assumption for our work with steel pins and nickel alloy LIGA parts, each of which have a modulus of about 190GPa and a Poisson's ratio of about 0.3.

Part Metrology

Obtaining and measuring or confirming the dimensions of the mating parts proved a challenge in itself. The pins were fabricated from steel plug gages purchased from Deltronic whom also supplied metrological reports for the gages. An SEM image of a sharpened pin is shown in Figure 1. On occasion, surface asperities were detected on the surface of the gages, one of which is visible on the shaft of the gage shown in Figure 1. Thus, surface roughness was measured using a Wyco NT3300 optical profiler to assure no or only minor concave asperities existed on the gages. Measurements indicated the average roughness of the gages to be generally about 200nm RMS with occasional isolated regions exceeding 1μm.

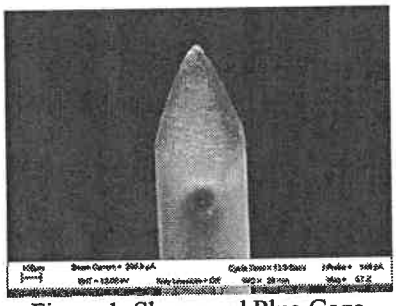

Figure 1. Sharpened Plug Gage

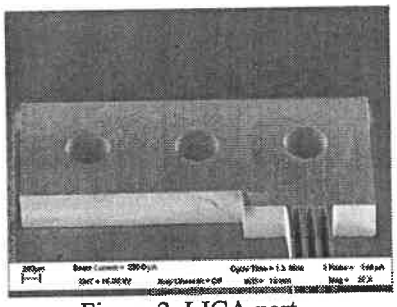

Figure 2. LIGA part

The parts possessing holes were fabricated by electroplating NiMn into LIGA molds. Top and bottom hole diameters were measured with a VIEW Engineering Voyager V6x12 optical microscope which has a measurement uncertainty of ±1.5μm. Side wall roughness was measured using the Wyco profiler and were generally less than 100nm with occasional regions up to 150nm average surface roughness. The roughness was measured on accessible sidewalls of the part and it was assumed that the sidewall roughness inside the holes was very similar.

Experimental Apparatus

The experimental apparatus consists of a Physik F-206 hexapod robot with controller that inserts the pin, an Eppendorf linear stage to position the LIGA part (hole), an ATI Nano17 load cell to measure insertion forces, and a Watec CCD camera with Navitar 5X lenses to align the parts, along with video monitor, personal computer, custom fixtures, tooling, and software. The apparatus is shown in Figure 3. Figure 4 shows a close up of the Physik platform, load cell with pin holder, and LIGA sample holder.

Figure 3. Experimental Apparatus

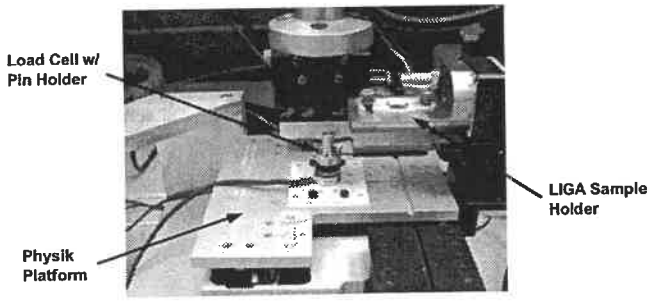

Figure 4. Close up

The load cell was calibrated using mass balance weights. The motion of the Physik was calibrated using a Starrett digital indicator which was calibrated though its full scale using gage blocks. In addition, experiments were performed to characterize and compensate for the compliance of the system.

To perform an insertion experiment, the pin and hole are aligned by viewing the overhead microscope while manually commanding the Physik and Eppendorf motion stages. Once coarsely aligned, the Physik moves the pin up until the hole in the LIGA part self centers on the point of the pin. After centering, a restraining plug is inserted over the LIGA part to prevent the part from moving vertically during pin insertion, but permits lateral part movement to compensate for any minor misalignment between the pin and hole. An experiment is performed by commanding the Physik to move upward, thereby inserting the pin into the hole while the force and displacement are recorded on the computer.

Results

Figure 5 shows the results of two experiments compared with the theoretical model. The tests consisted of inserting a 497.5μm diameter pin into an estimated 494.4μm diameter hole. Singer® sewing machine oil was used as a lubricant to assure a consistent coefficient of friction. Test 1 and test 2 were conducted in succession using the same pin and hole, the difference being that in test 2 the pin was inserted further through the approximately 500μm deep through hole to investigate the extent of the constant force region. There is excellent correlation between test 1 and 2, which indicates that the experiment is repeatable and no permanent deformation occurs to either the pin or the hole. However, the experimental results do not correlate with theory. The experimental results show that the insertion force initially increases and then decreases to about half of the peak force. In addition, the peak force occurs prior to full insertion of the pin and the insertion force does not become linear until the pin is well through the hole.

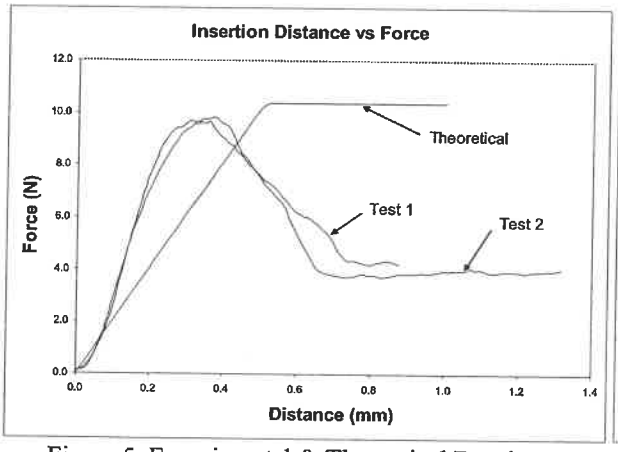

Figure 5. Experimental & Theoretical Results

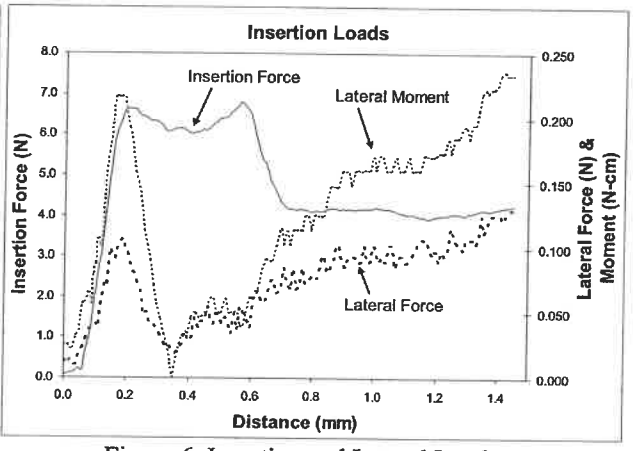

Figure 6. Insertion and Lateral Loads

Equation (3) shows that the contact pressure is a constant value for given geometries and material properties. Equation (1) states that the insertion force varies only as a function of insertion distance, thus the theoretical curve shown in Figure 5 reflects what the classical mechanics theory predicts. The magnitude of the insertion force that the theory predicts is subject to various assumptions, but none of the assumptions can account for the dramatic difference in the shape of the curves. The issue then becomes is the experiment or the classical theory in error.

Initially, it was hypothesized that the lubrication could be causing some sort of creeping effect. Thus, another set of experiments was run without lubricating the parts. The non-lubricated tests reviled the same characteristic curve as shown in Figure 5 with the exception of increased insertion force, which is to be expected. To further investigate this discrepancy, a simplified experiment was constructed that did not employ robotic systems to determine if the robot controllers were affecting the results. The simplified experiment again displayed similar behavior to that of tests 1 and 2. From this series of experiments we concluded that the original experiments were accurately depicting the insertion process. Another set of experiments was conducted in which the pin was inserted initially from the top and then from the bottom to determine if a slight taper in the hole could be causing the effect; however, the same result was obtained regardless of the direction of insertion.

Next we began investigating other theoretical models to explain the phenomenon. One possible explanation is that the classical model which is based on bi-axial strain is inadequate at this scale. The hypothesis was that the increasing axial load may cause a non-uniform bulge along the axis of the pin. To explore this possibility, we developed a simple finite element model based on tri-axial strain theory. Experiments with the model did display a slight drop in peak insertion force, but in general the tri-axial model more closely resembled the classical theory.

After more in depth considerations we realized that the shape of the curve is reminiscent of the force curve described by Whitney in his work on compliant insertion for clearance fits[8]. Thus, it is plausible that even though great care was taken to align the parts prior to insertion, some slight misalignment did exist and caused forces in addition to the force due to the interference fit. To evaluate this hypothesis, experiments were conducted that monitored the lateral forces and moments during insertions. The most dramatic instance is depicted in Figure 6 which shows insertion force and lateral forces and moments measured during insertion of a 497.5μm diameter pin into an estimated 494.8μm diameter hole. Note that insertion force is plotted against the left scale while both lateral force and moment are plotted against the right scale. In this experiment the peak force is less than that measured for the experiment in Figure 5, which seems reasonable given that parts having slightly less inference were used for this experiment. This experiment was unique because there appears to have been an initial misalignment that became aligned at about 0.35mm insertion distance, indicated by the lateral force and moment becoming nearly zero and possibly resulting in the plateau in the insertion force. Other experiments did not experience a dip in lateral force and displayed an insertion force curve similar to that in Figure 5. After 0.35mm insertion, the lateral loads gradually increase while the insertion force eventually drops to a steady state value. These experiments indicate that lateral loads do have an effect on the insertion force, but do not explain the unexpected shape of the insertion force curve.

Discussion

For the experiments conducted, the axial insertion force as a function of insertion distance displays unexpected nonlinear behavior. This behavior is repeatable and appears at odds with the classical theory describing insertion force of interference fits. Additional experiments confirmed that this behavior is not an artifact of the experimental procedure, due to effects from variation in dynamic and static friction, due to tapered holes, explainable with tri-axial strain theory, or due to extraneous lateral forces or moments.

It is possible that the behavior is a superposition of the effects mentioned above. It is also plausible that the behavior is caused, at least in part, due to a stress concentration between the tapering shoulder of the sharpened pin and the hole sidewall. It is even conceivable that the behavior is cause by the nature of the LIGA material or due to some sort of surface interaction effect. Several experiments were conducted with 500μm nominal diameter fits all of approximately the same magnitude of interference. Future work will explore this behavior for significantly different magnitudes of interference and nominal diameters. An experiment of particular interest would be to conduct an experiment at the macro scale to determine if this behavior is solely micro in nature.

Acknowledgements

Sandia is a multiprogram laboratory operated by Sandia Corporation, a Lockheed Martin Company, for the United States Department of Energy's National Nuclear Security Administration under Contract DE-AC04-94AL85000. The authors would also like to thank Dannelle Sierra for her assistance in conducting experiments, Joe Ceremuga and Kevin Krenz for their assistance in dimensional metrology, and Amy Rice for her work on the FEA model.

---

[1] Becker E.W., et al. "Fabrication of microstructures with high aspect ratios and great structural heights by synchrotron radiation lithography, galvanoforming, and plastic moulking (LIGA process)", *Microelectronic Engineering*, 1986, **4**, pp. 35-53.

[2] Hruby J., "LIGA Technologies and Applications", *MRS Bulletin*, 2001 26(4), pp. 337-340.

[3] Jones J. F., Kozlowski D.M., Trinkle J.C., "Micro-Scale Force-Fit Insertion", *Journal of Micromechatronics*, Vol. 2, No. 3-4., 2004, pp. 185-200.

[4] Gaillard J., "ISA Fits", *American Machinist*, July 15, 1936, pp.616-8.

[5] Christenson T.R., Buchheit T.E., Schmale D.T., Bourcier R.J., "Mechanical and Metallographic Characterization of LIGA Fabricated Nickel and 80% Ni- 20% Fe Permalloy", *Symposium on Microelectromechanical Structures for Materials Research*; April 15-16, 1998; San Francisco, CA, pp. 185-190.

[6] Ceremuga J.T., Aigeldinger G., "Inspection Strategy for LIGA Microstructures Using a Programmable Optical Microscope", *Sandia National Laboratories Report* SAND2004-2289, July 2004. Submitted to *Precision Engineering*.

[7] Vallance A., Doughtie V.L., *Design of Machine Members*, McGraw-Hill, 1943, p. 458.

[8] Whitney D.E., "Quasi-Static Assembly of Compliantly Supported Rigid Parts", *Journal of Dynamic Systems, Measurement, and Control, March 1982*, Vol. 104, pp.65-77.

MICRO-TURBO CHARGER FOR A PALMTOP GAS TURBINE GENERATOR

Shuji Tanaka[1], Kousuke Isomura[2], Shin-ichi Togo[3], Kousuke Hikichi[3], Satoshi Goto[3] and Masayoshi Esashi[1]

[1]Tohoku University, Sendai, Japan
[2]Ishikawajima-Harima Heavy Industries Co., Ltd., Nishi-Tokyo, Japan
[3]Tohoku Gakuin University, Tagajyo, Japan

Abstract

Micro-turbo chargers were manufactured and operated to test the compressor of a palmtop gas turbine generator at low temperature (< 100 °C). Impellers are 10 mm in diameter and have 3-dimensional blades machined using a 5-axis NC milling machine. The performance of the compressor were measured at 50 % (435,000 rpm) and 60 % (530,000 rpm) of the rated rotational speed (870,000 rpm). The measured pressure ratio is lower than predicted value, mainly because impeller tip clearance was larger than designed value. The measured adiabatic efficiency is unrealistically high due to heat dissipation from compressed air. The maximum rotational speed achieved using hydroinertia and hydrodynamic air bearings is 566,000 rpm and 165,000 rpm, respectively.

1 Introduction

In coming aging society with less working population, self-powered mobile machines like an autonomous robot are expected to work at construction sites, farms, hospices, homes etc. For the power source of such self-powered mobile machines, light weight, that is, high power density is highly important, and refueling is more convenient than time-consuming recharging especially at construction sites and disaster areas where an commercial electric power line is not available. From the social needs, 10-1000 W class miniature gas turbine generators are under development [1-6], because a gas turbine is potentially advantageous in power density compared to fuel cells and other heat engines.

We are developing a palmtop gas turbine generator with specifications shown in Table 1, because output power of 1 to several hundreds W/unit is often required by the self-powered mobile machines, and the limit of the miniaturization based on existing gas turbine configuration seems to be around 10 mm in the diameter of impellers [7]. To realize such a palmtop gas turbine, we must demonstrate that

(1) a compressor and a turbine achieve a required adiabatic efficiency of 68 %,
(2) a rotor stably rotates up to a rated rotational speed of 870,000 rpm,
(3) a combustor stably operates at a rated temperature of 1,050 °C, and
(4) the compressor is thermally isolated from a hot combustor and turbine to achieve required adiabatic efficiency.

Table 1 Specifications of the palmtop gas turbine generator under development

Compressor pressure ratio	3
Diameter of impellers	10 mm
Rated rotational speed	870,000 rpm
Turbine inlet temperature	1050 °C
Shaft output	130 W
Electrical output	100 W

In this study, micro-turbo chargers to demonstrate (1) and (2) at low temperature (< 100 °C) were manufactured and tested.

2 Structure

2.1 Overall structure

Figure 1 shows the cross-sectional structure of the turbo charger. The turbo charger is mainly composed of a compressor, a turbine, radial bearings and a thrust bearing. We tested two types of turbo charger: one with hydroinertia air bearings [6] and one with hydrodynamic air bearings. The details of the bearings are described in the next subsection. For the turbo charger with the hydrodynamic air bearings, the journal bearing air ports shown in Fig. 1 are not opened. The parts composing the rotor are made of titanium alloy with high specific strength, and the other parts are made of stainless steel.

Figure 2 shows the impellers with a diameter of 10 mm. The compressor impeller is designed to achieve possibly highest efficiency by computational fluid dynamics (CFD) simulation, and to keep required strength by stress and natural frequency analysis at the operation point shown in Table 1. The turbine impeller is designed in the same method to produce power required by the compressor (about 350 W) using cold driving air (< 100 °C). The impellers are machined using a tapered ball endmill with a diameter of 0.5 mm installed at a 5-axis NC milling machine (Toshiba Machine, F-MACH with an additional rotating stage).

The impellers and the shaft are assembled with preloading by the tie bolt and tie nut, and the rotor is balanced within 0.2 g·μm using a special rotational balancing machine (Kokusai). Because the rotor is disassembled and reassembled to be inserted into the turbo••

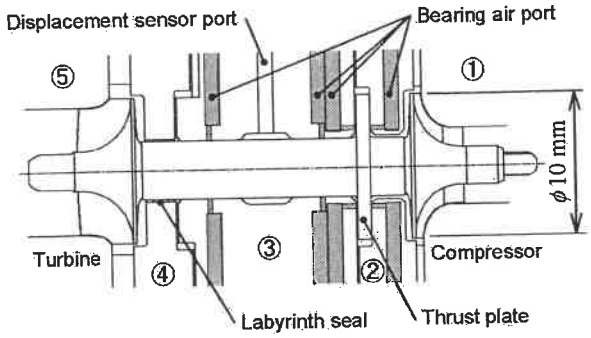

Fig. 1 Cross-sectional structure of the turbo charger

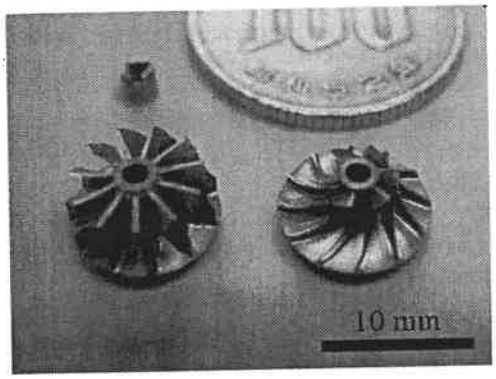

Fig. 2 Impellers (Left: Turbine, Right: compressor)

charger, the repeatability of the rotational balance is checked by repeating assembly and disassembly. The rotational imbalance deteriorates approximately to 1 g·μm after reassembly.

2.2 Bearings

At the rated rotational speed of 870,000 rpm, no existing bearing can be used. For the turbo charger, we designed and tested two types of air bearings: hydrointertia air bearings and grooved hydrodynamic air bearings.

Hyroinertia air bearing

The hydroinertia air bearing is a kind of externally-pressurized air bearing, which has a 2-3 times wider bearing gap than that of a conventional hydrostatic air bearing [6]. The hydroinertia bearing uses not only static pressure rise at the narrow side of the bearing gap but also static pressure drop due to the acceleration of supersonic air flow at the wide side to return a shaft to the bearing center. Air bearings make restoring force by static pressure difference between the wide and narrow bearing gap. In a conventional hydrostatic bearing, static pressure is positive at both wide and narrow bearing gap, but in the hydroinertia bearing, static pressure at the wide bearing gap becomes negative, so that larger restoring force, that is, higher load capacity is obtained.

The drawback of the hydroinertia bearing is large air consumption and relatively low rigidity at low eccentricity. Also, the wide bearing gap makes it difficult to tighten impeller tip clearance. In the turbo charger, the radial and thrust bearing gaps are designed at 30 μm and 40 μm, respectively, using the calculation method developed by Hikichi *et al* [8]. The measured radial and thrust bearing gaps are 25 μm and 44 μm, respectively.

Hydrodynamic air bearing

For the final gas turbine generator, a hydrodynamic air bearing is preferable, because it does not consume a part of air from the compressor, and has high whirl stability. Among several types of hydrodynamic air bearing, we first selected a herring-bone grooved air bearing and a spiral grooved air bearing for radial and axial support, respectively, because they are relatively easy to fabricate for a small shaft. The bearings are designed using a standard design method in Ref. [9]. The designed bearing gaps are 4.4 μm and 5.5 μm for the radial and thrust bearing, respectively. To keep such narrow bearing gaps, highly precise fabrication technology is required.

Figure 3 shows the shaft with bearing grooves fabricated by photolithography and wet etching. The herring-bone grooves on the cylindrical surface are fabricated using a special maskless exposure system with a rotating sample stage (Ball Semiconductor). Positive photoresist (Clariant, AZ 4400) is uniformly spread on the cylindrical surface by dipping the shaft into the photoresist and suspending it in solvent vapor. The image of the herring-bones is generated on a Digital Micromirror Device (Texas Instruments) in the maskless exposure system, and projected to the cylindrical surface by rotating the shaft step by step. After development and hard baking, the shaft is etched by the mixture of fluoric acid and hydrogen peroxide.

To fabricate the spiral groove on the thrust disc, the photoresist is first spread on the shaft by spinning the shaft. The spiral groove pattern is transferred using a

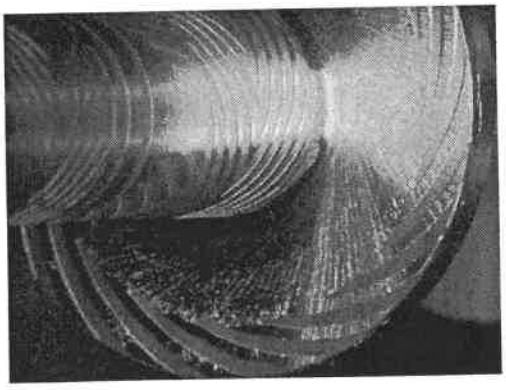

Fig. 3 Shaft with herring-bone and spiral grooves

special photomask with a hole where the shaft passes, and then the shaft is wet-etched. By repeating these steps, the spiral grooves are fabricated on both sides of the thrust disc.

3 Experimental

3.1 Experimental setup

The turbo charger is set with the turbine facing up and the compressor facing down. Driving air is supplied from a scroll compressor to the turbine through an air heater (Sakaguchi E.H VOC). The air heater is used, when turbine power generated by cold air is not enough to drive the compressor, but it was not used in this study. Air for the hydroinertia beaings is supplied from another scroll compressor, and its pressure is set at 0.5 MPa using a pressure regulator.

Rotational speed is measured by detecting a mark on the shaft using an optical fiber displacement meter (Philtec, D20) and counting up the pulse signals using a tachometer. Also, using similar optical fiber displacement meters, the radial and axial vibration of the rotor are measured at the center of the shaft and the back side of the turbine impeller, respectively. Temperature and pressure are measured using 10 thermocouples and 10 diaphragm pressure sensors (Keyence, AP-43/44), respectively. Air flow rate is measured using hot wire flow meters (STEC, SEF-52) at the inlets of the turbine and compressor, and using tapered tube flow meters at the outlets.

3.2 Experimental results

Compressor performance

Figure 4 and 5 show the pressure ratio and adiabatic efficiency of the compressor (compressor diagrams), which were obtained using the turbo charger with the hydroinertia bearings. The compressor diagrams were obtained at about 50 % (435,000 rpm) and 60 % (520,000 rpm) of the rated rotational speed. The measured pressure ratio is lower than predicted value. This could be mainly because the impeller tip clearance was too large compared to a designed value of 25 μm. In this study, the impeller tip clearance was set large enough to prevent the impeller tip from crashing to the shroud, because the machining error of the impeller and shroud as well as assembly error were not within tolerances, and the bearing gaps were large.

The measured adiabatic efficiency shows unrealistically high values. This is mainly due to heat dissipation from compressed air. Adiabatic efficiency, η_c, is the ratio of required adiabatic work calculated from measured pressure ratio to actual work calculated from measured temperature ratio, and is given by

$$\eta_c = \frac{\pi_c^{(\gamma-1)/\gamma} - 1}{T_{out}/T_{in} - 1},$$

where π_c is pressure ratio, T_{in} and T_{out} are inlet and outlet temperature, respectively, and γ is the ratio of specific heats. If T_{out} drops due to the heat dissipation from compressed air, the actual compressing work is underestimated, so that adiabatic efficiency is overestimated from the above equation. Heat isolation is necessary for compressed air, because heat dissipation relatively increases in such a small machine.

Characteristics of the hydroinertia air bearing

Using the hydroinertia air bearings, a rotational speed of 566,000 rpm, which is 65 % of the rated rotational speed, was achieved. Figure 6 shows the vibration of the rotor 240 ms before the crash at 566,000 rpm. In the radial vibration, an oscillation with low frequency (envelope) represents the whirl of the rotor, and that with high frequency synchronizes with rotation. The latter was influenced by uneven reflection rate on the shaft where the optical fiber displacement sensor approached, and does not represent just the rotation-synchronous mechanical vibration.

The rotor crashed to the radial bearing due to the whirl. The whirl ratio (rotational speed/whirl speed) observed in Fig. 6 is 8. The whirl is the precession of a rotor which is excited by the component of shaft load normal to the direction of eccentricity due to

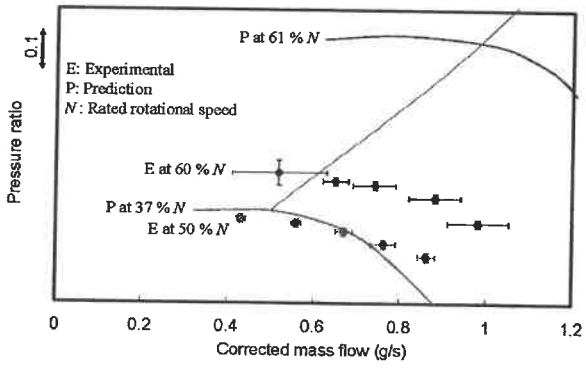

Fig. 4 Compressor diagram (pressure ratio)

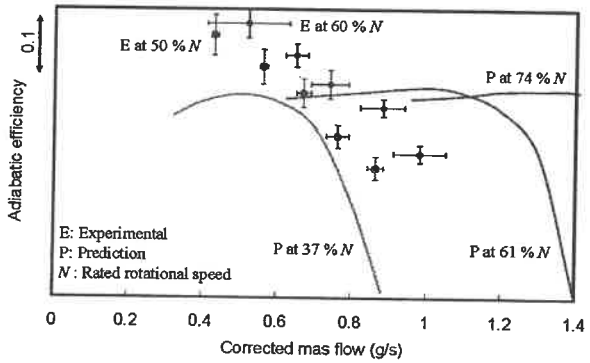

Fig. 5 Compressor diagram (adiabatic efficiency)

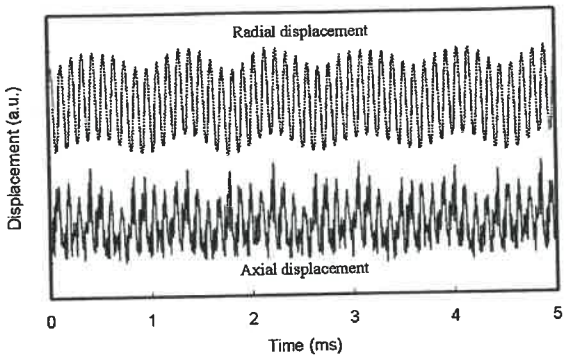

Fig. 6 Rotor vibration 240 ms before the crash at 566,000 rpm

hydrodynamic effect. The whirl speed is identical with the resonant speed of the bearing system. Thus, the product of the resonant speed and whirl ratio is the maximum achievable rotational speed. The resonant speed is determined by rotor weight and bearing stiffness, but the mechanism to determine the whirl ratio is not figured out. Simulation study based on CFD will help us to design the bearing with higher whirl stability.

Characteristics of the hydrodynamic air bearing

We tested the turbo charger with the hydrodynamic air bearing several times, but mostly the rotor crashed to the bearing below 100,000 rpm. The measured radial bearing gap is about 10 μm, which is approximately twice the designed value. From theoretical calculation shown in Fig. 7, the critical speed at this radial bearing gap is found to be several tens thousands rpm, and it is thought that the crash occurred due to the resonance of the bearing system. Using a better balanced rotor, the resonant peak becomes narrower, so that it becomes easier to pass the critical speed in acceleration. In this study, the rotor balance could not be good enough to pass the critical speed, because the rotor was disassembled and reassembled to be inserted into the turbo charger after balanced.

The maximum rotational speed achieved using the hydrodynamic air bearings is 165,000 rpm, which is in supercritical range. From the measured vibration of the rotor, we cannot find the reason of the crash. Further studies including fluidic simulation in the bearing gaps and the improvement of fabrication technology are necessary to approach the rated rotational speed.

4 Conclusion

In this study, a micro-turbo charger was manufactured and operated to test the compressor of a palmtop gas turbine generator at low temperature (< 100 °C). Impellers are 10 mm in diameter and have 3-dimensional blades machined using a 5-axis NC milling machine.

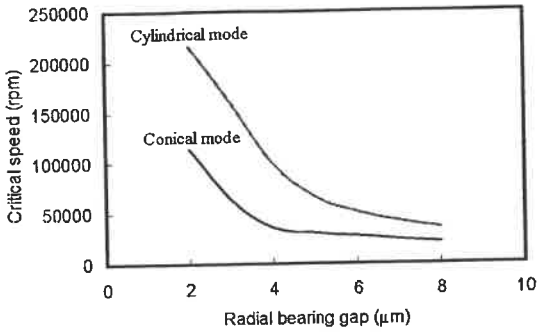

Fig. 7 Critical speed of the hydrodynamic air bearing

The performance of the compressor were measured at 50 % (435,000 rpm) and 60 % (530,000 rpm) of the rated rotational speed (870,000 rpm) by driving a turbine using compressed air at room temperature. The measured pressure ratio is lower than predicted value. This could be mainly because impeller tip clearance was larger than designed value. The measured adiabatic efficiency is unrealistically high due to heat dissipation from compressed air. The maximum rotational speed achieved using hydroinertia and hydrodynamic air bearings is 566,000 rpm and 165,000 rpm, respectively.

The obtained results are not satisfactory, but critical issues to be solved in future works were determined. This seems an important step toward the realization of the palmtop gas turbine generator.

Acknowledgements

This study was supported partly by the New Energy and Industrial Technology Development Organization of Japan, and partly by The Asian Office of Aerospace Research and Development.

References

[1] Alan H. Epstein, Proc. ASME Turbo Expo 2003 (2003) GT-2003-38866.
[2] Sangkyun Kang *et al.*, *Ibid.*, GT2003-38933.
[3] Kousuke Isomura *et al.*, *Ibid.*, GT2003-38151.
[4] Jan Peirs *et al.*, *J. Micromech. Microeng.*, 13 (2003) S190-195.
[5] P. Kang *et al.*, Proc. ASME Turbo Expo 2004 (2004), GT2004-53565.
[6] Shuji Tanaka *et al.*, *J. Micromech. Microeng.*, 14 (2004) 1449-1454.
[7] Kousuke Isomura *et al.*, Proc. ASME Turbo Expo 2001 (2001) 2001-GT-101.
[8] Kousuke Hikichi *et al.*, Proc. JAST Tribology Conference (2003) 309-310 [in Japanese].
[9] Shin-ichi Togo, Gas Bearing – From Design to Manufacturing –, Kyoritsu Shuppan (1984) [in Japanese].

Phase Plate Correction of Ocular Aberrations

Thomas W. Raasch, OD, PhD
The Ohio State University, College of Optometry, Columbus, OH
Allen Y. Yi, PhD
The Ohio State University, College of Engineering, Columbus, OH
Jeffery W. Roblee, PhD
Precitech, Inc., Keene, NH

Introduction

In recent years it has become possible to measure, and in some instances, correct the high-order aberrations of human eyes. This capability has been largely driven by the development of laser surgical procedures to treat refractive errors of the eye, such as myopia and astigmatism. Correction of high order aberrations is now also being pursued, using several types of correction methods, such as laser ablation of the cornea (Pettit 2001; Nakano, Portellinha et al. 2003), or via an intraocular (Marcos 2002), contact, or spectacle lens.

The technology for measuring aberrations of the human eye has developed recently and rapidly. A handful of techniques have been used to measure ocular aberrations; the most commonly used is wavefront sensing using a lenslet array. Light is focused on the retina to a point, and the light diffusely reflected from that point and exiting the eye through the pupil is captured by an optical system. The pupil is optically conjugated with the lenslet array, and the multiple spots formed by the individual lenslets are imaged on a CCD array. The spacing of the multiple focal spots in relation to that of the lenslets is used to derive the wavefront shape. This approach to evaluating the optics of the eye has borrowed heavily from astronomy. In astronomy, wavefronts distorted by traversing the atmosphere are measured using similar technology, and which can then be corrected dynamically with adaptive optics. This project is similar in that it also involves measuring an aberrated wavefront, and which is then corrected statically with the phase plate incorporated into a spectacle lens. We are investigating the use of precision engineering techniques to produce that static aberration correction in an otherwise standard ophthalmic lens.

For most human eyes, the potential visual benefit of reducing high order aberrations is relatively modest. Most normal eyes with well-corrected refractive errors have a residual RMS wavefront error of less than 0.3 micrometers. Even with perfectly corrected high order aberrations, visual performance would be limited by diffraction, scatter, and neural effects. Diffraction is an important limitation, so the theoretical limit of the resolving power of the eye depends heavily on pupil size. With a relatively large pupil, the theoretical limit of visual acuity, if affected only by diffraction and the limitations of the anatomy and physiology of the visual pathways, is approximately 20/12 to 20/8 (in clinical "Snellen" notation), corresponding to cut-off frequencies of 50 to 75 cycles/degree.

Some eyes, however, have substantially greater higher-order wavefront error due to aberrations. Because those aberrations can degrade the quality of the retinal image substantially, those eyes would be expected to benefit most from reduction in the aberrations. For example, corneal disorders such as keratoconus create corneal shape changes, and elevated levels of aberrations.

Similarly, corneal and refractive surgeries sometimes result in distorted corneal shapes and elevated aberrations. Since that type of surgery is becoming more widespread, the number of eyes with elevated high order aberrations follow surgery might also be expected to increase.

An important limitation of this approach is the positional relationship between the compensating phase plate and the eye pupil. That is, the line of sight should pass through the center of the phase plate, and any eye rotation will disrupt that relationship. This is not a limitation in corneal refractive surgery, since the aberration correction stays in registration with the line of sight (assuming the ablation zone is optimally placed during the surgery itself). This registration issue is also an important issue with aberration-correcting contact lenses, as contact lenses are not completely static on the eye. In a spectacle lens, the registration issue will likely limit the usefulness the aberration-correction to situations in which an object can be steadily fixated.

Methods

A commercial ocular aberrometer is used to measure the shape of the wavefront produced by the optics of the eye and spectacle lens combination. Wavefront shape and aberration types in the visual sciences are commonly expressed in terms of the Zernike polynomials (Thibos, Applegate et al. 2000). The lens used in combination with the eye is selected to correct as fully as possible the low-order refractive errors (e.g. myopia, astigmatism). As a result, only small residual low-order errors are expected, plus the high-order aberrations of the eye/lens combination. Those residual aberrations are then used to design the phase plate intended to correct those residual aberrations. Because the spectacle lens will typically have spherical, toric, or aspheric surface(s), those existing surface shapes must be accounted for in the design of the final phase plate surface.

We have prototyped this approach with a conventional CR-39 ophthalmic lens. Residual aberrations of an eye/lens combination (up through sixth order) were measured using an aberrometer (COAS, Wavefront Sciences, Albuquerque, NM). The pupil of the eye was dilated to greater than 6 mm, and accommodation paralyzed pharmacologically. The aberration structure was expressed in terms of Zernike coefficients over a 6 mm diameter circle. The seven Zernike terms of highest magnitude were used to design a correcting phase plate on the front surface of the lens. For this particular eye/lens combination, these seven terms, if perfectly implemented on the surface of the lens, would correct 97% of the wavefront variance.

The aberration-correcting phase plate consisted of a 6 mm diameter circle placed eccentrically on the front, convex surface of the lens. The front surface of this lens had a radius of curvature of 226.7 mm, and this base curve was incorporated into the phase plate surface. A fast tool servo (FTS) and an ultraprecision diamond turning machine were used to machine the phase plate. The single point diamond tool nose radius was 0.262 μm, the lens rotation was 200 rpm, and the tool traveled from periphery to center of the lens at 1 mm/minute.

Additional lens substrates are being investigated, including PMMA and polycarbonate, to determine which material and processing parameters produce the best surface finish.

Results

The first prototype was fabricated from a standard CR-39 spectacle lens. The surface finish of this lens without polishing was not adequate for an ophthalmic lens. The front surface was visibly hazy, making optical measurements and visual comparisons through the lens difficult. The surface finish was improved somewhat by manual polishing, using techniques that are commonly used clinically with rigid contact lenses. Polishing smoothed the surface and made possible the optical measurements, but it would also be expected to cause the phase plate shape to deviate from the intended shape, particularly in the higher-order terms.

The wavefront shape that was targeted is shown in Figure 1. It has a maximum peak-valley deviation of 3.6μm, and an RMS value of 0.68μm. Figure 2 illustrates the wavefront that was achieved through the phase plate on the CR39 lens. A 6 mm diameter region of the lens outside the phase plate was used as a reference region, so this wavefront shape represents the difference between inside to outside the 6mm phase plate circle. Multiple measurements through the lens were used to average down noise in the data, attributed to residual surface roughness and irregularities. The error phase plate had an RMS value of 0.49μm, indicating a modest reduction in the net aberration amplitude.

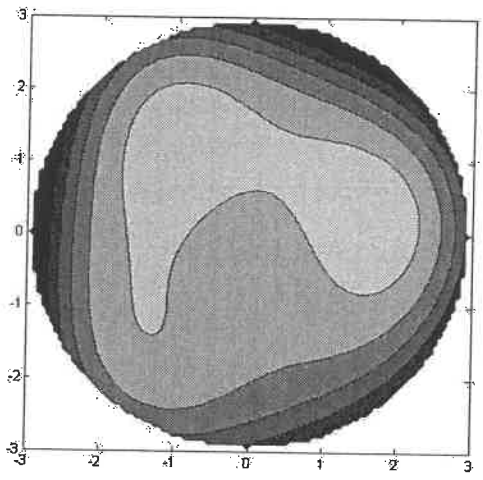

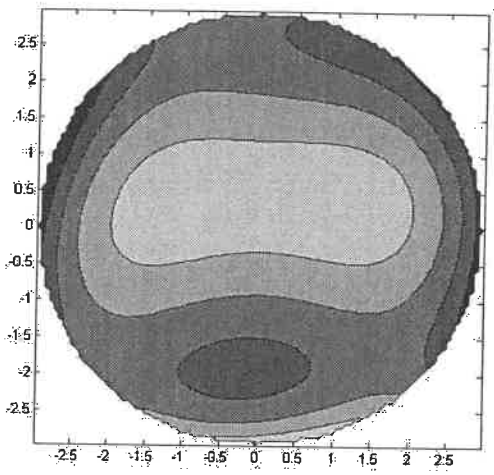

Figures 1 (left) and 2 (right). Fig. 1 illustrates the targeted wavefront to be produced by the phase plate. Fig 2 illustrates the wavefront that was achieved, on the same scale.

Visual comparisons through the lens, while inherently subjective, are consistent with the phase plate reducing aberrations. Surface roughness decreased resolution and contrast sensitivity both within and outside the phase plate. Visual comparison through those two regions indicated that the phase plate improved visual acuity by about ½ a "line" of acuity, or by about 12%. This is consistent with expectations based on the starting level of aberrations, and the partial correction of those aberrations in the phase plate.

Conclusions

The first prototype lens was not an acceptable result due primarily to the poor surface finish. Alternative lens materials and machining parameters are being investigated to determine optimum fabrication methods. In addition, phase plate correction will be applied to other individuals, particularly those who are likely to benefit most from aberration correction. This group consists mainly of those with optical (pre-retinal) abnormalities of the eye, but with an otherwise normal visual system at the retinal and post-retinal stages of the visual system.

References

Marcos, S. (2002). "Are changes in ocular aberrations with age a significant problem for refractive surgery?" J Refract Surg 18(5): S572-8.

Nakano, K., W. Portellinha, et al. (2003). "Refractive outcome of Nidek OPD-scan customized ablations." J Refract Surg 19(2 Suppl): S221-2.

Pettit, G. H. (2001). "The Alcon/Summit/Autonomous perspective on fixed vs. variable spot ablation." J Refract Surg 17(5): S592-3.

Thibos, L. N., R. A. Applegate, et al. (2000). Report from the VSIA taskforce on standards for the reporting of the optical aberrations of the eye. Vision Science and Its Applications, Santa Fe, NM, Optical Society of America, Washington DC.

ANAYSIS OF AN ELECTRON BEAM HEATING OF A SILICON WAFER

Shigeo KATO*, Hisashi NAKAMURA*,
Manabu ONO** and Norio SAITO***

*Nippon Institute of Technology, Miyashiro, Saitama 345-8501, JAPAN
E-mail:kato@nit.ac.jp
**Tokyo Metropolitan College of Technology, Shinagawa, Tokyo 140-0011, JAPAN
***Hitachi High-Technologies Corp., Minato, Tokyo 105-8717, JAPAN

1. Introduction

The semiconductor element has been integrated highly every year. Recently, the 90 nm level is produced. At the lithography process which makes the patern of a semiconductor device, electron beam drawing system (EB) is bearing the big role. With electron beam drawing system, the silicon wafer which is excellent in processability as aperture or a mask material which determines the form of an electron beam is used in many cases[1]~[4]. Since the electron beam of high energy is directly irradiated to aperture or the mask, the temperature analysis is indispensable in order to maintain stable operation of EB system and accuracy. However, since about one digit of heat conduction coefficients of silicon changed from room temperature between the melting point, temperature analysis was not easy. Consequently, the temperature of the silicon wafer which the electron beam irradiates was analyzed in considering of the radiation and the heat conduction.

2. Shape of silicon wafer

The sectional view of the silicon wafer heated by the electron beam is shown in Fig. 1. The radius r of the silicon wafer is 25 mm. A thick film part is between the radius of 25 mm and the radius of 10 mm with 500 μm thick. A thin film part is to the radius of 10 mm and the thickness is 20 μm. However, there is aperture (hole) between the radius of 1.55 mm and the radius of 1.63 mm with average thickness of 4 μm. The power of the electron beam is 2.5 W. When the electron beam is irradiated to the silicon wafer, the thin film part is heated and becomes high temperature. Therefore, the most of power is radiated from the irradiation area. The heat conduction which passes along the thin film occurs and radiates the heat due to high temperature. When the temperature is high in places other than an irradiation area, heat is radiated from the place.

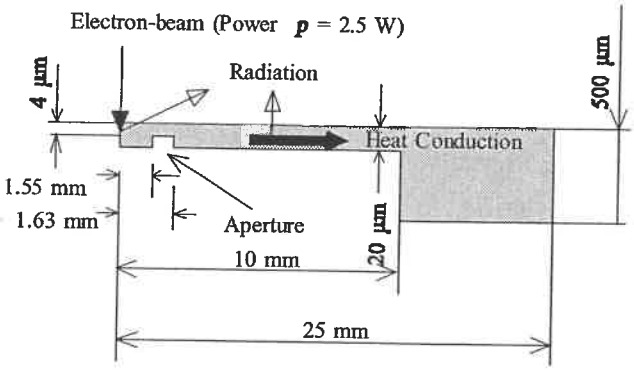

Fig. 1 Sectional view of a silicon wafer

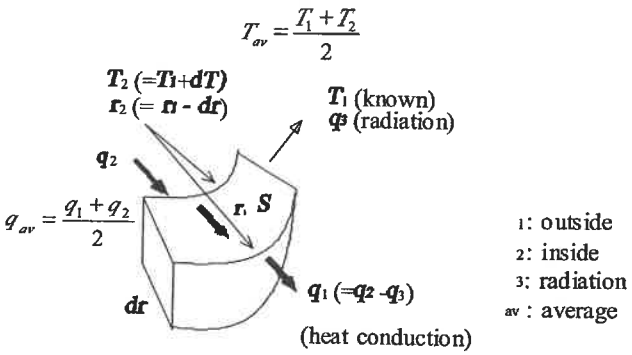

Fig. 2 Model of heat transmission

3. Model of heat transmission

The model of heat transmission of the silicon wafer is shown in Fig. 2. Subscript 1 which is shown in Fig. 2 is shown as outside of the silicon wafer. In addition, subscript 2 is shown as inside of the silicon wafer. Furthermore, subscript 3 is shown as radiation. Subscript av is shown as average. S is the area of radiation. The shape of the silicon wafer was assumed to be round. the passage quantity of heat is shown as:

$$q = -2\pi r l \lambda \frac{dT}{dr} \qquad (1)$$

Equation (1) has to add negative sign due to (dT/dr) is negative. From Equation (1) we get

$$dT = \frac{q}{2\pi r l \lambda} \frac{dr}{r} \qquad (2)$$

By integraling Equation (2) we obtain

$$T_1 - T_2 = \frac{q}{2\pi r_2 l \lambda} \ln\left(\frac{r_1}{r_2}\right) \qquad (3)$$

where T is the temperature of silicon wafer, T_1 is temperature of outside of silicon wafer, T_2 is the temperature of inside of silicon wafer, dT is increase of the temperature, dr is increase of the radius, q is the passage quantity of heat, r is the radius of silicon wafer, r_1 is the outer radius of silicon wafer, r_2 is the inner radius of silicon wafer, l is the thickness of silicon wafer. $?$ is the heat conductivity. Unknown temperature T_2 can be defined by equation (3). The quantity of heat q_2 which flowed into the area of inner radius of silicon wafer r_2 emits the quantity of heat of q_3, becomes $q_1=(q_2-q_3)$ and flows out of outer radius of silicon wafer r_1. The value of $T_{av}=(T_1+T_2)/2$ is used for the average temperature for determining the amount q_3 of the radiant energy. The value of $q_{av}=(q_1+q_2)/2$ is used for average quantity of heat for determining unknown temperature T_2.

4. Heat conductivity

The heat conductivity of the silicon is dependent on the temperature. The main temperature and the heat conductivity[5] are as follows. The heat conductivity is 148 W/mK at the temperature of 300 K, and is 61.9 W/mK at the temperature of 600 K. The heat conductivity is 42.2 W/mK at the temperature of 800 K and is 31.1 W/mK at the temperature of 1000 K. Furthermore, the heat conductivity is 25.8 W/mK at the temperature of 1200 K. The relationship between the heat conductivity and the temperature can be assumed as the following equation by making a and b into a constant.

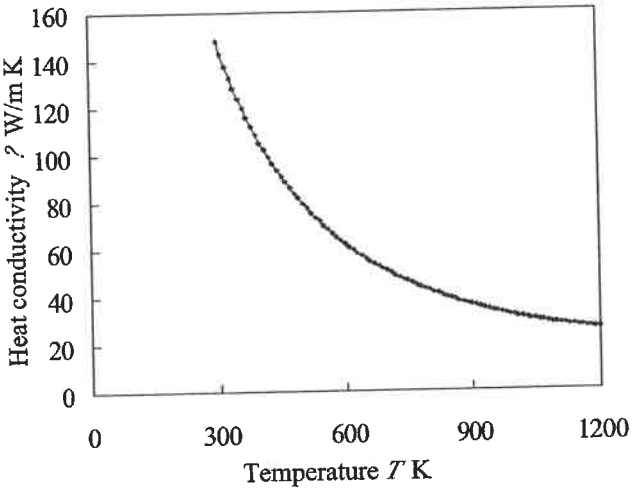

Fig. 3 Heat conductivity

$$\lambda = \frac{a}{T} + b \qquad (4)$$

The heat conductivity other than main temperature was calculated from the formula (2) using the heat conductivity of main temperature. The relationship between the heat conductivity and the temperature is shown in Fig. 3. Notice that the heat conductivity is inversely related to the temperature.

5. Radiant energy

Quantity of heat q_3 which is a certain temperature T and is radiated from the area of S is shown as:

$$q_3 = \varepsilon \sigma T^4 S \qquad (5)$$

where S is the radiation area, s is the Stefan-Boltzmann constant, q_3 is the radiant heat and e is the total emissivity. The radiant heat can be calculated from a formula (5).

6. Temperature and total emissivity

The relationship between the passage quantity of heat q and the temperature T is equivalent to the relationship between the current I and the electric potential difference V. The temperature difference T is equivalent to the electric potential difference V. In addition, the heat resistance is equivalent to the electric resistance R. The heat conductivity ? which is a factor in heat resistance changes a lot with the temperature T. Therefore, the heat resistance has to be changed, whenever it cannot consider as a constant but the temperature changes. In the high temperature part, since the heat is radiated, the passage quantity of heat is decreasing rather than the quantity of heat which is fixed. The boundary condition is as follows. Temperature $T1$ of the circumference part was assumed to 300 K. The temperature of the silicon wafer heated by the electron beam was calculated. Temperature calculation is begun from the place which the temperature of the outermost circumference (r_1=25 mm) is fixed as T_1=300 K. Concerning the selection of the radius of r_2, the radius of r_2 has to be chosen so that temperature difference becomes not large. If the electron beam is extracted to the radius of 1.5 mm and is

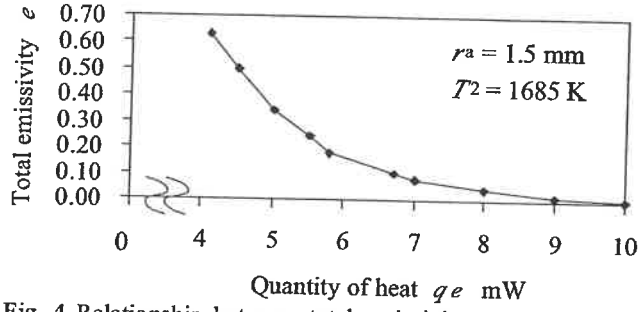

Fig. 4 Relationship between total emissivity and quantity of heat

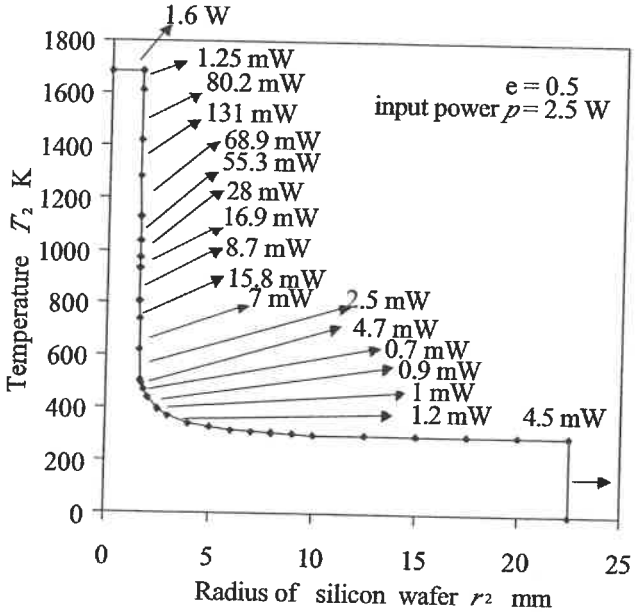

Fig. 5 Temperature of silicon wafer

irradiated, the silicon wafer will melt. The temperature distribution of the silicon wafer when the electron beam was extracted to the radius of 1.5 mm was calculated. In addition, The outermost circumference quantity of heat was changed. The total emissivity was changed so that the irradiation side temperature might be set to 1685 K which is melting point of silicon. The relationship between the outermost circumference quantity of heat q_e and the total emissivity is shown in Fig. 4. When the outermost circumference quantity of heat q_e is 4.5 mW, the total emissivity is about 0.5. In addition, when q_e is 5 mW, the total emissivity is about 0.3. The temperature of a silicon wafer is influenced by outermost circumference quantity of heat and the total emissivity was confirmed. The actual outermost circumference quantity of heat q_e is considered to be 4.5 mW from contact thermal resistance. The temperature distribution of a silicon wafer in case the outermost circumference quantity of heat q_e is 4.5 mW was calculated. The result is shown in Fig. 5. We confirmed that when the outermost circumference quantity of heat q_e is 4.5 mW, the total emissivity is about 0.5, and the heat of 1.6 W (64 % of input power) is radiated from an irradiation side. Furthermore, The irradiation side temperature in which electron beam is extracted and irradiated was calculated. The result is shown in Fig. 6. It is confirmed that if the electron beam is extracted and irradiated, the irradiation area becomes gradually high temperature.

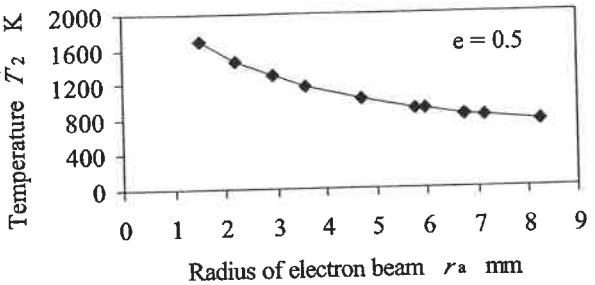

Fig. 6 Relationship between temperature and electron beam

7. Conclusion

(1) The temperature of silicon wafer which the electron beam which is extracted to the radius of 1.5 mm irradiates was analyzed in considering of the radiation and the heat conduction.
(2) We confirmed that when outermost circumference quantity of heat was 4.5 mW, the total emissivity was about 0.5, and the heat of 1.6 W (64 % of input power) was radiated from an irradiation area.
(3) The irradiation area temperature in which the radius of the electron beam is changed was confirmed.
(4) We confirmed that if the electron beam is extracted and irradiated, the irradiation area becomes gradually high temperature.

References

[1] H. Satoh, Y. Nakayama, N. Saitou, and T. Kagami, "Silicon shaping mask for electron-beam cell projection lithography", SPIE vol.2254 Photomask and X-Ray Mask Technology 123-132,1994.
[2] S. Kawata, N. Katakura, S. Takahashi, and K. Uchikawa, "Stencil reticle development for electron beam projection system", J. Vac. Sci. Technol. B17(6), 2864-2867,1999.
[3] B. Kim, R. L. Engelstad E. G. Lovell, S. T. Stanton, J. A. Liddle, and G. M. Gallatin, "Finite element analysis of SCALPEL wafer heating", J. Vac. Sci. Technol. B17(6), 2883-2887,1999.
[4] Isao Amemiya, H. Yamasita, S. Nakatsuka, I. Kimura, M. Tsukahara, S. Yasumatsu, and O. Nagarekawa, "Fabrication of complete 8 in. stencil mask for electron projection lithography", J. Vac. Sci. Technol. B20(6), 3010-3014,2002.
[5] A heat transmission handbook, the Japan Society of Mechanical Engineers

STIFFNESS ANALYSIS AND KINEMATIC MODELING OF STEWART PLATFORM FOR MACHINING APPLICATIONS

Satheesh G. Kumar, Bikshapathi M, Nagarajan T, Srinivasa Y. G.
PEIL Laboratory, Mechanical Engineering, IIT Madras, Chennai, India

Abstract: Today, the parallel manipulator robots play a very predominant role in Manufacturing Technology, because of their high stiffness, high payload capacity and simple structure. To machine complex shape of objects, the conventional machining equipments are not sufficient. For the improving product quality and reducing the product cost use of parallel manipulator is mandatory and the Stewart platform comes as a forerunner because of its 6-dof capability. In this paper a concise kinematic modeling of a Stewart platform and stiffness analysis is done. A MATLAB code was written implementing the Maximum stiffness model for the different trajectories within the workspace. The trajectory with maximum stiffness for different contours is obtained using the model.

Keywords: stiffness, Stewart platform, trajectory

Introduction: Stiffness is one of the important considerations in the design of Stewart platform based Parallel Kinematic Machines (PKM). The stiffness of the Stewart platform manipulator is not constant throughout its workspace. It depends on the position and orientation of the mobile platform. The stiffness varies with the direction in which it is computed, the posture (or configuration) of the manipulator. The stiffness matrix can be found out by using inverse kinematics through the position analysis and Jacobian matrix. A lot of research work has taken place in order to model the stiffness of the Stewart platform. The developed model is used for the benefit of less power consumption in machining operations without going for high-powered configurations and complex designs in Stewart platform.

This work focuses on stiffness variations of Stewart platform, varying positions and orientation of the moving platform offline for different trajectories within the workspace. An optimal solution is obtained for maximum stiffness with respect to each trajectory.

Stewart Platform as a Machine Tool: The most important properties of the industrial robots are the high speed, fast acceleration and a large working area compared with machine tools. Parallel kinematics combines successfully these properties. The kinematics is very simple, and it consists of three sections

- Struts (legs), which can change their length generally ball screws are used as these struts.
- One fixed and a movable platform. The fixed platform serves as a rigid frame, which does not deflect under load, and this platform contains the drive mechanism. The moving platform gives the space to the main spindle, gripper or any other unit.
- Joints connect the kegs and transfer the load energy.

The advantages of the parallel kinematics are reduction of moving masses and a higher stiffness. Bending moments do not take effect or they are minimized, therefore a small diameter strut can be used to make a stiff structure. Struts under compression have a tendency to buckle, usually it sets limit to the load. The disadvantages are the relatively small rotating range of the moving platform and due to the kinematics of the hexapod even a simple linear movement requires the simultaneous control of 6 axes.

INVERSE KINEMATICS

Position Analysis Of A Stewart Platform: The given fig 1 shows a spatial 6-dof, 6 SPS parallel manipulator having a six identical limbs connecting the moving platform to the fixed base through spherical joints at points B_i and A_i, for i = 1,2...6 respectively. First, we derive the location of each limb in terms of the location of the moving platform. The vector loop equation can be written as

$$a_i + d_i s_i = P + b_i \qquad (1)$$

where $a_i = [a_{ix}, a_{iy}, 0]^T$ denotes the position vector of A_i with respect to the fixed frame, ${}^B b_i = [b_{iu}, b_{iv}, 0]^T$ denotes the position vector of B_i with respect to the moving frame, $b_i = [b_{ix}, b_{iy}, b_{iz}]^T$ represents the vector ${}^B b_i$ expressed in the

fixed frame (i.e., $b_i = {}^A R_B \, {}^B b_i$), where s_i is a unit vector pointing from A_i to B_i and d_i is the length of limb i. Solving for s_i from the above equation,

$$s_i = \frac{P + b_i - a_i}{d_i} \tag{2}$$

where, $d_i = P + {}^A R_B \, {}^B b_i - a_i$ (3)

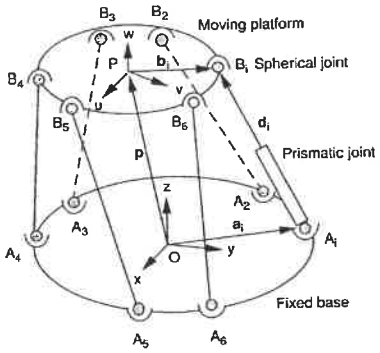

Fig.1: General Stewart platform

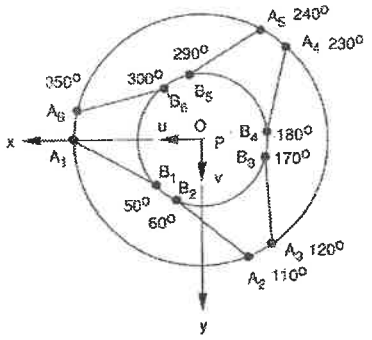

Fig.2: Top view of Stewart platform

For the inverse kinematics problem, the position vector P and rotation matrix ${}^A R_B$ of frame B with respect to A are given and the limb length d_i, i = 1, 2 ...6 are found to be,

$$d_i = \pm\sqrt{[P + {}^A R_B \, {}^B b_i - a_i]^T [P + {}^A R_B \, {}^B b_i - a_i]} \tag{4}$$

For i = 1, 2...6. Hence, corresponding to each given location of the moving platform, there are generally two possible solutions for each limb. However, the negative limb length is physically not feasible.

Jacobian Analysis of Parallel Manipulators: An important limitation of a parallel manipulator is that singular configuration may exist within its workspace where the manipulator gains one or more degrees of freedom and therefore loses its stiffness completely, which is undesirable. This property is included in the developed model using the Jacobian matrix. From the above fig 1, the output vector is given by $\Delta \dot{q} = [\dot{d}_1, \dot{d}_2, \dot{d}_3, \dot{d}_4, \dot{d}_5, \dot{d}_6]^T$, and the input vector is described by the vector of the centroid P and the angular velocity of the moving platform:

$$\dot{X} = [V_p, w_B]^T \tag{5}$$

The Jacobian matrix can be derived by formulating a velocity loop-closure equation for the i^{th} limb can be written as

$$\overline{OP} + \overline{PB_i} = \overline{OA_i} + \overline{A_i B_i} \tag{6}$$

Differentiating the above equation with respect to time yields

$$v_p + \omega_B \times b_i = d_i \omega_i \times s_i + \dot{d}_i s_i \tag{7}$$

where, bi and S_i denote the vector $\overline{PB_i}$ and a unit vector along $\overline{A_i B_i}$ respectively, and ω_i denotes the angular velocity of the i^{th} limb with respect to the fixed frame A. The above equation can be written in matrix form, which yields a scalar equation i.e.,

$$J_x \dot{X} = J_q \dot{q} \tag{8}$$

Hence the overall Jacobian matrix is given by

$$J = J_q^{-1} * J_x = \begin{pmatrix} s_1^T & (b_1 \times s_1)^T \\ s_2^T & (b_2 \times s_2)^T \\ s_3^T & (b_3 \times s_3)^T \\ s_4^T & (b_4 \times s_4)^T \\ s_5^T & (b_5 \times s_5)^T \\ s_6^T & (b_6 \times s_6)^T \end{pmatrix} \tag{9}$$

Stiffness Modeling: Stewart platforms in particular are increasingly being studied for possible use in multi-axis machine tools. An important consideration in the design of such machine is their stiffness. For a given design, stiffness varies with the direction in which it is computed, the posture (or configuration) of the mechanism and the direction of the actuation or disturbing force. The stiffness matrix for the parallel manipulator given by,

$$K = J^T \chi J \tag{10}$$

where, χ - the axial stiffness of the legs being equal and

J^T - the transpose of Jacobian matrix.

The above equation implies that the end-effector output force is related to its deflection by the stiffness matrix K. Further more, if the limbs are of the same type and the spring constants associated with all the drivelines are of the same valve (i.e., $k_1=k_2=k_3=k_4=k_5=k_6$), the stiffness matrix reduces to the form:

$$K = kJ^T J \tag{11}$$

COMPUTER SIMULATION AND DISCUSSION

CASE 1: For the first simulation, the orientation of the moving platform remains constant while the position vector of moving platform is given a sine wave motion. The displacement of the moving platform for this purpose is given by: $\Delta X = [0,0,1.0+0.2*\sin wt,0,0,0]$.

Conditions: $\psi = 0; \theta = 0; \phi = 0;$ P = [0 0 (1.0 + 0.2*sinwt)], where w = 3.0 rad/sec.

The moving platform is moving along Z direction alone without any orientation changes. Fig 3(a) shows the sine wave motion of the moving platform in y-axis and the x-axis shows the time in seconds. Fig 3(b) shows the leg length variation when the moving platform moves along the Z-direction. Fig 3(c) shows the stiffness variation of the Stewart platform when moving only in Z-direction without any rotation of moving platform. Fig 3(d) shows the corresponding actuators deflections.

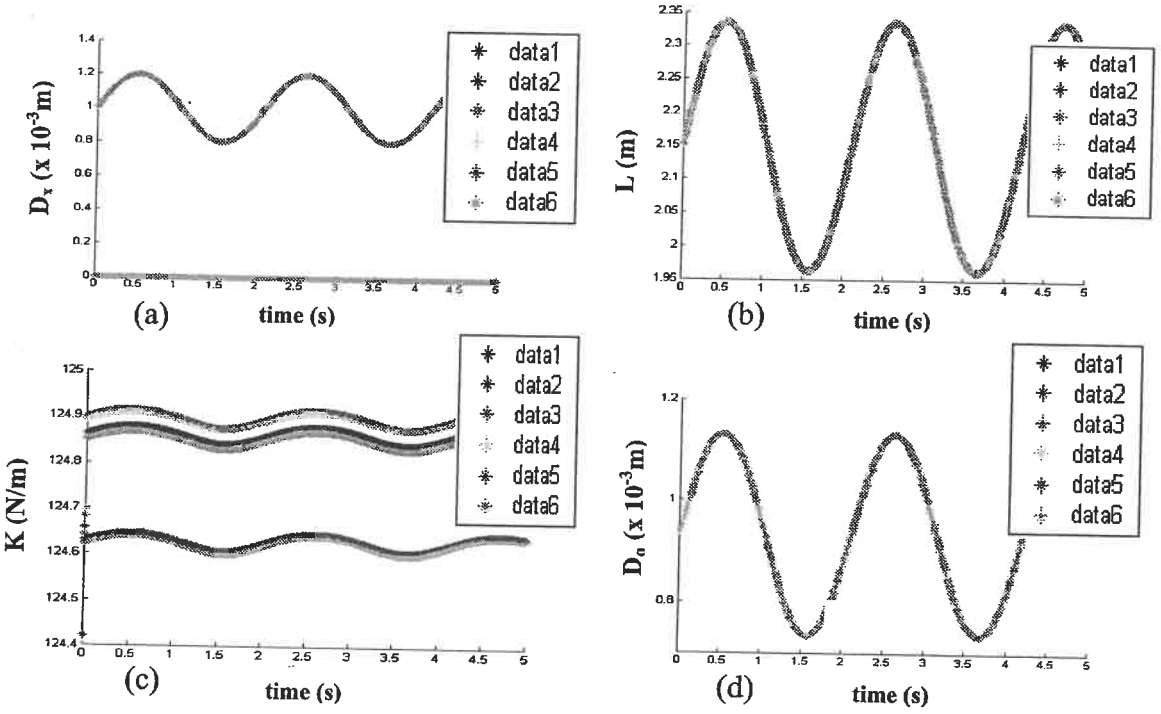

Fig. 3: Plots for Sine wave trajectory in Z direction

CASE 2: For the next simulation, the moving platform will follow the circular path, with a radius of 200mm along x and y directions and at a constant linear velocity of 0.0133m/s. For the circular trajectory displacement is given by,

$$\Delta x = [p_x + r*\sin\beta, P_y + r*(1-\cos\beta), p_z, \psi, \theta, \phi]$$

where r - the radius of the circular machining path trajectory which is 0.2 m

β - the cutter angle position with respect to the tool cutter (i.e. β = (feed rate/ radius) * time.

The orientation of the platform is varied as: ψ = -15 to15 deg; θ = -10 to 15 deg; ϕ = -15 to 20 deg.

Conditions: P_x = 0.8660; P_y = 0.5000; P_z = 3.0000; ψ = -10.0000; θ = 15.0000; ϕ = 0;

Maximum stiffness value is 7.1219e+004 N/m

From the fig 4(a) indicates that the moving platform displacement along the circular trajectory. For the corresponding circular path the leg length variations are shown in fig 4(b). The leg lengths, which are obtained from this simulation, are within range and satisfy the workspace criterion also. Fig 4(c) shows the trajectory, which has maximum stiffness and the stiffness variation within the trajectory. The maximum stiffness path has minimum stiffness variation along the trajectory. Fig 4(d) shows the variations of actuator's displacements when it starts at zero (at time t = 0).

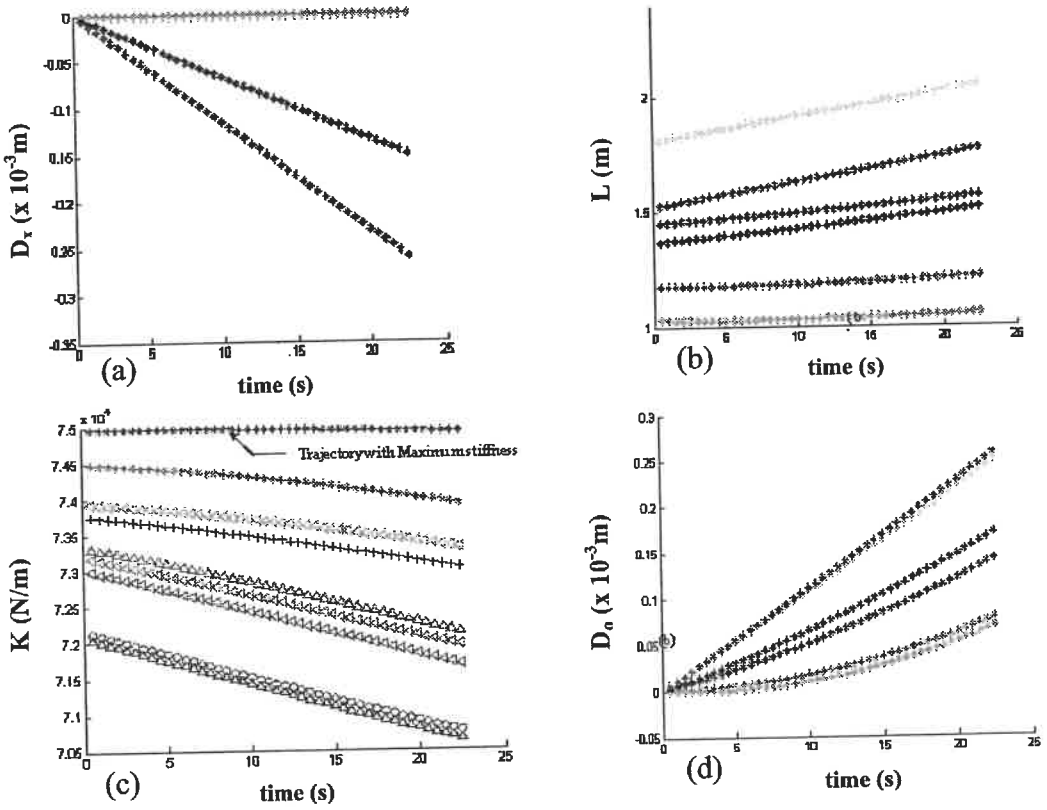

Fig. 4: Plots for circular trajectory

CONCLUSION

Mathematical model has been derived for the Stiffness of Stewart platform. A MATLAB code was written implementing the Maximum stiffness model for the different trajectories within the workspace. The trajectory with maximum stiffness for different contours were obtained with the above model, the results of which were shown for two cases. The results obtained with this stiffness model were found to be valid and implementable. By changing the position and orientation of the moving platform the model was tracked and was found to guarantee valid results throughout, although no attempt has been made to estimate the computational efficiency of the algorithm. The leg length variations and the corresponding actuator displacements were also studied and were found to be within the workspace. The output of this work can be used to get important design information with respect to stiffness of the Stewart platform manufactured for machining purposes.

LIST OF REFERENCES

[1] Tsai, L.W., Robotic Analysis: The Mechanics of Serial and Parallel Manipulators, John-Wiley & Sons, New York, 1999.

[2] Bhaskar Dasgupta, T.S Mruthyunjaya. "The Stewart platform manipulator: A review", Mechanism and Machine theory, Vol. 35, 15-40, 2000.

[3] S. Pugazhenthi, T.Nagarajan and M.Singaperumal, "Optimal trajectory planning for a hexapod machine tool during contour machining", Journal of Mechanical Engineering Science, Vol. 216, 1247-1257, 2002.

COMPENSATION FOR DISTORTION OF DYNAMIC SENSOR DATA USING RECEPTANCE COUPLING

Tony L. Schmitz
University of Florida, Department of Mechanical and Aerospace Engineering, Gainesville, FL 32611

1. INTRODUCTION

Sensors can be used to record a number of phenomena on mechanical structures. Applications of this sensor data include process metrology, condition-based maintenance, general fault diagnosis, and non-destructive evaluation, for example. In many cases, the recorded information is dynamic in nature and minimum requirements for the sensor frequency response, in addition to accuracy, resolution, and durability, are required. However, even if a satisfactory sensor (or sensors) is selected, if the sensor cannot be placed directly at the point of interest, the structural dynamics between the two locations can adversely affect the measured signal through both scaling errors and distortion of the frequency content. In this work, a unified mathematical approach for assembly dynamics prediction using receptance coupling techniques is presented. The predicted models can be applied to remove the effects of structural dynamics on the measured data and select high signal-to-noise ratio sensor mounting locations.

2. METHOD DESCRIPTION

Substructure analysis, or component mode synthesis, methods have been used for several decades to predict the dynamic response of assemblies using measurements and/or models of the individual components, or substructures. These components can be represented by spatial mass, stiffness, and damping data; modal data; or receptances [e.g., 1-4]. The latter representation is generally preferred in situations where the assembly receptances are the desired analysis output, as is the case here. This research builds on the previous receptance coupling work by including both translational and rotational degrees of freedom and applying the assembly dynamics models to sensor data compensation.

To demonstrate the method, consider the prismatic cantilever beam-cylinder assembly shown in Fig. 1, where a harmonic force, $F_1(t)$, is applied to the free end of the cylinder, coordinate X_1, and the resulting displacement $X_1(t)$ is to be determined. The preferred solution is to place an appropriate linear transducer at this location and record the required displacement directly. However, if access to the cylinder is obstructed, it may be required to place the sensor remotely at coordinate X_2, for example. Due to the change in cross-section and increased stiffness, there is reduced sensitivity to the X_1 vibrations for X_2 measurements. Additionally, the vibration measured at X_2 can be influenced by the assembly's structural response between coordinates X_1 and X_2. Finally, X_2 may be located at a node of one of the assembly mode shapes.

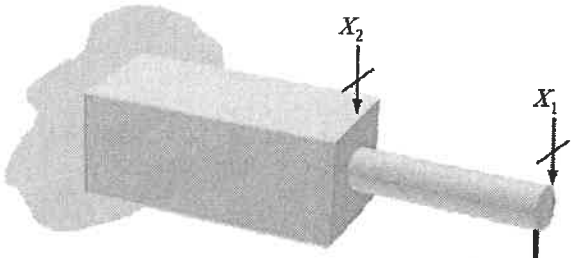

Figure 1: Method description example. The displacement, $X_1(t)$, due to the harmonic force, $F_1(t)$, is desired, but measurements can only be performed at coordinate X_2.

In order to determine $X_1(t)$ from X_2 measurements, the following three steps are carried out.

1. Measure the time-domain response $X_2(t)$ and Fourier transform to obtain the frequency-domain result $X_2(\omega)$.
2. The relationship between $X_2(\omega)$ and $F_1(\omega)$ can be expressed by:

$$X_2(\omega) = H_{21} F_1(\omega), \tag{1}$$

where H_{21} is the assembly displacement-to-force cross receptance between coordinates X_2 and X_1. Solving for F_1 gives $F_1(\omega) = H_{21}^{-1} X_2(\omega)$. This result can be substituted in the equation relating $X_1(\omega)$ and $F_1(\omega)$ to obtain:

$$X_1(\omega) = H_{11} F_1(\omega) = H_{11} H_{21}^{-1} X_2(\omega), \tag{2}$$

where H_{11} is the assembly displacement-to-force direct receptance at coordinate X_1.

3. Inverse Fourier transform $X_1(\omega)$ to obtain $X_1(t)$. This result now provides the required information and removes the influence of the structural dynamics between X_1 and X_2. Note that the time-domain force, $F_1(t)$, is also available by inverse Fourier transforming $F_1(\omega)$.

To carry out these steps, the assembly displacement-to-force receptances $H_{11}(\omega)$ and $H_{21}(\omega)$ must be known. The straightforward approach is to measure them directly using some external mechanical excitation, such as a hammer or shaker, and record the response using a linear transducer, e.g., accelerometer, vibrometer, or

displacement probe. However, there may be situations where either the measurements are difficult to carry out (due to mechanical obstruction) or the assembly changes regularly (for example, multiple tools and holders may be used in a single milling spindle [5-8]). In these cases, an accurate model is required.

One choice for developing the model is finite element analysis, or FEA, which can provide quality estimates of natural frequency and mode shapes. A current limitation of this method, however, is the treatment of joints, particularly the energy dissipation, or damping, at contact interfaces. This is critically important in the sensor data compensation proposed here because properly scaled assembly receptances, which depend strongly on damping, are required. In many cases, an FEA *a priori* prediction of assembly dynamics from design drawings is difficult or impossible. As an alternative, receptance coupling offers a hybrid method where measured receptances can be coupled to modeled receptances through appropriate connections, which can include both finite stiffness and non-zero damping. The general approach is to measure those components with difficult-to-predict behavior and model those components that are more suited to successful prediction using modeling techniques.

To determine the dynamics for the assembly shown in Fig. 1 by receptance coupling, several considerations must be made. First, only displacement-to-force receptances, H_{ij}, have been discussed so far. However, if accurate assembly predictions are to be made, all four bending receptances must be included in the component descriptions (i.e., displacement-to-force, H_{ij}, displacement-to-moment, L_{ij}, rotation-to-force, N_{ij}, and rotation-to-moment, P_{ij}). Second, the compatibility conditions at the component interfaces must be selected; these can be rigid, flexible with no damping, or flexible with damping. Third, the component receptances must be determined. If measurements are completed, care must be taken to accurately record all four receptances with adequate bandwidth and resolution. The steps required to predict the Fig. 1 assembly receptances follow.

1. Define the components and coordinates for the model. In this simple example, two components can be defined: a prismatic cantilever and free-free cylinder (see Fig. 2).
2. Describe the component receptances. Both measurements and models can be used. For the models, the closed-form receptance functions presented by Bishop and Johnson [1] for the analysis of flexural vibrations of uniform Euler-Bernoulli beams with free, fixed, sliding, and pinned boundary conditions are applied here. For example, the direct and cross receptances for the free-free cylinder due to the component forces $f_1(t)$ and $f_2(t)$, applied at coordinates $x_1(t)$ and $x_2(t)$, respectively, and moments $m_1(t)$ and $m_2(t)$, applied at $\theta_1(t)$ and $\theta_2(t)$, respectively, are compactly represented in Eq. (3) (lower case notation is used to designate component variables).

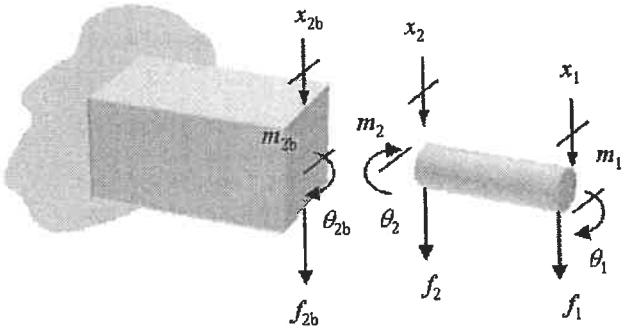

Figure 2: Components for the receptance coupling example. Two components are connected to form the assembly.

$$\begin{Bmatrix} x_1 \\ \theta_1 \end{Bmatrix} = \begin{bmatrix} h_{11} & l_{11} \\ n_{11} & p_{11} \end{bmatrix} \begin{Bmatrix} f_1 \\ m_1 \end{Bmatrix} \text{ or } \{u_1\} = [R_{11}]\{q_1\},$$
$$\begin{Bmatrix} x_2 \\ \theta_2 \end{Bmatrix} = \begin{bmatrix} h_{22} & l_{22} \\ n_{22} & p_{22} \end{bmatrix} \begin{Bmatrix} f_2 \\ m_2 \end{Bmatrix} \text{ or } \{u_2\} = [R_{22}]\{q_2\} \quad (3)$$
$$\begin{Bmatrix} x_1 \\ \theta_1 \end{Bmatrix} = \begin{bmatrix} h_{12} & l_{12} \\ n_{12} & p_{12} \end{bmatrix} \begin{Bmatrix} f_2 \\ m_2 \end{Bmatrix} \text{ or } \{u_1\} = [R_{12}]\{q_2\},$$
$$\begin{Bmatrix} x_2 \\ \theta_2 \end{Bmatrix} = \begin{bmatrix} h_{21} & l_{21} \\ n_{21} & p_{21} \end{bmatrix} \begin{Bmatrix} f_1 \\ m_1 \end{Bmatrix} \text{ or } \{u_2\} = [R_{21}]\{q_1\}$$

where R_{ij} is the generalized receptance matrix that describes both translational and rotational component behavior [8]. The individual entries in these matrices depend on the boundary conditions and include contributions from both the rigid body (if applicable) and flexural modes. For example, at the right end of the free-free cylinder, the R_{11} matrix terms are:

$$h_{11}(\omega) = \frac{x_1}{f_1} = \frac{-(\cos\lambda L \sinh\lambda L - \sin\lambda L \cosh\lambda L)}{EI(1+\eta)\lambda^3(\cos\lambda L \cosh\lambda L - 1)} \quad (4)$$

$$l_{11}(\omega) = \frac{x_1}{m_1} = n_{11}(\omega) = \frac{\theta_1}{f_1} = \frac{-(\sin\lambda L \sinh\lambda L)}{EI(1+\eta)\lambda^2(\cos\lambda L \cosh\lambda L - 1)}$$

$$p_{11}(\omega) = \frac{\theta_1}{m_1} = \frac{(\cos\lambda L \sinh\lambda L + \sin\lambda L \cosh\lambda L)}{EI(1+\eta)\lambda(\cos\lambda L \cosh\lambda L - 1)},$$

where $\lambda = \left(\frac{m\omega^2}{LEI(1+i\eta)}\right)^{\frac{1}{4}}$, m is the beam mass (kg), ω is the frequency (rad/s), L is the beam length (m), E is the elastic modulus (N/m^2), I is the 2nd area moment of inertia (m^4), and η is the structural damping factor (unitless).

[Damping was not included in reference [1], but has been added as part of this analysis.] These receptances can be used to couple components at their end points in order to determine assembly dynamics.

3. Based on the selected model from step 1, express the assembly receptances (see Eq. (5), where upper case notation is used to designate assembly variables). These receptances are determined by first writing the component displacements/ rotations as shown in Eq. (6).

$$\begin{Bmatrix} U_1 \\ U_2 \end{Bmatrix} = \begin{bmatrix} G_{11} & G_{12} \\ G_{21} & G_{22} \end{bmatrix} \begin{Bmatrix} Q_1 \\ Q_2 \end{Bmatrix}, \text{ where}$$

$$U_i = \begin{Bmatrix} X_i \\ \Theta_i \end{Bmatrix}, \quad G_{ij} = \begin{bmatrix} H_{ij} & L_{ij} \\ N_{ij} & P_{ij} \end{bmatrix}, \text{ and} \quad Q_i = \begin{Bmatrix} F_i \\ M_i \end{Bmatrix} \tag{5}$$

$$u_1 = R_{11}q_1 + R_{12}q_2 \quad u_2 = R_{21}q_1 + R_{22}q_2 \tag{6}$$
$$u_{2b} = R_{2b2b}q_{2b}$$

If the prismatic cantilever beam-cylinder assembly is considered to be a solid body with the cylindrical portion formed by turning one end of the beam down to its final diameter, for example, a rigid connection is applied at the component interface and the compatibility conditions are:

$$u_2 - u_{2b} = 0 \text{ and } u_i = U_i,\ i = 1 \text{ to } 2, \tag{7}$$

where the latter expression specifies that the component and assembly coordinates are defined at the same spatial positions. The equilibrium conditions vary with the external force/moment location. To determine the first column of the assembly receptance matrix in Eq. (5), Q_1 is applied to coordinate U_1. In this case, the equilibrium conditions are:

$$q_2 + q_{2b} = 0 \text{ and } q_1 = Q_1. \tag{8}$$

Substitution of the component displacements/rotations and equilibrium conditions into the compatibility conditions yields q_2 (see Eq. (9)). The expression for G_{11} is then given by Eq. (10). The other first column receptance is determined in a similar manner; G_{21} is shown in Eq. (11). To find the receptances in the second column, Q_2 must be applied to U_2.

$$q_2 = -\left(R_{22} + R_{2b2b}\right)^{-1} R_{21} Q_1 \tag{9}$$

Equations (10) and (11) contain the assembly receptances required to solve Eq. (2) for $X_1(t)$ from sensor data recorded at X_2. In this example, these receptances were developed analytically using material properties and component geometry. However, any of the component response terms could also be replaced by actual measurement data (no curve fitting or modal parameter estimation is required).

$$G_{11} = \frac{U_1}{Q_1} = \frac{u_1}{Q_1} = \frac{R_{11}q_1 + R_{12}q_2}{Q_1} =$$
$$R_{11} - R_{12}\left(R_{22} + R_{2b2b}\right)^{-1} R_{21} = \begin{bmatrix} H_{11} & L_{11} \\ N_{11} & P_{11} \end{bmatrix} \tag{10}$$

$$G_{21} = \frac{U_2}{Q_1} = \frac{u_2}{Q_1} = \frac{R_{21}q_1 + R_{22}q_2}{Q_1} =$$
$$R_{21} - R_{22}\left(R_{22} + R_{2b2b}\right)^{-1} R_{21} = \begin{bmatrix} H_{21} & L_{21} \\ N_{21} & P_{21} \end{bmatrix} \tag{11}$$

3. EXPERIMENTAL EVALUATION

To verify the receptance coupling approach, frequency response measurements were carried out on a 827.9 mm x 76.2 mm x 16.1 mm plastic beam using a small impact hammer (PCB 086D80) to excite the beam and low mass accelerometer (PCB 352B10) to record the response [9]. Free-free boundary conditions were approximated by suspending the beam vertically from a thin flexible wire (a 2 mm diameter hole was drilled at one end). The receptance coupling model of the constant cross-section prismatic beam was verified by measuring the direct frequency response function (FRF) at the 'free' end of the beam (away from the wire suspension) and comparing to the predicted response. The predicted and measured direct FRF are shown in Fig. 3. To populate the receptance model, the beam mass (944.3 g) and dimensions were recorded and the 2nd area moment of inertia was calculated. The modulus and structural damping factor were considered free parameters to enable a good fit between the model and data ($E = 1.37\text{x}10^9$ N/m^2 and $\eta = 0.035$).

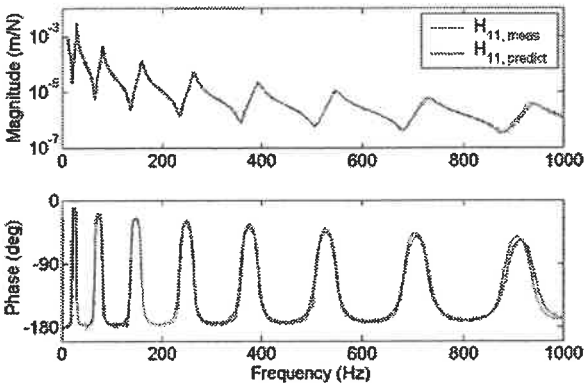

Figure 3: Measurement and model of plastic beam.

3.1 Force prediction using acceleration data

As described in Section 2, the externally applied force can be determined from the measured response and system FRF model. To verify this approach experimentally, the suspended plastic beam was excited at its 'free' end using the impact hammer and the response was measured at the same location using the accelerometer. Both signals were analog low-pass

filtered with a cutoff frequency of 1 kHz prior to digital sampling at 50 kHz for 2 sec. The measured acceleration, $a_1(t)$, was then Fourier transformed and pre-multiplied by the inverted direct accelerance, equal to the product of $-\omega^2$ and the modeled direct receptance $H_{11}(\omega)^{-1}$, to find the frequency domain force, $F_1(\omega) = \left(-\omega^2 \cdot H_{11}\right)^{-1} A_1(\omega)$. This result was then inverse Fourier transformed and compared to the input force due to the hammer impact. The force results and measured acceleration are shown in Fig. 4. The reader may note that the ringing in the hammer force is due to the analog low pass filtering.

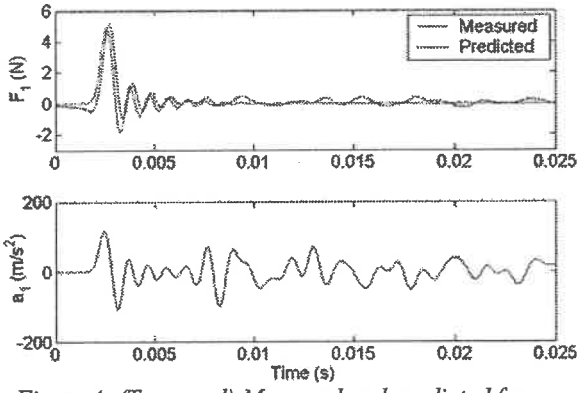

Figure 4: (Top panel) Measured and predicted forces; (bottom panel) acceleration response to F_1 force input.

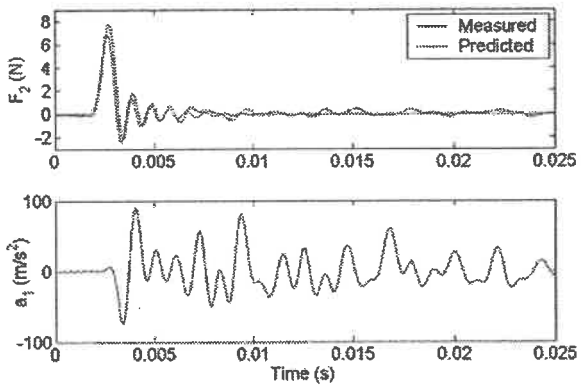

Figure 5: (Top panel) Measured and predicted forces; (bottom panel) acceleration response to F_2 force input.

3.2 Correction for accelerometer placement

The exercise in Section 3.1 was repeated, except the accelerometer was not placed at the hammer input location. In this case, the hammer impact occurred 254 mm from the beam 'free' end. If this position is referred to as X_2, then the receptance $H_{12}(\omega)$ can be used to determine the force, $F_2(\omega) = \left(-\omega^2 \cdot H_{12}\right)^{-1} A_1(\omega)$. The $H_{12}(\omega)$ receptance is found by artificially separating the beam into two components at X_2 and then joining the components with lengths of 254 mm and (827.9-254) = 573.9 mm. See Fig. 5. Note that incorrect results are obtained if only the displacement-to-force receptances are used.

4. CONCLUSIONS

This paper describes the use of receptance coupling techniques to build dynamic models of assemblies in order to compensate for scaling and frequency distortion errors arising from non-ideal sensor placement on mechanical structures. The receptance coupling equations provided here include both translational and rotational degrees of freedom, as well as the potential for non-rigid connections between substructures.

Experimental results are provided for a plastic prismatic beam and it is shown that force signals can be recovered from acceleration measurements at: 1) the force input position; and 2) other locations. An impact force was applied so that a broad range of structural modes would be excited simultaneously and, therefore, provide a rigorous test for the approach.

5. ACKNOWLEDGMENTS

The author gratefully acknowledges partial financial support for this research from the National Science Foundation (DMI-0238019) and Office of Naval Research (2003 Young Investigator Program). The author also thanks G. S. Duncan for contributions to this work.

6. REFERENCES

1. Bishop, R.E.D. and Johnson, D.C., 1960, The Mechanics of Vibration, Cambridge University Press, Cambridge.
2. Hurty, W.C., 1965, Dynamic Analysis of Structural Systems using Component Modes, *AIAA Journal* 3/4: 678-685.
3. Klosterman, A.L., and Lemon, J.R., 1969, Building Block Approach to Structural Dynamics, *American Society of Mechanical Engineering Annual Vibration Conference*, publication VIBR-30.
4. Ren, Y. and Beards, C.F., 1995, On Substructure Synthesis with FRF Data, *Journal of Sound and Vibration* 185: 845-866.
5. Schmitz, T.L. and Donaldson, R., 2000, Predicting High-Speed Machining Dynamics by Substructure Analysis, *Annals of the CIRP* 49/1: 303-308.
6. Schmitz, T.L., Davies, M.A., and Kennedy, M., 2001, Tool Point Frequency Response Prediction for High-Speed Machining by RCSA, *ASME Journal of Manufacturing Science and Engineering* 123: 700-707.
7. Schmitz, T.L., Davies, M.A., Medicus, K., and Snyder, J., 2001, Improving High-Speed Machining Material Removal Rates by Rapid Dynamic Analysis, *Annals of the CIRP* 50/1: 263-268.
8. Park, S.S., Altintas, Y., and Movahhedy, M., 2003, Receptance Coupling for End Mills, *International Journal of Machine Tools and Manufacture*, 43: 889-896.
9. Equipment manufacturers are specified for completeness. This does not imply endorsement by the author or the University of Florida.

A PRECISION ACTIVE AEROSTATIC SPINDLE WITH AN AXIAL POSITIONING ACTUATOR

Tadahiko Shinshi, Toshiki Hayashi, Yusuke Inami, Hitoshi Hashizume,
Kaiji Sato and Akira Shimokohbe
Precision and Intelligence laboratory, Tokyo Institute of Technology
4259 Nagatsuda Midori-ku Yokohama, 226-8503, Japan

1. Introduction

Many types of miniaturized machine tools have been developed for machining micro mechanical parts and to save energy, space and resources [1-3]. The next targets for the miniaturized machine tools will be multi-axis and ultra-precision machining. Conventional multi-axis machine tools are constructed from several stacked one-degree-of-freedom (one-DOF) positioning mechanisms to realize multi-degrees-of-freedom motion [4]. The stacked positioning mechanism is not suitable for miniaturization or ultra-precision motion control, due to the cumulative effect of the space occupied by several one-DOF positioning mechanisms and non-collocation of actuators with displacement feedback sensors.

In ordinary vertical milling machines, a two-DOF motion table and a spindle moving in the vertical direction are normally realized by assembling several one-DOF motion tables, consisting of lead screws, one-DOF linear guideways, servomotors and rotary encoders. The larger the number of the stacked one-DOF positioning mechanism becomes, the larger the actuators that are required to move the mass of the other DOF motion mechanisms. Furthermore, the mass centers of the positioning tables or the spindle and the locations of the displacement sensors are not collocated. Such non-collocations can cause motion and machining errors.

One solution for realizing an ultra-precision and miniaturized machine tooling is to develop a multiple-degrees-of-freedom-controlled positioning mechanism without stacking several one-degrees-of freedom-positioning mechanism, thus only one mass is directly moved multi-directionally by several actuators.

Our research group is developing a compact nano-machine tool (high-precision vertical milling machine) featuring nano-positioning resolution that can be placed on a normal-sized desk. The compact nano-machine tool consists of a novel X-Y-Θ motion table system, in which the square table is levitated with compressed air and is directly driven by six voice coil motors with three-axis laser feedback [5], and an aerostatic spindle integrated with an axial positioning actuator and an air motor, in which the ordinary precision spindle and the stacked one-DOF positioning mechanisms are not required.

This paper reports on the design and fabrication of a precision aerostatic spindle integrated with axial positioning actuator, precision measurement system and an air motor. The dynamic characteristics of the spindle have been evaluated.

2. Active Aerostatic Spindle

The principle of the proposed spindle is shown in Fig. 1. The main spindle is supported by two radial air bearings, placed at the both ends of the spindle housing. The aerostatic bearings not only support the radial motion of the main spindle, but they also work as a linear guideway in the axial direction of the spindle. As a result of the averaging effect of compressed air

in gaps between the main spindle and air bearings, the main spindle can rotate precisely and slide in the axial direction without restriction and friction. Thus a one-DOF table system to move the spindle in the axial direction can be omitted.

The main spindle is moved and positioned in the axial direction by utilizing the Lorentz force between a permanent magnet in the main spindle and air-core coils in the spindle housing. The Lorenz force, in proportion to the value of the current in the coil, acts in the axial direction. The reaction force against the Lorentz force moves the main spindle in the axial direction. Such a driving mechanism is as same as that in voice coil motors, except the spindle can also precisely rotate. The advantage of the air-core coil is the freedom from an unbalanced pull which would be generated in the radial direction between electromagnets and steel cores and having longer stroke than the electromagnets, while the draw-back is the small driving force in the axial direction, compared with that obtainable from electromagnets having steel cores. However, the small driving force may not be a major drawback for micro machining, because this operation does not require much axial force.

Feedback control is necessary in order to control the position of the main spindle in the axial direction. To measure the axial displacement of the main spindle with a laser interferometer system, a plane mirror is precisely attached at the end of the main spindle, in order to minimize the inclination of the mirror to the rotational axis. Abbe's principle and the collocation of the sensor and actuator are satisfied in this spindle system.

An air turbine is used to rotate the main spindle, being light and compact, and able to apply rotating torque while the spindle is moving in the axial direction. Furthermore the air turbine drive not only generates less

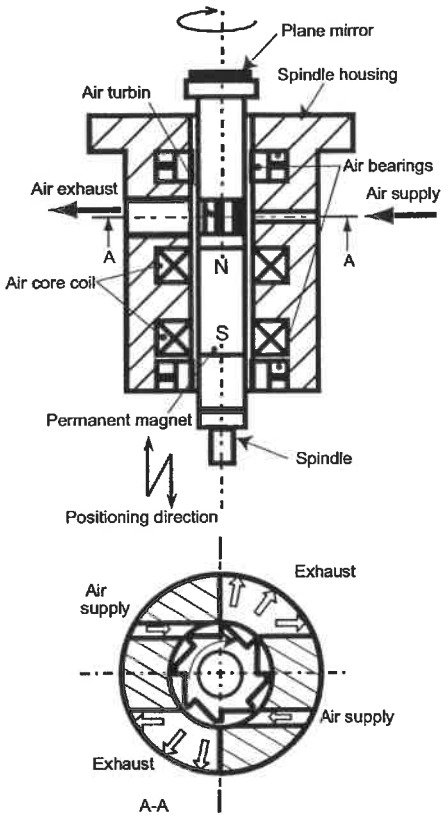

Fig. 1 Principle of an aerostatic spindle with an axial positioning actuator

disturbance force interfering with the axial magnetic actuator, but also is expected to have the effect of cooling the coils in the spindle housing due to adiabatic expansion of the air. Thus, thermal expansion of the spindle can be suppressed. The air turbine has eight blades and the turbine stator has two nozzles, placed symmetrically with respect to the rotational center to cancel the radial forces.

3. Fabrication

Figure 2(a) shows a fabricated main spindle. The length and diameter of the main spindle without the plane mirror are 147.5mm and 20mm respectively, and its weight, including a plane mirror, is 0.26 kg. The shaft core and the sleeves working as the air bearing rotor are made of SIALON (Si-Al-O-N) and alumina (Al2O3)

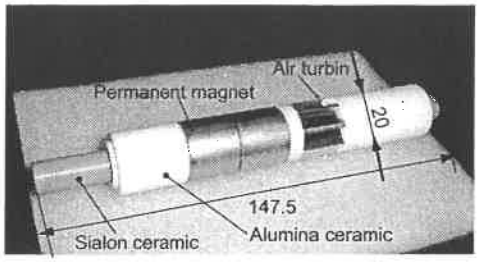

(a) Main spindle

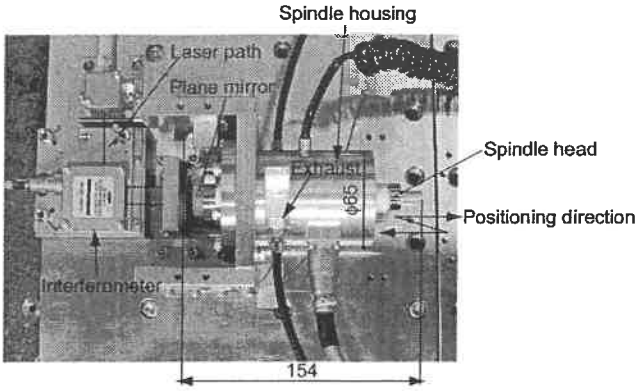

(b) Assembled spindle

Fig. 2 Test spindle

ceramic, respectively. SIALON is a ceramic with a large fracture resistance. The sleeves were precisely machined to attain concentricity of the order of sub-micrometer after being glued to the shaft core. The average air gap between the sleeves and air bearings in the spindle housing is 3μm. The measured stiffnesses of the air bearings at tool and plane mirror sides are 25N/μm and 50N/μm, respectively, while supplying compressed air at 0.5MPa at 1.7 NL/min.

The cylindrical permanent magnet, made from $Nd_2Fe_{14}B$, was glued to the shaft core, and was axially-magnetized after assembling and grinding the shaft. The air turbine, which is made of duralumin, was fixed to the shaft core using a shrink fit. The plane mirror for the laser interferometer measurement, with an effective diameter of 12mm, was precisely attached at the end of the shaft. The flatness of the plane mirror is 2.53nm rms.

In the spindle housing as shown in figure 2(b), a pair of coils, each comprising 357-turns, were placed and connected in series so that they generate magnetic flux in opposition. The coil current is supplied by a current-controlled amplifier. The actuator generates a driving force with 4.0 N/ Ampere.

The spindle is designed to have a 10mm positioning range in the axial direction. The displacement signal from a compact laser interferometer measuring system (Zygo Corp., ZMI 501), with the highest

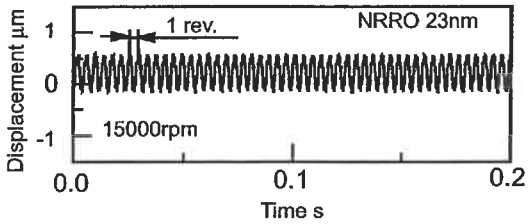

Fig. 3 Radial displacement at 15,000 rpm

resolution of 1.24 nm, with maximum velocity of 28.4 mm/s, provided a feedback signal. The position signal is input to a counter at 25MHz and used in a DSP board to calculate a control signal with a sampling period of 33 kHz. Precisely machined balance rings, which also act as sensor targets to evaluate the rotational accuracy, were attached at both ends of the spindle. The roundness of side surface of the balance rings is 0.11μm.

4. Positioning Test

The main spindle can be magnetically supported in the axial direction and can rotate at over 15,000 rpm, using the air motor turbine. The radial displacement of the main spindle was measured at the tool side using a capacitance type displacement sensor. The NRRO in the radial direction was about 23nm, as evaluated from the variation of positive displacement peak in the radial direction at 15,000rpm.

Figure 4 shows the 1μm step response of the main spindle in the axial direction while the spindle

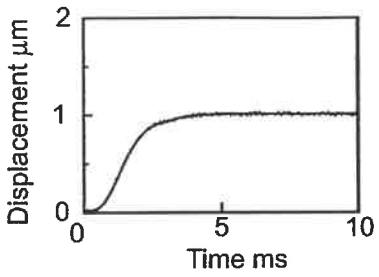

Fig. 4 Step response of 1μm

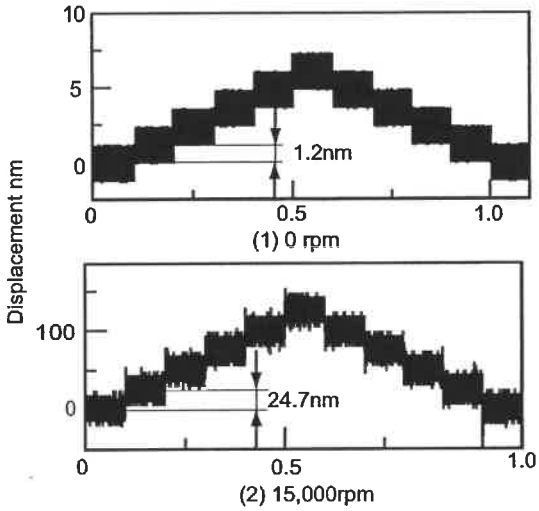

Fig. 5 Positioning resolution

was not rotating. Using the feedback signal from the high precision laser interferometer measurement system and feedforward compensation of the inverse transfer function of the closed loop system, both high speed and no overshoot response were attained. Long stroke positioning of ±5 mm was also verified.

Figure 5 indicates the positioning resolution in the axial direction with/without rotation. The positioning resolution decreases from 1.2nm at 0 rpm to 24.7nm 15,000rpm due to disturbing force of the air turbine. To improve the positioning resolution at a high speed, the bandwidth of the closed system needs to be extended.

The temperature rise on the spindle housing was measured while the spindle was rotating or stationary, as shown in Fig. 6. These data show the cooling effect of the air turbine.

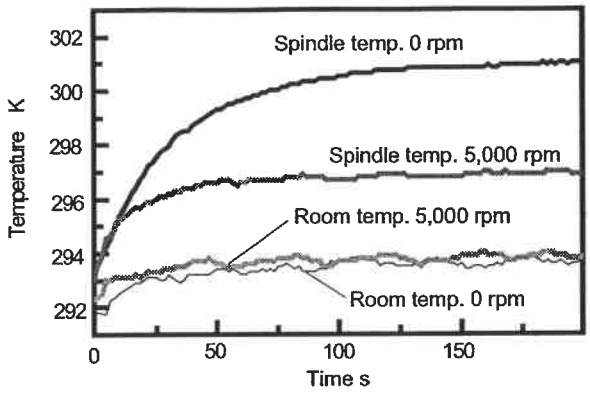

Fig.6 Temperature rise on the housing

5. Conclusions

A precision active aerostatic spindle with an axial positioning actuator was proposed and tested in order to realize a compact nano-machine tool. The spindle could rotate at over 15,000 rpm and had a positioning range and a resolution of ±5 mm and 24.7 nm, respectively, at 15,000 rpm. Future work will involve multi-axis and micro milling machining using the X-Y-Θ table system and this spindle. This research was supported by an Industrial Technology Research Grant Program in ' 02 from NEDO of Japan. The authors gratefully acknowledge the contribution of Dr. M. Fukuda of NTT for fabrication of the experimental spindle.

References

[1] Y. Okazaki and T. Kitahara, NC Micro-lathe to machine micro-parts, Proc. ASPE 2000 Annual Meeting, (2000) 575-579.

[2] T. Masuzawa: State of the art of micromachining, Annals of the CIRP,49, 2 (2000) 473-488.

[3] L. Alting, F. Kimura, H. N. Hansen and G. Bissacco, Micro Engineering, Annals of the CIRP, 52, 2 (2003) 635-657.

[4] K. Sawada, S. Odaka, K. Kawai, T. Hirai, Y. Takeuchi and T. Sata, Manufacture of diffraction grating on tiny parts by means of ultraprecision milling, Micro System Technologies, 5, (1999) 157-160.

[5]H. Shinno, H. Hashizume, et al., X-Y-Θ Nano-Positioning Table System for a Mother Machine, Annals of the CIRP, 53, 1 (2004) 337-340.

DESIGN OF AN EFFICIENT ACTIVE COOLED MESO-SCALE HEAT EXCHANGER USING FUNCTIONALLY GRADIENT MATERIALS

Ramkumar Subramanian, Patrick Kwon
Michigan State University, East Lansing, MI

The cooling system explored in this project is the fluid flow through an array of parallel micro-channels. Among the advantages of this cooling method is the closeness of the micro-channels to the heat source and therefore the thermal resistance is reduced. Among the disadvantages is the non-uniform variation of heat flux throughout the body of the heat exchanger. This in turn causes uneven expansion which results in high induced thermal strains, warping and even cracks. We propose to use Functionally Gradient Materials to offset this effect of thermal gradient loading.

1. INTRODUCTION

Micro-textured or Functionally Gradient Material (FGM) can be processed by spatially modulating the compositional ratio between two powders. An FGM ideally has continuous gradiency. One can approximate such gradient properties by preparing subcomponents in the form of layers. Each layer is prepared by homogeneously mixing two powders in various ratios, which can be stacked to form the 'discrete' gradiency in thermo-mechanical properties. One area of micromechanics is concerned with calculating the effective or bulk physical properties of locally inhomogeneous, but statistically homogeneous, materials such as composite materials. Composite materials consist of at least two distinct phases – the matrix material and the reinforcing material, whose properties are known. Rather than microscopically modeling each inclusion in a composite medium, a given inhomogeneous material can be replaced by an equivalent "effective medium". Structural and thermal properties of FGMs can be tailored by spatially varying the composition of the second-phase particles in the matrix material. This is achieved by modulating the concentration level of the second phase during fabrication. Therefore, the FGM fabrication processes should possess the ability to produce various distributions of particles to withstand assigned loading. For our finite element analysis, alumina and partially stabilized zirconia (PSZ) are chosen for their inherent interfacial strength and difference in their coefficient of thermal expansion (CTE) values. The Mori-Tanaka (1973) approach is used to solve for the properties of the FGM as a function of the volume fraction of the particles or fibers. Because of the almost similar sizes of the alumina and zirconia particles, the Mori-Tanaka mathematical model is solved twice, once for each of the two materials as the matrix. It is found that the properties of the intermediate discrete layers are almost similar by using either of the two models.

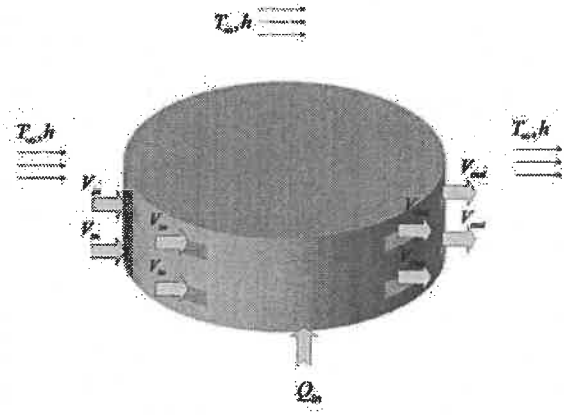

Fig 1: The Heat- Exchanger Model

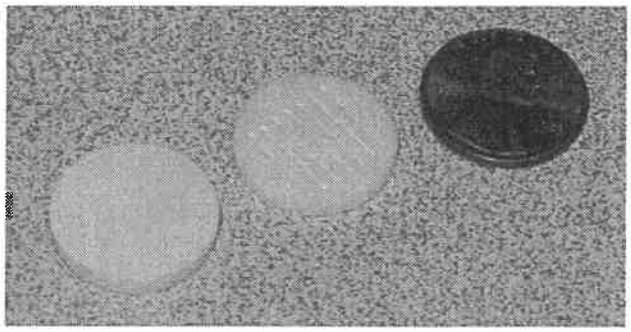

Fig 2: Photo of the micro-textured heat exchanger with internal and external micro-channels

2. DESCRIPTION OF DEVICE

The geometry of the proposed device (18mm diameter and 6mm thick) is as shown in Figure 1. This device is primarily designed to cool electronic chips or cutting tools. It is subjected to a high value of heat flux from its bottom surface as part of electronic package. The primary means of cooling this heat exchanger is through liquid coolants flowing through internal channels in the device. The device also looses heat to the ambient air through convection from its side walls and its top surface. A flux of 250,000 W/m^2 enters through its bottom surface. The coolant used is water and step-wise varying linear properties with temperature are assumed.

Water flows in all four channels with an inlet velocity of 0.5 m/s along the length of the channels. The water is discharged at the outlet to the ambient at atmospheric pressure. The ambient air is assumed to be at 25°C and its convective heat transfer coefficient is approximated to be 60 W/m^2/K. The objective is to prevent the temperature of the solid media from raising over 50°C. At the same time we also want to minimize the induced thermal stress in the body. For this the material of the bottom layer and the one nearest to the heat source should have the least CTE value. An attempt is made to study the values of thermal stresses via finite element analysis (FEA) for different gradiency in properties, which can be achieved by modulating thickness of each layer in the FGM. For the three layered model, the bottom layer (layer 1) is alumina, followed by a mixture of 50% alumina and 50% zirconia (layer 2), and finally a layer of partially stabilized zirconia (PSZ) (layer 3). The combination of layer thicknesses with the least induced thermal stress can then be chosen.

In addition, the FEA simulation is repeated for a six-layered FGM model with again the design objective being to choose the one with the least induced thermal stress. Again the six-layered model is built proportionately with the bottom layer being pure alumina, followed by the percentage of alumina in layer 2 being 80%, layer 3 with 60%, layer 4 with 40%, layer 5 with 20% and finally the top layer being pure zirconia. Table 1 lists the material properties of the composites with varying volume fractions computed using the Mori-Tanaka scheme [Mori and Tanaka, 1973 and Benveniste, 1987]. Because one cannot easily define which material is a matrix or reinforcement phase between alumina and PSZ, the mathematical model is solved twice, once taking almunia as the matrix phase and then taking PSZ as the matrix [Kwon et al., 1994 and Kwon and Dharan, 1995]. Thus, the average values are taken as the final material properties of the FGM.

Table 1: Properties of the FGM (from Mori-Tanaka scheme)

PSZ (%)	Alumina (%)	Young's Modulus (N/m^2)	Poisson's Ratio	CTE (/°C)	Thermal conductivity (W/m/K)
100	0	2.00000E+11	0.3	1.03E-05	3.00E+00
80	20	2.24150E+11	0.287085	9.77E-06	5.78E+00
60	40	2.50810E+11	0.273835	9.29E-06	8.82E+00
50	50	2.65127E+11	0.2672	9.07E-06	1.05E+01
40	60	2.80170E+11	0.26025	8.85E-06	1.22E+01
20	80	3.12796E+11	0.246085	8.46E-06	1.59E+01
0	100	3.50000E+11	0.23	8.10E-06	2.00E+01

3. FINITE ELEMENT MODEL

Our objectives here are two-fold:

i. Solve the fluid-thermal interactions for temperature distributions in the FGM model as well as in the cooling fluid.
ii. Solve the thermal-structure interactions in the solid part for induced thermal stresses.

Ansys Multiphysics is used to solve these coupled fluid-thermal-structure interactions. Extra care is taken to use only three-dimensional brick elements to mesh our models especially when computing flow through ducts. This is because it is important to align the grids along the direction of flow as they exert considerable influence on the flow and heat transfer.

For the fluid-thermal analysis, 3-D CFD flotran elements are used. The segregated solver is used for flow and TDMA solver is used for the velocity calculations. Here the thermal properties of the non-fluid material are several orders of magnitude different from those of the fluid, and this is called an *ill-conditioned conjugate heat transfer problem*. In this situation, it is known that the TDMA method probably will not yield useful results no matter how many sweeps we specify. The most robust but most memory-intensive method for solving conjugate heat transfer problems, the Preconditioned Generalized Minimum Residual method, is used as the temperature solver. Preconditioned Conjugate Residual method is chosen as the pressure solver because of its robustness for solving ill-conditioned heat transfer problems. Appropriate boundary conditions are applied (Figure 1) and the model is solved till desired convergence is achieved. Now the 3-D CFD flotran elements are replaced with 3-D structure elements in the solid regions, while null element is used in the fluid part. Then temperature boundary conditions are applied by importing the result file from the previous fluid-thermal analysis. Now the system is solved for thermal stresses only in the solid regions. The analyses are performed on all the three layered as well as six layered models.

4. RESULTS AND DISCUSSION

The results that are obtained from the finite element analysis are in agreement with our expected design objectives. First, the analysis is carried out on an alumina model and then the results are compared with the three layered and the six layered model.

4.1 Alumina model

Without the cooling channels, it is observed that the steady state temperatures are in the range of 250 °C to 280 °C. With the cooling channels we could bring down the steady state solid temperature range to 59 °C to 118 °C. After the thermal-fluid analysis, a structural analysis is performed to determine the maximum principal stresses in the model. It is observed that in the regions of high temperature gradients, the stress is the highest.

4.2 Comparing Results between – pure alumina, 3 layered FGM and 6 layered FGM

On comparing the results from the three models, it is found that the stress is least in the six layered FGM model, followed by the three layered model and it is maximum in the pure alumina model. Also for the models with the same number of layers, the ones with the smallest first layers produced the minimum stresses.

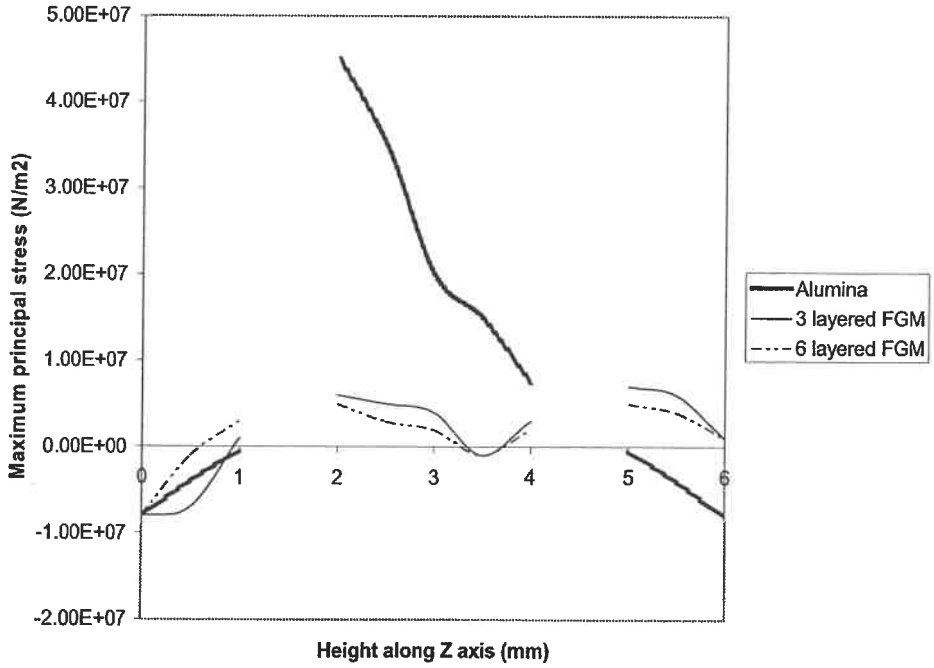

Fig 3: Maximum principal stresses- Section exactly through the centre of one set of cooling channels (x=0, y=3mm)

From the above results it is seen that we succeeded in reducing the tensile stresses significantly by building models using functionally gradient materials. Now, each of the two FGM models – the three layered and the six layered, are analyzed to see the effect in stresses by varying the thickness of each layer. The effect is not as pronounced as seen between an alumina model and a FGM model. However the effect is seen more in the case of the three layered FGM than the six layered FGM. For both the cases, the models with the thinnest bottom layers produced the minimum principal stresses. Perfect elastic behavior is assumed and the Rankine failure criterion is used in the models [Roeder and Sun, 2001a and b]. In all the cases, it is seen that the maximum principal stress in the models is well below the tensile limit.

5. VALIDATION

For validating our results, the finite difference approach is used. A simplified case of a two dimensional two layered FGM model of alumina and PSZ zirconia with only one cooling channel is considered. Starting from the simplified momentum and energy differential equations for fully developed (velocity and temperature profiles) flow in the two-dimensional parallel wall channel, the convective heat transfer coefficient is calculated when there is a constant flux through the lower wall but the upper wall is insulated. The finite difference equations are formed for each set of nodes corresponding to the boundary conditions and these are solved to obtain the nodal temperatures. Now, the model is assumed to be similar to a bimetallic strip and stress (tensile or compressive) on either material (alumina or PSZ) is calculated. These results are then compared with those obtained from a finite element model solved in *Ansys 7.0*. The results are within an error of 30%, which is considered reasonable considering the very rough estimate of the model.

6. CONCLUSIONS

Using eight parallel cooling channels is useful in bringing down the temperature in the operating range of the device. It is observed that the high thermal gradient created by the cooling channels results in high induced thermal stresses in the specimen. Hence to offset this effect, the concept of using a material with functionally gradient properties is used. From the results of the analysis, it can be inferred that the stresses in the FGM media are considerably less than the stresses in the alumina (homogeneous) media. Hence the incentive of using the FGM can be justified. The stresses in the six layered FGM model are further found to be lower than those in the three layered FGM model. Varying the thickness of the layers of the FGM also revealed interesting results. For both cases of three layered and six layered FGM models, it is found that the model with a thinner bottom layer had a lower value of stress than the other combinations. As far as future work on this topic is concerned, currently attempt is being made to powder process a three layered FGM model at MSU. Work can be done on finding what should be the optimum ratios of layer thicknesses with experimental validation of the heat exchanger being the final goal. Fugitive phases can be used and partially sintered ceramics are machined and joined after fully sintering for making the internal channels [Shin et al., 2000] and the heat exchanger can then be tested under actual conditions.

REFERENCES

[1] Mori, T., and Tanaka, K., 1973, "Average Stress in Matrix and Average Elastic Energy of Materials with Misfitting Inclusions," Acta Metallurgica et Materialia, Vol. 21, pp. 571-574
[2] Benveniste, Y., 1987, "A New Approach to the Application of Mori-Tanaka's Theory in Composite Materials," Mechanics of Materials, Vol.6, pp. 147-157.
[3] Shin, H.W., Kwon, P. and Case, E.D., ASM Fall 2000 Proceedings.
[4] Kwon, P., Dharan, C.K.H. and Ferrari, M., 1994, "Macroscopic Analysis of Axisymmetric Functionally Gradient Materials under Thermal Loading", *J. Eng. Res. Tech.*, 116, p. 115
[5] Kwon, P. and Dharan, C. K. H., 1995, "Effective Moduli of High Volume Fraction Particulate Composites," Acta Metallurgica et Materialia, 43, 3, pp. 1141-1147
[6] Roeder, B.A., Sun, C.T., 2001a, "Dynamic penetration of alumina/aluminum laminates: experiments and modeling", International Journal of Impact Engineering, 25, pp. 169-185.
[7] Roeder, B.A., Sun, C.T., 2001b, "Dynamic penetration of alumina/aluminum laminates: experiments and modeling", International Journal of Impact Engineering, 25, pp. 169-185.

Configuration and Control Aspects of High-Precision Planar Multi-Coordinate Drive Systems

Eberhard Kallenbach, Vladimir Kireev, Ralf Volkert, Johannes Zentner, Torsten Bertram
Mechatronics Department, Technische Universität Ilmenau, Germany

Abstract – Planar magnetic guidance system for an integrated multi-coordinate positioning system suitable for modern applications like coordinate inspection, laser cutting, circuit board assembly etc. is represented. Simulation of magnetic field and forces of actuators, control system synthesis has been carried out. A control structure of the electromagnetic guidance system has been investigated to identify factors limiting the achievable positioning precision, for the future system enhancement. Some experimental results from the test rig are shown.

I. INTRODUCTION

For many applications as laser cutting, coordinate inspection, circuit board assembly etc., high-precision multi-coordinate positioning systems are required, witch show accuracies in positioning in the sub-micrometer range and offer strokes of several 100 millimetres as well as high dynamics (100...200 mm/s planar track speed) at the same time. These demands are difficult to realize with conventional multi-coordinate drives that usually consist of several coupled linear drive modules with mechanical bearings and rotation-to-linear motion transmission. The number of the required linear and angular drive modules in a conventional positioning system corresponds to the required degree of freedom (DOF) of motion. Hence, such a multi-coordinate table would be too slow, heavy and complex especially when the positioning in 6 DOF has to be obtained.

A. Integrated Multi-Coordinate Direct Drives

Integrated multi-coordinate direct drives, in which a single moving platform is guided and propelled through magnetic field forces only, are suitable for such high-precision and dynamic positioning tasks [1]. Such drives possess a stator and a rotor facing each other without a mechanical contact. Therefore, the following advantages can be obtained:

1) no friction and no wear particles are generated, the operation of the motor in vacuum and in clean rooms is possible;

2) stiffness, damping, air gap width and other essential parameters of the bearing can be flexible varied and/or better stabilized with a suitable control system;

3) active vibration damping is possible with the magnetic bearings, that is advantageous for the high precision positioning;

4) number of degrees of freedom DOF = 6 can be obtained with a single movable element.

To achieve the advantages listed above, higher measurement and control effort and therefore higher costs are necessary [1]. As a rule, additional problems of magnetic guided systems are intrinsic non-stability and non-linearity of the electromagnetic actuators suitable for a planar positioning.

II. MAGNETIC GUIDANCE SYSTEM

A multi-coordinate drive with a rotor suspended by attracting forces and an electro-dynamic drive at the underside of the moving platform is shown in Fig. 1. The vertical position is measured with three eddy-current sensors placed in the stator mounting holes under the moving platform. Horizontal position in the *xy*-plane is determined using an incremental optical *xyφ*-measuring system [2].

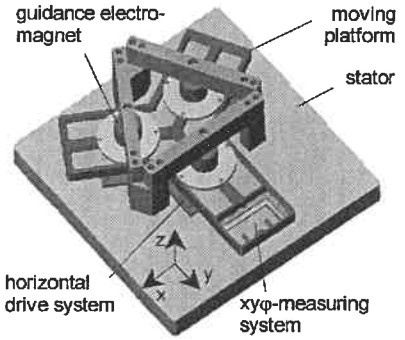

Fig. 1: Overall view of the system

Fig. 2 represents the used actuator arrangement in details.

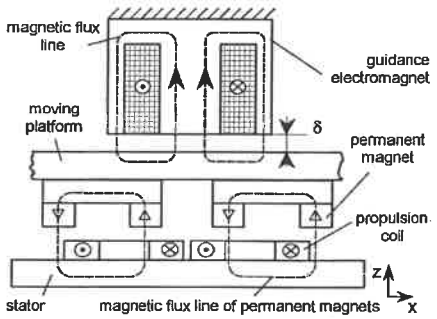

Fig. 2: Actuators' structure

III. MODELLING OF ACTUATORS FOR A MAGNETIC GUIDANCE SYSTEM

As shown in Fig. 1, three electromagnets forming a triangle are used to guide the moving platform

magnetically. The following system of differential equations describes the dynamic behaviour of a single electromagnet [4]:

$$U = iR + \frac{d\psi(z,i)}{dt}, \tag{1}$$

$$F_m(z,i) = m\ddot{z} + F_d, \tag{2}$$

$$F_m(z,i) = \frac{\partial}{\partial\delta}\int\psi(i,z)di, \tag{3}$$

where U denotes voltage, i – electric current, R – coil resistance, ψ – magnetic flux linkage, z – armature position, δ – air gap, m – mass, F_m – magnetic force, F_d – disturbance force.

To define plant properties of the magnetic guidance test rig (Fig. 3), to select a suitable control concept and to identify initial values of control parameters, the following study was carried out.

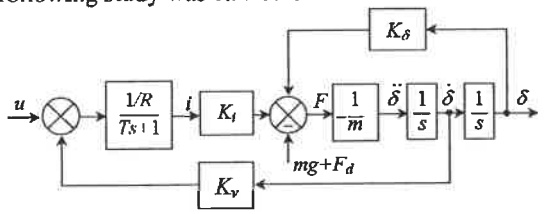

Fig. 3: Linearized plant structure

The static force-displacement and force-current characteristics of the guidance electromagnet have been calculated. Since the airgap has to be stabilised at an operating point with small deviations only, linear equations can be applied at first in place of non-linear (1) and (3):

$$U = iR + L\frac{di}{dt} - K_v\frac{d\delta}{dt}, \tag{4}$$

$$\Delta F_m = K_i i - K_\delta \delta, \tag{5}$$

where K_i and K_δ are proportionality coefficients between the magnetic force, current and air gap, respectively, $L = d\Psi/di$ – coil inductance, $K_v = d\Psi/d\delta$ – back-emf coefficient.

Strong current and airgap variation lead to strong changes relative to the initial values of L, K_v, K_i and K_δ and therefore the constant parameters can be applied only when position and current variation are small (2...5% from the corresponding initial values).

Using the Taylor decomposition at an operating point of the electromagnet ($\delta = 0.5$ mm, $i = 0.3$ A), the parameters of the linear plant model (Fig. 3) have been identified ($K_i = 175$ N/A; $K_\delta = -86\cdot10^3$ N/m, $T = L/R = 0.08$ s, $R = 7.8$ Ohm, $K_v = 100$ V/(m/s), $m = 0.5$ kg).

The overall input-output open loop transfer function in terms of the given input voltage:

$$G(s) = \frac{\delta(s)}{u(s)} = \frac{\frac{K_i}{K_\delta R}}{T\frac{m}{K_\delta}s^3 + \frac{m}{K_\delta}s^2 + \left(T + \frac{K_i K_v}{K_\delta R}\right)s + \frac{K_i}{K_\delta R} + 1} \tag{6}$$

with the parameters explained above.

The model is a dynamic system of third order with negative stiffness ($K_\delta < 0$). Therefore, the stabilising feedback vector has to include three state-space variables of the system, for example, $\delta, \dot{\delta}$ and $\ddot{\delta}$, taken from sensor and observer (Fig. 4).

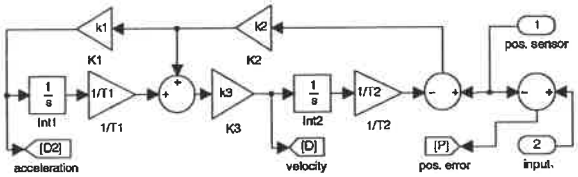

Fig. 4: Simple observer structure

For an adequate modelling the magnetic subsystem has been described by nonlinear characteristics, taking into account the saturation of electromagnets.

By implementing these characteristics as look-up-tables in SIMULINK, a model was created, which allows investigating of the dynamical behaviour of an electromagnet not only near a certain operating point, but within the whole possible movement range of the armature (Fig. 5).

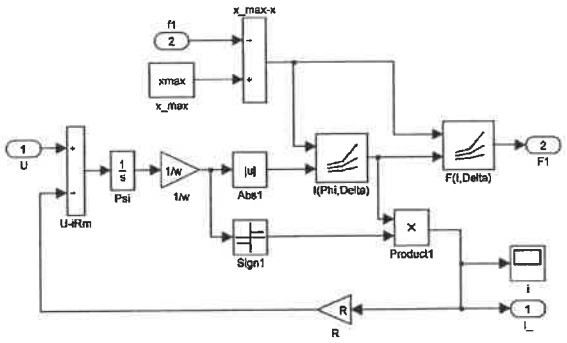

Fig. 5: Non-linear model of an electromagnet

IV. CONTROL SCHEME

The velocity and acceleration are calculated by an observer model (Fig. 4). For computing the PIDD²-controller's set value the following function is used:

$$U(s) = k_p\cdot(W(s) - Z(s)) + k_i\cdot\frac{W(s) - Z(s)}{s} + \frac{K_1}{1+\frac{K_1}{s}}\left(k_d\cdot Z(s) + k_{d2}\cdot Z(s)\cdot\frac{K_2}{1+\frac{K_2}{s}}\right) \tag{7}$$

$U(s)$ is the set value of the controller

$W(s)$ desired value
$Z(s)$ actual (measured) value

The control algorithm has been transformed into the discrete form for implementation in dSpace system.

V. GEOMETRY OF THE MAGNETIC GUIDANCE SYSTEM

The three electromagnets used for the guidance system form an equilateral triangle. Assuming a homogeneous distribution of mass, the moving platform's centre of gravity lies at the centre of the triangle. The platform is balanced by the forces of the electromagnets. If the point of origin is also placed at the centre of the triangle, the differential equations for the translation of the platform in z-direction and for the rotations around x-axis (φ_x) and y-axis (φ_y) are:

$$\ddot{z} = \frac{1}{m}\left(F_1 + F_2 + F_3 - mg - F_d\right), \tag{11}$$

$$\ddot{\varphi}_x = \frac{1}{J_x}\left(-F_1 \cdot c - F_2 \cdot c + F_3 \cdot a\right), \tag{12}$$

$$\ddot{\varphi}_y = \frac{1}{J_y}\left(F_1 \cdot \frac{b}{2} - F_2 \cdot \frac{b}{2}\right). \tag{13}$$

where $F_{1,2,3}$ denote forces of the electromagnets, F_d – disturbance force, m – mass, $J_{x,y}$ – moments of inertia, g –gravity acceleration.

The measuring system for the position of the moving platform consists of three eddy current sensors, which form an equilateral triangle with the length r_S at each side, as shown in Fig. 6. Every sensor is placed outside the actuator belonging to it. The triangle formed by the actuators itself has a length of r_{EM} at each side.

For converting the local coordinates referring to the electromagnets (z_{EM1}, z_{EM2}, z_{EM3}) into global coordinates (z, φ_x, φ_y), the following equations can be found due to the geometric dimensions:

$$z = \frac{z_{EM1} + z_{EM2} + z_{EM3}}{3}, \tag{14}$$

$$\varphi_x = \arctan \frac{-\frac{z_{EM1} + z_{EM2}}{2} + z_{EM3}}{r_{EM} \sin\frac{\pi}{3}}, \tag{15}$$

$$\varphi_y = \arctan \frac{z_{EM1} - z_{EM2}}{r_{EM}}. \tag{16}$$

The equations for the inverse transformation from global to local coordinates are:

$$z_{EM1} = z - \frac{r_{EM}}{3}\tan\varphi_x \sin\frac{\pi}{3} + \frac{r_{EM}}{2}\tan\varphi_y, \tag{17}$$

$$z_{EM2} = z - \frac{r_{EM}}{3}\tan\varphi_x \sin\frac{\pi}{3} - \frac{r_{EM}}{2}\tan\varphi_y, \tag{18}$$

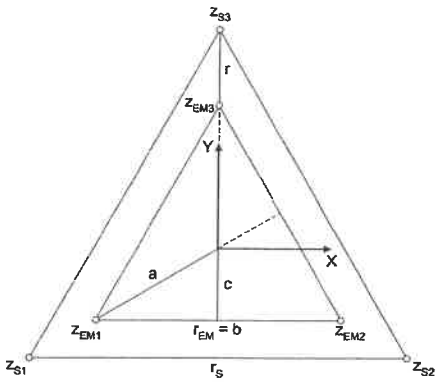

Fig. 6: Geometry of the magnetic guidance system

$$z_{EM3} = z + \frac{2}{3} r_{EM} \tan\varphi_x \sin\frac{\pi}{3}. \tag{19}$$

Furthermore, there is a coupling between the local coordinates referring to the electromagnets (z_{EM1}, z_{EM2}, z_{EM3}) and the coordinates measured by the sensors (z_{S1}, z_{S2}, z_{S3}).

The desired position of the moving platform is given in global coordinates z, φ_x and φ_y. The three eddy current sensors can only measure the local coordinates z_{S1}, z_{S2} and z_{S3}, but not the actual air gaps at the electromagnets themselves (z_{EM1}, z_{EM2}, z_{EM3}). Therefore several coordinate transformations are necessary. The entire control loop implemented in SIMULINK is shown in Fig. 7. This control structure requires the differential equations of movement for the local coordinates z_{EM1}, z_{EM2} and z_{EM3}.

Differentiating eq. (14), (15) and (16) twice we become some equations for $\ddot{z}_{EM1}$, $\ddot{z}_{EM2}$ and $\ddot{z}_{EM3}$ where $\ddot{z}$, $\ddot{\varphi}_x$ and $\ddot{\varphi}_y$ can be replaced by the differential equations of movement (11), (12) and (13). The calculation formulas for $\dot{\varphi}_x$ and $\dot{\varphi}_y$ can be obtained by differentiating the transformation equations (15) and (16) once.

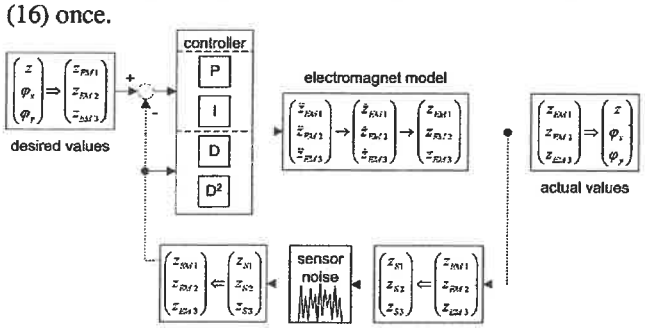

Fig. 7: Control loop implemented in SIMULINK

The velocities $\dot{z}_{EM1}$, $\dot{z}_{EM2}$ and $\dot{z}_{EM3}$ are computed by integrating equations for $\ddot{z}_{EM1}$, $\ddot{z}_{EM2}$ and $\ddot{z}_{EM3}$ received above. A second integration leads to the position values z_{EM1}, z_{EM2} and z_{EM3}, which can be converted into the global coordinates z, φ_x and φ_y.

If the parameters of the controller are chosen properly the step response with an overshoot of 15...20% and settling time of 100 ms for a 1 mm step can be obtained with the simulation. The cross-couplings between the movements of the platform in different degrees of freedom are visible, too. To prevent these, the control system has to be further improved during the forthcoming work steps.

VI. NOISE INFLUENCE

Noise of the position sensor and hysteresis of the actuators as well as the dynamic positioning uncertainty have been identified through a measurement (sampling frequency $f_s = 25$ kHz). Standard deviation of the position sensor signal σ is approximately 0.2...0.3 µm for the distances δ of 0.3...0.5 mm, thus the maximal noise amplitude 3σ is approximately of 0.9...1 µm for the unfiltered signal. The controlled z-position noise has an amplitude of about 1 µm too. The position uncertainty value can be improved if better sensors, for example, a capacitance measuring system or laser interferometer, will be used.

The force hysteresis of 2...3 N corresponds to the winding current variation of 1...1.5 A and has to be considered in an advanced actuator model.

During the xy-positioning, a cross-coupling of the horizontal and vertical position of the moving platform is obvious (Fig. 8, *a*). Using of an integral control part for the disturbance rejection and cancellation of the steady-state error, as described above, is necessary.

The reaction of integral feedback control on the horizontal positioning step is represented in Fig. 8, *b* (only for one magnet). The feedback control system must be extended with a feed-forward concept in order to reduce the control error.

VII. CONCLUSION

An electromagnetic guidance system has been analysed in order to determine the performance for a precision positioning system. Parameters and characteristics of the non-linear actuator model have been identified. Control structure with observer has been proved as a robust and effective solution for the vertical stabilisation of the moving platform. To improve system dynamics and to reduce overshoot, a non-linear observer can be used.

Linear transfer function analysis cannot be used to adequately determine disturbance rejection and realistic system bandwidth. Control must be pre-saturated since it protects the plant from extremes and allows saturation to be predictably modelled [6].

Because the position sensor noise cannot be changed as a design parameter, it is necessary to consider it as a constraint on the system bandwidth. An excessive bandwidth with noisy sensors leads to the large control effort, control saturation or even instability.

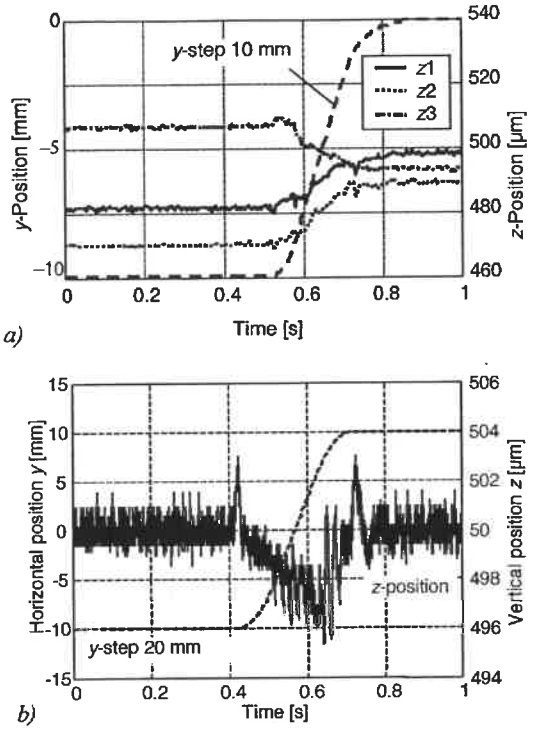

Fig. 8: Experiments show cross-coupling of the magnetic guidance and drive system

For demanding positioning tasks, extremely low-noise sensors have to be applied as the controller cannot control a plant output more accurately than it is measured.

The disturbances from the xy-drive system have to be considered in a suitable feed-forward scheme of the magnetic guidance system.

VIII. REFERENCES

[1] Kallenbach, E.; Saffert, E.; Schäffel, C.: Multi-coordinate Drive Systems – Opportunities and Limits. Int. Heinz Nixdorf, Symposium: On Mechatronics and Advanced Motion Control, Paderborn, 1999.

[2] Kovalev, S.; Saffert, E.; Kallenbach, E., Schäffel, C.: A Magnetically Guided Precision Drive with 6 Degrees of Freedom. The ASPE 13. Annual Meeting, October 1998. Proceedings pp. 614-617.

[3] Kovalev, S. Magnetisch geführter Mehrkoordinaten-Präzisionsantrieb. – Diss. TU Ilmenau, 2000.

[4] Kallenbach, E.; Eick, R.; Quendt, P.; Ströhla, T.; Feindt, K.; Kallenbach, M.: *Elektromagnete: Grundlagen, Berechnung, Entwurf und Anwendung*; B. G. Teubner, 2. Aufl., 2003

[5] Kallenbach, E.; Kireev, V.; Zentner, J.: Investigations for the Configuration of Integrated Magnetic Levitated Multi-Coordinate Drives. ICM: International Conference on Magnetics, Rome, Italy, 2003.

[6] Franklin, Gene F. Digital Control of dynamic systems.- 2nd ed.: Addison-Wesley Inc., 1990.

Identification of Friction Elements through Limit Cycle Analysis

Min-Seok Kim, Myong-Zoo Kim and Sung-Chong Chung

HYbrid Systems Design and Control LABoratory
School of Mechanical Engineering
Hanyang University, SungdongGu, Seoul 133-791, Korea

Abstract: A friction identification method in a frequency domain is proposed for a precision servomechanism. A nonlinear friction model including static, Coulomb, and viscous friction as well as Stribeck effect is considered in this paper. Friction models are formulated by using describing functions. Friction elements are estimated through the limit cycle analysis in a velocity control loop. A Butterworth filter is incorporated into the feedback loop to increase the accuracy of the friction identification process. A model-based friction compensator is applied as a feedforward controller to compensate for the nonlinear characteristics and to verify the effectiveness of the proposed identification method.

Keywords: Describing function, Friction identification, Limit cycle, Nonlinearity, Nyquist criterion, Servomechanism, Stribeck effect

1. Introduction

The need for high-density magnetic storage devices, assembly machines for semiconductors, and high-speed machine tools has increased the demand of high-performance servomechanisms. Friction is a dominant nonlinear factor that seriously deteriorates positioning accuracy of the servomechanism[1]. A friction compensator is indispensable to fabricate high-performance servomechanisms.

A lot of study concerning the identification and compensation of friction has been proposed so far[1-5]. Generally, friction elements in the servomechanism have been estimated from motor torque or current through recursive identification processes[2]. However, these methods require additional equipments such as torque meters and current sensors as well as time-consuming identification process.

This paper proposes a simple identification method to estimate friction elements in servomechanisms without additional equipment. A nonlinear friction model including static, Coulomb and viscous friction, as well as Stribeck effect is considered in this study. In order to identify friction coefficients of the servomechanism, an accurate linear element model of the system should be obtained in advance. A nonlinear element composed of two relays is devised to extract various limit cycle conditions in a velocity control loop[3]. The velocity control loop contains a linear element and two nonlinear elements. One nonlinear element refers to the friction model on the velocity feedback part and the other nonlinear element means the proposed nonlinear element to extract limit cycles in the velocity control loop of the servomechanism. Equivalent nonlinearity acting on the linear element is derived from the combination of two nonlinear elements in the form of a describing function[6-7]. Using this method, the friction identification becomes the estimation of describing function parameters.

Frequencies and magnitudes of stable limit cycles in the velocity control loop are obtained from several experiments. A Butterworth filter is incorporated intentionally into the velocity loop to satisfy the requirements of the describing function approximation and to increase accuracy of friction estimation. The identified accurate friction model is applied for a model-based friction compensator with a feedforward controller. Circular motion experiments are conducted to verify the effectiveness of the proposed identification method.

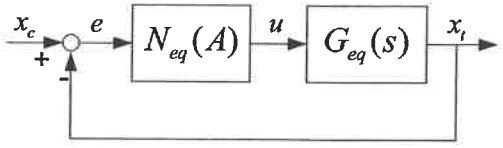

Fig. 1 Block diagram of a nonlinear system.

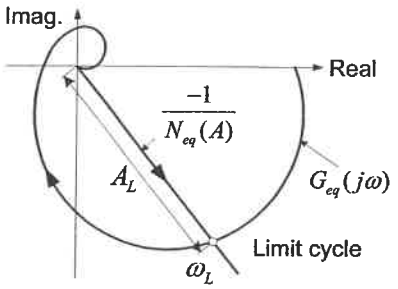

Fig. 2 Harmonic balance condition in polar coordinates.

2. Limit cycle analysis

Consider a nonlinear system composed of an equivalent linear element $G_{eq}(s)$ and an equivalent nonlinear element $N_{eq}(A)$ as shown in Fig. 1. The first step of the friction identification through the limit cycle analysis is an approximation of the nonlinear element to a quasi-linear element by using a describing function approximation. Following assumptions are required[6-7]: ①An input signal, x_c, fed to the system is zero. ②The nonlinear element has only the sinusoidal input. ③The linear element has low-pass property to filter out high-frequency harmonics of the nonlinear element.

The next step is to formulate the equation of a harmonic balance condition[6-7] used to predict the existence of limit cycles. The harmonic balance condition is derived from Nyquist criterion as follows:

$$1 + G_{eq}(j\omega) \cdot N_{eq}(A) = 0 \tag{1}$$

It is possible to plot both the frequency response function $G_{eq}(j\omega)$ (varying ω) and the negative inverse describing function (varying A) in polar coordinates as shown in Fig. 2. If the two curves intersect, then there exist limit cycles.

When some parameters (i.e. friction coefficients) of the describing function are unknown and characteristics of both the linear element and limit cycles are known, it could be used the harmonic balance condition to estimate the unknown parameters of the describing function.

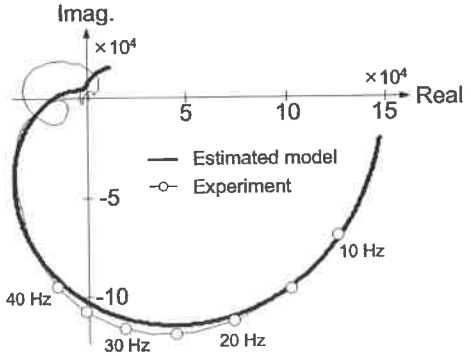

Fig. 3 Polar plot of the identified linear element.

3. Identification of a linear element

In order to identify friction elements of a servomechanism through the proposed method, an accurate linear element model should be obtained in advance. In order to obtain the accurate model of the linear element, a pair of biased square signals are applied for the excitation[3]. This method does not suffer from the problems due to the nonlinear effects and, therefore, is able to provide accurate results.

Fig. 3 shows a polar plot of the identified linear element of the servomechanism shown in Fig. 4. The linear element is a type 0 system in which $G_m(j\omega)$ locus starts at positive real axis and ends at the origin of polar coordinates as ω increases from zero to infinity.

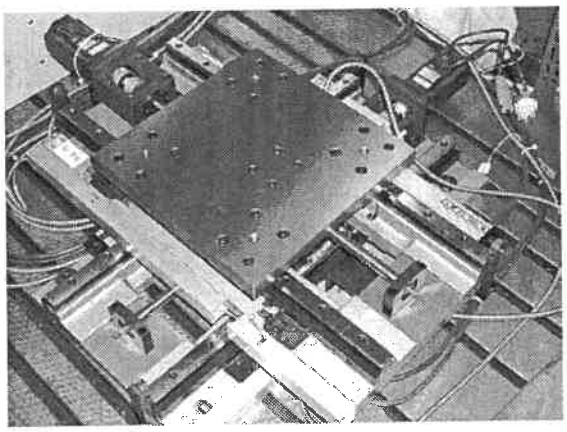

Fig. 4 Servomechanism for the case study.

4. Modeling of nonlinear elements

Friction models have been discussed extensively in the literature[1]. It is generally known that friction force or torque varies as a function of velocity. In this paper, a general nonlinear friction model including static, Coulomb and viscous friction, as well as Stribeck effect is proposed as shown in Fig. 5. Several basic nonlinear elements composed of a relay and a dead-zone are used to construct the friction model. By using describing functions of the corresponding elements, a quasi-linear element of the friction model is obtained as follows:

$$N_f(A) = \begin{cases} N_A(A) & , A \le \delta \\ N_A(A) - N_B(A) + N_C(A) & , A > \delta \end{cases}$$

$$\begin{cases} N_A(A) = 4f_s/\pi A & ,\forall A \\ N_B(A) = 4(f_s - f_c)\sqrt{1-(\delta/A)^2}\,/\pi A & , A > \delta \\ N_C(A) = f_v\{1 - N_d(\delta/A)\} & , A > \delta \\ N_d(x) = 2\left(\sin^{-1}x + x\sqrt{1-x^2}\right)/\pi \end{cases} \tag{2}$$

where δ is a boundary lubrication velocity, f_s, f_c, and f_v are static, Coulomb, and viscous friction element, respectively.

A velocity control loop composed of a linear and two nonlinear elements is devised to identify the

friction model as shown in Fig. 6.

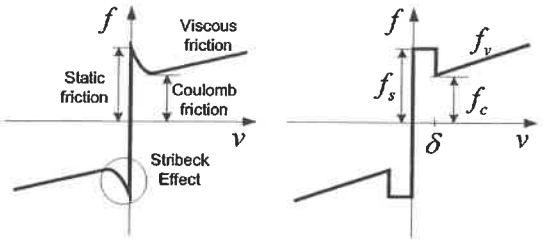

(a) original model (b) simplified model

Fig. 5 Proposed friction model.

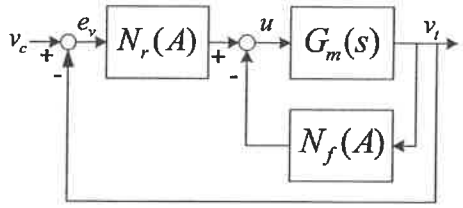

Fig. 6 System structure for friction identification.

In Fig. 6, $G_m(s)$ and $N_f(A)$ imply the linear element and the friction model, respectively. And $N_r(A)$ is the proposed nonlinear element to extract various limit cycle conditions in the servomechanism.

As described in section 3, the identified linear element is a type 0 system. Therefore, the frequency at which $G_m(j\omega)$ locus intersects the imaginary axis is the natural frequency of the system. In such a case, frequencies of limit cycles extracted to identify friction elements must exist in the fourth quadrant of polar coordinates. According to this condition, the nonlinear element, $N_r(A)$, is devised as a combination of two relays having different amplitudes given by

$$N_r(A) = -\frac{4d_1}{\pi A} - j\frac{4d_2}{\pi A} \tag{3}$$

where d_1 and d_2 are the magnitudes of two relays.

According to the assumptions described in section 2, nonlinear elements in the servomechanism must be represented as an equivalent nonlinear element. The describing function of the equivalent nonlinear element is determined as the parallel combination of the describing functions as follows:

$$N_{eq}(A) = N_r(A) + N_f(A) \tag{4}$$

When the limit cycle analysis is applied to a position control loop, the linear element has sufficient low-pass characteristics due to an integral element[4-5]. However, higher harmonics cannot be sufficiently filtered out in the velocity control loop. Therefore, in order to satisfy the assumptions of the describing function approximation and to increase the accuracy of friction estimation, a Butterworth filter $G_{lp}(s)$ is incorporated into the velocity control loop as shown in Fig. 7.

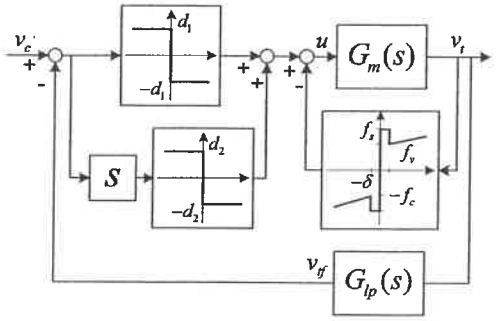

Fig. 7 System configuration for friction identification.

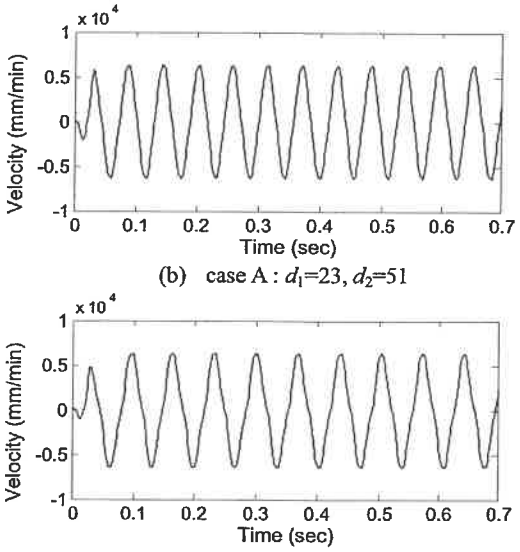

(b) case A : d_1=23, d_2=51

(b) case B : d_1=30, d_2=45

Fig. 8 Time responses of limit cycles.

5. Experiments

Experiments for friction identification are conducted in the precision x-y positioning system shown in Fig. 4. By varying amplitudes of the nonlinear element $N_r(A)$, various limit cycle conditions are intentionally extracted in the velocity loop. Fig. 8 shows limit cycle oscillations obtained from the experiments. Using amplitudes and frequencies of the extracted limit cycles, unknown parameters of the equivalent nonlinear element are obtained from the harmonic balance condition. Table 1 shows estimated friction coefficients.

A two-degree-of-freedom controller including a PID feedback controller and a model-based feedforward friction compensator shown in Fig. 9 is introduced to

verify the identified friction model. The model-based friction compensator estimates actual velocities of the table from the position command, and compensates for friction torque by adding voltage signal corresponding to the friction to torque command fed to the motor. Circular motion experiments are conducted for performance evaluation of the friction compensator. In the circular motion experiments, frictions, especially static friction and Stribeck effect, cause large position errors that appear every 90° interval around the circle, referred to as quadrant glitches. Fig. 10 shows the position error in a circular motion with and without the friction compensator. Clearly, position errors in the vicinity of zero-velocity are reduced through the friction compensator. Especially, quadrant glitches decrease from 20 μm to less than 5 μm.

Experimental results confirm that the friction elements in a servomechanism are effectively identified by using the proposed method.

Table 1 Identified friction coefficients.

Friction elements	Value	Unit
Static element	0.28	(N·m)
Coulomb element	0.17	(N·m)
Viscous element	2.56×10^{-2}	(N·min)
Sliding velocity (Stribeck)	122	(mm/min)

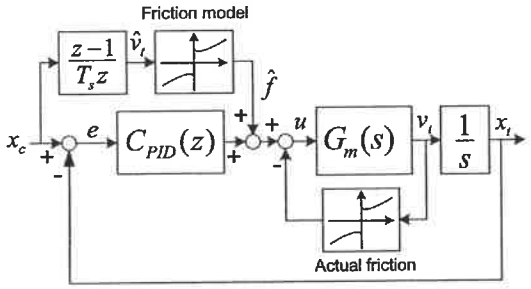

Fig. 9 block diagram for friction compensation.

6. Conclusions

This paper proposes a new application of the limit cycle analysis to identify friction elements in a servomechanism. A friction model including static, Coulomb, and viscous friction as well as Stribeck effect is formulated by using the describing function approximation. A nonlinear element composed of two relay elements is devised to extract various limit cycles. To improve the accuracy of friction estimation, a Butterworth filter is incorporated in the feedback loop to fulfill the requirements of the describing function approximation. Using the accurate model of a linear element and characteristics of the extracted limit cycles, friction elements in a servomechanism are simply identified. Another advantage of the proposed method is that existing control hardware is sufficient to identify friction coefficients and implement its compensation without excessive equipment. The estimated friction elements are applied for a model-based friction compensator. Circular motion experiments confirm that quadrant glitches are reduced to less than 5μm through the friction compensator.

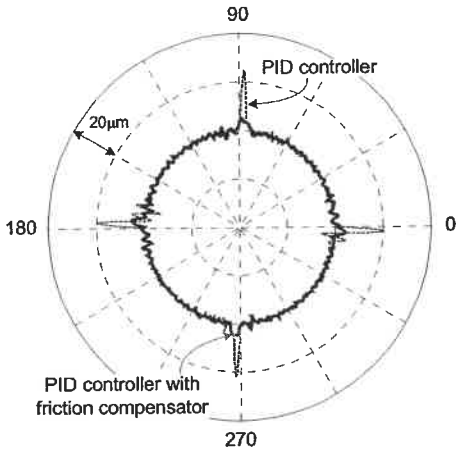

Fig. 10 Circular motion profiles.

References

(1) Armstrong-Hélouvry, B., Dupont, P. and Canudas de wit, C., 1994, "A Survey of Models, Analysis Tools and Compensation Methods for the Control of Machines with Friction," *Automatica*, Vol. 30, No. 7, pp. 1083~1138.

(2) Kim, M.S. and Chung, S.C., 2003, "Identification of Nonlinear Characteristics for Precision Servomechanisms," *Proceedings of the ASPE Annual Meeting*, pp. 167~170.

(3) Kim, S.C. and Chung, S.C., 1998, "Cutting Force Estimation Using Feeddrive and Spindle Motor Currents in Milling Processes," *Transactions of the KSME(A)*, Vol.22, No.11, pp. 2029~2038.

(4) Tan, K., K., Lee, T., H., Huang, S., N., and Jiang, X., 2001, "Friction Modeling and Adaptive Compensation Using a Relay Feedback Approach," *IEEE Trans. on Industrial Electronics*, Vol. 48, No. 1, pp. 169~175.

(5) Besançon-Vode, A. and Besançon, G., 1999, "Analysis of a two-relay system configuration with application to Coulomb friction identification," *Automatica*, Vol. 35, pp. 1391~1399.

(6) Slotine, J., J., E., and Li, W., 1991, *Applied Nonlinear Control*, Prentice Hall, Inc., New Jersey, pp.157~190.

(7) Atherton, D., 1975, *Nonlinear Control Engineering*, Van Nostrand Reinhold Co., London, pp.75~166.

Verification of Precision-limit Positioning of a Direct Drive System with the Existence of Friction

Bong-Yu Liu (p4692427@ccmail.ncku.edu.tw), Chen Hsieh (chsieh@mail.ncku.edu.tw)

High Precision Flexible Structure Control Laboratory

Department of Aeronautics and Astronautics

National Cheng Kung University, Tainan, Taiwan 701, ROC

Abstract

In this research, the verification of precision-limit positioning (PLP) of a direct drive system with the existence of friction is conducted experimentally. With regard to PLP, it means that the achieved positioning precision equals to the limit that the particular system hardware can offer. More specifically, in this research, the precision limit is defined to be the resolution of the sensor adopted for position feedback under the proved condition that all other parts of the system are capable of accomplishing this goal. PLP also enforces 100% repeatability when precision is of interest. Certainly, this is the limit of the precision that can be offered by a real positioning control system. But because of lacking of accurate knowledge about friction, especially the pre-sliding friction, PLP was not considered possible in the past. However, it has been shown in an earlier study that, with the help of newly revealed knowledge about pre-sliding friction, achieving PLP is possible. A simple and explicit criterion for the PID control design was also derived. In this research, such control design is applied to a direct drive DC torque motor system. Extensive experiments are arranged to observe the system performance. It has been shown that the repeatability of zero-count precision error is above 99.9996% according to more than 240,000 tests during a period of six months. Furthermore, all phenomena observed in these tests do coincide with what are expected by the friction model on which the PLP theory was based.

Keywords : Precision-limit Positioning, Direct Drive System, Pre-sliding Friction

1. Introduction

High precision positioning is a technology driver in the field of manufacturing. However, the task of positioning with extremely high precision was considered a difficult problem in the past because of lacking of accurate knowledge about friction, especially the pre-sliding friction. Therefore, when high precision is demanded in a positioning system, people usually use specially designed hardware and/or complicated control algorithms to reduce or compensate friction effects. Most of these approaches do improve the performance of positioning. But without thoroughly understanding the dynamics of pre-sliding friction, the system performance can not be guaranteed. Nevertheless, it has been shown in an earlier study [1] that, with the help of newly revealed knowledge about the pre-sliding friction, a positioning system can achieve the goal of zero-count error with 100% repeatability when a digital encoder is adopted for position feedback. With regard to this goal, a new term, precision-limit positioning (PLP), is defined. Of course, this performance is under the proved conditions that all other parts of the system are capable of achieving this goal, and the driven load is kept constant. Certainly, this is the ultimate precision that a real positioning control system can achieve.

In the following section, the pre-sliding

friction dynamics will be briefly summarized. Its influence on positioning is discussed in section 3. An explicit stability criterion for PID control in the pre-sliding phase is also given in the 3rd section. Section 4 describes experiments for verification of PLP and is followed by a conclusion.

2. Pre-sliding friction dynamics [1]

A traditional well-known friction model is the Amonton-Coulomb model. According to this model, there is no displacement in the pre-sliding phase. However, in 1899, Steven [2], with the help of an interferometer, discovered that an elastic displacement does exist before the normal slip occurs. This small displacement can be ignored when the requirement of precision is not high. But when talking about the precision of sub micrometer or higher, the displacement in the pre-sliding phase must be considered seriously.

As the motion of the pre-sliding phase is referred, it is well known in the tribology field that the parameters of any friction model are both time and position varying. But actually, the parameters are temporarily time-invariant and locally position-invariant. By temporarily time-invariant it means that the parameters remain constant during a short time interval which is, however, long enough for positioning control purposes. Besides, locally position-invariant means that the parameters are unchanged if the system stays in the pre-sliding phase. Because of this important property, consistent and repeatable qualitative properties can be discovered; the motion in the pre-sliding phase consists of two kinds of motion. The first is a non-linear elastic deformation that demonstrates a special Preisach hysteresis which has memory and wiping-out effects of reverse points. The second motion in the pre-sliding phase is plastic deformation which demonstrates creep and work hardening.

Based on these observations, a friction model consisting of several mechanical elements is established to match these qualitative properties. The parameters of this friction model can be treated as constants with "time-invariant" uncertainties. From the control point of view, PLP is thus possible. But it should be notified that 100% repeatable transient responses are not guaranteed.

3. Stability criterion of PID control in the pre-sliding phase

The widely accepted governing equation for a direct drive system is

$$m\ddot{x} + c_s\dot{x} = u - t_f \qquad (1)$$

, where t_f is the friction force, u is the control input and c_s is the damping coefficient in the slip phase. Based on the traditional Amonton-Coulomb friction model, any point $(x, \dot{x} = 0)$ in the state space is an equilibrium point when the control force u is less than the maximum static friction force. Therefore, the control force u can be released as the desired position, say x_d, is reached. However, this is not the case in a real positioning system. On the contrary, if a mass block is moved a small amount of distance in the pre-sliding phase, it will bounce back when the force is removed. This phenomenon is due to the retraction of the non-linear elastic deformation. Furthermore, once the plastic deformation has been work-hardened and no more creep can occur, the dynamic behavior of the system in the pre-sliding phase is very close to a mass-spring-damper system. The governing equation (1) is not valid anymore. Hence the real system is in fact composed of two different dynamic systems : a type-1 sliding system

and a type-0 pre-sliding system. Therefore, it is natural to take different control strategies for different phases to obtain a good response. The control design for coarse positioning in the sliding phase is well developed. So this research focuses on the fine position control in the pre-sliding phase.

In this phase, the system is basically a type-0 system. As a result, an integral type is needed for a zero steady state error. In this research, the controller structure of the pre-sliding phase is restricted to be a PID controller. It has been shown in [3] that the system is globally asymptotically stable about the desired position, x_d, if the following condition is satisfied :

$$k_I < \underline{k_I} = \frac{(c + k_D)(\underline{h} + k_p)}{m} \qquad (2)$$

,where k_p , k_i , k_d are the gains of the PID controller in the pre-sliding phase, m is the mass of the moving part, c is the damping coefficient of the pre-sliding phase, and $\underline{h}$ is the smallest slope of the elastic deformation.

4. Experimental verification and discussion

The system used in this research is shown in Fig. 1.

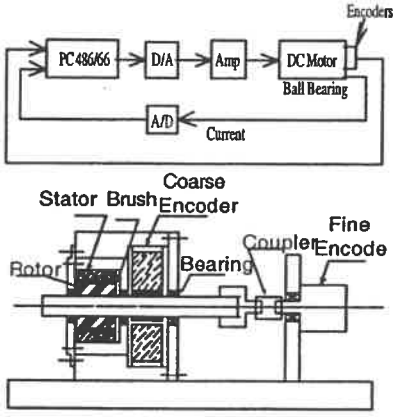

Fig. 1 The test platform

The plant is a drect drive DC torque motor mounted on ordinary ball bearings. The motor is driven by a linear amplifier. Two optical encoders with different resolutions, 86,400 counts/rev and 1,620,000 counts/rev, respectively, are mounted to measure the rotor position. The rotor angle is measured simultaneously by these two encoders. The outputs are compared to guarantee that the acquired data is correct. But only one encoder is used in the feedback loop in every test. The data acquisition and control is accomplished by a 486 PC with a D/A converter and an A/D one, each has a 12-bit resolution. The motor parameters such as moment of inertia and torque constant, etc., are identified using the method developed by Hsieh, etc. [4]

The stability of the two encoders used in this research is checked and the coincidence of data acquired from them is justified. This requirement is essential to get zero-count position error. The ratio of the readout of the coarse encoder to that of the fine one is fixed at 18.75. All other hardware parts in this system are also examined and verified to match the constraints mentioned in reference [3]. Hence the system is qualified for conducting PLP.

The verification of PLP consists of a series of batches of tests. 20,000 successive positioning tests are conducted in every batch. A total of 12 batches are accomplished during a period of six months. In addition to zero-count error test, every batch is arranged to verify some characteristics of the pre-sliding dynamics by assigning different positioning ranges and total time for each test. The time intervals between two successive batches are arranged from several hours to one month for testing the reliability of the system.

A typical result of the test is shown in the following figure.

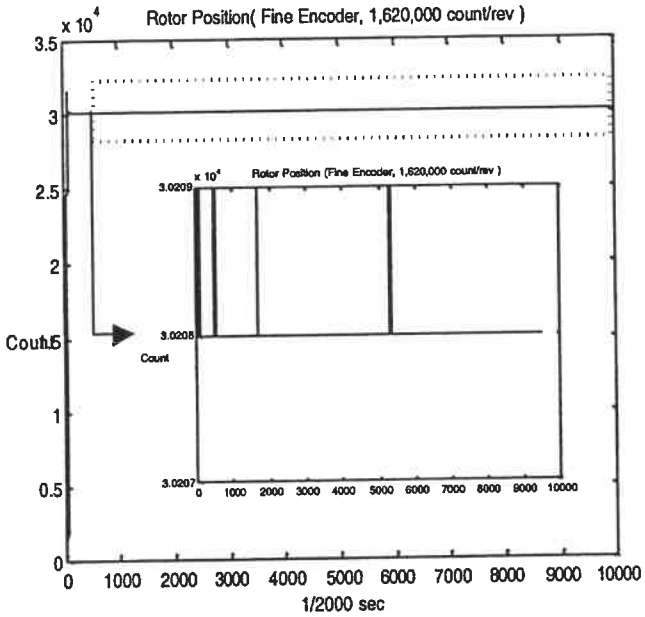

Fig. 2 Position response

The one count jerks that appear in single direction in Fig. 2 coincide with the plastic motion of the pre-sliding dynamics. [1] It is clear that the frequency of the jerks gets slower as the time goes by.

In this research, the settling time is defined to be the time when the position error reaches and stays within ±1 count. Its value depends on the positioning range and has an average of about 0.2 sec if the motion range is 360 degrees.

In all these 240,000 tests, only one test failed to get zero-count error. As a result, the repeatability of zero-count steady state error is 99.9996%. After analyzing that failure, it is found that the stiffness of the elastic deformation dropped to a much smaller value suddenly. This phenomenon is related to a more subtle characteristic of friction and is out of the scope of this paper. However, it is quite rare and can be ignored in most cases.

5. Conclusion

Precision-limit positioning of a direct drive system with the existence of friction is verified experimentally. The results of this research have shown that the repeatability of zero-count position error is above 99.9996%. The phenomena expected by the pre-sliding friction model do coincide with those observed in these tests. Furthermore, the only one failure is fixed by changing the gains of the PID controller dynamically. Further one million positioning tests were conducted to achieve zero-count error positioning successfully with the modified controller. This implies that the pre-sliding friction model and the PLP theory presented in [1] and [3] are quite precise.

Acknowledgment

This research is supported by the grants of 91-EC-17-A-65-S1-0014 and NSC86-2213-E-006-045.

Reference

[1] Hsieh, C. and Pan, Y.C., Dynamic behavior and modeling of the pre-sliding static friction, Wear, 242, pp.1-17, 2000

[2] Stevens, J.S., Some experiments in molecular contact, Physics, Vol. 8, No. 1, pp. 49-53, 1899

[3] Lin, T.Y., Pan, Y.C. and Hsieh, C., Precision-limit positioning of direct drive systems with the existence of friction, Control Engineering Practice, Vol. 11, No. 3, pp. 233-244, 2003

[4] Hsieh, C., Lin, C. and Pan, Y.C., Practicalhighly precise position control of direct drive PM DC torque motors, Proc. of 1996 IFAC, Vol. A, San Francisco, CA, pp. 283-288, 1996

THE DEVELOPMENT OF THE NC METHOD OF ELIMINATING MACHINING POINT ERRORS CAUSED BY MACHINING CENTERS

FIRST REPORT (Theory)

Toshihiro NAKAYABU*, Masatoshi HIRAO**, Toyoshiro INAMURA***, Takeshi YASUI†,
Hidetaka IMAI††, Masahiro OKAJI††, Hiroyuki KAWARA†††
* Industrial Research Institute of Ishikawa, 2-1 Kuratsuki, Kanazawa, Japan
** Dept. of Mech. System Engineering, Kanazawa University, 2-40-20 Kodatsuno, Kanazawa, Japan
*** Nagoya Institute of Technology, Gokiso, Shouwaku, Nagoya, Japan
† Industrial Exchange Institute of Kanazawa, 1400 Utsugi, Kanazawa, Japan
†† National Institute of Advanced Science and Technology, 1-1-1 Umezono, Tsukuba, Japan
††† Tsudakoma Corporation, 5-18-18 Nomachi, Kanazawa, Japan

1. INTRODUCTION

Rectilinear motions of the tables, columns, and heads of three-dimensional machines such as machining centers cause position errors, angle errors, and squareness errors between the axes of machining motion. It has been pointed out that these geometrical errors are complexly integrated to cause machining point errors. There has been no proposal for a method of eliminating the machining point errors. This report specifies a method of computing the actual position of a tool using a new geometrical error model based on the detected data of errors and the coordinates of the interferometers fixed to the machining center, and a method of feeding back the actual position of the tool to the feeding motors of X, Y and Z axes to eliminate the machining point errors.

2. WIRE FRAME REPRESENTATION OF THE MACHINING CENTER

Figure 1 shows the structure of the test machine, a vertical machining center with a moving column. (① ~⑤ represent the machine components; bed ①, table (X-axis) ②, column (Y-axis) ③, head (Z-axis) ④, tool ⑤) Line 120, which is discretionarily positioned on the bed, represents a virtual line parallel to the moving direction of the table. Point 121 is a virtual point that moves together with the table along Line 120, and is arbitrarily determined in the X direction of the table. Likewise, Lines 130 and 140 are virtual lines, and Points 131 and 141 are virtual points. Generally, movement of a rigid body consists of parallel

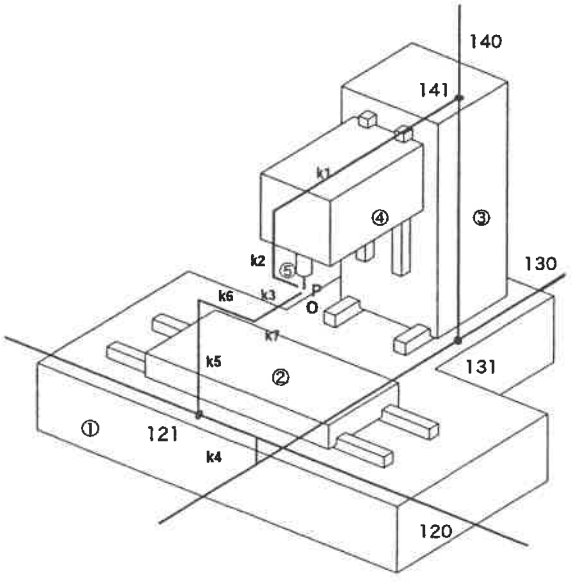

Fig 1. Arrangement of Virtual Lines and Points

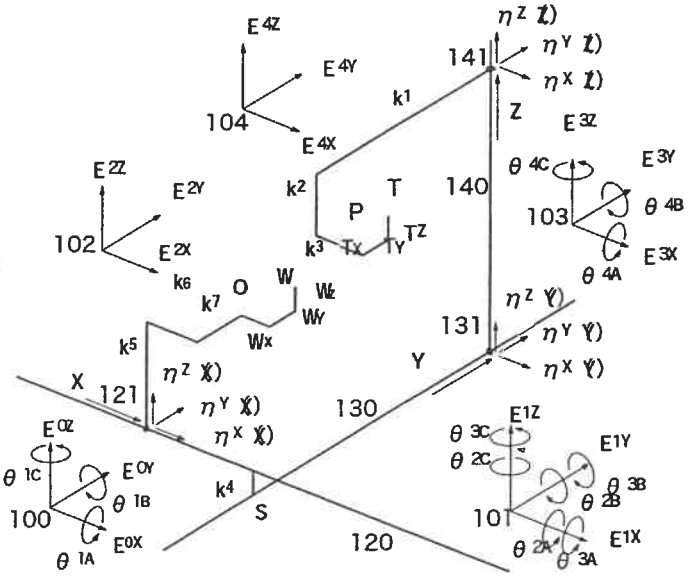

Fig 2. Model of the Machining Center with Error Vectors

motions and turning motions, and the travel can be separated into the turning motion centering on a discretionarily selected point on the body and the parallel motion of the center. Points 121, 131 and 141 in Figure 1 are selected as the centers of angle errors of the table, column and head respectively. Therefore, only the position errors in parallel motion occur at each virtual point.

Figure 1 is the state when the machine is at the starting position for processing. Point P is the tip of the tool, and Point O is the origin of processing on the table. When starting processing, virtual lines 120, 130, and 140 are in orthogonal positions, respectively. k_1, k_2, and k_3 are the lengths along each coordinate axis from Point 141 to tool tip P. k_4 is the distance between Line 120 and Line 130. k_5, k_6, and k_7 are the lengths along each coordinate axis from Point 121 to origin O.

3. MODELING OF MOTION WITH ERROR VECTORS

Figure 2 represents the wire frame showing the motion from the state in which tool tip P coincides with origin O to the state in which the table, column and head are simultaneously fed along the corresponding axis according to the feed command (X, Y, Z). Point T is the point on the head at a distance of (T_X, T_Y, T_Z) from tool tip P. Point W is the point on the table at a distance of (W_X, W_Y, W_Z) from origin O. Vector 100 (E_{0X}, E_{0Y}, E_{0Z}) is the unit vectors indicating the state of the coordinate of the laser fixed on the machine bed. Vector 101 (E_{1X}, E_{1Y}, E_{1Z}) on the bed, Vector 102 (E_{2X}, E_{2Y}, E_{2Z}) on the table, Vector 103 (E_{3X}, E_{3Y}, E_{3Z}) on the column, and Vector 104 (E_{4X}, E_{4Y}, E_{4Z}) on the head are the unit vectors, indicating the motion of each part respectively. When machining starts with tool point P at origin O, (E_{1X}, E_{1Y}, E_{1Z}), (E_{2X}, E_{2Y}, E_{2Z}), (E_{3X}, E_{3Y}, E_{3Z}) and (E_{4X}, E_{4Y}, E_{4Z}) should coincide and should not have angle errors.

$\eta_F(G)$ indicates positioning errors at Points 121, 131 and 141, where G represents the feeding direction and F represents the direction of the positioning error. θ_{1A}, θ_{1B} and θ_{1C} are the constant angle errors of E_1 from E_0, indicating the setting error of the laser optical axis on the machine bed. θ_{iA}, θ_{iB}, θ_{iC} (i=2,3, 4)are the angle errors of yaws, pitches and rolls. Vector R_T from Point S to Point T is expressed in Formula (1)

$$R_T=(Y+k_1+k_7)E_{1Y}+\eta_X(Y)E_{1X}+\eta_Y(Y)E_{1Y}+\eta_Z(Y)E_{1Z}+(Z+k_2+k_5+k_4)E_{3Z} +\eta_X(Z)E_{3X}+\eta_Y(Z)E_{3Y}+\eta_Z(Z)E_{3Z}+(k_3+T_X)E_{4X}-(k_1-T_Y)E_{4Y}-(k_2-T_Z)E_{4Z} \quad \cdots\cdots(1)$$

Similarly, Vector R_W from Point S to Point W is expressed in Formula (2).

$$R_W=(k_3-k_6+X)E_{1X}+k_4E_{1Z}+\eta_X(X)E_{1X}+\eta_Y(X)E_{1Y}+\eta_Z(X)E_{1Z} +(k_6+W_X)E_{2X}+(k_7+W_Y)E_{2Y}+(k_5+W_Z)E_{2Z} \quad \cdots\cdots(2)$$

Vector Δ from Point W to Point T is expressed in Formula (3) using the two vectors above. Δ_X, Δ_Y, Δ_Z are the components of E_{0X}, E_{0Y}, and E_{0Z} respectively.

$$\Delta=(\Delta_X E_{0X}, \Delta_Y E_{0Y}, \Delta_Z E_{0Z})=R_T-R_W \quad \cdots\cdots(3)$$

Vectors E_1, E_2, E_3 and E_4 are produced using E_0 [1], treating θ_{iD} (D=A, B, C) as the Eulerian angle. When incorporating these Vector into Formula (3) and ignoring $\eta_F(G)\ \theta_{jD}$ as the minimum, Δ_k, Δ_Y, Δ_Z, are calculated. For instance, Δ_X is expressed in Formula (4).

$$\begin{aligned}&\Delta_X(X, Y, Z, W_X, W_Y, W_Z, T_X, T_Y, T_Z)\\ &=-\eta_X(X)+\eta_X(Y)+\eta_X(Z)-X-W_X+T_X+\{Z+T_Z-W_Z\}\theta_{1B}\\ &-\{Y+T_Y-W_Y\}\theta_{1C}+\{Z+k_4+k_5+T_Z\}\theta_{3B}+\{k_1-T_Y\}\theta_{3C}\\ &+\{T_Z-k_2\}\theta_{4B}+\{k_1-T_Y\}\theta_{4C}+\{k_7+W_Y\}\theta_{2C}-\{k_5+W_Z\}\theta_{2B}\end{aligned} \quad \cdots\cdots(4)$$

X', the actual X-feed of tool tip P in the work coordinate system corresponding to the feed command X, is calculated by substituting zero for W_X, W_Y, W_Z, T_X, T_Y, and T_Z in Formula (4). The unknown numbers $\eta_F(G)$ are calculated in the way described in Section 4.

4. ARRANGEMENT OF THE ERROR DETECTORS ON THE MACHINING CENTER

Figure 3 shows the arrangement of the error detectors. Each detector is arranged separately to clarify its correspondence to the theory. Though the figure looks complicated, the actual constitution is simpler, thanks to multifunctionality and minimization of the detectors. 11, 12, 13, 14, 15, 16 and 17 are laser oscillators. Numbers from 51 to 56 are beam splitters to distribute laser beams. 21a, 24a,

25a, 26a, 31a, 34a, 35a, 36a, 41a, 44a, 45a and 46a are mirrors, and 21b, 24b, 25b, 26b, 31b, 34b, 35b, 36b, 41b, 44b, 45b and 46b are interferometers to detect feeds, pitches, yaws and rolls[2]. For example, 21a is attached to the table, and 21b is attached to the bed for detecting table feed.

61 and 62 are the pentagonal prisms used to reflect incident beams at a right angle. 61 is attached to the bed, and 62 is attached to the column. Beam 91 is the laser beam radiating from laser oscillator 17 and entering pentagonal prism 61. Beam 92 is the laser beam reflected through pentagonal prism 61 and entering pentagonal prism 62. Beam 93 is the laser beam reflected through pentagonal prism 62. Pentagonal prism 62 is attached to column, and it should be adjusted so that laser beams 93 and 91 cross orthogonally when the column starts to move. Vector E_0 indicates the states of 91, 92, 93. Numbers 22, 23, 32, 42 and 43 are the PSDs to detect rectilinear errors of moving lines. The units may be substituted by detectors using laser interference, which are composed of mirrors and interferometers[3].

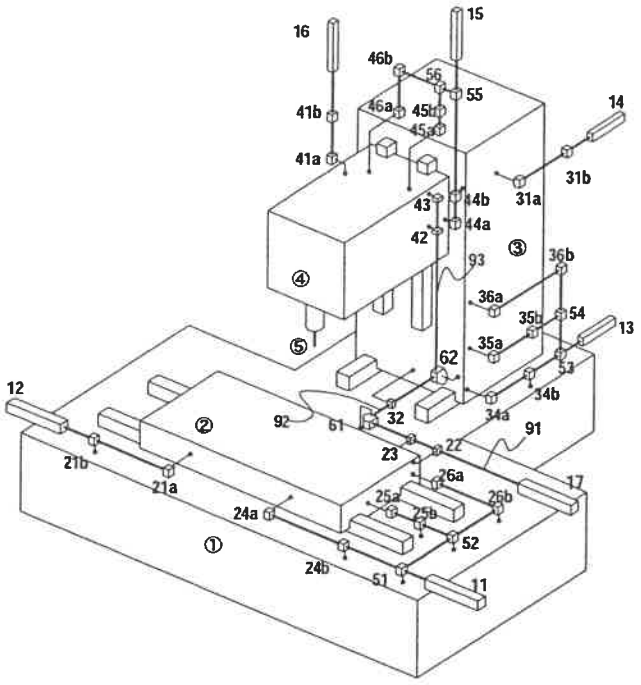

Fig3. Arrangement of the Error Detectors on the Machining Center.

The relation between the detected position errors and the fixed coordinates of the detectors can be calculated as follows. For instance, when $\delta_X(X)$ is defined as the feed error while feeding in the X-direction, and $(P_{X2},\ P_{Y2},\ P_{Z2})$ is defined as the fixed coordinate of detecting mirror 21a measured from origin O on the table at the start of processing, detected feed is not influenced by feed in the Y-direction or Z-direction, and it is, therefore, considered that Y=0 and Z=0, even though the machine feeds the head in three axial directions simultaneously. As a result, detected feed can be indicated as Formula (10) and an unknown value $\eta_X(X)$ is calculated from it.

$$X+\delta_X(X)=-\Delta_X(X,\ 0,\ 0,\ P_{X2},\ P_{Y2},\ P_{Z2},\ P_{X2},\ P_{Y2},\ P_{Z2})$$
$$=\eta_X(X)+X-(k_7+P_{Y2})\,\theta_{2C}+(k_5+P_{Z2})\,\theta_{2B} \qquad \cdots\cdots(10)$$

Calculate $\eta_F(G)$, i.e. the position errors at virtual points 121, 131 and 141, and incorporate them into Δ_X, Δ_Y, Δ_Z. Then, the actual feed $(X',\ Y',\ Z')$is calculated as indicated by formulas (12), (13) and (14), using the quantity of feed command, detected position error $\delta_F(G)$, detected angle error θ_{iD}, the coordinates of the position error detectors $(P_{Xi},\ P_{Yi},\ P_{Zi})$, $(H_{Xi},\ H_{Yi},\ H_{Zi})$, $(P_{Xi},\ P_{Yi},\ P_{Zi})$, and the coordinate of pentagonal prism 62 $(M_{Xi},\ M_{Yi},\ M_{Zi})$ measured when processing is started.

$$X'=X+\delta_X(X)-\delta_X(Z)-P_{Z2}\,\theta_{2B}+P_{Y2}\,\theta_{2C}+(M_Z-Z)\,\theta_{3B}-H_{Y4}\,\theta_{3C}+H_{Z4}\,\theta_{4B}-H_{Y4}\,\theta_{4C} \qquad \cdots\cdots(12)$$

$$Y'=Y+\delta_Y(Y)-\delta_Y(X)+\delta_Y(Z)+\delta_Z(Y)-H_{Z2}\,\theta_{2A}+H_{X2}\,\theta_{2C}+(P_{Z3}+V_{Z4}-V_{Y3}+M_Y-M_Z)\,\theta_{3A}$$
$$+(V_{X3}-M_X)\,\theta_{3B}-(V_{X4}-M_X+P_{X3})\,\theta_{3C}+V_{Z4}\,\theta_{4A}-V_{X4}\,\theta_{4C} \qquad \cdots\cdots(13)$$

$$Z'=Z+\delta_Z(Z)-\delta_Z(X)+\delta_Z(Y)+V_{Y2}\,\theta_{2A}-V_{X2}\,\theta_{2B}-V_{Y3}\,\theta_{3A}+V_{X3}\,\theta_{3B}-P_{Y4}\,\theta_{4A}+P_{X4}\,\theta_{4B} \qquad \cdots\cdots(14)$$

5. NUMERICAL CONTROL(NC) SYSTEM

In this method, the data of feed errors and angle errors detected by each interferometer, the data of rectilinear errors detected by each PSD, and the fixed coordinate of each detector are put into the high-speed calculation circuit. In the circuit, $(X',\ Y',\ Z')$, the actual position of tool tip P, is calculated using Formulas (12), (13) and (14). Next, the actual position is fed back to the motor controllers through pulse

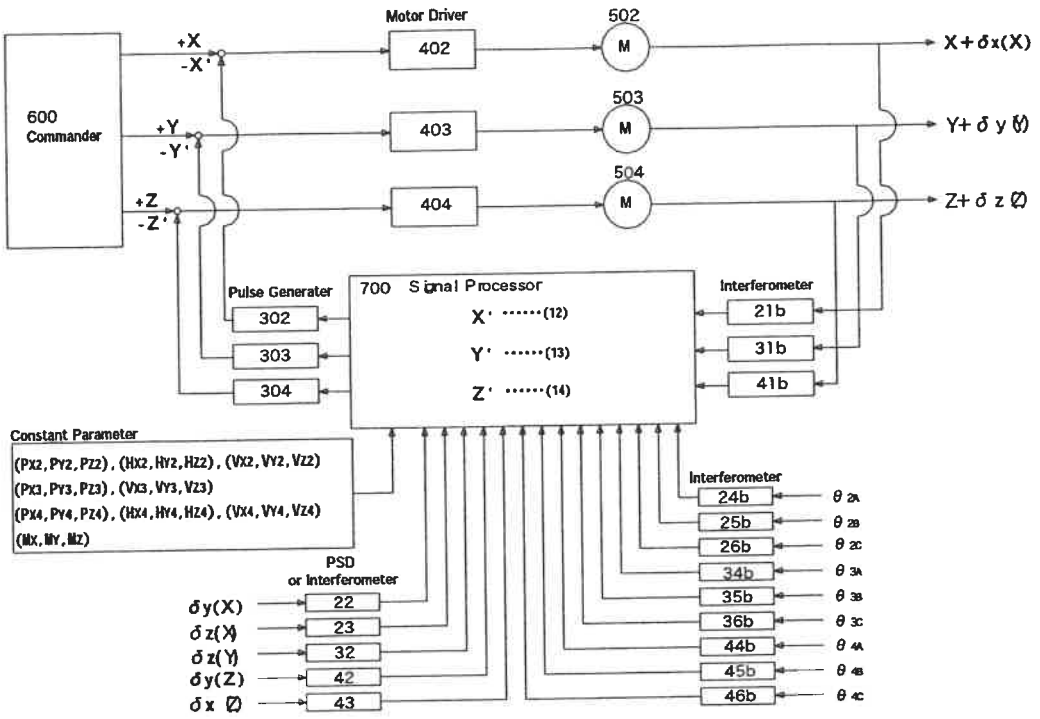

Fig4. Block diagram of the NC system to eliminate machining point error

generator circuit. In this way, the method aims to eliminate the machining points errors in feeding the tools. Rectilinear errors are detected by laser beams fixed on the bed crossing each other at a right angle, therefore, squareness errors between axes are included in rectilinear errors.

6. EFFECTS

The method controls the motion of the tool tip, which moves according to the orthogonal coordinate of the laser fixed on the machining center, and it enables highly precise processing without influence of irregular leads of feed screws, bending or uneven guide rails, or squareness errors between the axes which are caused during machine assembly. Moreover, even in the case of thermal deformation of a machine, rectangularity of the coordinate E_0 can be maintained. As a result, precision of machine operation can be maintained. When the theory is applied to a coordinate measuring machine, precision measurement can be attained while measuring the actual position of a measuring probe.

7. CONCLUSION

(1) The geometrical error vector model showed the relation of the machining point errors to the detected errors and the fixed coordinates of the detectors.

(2) The actual tool feed was calculated from the data of all detected in-process errors using the model above.

(3) Our NC method enabled the elimination of machining point errors by feedback of the actual tool feed to the servomotors of the tool.

REFERENCES

[1] Toyoshiro Inamura, Takeshi Yasui, Toshiaki Ozawa, Yukio Watanabe and Hiroyuki Yoshida: The Precision Test of Machining Centers Using the Geometrical Error Model, Jounal of Japan Society for Precision Engineering, 51, 05 (1985) 1060-1067

[2] Toshihiro Nakayabu, Masahiro Okaji, Hidetaka Imai and Goki Wakabayashi: The Development of the Simple Laser Interferometer for Measuring Rolling, The Thesis Collection of the Conference in Matsuyama, Japan Society of Mechanical Engineers, 25-2 (19/10/2002) 259-260

[3] Toshiriho Nakayabu and Hiroyuki Kawara: Laser Interferometers, Japan Patent Application No. 2003-9100

Error Compensation via Command Signal Deconvolution

Witoon Panusittikorn, Kenneth P. Garrard, Thomas A. Dow
North Carolina State University, Precision Engineering Center
Campus Box 7918, Raleigh, North Carolina USA

A signal processing technique has been developed to dramatically increase both the usable bandwidth and tracking accuracy of an actuator. All actuators exhibit varying amplitude and phase response to multiple frequency input signals. This makes it difficult to utilize their full small-signal bandwidth for high precision motion. For example, even a small phase lag in an axis of a turning machine may result in significant form errors due to the high relative velocity of the spinning workpiece and the cutting tool. The goal of this research is to use an understanding of the dynamics of an actuator to create an input command compensation technique to correct for anticipated motion errors. Deconvolution is a mathematical procedure that can produce a modified input to reverse the effects of attenuation and phase if the impulse response of the dynamic system is known. Since the modified signal is not calculated from the position feedback information, there is no delay in the response. The algorithm differs from feedback control in that it is implemented off-line to make use of the entire command signal to produce a modified actuator input signal. When the actuator is driven with this modified signal its motion will exhibit attenuation and phase lag that convolves with its dynamic response to produce the original desired position trajectory. In this way the individual motions of the axes can be synchronized to produce the correct machined surface. This technique critically depends on knowledge of the actuator dynamics and does not replace the feedback controller. Rather it works with the control system to improve the response of an actuator by compensating for high frequency dynamics that the servo feedback loop cannot correct due to its reactive nature and saturation of the drive system. When applied to a long-range fast tool servo, the result is a dramatic reduction in following error especially for high frequency motion [1].

Background A diamond turning lathe is capable of producing high quality surfaces in a variety of nonferrous materials. However, its use is normally limited to surfaces of revolution that are realized by moving the tool and/or workpiece through one-half of a cross section of the desired shape while the rotation of the workpiece on a spindle causes a symmetric surface of revolution to be machined. Advantages of turning are reduced process times as compared to milling or fly-cutting due to the continuous high cutting speed achieved via rotation of the workpiece, excellent form fidelity and optical quality surface finish.

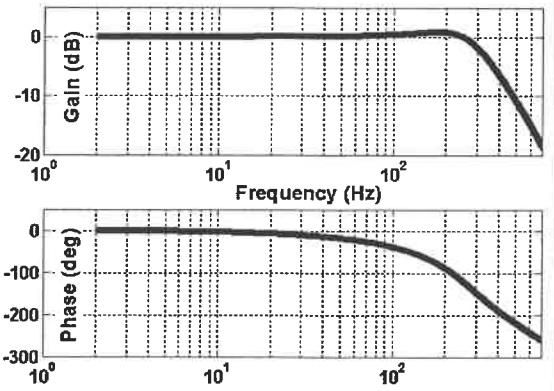

Figure 1. Dynamic response of the Variform.

It is desirable to produce optical systems with the diamond turning process that have features of high spatial frequency or are non-rotationally symmetric (NRS). The addition of a high-bandwidth fast tool servo (FTS) is one technique that has been used to add low amplitude, sub-revolution features to an asphere or sphere. Examples include torics and segmented off-axis conics. The slow-slide servo technique uses the axes of the machine to directly produce NRS features in a rotating workpiece. Both techniques depend on the proper synchronization of the machine tool axes at high relative frequencies.

This work experimentally validates an inverse dynamics command signal modification algorithm with a commercially available Variform fast tool servo and a diamond turning machine. The relevant linear systems theory, the algorithm, its implementation and preliminary experiments are described elsewhere [1,2]. The Variform has a 400 μm range and a bandwidth of 350 Hz. The response of this actuator is

predominately second order although nonlinearities are present for large amplitude command signals. The nominal dynamic response of the Variform is shown in Figure 1. The top graph shows the ratio of the amplitude of the output to the input as a function of frequency. At low frequency, the output is equal to the input and the ratio is unity giving a dB value of zero. As the frequency is increased, the amplitude response peaks at about 200 Hz and then drops rapidly for higher frequencies. The lower graph in the figure shows the phase angle between the input and the output. At lower frequencies these signals are nominally in phase, but even a small lag of less than a degree represents a significant length of arc if the actuator is at a large radius from the axis of spindle rotation. As the frequency rises the output increasingly lags the input. At 100 Hz this lag is about 45° and at 340 Hz it is about 180°. The goal of this project was to accurately machine NRS surfaces with a Variform operating at frequencies above 200 Hz. A significant complication is that the dynamics shown in Figure 1 are not correct for all amplitude and frequency combinations. The actuator velocity saturates at about 140 mm/sec and behaves nonlinearly if the driving command exceeds this limit. Figure 3 shows an expanded frequency response for the Variform as a function of excitation amplitude.

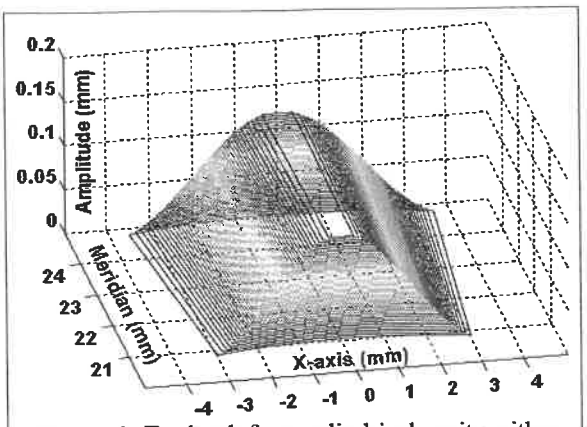

Figure 2. Toolpath for a cylindrical cavity with a cosine wave cross section.

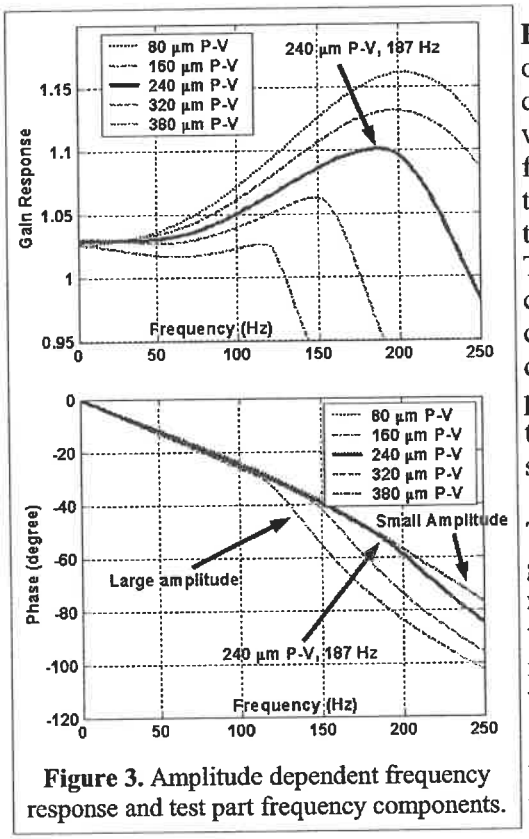

Figure 3. Amplitude dependent frequency response and test part frequency components.

Experimental Verification A cavity with the cross section of a cosine wave was selected as a test shape to verify the deconvolution technique. The shape is shown in Figure 2 where a full period cosine wave is smoothly integrated into a flat surface. As a result, no sharp corners exist in the tool trajectory and, since the cavity has a constant depth, the same tool excursion can be replicated for every revolution. Turning this feature does not require tool radius compensation so the input command modification technique can be clearly validated without the influence of other corrective schemes. This profile is easily measured with a profilometer and the machining parameters can be adjusted to obtain a specific frequency and amplitude in the command signal.

The desired shape is an 18-degree wide, off-axis cosine groove with a 240 µm peak-to-valley sag. If machined at 561 rpm, the dominant frequency will be 187 Hz[1], which is close to a peak of the gain response of the Variform FTS as shown in Figure 3(a). At this frequency, the output trajectory will be amplified by 10% and delayed by 52° resulting in a significant path difference with respect to the desired cosine wave. The overlap-add block convolution method [3] was used to filter the designated tool path with the inverse of the dynamics shown in Figure 3. The operation was performed in the time domain where the desired excursion is segmented into blocks of arbitrary size and each block is individually filtered (ie, convolved) with the inverse impulse response. The overlap-add algorithm prescribes how the resulting blocks are combined to produce a complete filtered output signal.

[1]If machined continuously around the part, there would be 20 waves and the temporal frequency would be 187 Hz.

A simulated output trajectory is shown in Figure 4. The actuator motion (points) associated with a modified input command (circles) is very close to the desired path (squares). The estimated error (a dashed line) is less than 200 nm P-V.

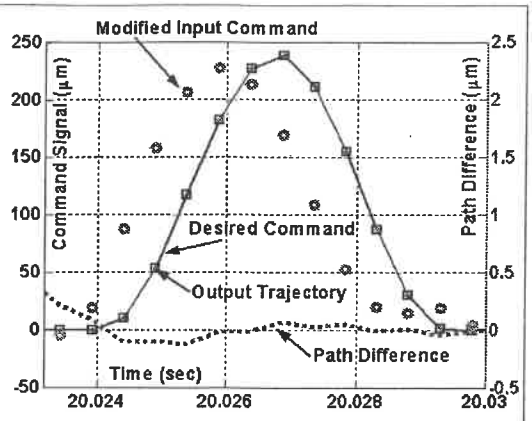

Figure 4. Simulation of modified toolpath yields an error of 200 nm P-V.

Next the modified input signal was experimentally verified by mounting the Variform FTS on an optical table and measuring its displacement with a distance-measuring laser interferometer. Figure 5(a) illustrates the agreement of the FTS motion (x marks) and that of the simulation (Figure 4). The output trajectory was in-phase and the path difference was ±1 μm near the peak and 8μm at the edges. A mismatch between the gain response used in the deconvolution operation and the actual response of the FTS may cause the path difference of the actual tool trajectory to be larger than that of the model. On the other hand, the tool trajectory (x marks in Figure 5 (b)) associated with an unmodified signal was, as expected, 10 μm bigger, and 52° out of phase with respect to the desired path (a solid line). The dynamic response of the Variform results in a path difference (a solid line) that resembles a sinusoidal profile with a magnitude of 225 μm P-V.

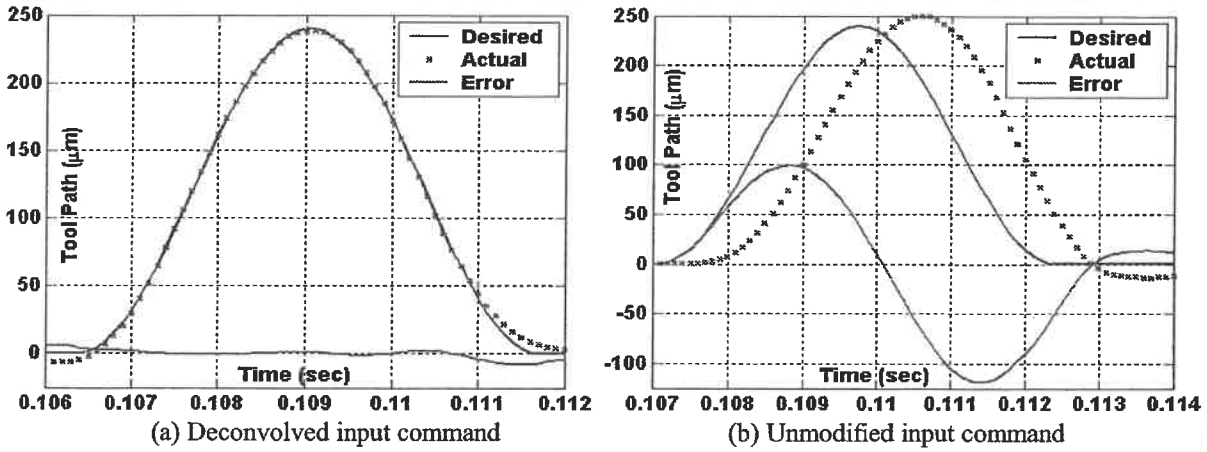

(a) Deconvolved input command (b) Unmodified input command

Figure 5. Comparison of path differences associated with modified and unmodified commands.

Machined Features The cylindrical cavity with a cosine cross section profile was fabricated into a copper blank. The location of the desired machined feature was created at 0° with respect to the reference flat. In Figure 6, the cosine groove close to the outside of the copper blank was machined using the modified input command whereas the other surface close to the center was associated with the unmodified input command.

A comparison of the form errors between the modified and unmodified surfaces was made using the Talysurf profilometer and the phase angles of the machined surfaces were measured using a microscope with linear scales on the axes of its sample translation table. This located the features in Cartesian coordinates which were then transformed to polar coordinates (r,θ). The profile of the machined surface associated with the deconvolved input command (measured along the trace (A) in Figure 7) is depicted as a solid line in the top graph of Figure 8(a), and the profile of the unmodified surface (measured along the trace (B) in Figure 7) is illustrated in Figure 8(b). The path differences with respect to the desired surface profile are plotted in the bottom graphs of both Figure 8(a) and 8(b) and show that the unmodified

surface was 50° out of phase resulting in a path difference of 122 μm P-V. The deconvolved surface was in-phase yielding a significant reduction in form error of almost two orders of magnitude (4 μm P-V) as shown in the bottom graph of Figure 8(a). However, the average of the path difference is about 10 μm. This means that the amplitude of the modified surface is short by 10 μm with respect to the desired surface.

Conclusions The modified input signal created by the deconvolution technique improves the form fidelity of a machined surface when compared to that of the unmodified signal. The figure errors can be reduced by two orders of magnitudes due mostly to the correction of the phase errors. This result is true even if the machining conditions do not exactly match those designated. The machining experiments corroborate the simulated results and the tool path measurements using the laser interferometer when the Variform is mounted on an optical table. The results are also superior to those obtained if the phase and gain were adjusted based on the attenuation and lag at the operating frequency because the shape of the desired input command will not be correct. The shape of the input command signal must be modified to yield the output tool path close to the desired excursion.

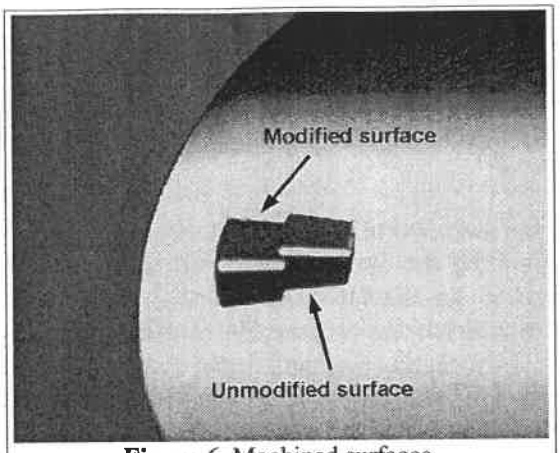

Figure 6. Machined surfaces.

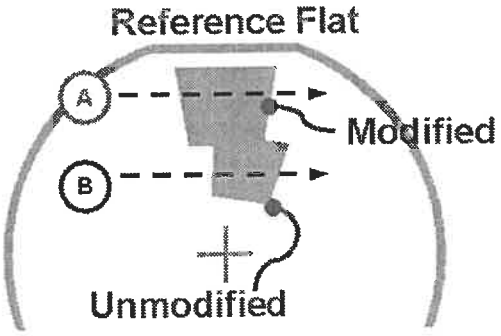

Figure 7. Profile measurements parallel to reference flat.

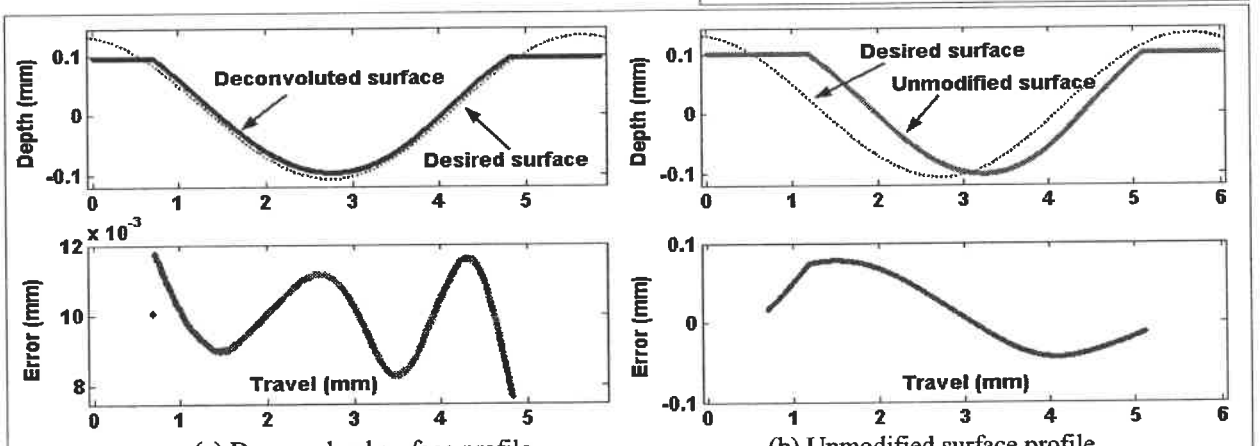

(a) Deconvolved surface profile
P-V error = 4 μm

(b) Unmodified surface profile
P-V error = 122 μm

Figure 8. Profile measurements of the modified and unmodified machined surfaces.

References

[1] Panusittikorn, W. Error Compensation using Inverse Actuator Dynamics. PhD Dissertation, North Carolina State University (2004).

[2] Panusittikorn, W., K.P. Garrard and T.A. Dow. Error Compensation using Inverse Actuator Dynamics. Proceedings of the Eighteenth Annual Meeting of the ASPE, 30, 107-110, (2003).

[3] Oppenheim, A.V. and R.W. Schafer. *Discrete-Time Signal Processing*. Prentice-Hall (1999).

Low Cost Flexure Alignment Features

Fadi Abu Ibrahim, Shorya Awtar, Jason Sutin, Alexander H. Slocum
Precision Engineering Research Group
Department of Mechanical Engineering
Massachusetts Institute of Technology
77 Massachusetts Avenue, Room 3-445
Cambridge, MA 02139 USA
slocum@mit.edu http://pergatory.mit.edu

Introduction

The alignment of components is often done using pins and slots; however, pins in holes and slots require some clearance between the features which reduces accuracy and repeatability. Removing such clearances deems the design over-constrained. True preloaded kinematic constraint between the parts to be pinned together can be obtained by treating the pins themselves as components of the assembly, and then properly constraining the pins against appropriate rigid surfaces and then preloading them against those surfaces with flexural elements. This method is particularly useful for assembling plates containing flexures cut using an abrasive waterjet or by EDM.

Design

Two plates 100 mm x 100 mm x 12 mm were made with 0.375" dowel pin restraints in their corners. All features were made using an OMAX[1] model 2626 Abrasive Waterjet Machining Center which had an accuracy of 50 microns[1]. One constraint was a right triangle with the hypotenuse as a flexural element. The flexural element preloaded a dowel pin into the corner. On the opposite corner of the plate, a groove aligned to the right triangle also had one side made as a flexure to preload a dowel against the rigid side. This allowed both plates to be made using the same part program, canceling the need for secondary machining. Figure 1 highlights these features with a black dotted circle. Another design utilized the concept of elastic averaging. The constraints consisted of equilateral triangles with all three sides functioning as flexural elements. The two constraints were positioned on opposing corners of the plates. Figure 1 highlights the features with a white dotted circle.

Experiment Setup:

The experimental setup used to measure the repeatability and the accuracy of the assembled plates had six mounting flexures designed to fixture capacitance probes with a uniform pressure on the probes' surface. 1/16" tapered pipe plugs where used to apply pressure to the clamping fixture. Figure 2 is a CAD model of the mounting flexures. The six probes were mounted in three pairs; probes of each pair were aligned vertically with an offset distance of 6mm between their centers. A three-pin kinematic coupling feature was added to the setup to easily mount and

[1] http://www.omax.com

unmount the test plates to the same location. The coupling was created by press-fitting three (1/4") dowell pins. The setup was machined with the OMAX waterjet cutter; secondary machining was done on a Bridgeport® mill. The machined setup with the Capacitance probes mounted in place is shown in Figure 3.

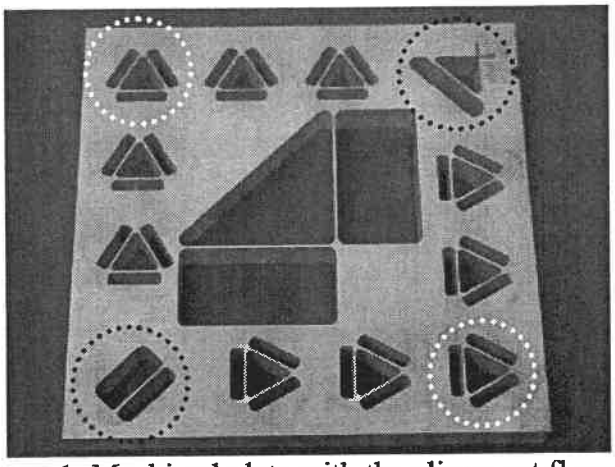

Figure 1: Machined plate with the alignment flexures

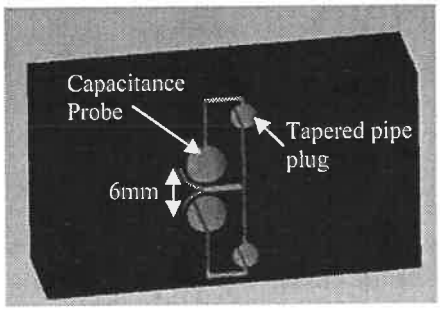

Figure 2: Solid model of the Cap-probe mounting flexures

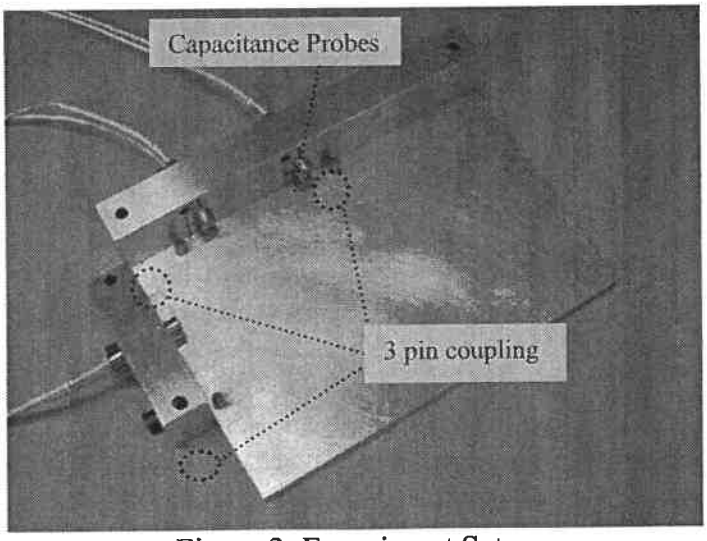

Figure 3: Experiment Setup

Experiment results

The accuracy of the experimental results were tested for via two sets of data. First the plates were placed on the experimental setup and left undisturbed. The drift in the probe readings over time was measured to be on the submicron level for all six probes. The submicron drift values are negligible and prove that the experiment readings are consistent and essentially independent of vibration, noise and temperature effects from the surrounding environment. Data from two of the probes are shown in Figure 4.

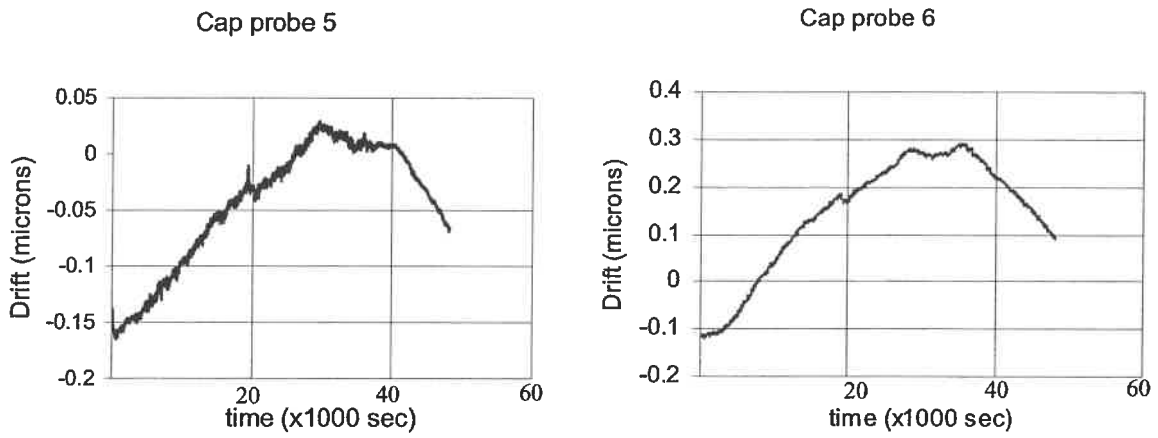

Figure 4: Cap probe drift readings

Test plates where removed and then reintroduced into the setup to measure the effects on repeatability of the measurements to repositioning of the plates relative to the probes. Charts shown in Figure 9 show the measurements of plate misalignment changing in a submicron range as well. The setup is repeatable and not sensitive to part or hand disturbances.

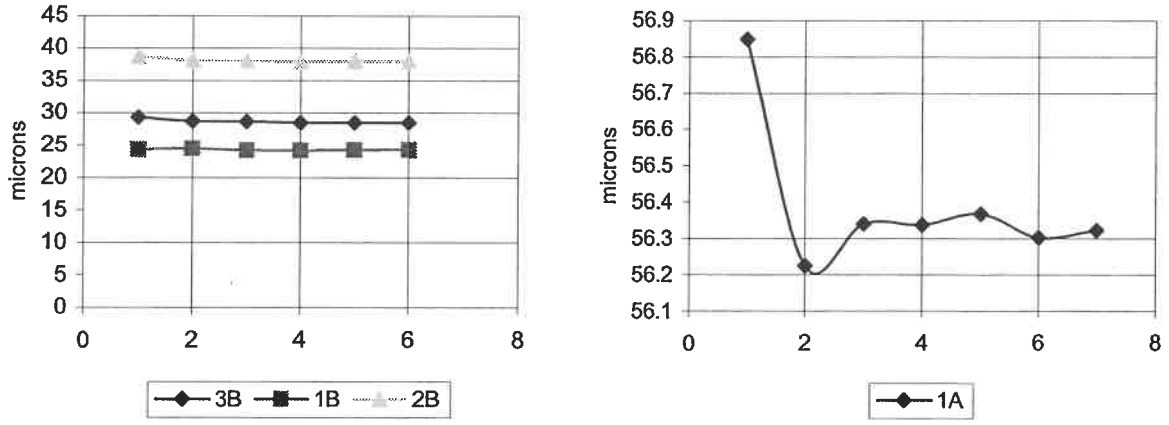

Figure 5: Charts of the results from removing and reintroducing the plate back into the setup at four points (3B, 1B, 2B and 1A)

To test the repeatability of the alignment flexures to disassembling and reassembling the plates, measurements for all six probes were performed several times in which the test plates were taken off the setup, decoupled from each other and then pinned back together again. Results were in

the range of 1 to 25 microns, where the large values are likely due to friction and shear at the flexure features. To measure the plate alignment a reference surface was used to measure the offset distance between the capacitance probes on the setup. Afterwards the plate misalignment, δ, was calculated based on the simple formula as shown in Figure 6. The alignment of the plates was in the range of 30 to 60 microns. A CMM machine was used to scan the test plates and the misalignment due to the water jet cutter resolution was corrected for. The corrected alignment was 13 to 43 microns.

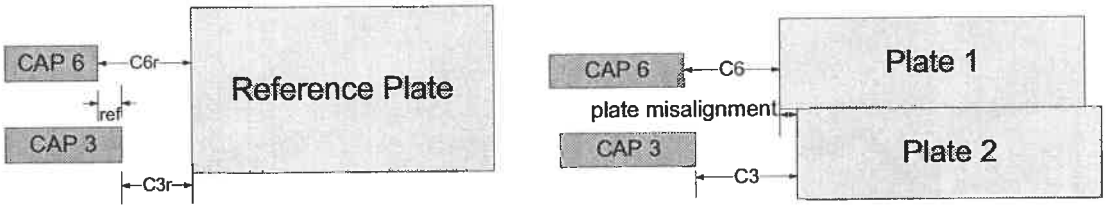

$$\delta = C_3 - C_6 + (C_{6r} - C_{3r})$$

Figure 6: Plate misalignment δ

Conclusion

An abrasive waterjet cut part can be 1/3-1/4 of the cost of a wire EDM cut flexure. Further cost reduction can be achieved and the taper created by a waterjet can be mitigated using the new alignment method. Thinner parts can be cut which saves cutting time and costs: cutting two 12 mm thick parts and then accurately aligning them reduces the total machining time by 40% as compared to machining a 24 mm thick part. Cutting thinner parts reduces the taper generated by the water jet, and the two plates can be assembled back-to-back. This reversal cancels the effect of the taper and places the shear center of the assembly at the center of the part. In addition to that damping materials can be sandwiched between the two plates. Future work will include studying the applicability of the features on plastics and sheet metal [4].

References

1 M Culpepper et al, *"Quasi-kinematic Couplings for Low-Cost Precision Alignment of High-Volume Assemblies"*, ASME journal of mechanical design, September 2002

2 A. Slocum, *"Precision Machine Design"*, SME Publishing, 1992

3 L. Hale, *"Principles and Techniques of Designing Precision Machines"*, MIT PHD thesis, 1999

4 B. Leibinger, *"The Fascinating World of Sheet metal"*, TRUMPF Gmbh, 2nd edition

Thin Optic Constraint

Mireille Akilian[1], Craig R. Forest, Alexander H. Slocum, David L. Trumper, and Mark L. Schattenburg
Massachusetts Institute of Technology, Cambridge, MA 02139

1 Introduction

X-ray telescopes utilizing monolithic mirrors have accelerated the progress of modern astrophysics due to their excellent resolution; however, the overall design suffers from weight and cost disadvantages. A proposed alternative approach to manufacturing x-ray telescopes is the use of thousands of segmented thin foil optics, such as glass and silicon substrates, as mirrors and gratings because of their low mass and high strength.

Over the past few years, progress has been made in the shaping and accurate assembly of the thin foils that provide x-ray reflecting mirror surfaces. The enabling technology for further improvements lies in the advances of surface metrology of thin optics. This paper covers the design of a holder that can be used to accurately measure the free-form surface topography of thin optics and thus evaluate their shaping processes. This device minimizes the effects of external loads acting on the thin substrate, such as gravity induced sag, frictional forces during optic manipulation, and thermal stresses. The significant effects of these loads contribute to the deformation of thin optics, leading to inaccurate metrology results. The optics of interest include borosilicate glass and single-crystal silicon with rectangular (100 mm×140 mm×0.4 mm) and circular (diameter 100 mm×0.4 mm) geometries.

The device will be used in conjunction with a Shack-Hartmann surface metrology system to provide accurate and repeatable surface maps [1]. The maximum tolerable deformation due to the optic's warp as a result of the external forces mentioned above and the repeatability of the metrology tool, is 0.5 μm.

The use of air bearings to constrain thin optics has been thoroughly analyzed and evaluated [2]. Air bearings eliminate contact with the optic and the associated problems of friction and thermal stresses; however, due to the extremely tight tolerances and design complexity associated with high cost, an alternative, passive design utilizing flexures is considered to fully constrain thin optics, as shown in Fig. 1 *(a)*.

Three double-sided, monolithic flexures are in contact with both sides of the optic, as shown in Fig. 1 *(b)*. Monolithic wire-electric-discharge machined (EDM) blade flexures are used to minimize the misalignment between the opposing flexure arms that leads to local torques on the optic.

2 Flexure Design

The monolithic structure is divided into two sets of flexures, as shown in Fig. 1 *(c)*. The vertical flexure opens to insert the optic and provides a preload once the optic is in proper position. The opposing flexures account for thermal expansion mismatch between the optic and the device.

2.1 Vertical Flexure Arm

The vertical flexure is designed to have a horizontal displacement of 1.6 mm with a maximum stress corresponding to 52% of the yield stress of aluminum. This large deflection is needed when inserting the optic between the opposing flexures. This flexure is actuated at its midpoint to minimize parasitic vertical motions associated with lateral deflections [3]. The tip of the vertical flexure undergoes very small vertical motion; however, the free end of one of the opposing flexure pair attached to the vertical arm undergoes a larger parasitic motion due to a sine error. This places an upper limit on the length of the opposing flexures, if misalignment between them is to be kept minimum. Upon removing the actuation force from the vertical arm, it springs back until contact with the optic is achieved. At this point the flexure acts as a cantilever with a stiffness of 2.45×10^{-4} N/μm. Upon placing the optic into the device, the vertical arm is displaced by 275 μm corresponding to a force of 0.067 N. The fact that this preload is small poses a risk on the overall stability of the device. Tests have shown that this does not manifest itself as a problem, and the optic does not vibrate while constrained; however, the countermeasure is to resize the dimensions to increase the stiffness of the vertical flexures, resulting in a smaller opening during optic insertion/removal.

[1]email: makilian@mit.edu.

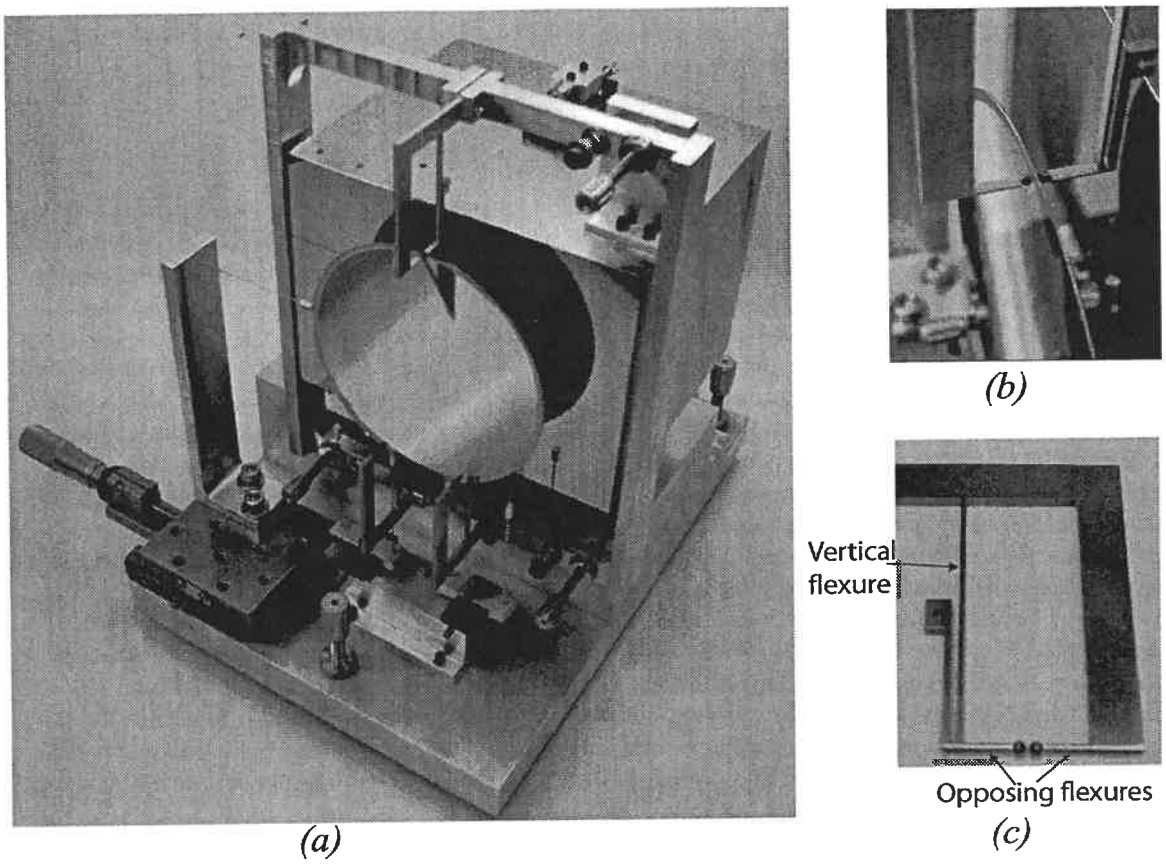

Figure 1: *(a)* The assembly of the double-sided flexures constraining a circular silicon optic during surface metrology. *(b)* A silicon wafer constrained by the monolithic flexure with two ruby balls mounted at the tip of the opposing arms. *(c)* Monolithic, wire EDM-ed, double-sided flexures made of stress-relieved Al 6061 T651. The left vertical arm is actuated back and forth at its center to allow for the optic insertion/removal. The opposing flexures accommodate thermal expansion mismatch between the optic and the Al device.

2.2 Opposing Flexure Arms

Blade flexures are compliant in one direction only, whereas thermal expansion occurs in all directions; therefore, the blade flexures must be held at different angles for best stability and performance. The flexures are placed such that the normals to the blades bisect the angles of the triangle formed by the three contact points with the optic, as shown in Fig. 2 *(left)*. This is analogous to the kinematic coupling lay out for best stability [3]. The top flexure is the most susceptible to thermal mismatch errors because the differential length between the optic and the device is a maximum at this point; therefore the top blade is placed such that its compliance is along the direction of maximum thermal growth.

The tips of the flexures have a post used for mounting drilled ruby balls, such that the gap between the two balls is 125 μm. Contact occurs between the ruby balls and the optic. Ruby is chosen for its hardness, leading to better repeatability and smaller Hertzian deformations.

When calculating the required compliance for the opposing flexures, it is assumed that the point of contact between the ruby ball and the optic, after the flexure mechanism preloads both sides of the optic, does not allow for slip. The flexures are modeled as cantilevers. An upper limit of 1°C temperature change per surface map measurement determines the amount of flexure deflection needed. For a coefficient of friction of 0.3 between ruby and glass [4], and a preload of 0.067 N, the corresponding friction force is 0.02 N. The

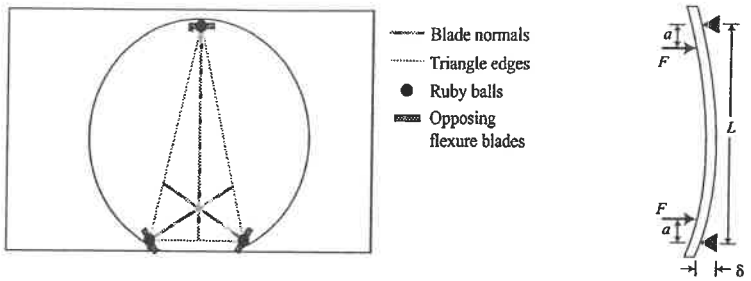

Figure 2: *(left)* The normals to the blades of the opposing flexures bisect the angles of the triangle formed by the three contact points between the circular/rectangular optic and the ruby balls. *(right)* Thin optic modeled as a simply-supported beam with twin loads to characterize the deflection caused by the misalignment of the ruby balls due to the parasitic motion. F is the preload from the flexure, a is the parasitic displacement, and L is the distance between the upper and lower monolithic flexures.

flexures are located at characteristic thermal lengths of 100 and 17 mm. For a 1°C temperature variation, the differential changes in length between the aluminum housing and silicon optic at both positions are 1.2 and 0.27 μm, respectively. These values correspond to the displacement at the flexure tip caused by the friction force calculated previously. Therefore, the required stiffness k ranges between 0.017 and 0.095 N/μm. To minimize the parasitic motion, a length of 6.75 mm is chosen for all opposing flexures with a thickness of 0.6 mm for ease of machining, which gives a stiffness of 0.024 N/μm. The associated parasitic motion calculated using finite element analysis is 6.6 μm. To see the effect of this displacement, the optic is modeled as a simply-supported beam with twin loads at a distance of 6.6 μm away from the supports, as shown in Fig. 2 *(right)*. The maximum deflection δ is found to be 8.65 nm using

$$\delta = \frac{Fa(3L^2 - 4a^2)}{24EI}, \tag{1}$$

where F is the preload, a is the parasitic displacement, L is the distance between the top and bottom flexures, E is Young's modulus of glass, and I is the moment of inertia. Measuring the surface of an optic over a period of 3 hours, during which the temperature of the room increases by 1.2°C reveals a maximum overall change of 47.5 nm in the second-order Zernike polynomials. This value is very close to the repeatability of 35.6 nm of the metrology tool.

2.3 Load-Carrying Flexures

To remove the effects of friction and thermal expansion while supporting the weight of the optic, "antenna" flexures are used to constrain the remaining three degrees of freedom. The flat on the circular optics is placed on an inner pair of flexures, whereas wider, rectangular optics are placed on an outer pair that is 0.5 mm longer than the inner one, as shown in Fig. 3 *(left)*. The optic sits on a hollow sapphire cylinder mounted at the tip of these flexures, as shown in Fig. 3 *(center)* to form a small line contact at the interface. While placing the thin sheet into the device, a temporary torque may unintentionally be applied onto the foil by the user. Friction at the interface may hinder the internal elastic force of the optic from restoring it to its natural shape, causing an artifical warp of the substrate during metrology. The role of the antenna flexures is to reduce the effects of this friction force, which can be calculated using the weight of the optic and the coefficient of static friction between the glass foil and sapphire tube [4]. The design stiffness of the antenna flexures is found to be 2.18×10^{-5} N/μm, using friction combined with the maximum distance d the optic can move while resting on the antennas. The finite stiffness of these flexures becomes an issue when the optic is placed at a distance d away from its nominal position as shown in Fig. 3 *(right)*. As the ruby balls constrain the optic, the two load-carrying flexure tips move a distance d, thus imposing an equivalent force of $2F$ on the foil, F being the restoring force of a single flexure. The optic is modeled as an overhung,

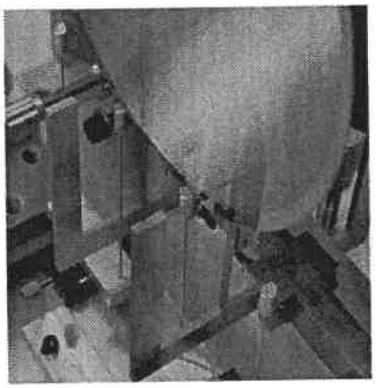

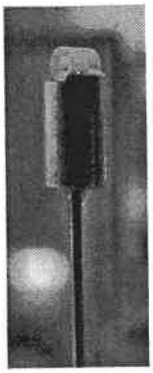

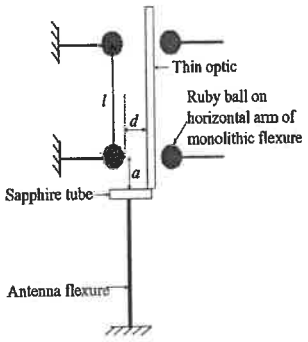

Figure 3: *(left)* Circular optics sit on the inner pair of antenna flexures, whereas rectangular ones contact the outer, longer pair. This allows for better stability with rectangular substrates, since the corresponding flexures are placed further apart; the length of the flat on circular optics (~31 mm) constrains the distance between the inner flexures. *(center)* Sapphire tube mounted on top of the antennas to facilitate optic placement on these flexures. *(right)* Thin optic placed at the very edge of the sapphire tube on the antenna flexures (figure not to scale). This leads to the motion of the flexures by distance d until the optic is fully constrained, resulting in a restoring spring force from the antennas onto the optic.

simply-supported beam to calculate the deformation δ caused by the flexures using

$$\delta = \frac{Fa^2(l+a)}{3EI}, \tag{2}$$

where a is the distance between the force from the antennas and the closest pin (ruby balls on the blade flexures), and l is the spacing between the two pins. The maximum deflection is found to be 148.55 nm. Experiment shows a maximum change of 157.5 nm in the second-order Zernike polynomial when the optic is misplaced, as shown in Fig. 3 *(right)*.

The placement repeatability of the system, where an optic is placed on the load-carrying flexures, fully constrained with the ruby balls, and removed and placed into the device again is 55 nm, which is very close to the repeatability of 35.6 nm of the metrology tool. This is sufficient to verify foil manufacturing and shaping processes and assure a surface non-flatness of <500 nm as required for x-ray optics.

3 Conclusions

A device for holding thin optics during metrology has been designed and manufactured. This device utilizes monolithic blade and tube flexures to kinematically constrain all degrees of freedom with a dynamic repeatability of 55 nm, while minimizing additional surface deformation caused by external forces.

References

[1] Craig R. Forest et al. Metrology of thin transparent optics using shack-hartmann wavefront sensing. *Optical Engineering*, 43:742–753, 2003.

[2] Craig R. Forest et al. Thin glass optic and silicon wafer deformation and kinematic constraint. *Proc. of the 18th Annual Meeting ASPE*, 30:39–42, 2003.

[3] Alexander H. Slocum. *Precision Machine Design*. Society of Manufacturing Engineers, 1990.

[4] Material property data. Available at: http://www.matweb.com.

Live Axis Turning

Nathan Buescher, Thomas A. Dow, Alex Sohn, Bruce Norlund*, Jeff Roblee*
Precision Engineering Center, North Carolina State University
*Precitech, Inc., Keene, NH

INTRODUCTION

The objective of the development of the Live Axis Turning (LAT) process is to apply recent advances in air-bearing slide design and linear motors to increase the velocity and range of tool motion and demonstrate a commercially viable device that will extend the fabrication capability of non-rotationally symmetric (NRS) surfaces. This technology, aided by high-resolution feedback devices and advanced control algorithms, will allow NRS surfaces to be machined efficiently and accurately on currently available diamond turning lathes. The goal is to create a tool axis capable of 4 mm displacement at 20 Hz.

Diamond turning has revolutionized optical fabrication because of its ability to accurately and rapidly create optical surfaces as well as opto-mechanical features used in optical alignment. An emerging trend in optical design is the use of optical surfaces that are not rotationally symmetric (NRS). When such surfaces are included in an optical system, the complexity, bulk and weight of the system can be reduced[1]. The shape of these surfaces can typically be divided into a best-fit sphere or asphere and a non-symmetric component as illustrated in Figure 1. It is this non-symmetric component of a surface that required the use of a fast axis.

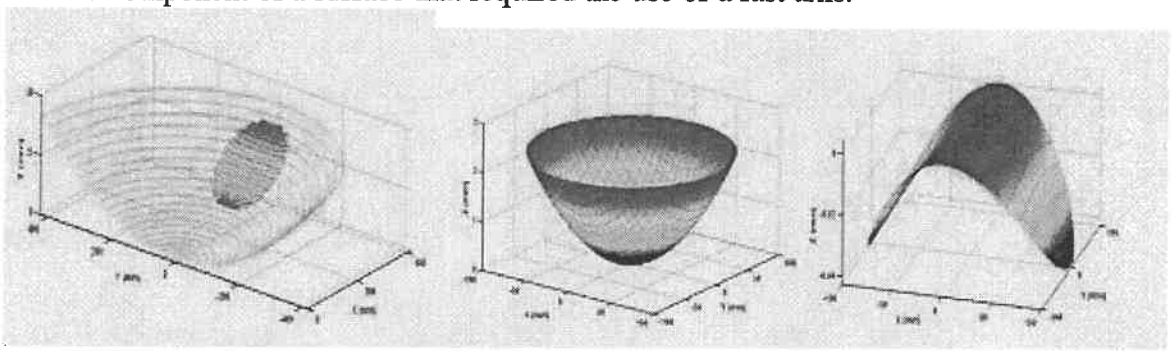

Figure 1: Decomposition of off-axis toroidal mirror surface (left) into symmetric (center) and non-symmetric (right) components for on-axis fabrication.

Presently, NRS surfaces can be created on a diamond turning machine (DTM) by using two slow-speed axes (slow) to generate the entire surface or three slow-speed axes with a fly cutter to raster scan the surface. Problems arise with these two methods: in the first method the spindle speed must be less than 50 rpm because of the low bandwidth of the slow-speed axes and thus the time for one pass of the tool for a 25 mm part will be over one hour. The second method requires exceedingly slow scans to produce an optical surface finish with a flycutter. Thus, long machining times and the associated thermal drift hamper both methods. Another technique is to add a Fast Tool Servo that is synchronized to the rotary position of the spindle on a 2D lathe. This arrangement will make a diamond turning machine more versatile and can efficiently produce an NRS optical surface. The main axes of the DTM create the symmetric component, the FTS adds the non-symmetric component and together they create the desired optical shape. The range of this auxiliary FTS axis dictates the maximum feature size possible while the feed rate and spindle speed have a direct bearing on the time to fabricate the surface and the cost. The

new LAT Axis exceeds the range of the commercial FTS by a factor of 10 while the operating frequency is more than 25 times greater than when using the machine slides.

ACTUATOR DESIGN

The goal is to develop a light-weight, high-speed, air bearing, linear motor driven slide that can operate with a stroke of 4 mm at 20 Hz. The LAT design consists of a lightweight aluminum-honeycomb slide driven by a linear motor and guided by stiff air bearings. A holder for a diamond tool is attached to the front of the slide. A drawing of the proposed LAT system is shown in Figure 2.

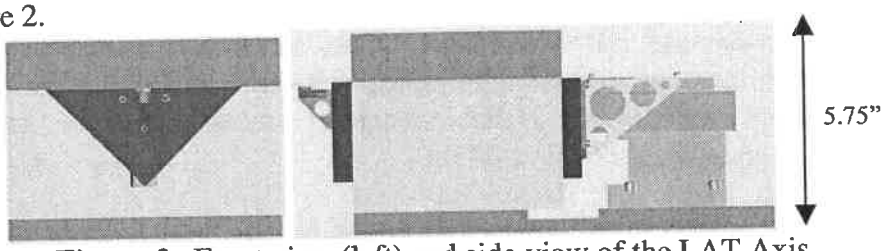

Figure 2. Front view (left) and side view of the LAT Axis

Slide Material The first step in the axis design was to select a material for the slide and develop the shape of the cross-section. The slide require a small moving mass, high stiffness to produce a high natural frequency for the system and sufficient surface area to produce a stiff air bearing. For these reasons, aluminum honeycomb was selected as the working material. Aluminum honeycomb consists of a honeycomb core of thin aluminum sandwiched between two thicker aluminum faces. The core cell structure holds the face sheets apart to generate the high bending stiffness but its low shear strength tends to decrease the theoretical stiffness by about 80%. The properties of flat honeycomb samples were calculated and measured, and a model for the actual material properties (modulus, density) was constructed. This model was used in the analysis discussed next.

FEM ANALYSIS

To help select an optimum cross-section shape, finite element models were created for different candidate shapes. Three basic shapes were analyzed: a box, a V-shape, and a triangle as illustrated in Figure 3. The properties of interest are the bending stiffness, mass, first natural frequency, center of gravity, location of the linear motor and location of the position sensing encoder.

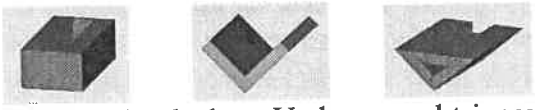

Figure 3: From left to right, the box, V-shape, and triangular slide designs

After simulating bending and frequency analysis tests for each slide shape, the box design was eliminated because removal of material to embed the motor caused a large drop in natural frequency. The remaining designs were compared using data obtained from simulations and shown in Table 1.

	Mass (g)	Nat. Freq. (Hz)	Lateral stiffness (N/μm)	Vertical stiffness (N/mm)	# Parts
V Shape	400	3450	8.145	8.17	4
Triangle	445	3950	25	10.5	2

Table 1: Comparison of V Shape and Triangle slide designs

Although slightly heavier, the triangle cross-section slide was selected because it proved more resistant to static forces resembling tool-tip loads and displayed a higher natural frequency than the V shape. Additionally, the air bearing structure supporting the slike consists of fewer parts, simplifying the assembly process.

Slide Length Another important design issue is the length of the moving slide. As the slide length increases, the bearing stiffness and natural frequency increase due to the larger surface area. However, the structural natural frequency of the moving slide decreases as the length increases. After analyzing the changes in natural frequency and the rate of change of stiffness with bearing length, a 7" slide in a 6" bearings was selected as the optimum length. This allows for 1" total stroke at lower frequencies. Also, the rear faceplate of the slide has a relieved area to accommodate the magnet track of the motor used to drive the system.

Motor Selection A brushless linear motor was chosen for its smooth motion characteristics, high accuracy, repeatability, high acceleration capabilities and stiffness. To reduce the moving mass of the system, the smallest/lightest motor capable of producing enough continuous force to drive the system was desired. Equation (1) was used to determine the force needed to drive the system:

$$F = mA\omega^2 \tag{1}$$

where m is the mass in Kg, A is the amplitude in m and ω is the frequency in Hz. For an assumed moving mass of 500 g, an operating frequency of 20 Hz , and amplitude of 2 mm (for a total stroke of 4 mm), 15.8 N are needed to drive the system. From the Airex Linear Motor P12 Series, the P12-1 is chosen (continuous force 27 N [2]. This motor weighs 100 g.

Mount Bracket The motor mount bracket connects the motor to the slide. The bracket must support the full weight of the motor coil, provide a rigid coupling to the slide and have minimum weight. The first bracket tested had a square faceplate to be bolted to the rear of the slide and a channel with 1/16" thick walls and vertical gussets to contain the motor as illustrated in Figure 4. However, this bracket was disappointingly flexible, allowing the motor and slide too much deflection. As a result of modeling, the faceplate was made taller to provide more resistance against vertical bending and horizontal gussets were added. Lightweighting holes were also added to the bracket in non-critical locations to reduce the mass.

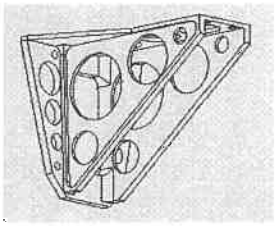

Figure 4: Improved final bracket

The new bracket performed well in dynamic simulations. The natural frequency of the slide-bracket-motor system was increased by nearly 50% and deformation was reduced to magnitudes seen in the slide and motor, indicating sufficient stiffness.

Experimental Verification When the moving slide was fabricated, accelerometers were used to observe its dynamic characteristics and compare those results to the predicted behavior. A free-free natural frequency test was used both with and without the motor and bracket. The setup for the experiment is shown in Figure 5.

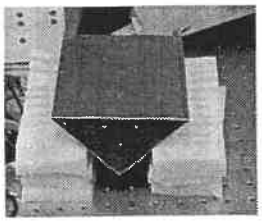

Figure 5: Setup for frequency analysis

A hammer was used to strike the slide resting on soft foam. The attached accelerometer then reported the vibration. The results are given below in Table 2.

	1st Natural Frequency (Hz)	2nd Natural Frequency (Hz)	Ratio of First/Second
Predicted Results	3950	5110	0.77
Actual Results	3540	4660	0.76

Table 2: Experimental results for natural frequency test (moving slide only)

With the values for the first and second natural frequencies showing a near match, two accelerometers were used to observe the vibration at different spots simultaneously on the slide. The relative magnitude and phase data of the two positions confirmed the predicted mode shapes – a twisting motion at the first frequency and a bending mode at the second.

CONTROL SYSTEM DEVELOPMENT

A linear motor depends on the control system to provide both static and dynamic stability. The following error, stiffness, disturbance rejection and stability depend on the drive system, the moving mass, the feedback sensor, the controller algorithm and update time. The control system must have fast loop update time, be flexible enough to support different control strategies and have the appropriate input/output configuration to support the required hardware. In this application, a straightforward proportional, integral, derivative (PID) control scheme may not be sufficient [3]. Feedforward gains will be investigated to eliminate following error. The UMAC controller from Delta Tau Systems is used to implement axis control.

MACHINING EXPERIMENTS

The goal will be to create optical surfaces that can be measured to evaluate the quality of the machining process. Two types of surfaces will be created. The first will be a tilted flat. For this type of surface, the LAT axis moves one cycle per revolution in a sine wave motion that linearly increases with radius. Because the resulting surface is flat, it can be easily measured using interferometers and profilometers to quantify the figure error and the surface finish. The second surface to be created will be a more complex NRS surface. Each of these surfaces will be used to test the capability of the LAT process to generate complex surfaces.

CONCLUSIONS

The 7" long slide for the Live-Axis turning system is made of aluminum honeycomb and has a triangular cross-section with faceplates at the front and back. In preliminary testing, the slide exhibits predicted behavior in dynamic applications. A linear scale encoder will be mounted on the flat top of the slide to provide position feedback to the controller.

1. K. Garrard, A. Sohn, R. G. Ohl, R. Mink, V. J. Chambers. "Off-Axis Biconic Mirror Fabrication." *Proceedings from the EUSPEN 2002 Annual Meeting* (2002).

Assessment of thin film UHMWPE bearings for precision slideways

Eric S. Buice, Hua Yang, Richard M. Seugling, Stuart T. Smith, Robert J. Hocken*
Center for Precision Metrology, University of North Carolina at Charlotte, NC 28223, USA.
**National Institute of Standards and Technology, Gaithersburg, MD 20899-8221, USA.*

Summary

In this extended abstract, results from tests on a novel, thin-film, Ultra-High-Molecular-Weight-Polyethylene (UHMWPE) bearing are presented. The goal of this investigation is to assess the performance and manufacture and to determine tribological conditions prevailing in the contact region. The bearings are comprised of a thin film of the polymer stretched over a spherical brass substrate. As of writing, two bearing geometries with substrate radii of 2.38 mm and 6.35 mm have been tested in air to determine both smoothness/repeatability of motion at traversal speeds of around 0.01 mm·s^{-1} to 1.00 mm·s^{-1} and durability under loads ranging from around 2.2 N to 28.0 N at speeds of up to 12.0 mm·s^{-1}. Smoothness of motion of the 2.38 mm radius bearing was assessed by using it as the counterface for traversing a carriage along an optically polished Zerodur® datum. A stylus-based measuring system was then used to profile a smooth, flat glass specimen and the repeatability of specific surface features measured with successive traces being used as a measure of both bearing noise and repeatability. While it is recognized that there are numerous other sources contributing to the measured signal, we believe this does represent a conservative estimate of the uncertainty of this bearing system. With this in mind, it was apparent that features of amplitude less than 10 nm could be repeatably measured. Durability was assessed using a custom built pin-on-disc testing apparatus. Wear of thin films is a particularly difficult measurement and we have used the criteria of catastrophic failure of the film as a measure of the durability. While the 2.38 mm bearing was observed to fail in one experiment, the larger radius bearing was observed to survive after sliding distances of over 2 km at loads and speeds of 28.0 N and 4.2 mm·s^{-1}, respectively*.

Introduction

This bearing represents a variant on the thin-film polytetrafluoroethylene (PTFE) bearings that are used in some profilometers[1, 2] and the Tetraform™ [3] grinding machine for motion control with sub-nanometer performance. The objective of this new bearing design is to produce a low-cost, robust, vacuum-compatible and modular dry rubbing bearing with sub-nanometer performance. To operate at these levels, it is necessary to address stiffness, heat removal from the interface, wear, thermo-mechanical characteristics, accuracy of the datum counterface and frictional characteristics (in particular, stiction and load dependence)[4].

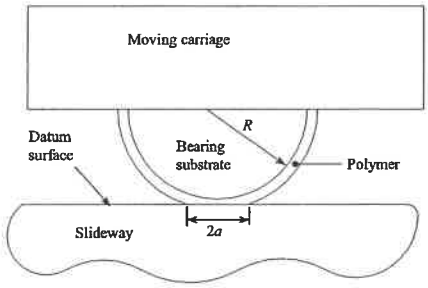

Fig. 1: Schematic diagram indicating key components of a precision slideway bearing utilizing a thin film polymer attached to a spherically shaped substrate.

While, initially, polymers might appear a poor choice of material for such demanding applications, there is plenty of evidence to suggest that they might provide a robust, inexpensive and easily fabricated solution. As far as can be determined, polymer bearings also appear to introduce little wear of the counterface that, in most designs, serves as a datum surface for controlled motion (linear or rotary). In contrast to fluid film and rolling element bearings that require either a pressurized or continuously coated fluid supply, polymeric bearings are passive mechanisms requiring no external supplies or connections. Competing bearing systems for linear slideway designs are the solid lubricant (steel on steel, lubricant filled metal composites on steel) and roller bearings.

Bearing Design

Given the criteria stated previously, two bearing designs have been built and tested as part of this study. The first design consists of a 4.76 mm (0.1875 inch) diameter brass sphere adhered to an aluminum substrate. A 0.15 mm (0.006 inch) thick UHMWPE film is then stretched over the sphere and held into place by a stamped metal cover, which is adhered to the substrate using a two-part epoxy while under a compressive load. A schematic illustration of the bearing is shown in Fig. 1. The dimensions of the bearing are approximately 10.0 mm × 10.0 mm × 12.7 mm. However, upon testing the bearing under various load conditions, it

* Certain commercial equipment, instruments, or materials are identified in this article in order to specify the experimental procedure adequately. Such identification is not intended to imply recommendation or endorsement by the National Institute of Standards and Technology, nor is it intended to imply that the materials or equipment identified are necessarily the best available for the purpose.

was found that the stress levels at the interface caused catastrophic failure at loads greater than 6.6 N at a surface speed of 4.7 mm·s^{-1}. To reduce the contact stress and increase the load capability of the bearing, a second bearing was designed with a radius of curvature nearly three times that of the original design. With suitable assumptions relating interface conditions, the contact radius of a rigid sphere in contact with a rigid flat surface through an elastic foundation can be estimated by[5]

$$a = \left(\frac{4PRh}{\pi E}\right)^{1/4}, \qquad (1)$$

where a is the radius of contact, P is the applied load normal to the surface, R is the radius of the sphere, h is the thickness of the film and E is the elastic modulus of the film. The contact area A, is given by

$$A = \pi a^2. \qquad (2)$$

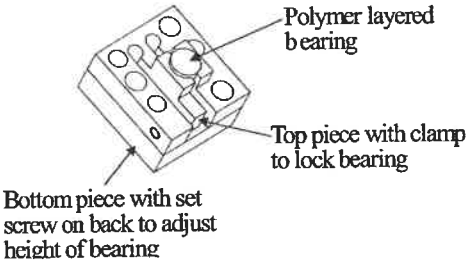
Polymer layered bearing
Top piece with clamp to lock bearing
Bottom piece with set screw on back to adjust height of bearing

Fig. 2: 2nd generation bearing incorporating brass cylinder with a 6.35 mm radius of curvature.

Increasing the substrate radius from 2.38 mm to 6.35 mm theoretically corresponds to a 60 % increase in contact area and a nearly 40 % reduction in contact stress given the assumptions stated above. As of writing, we are undertaking a theoretical investigation using continuum mechanics models and finite element studies to obtain a more complete model of this complex problem.

Based on the results and analysis described previously, a second bearing was designed. To keep the overall bearing size at a manageable level, a 12.7 mm brass sphere was machined to a 6.35 mm diameter cylindrical surface at the equator leaving the polar cap(s) as a spherical bearing surface with a 6.35 mm radius of curvature. The polymer is stretched over the pin and pushed through a reamed hole by a setscrew where the polymer/pin combination is secured by a squeeze clamp as shown in Fig. 2.

Table 1: Pin-on-disk results for the 2.4 mm radius UHMWPE bearing on float glass.

Direction	Load (N)	Speed (mm·s^{-1})	Dynamic Friction Coefficient	Comments
Forward	2.2	4.2	0.19	Bearings show no appreciable wear characteristics. Contact area shows little to no effect of sliding after a short run-in period.
		8.3	0.19	
	4.4	4.2	0.18	
		8.3	0.18	
	6.6	4.2	0.16	
		8.3	0.16	
	11.5	4.2	0.19	Bearing failed after approx. 700 meter traverse
		8.3	na	
Reverse	2.2	4.2	0.19	Bearings show no appreciable wear characteristics. Contact area shows little to no effect of sliding after a short run-in period.
		8.3	0.19	
	4.4	4.2	0.18	
		8.3	0.18	
	6.6	4.2	0.16	
		8.3	0.16	
	11.5	4.2	0.19	Bearing failed after approx. 700 meter traverse
		8.3	na	

The entire assembly can then be mounted to arbitrary structures. The total bearing and clamping system has dimensions of 25.4 mm × 38.1 mm × 12.7 mm. Although larger compared to the original bearing, this design allows for easy assembly and replacement of warn or damaged polymer material and the setscrew can act as a fine leveling mechanism if desired.

Results

To qualify these bearings for use in nanometer level systems, a number of important parameters would have to be tested. For the use in precision motion systems the criteria used to evaluate the performance of the bearings were friction/stiction, wear and repeatability. Two instruments were developed to evaluate these parameters. The first instrument was based on a pin-on-disk system commonly utilized for tribological investigations. The pin-on-disk system was designed to evaluate the friction/stiction and wear of the bearing sliding on a glass counterface. The second instrument is a profilometer based test apparatus that evaluates the repeatability of the bearings under loads during rectilinear motion.

Pin-on-disk

Both bearing designs have been tested for frictional force and durability over extended periods of time. Table 1 shows the results from the 2.4 mm radius bearing for various speeds and loads.

From the results given in Table 1 it is clear that the friction coefficient reduces as the applied load increases. However, there is a dramatic change in friction as the load increases over 6.6 N. It was observed that for loads over 6.6 N the bearing experienced catastrophic failure. In these cases the polymer tore from the substrate allowing for metal on glass interaction. From these observations a second bearing was designed allowing for an increase in radius of curvature and the ability to replace worn and/or damaged features. The new bearing was then tested in a similar manner and the results shown in Table 2.

As expected, the coefficient of friction decreased with an increase in load. At loads above 16.5 N the lateral force sensor became saturated and requires some modifications to properly evaluate the friction at higher loads. Fig. 3 contains examples of the data observed for the 6.35 mm diameter bearing. Included are plots of the friction coefficient as a function of time for short-term forward and reverse directions and long-term durability evaluations.

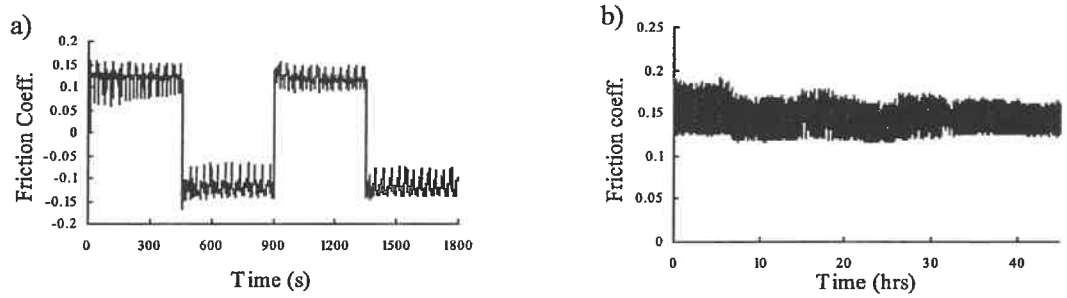

Fig. 3: a) Friction coefficient as a function of time for the 2nd generation bearing under an 11.45 N load at 4.2 mm·s^{-1}. Data includes three changes in direction. b) Friction coefficient as a function of time for a 6.65 N normal load over a 45 hour period.

A preliminary test was carried out to assess durability of the 6.35 mm bearing. At a load of 6.65 N, the bearing was run at a surface speed of 4.2 mm·s^{-1} for a period of 70 hours with no appreciable change in characteristics. In a further effort to determine the limit of performance, the bearing was subject to a maximum test-rig load of 27.8 N. Subsequent testing at a speed of 4.2 mm·s^{-1} for a period of 145 hours (total traverse distance of 2.2 km) indicated no visually observable damage or change in frictional characteristic.

Throughout all experiments, it was possible to infer a small stick/slip type behavior. Generally, the friction coefficient as measured appeared to increase by a factor of 0.05 upon reversal of traverse direction. A slightly higher initial friction was measured after the bearing had been in stationery contact with the counterface for a protracted time period (tens of minutes to days). As of writing, it is not possible to separate this variation between true bearing phenomena and instrument artifact.

Profilometer Test

The profilometer test evaluated the repeatability of the bearings sliding over a glass (Zerodur®) guide. A capacitance based contact probe measured the deviation of the rectilinear stage normal to the direction of motion as described previously. Data was collected using LABView™ software and written to spreadsheet where the data analysis was done. Initial analysis consisted of removing the tilt of the sample by removing a straight line fit to the original data. The residual values are the parasitic motion of the stage and represent the level of repeatability of the stage. Examples of the residual motion with the slideway being pushed and then pulled are shown in Fig. 4. Repeatability of the stage with the tilt removed was on the order of ±11.0 nm over a 10 mm travel range.

Table 2: Pin-on-disk results for the 6.35 mm radius UHMWPE bearing on float glass.

Direction	Load (N)	Speed ($mm \cdot s^{-1}$)	Dynamic Friction Coefficient	Comments
Forward	2.2	4.2	0.19	Bearings show no appreciable wear characteristics. Contact area shows little to no effect of sliding after a short run-in period.
	4.4	4.2	0.17	
	6.6	4.2	0.15	
	11.5	4.2	0.14	
	16.5	4.2	0.13	
	27.8	4.2	saturated	Outside sensors range
Reverse	2.2	4.2	0.19	Bearings show no appreciable wear characteristics. Contact area shows little to no effect of sliding after a short run-in period.
	4.4	4.2	0.17	
	6.6	4.2	0.15	
	11.5	4.2	0.14	
	16.5	4.2	0.13	
	27.8	4.2	saturated	Outside sensors range

From Fig. 4, it is apparent that there is a difference between profiles when the actuator is pushing or pulling the carriage. It is noted that when the micrometer is pushing the carriage, deflections due to bending moments generated by the offset between the line of action of the actuator force and the center of friction of the moving platform create an increase in the bending moment itself. In contrast, when pulling the carriage, perturbations create moments that tend to self-correct the error and reduce the magnitude. With this in mind, it is expected that the efficiency of the decoupling mechanism (cross roller bearing) between the actuator and moving carriage will worsen. In Fig. 4a, a periodic variation can be observed that closely corresponds to the pitch of the micrometer. However, even within this periodic variation, the profile is seen to repeat at nanometer levels. When the actuator is pulling the carriage, repeatable profiles are obtained with a total 'band' of deviations being within a few nanometers for the three profiles shown.

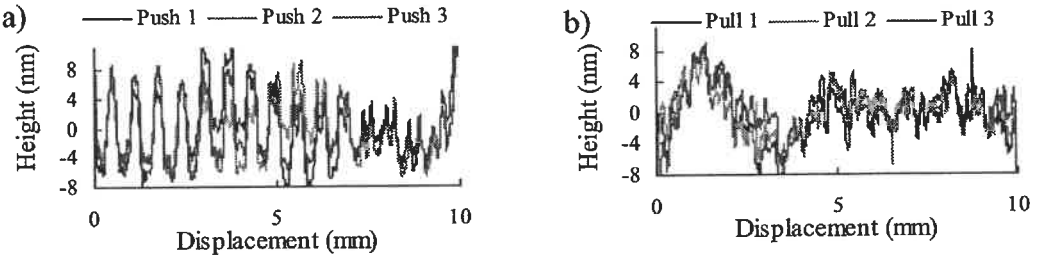

Fig. 4: a) Repeatability measurement of the profilometer height instrument as the rectilinear slide is being pushed. b) Repeatability measurement of the profilometer height instrument as the rectilinear slide is being pulled.

Acknowledgements

The authors of this paper would like to thank the University of North Carolina's Center for Precision Metrology and the National Science Foundation (NSF DMII #0210543) for providing support for this research.

[1] Lindsey K., Smith S.T. and Robbie C.J., 1988, Sub-nanometer surface texture and profile measurement with 'Nanosurf 2', *Annals of the CIRP*, **37**, 519-522.

[2] Leach R.K., 2000, Traceable measurement of surface texture at the National Physical Laboratory using Nanosurf IV, *Meas. Sci. Technol.*, **11**, 1162–1172.

- Garratt J.D. and Bottomley S.C., 1990, Technology transfer in the development of a nanotopographic instrument, *Nanotechnology*, **1**, 28-43.

[3] Lindsey K., 1991, Tetraform grinding, *SPIE*, **1573**, 129-135.

[4] Smith, S T, Yang, H and Seugling, R M, 2001, Polymer bearings for nanotechnology applications, *Proc. ASPE Summer Topical Meeting, Precision Bearings and Spindles*.

[5] Johnson, K L, 1985, *Contact Mechanics*, Cambridge University Press, Cambridge, UK.

High Frequency, Low Force Dynamometer for Micro-Milling Force Measurement

David Burton, G. Scott Duncan, John C. Ziegert, Tony L. Schmitz
University of Florida, Gainesville, FL 32611

Introduction

The need for miniature components in such applications as biomedical, aerospace, electronics, and mold production has led to the development of micro-milling processes that are characterized by high spindle speeds (up to 500,000 rpm) and low cutting force magnitudes (<1 N). Due to these high spindle speeds, the tooth passing frequency, and, therefore, the fundamental cutting force frequency, can reach 16 kHz for a two tooth cutter. Harmonics of the fundamental cutting force frequency are also present for partial radial immersion cuts. Many researchers have attempted to model cutting forces during the micro-milling process [1-3]; however, to better understand the micro-milling process and validate these cutting force models, there is a need to quantify cutting forces at high frequencies and low cutting force amplitudes.

Commercially-available dynamometers typically specify a bandwidth below the first natural frequency of the dynamometer structure (typically 1 kHz to 3 kHz in practice). Operation in this range enables the actual force to be determined by multiplying the time-domain dynamometer signal by a calibration constant. For operation outside this range, it is necessary to multiply the sensor signal (transformed to the frequency domain) by the inverted dynamometer frequency response function (FRF) to remove the influence of the dynamometer dynamics from the recorded signal [4]. However, this approach is limited because the frequency response magnitude is generally so small at higher frequencies that it is not possible to recover a valid force signal due to a poor signal-to-noise ratio. Additional difficulties in measuring low cutting forces at high frequencies include: 1) the requirement of a high resolution measurement device with a very large bandwidth, 2) a method to excite the structure with a known input at all frequencies of interest to determine the FRF of the dynamometer system, and 3) a dynamometer system design capable of limiting the effect of forces in coordinates other than the coordinate of interest.

This paper presents a concept for a dynamometer designed to operate within a frequency range of 10 kHz to 16 kHz while measuring cutting forces less than 1 N. The design is based on two coupled, single degree-of-freedom (SDOF) flexures that interact to produce vibration modes at the edge of the bandwidth of interest. These modes produce a FRF within the desired frequency band that has a magnified response and nearly constant value between modes. The workpiece is mounted to the first of the two flexures while a precision accelerometer with a frequency range up to 20 kHz is mounted to the second flexure. To limit the effect of additional structural modes, finite element analysis (FEA) is used to optimize the flexure design by forcing the natural frequencies of additional modes above the bandwidth of interest. To validate the dynamometer design prior to manufacture, an uncertainty analysis is performed.

System Model

The flexure design goal was to include only two vibration modes below 16 kHz, specifically, linear translation of both the workpiece and accelerometer flexures. The system was initially modeled as a 2DOF lumped mass, spring, damper system with stiffness determined from flexure theory [5] and mass and damping characteristics determined from flexure geometry and material properties. To refine the model, Ansys Workbench 8.0 [6] was selected as FEA software. The final 2DOF flexure design is shown in Fig. 1 along with the desired first two system modes (at 9628 Hz and 17688 Hz).

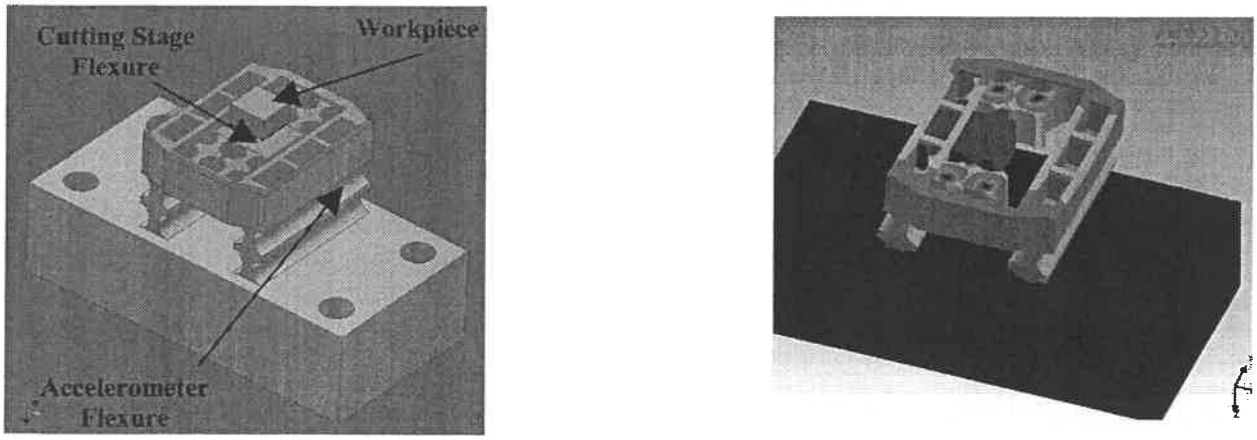

Figure 1: 2DOF flexure design; the workpiece flexure is carried on the accelerometer flexure

The critical flexure parameters are shown in Fig. 2 with the corresponding values provided in Table 1. Due to its high strength to density ratio, the flexure material was selected as tungsten carbide. The FEA-predicted FRF of the 2DOF flexure design is displayed in Fig. 3. As seen in the figure, the FRF has a nearly constant value in the frequency bandwidth of interest, between the 9628 Hz and 17688 Hz modes.

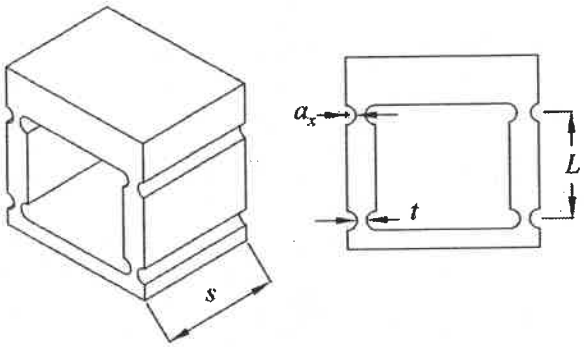

Figure 2: Flexure design parameters

Parameters	Accelerometer Flexure	Workpiece Flexure
a_x (mm)	1.75	1.75
s (mm)	29.00	5.00
t (mm)	1.50	1.00
L (mm)	4.50	4.50

Table 1: Flexure geometry values

Uncertainty Analysis

The uncertainty analysis developed in this section provides 95% confidence intervals on the measured cutting force. The uncertainty analysis is dependent on the cutting force signal; therefore, simulation [7] is used to generate two input signal cases for a 420 krpm spindle speed using a two tooth cutter: 1) a slotting cut, and 2) a 50 percent radial immersion cut. To convert the simulated cutting force signal to an acceleration signal, the force signal is Fourier transformed to the frequency domain, multiplied by the acceleration to force frequency response of the dynamometer system (produced from FEA), and inverse Fourier transformed back to the time domain. Chip loads were selected to generate cutting force amplitudes that approximated previously predicted and measured values for micro-milling operations [1-3]. Figure 4 displays the input cutting force signal for both uncertainty analysis cases.

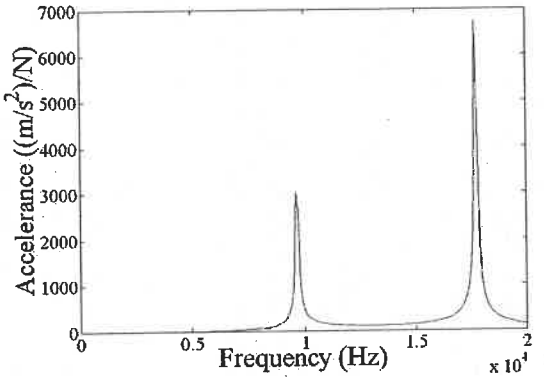

Figure 3: Model FRF results

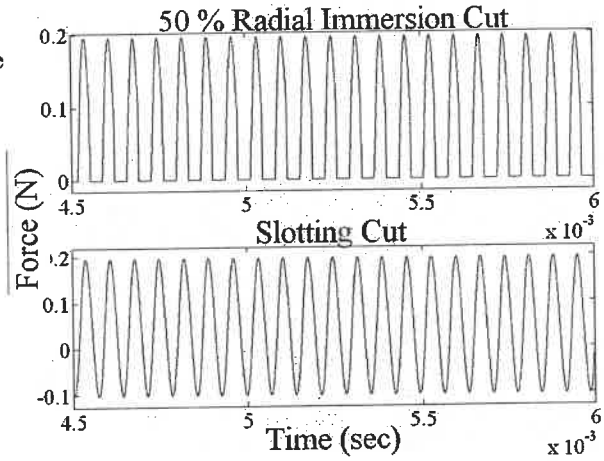

Figure 4: Cutting force signals

Uncertainty contributors occur on each time sample of the acceleration signal in the time domain and on each point of the measured FRF in the frequency domain. The uncertainty contributors in the time domain include: (1) accelerometer resolution, (2) electrical noise and external vibration, and (3) contributions from additional system modes, and the uncertainty contributors in the frequency domain include: (1) measurement variation, (2) ambient temperature, (3) dynamic changes due to material removal, and (4) dimensional and material variation. Each of the contributors is assumed to have a uniform distribution across a selected range. For the accelerometer resolution, the distribution range (0.04 m/s^2) was specified as twice the resolution of the device and the electrical noise and external vibration range (0.3 m/s^2) was determined by measuring the signal of an accelerometer mounted to a tombstone while a spindle rotated and completed linear moves. The range of the additional system modes was determined by multiplying a Fourier transformed cutting signal for the direction (y) orthogonal to the desired force measurement direction (x) by an FEA-predicted FRF for two cases: 1) the x direction flexure motion to the y

direction input force at the center of the work piece; and 2) the x direction flexure motion to the y direction input force at the edge of the work piece. The frequency domain uncertainty was then inverse Fourier transformed to the time domain and applied to each time sample. For the measurement variation in the frequency domain, the distribution range was set using the statistical variation determined from previous modal testing (2% of the measured FRF). The temperature distribution range was determined by subtracting the FEA-predicted FRF at 20 °C from FRF at 25 °C. The geometric and material variation properties included the dimension of the notch radius, the modulus of elasticity, Poisson's ratio, and material damping. The FEA model was used to produce FRFs for ±5% of the nominal values for each of the properties and the distribution range was set by subtracting the low value FRF from the high value FRF. Finally, the material removal distribution range was determined by subtracting the FEA-predicted FRF with 10% of the work piece material removed from the FRF with a complete work piece. The individual time domain uncertainties were joined to create a combined uncertainty as shown in Eq. (1), where σ specifies the standard deviation and n is the total number of uncertainty contributors. The procedure was repeated for the frequency domain uncertainties. The standard deviation of a uniform distribution was calculated from Eq. (2) [8].

$$\sigma^2_{combined} = \sigma_1^2 + \sigma_2^2 + \ldots + \sigma_n^2 \qquad (1)$$

$$\sigma^2 = \frac{Range^2}{12} \qquad (2)$$

To account for uncertainties in both the time and frequency domains, a Monte Carlo simulation was completed to generate the 95% confidence intervals around the x-direction cutting force signal. The following steps were used to determine this result: 1) the acceleration signal, based on the initial cutting force signal, was multiplied by a randomly generated value based on the combined standard deviation of the time domain uncertainties; 2) the new acceleration signal was Fourier transformed to the frequency domain; 3) the FRF of the dynamometer (produced by FEA) was multiplied by a randomly generated value based on the combined standard deviation of the frequency domain uncertainties; 4) the new acceleration signal was multiplied by the inverse of the new dynamometer FRF to produce a cutting force signal in the frequency domain; and 5) the cutting force signal was inverse Fourier transformed back to the time domain. These steps were repeated 1000 times to determine a mean cutting force signal and standard deviation in the time domain. To create 95% confidence intervals, two times the standard deviation was added to the mean of the cutting force signal at each time sample. The original cutting force signal, the Monte Carlo mean, and the 95% confidence intervals are shown in Fig. 5 for the slotting cut and Fig. 6 for the 50 percent radial immersion cut.

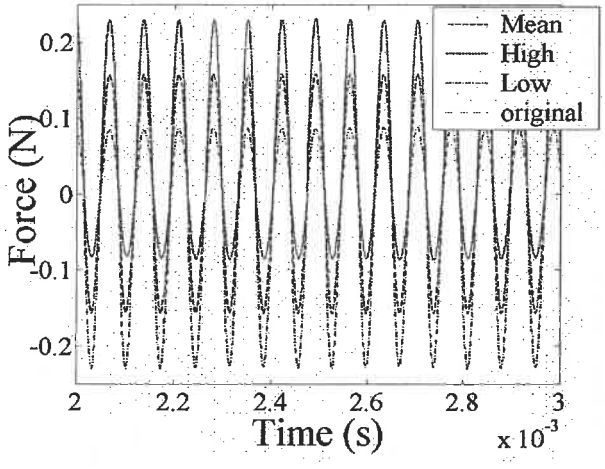

Figure 5: 95 percent confidence intervals for slotting

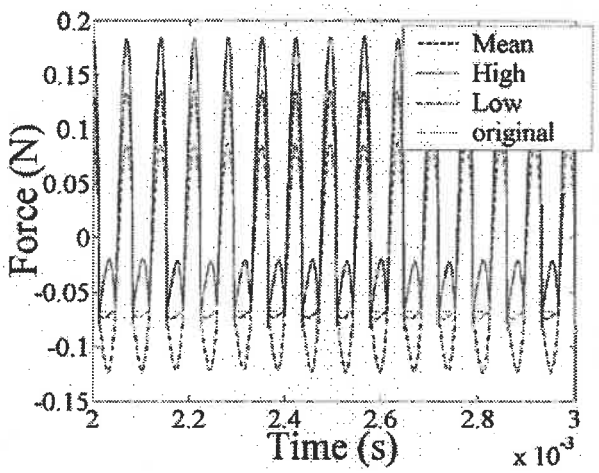

Figure 6: 95 percent confidence intervals for 50 percent radial immersion cut

A large percentage of the uncertainty is due to material property and dimensional variation. This is very important in producing a dynamometer that will operate in the specified range; however, these properties will be captured in the measured FRF of the actual dynamometer system, effectively removing their uncertainty from the measured cutting force signal. As an approximation to the final 95% confidence intervals of an actual dynamometer, the

confidence intervals for a slotting cut and 50 percent radial immersion cut with material property and dimensional uncertainties removed are shown in Figs. 7 and 8, respectively.

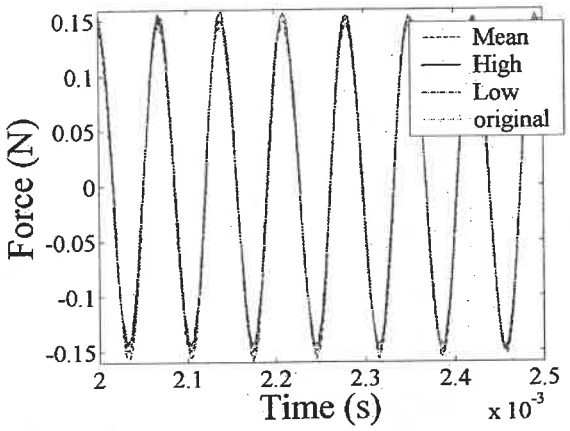

Figure 7: 95 percent confidence intervals for slotting cut excluding material property and dimensional uncertainties

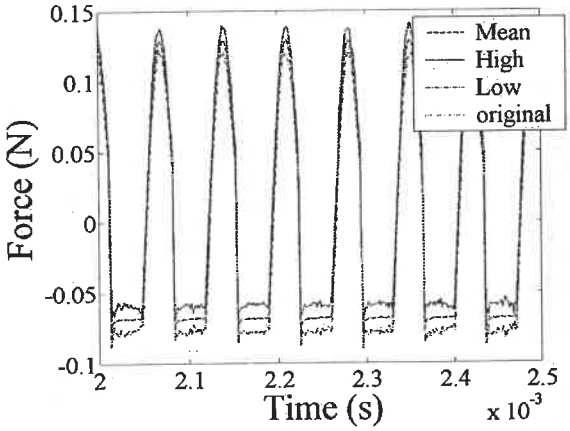

Figure 8: 95 percent confidence intervals for 50 percent radial immersion cut excluding material property and dimensional uncertainties

Measurement and Excitation Issues

Determination of the FRF of the dynamometer system requires exciting the structure across the desired bandwidth, 10 to 16 kHz, and providing a measurement device that is capable of sensing the response across the same bandwidth. To verify that excitation is possible for this bandwidth, testing was performed using a small piezoelectric impact hammer with a hard, steel tip on a hard surface. The time response of the hammer impact was Fourier transformed to the frequency domain and the excitation bandwidth was approximately 20 kHz. The dynamometer system accelerometer with a 20 kHz bandwidth can be used to measure the response. To validate the dynamometer system, a piezoelectric shaker in conjunction with an integral high frequency force transducer is capable of exciting the dynamometer system with a bandwidth of 20 kHz with a known input. In this manner, the operation of the dynamometer output can be verified and calibrated to a known input.

Conclusions

A 2DOF, flexure based design for a high frequency, low force dynamometer to measure micro-milling cutting forces was investigated using analytical and FEA techniques. The dynamometer design limited the effect of unwanted structural modes and provided an acceptable resolution-to-response ratio for the sensing device. An uncertainty analysis, based on Monte Carlo techniques, was also performed. The results of the analysis predict that the proposed dynamometer will be capable of providing cutting force measurements with acceptable uncertainty.

References

[1] Dow, T., Miller, E., Garrard, K., 2004, "Tool Force and Deflection Compensation for Small Milling Tools", Precision Engineering, **28**, pp. 31-45.

[2] Bao, W., Tansel, I., 2000, "Modeling Micro-End-Milling Operations. Part I: Analytical Cutting Force Model", International Journal of Machine Tools and Manufacture, **40**, pp. 2155-2173.

[3] Rahman, M., Kumar, S., Prakash, J., 2001, "Micro Milling of Pure Copper", Journal of Materials Processing Technology, **116**, pp. 39-43.

[4] Tounsi, N., Otho, A., 2000, "Dynamic Cutting Force Measuring", International Journal of Machine Tools and Manufacture, **40**, pp. 1157-1170.

[5] Smith, S., 2000, Flexure Elements of Elastic Mechanisms, Gordon and Breach Science Publishers, Amsterdam, The Netherlands.

[6] Ansys, Inc., 2003, Ansys 8.0 Workbench: Finite Element Analysis Software, Canonsburg, Pennsylvania.

[7] Smith, S., Tlusty, J., 1991, "An Overview of Modeling and Simulation of the Milling Process", ASME Journal of Engineering for Industry, **113**, pp. 169-175.

[8] Wackerly, D., Mendenhall, W., Scheaffer, R., 2002, Mathematical Statistics with Applications, Duxbury, Pacific Grove, CA.

Development of a Precise Positioning Stage Traveling on Micro-pitch Racks

Tomoyuki Iwata and Satoshi Honda
Tokyo Metropolitan Institute of Technology

1. Introduction

Recently, precise positioning stages are indispensable elements for measuring instruments and precise machine tools because abilities of these positioning stages raise sensing abilities of the measuring instruments directly and improve a cutting accuracy of the machine tools. Performances of the stages mounted on the measuring instruments affect data sensitivity, data resolution, and data accuracy. Performances of the stages mounted on the precise machine tools decide dimension accuracy and surface roughness of machined works. Therefore, many precise positioning stages with some advantages have been developed[1) 2) 3)] . The advantages for positioning mean followings; accuracy for positioning is less than several micrometers, resolution of positioning is less than one micrometer, and repeatability of positioning is less than several micrometers. The advantages for mechanical specifications mean followings; size of the stage is small and compact, structure of the stage is simple, stiffness of the stage is high, and lost motion is small. The advantages for controlling mean followings; control system is simple, control rule or control algorithm is not complicated, and motion for positioning is smooth without meandering on guide rails.

One of the developed stages consists of a ball screw, an air slider and a laser interferometer[1)] . However, the first stage is bulky because individual elements are assembled without merging. If the ball screw and the air slider should be more rigid, and accuracy of positioning become higher, yet those elements become bigger and heavier. Control system is complicated for combining those elements. Other stage is formed into a linear motor with a precise linear encoder combining a grating and a laser[2)] . Although the second stage is compact, a control system is complicated because the linear motor cannot control the position without accurate regulating of electric current. Last stage is composed an inchworm mechanism by using piezoelectric actuators[3)]. Control system of the third stage is constructed easily because inchworm motion can be accomplished in an open-loop system, yet the stage can not be positioned without slipping even if cramp blocks grip guide rails tightly.

In the last paper[4)] , we presented a novel precise positioning stage traveling on micro-pitch racks. The stage is positioned every 60μm over the travel distance of 40 mm in the inchworm motion in which cramp blocks with micro-pitch teeth alternately grip on the micro-pitch racks. The structure is compact and simple, and the open-loop control system is used as the control rule; besides, the stage does not slip in the inchworm motion. In this paper, a new micro-pitch rack with fine pitch of 100μm is developed for reducing the positioning accuracy and the positioning resolution, and a new cramp and release mechanism is developed to reduce the positioning repeatability and lost motion and to heighten the stage stiffness.

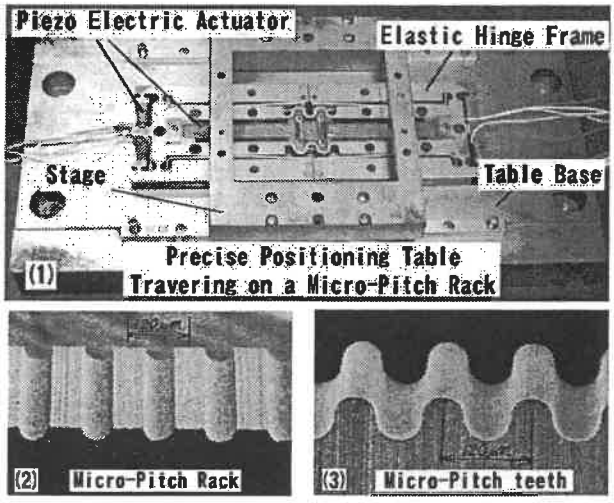

Figure 1 The precise positioning stage traveling on the micro-pitch rack

2. Structure of the precise positioning stage

The precise positioning stage consists of a stage board, an elastic hinge frame, a table base, and piezoelectric actuators as shown in figure 1. Two micro-pitch racks facing each other are attached under

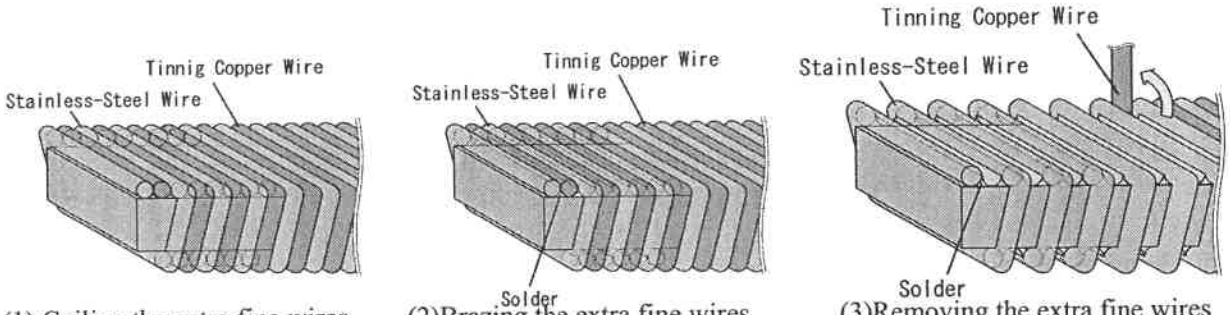

(1) Coiling the extra fine wires (2)Brazing the extra fine wires (3)Removing the extra fine wires

Figure 2 Making process for the new micro-pitch

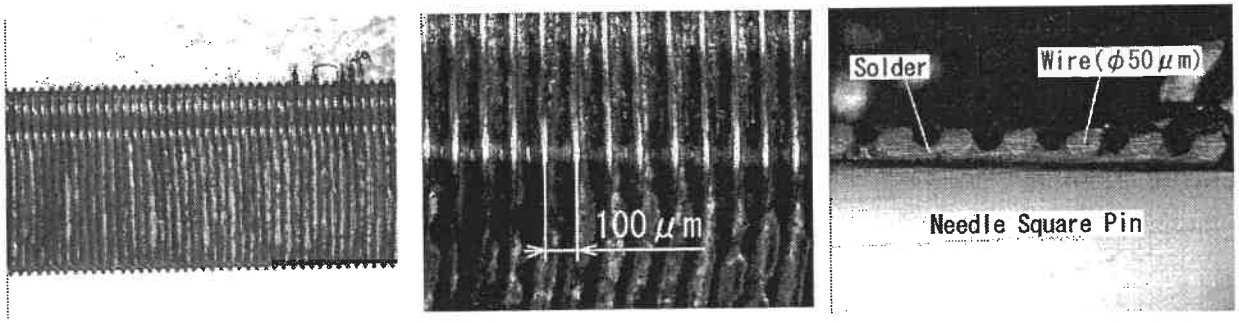

Figure 3 The new micro-pitch rack (general view, close-up, cross section)

the stage board. Four engage blocks with the micro-pitch teeth are attached at the centers of both sides of the elastic hinge frame. The stage board traverses right and left accurately in the inchworm motion in which the piezoelectric actuators extend or contract sequentially.

The positioning accuracy of the stage was 2.5μm and the positioning resolution was 60μm which value was half pitch of the micro-pitch rack. The micro-pitch rack as shown in figure 1-(2) was made of special steel for dies (JIS: SKD11), and depth of grooves was 30μm in radius. The engage block as shown in figure 1-(3) was made of cemented carbide (JIS: WC3), and section profile of the teeth is a series of arcs that combined semicircles of 30μm in radius. Both pitches of the micro-pitch rack and the engage block were 120μm.

3. The new micro-pitch rack with fine pitch of less than 100μm

To reduce the positioning accuracy and the positioning resolution, the new micro-pitch rack with fine pitch of less than 100μm is required. The micro-pitch rack is made through following processes as shown in figure 2. Firstly, a pair of one extra fine wire to be firmly soldered on the needle squire pin and another extra fine wire to be hardly soldered on a needle square pin is closely coiled each other around the needle squire pin like a double-start thread. We used a tinning copper wire as the extra fine wire to be firmly soldered and used a stainless-steel wire as the extra fine wire to be hardly soldered. Both diameters of the tinning copper wire and the stainless-steel wire are same size of 50 micrometers. The pair of the wires is coiled by hand. Secondly, the double-coiled part mentioned above is soaked in melted solder, and the melted solder flows into gaps between the needle pin and the coiled wires. The extra fine wire to be firmly soldered is brazed around the squire pin, yet the extra fine wire to be hardly soldered is not brazed around the squire pin. We used the solder which consists of 63 percents tin (Sn) and 47 percents lead (Pb). Finally, the wire to be hardly soldered is removed, and the extra fine wire to be firmly soldered is remained as a micro-pitch rack. Axial cross section of the micro-pitch rack shapes a profile to connect semicircle concave ditches and semicircle convex ridges alternatively as shown figure 3. We removed the stainless-steel wire by hand.

By using super fine wire which diameter is less than 50μm for example of tungsten wire and by using a long needle squire pin, it is possible to make a long micro-pitch rack with super fine pitch.

4. The new cramp and release mechanism

The new cramp and release mechanism is developed to reduce the positioning repeatability and lost motion and to heighten the stage stiffness. Two types of the cramp and release mechanism are developed one after another. Type A of the cramp and release mechanism consists of two micro-pitch teeth, two parallel plate springs, and a center slider, and stopper as shown in figure 4-(1). The parallel plate spring is attached at a center protuberance of the center slider and behind the micro-pitch teeth. When the center slider is pushed by weak force toward left, the parallel plate spring pushes the micro-pitch teeth strongly and the micro-pitch teeth mesh with the micro-pitch rack tightly. While the protuberance of the center slider is making contact with the stop bar, the micro-pitch teeth cannot move vertically and horizontally because the micro-pitch teeth is tightly propped with the parallel plate spring and the shape of the parallel plate spring is settled in the space between the stopper and the center slider. Therefore, stiffness of the cramp and release mechanism becomes higher. If many rings is inserted between the parallel plate springs like a type B, the stiffness of the cramp and release mechanism becomes more higher.

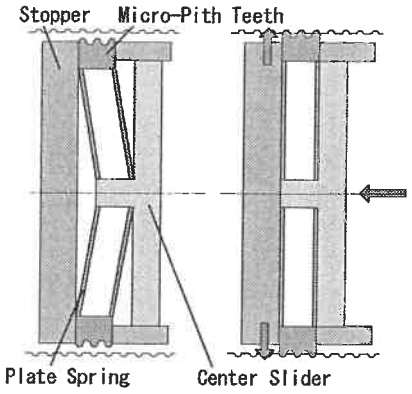

(1) Type A

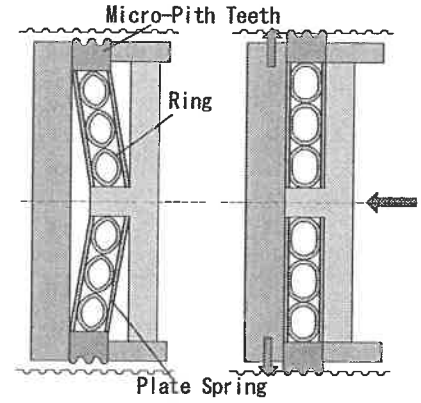

(2) Type B

Figure 3 The new cramp and release mechanism

4. Experimental apparatus and results

In the experiment, the stiffness of the cramp and release mechanism was measured. When the center slider was set to a certain position, we call the cramp position, and a certain force loaded to the engage block horizontally, displacement of the engage block was measured by laser instrument. Figure 4 shows the experimental apparatus. Size of the engage block was 8 mm in width, 5 mm in height, 16 mm in depth. Size of the plate spring was 0.1 mm thickness, 5 mm height, 25 mm in length. Width between the parallel plate springs was 6 mm, and its material was SUS304.

Figure 5 shows the displacement (y1) of the right engage block against the force (F1) loaded to the right engage block when the center slider is fixed at the set positions in the type1. The displacement (y1) increased against the loaded force (F1), and slopes of the experimental lines decreased against the cramp position. Figure 6 shows the displacement (y2) of left engage block against the loaded force (F2), and figure 7 shows the relationship between total displacement, that is (y1+y2), and total force, that is (F1+F2).

Figure 8 shows the stiffness of the cramp and release mechanism of type 1. The stiffness became much higher when the cramp position was 2mm.

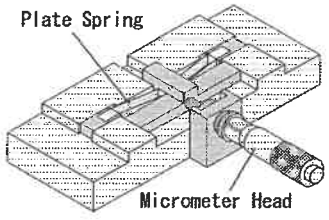

(1)The engage block and the parallel plate spring

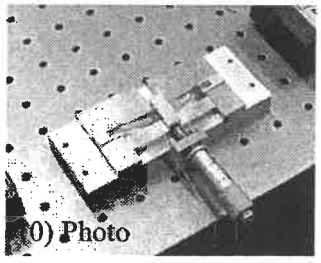

(0) Photo

Figure 4 The experimental apparatus

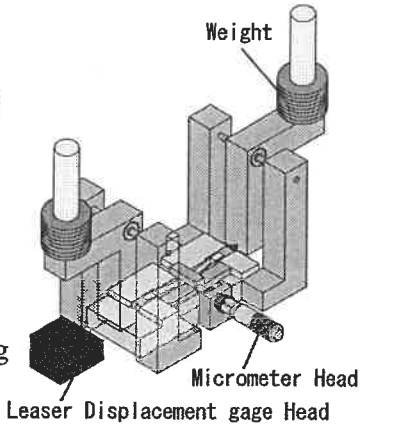

(2) Loading apparatus

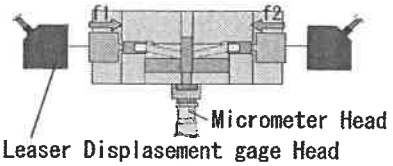

(3) Measuring apparatus

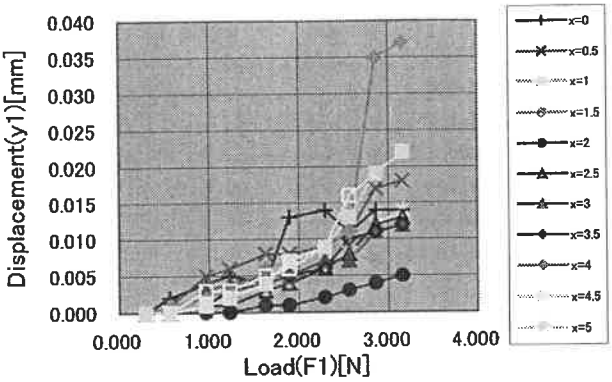

Figure 5 The displacement (y1) against Load (F1)

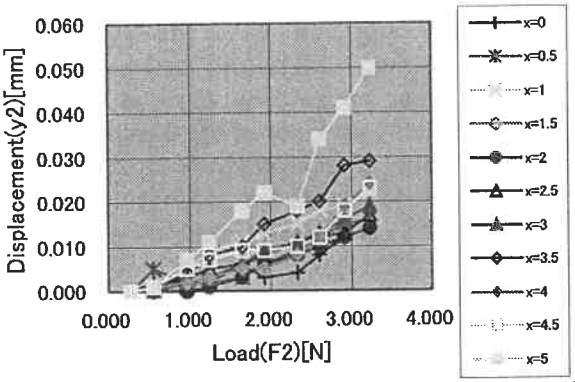

Figure 6 The displacement (y2) against Load (F2)

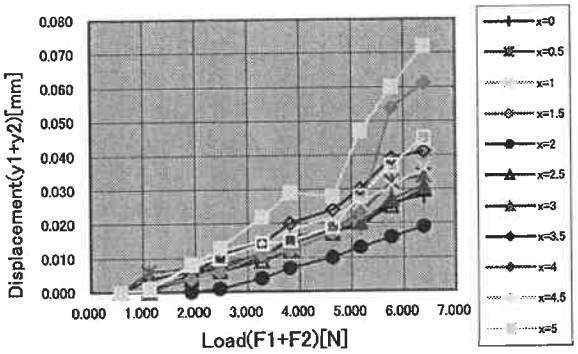

Figure 7 The displacement (y1+y2) against Load (F1+F2)

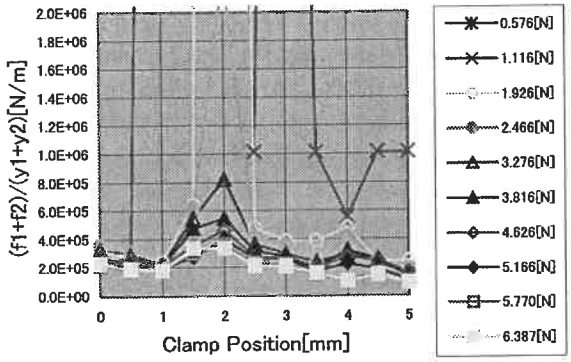

Figure 8 Stiffness of the cramp and release mechanism (F1+F2)/(y1+y2)

Figure 9 shows the relationship between total displacement, that is (y1+y2), and total force, that is (F1+F2) in the type 2. Figure 10 shows the stiffness of the cramp and release mechanism of type 2. The stiffness became much higher when the cramp position was 1.5mm.

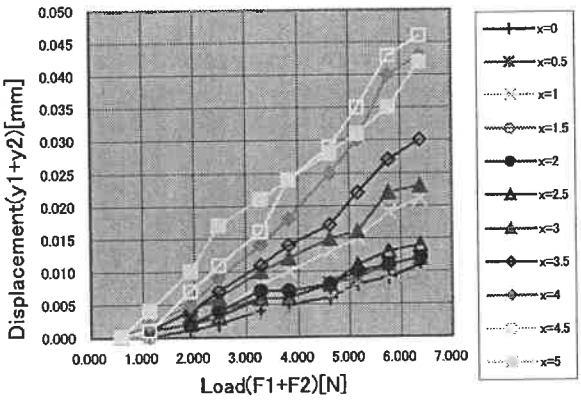

Figure 9 The displacement (y1+y2) against Load (F1+F2)

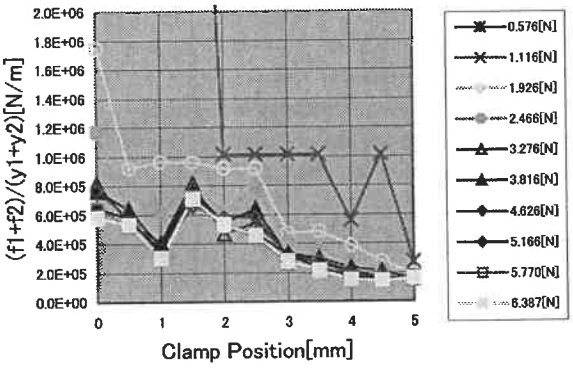

Figure 10 Stiffness of the cramp and release mechanism (F1+F2)/(y1+y2)

5. Conclusions

The new micro-pitch rack with pitch of 100μm is developed. The new cramp and release mechanism is developed and the stiffness was measured. The stiffness of type 1 and type 2 became much higher.

6. References

1)Jiro Otsuka, et al.: JSPE, 59, 10, (1993) 1655. 2)Shigeru Futami, et al. : JSPE, 57, 10, (1991) 1808.
3)Tetsuro Sakano et al.: JSPE, 63, 9, (1997) 1246. 4)Satoshi Honda et. al. : Proc. 1st EuSPEN (1999) 116.

PRECISION PRODUCT DESIGN – FROM UNIVERSITY LABS TO COMPANY CATALOG

Nathan R. Kane[1], Joachim Sihler[2],
Jeffrey W. Roblee[3], Mark M. Walter[3], Bob Blair[3], Robert J. Koning[3]
Alexander H. Slocum[4]

[1]MicroChips, Inc., Bedford, MA, USA.; [2]Schlumberger-Doll Research, Cambridge, MA, USA; [3]Precitech, Inc., Keene, NH, USA; [4]Massachusetts Institute of Technology, Cambridge, MA, USA.

Introduction

This paper traces the development of a novel hydrostatic rotary bearing from its inception at the Massachusetts Institute of Technology to its integration into a commercial rotary table manufactured by Precitech Inc., in Keene, NH. The bearing utilizes a new type of self-compensation that allows a large number of bearing pockets to be present while using only a few precision round parts, as shown in Figure 1, thus allowing high hydrostatic averaging with relatively low design complexity. A stand-alone prototype was built and tested by a research team at the Massachusetts Institute of Technology. The prototype's unusually high error averaging, resulting in a radial error motion of less than 50 nm with parts accurate to only 2.5 μm, in combination with the relative compactness and design simplicity, motivated Precitech Inc. to incorporate the technology into a servo controlled rotary table. The performance benefits of the bearing are presented along with the integration and technology transfer issues.

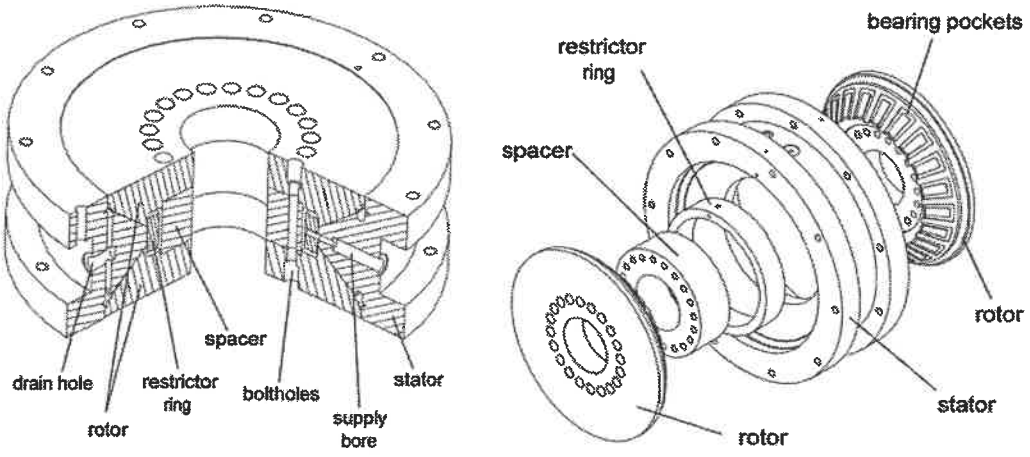

Figure 1: Cross section and exploded view of the angled surface self-compensated rotary hydrostatic bearing

Development at the Massachusetts Institute of Technology (M.I.T.)

During the 1990's, the Precision Engineering Research Group (PERG) at M.I.T. developed several novel linear and rotary hydrostatic bearing systems [1-4] in an effort to create a family of compact, modular bearings that would allow simplified integration into precision machine tools. One of these projects, sponsored by the Defense Logistics Agency (DLA) Manufacturing Technology Program, was the development of a modular linear hydrostatic guideway that is bolt for bolt compatible with standard rolling element linear rails [5,6]. The bearing utilizes a novel variation of self-compensation, for which a unique profile rail shape provides restricting lands that are oriented at an acute angle relative to adjacent bearing pockets. The design eliminates the restricting orifices required by conventional uncompensated hydrostatic systems, as well as the network of restrictor-to-pocket passages required for conventional self-compensating systems.

Shortly after the modular hydrostatic linear rail system was developed, the researchers at M.I.T. realized that the rail profile could also be revolved to create a rotary bearing having numerous pockets without the need for individual restricting elements or a network of drilled holes, thus allowing high error averaging with minimal complexity [7,8]. The first prototype, internally named the "HydroRound", was manufactured by Elk Rapids Engineering, a division of Star Cutter Company (Elk Rapids, MI) and tested for precision by Moore Tools

(Bridgeport, CT). After meetings and conversations with the precision manufacturing experts at Elk Rapids Engineering, the smooth fillets and rounds on the original bearing's cross sectional profile (derived from the profile linear rail design) proved problematic for the rotary bearing's manufacture. The solution was to construct a profile via an assembly of simpler, non-profiled parts that was functionally the same but could be more easily precision ground with non-profiled, straight grinding wheels. An initial concern was that the new profile included a sharp edge instead of a rounded edge near the restrictor surface, and hence was more vulnerable to being damaged during manufacturing and assembly. Upon further review, however, the machinists felt that the sharp edge was of less concern, and they expressed enthusiasm and support for the manufacturability of the new design. The re-designed HydroRound then seemed feasible in all aspects, and the engineers at Elk Rapids Engineering were galvanized to proceed with making the first prototype.

The prototype was assembled in M.I.T. labs and the stiffness was tested using custom fixtures, a load cell, and high accuracy capacitance probes. Measured stiffness values were initially lower than predicted, but the problem was solved by applying correction factors obtained by a thorough finite element analysis which took into account the elastic compliance of the bearing parts and the setup. Moore Tools Company, a manufacturer of high precision machines and machining accessories agreed to help with error motion measurements. The prototype bearing and a hydraulic pressure supply unit were brought to Connecticut, and set up on a Moore Tool precision coordinate measuring machine. Using custom fixtures, the bearing was slowly rotated by the measuring machine's drive spindle while the error motion was measured against a high precision spherical artifact attached to the bearing rotor. The recorded polar plot traces showed that the error motion of the bearing was actually on the order of the resolution of the coordinate measuring machine of 1 micro-inch. The bearing was then disassembled and the accuracy of the individual parts was measured and compared to the error motion, suggesting a hydrostatic averaging factor on the order of 50 to 1.

Development at Precitech Inc.

To provide additional data for a technical publication, further part accuracy and flow rate measurements were done with the help of Precitech, Inc., a manufacturer of ultra high precision diamond turning and milling machines in Keene, NH. After seeing the exceptional error motion and stiffness data of the bearing prototype in combination with it's relatively simple design, Precitech expressed interest in integrating the bearing into precision rotary tables for use on Precitech's Nanoform® series diamond turning machines and Freeform® series milling and grooving machines. A meeting with several Precitech engineers was set up to discuss the advantages, tradeoffs, and integration challenges.

The engineering team decided the technology could provide enough improvement in error motion and cost reduction to warrant development. The first application would be an improved B-axis rotary table, in part because of a need to improve the radial error motion of existing tables, and in part because it would serve as a straightforward test bed for the technology. A new B-axis would require the least changes to the M.I.T. prototype's configuration, and thus would most likely be successful and motivate future use in other rotary machine axes. Photos of the HydroRound B-Axis rotary table developed at Precitech are shown in Figure 2.

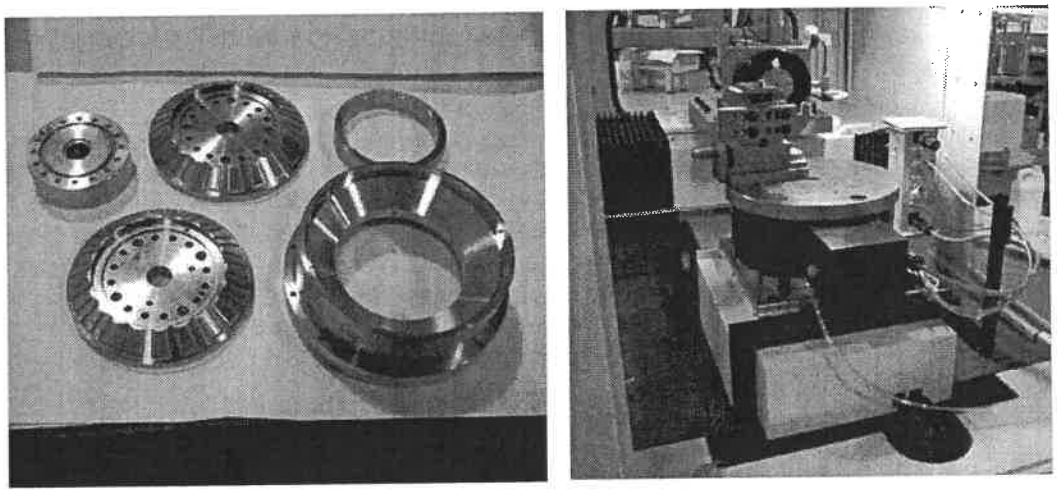

Figure 2: Photographs showing HydroRound bearing components manufactured at Precitech Inc. (left), and a 330 mm diameter HydroRound B-Axis rotary table mounted on a Nanoform®700 (right).

The engineering team at Precitech added features to the bearing developed at M.I.T. that were required for use as a CNC axis on a machine tool. The oil bearing dimensions were copied from the M.I.T. design. A direct drive DC brushless motor was found that packaged outside and concentric with the oil bearing, keeping the overall profile low. An integral encoder was packaged over the oil bearing to keep the encoder disk safe from oil contamination. The encoder has 47,200 lines per revolution, and with subsequent interpolation provides an angular resolution of 0.07 arc seconds. The table top was designed to be removable without disturbing the encoder or the bearing, for the cases in which the table top needed to be modified. A labyrinth seal was designed into the table top to keep chips out and oil inside, while eliminating static friction. The oil from the bearing was ported to a common drain through the base plate. Limit switches and hard stops were added for the customer applications that required limited travel, and were designed to be easily removable for multi rotation use. A brake system for stopping the axis from drifting when the machine is in emergency stop mode was added. A rotary vacuum pass-through joint was provided for applications that require vacuum at the table top. The locking feature of the M.I.T. prototype using separate pressure supply lines to the top and bottom bearing section was used for locking the rotary axis when it is not needed. M.I.T. and Precitech worked together on some of the more challenging aspects of this integration effort.

The B-axis rotary table incorporating the HydroRound bearing provided significantly improved error motion and tilt stiffness over previously used rotary B-axes. Table 1 shows a comparison of measured values for the new bearing versus two previously used systems.

Table 1: Comparison of Measured Performance Characteristics for B-Axis Rotary Tables

	Air Bearing B-Axis	Previous Oil Bearing B-Axis	M.I.T. HydroRound Oil Bearing
Table Outer Diameter	330 mm	330 mm	330 mm
Axial Error Motion	.076 μm	0.051 μm	0.025 μm
Radial Error Motion	.100 μm	0.091 μm	0.064 μm
Load Capacity *	227 kgf	450 kgf	550 kgf
Axial Stiffness *	350 N/μm	525 N/μm	350 N/μm
Radial Stiffness *	290 N/μm	350 N/μm	788 N/μm
Tilt Stiffness *	NA	3.3 N-m/arcsec	9 N-m/arcsec

* Values measured at 17 bar supply pressure for oil bearings, 6 bar for air bearing

The new rotary table provides a 50% better axial, and a 30% better radial error motion. The low error motions were achieved using bearing components with a measured roundness of 1.3 μm. The error motions indicate a 50 to 1 axial, and a 20 to 1 radial hydrostatic averaging effect that is afforded by the design. Because part roundness values of the previously used B-axis bearings are not available, it is not possible here to directly compare the error averaging characteristics. Comparing the two oil bearings, the radial stiffness was improved more than 2 fold and the tilt stiffness was improved 3 fold, given the same operating supply pressure of 17 bar.

As a result of the promising performance characteristics of the first B-axis table, additional units have been manufactured at Precitech and shipped to customers. The main applications are tool-normal diamond turning, and ultra precision milling of freeform surfaces such as F-Theta lenses, torics, progressive lenses, variable angle grooved patterns, and diffractive surfaces. The tool-normal feature, for which a rotary axis is necessary, allows a tool or grinding spindle to be kept normal to the workpiece surface during cutting, allowing deep concave molds and lenses to be fabricated to high accuracy.

Figure 3 shows a contour plot of a spherical test surface. The part was continuously turned by an air bearing spindle while the tool was swept through a 52 degree horizontal arc via a coordinated move by the X, Z and B-axes. The HydroRound B-Axis was used to keep the diamond tip always normal to the part surface. The maximum deviation of the resulting part from a perfect sphere was measured to be +/- 0.030 μm. Since the spherical surface was the resultant of the simultaneous motion of the X, Z, B, and spindle axes, each of which have their own imperfections, the error motion of the B-Axis over the move must have been only a fraction of +/- 0.030 μm.

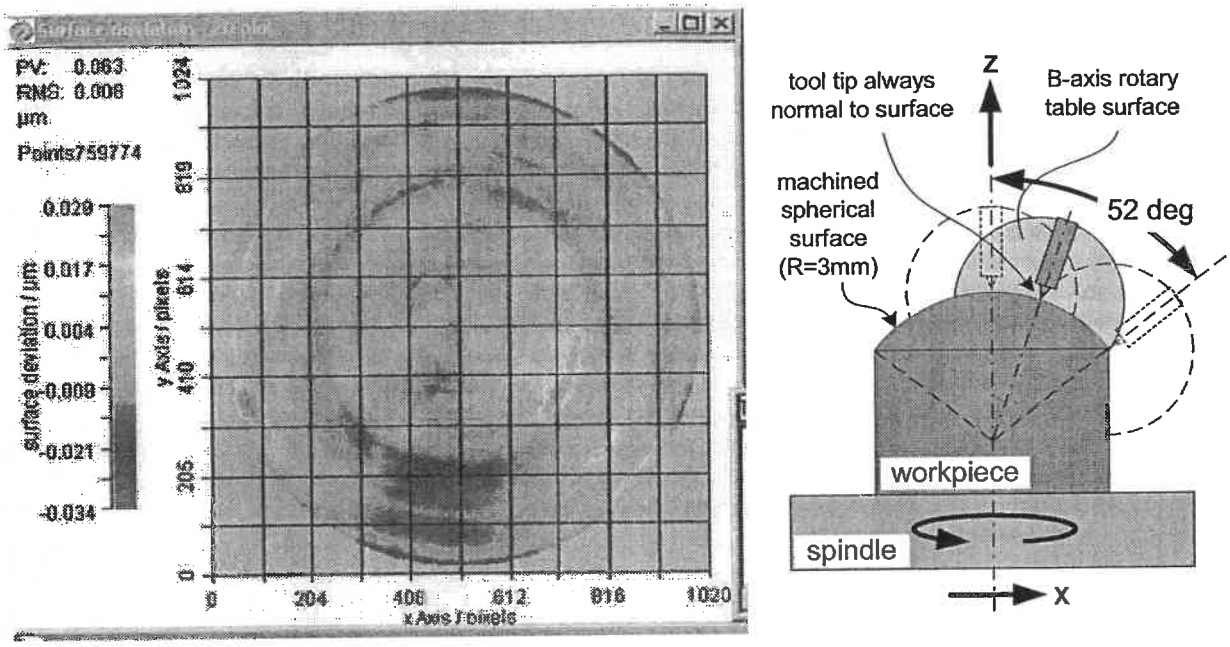

Figure 3: Contour plot showing deviation of a test part surface from a true sphere. The diamond tool was clamped onto the HydroRound B-Axis rotary table with the tool tip coinciding with the B-axis centerline. Mounted on linear axes, the B-axis table is moved in the Z-direction while the spindle is moved in the X-direction. The B-axis is rotated to keep the tool always normal to the part surface during cutting. The part was machined on a Precitech Nanoform® 700.

Conclusion

A case study has been presented detailing the process by which a novel precision rotary bearing has been brought to commercialization. Sufficient data was gathered at the research stage to demonstrate the benefits of the new design. The next step involved providing consulting services to assist in integrating the new design into a product. The success of the B-Axis project has motivated further efforts to exploit the advantages of the new design for other applications. Future developments at Precitech could include designing the HydroRound into a metrology spindle for high accuracy roundness measurements, a work holding spindle, or an added rotary axis for multi-axis machining centers.

References:

[1] Slocum, A.H.; Self Compensating Hydrostatic Linear Motion Bearing, US Patent 5,104,237, April 14 1992

[2] Slocum, A.H., Scagnetti P. E., Kane N. R., Brünnner C.: Design of Self Compensated Water-Hydrostatic Bearings, Precision Engineering, Vol. 17 No. 3, 1995, pp. 173-185

[3] Wasson, K.L.; Slocum, A.H.: "Integrated Shaft Self-Compensating Hydrostatic Bearing", US Patent 5,700,092, Dec. 23 1997

[4] Kotilainen, M.S., Slocum, A.H.: Manufacturing of Cast Monolithic Hydrostatic Journal Bearings, Journal of the International Societies for Precision Engineering and Nanotechnology, Vol. 25 (2001), pp. 235-244.

[5] Kane, N.R., Slocum, A.H.: Modular Hydrostatic Bearing with Carriage Form-Fit to Profile Rail, US Patent 5,971,614, Oct. 1999

[6] Kane, N.R.: Surface Self-Compensated Modular Linear Hydrostatic Bearings, Ph.D. Thesis, Department of Mechanical Engineering, Massachusetts Institute of Technology, June 1999.

[7] Sihler, J.: Design, Manufacturing and Test of a Self-Compensating Hydrostatic Rotary Bearing for Rotary Machine Axes, Dipl.-Ing. Thesis, University of Stuttgart and Massachusetts Institute of Technology, 1998.

[8] N. R. Kane, J. Sihler, A.H. Slocum: A Hydrostatic Rotary Bearing with Angled Surface Self-Compensation, Precision Engineering, Vol. 27, No. 2, pp. 125-139, April 2003

DEVELOPMENT OF A MINIATURE ADJUSTING DEVICE SCULPTED INTO A PARALLEL LINKAGE

Yu Masuya and Satoshi Honda
Tokyo Metropolitan Institute of Technology, Tokyo, Japan

1. Introduction

Recently, sensor units and machine elements are miniaturized into the size of less than several millimetres in order to downsize machines and equipments; and also, the sensor units and the machine elements are produced into ultra precise dimensions and with high quality materials in order to detect signal sensitively and to accomplish delicate functions. Therefore, it is necessary to adjust positions and postures of these miniature parts finely; and it is necessary to fix these miniature parts on the equipments at their ideal positions and ideal postures firmly; and it is necessary to hold positions and postures of these miniature parts on the equipments permanently. If the miniature parts are not adjusted accurately and are not fixed on the equipments firmly, and are not held in their position and posture lastingly, their abilities are not realized sufficiently.

Several systems to adjust position and posture for a component, and to fix the component on the equipment, and to hold its position and posture were developed.

Firstly, the system of fits is mentioned, in which the component is inserted into a groove of the equipment. Accuracy of the positioning and the posturing in the system is always settled into fit tolerance. The component is easily adjusted without troublesome operations if the fit tolerance is smaller than acceptable error for assembling the component and the equipment, and the component is usually fixed by bolts and so on. However, it is impossible to adjust the position and the posture of the component into the acceptable error if its value is less than several micro-metres. If the excessive force acts to the component, or if the bolts are loose, the component is slid within a width clearance between the components and the groove. The component is not positioned and is not postured definitely.

Secondly, the system of a dowel is mentioned, in which a cylindrical pin or a shoulder-bolt is inserted into a reamed hole bored through the component and the equipment. The reamed hole is made in one boring process after the components is finely adjusted and is temporarily fixed to the equipment by the bolts. Accuracy of the positioning and the posturing in the system are settled into the adjusting error and a temporary fixing error. Although a lot of troublesome operations are required for the adjustment, the component is permanently held its position and its posture. However, it is impossible to bore the reamed hole without deviation of several micro-metres because cutting force for drilling and reaming is occurred vibrations and deformations of the component. Even if the reamed hole is bored at the adjusted point accurately, a lot of chips are scattered around the component.

Thirdly, the system of adjusting stages is mentioned, in which the component is fixed on the top of the stage and its position and its posture are adjusted by rotating of control screws. Accuracy of the positioning and the posturing in the system are settled into the adjusting error, backlash, and stiffness error. The component is finely adjusted toward six directions of x, y, z, θx, θy and θz. However, it is difficult to hold the position and the posture permanently because the elements of the stage are wobbled in the backlash and the stiffness of the stage consisting of small elements is not raised higher. Moreover, if the system is used, advantages of the miniaturized parts are lost entirely because the stage becomes much bigger than the component.

A novel miniature device for adjusting, fixing and holding the miniature parts is thought up in this paper. The device can easily adjust the positions and the postures toward six directions of x, y, z, θx, θy and θz. The device is monolithically sculpted into a parallel linkage. The stiffness is strongly. The device is held in the position and the posture permanently.

2. Structure of the miniature adjusting device

The miniature adjusting device consists of an top plate, a bottom plate, and six elastic hinge frames arranged between the top plate and the bottom plate as shown in figure 1 and figure 2. These parts are sculpted in a small hexagonal prism like an openwork, and the device composes a seamless parallel linkage in which the elastic hinge frames are connected to the top plate and the bottom plate with universal flexure hinge joints. The elastic hinge frames are individually extended or are individually shrunk, and the top plate is adjusted into a reference position (i.e., x, y, z) and a reference attitude (i.e., θx, θy and θz).

The miniature adjusting device was made of aluminum alloy. A side of the hexagonal prism was forty millimeters and its height was fifty millimeters.

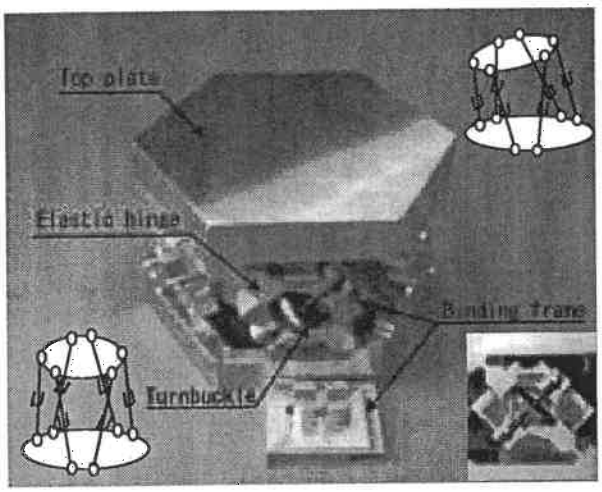

Figure 1. The miniature adjusting device sculpted into a parallel linkage

3. Structure of the elastic hinge frames

In the parallel linkage, if a movable range for the top plate is required widely, the elastic hinge frames must be extended widely and must be shrunk widely; besides, joint of the elastic hinge must be bend to any directions flexibly. Therefore, the elastic hinge frame is formed in the special shapes.

The elastic hinge frame consists of an elastic hinge plate, a turnbuckle, and two binding frames as shown in figure 3. Shape of the elastic hinge plate is the shape in which four quarter circles are connected inversely. The turnbuckle is inserted between horizontal edges, and the elastic hinge plate is extended, or is shrunk by rotating the turnbuckle. As the elastic hinge plate is inserted in two binding frames, the quarter circle is deformed along the ditch composed by the binding frame A

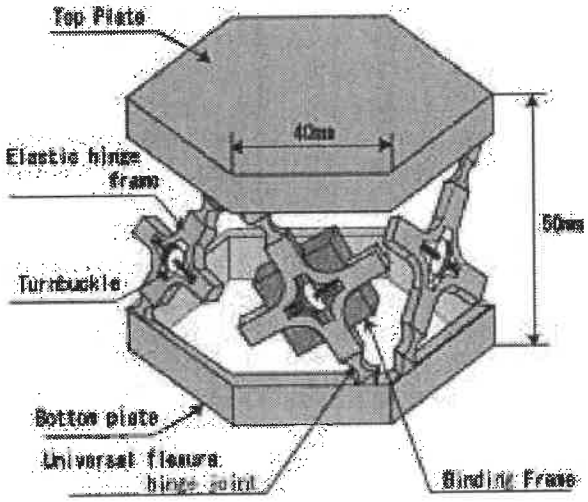

Figure 2. Structure of the miniature adjusting device

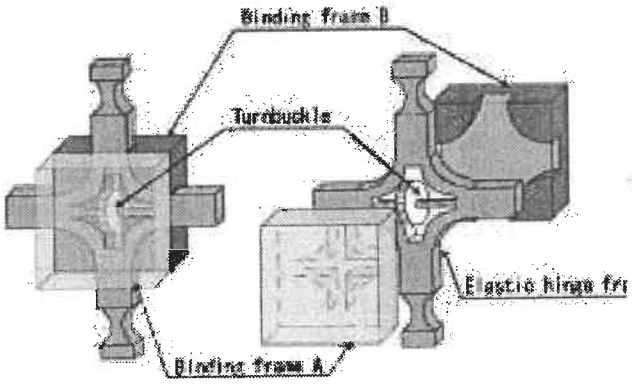

Figure 3. Structure of the elastic hinge frame

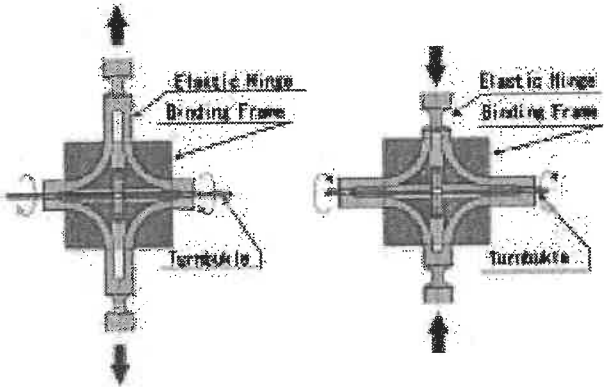

Figure 4. Deformation of the elastic hinge plate

and B. If the quarter circle is thin, the quarter circle is slid with a little resistance force, so the elastic hinge plate is extended widely and is shrunk widely as shown in figure 4. However, stiffness of the elastic frame is high because two binding frames limited the deformation of the quarter circle.

Thickness of the quarter circle was 0.5 millimeters. Radius of the quarter circle is 5 millimeters.

3. Experimental Results

In the experiments, attitudes and positions of the miniature adjusting device were measured when the turnbuckles rotated several times clockwise or counterclockwise, and stiffness of the elastic hinge frame was also measured when the binding fran fit to the elastic hinge plate or does not fit to t elastic hinge plate.

The displacements at six edge of the top pl were measured under the coordinate frame sho in figure 5. Figure 6-(1) shows the displaceme of z direction, that is a height displacement, wh the turnbuckles of six elastic hinges were rota until quarter one after another. When turnbuckles were rotated, the height displacem is nearly same. The figure is graphed convenient Figure 6-(2) shows the location of the six edge the top plate into the x-y plane when t turnbuckles of hinge 1, hinge 3 and hinge 5 w rotated until quarter. The figure is graph conveniently. The top plate was rotated about 0.14 degrees.

The stiffness of the elastic hinge frame with fitting the binding frames or without fitting the binding frames was calculated by measuring width and height of the elastic hinge frame under loading force as shown in the figure 7. Figure 8 shows the horizontal displacement, that means the width displacement, and the vertical displacement, that means height displacement, against the rotations of the turnbuckle. Figure 9 shows the relationship between the vertical displacement and horizontal displacement. When the turnbuckle was rotated once, that means 360 degrees, width of the elastic hinge frame was reduced 0.25 millimeters which correspond to the screw pitch of 0.25 millimeters, and height of the elastic hinge frame was extended 0.1 millimeters.

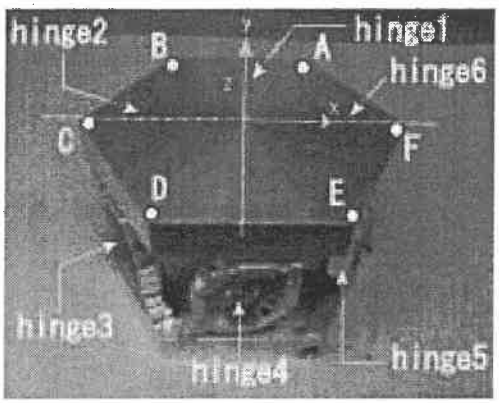

Figure 5. Coordinate frame for experiments

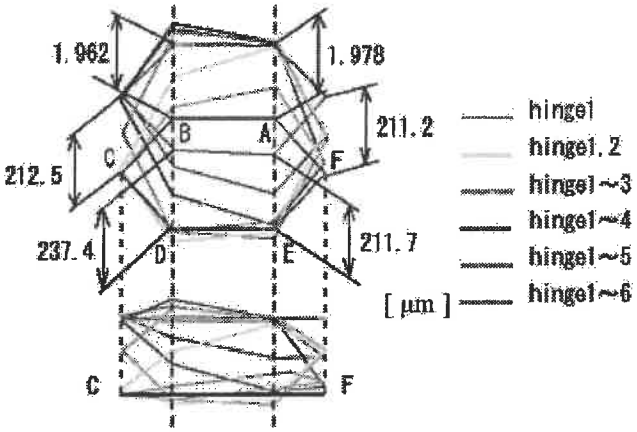

Figure 6-(1) Experimental result (1)

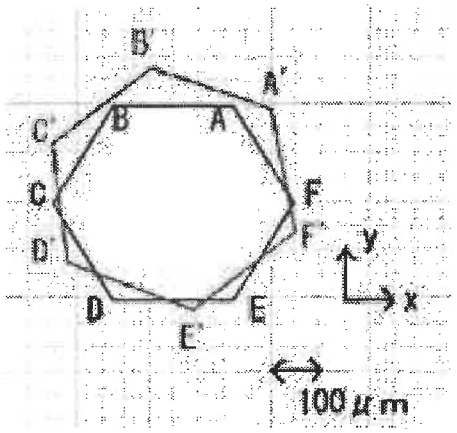

[Location by rotating of turnbuckles of 1,3,5]

Figure 6-(2). Experimental result (2)

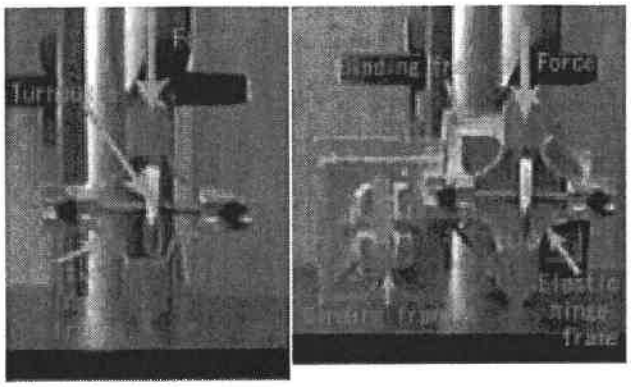

Figure 7. Stiffness experiment with the binding frame and without the binding frame

Figure 10 shows a vertical stiffness and a horizontal stiffness of the elastic hinge frame. The vertical stiffness was calculated by dividing loading force by the vertical displacement, where the compressive stiffness was expressed by a negative number and tensile stiffness was expressed by a positive number. The horizontal stiffness was calculated by dividing loading force by the vertical displacement.

The stiffness of the elastic hinge frame with the binding frames was much higher than the stiffness of the elastic hinge frame without the binding frames.

6. Conclusions

The miniature adjusting device sculpted into a parallel linkage was developed. The device could easily adjust the positions and the postures toward six directions of x, y, z, θx, θy and θz. The stiffness of the elastic hinge frame with the binding frames was strong.

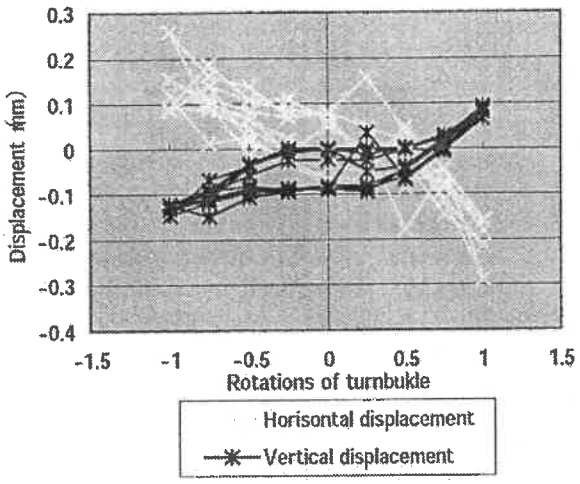

Figure 8 Horizontal and vertical displacement of the elastic hinge frame against the rotations of the turnbuckle

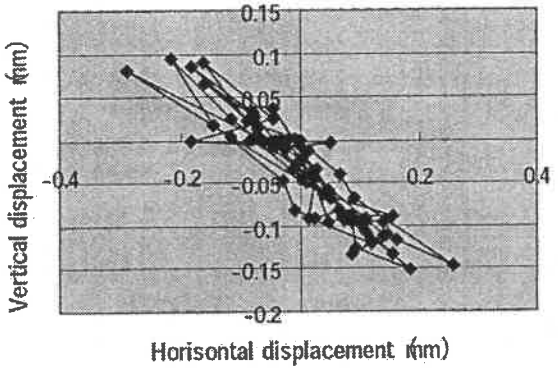

Figure 9 Relationship between vertical and horizontal displacements

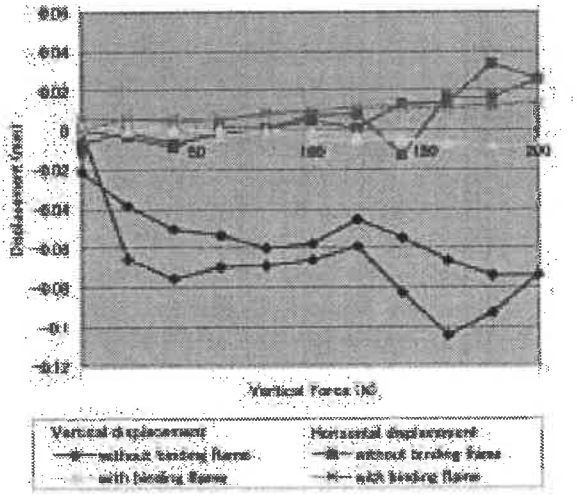

Figure 10• Stiffness of the elastic hinge frame

A STUDY ON OPTIMIZATION OF MINIATURE MACHINE TOOL DESIGN

Nozomu Mishima
National Institute of Advanced Industrial Science and Technology
1-2 Namiki, Tsukuba, Ibaraki, 305-8564 JAPAN

Abstract

AIST, Japan proposed and prototyped some new miniature machine tools for micro mechanical fabrication. Although the miniature machine tools had considerable machining capabilities, design optimizations of the machines have not been studied enough. Since the miniature machine tool designs are not fully supported by existing design experience, strategies and guidelines of designs are strongly demanded. In order to support miniature machine tool design, a design tool combines the form-shaping theory of machine tools and the Taguchi method was proposed.

This paper applied the design tool to a new machine tool design procedure of not only miniature machine tools but also wide range of design variations. The tool was effective identifying which of the several designs had the best performance and which of the design parameters had the critical effect on improving the machining accuracy of machine tools. Finally, the paper concludes that the design tool is useful in design optimization of machine tools.

1. Introduction

"Microfactory" is a name of an extremely small manufacturing system that consists of miniature machine tools and manipulators. The concept was proposed by AIST, Japan, in 1989. The first prototype of the microfactory was developed in 1999 by the author's research group in AIST [1]. It could perform manufacturing processes involving machining and parts assembly in a desktop space. Key components of the microfactory were miniature machine tools such as micro-lathe [2] and micro-mill [3]. However, although each miniature machine tool demonstrated rather good machining capability, there was no assurance that the individual machine designs were optimized. There was no theoretical background for those designs, including an analysis of structures and so on. Since, for miniature machine tools, existing experience with normal machine tool designs may not be applicable and the miniature machines have wider design choices than normal machine tools have, (due to its small size and fewer constraints), there is a strong demand for a design tool to analyze machine performance without the need for prototyping. The proposed design tool [4] is used in this paper for design optimization of machine tools.

2. Design Evaluation Method

A machine tool structure can be thought of as a chain of directly linked rigid components extending from the product through the cutting tool. An orthogonal coordinate system S_i corresponding to element i (i=0 to k) is defined. The transformation from S_i to S_{i+1} represents a coordinate transformation between components. Form-shaping theory [5] represents these respective coordinate transformations by homogeneous transformation matrices [6]; A_i. In an ordinary machine tool, A_i is represented by one of either parallel transformation along the x, y or z axes or rotation around the axes. Each of these six coordinate transformations is assigned a number to distinguish them, with parallel movement along the x-axis being 1, and so on. When the homogeneous transformation matrices A_i are represented by the transformations j_i, (=1 to 6), and the amounts of motions are represented by l_i, we define $A(i)(j_i)(l_i)$ as the expressions of the matrices. Vector $\vec{r}_0$ represents the relative displacement between the product and the tool, and the tool shape vector $\vec{r}t$ is also defined. The relation between $\vec{r}_0$ and $\vec{r}t$ is as given by eq. (1), and $\vec{r}_0$ is the definition of the form-shaping function that expresses the cutting motions of the machine tools. An actual machine tools have alignment errors, thermal deformation, wear and many other sources of errors. Such errors may for convenience's sake be treated as errors in transformations between elements. We define another homogeneous transformation matrix $A_{\varepsilon i}$ to generally represent transformation error between elements. By inserting the error component matrix $A_{\varepsilon i}$ between $A(i)(j_i)(l_i)$ and $A(i+1)(j_{i+1})(l_{i+1})$ in equation (1), the form-shaping function including errors, $\vec{r}_{\varepsilon 0}$ is written as equation (2). And the form-shaping error function $\Delta\vec{r}_0$, expressing the error amount from the target value, is defined as the difference between the form-shaping function not containing errors and that containing the errors, as equation (3).

$$\vec{r}_0 = A(0)(j_0)(l_0)\cdots A(i)(j_i)(l_i)A(i+1)(j_{i+1})(l_{i+1})\cdots A(k-1)(i_{k-1})(l_{k-1})\vec{r}_t \qquad (1)$$

$$\vec{r}_{\varepsilon 0} = A(0)(j_0)(l_0)A_{\varepsilon 0} \cdots A(i)(j_i)(l_i)A_{\varepsilon i}A(i+1)(j_{i+1})(l_{i+1}) \cdots A(k-1)(j_{k-1})(l_{k-1})A_{\varepsilon k-1} \cdot \vec{r}_t \quad (2)$$

$$\Delta\vec{r}_0 = \vec{r}_{\varepsilon 0} - \vec{r}_0 \quad (3)$$

To achieve machining tolerance that is stable under a variety of machining conditions, a method is needed for obtaining a design which is robust with respect to unknown local errors. The Taguchi method [7], [8] is widely used in the field of quality engineering, and provides an environment for robust design. This study uses the Taguchi method to evaluate the dimensional effect imposed on machining errors by the machine structure, when local errors are unknown. Analysis was performed applying the method to the form-shaping error function. The Taguchi method allows us to calculate combinations of values of control factors to optimize an evaluation function, when given noise factors fluctuate within given ranges. In this study, the primary objective is to determine the effect on machining performance of structural design, when some local errors exist in the various components of the machine tool. Therefore, it is appropriate to take the design parameters and product dimensions as control factors and the local errors as noise factors. We defined Δx, Δy, Δz as the error amounts in each direction.. Then, $(\Delta x^2+\Delta y^2+\Delta z^2)^{1/2}$ was set to be the evaluation function. When the value of the evaluation function at the ith trail is expressed as equation (4) and the number of trial is expressed by "n", the average of the function is shown in equation (5).

$$f_{ei} = (\Delta x^2 + \Delta y^2 + \Delta z^2)^{1/2} \quad (4)$$

$$f_{em} = \sum_{i=1}^{n} f_{ei} / n \quad (5)$$

3. Selection of Design Candidate

In creating a new design concept, there are many possible structures that have different sequences of motion axes. The issue is how to apply the proposed design evaluation method to create a design concept for a machine tool. The performances of the designs can be compared by introducing some assumptions to the Taguchi method. By assuming that every design concept has the same control factors, noise factors and its variation ranges, the calculation results based on the Taguchi method are expected to show the priority of the designs directly. By this extension, a machine tool designer can determine the best design concepts for miniature machine tools from several listed designs. Tracking the components from the workpiece to the cutting tool, it is possible to categorize machine tool structures by the number of the components that appear before the machine tool base. It is common to express transitional motions along the *X, Y* and *Z*-axis as 1,2 and 3, and rotational motions around the *X, Y* and *Z*-axis as 4,5 and 6. By using this expression, structure types of milling machines that have three transitional motions and one spindle rotation are categorized to 4 major structures, by the distribution of DOF. Those 4 are shown in Fig. 1. Type 12036 is frequently seen for tabletop drilling machines. Type 20136 is called column-traverse type machine and often used for relatively large product such as automobile parts, because it doesn't require extra space for table movement. Type 01236 is sometimes seen in a manufacturing system called "transfer line". Whereas type 12306 is rare for actual machine tools. A significant question is which of the four typical types has the best theoretical performance.

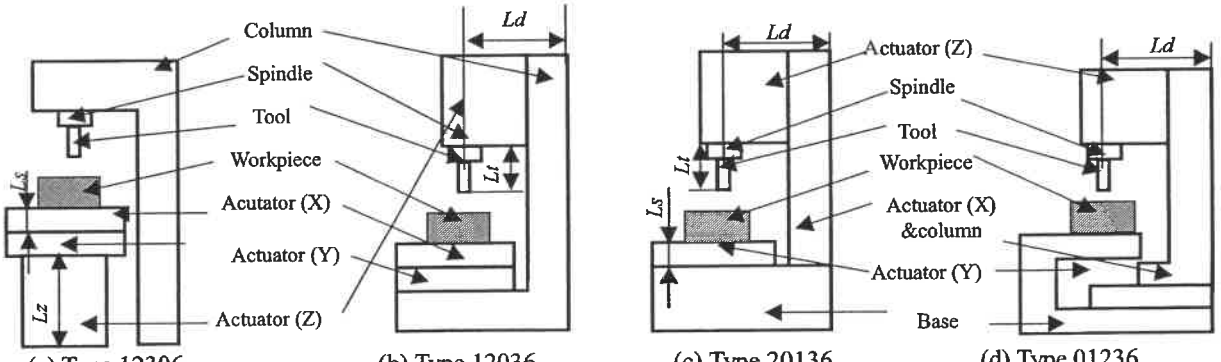

(a) Type 12306 (b) Type 12036 (c) Type 20136 (d) Type 01236

Fig.1 Four major types of mills

To apply the design evaluation method and perform parametric optimization to the structures, 6 design parameters was defined. And 3 of them were shown in the figure. Table 1 is the list of defined design parameters and its deviation ranges. Also, we defined 15 error factors to take the effect of error sources into account. Tables 2 is the list of defined error factors and its deviation ranges obtained from catalog data of machine components and so on.

Table 1 Design parameters and its ranges

Factor name	Variable	Ranges
Workpiece size	*Ws*	5, 7.5, 10, 12.5, 15cm
Bearing diameter	*Db*	25, 37.5, 50, 62.5, 75 mm
Tool length	*Lt*	5, 7.5, 10, 12.5, 15cm
Rotational speed	*N*	4000, 6000, 8000, 10000, 12000 rpm
Spindle - column distance	*Ld*	25, 37.5, 50, 62.5, 75cm
Thickness of the linear slides	*Ls*	5, 7.5, 10, 12.5, 15cm

Table 2 Error factors and its ranges

Name of the factor	Variable	Ranges
Angular error of the linear actuator	α_1	+-15"
	β_1	+-15"
	γ_1	+-15"
Scale error of the linear actuator	δ_{x1}	+-2μm
Straightness error of the linear actuator (H)	δ_{y1}	+-2μm
Straightness error of the linear actuator (V)	δ_{z1}	+-2μm
Angular error of the vertical Actuator	α_3	+-15"
	β_3	+-15"
	γ_3	+-15"
Straightness error of the vertical actuator (H)	δ_{x3}	+-2μm
Straightness error of the vertical actuator (V)	δ_{y3}	+-2μm
Scale error of the vertical actuator	δ_{z3}	+-2μm
Angular error of the spindle	α_4	+-30"
Eccentricity of the spindle	δ_{x4}	+-5μm
Expansion of the spindle	δ_{z4}	0~20μm

Six control factors shown in Table 1 were set to be independent control factors and L25 array was used for the control factors. L16 array was used for 15 error factors shown in Table 2. Four different form-shaping error functions; $\Delta\vec{r}_0$, corresponding to the four designs shown in Fig.1 can be expressed using the parameters defined in table 1 and 2. Equations (6) is an example of a form-shaping error function which corresponds to the structure called "type 12036" in Fig.1. One needs to calculate the value of the equation to evaluate the performance difference of the designs, under the same design parameters and error factors.

$$\Delta\vec{r}_0 = \begin{bmatrix} \delta_{x1}+\delta_{y1}+\delta_{x3}+\delta_{x4}-(\beta_3+\beta_4)\cdot Lt+\alpha_1\cdot(2Ls+h)+\beta_1\cdot(Ls+h)-\gamma_1 d \\ \delta_{x1}+\delta_{y1}+\delta_{y3}+\delta_{x4}+(\alpha_3+\alpha_4)\cdot Lt-\beta_1\cdot(2LS+h)-\alpha_1\cdot(Ls+h) \\ 2\delta_{z1}+\delta_{z3}-\delta_{z4}+\alpha_3\cdot Ld+\alpha_1\cdot d \\ 0 \end{bmatrix} \quad (6)$$

4. Analysis of Design Parameters

Same ranges of the error factors shown in table 2, which are roughly assumed, are substituted to the calculated form-shaping error functions corresponds to 4 major structure types shown in Fig.1. In the calculation, size effects of error factors were also considered. For example, "expansion of the spindle" is likely to be smaller, when the machine tool size is small. On the other hand, straightness error of slides would not be affected by machine size. Considering these size effects, Fig. 2 shows the comparison of the theoretical performances. According to the figure, when the

design parameters vary within the defined ranges, lines to express the positioning error of type 12036 are always the lowest, and those of type 02136 are the largest. Among the 6 design parameters, "spindle-column distance" is the most critical parameter to affect the machine performance. The figure shows that the design with distributed DOF (type 12036) has better theoretical performance than the concentrated DOF (type 12306 or type 01236) has, although the differences between the types are not very large when the machine tool sizes are small. By these results, type 12036 was selected for the design of the miniature mill to be used in the aforementioned microfactory project.

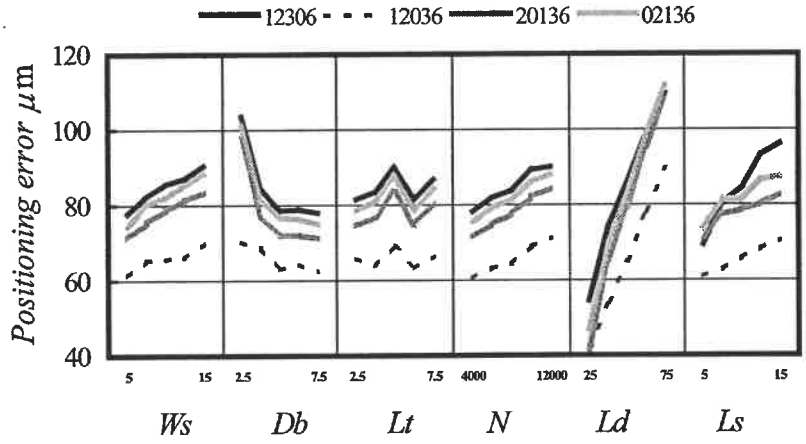

Fig. 2 Comparison of the theoretical performance

From the figure, it is concluded that "type 12036" has the best theoretical performance among four structure types. Among the six design parameters, *Ws*, *N*, *Ld* and *Ls* have positive impact on machine performance, where as *Db* has a negative effect. And "*Ld*" which expresses "spindle-column distance" has the most critical influence on machine performances.

5. Conclusions

The proposed design evaluation tool was effective in identifying the proper design from the design candidates for milling machines. "Type 12036" was estimated to have the best theoretical performance.

It was also possible to determine design parameters that had significant influences on machine performance. "*Ld*" which expresses "spindle-column distance" of machine tools had the most critical effect on machine performances. "Thickness of the linear slides; *Ls*" and "bearing diameter; *Db*" had relatively large influence on machine performances, as well.

References

[1] Mishima, N., Ashida, K., Tanikawa, T. and Maekawa, H., *Design of a Microfactory*, Proc. of ASME/DETC 2002, Montreal, Sept. 2002.

[2] Kitahara, T., Ishikawa, Y., Terada, K., Nakajima, N., and Furuta, K., *Development of Micro-lathe,* Journal of Mechanical Engineering Laboratory, Vol. 50, No. 5, p. 117-123 (1996).

[3] Mishima, N., Ashida, K., Tanikawa, T. and Maekawa, H., *Design of a Microfactory*, Proc. of ASME/DETC 2002, Montreal, Sept. 2002.

[4] Mishima, N. and Ishii K., *Robustness Evaluation of a Miniaturized Machine Tool*, Proc. of ASME/DETC99. Las Vegas, Sept. 1999.

[5] Reshtov, D.N. and Portman, V.T., *Accuracy of Machine Tools,* ASME Press, New York, (1988).

[6] Paul, R.P., *Robot Manipulators*, THE MIT press, Cambridge (1981).

[7] Taguchi, G. and Konishi, S., *Quality Engineering Series* Vol.1-4, ASI Press. (1994).

[8] Folkes, W.Y. and Creveling, C.M., *Engineering Methods for Robust Product Design*, Addison Wesley, (1995).

PERFORMANCE OF WATER ENERGY DRIVE SPINDLE SUPPORTED BY WATER HYDROSTATIC BEARING

Yohichi Nakao, Fumiyuki Kobayashi and Yuji Sagesaka

Department of Mechanical Engineering, Kanagawa University
3-27-1, Rokkakubashi, Kanagawa-ku, Yokohama 221-8686, JAPAN
(Email: nakao@kanagawa-u.ac.jp)

Key Words: *Water-Driven Spindle, Water Hydraulic Built-in Motor, Water Hydrostatic Bearing, Ultra-Precision Machine Tool, Bearing Stiffness*

1. Introduction

Spindles used for recent diamond turning machines are typically supported by hydrostatic bearings. Especially, air hydrostatic bearings are the most common because of low viscosity of air. Low viscosity of lubricant fluid is an important requirement for operating the spindle in a range of higher rotational speeds. However, from a stiffness viewpoint of the bearings, higher compressibility of the air can be a disadvantage. From viewpoints of stiffness and stable operation of the hydrostatic bearing, incompressible fluid is desirable. Oil hydrostatic bearings may be an alternative for such case. However, higher viscosity of the oil makes it difficult to operate the spindle in a range of higher rotational speeds. A spindle supported by water hydrostatic bearing would be a better alternative.

An electrically driven built-in type motor is recently designed for the most of the spindles for diamond turning machines. In this case, heat generation at the electric motor can deform the spindle, which must cause serious problems during the spindle operation. In order to attain higher bearing stiffness of the air hydrostatic bearing, the gap between spindle body and housing is usually designed to be very small. Hence, the deformation may cause metal contacts between the two parts. To cope with these problems, a water-driven spindle supported by water hydrostatic bearings has been proposed and developed [1]-[3].

2. Developed Spindle

Figure 1 shows the spindle structure. The spindle driven by pressurized water flow can effectively use the water for three spindle functions, i.e., motor, bearing and cooling functions.

(1) Motor function

In the spindle body, simple bend channels, named flow-out channels, are designed in order that pressurized water flow in the bend channels can generate torque for rotating the spindle. Therefore, the flow channels can be used as a motor. An advantage of the motor is that it can be easily fabricated inside the spindle body. As an additional advantage, the motor structure allows us to design compact spindle.

(2) Bearing function

Water hydrostatic bearings are designed to support the spindle, which makes it possible to

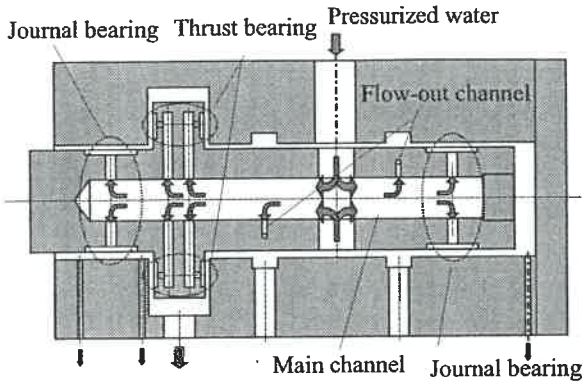

Fig. 1 Spindle structure

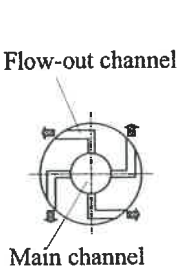

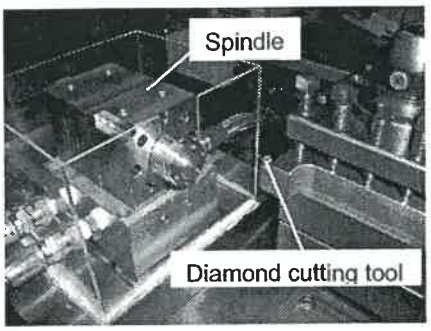

Fig. 2 Spindle set on precision machine tool

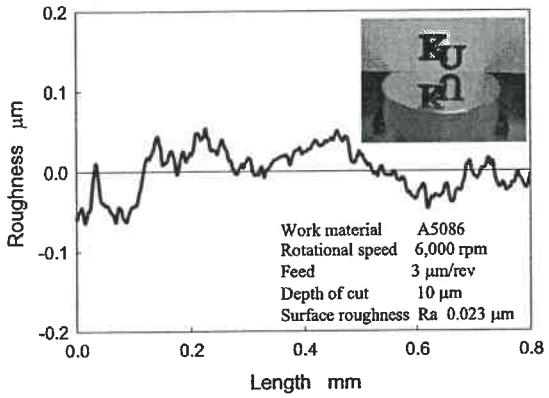

Fig. 3 Surface roughness and machined surface

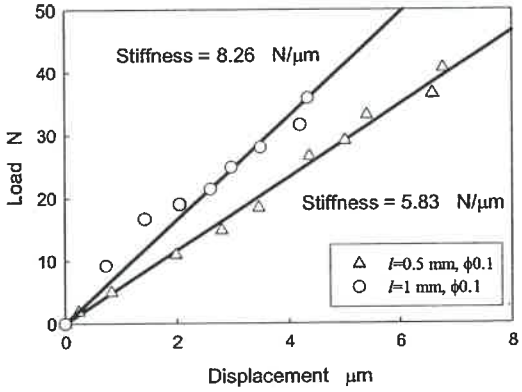

Fig. 4 Stiffness of water hydrostatic bearing

design both higher spindle rotation and bearing stiffness.

(3) Cooling function

Water supplied for the motor and hydrostatic bearing can be used for cooling water as well, which can effectively maintain temperature of the spindle. As a result, a serious deterioration in the machining accuracy due to thermal deformation of the spindle can keep minimum. In addition, the cooling function can effectively avoid the mechanical contacts between spindle body and housing.

In this paper, an experimental result of diamond turning, which has been conducted with the spindle, is presented. In addition, measurement results of the bearing stiffness, which have been conducted in order to consider a cause of unsatisfactory machining result, are also presented.

3. Diamond Turning Test

Developed water driven spindle has been tested for diamond turning. Figure 2 shows the spindle placed on a commercial precision machine tool. Face cutting tests using a single point diamond cutting tool have been conducted in order to investigate performances of the spindle. Aluminum and cupper alloys, A5086 and C1020, have been used as workpiece materials. A surface roughness and a machined workpiece are shown in Fig. 3. In this case, optical quality surface can be successfully obtained. However, the surface roughness, Ra =23 nm, is considerably larger than

the target level in our study.

From the viewpoint of the spindle performance, important factors that affect the surface roughness would be the followings:

(1) Stiffness of the water hydrostatic bearings

(2) Rotational accuracy

In this paper, the issue of bearing stiffness is investigated. The influence of rotational accuracy of the spindle on the machining results will be considered in the future.

4. Measurement of Stiffness of Hydrostatic Bearing

Figure 4 shows a relationship between radial direction forces to the spindle and resultant displacement. In a series of the experiments, the stiffness of the journal bearing has been measured using bearing chokes with two different lengths, i.e. 0.5 and 1.0 mm, respectively. A choke with 1mm in length is originally designed, however, the experiments with the choke, 0.5 mm in length, were conducted in order to examine the influence of the length.

Journal bearing stiffness, when no load torque is applied to the spindle, was designed to be 29 N/μm. However, it is found that actual bearing stiffness is only 29 % of the required stiffness. Because of the insufficient bearing stiffness, slight changes in cutting forces could affect positions of the spindle during diamond turning. It is considered that the insufficient stiffness is a possible reason of the relatively large surface roughness.

Next, a reason of the insufficient bearing stiffness is discussed. Pressure ratios of the hydrostatic journal and thrust bearings were designed to be 0.5, which is the theoretical optimum condition for obtaining maximum bearing stiffness. In this case, theoretically, the recess pressure, p_r, should be a half of the supply pressure, p_s. Pressure-flow characteristics, i.e. flow resistances, of both bearing chokes and hydrostatic bearing surfaces are crucial factors to determine the pressure ratio, p_r / p_s.

Figure 5 shows the pressure-flow characteristics of the choke designed for the hydrostatic journal bearing. The characteristics obtained by the experiments significantly differ from the theoretical relationship. In this case, the actual flow resistance of the choke was approximately 24 times of that of theoretical relationship. If the actual flow coefficient of the hydrostatic journal bearings is the same to the theoretical relationship, actual recess pressure, p_r, becomes approximately only 8 % of the theoretical value.

5. Spindle Speed

Water, supplied from a pump to the spindle, flows primarily into the motor and hydrostatic bearing besides leakage. Flow distributions for the motor and hydrostatic bearings are determined by flow resistances of the two parts. Therefore, the characteristics of the bearing choke presented in Sec. 4 affect not only the characteristics of the hydrostatic bearing but also that of the spindle motor. More specifically, the motor flow should be larger than the expected since the actual flow resistance of the bearing choke became significantly large.

Figure 6 shows the spindle speed characteristics. In fact, it is found that the spindle speed obtained theoretically, which is given by a dashed line, is lower than that of experimental result. In contrast, the solid line, which is calculated with the measured flow coefficient of the bearing choke, shows the relatively similar trends to the experimental result. From these results, it is verified that the

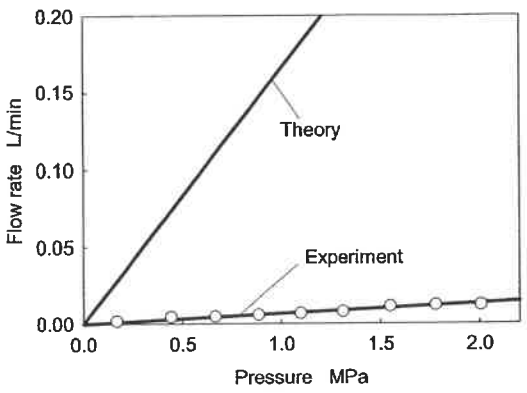

Fig. 5 Characteristic of bearing choke

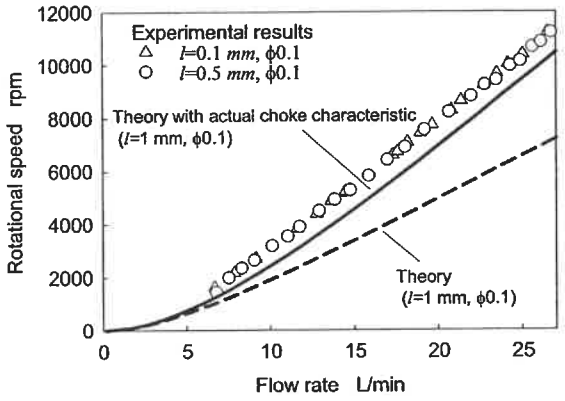

Fig. 6 Rotational speed of water driven motor

characteristics of the bearing choke play an important part of the spindle motor performances as well as the bearing stiffness.

6. Summary

A water-driven spindle developed for ultra-precision machine tools was tested for diamond turning. An optical quality surface was generated in the test. However, the surface roughness did not reach required level.

In order to investigate the unsatisfactory result of the diamond cutting test, a stiffness of the water hydrostatic bearing has been measured. As a result, low stiffness of the bearing was appeared. An experiment to measure the pressure-flow characteristic of the choke of the hydrostatic bearing has been conducted. The result shows that the flow resistance of the choke is too high to obtain an optimum stiffness of the bearing. This issue is now being investigated in our study.

It is considered that the rotational accuracy of the spindle must be another factor to determine the diamond cutting performance. Therefore, the rotational accuracy of the spindle will be measured and investigated. Especially, an influence of supply water pressure pulsation on the machining performance could play important factor.

Acknowledgements

This research work is financially supported by the Grant-in-Aid for Scientific Research (C) of Japan Society for the Promotion of Science. The support of Nano corporation for the diamond turning tests is gratefully acknowledged.

References

[1] Y. Nakao and M. Mimura, Spindle Motor Driven by Fluid Energy for Ultra-Precision Machine Tool, Proc. of ASPE 2001 Annual Meeting, pp.215-218, (2002).

[2] Y. Nakao and M. Mimura, High-Speed Motor Driven by Fluid Power, Proc. of 5th JFPS, pp.543-548, (2002).

[3] Y. Nakao, M. Mimura and F. Kobayashi, Water Energy Drive Spindle Supported by Water Hydrostatic Bearing for Ultra-Precision Machine Tool, Proc. of ASPE 2003 Annual Meeting, pp. 199-202, (2003).

DESIGN PRINCIPLES FOR HIGHEST PRECISION APPLICATIONS

R. Theska, T. Frank, T. Hackel, G. Höhne and M. Lotz
Technische Universität Ilmenau, Germany

Introduction

Ultra precise multi-axis positioning and measuring machines have been identified as an enabling tool in the current developments in nanotechnology and further beyond. Therefore machines with an increasingly large spatial travel are being demanded while reaching accuracy in the nanometer range. High flexibility for various applications in metrology, micro-mechanics and nanotechnology is feasible. Known machines show that requirements of highest precision applications cannot be reached only trough the use of closed loop control [1, 2, 3]. With a systematic machine design it is possible to better handle environmental influences and machine behavior.

State of the Art

Machines with best accuracy and precision are required for measurement tasks in various precision applications. Therefore universal coordinate measuring machines (CMM) are used, conducting a relative motion between an object and a special tool like probe head, AFM-tip, optical sensor or another.
CMM can be divided into three categories, depending on the working range, as to be seen next (Figure 1).

	Large Range		Small Range		
Name	Leitz PMM-C	Zeiss UPMC 850	Vecco Explorer SPM		
Structure					
Moving range	1.2 x 1.0 x 0.7 m³	1.15 x 0.8 x 0.6 m³	70 x 15 x 15 µm³	100 x 100 x 10 µm³	
Developer	Leitz Messtechnik Germany [Leitz 2004]	Carl Zeiss IMT Germany [Zeiss 2004]	TU Ilmenau / PTB Germany [Jäger 1998]	Vecco Instruments USA [Vecco 2004]	
	Medium Range				
Name	NMM 1	Molecular Measuring Machine	Ultra Precision CMM	Ultra Precision CMM	
Structure				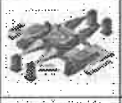	
Moving range	25 x 25 x 5 mm³	50 x 50 mm²	100 x 100 x 40 mm³	300 x 300 x 300 mm³	
Developer	TU Ilmenau Germany [Haessler 2002]	NIST USA [Kramar 2001]	TU Eindhoven Netherlands [Ruijl 2002]	BUPE Korea [KAIST 2003]	

Figure 1 – State of the Art machines

To reach best as possible accuracy all different error sources have to be considered for machine control and correction of the measurement result. One example is the CMM Sirio from Leitz Messtechnik which is equipped with 28 temperature sensors to estimate machine deformations [4].

Methods

To design machines for highest precision applications successfully a systematic approach is necessary.
One possible approach is a four stage process (Figure 2) consisting of task specification, analysis and determination of the technological process, synthesis of functional structures including the design of solution principles and at last the design of the overall system. For the development of a nanopositioning device with a moving range of 200 x 200 x 15 mm³ [5] this four stage process has been used.

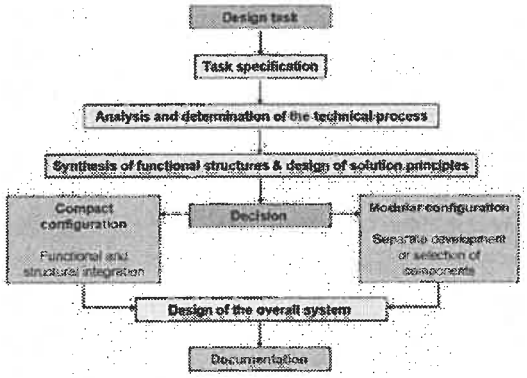

Figure 2 – Four stage design process

It starts with the specification of the task that has to be fulfilled. The next step is the analysis of the required technological processes and the given boundary conditions. Therefore all operations which have to be carried out have to be described. It leads to a generalized model that describes the overall function of the machine as well as the interactions with the expected environment.

In the next step a general functional structure can be established which serves as a base for the whole design. All necessary functions are in it included and described. Figure 3 shows a functional structure for a positioning and measuring system. It is used as a maximum functional structure this means it can be reduced if functions are not needed. For example tool movements are reduced to avoid error sources.
The functional structure leads to the design of the solution principles. These principles are the base of the whole machine design. Because of this they have to be developed with care. Design principles are applied to reach an optimum design beginning in this early phase

of development. Virtual Prototyping methods are used to check that the principles will work.

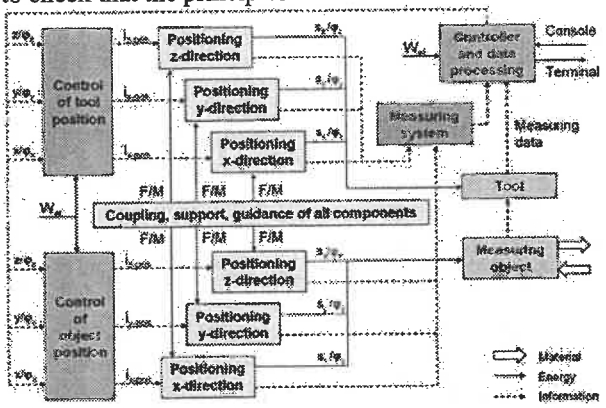

Figure 3 – Functional Structure

Tools and objects can vary according to the technology needs of the application. Therefore the tool and the mount of the object are so called non-platform elements designed or selected specially for each variant of machine. This function-oriented configuration is indicated because the machines are only produced in small numbers.

In the next stage the structures will be designed around the functions. The specified functional structure and the determination of the movements are the basis to realize the function-oriented configuration of the machine. A configuration matrix can be used to find possible solutions. This matrix can be easily expanded to include new potential solutions.

The last stage in the methodology concerns the design of the embodiment and ends with the detail design including all necessary documentations.

Design Principles

High precision applications require machines with outstanding performance, which means very good dynamic behavior combined with highest precision. It is obvious and recommended that design principles should be used consequently for the whole machine design to reach these requirements [5, 6].

Unfortunately in times of high speed computers and closed loop control the importance and the benefits of design principles are underestimated. They can be used to:

- avoid random errors and reduce systematic errors,
- reduce the effects of environmental influences (e.g. temperature, vibration),
- realize a predictable system behavior,
- simplify the machine control.

The design of the technical principle is crucial for the whole machine design. This phase allows to find the most critical error sources and crucial components of the whole machine and the measurement circle at this early design stage. Error calculations and the development of adjustment strategies can be carried out.

Because of this design principles should be applied beginning in this early stage of design. Nevertheless if highest precision is desired it is necessary to apply design principles in all phases of the design process. The most important ones will be described next.

Principle of Small Error Arrangement

Systematic and random errors should be avoided as best as possible. For example first order measuring errors can be eliminated by the arrangement of object and measuring system in one line according to the so called Abbe principle. This principle can be expanded also to three axes (Figure 4).

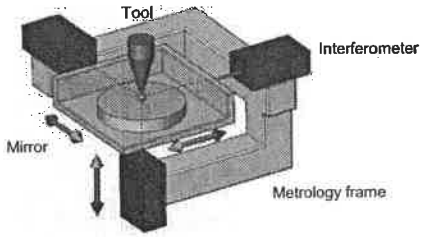

Figure 4 – Abbe principle for three axes

Principle of Function Separation

Depending on the level of abstraction, the overall functional structure can be broken down into sub-functions. A function defines the desired output, which has to be fulfilled by the machine components, from the input.

For high precision and reliability it is inevitable to apply the principle of function separation. One component or subassembly has to fulfill a single defined function which reduces negative influences from interactions of several functions on the control loop. Also the adjustment as well as calculation of dimensions and tolerances is simplified. But this principle results in an increasing number of parts and interfaces which leads to an increased mass and volume.

Principle of Function Integration

On the opposite, the principle of function integration combines several functions in one component. It is applied for compact, miniaturized and lightweight design and less number of mechanical interfaces. Especially for auxiliary functions it is useful to apply this principle.

It strongly depends on the special case which of both principles should be applied.

Principle of Force Transmission

A general principle of the precision machine design is to reach a short and direct force flow. To minimize deformations and to use part and material capacity in the best

possible way the forces should preferably cause tensile or compressive stresses instead of bending and torsional stresses. Methods of Virtual Prototyping can be used to simulate and optimize the force flow.
If a direct force flow without resulting moments is not possible additional measures should be taken. For example force should not result in a small contrary motion, as to be seen in the following picture (Figure 5).

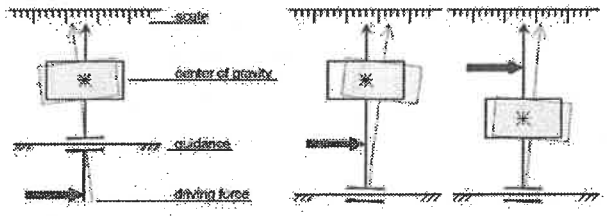

Figure 5 – Dynamic Force Compatible Arrangement

In the left figure the driving force results in a small motion opposite to the force which can confuse the controller. To optimize the dynamic performance the right hand setups should be preferred.

Principle of Symmetry

In order to average and to reach uniform systematic and random errors, precision machines should apply symmetric design not only for mechanical components and forces, but also for thermal design. All actuators, which are heat sources, are placed symmetrically to minimize temperature gradients in the machine. Combined with the principle of exact-constraint design symmetric 3-point supports are arranged at 120° angles, resulting in triangular shapes.

Principle of Exact Constraint Design

The entire machine can be seen as kinematic chains with rigid bodies and joints as elements. Either mechanical interfaces or elastic zones of a part serve as joints. Using exact constraint design, the kinematic chains or subchains must satisfy the desired and preliminarily specified degree of freedom. This can easily be calculated using Chebyshev's equation.
Over constrained mechanisms require small geometrical tolerances that result in the need for high precision manufacturing or adjustment devices. Yet an over constrained mechanism is very sensitive regarding disturbing influences. Because of that, precision components should be based on a deterministic design.

Example

One possible solution for a high precision machine is shown in Figure 6. The given design principles will be described on this example of a machine design.
The position of a three-face mirror, which carries the object is measured by three fixed laser interferometers. First order position errors are eliminated by the arrangement of the interferometers. Abbe's principle will be respected in all three axes because the extensions of the three laser beams meet in a single point (so called Abbe point), which is in coincidence with the tool's working point [2].
The metrological frame is separated from the machine frame (Figure 4). This isolates the metrological frame from unwanted forces and vibrations. Another example is the separation of static (gravitational) and dynamic forces. A separate mechanism has to carry the weight of all components to be moved in z direction. The z actuator only generates dynamic forces to move the platform with highest resolution. To reach unidirectional forces, the weight is not compensated entirely.

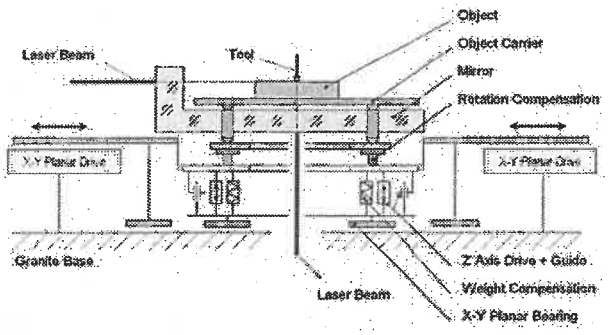

Figure 6 – Technical Principle

Being an example of function integration as well, the x-y planar drive generates the driving forces in only one plane, which is close to the centre of gravity of the moving parts. This minimizes moments of tilt, which cause second order measurement errors.
To avoid hot spots and unwanted thermal influences the design is symmetric. The x-y planar drives are shielded by a plate to reduce convection. Therefore thermal influences to the laser beams can be reduced.
All couplings of functional elements are well constraint. This is very important to avoid deformations induced by dynamic forces or different expansion coefficients.

Virtual Prototyping

Beginning in early phases of design the virtual prototyping method [7, 8, 9] can be used to check that the technical principles and the embodiment design consisting of parts and assemblies will work. For this purpose there are several different tools.
MASP, a tool for constraint solving, is used in our case to simulate movements, forces and tolerances of a principle solution. Following tools are that of simulation with multi-body systems (ALASKA) and that of finite element analysis (CosmosWorks and ANSYS).

One typical component for high precision machines is the measuring mirror of the interferometric measuring

system. It is necessary to measure the position of the object in three coordinates.

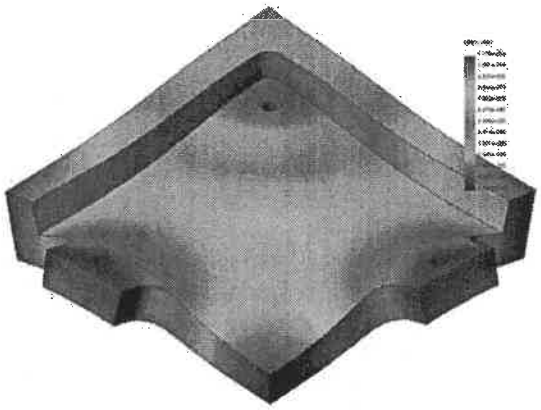

Figure 7 – FEA deformation of measuring mirror

For the given example of the measuring mirror (Figure 7) it is important to optimize the position of its supporting points. The aim is to minimize the mirror deformation under gravity. Because the material of the mirror is a ceramic glass only little stress is allowed.
To solve this problem a parametric CAD-model was generated to change the position of the supporting points easily by only one parameter. The supporting points themselves were modeled as a contact area to comply with the real system as best as possible.

Virtual Prototyping is very useful and more and more necessary especially for important machine components which are often very complex and expansive. They can be tested without physical prototypes during the design phases. Therefore results of the simulations and knowledge of the future behavior can be integrated in the whole system design earlier.
The aim is to make important decisions on the optimum design in early phases of design. Thus it is possible to save time and money and to reach better design solutions.

Conclusion

The design of a high precision machine should be as simple and reliable as possible, and exactly determined. To achieve this goal, the persistent use of the design methodology and principles is a powerful tool in the design process of ultra-precision instruments with extreme accuracy, repeatability and stability requirements. Already at the earliest stages of the design process, they are a great help to elaborate a machine concept on a more deterministic and comprehensible way.
By using virtual prototyping techniques it is possible to optimize the arrangement and the shape of the machine components. Because a high precision machine is an extremely complex system it is useful to treat the components separately but also the interaction of the components must be considered.
Further research has to be done to experimentally test the design principles and evaluate the results of the virtual prototyping. So it will be possible to get a feedback for the current development of methods and tools.

References

[1] Takamasu, K. et al., "Development of nano-CMM and parallel-CMM – CMM in the 21th century", Proceedings of International Dimensional Metrology Workshop 1999, Tennesse, 1999

[2] Jäger, G. et al., "Operation and Analysis of a Nanopositioning and Nanomeasuring Machine", ASPE Annual Meeting 2002

[3] Hausotte, T., "Nanopositionier- und Nanomessmaschine", Dissertation, Isle, Ilmenau, 2002

[4] Leitz 2004 „Leitz PMM-C" brochure Leitz Messtechnik GmbH

[5] Theska, R. et al., "Advanced Design Principles to Develop Nanopositioning Machines", Proceedings of 4th euspen, Glasgow, 2004, pp 440-441

[6] Krause, W., "Gerätekonstruktion in Feinwerktechnik und Elektronik", Carl Hanser Verlag, München, 2000

[7] Kunz, A. et al., "Innovation at the digital product - the use of virtual product development process", Proceedings of ICED 01, Vol. 1, Glasgow, 2001, pp.693-700

[8] Brix, T. et al., "Multi-stage modelling in early phases of design", Proceedings of ICED 03, Stockholm, 2003, pp 279-280

[9] Hochmuth, R. et al., "Approach to evaluate the precision of technical systems", Proceedings of ICED 01, Vol. 3, Glasgow, 2001, pp.C586/031

Acknowledgement

The authors would like to thank the members of the Collaborative Research Centre 622 "Nanomeasuring and Nanopositioning Machines" and the Deutsche Forschungsgemeinschaft for their support.

Key words

design principles, virtual prototyping, design methods

DEVELOPMENT OF FORCE AND MOMENT CONTROL MECHANISM FOR ROTATING PARTS USING ELECTROMAGNETIC FORCE (APPLICATION OF CMP HEAD)

Yutaka Uda, Takeshi Soma, Takanori Fujiwara, Isao Sugaya
Nikon Corporation, Tokyo, Japan
Thomas Novak, Douglas Watson, Bausan. Yuan, Yi-Ping Hsin
Nikon Research Corporation of America, Belmont, CA, USA

1. Introduction

Semiconductor devices have achieved high performance, high function and high density with incredible speed. This trend is accelerated by introduction of CMP technology. For miniaturization and integration in semiconductor process of <90 nm node, it is indispensable to achieve Cu/low-k CMP process at low pressure of <1psi. The lower the dielectric constant (=k), the lower the mechanical strength and adhesiveness. Therefore, lower pressure polishing CMP system is necessary. Especially in case of ultra low-k material of k<2, which consists of low-density and high-porosity material, development of CMP technology at <0.1psi (690Pa) ultra low pressure is required.

• However, in the CMP process with low pressure, we have to face a difficult issue: poor uniformity. To obtain as good uniformity as at high pressure polishing, a capability of removal profile control is required. Our CMP system (NPS3301) is developed by the concept of local polishing using a smaller polishing pad. The local polishing mechanism has a capability of removal profile control by changing the polishing parameters: wafer spindle speed, polishing pad spindle speed, and oscillation stroke & start position. Then Nikon CMP tool is the first successful system in the world that achieved <0.1psi (690Pa) polishing for Cu/ultra low-k films.

In mechanical polishing, the removal amount can be determined by polishing pressure, relative velocity, and polishing time (Preston's equation). In local polishing method, the removal amount is to be controlled by changing relative velocity and polishing time. To enlarge the range of polishing profile, the control of polishing pressure is required. On the current CMP mechanism, polishing pressure is generated by air pressure. Air pressure control is good for maintaining constant pressure, and it is not good for changing pressure quickly. Moreover the pneumatic mechanism for controlling the moment of rotating parts is very difficult. So we developed new mechanism using electromagnetic force. Changing the electric current, generated electrical magnet force is changed. In the case of CMP, a polishing pad is to be dressed each time after wafer polish. The pad thickness becomes thinner. Using electrical magnet force, the relation ship between force and gap is non-linear. A general mechanism needs a gap sensor and a force transducer. Our force control system uses only force transducer and achieves to have a good response enough to adapt for CMP head.

• This presentation refers to the force control mechanism and the force control system newly developed. To verify the system design and concept, the basic experiment was carried out, and the results are reported.

2. Polishing System

The polishing mechanism on this system uses a smaller polishing pad than wafer as shown

in Fig.1 enabling local polishing. It is judged that the product of relative speed and polishing time is more precisely controllable than the polishing pressure on Preston's empirical formula. This system has the mechanism to control the oscillation position and the speed of polishing pad. Slurry is delivered to a wafer rotating face up from a center of polishing pad, which pushes polishing pad downward. This mechanism enables uniform chemical effect by flowing slurry over polishing area almost uniformly.

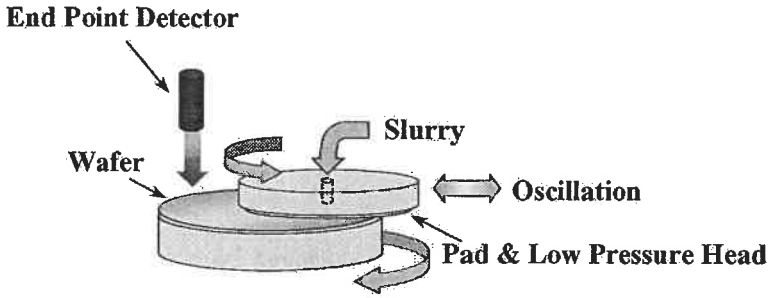

Fig.1 Polishing Mechanism

3. Development of CMP Polishing Head

3-1.Mechanizum

The mechanism is required non-contact for used in a clean room. The electromagnetic force system (CI-core) is adopted to maintain the uniform pressure on the pad/wafer contacted area. The force pulling up I-core is generated by supplying electric current to the coil attached in C-core. Controlling a rotating part, I-core is made ring-shaped and attached to the rotor. (Fig.2) C-core which needs wiring is fixed to non-rotating part. In order to control force and moment for a rotating part, the system needs three C-cores at least. Figure 3 shows the wafer polishing force distribution with the side-view plot. To obtain the uniform contact pressure on the pad/wafer contacted area, the following equations are required.

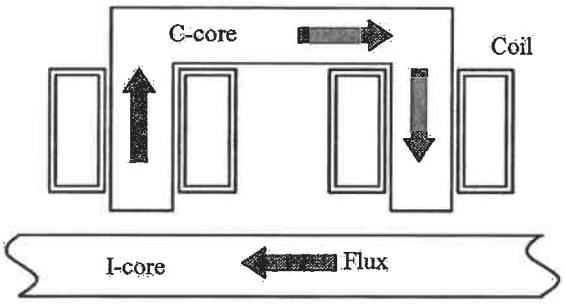

Fig.2 C-I Core

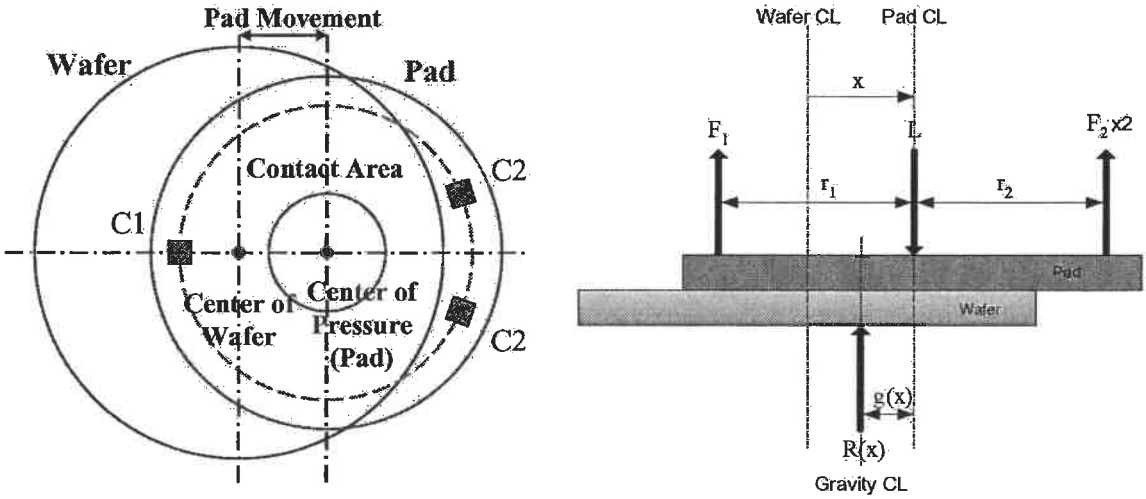

Fig.3 Wafer Polishing Force Distribution

$$F1+2*F2+R(x)=L \quad (1)$$
$$F1*r1+R(x)*g(x)=2*F2*r2 \quad (2)$$

Using CI-core, the relationship between a gap distance and a generated force is not non-linear in the case of constant supply current. In CMP process, the pad is dressed and its thickness is reduced after polishing a wafer every time. The reduction of pad thickness changes the gap and causes the non-linearity problem. The load cell is attached to C-core.

3-2.Controller

For a controller, two items are required mainly. One is how to calculate the output signals of three C-cores. The other is how to optimize the gain caused by the mentioned non-linear relationship. About the first item, the contact area and its gravity center distance can be calculated by geometric equations (1), (2) as the pad position is known during polishing by a rotary-encoder attached to the oscillation arm. About the non-linearity problem, the adaptive gain adjustment (AGA) servomechanism was developed. The AGA servomechanism includes the real-time force gain estimate scheme and the extra adaptive gain adjustment block in the servo loop. If the adaptive gain adjustment block has the fixed gain one, it would be the conventional feedback control system.

4. Experiment

Before assembling the developed mechanism to CMP polishing head, the basic experiment was conducted. I-core was attached to the spindle of milling machine and C-core with the load cell is fixed on the table, and the gap sensor detects the gap between cores. A result is shown in figure 4. The output of the load cell is the almost same value as the command signal. The gap signal is combined two sine waves. One is synchronized with number of rotations, and the other is synchronized with the force generated by C-core. It has checked that the force can be transmitted to a solid of revolution by non-contacting, and that the nonlinear measure in a controller had been successful.

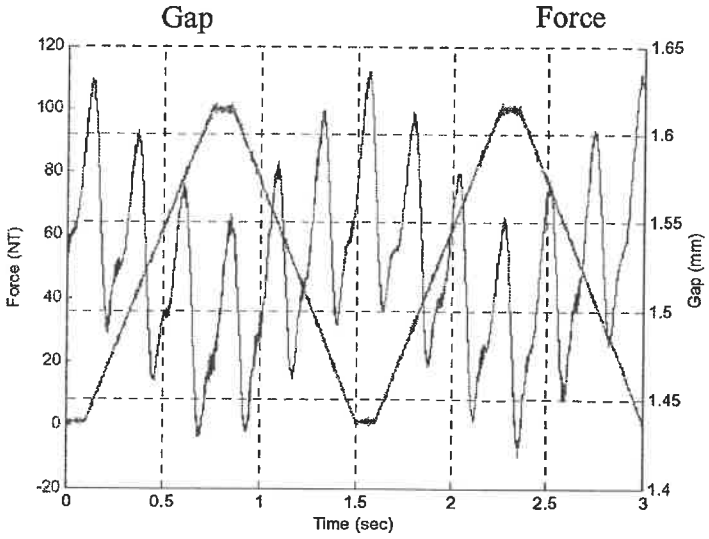

Fig.4 Force Control and Gap

After assembling the mechanism to CMP system, a pressure distribution on the wafer surface is measured by a pressure measurement sheet to investigate the moment compensation. The results show figure 5 The pressure concentration at the upper right can be decreased by C-core force controlling. Then a polishing experiment is carried out and the polishing profiles is shown in figure 6. Since the pressure concentration at the edge of wafer is decreased, the profile is changed from concave to convex. Thereby the effectivity of the developed system is confirmed.

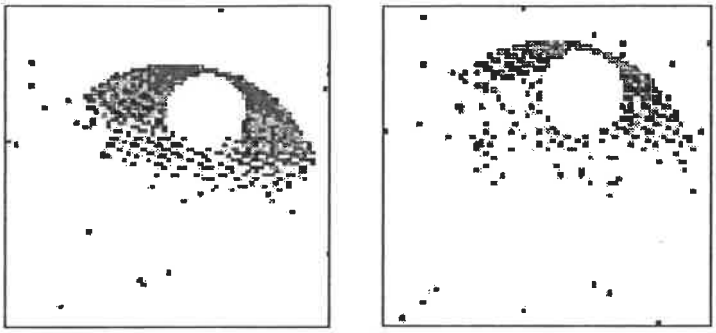

OFF ON

Fig.5 Pressure Distribution on Wafer Surface

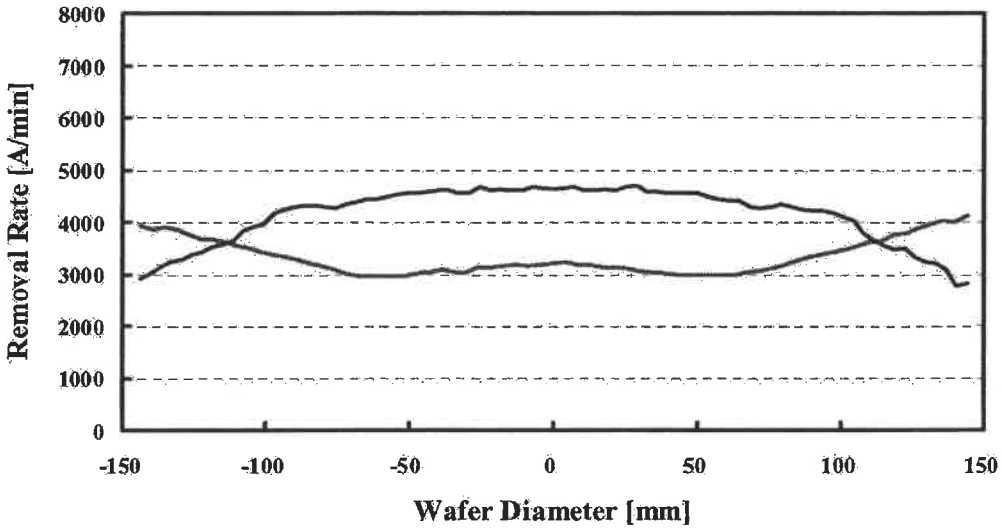

Fig.6 Polishing Profile

5. Conclusion

The force & moment control mechanism for rotating parts is developed using electromagnetic force. Then it is applied to CMP polishing head. The basic and polishing experiments are conducted and the effectivity of the developed system is confirmed. Thereby the control range of polishing profile will be able to expand

References

1. T.Doi, Details of Semiconductor CMP Technology, Kogyo Chosakai Publishing Co., Ltd. 2001
2. International Technology Roadmap for Semiconductors, 2003 Edition
3. F.W.Preston, The theory and design of plate glass polishing machines, J. Society of Glass Tech., 1972, 214-256
4. Y. Uda, T. Senga, A. Ishikawa, E. Yamamoto, T. Mitsui, S. Hoshino: Digital Polishing Method for CMP System using a Smaller Diameter Polishing Pad, ASPE on 12th, Nov.2001
5. S. Hoshino, Y. Uda, E. Yamamoto : Characteristics of Cu CMP Process on Ultra-Low Pressure, CMP-MIC, Feb.2004

Improvement of Visual Based Motion Error Compensation for Precise Versatile Micro Robot

O. Fuchiwaki, D. Misaki* and H. Aoyama

Dept. of Mechanical Engineering
& Intelligent Systems,
Univ. of Electro-Communications, Chofu,
Tokyo 182-8585
Japan
[URL http://www.aolab.mce.uec.ac.jp]

*Dept. of Mechanical Engineering
Shizuoka Inst. of Tech.
Fukuroi, Shizuoka, 437-8555
Japan

1. Introduction

In MEMS technology and precision engineering, there have been developed many reports about micromechanisms and microrobotics. Some are based on advanced technology including microbatteries, micromotors, and miniscule computational facility, the others are made by sophisticated precision machining techniques. However it is still very important to find industrial applications where such microrobots can provide effective benefits. Recently, in-situ microprocessing becomes more important for biochemical operation and real time processing inside SEM vacuum chamber[1][2]. In order to provide microscopic manipulation, we have developed the unique locomotion mechanism which is composed of four piezoelectric elements and two electromagnets. Here two legs arranged on cross each other are connected by four piezoelectric elements so that it can move in any directions, i.e. in X and Y directions as well as rotate at the specified point precisely with the manner of an inchworm as shown Fig.1. Moreover the combination of particular wave forms for piezoelectric elements can provide "arc trajectory with facing center", that is important for the micro manipulator to keep its tip end within the microscopic view area as shown Fig.2. In previous report, we attached three miniature robots under microscopes and demonstrated the precise and flexible control of miniscule pipe as shown Fig.3[3]. We have concluded that our robot is effective for microscopic operations such as microinsemination, in-situ manipulation inside the SEM vacuum chamber because we could easily install our robots under various microscopes and our robots are more reasonable and more flexible than conventional

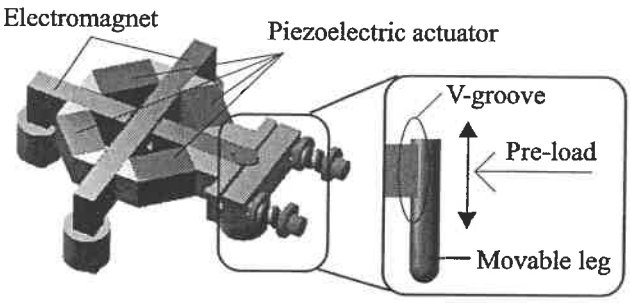

Fig.1 Structure of versatile microrobot

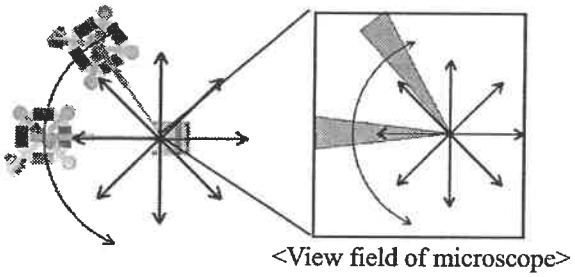

Fig.2 Motion pattern required at microscopic operation

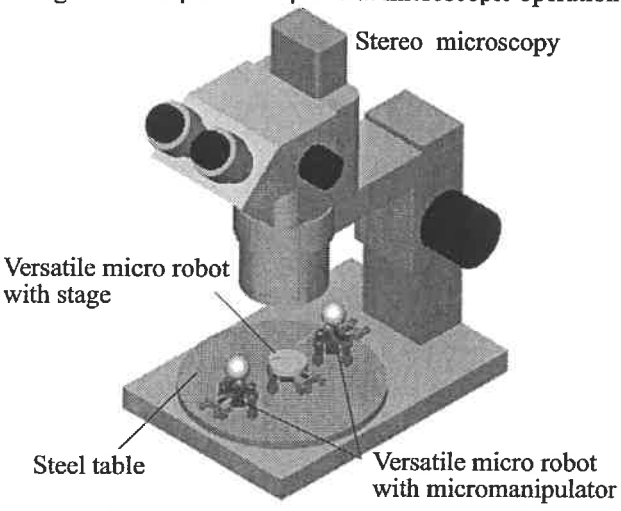

Fig.3 Flexible micromanipulation collaborated by three versatile micro robots under microscopy

instruments.

However, the versatile micro robot could not move precisely without the motion compensation because of the difference of characteristics of four piezoelectric elements and the assembling error of four piezoelectric elements and two electromagnets. In previous report, we analyzed the mechanical kinematics for locomotion and propose the competitive compensation system supported by the CCD camera based image tracking system as shown Fig.4[4]. In this paper, we analyze the mechanical kinematics of our robot more precisely to improve the competitive compensation. In experiments, we confirm that newly developed compensation system is more effective than previous one especially in forward, back, right and left directions. The design procedure, basic performance and biomedical application of this tiny robot also are discussed to open the new field for micro-robotics in precision region.

2 Sequence of Compensation

In order to explain the problem of the previous compensation, we describe the sequence of the previous compensation. We analyze the motion mechanism at a half step to investigate relationship between displacements of 4 piezo elements and motion of the free electromagnet as shown Fig.5 and FIg.6. Fig.5 shows the kinematic model of this small robot. In this figure, we consider that the displacement of each PZT element A0, A1, A2 and A3 move the specified points K1 and K2 on the free magnet to K1' and K2' . Fig.6 shows the definition of parameters at a step motion. In the experiment, the robot are measured by the CCD camera based microscope image tracking system. We calculate experimental displacements of 4 piezo elements by the geometric analysis of the orbit and the kinematic model of the robot as shown Fig.5 and Fig.7. Finally, we apply the compensation formula to compensate the robot motion as depicted in Fig.8. The robot can move more precisely with repetitive these procedures. The best calculation results are stored in PC as unique parameters. Fig.9 shows the experimental results of previous compensation. We know that four diagonal motions are well compensated, but the forward, back, right and left straight motions are not compensated very much. We have concluded that we should improve the kinematic model in order to involve the assembling error of four piezoelectric elements and two electromagnets into the procedure of compensation.

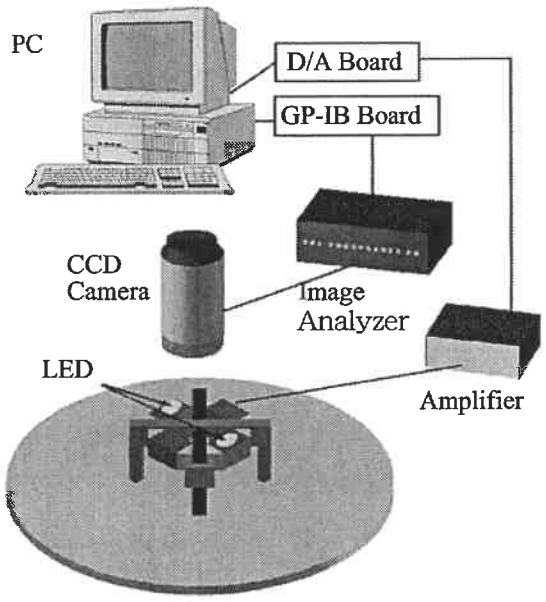

Fig.4 Experimental set up of repetitive compensation

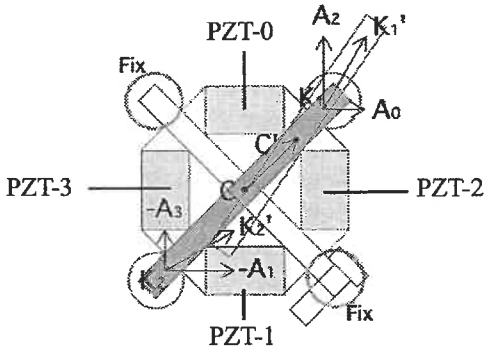

Fig.5 Previous kinematic model

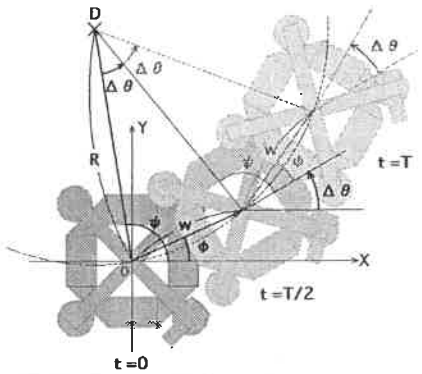

Fig.6 Definition of parameters at a step motion

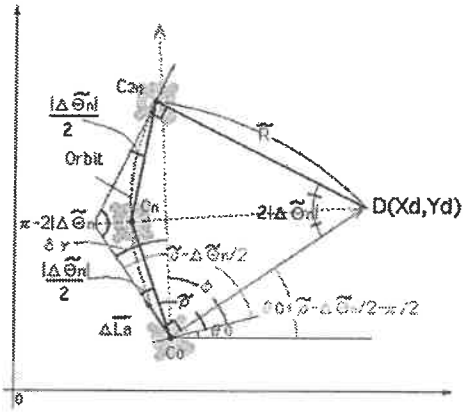

Fig.7 Geometric analysis of the orbit

$$PGain[k]' = PGain[k] \times \frac{Ak'}{Ak} \quad (k = 0,1,2,3)$$

Ak': **Ideal displacement of PZT-k**

Ak: **Experimental displacement of PZT-k**

PGain[k]': **Sinwave's amplitude of PZT-k after compensation**

PGain[k]: **Sinwave's amplitude of PZT-k at experiment**

Fig.8 Compensation equation

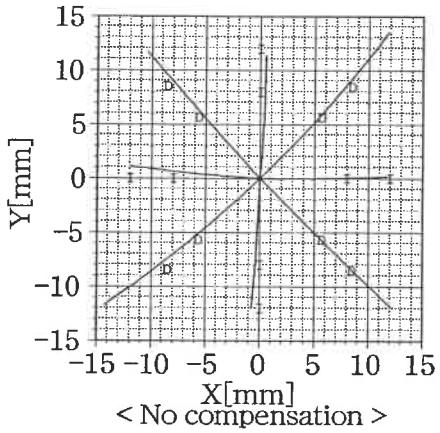

< No compensation >

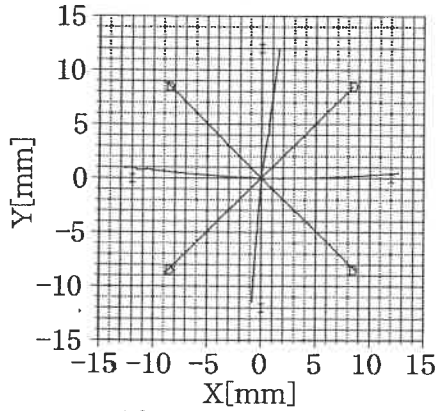

< After compensation >

Fig.9 Experimental results of previous compensation

3 Improvement of the Kinematic Model

In order to involve the assembling errors of four piezoelectric elements and two electromagnets into the kinematic model, we define the four unique angles. When the robot moves to forward, back, right and left, we use the two piezoelectric elements. If we adjust the two piezoelectric elements so that the robot

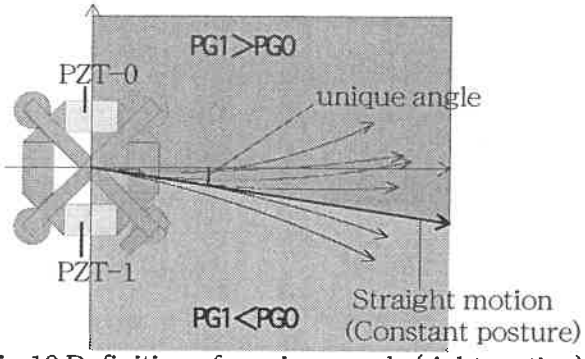

Fig.10 Definition of a unique angle (right motion)

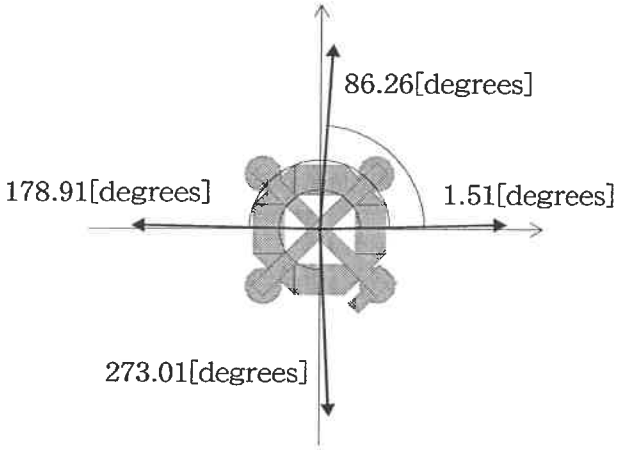

Fig.11 Experimental results of unique angles

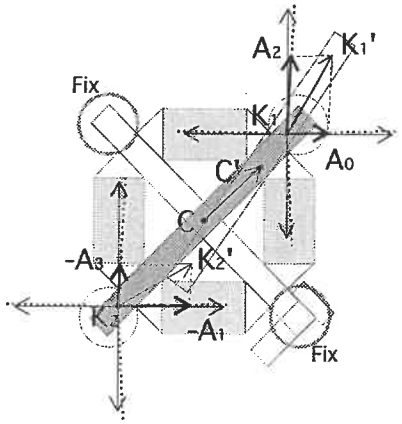

Fig.12 Kinematic model by use of unique angles

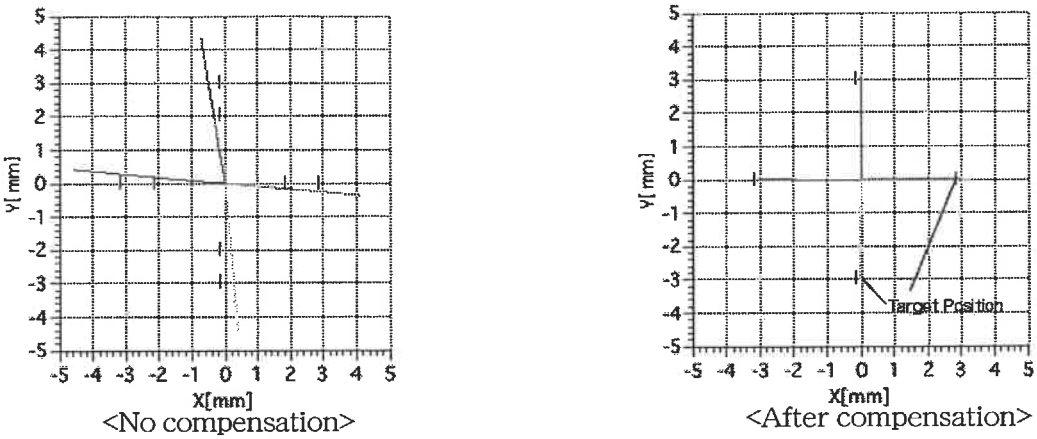

<No compensation> <After compensation>

Fig.13 Experimental results of newly developed compensation

would not change its own posture, the robot should move straight to the unique angle. Fig.10 shows the how to get the unique angle at right motion. In this figure, PG0 means displacement of PZT-0 and PG1 means that of PZT-1. We could adjust the PG0 and PG1 so that the robot would not change its own posture. Fig.11 shows the experimental results of unique angles. If there are not assembling errors, the four unique angles should become 0, 90, 180 and 270. We define the new kinematic model which is involved the four unique angles as shown Fig.12. In this figure, we consider the four piezoelectric elements push the free magnet to the corresponding unique angles.

4. Experimental Results

We recalculate the compensation equation by use of the newly developed kinematic model. And then we conducted the repetitive compensation 5 times at each motion. Then we have checked its motion accuracy by use of CCD based image analyzer. Fig.13 shows the compensational results of forward, back, right and left straight motion. The ratios of locational errors to length of path become less than 1%. We also check that the posture errors become less than 0.2 degrees in the experiments. We confirm that we could compensate the robot motion in forward, back, right and left straight motion very well if we use the newly developed kinematic model.

5. Conclusions & Future Works

Visual based motion error compensation system for precise versatile micro robot is improved by use of newly developed kinematic model. We define the unique angles to involve the assembling error into the kinematic model. We confirmed that we could compensate the robot motion in forward, back, right and left straight motion very well if we use the newly developed kinematic model. Furthermore, in order to develop the motion performance, improvement of the whole system by both side of hardware and software is required. In addition, development of the PC controlled system with the help of the visual feedback system is also required. Moreover, micro tools which can be implemented on this robot to achieve the flexible micro processing under the collaboration by this versatile micro robots have been developing.

References

(1) Y.Hatamura,M.Nakao and T.Sato: Construction of Nano Manufacturing World as a Desk-top Factory, Microsystem technologies 1, pp.155-162(1995)

(2) Y. Sun and B. J. Nelson: Biological Cell Injection Using an Autonomous Microrobotic System, Journal of Robotic Research, Vol.21, No.10-11, pp.861-868 (2002)

(3) O. Fuchiwaki, H. Aoyama :Precise manipulation control on three versatile microrobots for flexible micro handling, Proc. of18th ASPE Annual meeting, pp.287-290(2003)

(4) O. Fuchiwaki, H. Aoyama :Visual Based Motion Error Compensation for Precise Versatile Micro Robot, Proc. of 17th ASPE Annual meeting, pp.148-151(2002)

DEVELOPMENT OF INCHWORM TYPE MOBILE ROBOT MOVABLE IN PIPES WITH T-JUNCTION

Shigeo KATO*, Mitsuhiro KATO*,
Shinnosuke OGAWA* and Manabu ONO**

*Department of Systems Engineering, Nippon Institute of Technology
Miyashiro, Saitama 345-8501, JAPAN
Phone: +81-480-337725, Fax: +81-480-337745
E-mail: kato@nit.ac.jp
**Department of Mechanical Engineering, Tokyo Metropolitan College of Technology
Shinagawa, Tokyo 140-0011, JAPAN
Phone: +81-33471-6331, Fax: +81-33471-6338
E-mail: m_ono@tokyo-tmct.ac.jp

1. Introduction

We have many small diameter pipes, which are gas and water pipelines for individual or corporate houses. They must be inspected in order to protect the accident previously. Since these pipes are buried in the underground or buildings, it is very difficult to inspect the pipes from the outside. Moreover, the pipes have T-junction at the point where the main pipe and the branch pipe connect. Therefore, the inspection robot must move in the pipes and turn the T-junction of rectangular.

Authors have been researched in-pipe robots which are driven by the air pressure and can pass the Y-junction which is about 60 degrees [1], [2]. But they could not pass the T-junction of rectangular. Now, authors fabricate a robot which can pass the T-junction. The fabricated robot is structured by a moving mechanism to move in the pipe and a steering mechanism to pass the T-junction of the pipe. For the moving mechanism, we used three rubber bellows actuators which are 33 mm in outer diameter and 60 mm long. Two outer rubber bellows actuators are provided four bulging rubber sheets. These are called as friction braking mechanism. The friction brake mechanism works as a brake of the moving mechanism. The center rubber bellows actuators is called as a moving element, because the rubber bellows actuators drives the moving mechanism by its stretching and shrinking motion. For the steering mechanism, we use four rubber bellows actuators, which are arranged in the shape of a matrix, and 16 mm in outer diameter and 60 mm long. Seven electromagnetic valves, which switch the pneumatic pressure and the vacuum pressure, are connected to the seven rubber bellows actuators. The sequence of operation is programmed by a computer and carried out through the valve controller. The matrix shaped rubber bellows steering actuators are controlled by a joystick connected to the computer.

The steering actuators can steer the head of the robot for the eight directions in 45 degrees. The seven rubber bellows actuators are stretched by the pneumatic pressure of 0.05 MPa and shrunk by the vacuum pressure of -0.08 MPa. The fabricated robot was confirmed to pass the T-junction of rectangular with speed of 21 mm/s.

2. Structure of the fabricated robot

An in-pipe mobile robot which is able to move in T-junction pipes is shown in Fig. 1.

The fabricated robot is structured by a moving mechanism to move in the pipe and a steering mechanism to pass the T-junction of the pipe. For the moving mechanism, we used three rubber bellows actuators which are 33 mm in outer diameter, 22 mm in inner diameter and 60 mm long. Two outer rubber bellows actuators are provided six bulging rubber sheets. These are called as friction braking mechanism. The friction braking mechanism works as a brake of the moving mechanism. The bulging rubber sheets are 60 mm long, 20 mm wide and 2.5 mm thick. The center rubber bellows actuators is called as a moving element, because the rubber bellows actuators drives the moving mechanism by its stretching and shrinking motion. For the steering mechanism, we use four rubber bellows actuators, which are arranged in the shape of a matrix, and 16 mm in outer diameter, 10 mm in inner diameter and 60 mm long. Seven electromagnetic valves, which switch the pneumatic pressure and the vacuum pressure, are connected to the seven rubber bellows actuators.

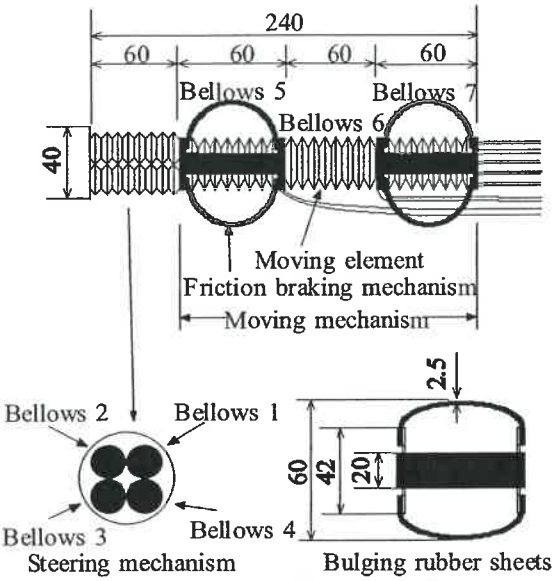

Fig. 1 Structure of in-pipe robot

3. The control system of the robot

The control system for measuring the characteristics of the mobile moving mechanism is show in Fig. 2. The sequence of operation is programmed by a computer and carried out through the valve controller. The matrix shaped rubber bellows steering actuators are controlled by a joystick connected to the computer. The other ends of air-feeding tubes are attached to the air-compressor and the vacuum pump.

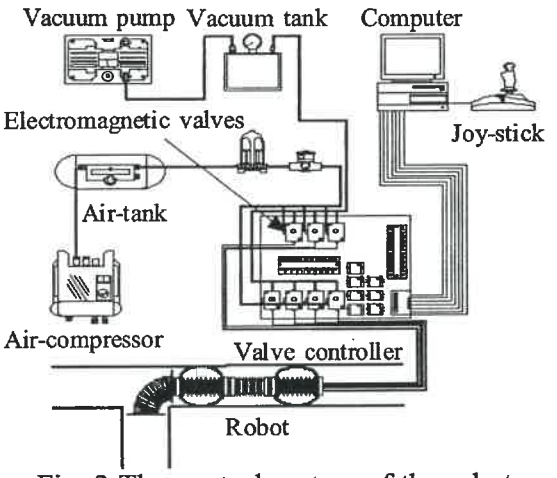

Fig. 2 The control system of the robot

4. Moving principle of the robot

The seven rubber bellows actuators are stretched by the pneumatic pressure of 0.05 MPa and shrunk by the vacuum pressure of -0.08 MPa.

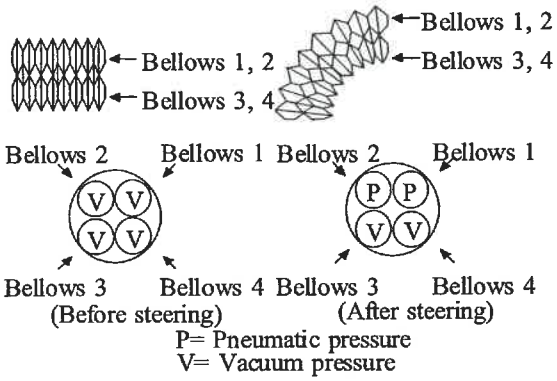

Fig. 3 Steering motion of the rubber bellows at the junction (Downward direction)

4.1 Moving of steering mechanism

First, to the four rubber bellows the vacuum pressure in given before steering motion. If

the pneumatic pressure is given to two or three bellows and the vacuum pressure is still given to another bellows, the four bellows bend their head to the vacuum bellows. The steering mechanism is able to displace its head eight directions of each 45 degrees.

For example, if the bellows 1 and bellows 2 are stretched and the bellows 3 and the bellows 4 are shrunk, the four bellows bend their heads to the side of the bellows 3 and the bellows 4. Bending motion of the four rubber bellows at T-junction is shown in Fig. 3. In this case, the robot is steered to the downward direction.

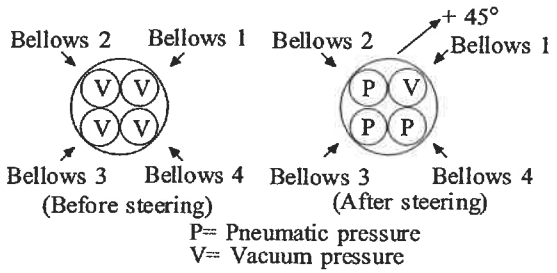

Fig. 4 Steering motion of the rubber bellows at the junction (+ 45 degree direction)

When three bellows within the three bellows are stretched and one bellows is shrunk as shown in Fig. 4, the robot is steered to the direction of 45 degree from horizontal and vertical direction.

4.2 Moving principle

The air-feeding time schedule and moving principle of the robot are shown in Fig. 5.

Step 0: At initial, all the bellows are in the shrinking by the vacuum pressure. The front and rear friction braking mechanisms are at the condition of the braking and hold the pipe.

Step 1: The pneumatic pressure is supplied to the front friction braking mechanism and the braking is free. The friction braking mechanism is pushed out in the length direction of a pipe.

Step 2: The pneumatic pressure is supplied to the central moving element and the mobile moving mechanism is stretching. Then the front part of the mobile moving mechanism can move to the forward direction, because the rear friction braking mechanism is still at the condition of the braking and holds the pipe.

Step 3: The pneumatic pressure is supplied to the rear friction braking mechanism and the braking is free. At the same time, the vacuum pressure is supplied to the front friction braking mechanism and it is at the condition of the braking. The friction braking mechanism is swelled out in the diameter direction of a pipe.

Step 4: The vacuum pressure is supplied to the central moving element and the mobile moving mechanism is shrinking. Then the rear part of the mobile moving mechanism can move to the forward direction, because the braking of the rear friction braking mechanism is free. After that, all the bellows are shrunk by the

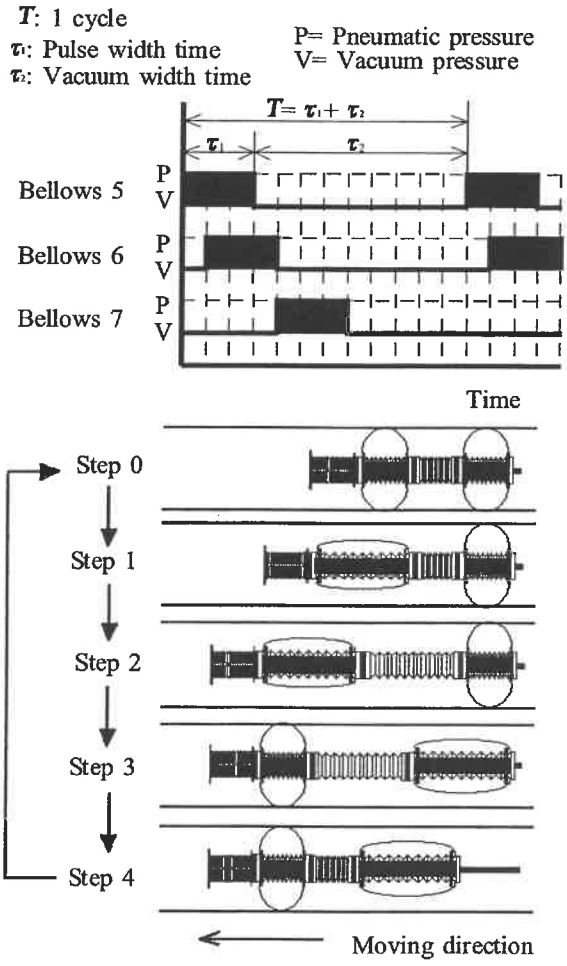

Fig. 5 Moving principle of the in-pipe robot

vacuum pressure. The braking mechanism of the front and rear holding element are in the condition of braking and hold the pipe. It is same as the initial condition and one cycle is over. The moving mechanism moves the stretching displacement of the moving element.

5. Moving experiment

5.1 Moving speed of the robot

The moving speed of each direction of a robot is shown in Fig. 6. The rubber bellows actuators are stretched by the pneumatic pressure of 0.05 MPa and shrunk by the vacuum pressure of -0.08 MPa. The cycle time is 2.4 s.

The robot could move forward and backward with the speed of 26 mm/s. The robot was confirmed to pass the T-junction of rectangular with the speed of 21 mm/s in the right-turn and the left-turn. Right-turn and left-turn is slower than straight pipe. But, it is enough speed to moving a T-junction.

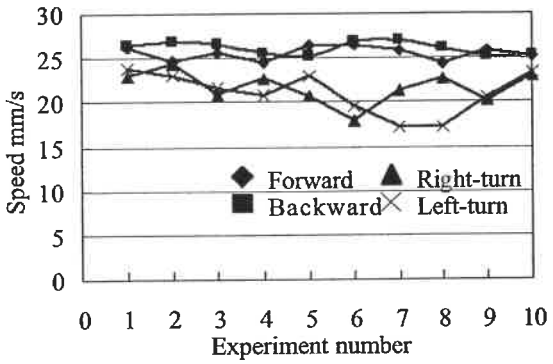

Fig. 6 Moving speed

5.2 Steering characteristics

The steering mechanism is steered to any direction from 45 till 315 degrees. The photograph of the bending four bellows to +45 degrees direction is shown in Fig. 7.

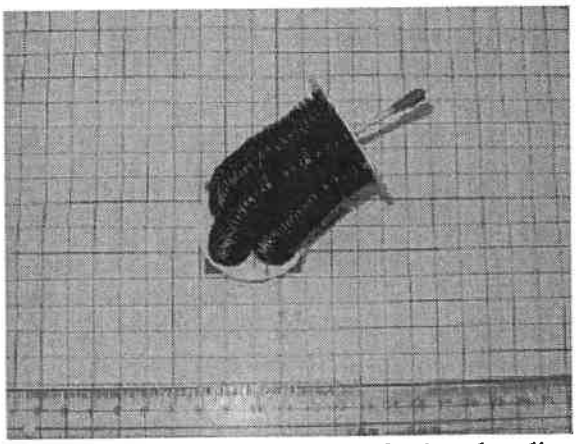
Fig. 7 The photograph of the bending steering mechanism (+45 degree direction)

6. Conclusions

(1) We fabricated a robot which is structured by a moving mechanism to move in pipes and a steering mechanism to pass the T-junction of pipes.

(2) We used four rubber bellows actuators which are arranged in the shape of a matrix for the steering mechanism.

(3) The fabricated robot was confirmed to pass the T-junction of rectangular with speed of 21 mm/s.

References

[1] S. Kato, M.Shirakawa, M. Ono and S. Fukumoto: Fabrication of In-pipe Mobile Micromachines Driven by Pneumatic and Vacuum Pressure, Proceedings of ASPE 1999 (Fourteenth) Annual Meeting , pp. 37-40.

[2] S. Kato, H. Sugiyama, T. Saito, M. Ono and N. Kato: 3D Mechanical Steering Control of an In-pipe Mobile Microrobot, Proceedings of IASTED International Conference Control and Applications, pp. 450-454.

FABRICATION OF AN INCH-WORM TYPE MOBILE MICROROBOT MOVABLE IN DIFFERENT DIAMETER PIPES

*Shigeo KATO, *Yoshiaki AIZAWA, *Tsubasa OSADA and **Manabu ONO

*Department of Systems Engineering
Nippon Institute of Technology
Miyashiro, Saitama 345-8501, Japan
E-mail: kato@nit.ac.jp
** Department of Mechanical Engineering,
Tokyo Metropolitan College of Technology,
Shinagawa, Tokyo 140-0011, Japan
E-mail:m_ono@tokyo-tmct.ac.jp

1. Introduction

We have many small diameter pipes which are cooling pipes for atomic power stations, boiler pipes for industries, gas and water pipe lines for individual or corporate houses. They must be periodically inspected in order to protect the accident previously. Some of these pipes are long and their diameters are different at the place where pipes change from the main to the branch. The inspection robot for these pipes must move different diameter .

A step comes where the pipe changes its diameter. The in-pipe robot driven by wheels is very difficult to cross the step [1]. We have used cone-shape friction rings for the driving legs of the in-pipe robot. However, the robot driven by friction rings is also difficult to move in the pipe where diameter changes more than 3 mm [2].

Now, we propose a mobile robot that can surely move in the diameter changes. We are needed to hold the different diameter pipe to the radius direction and to drive the robot to longitudinal direction using the friction force by the holding the pipe, in order to move surely in the different diameter pipe. In order to achieve this motion, we developed a new mechanism which is made of three rubber bellows in series. In the mechanism, two outer rubber bellows are provided six bulging rubber sheets. These are called as holding elements with braking mechanisms. So, the holding element works as a brake of the moving mechanism. The center rubber bellows is called as a driving element, because the rubber bellows drive the moving mechanism by its stretching and shrinking motion.

When the rubber bellows of the holding element shrinks, six bulging rubber sheets spread to the radius direction and touch the different diameter pipe. Then the spread bulging rubber sheets surely hold the different diameter pipe. When the rubber bellows of the holding element stretches, spreading to the radius direction of the six bulging rubber sheets and touching to the different diameter pipe are canceled. The rubber bellows are stretched by air pressure and shrunk by vacuum pressure. The stretching and shrinking of the rubber bellows are controlled by a computer and electromagnetic valves.

The inspection robot is required to move long distance in the pipe. However, large time is needed to send air pressure pulse to the air actuators which are laid at the end of long air-feeding tube because of the compressibility of air, if the electromagnetic valve is laid near at the air pressure generators. Robots whose electromagnetic valves are laid near at the air pressure generators could not move long distance[3], [4]. So, we arranged electromagnetic valves, which make air pressure pulse, near the air actuator in the case of the fabricated mobile robot. We confirmed that the new mobile robot can move in the long pipes.

2. Structure of fabricated robot and characteristics of elements

An in-pipe mobile robot which is able to move in pipes whose inner diameters are among 70 mm and 140 mm is shown in Fig. 1. The robot consists of two holding elements and a driving element. The holding elements are driven by bellows which are 33 mm in outer diameter, 22 mm in inner diameter, 79 mm long. The driving element is driven by bellows which is 100 mm long. They are made of nytrile butyl rubber (NBR). Each bellows is an independent vessel. Electromagnetic valves are arranged near three bellows of the holding elements and the driving element. Consequently, these electromagnetic valves move with the mobile robot. Two air-feeding tubes which supply air pressure and vacuum pressure and 4 mm in outer diameter, 2 mm in inner diameter are connected to the electromagnetic valves. The rubber bellows are stretched by the supply of the air pressure and are shrunk by the supply of the vacuum pressure. The stretching and shrinking of the bellows are controlled by electromagnetic valves and a computer.

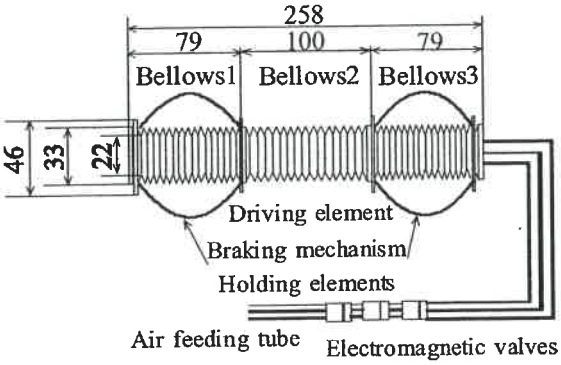

Fig. 1 Structure of the fabricated mobile robot movable in different diameter pipes

A braking mechanism of the holding element is shown in Fig. 2. The braking mechanism consists of six bulging rubber sheets which are 15 mm wide, 2.5 mm thick, 140 mm long and made of NBR. The length of the braking mechanism is 140 mm and the outer diameter of the bulging brake is 67 mm in the condition where the pressure in the bellows is +50 kPa. The length of the braking mechanism is 46 mm and the outer diameter of the bulging brake is 153 mm in the condition where the pressure in the bellows is vacuum of -80 kPa. Then the bulging rubber sheets are strongly pressed to the pipe whose diameter is less than 140 mm. The friction force in the pipe are made by the radial force of the bulging rubber sheets.

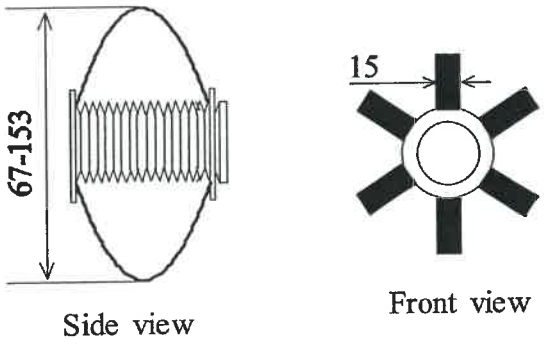

Fig. 2 Structure of the braking mechanism of the holding element

3. Mobile robot system

An experimental apparatus for measuring the characteristics of the mobile robot is shown in Fig. 3. A computer controls electromagnetic valves through a valve controller. Three air-feeding tubes are connected from the electromagnetic valves to two holding elements and the driving element of the mobile robot. These electromagnetic valves move with the mobile robot. An air-compressor is connected to the entrance port of the electromagnetic valves through long air-feading tubes to feed air pressure and to stretch the bellows. A vacuum pump is connected to the exit ports of the electromagnetic valves and feeds vacuum pressure to shrink the bellows.

4. Principle of the moving of the mobile robot

The mobile moving motion is shown as Fig. 4.

(1) At initial, all the bellows are shrinking by the vacuum pressure. The braking mechanisms of the front and rear holding element are at the condition of the braking and hold the pipe.

(2) The air pressure is fed to the front holding element and the braking is free.

(3) The air pressure is fed to the central driving element and the mobile robot is stretching. Then the front part of the mobile robot can move to the forward direction, because the rear holding element is still at the condition of the braking and holds the pipe.

(4) The air pressure is fed to the rear holding element and the braking is free. At the same time, the vacuum pressure is fed to the front holding element and it is at the condition of the braking.

(5)The vacuum pressure is fed to the central driving element and the mobile robot is shrinking. Then the rear part of the mobile robot can move to the forward direction, because the braking of the rear holding element is free.

(6) All the bellows are shrunk by the vacuum pressure. The braking mechanisms of the front and rear holding element are in the condition of braking and hold the pipe. It is same as the initial condition and one cycle is over. The mobile robot moves the stretching displacement of the driving element. Consequently, the speed is shown by (stretching displacement) / (cycle time).

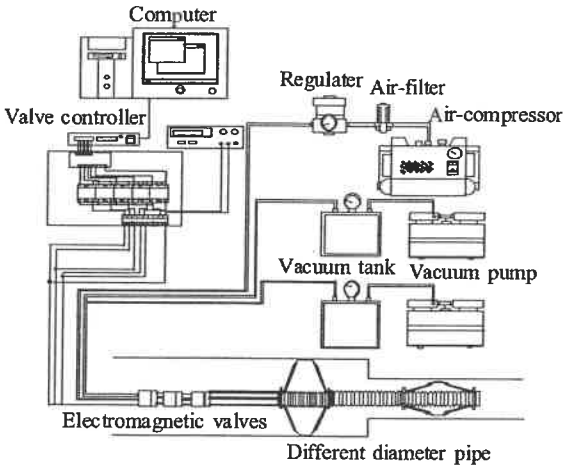

Fig. 3 Experimental apparatus of the mobile robot system

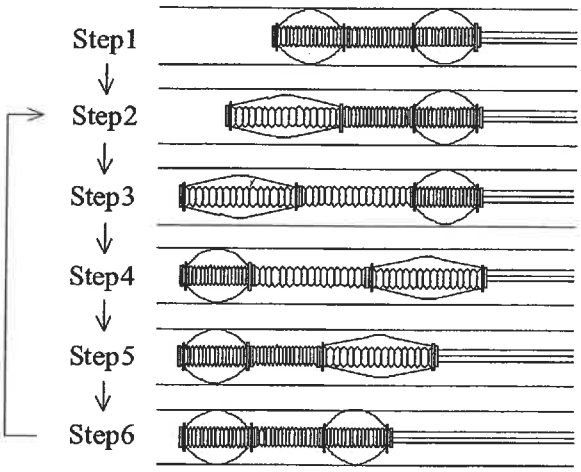

Fig. 4 Principle of the moving of the mobile robot

5. Principle of the moving different diameter pipes of the mobile robot

The principle of holds of different diameter pipe is shown in Fig. 5. In the ease of 140mm pipe, the bulging rubber sheets spread in the radius direction of a pipe. They are at the condition of the braking and hold the pipe. In the ease of 70mm pipe, the bulging rubber sheets spread in the radius direction of a pipe. After that, they spread longitudinalley. Consequently, the braking mechanisms can hold, the microrobot can move different diameter pipes.

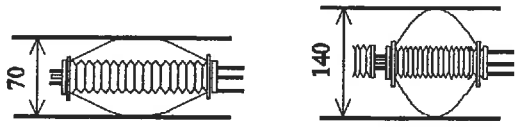

Fig. 5 Principle of the moving different diameter pipes of the mobile robot

6. Experiments

6.1 Measurement of the traction force

We measured the generated traction force of the microrobot which moves to perpendicular direction. Relationship between the tractionforce and diameter pipe is shown in Fig. 6. The maximum traction force is obtained at the diameter of the pipes which is 90mm 100mm 110mm. The mobile microrobot was confirmed that the maximum traction force is 13 [N]. The traction force is confirmed to be nearly equal to the friction force of the braking mechanism.

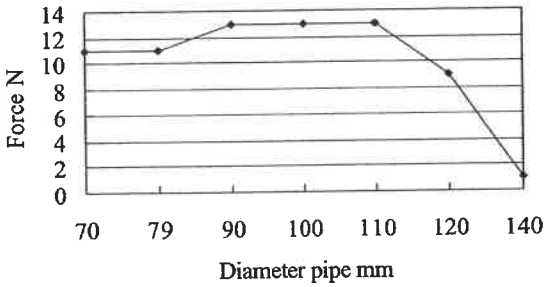

Fig. 6 Relationship between the traction force

6.2 Measurement of the speed

We measured the speed of the mobile microrobot supplying the air pressure of 0.05 [MPa] and the vacuum pressure of -0.08 [MPa]. The diameters of pipes are seven, including 70mm. Moving is done from larger diameter to smaller diameter pipe. We have steps of 5 mm in minimum and 35 mm in maximum between two pipes. However, the fabricated mobile microrobot could move the steps. The moving speed characteristics of differene diameter pipes is shown in Fig. 7. The mobile microrobot was confirmed to move different diameter pipes at the speed of 20 [mm/s]. The observed moving speed is almost the same. It shows that the microrobot can move the different diameter pipes certainly.

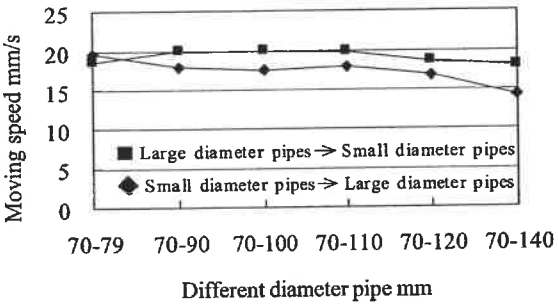

Fig. 7 The moving speed characteristics of different diameter pipes

7. Conclusions

(1) We proposed a mobile microrobot that can surely move in different diameter pipes. The microrobot consists of two holding elements and a driving element. The holding element has a braking mechanism which consists of six bulging rubber sheets.

(2) The friction force between the holding element and the pipe was measured. Friction force of 1 N is obtained at the large diameter pipe of 140 mm and 13N is obtained at the pipe of 90mm, 100mm and 110mm.

(3) The mobile microrobot was confirmed to move in different diameter pipes whose diameter are 140 mm and 70 mm. Its speed was 20 [mm/s] . And it can move in the pipe where diameter changes 35 mm.

References

[1] K. Kawaguti, O. Yoshida, K. Iwao and T. Kikuta, Journal of the Robotics Society of Japan, Vol 15, No. 3 (1997), 387.

[2] S. Kato and T. Hirayama, Proceedings of the Japan Society of Mechanical Engineers, Centennial Grand Congress, Intelligent Motion-control, Power transmission and Tribology, (1997), 661.

[3] M. Takahashi, I. Hayashi, N. Iwatsuki, K. Suzumori and N. Ohki, Journal of the Japan Society for Precision Engineering, Vol. 61, No. 1 (1995), 90.

[4] T. Noritugu and M. Kubota, Journal of the Robotics Society of Japan, Vol 18, No. 6 (2000), 831.

A HYBRID STEREO ALGORITHM WITH 3D DISPARITY SPACE FOR RECONSTRUCTION OF SURFACE MORPHOLOGY WITH DEPTH DISCONTINUITY

Gyung-Bum Kim*

*Applied Opto-Mechatronics Lab., Department of Mechanical Design Engineering

Chungju National University, Chungju, Chungbuk, 380-702, Korea

Abstract: A critical issue in area-based stereo matching lies in selecting a fixed rectangular window size. Previous stereo methods doesn't deal effectively with occluding boundary due to inevitable window-based problems, and so give inaccurate and noisy matching results in areas with steep disparity variations. In this paper, a hybrid stereo vision approach is presented to estimate rapid, accurate, detailed and smooth disparities in depth discontinuity. It makes the smoothing of depth discontinuity reduced by evaluating corresponding correlation values and intensity gradient-based similarity in the three-dimensional disparity space. In addition, it investigates maximum connected match candidate points and then devises the novel variable window to treat with general surface morphologies. We show how our results improve on those of closely related techniques for accuracy, robustness, matching density and computing speed

Keywords: Correlation values, Disparity, Intensity gradient-based similarity, Match candidate points, Projective distortion, Three-dimensional(3D) disparity space

1. Introduction

For machine stereo vision available for 3D reconstruction, the appropriate window size selection is critical to obtain smooth, detailed and accurate disparity map in area-based stereo methods. These stereo methods have used fixed windows experimentally selected, and then the contradiction of disparity maps are followed according to selecting window size.

In this paper, a hybrid stereo algorithm is tried to estimate a rapid, detailed and accurate disparity in depth discontinuity. For match candidate selection, the incorporation of both a new correlation function and intensity-gradient based similarity makes smoothing around depth discontinuity decreased. The connectivity of match candidate points in 3D disparity space is investigated to improve robustness to noise. A new variable window[1] is devised to cope with general surfaces as well. Sub-pixel disparity is accurately estimated through formulating the error function in the variable window.

The proposed hybrid stereo method has obtained a detailed, accurate and robust disparity, and also has relatively quick disparity estimation speed. Experiments show that the proposed algorithm easy to effectively implement outperforms previous ones.

2. Disparity distribution models

All stereo algorithms have been so far developed to examine how much support they receive from their local neighborhood. Prazdny[2] incorporates the function to specify the support amount between neighboring points based on disparities into stereo algorithm. Three requirements for the function are set. Kanade's model[2] is exactly the same as that of Pradzny in that the disparity difference between two pixels follows a zero-mean gaussian distribution whose variance increases with their distance apart. The only difference between Pradzny's model and Kanade's one is that the variance is proportional to the square of the distance between the pixels, instead of the distance itself.

Analyzing above disparity distribution models, physical meanings that small match areas are straight planar and parallel to baseline, are implied. However, the larger matching areas, more distorted planes or surfaces are expected. In addition, match error is seriously generated in depth discontinuity, due to projective distortion resulting from different viewpoints. Thus, Arbitrary match support areas to deal with various surface morphologies are needed. In order to incorporate these ideas into our algorithm, we have devised a novel variable window Ψ and then

proposed the disparity model shown by Eq. (1).

$$d(u,v)-d(0,0)=d_c \quad (u,v)\in\Psi \tag{1}$$

3. Hybrid stereo approach with 3D disparity space

3.1 Match candidate selections in 3D disparity space

The selection of match candidates is performed in the 3D disparity space composed of image row, column and disparity, as shown in Fig. 1. The 3D space voxels $\Gamma(u,v,d)$ have correlation values which mean the probabilities to be matched disparity d for the left image pixel.

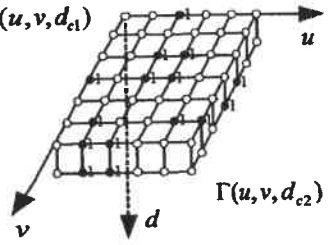

Fig. 1 Descriptions of 3D disparity space

This correlation values use the sum of absolute difference ε_{SAD} within fixed windows Ω, and are defined as Eq. (2). These correlation values have to have high match probabilities for correct matches. The lower ε_{SAD}, the correlation is high and then correlation values are close to 1.

$$\begin{aligned}
&\varepsilon_{SAD(u,v,d)}=\sum_{(u',v')\in\Omega}\left|f_L(u+u',v+v')-f_R(u+u'+d,v+v')\right| \\
&\varepsilon_{max}=\max_d \varepsilon_{SAD(u,v,d)} \\
&\varepsilon_{min}=\min_d \varepsilon_{SAD(u,v,d)} \\
&\text{where} \quad d_{min}\le d\le d_{max} \\
&\rho(u,v,d')=\frac{1}{1+\beta\dfrac{\varepsilon_{SAD(u,v,d)}-\varepsilon_{min}}{\varepsilon_{max}-\varepsilon_{min}}}
\end{aligned} \tag{2}$$

In opposite case, the values are close to 0. In order to improve the consistency of computed correlation values, the voxels of the 3D space are updated by averaging the correlation values in certain support areas.

In this paper, the 3D support to cope with sloping and more general surfaces is devised in the 3D disparity space, and the criterion function for the choice of match candidate voxels is suggested in Eq. (3) using Eq. (2) and intensity-gradient based similarity S_G.

$$\begin{aligned}
&\Gamma(u,v,d)=\frac{1}{N_v}\sum_{(u',v',d')\in\Phi}\rho(u+u',v+v',d+d') \\
&S_G=\frac{|\nabla f_L(u,v)|+|\nabla f_R(u+d,v)|}{2}-|\nabla f_L(u,v)-\nabla f_R(u+d,v)| \\
&\textit{if } \Gamma(u,v,d)>\Gamma_{th} \textit{ and } S_G>0 \\
&\quad \Gamma(u,v,d)=1 \\
&\textit{else} \\
&\quad \Gamma(u,v,d)=0
\end{aligned} \tag{3}$$

This intensity gradient-based similarity represents the measure of the intensity variation and is computed with the sobel operator. Here, for simplicity, the 3D support area Φ is defined as a cube with a fixed row, column and disparity(depth), and N_v is the voxel number of 3D support. The positive S_G means the intensity changes of corresponding point are consistent. Here, we have tried to improve the reliability of the selection of match candidates by incorporating intensity changes into the criterion function, as well.

3.2 Connectivity of match candidates

Fig. 1 shows match candidate points are described with both black color and '1' in the 3D space, and they mean voxels corresponding to a specific disparity d_{c1}, d_{c2}. In the case of projecting the arbitrary point of 3D surface morphology to stereo images, we have surveyed that a same disparity near to an interested pixel is very likely to exist through the assumption of several stereo methods. To include this physical meaning, the connectivity of a voxel is investigated with labeling techniques, and then the 3D disparity space is renewed at every disparity plane. Here, connected components C of match candidates can be found at a voxel. The connected components mean the set of a voxel with the same disparity, and also the connected number of the match candidates in each component can be computed. The integer disparity in the updated 3D space is estimated by determining the plane with maximum connected candidates in the

connected components. This can be expressed as follows.

$$\bar{d} = \arg\max_{d} \; N_c(L) \text{ of } C(\Gamma(u,v,d)) \quad \text{where } N_c\text{:Number of connected label}(L) \tag{5}$$

3.3 Sub-Pixel Disparity Estimation

In the case of projecting an arbitrary point of 3D surface morphology to stereo images, there is ambiguity of ±1/2 pixel in an image coordinate. These problems make stereo matching get more difficult. Sub-pixel disparity estimation for identifying the ambiguity is performed with only the intensity of the variable window and then the intensity changes resulting from viewpoints is assumed not to be. The possible solution to the smoothing of depth discontinuity is to use non-uniform and variable support regions, that is the variable window, since the boundary blurring is caused by support regions that span object boundary.

This variable window is defined as Eq. (4) where Ω_v is to limit the variable window range.

$$\Psi = \left\{ w \mid w \in C(\Gamma(u,v,\tilde{d})) \cap \Omega_v \right\} \quad \text{where } \Omega_v\text{:Variable window mask} \tag{4}$$

The intensities of corresponding points in the variable window are given by Eq. (5) where $\delta\tilde{d}(w_i)$ is a correction value for sub-pixel disparity.

$$f_L(w_i) = f_R\left(w_i - \tilde{d}(w_i)\right) + n(w_i),\ w_i \in \Psi \quad \text{Where } \tilde{d}(w_i) = d_0(w_i) + \delta\tilde{d}(w_i) \tag{5}$$

The intensity function f_R is linearized at $w_i - d_0(w_i)$ and then high order terms are assumed to be negligible. Thus, as shown in Eq. (6), the correction value can be determined to minimize the error function E, which is defined as the sum of squared noise in the variable window.

The proposed hybrid method with the variable window makes match error reduced rather in a general surface morphology with both depth discontinuity and smooth areas. The rapid and accurate stereo method has been verified through experiments in next section.

$$E = \sum_{w_i \in \Psi} n^2(w_i), \quad \frac{\partial E}{\partial \delta\tilde{d}} = 0$$

$$\delta\tilde{d} = -\frac{\sum_{w_i \in \Psi} f_R'(w_i - d_0(w_i))\left(f_L(w_i) - f_R(w_i - d_0(w_i))\right)}{\sum_{w_i \in \Psi} f_R'^2(w_i - d_0(w_i))} \tag{6}$$

4. Experiments

Fig. 2(a) is synthetic stereo images which are constructed with the disparity range of 0 to 24, including depth discontinuity. An actual disparity map of the stereo images is described in Fig. 2(b). The larger the disparity, the brighter the disparity map is represented. Fig. 3 shows disparity maps estimated by area-based(SSD, NCC), pixel-based[3] and the proposed method. A window Ω was applied as 7 in area-based methods, and several parameters $\Omega, M_{Th}, \beta, \Phi$ were inputed as 3, 0.7, 9, 3 in the proposed method, respectively. Large matching errors occur due to the smoothing of depth discontinuity resulting from rectangular window based problems in area-based methods. Meanwhile, no the proposed method gives more detailed discontinuity than pixel-based one, but it represents more accurate disparity than area-based techniques.

Table 1 is to evaluate estimated disparity maps for RMS(root-mean-squared) error, BMR(bad match ratio), NMR(no match ratio), computation time. Equations of these items are in Eq. (7).

SSD makes RMS error minimized according as the window size is larger, but we confirm via BMR that match errors instead get bigger, due to projective distortion. Also, computation time gets rapidly increased. The results of NCC are similar to those of SSD as well. MLMHV gives excellent results of 34% compared with the RMS error of the proposed method.

We are aware that the pixel-based method, MLMHV gives detailed and sharp disparities in depth discontinuity through RMS and BMR values. However, one of the reasons that these values are low is not to include non-matched pixels, and so MLMHV has very large NMR. It has been expected that the bigger NMR can be generated in stereo images with noise and severe intensity variations and it takes long time to reconstruct a surface morphology with the stereo images.

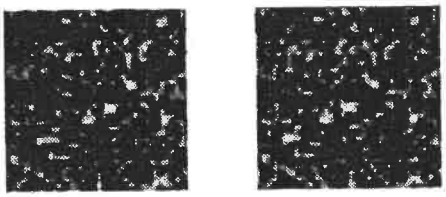

(a) Stereo images

(b) A true disparity map with depth discontinuity

Fig. 2 Synthetic stereo images

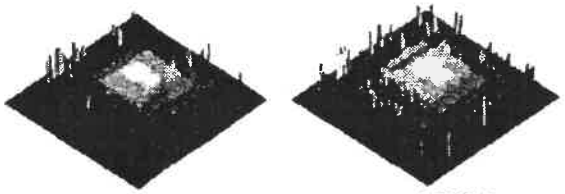

(a) SSD (b) NCC

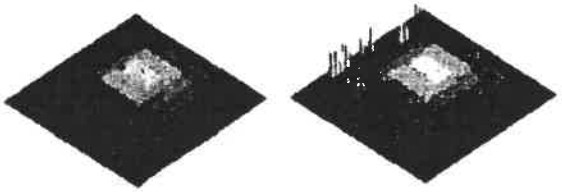

(c) MLMHV (d) Proposed

Fig. 3 Computed disparity maps

$$\mathrm{RMS}=\left(\frac{1}{N_m}\sum_{(u,v)}\left|d_T(u,v)-\tilde{d}(u,v)\right|^2\right)^{\frac{1}{2}}$$

$$\mathrm{BMR}=\frac{100}{N_m}\sum_{(u,v)}\left(\left|d_T(u,v)-\tilde{d}(u,v)\right|>\Delta_d\right)$$

$$\mathrm{NMR}=\frac{100(N_p-N_m)}{N_p}$$

where d_T : True disparity (7)

N_m : Total number of matched pixels

Δ_d : Disparity error tolerance

N_p : Total number of pixels

The proposed method reduces 12%, 13%, 72% in terms of RMS error, BMR and computation time, compared with area-based methods, respectively and 82% for NMR compared with MLMHV as well. Finally, we confirm that the proposed method makes up for the weak points of two stereo techniques.

Table 1 Evaluations of stereo methods for Fig. 3

Method (Ω)	RMS (pixel)	BMR (%)	NMR (%)	Time (sec)
SSD(3)	2.11	23.88	0.31	3.05
SSD(11)	1.87	28.11	0.36	40.25
SSD(15)	2.01	30.12	0.24	74.67
NCC(3)	2.32	24.35	0.60	3.58
NCC(11)	2.02	28.32	0.45	42.09
NCC(15)	2.11	30.31	0.14	77.65
MLMHV	1.21	16.95	6.93	1.05
Proposed	1.86	20.74	1.21	0.83

5. Conclusions

A hybrid stereo algorithm with 3D disparity space has been proposed to give a detailed, sharp and smooth disparity in a surface morphology including depth discontinuity. In 3D disparity space, a correlation value and intensity-gradient based similarity are defined, and then smoothing in depth discontinuity is reduced with them. Maximum connected match candidates in the 3D disparity space are investigated to deal effectively with general surface morphology.

The performance of the proposed method has been evaluated and verified with several items. The proposed algorithm gives more excellent data for each item and is easy to implement. In addition, it has been regarded the hybrid stereo algorithm could be widely applied to machine vision system required three-dimensional information

Acknowledgement

The work was supported by research funding 2003 provided by Chungju National University and Korea Science and Engineering Foundation Grant.(R05-2004-000-10512-0)

References

[1] Kim, G. B. and Chung, S. C, 2004, An Accurate and Robust Stereo Matching Algorithm with Variable Windows for 3D Measurements, *Mechatronics*, 14, 715-735.

[2] Kanade, T. and Okutomi, M., 1994, A Stereo Matching Algorithm with an Adaptive Window:Theory and Experiment, *IEEE Trans. Pattern Anal. Machine Intell.*16(9), 920-932.

[3] Cox, I. J., Hingornni, S. L. and Rao, S. B., 1996, Maximum Likelihood Stereo Algorithm, *Computer Vision and Image Understanding* 63(3), 542-567.

Electromagnetically Driven UltraFast Tool Servo*

Xiaodong Lu, David L. Trumper
Massachusetts Institute of Technology

Abstract

This paper presents an ultra-fast motor design for actuating tool servos. In comparison with conventional fast motors, higher acceleration and better-structural design can be achieved. Based on the ultra fast motor, a linear ultra-fast tool servo is designed for diamond turning. The material selection, real time computer, and power amplifier design for the ultra-fast tool servo control are also described.

Introduction

Fast Tool Servo (FTS) technology plays important roles in precisely manufacturing complicated free-form surfaces for the modern optics industry. The increasing complexity of surfaces requires more components in shorter spatial wavelength, and thus drives simultaneously the need for high bandwidth, high acceleration and high accuracy of the FTS. The conventional drive solution for an FTS is high-voltage driven piezoelectric stacks [1], which suffer from structural resonance modes and large hysteresis energy loss and are thus challenging to operate at high frequencies. As an alternative solution, variable reluctance actuators can be used with fast tool servo [2]. In earlier paper, we demonstrated an electromagnetically actuated fast tool servo with 163G acceleration and 10kHz bandwidth [3]. This paper presents a new design of electromagnetically driven ultra-fast tool servo, which has been significantly improved over the first prototype. The power amplifier design and the real time control issues are also addressed.

Ultrafast Motor

Electromagnetic motors have significantly higher force density in the air-gap normal direction than in the shear direction. However, a motor working on normal stress has of necessity a relatively short motion range. For fast tool servo application, such a short stroke is generally acceptable.

A typical normal force solenoid-type actuator is shown in Fig 1. This actuator has a very strong nonlinear characteristic: the actuating force is proportional to the exciting current squared and inversely proportional to the air gap squared. In order to control such a strongly nonlinear actuator, a biasing current is usually applied. However, the actuator is then linear to exciting current only at the neutral position (equal air gap on both sides of the armature) with a constant biasing current. When biasing force is applied with dynamic feedback linearization, the actuator can be linearized globally and dynamically [4]. However, this linearity suffers at high frequencies where significant modeling errors exist.

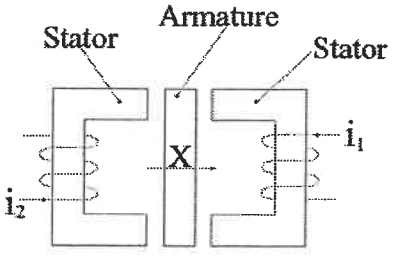

Fig 1. Solenoid-type fast motor

Flux bias can be utilized to achieve better linearity and power efficiency. Fig 2 shows a hybrid motor design using permanent magnets to generate biasing flux. As opposed to the solenoid-type actuator, the actuating

* This research is supported by National Science Foundation under grant DMI-0322590.

force is linear with both air gap and exciting current, because the permanent magnets permeability is near that of air, and thus the DC bias flux doesn't change significantly with armature position.

All of these motors above have a common problem: the middle part of the armature is part of the flux path but has no contribution to the force generation. This leads to excess inertia, thus limiting the achievable acceleration. Moreover, the middle part cannot be reduced in size because the bias flux will saturate the armature or stator if the middle part of the armatures in Fig 1 and Fig 2 are too narrow.

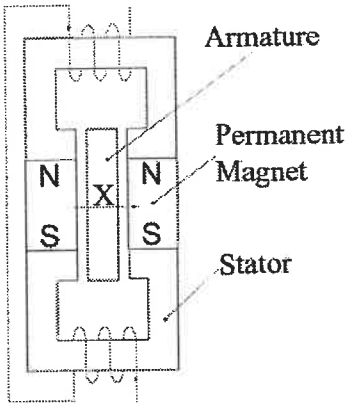

Fig 2. A hybrid fast motor

In order to fully realize the potential of a normal-stress motor, we have developed the ***ultra-fast motor*** as shown in Fig 3. This motor is linear in principle, *e.g.* the actuating force is a linear function of both exciting current and armature displacement. Further, the moving part is a combination of armature and motion backbone with high specific stiffness. All of the armature normal area in this motor generates normal force, since the flux bias is brought in through the radial faces of the armature. Moreover, the excitation coils are fully enclosed by the armature pole faces. Thereby, more coil area can be accommodated, and the leakage flux is significantly reduced. Consequently, more actuating force can be generated without overheating the coils or saturating the flux path in the solenoids.

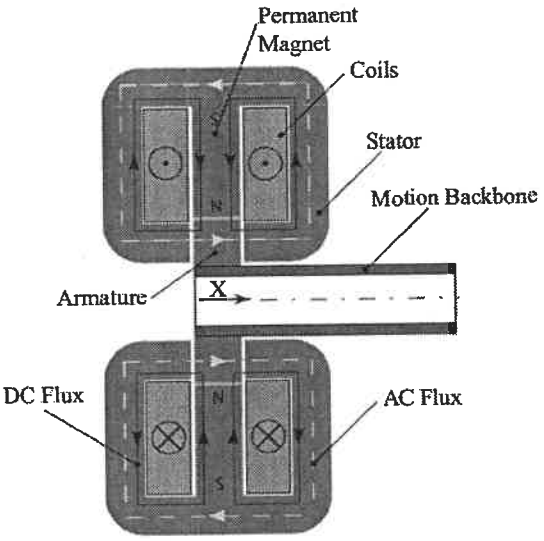

Fig 3. Ultra-fast motor working principle

Since the ultra fast motor does not require the middle part of the armature in the flux path, the motor can easily be paralleled with multiple armatures. For example, Fig 4 shows a prototype rotary ultra fast motor with multiple armatures demonstrating such parallelism.

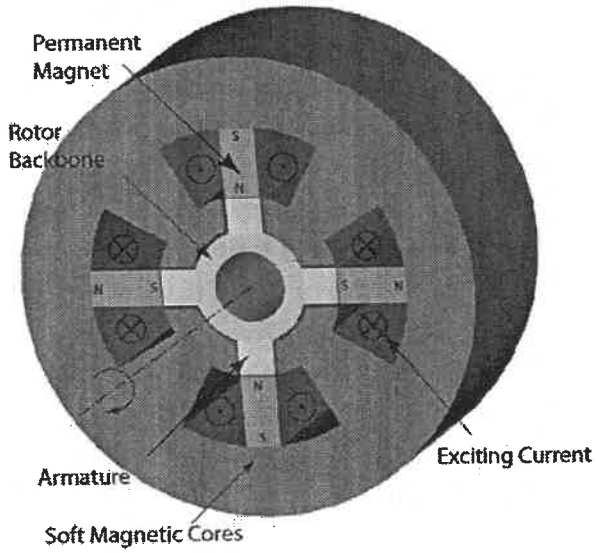

Fig 4. Rotary ultra-fast motor concept.

UltraFast Tool Servo

The design details of our ultrafast tool servo are shown in Fig 5. The moving part is composed of the armature, the moving backbone, and the diamond tool holder. The moving backbone is made from ceramic with high specific stiffness. The moving part is supported by a front spring steel flexural bearing and a

rear rubber sheet bearing of the type proposed by Rivin [5]. A capacitance probe directly senses the tool holder motion from behind. Therefore, the tool can be controlled accurately and independently of structural length variations induced by thermal expansion or cutting/inertial forces.

The actuating force F is a linear function of exciting current I and the armature position X, which greatly simplifies the associated control laws. By normalizing these variables with F_0, I_0, and X_0, the force relation can be formulated as:

$$f = \eta\lambda,\ \lambda = i + \eta x$$

where f, η, λ, i, and x are normalized force, permanent magnet biasing strength, flux, and excitation current as defined below:

$$f = F/F_0,\ i = I/I_0,\ \eta = B_{pm}/B_0,$$
$$x = X/X_0, F_0 = A_e B_{sat}^{\ 2}/2\mu_0,$$
$$B_0 = B_{sat}/2, B_{pm} = B_r A_{pm}/2A_e,$$
$$I_0 = 2X_0 B_0/\mu_0 N.$$

Here X_0 is the air gap at neutral position, B_{sat} is the saturation flux of the armature, B_r is the remanence flux of the permanent magnet, A_e is the effective armature pole face area, A_{pm} is the pole face area of permanent magnet, and N is the turn number of excitation coil winding. From this result, it is clear that the actuating force f is more directly related to flux λ than to exciting current i. By using a flux feedback method as shown later, we can thus achieve better linearity than using current control alone.

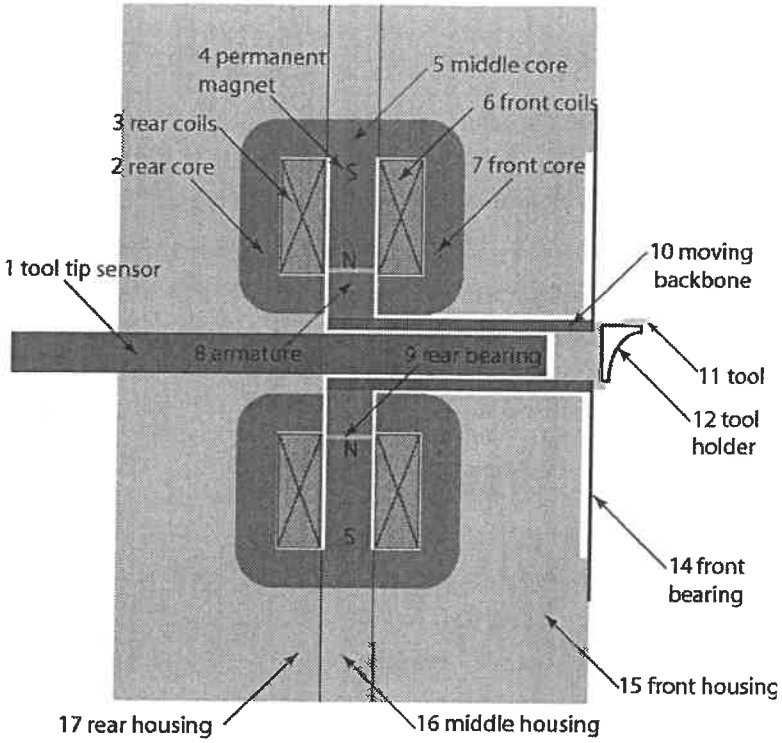

Fig 5 Linear ultra fast tool servo design details.

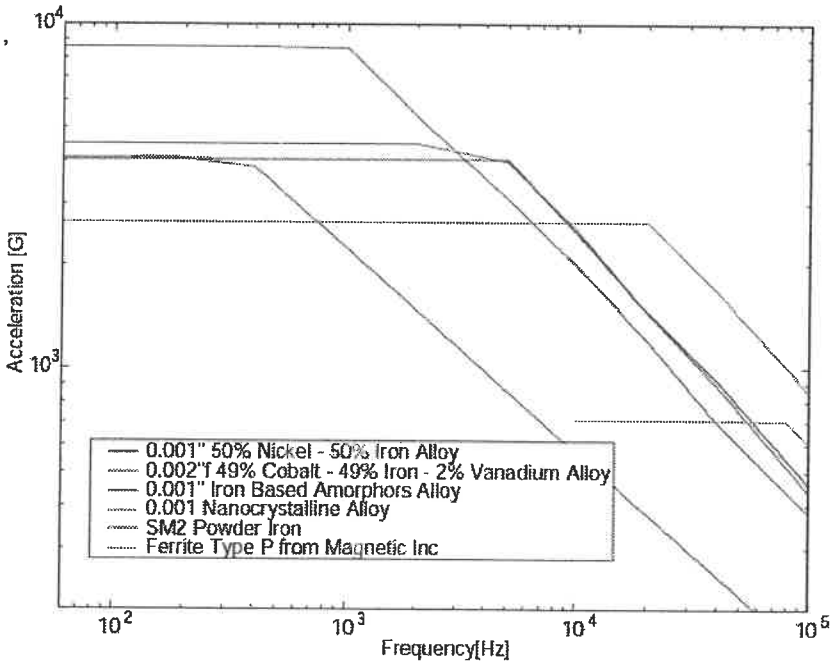
Acceleration [G]
Frequency[Hz]
0.001" 50% Nickel - 50% Iron Alloy
0.002"f 49% Cobalt - 49% Iron - 2% Vanadium Alloy
0.001" Iron Based Amorphors Alloy
0.001 Nanocrystalline Alloy
SM2 Powder Iron
Ferrite Type P from Magnetic Inc

Fig 6. Typical soft magnetic materials acceleration performance. The energy loss is limited by $0.25 W/cm^3$.

Magnetic Materials

A key issue for the ultra fast tool servo design is soft magnetic material selection. Promising candidates include silicon-iron, nickel-iron, metallic glass, and powder iron. In order to reduce the eddy current loss, the soft magnetic material is either laminated or in powder format. The laminated material shows much lower core loss, especially the nanocrystalline material developed by Hitachi Metal. But the powder iron has structural advantages and can easily be accommodated in a 3-D flux path. Fig 6 shows the calculated maximum acceleration over frequency for different materials for 3mm armature thickness. At low frequencies the acceleration is limited by the material saturation flux, while at high frequencies acceleration is limited by eddy current and hysterisis induced heat.

Real Time Computer

In order to control this ultra-high bandwidth FTS, we have designed a real time computer with a total computation power of 5.4GFLOPS by using 3 DSPs running in parallel at 300MHz. A 1MHz control loop speed has been achieved with 1.8us total delay. The total harmonic distortion of the A/D and D/A is less than –88dB up to 50kHz. This real-time computer will support FTS tool servo research up to 50kHz bandwidth.

Power Amplifier

We have designed a 1kW linear amplifier to drive the FTS using four APEX PA52A amplifiers in parallel to drive the excitation coils. Using fluxing sensing coils [6], a flux sensing circuit is integrated into the current feedback path as shown in Fig 7 to feed back the generated flux at high frequencies. Thereby, this amplifier works in current mode at low frequencies, and works in flux mode at high frequencies where the current feedback signal rolls down and the flux feedback signal rolls up. Consequently better linearity can thereby be achieved at high frequencies. Additionally, armature position x is fed back to compensate the negative spring effect of the ultra fast motor with an analog feedback loop, which has higher bandwidth than a digital implementation.

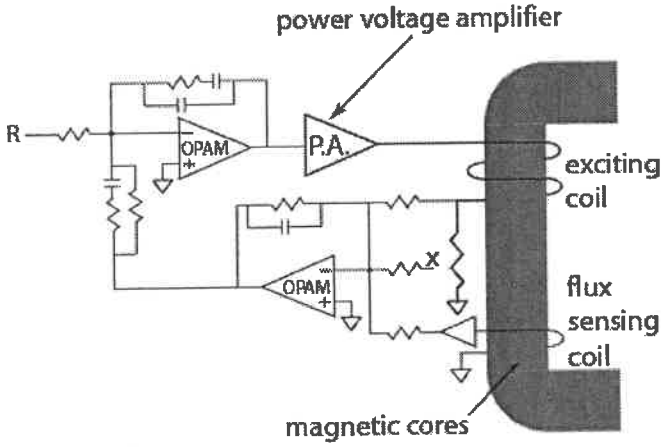

Fig 7. Power amplifier control circuit with flux feedback..

References

[1] S. Patterson, E. Magrab, "The design and testing of a fast tool servo for diamond turning," *Precesion Eng.*, Vol 7, No. 3, 1985

[2] H. Gutierrez, P. Ro, "Parametric Modeling and control of a long-range actuator using magnetic servo-levitation", *IEEE Tran. on Magnetics*, Vol 34, No. 5, 1998.

[3] X. Lu and D. Trumper, "Electromagnetically Driven Fast Tool Servo", *Pro. of ASPE 2003 Annual Meeting.*

[4] X. Lu and D. Trumper, "High Bandwidth Fast Tool Servo Control", *Proc. of 2004 American Control Conference.*

[5] E. Rivin, "Properties and prospective applications of ultra thin layered rubber-metal laminates for limited travel bearings", *Tribology Int.*, Vol 18, No. 1, 1983.

[6] T. Lipo, "Flux sensing and control of static ac drives by the use of flux coils", *IEEE Tran. on Magnetics*, Vol 13, No.5, 1977.

3D Micro Image Recognition for in Bio-Cell Operation by Micro Robots

Daigo Misaki, Naoto Chiba, Takashi Usuda, Ohmi Fuchiwaki and Hisayuki Aoyama
University of Electro-Communications,Department of Mechanical Engineering and Intelligent Systems,
Chofugaoka 1-5-1,Chofu, Tokyo 182-8585,Japan
[misaki@sys.aolab.mce.uec.ac.jp]

1. Introduction

With the demand for microscopic operation such micro parts handling and bio cell manipulation, it become much important to control the micro robots system with fine tool on the desktop. For these years, many tiny robots have been developed and they provided several unique accurate applications such fine surface machining, micro parts conveying and surface roughness measurement in our group [1]. In order to provide such microscopic operations automatically under the microscope by multiple micro robots, we have investigated the navigation strategy and the positioning method based on microscopic image recognition in 2-dimensional space [2]. However, in order to achieve more advanced microscopic biological operations in the bio cell, the more advanced image recognition and the fine tool guidance in 3 dimensions were required. For example, when conveying a micro injection tool and carrying out such a nuclear transplantation under a microscope with preventing from the breakage of bio cell, we must check the position for insertion and maneuver the small robots to approach from the specified direction.

In this report, a unique non contact rotating mechanism in-situ is proposed at first. When the thin pipette on the small robot is vibrated near the bio cell, the micro flow can be generated around it and then the cell can be rotated without any mechanical contact. And then several cell images at every rotating angle can be monitored by a microscope with CCD device and a 3D image can be reconstructed after the image processing computation to provide the precise location of the bio cell elements. After the identification of each element in the bio cell, the small robots can be controlled to execute the fine operation. We aim development of the micro robots system can provide the automatic bio cell operation combined with the 3D image recognition property.

2. System Configuration

Fig.1 shows the flexible micromanipulation by using versatile micro robots under microscope which is ongoing development in our laboratory. These micro robots can be controlled using a PC in real-time analyzing of microscopic images. All micro robots are set on a steel table. In this basic setup, this system can execute flexible microscopic tasks with easy operation. All positioning facilities are given by micro robots' movement so all mechanical functions are simply divided. This unique arrangement allows the system good flexibility and high mechanical stability although sophisticated control is required. This may be a good application for micro robots practically. We can easily attach micro robots to micro processing instruments. This flexibility meets the requirements of users, and the use of small robots avoids reparation of microscopes and easily implements processing with low cost.

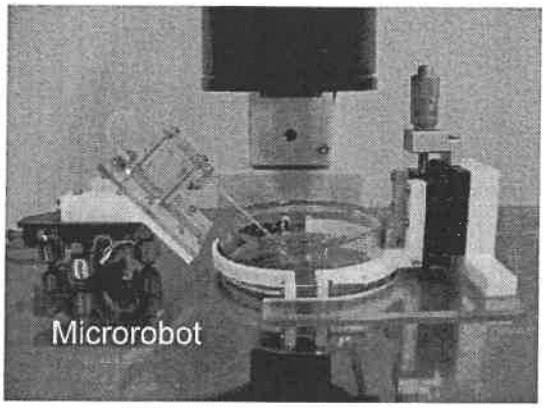

Fig.1 The flexible micromanipulation system by using versatile micro robots under microscope.

3. Versatile micro robot

In microscopic operations, an operator needs to operate a tool intricately. Fig.2 shows motion patterns required during microscopic operation. Because there is no surplus space in such a narrow area, such movement was difficult for the old micro robot [3]. To realize these motion patterns at the same time, a structure was need that could move in XY directions and in rotation in θ independently, namely holonomic behavior. Fig.3 shows the structure of the versatile micro robot which is proposed to satisfy the requirements above. Two u-shaped electromagnets which are arranged to cross each other are connected by four piezo elements so that the micro robot can move in any direction like an inchworm. Also we designed the special joint at one of the 4 legs to ensure

all legs smooth simultaneous contact on the surface. This layout of actuators can allow it to move precisely in a holonomic locomotion manner.

As shown in Fig.4, the robot is 35mm in length, 35mm in width and 15mm in height. We use the stacked type PZT elements of 5mm x 5mm x 10mm. Each piezo element is connected to each electromagnet with a plastic insulator. In experiments, we confirmed that the micro robot can move in XY directions. We also design the spherical 3D micro manipulator as a microscopic manipulator [4] as shown in Fig.5. The manipulator is composed of three piezo elements with a small accurate sphere and a large accurate sphere on the top of them and can be set on this micro robot.

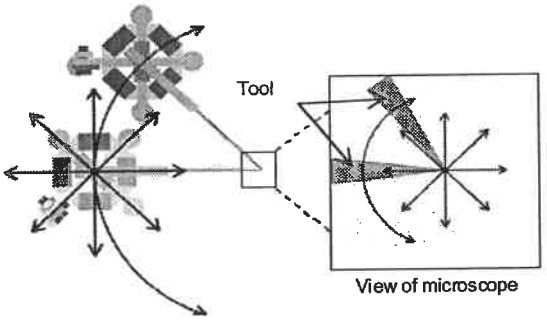

Fig.2 Motion pattern required during microscopic operation.

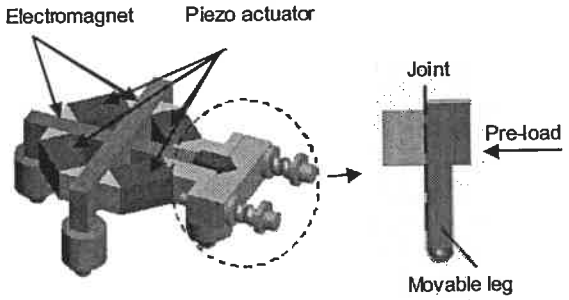

Fig.3 Structure of versatile micro robot

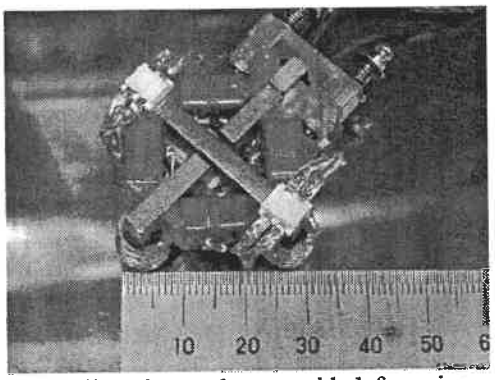

Fig.4 Versatile micro robot provided for microscopic operation.

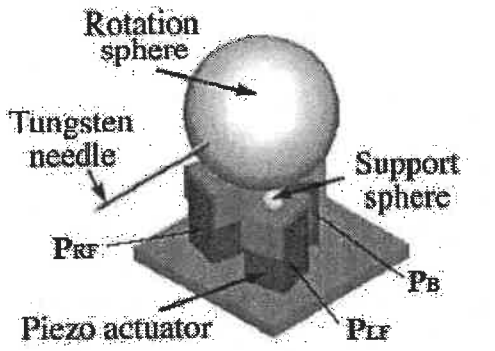

Fig.5 Structure of spherical 3D micro manipulator

4. Non contact rotation positioning of the egg cell by pipette vibration

To perform more precise cell operation, the operation of direction of Z as well as the operation of XY is needed. Three-dimensional micro operations are difficult to operate by using a 2D image from the CCD camera. In order to construct the 3D information, it is necessary to observe the object from any direction by rotating a CCD camera centering on an object, or rotating the object itself. In the microscopic operation under microscope, because it is difficult to move a camera by spatial constraint, constructing 3D information for precise micro manipulation is carried out by fixing a camera and rotating an object. Rotating an object mechanisms have been studied from the former. Those systems using an electromagnetic field may damage bio-samples which are sensitive to environmental change and are not suitable in order to handle a bio cell [5].

In this paper we proposed and used the non contact rotation positioning of an egg cell by pipette vibration, which makes a rotational flow near the pipette. In our system, this rotational flow is generated by using the versatile micro robots. First, as shown in Fig. 6, a robot's electromagnet 1 is always adsorbed and electromagnet 2 is always not adsorbed. And the position Fig. 6 (a) and (b) is repeated by expanding and contracting the piezo-electric element between both electromagnets. By this motion, the pipette on a micro robot can be vibrated with the amplitude of tens of microns. This proposed mechanism can be carried out non contact rotation operation, without using some additional actuators for a micro robot. This is a very important factor, in order to construct a simple and low cost microscopic operation system.

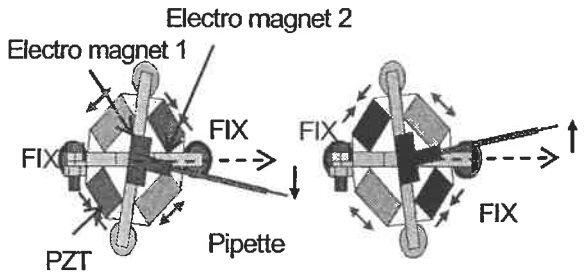

Fig.6 The flow generating mechanism by using a versatile micro robot.

In this experiment, the rotational follow in water of schale was generated using the holding pipette of the bore 15 [μ m] and an outside diameter 100 [μ m] at a tip of micro pipette. The pipette tip was bent to 45 [°], and it placed in parallel to the schale bottom, and observed from the schale bottom. To tracing partial flows, water mixed with black sumi was used. The flow pattern when vibrating a piezo-electric element by the sine wave of pitch 200 [Hz] and the seal-of-approval voltage±45 [V] is shown in Fig. 7 (a) and (b).

These experimental results show that pipette vibration can generate constant flows, which shows a fixed flow pattern near the pipette. When changing the pitch and seal-of-approval voltage of a piezo-electric element, the flow velocity changed, but this flow pattern was about fixed. Therefore, the proposed mechanism may be effective in order to control rotation of a miniature ball such as an egg cell for bio cell operations.

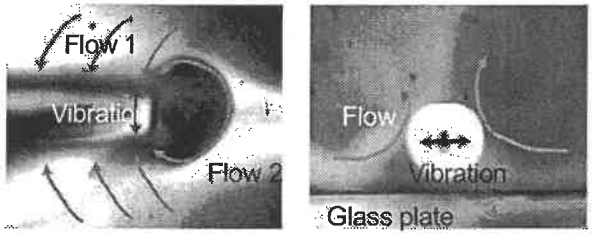

Fig.7 Flow pattern near a micro pipette. [Scale:×200]

As a basic experiment, the rotation positioning of the minute ball placed around a pipette was tried using our proposed mechanism. The glass minute ball of a diameter 130 [μ m] (UB-67L Union Co. Ltd) was used for this experiment. When vibrating a piezo-electric element by the sine wave of pitch 200 [Hz] and the seal-of-approval voltage±45 [V], a minute ball rotates counterclockwise in the same position at the pipette tip as shown in Fig. 8 (a). This motion occurs based on the straight flow and circle flow shown in Fig.7 (a). Rotational movement is shown in Fig.8 (b) is also occurs based on the flow pattern in Fig.7 (b). The direction of rotation of the minute ball in the experimental result of Fig. 8 is the same as the direction of a flow observed in Fig. 7. Therefore, it is guessed that rotation movement is caused by this rotational flow. From these experimental results show that the proposed mechanism can be used non-contact rotation positioning in three dimensions. In the conditions of dealing with a minute object, viscous power acts on a minute object greatly rather than force of inertia. Therefore, it is possible to stop rotation of a minute ball immediately by suspending vibration of a pipette. The degree of rotation angle of a minute ball can be determined with the resolution of several degrees by controlling the oscillating time of a pipette. This is very effective function in order to carry out precise microscopic operations.

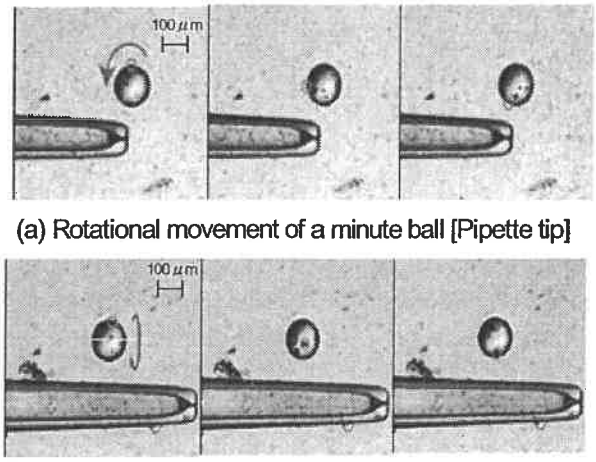

Fig.8 Non contact rotation positioning of the minute ball using vibration by pipette vibration [Scale:×160]

When the egg cell of the mouse of a diameter 120 [μ m] was used as an object of microscopic operations, the non contact rotation positioning of the egg cell by pipette vibration of a micro robot was also available in a similar manner. A general sequence of microscopic operations (rotation positioning of an egg cell in a pipette tip, movement of a pipette and aspiration fixation) required for an operation can be carried out by using only this mechanism without some special additional actuators.

5. 3D Micro Image Recognition for in Bio-Cell Operation

Using the non-contact rotation positioning mechanism, the object of microscopic operation is recognized in three dimensions. A minute glass ball is used as an object of a basic experiment for bio cell operations.

This ball is a diameter 130 [μ m] (UB-67L Union Co. Ltd). The diameter of this ball is equivalent to the egg of a mouse.

To a preparation of 3D micro image recognition, the 3D sphere model corresponding to the size of this ball is generated on a computer based on the information on the scale factor of a microscope, and the diameter of the circle on a screen. The sphere on a computer and an actual sphere are rotated 360 degrees by the resolution of a unit 10 degrees towards being shown in Fig. 8 (b). The circle shape on the surface model of a sphere of the boundary for recognition of front area is extracted.

Pre-processing of recognition of the object of circle shape assigns a label number to a continuous pixel area, after binary-izing the bit map image of a CCD camera. The circular value (Value shows circle-likeness) is calculated to each labeling area. A circular domain is extracted using this value and threshold value. The circular value e is calculated by the following equation using the neighboring length l and the area S of a area.

$$e = \frac{4\pi S}{l^2} \qquad (0 < e < 1)$$

When a local area is a perfect circle, e is set to 1.0. This value becomes small, so that area is no like a circle. When a circle is extracted, the position and size are measured and the result plotted on the surface-of-a-sphere model is shown in Fig. 9.

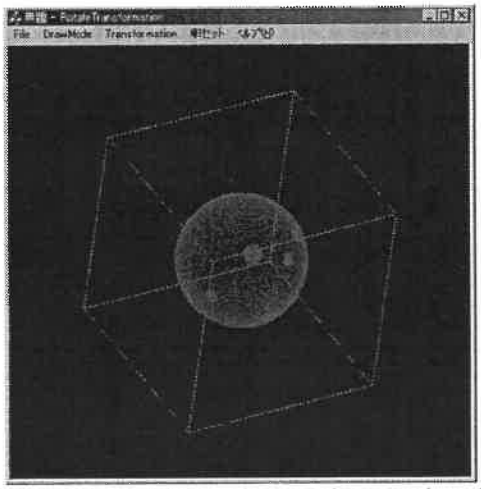

Fig.9 The 3D model for microscopic operations based on the non contact rotation positioning mechanism

To generate this 3D surface model in the computer previously is useful to execute more precise operation and this model can be used creating control signal of micro robots.

6. Conclusions and Future Works

Flexible micro-processing organized by versatile micro robots under microscopes was proposed and developed 3D model for microscopic operations based on the non contact rotation positioning mechanism.

In future work, our spherical micro manipulator which can control the bio operation tool in Z direction as well as angles precisely and this 3-D image recognition approach will be combined, and then we're going to develop a more precise bio operation system.

Acknowledgement

This research was partially supported by the Ministry of Education, Science, Sports and Culture, Grant-in-Aid for Young Scientists (B), 16760194, 2004 and Research Foundation for the Electrotechnology of Chubu, E-16148 ,2004 . We would also like to thank Prof. Tadashi Masuda and Dr. Yuji Teshima Institute of Science and Technology for their comment to this paper.

References

[1] Hisayuki Aoyama and Akira Hayashi: Multiple Micro Robots for Desktop Precise Production, Proc. of 1st Conf. of EUSPEN,(1999) pp.60-63

[2] Daigo Misaki Ohmi Fuchiwaki and Hisayuki Aoyama: Microscopic Image Analyzing for Navigation and Positioning of Micro Robots with fine tool, Proc. of 9th Conf. ofRobotics Symposia, (2004) ,pp.431-436, (In Japanese)

[3] H. Aoyama, F. Iwata, and A. Sasaki: Desktop flexible manufacturing system by movable micro robots, Proc. Of Int. Conf .on Robotics and Automation, (1995) pp.660-665

[4] O. Fuchiwaki, H. Aoyama : Precise manipulation control on three versatile microrobots for flexible micro handling, Proc. of 18th ASPE Annual meeting, pp.287-290

[5] F. Arai, A. Ichikawa, M. Ogawa, T. Fukuda, K. Horio and K. Itoigawa, "High Speed Separation System of Single Microbe by Laser Trap and Dielectrophoresis, " Trans. of JSME, Vol. 67, No. 653, C, JSME, pp. 146-153, 2001 (in Japanese).

Desk-Top Ultra-High-Speed Milling Machine with 300krpm spindle and linear motor stages

Yuichi Okazaki
The National Institute of Advanced Industrial Science and Technology
1-2-1 Namiki, Tsukuba, 305-8564, Japan
okazaki-u1@aist.go.jp

1 Background

Downsizing of machine tools can improve space utilization factor, and reduce the price and energy consumption including air conditioning and facility investment. The agility in reconfiguring the manufacturing lines in the factories will be elevated. Furthermore, location of the machines can be spread off the factory floor, to the design office, classrooms and distributed to small manufacturing laboratories, even in residential areas. As technical aspects, the downsizing makes it easier to achieve high-speed machining and high-precision/rigidity motion control due to reduced inertia, and in turn, it leads to higher precision, quality and productivity. With these objectives, the first prototype of desktop NC milling machines was developed using a miniature high-speed spindle[1]. To emphasize the rapid milling capability of small works, a new machine has been developed, employing a high-acceleration X-Y stage and a miniature ultra-high-speed spindle with more elevated rotation speed.

2 Mechanical Design

The machine as the second prototype is basically succeeding the original mechanical design concept of the first prototype. It consists of a direct-driven X-Y stage and a Z-axis drive unit holding a spindle unit at the end. The Z-axis drive unit is mounted on the top of a rugged housing surrounding the X-Y stage (**Fig. 1**). The machine itself is 470 mm high, 480 mm wide, and 480 mm deep, weighing 42 kg.

The X-Y stage is originally designed one using crossed roller guides and linear motors. The X- and Y stage elements use one and two linear coreless motors respectively. Though the two stages are kinematically stacked, the guides are

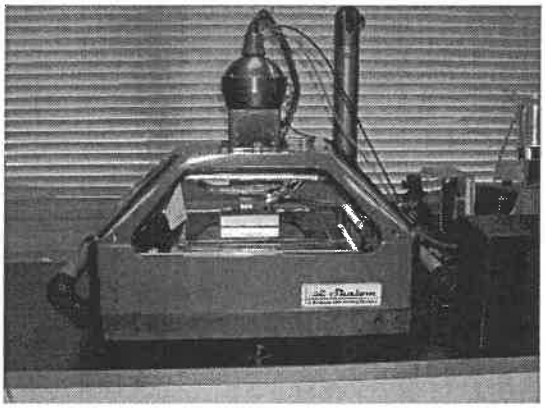

Fig. 1 Structure of the desktop milling machine

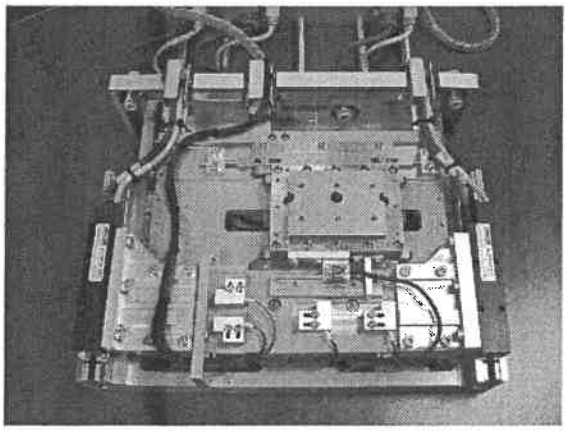

Fig. 2 Linear motor-driven X-Y stage

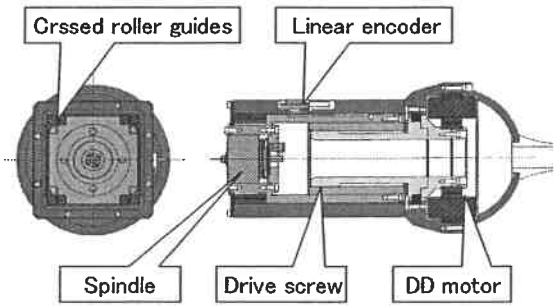

Fig. 3 Structure of Z axis drive

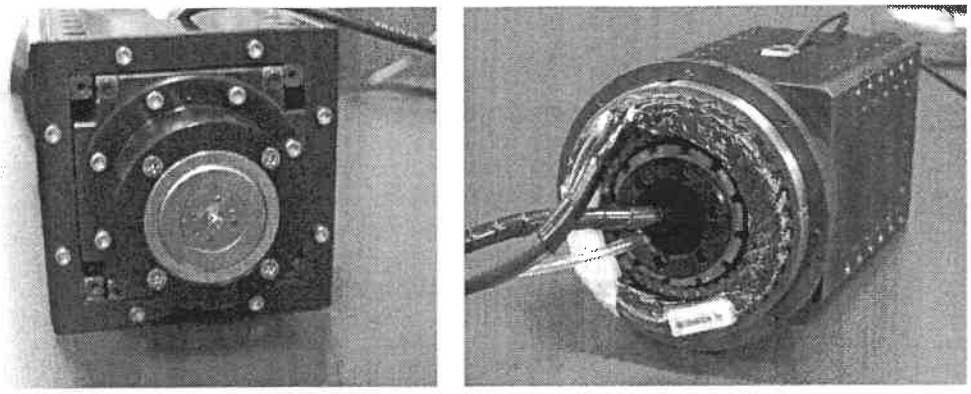

Fig. 4 Views of Z axis drive (from bottom and top with cover removed)

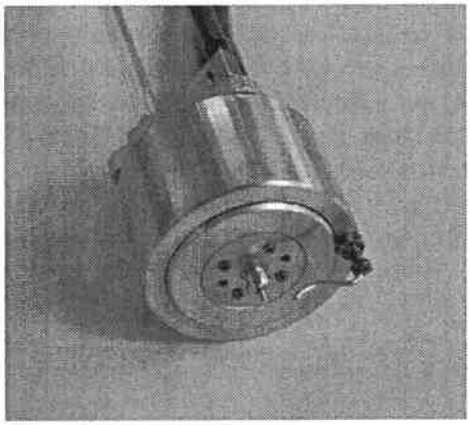

Fig. 5 Spindle with jacket

aligned at almost the same level to eliminate overhang problems. The linear motors are aligned as "H-configuration" as shown in **Fig. 2.**

The Z-axis drive unit uses a vertical hollow drive screw, and is driven by a brushless direct drive torque motor **(Fig. 3-4)**. The sliding part of the unit is guided by four crossed roller guides, which are located at the four corner of the slide. The drive screw is supported by a thin rotary ball bearing. The screw, the spindle unit and the DD motor are allocated in a line.

The spindle, as shown in **Fig. 5**, is a miniature high frequency AC motor specially designed to provide 60W rated power and 300 krpm of maximum rotation speed. It is 27mm in diameter and 26 mm long. The motor is slightly cooled by airflow in a jacket, and the air is also used as a clearing jet at the cutting point. The motor uses a pair of miniature ceramics ball bearings, and lubricated by oil mist system. The spindle end holds a milling tool by a directly machined collet chuck of 1.0 mm shank diameter.

The spindle run-out was measured as less than 0.3 μm as NRRO.

3 Motion Control System

3.1 Numerical Controller

Full closed loop numerical control system with 0.1-μm resolution is installed. The position feedback is given by optical linear encoders with 50 nm resolution (MicroE M3000) at the stages. The compact custom-made NC system consists of a microprocessor-based controller, operational panel, and a notebook PC for monitoring and program control. DNC operation is available. **Table 1** summarizes the specifications of the axis. For X and Y axes,

Table 1 Specification of axis mechanisms

Axis	X (upper)	Y (lower)	Z (top)
Guide	Two crossed-roller guides	Two crossed-roller guides	Four crossed-roller guides
Travel	50mm	50mm	50mm
Feed mechanism	Direct drive	Direct drive	Lead screw
Actuator	Linear motor	2 Linear motors	AC DD motor
Maximum feed rate	400mm/s	400mm/s	5mm/s
Maximum acceleration	$21mm^2/s$	$21mm^2/s$	$1mm^2/s$
Encoder (resolution)	Optical linear scale (50nm)	Optical linear scale (50nm)	Optical linear scale (50nm)

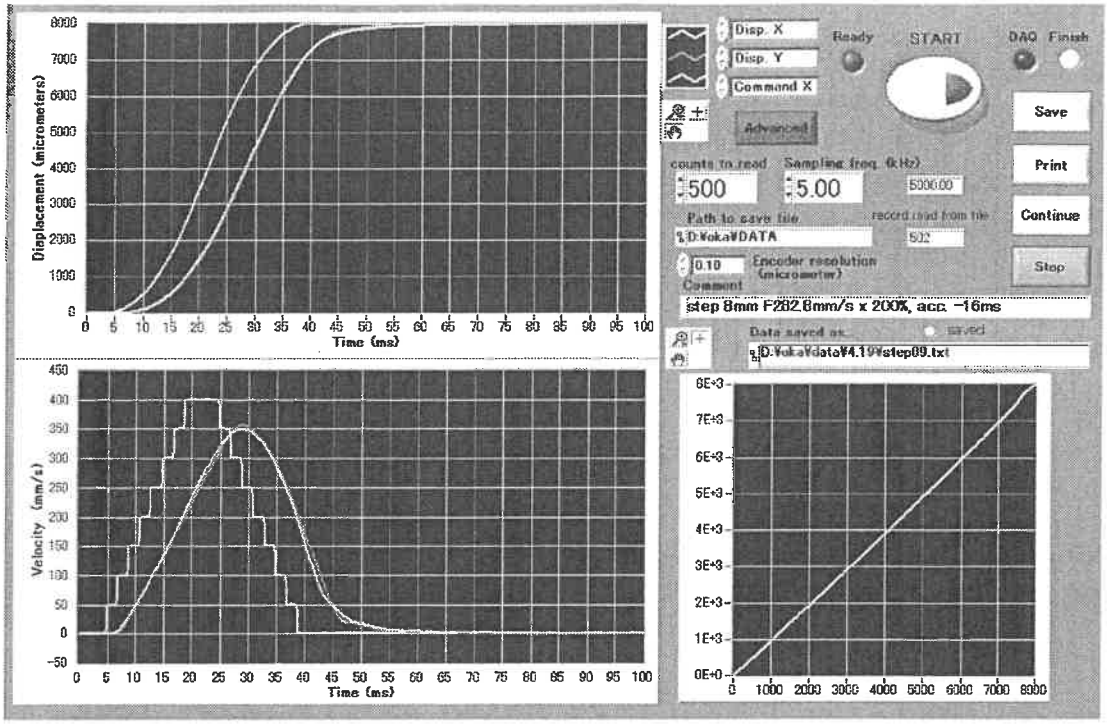

Fig. 6 Response of X-Y stage

the maximum feed rate is limited by the maximum acceptable pulse rate (4Mpps) of the drivers.

Response of the axis motion control was evaluated observing the encoder signals for each axis. Actually, positioning resolution of 0.1 μm is achieved for all the axes. High acceleration step motion has been also tested. As X-stage is much lighter than Y-stage, maximum acceleration reached to 4.1G and 2.1G for X and Y stage, respectively. In order to maintain shock-free and synchronizing motion of the two axes, position loop gain and command velocity profile are adjusted, as shown in **Fig. 6.**

3.2 Positioning repeatability

A target block was set at the low end of the Z-slide in place of the spindle, and a capacitance gage was encountered to it. Short-term positioning repeatability was measured as better than 50nm (**Fig. 7**).

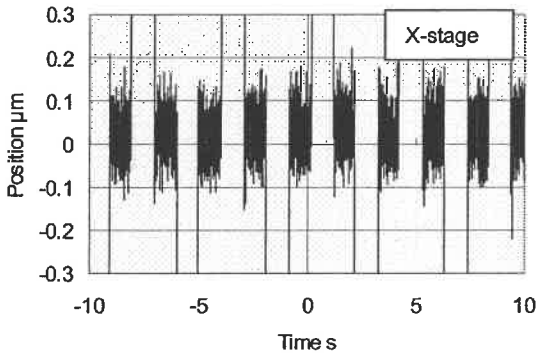

Fig. 7 An example of positioning repeatability tests

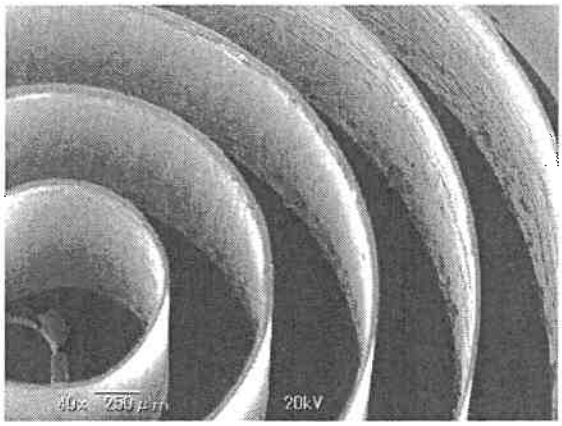

Fig. 8 Thin wall machining

4 Machining

4.1 High aspect-ratio machining

Thin walls were machined out of high strength aluminium alloy, A7075 (**Fig. 8**). The tool used was a straight two-flute end mill of 0.5 mm diameter with straight edges. Annular slots were made by helical milling with 200,000 rpm of spindle speed, and they saved thin walls of 30 μm thick and 1.5 mm high between them. No serious damage on the wall was observed. When the spindle rotation speed was reduced down to 50,000 rpm, the tool has broken due to an excess cutting force.

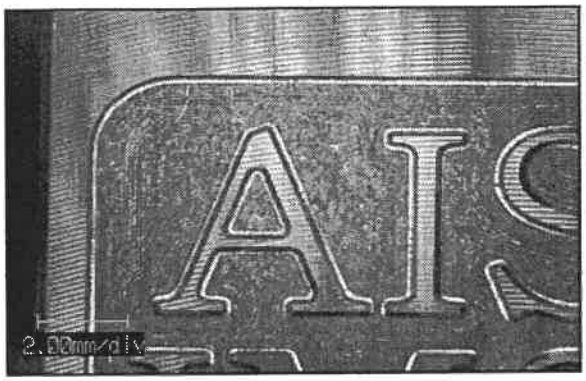

Fig. 9 Figure pocketing

4.2 Pocketing

Three-dimensional milling was also made using DNC function, processing machining program files generated by a CAM system. The pocketing sample shown in **Fig. 9** was machined under the condition listed in **Table 2**. The advantage of the miniaturized milling machine has been taken, so that the stage traced a series of tiny segments quickly enough at high acceleration.

Table 2 Cutting conditions for pocketing

Material of workpiece	A7075
Depth of cut	0.1 mm x 3
Feed rate	50 mm/s
Pick feed	0.1 mm
Nose radius of tool	0.2 mm
Spindle rotation speed	200,000 rpm

5 Power consumption

One of the advantages of downsized machine tools is their minimized power consumption. In this system, the total power consumption in the idling state was about 250W. Its major part is consumed at the linear motor drives, not the motors themselves. Spindle rotation and stage motion raised the consumption up to over 400W.

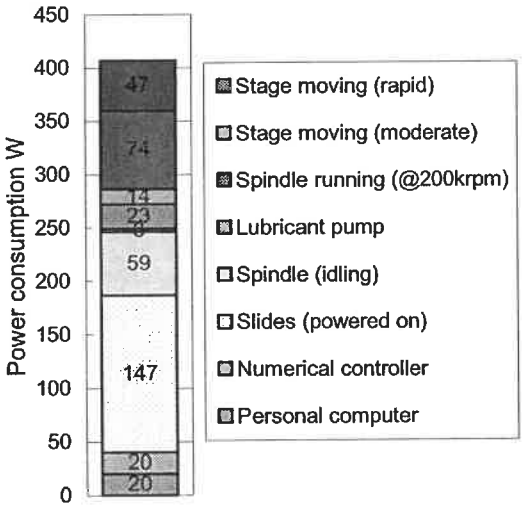

Fig. 10 System power consumption

6 Conclusion

The second prototype of miniaturized milling machines has been developed and evaluated. The X-Y stage employing linear motors performs quick motion suitable for contouring small figures. The ultra-high speed spindle enables high-speed milling and high aspect ratio machining by reducing cutting force.

7 Acknowledgements

This research has been done as a part of the national R&D project, "Digital Meister" in duration of FY2001-2003.

8 Reference

1) Okazaki, et al: Desk-Top NC Milling Machine with 200 krpm Spindle, Proc. ASPE 2001 Annual Meeting, 192

A MICROROBOT MOVABLE IN FLEXIBLE PIPES LIKE THE LARGE INTESTINE

Manabu ONO*, Tomoya SASAZAKI**, Manabu OTSUKI**,
Norihiko KATO** and Shigeo KATO**

*Department of Mechanical Engineering,
Tokyo Metropolitan College of Technology,
Shinagawa, Tokyo 140-0011, Japan
Phone:+81-3-3471-6331, Fax:+81-3-3471-6338
E-mail:m_ono@tokyo-tmct.ac.jp
**Department of Systems Engineering,
Nippon Institute of Technology
4-1 Gakuendai, Miyashiro, Saitama 345-8501, Japan
Phone:+81-480-34-4111, Fax:+81-480-33-7745
E-mail:kato@nit.ac.jp

1. Introduction

An inspection of the large intestine is very effective in order to prevent the large intestine cancer. A fiberscope is excellent for the inspection of the large intestine. However, the inspection by the fiberscope often attends many pains and injuring of the intestine. We are hoping the inspecting method for the intestine with no pain and no injuring of the intestine before the operation by the fiberscope. Many microrobots which can move in the large intestine have been proposed by several research groups [1], [2]. However, the sure moving in the large intestine has not been confirmed, because the actual large intestine in our human body is especially very flexible to the radius direction and the mobile moving in the flexible pipes is very difficult.

Now, we propose the new microrobot movable in a flexible pipe like the large intestine. We need the mechanism for moving in a flexible pipe surely. This mechanism is using friction force. The microrobot is able to holds a flexible pipe in the radius direction, and moves in the length direction. We use three rubber bellows in series. Six bulging rubber sheets are provided to the rubber bellows of two outsides. They are called friction braking mechanism. The friction braking mechanism works as a brake of the microrobot. The center rubber bellows is called as a moving element, because the microrobot is moves by stretching and shrinking of a rubber bellows.

When the rubber bellows of the friction braking mechanism is shrinking, six bulging rubber sheets spread in the radius direction and touch the flexible pipe. Then the spread bulging rubber sheets surely hold the flexible pipe. When the rubber bellows of the friction braking mechanism is stretching, spreading to the radius direction of the six bulging rubber sheets and touching to the large intestine are canceled. The rubber bellows are stretched by pneumatic pressure and shrunk by vacuum pressure. The stretching and shrinking of the rubber bellows are controlled by a computer and electromagnetic valves.

The new microrobot was confirmed to move at the speed of 12 mm/s in the pig's raw small intestine. We confirmed moving speed of 20.8 mm/s in the curving pipe. In this experiment, it was also confirmed that the microrobot is able to generate the traction force of 0.3 N.

2. Structure of the fabricated microrobot

Structure of the fabricated microrobot is shown in Fig. 1. The microrobot consists of two friction braking mechanisms and a moving element. These elements are driven by three bellows which are 16 mm in outer diameter, 11 mm in inner diameter, 27 mm, 31 mm long

and made of nytrile butyl rubber (NBR). Each bellows is an independent vessel. Three air feeding tubes, which are 2.0 mm in outer diameter, 1.2 mm in inner diameter, 2.0 m long, and 4.0 mm in outer diameter, 2.5 mm in inner diameter, 1.0 m long, are connected to three bellows of the friction braking mechanisms and the moving element. The rubber bellows are stretched by the supply of the pneumatic pressure and are shrunk by the supply of the vacuum pressure. The stretching and shrinking of the bellows are controlled by three electromagnetic valves and a computer.

Structure of a bulging friction sheet is shown in Fig. 2. The bulging friction sheet consists of six bulging rubber sheets which are 5 mm wide, 0.5 mm thick, 23 mm long and made of NBR. The length of the bulging friction sheet is 17 mm in the free condition and 14 mm when the pressure in the bellows is vacuum. The diameter of the bulging friction sheet becomes to about 32 mm. Then the bulging rubber sheets are strongly pressed to the flexible pipe like the large intestine. The friction force in the flexible pipe are made by the radial force of the bulging rubber sheets.

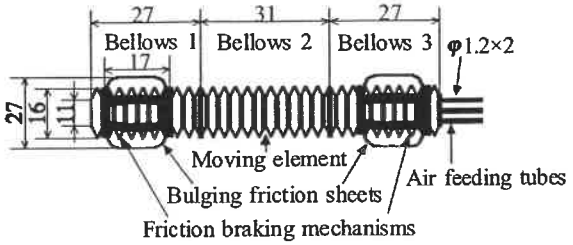

Fig. 1 Structure of the fabricated microrobot

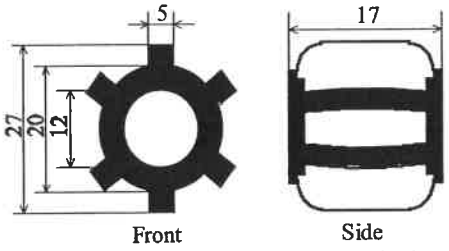

Fig. 2 Structure of a bulging friction sheet

3. Experimental apparatus

An experimental apparatus for measuring the characteristics of the microrobot is shown in Fig. 3. A computer controls three electromagnetic valves through a valve controller. Three air feeding tubes are connected from the electromagnetic valves to two friction braking mechanisms and the moving element of the microrobot. An air compressor is connected to the entrance ports of the electromagnetic valves and feeds pneumatic pressure to stretch the bellows. A vacuum pump is connected to the exit ports of the electromagnetic valves and feeds vacuum pressure to shrink the bellows.

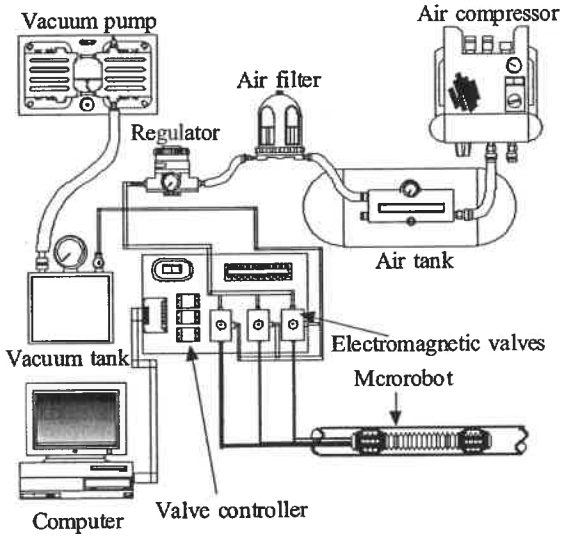

Fig. 3 Experimental apparatus

4. Moving principle of the microrobot

The pneumatic and vacuum pressure are fed like as a time chart shown in Fig. 4. The mass flow rate through the electromagnetic valve is proportional to the absolute pressure of the upstream flow, because the electromagnetic valve is a kind of an orifice. The absolute pneumatic pressure at the time of stretching motion is more than two times of the pressure in the bellows in the time of shrinking motion. Then the supplying time of the vacuum pressure in the shrinking motion ($=t_2$) must be more than two times of the supplying time of the

pneumatic pressure in the stretching motion ($=t_1$). The sum of t_1 and t_2 is called as the cycle time ($=T$).

We make a time difference of $t_1/2$ in the pneumatic supplying time among the front friction braking mechanism, the central moving element and the rear friction braking mechanism. The moving principle of microrobot is shown in Fig. 5, when the pneumatic and vacuum pressure are supplied as shown in Fig. 4.

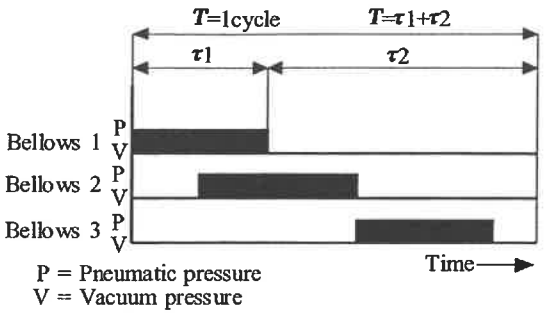

Fig. 4 Time chart of the pneumatic and vacuum pressures for the each bellows

Step 0: At initial, all the bellows are shrinking by the vacuum pressure. The bulging friction sheets of the front and rear friction braking mechanisms are at the condition of the braking and holds the flexible pipe.

Step 1: The pneumatic pressure is fed to the front friction braking mechanism and the braking is free.

Step 2: The pneumatic pressure is fed to the central moving element and the microrobot is stretching. Then the front part of the microrobot can move to the forward direction, because the rear friction braking mechanism is still at the condition of the braking and holds the flexible pipe.

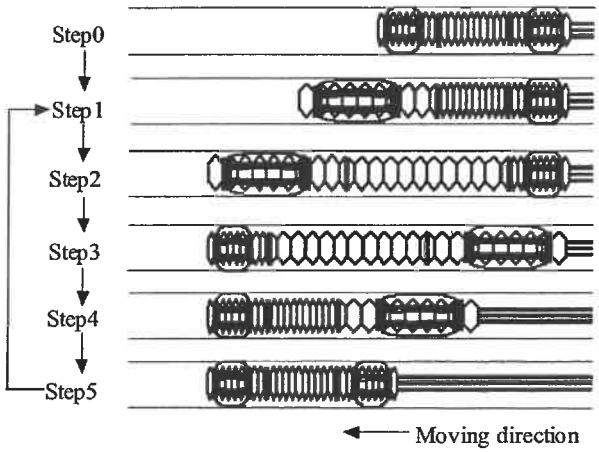

Fig. 5 Moving principle of microrobot

Step 3: The pneumatic pressure is fed to the rear friction braking mechanism and the braking is free. At the same time, the vacuum pressure is fed to the front friction braking mechanism and it is at the condition of the braking.

Step 4: The vacuum pressure is fed to the central moving element and the microrobot is shrinking. Then the rear part of the microrobot can move to the forward direction, because the braking of the rear friction braking mechanism is free.

Step 5: All the bellows are shrunk by the vacuum pressure. The bulging friction sheets of the front and rear friction braking mechanisms are in the condition of braking and hold the intestine. It is same as the initial condition and one cycle is over. The microrobot moves the stretching displacement of the moving element. Consequently the speed is shown by (stretching displacement) / (cycle time).

5. Experiments

5.1 Measurement of friction force

The relationship between the pressure in a bellows and friction force is shown in Fig. 6. The experiment had done using the pig's small intestine. The pressure in bellows was changed from 0 MPa to -0.08 MPa. Friction force had been measured using the force gauge. When the pressure of the bellows was -0.08 MPa, maximum friction force of 0.8 N was confirmed.

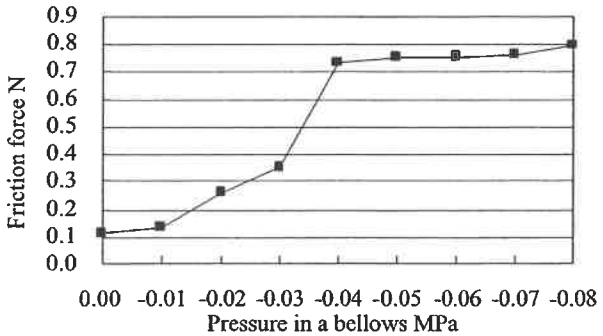

Fig. 6 Relationship between the pressure in a bellows and friction force

5.2 Measurement of the moving speed

We measured the traction force of the microrobot supplying the pneumatic pressure of 0.08 MPa and the vacuum pressure of -0.08 MPa. We chose that the supplying time of the pneumatic pressure in the stretching motion ($=t_1$) is 0.35 seconds. The supplying time of the vacuum pressure in the shrinking motion ($=t_2$) was 0.7 seconds. Relationship between the load and the moving speed is shown in Fig. 7. The microrobot was confirmed to generating the maximum traction force of 0.3 N and the moving speed of 12 mm/s.

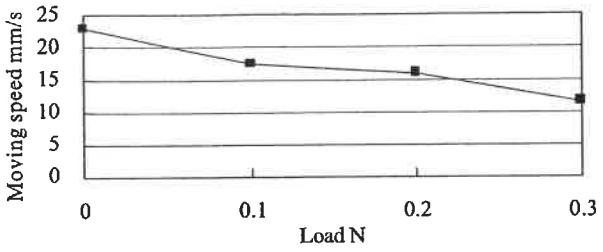

Fig. 7 Relationship between load and moving speed

5.3 Moving experiment of the curving pipe

The curving pipe of pig's small intestine for moving experiment is shown in Fig. 8. The small intestine is curving pipe that 181 mm of curvature radius, 27 mm of outer diameter, 1190 mm long. The pneumatic pressure of 0.08 MPa and vacuum pressure of -0.08 MPa were taken the cycle time was 1.05 seconds. It confirmed that a moving speed was 20.8 mm/s.

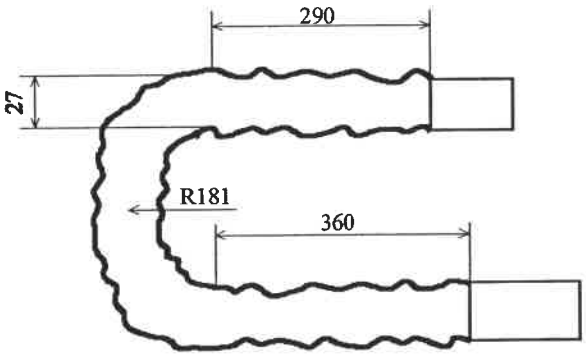

Fig. 8 Curving pipe of pig's small intestine

6. Conclusions

(1) We fabricated a new microrobot that can surely move in a flexible pipe like the large intestine. The microrobot consists of two friction braking mechanisms and a moving element. The friction braking mechanisms has a bulging friction sheet which consists of six bulging rubber sheets.

(2) We confirmed by the experiment that the microrobot can move to the forward and backward direction in the pig's small intestine. The moving speed is 12 mm/s and to generated traction force of 0.3 N.

(3) We confirmed by the experiment that the microrobot can move to the curving pipe in the pig's small intestine. The microrobot was confirmed to move at the speed of 20.8 mm/s.

(4) The microrbot may be used to the inspection mobile microrobot for the human large intestine, because the pig's small intestine is very similar to the human large intestine.

Reference

[1] L. Phee, C. Stefanini, A. Arena, D. Accoto, A. Menciassi, G. Pernorio, M. Boccadore, P. Dario, Mechanical Clamping Mechanism for Locomotion in the Gastrointestinal Tract, Proceedings of the 2nd International Conference of EUSPEN, pp. 770-773.

[2] M. Ono, E. Arakawa, S. Kyoumine, S. Kato, Fabrication of a Microrobot Movable in a Freely Held Pig's Small Intestine, Proceedings of the 2nd International Conference of EUSPEN, pp. 806-809.

FABRICATION OF AN ARTIFICIAL EARTHWORM TYPE IN-PIPE MOBILE ROBOT MOVABLE IN PRIMARY COOLING-WATER PIPE OF AN ATOMIC POWER PLANT

Manabu ONO*, Takayuki NAITO** and Shigeo KATO**

* Department of Mechanical Engineering,
Tokyo Metropolitan College of Technology,
Shinagawa, Tokyo 140-0011, Japan
Phone: +81-33471-6331, FAX: +81-33471-6338
E-mail: m_ono@tokyo-tmct.ac.jp
** Department of Systems Engineering,
Nippon Institute of Technology,
Miyashiro, Saitama 345-8501, Japan
Phone: +81-480-34-4111, FAX: +81-480-33-7745
E-mail: kato@nit.ac.jp

1. Introduction

A few years ago, we had an accident that radioactive cooling-water flowed out from the primary cooling-water pipe of an atomic power plant in Japan. The cooling-water pipe whose inner diameter is 3 inches was cracked by vibration of the cooling-water. The cracked location was inspected after removal of heat insulating materials around the pipe. If we can insert an inspection robot and inspect the pipe, we are avoidable from the difficult removal of the heat insulating materials and radioactivity of the flowed water. The cooling-water pipe is 76 mm in inner diameter, about 30 m long and has some elbows and vertical parts. Robots driven by electric motor are difficult to move in the vertical pipes, because the ratio between the power and the weight of the electric motor is not large[1], [2].

Many researchers have researched a new inspection robot which is able to move in the long pipe that has some elbows and vertical parts and driven by pneumatic actuators, because the pneumatic actuators are advantageous concerning the ratio between the power and the weight. However, they could not move the long distance[3]-[5]. The former reason that robots driven by pneumatic actuator could not move the long distance is caused by the long distance between the air pressure generators and pneumatic actuators. Accordingly, we propose an idea that the robot is moved in the condition where the pneumatic actuators are worked near the air pressure generators. The idea was realized by attaching electromagnetic valves direct behind of the pneumatic actuators.

We fabricated an artificial earthworm type robot in which we use three rubber bellows of pneumatic actuators. 12 rubber friction rings are used to get friction force between bellows and the pipe. Three electromagnetic valves that control pneumatic pressure to the three bellows are attached direct behind of the robot in order to evade the flowing time-lag of the air pressures. The electromagnetic valves and air-feeding tubes are carried on trolleys in order to decrease friction force between the pipe and them. The Air-feeding tubes conveying mechanism consists of a chassis made of vinyl chloride pipe, 8 legs made of aluminum and 8 wheels made of plastics. The wheels smoothly rotate. The air-feeding tubes conveying mechanism can carry the air-feeding tubes in pipe whose inner diameter is more than 74 mm.
The fabricated artificial earthworm type mobile robot was confirmed to move in the pipe that has 4 "U" letter curving vertical pipes (double elbows) and is 32 m long.

2. Structure of the fabricated robot

An in-pipe mobile robot which is able to move in pipes whose inner diameter is 3 inches is shown in Fig. 1. The robot is constructed by three bellows for the pneumatic actuators, friction rings and three electromagnetic valves. The bellows are made of Nitrile Butyl Rubber whose outer diameter, inner diameter and natural length are 60 mm, 43 mm and 135 mm. Total 12 friction rings are attached at the end of the three bellows as moving legs of robot. The friction rings are 84 mm in outer diameter, 42 mm in inner diameter and 1.5 mm thick. When the friction ring is attached at the bellows, the inner diameter is enlarged, because the inner diameter of the friction ring is 4 mm smaller than the inner diameter of the bellows. Then, friction ring comes to the shape of a cone. Three electromagnetic valves which control pneumatic pressure and vacuum pressure to the three bellows. They are attached direct behind of the robot in order to evade the flowing time-lag of the air pressures. Three air-feeding tubes made of polyurethane (inner diameters is 4 mm) are attached to the electromagnetic valves in order to feed pneumatic and vacuum pressure. A power line for the electromagnetic valves is bundled with air-feeding tubes. They are 40 m long. The air-feeding tubes are carried on conveying mechanisms in order to decrease friction force between the pipe and them. The air-feeding tubes conveying mechanism consists of chassis made of vinyl chloride pipe, 8 legs made of aluminum and 8 wheels made of plastics. The wheels smoothly rotate.

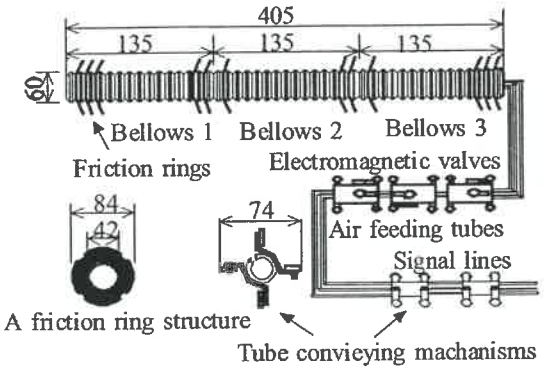

Fig. 1 Structure of the fabricated mobile inspection robot

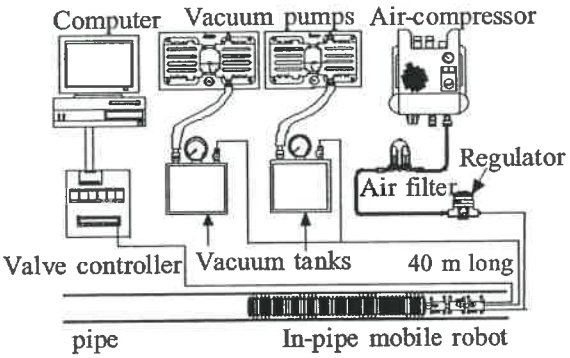

Fig. 2 Experimental apparatus of the mobile robot

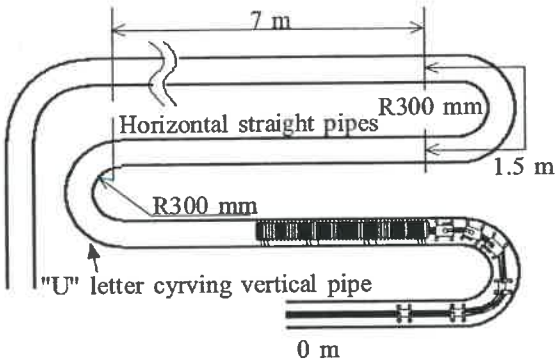

Fig. 3 The pipeline for an experiment

Experimental apparatus of the mobile robot is Fig. 2. Moving sequence is programmed in a computer. The computer controls the electromagnetic valves which are 40 m long far away through a valve controller, using the air-feeding time schedule program for the actuators. The other ends of air-feeding tubes are attached to the air-compressor and two vacuum pumps.

The pipeline for an experiment is shown in Fig. 3. The pipeline is 79 mm in inner diameter whose horizontal straight pipes are 7 m long and "U" letter curving vertical pipe are R300 mm, 1.5 m long.

3. Moving principle

The air-feeding time schedule and moving principle of the robot are shown in Fig. 4. The bellows are stretched by pneumatic pressure of 0.1 MPa, and shrunk by vacuum pressure of

-0.08 MPa. The supplying time of the pneumatic pressure ($=\tau_1$) is 1.5 seconds and the supplying time of the vacuum pressure ($=\tau_2$) is 7.0 seconds. Consequently, the supplying time of the one cycle is 8.5 seconds.

Step 0: All bellows are in the shrunk condition, because the vacuum pressure is supplied.

Step 1: The pneumatic pressure is supplied to the bellows 1 and the bellows 1 is stretched. Front end of the bellows 1 moves to the forward direction, because the friction force of the friction rings at the front end of the bellows 1 is smaller than friction force of the friction rings at the junction between bellows 1 and bellows 2.

Step 2: The vacuum pressure is supplied to the bellows 1 and the bellows 1 is shrunk. At the same time, the pneumatic pressure is supplied to the bellows 2 and the bellows 2 is stretched. The junction between bellows 1 and bellows 2 moves to the forward direction, because the friction force of the friction rings at the front end of the bellows 1 is larger than friction force of the friction rings at the junction between bellows 1 and bellows 2, beside the friction force of the friction rings at the junction between bellows 1 and bellows 2 is smaller than the friction force of the friction rings at the junction between bellows 2 and bellows 3.

Step 3: The vacuum pressure is supplied to the bellows 2 and bellows 2 is shrunk. At the same time, the pneumatic pressure is supplied to the bellows 3 and the bellows 3 is stretched. The junction between bellows 2 and bellows 3 moves to the forward direction, because the friction force of the friction rings at the junction between bellows 1 and bellows 2 is larger than friction force of the friction rings at the junction between bellows 2 and bellows 3, beside the friction force of the friction rings at the junction between bellows 2 and bellows 3 is smaller than the friction force of the friction rings at the end of bellows 3.

Step 4: The vacuum pressure is supplied to the bellows 3 and the bellows 3 is shrunk. The end of bellows 3 moves to the forward direction, because the friction force of the friction rings at the junction between bellows 2 and bellows 3 is larger than the friction force of the friction rings at the end of bellows 3. One cycle of stretching and shrinking motion of the robot becomes end. The robot can move a stretching distance in the cycle time. If the cycle is reversed, the robot can move to the

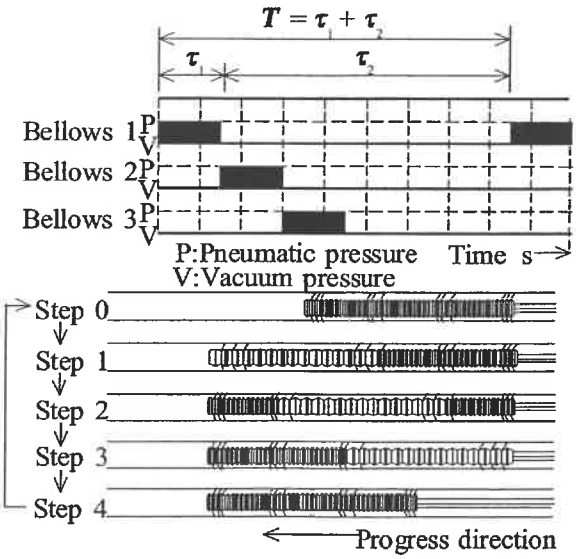

Fig. 4 Moving principle of mobile robot

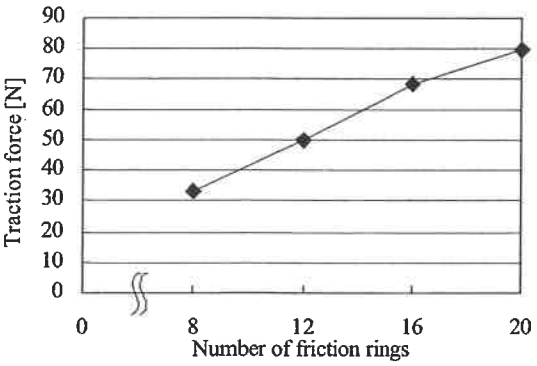

Fig. 5 Relationship between number of friction rings and traction force

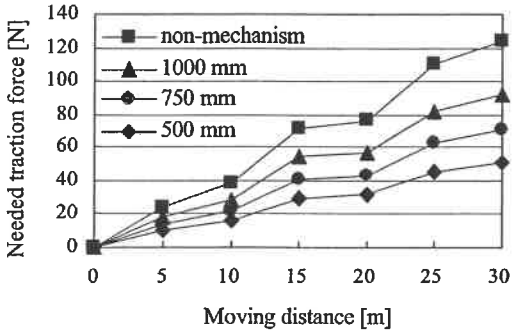

Fig. 6 Relationship between moving distance and needed traction force

backward direction.

4. Moving experiment

Traction force generated at the friction ring is measured and shown in Fig. 5. The traction force of about 53 N is generated by 12 friction rings of 1.5 mm thick. Friction force of the air-feeding tubes conveying mechanism in the pipe is measured. Space between each mechanism is selected as 500 mm, 750 mm and 1000 mm.

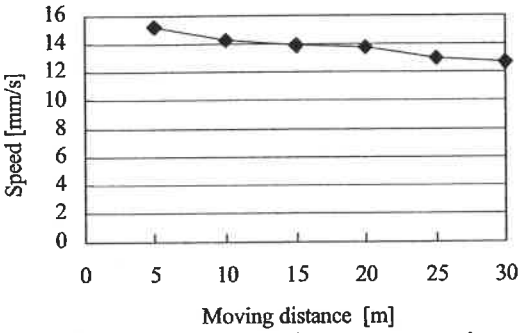

Fig. 7 Relationship between moving distance and speed

(a) Horizontal straight pipe

Friction force is constant and 0.41 N/m at any space of mechanism.

(b) "U" letter curving vertical pipe

Friction force depends on space of mechanisms, and is 12.3 N at 500 mm, 18.1 N at 750 mm and 24.7 N at 1000 mm. Relationship between the friction force and the moving distance of the robot is shown in Fig. 6. Friction force for the robot move to 30 m (passing of 4 "U" letter curving vertical pipes) may be 51 N, if we choose the space of the mechanisms to be 500 mm. Consequently the robot attached 12 friction rings is expected to move more than 30 m.

Relationship between moving distance and speed is shown in Fig. 7. The moving speed decreases according to the increasing of moving distance, and is 13 mm/s at 30 m. Finally, maximum moving distance was confirmed to be 32 m.

5. Conclusions

(1) We fabricated an artificial earthworm type mobile robot which is constructed by three bellows, 12 friction rings and three electromagnetic valves.

(2) The robot was confirmed to move in the pipe which has 4 "U" letter curving vertical pipes and is 79 mm in inner diameter and 32 m long.

(3) The traction force depends on the number of friction rings. The increasing to 20 friction rings may be able to move more than 40 m. We obtained feasibility on an in-pipe inspection robot for the primary cooling-water pipe of atomic power plant.

References

[1] Miyagawa, T., Suzumori, K., Kimura, M. and Hasegawa, Y.,: Development of Micro-Inspection
Robot for Small Piping, Proceedings of tenth World Congress on the Theory of Machines and Mechanism Vol. 2 (1999), 856.

[2]Kawaguti, K., Yoshida, O., Iwao, K. and Kikuta, T.,: Control of an In-pipe Inspection Robot for Iron Pipes, Journal of the Robotics Society of Japan, Vol 15, No. 3 (1997), 387.

[3] Noritugu, T. and Kubota, M.,: Development of In-pipe Mobile Robot using Pneumatic Soft-Actuator, Journal of the Robotics Society of Japan, Vol 18, No. 6 (2000), 831.

[4] Kato, S. and Hirayama, T.,: Fabrication of Artificial Earthworms Driven by Pneumatic Pressure, Proceedings of the Japan Society of Mechanical Engineers, Centennial Grand Congress, Intelligent Motion-control, Power transmission and Tribology, (1997), 661.

[5] Takahashi, M., Hayashi, I., Iwatsuki, N., Suzumori, K. and Ohki, N.,: The Development of an In-pipe Microrobot Applying the Motion of an Earthworm, Journal of the Japan Society for Precision Engineering, Vol. 61, No. 1 (1995), 90.

Wear Measurement of Valve Assemblies by using the Machine vision

Chang-Woo Park*, Keyoung-Jin Chun+ and Sung-Chong Chung*

*** HYbrid Systems Design & Control LABoratory, School of Mechanical Engineering, Hanyang University, Sungdong-Gu, Seoul 133-791, KOREA**

+ Korea Institute of Industrial Technology, 35-3,HongChonRi, IbJangMyun, ChonAnSi, ChungNam 330-825, KOREA

Abstract: Engine performance depends upon wear of valves and seat inserts. To improve quality and life of valve assemblies, wear mechanism and 3D surface topography should be analyzed according to operating conditions. After developing an engine simulator that generates valve speed up to 90Hz and high temperature up to 900℃ as well as controls test load, wear tests have been conducted for two different operating conditions. In order to observe the wear characteristics of the valve assemblies, a cost-effective measurement system based on the shape from focus (SFF) has been fabricated in this paper. 3D surface topography of the valve assemblies has been analyzed to understand the wear behavior according to the operating conditions.

Keywords: Machine vision, Shape from focus, Valve and seat wear, Wear measurement, 3D topography

1. Introduction

Performance of vehicle engines is evaluated from several criteria such as power output, durability and fuel economy. Manufacturers invest a lot of money and time to improve fuel economy and engine power, as well as to reduce emission. Major component of the engine that affects above problems is the valve assembly composed of a valve and a seat insert.

Wear of the valve assembly is observed in various ways according to the operating conditions of engines. Condition monitoring of wear mechanism of the valve assembly is important to produce high quality engines. However, as the valve assembly is small and has a groove, wear measurement of the valve assembly is very difficult. In order to measure wears of the valve assembly, measurement systems such as SEM and confocal microscopes have been used[1-2]. However, these measurement systems are expensive and impossible to apply in the rugged factory.

In this paper, a machine vision technique using a SFF method[3-4] is applied to measure surface wear on a precision servo-stage. A novel illumination unit fabricated with LEDs and halogen lamps is devised to obtain clear images and reduce noises due to reflection. Wear experiments of the valve assembly are conducted on the engine simulator according to engine operating conditions. Visual and parametric characterizations have been studied to analyze wear behavior of the valve assembly[5-6].

2. Wear Test Apparatus and Valve Assembly

The valve assembly wear simulator used for the wear experiments has been fabricated, which is similar to an internal combustion engine[2]. The engine simulator consists of three modules: a hydraulic power unit, a control unit and a mechanical unit. The hydraulic unit simulates combustion pressure of engines to regulate the wear simulator pressure and transmit force to the valve head. The control unit composed of a computer, signal generator, data acquisition system, etc. It controls experimental conditions such as the force imposed to the valve head, seat insert temperature, distance between the valve and the seat insert, and so on.

Actual valve assemblies are used for experiments. Valves are made of STR35. HVS1-2 is used for seat inserts. Hardness of the valve is 419 (Hv500g) and of the seat insert is 397.7 (Hv500g). Fig. 1 shows the valve and seat insert geometries.

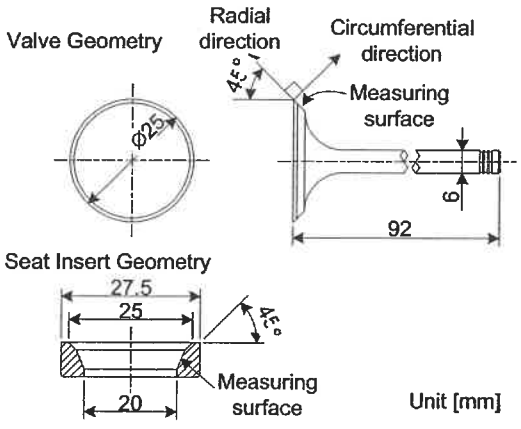

Fig. 1 Geometries of the valve and seat insert.

Wear experiments are conducted for two engine speeds, 10Hz and 25Hz. Temperature conditions are

350℃ and 760℃ at the outer surface of the seat insert and at the valve surface, respectively. LPG is used for experiments. The valve is opened and closed 2.1×10^6 times, and the test load is selected with 1960N.

3. Machine Vision System

3.1 Shape from focus

When the object point **P** is blurred on the image detector plane ID shown in Fig. 2, the radius **r** of the blurred circle **Q'** is obtained. This image *h(x,y)* is the point spread function (PSF) of the camera. It is also called the blurring function. A two-dimensional Gaussian function is used to approximate this physical model. Then, the blurred or defocused image *g(x,y)* at the small image region on the image detector ID is equal to the convolution of the focused image *f(x,y)* and the PSF *h(x,y)*. If *G, F* and *H* are the Fourier transforms of *g, f* and *h*, respectively, then *G=HF*. H has characteristics of a low-pass filter where the bandwidth decreases with increase in defocusing.

Defocused images are obtained by moving the lens every Δd with respect to the reference plane. If the camera moves toward an object focus position, the image will gradually increase its degree of focus (high frequency energy) and will be optimally focused at the focused object plane. When the object plane has a perfect focus at *d*, object height d_z is given by

$$d_z = d = N \times \Delta d \tag{1}$$

This approach should be applied to wear surface to characterize 3D wear scars of valve assemblies.

Since defocusing is a low-pass filtering process[3-4], its effects on the image are more pronounced and detectable if the image has strong high-frequency content. In order to obtain sharp peaks of the image, a modified Laplacian operator is used. It is generated by the convolution of input image $I(x, y)$ and the kernel $H_L(x, y)$ in spatial domains as follows:

$$\begin{aligned} ML(x,y) &= I(x,y) \otimes H_L(x,y) \\ &= |2I(x,y) - I(x-step,y) - I(x+step,y)| \\ &+ |2I(x,y) - I(x,y-step) - I(x,y+step)| \end{aligned} \tag{2}$$

where *step* means variable spacing between the pixels used to compute the derivatives.

The focus measure at a window is computed as the sum of the modified Laplacian values, in a small window around a pixel (i, j), that are greater than a threshold value as follows:

$$f(i,j) = \sum_{x=i-M}^{i+M} \sum_{y=j-N}^{j+N} ML(x,y) \quad for\ ML(x,y) \geq T_L \tag{3}$$

where parameters *M* and *N* determine the window size to compute the focus measure. The window size is selected empirically according to the object geometry. Gaussian interpolation with step size of 0.1 ㎛ is applied to find the optimal values of the peak FMI.

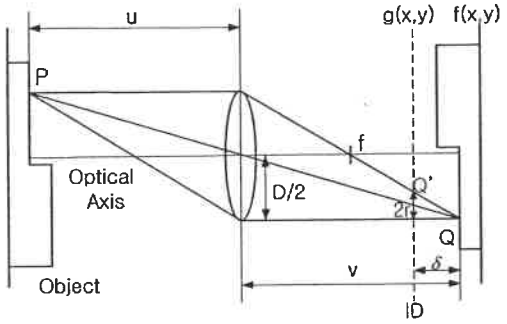

Fig. 2 Image formation of focus and defocus.

3.2 Measurement setup

Developed measurement system consists of a CCD-camera with a zoom lens attached to the precision servo-stage equipped with AC-servos, illumination units, a digital image processing unit and a personal computer as shown in Fig. 3. Both the halogen and LED-array lights are devised to provide adequate illumination to inspect surface wear and roughness of valves and seat inserts. Images are captured through the CCD camera and a frame grabber with 256 digitized gray levels. The image has 640×480 pixel elements with a pixel size 2.17 ㎛. The camera axis is perpendicular to measuring surfaces of the valve and seat.

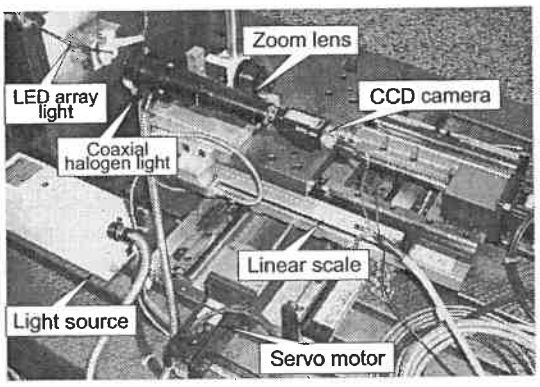

Fig. 3 Developed machine vision measurement system.

4. Results and Discussions

In order to characterize surface wear of the valve assembly, the SFF method described in the previous chapter is applied to valve and seat inserts. To assess the

surface wear, 3D visual and parametric characterizations are performed for the valve assembly according to the engine operating conditions. The visual and parametric characterizations are performed with respect to the least squared mean plane $f(x_i, y_j)$. Eq. (4) means a residual surface to characterize the 3D topography.

$$\eta(x_i, y_j) = z(x_i, y_j) - f(x_i, y_j) \tag{4}$$

where $z(x_i, y_j)$ is the original surface measured through the SFF method. x_i and y_j are i and jth pixel of the radial and circumferential direction, respectively, as follows:

$$\begin{cases} x_i = i\Delta x, \; i = 1 \sim 640 \\ y_j = j\Delta y, \; j = 1 \sim 480 \end{cases} \tag{5}$$

where Δx and Δy are sampling intervals in the radial and circumferential direction, respectively.

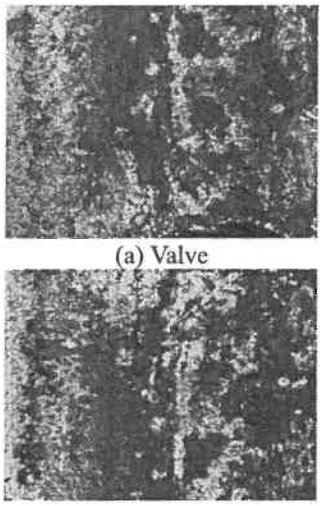

(a) Valve

(b) Seat Insert

Fig. 4 Raw wear images of the valve assembly (25Hz case).

4.1 Visual Characterization

Fig. 4 shows raw wear images of a valve and a seat insert after the running speed of 25Hz for 2.1×10^6 times of operation. Fig. 5 and 6 show isometric plots of the worn valve assembly. Fig. 7 and 8 show the mean depth along the radial direction. Both wear surfaces are almost matched together along the radial direction. Fig. 9 shows peaks over the reference plane on the seat insert. Fig. 10 shows valleys on the worn seat insert. The peak and valley are formed circumferentially on the valve and the seat insert. They are formed owing to the combustion load, adhesive and abrasive wear, as well as corrosive wear[1]. The adhesive wear comes form micro-welding or bonding between contact surfaces. The abrasive wear is due to sliding of the mating surfaces. Corrosive wear occurs due to the high temperature and the chemical reaction in the valve assembly. Plastic deformation due to the combustion load makes scars on the valve assembly too. Truncated plots shown in Figs. 9 and 10 distinguish wear scars well. Using the truncation plot, magnitudes of the wear scar can be observed well according to the truncation height level.

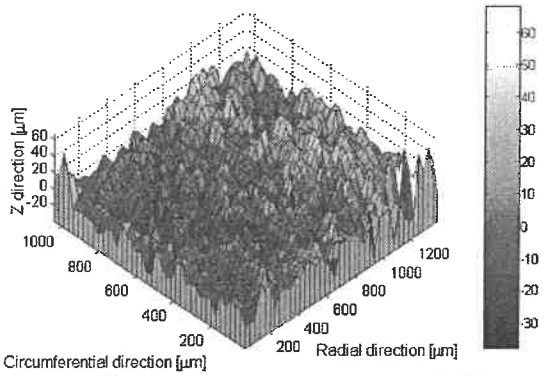

Fig. 5 Isometric plot of the worn valve at 25Hz.

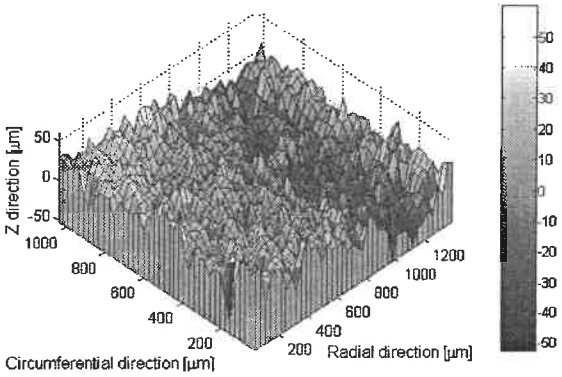

Fig. 6 Isometric plot of the worn seat insert at 25Hz.

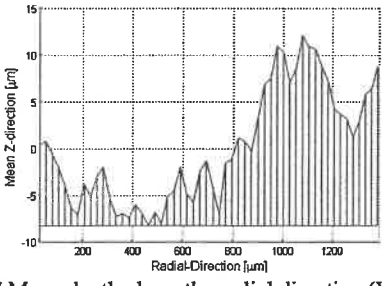

Fig. 7 Mean depth along the radial direction (Valve).

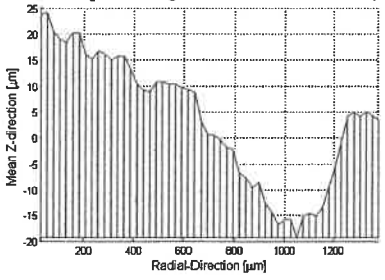

Fig. 8 Mean depth along the radial direction (Seat Insert).

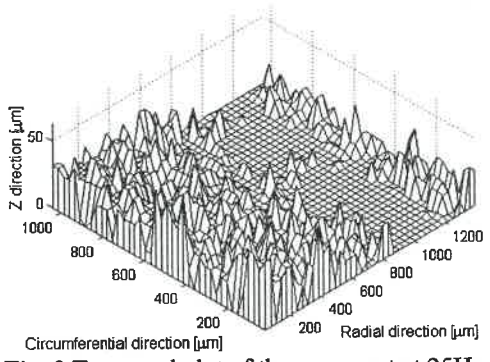

Fig. 9 Truncated plot of the worn seat at 25Hz.

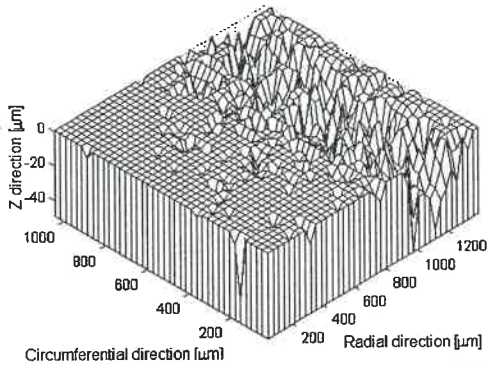

Fig. 10 Truncated plot of the worn seat at 25Hz.

Table. 2 Three-dimensional parameters.

	10 Hz		25 Hz	
	Valve	Seat	Valve	Seat
$S_q(\mu m)$	9.71	13.88	12.87	17.27
S_{sk}	-0.34	0.78	0.56	0.57
S_{ku}	3.08	3.37	4.34	2.89
S_{tp} (%)	49.84	49.36	51.2	46.8
$S_{ds}(mm^{-2})$	1738	2441	2313	2081
$S_{\Delta q}(\mu m/\mu m^{-1})$	0.40	0.49	0.60	0.61
S_{dr} (%)	7.35	10.94	15.22	15.77

4.2 Parametric Characterization[5-6]

RMS deviation S_q describes the statistical RMS height of the surface topography.

Skewness S_{sk} is a measure of the asymmetry of surface deviations about the mean plane.

Kurtosis S_{ku} is a measure of the peakedness or sharpness of the surface height distribution.

Surface bearing area ratio S_{tp} is the ratio of the total contacting area, obtained by truncating the surface summits by a plane parallel to the mean plane at a given truncation level, over the sampling area.

Density of summit S_{ds} defines the number of summits per unit sampling area.

RMS slope S_q is the RMS value of the surface slope within the sampling area.

Developed interfacial area ratio S_{dr} is the ratio of the increment of the interfacial area of a surface over the sampling area.

Table 2 shows parameters of 3D surface topography obtained from valve assemblies according to the running conditions.

5.Conclusions

A SFF-based vision measurement system is fabricated on a precision servo-stage to characterize surface wear of engine valve assemblies. The machine vision system consists of a CCD camera with a zoom lens, a novel illumination unit and image processing modules.

Visual and parametric characterizations of wear scars of engine valve assemblies are conducted by using the isometric and truncation plots, as well as 3D topographic parameters.

The wear mechanism composed of combustion load, adhesive and abrasive wear, as well as corrosive is observed and analyzed efficiently through 3D plots and parameters.

Although wear scars show asymmetric surface wear height distributions for both the valve and the seat insert, both wear surfaces are almost matched together along the radial direction. Wear scar develops rapidly as the engine speed increases.

References

[1] Wang, Y. S., et al, 1996, "The effect of operating conditions on heavy duty engine valve seat wear," *Wear*, Vol. 201, pp.15~25.

[2] Chun, K. J., et al., 2004, "A study on Engine Valve and Seat Insert Wearing Depending on Speed Change," *2004 SAE International*, ANNUAL-136.

[3] Nayar, S.K. and Nakagawa, Y., 1994, " Shape from Focus," *IEEE Transactions on Pattern Analysis and Machine Intelligence*, Vol. 16, No. 8, pp.824-831.

[4] Yoon H. S. and Chung S. C., 2004, "Vision Inspection of Micro-drilling Processes on the Machine Tool," Transactions of the NAMRI/SME, Vol. 32, pp. 391~398.

[5] Dong, W.P., Sullivan, P. J. and Stout, K. J., 1994, "Comprehensive Study of Parameters for Characterizing Three Dimensional Surface Topography Ⅲ: Parameters for Characterizing Amplitude and Some Functional Properties," *Wear*, Vol. 178, pp.29~43.

[6] Dong, W.P., Sullivan, P. J. and Stout, K. J., 1994, "Comprehensive Study of Parameters for Characterizing Three Dimensional Surface Topography Ⅳ: Parameters for Characterizing Spatial and Hybrid Properties," *Wear*, Vol. 178, pp.45~60.

COMPLIANT MECHANISMS FOR MICRO-SCALE SPATIAL MANIPULATORS: APPLICATIONS IN NANOMANIPULATION

Shih-Chi Chen
MIT Department of Mechanical Engineering
77 Massachusetts Avenue, Room 3-446
Cambridge, MA 02139
Tel: 617-452-4957, scchen@mit.edu

Martin L. Culpepper
MIT Department of Mechanical Engineering
77 Massachusetts Avenue, Room 3-449b
Cambridge, MA 02139
Tel: 617-452-2359, culpepper@mit.edu

Keywords: Flexure, compliant mechanism, stiffness, parasitic error, MEMS, spatial, six axis

1 Introduction

Traditional macro and micro-scale [1] six-axis mechanism utilize jointed, three dimensional mechanisms to achieve in and out-of-plane manipulation. The focus of this work is to generate a planar, monolithic, micro-scale Nanomanipulator which generates controlled displacements/motions via compliance of the device's structure. Such a device would not require joints and could therefore avoid the friction, wear and hysteresis errors which preclude jointed mechanism from use in Nanomanipulation applications. In this paper, we present a concept for achieving six-axis manipulation via a micro-scale compliant mechanism with integrated actuators. This manipulator, the Micro-HexFlex (MiHx) shown in Fig. 1A, was inspired by the macro-scale equivalent, the HexFlex [2]. The MiHx, uses layered compliant mechanisms with integrated U-shaped thermal actuators [3] to achieve six-axis positioning. The results of preliminary static and dynamic response tests are reported and compared against FEA simulations.

2 HexFlex six-axis compliant mechanism *(patent pending)*

It is important to understand the general concept of the HexFlex compliant mechanism before we study the micro-scale version. The HexFlex consists of a central stage, supported by six flexure bearings as shown in Fig. 1B. Six actuators act upon the tabs, three in-plane and three out-of-plane.

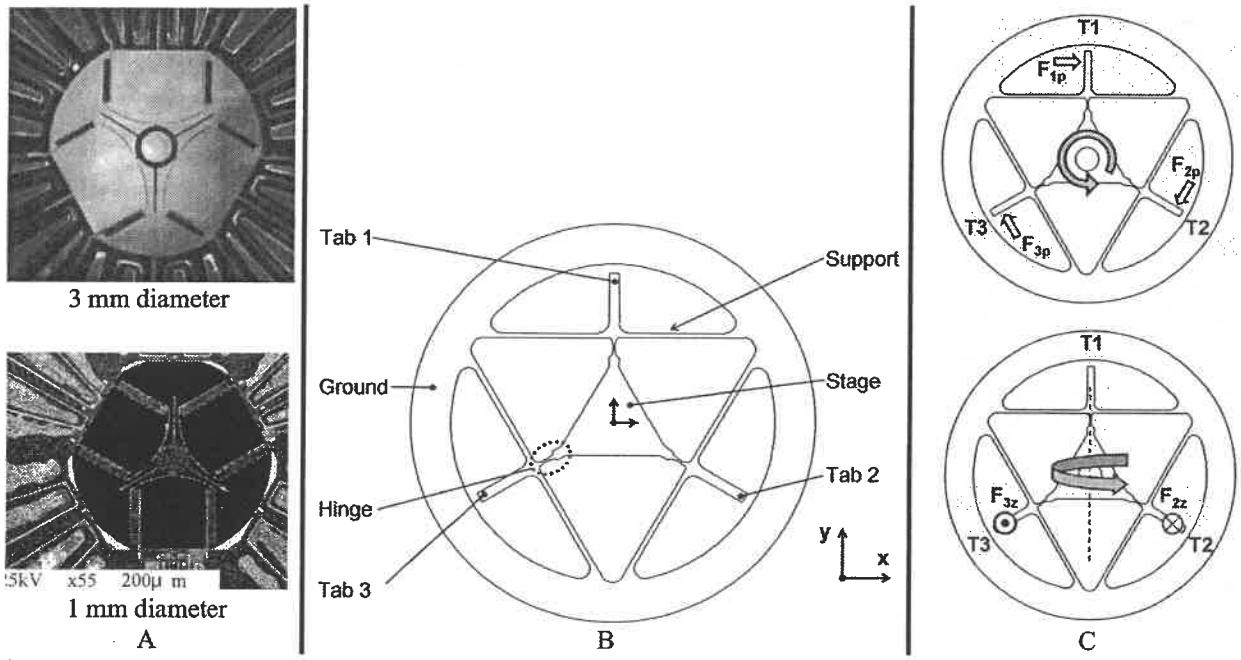

Figure 1: The MiHx (A) and HexFlex (B, C) designs

[x's indicate directions into the plane, •'s indicate directions out of the plane, hollow arrows show actuator inputs and shaded arrows show stage displacement]

In-plane displacements (x, y, θ_z) are generated by in-plane actuation forces applied to the tabs and out-of-plane displacements (z, θ_x, θ_y) are generated by applying an out-of-plane force to the tabs. Combinations of in and out-of-plane actuations may be used to achieve six-axis positioning. Examples of single-axis actuation-displacement combinations are shown in Fig. 1C.

3 Actuators

A tri-layer, two degree-of-freedom thermal actuator was designed and optimized for in-plane and out-of-plane actuation. The sandwich actuator, shown in Fig. 2, consists of a one micron silicon dioxide layer sandwiched between two device layers (we us a double SOI wafer) of single crystal silicon, each 8 μm thick. When actuators in both device layers are activated, the actuator moves in-plane. When one layer is activated, the actuator displaces out-of-plane. The critical dimensions of the sandwich actuator were optimized via a combination of FEA [4] to drive the stage through a minimum range of 5x5x5 microns^3 and 3x3x3 degree.

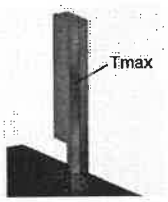

A: Simulated temperature distribution

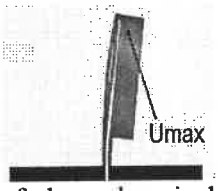

B: Actuation out-of-plane when single layer is actuated

Figure 2: Sandwich actuator

4 Compliant mechanism and flexure design

Figure 3 shows the layout of actuators about the MiHx stage. The geometry of the bow-shaped flexures was optimized via FEA to maximize the ratio of stiffness (> 10) in the directions depicted in Fig. 3A.

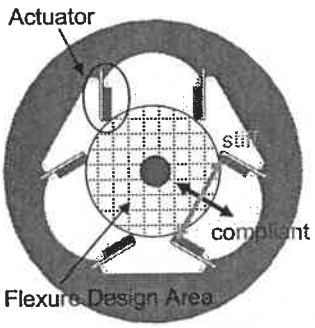

A: Design criteria

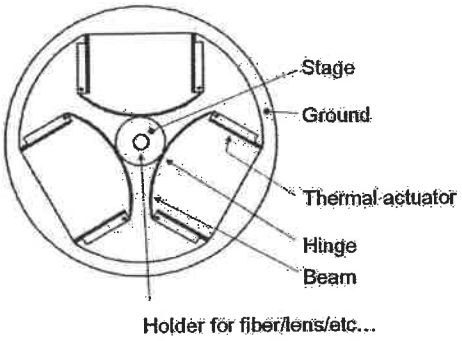

B: Optimized flexure

Figure 3: Flexure characteristic stiffness and components of the MiHx

With respect to the magnitude of stiffness in the noted directions:

(1) The flexures connecting the actuators to the stage must be stiff in the lateral direction and compliant in the longitudinal direction to ensure proper constraint and efficient transfer of actuation inputs to the stage.

(2) The flexures must be compliant as shown in Fig. 3A so as not to over constrain the stage [4].

Figure 4A and B show how in-plane displacements are generated by the actuators. Figure 4C shows how the MiHx generates out-of-plane motions. As mentioned in section 3, the MiHx is fabricated from two single crystal silicon layers joined by a 1 μm thermal oxide layer. If actuators in one layer are activated, the stage will move out-of-plane. For example, if the thermal actuators on the top layer are activated, the stage moves in the negative Z direction as shown in Fig. 4C. Six-axis displacements may be achieved via superposition of in and out-of-plane actuation inputs.

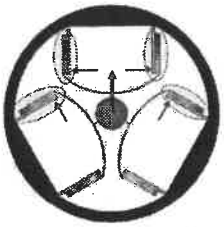

A: Pure Y displacement

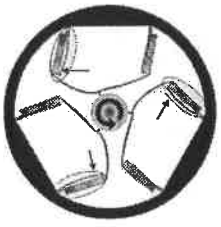

B: Pure θ_Z displacement

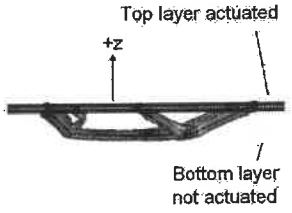

C: Pure z displacement

Figure 4: Generating displacements in the MiHx

5 Preliminary test results

Preliminary tests were conducted on a 3mm MiHx device. Out-of-plane and in-plane tests were conducted on a ZYGO white light interferometer and a Micro-vision system respectively. The goal of these tests was to obtain a first look at the HexFlex static and dynamic functions. Figure 5A contains surface plots which show the static response before (top) and after (bottom) supplying current to one actuator on the top layer of the device. Due to errors in flexure thickness (taper from the DRIE processes) the device exhibited 13% error from FEA simulated behavior. When the correct values were placed within the FEA, the behavior matched within 5%. The improved agreement is shown in Fig. 5B.

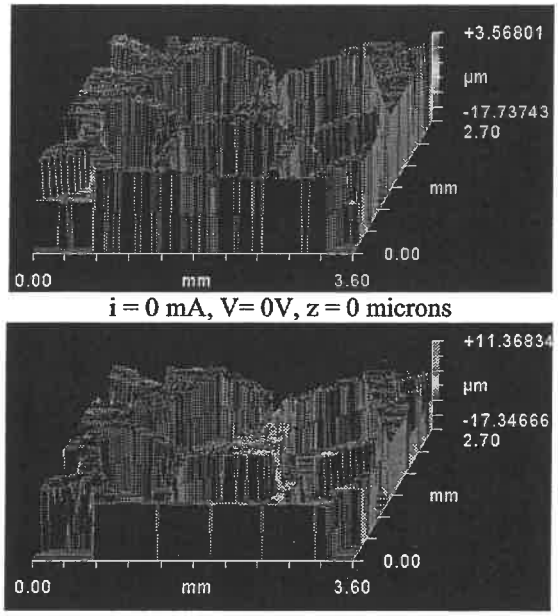

A: Stationary scan for out-of-plane displacement

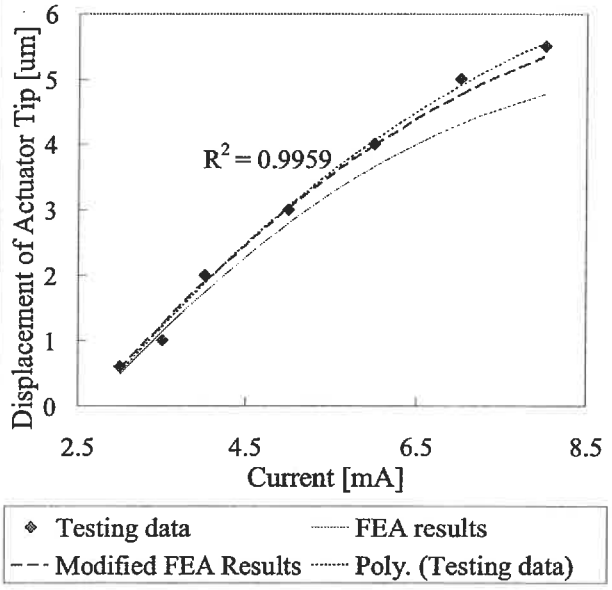

B: Displacement vs. current

Figure 5: Static z axis displacement tests (A) and comparison of FEA simulations and test results

Figure 6 shows the dynamic response of the mechanism for two different motion actuation scenarios. The resonant frequency of the MiHx (3mm in diameter) is higher than the operating range of the thermal actuator; therefore a peak in the frequency plot is not expected. The theoretical minimum step of the stage is determined by the resolution of the current source. The power supply is capable of a 0.01 mA minimum increment, which relates roughly to a 15 nm displacement. We are in the process of verifying the resolution and repeatability experimentally.

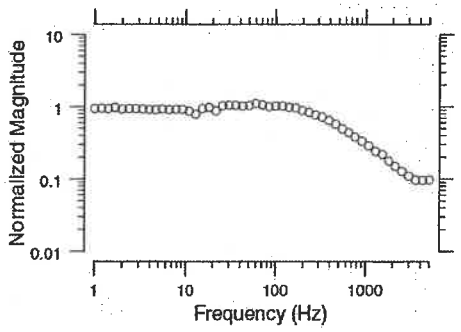

A: Y-axis response plot

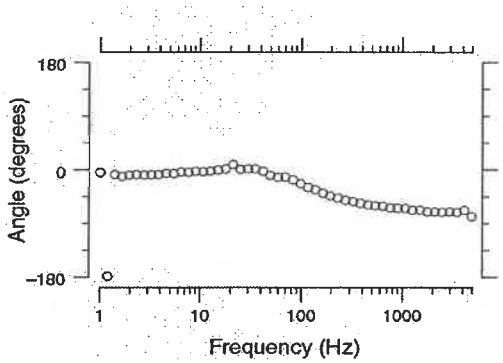

B: θz response

Figure 6: Dynamic tests - vertical axis normalized with respect to the device's full range in the respective axis

6 Summary

In this paper, we have been able to provide an introduction to a micro-scale, six axis device which is being designed for micro-component alignment and Nanomanipulation. The project is in its nascent stage, however the preliminary

tests on the first prototypes are encouraging. The concept of the sandwich beam and the means to couple a multiplicity of them to a stage has been developed using FEA simulation and shown to move in a manner close to that predicted by FEA. Tests indicate that more than 5 micron displacement is possible (the single actuator moved the stage 5 microns) and that it is possible to drive the device at tens to perhaps a few hundred Hz. Much work remains to be completed. We have generated FEA simulations which will guide us through open-loop performance tests. We will test the kinematic solutions and the device's repeatability, resolution, linear range and angular range.

Acknowledgements

We would like to thank Prof. Dennis Freeman (MIT EECS) and Salil Desai for the use of their six-axis MEMS measurement station and the assistance in test setup and data analysis.

7 References

[1] Bernhard Jokiel, et al, "Planar and spatial three degree-of-freedom micro-stage in silicon MEMS", Sandia National Lab., March 2001. http://www.aspe.net/meetings/2001annual/Short_Abst/1160.pdf.

[2] Culpepper, ML, Anderson, G, "Design of a low-cost Nanomanipulator which utilizes a monolithic, spatial compliant mechanism", Prec Eng 2003.

[3] Guckel, H.; Klein, J.; Christenson, T.; Skrobis, K.; Laudon, M.; Lovell, E.G., "Thermo-magnetic metal flexure actuators," Solid-State Sensor and Actuator Workshop, 1992. 5th Technical Digest., IEEE , 22-25 1992, pp. 73.

[4] Shih-Chi Chen, "A Six-Degree-of -Freedom Compliant Micro-Manipulator for Silicon Optical Bench", pp.43-100, M.S. Thesis, MIT, 2003.

8 Appendix

The following diagram provides a shortened description of the materials/fabrication process used to make the MiHx.

Step	Recipe/Description
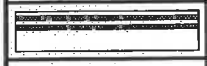	Double deck SOIOI; Device layers @ 8 microns thickness; Oxide at 1 micron thickness
	Photoresist and pattern
	DRIE (Si) and BOE Oxide
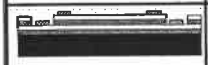	Pattern AL contacts at 350 nm thickness
	Photoresist and pattern
	DRIE (Si) and BOE Oxide and DRIE (Si)
	Pattern handle wafer; Mount to quartz wafer; DRIE backside etch
	Release with vapor HF
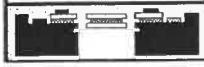	Remove resist via plasma etch

SMALL-SCALE MICRO / NANO-MANIPULATORS IN PRECISION ALIGNMENT AND POSITIONING

Dariusz Golda
MIT Department of Mechanical Engineering
77 Massachusetts Avenue, Room 3-446
Cambridge, MA 02139
Tel: 617-452-4957, dgolda@mit.edu

Martin L. Culpepper
MIT Department of Mechanical Engineering
77 Massachusetts Avenue, Room 3-449b
Cambridge, MA 02139
Tel: 617-452-2359, culpepper@mit.edu

Keywords: MEMS, flexure, compliant mechanism, Nanomanipulation, actuator, accuracy, precision

1 Introduction

Micro-electro-mechanical systems (MEMS) are small-scale machines which are generally a few millimeters to a few microns in size. They are of interest to precision engineers because of their favorable dynamic characteristics (potential for tens to 100s of kHz bandwidth), favorable thermal characteristics (small size and high thermal diffusivity materials can be used to limit thermal strain errors) and potential for low cost and small packaging that follow when machines are miniaturized. Although the technology required to make simple MEMS devices has existed for several decades; the rate at which the technology has developed solutions for small-scale, precision machines has been slow. This is due in part to the challenges that the small-scale machine designer faces: (1) Design using materials with non-isotropic material properties and which experience non-isotropic material removal rates in MEMS fabrication processes, (2) Many MEMS process rely on chemical processes with rates that may form micron-sized parts, yet the reproducibility of critical feature size and location dimensions is difficult as the sources of variation in micro-fabrication processes are chemical/diffusion-based in nature and not as easily controlled, (3) The design and integration of actuators, sensors and electronics is complicated due to the need to ensure process compatibility between the types of devices which are fabricated on the same wafer, (4) Lack of reliable, low cost metrology equipment for characterizing the multi-axis performance and stiffness of MEMS devices (although interferometer-based systems have started to appear in recent years) and (5) difficulty fabricating robust precision contact bearings and motion constraints in MEMS devices.

This is not an exhaustive list of problems and the preceding points do not represent ubiquitous problems, rather they reflect the types of challenges which the precision engineer is likely to face when adjusting their methods to adapt to the constraints which will be placed on their thinking, and therefore the machines can design, at the small-scale. This document is mean to (1) provide a collection of references on MEMS technologies which have promise for use in precision alignment equipment/manipulators with nanometer-level accuracy/precision and (2) provide a brief introduction to the technologies which show promise for practical application in small-scale precision machines. Within the 4 page limit of this document, we have decided to separate the text into roughly $^2/_3$ explanation of the basic technologies and $^1/_3$ references which we believe will be of interest to precision engineers.

2 Manipulators overview

Manipulators consist of actuators, power transmission systems, and sensors. Many micro-scale fabrication processes preclude the integration of sensors in most micro-manipulation devices. Thus most micro-precision machines are forced to run open-loop. These systems may be classified according to actuator species, including electrostatic, electromagnetic, thermal, piezoelectric, electro-active polymer, etc.... Devices with one to six degrees of freedom have been micro-fabricated that employ linkages, gears, hinges, and compliant mechanisms. Unfortunately, the friction, wear and fit tolerances (e.g. "slop) in these components preclude their use in small-scale precision machines which perform Nanomanipulation tasks. Flexures are often used (generally easily fabricated) as precision motion bearings/guides for practical micro-precision machines. In many cases, this limits the range of the devices to a few percent of the device size.

3 Electrostatic manipulators/actuators

The seminal paper by Tang, et al, ignited the development of MEMS electrostatic comb-drive actuators. These actuators use electrostatic force between charged electrodes to create force/motion. Comb-drive actuators (Fig. 1A) use interdigitated electrode fingers to create motion, as opposed to parallel plate actuators which utilize parallel electrodes.

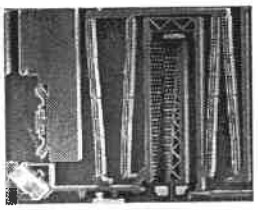

A: Electrostatic comb drive actuator [2]

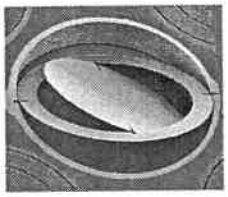

B: Electrostatic parallel-plate actuated mirror

Figure 1: Electrostatic actuators/manipulators

Several variations of the classic comb-drive actuators have been developed for positioning mirrors in optical switches, tuning micro-lasers, rotating gears, Nanopositioning, and data storage [2- 9]. Likewise, a variety of parallel-plate configurations have been designed for positioning of memory read heads, diffraction gratings, optical switching, and inchworm-type, large-travel drives [10-16]. In addition, Hoen, et. al., have developed a unique X-Y electrostatic dipole surface drive micro-positioner capable of 50 micron travel and 4nm open-loop repeatability [17].

4 Electromagnetic manipulators/actuators

Electromagnetic actuators are commonly used in high-power switches, and valves. More recently, a high-performance macro-scale 6-axis manipulator has been developed using electromagnetic actuators [18]. However, the complexity of fabricating micro actuator magnets and coils has been a progress bottleneck at the small-scale. An overview of magnetic MEMS, including some positioning applications can be found in [19]. Despite issues with process control, researchers have been able to fabricate micro-electromagnetic manipulators for data storage, scanning probes, and optical scanning/switching [20- 23]. Figure 2 shows an electromagnetic microactuator used for rotating micro mirrors (conductive paths may be seen) in an optical switch.

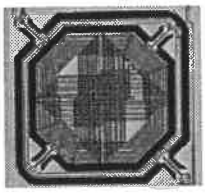

A: 2-axis EM-actuated optical switch [23].

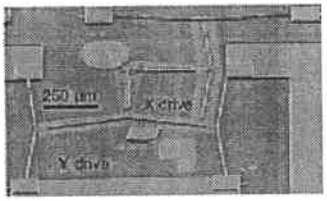

B: Thermally-driven chevron-beam rotary actuator [27].

Figure 2: Electromagnetic and thermally driven Microactuators

5 Thermally driven manipulators/actuators

Thermal actuators make use of Joule heating and subsequent thermal expansion of materials, notably silicon, to generate displacements. Silicon-based thermal actuators can be (though not always) highly repeatable due to the predictable and reversible nature of single-crystal thermal expansion. Although strains are small in silicon devices, several configurations have been implemented to amplify the strain, including the chevron beam, differentially heated beams, and bimorph beams [24 - 26]. Applications include mirror positioning, linear drive systems and rotary drive systems [24, 27]. Figure 2B shows a rotary actuator driven by an orthogonal pair of thermal chevron-beams. Resolution on the order of tens of nanometers is possible with fine resolution current control. Compared to electromagnetic and electrostatic devices, bandwidth is generally lower due to the difference between electromagnetic/electrostatic time constants and thermal time constants (heating/cooling time).

6 Piezoelectric manipulators/actuators

Research on the integration of piezoelectric thin films into MEMS devices has been growing steadily in recent years. Fabrication complexity and reproducibility are the main risks in applying this technology. The most common type of actuator is the simple bimorph cantilever beam (this type of design is used in some SPMs) as shown in Fig. 3A [28-30]. In addition to the bimorph beam, several devices have been made, including tunable optical gratings, linear drive systems, and rotary motors [31-35].

A: Image of a piezoelectric bimorph cantilever beam [29].

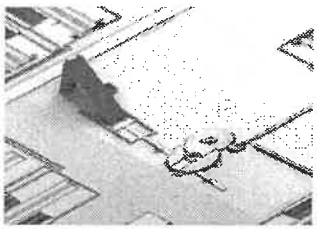

B: SEM image of an electrostatic rotary actuator driving a hinge-mounted mirror via a rack and gear system [36].

Figure 3: Piezoelectric and electrostatically driven, non-planar mechanism

7 References

[01] W. Tang, et. al., "Laterally Driven Polysilicon Resonant Microstructures," Sensors and Actuators, 20, p. 25-32, 1989.

[02] J. D. Grade, et. al., "Design of Large Deflection Electrostatic Actuators," J. Microelectromechanical Systems, 12, p. 335-343, 2003.

[03] J. D. Berger, et. al., "Widely Tunable External Cavity Diode Laser based on a MEMS Electrostatic Rotary Actuator," Proc. Optical Fiber Communication Conf., Anaheim, CA, 2001.

[04] M. S. Rodgers, et. al., "A New Class of High Force, Low-Voltage, Compliant Actuation Systems," Proc. Solid State Sensor and Actuator Workshop, Hilton Head, NC, 2000.

[05] H. Xie, et. al., "A CMOS-MEMS Mirror with Curled-Hinge Comb Drives," J. Microelectromechanical Systems, 12, p. 450-457, 2003.

[06] J. J. Sniegowski, et. al., "Surface-Micromachined Gear Trains Driven by an On-Chip Electrostatic Microengine," Electron Device Letters, 17, p. 366-368, July 1996.

[07] D. M. Tanner, et. al., "Pin-Joint Design Effect on the Reliability of a Polysilicon Microengine," Proc. 38th Annual IEEE Intern. Reliability Physics Symposium, p. 139-145, April 2000.

[08] W. C. Lee, et. al., "Nonlinearly Modulated Digital Microactuators for Nano-Precision Digital Motion Generation," 15th Intern. Conf. on MEMS, p. 594-597, 2002.

[09] C. H. Kim, et. al., "Silicon Micro XY-Stage With a Large Area Shuttle and No-Etching Holes for SPM-Based Data Storage," J. Microelectromechanical Systems, 12, p. 470-478, 2003.

[10] F. Chen, et. al., "A MEMS-Based Monolithic Electrostatic Microactuator for Ultra-Low Magnetic Disk Head Fly Height Control," IEEE Trans. Magnetics, 37, 1915-1918, July 2001.

[11] E. R. Deutsch, et. al., "A Large-Travel Vertical Planar Actuator with Improved Stability," Transducers '03- 12th Intern. Conf. Solid State Sensors, Actuators, Microsystems, p. 352-355, 2003.

[12] E. S. Hung, et. al., "Extending the Travel Range of Analog-Tuned Electrostatic Actuators," J. Microelectromechanical Systems, 8, p. 497-505, 1999.

[13] H. Toshiyoshi, et. al., "Electrostatic Micro Torsion Mirrors for an Optical Switch Matrix," J. Microelectromechanical Systems, 5, p. 231-237, 1996.

[14] D. S. Greywall, et. al., "Crystalline Silicon Tilting Mirrors for Optical Cross-Connect Switches," J. Microelectromechanical Systems, 12, p. 708-712, 2003.

[15] R. Legtenberg, et. al., "Electrostatic Curved Electrode Actuators," J. Microelectromechanical Systems, 6, p. 257-265, 1997.

[16] M. V. Shutov, et. al., "Electrostatic Actuators with Long Range Translation," Transducers '03- 12th Intern. Conf. Solid State Sensors, Actuators, Microsystems, p. 356-359, 2003.

[17] S. Hoen, et. al., "A High-Performance Dipole Surface Drive for Large Travel and Force," Transducers '03- 12th Intern. Conf. Solid State Sensors, Actuators, Microsystems, p. 344-347, 2003.

[18] Culpepper, ML, Anderson, G, "Design of a low-cost Nanomanipulator which utilizes a monolithic, spatial compliant mechanism", Prec Eng 2003.

[19] D. Niarchos, "Magnetic MEMS: Key Issues and Some Applications," Sensors and Actuators: A, 109, p. 166-173, 2003.

[20] J. Choi, et. al., "Electromagnetic Micro X-Y Stage for Probe-based Data Storage," J. Semiconductor Tech. and Science, 1, p. 84-93, 2001.

[21] H. Rothuzien, et. al., "Fabrication of a Micromachined Magnetic XYZ Scanner for Parallel Scanning Probe Applications," Microelectronic Engineering, 53, p. 509-512, 2000.

[22] H. Miyajima, et. al., "A MEMS Electromagnetic optical Scanner for a Commercial Confocal Laser Scanning Microscope," J. Microelectromechanical Systems, 12, p. 243-251, 2003.

[23] J. J. Bernstein, et. al., "Electromagnetically Actuated Mirror Arrays for Use in 3-D Optical Switching Applications," J. Microelectromechanical Systems, 13, p. 526-535, 2004.

[24] J. H. Comtois, et. al., "Applications for Surface-Micromachined Polysilicon Thermal Actuators and Arrays," Sensors and Actuators: A, 58, p. 19-25, 1997.

[25] L. Que, et. al., "Bent-Beam Electro thermal Actuators – Part I: Single Beam and Cascaded Devices," J. Microelectromechanical Systems, 10, p. 247-254, 2001.

[26] D. Yan, et. al., "Design and Modeling of a MEMS Bidirectional Vertical Thermal Actuator," J. Micromech. and Microeng., 14, p. 841-850, 2004.

[27] L. Que, et. al., "Bent-Beam Electro thermal Actuators – Part II: Linear and Rotary Motors," J. Microelectromechanical Systems, 10, p. 255-262, 2001.

[28] Ph. Luginbulh, et. al., "Piezoelectric Cantilever Beams Actuated by PZT Sol-Gel Thin Film," Sensors and Actuators: A, 54, p. 530-535, 1996.

[29] D. L. DeVoe, et. al., "Modeling and Optimal Design of Piezoelectric Cantilever Microactuators," J. Microelectromechanical Systems, 6, p. 266-270, 1997.

[30] M. S. Weinberg, "Working Equations for Piezoelectric Actuators and Sensors

[31] C. W. Wong, et. al., "Analog Tunable Gratings Driven by Thin-Film Piezoelectric Microelectromechanical Actuators," Applied Optics, 42, p. 621-626, 2003.

[32] W.P. Robbins, et. al., "Design of Linear-Motion Microactuators using Piezoelectric Thin Films," J. Micromech. and Microeng., 1, p. 247-252, 1991.

[33] M. A. Dubois, et. al., "PZT Thin Film Actuated Elastic Fin Micromotor," IEEE Transactions on Ultrasonics, Ferroelectrics, and Frequency Control, 45, p. 1169-1177, 1998.

[34] P. Cusin, et. al., "Compact and Precise Positioner based on the Inchworm Principle," J. Micromech. and Microeng., 10, p. 516-521, 2000.

[35] N. J. Conway, et. al., "Large-Strain, Piezoelectric, In-Plane Micro-Actuator," 17th Intern. Conf. on MEMS, p. 454-457, 2004.

[36] S. L. Miller, et. al., "Failure Modes in Surface Micromachined Microelectromechanical Actuators," 36th Annual International Reliability Physics Symposium, p. 17-25, 1998.

DEVELOPMENT OF A MICRO SCREW THREAD AND A MICRO GEAR COILED EXTRA FINE WIRES

Satoshi Honda
Tokyo Metropolitan Institute of Technology

1. Introduction

Micro-mechanical parts for a micro-machine are mostly produced by two methods of a photolithography1) 2) or an ultra-precise milling3). If we choose the photolithography method to make the micro parts, we can produce a lot of the micro-mechanical parts at a time like IC manufacturing; also, the parts are fabricated into the micro-machines through the processes of multi-layered deposition/electroforming and etching of sacrificial layers. However, the parts are shaped into a planar figurer with constant thickness, and their materials are selected from a few materials example of poly-silicon or tungsten. Moreover, the method requires photolithography equipments for IC manufacturing systems; besides, their equipments must be kept in a clean room. The price of the lithography equipments is over several million dollars and running cost for the clean room runs up to considerable sum. Therefore, the researchers working on the development of the micro-machines which parts are produced by the photolithography method are only a handful of researchers in a few research institutes.

If we choose the ultra-precise milling method to make the micro parts, we can produce only one micro part in one manufacturing cycle; also, the part is not fabricated into the micro-machine. Nevertheless, the micro part is shaped into three-dimensional shape by CNC (computerized numerical control) machine tool with CAD/CAM system, and their materials are selected from many materials. However, the method requires a super-precision CNC machining center to enable to control five-axis machining simultaneously; besides, the CNC machining center needs diamond tools which cutting edges are fabricated to special profiles with the accuracy of sub-micrometer. The price of the super-precision CNC machining center is over several million dollars. Therefore, advanced researches for the micro-machine which parts are produced by the ultra-precise milling method are carried on the shoulders of limited researchers.

Many researchers and engineers wait for the third method to developed micro-mechanical parts with simple and inexpensive processes and without special equipments. A novel method to make the micro mechanical parts utilized extra fine wires was thought up4). In this paper, a micro mechanical system composed by the micro-screw and the micro-nut is developed, and an external micro gear and an internal micro gear utilized extra fine wires are developed, also rotations of gear trains are confirmed by experiments.

2. Micro screw and Micro nut utilized extra fine wires

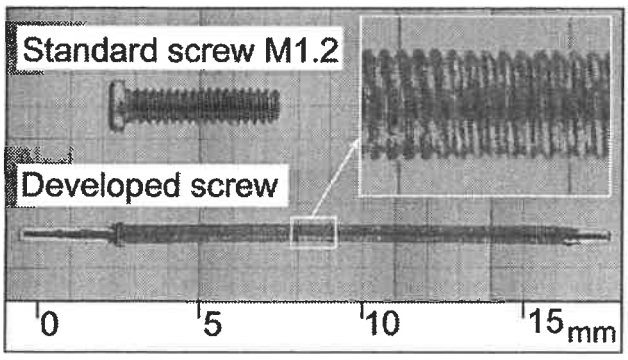

Figure 1. Micro screw utilized extra fine wires and the standard screw of M1.2.

The micro screw utilized extra fine wires and the standard screw of M1.2 are shown in figure 1. The micro screw is made by brazing an extra fine wire which is coiled around a needle pin. The micro screw has following dimensions; its major diameter is 0.6 millimeters, its pitch is 0.1 millimeters (i.e. 100 micrometers), and its length of threaded portion is 14 millimeters. Just for reference, the standard screw of M1.2 has following dimensions; major diameter is 1.2 millimeters, its pitch is 0.25 millimeters (i.e. 250 micrometers), and its length of threaded portion is 6 millimeters.

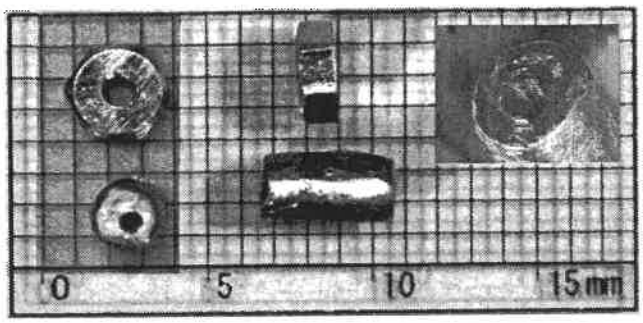

Figure 2. The micro nut utilized extra fine wires and the standard nut of M1.2.

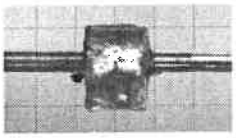

Figure 3. Fitting the micro nut and the micro screw.

The micro nut utilized extra fine wires and the standard nuts of M1.2 are shown in figure 2. The nut utilized extra fine wires is made by brazing an extra fine wire which is coiled on the inside of a small tube. The micro nut has following dimensions; its major diameter is 0.65 millimeters, its pitch is 0.1 millimeters (i.e. 100 micrometers), and its thickness is 4 millimeters. Just for reference, millimeters. The micro nut utilized extra fine wires and the standard nut of M1.2 has following dimensions; its major diameter is 1.2 millimeters, its pitch is 0.25 millimeters (i.e. 250 micrometers), and its thickness is 1.2 millimeters.

3. Micro mechanical system composed by the micro-screw and the micro-nut

3-1. Micro stage

A micro-stage composed by the micro-screw and the micro nut is developed as shown in figure 3. and figure 4. The micro screw with pitch of 100 micrometers acts as a lead screw of the stage, and the micro nut with pitch of 100 micrometers acts as a driving nut of the stage. An angle plate is attached to the micro nut for restraining rotations of the nut. The driving nut travels 100 micrometers by one turn of the micro screw. Position accuracy of the stage was followings: the mean travel of strides in which the micro screw rotated one turn was 103.3 micrometers, standard deviation of the strides (i.e. 3σ) was 1.9 micrometers.

3-2. Screw-worm mechanism

A screw-worm mechanism composed by the micro-screw, the screw-worm gear is developed as shown in figure 5 and figure 6. The screw-worm gear consists of the stander screw of M2 and a flexible screw in which the extra fine wire is brazed around a flexible wire made by same manufacturing method for the micro screw. The flexible screw is coiled and is brazed along a groove of the standard screw. The screw-worm gear is moved to its axial direction with spiral motion guided to the standard nut of M2 by the rotation of the micro screw. Each pitch of the micro screw and the flexible micro screw is 400 micrometers, and reduction ratio between the micro screw and the screw-worm gear is 1/34.5. Therefore, travel distance becomes 11.6 micrometers in one turn of the micro screw because the pitch of the

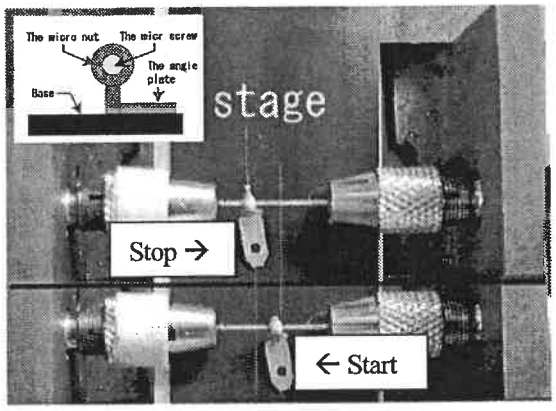

Figure 4. The micro stage.

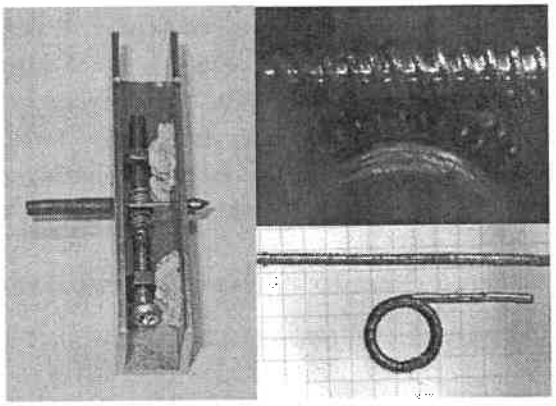

Figure 5. The micro stage.

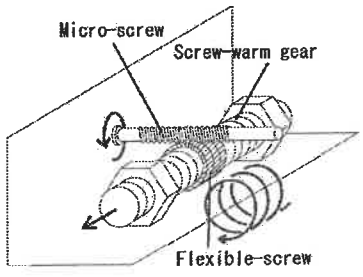

Figure 6. Structure of the screw-worm mechanism.

standard screw of M2 is 400 micrometers and travel distance is 400/34.5 micrometers.

4. The external micro gear and the internal micro gear utilized extra fine wires

The external micro gear and the internal micro gear utilized extra fine wires are shown in figure 7. Pitch of these gears is 400 micrometers. Module of the gears is 127.3 micrometers.

The external micro gear utilized extra fine wires are made through following processes as shown in figure 8. Firstly, a needle pin to be hardly soldered is prepared. We used a hypodermic needle as the needle pin. The pin is made of stainless steel and is hardly soldered. Its diameter is 800 micrometers. Secondly, an extra fine wire to be firmly soldered is closely coiled around the needle pin. We used a tinning copper wire as the extra fine wire to be firmly soldered and its diameter is 200 micrometers. Thirdly, the extra fine wires to be firmly soldered and the extra fine wires to be hardly soldered are arranged around the coiled needle pin. We used the tinning copper wire as the wire to be firmly soldered and used a tungsten wire as the wire to be hardly soldered. Both diameters of the wires are 200 micrometers. Fourthly, these wires are bound by the extra fine wire to be hardly soldered. Fifthly, the bound and coiled needle pin is soaked in melted solder, and the wire to be firmly soldered is brazed around the coiled needle pin, yet the wire to be hardly soldered is not brazed. Finally, the wire to be hardly soldered is removed, and the wire to be firmly soldered is remained as teeth of the micro gear. The needle pin is removed from the coiled and brazed wire. The coiled and brazed wire forms a hub of the gear.

We coiled and removed the wires by hand. The solder consists of 50 percent tin (Sn) and 50 percent lead (Pb).

The internal gear utilized extra fine wires are made through almost same processes as shown in figure 8. We use a little thick pin as the substitute of the needle pin. On coiling process as shown in figure 8-(2), the extra fine wire to be hardly soldered is closely coiled around the needle pin. After the binding process as shown in figure 8-(4), a the bound and coiled thick pin is inserted in a ring and is soaked in melted solder. Finally, the wires to be

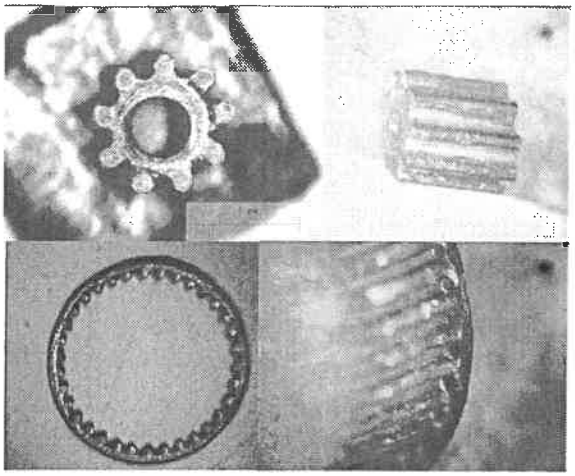

Figure 7. The external micro gear and the internal micro gear utilized extra fine wires.

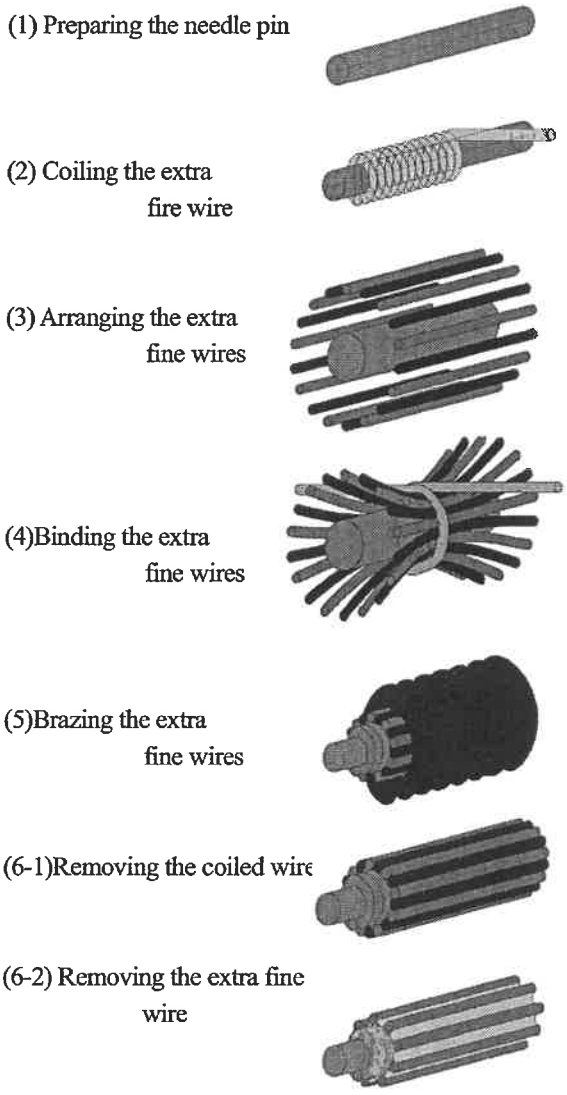
(1) Preparing the needle pin
(2) Coiling the extra fire wire
(3) Arranging the extra fine wires
(4)Binding the extra fine wires
(5)Brazing the extra fine wires
(6-1)Removing the coiled wire
(6-2) Removing the extra fine wire

Figure 8. Making processes for the micro gear.

hardly soldered and the a little thick pin are removed. The internal micro gear is manufactured.

5. Rotational test for the gear trains

A gear train engaged two external gears was rotated in the experiments as shown in figure 9-(1). Drive gear having nine teeth rotated with the angular velocity of 1000 rpm, and the other gear having eleven teeth had been rotated over 10 minutes. Other gear train engaged the external gear and the internal gear was also rotated over 10 minutes as shown in figure 9-(2). These gears have not broken yet.

The external micro gear and the internal gear have a same module of 127 micrometers (i.e. their pitches are same length of 400 micrometers).

6. An external micro gear constructed around a tube mesh.

The external micro gear constructed around the tube mesh is shown in figure 10. We used a tube mesh as the substitute of the coiling wire in figure (8)-2, so the melted solder permeated enough between the extra fine wire and the tube mesh. The extra fine wire that composes gear teeth was strongly brazed to the tube mesh that becomes the gear hub.

7. Prompt results of other trial micro parts utilized the extra fine wires

A micro stage supported by six linkages is shown in figure 11-(1). The linkages were made by coiling and knotting of the extra fine wire. A slider crank mechanism is shown in figure 11-(2) as an application of the linkage.

9. Conclusions

The micro mechanical systems composed by the micro-screw and the micro-nut are developed, and the external micro gear and the internal micro gear utilized extra fine wires are developed, also rotations of the gear trains were confirmed by experiments.

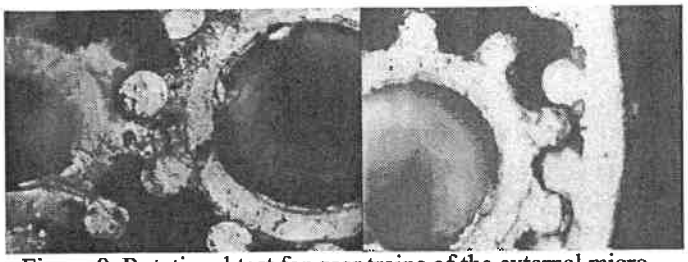

Figure 9. Rotational test for gear trains of the external micro gears and the internal micro gears.

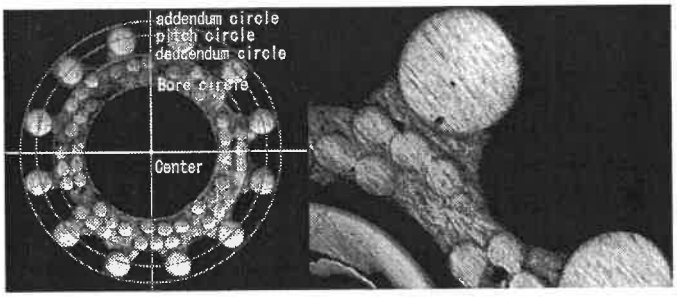

Figure 10. The external micro gear constructed around the tube mesh.

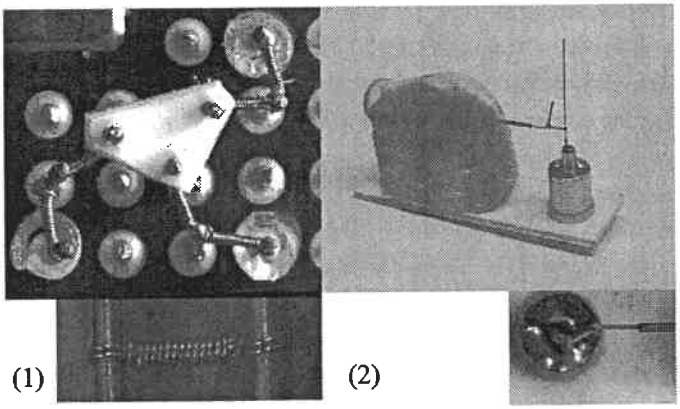

Figure 11. The micro stage and slider crank mechanism.

References

1)Y. C. Tai, et al.: "IC-processed electrostatic synchronous micromotors", Sensors & Actuators, Vol.20(1989), pp49-56.

2)W. Menz, et al.: "The LIGA Technique –a Novel Concept for Microstructures and the Combination with Si-Technologies by Injection Molding", Proc. of IEEE Workshop on Micro Electro Mechanical Systems, Nara, Japan Feb. (1991), pp69-73.

3) Y.Takeuchi, K. Sawada and T.Sata: "Ultraprecision 3D Micromachining of Glass", Annals of the CIRP, Vol.45/1 (1996) , pp401-404.

4)Satoshi Honda: "Development of a micro screw thread and a micro gear utilized extra fine wires, Proc. of 18th annual meeting of ASPE, October 26-30th, Portland Oregon U.S.A, pp208-211 (2003).

Nano Structure Patterning Using a Scanning Nanopipette Probe Microscope

Futoshi IWATA, Yosuke SUMIYA, Shinichirou NAGAMI and Akira SASAKI
Department of Mechanical Engineering,
Faculty of Engineering, Shizuoka University
3-5-1, Johoku, Hamamatsu, 432-8561, Japan
Phone: +81-53-478-1072, Fax: +81-53-478-1072
E-mail: tmfiwat@ipc.shizuoka.ac.jp

Key words: Micropipette probe, SPM, Shear-Force, surface fabrication

1. Introduction

Scanning Probe Microscopes (SPMs) are well known as surface imaging techniques at nanometer scale resolution. SPM can be used not only for surface observation but also for local surface fabrication. The typical fabrication technique using SPM is directly scratching on surfaces with the probe. However in this case, high loading force must be applied between the probe and the surface, which induces some undesirable problems such as cutting particles and probe edge wearing. Therefore, other fabrication techniques are required.

In this paper, we report a novel technique of nanometer-scale fabrication using a scanning shear-force microscope. A pulled micropipette has been employed as a novel probe, "micropipette probe" for SPMs. The micropipette probe was used for delivering materials to any points on the substrate surface. Using the micropipette probe filled with organic solvent, polymer surfaces could be fabricated. The fabrication properties of sub-micrometre dots on the polymer surfaces were systematically investigated. Furthermore, local metal plating was also achieved using the micropipette probe filled with metal ionic electrolytes. Dot array and line pattern were sequentially fabricated on the Si substrates.

2. Experimental method

Figure 1 shows a schematic diagram of a scanning shear-force microscope using a micropipette probe for local surface fabrication. This scanning probe microscope system was constructed by us. A capillary grass tube, having 1.0 and 0.6 mm outer and inner diameters, respectively, was thermally pulled using a filament-type micropipette puller (Narishige, PD-5). The diameter of the probe aperture was approximately 200 nm as shown in Fig. 2. The micropipette probes could be filled with any kind of liquids for delivery and fabrication. In regard to the topographical observation of the surface, the shear-force control technique was employed. The pipette probe was fixed on a dither PZT and oscillated laterally at its resonant frequency of approximately 20 kHz.

As for the polymer surface fabrication, polycarbonate surfaces were fabricated using the pipette probe filled with organic solvent of 1,4-dioxane (Wako Co. Ltd). On the other hand, as for the local metal plating, copper sulfate was filled into the pipette probe. Cu dots were electrochemically deposited on Si surfaces.

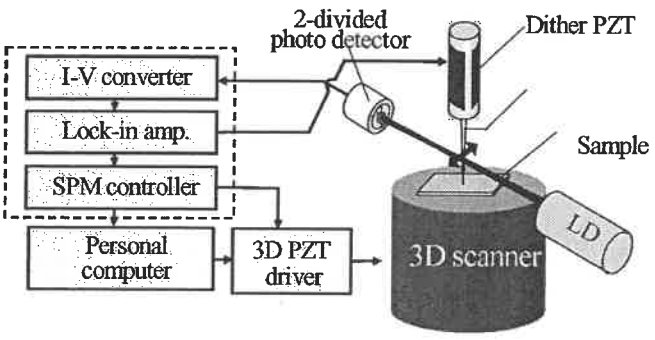

Fig. 1 Experimental setup of the micropipette probe microscope

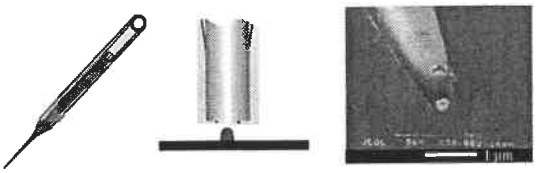

Fig. 2 Micropipette probe

3 .Experimental result

3.1 Surface observation

In order to observe the surface using the solvent-filled micropipette probe, a significant distance between the probe and the surface should be maintained so as to avoid undesirable surface distortion. In this experiment, the probe-surface distance was maintained by feedback control at a set-point ratio $r_{sp} = A_{sp} / A_0$, where A_{sp} is the set-point amplitude and A_0 the free amplitude. Figure 3 shows the CD surface observed using the solvent-filled probe at the set-point ratio $r_{sp} = 0.9$. As shown in this figure, the pit patterns of the CD surface are clearly observed without any surface modification. Even after several surface scanning, topographical distortion was hardly observed. Thus, it is possible to observe the surface with the micropipette probe at the solvent-filled state.

3.2 Polymer fabrication[1]

Figures 4 show the width and height of the fabricated dots as a function of the set-point ratios. Those fabrications were carried out at the same pausing time (1 s) at the probe approaching states. The height and width of the dot patterns decreases with increases the probe-sample distance. Below a set-point ratio of 0.6, dot patterns could be fabricated. The diameter of the smallest dot was 200 nm, which corresponds the aperture size of the probe (see in the inset). Thus it is possible to fabricate the dot structure controllably by adjusting the shear-force distance. On the other hand, above the set-point ratio of 0.6, no structures were confirmed, which means that surface observation can be carried out without any topographical distortion at set-point ratios above 0.6. Thus, it is possible to switch between the fabrication mode and the

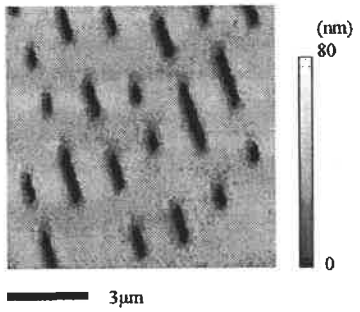

Fig. 3 Topographical image of CD surface observed using the solvent filled probe. The image was obtained at the set-point ratio of 0.9.

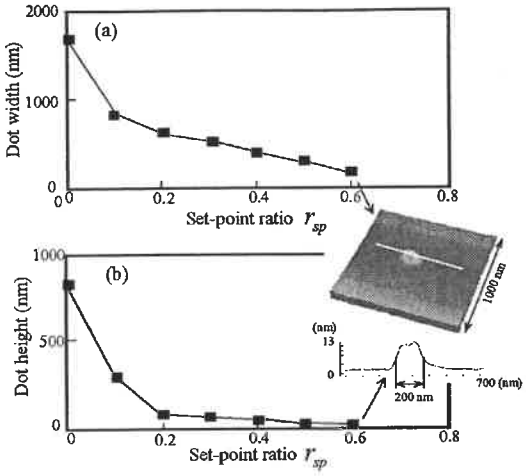

Fig. 4 Width and height of the fabricated dots as a function of the set-point ratios. The image of the smallest structure is shown in the inset.

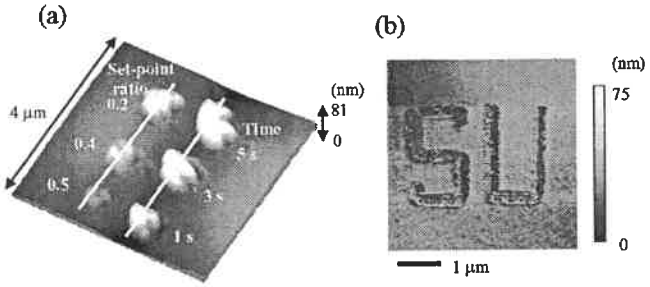

Fig. 5 Dot array and line patterns sequentially fabricated during surface scanning by shear-force distance control. (a)Dot array modified by changing the modification time and distance control. (b) Line pattern of alphabet SU (Shizuoka Univ.)

observation mode by controlling the shear-force distance by adjusting only the set-point ratios ($r_{sp} \leq 0.6$ for fabrication and $r_{sp} = 0.9$ for observation).

Figure 5(a) shows the dot array sequentially fabricated during surface scanning by modulating between the probe-surface distance and pausing time under shear-force distance control. The dot size could be controlled by changing the set point ratio and pausing time for the fabrication. Figure 5(b) shows letter patterns fabricated by line scanning. The letter patterns of "SU", the initials of Shizuoka University, were clearly fabricated.

3.3 Metal plating[2]

As another performance, local metal plating was carried out using the pipette probe system. For the fabrication process, the Si surfaces were first imaged in shear-force mode to find a suitable location for lithography, and then the pipette probe was brought into nearly contact with the surface by reducing the set point ratio of $r_{sp} = 0.1$, which resulted in forming electrolyte meniscus between the pipette probe and the surface. At the condition, a positive DC bias was applied on the electrode wire inserted into the pipette probe. During the fabrication process, $CuSO_4$ dissolved in the aqueous solution is electrochemically reduced from Cu(•) to Cu(0) metal at the cathodic Si surface (Cu^{2-} + 2e⁻• Cu) and deposits as Cu nanofeatures. After the deposition process, the topographical images were sequentially obtained using the same pipette probe at the setpoint ratio of $r_{sp} = 0.9$.

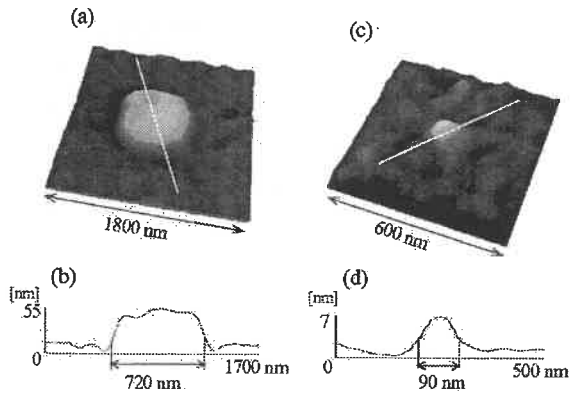

Fig. 6. Topographical images of Cu dot electrochemically deposited on the Si surface. (a) Cu island deposited with voltage of 2 V for 5 s. (b) Cross-sectional profile of the island structure in image (a). (c) Cu dot deposited with voltage of 0.2 V for 0.1 s. (d) Cross-sectional profile of the dot structure in image (c).

Figure 6(a) shows the topographic image of a Cu island formed on the Si surface. The Cu island structure was electrochemically deposited by approaching the pipette probe at the center point of the image with applying voltage of 2 V for 5 s. The circular island structure is seen at the center of the image. Figure 6(b) shows the cross-sectional profile of the island structure. The width and height of the island structure are 720 nm and 50 nm, respectively. The diameter of the island structure is much larger than that of the aperture of the pipette probe. Thus the deposition area might expand around the probe in the case of large amount of deposition. The amount of the Cu deposition depends on the deposition parameters of the electrochemical process. Thus, a smaller structure might be fabricated by reducing the voltage and deposition time. Figure 6(c) shows a Cu dot deposited with applying voltage of 0.2 V for 0.1 s. The dot size is much smaller than that of the image in Fig. 6(a). The cross-sectional profile of the dot structure is shown in Fig. 6(d). The width of the dot is 90 nm and height is 6 nm.• The amount of deposited metal could be varied by the deposition conditions. The dot shown in Fig. 6(c) was the smallest one confirmed in this experiment, which means the micropipette probe techniques allow us to deposit dot materials in a diameter of less than 100 nm.

In order to evaluate the lithography technique of local metal plating, dot array deposition was performed. Figure 7 (a)

shows the dot array of the Cu deposition. The dots was sequentially fabricated during surface scanning by varying the probe-surface distance under shear-force control. At the fabrication points, the probe was approached to the surface for the deposition mode ($r_{sp} = 0.1$) and then withdrawn to the significant distance ($r_{sp} = 0.9$) for stepping to the next deposition point. Each Cu dot was deposited with applying voltage of 1 V for 1 s. As shown in this image, the dots could

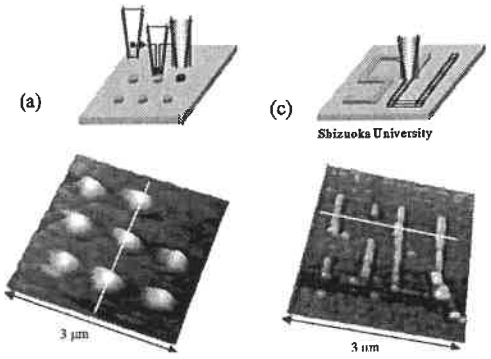

Fig. 7 (a) Dot array continuously deposited during surface scanning by changing the probe-surface distance under shear-force control. (b) Cross-sectional profile of the dots structure. (c) Line patterns of the alphabets "SU". (Initials of Shizuoka University) deposited by line scanning. (d) Cross-sectional profile of the line patterns.

be successfully deposited on the Si surface. Figure 7(b) shows the cross-sectional profile of the dots structure. Typical width of the island structure is 350 nm and its height is 23 nm, respectively. All dots indicate almost the same size, which means the plating technique presented here indicates high reproducibility of the electrochemical deposition. The micropipette probe provides small amount of electrolyte droplets on the surface passing through the probe aperture, which sequentially produces Cu dots as a result of electrochemical reaction. Figure 7(c) shows line patterns fabricated by line drawing process. The alphabet patterns of "SU", the initials of Shizuoka University, were successfully fabricated.

4. Conclusion

Novel fabrication techniques of local surfaces were performed using a scanning probe microscope with various liquids filled micropipette probes. Polymer surfaces could be fabricated using an organic solvent filled pipette probe. Local meal plating could be realized using an electrolyte filled probe. These fabrication techniques might be conceivable for many fields such as precision engineering and biological manipulations.

References

[1] F. Iwata, Y. Sumiya, S. Nagami and A. Sasaki: "Submicrometer-scale fabrication of polycarbonate surface using a scanning micropipette probe micrscope", Nanotechnology 15 (2004) 422-426.

[2] F. Iwata, Y. Sumiya and A. Sasaki: "Nanometer-Scale Metal Plating Using a Scanning Shear-Force Microscope with an Electrolyte-Filled Micropipette Probe", Jpn. J. Appl. Phys 43 (2004) 4482-4485.

MICRO TUBE MANUFACTURING METHOD OF TUBE-SHAPED DILATATION MICROMANIPULATOR MADE OF SHAPE MEMORY POLYMER

Daiki Kamiya[a], Yoshihiro Gamo[b], Mikio Horie[a]
[a]Precision and Intelligence Laboratory, Tokyo Institute of Technology,
4259-R2-14, Nagatsuda-cho, Midori-ku, Yokohama, Kanagawa, 226-8503, Japan
dkamiya@pi.titech.ac.jp, mahorie@pi.titech.ac.jp
[b]Graduate student• Ðept. of Precision Machinery Systems, Tokyo Institute of Technology

1 Introduction

There are shape-memory materials among advanced functional materials which have been developed recently. Above all, shape-memory alloys and a shape-memory polymer are proceeding toward practical utilization. A shape-memory polymer has low density compared to shape-memory alloys, and it is easy to deform as well as suitable for microminiaturization. A notable property of the shape-memory polymer is that its recovery distortion is more than 100 % while that of shape-memory alloys is only 6~8%[1]-[5]. This also indicates that a significant deformation of the shape-memory polymer is possible. The shape-memory polymer can be considered to be one of the most suitable materials for a micromanipulator, making use of the deformation property of materials.

This study presents a tube-shape dilatation micromanipulator made of a shape-memory polymer, which is suitable for microminiaturization. The manufacturing process of the tube and its heater is shown to explain the characteristics of the manipulator, as well as to point out its problems. Moreover, another new method to manufacture the tube of a uniform wall thickness is examined and presented to resolve the problems.

2 A proposal of a dilatation micromanipulator made of a shape-memory polymer

When a shape-memory polymer is heated and its temperature exceeds the glass transition temperature, it becomes as soft as rubber to be deformed significantly. After the temperature is lowered less than the glass transition temperature, the polymer becomes solid maintaining the changed shape. Moreover, it returns to its original shape when it is heated again and its temperature exceeds the glass transition temperature. The objective of this study is to develop a tube-shape dilatation micromanipulator 1mm in internal diameter and 100 mm long utilizing the properties of a shape-memory polymer mentioned above.

• • The manipulator proposed in this study is a tube of a shape-memory polymer to which a heater is attached as shown in Fig. 1. As shown in Fig. 2, when a part of the tube is heated with the heater and its temperature exceeds the glass transition temperature, it dilates due to the internal pressure, which causes the tube to bend. When the temperature is lowered, while maintaining the internal pressure, the changed shape is maintained. On the other hand, it restores its original shape when it is heated again, removing the internal pressure and its temperature exceeds the glass transition temperature.

• The characteristic of this micromanipulator lies in that the large elastic deformation property of a shape-memory polymer is utilized in its deformation. This micromanipulator has a lot of advantages. It is easy to manufacture and assemble as well as suitable for microminiaturization because its shape is a simple tube. The arm section and end effecter can be manufactured as a unit. It is actuated with its internal pressure without a built-in actuator, which makes microminiaturization possible. Moreover, it can be bent toward random positions or directions by devising a method of heating. Also, it can even be expanded and contracted.

3 Manufacturing of the tube

Casting, injection molding, and dip molding methods were tried and examined in manufacturing a shape-

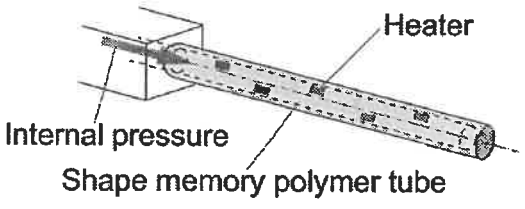

Fig. 1 • Manipulator made of SMP

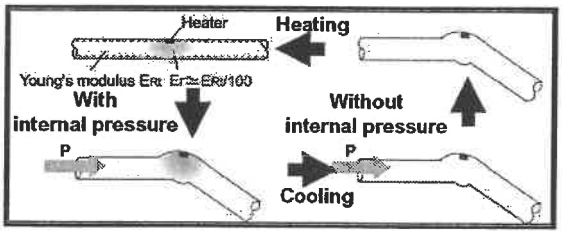

Fig. 2 Motion principle of SMP

memory tube as the body of the micromanipulator. By using the casting and injection molding methods, it was difficult to separate the tube from the moldings. Therefore, a dip molding method was adopted. The procedures are shown in Fig. 3. First, a wire was put through a Teflon tube, and a plummet was attached to the end of the wire to straighten the tube, which was dipped into a container filled with the shape-memory polymer. The tube was pulled up at a constant speed to be coated with the shape- memory polymer. After the tube was pulled out of the container, a solvent of the polymer on it was volatized to make the polymer solid. When the polymer became solid enough, the Teflon tube inside was pulled out of it, which completed the process of making a shape-memory polymer tube. An external view and a section view of the tube 1 mm in internal diameter made using the dip molding method are shown in Fig. 4.

4 Heating experiment at a joint part of the manipulator

As shown in Fig. 5(a), a type of energized heater, which makes the joint section of the manipulator, was experimentally manufactured by soldering a copper wire on a Nichrome foil 1-mm square and 20μm thick in order to examine the heating method. The heater was glued to the polymer tube mentioned above, and an actuating experiment was conducted. The relationship between the passed current and the temperature at the experiment is shown in Fig. 5(b). As a consequence, a film of the polymer tube ruptured at the end of the portion where the heater was glued.

It is conceivable that it was because a stress concentration arose in the area where hard Nichrome was glued to soft polymer, which caused an inadequate heat distribution, and the wall thickness of the tube was not uniform.

5 Problems in manufacturing a polymer tube

In manufacturing polymer tubes using the dip molding method, there were problems. Knots were sometimes generated against the axial direction of the tubes as shown in Fig. 6(a). Even if knots were not generated, the wall thickness of some tubes was not uniform and their cross sections were eccentric. It is conceivable that this could be due to the viscosity of the polymer and pulling-up speed. Also, the humidity in the manufacturing environment is considered to have an influence on the tube. As shown in Fig. 6, a whitish part was generated on some polymer tubes, which could be due to the humidity while being manufactured.

Therefore, it was decided that the viscosity of polymer, pulling-up rate, temperature and humidity should be controlled in manufacturing the tubes to resolve the problems mentioned above.

6 Dip molding equipment

A diagrammatic sketch of the new dip molding equipment is shown in Fig. 7. The equipment consists of the pulling-up segment and the environmental controlling segment.

• • Pulling-up segment: A wire sticking out of a Teflon tube dipped in the shape-memory polymer is attached to a ball screw on the mobile part of the equipment. The tube is pulled up with the ball screw actuated by a stepping motor. The tube can be pulled up at a speed between 0.001 mm/s and 1 mm/s.

• • Environmental controlling segment: A container with the shape-memory polymer in it was placed in a thermostatic chamber made of an acrylic case covered with an insulator, in which the tube was dipped and then pulled up. A heater was set in the thermostatic chamber to control the temperature inside by turning on or off the current through the heater with a thermo-comparator. Also, a fan was set to make the temperature inside the chamber

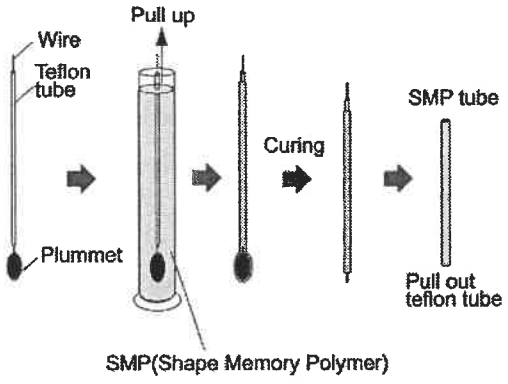

Fig. 3 Manufacturing method of tube

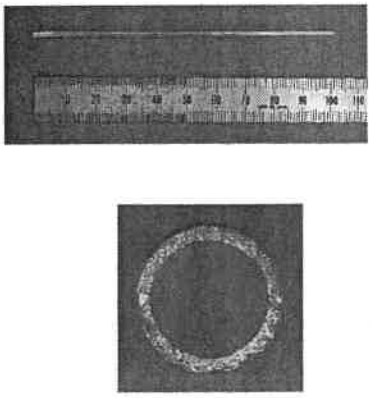

Fig. 4 Trial manufactured tube

uniform. The temperature inside the chamber can be controlled between the room temperature and 80°C. Moreover, it was confirmed that the humidity inside the chamber can be controlled below 10 % by sending nitrogen into it.

The new dip molding equipment manufactured experimentally is shown in Fig. 7. The left part of the figure shows the pulling-up segment (the upper part of the equipment) while the right part shows the thermostatic chamber as the environmental controlling segment (the bottom part of the equipment), in which the container with the shape-memory polymer is placed.

• • The pulling-up speed, V [mm/s] and the viscosity of shape-memory polymer, μ [Pa·s] were used as parameters in manufacturing the tubes because they exert an influence on the wall thickness of the tubes. By varying these parameters, the tubes were manufactured as shown in Fig. 8, and their wall thickness was measured.

7 Examination of the wall thickness of new tubes according to the pulling-up speed and viscosity of polymer

Remarkable variations of the wall thickness in the axial direction among the measurement results are investigated. In the results, the horizontal axis indicates the distance between the top end of a polymer tube and a position of each cross section of the tube examined in the experiment. Each value is the measured wall thickness.

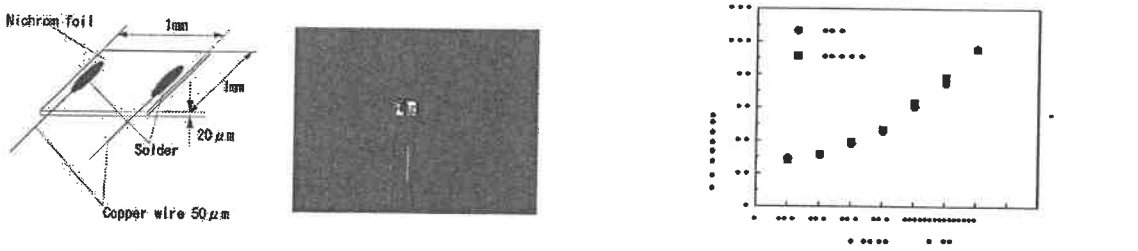

(a) Manufactured heater at the joint part (b) Relationship between current and temperature

Fig. 5 Trial manufacturing of heater

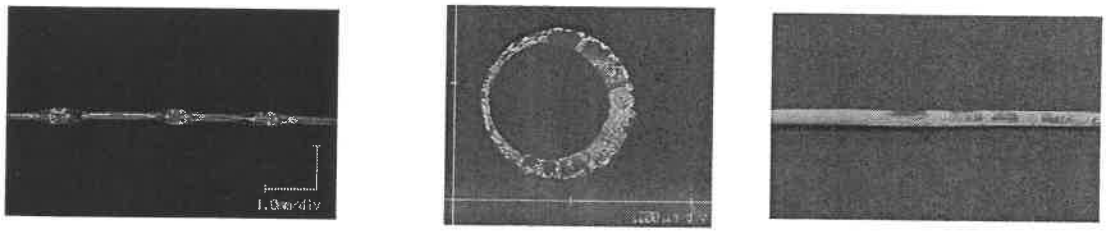

(a) Knots generated at the tube (b) Eccentricity of the tube (c) Whitish part in the tube

Fig. 6 Manufactured failure tube

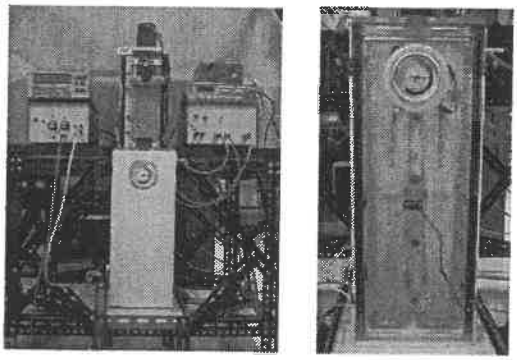

Fig. 7 Manufacturing machine of the new tube

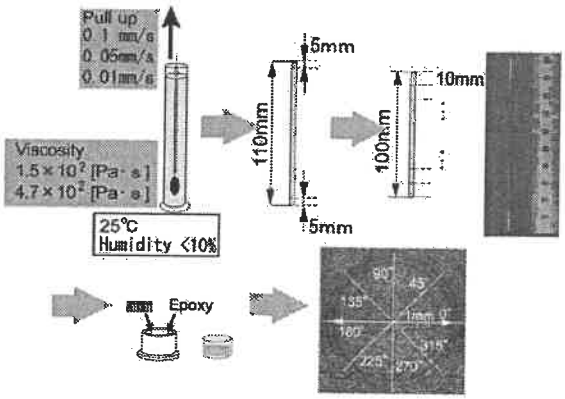

Fig. 8 New tube manufacturing method and manufactured tube

When the viscosity of the polymer is high and the pulling-up speed is fast, specifically, the viscosity is $4.7*10^2$ Pa·s, and the speed is 0.1mm/s, the wall thickness of tubes increases toward the bottom of the tube and its deviation increases from the top toward the bottom. On the other hand, the wall thickness and its deviation are constant when the viscosity is low and the pulling-up speed is slow, specifically, the viscosity is $1.5*10^2$ Pa·s, and the speed is 0.01 mm/s.

In order to compare the wall thickness of the tubes according to the different length of internal diameter, 300-μm-internal diameter-polymer tubes 30 mm long were manufactured under the same manufacturing conditions as the 1-mm-internal diameter-tubes and their wall thickness were measured. The mean value and the deviation of the wall thickness are shown in Fig. 9 along with the results of the 1-mm-internal diameter-tubes. The results of the 300-μm-internal diameter-tubes are shown in a dark color while those of the 1-mm-internal diameter-tubes are in a light color.

• Polymer tubes manufactured when the viscosity was $1.5*10^2$ Pa·s and the pulling-up speed was 0.01 mm/s were too thin to measure their wall thickness. They deformed when they were dipped in epoxy resin. It was shown that the deviation was smaller as the internal diameter was shorter. Especially, when viscosity was $4.7*10^2$Pa·s, the deviation of 1-mm-internal diameter tubes became large at a speed of under 0.05 mm/s while the deviation of 300-μm-internal diameter-tubes was small. The average wall thickness of 300-μm-internal diameter-tubes was thinner than that of the 1- mm-internal diameter-tubes. Moreover, the 100-μm-internal diameter-tubes were experimentally manufactured under the same conditions as the 1-mm-internal diameter-tubes. Finally, a 100-μm-internal diameter-tube was experimentally manufactured when the pulling-up speed was 0.01 mm/s and the viscosity was $4.7*10^2$ Pa·s. Its wall thickness was 11 μm.

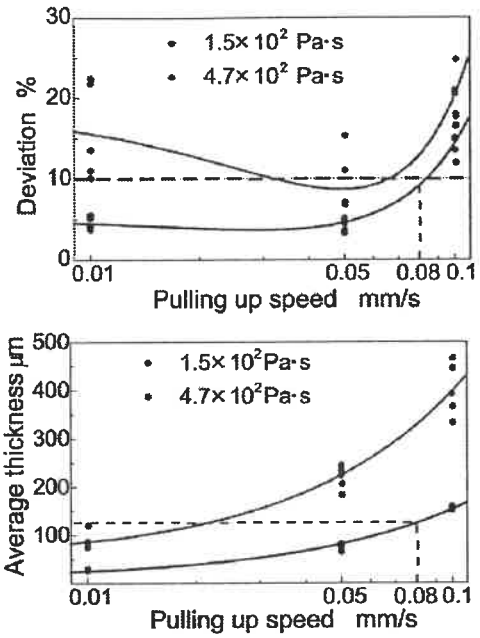

Fig. 9 Average thickness and its deviation vs. pulling up speed of the tube

8 Conclusions

We have proposed and discussed the tube-shape dilatation micromanipulator made of the shape-memory polymer and the new tube manufacturing method to obtain the constant thickness tube. In the results, we have the following conclusions.

(1) This study presented a dip molding method as a method of manufacturing shape-memory polymer tubes aiming at microminiaturization and pointed out the problem of their non-uniform wall thickness.

(2) Dip molding equipment was experimentally manufactured, while taking account of the pulling-up speed, viscosity of the polymer, temperature and humidity in the manufacturing environment.

(3) The relationship of the viscosity of the polymer and pulling-up speed with the wall thickness of tubes in manufacturing polymer tubes 1 mm in internal diameter and 100mm long was explained, and the manufacturing conditions to keep the deviation of the wall thickness below 10% were shown in this study. Under these conditions, the wall thickness was between 30 μm and 120 μm.

(4) This study indicated that manufacturing polymer tubes 300μm and 100μm in internal diameter was possible under the same conditions as manufacturing 1- mm-internal diameter-polymer tubes.

References

[1] Irie, M., 'Material development of shape memory polymer', CMC Publishing Co. Ltd. 10-6,5(2000) (in Japanese).

[2] Hayashi, S, 'Shape memory polymer', *Nikkei Mechanical*, 7-24,(1989), pp.116-120 (in Japanese).

[3] Yamamoto, E., 'Characteristics of shape memory functional plastics and its use development', *Plastics*, 38, 12,(1986), pp.107-111 (in Japanese).

[4] Tobuse, T., 'Development and Application of the shape memory polymer', *Machine Research*, 45-11, (1993), pp.136-141 (in Japanese).

[5] Tobuse, T., 'Characteristics and application of polyurethane shape memory polymer', *Machine Research*, 46-6, (1994), pp.646-652 (in Japanese).

Control method for pushpull type piezo-driven linear motion stage with smooth motion, long travel range and high resolution

Kyoung-Soo LIM[a], Daichi ABIKO[b], Sun-Kyu LEE[a], Masato AKETAGAWA[b], Koji TAKADA[c], Yutaka MUNAKATA[d], Jinmo LEE[d], Kohsei TERAO[d], Takashi MURAKI[d], Kenji MAGARA[d], Masashi ONO[d]

[a] Department of Mechatronics, Kwangju Institute of Science and Technology, 1 Oryong-dong, Buk-gu, Gwangju City 500-712, Republic of Korea
[b] Department of Mechanical Engineering, Nagaoka University of Technology, 1603-1 Kamitomioka, Nagaoka-City, Niigata-Prefecture, 940-2188 JAPAN
[c] Nagaoka National College of Technology, 888 Nishikatakai, Nagaoka, Niigata 940-8532, Japan
[d] CHUO PRECISION INDUSTRIAL CO., LTD. 112-5 Kawa, Ageo-City, Saitama-Prefecture, 362-0048 JAPAN

Abstract

This paper presents new control methods to reduce vibration errors, which occur in clamping operation. Firstly, optimal clamping force is adjusted experimentally. Secondly, optimal control parameters of PID control are determined using a genetic algorithm. The new parameters are compared with ones from the conventional method. Finally, a power supply procedure for feed and clamp actuators is proposed and tested to reduce interference between push-pull feed motion. The proposed methods improve the vibration errors significantly.

Key words: Piezoelectric actuator, Smooth motion, Nanometer, Inchworm, PI control, Genetic Algorithms.

Introduction

Development of precision measurement/ control technology in the Precision Engineering has made an ultra-precision positioning whose displacement resolution is 0.1 nm since 1990s [1]. Relative uncertainty to quantitatively show density between resolution and stroke range is expressed to ratio of resolution and stroke range. Nowadays, an attained uncertainty level in the Precision Engineering exists in the range of 10^{-3} and 10^{-6}. It is real condition that Precision Engineering of the 10^{-9} uncertainty (BUPE: Billionth Uncertainty Precision Engineering) is urgently required [2]. Therefore, it is required the stage that has a high resolution and long stroke range. In order to realize this requirement, many types of control methods have been introduced so far. For example, friction drive, ball screw, dual servo type and inchworm type are representative. Inchworm type is ultra feed device that overcome the limited displacement in combination with fine displacement of PZT and motion apparatus. This type is controlled by electrostatic clutch mechanism to improve motion controllability and force transmission. This paper has developed a pushpull type linear motion stage that is composed of two clamp and two feed actuators. The newly developed stage provides continuous motion, but vibration error still exists during clamping and feeding operations [3]-[6].

This paper presents new control methods to reduce the vibration error. At first, the optimal control parameters of PID control are determined through the Genetic Algorithm, and compared with the conventional method. Secondly, the optimal clamping force is applied that affects strongly on the residual vibration. The suggested methods improved the vibration error significantly.

Pushpull type motion stage

Existing inchworm stage that is composed of one feed piezo actuator and two clamp actuators is not continuous but stepwise.

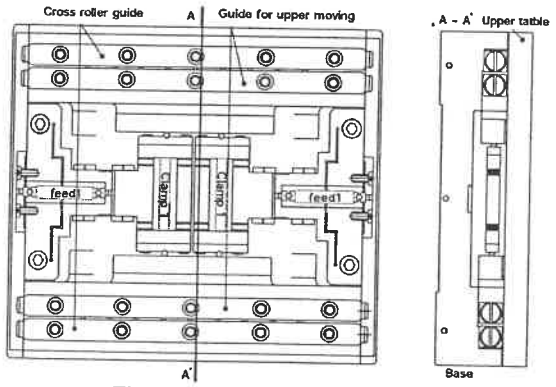

Fig. 1 Inner side of inchworm stage

In order to overcome, authors have developed a pushpull type linear motion stage that is composed of two clamp and two feed actuators. The inner side of pushpull stage is indicated in Fig. 1.

Principle of stage motion

The two clamp piezo actuators (clamp1, clamp2) are linked with the outer two feed piezo actuators (feed1, feed2) with lateral symmetrical fashion. Each piezo actuator is fixed on the base. The moving part is clamped on the clamp piezo actuators, and actuated by the feed piezo actuators along the guide. The operation procedure includes simultaneous extending and shrinking of the two feed piezo actuators in opposite polarities in cooperation with clamping and unclamping action of the clamp piezo actuators. The pushpull stage is actuated by motion of 6 steps in 1 cycle. The cyclic repetition enables the moving table to move long stroke range with smooth and continuous fashion, theoretically.

The principle of stage driving is indicated in Fig. 2. **Step 1:** Clamp 1 and Clamp 2 PZTs are clamped, and Feed 1 and Feed 2 keep half elongation. **Step 2:** Clamp 1 unclamps and the moving table is moved by shrink of Feed 2. **Step 3:** Feed 1 shrinks immediately and Feed 2 continuous to shrink. **Step 4:** Clamp 1 clamps the moving table, and Feed 1 extends. The Clamp 2 unclamps **Step 5:** Feed 2 extends immediately. **Step 6:** Clamp 2 clamps, and the moving table is moved by extension of Feed 1 and shrink of Feed 2.

At here, extension of Feed 1 and shrink of Feed 2 provides Push and Pull motions, respectively. Through these repeated motions, the stage moves continuously [7].

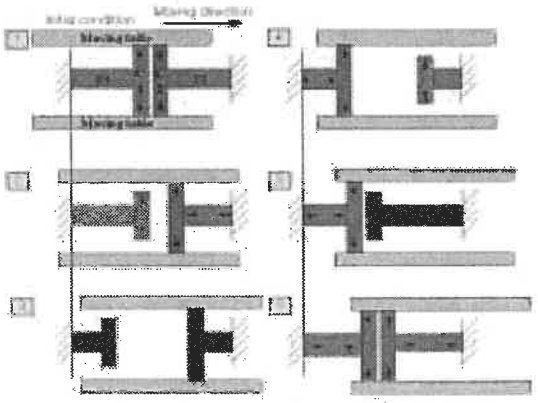

Fig. 2 Principle of Pushpull drive

Optimal PID parameters

The population is typically chosen over 30, sometimes over 1000. The lower boundary of a population size that guarantees with 95% probability, that allele loss does not occur in the first generation, is 10[8]-[10]. Crossover rates should be kept high, generally between 0.7 and 0.9, since recombination produces highly fitted chromosomes that are different from their parents, yet retain some of their parents' characteristic. A high probability of mutation rate may increase population diversity, but will decrease average population fitness, hence typical mutation rates range from 0.01 to 0.05[11]-[13].

The procedure of the control loop indicated in Fig. 3 is as follow:

Step 1: Initial population about each gain K_p, K_i, and K_d is provided randomly. At here $y(t)$, M_p, and T_s represent input, overshoot, and settling time respectively. r and y mean reference input and output of plant respectively.

Step 2: The gotten population is given to the system, and $y(t)$, M_{py}, and T_{sy} are received. And then the response is calculated by the system reference.

Step 3: New population of string about PID gains is given and converted into decimal number.

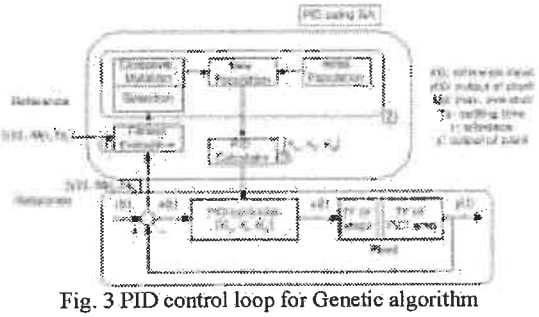

Fig. 3 PID control loop for Genetic algorithm

This cycle is repeated as much as generation number. Plant is given by the transfer functions of stage and PZT amp that are obtained from experiment. The transfer functions of stage and PZT amp are $G_{stg} = \frac{1.3}{1.3s^2 + 247s + 3.9\times10^6}$ and $G_{Amp} = \frac{7.5}{0.88\times10^{-3}s + 1}$.

Using this Genetic Algorithm, it could be determined the PID parameters such as K_p=0.15, K_i=100, and K_d=0. Fig. 4 shows the comparison between the new results and the existing one.

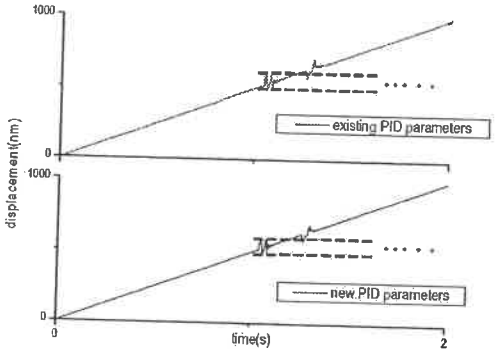

Fig. 4 Comparison results between existing and calculated PID gains

From the result, it could be reduced clamping vibration from 114nm to 100nm using PID parameters got from genetic algorithm.

Optimal clamping voltage

Clamping actuations are considered as major existing sources in the pushpull operations. Fig. 5 shows a clamping mechanism design. Clamping is achieved by PZT extension through the ball contact.

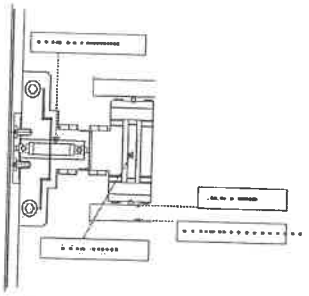

Fig. 5 Clamping mechanism design

The optimal clamping force not only provides rigidness appropriately but minimizes vibration excitation. To investigate the optimal input voltage of PZT, the resonant frequency of the displacement according to the clamp voltage was observed. As shown in the Fig. 6, sweep sign signal is provided to the Feed 1 PZT via function generator while the clamping voltage to the clamping 1 PZT. The signal was changed from 0.1 Hz to 1000 Hz for 15 sec with amplitude of 5V for each clamp voltage, which was changed from 40V to 150V. The displacement of stage was measured by the laser interferometer during those operations.

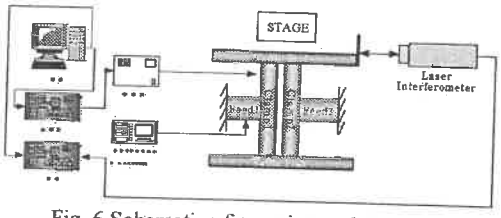

Fig. 6 Schematic of experimental equipment

Using the displacement measurements, it could be obtained the corresponded resonant frequency of each clamping voltage. And then relationship between this natural frequency and real vibration error was compared when the clamping voltage is changed. Fig. 7 illustrates about the relationship.

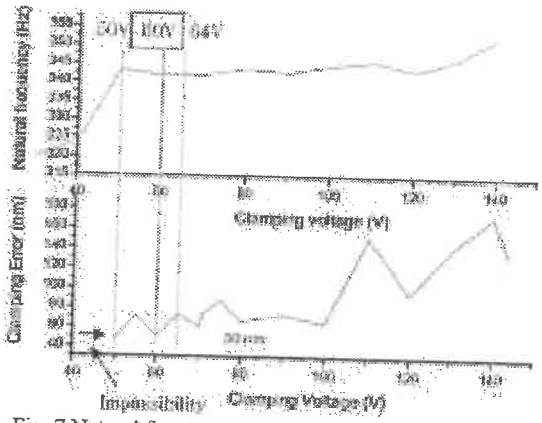

Fig. 7 Natural frequency and measured real error about each clamping voltage

As indicated in Fig. 7, the resonant frequency almost converged over 50V.

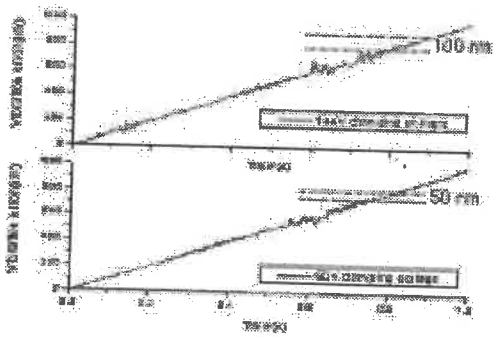

Fig. 8 Comparison of vibration error due to clamping voltage

It indicates that 50V is enough for the clamping rigidness to provide the feed actuation of the stage. On the consideration of stable clamping, the optimal voltage was applied 60V for this stage.

As a result, the vibration error was reduced from 100nm to 50nm by applying the optimal

clamp voltage. The results are compared in Fig. 8.

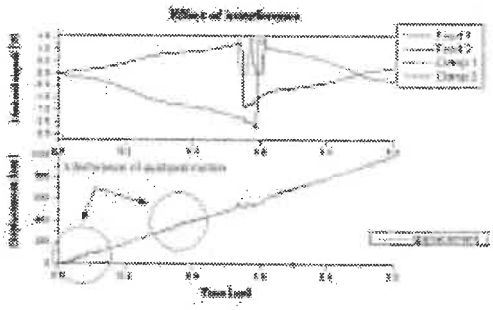

Fig. 9 Existing driving signal

As indicated in Fig. 9, existing signal has the interference during pushpull motion. In order to overcome this problem, this paper presents new driving signal which remove the interference of pushpull motion.

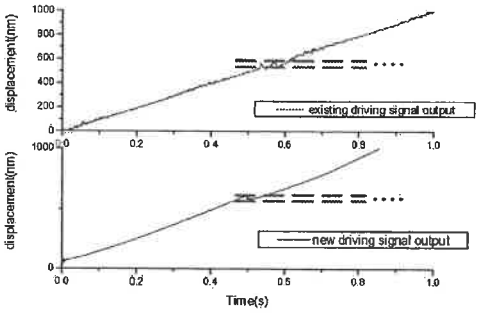

Fig. 10 Results about existing and new driving signal

Fig.10 shows the results of each driving signal. Through the comparison of each result, it is verified to the superiority of new driving signal.

Conclusion

In order to reduce clamping vibration, this paper presents new control methods. At first, the optimal control parameters of PID control are determined through the Genetic Algorithm, and compared with the conventional method. Secondly, the optimal clamp voltage was determined by examining the rigidness of feed stage. Finally, the interference during pushpull motion is removed using the new driving signal. Consequently, the vibration error was decreased to 45nm.

Reference

[1] N. Taniguchi, "current status in the future trends of ultra precision machining and ultra fine materials processing," Annals of CIRP32/2, 573, 1983

[2] D. Swyt, "Uncertainties in dimensional measurements at nonstandard temperatures," J. of Res. NIST, 1993. Thermacore Inc, "Heat pipe design guide," 1994

[3] V. G. Dudnikov, D. V. Kovalevsky, and A.L. Shavalin "Simple, high precision linear-motor-driven XYθ positioner (walker)", Rev. Sci. Intrum., Vol. 62. No.10, pp.2492, 1991

[4] Li Y, Hu M, Zhou ZY, Wang XJ. "An inchworm type of micro feed and ultra-precision positioning mechanism characterized with high thrust force, Piezoelectric & Acousto-optic," (in china), 1999; 21(5): 407-10.

[5] P. Cusin, T.Sawai, S. Konishi, "Large travel range, high accuracy inchworm-type stepper positioner," in: Proceeding of the Euro sensors XIV, 2000, pp. 177-178.

[6] P. Cusin, T.Sawai, S. Konishi, "Compact and precise positioner based on the inchworm principle", J.Micromech. Microeng. 10 (2000) 516-521.

[7] Daichi ABIKO, Koji TAKADA, Masato AKETAGAWA, "Piezo-driven linear motion stage with smooth motion, large travel range and high resolution", Leading Edge Manufacturing in 21 century.

[8] Reeves, 1993, "Using genetic algorithm with small population. Proc. of the Fifth Intern. Conf. on Genetic Algorithms, pp. 92-99.

[9] Dozier et al., 1994, "Solving small and large scale constraint satisfaction problems using a heuristic-based microgenetic algorithm. First IEEE conf. on Evolutionary Computation, pp. 306-377.

[10] Lance Chambers, "The Practical Handbook of GENETIC ALGORITHMS application", 2001

[11] Yong-Soo Jeon, Chung-Oh, Ye-Sun Hong, "Optimization of the control parameters of a pneumatic servo cylinder drive using genetic algorithms, Control Engineering Practice 6 (1998) 847-853

[12] H. H. Kim, K. C. Kee, S Lee, "Remote Controller Design of Networked Control System using Genetic Algorithm, KSPE, KOREA, pp. 598 - 601, 2001

[13] Daichi ABIKO, Koji TAKADA, Masato AKETAGAWA, Kyoung-Soo Lim, Sun-Kyu Lee, "New controller for piezo-driven linear motion stage with smooth motion, long stroke range and high resolution", ICPT2004, Japan

CONTROL OF WETTABILITY WITH SURFACE TEXTURING AND ITS APPLICATION

Nobuyuki Moronuki, Kentaro Ryu and Arata Kaneko
Tokyo Metropolitan University, 1-1 Minami-Ohsawa, Hachiohji, Tokyo 192-0397, JAPAN

1. Introduction

Textured solid surface can provide various functions. Modification of wettability is the typical example, which is expected to provide hydrophobic or hydrophilic surface character for various situations. Young's and Wensel's equations are the most basic theories of wettability related to surface geometry. Extended explanation on periodically grooved surface was demonstrated both theoretically and experimentally by Oliver et al. [1]. Bico [2][3] also demonstrated the modification of wettability with surface geometric texture which consists of micro pillar array. Wettability can be also modified with coating of low surface-energy material such as PTFE [4] independently of the surface geometry. However, there is little approach that suggests a design methodology of surface texture to obtain intended wettability combining the effect of surface geometry and coating, especially considering the effect of gravity. The goal of this study is to establish such a design method. This paper aims to make clear the effect of patterned hydrophilic/hydrophobic pattern by coating on the wettability, including the effect of gravity. Then an application is demonstrated.

2. Definition of wettability

Wettability is often referred as the contact angle of liquid droplet as the measure of characteristics for hydrophilic or hydrophobic surface. However, contact angle is not the only parameter to decide the wettability. CJ. Kim et al [4]. evaluated the flow resistance of microchannel with the sliding angle of water droplet on tilted surface. Sliding angle is the effective parameter for the evaluation of adhesive force between liquid and solid, which is sometimes important in practice. Actually, the relationship between the contact angle and sliding shown in Fig.1 has not been made clear. This, in this paper, both of the contact angle and sliding angle are employed for the evaluation of wettability.

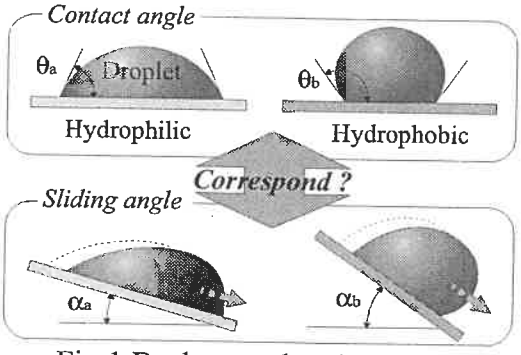

Fig.1 Background and problem

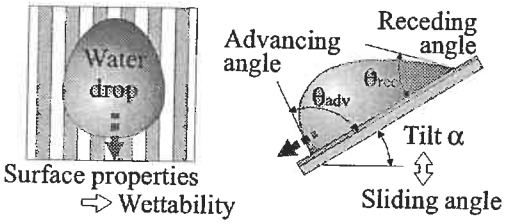

Fig.2 Experiments in this study

3. Experiments

Figure 2 shows what done in the experiment.
Firstly, Line-and-space pattern of hydrophilic and hydrophobic region was prepared on silicon substrate. Hydrophobic regions were produced by sputtering PTFE, and hydrophilic regions were produced by oxidation of silicon surface with SPM (H_2SO_4:H_2O_2=3:1) solution after the lithography and lift-off process. The thickness of the PTFE layer was less than 10nm and the original roughness of the substrate was less than 1nm. Thus, the effect of the surface geometry is

negligible and the effect of wettability only can be discussed. Hereafter, these patterns are referred as "PTFE/SiO_2 texture". The specifications of the pattern are summarized in Table 1. Secondary, the sliding angle and contact angle were measured using the setup shown in Fig.3. In order to evaluate the effect of droplet volume, a motorized micro-syringe was used and the shape of the droplet was analyzed using a CCD camera and capture board. The tilt angle was given by inclining the whole system. The conditions are shown in Table 2. Sliding direction was set parallel to the texture line. In addition to the sliding angle, the advancing angle and the receding angle were analyzed in order to investigate the detail of the phenomenon.

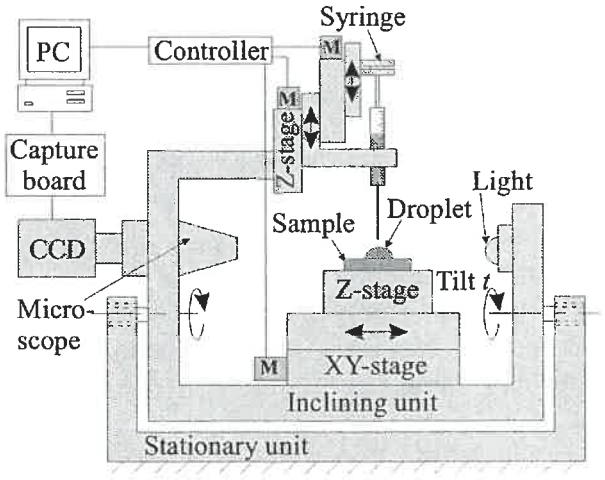

Fig. 3 Setup for experiments

Table 1 Properties of fabricated PTFE/SiO_2 textures

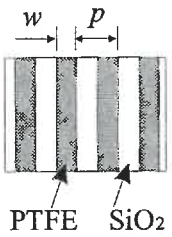

No	Line width of PTFE and SiO_2					
	Different ratio			Constant ratio		
	PTFE w	SiO_2 p-w		No	PTFE w	SiO_2 p-w
1	100	750		5	100	100
2	250	600		6	250	250
3	500	350		7	500	500
4	750	100		8	750	750

unit : μm

Table 2 Experimental conditions

Liquid	Pure water
Droplet volume	20-70 [μl]
Inclining speed	0.5-1.0 [deg/sec]

4. Results and discussions

Figure 4 shows the relationship between droplet volume and sliding angle (bottom) and the contact angle (top) of sliding droplet on the PTFE/SiO_2 textures respectively. Sliding angles on PTFE and SiO_2 without texture were also shown. For PTFE, there is a tendency that sliding angle decreased with the increase in droplet volume, while that of SiO_2 is almost constant. Droplets did not slide down when their volume was less than 20μl because the strong surface force. When the volume becomes larger, they slipped down due to the effect of increased mass.

It was found from sliding angle point of view that the droplet adhered to PTFE surface stronger than that of SiO_2, which seem to be the opposite in terms of contact angle. As shown in the upper figure in Fig.4, the advancing angle of PTFE is larger than 90 degrees.

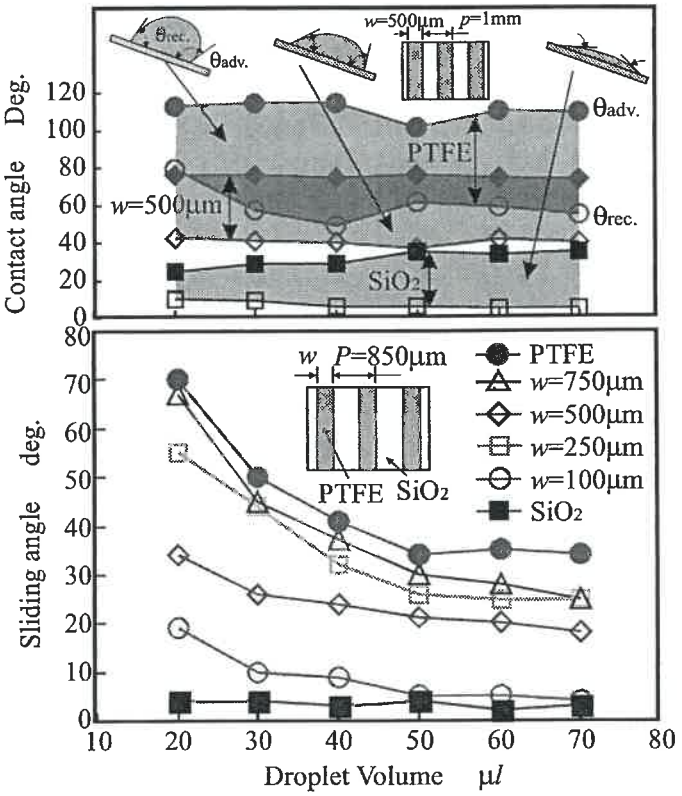

Fig. 4 Sliding angle and contact angle vs. drop volume

However, it was found that the hysteresis of contact angle, $\theta_{adv.}$-$\theta_{rec.}$, of PTFE is the largest in the case of PTFE. This fact suggests the work necessary to move the droplet on PTFE surface is larger and thus the sliding angle became large. It was also found that applying the texture the sliding angle can be set at desired value between PTFE and SiO_2 surface depending on the area ratio of PTFE/SiO_2 and droplet volume.

In addition to the ratio of PTFE/SiO_2 pattern, the width is also one of the design parameters. Figure 5 shows another results in which the pattern width was changed while keeping their ratio at constant. It was found that the sliding angle slightly decreased with the increase in the pattern width. These results indicate that both the area ratio of hydrophilic/hydrophobic region and the width of patterns should to be specified appropriately in the design of wettability.

The profiles of sliding droplets were also observed from the normal direction of the surface using another microscope. It was found that the advancing line of the droplet was arc-shaped but the receding line was undulate exactly with the pitch of hydrophilic/hydrophobic line as shown in Fig.6. This was due to the difference of the wettability or drag force between PTFE and SiO_2. The amplitude of this undulation varied depending on the line width. It is seen that the amplitude or drag height H increased almost linearly with the increase in PTFE line width.

To elucidate this phenomenon, various force components should be taken into account such as volumetric force and surface force. This is, of course, one of the important future works. However, this type of wettability pattern can be applied for the self-assembling of fine particles.

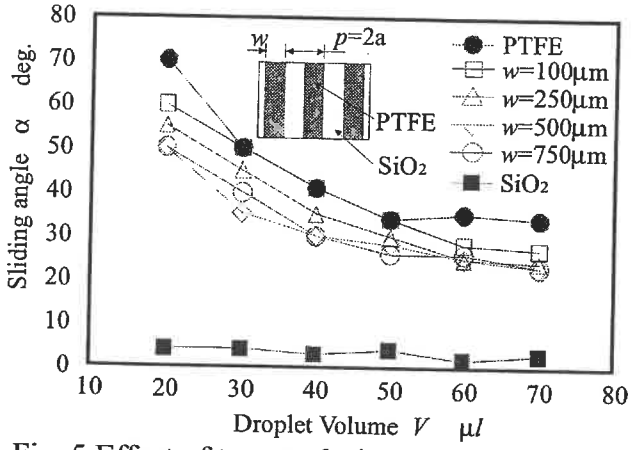

Fig. 5 Effect of texture design on sliding angle

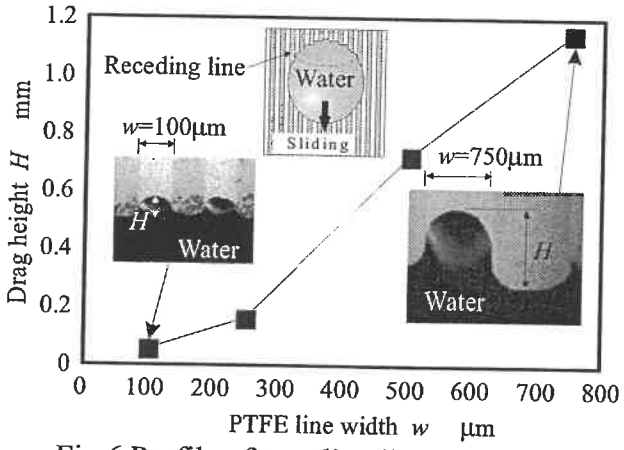

Fig.6 Profile of receding line of the droplet

5. Application of wettability pattern to continuous convective assembling of fine particles

We applied the wettability pattern to so-called "continuous convective assembling of fine particles". Figure 7 shows the principle. Drawing the patterned substrate from the suspension that include fine particles at specific angle, the particles gathered selectively on the hydrophilic regions due to the meniscus force between the particles while evaporation. In this process, the difference of contact angles between hydrophilic and hydrophobic region should be large as possible to gather them only on the hydrophilic region. Thus, in this experiment, octa-decyltrichlorosilane self-assembly monolayer (OTS-SAM) was used for hydrophobic material of which static contact angle was 105 degrees.

The condition of this experiment corresponds to the extreme on the right side in Fig. 4 and 5 because the droplet volume is considered as infinite. Therefore the assembling process was affected by behavior of the receding line shown in Fig. 7. Figure 8 shows the photos of particles

assembled on different hydrophilic region width and pitch. It was found that the particles were assembled with closest packing in monolayer on hydrophilic region. However, it is also seen that edge profile of assembled area is more continuous in the case of 70μm width while that of 35μm is discontinuous or no particles on the region. This is because receding undulation is larger for the texture of 70μm so that much more particles are supplied from hydrophobic region onto the hydrophilic region. These results are well explained by the former results and discussion. The assembled particles can be applied in various fields such as photonic crystal.

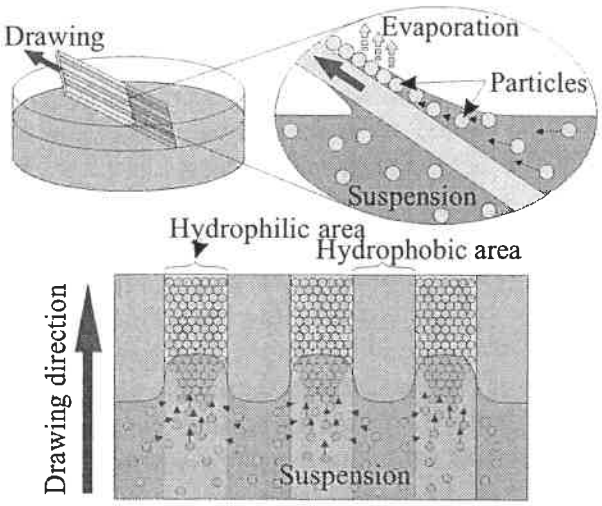

Fig.7 Continuous convective assembling of fine particles

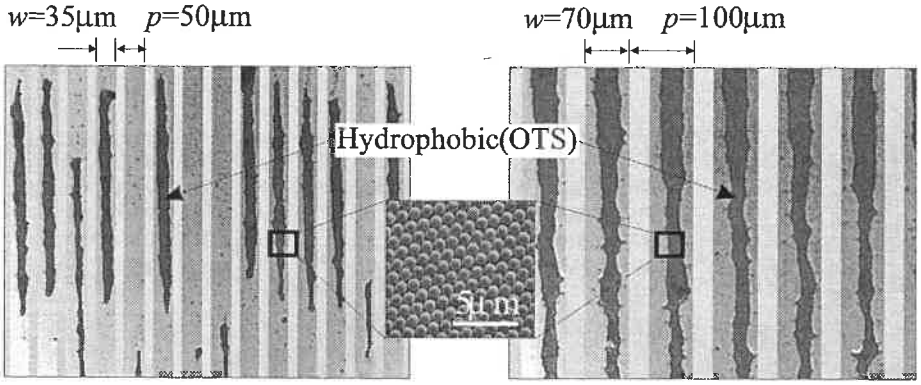

Fig.8 Assembled fine particles on OTS/SiO2 textures of different width and pitch

6. Conclusions

For the purpose of establishing the design methodology of surface texture to obtain intended wettability, influences of droplet volume and hydrophilic/hydrophobic pattern on sliding angle were investigated. The relationship among them indicated the possibility of controlling wettability by designing texture appropriately.

Continuous convective assembling of fine particles was carried out as the application of droplet sliding on hydrophilic/hydrophobic alternate lined texture. Influences of line width and pitch were shown to have relation with assembling rate of particles in intended place on substrate.

References

[1] Oliver J. F. et al, The Apparent Contact Angle of Liquid on Finely-Grooved Solid Surface, Journal of Adhesion, 8 (1977), 223-234.

[2] Bico J., Marzolin C. and Quere D., Pearl drops, Europhysics letters, 47-2 (1999), 220-226.

[3] Bico J., Thiele U. and Quere D., Wetting of textured surfaces, Colloids and Surfaces, A: Physicochemical and Engineering Aspects 206 (2002), 41-46.

[4] Kim J., Kim CJ., Nanostructured Surfaces for Dramatic Reduction of Flow Resistance in Droplet-Based Microfluidics, MEMS Conference, IEEE, (2002) ,479-482.

Shape of microtweezers fabricated for gripping micro objects

Yuichi NAKAZATO, Takahito OOIDE, Hajime MIYAZAWA,
Yukinori ARIGA, Sadao TAKEUCHI and Masao MURAKAWA

Nippon Institute of Technology, Miyashiro-machi, Minamisaitama-gun Saitama Pref. , JAPAN

1. Introduction

The ultimate goal of this study is the construction of an entire micromanipulation system. In this paper, we report only the results of the development of an end effector, in this case, microtweezers. Therefore, systems other than those of end effector, such as the observation system for the object to be gripped and the positioning system incorporated into the end effector, are excluded from this study; these were obtained commercially. Figure 1 shows the systems addressed in this study.

2. Material selection and fabrication

We developed end effector fingertips, i.e., microtweezers, on the basis of the concept described in Section 1 and have produced practical micro-tweezers [1]. Figure 2 shows an external view of the end effector of the micromanipulator and its design drawing. A flat diamond film 50-100 um thick, produced by chemical vapor deposition (CVD) using diamond fabricated by the hot filament method in our laboratory, was used and successfully processed into the required shape using an excimer laser processor [2]. In the CVD of thick diamond film, automorphic and ball-like layers were synthesized and a multilayer structure was constructed. A multilayer film has better elasticity than DLC and automorphic diamond films. It is also highly resistant to microcracks [3]. Therefore, an elastic hinge mechanism can be easily adopted and it is suitable for use in microtweezers at the hinge section.

3. Selection of shape of microtweezers

As described in Section 2, although the thick diamond fabricated using CVD, which has a layered structure, has better elastic properties than other diamond materials, it has a higher stiffness than polymer and metallic materials. Thus, its toughness is low; in contrast to the many excellent properties discussed in Section 2.3, the layered diamond is brittle and weak against impulsive loads. Therefore, when an elastic hinge is used to open and close the end effector fingertips, i.e., a component of the tweezers made of diamonds; its shape is very important for the component of microtweezers.

An end effector fingertip must be designed which can hold an object using a minute deformation developed at the tip which does not generate stress concentration. Unfortunately, the design optimization procedure for microcomponents has not been established and experimental verification has not been carried out. Furthermore, the shapes of the micromanipulators fabricated thus far have been designed on the basis of past experience; it is not clear if these shapes are theoretically optimally designed for manipulation. Therefore, to prevent the manipulator fingertip from breaking due to unexpected stress concentration while its gripping force is being maintained, we improved the shape of the end effector fingertip by repeating simulations using design optimization as an analytical method.

3-1 Selection of a method for design optimization

We carried out design optimization using linear mathematical programming. Design optimization is effective in reducing the area and volume of microobjects which have been designed in the past; it

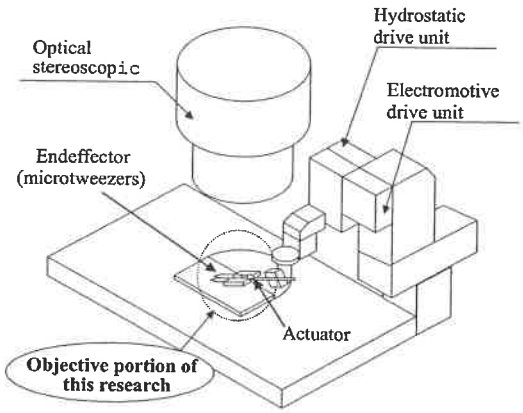

(a) Schematic illustration .

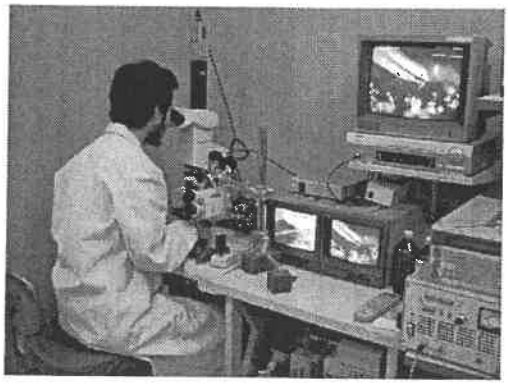

(b) Photograph

Fig.1 Micro manipulator system

is a method adopted in the middle and latter stages of the design process [4]. This procedure has already been used in many industrial fields and is fairly reliable. In this study, we improve the shape of the microtweezers obtained from experiments; thus, the design optimization approach was adopted. Linear mathematical programming is an effective method of obtaining solutions when the design space is simple and the gradient of the target function is continuous [5]. Because the gradient of the selected target function is continuous, the method can be applied to our analysis without any problems. The target function is used to relax stress concentration while minimizing volume.

3-2 Design variable

Figure 3 shows the initial shape before design optimization. The initial shape of the microtweezers was determined on the basis of experience by researchers. The entire length of the microtweezers is 7.6 mm, and the hatched area on the right is the fixed section. A load F is applied in the direction of the X-axis via the hole at the center. The load set is calculated by setting the force generated by the shape memory alloy, which is an actuator, to 0.3 N. The following three values are adopted as design variables. First, we considered that the two sections, the gripping and elastic hinge sections, are important; thus, the dimensions of these sections, namely, the total width and radius at the elastic hinge section, were selected as variables. Then we focused on the section connecting the two sections and the radius is set as a variable. Although the possibility of using the length between the gripping and hole sections and the distance between the gripping sections as variables was considered, these were abandoned because of the increase in the number of analyses and the difficulty of comparison with conventional shapes. Thus, the following is a list of variables:

1)width of the gripping and hinge sections (beam),
2)radius at the arc section of the hinge (radius) and
3)radius of the arc section connecting the gripping section and the hinge (fillet)

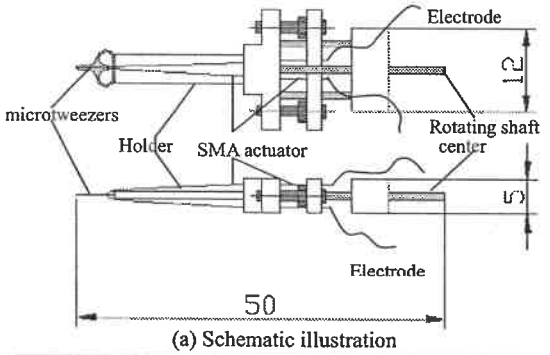

(a) Schematic illustration

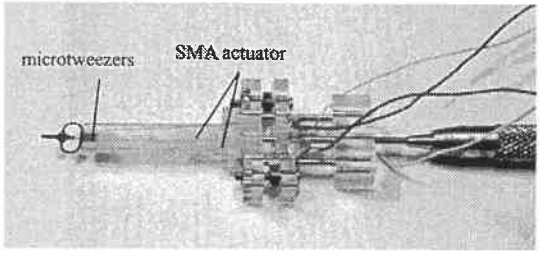

(b) Photograph

Fig.2 End effector system

3-3 Constraint

We optimize the above three elements as variables. As a constraint, a safety factor, which was set to 3, was adopted; considering the bending strength of the multilayer diamond as 1500 MPa, the maximum stress was decreased to less than 500 MPa. Furthermore, a deformation of 0.050 mm, by which the fingertips of the grip can be closed, must be obtained. Thus, 0.025 mm deformation of one finger of the grip, must be produced. The optimal design which provides the minimum volume while conforming to the constraint is then designed.

3-4 Design variable

ANSYS ED 5.7 by Cybernet Systems Co., Ltd. was used as software for the analysis. Equations (4.1)-(4.6) represent the design variables used in this study. The target function represents the volume; it is minimized by the variable f(x). The amount of deformation during gripping when a load is applied is g 1: a design which produces at least 0.025 mm deformation is acceptable. The maximum stress when a load is applied is g 2, a design is acceptable when the maximum stress is less than 500 MPa. The terms x1, x2 and x3 show the ranges of variables for beam, radius and fillet, respectively. The step adopted in the analysis is 0.01 mm for all cases.

Target function:	f(x) >> min	(4.1)
Constraints:	g1(x) > 0.025 mm	(4.2)
	g2(x) > 500 MPa	(4.3)

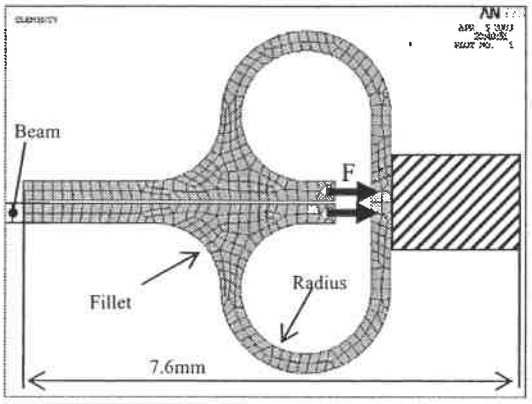

Fig.3 Initial shape of microtweezers used for design optimization

Design variable: $0.2 <= x1 <= 0.3$ (4.4)

$0.6 <= x2 <= 1.0$ (4.5)

$0.1 <= x3 <= 1.0$ (4.6)

4 Results of the analysis

4-1 Results of the analysis using one variable

Figures 4 through 6 show the design optimization results using one of the three variables, beam, fillet, or radius, as the design variable. In these figures, the X- and Y-axes represent the ranges of the variables and maximum stress for the shape, respectively. As shown in Figs. 4 and 5, maximum stress changed substantially when beam and radius were changed. However, as shown in Fig. 6, when fillet was used as the variable, maximum stress changed only slightly, from 493 MPa to 498 MPa. Maximum stress did not change substantially when fillet was changed; maximum stress is independent of fillet.

4-2 Results of analysis using two variables

On the basis of the results shown in Fig. 5, we assumed that the results would not be affected even if fillet were fixed. Therefore, the fillet was set at 0.1 mm, the values of the two other variables, beam and radius, were altered, and the design optimization was carried out. Figure 7 shows the results of optimization. In the figure, the X-, Y-, and Z-axes represent beam, radius and maximum stress, respectively. Figure 8 shows the relationship between volume and maximum stress.

As shown in Fig. 7, maximum stress is reduced by decreasing radius and increasing beam. Furthermore, on the basis of the results shown in Fig. 8, we adopted design variable values which produce the minimum volume when the maximum stress is at or below 500 MPa. The adopted values were 0.27 mm for beam and 0.6 mm for radius. The values obtained by this analysis are shown by empty circles in Figs. 7 and 8.

Table 1 show the design results obtained by these analyses. As shown in Fig. 9(a), the stress distribution disappeared from the front of the fillet in the conventional design; however, it extended to the gripping section in the design into which our new approach is incorporated (Fig. 9(b)). However, in both cases, the maximum stress is located at the central section of the hinge; there was no difference in the results between the two designs. According to Table 1, the volume was reduced by approximately 21.4% successfully without significantly affecting maximum stress, which contributed to the miniaturization of the micromachines.

5 Conclusions

To construct a three-dimensional object by directly handling micrometer-sized components, we proposed a method of designing diamond microtweezers for use as an end effector for a micromanipurator. In

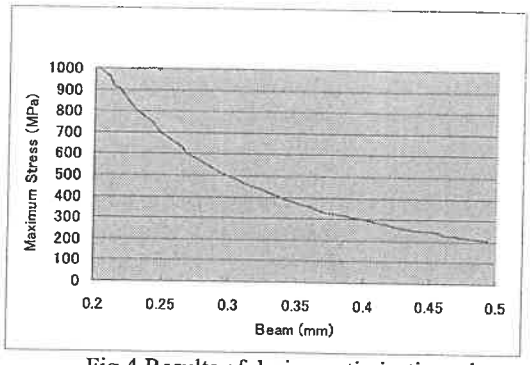

Fig.4 Results of design optimization when only beam is used as variable

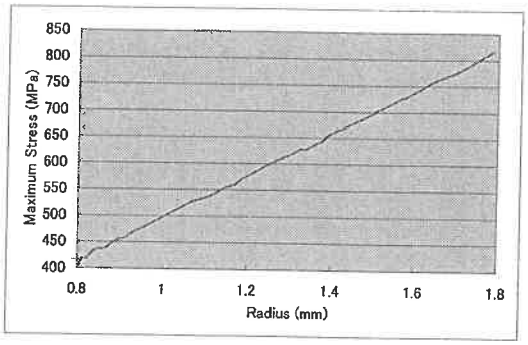

Fig 5 Results of design optimization when only radius is used as variable

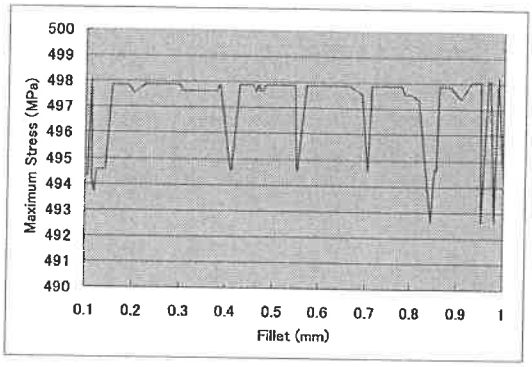

Fig.6 Results of design optimization when only fillet is used as variable

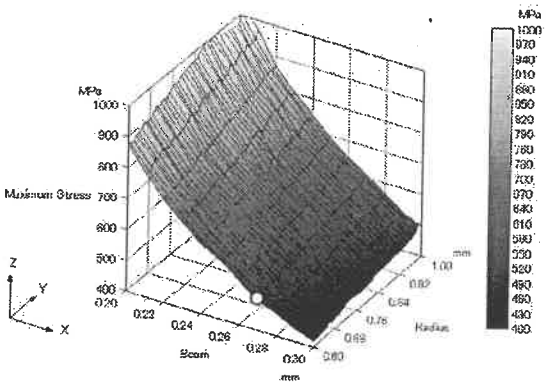

Fig.7 Result of analysis after design optimization (beam-radius-stress)

designing the tweezers, the initial shape of the tweezers was determined based on our experience, considering 1) the use of diamond, 2) fabrication of an actuator taking the effect of dimensions into consideration, and 3) the use of a hinge mechanism. We then simulated the relationship between deformation and stress concentration using design optimization software based on linear mathematical programming and obtained the optimal shape of the microtweezers. By optimizing the design of tweezers, which were originally designed based on experience during past studies, we succeeded in reducing the original volume by approximately 21.4% without altering maximum stress. Furthermore, the design method proposed in this study was confirmed to be effective in simulations; the miniaturization of tweezers was successful.

Acknowledgements

We appreciate the support provided through the High-Tech. Research Project and Grants-in-Aid for Scientific Research (C) from the Ministry of Education, Culture, Sports, Science and Technology.

References

[1] Y. Nakazato, A. Sekine, H. Miyazawa, S. Takeuchi Y. Ariga and M. Murakawa, "Development of a micromanipulator made of diamond having reversal mechanism", A Proceedings of IIP/ISPS Joint MIPE'03, pp.123-124, 2003.

[2] Hajime MIYAZAWA, K, Hotta, H. Hirose, Basic Study on the
Formation of Superconductive Circuit on the Bulk of Press Formed Bi System by Laser Technique, CIMTEC'02 ABSTRACTS, pp.156, 2002.

[3] S. Takeuchi, M. Murakawa, Synthesis and Evaluation of High-quality Homo epitaxial Diamond Made by the Combustion Flame Method, Thin Solid Films Vol. 377-378, pp. 290-294, 2000.

[4] ZIENKIEWICZ O. C .,CAMPHBELL O. C. "Shape Optim- ization and Sequential Linear Program-ing in Optimum Structural Design" , John Wiley & Sons, 102, 1973.

[5] N.Karmarkar, "A new poly nomial-time algorithm for linear programming", Combinatorica4, pp. 373–395. 1984.

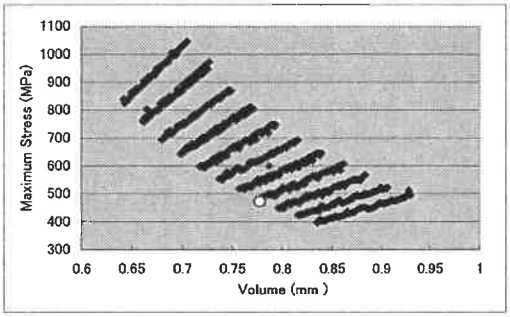

Fig.8 Result of analysis after design optimization (volume-stress)

Table 1 Results of analysis

	Before improvement	Afetr improvement
Beam(mm)	0.3	0.27
Fillet(mm)	1.0	0.1
Radius(mm)	1.0	0.6
Volume(mm^3)	1.01398	0.79609
Maximum stress(MPa)	494.548	494.554
Length(mm)	7.6	7.2

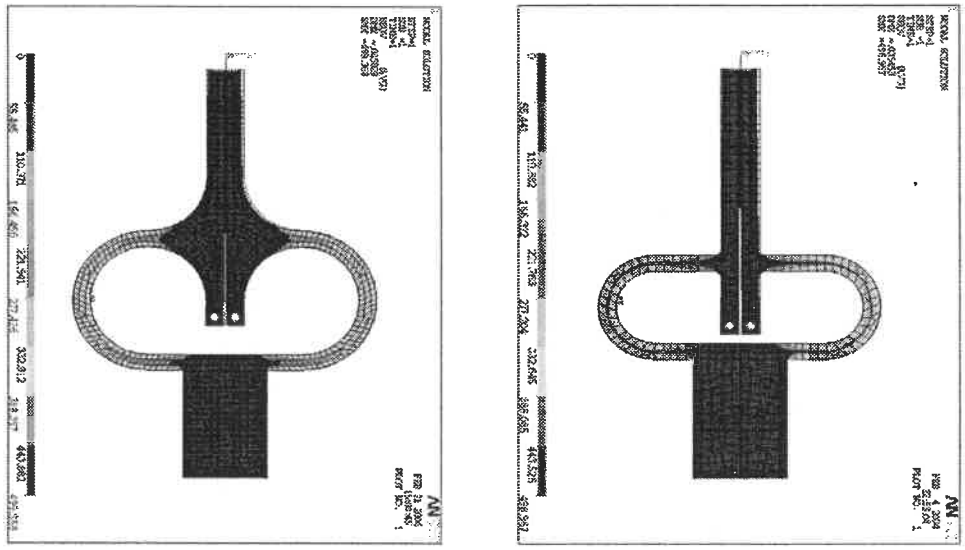

(a) Before improvement (b) After improvement

Fig.9 Comparison of stress distributions

SELF-ALIGNMENT OF MICROPARTS USING LIQUID SURFACE TENSION – EXTENSION OF FUNCTION BY VIBRATION FORCE: SELF-ALIGNMENT OF A GROUP OF MICROPARTS AND SELF-STANDING

Kaiji SATO, Shioich HOSHINO and Shintaro KOBAYASHI
Tokyo Institute of Technology, 4259-G2-17 Nagatsuta, Midori-ku, Yokohama, 226-8502, Japan

INTRODUCTION

Microsystems have become an important research field and 2D or 3D microsystems composed of microparts of which materials and shapes differ have been investigated. In order to realize such systems as industrial products, an assembly technique of the microparts is necessary with alignment being a very important task in the assembly. The purpose of this research is to establish a self-alignment technique for microparts assembly using liquid surface tension[1][2]. Up to date, the method for aligning the flat microparts one by one has been proposed and evaluated experimentally.

This series alignment can be widely used and it is reliable. However, the time required for the alignment becomes long as the number of the microparts increases. Thus, the method to align a group of microparts at a time is also needed in addition of the series self-alignment method. For manufacturing 3D microsystems, the methods of rotational alignment out of the base plane using surface tension of melting solder and some electrostatic actuators are examined[3][4]. However the out of plane rotational alignment methods using liquid surface tension are not shown yet.

This paper describes the extension of function of the self-alignment using liquid surface tension. The extended functions are the self-alignment of a group of microparts at a time and the self-standing as an important function of the out of plane rotational alignment. For the functions, the vibration force is used with liquid surface tension.

SELF-ALIGNMENT METHOD OF A MICROPART GROUP USING LIQUID SURFACE TENSION

The surfaces of the microparts used in the self-alignment of [1][2], are divided into two areas, namely, high and low wettability areas and have the same pattern of the high wettability area. In the alignment, a micropart needs to be put on the other micropart so that a liquid droplet comes in contact with the high wettability areas of the two microparts. It becomes more difficult to put all the microparts under the condition simultaneously as the number of the microparts increases. This may become an obstacle of practical use in mass production although the series alignment can be widely used and reliable.

For overcoming this problem, the vibration force is used with the liquid surface tension in the alignment. Figure 1 shows the method of the self-alignment of a micropart group at a time. It is carried out as follows;

(Step 1) Droplets of the liquid are put on the high wettability area of a base part. As described later, they can be put on all the areas at a time.

(Step 2) Microparts are put on the base part. In this case, the droplets do not need to always come in contact with the

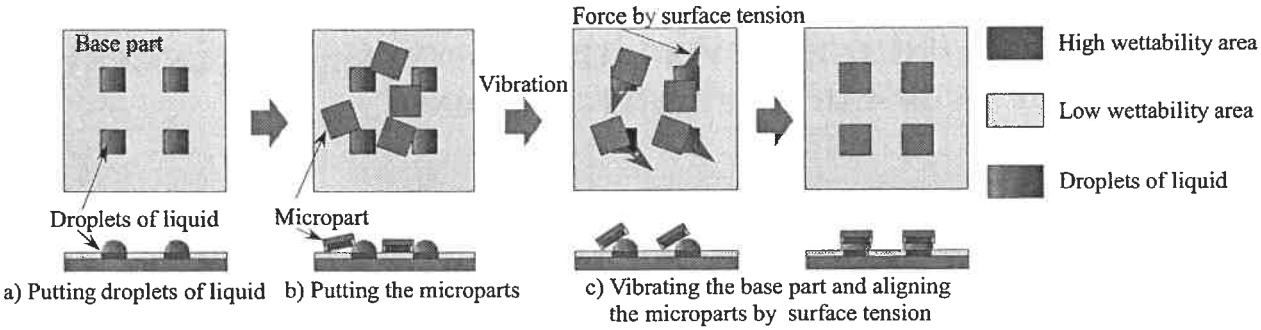

Fig.1 Method of self-alignment of a group of microparts

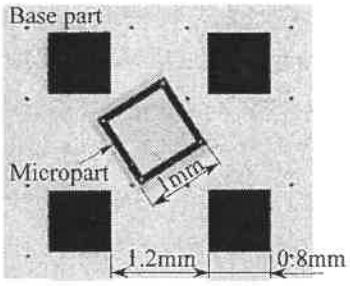

Fig.2 Experimental base part and micropart

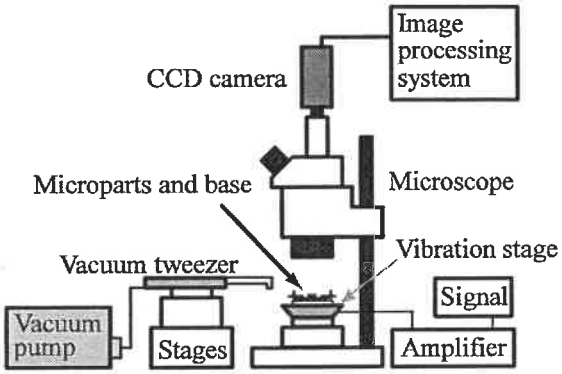

Fig.3 Experimental setup

high wettability areas of the parts.

(Step 3) The base part is vibrated so that the microparts move on the base part. When the high wettability areas of the microparts come in contact with the droplets, the liquid surface tension force drives the microparts so that the high wettability area patterns of the microparts overlap with that of the base part.

In [2], the friction force between the parts often deteriorates the accuracy of the alignment using only liquid surface tension. However the vibration force reduces the bad influence and can improve the alignment accuracy.

EXPERIMENTAL SELF-ALIGNMENT

Self-alignment of a micropart group using conventional microparts

The experimental micropart and base part shown in Fig.2 are used in this experiment. Figure 3 shows the experimental setup for the self-alignment. Circular symbols are marked on the parts. The position and the inclination angle of the microparts are measured by using these symbol and an image acquisition and processing system with a CCD camera connected to a microscope. The stage which the base part is set on (vibration stage) can be vibrated by a voice coil actuator. Water is used as the liquid which produces a surface tension force.

The alignment experiments were carried out as follows. (1) A large liquid drop is put on the base part so that the drop comes in contact with all the high wettability areas of the base part(four areas) and then is absorbed by a syringe. This action results in the liquid being only on the high wettability areas. (2) Four microparts are put on a

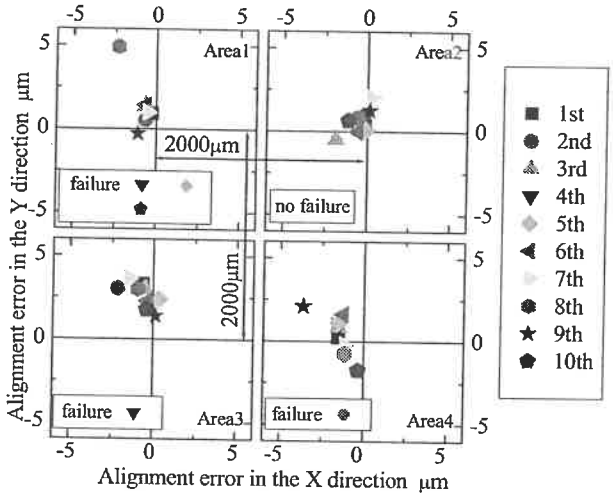

Fig.4 Experimental alignment error in the x and y directions

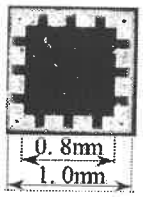

Fig.5 Improved experimental micropart

base part. (3) The vibration stage is vibrated. The alignment experiment based on this procedure was made 10 times. Figure 4 shows experimental alignment error in the x and y directions. In the experiments, 35 out of 40 microparts used were finally aligned by liquid surface tension. The average and standard deviation of alignment errors of the aligned microparts are almost the same as those by the method in [1]. Some out of the misaligned microparts were turned upside down and the others were moved far from the goal. These motions are caused by the low wettability area around the high wettability one of the microparts. The low wettability area sometimes prevents the liquid droplet from coming in contact with the high wettability area.

Improvement of reliability of the self-alignment

The low wettability area of the micropart sometimes hinders the liquid droplet coming in contact with the high wettability area of the micropart and forces the microparts fail in the alignment. On the other hand, the restoring force caused by the liquid surface tension is proportional to the length of the boundary line between the low and high wettabiluty areas. For improving the reliability of the self-alignment, in this paper, the low wettability area on a micropart is divided into several areas so that the liquid is easy to spread over the high wettability areas of the microparts. Figure 5 shows the improved experimental micropart. The experimental self-alignment using these improved microparts and the conventional base part was made. In the experiment, all the improved microparts were not turned upside down and not moved far from the goal.

Self-standing

In manufacture of 3D microsystems, the out of plane rotational alignment is often needed. The 3D microsystems often include standing microparts. In this section, a self-standing method using liquid surface tension and vibration force is proposed and the experimental self-standing result is shown. The self-standing method is based on the self-alignment one of a micropart group. Only one surface of the micropart used in the self-standing includes the high wettability area. The base part has the same high wettability area on its one surface. Figure 6 shows the behavior of the micropart in the experimental self-standing experiment. The size of the micropart in Fig.6 is 1.0mm

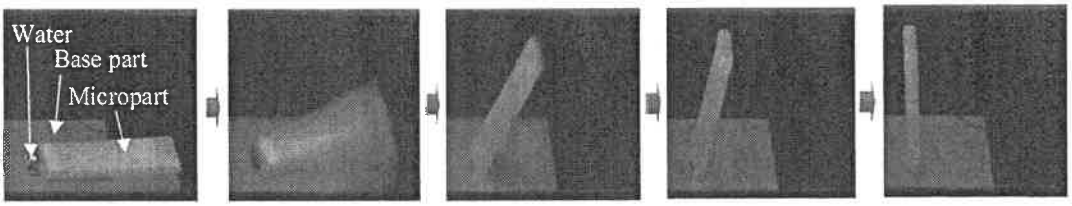

(a) Initial state (b) Vibration of the parts (c) Evaporation of the liquid

Fig.6 Behavior of the micropart in the experimental self-standing

x 2.6mm x 0.15mm. The areas of high wettability on the parts are 1.0mm x 0.15mm. The edge of the micropart keeps in contact with the base part by the liquid surface tension even if the vibration force is applied. The micropart stood up as the liquid evaporates and the droplet shranks. In case the length of the micropart is short enough, the micropart can stand up with the only liquid surface tension.

CONCLUSION

Microsystems which has 3D structure and comprises various microparts have been studied as advanced systems. In the assembly process for the microsystems, the alignment of a micropart group at a time and the out of plane rotational alignment are very important tasks. In this paper, first, the alignment methods for them using liquid surface tension and vibration force were introduced. And then their performances were evaluated experimentally. The experimental results show that the reliability of the introduced self-alignment method of a micropart group is very high by using the improved microparts and the proposed self-standing method is useful.

ACKNOLEDGEMENTS

This research was supported by a grant from Mitutoyo Association for Science and Technology. The research was carried out at the Vacuum Machining Laboratory in the Tokyo Institute of Technology.

REFERENCES

[1] Kaiji Sato, Seiichi Hata and Akira Shimokohbe: "Self-alignment for Microparts Assembly Using Water Surface Tension", Proceedings of SPIE, Vol.3892, (1999) 321-329.

[2] Kaiji SATO, Kentaro ITO, Seiichi HATA and Akira SHIMOKOHBE: "Self-alignment of Microparts Using Liquid Surface Tension –Behavior of Micropart and Alignment Characteristics", Precision Engineering, Vol.27, No.1(2003)42-50.

[3] R.R.A.Syms: "Equilibrium of Hinged and Hingeless Structures Rotated Using Surface Tension Forces", J.of MEMS, Vol.4, No.4(1995)177-184.

[4] Emmanuel Quevy, Patrice Bigotte, Dominique Collard and Lionel Buchaillot: "Large Stroke Actuation of Continuous Membrance for Adaptive Optics by 3D self-assembled microplates, Sensor and Actuator A, No.95(2002)183-195.

A SIX DEGREE-OF-FREEDOM TRI-LAYER CHEVRON BEAM THERMAL ACTUATOR

Shih-Chi Chen
MIT Department of Mechanical Engineering
77 Massachusetts Avenue, Room 3-446
Cambridge, MA 02139
Tel: 617-452-4957, scchen@mit.edu

Martin L. Culpepper
MIT Department of Mechanical Engineering
77 Massachusetts Avenue, Room 3-449b
Cambridge, MA 02139
Tel: 617-452-2359, culpepper@mit.edu

Keywords: Flexure, compliant mechanism, stiffness, MEMS, manipulation

1 Introduction

In recent years, micro-electro-thermal actuators have been used for single-axis positioning. For example, the bent-beam electro-thermal actuator, developed in 1999, provides 20 μm stroke and more than 100 μN force output. [1, 2]. Although thermally driven micro-manipulators/actuators have a limited operating frequency (generally less than 1 kHz), there are many small-scale, precision alignment and manipulation applications which do not require ultra-high bandwidth. For example micro-photonics alignment is a reasonable candidate. Unfortunately, the state-of-the-art in MEMS electro-thermal actuators is only capable of generating single degree-of-freedom motion [3]. These actuators would be more useful in small-scale precision manipulators if they were capable of multi-axis actuation and high force output. This paper introduces the concept of a multi-axis, tri-layer electro-thermal actuator. The actuator, shown in Fig. 1, has been designed to move in 5 or 6 axes. The actuator exhibits an unexpected motion displacement which affects the precision of its motion. In this paper, we examine a 1st order model used to predict when this phenomenon occurs. This is a necessary first step before we seek to use this actuator in a small-scale precision manipulator.

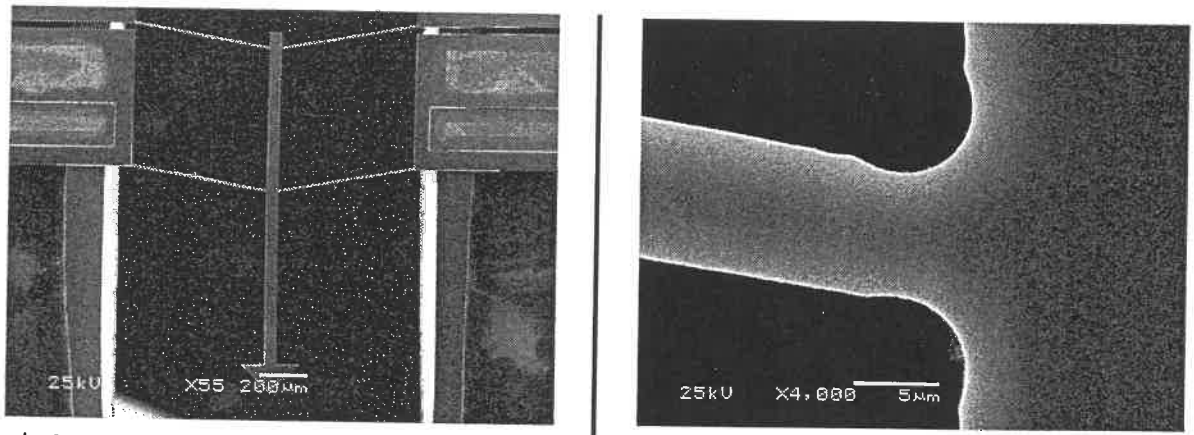

A: Top view of a tri-layer chevron beam actuator

B: SEM view of flexure joint near ground

Figure 1: A SEM of the tri-layer chevron beam actuator

2 Actuator design concept

As shown in Figure 2A, the tri-layer chevron beam actuator is made of two identical device layers bonded together via a 1 μm thick thermal oxide layer at selected locations (Fig. 2B). Each device layer is 8 μm

thick and comprised of two parallel bi-layer chevron beams of 6μm width. Thus each device layer contains two identical chevron actuators which can be independently or simultaneously actuated. The beams of the actuators connect to the central structure which is 50 μm wide x 1.2 mm long. The beams intersect the central structure at a 10° angle.

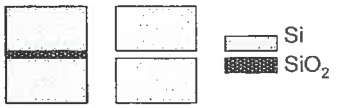

A: Cross section views tri-layer actuator.

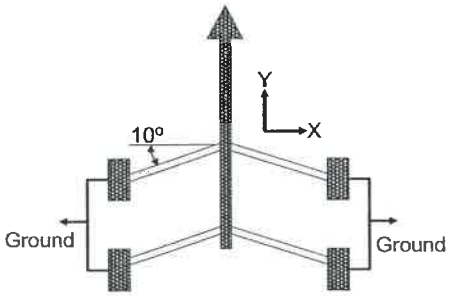

B: Blue regions show the spots connected by SiO_2.

Figure 2: A SEM of the tri-layer chevron beam actuator

3 Generating displacements in six axes

The tri-layer actuator has the ability to achieve six-axis displacement by selectively actuating the electro-thermal actuators. Motion generations are explained in Figure 3A - F. The dashed lines represent a driving current through the top layer, and the dotted lines represent current through a bottom layer. To obtain pure y-axis motion, current is supplied to both top and bottom layers as shown in Figure 3A. To obtain z motion, the current is run through both of the chevron beams on the bottom layer. These beams then cause the actuator to buckle out of plane in the z direction. To obtain the angular displacement θx (Fig. 3C), the currents is routed through the top and bottom layer at either the front or back chevron beams. Figures 3D – 3F show how other displacements are achieved.

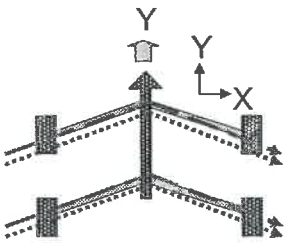

(a) Pure Y motion

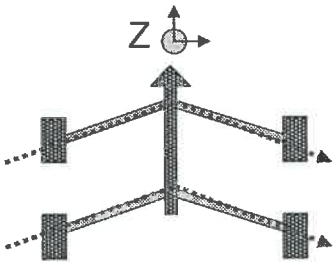

(b) Z motion

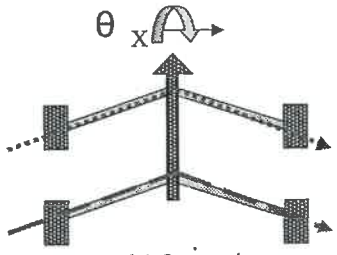

(c) θ_X motion

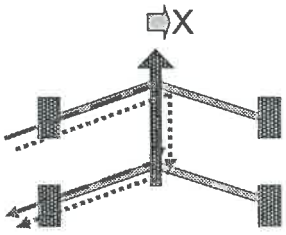

(d) X motion

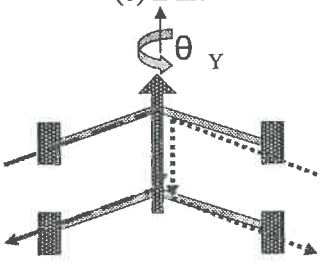

(e) θ_Y motion

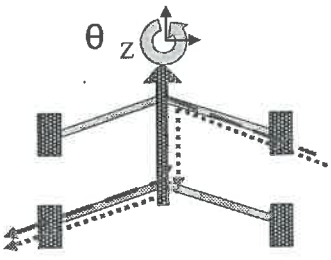

(f) θ_Z motion

Figure 3: Demonstration of six-axis actuation.

4 Modeling out-of-plane motion sensitivity

The ratio of in-plane stiffness to out-of-plane stiffness of the tri-layer actuator is considered to determine the adequate thicknesses and ratios of the silicon and oxide layer. As the top or bottom layer is heated, the chevron beam on that layer expands. The heated chevron beam moves forward and bends out-of-plane by a small amount at first, then by a rapidly increasing amount as more current is applied. For now, we choose to model this out-of-plane bending displacement by using a model which treats the shallow angle chevron beam as a straight beam which is grounded on both ends. As the beam strains thermally, the beam bends out-of-plane, the length of the beam increases and the out-of-plane curvature changes. The curved beam equations [3] shown in Fig. 4A and the dimensions of the chevron beam actuator were used to generate the stiffness graph in Fig. 4B.

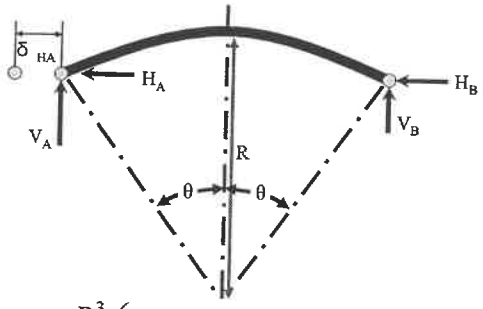

$$\delta_{HA} = \frac{R^3}{EI}\left(A_{HH} H_A + A_{HM} \frac{M_A}{R} - LP_H \right)$$

A: Curved beam displacement

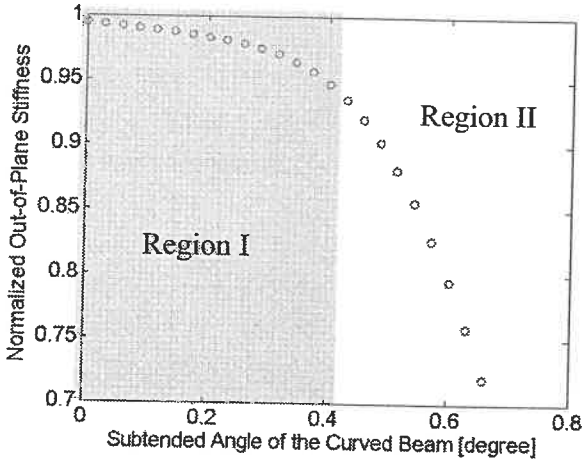

B: Out-of-plane stiffness is a function of curvature

Figure 4: Out-of-plane stiffness model (A) and out-of-plane stiffness (B)

Figure 4B shows the out-of-plane stiffness of a curved beam as a function of the curvature. A decrease in stiffness is observed as the curvature increases. As the out-of-plane included angle approaches 0.4 degree, a decrease in the stiffness is observed. Regions I and II are defined to the left and right of the 0.4 degree angle. Initially, the in-plane stiffness of the actuator is smaller than the out-of-plane stiffness. This is required to ensure that the displacement of the chevron beams will be confined to in-plane directions. However, the out-of-plane stiffness is a function of the out-of-plane curvature. Should the out-of-plane stiffness decrease below a specific stiffness value (at the boarder between Regions I and II), the actuator will find it is easier to deform out of plane than in-plane. At this point, an actuator which is told to move in plane will actually move out of plane.

5 Experimental results

Testing of the tri-layer chevron beam actuator was performed with the white light interferometer for motion in three major axes θx, y, and z. Figure 5A and 5B show the input current versus actuator tip displacement in θx and z axes. Both plots can be divided in two regions as in Figure 4B. In Region I, the displacement outputs vary from 0 to 3μm where, as the input current increases, the displacement increases

at slightly more than linear. This result corresponds to Region I in Figure 4B. Likewise, Region II in Figure 5 corresponds to Region II in Fig. 4B.

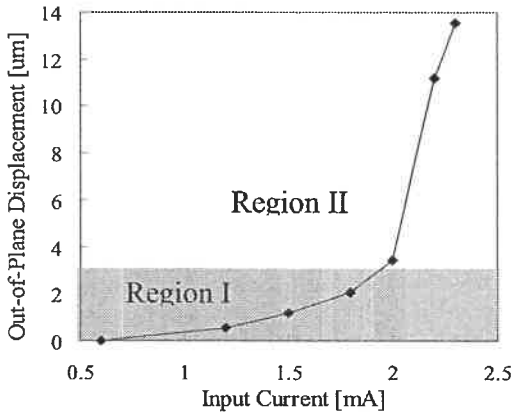

A: θ_X motion plot. First chevron, bottom layer actuated.

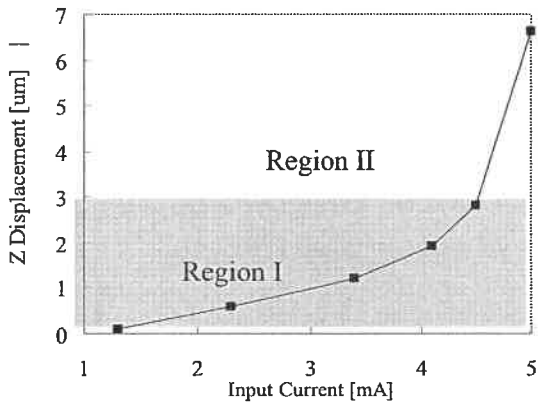

B: Pure Z motion plot. Both chevron, top layer, actuated

Figure 5: The plots of θx and z error motion which occur as chevron beam stiffness changes

The buckling beam model accurately predicts the error transition point between Region I and Region II and the amount of error at this transition, yet fails to predict the correct behavior of the actuator within Region II. We are presently examining how to make the transition in the curve more pronounced so that we might use these actuators as binary actuators.

6 References

[1] Que, L.; Park, J.-S.; Gianchandani, Y.B., "Bent-beam electro-thermal actuators for high force applications," Micro Electro Mechanical Systems, 1999. MEMS '99. Twelfth IEEE International Conference, 1999, p.: 31 – 6

[2] Long Que; Jae-Sung Park; Mo-Huang Li; Gianchandani, Y.B., "Reliability studies of bent-beam electro-thermal actuators," Reliability Physics Symposium, 2000. Proceedings. 38th Annual 2000 IEEE International, April 2000, Pages: 118 – 22

[3] Shih-Chi Chen, "A Silicon X-Degree-of -Freedom Compliant Micro-Manipulator for Silicon Optical Bench," MSME Thesis, MIT, 2003

[4] Warren C. Young, Richard G. Budynas, "Roark's formulas for stress and strain," p. 333-5, 7th edition, McGraw-Hill, NY, 2002

DESIGN AND MANUFACTURE OF MONOLITHIC, 3D COMPLIANT MECHANISMS FOR NANOMANIPULATION EQUIPMENT

Martin L. Culpepper
MIT Department of Mechanical Engineering
77 Massachusetts Avenue, Room 3-449b
Cambridge, MA 02139
Tel: 617-452-2359, culpepper@mit.edu

Shih-Chi Chen and Samuel Korb
MIT Department of Mechanical Engineering
77 Massachusetts Avenue, Room 3-446
Cambridge, MA 02139
Tel: 617-452-4957, scchen@mit.edu / skorb@mit.edu

Keywords: Monolithic compliant mechanism, 3D compliant mechanism, plastic deformation, precision flexures.

1 Introduction and summary

Compliant mechanisms provide motion/positioning via the compliance of the mechanism's structure. Monolithic, or single piece compliant mechanisms (1) do not require assembly, (2) are capable of nanometer-level repeatability, (3) do not suffer from contact wear or friction and (4) exhibit low hysteresis. This technology is useful for instance in making compliant hexapods for Micro and Nanomanipulation. Hexapods are popular mechanisms used to achieve six-axis positioning. Unfortunately, their 3D structures and mechanisms (rigid or compliant) must be carefully manufactured and assembled from many precision components. As a result, these devices may cost several hundred to several thousand dollars. This paper presents a summary of work which is aimed at generating monolithic, three-dimensional compliant mechanisms for Micro and Nanomanipulation processes. This is accomplished by plastically deforming 2D flexures into a 3D shape. The purpose of this paper is to examine the magnitude and timing of stress relaxation/creep errors which might limit the performance of a precision manipulator. Tests on a monolithic, 3D compliant hexapod indicate that stress relaxation induced errors subside with time and are of magnitude and time scale such that they may easily be addressed via closed-loop control in Nanomanipulation systems.

2 A brief synopsis of plastic deformation in precision flexures

A precision engineer's first instinct is to think of plastic deformation as a phenomena to be avoided at all costs. A review of past work shows that limited plastic deformation (a few small-strain bending cycles) has a long and successful history in the alignment of laser cavity components [1,2,3,4], photonics devices [5,6,7,8,9,10,11,12] and automotive components [13, 14]. Unfortunately, the use of plastic deformation requires an iterative, "tweaking" process which is not well-understood. This process is analogous to the bending imposed on the frames of eye glasses to achieve a better fit. This work is a first step in better understanding the process in the context of precision manipulators.

3 Design techniques for the forming tooling

The process used to make monolithic, 3D compliant mechanisms is shown in Figure 1. The figure traces the process used to form a monolithic 3D compliant hexapod. The process has four steps:

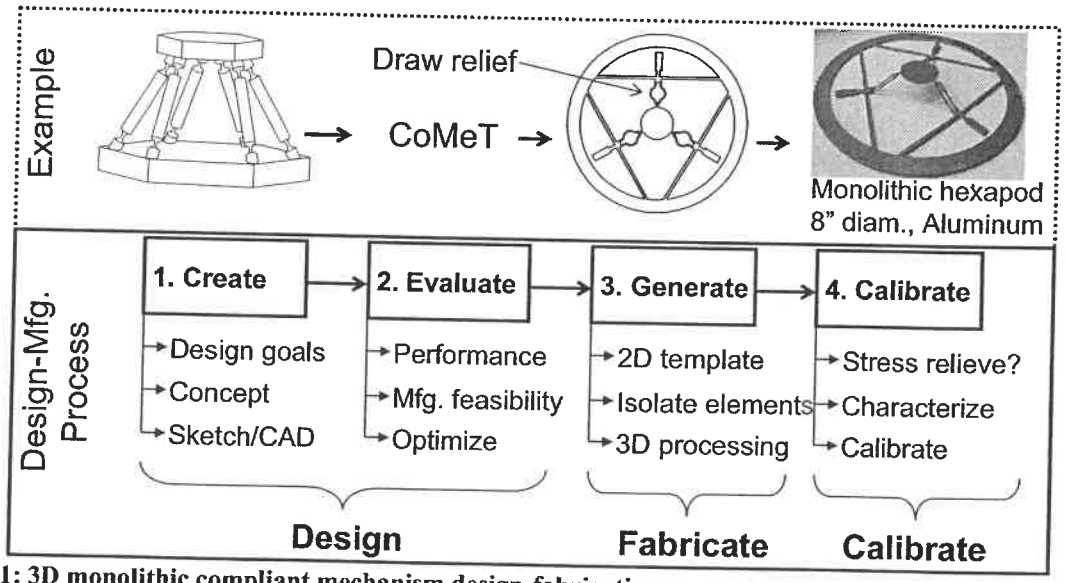

Figure 1: 3D monolithic compliant mechanism design-fabrication process

Step 1: Create - A 3D mechanism concept is synthesized by analogy to a 3D mechanism

Step 2: Evaluate –The design, in its final 3D form, is evaluated for proper kinematic function and identification of processed/deformed stress limits.

Step 3: Generate – The 3D geometry is mapped onto a 2D surface, called a template, which is machined into a sheet of material using laser cutting, abrasive waterjet, or DRIE. Forming processes transform the template into a 3D compliant mechanism.

Step 4: Calibrate – The mechanism or control system is calibrated to achieve the desired functional performance characteristics. This step eliminates the need for hyper-accurate forming of mechanism dimensions. In this way, the effects of spring back are made irrelevant. This stage may also include stress-relief of the mechanism structure.

At present, much of steps 1-3 depend upon human skill and experience. A long-term goal of this work is to develop a parametric, matrix-based design theory which enables us to automate steps 2 and 3.

4 Modeling techniques

The modeling and evaluation in step 2 is currently performed via FEA. The mechanism is modeled in CAD or CoMeT [15] and then simulations are run to link geometry parameters to mechanism performance. The mechanism geometry is then optimized to achieve a desired goal. It is often helpful to plot important performance metrics such as transmission ratio, T_{rz}, and range (or normalized range) vs. an independent design parameter. For instance, the included angle, θ_{inc}, in Fig. 2A may be set to achieve a given mechanism performance as indicated in Fig. 2B.

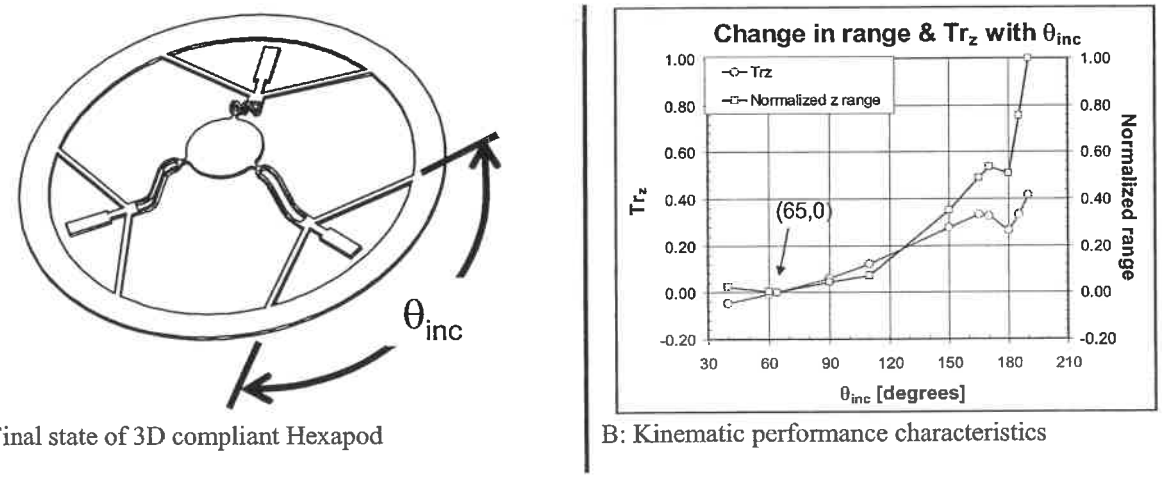

A: Final state of 3D compliant Hexapod

B: Kinematic performance characteristics

Figure 2: Relationship between tuning variables and performance metrics

Once the final geometry is set, the designer maps the 3D shape onto a 2D sheet. For the example shown in Fig. 2A, this mapping is relatively easy. The problem becomes much more complex when one wishes to form mechanisms with overlapping features or mechanisms in which flexures/structures must be sequentially formed. Long-term research is focused on mapping of template-performance variables as laid out by the logic in Eqxns. 1 and 2.

$$T_{3D} = L_{2D} \cdot K_{2D} \cdot T_{2D} + S_{process} + e_{process} \tag{1}$$

$$D_{3Di} = L_{3Di} \cdot K_{3Di} \cdot T_{3D} + S_{3Di} + e_i \tag{2}$$

Here, $\boldsymbol{T}$ = Topology (geometry) descriptor, $\boldsymbol{S}$ = Spring back, $\boldsymbol{L}$ = Applied loads, $\boldsymbol{D}$ = Displacements, $\boldsymbol{K}$ = Kinematic relation between mechanism input-output, $\boldsymbol{e}$ = error. Subscripts denote either the source of the error (actuated, process) or the starting geometry of the mechanism (2D or 3D). Equation 1 links the final mechanism topology ($\boldsymbol{T_{3D}}$) with the template parameters ($\boldsymbol{T_{2D}}$) and forming process parameters. Equation 2 links the 3D mechanism outputs, $\boldsymbol{D_{3Di}}$ ($i = f$ for force based actuation and d for displacement-based actuation) with 3D topology, loading and kinematic behavior. $\boldsymbol{S_{3D}}$ captures any subsequent spring back which may occur during use (ideally this is 0) and $\boldsymbol{e}$

represents the combined systematic and random errors of the device. Using Eqxns. 1 and 2, we may link template topology (T_{2D}) to final mechanism performance characteristics (D_{3Di}). The development of this theory is ongoing. In this paper we will use the intuitive example in Fig. 2B as a means for creating a mechanism to demonstrate the technology, characterize transient errors, and generate data for subsequent validation of Equations 1 and 2.

5 Case study: 3D compliant Hexapod

A template was designed in CAD and used to generate the 2D template shown in Fig. 3. Tooling was designed to simultaneously fixture and form the template. The template is rigidly attached to the tooling at points a, b, and c. The template is clamped between two pieces of tooling at points d, e, and f. The clamping is required to prevent the delicate, motion generating parts of the mechanism from deforming during the forming process. These elements are located between a-e, e-b, b-f, f-c, c-d, and d-a. The tooling is designed to draw the reliefs (oval shaped features at the apex of the triangle stage) as the device is formed. These draws are shown, post-forming, at location g. By using this process, we are able to isolate the formed and motion generating parts of the mechanism. It is important to make sure that the formed parts are an order of magnitude stiffer than the compliant parts. This ensures that subsequent actuation will not induce significant stresses (S_{3Di} in Eqxn. 2 ~ 0) in the parts of the mechanism which were irreversibly deformed during processing. The mechanism was actuated with micrometer heads and displacement measurements (for motion tests) were taken with 1.25 micron resolution dial gauges. The long-term error tests (e.g. creep, stress relaxation, etc...) were measured with a capacitance probe (5 nm resolution) in the z axis. The testing was performed in a thermal isolation chamber.

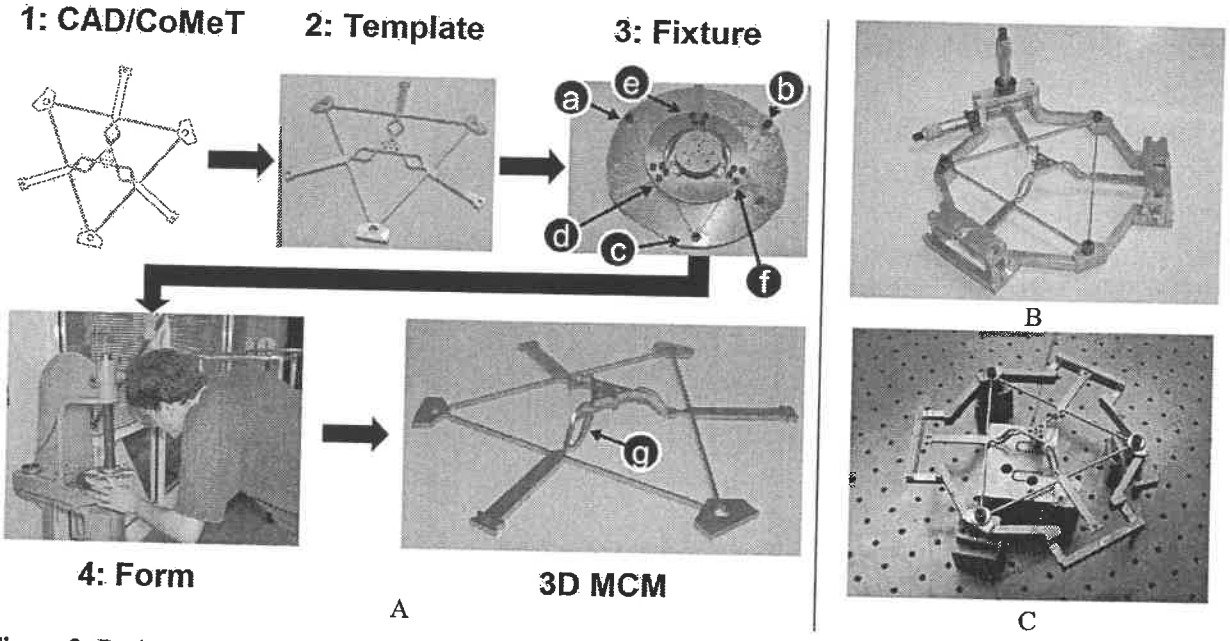

Figure 3: Design process for the case study (A), method of actuation (B) and z axis measurement (C)

The results of long-term error tests are shown in Fig. 4. The stress relaxation behavior immediately following the forming process is shown in Fig. 4A. Please note that the measurements in Fig. 4A and 4B contain a cyclical thermal error of approximately 2 microns peak-to-peak. Figure 4B shows the results of stress relaxation after the device rested in a constraint-free position for one week at room temperature. The differences in Fig. 4A and 4B indicate that the higher transient stress relaxation errors can be made to occur within a few days of forming. As we would like, the magnitude of this error and time constants (at t = 0 and t = 8 days) of the error is small compared to those of the actuation-control system which would force the mechanism to the correct location in a Nanomanipulation system. Even so, one might consider thermal stress relief of these mechanisms. Subsequent creep measurements (constant load on the mechanism) showed no discernable creep over a 24 hour period [16]. Additional, longer-term, creep tests are in process.

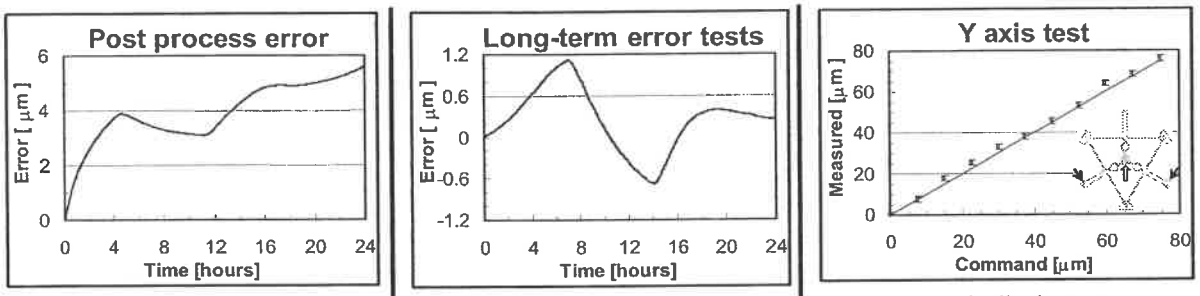

A: Post-process z axis σ relaxation | B: Long-term z axis σ relaxation | C: Single axis displacement test

Figure 4: Experimental results of post process drift (A), stress relaxation (B) and y axis displacement (C)
Several tests were run to characterize the displacement behavior of the mechanism. Figure 4C shows the difference between command and measured displacement. The data has a higher slope (3%) than predicted by FEA (probably a consequence of Young's Modulus difference between material and FEA) and an error from line fit of less than 2.5% FS. This is approximately the error of the measurement system, 2% FS. The tests show the mechanism has near linear behavior and is therefore suited for more rigorous testing once a capacitance-based measurement system is set up to more accurately measure the six-axis performance.

6 References

[01] Goedertier, P. V., "Unitary Q-switch laser device," US Pat. No. 3,500,234, 1966.

[02] Kindl, H., Westermeier, H., "Gas Laser," US Pat. No. 3.826,998, 1974.

[03] Knowles, K. H., "Laser components and fabrication method," US Pat. No. 3,978,425, 1976.

[04] Van den Brink, H. G., Van Hoof, A. J. F. M., Van Kleef, J. H. K. C., Lamboo, T. F., "A method of adjusting gas laser mirror," US Pat. No. 4,217,559, 1980.

[05] Heyler, R., "Package design considerations for automated assembly," www.newport.com/support/magazine_features/fpn01.asp

[06] Shimaoka, M., Kumazawa, T., Yagiu, Y., Sasayama, A., "Optical coupling apparatus and manufacturing of the same and lens holder," US Pat. No. 5,195,155, 1993.

[07] Verviell, J., "Optical electronic assembly having a flexure for maintaining alignment between optical elements," US Pat. 6,207,950B1, 2001.

[08] Masghati, M., Racz, L. M., "Re-entrant alignment features for optical components," US Pat. Application. No. US2002/0048446A1, 2002.

[09] Pan, J., Jiang, P. S., Shih, M., Chen, J., Wang, L., "Fiber optic support clip," US Pat. No. 5,619,609, 1997.

[10] Verviell, J., "Opto-electronic assembly and method of making the same," US Pat. No. 5,977,567, 1999.

[11] Jang, S., Heyler, R., "Process for detecting and correcting a misalignment between a fiber cable and a light source within a fiber module," US Pat. No. 6,184,987B1, 2001.

[12] Katagiri, T., Tachikura, M., Murakami, Y., "Basic design for stable fiber clamping in multi-fiber ribbon mechanical splice," IEICE Transactions of Communication, vol. E84-B, No. 8, pp. 2161-69 August 2001.

[13] Culpepper, M. L., A. H. Slocum and F. Z. Shaikh, "Quasi-kinematic Couplings for Low-cost Precision Alignment of High-volume Assemblies," Journal of Mechanical Design, Vol. 126 (4), pp. 456-63.

[14] Culpepper, M. L., "Design of Quasi-Kinematic Couplings," Journal of Precision Engineering, Vol. 28, Issue 3, July 2004, Pages 338-57.

[15] Culpepper, M. L. and Kim, S., "Framework and Design Synthesis Tool Used to Generate, Evaluate and Optimize Compliant Mechanism Concepts for Research and Education Activities," Proc 2004 ASME DETC.

[16] Korb, S, "Design, Fabrication, and Testing of a Three-Dimensional, Plastically-Deformed, Monolithic Compliant HexFlex Nanomanipulator," BS Thesis, MIT, 2004.

PRECISION ENGINEERING EDUCATION AT MIT VIA HANDS-ON DESIGN PROJECTS: THE MIT NANO-ETCHA-SKETCH PROJECT

Martin L. Culpepper
MIT Department of Mechanical Engineering
77 Massachusetts Avenue, Room 3-449b
Cambridge, MA 02139
Tel: 617-452-2359, culpepper@mit.edu

Shih-Chi Chen and M.V. Kartik
MIT Department of Mechanical Engineering
77 Massachusetts Avenue, Room 3-446
Cambridge, MA 02139
Tel: 617-452-4957, scchen@mit.edu / mvkartik@mit.edu

Keywords: Flexure, compliant mechanism, magnet-coil actuator, capacitive sensing, education

1 Introduction

Project-based courses have long been used to teach the fundamentals of engineering design. This hands-on approach is used at MIT to teach engineering students several fundamental principles of precision engineering:

(1) Flexure design (2) Magnet-coil design (3) Basic electronics/control
(4) Precision fixturing (5) Precision measurement (6) Natural frequency and mode shapes
(7) Vibration isolation (8) Thermal sensitivity/design (9) Deterministic design practices

These fundamentals are taght in 2.000: How and Why Machines Work [01]. During this semester-long course, freshmen engineering students are tasked with two separate precision design projects:

(1) Nano-etch-a-sketch: Modeling, design, fabrication and characterization of a two-axis, macro-scale Nanomanipulator (a Nano-etch-a-sketch).

(2) MEMS accelerometer: Modeling, design and characterization of a MEMS mass-spring accelerometer.

The following sections describe the projects and philosophy/tools the students use to learn the preceding fundamentals. The curriculum which supports these activities is freely available. Contact culpepper@mit.edu with questions / requests.

2 Teaching philosophy

A failing of many engineering design courses is that they turn "technically impressionable" students into applied mathematicians with engineering knowledge. By this, we mean that most engineering courses present engineering theory and quantitative methods rather than a balanced set of theory, qualitative skills and quantitative skills. The approach taken in these projects, aims to make the students develop qualitative skills by helping them figure out the important characteristics of a problem and performance sensitivity to important variables before they delve into equations. They then use dimensional analysis to form relationships between the important variables/characteristics and performance. This often starts with analogy. For example, when the students are asked to design a mass-spring-damper system (see Section 5) with a particular natural frequency, they are asked to think about how a car's suspension system characteristics affect its natural frequency. After several thought experiments, the students are able to determine that the mass and stiffness are the important variables. They then perform dimensional analysis to develop relationships between the design and performance parameters and run experiments to flesh out the relationships. Activities such as these build confidence in the student's innate ability to understand what is important and then use this knowledge to solve an engineering problem. Once the students understand the important variables, they are taught the engineering theory in the classical, analytically intense manner.

3 CoMeT – A compliant mechanism/flexure design tool

The projects in subsequent sections rely on flexures and compliant mechanisms. We have developed a software package and curriculum which students use to understand, design, fabricate and integrate flexure-based machines into precision equipment [02]. This tool, CoMeT (Compliant Mechanism Design Tool), has also been used to

design R&D 100 award (2004) winning flexures and compliant mechanisms for Nanomanipulation equipment [03] for research projects. *CoMeT* is a *Matlab*^{TM} script designed to enable:

Rapid concept evaluation – The GUI, shown in Fig.1, reads hand sketches of mechanism concepts (e.g. via pen on tablet PC) to automatically generate matrix based analysis models that use beam equations (i.e. no meshing). This is equivalent to having a smart "back of the envelope" which can help you optimize/explore designs.

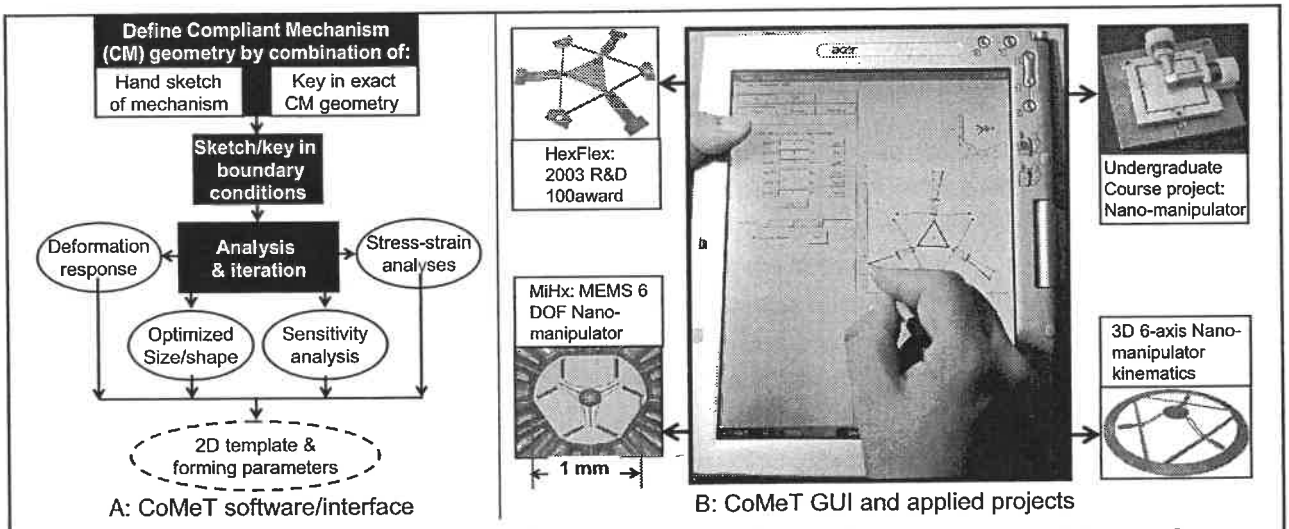

Figure 1: *CoMeT* design tool used in MIT undergraduate flexure design courses and research

4 Nano-etch-a-sketch contest

An example of a student-designed Nanomanipulator is shown in the upper right hand corner of Figure 2. The Nanomanipulator consists of an x-y flexure stage which is driven by two magnet-coil actuators. The steps follow as they design their device are shown in Fig. 2 and outlined below the figure.

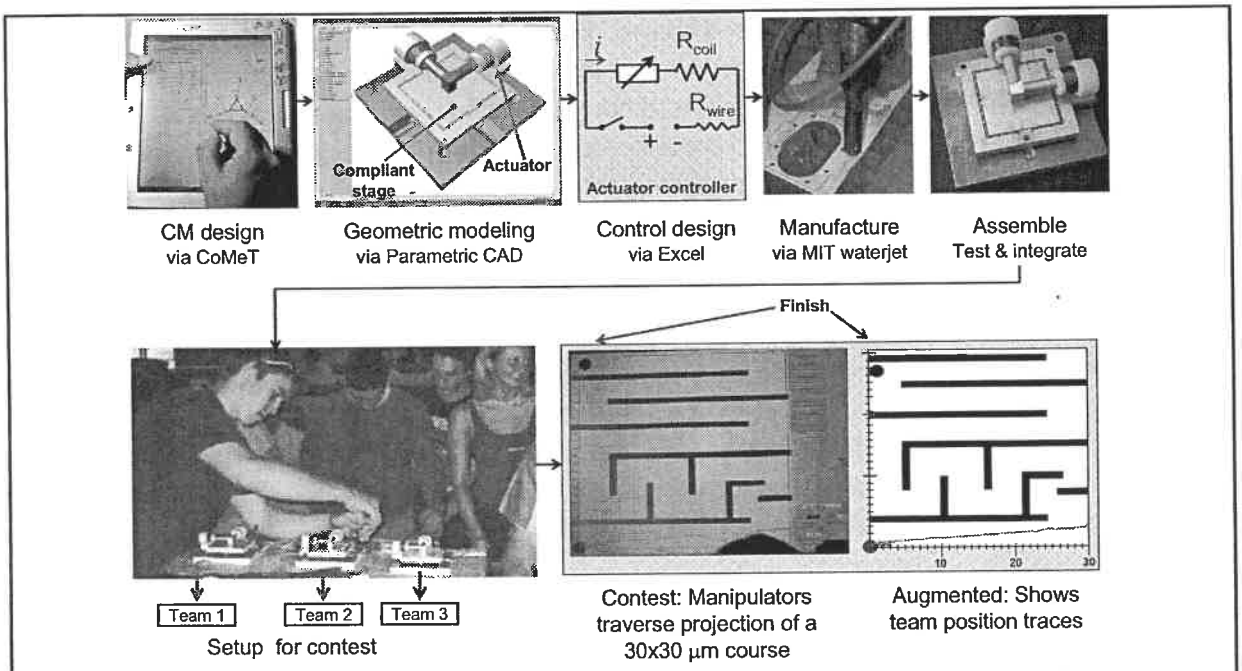

Figure 2: 2.000 How and Why machines Work; (A) Nanomanipulator contest and (B) MEMS project
Note: Traces on bottom right images show position of each manipulator in maze during a race

The following steps trace the flow shown in Fig. 2:

Step 1: Students conceive of an x-y flexure stage design and model it using the CoMeT flexure design software.

Step 2: Students design the geometry of auxiliary equipment (actuators, sensors, fixtures) using a CAD program.

Step 3: Students design and build the electronics and the magnet coil actuators.

Step 4: Students use an abrasive waterjet to fabricate their flexure stage.

Step 5: Students assemble, test and calibrate their Nanomanipulators. At this stage, students learn to use precision measurement probes (capacitance probes) which they set up to track the motion of their Nanomanipulator. Students also equip their Nanomanipulator with a kinematic interface which enables them to quickly/repeatably dock and undock their Nanomanipulator to the capacitance probe fixture.

At the end of the course, students "race" their Nano-manipulators through a virtual 30x30 micron race track. The bottom left of Fig. 2 shows three teams lining up to race. To successfully complete the track, the student's needed to design a Nanomanipulator which can move over a 30x30 micron range. Each Nanomanipulator must be capable of 50 nm resolution (to make the tightest turns). Students quickly learn not to "jump up and down' when they get excited during the race (some students design low-cost, but effective vibration isolation tables for their machines by supporting the Nanomanipulators with bubble wrap) In addition, design for thermal insensitivity is impressed on the students as they run experiments to determine the affect of temperature variation on their ability to drive the Nanomanipulator through the course. They quickly learn that they can not handle the Nanomanipulators without gloves (due to thermal energy transfer from their hands). Clever students lean how to integrate friction damping to limit the effect of vibration-based disturbances. To date 28 of 32 students have been able to successfully complete the maze with their machine.

5 MEMS accelerometer project

The 2.000 students are also tasked with designing and testing the hardware components of a MEMS accelerometer. The students are given targets with respect to natural frequency, size constraints, the CoMeT tool and material properties of single crystal silicon. The students then go through the thought experiments described in Section 2, to determine the important variables and relationships which relate stiffness and mass to dynamic performance. The students use the CoMeT tool to develop concepts and simulate their performance. After two weeks, they are required to hand in a DXF file of their design which is then transformed into a mask pattern. The course TA fabricates the devices in the MIT Micro Technologies Laboratory (see wafer in Fig. 3). Several examples of student designs are shown on the right hand side of Fig. 3. Students then use capacitance probes to measure the vibration properties (displacement vs. time) of their device, perform a FFT and determine the device's natural frequency. To date, their calculations have matched measured data within 5%.

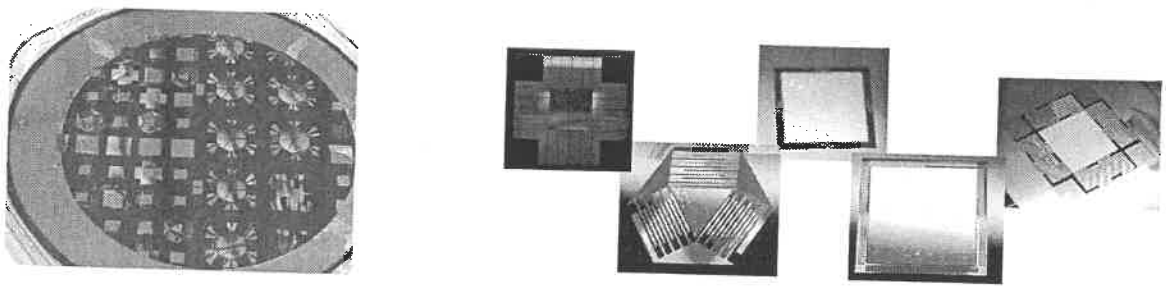

Figure 3: 2.000 How and Why machines Work; MEMS accelerometer project

6 Graduate student projects in precision engineering

During the Fall of 2004, Graduate students at MIT will take 2.76: Multi-scale systems design and manufacturing [04]. Multi-scale systems consist of components from two or more length scales (nano, micro, meso, or macro-scales) and thus require precision engineering to ensure proper design and fabrication. The students will be tasked with the design, modeling, fabrication and characterization of a STM which is capable of better than 0.5 nm resolution over a range of 500 x 500 x 500 nm^3. Problem sets guide the design of each key component of the SPM. Figure 4 shows the original concept for the STM project.

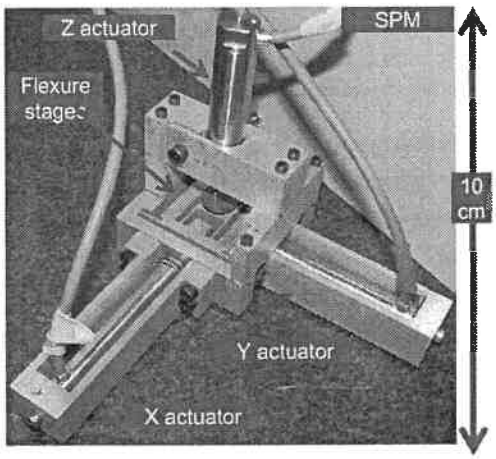

Figure 4: 2.76: Multi-scale design and manufacturing course project (STM)

7 Acknowledgements

The authors would like to thank Microsoft and the MIT iCampus project [05] for providing the funding to develop the CoMeT design tool. We would also like to thank Ford Motor Company for providing the funding and technical support required to make the MEMS accelerometer project possible. We also extend our thanks to GM for providing access to engineering design tools via the PACE program and funding PACE curriculum development.

8 References

[01] 2.000 Course web site: http://psdam.mit.edu/2.000/start.html.

[02] Culpepper, M. L. and Kim, S., "Framework and Design Synthesis Tool Used to Generate, Evaluate and Optimize Compliant Mechanism Concepts for Research and Education Activities," Accepted for publication in the proceedings of the 2004 ASME Design Engineering Technical Conference, Salt Lake City, UT, September 2004.

[03] Culpepper, M. L. and G. Anderson, "Design of a Low-cost Nano-manipulator Which Utilizes a Monolithic, Spatial Compliant Mechanism," Accepted for publication in the Journal of Precision Engineering, 2002.

[04] 2.76 Course web site: http://psdam.mit.edu/2.76/index.html

[05] MIT iCampus web site: http://icampus.mit.edu

Making wooden reconstruction models from the Codex written by Leonardo da Vinci

Kazuhide KAMIYA[*a], Nagayuki KAMIYA[**], Takashi NOMURA[*a], Hatsuzo TASHIRO[+b]

[a] Faculty of Engineering, Toyama Prefectural University,

[b] Faculty of Engineering, Toyama University,

* Kurokawa, Kosugi-machi, Toyama 939-0398, Japan,

** Ronchi-machi, Takahama, Aichi 444-1314, Japan,

+ Gofuku, Toyama, Toyama 930-8555, Japan

Keywords: Leonardo da Vinci, Reconstruction, The Madrid Codices, The Atlanticus Codex, Mechanics

Introduction

Leonardo da Vinci is not only famous as the artist who painted master pieces such as "The Last Supper" and "Mona Lisa", he is also a great scientist and engineer. He left records of many original scientific inventions and explorations in books now known as Leonardo's Codices. Although parts of the codices have now been scattered and lost in Europe about 5000 pages of the codices have been preserved. These codices include anatomical charts, mechanical equipment, civil engineering concepts, and drawings related to architecture, astronomy, botany, and so on. In particular, descriptions of mechanical equipment are included in the Madrid Codices and the Atlanticus Codex. The contents of these Codices are interesting for beginners who are studying mechanical engineering, although beginners are not used to recognizing a solid from a drawing. Therefore, models were reconstructed from the drawings in these codices, to be used as teaching materials for the study of mechanical engineering. This paper describes the reconstructed models and their use in education.

Codices written by Leonardo da Vinci

The Madrid Codices and the Atlanticus Codex were used on the basis for constructing wooden reconstruction models. The Madrid Codices and the Atlanticus Codex are about 600 pages and about 1200 pages long, respectively. These codices are exceptional as works of art

but they present difficulties when considered as technical drawings. These difficulties are as follows. The drawings do not specify the scale of models, and the relative size is not accurate because the drawings are made using the axonometric projection. Therefore, in the codices, the structure of the hidden side of the model is unknown, and furthermore, drawings of individual elements are very rare. Figure 1 shows a rare codex drawing that shows the assembly of the elements of the mechanism.

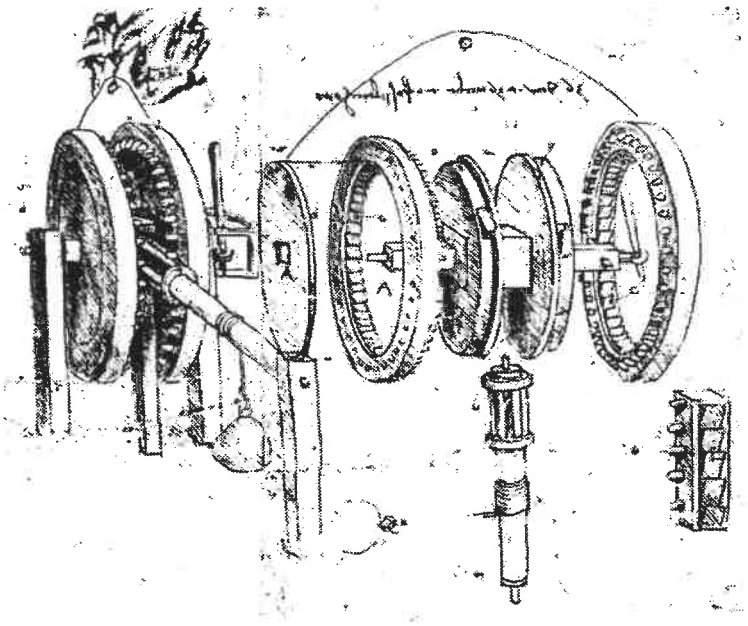

Figure 1 Example of codex assembly drawing; hand-powered winch.

Reconstruction from the codices

Reconstruction of the models was performed on the basis of the drawings in these codices as faithfully as possible, with the limitation that the footprint of all models was fixed at no more than 8-1/2" x 11" due to the restrictions of the exhibition space. Assuming that the models would still function appropriately, the unknown parts were constructed based on present-day technology. Various kinds of wood were used as model materials. More than 50 models were reconstructed from the Madrid codices and the Atlantico codex over a period of about 10 years. Figure 2 shows an example of a model that was reconstructed on the basis of the codex drawing shown in figure 1. As a result of the reconstruction work, even if all models were faithfully manufactured according to the codices, there were still some models that did not function satisfactorily. The author considers that a number of concepts which had not been subjected to trial manufacture were recorded in the codices.

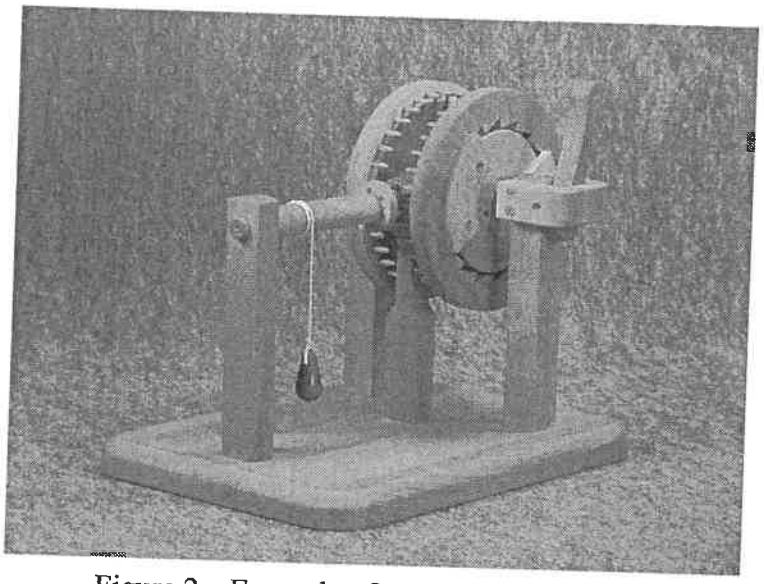

Figure 2 Example of reconstructed model.

Education using the reconstructed models

The reconstructed models were used in a lecture as part of a mechanics course. After the lecture based on a textbook, the reconstructed da Vinci models were shown to students. The reconstructed models attracted much more attention than the textbook. It was possible to generate an interest in mechanical engineering among students who studied mechanics using the reconstructed models. Figure 3 shows a photograph of the DA VINCI Festival held at Toyama Prefectural University. The purpose of the DA VINCI Festival was to give young scientists insight into points of interest in science and technology. Though the majority of primary school children could not understand the meaning of advanced mechanisms, they enjoyed interacting with the reconstructed models in the festival. Similarly, an opportunity to consider the field of mechanical engineering was given to students of primary schools, junior high schools, senior high schools and their parents, by the reconstructed models presented in the festival.

Conclusions

Models were reconstructed on the basis of the Madrid Codices and the Atlantico Codex written by Leonardo da Vinci, so that they could be used as teaching materials for students studying mechanical engineering. As a result of the reconstruction work, even if all models were faithfully manufactured according to these codices, there were still some models that did

not function satisfactorily. The author considers that a number of concepts which had not been subjected to trial manufacture were recorded in the codices. In a lecture as part of a mechanics course, it was possible to generate an interest in mechanical engineering among beginners who studied the mechanics by using the reconstructed models. Similarly, an opportunity to consider the field of mechanical engineering was given to students of primary schools, junior high schools, senior high schools, and their parents, by the reconstructed models presented in the DA VINCI Festival at Toyama Prefectural University.

Figure 3 Photograph of DA VINCI Festival.

Acknowledgements

The authors would like to thank the Crossland Oyabe Foundation for providing copies of the codices. This study was financially supported in part by a special grant in aid from Toyama Prefectural University.

References

1) Leonardo da Vinci and Reti Ladislao: Tratado de estatica y mechanica en Italiano; Codices Madrid.
2) Leonardo da Vinci and Carlo Pedretti: The Codex Atlanticus of Leonardo da Vinci : a catalogue of its newly restored sheets.

STABILITY AND ACCURACY OF THIN, PRECISION FLEXURE AMPLIFICATION MECHANISMS

Nathan Landsiedel
MIT Department of Mechanical Engineering
77 Massachusetts Avenue, Room 3-446
Cambridge, MA 02139
Tel: 617-452-4957, nate1@mit.edu

Martin L. Culpepper
MIT Department of Mechanical Engineering
77 Massachusetts Avenue, Room 3-449b
Cambridge, MA 02139
Tel: 617-452-2359, culpepper@mit.edu

Keywords: Flexure, compliant mechanism, stiffness, parasitic error, MEMS

1 Introduction

Elliptically-shaped amplification flexures, such as the one shown in Fig. 1A, are generally designed with r_{max} / w ratios of 5 or less to avoid out-of-plane error motions. Emerging applications in MEMS manipulators (Fig. 1B) and thin-walled tube actuators (Fig. 1C) are constrained to use flexure with ratios larger than 25. The in and out-of-plane stiffness-error characteristics of low-width amplification flexures are not well understood. In this paper we present the steps in a method which can be used to model transmission ratio and out-of-plane error motions of thin-width flexures. This method links flexure transmission ratio, out-of-plane errors, error causing loads and flexure characteristics. The theory has been implemented in an *Excel*™-based design tool and may be downloaded at http://psdam.mit.edu/download.html. The tool is particularly useful for designers who seek to generate amplification flexures for use in micro-scale, precision machines such as micro-scale Nanomanipulators. The theory is also generally applicable for optimization of meso and macro-scale elliptical amplification flexures.

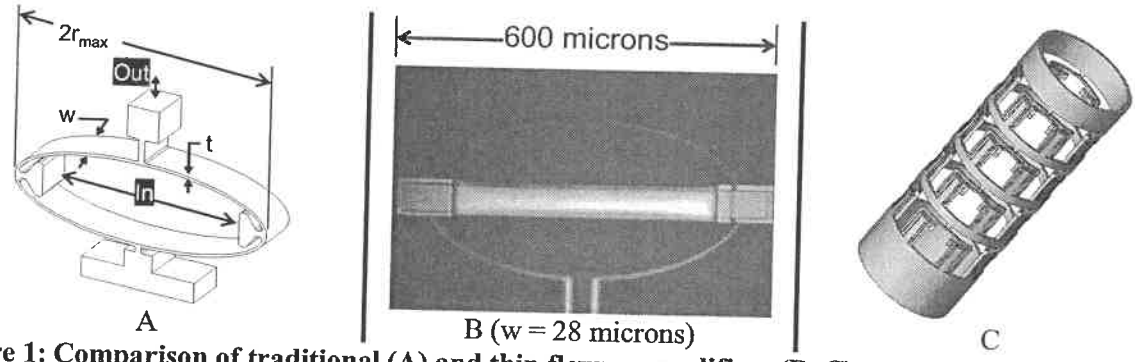

A B (w = 28 microns) C

Figure 1: Comparison of traditional (A) and thin flexure amplifiers (B, C) MEMS flexure shown in (B) has r_{max} / w ratio ~ 21

2 Modeling

Figure 2 is labeled to indicate the characteristic dimensions of an elliptical amplification mechanism.

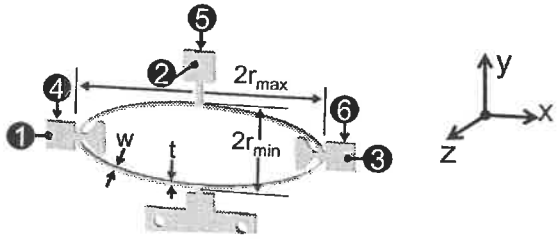

Figure 2: Flexure design parameters

2.1 Out-of-plane errors

We are interested in errors due to moment loads which result from mounting an actuator on one side of the flexure (e.g. piezo actuators deposited on one side of a flexure, see Fig. 1B) and/or a misaligned actuator. The model for out-of-plane motion uses the standard elastic deformation theory which relates the out-of-plane motion, z, to material properties, loading and flexure geometry [2]. The loading, M, is the actuator force multiplied by the moment arm between the mid plane of the flexure (at ½ w) and the x component of the actuator force. This moment would be applied at attachment points 1 and 3 in Fig. 2.

$$z(x) = \iint \frac{M}{EI(x)} dx\, dx \quad \text{for} \quad I(x) = \frac{b(x) \cdot w^3}{12} \tag{1}$$

The area moment of inertia of the ellipse is different from that of a straight beam because the cross-sectional area of the ellipse varies with x. Eqxn. 2 was derived to capture the effect of b variation with x

$$b(x) = 2\left[\sqrt{r_{\min 2}^2 - \frac{r_{\min 2}^2 x^2}{r_{\max 2}^2}} - \sqrt{r_{\min 1}^2 - \frac{r_{\min 1}^2 x^2}{r_{\max 1}^2}}\right] \tag{2}$$

Subscripts *2* and *1* refer to the referenced dimension taken just outside and inside of the elliptical flexure's 2D envelope. For instance, $r_{min\ 2} - r_{min\ 1} = t$. When Eqxn. 2 is substituted into Eqxn. 1, the right side of Eqxn. 1 may be integrated to form a relationship between out-of-plane error, flexure loading and flexure geometry.

2.2 In-plane displacements

The in-plane motions have been modeled using Castigliano's theorem as applied to thin, curved beam of varying radius [3]. In this approach, the displacement of a beam is related to the energy stored in the beam as shown in Equation 3. The ellipse was treated in the study as one quarter of the ellipse. The model enforces a ground constraint on one end and assumes the other end has a no slope constraint. One quarter of the actuator force, F, is applied to load the model.

$$\delta_i = \frac{\partial U}{\partial F_i} = \int \frac{M}{EI} \frac{\partial M}{\partial F_i} dx \tag{3}$$

Equation 6 gives the relationship for the moment and the partial derivatives of the moment equations which are substituted into Equation 5.

$$M = F\left(\frac{w}{2}\right) + M_o = F\left(\frac{w}{2}\right) + F k\left(r_{\max} - \frac{w}{2}\right) \tag{4}$$

$$\frac{\partial M_y}{\partial F} = y \quad \text{and} \quad \frac{\partial M_x}{\partial F} = \left(r_{\max} - \frac{w}{2}\right) - x \tag{5}$$

Here k is a value obtained from Roarke [2]. When Eqxns. 4 and 5 are substituted into Eqxn. 3, the right side of Eqxn. 3 may be integrated to form a relationship between actuator input and flexure output (essentially the transmission ratio) as a function of load and flexure geometry.

3 Experiment

3.1 Test rig and flexure prototypes

Two flexure geometries were tested during this experiment to ascertain the accuracy of the theory developed in section 2. Prototype dimensions are provided in Table 1. The flexures were fabricated on an abrasive water-jet. The flexures were cut from 7075-T651 Aluminum sheet. Figure 3 shows the test rig used to actuate the flexure and measure its response. Both prototypes were assembled within the test rig so as to provide equivalent out-of-plane error loads on the flexures.

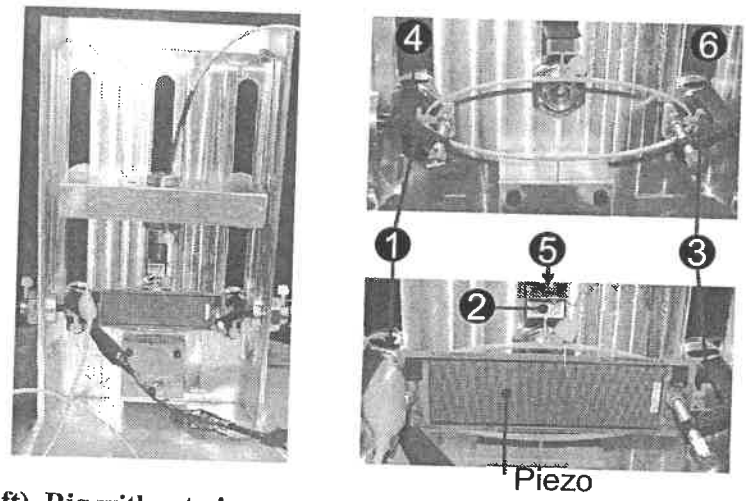

Figure 3: Test rig (left), Rig without piezoactuator (top right), rig with piezoactuator (bottom right)

Table 1: Prototype dimensions (t = 1.3 mm for both flexures)

Dimension	For w = 1.3 mm	For w = 3.2 mm
r_{max} [mm]	57.2	57.2
r_{min} [mm]	19.1	19.1
t [mm]	1.2	1.2
r_{max} / w	47.6	17.8

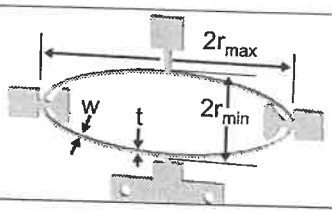

3.2 Measurement

A calibrated piezoactuator with low bending stiffness was used to actuate the flexure. The actuator was mounted on one side of the flexure. This emulates the situation in Fig. 1B.

3.3 Actuation

Slots in the fixture accept capacitive sensors capable of 60 nm displacement measurements. Figures 2 and 3 show the location of in-plane (points 1, 2, 3) and out-of-plane measurements (points 4, 5, 6).

3.4 Experimental error sources

The error sources in the test rig, provided in Table 2, sum to less than 3 % of the measured outputs.

Table 2: Experimental error sources

Source	Error [μm]	Comments
Manufacturing and assembly	2	Waterjet taper measured at 5 degrees
Vibration	< 1	Optical table used for vibration isolation
Measurement	0.06	Capacitance probes capable of 60 nm resolution

4 Results and discussion

Figure 4 compares the relationship between actuation input and flexure output as defined in Fig. 1A.

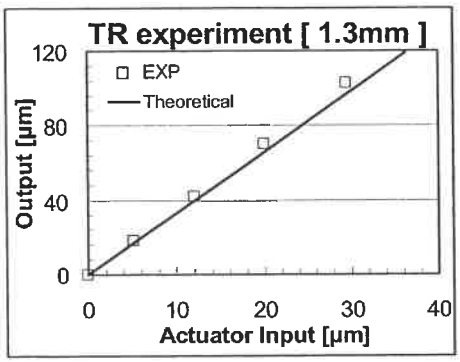

A

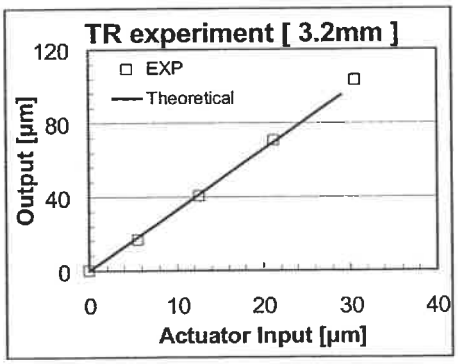

B

Figure 4: Results of transmission ratio tests

The theory and experiment match to within 2% and 6% for the 3.2 and 1.3 mm width flexures respectively. Figure 5A and Fig.5B compare the relationship between flexure motions and out-of-plane errors. As expected, the 3.2 mm flexure exhibited less out-of-plane error (4.4 microns or 4.3 % of flexure's desired output motion) than the 1.3 mm flexure (11 microns or 10.8 % of the flexure's output motion).

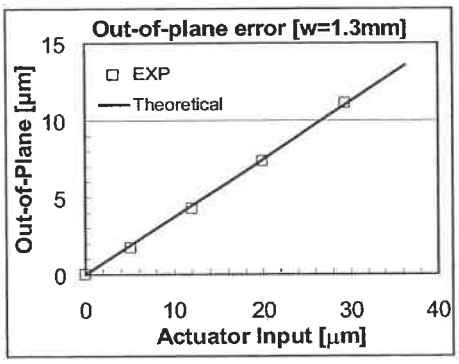

A

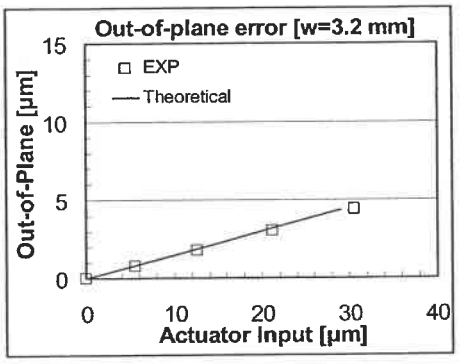

B

Figure 5: Results of out-of-plane errors tests

The tests indicate that the theory is accurate enough to ascertain out-of-plane errors for $r_{max} / w < 15$. This is adequate for setting design limits on the tube-flexures and MEMS devices shown in Fig. 1. For instance, for a given MEMS device size (r_{max}), the theory can be used to select a device layer thickness (w_{device}) which is needed to prevent out-of-plane errors from exceeding design specifications. The theory can also be used to generate surface plots which relate TR and out-of-plane errors to independent variables w, t, r_{max} and r_{min}. The design theory has been implemented in an Excel™ file and posted for download at http://psdam.mit.edu/download.html.

Improving the accuracy of the theory is a goal of the continued research. The tube-actuators and MEMS device shown in Fig. 1B will be tested and error results will be presented vs. the results of this work in the near future. More effort will be focused on reducing the experimental error and improving the model's accuracy by incorporating components which capture the effect of the flexure beam taper one would find in flexures fabricated by EDM, waterjet cutting or DRIE.

5 References

[1] Conway, NJ and Kim, SG, Large-strain piezoelectric in-plane micro-actuator, 17th IEEE MEMS Conf, 2004, p.454-57.

[2] Young, WC and Budynas, RG: "Roark's Formulas for Stress and Strain," 7th ed., McGraw-Hill, 2002.

[3] Budynas, RG: "Advanced Strength and Applied Stress Analysis," Mcgraw-Hill, 1977.

Structured Surfaces Damping Enhancements at Mechanical Interfaces

Eric R Larsen, Matthew A Davies, K. Scott Smith, Melissa M Nuttall
University of North Carolina at Charlotte, Charlotte, NC

The development of high-power, high-speed machine tools has lead to a practical need to predict, enhance and control regenerative chatter. While techniques such as tool tuning have been used to significantly enhance machining stability in high-speed machining, increasing system damping is a more effective means of enhancing the overall stability of the machining system. However, the damping properties of machine structures are extremely difficult to predict or control because it depends strongly on the microscopic contact conditions at the mechanical interfaces in the system. We aim to design structured surfaces that intentionally create contact conditions that enhance the damping and the dynamic repeatability of the mechanical connections in a machine tool without compromising the kinematic repeatability and accuracy. This will result in increased stability, productivity and machine utilization.

Determining the cause of the variation in dynamic stiffness between nominally identical unaltered toolholders presents a significant challenge in itself. In order to better understand the spindle – toolholder dynamic interactions, three toolholders were placed into a control group and analyzed. Two toolholders were AT-4 fit class and one toolholder was AT-5. The Frequency Response Functions (FRF) of the two AT-4 toolholders, nicknamed Frick and Frack, were compared from impact modal tests in the Spindle Test Stand (STS) with a 34.1 kN drawbar load.

These two toolholders, Frick and Frack, which look nominally the same, differ in weight by less than 0.01 %, and differ in natural frequency by less than 0.6 %, differ in damping ration by more than 54 %. Their dynamic stiffness also differs by around 52 %. Small changes in damping ratio yield large changes in dynamic stiffness. Since no alteration was made to the contact surface of the toolholders and they were both tested in the same spindle nose with the same drawbar load, the difference in dynamic stiffness must come from the geometry of the toolholders themselves. The geometry of the tapers of the two toolholders was measured, revealing lobing of the taper consistent with parts that were OD ground. Since the toolholders can be inserted into the test stand in two orientations (at 0 degrees and rotated 180 degrees) dynamic measurements were taken in both orientations. Both toolholders proved to have preferred orientations in the spindle test stand resulting in more repeatable results across consecutive measurements than their alternate insertion orientations.

Table 1. AT-4 CAT 40 toolholders.

Toolholder	Natural Frequency	Damping Ratio
Frick	2100.0 Hz	0.46 %
Frack	2089.5 Hz	0.72 %

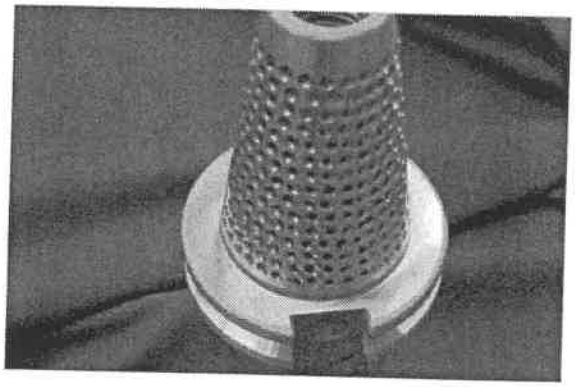

Figure 1. CAT 40 toolholder with altered contact surface.

Additionally, an AT-5 fit class toolholder was tested to establish its baseline FRF and then its tapered surface was altered on a micro level using a fine grit sandblast. The surface was iteratively sandblasted and surface texture and FRF measurements were taken three times. The sandblast resulted in a change in surface texture measured by an 18% increase in Ra, 11% increase in Rq, 4.8% increase in Rmax, 6.5% increase in Rz, and a 42% more negative skew than the original surface. A two factorial experiment was designed to test the effects of drawbar load, orientation, and surface (before and after sandblasting) on the first natural frequency (cantilever bending mode) and damping ratio. The experiment showed quantitatively that the drawbar load had a statistically significant effect on the natural frequency. The experiment also showed qualitatively that the drawbar load had an effect on the damping ratio. These experiments again showed a preferred orientation of the toolholder in the spindle resulting in more repeatable results across consecutive measurements. These results statistically verify the earlier work of Smith and Jacobs (2000).

Fabrication of structured surfaces and evaluation of the contact between two surfaces is difficult enough without the added complexity of the two surfaces comprising the spindle-toolholder interface being conical. In order to simplify this problem, it was decided to investigate the effects of structured surfaces on the contact interaction of two flat, parallel surfaces. In essence, this simplified configuration gives a cut-away look at the spindle-toolholder interface during the experiments. Once candidate surfaces have been identified and their effects documented in the 2-D test stand, they can then be replicated on toolholders and tested in the STS and machines.

The 2-D surface test stand was designed to focus on the contact interaction be the two surfaces while mimicking the conditions seen in the spindle-toolholder interface in a machine tool. In a machine tool, toolholders are placed in the spindle and held in place with a drawbar. This introduces a load that elastically deforms the surface of the toolholder. We chose to replicate the contact pressure at the interface between the spindle – toolholder combination. To do so, the area and loading method were designed so that these contact pressures could be easily replicated using a loading bolt as shown in Figure 2. Another important loading consideration was uniformity of the loading. We hypothesize that the cause of the increased dynamic stiffness seen with the original altered toolholder was that the surface had somehow enhanced, exaggerated, or caused the onset of stick-slip friction at the interface. If this is true, then non-uniformity in the loading would change the behavior of the interface and not isolate the effects of the structured surface.

Choice of material was also driven by the interface we were trying to replicate. Toolholders and spindle noses are commonly made from AISI 8620 steel case – hardened at 58 – 60 HRC to 1.5 – 2.0 mm deep. The surface samples and test stand therefore were made from AISI 8620 steel. Case hardening of the entire flexure was not desirable since it would make future machining for fixturing extremely difficult and would cause non-uniform deflection of the arms with load application since the shell of the arms would be harder than the core. Therefore, the contact portion of the flexure was cut first with the wire EDM (WEDM), and the remainder of the flexure was coated with copper to prevent carbon from leaching into surfaces that were not inteded to be hardened. The flexure was then carburized, hardened, and final WEDM of the flexure was completed. The rest of the features were machined and a final pass was made on the contact surfaces with the WEDM. This resulted in a completed test stand with a case hardened contact area.

Loading and unloading of samples also made it necessary for the test stand to actuate. Since we planned to characterize the surfaces with dynamic excitation, we also needed a way to load the samples in nominally the same location every time and have no contact interfaces besides the one under consideration in the metrology loop. All these considerations led us to a flexure design for the surface test stand, dubbed the Flexural Test Stand (FTS). A flexural design allowed for uniaxial actuation with no interfaces in the test stand thus fulfilling all the requirements set earlier. A picture of the FTS is shown in Figure 2 below.

Measuring the load applied to the sample is done with a strain gage load cell. Since the load cell could not be placed between the clamping arms of the test stand and the sample, a calibration had to be done between the load it measures through the flexure and the load actually applied to the sample. A second strain gage load cell was calibrated to the one used in the test stand in a separate fixture. The load cell was placed in the test stand and the second load cell was placed in the contact area. The output of the first load cell was then calibrated to the output of the second load cell. In this way, the output of the load cell in the test stand is calibrated to reflect the load actually applied to the samples. The calibration curve is show in the figure below.

The experimental surfaces being tested range from macro geometric features with size scales on the order of millimeters, to micro texturing with size scales on the order of micrometers characterizable in terms of surface finish. The operating assumption

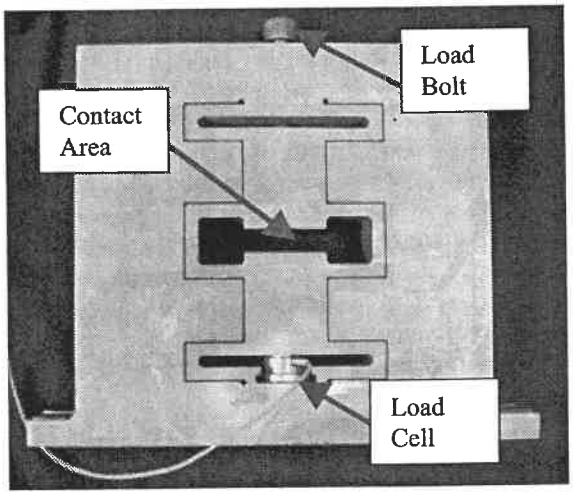

Figure 2. Flexural Surface Test Stand.

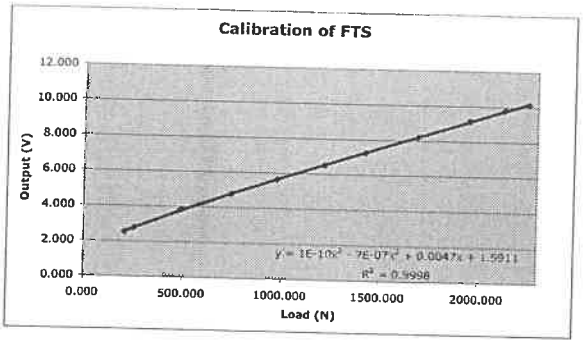

Figure 3. Calibration curve of clamping load in FTS.

of this project is that a given surface exists, which may be a combination of surface finish and macro geometry, resulting in a maximum dynamic stiffness, for a given clamping load, in the frequency range of interest. Several test surfaces have been fabricated with macro geometric feature sizes from 10 millimeters to 1 millimeter.

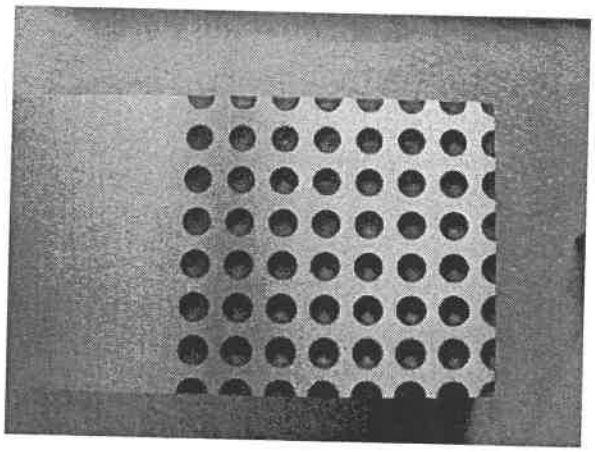

Figure 4. Dimpled 2-D surface sample.

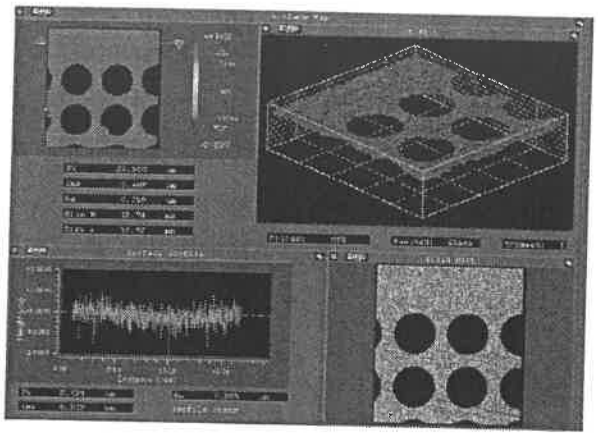

Figure 5. Surface roughness measurement of dimpled surface sample.

The samples all have surface roughness of approximately 0.3 microns Ra. A stitched surface roughness scan of one of the samples from a white light interferometer is shown the figure above. This sample is the 2-D version of the surface applied to the toolholder in figure 1. A 6 millimeter diameter ball-nose end mill was used to create dimples 1 millimeter deep in the surface of the sample.

Alteration of the contact surface in the spindle – toolholder interface has been proven to effect the dynamic stiffness of the system. During the last year, the focus has been on determining the optimum surface for damping enhancement at the spindle – toolholder interface.

Real-time Collaborative Design and Dimension Verification over the Internet

In-Ho Song, Kwang-Heum Yeon and Sung-Chong Chung

Hybrid Systems Design & Control LABoratory
Department of Mechanical Design & Production Engineering
Hanyang University, SungdongGu, Seoul 133-791, KOREA

Abstract: The objective of this paper is not only the development of a real-time viewer for the real-time collaboration of design reviews, but also the real-time verification of dimensions over the Internet. As the anytime-anywhere access is possible via the Internet, remote collaboration in the design and manufacturing process is realized. The developed system is also designed to eliminate network dependency, so that it reduces the cost of implementation and management of the system. This system runs on all types of networks from high-speed LANs to wireless connections. Collaborators can check dimension errors, human factors, form errors, as well as mark up the important parts and make a statement of their views over the Internet. 2D and 3D data viewing, markup and annotation, dynamic sectioning, printing services, and real-time conferencing combined with PDM bring real-time benefits to reduce production time to market and design cost. The usefulness of the developed system is confirmed through a case study.

Key Words: ActiveX, Apache, Dimension verification, HTTP, Internet, Native file, Real-time Collaboration

1. Introduction

Concept of remote collaboration in the design and manufacturing processes is strongly required to reduce design conflicts and uncertainties in the early design stage and manufacturing processes, as well as cost and time-to-market. Internet based CAD/CAM conference systems assist designers to review design results through real-time viewers, to communicate design ideas through markups and chatting, as well as to simulate manufacturability and to measure dimensions for correction of design conflicts. Real-time collaboration reduces production ambiguity, product development lead-time and manufacturing cost to a large extent. The objective of this paper is not only the development of a real-time viewer for the real-time collaboration of design reviews, but also the real-time verification of dimensions over the Internet.

Kan, et al [1] have discussed the real-time collaborative system for product design in Internet environment using Virtual Reality Modeling Language(VRML) form and Java applet. Huang, et al [2] have begun to create a standard Internet based Design for X (DFX) shell that provides a framework in which many types of DFX tools can operate. Chen, et al [3] developed the Internet-enabled real-time collaborative assembly modeling system using Java RMI and STEP. However, they have following problems: (1) Previous systems use the middleware such as CORBA. CORBA requires high performance hardwares and is very expensive. (2) Since a lot of data is transmitted during the collaborative operation, it is impossible to realize the real-time collaboration over the low speed network environment. (3) It is impossible to transmit information across the firewall installed in most companies. (4) Since the program to be installed in a client side is very large, it takes much time to execute the viewer.

To overcome these disadvantages of the previous viewing systems, a real-time multi-viewer is developed on the open-architecture web server, Apache, in this paper. As the Apache is used for the viewer, it is inexpensive and does not require high-performance hardwares. In order to increase the data transmission capability, all transmission data are converted into parameters. This conversion decreases the transmission time. And the developed system works well even on the low speed network environment. It runs on all types of networks such as high-speed LAN, dial-up modem, wireless connection and so on.

As the real-time viewing functions are constructed over the ActiveX control environment, client application for the design and dimension verification does not need to install the developed software before using the system. Collaborators are able to perform real-time 2D and 3D viewing, precision measurement, markup and annotation, dynamic sectioning, printing services, real-time conferencing combined with PDM and so on over the Internet Explorer. The proposed system helps to reduce production cost, errors and lead-time to market. Performance of the developed system is

confirmed and verified through a case study.

2. System Architecture

Fig. 1 shows the architecture of a collaborative server. As the collaboration server, four-tier architecture is proposed to enable a distribution processing when multiple users connect to the server at once. Four-tier client/server architecture is proposed to realize the real-time collaborative product design and dimension verification system. The first tier in the client region consists of an administration web page and viewing ActiveX control. The second tier is the web server. It controls clients by using the administration page. Clients communicate with the server through the HTTP protocol. The third tier, which is realized through the JSP(Java Server Pages) and the Servlet engine(Tomcat), is the web container dealing with dynamic web service. Tomcat of the Apache Software Foundation is selected to act as the engine of JSP and Servlets. The fourth tier, collaboration extension module, takes charge of the collaboration functions such as transmission of parametric data, files, markups and chatting information. This is realized through Java. Real-time viewing functions are constructed over the ActiveX control environment.

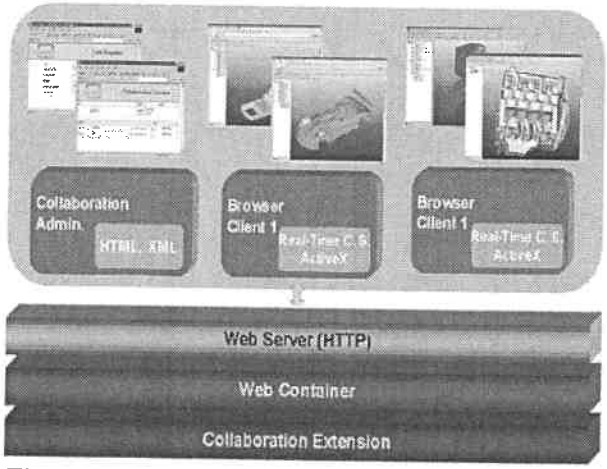

Fig. 1 Structure of the real-time collaboration system.

3. Real-time Collaboration Work

Collaborators are able to conduct real-time 2D/3D viewing, precision measurements and markup through the proposed real-time collaborative system.

ActiveX control is downloaded directly into the client system from the server. In order to protect the collaboration work, communication between the client browser and the collaborative server is performed through the encrypted mode. Functions of the real-time viewer are constructed over the ActiveX control using the visual C++ and OpenGL. Fig. 2 represents a configuration of the collaborative ActiveX control.

In the previous system[4], it is impossible to conduct real-time collaborative processes on low-speed network environment because a share of CAD data causes overload to the network. In order to accelerate the data transmission capability, the developed system is constructed to share the native file instead of the CAD file, and all transmission data are converted into the parameters.

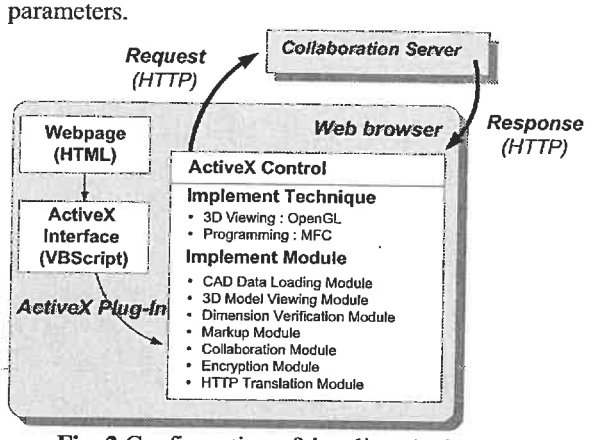

Fig. 2 Configuration of the client ActiveX for the real-time collaboration.

Functions of the developed system have been constructed by using the ActiveX control plugged in the Internet Explorer. All contents of collaborative works are transmitted to multiple users through the collaboration server as shown in Fig. 2.

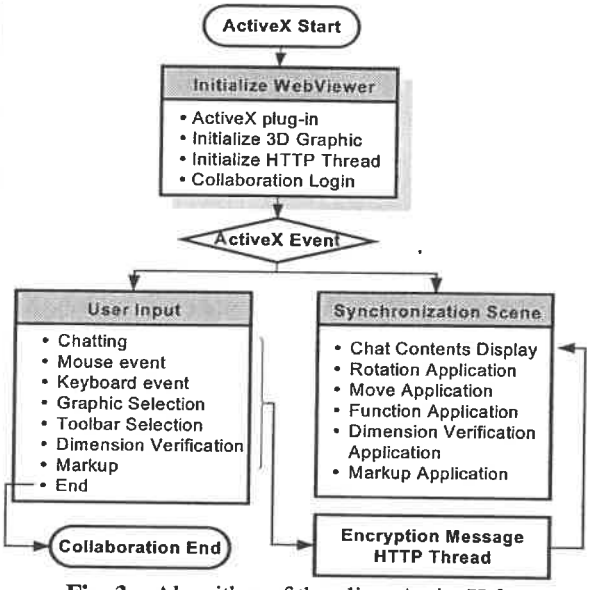

Fig. 3 Algorithm of the client ActiveX for the real-time collaboration.

In order to protect the collaborative work, communication between clients and the collaboration server is performed through the encryption mode. Moreover, the proposed system applies HTTP protocol to transmit data and to overcome firewall systems in companies. Fig. 3 represents work flows of the collaborative ActiveX control[5-7].

4. Design of the Native File

In general, VRML is considered as a viewing tool of CAD data on the Internet environment. However, it takes much time to transform the CAD data into ASCII format by using the CAD API. Moreover, VRML has only the facet data. It is not sufficient for the dimensional verification. In order to overcome these problems, the proposed system uses the native file transforming the CAD data into optimal format through the translation server constructed by using the ACIS kernel and InterOP. The native file includes not only facet data for design verification, but also edge and topological information of CAD data for the dimension verification. New dimension verification results or mark up messages are included in the mark up file followed by a separator. In order to allow a lot of consultation from the clients, a hyperlink function is also used in the mark up function[5]. The native file size is reduced to around 90% through a binary conversion and compression processes.

Fig. 4 shows a structure of the native file converter.

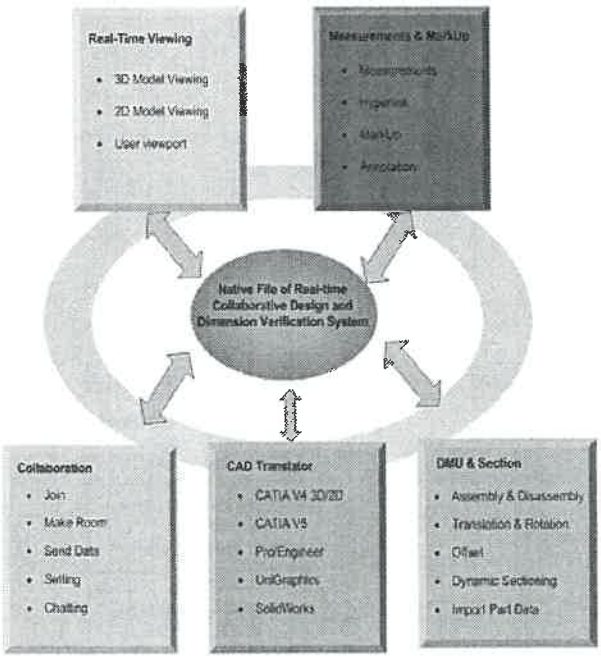

Fig. 4 Structure of the native file converter.

5. Case Study

Effectiveness of the proposed system is verified through design verification of car clutch parts. Fig. 5 shows a Graphic User Interface(GUI) and a start-up process of the real-time collaboration system. The symbols [A], [B], [C], [D], [E] and [F] in Fig. 5 mean verification and markup toolbar, management treeview, a login window, a dialog box for chatting, graphic set up toolbar and display area, respectively. Real-time collaboration procedure is described as follows:

(Step 1) Access the web page and plug the real-time collaboration system in the user's web browser.

(Step 2) Click the collaboration start icon, and input ID and a password through the login window.

(Step 3) Select a session for collaboration.

Fig. 6 shows a design and dimension verification example. Collaborators related to the development of a new product are able to perform real-time collaboration according to the above steps.

If collaborators do not satisfy certain design results after the dimension verification procedure, they will leave verification message by using the markup and annotation function. As shown in [A] of Fig. 6, the rectangle and the arrow existing in the markup function deliver another verifier's message regarding the problem of the current design. Since this markup function can be added on the verification file as a hyperlink function, clients are able to deliver their opinions in detail.

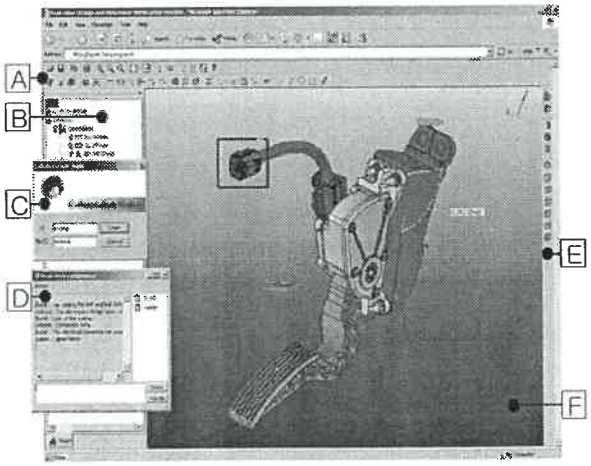

Fig. 5 Graphic user interface of the developed system.

If a collaborator wants to verify the thickness of the clutch cover, the collaborator should select the lines [B] and [C] after selecting the icon existing on the

verification and markup toolbar shown in [A] of Fig. 5. These actions compute the minimum length between the lines. Dimension verification data of the clutch cover is given by 32.197 mm as [D] of Fig. 6.

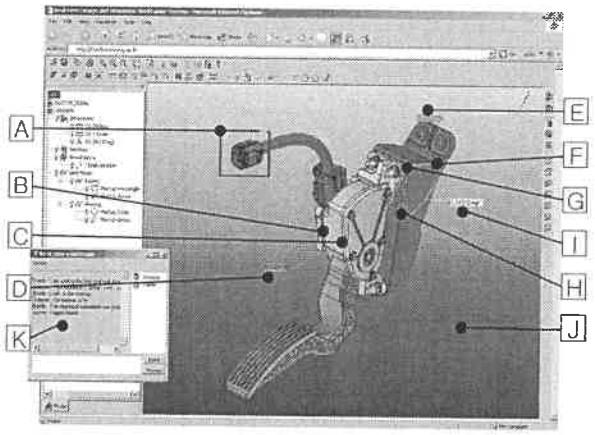

Fig. 6 Design and dimension verification.

[E] of Fig. 6 shows the distance of 28.000 mm between bolts by using the function to compute the minimum gap between circles. After selecting the angle measurement icon and clicking [F], [G] and [H] points successively, the angle of 3 points, 83.342° , is obtained as [I] of Fig. 6.

[K] in Fig. 6 shows a communication example among three collaborators by using a chatting function. This function assists collaborators to communicate design ideas in detail. Moreover, all collaboration contents, such as precision measurement, markup, annotation and chatting contents, are saved as a native file. After disconnecting the server, a design supervisor can modify the current design as an updated design according to the collaboration contents.

All contents described above have been observed and controlled by collaborators participating the collaboration at the same time. Collaborators attending the collaboration session are able to express their design and production ideas at real-time.

6. Conclusions

A real-time collaborative design and dimension verification system is proposed for the rapid design and manufacture. The developed system is executed on the Internet Explorer without using the commercial CAD systems. Designers, customers and manufacturers, who are geographically separated, are able to verify design results and dimensions over the Internet.

The native file converter is developed to make a real-time collaboration system over the Internet. Using the ActiveX control, users do not need to install the developed system prior to using the system. System updates are accomplished through the server. It is adequate for the distributed environment.

In order to protect the collaborative work, communication between clients and the collaboration server is performed through the encryption mode. To overcome the firewall in companies, HTTP protocol is used for the data transmission. As the system is an open-architecture and does not use CORBA, additional functions could be added to the system moderately and easily.

The usefulness of the developed systems has been confirmed through a case study.

References

(1) Huang, G. Q., 2002, "Web-Based Support for Collaborative Product Design Review," *Computers in Industry*, Vol. 48, pp. 71～88.

(2) Kan, H. Y., Duffy, V. G. and Su, C. J., 2001, "An Internet Virtual Reality Collaborative Environment for Effective Product Design," *Computers in Industry*, Vol. 45, pp. 197～213.

(3) Chen, L., Song, Z. and Feng, L., 2004, "Internet-enabled Real-time Collaborative Assembly Modeling via an e-Assembly System: Status and Promise," *Computers-Aided Design*, Vol. 36, No. 9, pp. 835～847.

(4) William, R., 1997, "Internet-enabled Computer-Aided Design," *IEEE Internet Computing*, pp. 39～50.

(5) Song, I. H. and Chung, S. C., 2003, "Web-based Precision Dimensional Verification System for Rapid Design and Manufacture," *Proceedings of the Annual Meeting, American Society for Precision Engineering*, pp. 359～362.

(6) Kim, K. D. and Chung, S. C., 2001, "Synthesis of the Measurement System on the Machine Tool," *International Journal of Production Research*, Vol. 39, No. 11, pp. 2475～2497.

(7) Song, I. H., Kim, K. D. and Chung, S. C., 2003, "An Internet-based Dimensional Verification System for Reverse Engineering," *Transactions of the Korean Society of Mechanical Engineers, Series A*, Vol. 27, No. 8, pp. 125～133.

Implementation of Kinematic Web Handling

Alexander D. Sprunt, Alexander H. Slocum
Department of Mechanical Engineering, Massachusetts Institute of Technology, Cambridge, MA

Abstract— **This paper presents simple mechanisms for kinematic web handling, including a castoring and gimbaling roller, a pinch roller, and an edge constraint. Developed as part of a system for in-situ measurement of spring probe contact resistance on virgin material, the machine uses a 51mm wide, 0.13mm thick foil, or web, of solder clad Alloy 42 as a proxy for semiconductor leadframes. Storage on a roll was the most straightforward way to manage the large area of virgin material required by the study.**

I. Kinematic Web Handling

A web is "a strip of flexible material whose width is much greater than its thickness and whose length is much greater than its width" [1]. As Blanding states, kinematic web handling can eliminate calibration, facilitate precise web placement, and unlike crowned or flanged rollers can be used to guide stiff webs. The web's six degrees of freedom are reduced to three because it is confined to travel in the planes defined by the rollers around which it winds. The motion imposed by the feed roller further reduces the web's degrees of freedom to two: rotation and motion perpendicular to the feed. Blanding recommends these two remaining degrees of freedom be exactly constrained with gimbaled rollers, zero constraint rollers, and edge constraints. Such rollers have been designed before (US Patents 4,221,480 and 5,244,138 are two examples), but they are not readily available and are not amenable to fabrication as singletons. For our spring probe testing machine, we designed and tested several new roller concepts, as well as a kinematic pinch roller, and a kinematic edge constraint.

II. Test Machine Concept

Our concept for the spring probe testing machine is shown in Figure 1. The web is wound off the supply spool, around an idler roller, past the array of spring probes being tested, through an edge constraint, around the index roller, and onto a take-up roll. The web is tensioned between a DC motor on the take-up roll shaft and a slip clutch attached to the supply roll. To advance the web, a stepper motor fixed to the index roller is incremented, breaking the equilibrium between the DC motor and the slip clutch. The index roller's diameter makes one count on the stepper equivalent to 0.35mm of web advance.

III. First Bench Level Prototype

A Bench Level Prototype (BLP) was built using universal joints to create gimbaled and castored rollers

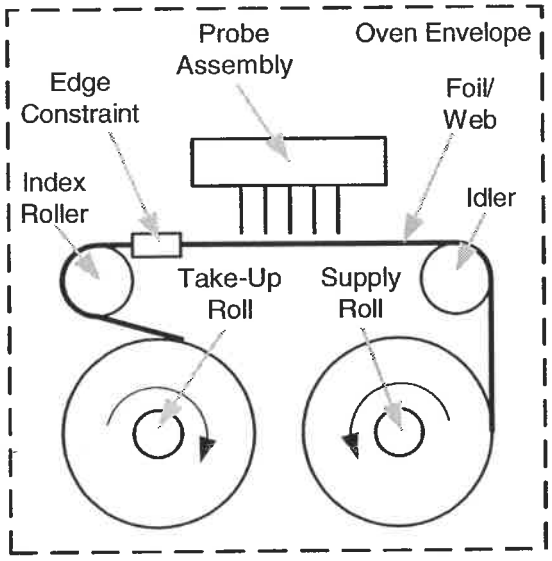

Fig. 1. Spring probe testing machine concept. High temperature testing required the whole machine be placed in an oven, a significant design constraint.

(Figures 2 & 3). Castored rollers are a type of zero-constraint roller, but instead of having a compliant surface like the rollers in the aforementioned patents, they are mounted so they may pivot about an axis normal to the web's plane of travel (Figure 4) to self-align with the web's path as defined by other constraints. Imagine a cart's castored wheel aligning itself to the cart's direction of travel, or rather to the ground's direction of travel with respect to the cart. Gimbaled rollers are mounted to rotate about an axis parallel to the plane of the incoming web. The twist accommodated upstream of the roller relieves the web of one degree of freedom. The two orthogonal axes of the universal joint combine to gimbal and castor the attached roller.

The prototype worked, but even after the addition of counterweights, substantial web tension was required to overcome the destabilizing effect of gravity. Still more tension would have been required if the rollers had not been positioned to hang from the couplings pendulum-fashion (rather than stand inverted from them), a limitation severely constraining the configuration of the system, and preventing implementation of the concept in Figure 1.

A kinematic edge constraint (Figure 5) was designed

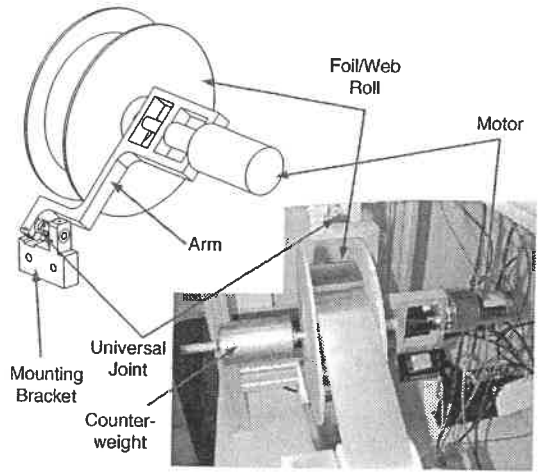

Fig. 2. A gimbaling and castoring roll assembly from the first BLP. Note how the assembly hangs down from its mount.

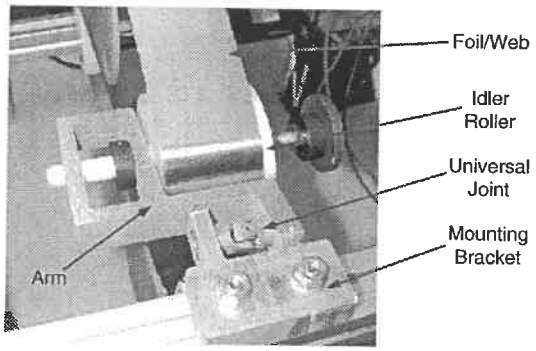

Fig. 3. An idler roller assembly from the first BLP. Note how web tension holds the assembly in position. Without the edge constraint (Figure 5, the web had a tendency to ride against the side of the arm supporting the roller.

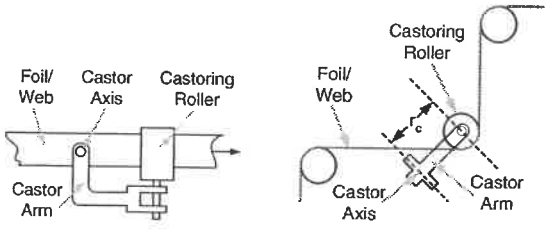

Fig. 4. Castored rollers rotate to align themselves with the path of the web. The distance the web must travel before alignment occurs is a function of the castor radius (r_c) [1].

to guide the edge of the web. One edge of the foil was pressed against a fixed cam follower by the "nesting force" of a second follower mounted on a spring arm. Concerns about lead particle generation from the solder on the foil necessitated rolling rather than sliding contact between the web and the edge constraint.

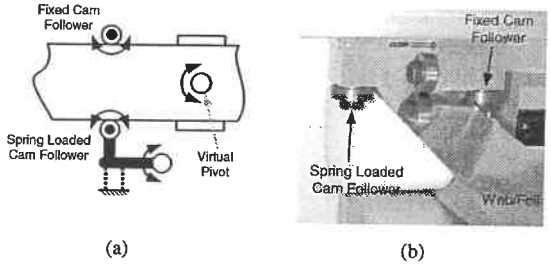

Fig. 5. A diagram and a picture showing the operation of the kinematic edge constraint. The force of the spring loaded cam follower keeps the web "nested" against the fixed cam follower. Obviously, too high a force will buckle the web.

IV. Second Bench Level Prototype

BLP-2 moved the universal joints from the roller arms to the rollers' axes (Figure 6). The rollers were now supported at their center of mass while still providing gimbaling and castoring axes. This prototype improved on BLP-1 by eliminating the need for counterweights, and greatly simplifying the mounting of motors, brakes, and sensors on roller shafts, but it required a disappointingly large amount of tuning; lateral misalignments tolerable in BLP-1 were unacceptable to BLP-2.

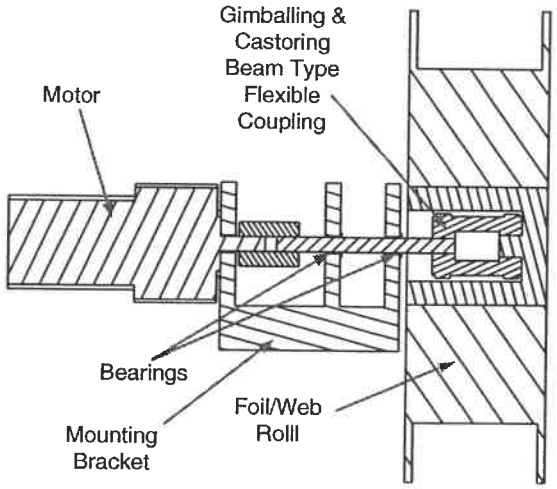

Fig. 6. Cross section of a flexible coupling mounted gimbaling (and perhaps castoring) roll assembly. BLP-2 was similar, but with a universal coupling in place of the flexible coupling. This was a much more adaptable concept than the first BLP.

Replacing the universal joints with beam type flexible couplings from Helical Products solved these problems and provided a restoring force to support the rollers

after the web had been unloaded, though it was unclear whether true castoring was still occurring [2] because the castor radius (r_c) had been reduced to zero.

V. Kinematic Pinch Roller

For the testing machine, a kinematic pinch roller was added to eliminate slip between the drive roller and the web (Figures 7 & 8). Pinch rollers are not often found in kinematic web handling systems because in combination with the other rollers they invariably overconstrain the web [1]. To prevent this, the web was pinched between a compliantly mounted self-aligning bearing and a fixed roller; the foil may thus still pivot about the drive roller. This combination provided the grip of the pinched roller configuration without overconstraint.

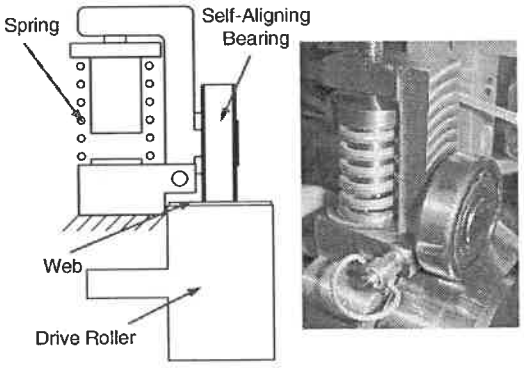

Fig. 7. The kinematic pinch roller provides the advantages of a clamped connection without overconstraint.

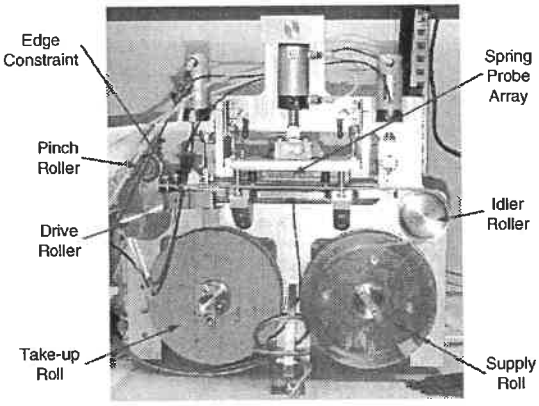

Fig. 8. The final machine. Note the foil path in blue. Over half a million trouble free cycles have been completed.

VI. Conclusion

The testing machine has completed over half a million trouble free cycles of advancing the web by 0.35mm, clamping the web, plunging an array of contactors into the web, and then advancing the web another 0.35mm to start the next cycle, all while intermittently measuring the contact resistance of the spring probes. Those results, an example of which can be seen in Figure 9 are described elsewhere [3]. A similar machine could readily be adapted for other tribological experiments requiring large areas of virgin material.

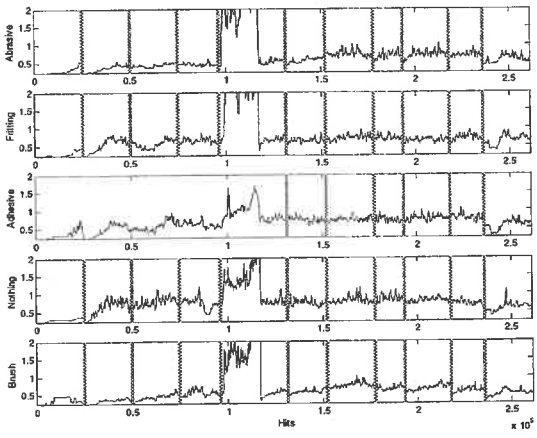

Fig. 9. One experiment run with the machine tested the effectiveness of various different cleaning techniques. The figure plots the window averaged contact resistance measurements (ohms) of probes cleaned with each different cleaning method. Fritting [4], [5] is a phenomenon exploited to lower contact resistance by forming a spark between electrodes to breakdown any intermediate oxide.

Acknowledgment

The authors are grateful for the support of the Teradyne Corporation.

References

[1] Douglas K. Blanding. *Exact Constraint: Machine Design Using Kinematic Principles*. ASME Press, New York, NY, USA, 1999.

[2] Douglas K Blanding. Personal communication: July 2001.

[3] David Gessel, Alexander Slocum, Alexander Sprunt, and Scott Ziegenhagen. Realistic spring probe testing methods and results. In *Proc. International Test Converence*, pages 417–423. IEEE, October 2002.

[4] Paul G. Slade, editor. *Electrical Contacts - Principles and Applications*. Marcel Dekker, New York, NY, 1999.

[5] Ragnar Holm and Else Holm. *Electrical Contacts: Theory and Application*. Springer-Verlag, New York, NY, 1967.

Precision Connector Assembly using Elastic Averaging

Patrick J. Willoughby, Alexander H. Slocum
Massachusetts Institute of Technology, Cambridge, MA

In precision assemblies, exact constraint techniques have been used to align removable components in automobile engines, robotics, and many measurement devices. Exact constraint typically requires controlled precision machining to allow an interface to be repeatable and interchangeable. Elastic averaging techniques can be used instead of exact constraint to create slightly less repeatable interfaces with more generous machining requirements. Averaging techniques work by averaging out errors through controlled compliance between precision surfaces. The key to elastic averaging is to control a large number of features spread over a broad region that elastically deform when separate parts are forced into geometric compliance with each other. Examples include curvic or Hirth couplings [1], waffle trees, and plastic building blocks such as Lego™. Recent research has shown that KOH etched pyramids and grooves in silicon wafers can be used to enable pure mechanical alignment of silicon wafers with sub-micron precision [2].

In this research, elastic averaging techniques are applied to a precision assembly intended to align a line of cylinders contained within two separate hexagonal connector elements. As shown in Figure 1, the hexagonal elements are formed by joining two injection molded trapezoidal parts containing a number of V-groove features. Before joining, cylinders are placed in the grooves of one trapezoidal element. The second trapezoidal element is aligned to the first using elastic deformation of each groove-cylinder interface, averaged across the set of grooves. The optimal number of grooves is a balance between the increase in repeatability between the connector halves due to a large number of contacts and the decrease in the accuracy of cylinder alignment due to a large number of contacts. As the number of cylinders increases, sine errors about the center of stiffness cause misalignment between cylinders in separate hexagonal elements.

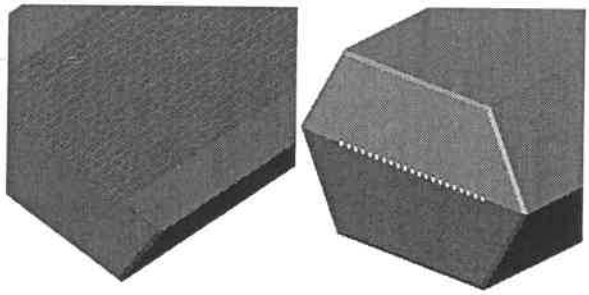

Figure 1 - Trapezoidal half showing grooves (top) and Joined hexagon element with 21 cylinders laid in V-grooves (bottom)

Two separate connector elements are subsequently aligned using a separate sleeve element employing elastic averaging in a circular fashion. In summary, the sleeve is a series of 12 bumps located around a thin circular metal extrusion. During assembly, each of the side surfaces on the hexagonal connector elements will connect with two of these bumps, causing the metal sleeve to deform elastically in the radial direction. To maintain contact between the two hexagonal connector elements, beam springs are formed into the sleeve to provide a preload force along the axis of the sleeve. In Figure 2, the springs are shown as fixed-free cantilever beams but can also be realized as simply supported beams.

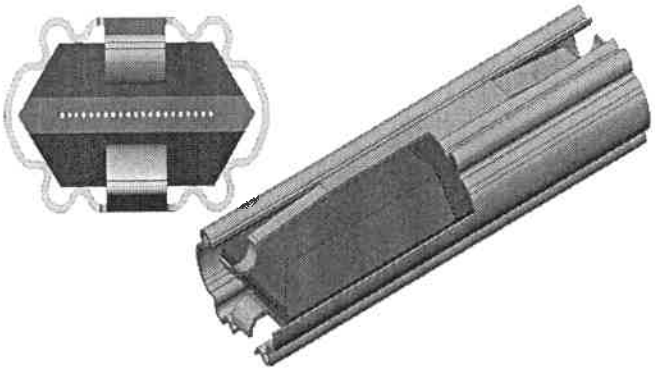

Figure 2 – Two connector elements shown mated inside sleeve – end view (left) and isometric view with cutout showing preload beam (right)

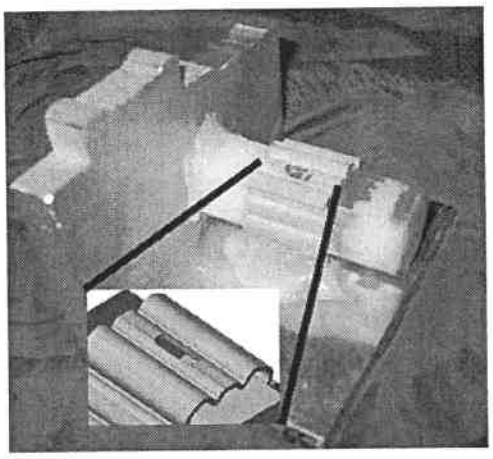

Figure 3 – Scaled experimental setup with aluminium sleeve and Delrin hexagonal connectors

Initial large-scale models of the connector were created using approximately 1mm thick waterjet aluminum for the sleeve and a 1-inch wide Delrin hexagonal rod for the connector elements. These models were joined then measured using a white light profilometer to determine the repeatability of the height difference between the two elements. As white Delrin is difficult to measure using a profilometer, small silicon targets were glued to the plastic. Figure 3 illustrates the test setup for this experiment. Results with this fairly basic model show that the standard deviation of the height difference is approximately 5 micrometers and the angular difference is 0.03 degrees. Complete results for 20 trials are shown in Figure 4. However, baseline repeatability of the measurement system is on the same order as these results, indicating that the models should be more repeatable. The main source of measurement error is the motion of the x-y stage when traveling between the two targets.

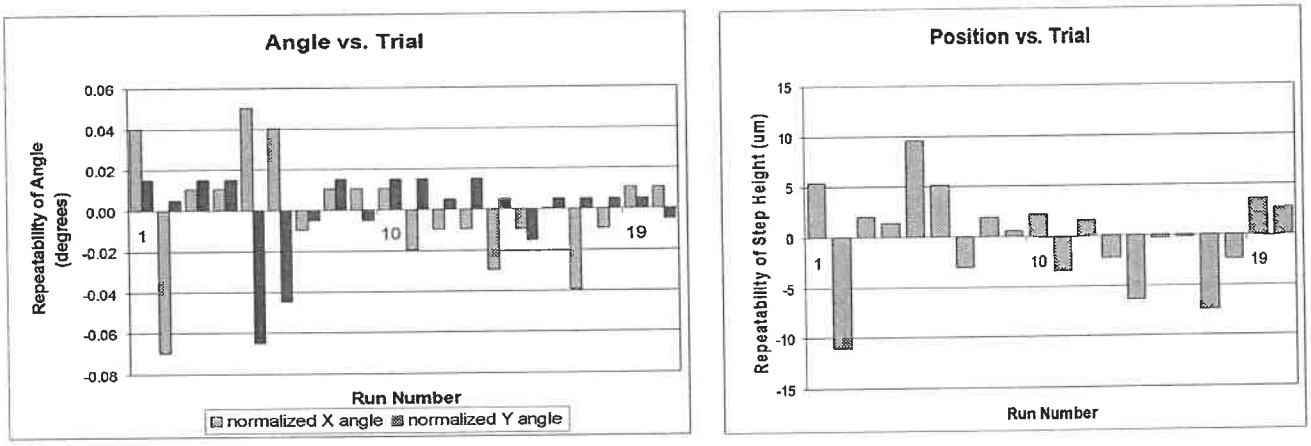

Figure 4 - Angle vs. Trial and Position vs. Trial result for large-scale model of assembly

Additional experiments are currently underway on a system with a constrained sleeve so that all elastic deformation occurs due to Hertzian contact effects. Preliminary results indicate that repeatability of the fixed sleeve system is comparable to the flexible sleeve model; however, material damage is more apparent along the contact lines due to increased contact force. Further

large-scale experiments are planned using precision extruded aluminum sleeves and higher quality Delrin connector elements. The profilometer measurement system will be replaced with a capacitance probe system, allowing for increased resolution. In addition, four-point bending tests will be performed to gauge angular stiffness against side loads and repeatability tests will be performed on the multiple groove-cylinder interfaces between trapezoidal connector halves.

Currently, analytical models have been created to describe the forces involved in the system. Due to geometric complexity, a closed form solution for sleeve stiffness was not attempted. Instead, a series of linear finite element analyses was performed using the IDEAS software from UGS. A quarter model of the large-scale system was created using 2D plane strain shell elements with appropriate boundary conditions, including a 10N load applied normal to the contact points. Deflections of appropriate nodes were recorded for models with varying part thickness, gap thickness, and contact radius. These results were then fitted to a product of exponential factors to yield a parameterized geometric stiffness equation. By combining geometric stiffness with Hertzian contact stiffness and friction, the axial insertion and removal force for a hexagonal connector can be determined. A simple verification test using the prototype shown in Figure 3 matched the predicted removal force to within 2%. These forces can then be used to determine the required geometric and material parameters for the preload beams shown in Figure 2Figure 5.

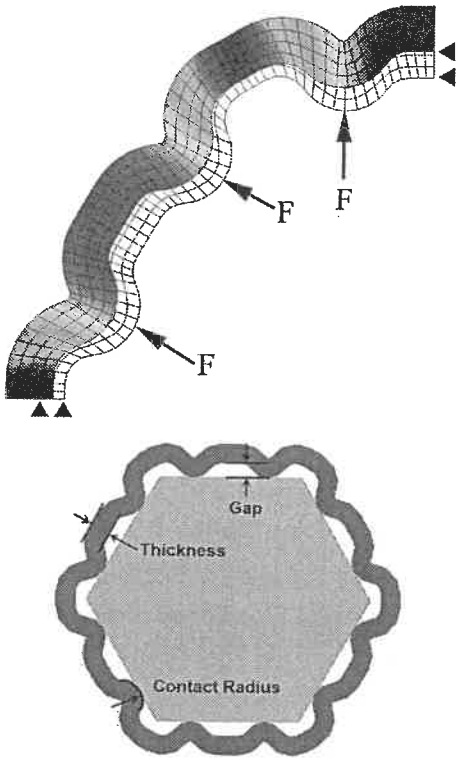

Figure 5 - Finite element model of sleeve (top) showing boundary conditions and displacement (red is 1μm and blue is 0.5μm) and Important sleeve parameters (bottom)

These analyses are being combined into a tolerance-based analysis that will statistically predict final device characteristics using a Monte Carlo analysis. Work is also ongoing to experimentally identify design parameters, such as the extruded sleeve tolerances, and methods for determining their tolerance limits as a function of obtainable system accuracy.

Key words: precision assembly, elastic averaging

References:

[1] M. Balasubramaniam, H. Dunn, E. Golaski, S. Son, K. Sriram, A. Slocum, "An anti backlash two-part shaft with interlocking elastically averaged teeth", Precis. Eng., Volume 26, No. 3, pp. 314-330, 2002.

[2] A. H. Slocum and Weber A. C. "Precision passive mechanical alignment of wafers", Journal of Microelectromechanical Systems, Vol 12, No. 6, pp. 826 – 834, 2003.

Research sponsored by NSF Grant DMI-0303738

FLUID FILM BEARINGS REQUIRING NO PRECISION MACHINING PROCESSES, FORMED BY WRAPPING OF 2D SHEETS

Amos G. Winter V
MIT Department of Mechanical Engineering
77 Massachusetts Avenue, Room 3-446
Cambridge, MA 02139
Tel: 617-452-4957, awinter@mit.edu

Martin L. Culpepper
MIT Department of Mechanical Engineering
77 Massachusetts Avenue, Room 3-449b
Cambridge, MA 02139
Tel: 617-452-2359, culpepper@mit.edu

Keywords: Hydrostatic bearing, stiffness, compensated bearing, spiral network, spinning

1 Introduction

This paper presents a means to use Spiral Networks (SPIN) to reduce bearing/bushing cost. A SPIN fluid bearing starts as a flat sheet of shim stock (a template) which contains 2D through cuts. When the template is wrapped on a mandrel, the overlapping features form a 3D fluid network. The network paths may run/interconnect in the axial, radial and circumferential directions. In this paper we explain the SPIN bearing concept and experimental observations obtained from tests on a hydrostatic, self-compensating design which exhibits bearing stiffness of 17.8 $^{N}/_{\mu m}$ (+4.6% error between theory and experiment).

Hydrostatic bearings are often used to achieve high stiffness motion guidance and essentially no wear when used properly [1]. The bore size tolerances (several microns) and surface finish requirements (~ ¼ bearing gap [2]) of these bearings lead to inherent precision fabrication costs. In previous work, it has been shown that hydrostatic compensating features may be cast into a bore which is then machined to the desired size and surface finish [2, 3]. The object of this work is to develop a self-compensating bearing which is made from materials, e.g. shim stock, that do not require subsequent precision fabrication.

2 Spiral Network fluid bearings

Figure 1A shows the concept of a SPIN hydrostatic bearing. A designer lays out 2D through cuts on a template such that the 2D geometries align and the layers seal to form a 3D fluid network when the template is rolled ("spun") on a mandrel. This includes pockets, restrictors, etc. The design under study in this work is shown after spinning in Fig. 1B, and after potting in a support sleeve in Fig. 1C.

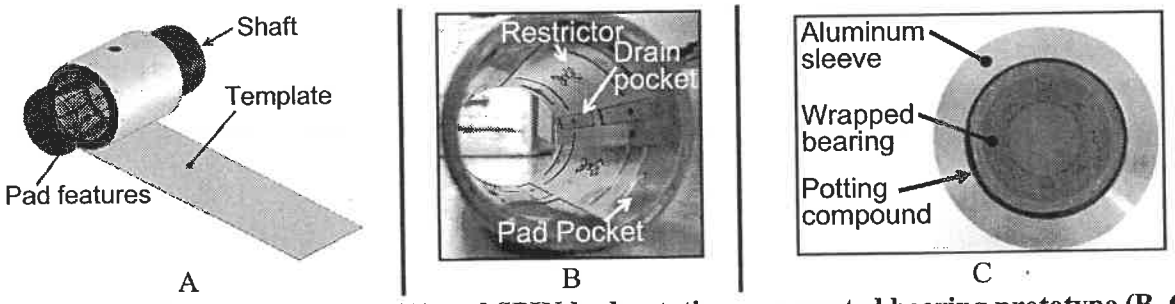

Figure 1: Spiral network concept (A) and SPIN hydrostatic compensated bearing prototype (B, C)

The 2D template for the SPIN bearing prototype is shown in Fig. 2.

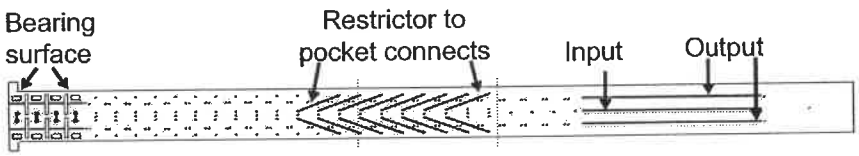

Figure 2: Template for SPIN bearing prototype (170 mm long)

In using the SPIN fabrication process, the tolerances/finish requirements are placed upon the shim stock material for the template (~ $ 0.01 / cm^2) and ground bar stock for the mandrel (~ $ 1/cm length at 5 cm diameter). These are easily obtained to specification via on-line catalogues such as McMaster.com.

3 Prototype modeling

Successful layout of template features and the mapping processes which turn the templates into the proper 3D SPIN geometry require models which relate the wrapped geometry to bearing design. Figure 3 will be used with the methods described in the following sub-sections to explain the modeling approach.

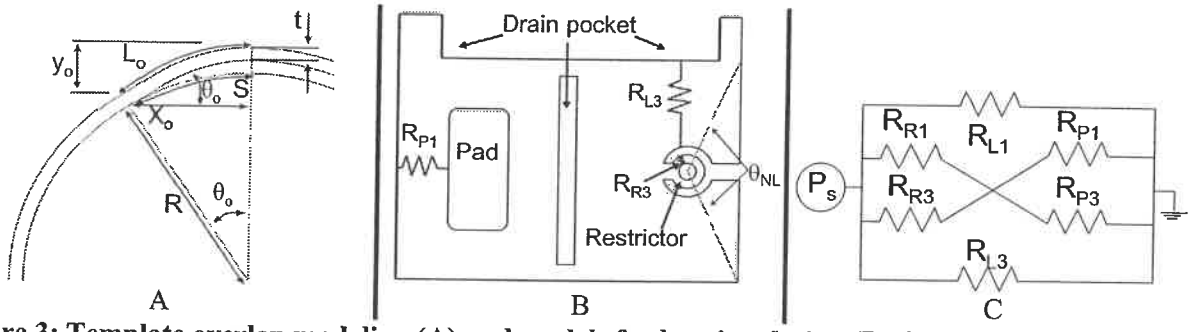

Figure 3: Template overlap modeling (A) and models for bearing design (B, C)

3.1 Template – SPIN mapping

In the overlap region shown in Fig. 3A, the shim stock breaks contact with the mandrel as it continues on to start the second layer, thereby leaving a void. This void is essentially a fluid draining feature which must be accounted for in bearing modeling. If features such as additional drainage features (Fig. 1B) are similarly sized and symmetrically placed around the bore, the resultant force from each pad will be balanced, thereby eliminating the impact of the void. The overlapping material may be modeled as an elastic beam of length L_o. The left end of this beam is tangent to the mandrel, with slope θ_o. By using elastic beam bending theory, the geometry of the beam and trigonometry, we obtain:

$$0 = \frac{3R}{2S}\left[t + R\left(1-\cos\left(\frac{S}{R}\right)\right)\right]\left[1-\sqrt{1-\frac{R\sin\left(\frac{S}{R}\right)}{S}}\right] - R\sin\left(\frac{S}{R}\right) \qquad (1)$$

This expression was used in a spreadsheet to solve for:

(1) The void size which in turn drives the geometry of the other drainage features.

(2) Variations in values of S for each wrapped layer. The value of S changes with each wrapped layer and thus we use Eqxn. 1 to ascertain the amount of ΔS per layer. We use this information to ensure proper alignment between features in adjacent layers. In successive layers, $R + n \bullet t$ must be substituted for R in Eqxn. 1 to capture the increase in radius with each n layer. The extra material, Δ, required per layer is:

$$\Delta = L - x_o \qquad \text{(variables are local to the wrapped layer)} \qquad (2)$$

3.2 Bearing circuit design

The bearing restrictor design, an annular feed concept (see right side of Fig. 3B), were modeled using existing bearing theory [1, 4, 5]. The bearing system was modeled as a network of resistive fluid circuits (Fig. 3C). The resistance names correspond to their location in the bearing, starting with one at the top and proceeding clockwise. Two pads are shown in Figure 3. Each restrictor feeds the pad which is diametrically opposed. This particular bearing is therefore modeled as four sets of pads. The pressurized regions of the bearing are axi-symmetric. The input and drainage channels encircle the bearing. The flow

is modeled as fully developed since the characteristic dimensions of the bearing are orders of magnitude larger than the bearing gap.

3.3 Bench-level prototype characteristics, fabrication and assembly

Figure 4 shows details of the bearing template and snapshots of the process by which the template is bonded and wrapped (called spinning). The bearing bore-shaft pair was specified to have a 50.902 mm bore and a 50.8 micron gap height. This relatively large gap was chosen to help filter unknown gap variations which might result from the spinning processes. The required surface finish of the bearing bore is met by the surface finish, RA = 0.1 – 0.5 μm, of off-the-shelf shim stock. The bearing prototype consisted of 10 layers (in the rolled state) of 170x100x0.152 mm 302 stainless steel. Double-sided epoxy tape, 3M 9244, was used to bond and seal the layers.

The template was fabricated on a laser cutter. Size and location tolerance of features within the template are +/- 500 microns. The epoxy tape was cut to have matching features and then applied to the back of the template. Prior to spinning, a layer of shim stock with thickness equal to the desired bearing gap was placed between the mandrel and template. After spinning, the tape-template assembly was clamped with constant pressure hose clamps and then cured in a convection oven at 120° C for 150 minutes. The gap-setting shim stock was then removed. The SPIN bearing was potted within an aluminum sleeve which contained a $^1/_4$ NPT supply port. Filtered air was run through the bearing after fabrication to ensure all paths were passing fluid flow.

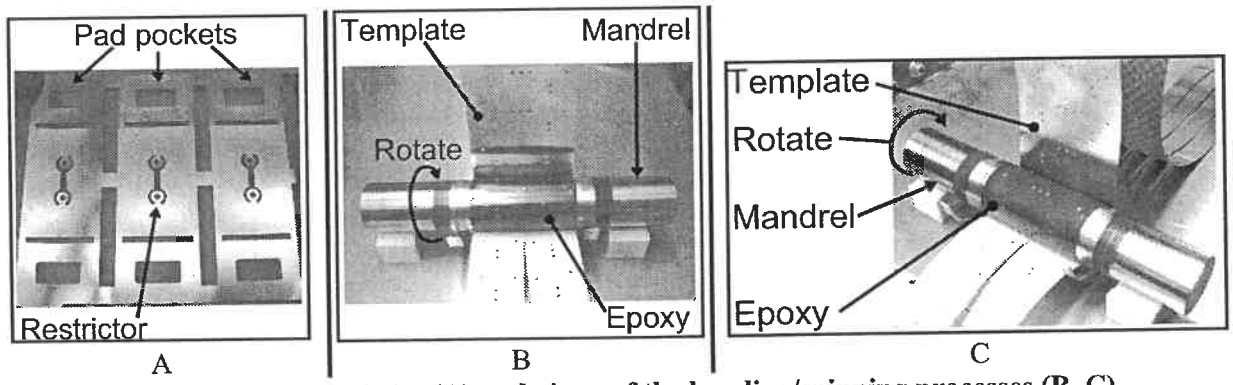

Figure 4: Template characteristics (A) and views of the bonding/spinning processes (B, C)

4 Experiment

The experimental setup shown in Fig. 5A included an accumulator (not shown) which provided constant fluid pressure at 565 kPa. Oil was pumped through a 25 micron filter before it was routed to the bearing.

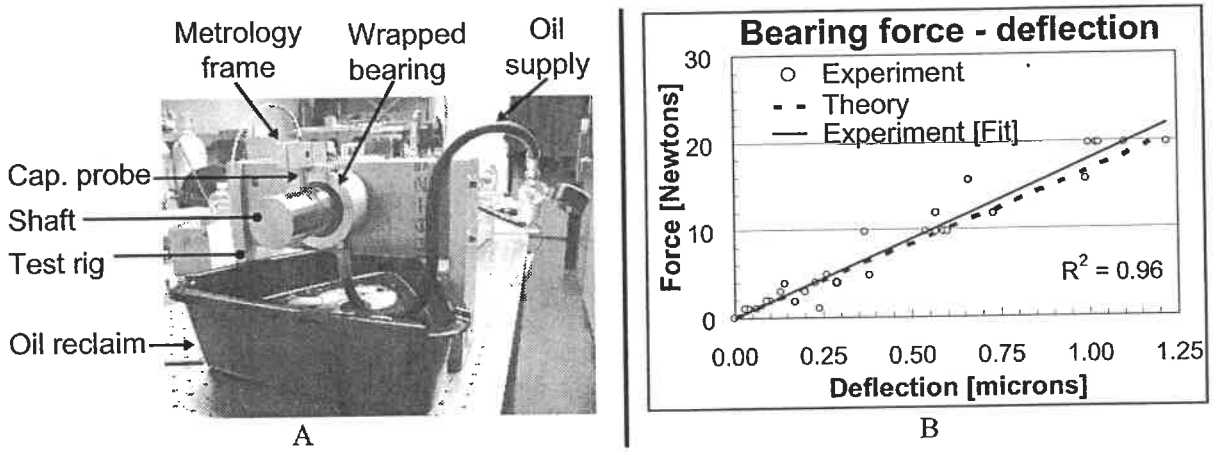

Figure 5: Experimental setup and results

A metrology frame was hard-mounted to the bearing sleeve, thereby removing the frame from the load path within the test rig's structure. Capacitance probes, measured shaft displacement with 5nm resolution. Radial stiffness tests were conducted in which combinations of masses were loaded on each end of the shaft. Flow rate was obtained by measuring the amount of oil collected per unit time.

5 Discussion of results

5.1 Observations on design and process improvements

During trial runs, the bonding epoxy was found to have extruded (by tens of microns) along the edges of some surface features (e.g. edges of the pads). As a result, the flow was obstructed in several areas and the bearing did not initially function. Uniform pressure pipe clamps had been used to clamp the bearing during processing. Observations indicate the clamps did not exert uniform pressure and as a result, the epoxy and template were bowed in several places. This led to warping of the bore and extrusion of the epoxy. These problems may also account for the periodic, torsional stick-slip which we initially observed in the bearing. The bearing appeared to functioned properly after the unwanted epoxy was removed via razor blade. In this orientation, we observed self-compensation as the shaft recovered by 20 nm when loaded.

5.2 Differences between expected and observed performance

The results from the radial stiffness test are displayed in Fig. 5B. The average stiffness of the bearing is within 4.6% of the theoretical prediction. This is encouraging for a bench-level prototype; however the variation in the measured data yields higher than expected percentage error (maximum error of 55%, $\sigma_{\%\ error}$ = 23%) between the average experimental stiffness and the observed data. It is probable that the epoxy extrusion problem is only partly solved and this in combination with the bore warping and random "stiction" may be responsible for the variability. Most of the "outliers" are above the average force-displacement linear fit. This may indicate "stiction" forces of several Newtons are randomly engaging within the bearing. We are planning additional tests to measure the stiffness after the epoxy extrusions areas have been re-inspected and modified if necessary. Improved measurements are planned for future tests on second SPIN prototype.

In summary, the results are encouraging for a bench-level prototype. Fully understanding the differences between theory and observation will depend on additional tests in which we will also examine the bore on a CMM (for roundness) and improve the spinning process.

6 Acknowledgements

Special thanks to Cynthia Walker and Nathan Landsiedel for help with bearing fabrication and testing.

7 References

[1] Slocum, AH. Precision Machine Design; Society of Manufacturing Engineers, 1992.

[2] Kotilainen, M. Design and manufacturing of modular self-compensating hydrostatic journal bearings. PhD Thesis, MIT, Cambridge, Ma, 2000.

[3] Kotilainen, M., Slocum, AH. "Manufacturing of cast monolithic hydrostatic journal bearings." Prec Eng. 25 (2001): 235-44

[4] Slocum, AH. Design of self-compensated water-hydrostatic bearings." Prec Eng 17 (1995): 173-85.

[5] Slocum, AH. Self Compensating Hydrostatic Linear Bearing, US Patent No. 5,104,237, 1992.

IN-SITU METROLOGY OF SWELLING EFFECTS ON CRITICAL DIMENSIONS IN LIGA PMMA MOLDS

Georg Aigeldinger, Joseph T. Ceremuga and Kevin D. Krenz
Sandia National Laboratories, 7011 East Ave., Livermore, CA 94550, USA
Email: gaigeld@sandia.gov

Sandia National Laboratories manufactures high precision microparts using LIGA technology. LIGA is the German acronym for x-ray lithography (Lithographie), electrodeposition (Galvanoformung) and molding (Abformung) [1]. Fabricating large batches of high aspect ratio metal microstructures has been demonstrated at Sandia and provides a unique opportunity to produce centimeter scale macroscopic parts with micrometer scale precision. [2, 3].

A challenge in LIGA processing is the fact that the favored x-ray lithography resist, polymethylmethacrylate (PMMA), swells approximately 0.4% in the aqueous electrolyte solution during electrodeposition [4]. The effect is significant in thick molds and for long electroplating times, and seriously impacts the fidelity of critical dimensions. Other geometric distortion occurs due to the bottom surface boundary condition of the PMMA; being fixed to the mold substrate [5, 6]. Auxiliary surrounding features which are put adjacent to features of critical dimension can limit the primary swelling [3, 6]. Complicated geometries pose a challenge for designing auxiliary features because the features must follow the perimeter of the part uniformly. Complex non uniform geometries of the auxiliary structures can lead to swelling effects that are difficult to predict.

In situ PMMA swelling measurements enable quick prototyping for the design of auxiliary structures to minimize the effects of swelling. When the PMMA mold can be measured in situ, as it swells, no time has to be spent electrodepositing metal into the mold and examining the final product. Some of the electrodeposited structures at Sandia may take several weeks to fully grow. In addition, with the presented methods, it is possible to monitor other time-dependent effects such as PMMA unwantedly delaminating from the mold substrate.

While final LIGA part metrology at Sandia is well understood [3, 7], methods to measure a submerged or wet PMMA mold had to be established. A View Engineering Voyager V6x12 programmable optical microscope is used for this metrology [8]. Experiments were conducted immersing the objective lens in a container of water, together with the PMMA, as well as keeping the objective lens above the water level. Both methods showed to be too sensitive towards movement of the water, which is unavoidable, because the stage of the microscope has to move to inspect all regions of the mold. We found that extracting the mold from the water solution under a 90 degree angle towards the water surface leaves water in the open areas of the mold without wetting the top edge of the mold, which is the edge of interest for the measurements to be conducted. Figure 1 shows the video capture of a structure edge in PMMA with the mold cavity filled with

water. The image shows excellent contrast of the edge, making edge detection just as straight forward as it is in a dry mold. Illumination using high levels of coaxial light, versus colored LED ring light, produced the most suitable edge contrast.

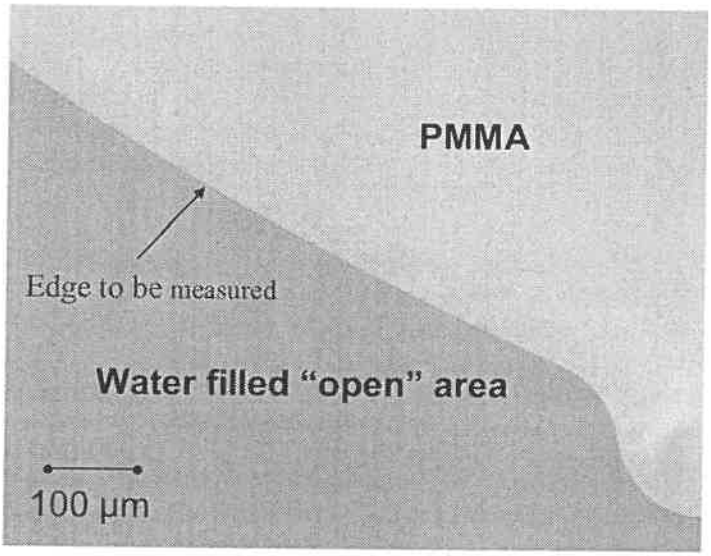

Figure 1: Typical microscope video image used for edge detection and measurement of the wet PMMA mold . The mold is taken out of the immersion bath and water remains in the mold without wetting the top edge that is inspected.

The top edge of a wet mold is examined in regular time intervals, thus following the swelling over the course of several days. Since the cavities of the mold are well saturated with water, drying of the mold during inspection is insignificant, especially because the mold generally is examined for less than one hour at a time.

Once the coordinate data is captured, the evolution of part geometries can be visualized against time. Even evolving coordinate point clouds can be compared to the part design (CAD). As an example, Figure 2 shows 143 µm line widths of a 1500 µm thick mold that are measured and show non-uniform narrowing from swelling over time.

Wafer bow from swelling PMMA resist can also be analyzed from the captured Z-axis coordinate data. Figure 3 shows a graph indicating total wafer bow evolving over time.

The demonstrated method to measure resist swelling in situ, is valuable for process control and quick prototyping. Future work will include the examination of simple mold structures to compare their swelling behavior with theoretical calculations.

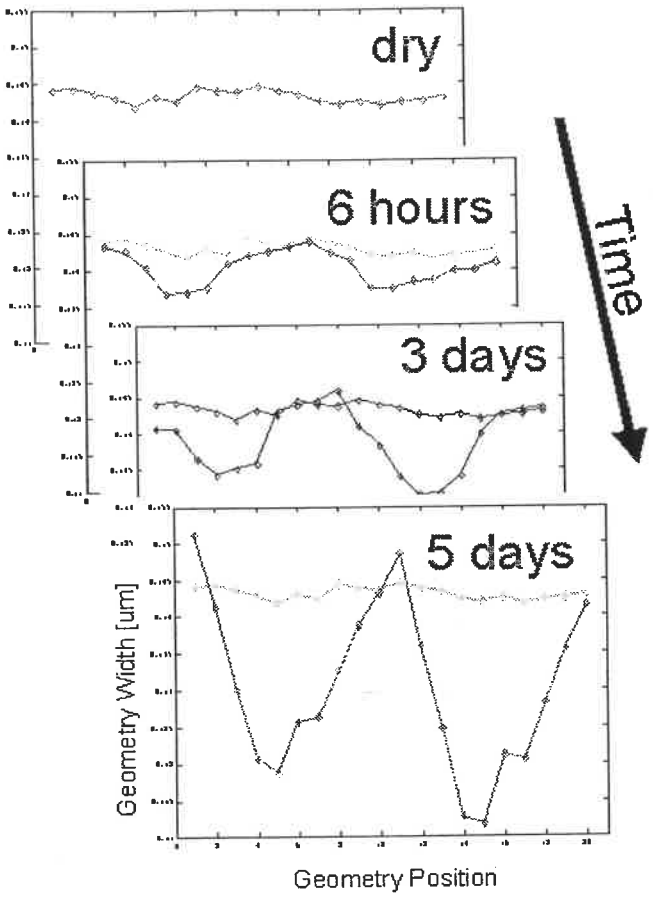

Figure 2: Line width measurements evolving over time from PMMA swelling. The dry data is presented in all graphs for reference. Between 3 and 5 days, resist delamination leads to large linewidth deviations.

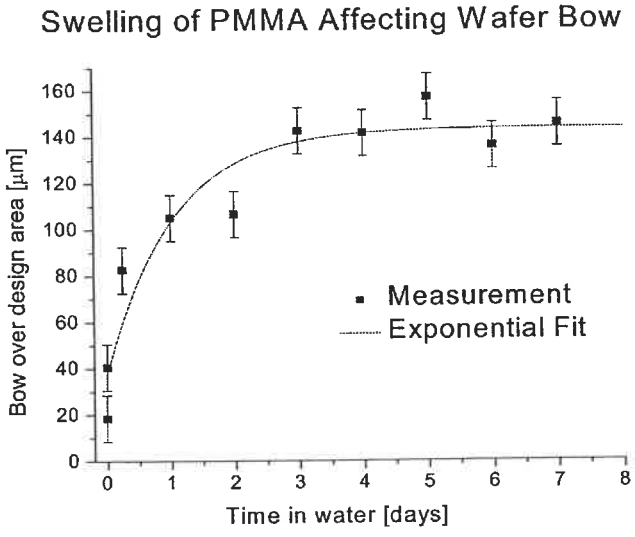

Figure 3: Total bow of the wafer (amplitude) from the thick PMMA resist swelling. An exponential saturation peaks after about 3 days.

Acknowledgements:

Sandia is a multiprogram laboratory operated by Sandia Corporation, a Lockheed Martin Company, for the United States Department of Energy's National Nuclear Security Administration under Contract DE-AC04-94AL85000.
All x-ray lithography exposures for this research have been conducted at the Advanced Light Source, Berkeley, CA. The ALS is supported by the Director, Office of Science, Office of Basic Energy Sciences, Materials Sciences Division, of the U.S. Department of Energy under Contract No. DE-AC03-76SF00098 at Lawrence Berkeley National Laboratory.

References:

1. Becker, E.W., et al., *Fabrication of microstructures with high aspect ratios and great structural heights by synchrotron radiation lithography, galvanoforming, and plastic moulding (LIGA process).* Microelectronic Engineering, 1986. **4**: p. 35-53.
2. Hruby, J., *LIGA Technologies and Applications.* MRS Bulletin, 2001. **26**(4): p. 337-340.
3. Aigeldinger, G., et al., *Final-Part Metrology for LIGA Springs, Build 1.* SAND REPORT, Sandia National Laboratories, 2004(2004-8153).
4. Goods, S.H., R.M. Watson, and M. Yi, *Thermal Expansion and Hydration Behavior of PMMA Molding Materials for LIGA Applications1.* SAND REPORT, Sandia National Laboratories, 2003(2003-8000).
5. Ruzzu, A. and B. Matthis, *Swelling of PMMA-structures in aqueous solutions and room temperature Ni-electroforming.* Microsystem Technologies, 2002. **8**(2-3): p. 116 - 119.
6. Griffiths, S.K., et al., *Dimensional errors in LIGA-produced metal structures due to thermal expansion and swelling of PMMA.* Journal of Micromechanics and Microengineering, 2004(14): p. 1548-1557.
7. Aigeldinger, G., J. Ceremuga, and D. Skala, *Large Batch Dimensional Metrology Demonstrated in the Example of a LIGA Fabricated Spring.* Book of Abstracts, HARMST 2003, USA. Microsystems Technology accepted., 2003: p. 263-264.
8. Ceremuga, J.T. and G. Aigeldinger, *Inspection Strategy for LIGA Microstructures Using a Programmable Optical Microscope.* SAND REPORT, Sandia National Laboratories, 2003(SAND2004-2289 / Submitted to Precision Engineering).

NON-STATIONARY SYSTEMATIC ERROR DETECTION WITH EXPERIMENTAL VERIFICATION ON AN OPTICAL PROFILER

Y. Gao *, S. Tse, C. Lo
Department of Mechanical Engineering, Hong Kong University of Science and Technology,
Clear Water Bay, Kowloon, Hong Kong, China
* E-mail: meygao@ust.hk

Introduction

Variable or dynamic systematic errors existed in many measurement processes. It is caused by deviations or changes in measurement conditions. It is very difficult to detect for removal because stable measurement conditions are not easy to be maintained in many practical applications. One example is temperature drift. It occurs in many measurement devices involving electronic circuits because the temperature in the instruments will typically keep increasing for a certain period of time after power being switched on. For the cases where dynamic systematic errors exist together with random errors, the changes in system conditions are hard to notice. This will make the detection more difficult. In many cases, the effects due to dynamic systematic errors are ignored and the reliability of measurement results seriously affected. Measurement errors of the kind may be classified into two types, the stationary type and the non-stationary type. For the stationary type, systematic errors may be identified and reduced through a number of comparative experiments. For the non-stationary type, suitable data treatment methods may be applied. A number of statistical methods have been proposed to solve the problem, such as curve fitting data evaluation coupled with a statistical sensitivity analysis, Markov estimator, and residual error [1-3]. However, most of the methods are highly dependent on the use of statistics that inherently require the sampling size to be large and the distribution to be known in advance. For the cases of small sampling size and unknown distribution, the methods may become ineffective. A new dynamic systematic error detection method based on fuzzy set theory was proposed [4]. The new method works effectively when the sampling size is small and the sample distribution is unknown. Mathematical models and dynamic systematic error detection criteria are presented. In order to verify the effectiveness of the proposed method, a series of experiments were conducted on a precision optical profiler. Changes in system conditions, such as warm up, focus, magnification, measurement location, and temperature drift during a measurement process in the optical profiler were made and the effects of the conditions were examined.

Error Detection Model

Assume that there are m quantities measured in measurement processes. In each of the process, an equal number of samples, noted as n, are measured. These set of data can form a measurement data matrix, noted as $\mathbf{Y}$, as shown in Eq. (1).

$$\mathbf{Y} = \begin{pmatrix} y_{11} & y_{12} & y_{13} & \cdots & y_{1n} \\ y_{21} & y_{22} & y_{23} & \cdots & y_{2n} \\ y_{31} & y_{32} & y_{ik} & \cdots & y_{3n} \\ \vdots & \vdots & \vdots & \ddots & \vdots \\ y_{m1} & y_{m2} & y_{m3} & \cdots & y_{mn} \end{pmatrix}, \tag{1}$$

where $y_{ik} \in \mathbb{R}$, $i = 1, 2, \ldots, m$, and $k = 1, 2, \ldots, n$. $\mathbb{R}$ is a real number set. After normalization, a new data set $\mathbf{X}$ is obtained and it is a function of the original measurement data set $\mathbf{Y}$, $\mathbf{X} = f(\mathbf{Y})$. The normalization should not change the characteristics of errors in the original data [4]. The relation R can be considered as

$$R = \sum_{(x_i, x_l) \in \mathbb{R}^2} \mu_{\mathbf{R}}(x_i, x_l)/(x_i, x_l), \tag{2}$$

where $i,l = 1, 2,\ldots, m$. The term $\mu_{\mathbf{R}}(x_i, x_l)$ is the fuzzy membership grade of any two quantities x_i and x_l in the measurement data matrix. It is in the relation subset $\mathbf{R}$ of the real number set $\mathbb{R}$, $\mathbf{R} \subset \mathbb{R}$. The relation can also be represented as $\mathbf{R} = [r_{il}, i = 1, 2, 3 \ldots m, l = 1, 2,\ldots, m]$, where $r_{il} = \mu_{\mathbf{R}}(x_i, x_l)$, $i,l = 1, 2,\ldots, m$, and $(x_i, x_l) \in \mathbb{R}^2$. The matrix $\mathbf{R}$ can be used to represent the degree of associations among the quantities. A suitable model should be chosen to obtain each of the membership grades r_{il} [4]. In considering a simpler case, a min-max model is utilized as

$$r_{il} = \frac{\sum_{k=1}^{n} (x_{ik} \wedge x_{lk})}{\sum_{k=1}^{n} (x_{ik} \vee x_{lk})}, \tag{3}$$

where $\wedge$ and $\vee$ are the fuzzy operations representing the minimum operation and the maximum operation respectively. The membership grade matrix $\mathbf{R}$ is symmetric as $r_{il} = r_{li}$. The diagonal of the matrix is equal to 1 when $i = l$.

The relationship between any one of the m quantities and the remaining m-1 quantities can be assessed by obtaining a transitive closure matrix $\mathbf{T}$. It is obtained by applying max-min closure of $\mathbf{R}$ [4]. The closure matrix is symmetric and the diagonal is equal to 1 (Eq. (4)).

$$\mathbf{T} = \begin{pmatrix} 1 & v_{12} & v_{13} & \cdots & v_{1l} & \cdots & v_{1m} \\ v_{12} & 1 & v_{23} & \cdots & v_{2l} & \cdots & v_{2m} \\ v_{13} & v_{23} & 1 & \cdots & v_{3l} & \cdots & v_{3m} \\ \vdots & \vdots & \vdots & \ddots & \vdots & \vdots & \vdots \\ v_{1l} & v_{2l} & v_{3l} & \cdots & 1 & \cdots & v_{im} \\ \vdots & \vdots & \vdots & \vdots & \vdots & \ddots & \vdots \\ v_{1m} & v_{2m} & v_{3m} & \cdots & v_{im} & \cdots & 1 \end{pmatrix}, \tag{4}$$

where $0 \le v_{il} \le 1$, and $i,l = 1, 2,\ldots, m$. Each element, v_{il}, in the transitive closure matrix $\mathbf{T}$ represents the fuzzy equivalence relation or the similarity relation between two quantities, y_i and y_l. If the value of the element v_{il} is close to 1, this represents the two quantities have a stronger level of association and the possibility of having systematic errors is low. However, if the value of the element v_{il} is close to 0, this means the two quantities have a weaker level of association and the systematic errors are existed.

Error Detection Criteria

Having obtained the transitive closure matrix $\mathbf{T}$, the detection of systematic errors can be done by comparing the elements v_{il} with an optimum level, λ. The level was chosen to be $\lambda = 0.5$ because it is the average value of the minimum level of association, $\lambda = 0$, and the maximum level, $\lambda = 1$. The systematic errors exist between the quantities y_i and y_l if the value of the elements v_{il} is smaller than or equal to λ, and vice versa [4]. In order to compare the elements with the optimum level, a λ-cut subset matrix $\mathbf{R}_\lambda$ is defined as

$$\mathbf{R}_\lambda = [r_{\lambda il}], \tag{5}$$

where $r_{\lambda il} = \begin{cases} 1, & v_{il} \ge \lambda \\ 0, & v_{il} < \lambda \end{cases}$, $i,l = 1, 2, \ldots, m$.

Experimental Results and Discussion

In order to verify the effectiveness of the method [4], several experiments conducted on a Veeco Wyko NT3300 optical profiler (Fig. 1) in PSI and VSI modes were performed. It can measure heights from angstroms to millimetres. The vertical resolution is up to 3Å. The measurement samples are shown in Fig. 2-3.

Fig. 1 Optical profiler

Fig. 2 Testing sample for PSI

Fig. 3 Testing sample for VSI

Totally 6 cases of conditions were examined (Table 1). In each case, 6 data sets with 5 data points in each of the data sets were collected. Based on the models (Eq. (1)-(5)), for each of the 6 cases, the measurement data matrix **Y**, the transitive matrix **T**, and the λ-cut matrix $\mathbf{R}_\lambda$ for both VSI and PSI modes are determined.

The results of **Y**, **T**, and $\mathbf{R}_\lambda$ for the change of location condition are presented. The variations in **Y** for the case are not large (Fig. 4) and it would be difficult to determine the existence of systematic errors.

$$\mathbf{Y}=\begin{pmatrix} 1.92 & 1.92 & 1.92 & 1.92 & 1.92 \\ 1.92 & 1.92 & 1.92 & 1.92 & 1.92 \\ 1.95 & 1.95 & 1.95 & 1.95 & 1.95 \\ 1.95 & 1.95 & 1.95 & 1.95 & 1.95 \\ 1.97 & 1.97 & 1.97 & 1.97 & 1.97 \\ 1.94 & 1.96 & 1.96 & 1.96 & 1.96 \end{pmatrix},\quad \mathbf{T}=\begin{pmatrix} 1.00 & 1.00 & 0 & 0 & 0 & 0 \\ 1.00 & 1.00 & 0 & 0 & 0 & 0 \\ 0 & 0 & 1.00 & 1.00 & 0.72 & 0.74 \\ 0 & 0 & 1.00 & 1.00 & 0.72 & 0.74 \\ 0 & 0 & 0.72 & 0.72 & 1.00 & 0.72 \\ 0 & 0 & 0.74 & 0.74 & 0.72 & 1.00 \end{pmatrix},\quad \text{and}\quad \mathbf{R}_\lambda=\begin{pmatrix} 1 & 1 & 0 & 0 & 0 & 0 \\ 1 & 1 & 0 & 0 & 0 & 0 \\ 0 & 0 & 1 & 1 & 1 & 1 \\ 0 & 0 & 1 & 1 & 1 & 1 \\ 0 & 0 & 1 & 1 & 1 & 1 \\ 0 & 0 & 1 & 1 & 1 & 1 \end{pmatrix}.$$

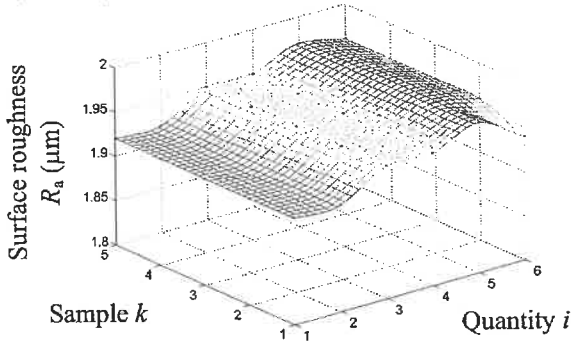

Fig. 4 Measurement results under the change of location condition

For this case (Fig. 4), the minimum value of the elements in the transitive closure matrix **T** was 0. The value was much smaller than $\lambda = 0.5$. The minimum value of the elements in $\mathbf{R}_\lambda$ had zero values. Therefore, systematic errors were identified in the measurement data set (Fig. 4).

Table 2 shows the minimum value of the elements in the λ-cut matrix $\mathbf{R}_\lambda$. If it is 0, the systematic errors would exist. It was found that two conditions, the change of magnification and the change of measurement location, in the PSI mode were the most significant involving systematic errors, since more zero value elements in $\mathbf{R}_\lambda$ are observed (Table 2). It can be seen that for the VSI mode, there were two failures (Table 2). This could be due to the measurement

resolution in the VSI mode being not high and the changes introduced in the two cases being not sufficiently large. However, the proposed method [4] could successfully determine if systematic errors exist for case of no condition change and for the five cases in the PSI mode (Table 2).

Table 1 Experimental conditions examined

Condition	Condition changes	No. of repetition of a state N_c
No change	None	6
Change of magnification	10x, 20x, 50x	2
Change of measurement location	Three arbitrary positions	2
Focusing	Three arbitrary trials of focusing	2
Warm up	Switch on and off the machine	3
Temperature drift	Switch on for 0 or 2 more hours	3

Table 2 Results of the λ-cut matrix $\mathbf{R}_\lambda$

Condition	Minimum value $\min(\mathbf{R}_\lambda)$	Total no. of zero value elements $N(\mathbf{R}_\lambda\|_{\mathbf{R}_\lambda(i,l)=0})$	Minimum value $\min(\mathbf{R}_\lambda)$	Total no. of zero value elements $N(\mathbf{R}_\lambda\|_{\mathbf{R}_\lambda(i,l)=0})$
	PSI		VSI	
No change	1	0	1	0
Change of magnification	0	24	0	16
Change of location	0	25	0	16
Focusing	0	10	1	0
Warm up	0	22	0	22
Temperature drift	0	22	1	0

Conclusions

Experiments conducted on the optical profiler are presented. Based on the analysis of the experimental results, the proposed method has shown to be quite effective in identifying the systematic errors. The method has shown to be effective for small changes, as long as the measurement resolution is sufficient, in the system condition that could be difficult to detect.

References

[1] T.M. Souders, D.R. Flach, C. Hagwood, and G.L. Yang, Effects of timing jitter in sampling systems, *IEEE Trans Instrumentation & Measurement*, 39(1), 1990, pp. 80-85.

[2] J.L. Settle, and Z. Nagy, Metal deposition-dissolution in molten halides: on the question of measurability of very fast electrode reaction rates, *J Electrochemical Society*, 132(7), 1985, pp. 1619-1627.

[3] H. Turner, and D. Steiner, Digital image processing techniques to extract metric data on buildings from shadows on simulated air photos, *Photogrammetria*, 35(4), 1979, pp. 141-160.

[4] Y. Gao, X. Xia, Z. Wang, and Z. Tao, Detection of systematic errors in a measurement process using fuzzy set theory, *Review Scientific Instruments*, 73(4), 2002. pp. 1786-1794.

A study of CMM measurement variation in precise, thin-wall iron castings

Krishnakumar Gopal, Edward P. Morse, James F. Cuttino
Center for Precision Metrology
Department of ME&ES
UNC Charlotte, Charlotte, NC

Abstract

The role of coordinate measuring machines in foundries has historically been somewhat different than in other industries. In the foundry layout room, the CMM is often used simply to see if there is enough material at specific gage points – measurement techniques such as establishing complex datum reference frames [1,2] and considering the number and spacing of sample points are usually not an issue. However, as modern foundries develop better production techniques to make competitive thin wall and precision castings [3], the measuring methods must keep pace. This paper analyses measurement techniques used by various metrology shops with the goal of determining best measurement practice for reducing the variations in measurements. A set of 10 artifacts (castings) were sent to different metrology shops and the measurement techniques and thickness results were recorded for each shop. The thickness of the castings reported by each metrology shop is compared to other shops in a method similar to a Gage Repeatability and Reproducibility (GR&R) study [4,5]. We extend this analysis to consider the effects of different measurement techniques, and then propose a procedure to reduce the variation caused due to different measurement techniques.

Keywords: CMM measurement techniques, Datum reference frames, iron castings, GR&R

Introduction:

The metrology round-robin study was conducted by shipping a set of ten castings to different metrology shops in turn. The measurements were performed at a CMM manufacturer's demonstration laboratory, two foundry layout rooms, and at a pattern shop and also two different measurements at UNC charlotte. The most common questions that arose when the artifacts arrived at the round-robin participants were how to establish the co-ordinate system and how many points should be taken on each web. To address these questions, the number of points to be taken and a suggested co-ordinate system were documented, and these instructions accompanied the artifacts to the participants. The co-ordinate system suggested is shown in Figure 1. The +Z axis is along the central cylindrical feature of the star casting and the +Y axis is along the thickest undrafted web. The undrafted webs occur at the parting line of the mold (see figure) where draft is not required for the pattern to be removed from the mold. The +X axis is perpendicular to the other two axes.

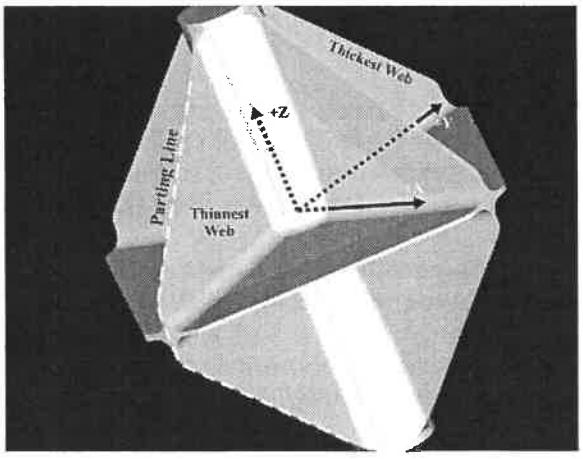

Figure 1: Initial co-ordinate system suggestion

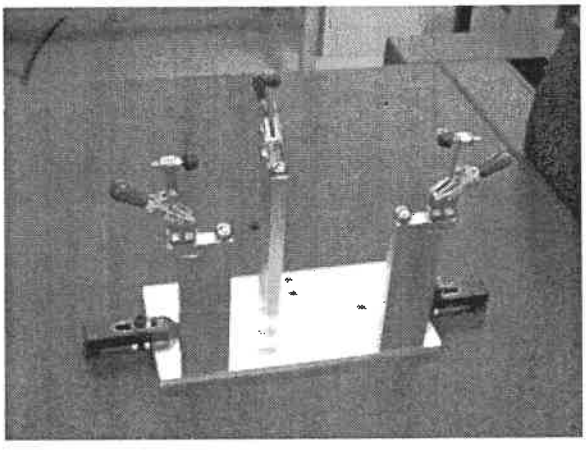

Figure 2: Locating Fixture

Experimental Approach:

At UNC Charlotte, a Brown and Sharpe XCel 765 Coordinate Measuring Machine (CMM) was used to measure the castings, and direct computer control (DCC, or automatic) programs were written to conduct the measurements using both QUINDOS and PC-DMIS software. The fixture shown in Figure 2 was used to kinematically restrain the casting in all six degrees of freedom on the CMM. The fixture consisted of three precision balls mounted on pillars, each ball contacting the casting on two orthogonal sides to constrain part motion. The CMM probe was oriented for each sampling such that it avoided interference with the fixturing. The measuring program establishes a coordinate system by sampling a subset of the webs (or fins) on the casting. The planes of the coordinate system nominally pass through the middle of the fins (e.g., the x-y plane passes through the middle of the four horizontal fins). Each fin was then sampled with either ten or eleven points depending on the location of the fins. Measurement points were collected from each side of the fin, and a midpoint and thickness were calculated for each location. The sampling patterns used for QUINDOS program are shown in Figure 3. The pattern shown in Figure 3(b) allows for the fixture on some of the webs.

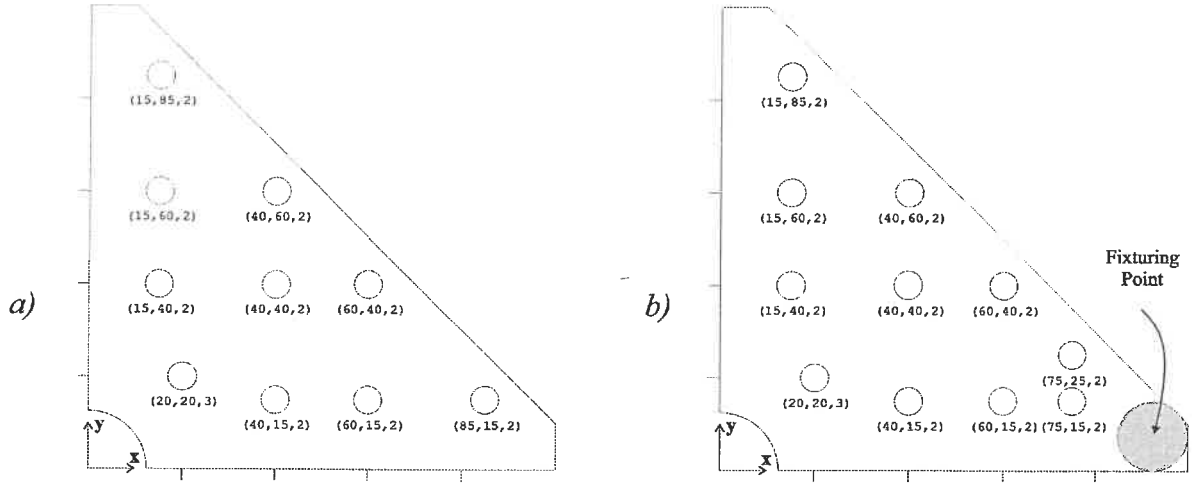

Figure 3: Sampling Patterns

The setup used at UNC Charlotte to measure the artifacts is shown in Figure 4 . The cylindrical section is vertical and the parting plane webs are from front to back. The horizontal webs were used to establish the primary datum (*xy-plane*) and the parting line webs were used to establish the secondary datum (*y-axis*) and the other vertical webs perpendicular to these datum's were used to establish the tertiary datum (*z-height of the origin*). The setup used for measurement of the artifact by one of the participants is shown in Figure 5. In this setup the cylindrical section is in horizontal orientation. Although it shouldn't matter, we suspect that the difference in setup increases the uncertainty in the measurement results. The primary difference in coordinate systems is due to difference choices in the reference surfaces for the datums.

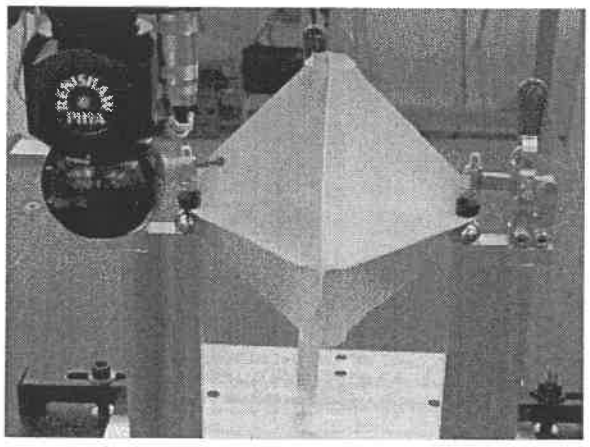

Figure 4: UNC Charlotte setup

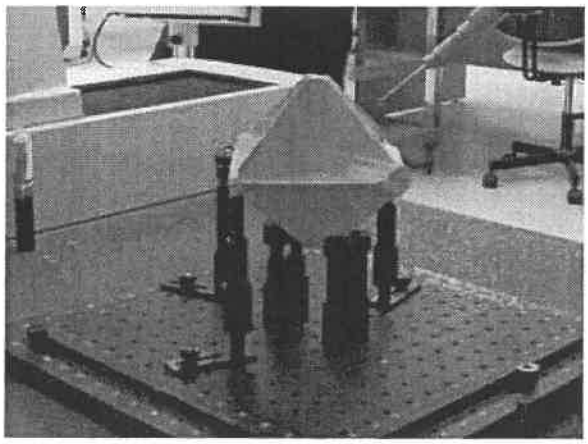

Figure 5: One of the participant's setups

Data Analysis and Results:

The thickness measurements reported by each participant were averaged by web for all ten castings. The overall average for each web was also calculated. Each participant's deviation in thickness from the average was calculated for each web. This deviation was plotted against web number and sorted in descending order by the range of the thickness over the five participants, as shown in Figure 6. Each bar in the figure represents a participant in the study. The graph illustrates the range of values obtained by different metrology shops. Each shop fairly consistent, in that most reported values on the same side of the average for most webs. For example, the shop indicated by the white bar is consistently high for all but the parting line webs. Note that the range of values for many of the webs exceeds 1mm – this indicates a need for improvement and standardization in the inspection process.

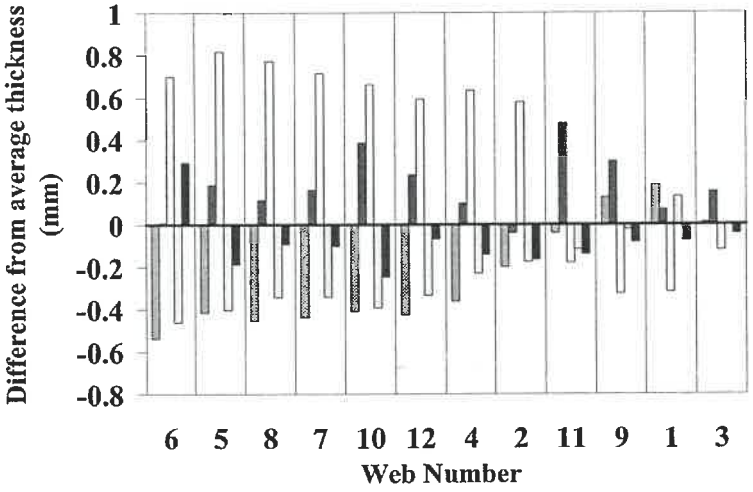

Figure 6: Deviation in thickness from the average vs. Web number

In Figure 6 it can be seen that the deviation is less for the four webs along the parting line (web numbers 11, 9, 1, 3) for most of the participants, regardless of how they set the part up for measurements. It is interesting to note that the part-to-part variation of these webs is not necessarily low. In Figure 7 the standard deviation of the 10 parts' thicknesses is plotted on a per-web basis, and the parting line webs have some of the highest variability.

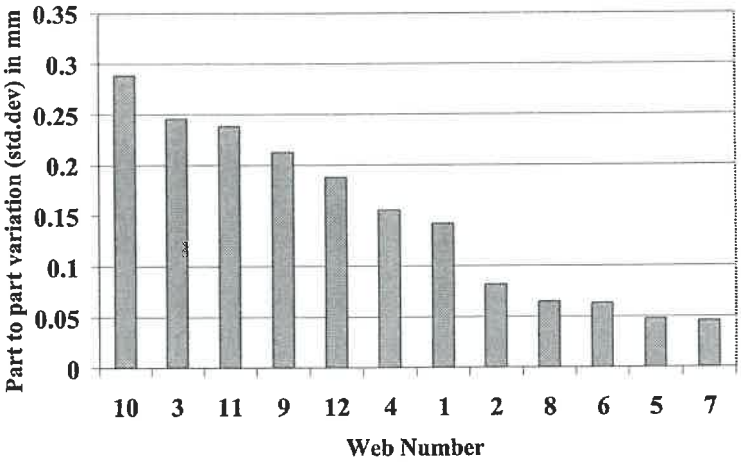

Figure 7: Standard Deviation in Thickness among the 10 sample parts vs. Web Number

Conclusions and future work:

The variation in the measurements obtained from the different metrology shops is evident from Figure 6. We believe that these variations could be greatly reduced if proper datum targets were shown in the drawing instead of a picture showing the desired axes. This would allow the measurement points for thickness values to be specified with basic dimensions from the datum reference frame, rather than stating "measure points 15mm from the edge of the web." The desired datums from the part model are shown in Figure 8. The appropriate specification of datum targets is needed, as shown in Figure 9. By using datum targets on the drawings the uncertainty due to different measurement techniques can be reduced. Future work includes sending the artifacts to the various participants with drawings with proper datum targets on them. The CMM measurement variation will (we hope) be reduced using this datum target scheme.

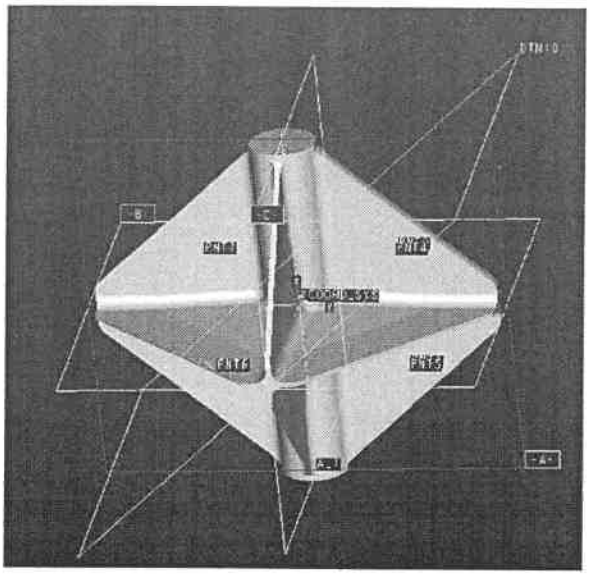

Figure 8: Part model showing Datums and points used to create Datum Targets

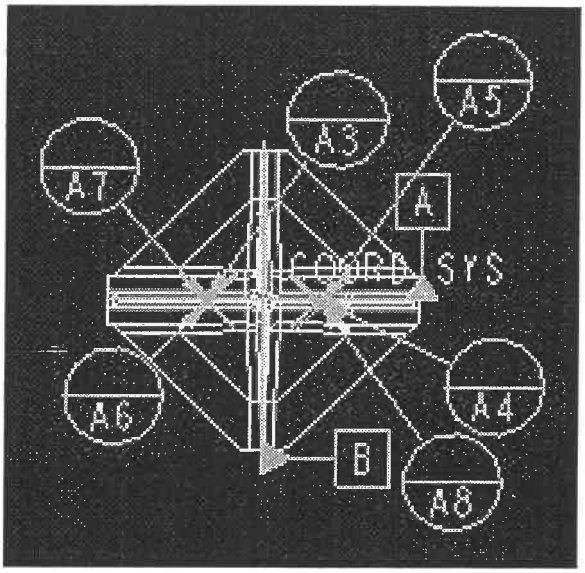

Figure 9: Part drawing showing example of Datum Targets Symbols and Datums

Acknowledgement:

This project was funded partially by Cooperative Agreement DE-FC07-02ID14231 with the United States Department of Energy. The opinions expressed in this paper are those of the authors and not necessarily those of the Department of Energy. The authors also wish to acknowledge the support of the UNC Charlotte Center for Precision Metrology, an NSF funded Industry/University Cooperative Research Center, for the use of the center's equipment and the expertise of its personnel

References:

1) ASME Y14.8M-1996 *Castings and Forgings*
2) ASME Y14.5M-1994 *Dimensioning and Tolerancing*
3) Kachru, A., *Molding Capability Study for Thin Wall Iron Castings*, Master's Thesis, University of North Carolina at Charlotte, 2001
4) F.E. Peters, R. Velaga, and R.C. Voigt, "*Assessing Dimensional Repeatability of Metalcasting Processes*," AFS Transactions 224, 181-190 (1996).
5) ***Measurement System Analysis***, AIAG Reference Manual, 1990.

Surface Roughness Evaluation of a LIGA Micro Component

Kevin D. Krenz, Georg Aigeldinger, Joe T. Ceremuga
Sandia National Laboratories, PO Box 0969 M/S 9401, Livermore, CA 94551-0969
Email: kdkrenz@sandia.gov, gaigeld@sandia.gov, jtcerem@sandia.gov

Sandia is a multiprogram laboratory operated by Sandia Corporation, a Lockheed Martin Company, for the United States Department of Energy's National Nuclear Security Administration under Contract DE-AC04-94AL85000

INTRODUCTION

LIGA technology capabilities at Sandia National Laboratories are able to manufacture very accurate high aspect ratio microstructures such as the LIGA Spring. LIGA is the acronym for the German words lithography (Lithographie), electrodeposition (Galvanoformung) and molding (Abformung) [1]. At Sandia, we primarily use "direct LIGA" [2], where the mold produced by x-ray lithography is directly used to manufacture the final parts. However, the mold must be sacrificed after the metal deposition step to release those parts.

This work focuses on the methods and techniques established to measure a prototype part that has been manufactured in large numbers. This part is electroformed with a nickel manganese alloy and then gold plated as a final production step. Surface roughness is measured before and after the gold plating step, then again after testing the part.

The instrument used for this inspection is a Wyko NT3300 white light optical profiler. The details about handling and mounting of the delicate parts are discussed along with the analysis of the obtained data sets. Artifacts in the sidewall topology that can give valuable feedback to processing are shown in detail. This study allows for defining a sidewall surface roughness value that represents the state of the art of the LIGA process at Sandia.

LIGA SPRING

The spring arm geometry has high aspect ratio of 10:1, 150 um wide by 1.5 mm tall. The hub center and two extending arms must pass the stringent CAD-designed lateral dimension contour analysis; the arm sidewall then must satisfy surface roughness criteria specified by the designer. [3] The position for any point on the arm cannot deviate more than 5 um from the lateral CAD dimensions. The arm being relatively long, a small angular deformation at the base amplifies the positional change at the tip. Handling of the parts is minimized but when required, carbon fiber tweezers, to prevent galling, are used to handle the hub only. The arms are never touched by hand, for this is a high risk to future qualification.

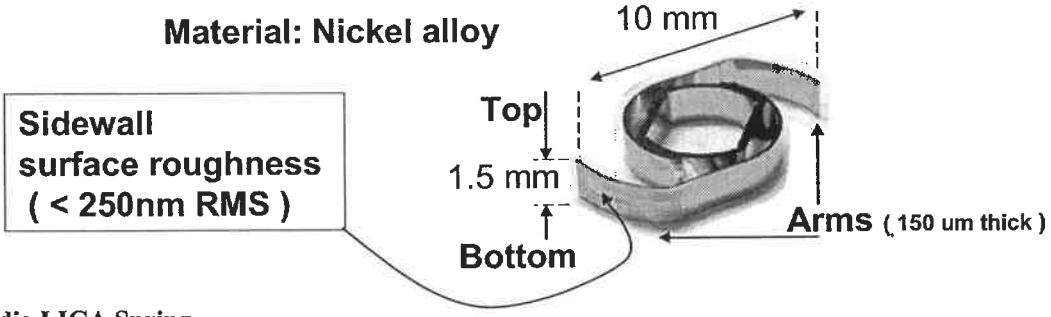

Figure 1: Sandia LIGA Spring.

The sidewall surface roughness of 250 nm RMS is a key parameter to be met before delivery to the customer. Measuring surface roughness on a fragile complicated micro component is not a trivial task. The Wyko NT3300 optical profilometer tool provides non-contact measurements, alleviating damage concerns and provides less than 1 nm precision to the 250 nm RMS surface roughness specification. Dozens of spring sidewalls have been measured to benchmark the surface quality. Collaborators provided a mounting base to inspect the same arm regions on all springs.

LIGA PROCESS OVERVIEW

The LIGA Spring sidewall topology provides important feedback that gages the quality of the LIGA process. The topographical orientation can direct attention to the process steps responsible for the defects. The vertical striations,

top-down trenches and peaks that are perpendicular to the stretch of the spring arm, result from steps before the x-ray exposure and are projected in the direction of the x-rays. In contrast, horizontal ridges parallel to the stretch of the arm develop after the exposure during the wafer processing steps. For illustration, key steps in the LIGA process are grouped into two stages: Exposure stage and Wafer Processing Stage. See figure 2.

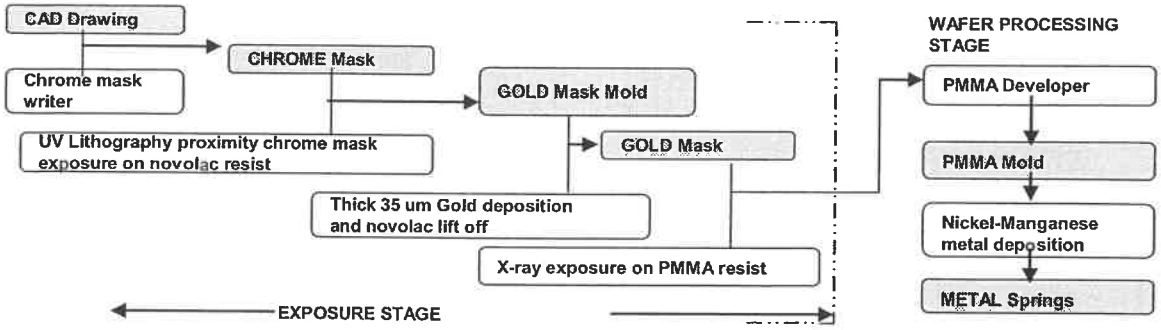

Figure 2: Flow chart of Sandia LIGA process.

VERTICAL STRIATIONS AND EXPOSURE STAGE

The Exposure Stage contains all the mask preparation steps ending with the x-ray dose illumination at the synchrotron beam line. The top-down striations are formed from gold mask imperfections along the feature edges, either from random gold mask imperfections or from unwanted programmed defects at earlier mask production steps.

Two forms of striations formed in the early mask production steps will be discussed. First, periodic striations with 500 nm P-V amplitudes can be traced to the first step. The CAD model had wafer layouts where a few springs were not represented in sufficient resolution about the curves. The arm curvatures were written to the chrome mask with polygonal facets at lower resolution, and then transferred through the remaining steps onto the gold mask, the result being springs with polygonal sidewalls. Figure 3 shows how the Wyko surface height contour plot views those facets, with the localized arm curvature subtracted from the data.

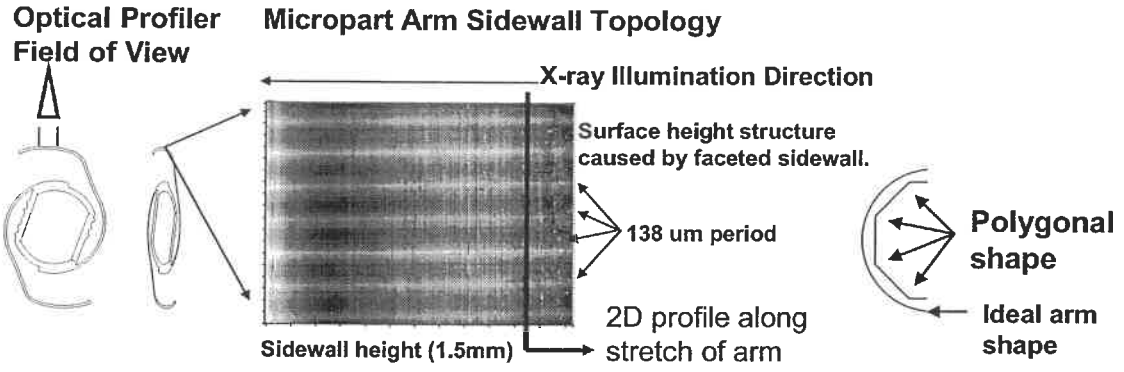
Optical Profiler Field of View
Micropart Arm Sidewall Topology
X-ray Illumination Direction
Surface height structure caused by faceted sidewall.
138 um period
Polygonal shape
Ideal arm shape
2D profile along stretch of arm
Sidewall height (1.5mm)

Figure 3 Contour plot showing gray scale relative height of LIGA spring sidewall.

The 2D profile of the facets shows a banded structure that follows the mathematical subtraction of the designed arm curvature from the faceted polygonal shape of the sidewall, as indicated in figure 4. The surface roughness from the

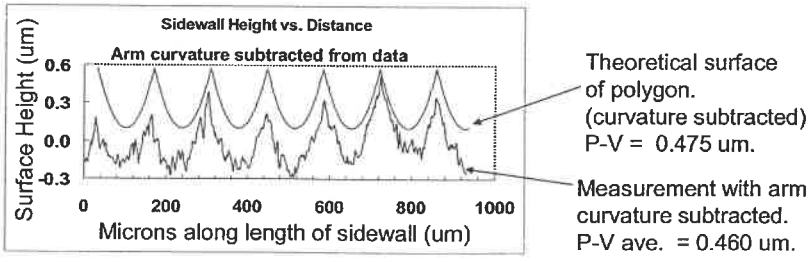

Figure 4: 2D profile from Figure 3 contour compared to theoretical values.

polygonal structure increases the surface roughness to near the specification of 250 nm, however, this can be corrected easily with a CAD file revision.
The second type of vertical striations is also periodic, resembling the look of the polygonal structure, but at approximately half the peak-to-valley amplitude, 200 nm P-V. Unlike the previous structure, this type is observed readily on straight edge sidewalls with spatial periods starting at 200 um or 250 um instead of the 138 um period. The 200 um or 250 um period corresponds to the vendor-documented chrome mask writing tool laser sweep. As the mask writer tool sweeps the resist-exposing laser, the mask is scanned perpendicular. The 5-inch wide mask must have several sweep areas stitched, and 200 nm P-V amplitudes span adjacent sweep areas. If the straight sidewall is not parallel to the laser sweep, the spatial period should be lengthened by a 1/cosine factor. Measurements of angled straight edges support the cosine factor prediction. See figure 5.

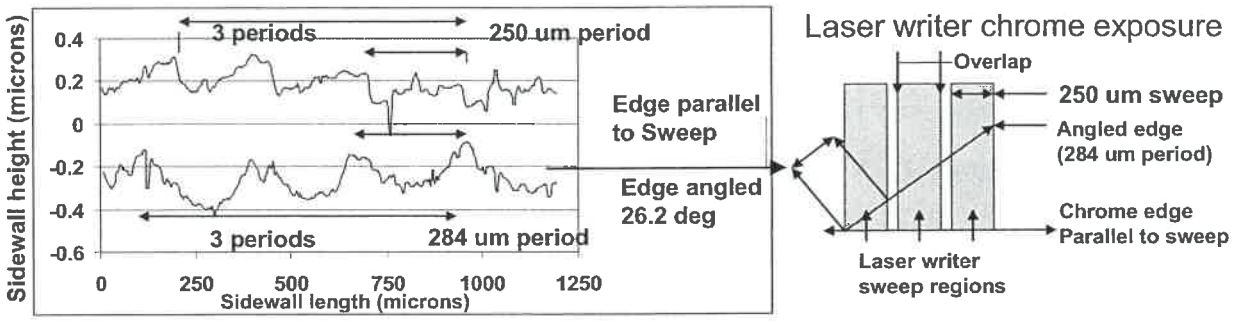

Figure 5 Graph comparing flat sidewall undulations with spatial periods formed by chrome edges, one parallel and one angled to laser sweep direction.

In addition to the repeating sidewall striations, there are large isolated vertical striations on the nickel sidewalls also. These appear as grooves extending down the sidewall, distributed at random, and typically 1-3 microns deep stretching across 50 microns along the arm. If these occur at key positions on the spring arm, the surface roughness is severely compromised, and the part will fail. Deeper grooves of 3 um are discovered by top view lateral dimensional metrology as well. The grooves are not written from artifacts on the chrome mask but from ones introduced later during the gold mask deposition. The resist mold created from the chrome UV exposure develops sidewall imperfections of its own which the gold deposition process will fill, forming isolated nodules. Additional gold masks fabricated from the same chrome mask will form nodules in different locations.

HORIZONTAL FEATURES AND WAFER PROCESSING STAGE

Horizontal feature refer to in-line ridge patterns running parallel to the PMMA substrate surface. There are two patterns of formation, both occurring in the wafer processing stage of the LIGA process. Refer to Figure 2, the LIGA Process Overview Chart.

The most severe horizontal defects, sidewall variations greater than a micron, appear from the PMMA development step. Cracks can form along the resulting channel sidewalls before the exposed PMMA is chemically developed away. The extent of those cracks correlates to x-ray dose and longer transfer delay times between x-ray exposure and immersing the wafer into the developer. Fortunately, minimizing the delay time has eliminated crack formation issues.
Sidewall ridges also occur during the nickel electroplating step, though much less severe than the crack formations. Throughout the slow deposition process, the ridges resemble captured growth levels of the metallization at any given moment, producing 30-50 nanometer oscillations up the sidewall. In figure 6, an unwanted void from a bubble that formed early during electroplating reveals how the developing grain structure must be related to subsequent metal deposition. The void or defect upsets the flat level formation of the nickel, but gradually the subsequent layers flatten the bump.

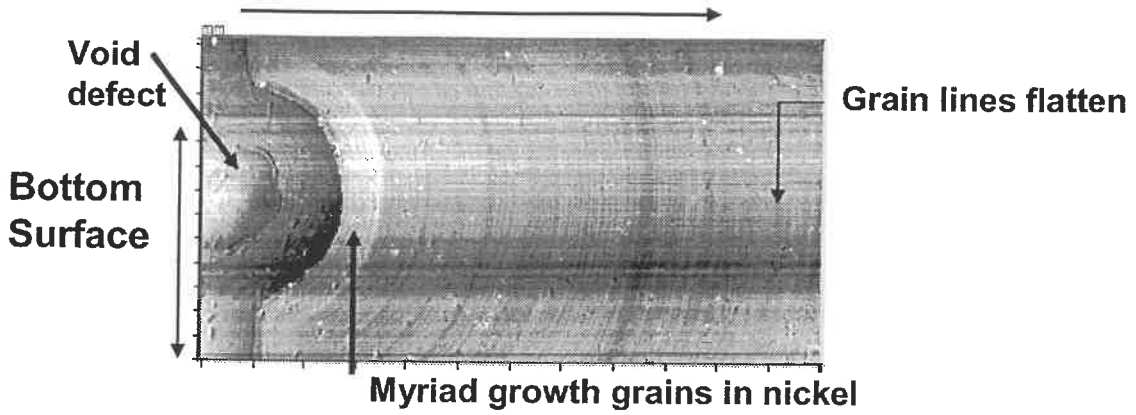

Figure 6. Horizontal sidewall structure showing a void defect early in plating step, then growth grains straightening around the defect toward the latter period.

The structure of the growth grains is thought to be related to localized chemical saturation that could slow and then increase the rate of metal deposition as the chemistry works in relatively low mixing regions of the channels. The surface roughness contribution of these growth grains does not pose problems for meeting our specification, but the LIGA group is exploring bath chemistry to better understand and eliminate this plating effect.

GOLD COATING AND SURFACE ROUGHNESS

As a final processing step, the spring is coated with gold to minimize corrosion. The protective layer is electroplated after the springs pass quality inspection tests. For spring qualification measurements, the surface roughness on the sidewall is typically measured over a 1 mm square area. Effects of the gold coating on surface roughness are seen best at five times higher magnification where surface shape cannot mask the finish attributes. Distinguishable locations on the hub top are also used to repeat surface measurements before and after, a more controlled comparison. The surface roughness as expected was measured to increase, but spanned a broad range from 60% to 100%. The gold plating process depends on multiple parameters and has been inconsistent as the plating recipe requires adjustment in order to improve the adhesion. Gold electroplates more efficiently to sharp points, serving to accent any topography rather than smooth it. Though the gold increases the surface roughness significantly over a localized region, the P-V amplitude remains small compared to the longer spatial periods previously discussed.

CONCLUSION

The LIGA process has produced hundreds of springs. Surface roughness is a key parameter that must be measured carefully. Vertical striations are formed from the Exposure Stage of the LIGA process and contribute most to the surface roughness. Most vertical striations are attributed back to the chrome mask. The horizontal sidewall ridges are formed during the wafer processing stage and contribute less to the surface roughness overall. Gold plating increases localized surface roughness from 50 – 100%.

References:

1. Becker, E.W., et al., *Fabrication of microstructures with high aspect ratios and great structural heights by synchrotron radiation lithography, galvanoforming, and plastic moulding (LIGA process).* Microelectronic Engineering, 1986. **4**: p. 35-53.
2. Guckel, H., et al., *Direct high throughput LIGA for commercial applications: a progress report.* Microsystem Technologies, 2000. **6**(3): p. 103 - 105.
3. Ceremuga, J.T. and G. Aigeldinger, *Inspection Strategy for LIGA Microstructures Using a Programmable Optical Microscope.* American Society for Precision Engineering, Annual Meeting, Book of Abstracts, 2003.
4. Dewa, A.S., *Mesoscopic systems: bridging from micromachined devices to macroscopic systems.* Mechatronics, 1998. **8**(5): p. 521-534.

Measuring two-axis stage mirror non-flatness using linear/angular interferometers

J. Montoya, R.K. Heilmann, and M.L. Schattenburg

Space Nanotechnology Laboratory, Massachusetts Institute of Technology, Cambridge, MA 02139

Abstract

Typically, high accuracy two-axis (x,y) stages use displacement interferometers to determine stage position and velocity. A stage controller uses these quantities as feedback to minimize the error between the desired and actual stage travel. This method, however, is prone to error due to the non-ideal flatness of the stage mirrors. In order to compensate for the mirror non-flatness, knowledge of the mirror profile over the length scale of interest is required. We have developed a method to measure the stage mirror non-flatness by using two linear/angular interferometers mounted on opposing axes. By performing discrete sampling of the stage mirrors along the range of travel, we show that both the stage rotation and a filtered mirror profile can be obtained. Here we present the measurement transfer function which describes the spatial frequencies of the mirror profile that can be recovered using this approach. A novel inverse transfer function was developed which eliminates the instability due to zeros in the transfer function. Moreover, we will apply this technique to measure non-linearities of a 300 millimeter stage mirror. In the context of this measurement, we will describe the assumptions and limitations of this approach.

1. Introduction

Techniques for calibrating mirror nonflatness exist in the literature. One promising method uses a self-calibration approach known as the 3-flat test (1). This method uses three reference flats which are compared to each other interferometrically. By comparing three combinations of the reference flats, followed by a fourth combination in which one of the flats is rotated, a resulting set of equations are obtained. These equations may be solved to obtain the nonflatness of the reference flats (2).

Once a reference flat is calibrated, it can subsequently be employed to calibrate an interferometer, which itself is subject to non-ideal optical components. While these measurement approaches have been demonstrated successfully, the equipment required may be expensive or require extensive design. For a 300 mm stage mirror, a nonflatness measurement would require a pre-calibrated interferometer with a large aperature. Another approach would be to perform a 3-flat test on the mirror itself, which would require extensive design for rotation and probing equipment. Moreover, there is also the possibility that distortion will be added to the mirror by the installation procedure (3).

Here we will present an alternative technique which allows us to measure the mirror nonflatness after it is mounted on a stage. This eliminates the measurement uncertainty resulting from the mounting process. The measurement procedure involves using two opposing axis (X-Y) measurements. Each axis measurement uses a Zygo angular/displacement interferometer. Here, we will focus on measuring the X-stage mirror. The Y-stage mirror may be measured similarly.

2. Measuring the X-Stage Mirror

In order to measure the X-stage mirror, both X and Y interferometers are used as the stage travels along y. The X interferometer measures $X_m(x, y)$, the X-axis mirror displacement as a function of the

desired stage coordinates (x, y), and $\theta_x(x, y)$, the measured stage angle (yaw). Similarly, the Y-axis interferometer yields $Y_m(x, y)$ and $\theta_y(x, y)$. Both X- and Y-axis interferometers use a four-pass heterodyne measurement scheme (4).

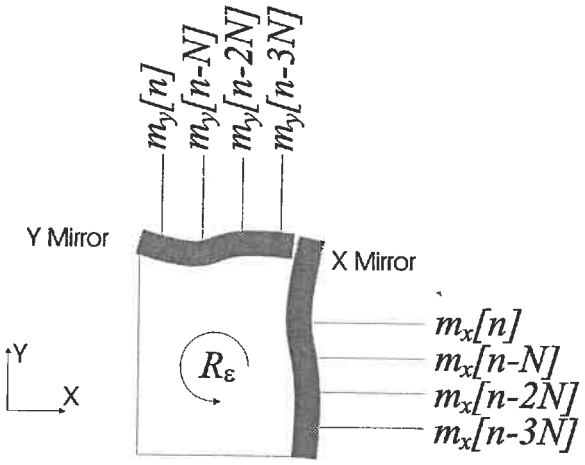

Fig. 1. The X-Y interferometers use a four-pass scheme to measure stage angle and displacement. The four measurement points are shown for each stage mirror. As the stage travels along Y, keeping the X displacement constant, small rotation errors R_ϵ may occur.

In order to generate a profile of the stage mirror, a closed feedback loop is used to hold the measured X-mirror displacement $X_m(x, y)$ constant as the stage travels along y. The four-pass X-axis mirror displacement measurement may be expressed as

$$X_m(x, y) = \frac{m_x(x, y) + m_x(x, y \quad h)}{2}, \tag{1}$$

where h is the distance between two beam spots on the stage mirror. The displacement of the X-stage mirror from a choosen reference location, at a point y along the mirror, is given by $\hat{m}_x(x, y)$. However, since we are dealing with beams of finite size, the measurement results in m_x which is modeled as a moving average version of $\hat{m}_x$ over the beam spot size d. Accordingly, spatial frequencies present in the mirror which are greater than $1/d$ will be attenuated by the averaging process.

The Zygo linear/angular displacement interferometer uses an optical differencing scheme to determine the angle (yaw) of the stage. This may be defined in terms of the displacement measurement at four points on the X-stage mirror as follows

$$\theta_x(x, y) = \frac{X_m(x, y) \quad X_m(x, y \quad 2h)}{2h} + R_\epsilon(x, y), \tag{2}$$

where $R_\epsilon(x, y)$ is a small rotation error of the stage at coordinate (x,y) about the normal axis of the stage (i.e., the yaw). For example, in our air-bearing stage, the nonflatness of the reference surfaces (granite and ceramic) on which the air-bearings glide are assumed to be the main source of this error. The total yaw $R_\epsilon(x, y)$ could be further decomposed as functions of the X (ceramic surface) yaw $R_x(x)$, and the Y (granite surface) yaw $R_y(y)$ as $R_\epsilon(x, y)$=$R_x(x) + R_y(y)$. Note that in the context of measuring the X-stage mirror, x is held constant and the total yaw error $R_\epsilon(x, y)$ will be a function of y only with x as a parameter.

Similarly, the Y-axis interferometer measurement provides

$$Y_m(x, y) = \frac{m_y(x, y) + m_y(x \quad h, y)}{2} \tag{3}$$

$$\theta_y(x, y) = \frac{Y_m(x, y) \quad Y_m(x \quad 2h, y)}{2h} + R_\epsilon(x, y), \tag{4}$$

In order to progress, we will discretize the former equations and introduce a standard notation. The discretization occurs because our controller samples the interferometers at finite intervals during the stage travel. If we represent the discretized stage coordinate $y = n\Lambda$ and remove the redundant notation, we may rewrite equations (1) - (4) as

$$X_m[n] = \frac{m_x[n] + m_x[n \quad N]}{2} \tag{5}$$

$$\theta_x[n] = \frac{X_m[n] \quad X_m[n \quad 2N]}{2h} + R_\epsilon[n] \tag{6}$$

$$Y_m[n] = \frac{m_y[n] + m_y[n \quad N]}{2} \tag{7}$$

$$\theta_y[n] = C + R_\epsilon[n]. \tag{8}$$

Since we are holding the X-displacement constant and moving the stage along Y, the θ_y measurement results in a direct measurement of the stage rotation with a constant offset C. For instance, the difference $m_y[n] + m_y[n \quad N] \quad m_y[n \quad 2N] \quad m_y[n \quad 3N] = C$ is constant for all y. Furthermore, since we are only interested in measuring the nonlinear mirror flatness deviation, we may

neglect this constant offset in our analysis. This allows us to use equation (8) to measure the stage rotation error at the sampled intervals $y = n\Lambda$ where Λ is the spatial sampling period. In order to use this formalism, we must choose the sampling period $\Lambda = h/N$ where N is an integer. This is necessary to insure that the measurement points are located at integer sampling distances from each other. Moreover, since the spot size limits the spatial frequency content to $1/d$, a sampling period $\Lambda < 2d$ will lead to oversampling.

3. Measurement Transfer Function

With the desired notation in place for the various quantities, discrete Fourier analysis will allow us to investigate the spatial frequency spectrum of the mirror profile. By holding the X-displacement constant, equation (6) for the θ_x measurement results in a measurement of the mirror profile with an error term due to the stage rotation. The rotation may be removed by subtracting out the Y-axis angle measurement. Subtracting equation (8) from equation (6) results in

$$\Delta\theta[n] = \frac{m_x[n] + m_x[n \quad N]}{4h} \qquad (9)$$
$$\frac{m_x[n \quad 2N] + m_x[n \quad 3N]}{4h},$$

where $\Delta\theta[n] = \theta_x[n] \quad \theta_y[n]$. The measurement transfer function may then be defined in terms of the discrete Fourier transforms $\Delta\Theta(e^{j\omega})$, and $M_x(e^{j\omega})$ of the quantities $\Delta\theta[n]$, and $m_x[n]$ respectively. To relate these quantities, we define the measurement transfer function $H(e^{j\omega})$ as

$$H(e^{j\omega}) = \frac{\Delta\Theta(e^{j\omega})}{M_x(e^{j\omega})} \qquad (10)$$

$$H(e^{j\omega}) = \frac{(1 + e^{\ j\omega N} \quad e^{\ j\omega 2N} \quad e^{\ j\omega 3N})}{4h}. \qquad (11)$$

The measurement transfer function may be interpreted as follows. When we subtract the stage rotation given by the Y-interferometer θ_y from the X-interferometer θ_x, we measure a filtered mirror profile. The filter that is applied to the mirror profile is given by the measurement transfer function. A key property of the measurement transfer function is that it does not have a dc (zero frequency $\omega = 0$) component. This component would provide information about the X-displacement of the stage mirror, which is not of interest. Moreover, we would like for our measurement to be immune to the stage X-displacement since there may be additional stage error associated with maintaining a constant displacement.

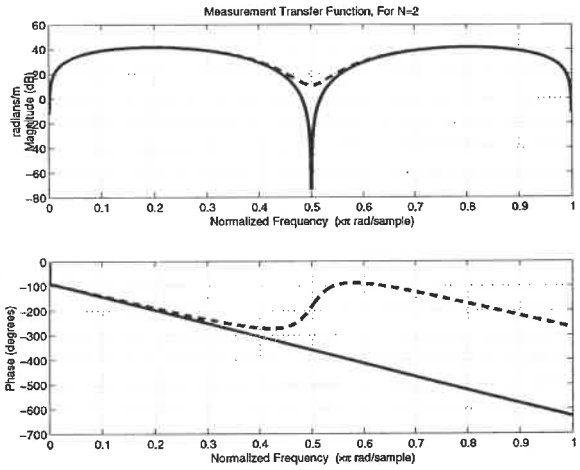

Fig. 2. The solid line shows the frequency response of $H(e^{j\omega})$, while the dashed line corresponds to an approximation where the double zeros corresponding to a normalized frequency of 0.5 have been moved inside the unit circle. These zeros would result in an unstable inverse transfer function. Any spatial frequencies in the mirror corresponding to the zeros in $H(e^{j\omega})$ will be lost. For the case of $N = 2$, the first zero location beyond the zero frequency corresponds to spatial periods equal to the spacing h between the four beam spots on the mirror.

To recover the mirror profile, we must apply the inverse transfer function $H(e^{j\omega})^{-1}$. Unfortunately, investigation of the zeros of $H(e^{j\omega})$ reveal that they reside on the unit circle, which by definition does not have a stable inverse transfer function. In order to obtain a stable inverse, we must find an approximation to $H(e^{j\omega})$ with zeros inside the unit circle. Subsequently, we may take the inverse of this approximate function and apply it to the data to recover the mirror profile. Figure (2) shows an approximate transfer function for $N = 2$.

4. Conclusions and Future Work

We have applied this technique to measure the profile of a 300 mm stage mirror. This technique has shown promise in simulations which generated random mirror profiles containing a uniform frequency distribution (white noise). Moreover, we hope to apply this formalism to measure distortions in diffraction gratings and other patterns of interest. Future work will involve investigating the consequences of interferometer alignment on this technique, and improving the alignment to insure accurate results.

References

[1] Evans, C.J, Davies, A. D., Schmitz, T., Parks, R., Interferometric figure metrology; enabling in-house traceability, Proc. SPIE, **Vol. 4450**, pp:81-93, 2001

[2] Schulz, G., Grzanna, J., Absolute flatness testing by the rotation method with optimal measuring-error compensation, Applied Optics, **Vol. 31**, pp:3767-3780, 1992

[3] Ruijl, T.,Ultra Precision Coordinate Measuring Machine Design, Calibration and Error Compensation, PhD Thesis, Eindhoven, the Netherlands 2001

[4] ZYGO 2/20 Integrated Interferometer System Reference Manual OMP-0229B, 1993 (Zygo Corp., Middle Field, CT.)

DIMENSIONAL ANALYSIS OF CROSS SECTIONED HIGH ASPECT RATIO MICROSTRUCTURES

Joseph T. Ceremuga, Georg Aigeldinger, and Kevin D. Krenz
Microsystems Processing Dept., Sandia National Laboratories, Livermore, CA
email: jtcerem@sandia.gov

INTRODUCTION

The LIGA microfabrication process can be used to produce high aspect ratio metal microstructures with nearly vertical sidewalls. LIGA is the German acronym for lithography (Lithographie), electrodeposition (Galvanoformung), and molding (Abformung) [1]. At Sandia National Laboratories, "direct LIGA" [2] is used for several applications. In this process, the x-ray lithography fabricated polymethyl methacrylate (PMMA) mold is directly filled by electrodeposition to fabricate individual metal components. Some LIGA part designs at Sandia involve the use of flexures, whose performance characteristics rely upon precise geometries. Generally there are several factors that affect the sidewall normality, or degree of verticality from the wafer plane: Secondary radiation effects during the x-ray exposure step [3,4], PMMA swelling during electrodeposition [5,6], thermal expansion of PMMA during electrodeposition, and the stress of the electrodeposit itself.

The sidewall normality in a complicated part design is a challenge to measure and evaluate. While top and bottom critical dimensions can be measured, along with samples of sidewall topologies, these methods do not give a complete assessment of sidewall normality. To acquire sidewall data, the part is typically cross-sectioned, and is ultimately destructively tested. This study demonstrates methods for measuring and digitizing cross-sectioned structures using an optical coordinate measurement machine, and presents a data-processing method to fortify the understanding of high aspect ratio structures.

EXPERIMENTAL SETUP

The part evaluated in this study is a LIGA fabricated spring mechanism. The spring laterally spans approximately 1 cm², has two curved flexures of over 1 cm arc length and 143 μm in thickness, depending on its design. The aspect ratio of the flexures is 10:1, height to thickness, respectively. Figure 1 shows a drawing representing the spring and the locations of the cross-sections.

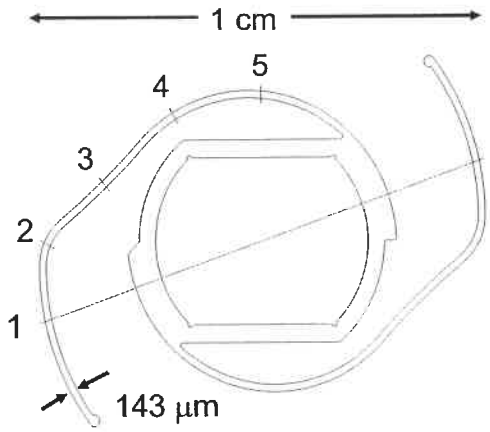

Figure 1: Top view of spring design and the locations of cross sections.

As seen in Figure 1, the flexure geometry is comprised of multiple curvatures. The locations of the cross sections are chosen to capture each curvature. Springs from various wafers are placed in a fixture, positioned for planarization, mounted in epoxy, and then cross-sectioned. Figure 2 shows an optical microscope image of a cross section in the #5 position shown in Figure 1.

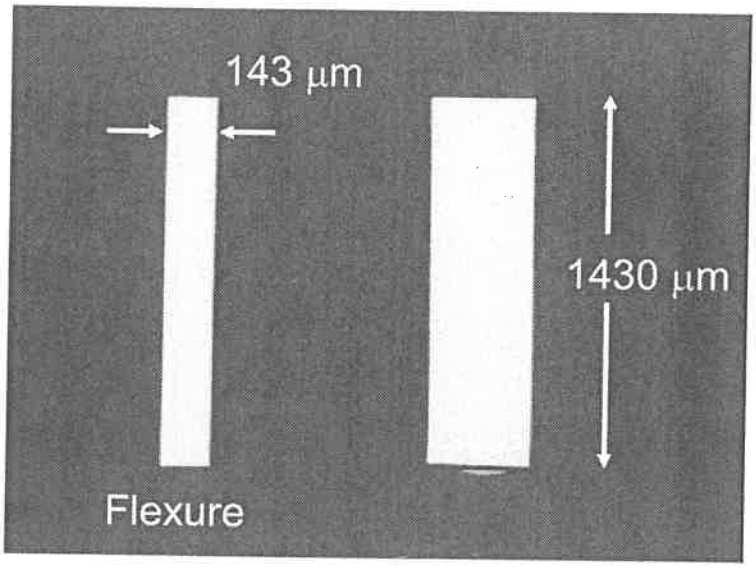

Figure 2: Optical microscope image of cross section #5.

Five thickness measurements are taken at equidistant heights of the cross section, and the perimeter is digitized. Digitizing a part refers to inspecting the perimeter of a part, then extracting the coordinate data generated during edge detection. A 20x objective is used for inspection, translating into a pixel size equal to 0.55 μm for image processing. Specimens are illuminated using backlighting as the primary source, with supplemental LED ring lighting and coaxial lighting to refine the image contrast. The microscope uncertainty for the thickness measurements is ±1.5 μm, and the digitization uncertainty is ±1.8 μm for the part scale in which stage movement is necessary [7]. The digitized data is imported into a commercial point-to-CAD comparator, along with the CAD model representing the cross-section geometry [8].

The data analysis flow is illustrated in Figure 3. Data fitting is performed by overlaying the digitized cross section (point cloud at left in the figure) onto the CAD model with a numerically weighted fit to the planarized top surface geometry so that deviations due to wafer bow do not skew the results. The fit model shows a 10x scaled vector plot of the deviations. The point-to-CAD deviations of each sidewall are then plotted with respect to the vertical axis and combined into one graph, spanning a total of five sidewall sections. The graph shows a repeated saw-toothed pattern in the vertical direction. This is due to the sub-pixel interpolation of the image processing [9].

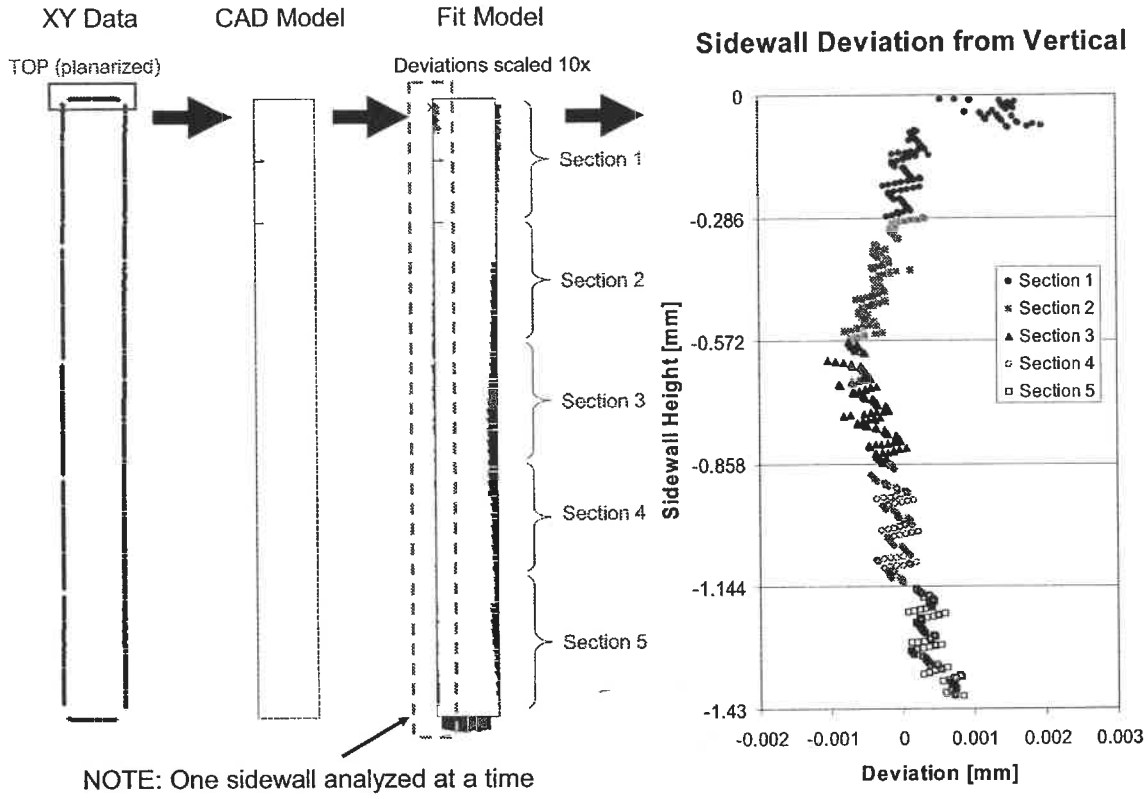

Figure 3: Metrology data analysis flow, starting with a point cloud (left) and finishing with the extraction of the deviation from a vertical sidewall.

The data is sorted and analyzed with respect to the inside or outside location from which the cross-section was taken. The inside location refers to the sidewall closest to the center of radius of the flexure, whereas the outside refers to the sidewall furthest from the center of radius. Figure 4 shows this inside/outside sidewall convention used for data analysis.

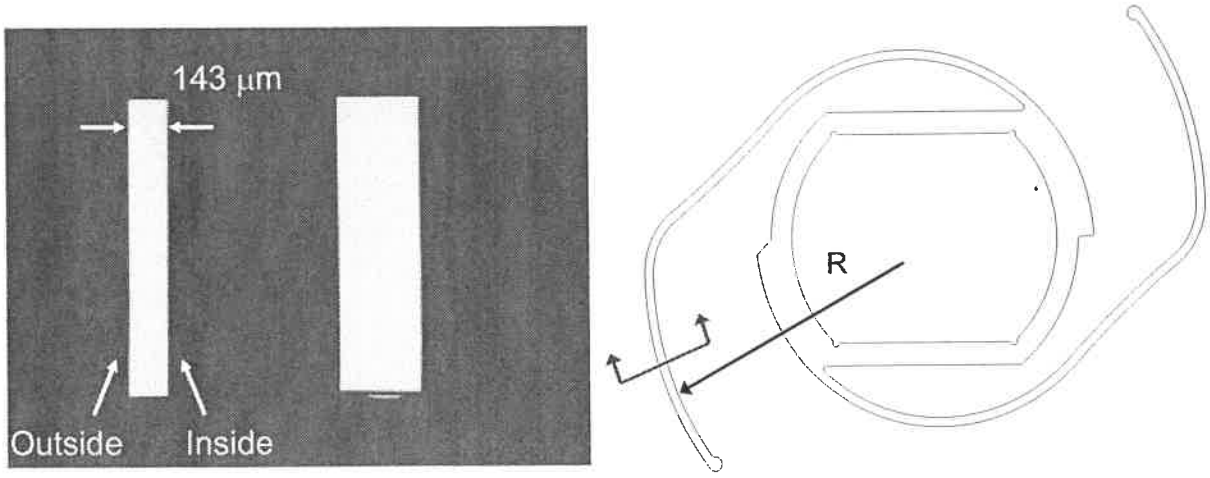

Figure 4: Inside and outside sidewall convention

CONCLUSIONS

We have demonstrated a precision method to dimensionally capture cross sections of high aspect ratio microstructures. We have developed and applied software analysis tools and methods that evaluate sidewall normality and topology. This novel metrology method can now be used for better process control. More importantly, the method greatly supports process development by precisely quantifying deviations and effects that would otherwise be qualitative observations at best.

ACKNOWLEDGEMENTS

Sandia is a multiprogram laboratory operated by Sandia Corporation, a Lockheed Martin Company, for the United States Department of Energy's National Nuclear Security Administration under Contract DE-AC04-94AL85000. The authors would like to thank the LIGA group staff, Andrew Gardea and Nancy Yang, Sandia National Laboratories, for the cross sectioning of the microstructure samples.

REFERENCES

[1] Becker, E. W., et al., Fabrication of Microstructures with High Aspect Ratios and Great Structural Heights by Synchrotron Radiation Lithography, Galvanoforming, and Plastic Moulding (LIGA Process). Microelectronic Engineering. 4:35-53 (1986).

[2] Guckel, H., et al., Direct high throughput LIGA for commercial applications: a progress report. Microsystem Technologies. **6**(3):103-105 (2000).

[3] Griffiths, S.K. and A. Ting, The influence of X-ray fluorescence on LIGA sidewall tolerances. Microsystem Technologies. **8**(2-3):120-128 (2002).

[4] Pantenburg, F.J. and J. Mohr, Influence of secondary effects on the structure quality in deep X-ray lithography. Nuclear Instruments and Methods in Physics Research, Section B, **97**(1-4):551-556 (1995).

[5] Goods, S., Howard, S., et al., Thermal Expansion and Hydrogen Behavior of PMMA Molding Materials for LIGA Applications. Sandia Report, Sandia National Laboratories, Livermore, CA (2003).

[6] Griffiths, S. K. and J. A. Crowell. Dimensional Errors in LIGA-Produced Metal Parts due to Thermal Expansion and Swelling of PMMA. HARMST 2003, Monterey, CA (2003).

[7] Ceremuga, J.T. and G. Aigeldinger, Inspection Strategy for LIGA Microstructures Using a Programmable Optical Microscope. SAND REPORT, Sandia National Laboratories, 2003(SAND2004-2289 / Submitted to Precision Engineering).

[8] ICAMP, Inc., Best-fit software. Virtual functional gaging software for quality control. For more information, see http://www.icamp.com

[9] VIEW Engineering, Inc. Precision measurement solutions for process control. For more information, see http://www.vieweng.com

Wear Measurement of Engine Valve and Seat Insert Using a Confocal Laser Microscope

Keyoung Jin Chun, Jae Soo Hong

Korea Institute of Industrial Technology,
35-3, HongChonRi, IbJangMyun, ChonAnSi, ChungNam, 330-825, Korea

Abstract : The minimization of valve and seat insert wear is a critical factor for consideration in the pursuit of engine performance improvement. In order to achieve this goal, an innovative simulator was developed with the ability to generate and control high temperatures up to 900℃ and various speeds up to 80Hz during motion, just as in the case of an actual vehicle engine. This wear simulator is considered to be a valid reproduction of the engine valve and seat insert wear process operating with various speeds during engine activity.

This work focuses on the different degrees of wear at three different singular test speeds (10Hz, 25Hz & multi-Hz). In this study, the seat insert's exterior surface temperature was controlled at 350℃, the cycle number was 2.1×10^6 and the test load was1960N. The wear depth was measured before and after the testing using a confocal laser microscope. The wear depth of the valve and the seat insert for each speed (Hz) with statistical data. The mean (± Standard Deviation) wear depth of the valve and seat insert at 10Hz was 29.9 (± 4.8)㎛ and 34.7 (± 1.4)㎛, respectively. The mean (± Standard Deviation) wear depth of the valve and seat insert at 25Hz was 74.7 (± 3.5)㎛ and 82.9 (± 2.7)㎛, respectively. In the case of multi-Hz it was 48.5 (± 6.3)㎛ and 61.4 (± 5.4)㎛, respectively. It was found that higher speeds caused a greater degree of wear than lower speeds under identical test conditions.

1. Introduction

The vehicle engines of today must function with a high level of power output, demonstrate superior fuel economy and perform with high durability. Such needs require strict control on the wear of the valve and seat insert, which are major components of any vehicle engine. The valve collides with and slides in the seat insert at high temperatures by means of the action of the valve spring. Occasionally, friction between the valve and seat insert is accompanied by a sliding phenomenon [1]. Certain phenomena of the valve and seat insert wear can be observed depending on the engine operation status. These include internal temperature, power output, speed or RPM (revolutions per minute) [2, 3]. Among them there has been no analysis of the wear rate and wear mechanism due to speed (RPM) change. A great amount of research throughout numerous studies has taken place concerning the valve and seat insert. However, the majority of such inquiries have only taken factors into consideration at a constant RPM while the actual condition for driving vehicles is fluctuation in the operational RPM. As such, it is difficult to examine the wear rate and the wear mechanism of the valve and seat insert depending on the engine RPM.

The objectives of this study focus on measuring the wear rate using a confocal laser microscope and observing the wear mechanism of the valve and seat insert depending on speed (RPM) changes.

2. Test Device and Method

2.1 Test Device

In order to examine the wear rate and the wear mechanism of the valve and seat insert [8, 9, 10], this study has applied a simulator that is exclusively used for valve and seat insert wear. This simulator takes

into account such aspects as speed change, temperature, load and friction between the valve and seat insert, etc., that represent the internal conditions of an actual vehicle engine.

The simulator exclusively used for this study has been designed to be similar to an internal combustion engine. It consists of three components: a hydraulic power unit, a control unit and a mechanical unit. The internal temperature of the chamber is monitored by five thermocouples. Three thermocouples are located 120° apart along the outer surface of the seat insert. The remaining two thermocouples are used to monitor the cooling system. In order to constantly maintain the desired internal temperature, cooling channels have been installed, which can control the temperature up to 900℃.

2.2 Test Method

The exhaust valves and seat inserts, currently used for an existing vehicle, were used as specimens. The valve material consists of STR35, a valve steel, and the seat insert material consists of HVS1-2, a sintered iron alloy. Table 1 shows the chemical composition of each material.

Table 1 Chemical compositions (wt. %)

Materials	C	Si	Mn	Cr	Mo	Ni	Cu	Fe
Valve (STR35)	0.53	0.31	9.00	21.00	-	3.87	-	Bal
ValveSeat (HVS1-2)	1.1	-	-	7.5	2.0	2.0	15	Bal

The hardness of each specimen was measured after having been ground using a Vickers hardness tester. The hardness obtained in this manner was 419 (Hv 500g) for the valve and 397.7 (Hv 500g)for the seat insert.

Wear tests were performed for three speeds, 10Hz, 25Hz and multi-Hz (10Hz-25Hz). To achieve objectivity and consistency, the tests were performed for six specimens per speed under identical test conditions. The applied test temperature was 350℃ at the outer surface of the seat insert (760℃ at valve face). The valve was opened and closed 2.1×10^6 times, and the test load was 1960N.

Wear depth was measured before and after the test using a confocal laser microscope (Model OLS 1100 made by Olympus, Resolution 0.01㎛). Then, the measured values before and after the test were analyzed and compared. In addition, using a SEM (Model JSM 6400JEOL made by JEOL, Resolution 4nm), the valve face and seat insert surfaces were observed before and after the test to examine the wear mechanism.

3. Test Results

3.1 Wear Depth

To guarantee the reliability of the measurements and minimize differences of the wear depth caused by eccentricity, the measured area was divided 90° apart along the surface of the valve and seat insert (see Fig. 1).

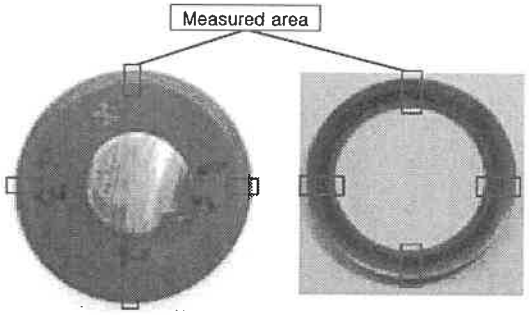

Fig. 1 Measured area of a valve and seat insert

Each measured area was scanned 10 times (see Fig. 2), and the scanned datas were averaged for the wear depth of the each measured area.

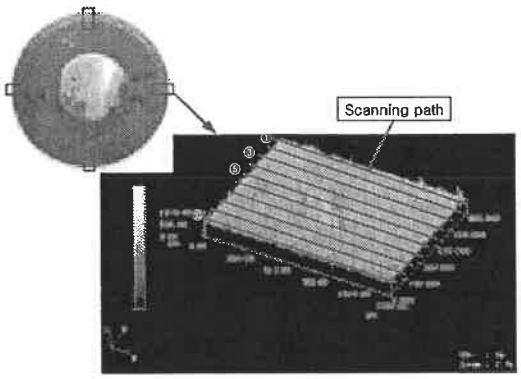

Fig. 2 Scanning path of the wear face

Fig. 3 shows one example of the three-dimensional wear scar profile at the maximum contact area of a seat insert at 25Hz, which was measured using the OLS1100.

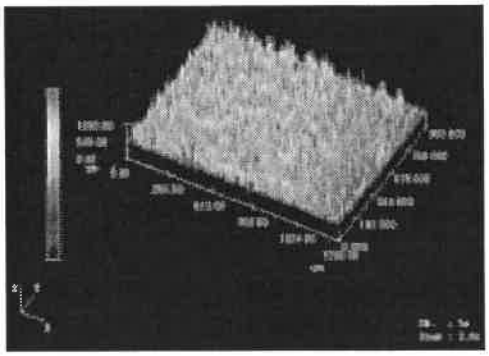

Fig. 3 Three-dimensional wear scar profile at the maximum contact area of a seat insert at 25Hz, which was measured from the OLS 1100.

Fig. 4 illustrate the wear depth of the valve and the seat insert for each speed (Hz) with statistical data. The mean (± Standard Deviation) wear depth of the valve and seat insert at 10Hz was 29.9 (±4.8)㎛ and 34.7 (±1.4)㎛, respectively. The mean (± Standard Deviation) wear depth of the valve and seat insert at 25Hz was 74.7 (±3.5)㎛ and 82.9 (±2.7)㎛, respectively. In the case of multi-Hz it was 48.5 (±6.3)㎛ and 61.4 (±5.4)㎛, respectively.

As can be seen from the measured values in Table 3, wear depth increases as the speed (Hz) increases. Here, since an increase in the Hz signifies an increase in the RPM of the vehicle engine, a severe increase in RPM may be responsible for such drastic increase in the valve and seat insert wear.

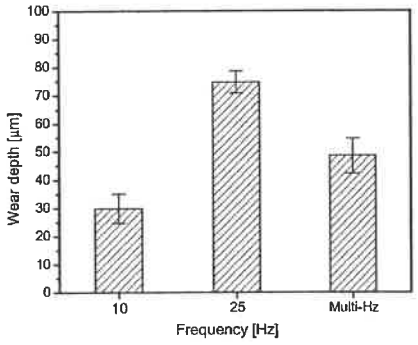

(a) Valve

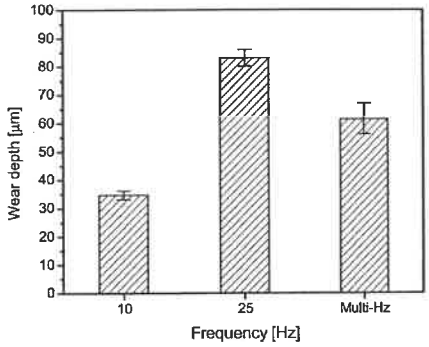

(b) Seat Insert

Fig. 4 Histograms show the means for wear depth of worn valves and seat inserts. Error bars indicate standard deviation of the mean.

3.2 Wear Mechanism

(1) Adhesive Wear

During sliding, fragments from one surface contact fragments from the other surface. When such contact does not take place, fragmentation may not occur at the interface. As a result, movable fragments will be generated. The roughness of each surface has substantial impact on the adhesive wear.

(2) Shear Strain

The result of shear strain exceeding the limit of the plastic deformation of the material surface can be classified as wear. It can be observed that in the case of the valve and seat insert, the typical

appearance of the shear strain generated due to wear is identical to the flow in the ridge or radial direction.

(3) Abrasive Wear

Abrasive wear occurs due to the cutting action of asperities or hard particles on a hard surface. The surface is damaged by the interaction of the separated particles that are confined between the sliding surfaces of the valve and seat insert.

(4) Surface Fatigue Wear or Pitting

The loading and unloading cycles that expose the material cause a crack to form on or below the material surface, creating a large fragment or damaging the surface leaving large holes in its end. The form of wear similar to this type of surface fatigue wear can be seen from a brittle material that breaks into large fragments. Upon repeated sliding or rotation of surfaces, surface fatigue wear is frequently noticed from the seat insert as it sinters from the iron powder.

4. Discussion and Conclusion

1) The mean wear depth (± Standard Deviation) of the valve and seat insert at 10Hz was 29.9 (±4.8) ㎛ and 34.7 (±1.4) ㎛, respectively. In addition, the mean wear depth (Standard Deviation) of the valve and seat insert at 25Hz was 74.7 (±3.5) ㎛ and 82.9 (±2.7) ㎛, respectively. Lastly, the mean wear depth (± Standard Deviation) of the valve and seat insert at multi-speeds (variable from 10Hz to 25Hz) was 48.5 (± 6.3) ㎛ and 61.4 (±5.4) ㎛, respectively. Therefore, it can be seen that the wear depth of the valve and seat insert increases sharply in accordance with a rise in the speed (Hz). According to these results, an increase in the engine revolution may cause the engine performance of a vehicle to decrease due to the rapid wear of the valve and seat insert.

2) From the valve wear mechanism, the following phenomena were observed:

- At 10Hz, the following types of wear were observed: adhesive wear causing sliding of the valve and seat insert due to friction between the valve and seat insert; and shear strain wear in a radial direction resulting in the breakdown of metal particles due to the plastic deformation in the material, or fragments being created.
- At 25Hz and multi-Hz, abrasive wear that occurs due to metal particles created by shear strain was observed.

3) From the seat insert wear mechanism, the following phenomena were observed:

- At 10Hz, adhesive wear occurring at the beginning stage of metal wear was primarily observed.
- At 25Hz and multi-Hz, surface fatigue wear was noticed because the seat insert was made from a sintered iron powder.
- In addition, at 25Hz and multi-Hz, abrasive wear by metal particles was often seen.

References

1 Ootani, T., Yahata, N., Fujiki, A., Ehira, A., Impact wear characteristics of engine valve and seat insert insert materials at high temperature (impact wear tests of austenitic heat-resistant steel SUH36 against Fe-base sintered alloy using plane specimens), 1995, Wear 188, 175-184.

2 Sato, K., Midorikawa, T., Takahashi, T., Oshige, H., Development of Seat insert Material for Gas-Fueled Engines, SAE Paper 2000-01-0911, 2000.

3 Scott, C. G., Riga, A. T., Hong, H., The erosion-corrosion of nickel-base diesel engine exhaust valves, 1995, Wear 181-183, 485-494.

4 Fujiki, A., Kano, M.,New PM Seat Insert Materials for High Performance Engines, SAE Paper 920570, 1992.

5 Pyle, W. R., Smrcka, N. R.,The Effect of Lubricating Oil Additive on Valve Recession in Stationary Gaseous-Fueled Four-Cycle Engine, SAE 932780, 1993.

6 Zhao,R., Barber, G. C., Wang, Y. S., Larson, J. E.,Wear Mechanism Analysis of Engine Exhaust Seat inserts with a Laboratory Simulator, STLE, 1997, Vol 40, 209-218.

A multi-purpose linear measuring system with laser interferometer

TaeBong Eom and JinWan Han

Korea Research Institute of Standards and Science, Yousong , Daejeon 305-666, Korea

Abstract

The paper presents a new linear measuring machine being designed and fabricated in the Korea Research Institute of Standards and Science. The main requirement of the machine is to achieve a flexibility to calibrate a variety of different standards such as step gages, line scales and gauge blocks with high accuracy. The main parts of the system are a precision linear stage, an alignment system for the specimen, a system for detecting measurement points, and a laser interferometer. Measuring range of the system is 1,000 mm, and target accuracy for 1,000 mm gauge block calibration is 0.35 um at the 95% confidence level.

Introduction

Most of demands on dimensional measurement are related to the linear measurement. The national metrology laboratories should maintain the primary standards such as end standards and line standards. These length standards are usually calibrated using the precise and accurate laser interferometers that are designed to operate in temperature-controlled chambers. Many kinds of interferometric calibration systems for gauge blocks or graduated line scales have been built at many national metrology laboratories. These systems need larger outlay of equipment and larger metrological effort. Recently demands of industry for the calibration of a step gauge, which can be used in calibration of CMMs, is increased more and more, so many metrology laboratories have developed special calibration systems for step gauge. Some laboratories modified commercial machine such as coordinate measuring machine or universal measuring machine for their purposes, and others specially developed their own systems. Generally these calibration systems are designed for calibrating one or two artifacts, so standard laboratories need several calibration systems as well as spaces in order to measure a variety of different artifacts. [1-4] For this reason, 4 years ago, we designed and constructed the universal measuring system that could calibrate many kinds of linear artifacts from industry. [5] However, this system was not designed for calibrating standard grade gauge block or primary standard line scale.

To calibrate standard grade gauge block, standard line scale and step gauge, Korea Research Institute of Standards and Science have designed a new linear measuring machine. On designing, we consider accuracy as well as flexibility to calibrate many kinds of different linear artifacts. The main parts of the system are a precision stage, a detecting system and a laser interferometer. To detect the measuring surface of gauge block or step gauge, we designed the special probing system with flexure structure. A double-pass plane mirror interferometers based on the heterodyne technique measure the displacement of the stage. The laser interferometer has Abbe' error free structure.

Design and fabrication of the linear measuring system

Fig. 1 shows the structure of the linear measuring machine. System consists of six main parts: machine body, linear translating system, alignment system for measuring artifact, laser interferometer, detecting apparatus, and electronic system. The granite surface plate (2,200 mm x 400 mm x 450 mm) is used as a base of the machine body and a vertical guide of the linear translator. The granite parallel bar is fixed on the granite surface plate and used as the horizontal guide of the linear translator. The translating system, which carries the alignment system for measuring artifact, reference gauge block and the interferometer reflector, makes relative displacements between the measuring artifact and the detecting apparatus. This translator, which incorporates air bearings for smooth movement, is driven by the micro-stepping motor and the lead screw. It has a traverse length of 1,100 mm. (the maximum range in gauge block measurement is 1,000 mm)

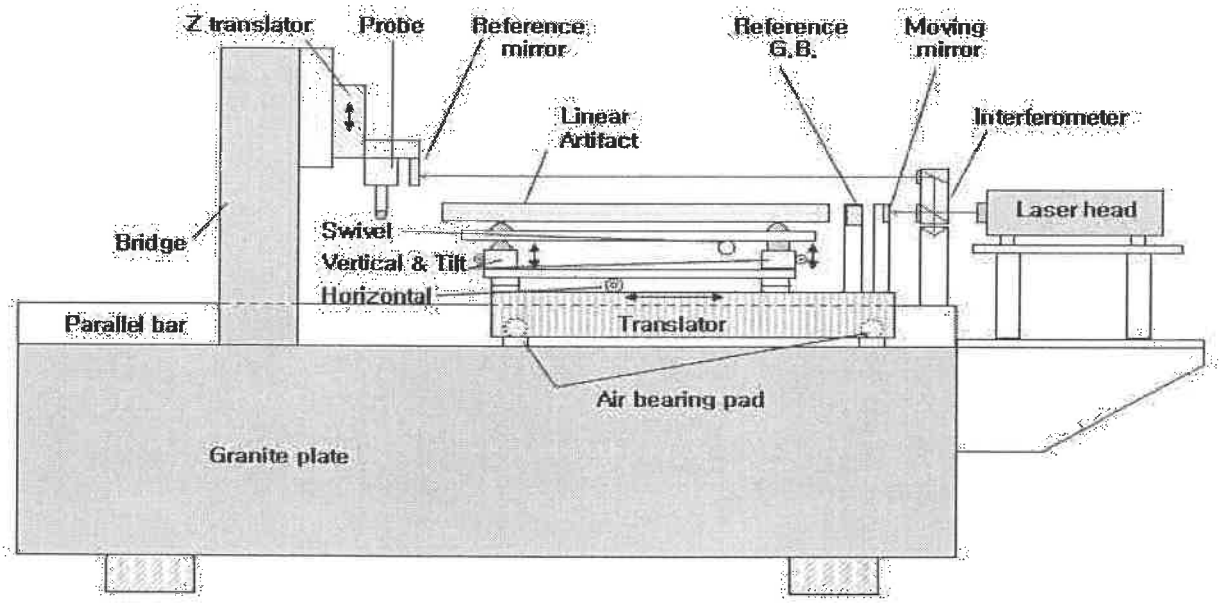

Fig. 1 Schematic diagram of the linear measuring machine

The alignment system for linear artifact consists of a horizontal translator, two vertical translators and a swivel system. The horizontal translator is driven by a micrometer with a DC geared motor and used for selecting the measuring gauge block. The vertical position and tilt angle of the artifact can be adjusted by two vertical translators.

The displacement measurement of carriage is realized by a heterodyne laser interferometer (HP5518 laser head and home-built plane mirror interferometer). The measuring axis of length standards is vertically and horizontally on same position with laser beam incident on moving interferometer reflector in order to reduce the Abbe' error. The reference beat signal and the measurement beat signal are detected before and after interferometer, respectively. These are sinusoidal signals with frequency of about 1.8 MHz. When the linear translator (moving reflector) moves $\lambda/4$ (about 0.16 μm), the phase between two signals changes 360°. In order

to encode the phase difference between reference signal and measurement signal of the heterodyne interferometer, the phase-quadrature mixing technique is used. Two outputs of phase demodulating electronics become sinusoidal signals with phase quadrature. Whenever the plane mirror moves $\lambda/4$, sine and cosine signals change 360°. These are resolution-extended up to X20 electrically. (interpolator : X5 and counter : X4) Therefore the resolution of $\lambda/80$ can be obtained. (optical : $\lambda/4$ and electrical : X20)

The detecting apparatus is used to detect the measuring point of linear artifact. Two detectors are generally used. For probing the measuring surface of gauge block, step gauge and ring gauge, parallelogram with an inductive probe and a spherical ball probe is used. The parallelogram of Invar is machined by a wire cutting machine. A solenoid coil and a permanent magnet make attractive and repulsive force. An inductive sensor measures the displacement of the hinge spring. However it is usually used as a zero detector. The measuring force is adjusted electronically by controlling the voltage applied to the solenoid. For observing the scale of line standards and detecting its center, an optical microscope with CCD camera is also used. The detecting apparatus and the reference interferometer reflector are attached to a vertical translator driven by step motor. The vertical translator is a fixed on a bridge which is also rigidly fixed on the granite surface plate.

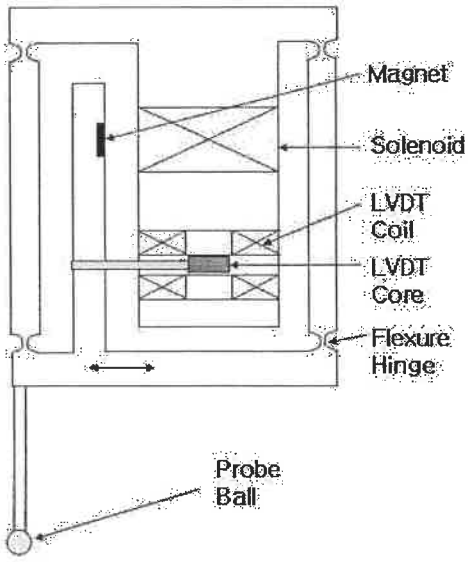

Fig. 2 Schematic of parallelogram sensor

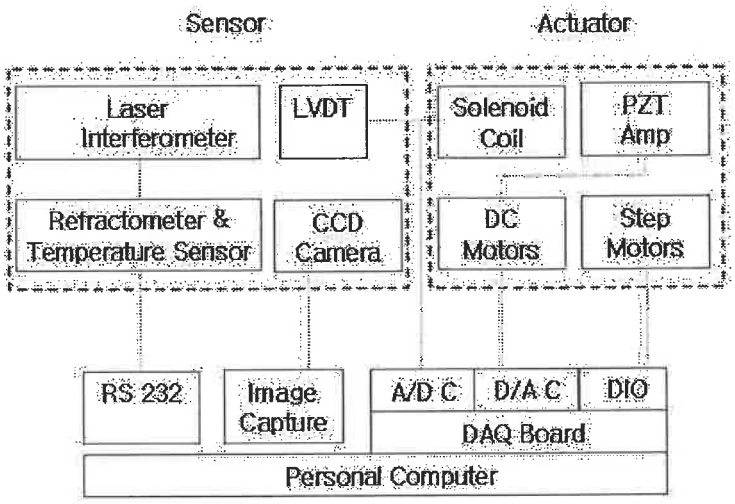

Fig. 3 Schematic of electronic system

The linear measuring system is controlled by a personal computer (PC). The schematic diagram of an electronic system is shown in Fig. 3. Two step motors are used for driving the main translator and Z-translator. For fine positioning of main translator, micro-translator with a PZT is used. Air temperature, pressure, humidity and concentration CO_2 are measured and the refractive index of the air is calculated using the

modified Edlen equation. And also material temperature is measured to compensate a thermal expansion.

Operation of the system

In order to reduce the dead path error and air turbulence effect, the measuring object is positioned as close as possible to the interferometer. And the measuring object must be aligned coaxially with center of laser beam to minimize Abbe's error and cosine error. On measuring the step gauge, ring gauge or gauge block, a reference gauge block is used to calculate the effective probe diameter. The computer controls the position of a horizontal stage (main translator) and a vertical stage (Z-translator) to allow the electronic probe to touch the front or rear measuring face. On touching the measuring surface, the main translator is controlled to stop at zero position of the inductive sensor. For measuring the scale, an optical microscope with a CCD camera and an illumination system is used. The image processor board captures the image of the scale marker and displays it on the CRT monitor with reference cross line which is generated by computer.

Conclusion and future work

In order to calibrate a variety of different standards such as step gages, line scales and gauge blocks with high accuracy, we have designed the new linear measuring machine. Its main feature is similar to old one. However its target accuracy for 1,000 mm gauge block calibration is 0.35 μm at the 95% confidence level. This value is about 3 times better than uncertainty of the old system. (Expended uncertainty (k=2) of the old system is (0.2 + 0.63 * L) μm, where L is in m.) Now we are integrating the electronic system, and we will evaluate the performance of the system.

References

[1] J. Flügge, H. Dangschat, A. Spies, J. Tschirnich and H. Pieles 1999 Concept of an interferometric length comparator with measurement uncertainties in the nanometer range *EUSPEN* **2** 27-30

[2] C Quan and G Xu 1997 A laser measurement system for automatic calibration of a height-setting micrometer *Meas. Sci. Technol.* **8** 520-24

[3] Busch K, Kuppers R, Rademacher H J and Schaller M 1984 Interferometric displacement comparator for large lengths *Feinwertech. Messtech.* **92** 313-15 (In German)

[4] R Thalmann 1997 A new high precision length measuring machine *8e Congress International de Métrologie* 1-4

[5] TaeBong Eom, and JinWan Han 2001 A precision length measuring system for a variety of linear artifacts *Meas. Sci. Technol.* 12 698-701

[6] Birch K P and Downs M J 1994 Correction to the updated Edlen equation for the refractive index of air *Metrologia* **29** 315-6

ALTERNATIVE ARTIFACTS FOR EVALUATING SCANNING CMM PERFORMANCE

Sami A. Farooqui, Edward P. Morse
Department of Mechanical Engineering and Engineering Science
The University of North Carolina at Charlotte
Charlotte, NC 28223

1. Introduction

Coordinate measuring machines (CMMs) with continuous-contact scanning capabilities are being widely used throughout many industries. Most CMM users, if asked, say they require high density scans at high speeds with high accuracy. Obviously, there will be some point at which the accuracy of the scanned data begin to decrease with an increase in the scanning speed. Previous research [1] at UNC Charlotte has revealed that the scanning errors increased in a predictable relationship with the speed when measuring ring gages. There was also found to be a large difference between the results obtained during single point probing and scanning on the same CMM. Other research [2] at UNC Charlotte has developed a compensation model to reduce the scanning errors at high speeds, but this model is only valid for circular features. To date, our literature search has found no standard method (aside from ISO 10360-4) for comparing different CMMs based on their ability to scan at different speeds. A necessary step in comparing scanning CMMs to each other, or to discrete point CMMs, is to use a standardized test method [3]. The current ISO 10360-4 [4] standard describes circular scans on a calibrated sphere. As this sphere is of good quality, we feel that this certification test is more an exercise of the CMM motion controller than a test of the behavior of the measuring system under the excitation of measuring a real part surface. Other tests [5] have been proposed, including one that involves scanning over a gage pin with the same diameter as the probe stylus. This test produces double contacts between the stylus and the artifact where the pin is first contacted, and resulted in large errors at higher scanning speeds. Our current work examines the roles of a linear and a circular artifact, both with a sinusoidal waveform superimposed on a flat surface. By supplementing the ISO scanning tests with the measurement of these artifacts along different machine axes, and at different speeds, we can excite different frequencies in the probing system and in the machine structure. Our goal is to develop a means of distinguishing between scanning CMMs based on their accuracy at different speeds, direction of scanning. This paper describes our work in developing and measuring artifacts that will better capture how a scanning CMM will perform when measuring actual parts.

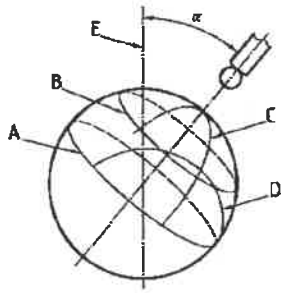

Figure 1: Target Scan Planes on the Test Sphere per ISO 10360-4

2. Current Work

To date, following three sinusoidal artifacts (See Figure 2) have been measured to compare the performance of different CMMs by varying scanning speed and direction of scan. The linear artifact was cut with a wire EDM, while the disc artifacts were turned on a diamond turning machine – the high amplitude disc using a diamond tool, and the low amplitude disc using a conventional tool.

- Linear Sinusoidal Artifact with amplitude ±2mm and wavelength 20mm.
- High Amplitude Sinusoidal Disc with amplitude ±2mm and wavelength 10mm.
- Low Amplitude Sinusoidal Disc with amplitude ±10μm and wavelength 5mm.

These artifacts have been measured on following CMMs:

- Brown & Sharpe Gage 2000 DCC using PH10T (TP20) for single point probing.
- Brown & Sharpe Global Image A using PH10M (SP600M) probe head for scanning.
- Zeiss Contura and Contour Select CMMs using VAST XT probe head for scanning.
- Leitz PMM 654 for scanning.

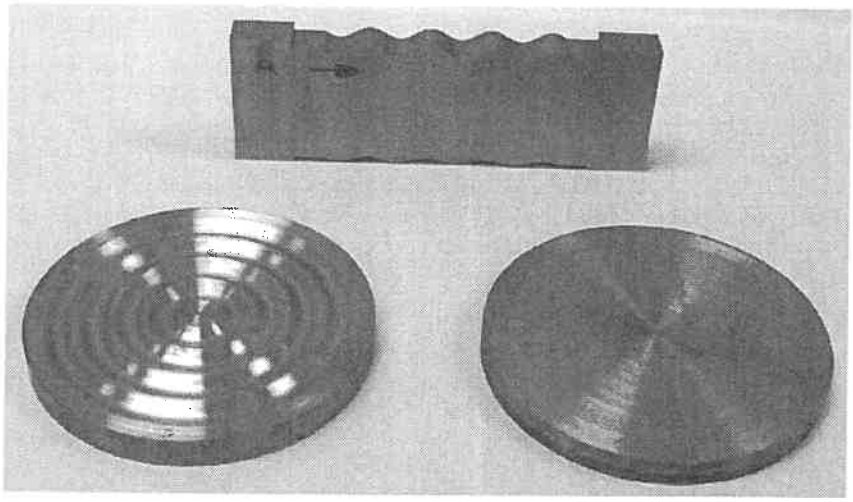

Figure 2: Sinusoidal Artifacts: Linear (Top), High Amplitude (Left), and Low Amplitude (Right) Artifacts

3. Scanning the Artifacts and Data Analysis

By scanning the artifact along a single axis, errors related to that axis could be isolated. The main advantage of using a disc artifact is that it could be scanned along Machine X and Y axes without moving the artifact. The scans obtained on different CMMs can be compared using two methods. One method is to fit a least square sine wave to the scanned data using MATLAB's optimization toolbox. This method gives the form error of the artifact with respect to a perfect sine wave. The deviation value, which contains both artifact and CMM errors, can be compared with data obtained from other CMMs. Other comparison method, more directly related to CMM performance, involves starting with a reference shape for the wavy surface (See Figure 3), and then comparing different scans to this reference scan. This allows us to compare different scans without fitting a least squares sine wave each time. The reference shape for the low amplitude sinusoidal disc was obtained by single point probing using Brown & Sharpe Gage 2000 DCC with a PH10T probe head and a 3×10 mm stylus. The disc was measured two times along the radius; once in forward direction and then in reverse direction. The average of the two measurements was considered as the reference. This averaging was done to reduce any noise in the data. For a more accurate reference curve, we will perform a reversal on measurements taken from a highly repeatable single point CMM, but the current reference scan is suitable for identifying differences between CMMs.

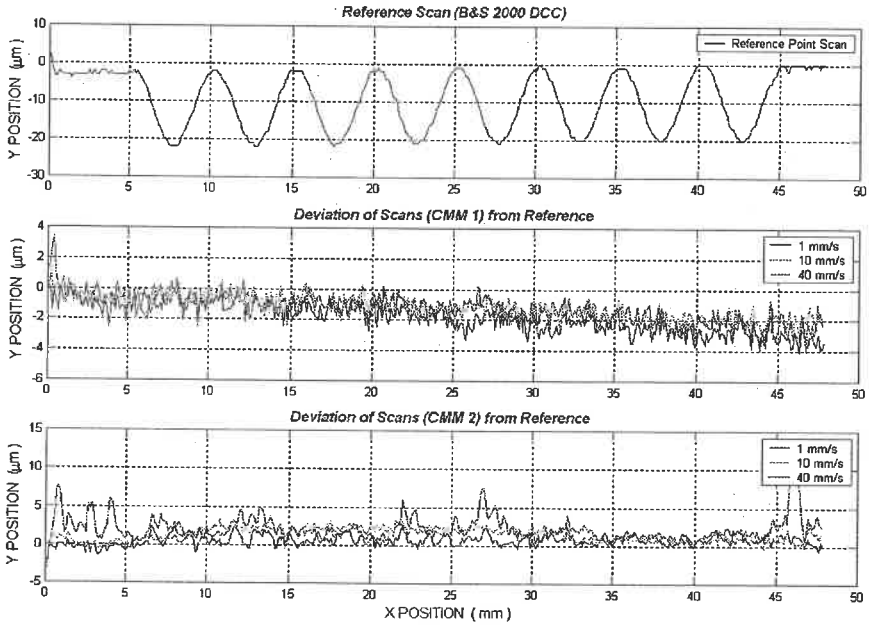
Reference Scan (B&S 2000 DCC)
Reference Point Scan
Y POSITION (µm)
Deviation of Scans (CMM 1) from Reference
1 mm/s
10 mm/s
40 mm/s
Deviation of Scans (CMM 2) from Reference
X POSITION (mm)

Figure 3: Comparison of scans on low amplitude sine disc scanned on two different CMMs

4. Results

While scanning the low amplitude sine disc in the xy-plane of the CMM the probe head itself does not move in Z direction. Instead, the Z coordinates are recorded by the vertical deflection of the stylus. This enables the CMM to scan at higher speeds (up to 40 mm/s) without observing much increase in the scanning error (See Figure 5 and Table 1). As the CMM is moving in a straight line for these scans, the errors observed as a result of increased speed may be associated with the probe rather than the CMM. Similar measurements on the high amplitude sine disc showed that much larger errors are observed at higher scanning speeds (See Figure 4). The reason for this increase in errors is that the CMM is no longer moving in a straight line and it has to struggle to maintain contact with the surface as it scans the artifact. Analysis of the scans on low amplitude sinusoidal disc showed that one of the CMM performed better than the other at higher scanning speeds (See Figure 5).

Table 1: Range of Deviations (μm) from Reference while scanning low amp sine disc

CMM	Scanning Speed (mm/s)					
	1	2	5	10	20	40
CMM 1	4.30	5.12	3.96	4.55	4.79	7.38
CMM 2	5.10	5.69	5.61	6.30	20.25	16.30

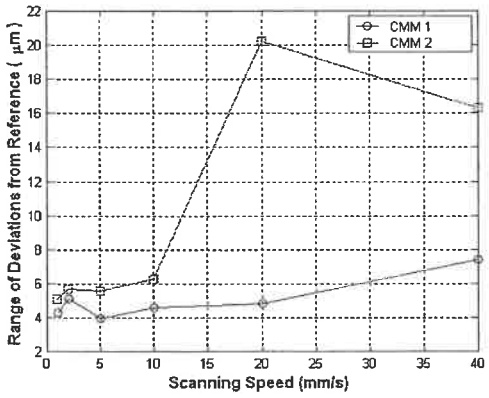

Figure 5: Performance of two CMMs while measuring low amp sine disc

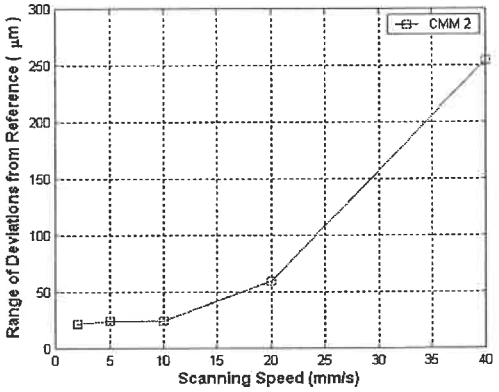

Figure 4: Effect of speed while scanning high amp sine disc

The linear artifacts have been measured in two different positions: along machine x-axis and 45° from machine x-axis. Larger errors are observed when the CMM is traveling along both the axes (See Table 2). In these scans the 1 mm/s scan was considered as a reference. All other scans were compared to the reference (See Figure 6). Other measurements have revealed that the scanning performance gets worse when the CMM is moving in all three axes.

Table 2: Range of Deviations (μm) from Reference while scanning linear artifact

Direction of scan	Scanning Speed (mm/s)			
	2	5	10	20
X-axis	2.96	4.78	36.93	150.63
45° from X-axis	3.02	5.03	40.65	165.40

All of the measurements reported here were taken using **closed-loop** (the path is not known *a priori*, only the starting and ending points) scanning mode. Scanning performance improves when the scanning is done in **open-loop** mode – i.e., the scan path is pre-defined.

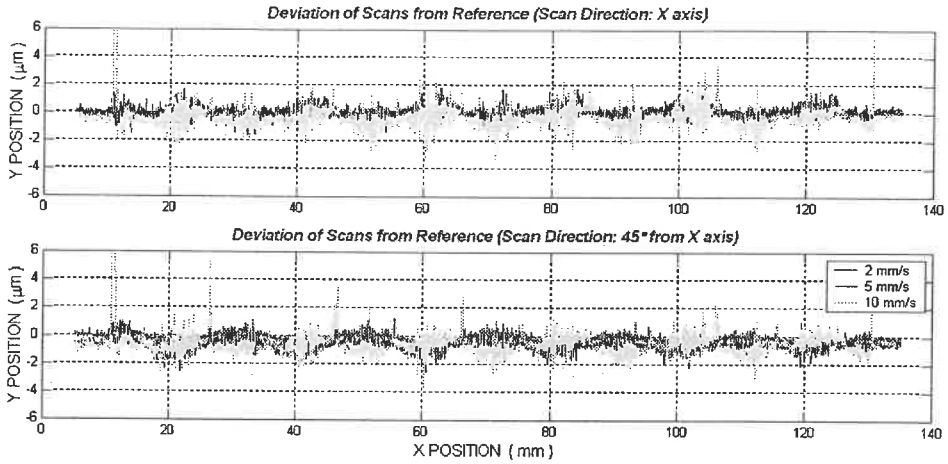
Deviation of Scans from Reference (Scan Direction: X axis)
Y POSITION (µm)
Deviation of Scans from Reference (Scan Direction: 45° from X axis)
2 mm/s
5 mm/s
10 mm/s
X POSITION (mm)

Figure 6: Comparison of scans on linear artifact scanned on CMM 3

5. Future Work

Analysis of the low amplitude sinusoidal disc reveals that there is a slope present along the wavy surface, due to out-of-squareness of our Diamond Turning Machine cross-slide. This will be corrected before the final artifact is cut. The artifacts will continue to be scanned on more CMMs to observe the performance at different speeds and in different orientations. Scanning Tests as per ISO 10360-4 will also be performed on different CMMs – varying scanning speeds will be used to study the relationship between the "official values" obtained from ISO tests and those from scanning the sinusoidal artifacts. The ultimate goal is to produce graphs similar to Figure 7, in which the difference between scanning CMMs based on their accuracy at different scanning speeds would be characterized.

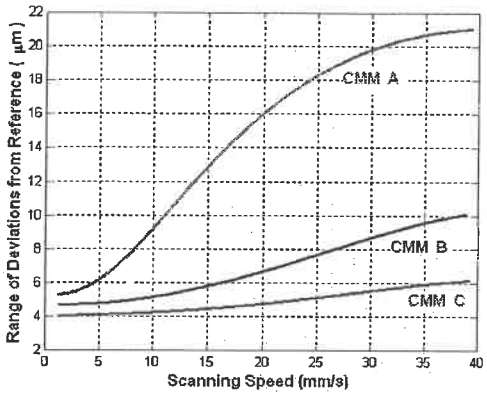

Figure 7: Desired plot comparing different CMMs

Acknowledgements

This work was supported by the industrial affiliates of the Center for Precision Metrology, a National Science Foundation Industry / University Cooperative Research Center supported under grants #EEC9811556 and #EEC0331950. Any opinions, findings, and conclusions or recommendations expressed in this material are those of the author(s) and do not necessarily reflect the views of the National Science Foundation. We also thank the Brown & Sharpe Manufacturing Company and J&H Machine Tools for the use of their machines and personnel for comparison testing of our artifacts.

References

[1] Muralidhar, A., Characterization of scanning probe CMMs. Thesis, UNC Charlotte; 1998.

[2] Pereira, P. H., Characterization and compensation of dynamic errors of a scanning coordinate measuring machine. Dissertation, UNC Charlotte; 2001.

[3] Morse, E. P., Testing scanning CMMs – How much do the standard tests tell us? International Dimensional Workshop, Nashville, TN, May 2004.

[4] ISO 10360-4: Geometrical Product Specifications (GPS) – Acceptance and reverification tests for coordinate measuring machines (CMM) – Part 4: CMMs used in scanning measuring mode; 2000.

[5] Freire, A. S., Dynamic performance of a coordinate measuring machine measuring small radii, corners and edges. Thesis, UNC Charlotte; 2000.

Three-dimensional Measurement of the Surface Geometries of Grinding Wheel by Using a Laser Displacement Sensor

Hwa-Soo LEE, Kazuki KAWAGUCHI and Takazo YAMADA
Department of Mechanical Engineering, College of Science and Technology, Nihon University, Tokyo

Abstract: In order to improve the surface accuracies in grinding process, it is important to evaluate the geometrical shapes of grinding wheel surfaces as a tool used grinding process. In this study, a new three- dimensional measuring method for the surface geometries of grinding wheels by using a laser displacement sensor is proposed. As experimental considerations, it is confirmed that three-dimensional shapes of grinding wheel surfaces can be evaluated quantitatively in the proposed method.

1. Introduction

In grinding operations, workpiece surfaces are generated depending on the copy principle. And then, in order to improve the accuracies of ground surfaces, three-dimensional geometrical shapes of grinding wheels have to be measured and evaluated quantitatively. In this study, a new measuring method of whole external surfaces of grinding wheels by using a laser displacement sensor is proposed. As the experimental evaluation of the proposed measuring method, it is clarified that the surface geometries of grinding wheels can be measured in three-dimension and the distributions of cutting edges can be evaluated precisely.

2. Three-dimensional measuring principle of grinding wheel surfaces

Rotating measured grinding wheels in wheel spindle axis Z, distances Δx in X axis are measured by a laser displacement sensor. Figure 1 shows a three-dimensional displaying method for measured data. That is, displacement data showing geometrical shape in a certain periphery Δx is measured and this data is named as data 1. Feeding the monitoring position in Δz in Z axis, data 2 is monitored as same as data 1. Repeating such manner in n times, geometrical shapes surrounding grinding wheel periphery, (Ym, Xn), are monitored.

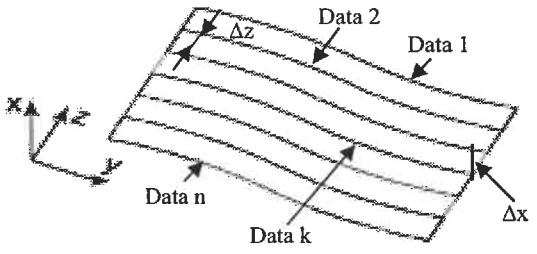

Fig.1 Principal of surface measurement for grinding wheels

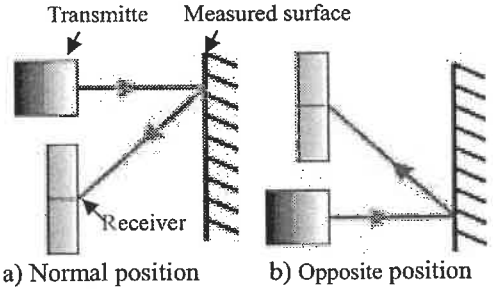

Fig.2 Direction of laser displacement sensor

The laser sensor applied in this measurement uses diffused reflections for measuring displacements. And then, in case of that measured objects have some large steps in its surfaces, accurate measurement cannot be preformed and measuring errors take place. In order to avoid such errors, a new measuring method is proposed. Namely, wheel surfaces are measured in two opposite directions as shown in figure 2 and these two data Δx are compared. In case of that these two data are not same, larger data is treated as a data at this point. In such a treatment, measuring errors due to large steps in measured surfaces can be avoided.

3. Measuring equipment

A laser displacement sensor is located on a table of NC milling machine and measured grinding wheels are fixed to the spindle of this machine as shown in figure 3. Specification of the used laser displacement sensor is shown in table 1.

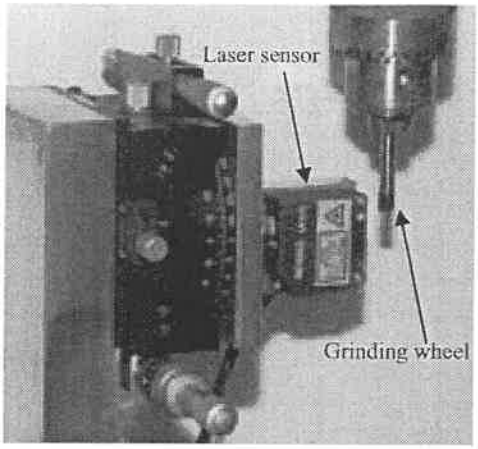

Fig.3 Arrangement of the Laser sensor

Table1 Specification of the Laser Displacement Sensor

Reference length	10mm
Span of measurement	±1mm
Kind of Laser	Red laser diode
Spot diameter	20μm~100μm
Resolution	0.1μm
Sampling interval	2048μs

4. Measuring of single abrasive grain

In order to evaluate the effect of the characteristics of measured abrasive grains on measuring performances, geometrical shapes of single abrasive grains, that is C, GC, A, WA, PW, SD, SDC, CBN and CBNC, are measured. Figure 4 shows an example of measured. In this evaluation, it is clarified that some of these grains can be measured as it is and others cannot be. Table 2 shows the evaluated results, in which signal OK shows the grains can be measured and signal NG shows grains cannot be measured as it is.

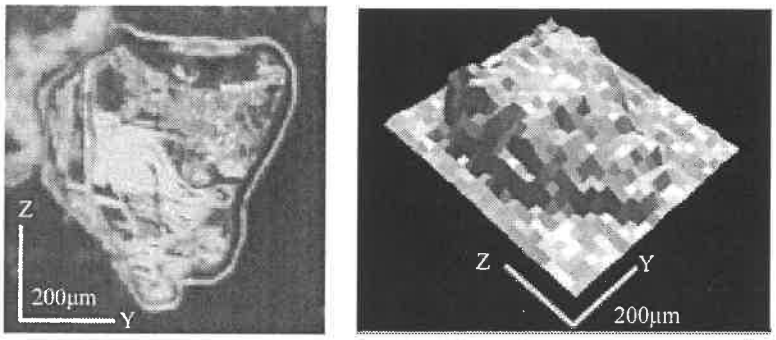

Fig.4 A measured example of single GC abrasive grain

Table2 Evaluated result of single grain measurement

Kind of grain	WA	A	PW	C	GC	CBN	CBNC	SD	SDC
Grain size	#60	#60	#60	#60	#60	#80	#80	#80	#80
Result	NG	NG	NG	OK	OK	NG	OK	NG	OK

As the monitoring with an optical microscope, it is known that the grains which cannot be measured as it is have transparent characteristics itself and they are difficult to be measured by laser beam. In order to confirm the laser measuring characteristics in transparent part, experimental evaluation has been carried out.

5. Measurement of transparent part

In order to evaluate the measuring characteristics of laser displacement sensor, a plastic specimen shown in figure 5 is measured. In this specimen, some parts are transmitted and other parts are avoided laser transmission by coating color spray. The height of a reference is 3 mm. A measured result is shown in figure 6.

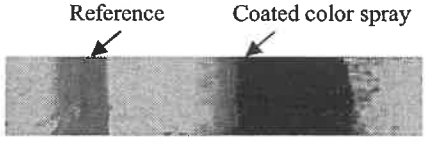

Fig.5 A measured plastic specimen

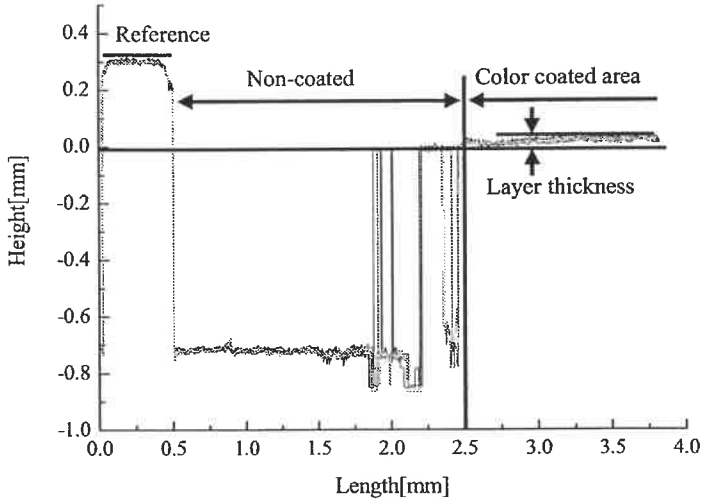

Fig.6 Measured result of specimen

From the measured result, it is known that the output in the reflected area is 0.03 mm and that in transparent area is -0.7 mm. In these results, it is known that the depth of coated layer 0.03 mm can be measured well. On the other hand, in the area laser beams trampers this specimen, measuring error -0.7 mm due to the transparence of laser beams takes place. From these experimental results, it may be known that the geometrical shapes of abrasive grains can be measured by covering the surfaces with reflecting layers.

6. Measurement of the surface of grinding wheels

A three-dimensional surface geometric shape of an electro deposit grinding wheel is measured, in which abrasive grain is CBN and grain size is #60. Before carrying out this measurement, wheel surface is covered by a black spray. In this experiment, measured area is 2 mm square. Microscopic photograph of measured area is shown in figure 7 and three-dimensional display of measured result is shown in figure 8.

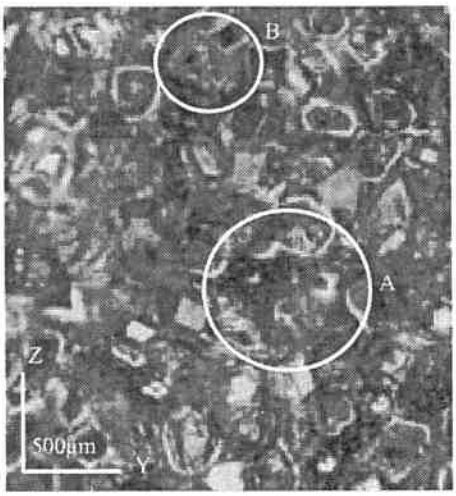

Fig.7 Microscopic photo

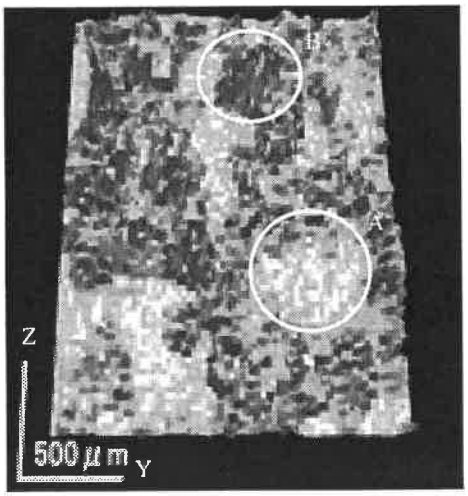

Fig.8 Measured result

Comparing figure 7 and 8, it is known that the area A, an electric deposit base, and area B, grain geometry, can be measured. From such an example, by using this proposed method it may be possible to measure the complicated surface geometry of grinding wheel.

7. Measurement of surface geometry of grinding wheel periphery

Based on the measuring performance shown above, three-dimensional geometric shape of grinding wheel periphery is measured, in which abrasive grain is CBN and grain size is #120. This measurement is carried out in 3 mm width in spindle direction. Figure 9 shows one quarter part, 90 degree, of measured geometric surface of the grinding wheel. And interfering part of this grinding wheel to workpiece under the condition that depth of cut is 50 μm is shown in figure 10. Figure 11 shows in case of that depth cut is 100 μm.

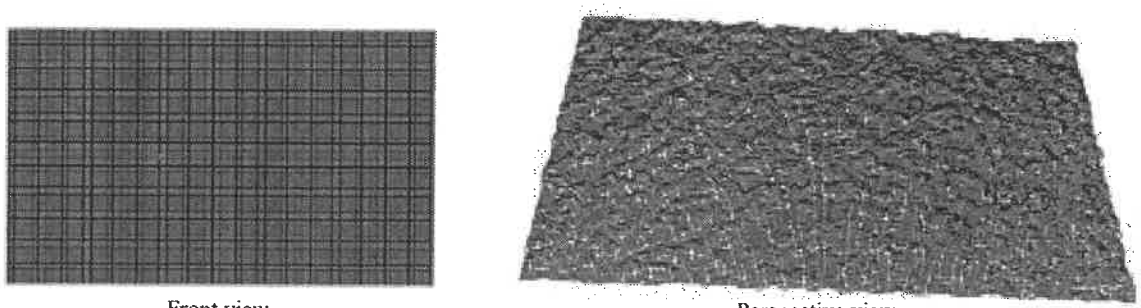

Front view Perspective view

Fig.9 Quarter part of measured geometrical shape of grinding wheel

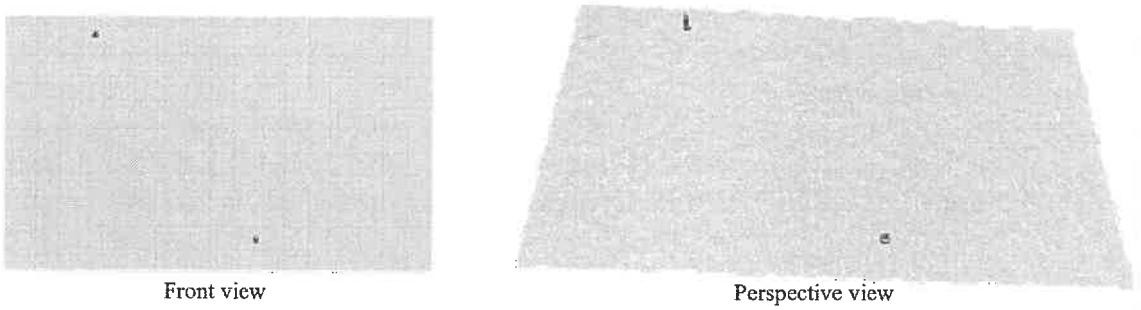

Front view Perspective view

Fig.10 Interfering part of grinding wheel (depth of cut is 50μm)

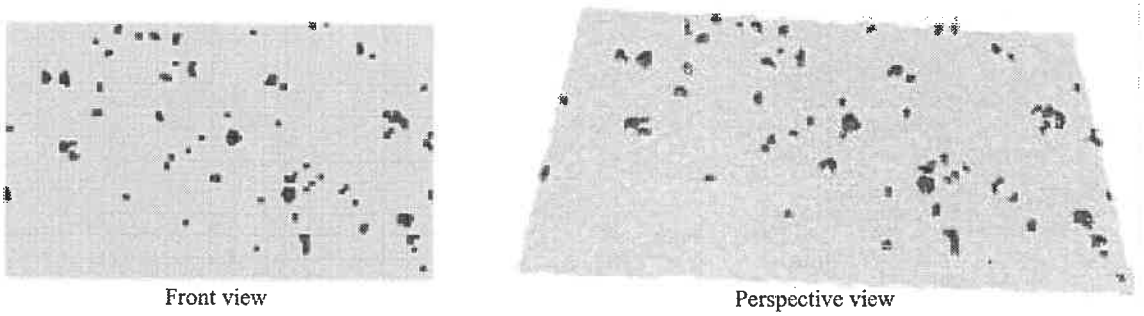

Front view Perspective view

Fig.11 Interfering part of grinding wheel (depth of cut is100μm)

From figure 9, it is known that whole surface geometrical shapes of grinding wheel can be monitored, and the interfering part of grinding wheel surfaces can be also evaluated quantitatively by the proposed measuring method in this study.

8. Conclusions

A measuring method of three-dimensional surface geometrical shapes of grinding wheels is proposed. By using this measuring method, the distribution of cutting edges and the height of them can be evaluated quantitatively and then the effect of these cutting edges in the grinding process may be evaluated accurately.

Six Sigma Comparison of Precision Typological Equipment for the Production of Gas Bearings
Extended Abstract

Rochelle Moore
Draper Laboratory
555 Technology Square
Cambridge, Ma 02139
617-258-4852 Phone
rmoore@draper.com

Overview

Gas bearings wheels, which are used in high performance inertial instruments, have precision surfaces which run long hours with minimal degradation in performance. This requires measurement of the surface shape, form and finish to be well understood in order that the parts can perform consistently over long periods of time. The present spool and hemispherical wheels have been traditionally measured by the Taylor Hobson (Form Talysurf Series 2 PGI Plus) and more recently by the Zygo (NewView 5000 and Metro Cell). A Six Sigma approach is used to evaluate actual gas bearing component data, compare these two types of measuring systems and assess cost savings involved when choosing a measuring system to be used in the production of the Gas Bearing. This paper outlines the steps being taken by Draper Laboratory to define the need for a uniform measuring system to be used for production, to set up the measurement systems so that the appropriate data needed is collected, to analyze this data, to improve the current system, and to control to ensure training; auditing practices and knowledge transfer are complete. This will include evaluating the differences between contact and non-contact precision typological equipment to see how shape, form and finish are obtained for the coated surfaces obtained from a critical semi-automated finishing operation.

Introduction

Draper Laboratory currently has the Taylor Hobson (PGI Plus) and access to a Zygo system to evaluate precision gas bearing components. The surface finish and radius of curvature of parts are critical to the bearing components yet difficult to measure.

Six Sigma Approach

The roadmap to six sigma follows **DMAIC-D**efining the project, evaluating the **m**easuring system, collecting data and **a**nalyzing, **i**mproving by evaluating tradeoffs and **c**ontrolling by validating performance improvements and impact.

Definition: The objective of this project is to look at two different of measuring systems (contact and non-contract) and evaluate their suitability for measuring gas-bearing components. There are several pieces of measuring equipment used to measure form, and surface finish on the factory floor. The set-up time and operator sensitivity makes it difficult to duplicate and the exact measurement for radius of curvature is not obtainable.

Measuring System Evaluation: The Taylor Hobson Form Talysurf Series 2 PGI Plus is a measurement system using a stylus to contact the work surface. The motion of the in-house device is in the X and Z directions (in-out, up-down). A manual Y stage is mounted on the base to position part being measured under the sensing head. The output from the system is collected

by an attached computer system that stores and processes the data. Figure 1 shows typical output from this system. The form, waviness and roughness from an ideal shape are recorded as the output results. A 3-D profile may be obtained with this system by multiple data logging at a number of parallel profiles at predetermined spacing using a Y-axis computer controlled and monitored translation stage.

The Zygo NewView 5000 and Zygo Metro Cell are non-contract measuring systems. The NewView is used for performing 3-D surface profiling. Figure 2 shows the data output. This piece of equipment was designed to measure surface roughness, part shape, and step heights in a non-contact manner. It utilizes a three-dimensional scanning white light and optical phase shifting interferometry. Its field of view and resolution is dependent on the objective used in the measurement. The 1X has a field of view of 7.00 by 5.30 mm, while the 100X is .070 by .053 mm. The Zygo MetroCell utilize the Zygo GPI measurement system on the production floor. The GPI is a laser based, three-dimensional system using optical phase-shifting interferometry as the measurements technique. It measures the overall form of a reflective surface and optics, transmitted wave fronts of optics and radius of curvature of surfaces. The MetroCell output is shown in Figure 3. The data is stored on the mating computer and can be retrieved at a later date for additional analysis.

Analysis: Table 1 presents a comparison of the two types of measuring systems. When making similar measurements the two systems provide comparable results.

System	Contact	Non-Contract
	2-D	3-D-more info available
	Operator intensive	Less operator intervention
	Opportunity for damage to part-stylus travels over part for measurement	No contact to critical surfaces by measuring equipment
	Only form can be obtained	Actual radius of curvature can be measured
	Data can be retrieved yet additional measurements cannot be made without the part.	Part data can be stored and retrieved at a later date to perform additional measurements without actual part present

Table 1-Comparing Contact and Non-contact Measuring Equipment

The specific Taylor-Hobson and Zygo systems are compared in Table 2.

Improvement: The current method for measuring can be improved by changing to a non-contact system. This will reduce operator induced error and provide accurate measurements. The surface finish measurement has good correlation (1.96 on Taylor-Hobson vs. 1.41 on the Zygo NewView 5000). The Taylor Hobson does not provide a radius of curvature measurement on a single line and the MetroCell provides measurement of .18711. The contact system has difficulty in providing absolute measurements. Further investigation on these systems in planned for evaluation of other parts.

Control: The performance improvement of a 3-D non-contact system is needed for these parts. Although the Taylor Hobson is less expensive to purchase (Table 2), the cost to operate is higher due to the need for experienced operators and the absence of the absolute radius of

curvature. The impact, of not being able to measure the radius of curvature, compounds the error in the upward assembly which can escalates the unit cost.

Conclusion: The differences between contact and non-contact precision typological equipment were evaluated when measuring the coated surfaces obtained from a semi-automated finishing operation. The non-contract system should be considered when the measurement of absolute radius of curvature is critical.

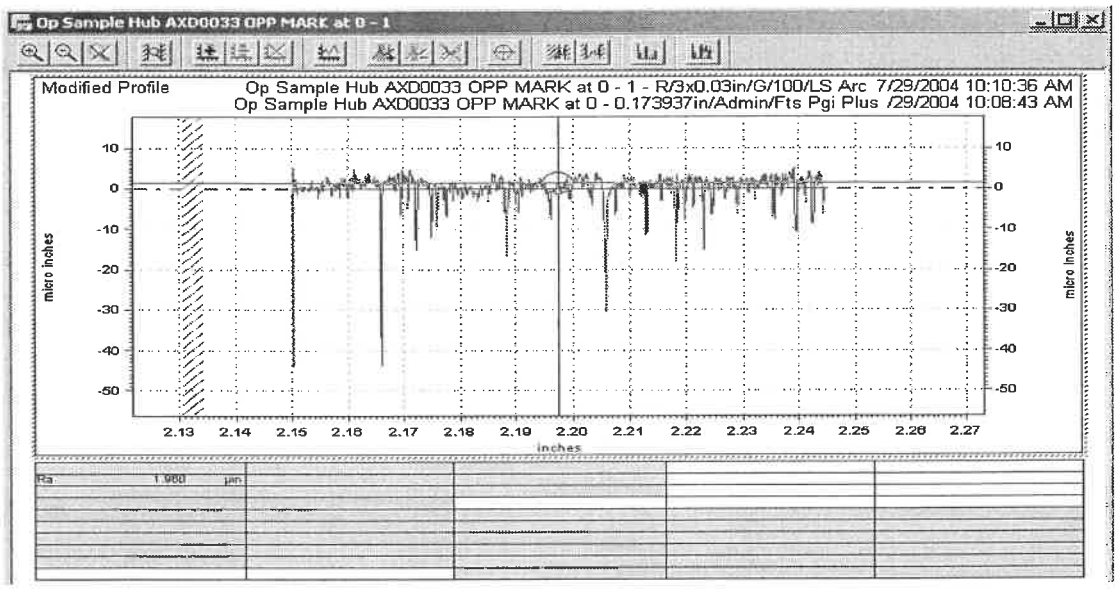
Op Sample Hub AXD0033 OPP MARK at 0 - 1
Modified Profile
Op Sample Hub AXD0033 OPP MARK at 0 - 1 - R/3x0.03in/G/100/LS Arc 7/29/2004 10:10:36 AM
Op Sample Hub AXD0033 OPP MARK at 0 - 0.173937in/Admin/Fts Pgi Plus /29/2004 10:08:43 AM
micro inches
inches
Ra 1.980 µin

Figure 1 Talysurf Chart Output

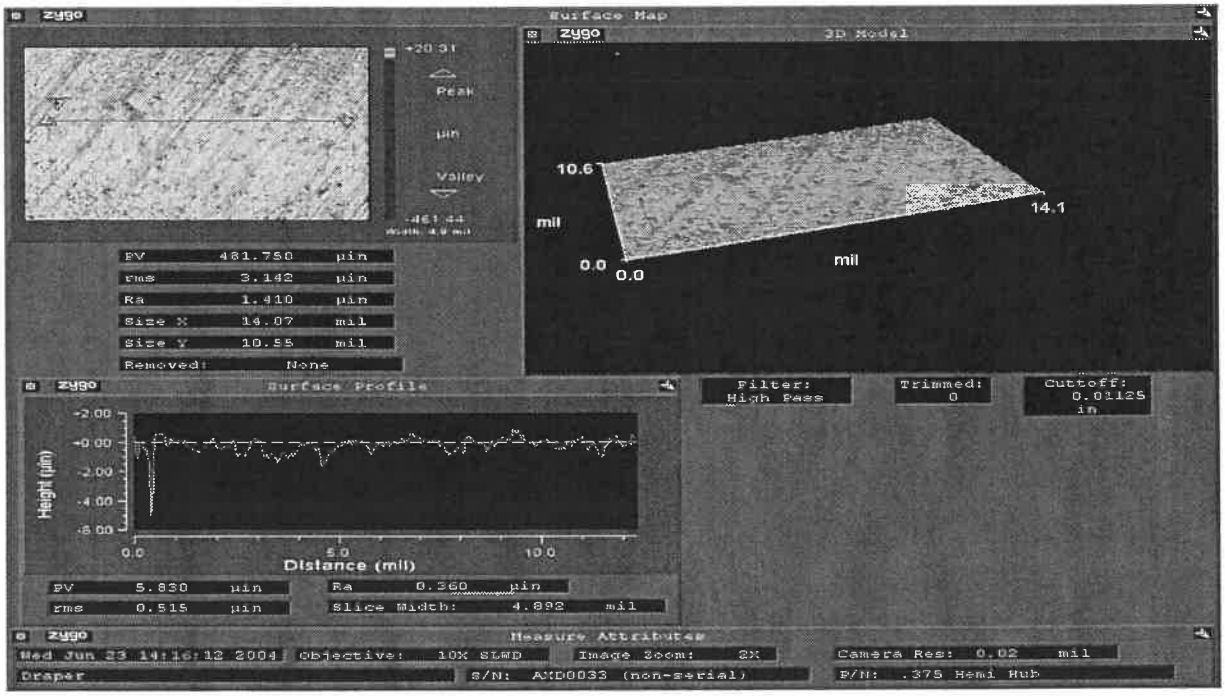

Figure 2 Outputs from NewView 5000

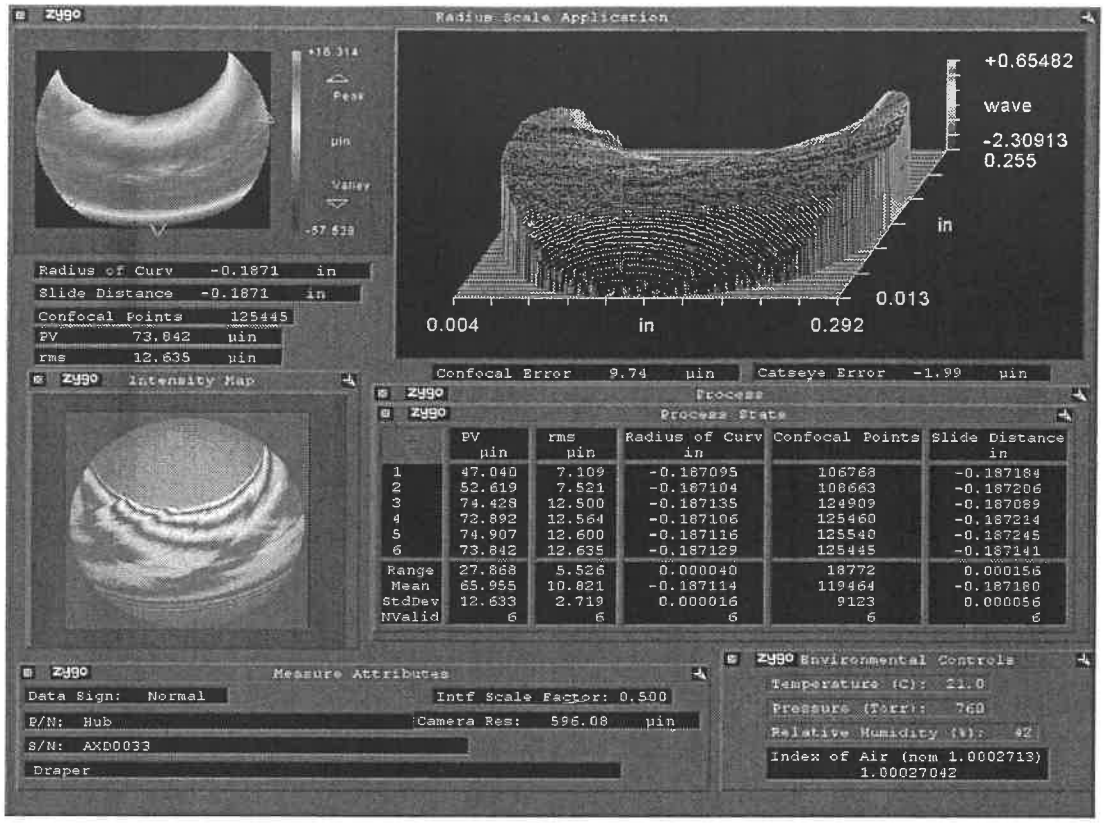

Figure 3 Metro Cell Output

Device	Taylor Hobson (Series 2 PGI Plus)	Zygo
Range	10mm(.4in)	.06-13mm-nuView
Resolution	1nm (.04µin)	.01µm-Simetra Vertical-.1nm Laterial-.64 to 4.72µm: objective dependent. NewView
Accuracy	Calibrated over a sphere accuracy of ¼ wavelength of light	.1 µm –flatness, .15 µm –parallelism .30 µm -thickness
Time to measure Surface finish	1 min	≤10 sec
Time to measure radius of Curvature	unable	(≤ 1 min),100 parts/hour
Positive features	Programmable for automatic inspection and analysis routines	Non-contact system. One button operation. Data storage capability for future retrieval.
Negative features	-Contact system, potential for damage to components during set-up and tests -Not accurate for radius measurements. Single line used to determine a 3D feature.	Two pieces of equipment needed for measurements
Price	~130K	~275Metro Cell ~200K-NuView 5032

Table 2-Comparison of Contact (Taylor Hobson) and Non-contact (Zygo)

A Practical Method of Determining Orthogonal Sampling Distances for Flatness Deviation Measurement Using an Electric Capacitance Displacement Sensor

Teruaki Saito* and Kazuhisa Yanagi*

** Nagaoka University of Technology, School of Mechanical Engineering, Kamitomioka 1603-1, Nagaoka, Niigata 940-2188, Japan*

e-mail:xitou@stn.nagaokaut.ac.jp http://orion.nagaokaut.ac.jp/

Specification

1. Introduction

In order to assess the surface form deviation or surface texture of industrial products, surface topography data is usually obtained as orthogonal discrete data using a displacement sensor and its scanning instruments. It is desirable that the measurement model conditions are regulated to some extent. ISO/TC213 related to dimensional and geometrical product specifications and verification has discussed about rules and procedures for the assessment of deviations from straightness, flatness and so on. However, complete ISO standards have not been established due to various technical problems. Especially, in the case of areal measurement , there are many factors to be considered such as filters selection ,cutoff wavelength, evaluation area and sampling distance. This paper deals with the appropriate measurement conditions for non-contact displacement sensor which is alternative to contact stylus which in the ISO/TC213 for assessing surface form deviation. We try to derive the sampling distance from characteristics both of displacement sensor and surface topography of object surface.

2. Areal surface form measurement

2.1 Conventional measuring conditions and alternative displacement sensor

As to the ISO standards about surface form deviation or surface texture, except some special cases such as surface plate and optical parts, so-called profile instrument with a contacting displacement sensor is recommended as a measuring device. However there exist some problems in the contact method. The measurement time for areal measurement is extraordinarily large due to its low traversing speed. And it is inevitably sensitive to acute projections of micro irregularity. Its influence on the final assessment can not be removed even by Gaussian lowpass filter(LPF)[1] recommended in the Technical under consideration in ISO/TC213. The measuring conditions for flatness assessment by a contacting probe are given in ISO/TS12781-2[2]. By knowing the size of object surface, stylus tip radius and cutoff wavelength of LPF are determined and the sampling distance for discrete measurement is derived. In consideration of above problems, we apply an electric capacitance displacement sensor to areal profiling instrument. Electric capacitance displacement sensor has, in general, a circular electrified plate. It principally measures the arithmetic mean gap between the sensor area and spot on the object surface (effective sensor diameter). This means that the influence of short wavelength component of the object surface can be attenuated.

2.2 Sampling distance for surface form measurement

In order to assess a wide range of surface wavelength in the areal discrete surface measurement, a large number of sampling points are required. However, in the case of relatively large sampling interval, additional problem of aliasing would arise. Once an electric capacitance displacement sensor with larger electrified plate, the sampling distance can be increased according to its sensor area.

First of all we propose a method of determining lower limit of data sampling distance from amplitude transmission characteristic against surface wavelength. On the other hand we derive upper limit of data sampling distance from autocorrelation curve of measured surface profile so that adjacent sampled points could be well correlated.

3. Determination of sampling distance from sensor characteristic

3.1 Effective sensor diameter

In order to evaluate effective sensor diameter of the displacement sensor, its output signal was recorded

when traversing over a step height gage. Two kinds of gages with 30um and 50um height differences were prepared for the experiment. And two displacement sensors of 4mm and 6mm diameters (AX30-100 of Photonics Co.) were examined. The specifications of the sensors under test are tabulated in Table 1. Recorded output signals of the sensors against their lateral distance are shown in Fig.1 from which the effective sensor diameter of each sensor can be drawn. Experimentally obtained diameters are 3.2mm for the ϕ4mm sensor and 2.2mm for the ϕ6mm sensor, respectively.

Table 1 Specifications of electric capacitance sensor

Probe diameter	4.0mm	6.0mm
Core diameter	2.5mm	3.5mm
Resolving power	»30nm	»45nm
Measuring range	100μm	150μm
Frequency response	1kHz(-3DB,4th Butterworth)	
Linearity	¶0.1%/FS	

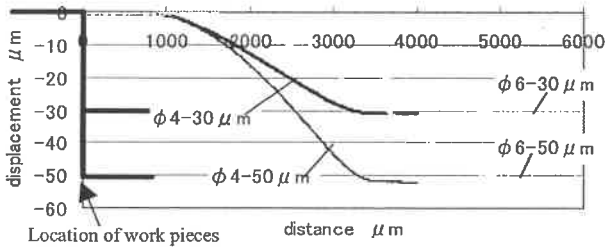

Fig.1 Estimation of effective sensor diameter

3.2 Amplitude transmission characteristic against surface wavelength

The amplitude transmission characteristic of the displacement sensor was experimentally obtained using test surface specimens with sinusoidal undulation. The transmission curve seems to be unnaturally attenuated in the range of shorter surface wavelength.

In order to get certain theoretical evidence, numerical simulation was conducted in consideration of circular weighting function derived from circular electrode. It was assumed that electric field between electrode and object surface is perpendicular to the mean plane of the object surface and the electric capacitance is in inverse proportion to local gap between the two surfaces.

Fig.2 shows both experimental results and simulations ones. Its abscissa means surface wavelength divided by effective sensor diameter. Both of the results are fairly in good agreement to each other.

In the range of shorter wavelength than the effective sensor diameter, unnatural transmission curve may cause an unreasonable measurements. That unnatural part should be attenuated by a LPF. Although the Gaussian LPF is recommended in ISO/TS12781-2, the amplitude transmission characteristic of the spline LPF[4] is functionally better than that of Gaussian LPF and the end-effect is also smaller than that of Gaussian LPF. Thus, we apply the spline LPF instead of the Gaussian LPF.

Fig.3 shows the amplitude transmission characteristic of spline LPF with the cutoff wavelength identical to the effective sensor diameter and also shows the characteristic which is product of the simulation result and the spline LPF. From Fig.3, the amplitude transmission is at most 4% in the range of shorter wavelength than the effective sensor diameter. And the amplitude transmission becomes 50% when the wavelength is 1.7 times of effective sensor diameter. We determine the sampling distance from transmission characteristic of spline LPF.

The filtered result by the spline LPF suffers from aliasing in the case of lager sampling distance. The amplitude transmission characteristic obtained from discrete data agrees fairly well with theoretical characteristic of the spline LPF, when the sampling distance for the former case is smaller than 1/10 of the cutoff wavelength. Therefore, when the effective sensor diameter is chosen as the cutoff wavelength, the sampling distance becomes 1/10 of the effective sensor diameter.

Determined sampling distances were 220μm for the ϕ4mm probe and 320μm for the ϕ6mm probe. These

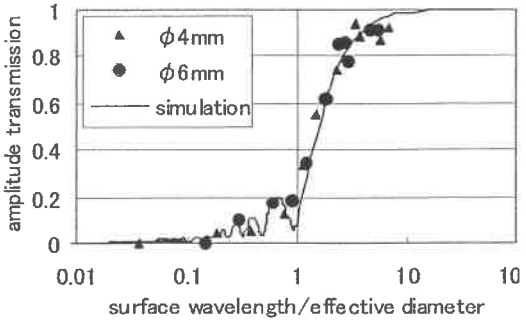

Fig.2 Amplitude transmission of the capacitance sensor against surface wavelength

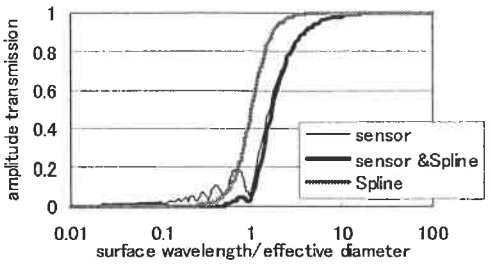

Fig.3 Amplitude transmission curve of the capacitance sensor and effect of spline LPF

sampling distances could be applied to measurement in any direction because the electric capacitance sensor is geometrically isotropic.

4. Determination of sampling distance based on autocorrelation of surface profile

4.1 Autocorrelation curve

In order to determine the sampling distance from surface wavelength distribution of test surface, profiles were measured in two orthogonal directions with very small sampling distance , along each evaluation length L by electric capacitance sensor. We introduce the sampling distance for surface form measurement on a basis of the autocorrelation value from measured profile. Measured profile data z(x) and z(y) are composed of finite discrete data points N=L/ , respectively.

Therefore, autocorrelation function R(τ) have to be calculated from limited length as shown in equation (1).

$$R(\tau) \approx \frac{1}{N-k\Delta}\sum_{i=1}^{N-k\Delta} z(x_i)z(x_i+k\Delta) \qquad (1)$$

Where τ is lag distance and its value is multiple of the sampling distance , and expressed by k . However, the calculation span decreases with the increase of τ. The autocorrelation curve was affected by the amplitude of long wavelength components. When the calculation span is smaller than the length of period of the long wavelength, reasonable correlation value would not obtained. Therefore, highpass filter(HPF) was applied to the measured profile to remove the long wavelength components before calculating the autocorrelation curve. We utilized spline HPF.

Pekleink[5] regarded the lag distance as averaged wavelength of surface topography which is called correlation length at which the correlation value of roughness profile attenuates down to 0.5. On the other hand, Whitehouse[6] defined the lag distance at which the correlation value decrease to 1/e as correlation length.

We adopt the value as the sampling distance which was proposed by Whitehouse and applied to areal measurement.

4.2 Experimental analysis

Following the above-mentioned procedure, we tried to obtain the sampling distance for a 80x60mm ground surface of S50C. Three profiles were measured in each direction. Due to the width of effective diameter, the evaluation length in the X-direction was 70mm and 50mm in the Y-direction with sampling distance was 5μm. The electric capacitance displacement sensor of ϕ6mm probe diameter was used for the measurement. Because the sensor has unnatural amplitude transmission characteristic, spline LPF is applied to the measurement result prior to the calculation. Since short wavelength components below effective diameter are attenuated, the correlation distance would be increased. After calculation of the correlation lengths from three autocorrelation curves, the shortest correlation length was adopted as the sampling distance in the related direction.

Three measured profiles in the X-direction are shown in Fig.4. LPF and HPF were applied to these profiles. Fig.5 shows calculated autocorrelation curves with different cutoff wavelengths in the range of small τ. Fig.6 shows the relation between the sampling distance and cutoff wavelengths of HPF. And the effect of LPF on that relation is also indicated. We can see the sampling distance was rapidly decreased with the cutoff wavelength down to L/3. Because the amplitude of long wavelength components of measured profile is larger than that of short wavelength component. The sampling distance decreases gradually when the cutoff wavelength is smaller than L/3. Since amplitude of wavelength component below the cutoff wavelength is attenuated by the amplitude transmission characteristic of the HPF. Experiments were carried out using some test surfaces which were ground under different machining conditions. As a result, almost constant sampling distance could be obtained after having applied HPF with the cutoff wavelength smaller than L/3. Thus we determine the cutoff wavelength of HPF

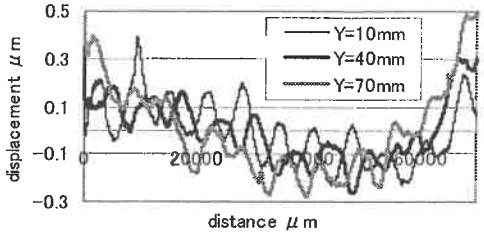

Fig.4 Variation of measured profile

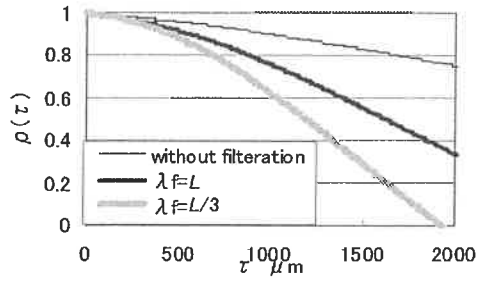

Fig. 5 Auto-correlation curves for the original and filtered profiles

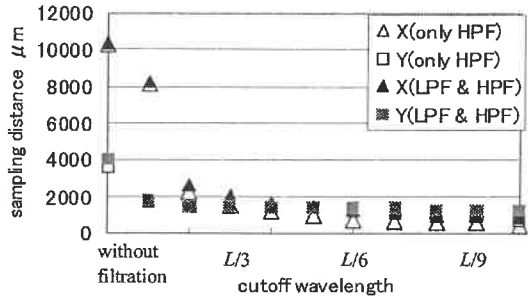

Fig. 6 Variation of sampling distance with cutoff wavelength

to be 1/3 of evaluation length.

It should be noted that, the sampling distance when the LPF was applied larger than that without LPF. Because the short wavelength components are attenuated and the correlation value increases.

As far as this test surface in concerned, sampling distances determined by the proposed procedure were 2020μm in the X-direction and 1415μm in the Y-direction.

5. Experimental result and discussion

The obtained total numbers of sampling points for the test surface of 80mm×60mm are tabulated in Table 2. Both of the numbers derived from sensor characteristic and autocorrelation curve are smaller than those given in the ISO/TS12781-2. In this case the sampling condition of 1260 data points is recommended for assessing the flatness deviation. This is because of amplitude transmission characteristic of the displacement sensor and the surface wavelength distribution of the test surface.

Table 2 Number of sampling points

Method	Number of points
Sampling theorem based on effective diameter	34383
1D Auto-correlation curve	1260
ISO/TS 12781-2 (2)	269985

6. Concluding remarks

Experimental analysis for reasonable measuring conditions were carried out on the areal surface form measurement using the electric capacitance displacement sensor, and following results ware obtained.

Since the amplitude transfer characteristic of electric capacitance displacement sensor against surface wavelength shorter than its effective sensor diameter is unnatural, the spline LPF is applicable in this case. A cutoff wavelength smaller than 1/10 of the effective sensor diameter is desirable to compensate it.

Measured autocorrelation curve is easily influenced by long wavelength component of object surface. Stable autocorrelation curve for the determination of sampling distance can be introduced by using the spline HPF with a cutoff wavelength smaller than 1/3 of autocorrelation evaluation length.

References

(1)ISO 11562, Geometrical Product Specifications (GPS) – Surface Texture : Profile method Metrological characteristics of phase correct filters (1996)

(2)ISO/TS 12781-2, Geometrical Product Specifications (GPS) Flatness Part 2: Specifications operators (2003)

(3)Saito, T; Yanagi, K; Togawa, K : A fast and accurate non-contact profiling instrument for assessing areal surface texture and flatness, Proceedings of ASPE the 17th Annual meeting, (2002)438-441

(4)M.Krystek : Form filtering by Splines, Measurement ,18,9(1996),9-15

(5)J.Peklenik : New Developments in Surface Characterization and Measurements by Means of Random Process Analysis, Proc. Instn. Mech. Engrs, 182 (1967-1968),108

(6)D.J.Whitehouse : Handbook of Surface Metrology, Institute of Physics Pub., (1994),53

Long Scan Stage for the Metrological Atomic Force Microscope

TaeBong Eom, JaeYun Lee and JongAhn Kim
Korea Research Institute of Standards and Science, Youseong , Daejeon 305-666, Korea

Abstract

This paper presents the design and fabrication of a long scan stage for metrological atomic force microscope. On designing the system, we mainly consider a simple structure with low vibration and high accuracy. In stead of the traditional two level stages, we used a surface plate as the reference of the main stage. Therefore, it has low profile and simple structure. Surface plate was made of the ceramic glass with very low thermal expansion. The stage is positioned on the surface plate of 800 mm x 800 mm. It is guided horizontally by a cross structure with two precision bars perpendicularly linked and vertically by the surface plate. The sliding pads of PTFE are used at X- and Y-axes, and also used for vertically supporting the stage. The X-axis guide bar with a moving plate is glued on the surface plate. The Y-axis guide bar is attached to the X-axis moving plate and moved to the Y-direction. Finally the Y-axis guide bar guides the XY-stage plate, so the XY-stage plate can be moved to two directions. This global stage also has the two-axis flexure structure machined by the precision wire-cutting machine. By combining global stage and micro-stage, the fast and long movement and the fine positioning can be provided. A two-axis tilt stage for adjusting the pitch motions of the stage and a L-shaped mirror for laser interferometer is positioned on the tilt stage.

Introduction

Atomic force microscopes (AFMs) have been used frequently to observe the surface texture. With the development of nanotechnology, there has been growing demand for measuring the dimension of the very small structure. For this purpose, several metrological AFMs have been developed. Most of them have the precision flexure stages and displacement measuring systems such as capacitance type sensor or laser interferometer [1, 2]. These metrological AFMs are used mainly for measuring the pitch and step-height. However, these measuring systems have the short measuring range of a few ten μm. For measuring the image placement of the photomask and wafer, a special metrological system having long measuring range is required. National Institute of Standards and Technology is developing a STM based Molecular Measuring Machine having an accuracy of 1 nm and a measuring range of 50 mm x 50 mm x 0.1 mm [3]. PTB also developed a SEM-based Electron-Optical Metrological System with a measuring range of 300 mm x 300 mm [4]. Recently PTB reported a large range scanning probe microscope (LR-SPM). It has a large measuring volume of 25 mm x 25 mm x 5 mm and is applicable to topography

measurements.[5] At present, we are also constructing a metrological AFM with a large scanning range. The aim of the project is to develop a nano-measuring system presenting a resolution of sub-nanometer with a measuring range of 250 mm x 250 mm x 20 μm.

Design and construction of the stages

Two years ago, we had designed and fabricated a long scanning stage for test purpose.[6] The main structure of the present system is similar to the old version. Fig.1 shows two-axis translation system. On designing the system, we mainly consider an Abbe's offset free arrangement and a simple structure with low vibration and deformation. In stead of the traditional two-level X and Y stages, we used one level X-Y stage. The surface plate is used as the reference of the stage. Therefore, it has low profile and simple structure. Surface plate was made of the ceramic glass with low thermal expansion coefficient and its flatness is below 1.3 micrometer over the size of 800 mm x 800 mm. The X-Y stage is positioned on the surface plate. It is guided horizontally by a cross structure with two precision parallel bars rectangularly linked and vertically by the surface plate. The X-axis guide bar, which is made of aluminum alloy and grinded precisely, is glued on the surface plate. It carries a X-axis moving plate. A Y-axis guide bar is fixed to the X-axis moving plate and moved to the X direction by motion of the X stage. Finally the Y-axis guide bar guides the Y-axis moving plate on which the X-Y moving plate with flexure hinge structure is mounted, so it can be moved to two directions. The sliding pads, which are made of PTFE, are used as bearings of X-Y translation system. X- and Y-axis moving plates are vertically guided by four sliding pads respectively. One sliding pad is rigidly fixed to the moving plate and three sliding pads are fixed to flexure mechanism for adjusting the contact force with guide bar and the

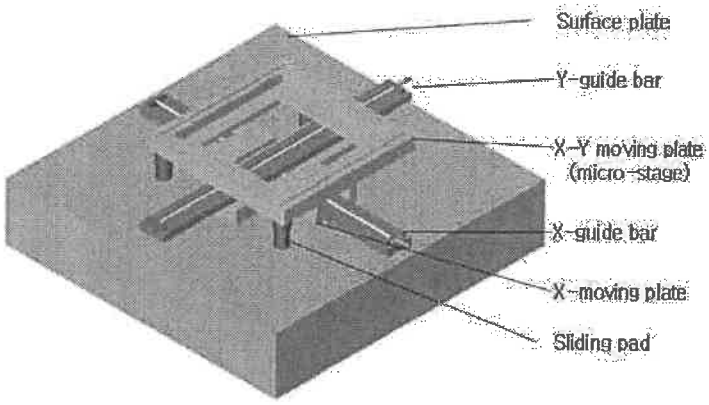

Fig. 1 Schematic diagram of two axis translator.

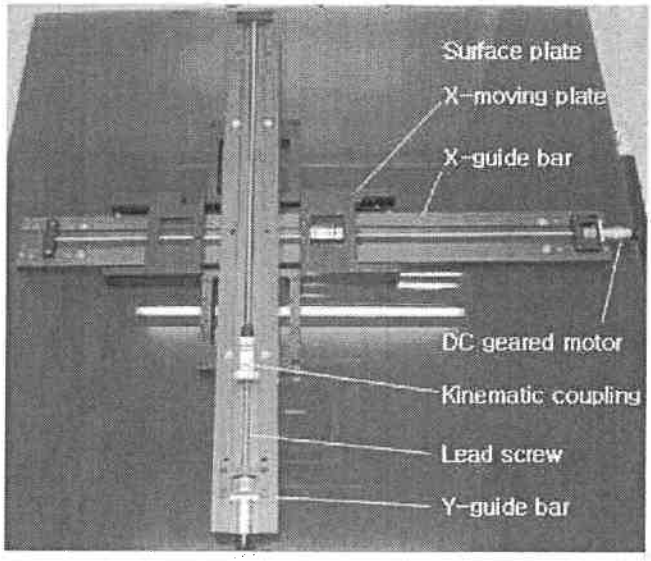

Fig. 2 Guiding system of two axis translator.

squareness between two guide bars. The X-axis moving plate and the X-Y moving plate are vertically guided with the surface plate by 3 sliding pads respectively. X- and Y-axis moving plates are driven by the lead screws with the geared DC servo motors and have the moving range of 250 mm and 250 mm. The X-Y moving plate, which is made of a single aluminum block, has the two-axis flexure hinge structure machined by the precision wire-cutting machine. This flexure stage (micro-stage) consists of two micro-stages which are decoupled avoiding the cross-talk effect. The X micro-stage and Y micro-stage are driven by two PZTs and one PZT respectively. The micro-stage provides a linear translation of 40 μm x 40 μm and angular motion of about 1 minute for adjusting yaw motion (see Fig. 3). By both global stage and micro-stage, the fast and long movement, and the fine positioning are provided. The tilt stage, on which L-shaped mirror and specimen to be measured are mounted, is kinematically coupled to the inner moving part (equivalent to Y micro-stage) of the micro-stage. Two pitch motions of the tilt stage are provided by two PZTs of the micro-stage. To measure the displacement of the X-Y stage, we use a heterodyne type laser interferometer. The Agilent 5517 He-Ne laser, of which beat frequency is about 1.8 MHz, is used as a light source. At X-axis, three plane-mirror type interferometers are used for 1 displacement and 2 angular measurements. At Y-axis, one plane-mirror interferometer is used for only displacement. In order to encode the phase difference between reference signal and measurement signal of the heterodyne interferometer, the phase-quadrature mixing technique is used. Two outputs of phase demodulating electronics become sinusoidal signals with phase quadrature.

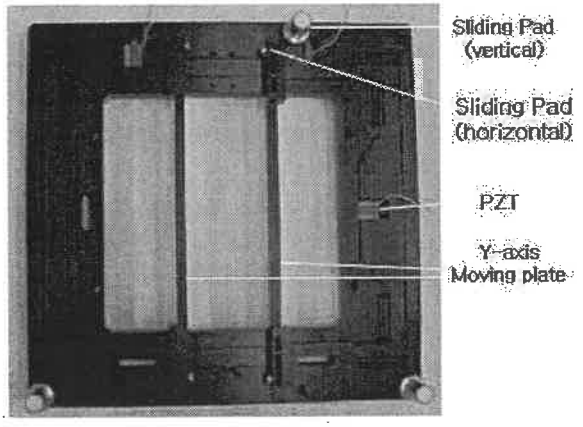

Fig. 3 Flexure hinge type micro-stage. (bottom view)

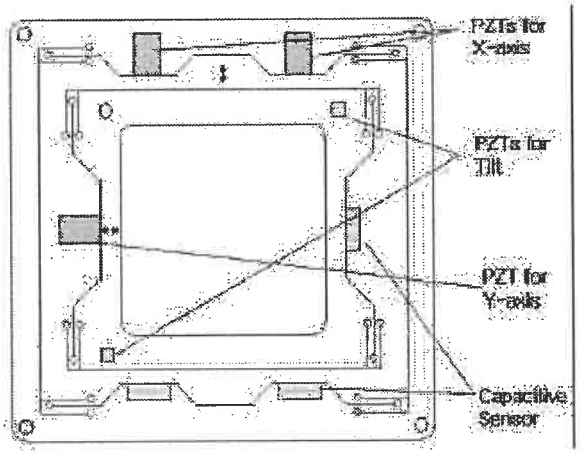

Fig. 4 Schematic diagram of micro-stage.

A compact flexure with PZT is used for actuation of AFM tip and a capacitive sensor reads the displacement of the tip. The PZT actuator with cantilever and capacitive sensor is mounted on a

stage driven by Pico-motor, which is used for coarse adjustment of the AFM tip relative to sample surface. In order to view the sample surface and the AFM tip, an optical microscope with CCD camera is also used.

Further works

Now we are constructing the large range nano-measuring machine for semiconductor metrology applications. For this, a long scan stage with a measuring range of 250 mm x 250 mm x 20 μm is fabricated. The preliminary test shows that the long range stage works well. Further study is to combine the stage with laser interferometer and develop the control algorithm.

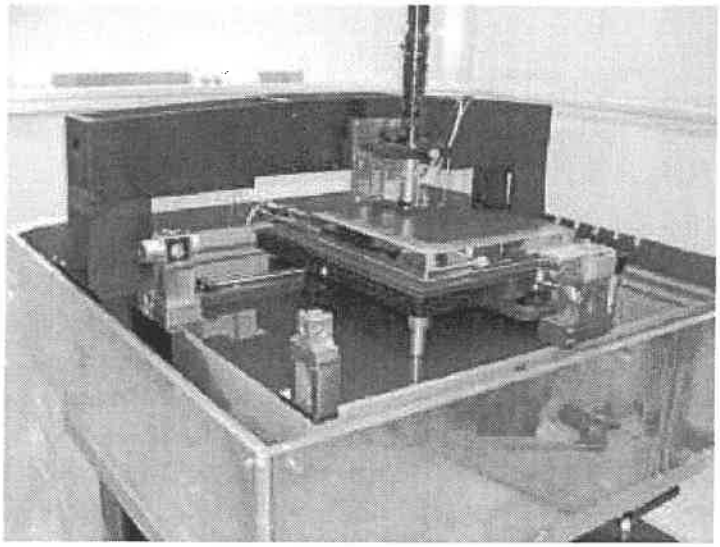

Fig. 5 Nano-measuring machine under construction.

References

[1] T. V. Vorburger, *et al.,* Industrial uses of STM and AFM, Annals of the CIRPS, 46(1997) pp 597-620.

[2] G. B. Picotto and M. Pisani, A metrological SPM for dimensional surface measurement, Proceedings of the EUSPEN, 1(2001), pp 402-405.

[3] E. C. Teague, Nanometrology, Scanning Probe Microscopy, Gaithersburg, MD 20899, NIST (1991)

[4] W. Häßler-Grohne and H. Bosse, An electron optical metrology system for pattern placement measurements, Meas. Sci. Technol. 9(1998) pp1120-1127

[5] T. B. EOM, H. S. Choi and S. K. Lee, Long range stage for the metrological atomic force microscope, Proceedings of ASPE, (2001)

[6] Dai *et al,*. A novel metrological large range scanning probe microscope applicable for versatile traceable topography measurements Proceeding of EUSPEN, 4(2004), pp 228-229

Optimum clearances for shearing work of sheet metals

Y. OKADA*, S. YOSHIDA** and K. MITSUI***

* Graduate School of Science and Technology, Keio University
3-14-1 Hiyoshi, Kohoku-ku, Yokohama 223-8522 JAPAN
E-mail: mr032118@hc.cc.keio.ac.jp

** Graduate School of Science and Technology, Keio University
3-14-1 Hiyoshi, Kohoku-ku, Yokohama 223-8522 JAPAN
E-mail: satoshi1981@mpd.biglobe.ne.jp

*** Department of mechanical engineering, Keio University
3-14-1 Hiyoshi, Kohoku-ku, Yokohama 223-8522 JAPAN
E-mail: mitsui@mech.keio.ac.jp

1. Introduction

Recent rapid progress in the field of mechanical and electrical technologies accelerates the needs for precision manufacturing technologies. Etching and micro-EDM are general machining methods for sheet metals. However, shearing work is consequently appropriate for mass-production.

In general, shearing work of sheet metals are affected by the thickness of sheet metals, clearance of the die and punch [1], shearing velocity [2], [3], and so on. In particular, the clearance is the most important factor in the shearing work of sheet metals. For general shearing work of various sheet metals, the optimum clearances have been already proposed [4]. However, optimum clearances for thin sheet metals have not been proposed yet. It is not made clear that the optimum clearances for general shearing work can be applicable for also thin sheet metals or not. Recently, numerical simulation for clearances in shearing work of thin sheet metals and optimization seems to be started [5], but the research to propose the optimum clearances for thin sheet metals through experiments and measurements has not been reported.

From these points of view, the purposes of this study are, 1) development of a stamp out machine for thin sheet metals, 2) find out the relation between machining conditions and dimensional accuracy of holes and wear of the die, 3) proposal of the optimum clearances for shearing work for thin sheet metals.

2. Development of stamp out machine

In order to investigate optimum clearances in stamp out machining that is a kind of shearing work, it is an indispensable function to stamp out in the condition of the exact coincidence of the center of the die and punch. However, in ordinary stamp out machines, it is impossible to coincide the center of the die and punch exactly. Therefore, as shown in Fig.1, a stamp out machine, which enables adjustment of the center of the die and punch, has been developed.

The developed stamp out machine has the structure in which the die and punch are completely split into two parts. The coordinates of the center of the die and punch are measured by image processing system, and then both centers are adjusted by moving the die, which is set on PZTs driven X-Y micro-stage.

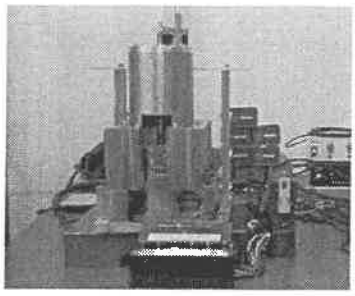

Fig.1 Stamp out machine

3. Measurement and adjustment systems for center of the die and punch

The 2D images of the die and punch are taken by an optical microscope with magnification 2, which is installed with a CCD camera (Fig.2). Then, these images are processed by machine vision software "Hexsight (by Adept Technology, Inc.) as shown in Fig.3.

In order to adjust the center of the die and punch, it is easier to move the die. The most popular devices of carrying a die are commercially available X-Y micro-stages. However, the stiffness of these X-Y micro-stages is not robust enough to survive the press load conditions applied through the die. From the reason, we have developed PZTs driven X-Y micro-stage, which consists of flexure hinge mechanisms, as shown in Fig.4.

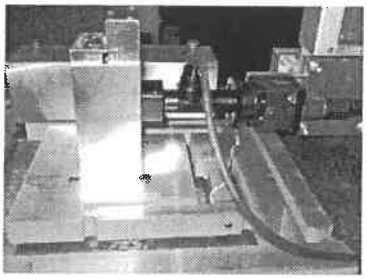

Fig.2 Layout of a CCD camera

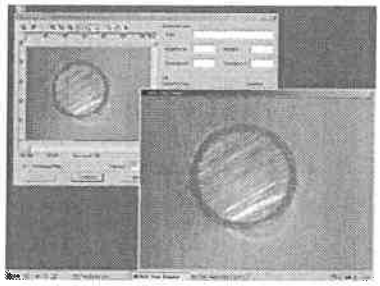

Fig.3 Machine vision software "Hexsight"

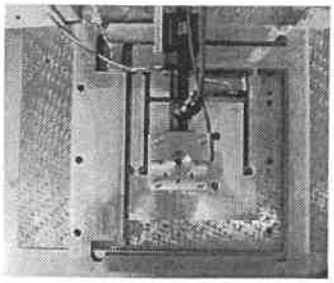

Fig.4 PZTs driven X-Y stage

4. Measuring instrument for Shape and Dimension of Micro-Components

In this study, quantitative measurements of dimension of holes, roll over and burrs, the ratio of a shear plane and a fractured section are very important. The measuring method that has small measuring force and applicable especially to the measurements of roll over and burrs is required. Then, a small 3D-CMM for the measurement of shape and dimension of micro-components [6], which had been developed in our laboratory, was used. The configuration of the apparatus is shown in Fig.5.

In the measuring instrument, the probe detecting proximity to the object through tunneling effect. So we can measure without contact to surface of a measuring target. A Z-axis micro-stage and a linear motor driven X-Y micro-stage are used for coarse positioning. For the fine positioning, PZTs driven X-Y-Z micro-stage that has 100 μm travel are set on the linear motor micro-stage. The measuring targets are set on the PZTs driven X-Y-Z micro-stage.

Another flexure hinges movable to X-Y-Z direction with piezoelectric actuators (PZTs) are set on the Z –axis micro-stage. The maximum driving range of these flexure hinges is about 10 μm along each axis. The flexure hinges equipped with PZTs are used as the probe over travel protection mechanism.

As for the radius of probe tip is 1 μm or less. The probe is fabricated by micro-EDM. The measuring resolution of the small 3D-CMM is 0.2 μm.

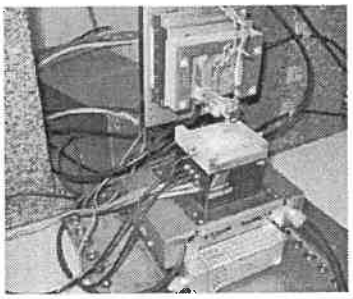

Fig.5 Small 3D-CMM

5. Experimental results

The machining conditions used in the experiments are shown in table 1. In the experiments, the center of the die and punch are adjusted by the previously mentioned procedures. The error of the adjustment is less than 1μm. After the stamp out experiments, we took photomicrographs of the cross section of the thin sheet metals with a laser microscope. The photographs of the cross section are shown in Fig.6 through Fig.10. We have measured the roll over and burrs by small 3D-CMM. The examples of the measurements are shown in Fig.11 and Fig.12.

In general shearing work of various sheet metals, optimum clearances for phosphorus bronze are 6%t to 10%t (for one side). From the result of our experiments, when the clearances are set at 5%t and 10%t, the thickness of a shear plane and a fractured section is nearly at 1:1 ratio. These results are consistent with the optimum clearances for general shearing work. When a clearance is set at 15%t, the thickness of a shear plane and a fractured section is nearly at 1:1 ratio. However, the clearance of 15%t is out of range in the optimum clearances for general shearing work. For phosphorus bronze (t=0.2mm), optimum clearances might have possibility larger than the optimum clearances for general shearing work. We would like to propose the optimum clearances with also roll over and burrs taken into consideration in future.

Table 1 The machining conditions used in the experiments

external diameter of a punch	1.000mm
internal diameter of dies	1.010, 1.020, 1.040, 1.060, 1.080mm
clearances (for one side)	2.5%t, 5%t, 10%t, 15%t, 20%t
material of work piece	phosphorus bronze JIS C5191 (ISO CuSn6)
thickness of work piece	0.2mm
pressure of a stripper	58.634N
velocity of stamp out	1.004mm/s

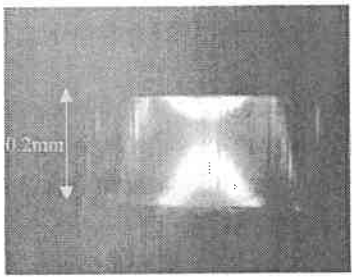

Fig.6 A cross section (clearance=2.5%t)

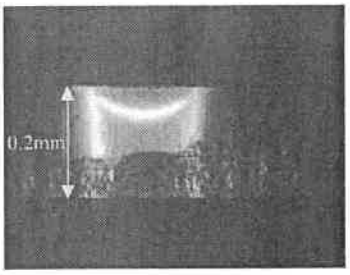

Fig.7 A cross section (clearance=5%t)

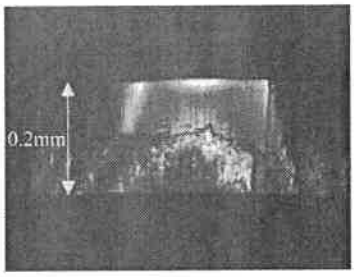

Fig.8 A cross section (clearance=10%t)

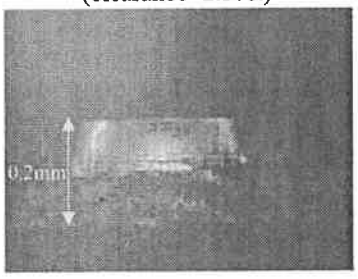

Fig.9 A cross section (clearance=15%t)

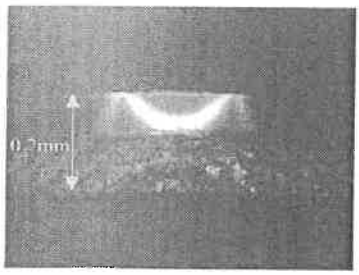

Fig.10 A cross section (clearance=20%t)

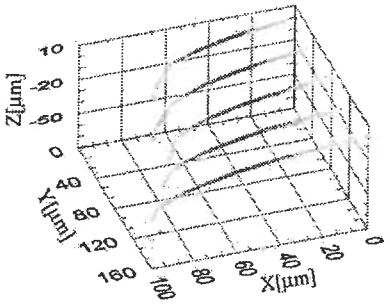

Fig.11 result of measuring of roll over (clearance=10%t)

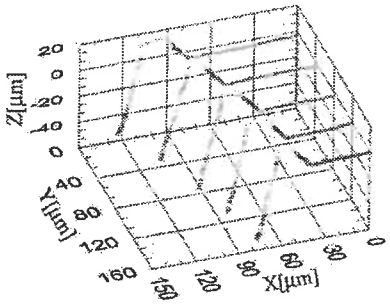

Fig.12 result of measuring of burrs (clearance=10%t)

6. Conclusions and Acknowledgements

In this report, we have tried to make clear the optimum clearances for thin sheet metals stamp out machining through experiments and measurements. The results are summarized as follows:

(1) For phosphorus bronze (t=0.2mm), when the clearances are set at 5%t and 10%t, the thickness of a shear plane and a fractured section is nearly at 1:1 ratio. The result is almost same as the optimum clearances for general shearing work.

(2) For phosphorus bronze (t=0.2mm), when the clearance between the die and punch is 15%t, the ratio of a shear plane and a fractured section is nearly at 1:1 ratio. The result is different from the optimum clearances for general shearing work.

(3) For phosphorus bronze (t=0.2mm), optimum clearances have possibility larger than the optimum clearances for general shearing work.

The authors gratefully acknowledge the contribution of AMADA foundation for metal work technology that supported this study.

7. References

[1] Shinzi FUKUI and Teizo MAEDA: A commentary on the optimum clearances of shearing tools of sheet metal, Journal of the Japan society of precision engineering, (in Japanese), Vol.25, No.11 (1959) 602-629.

[2] Teizo MAEDA: Velocity Effect on Shearing of Sheet Metal Vol.1, Journal of the Japan society of precision engineering, (in Japanese), Vol.25, No.8 (1959) 364-379.

[3] Teizo MAEDA: Velocity Effect on Shearing of Sheet Metal Vol.2, Journal of the Japan society of precision engineering, (in Japanese), Vol.25, No.11 (1959) 439-451.

[4] Japanese Society of Die and Mould Technology, Die and Mould Handbook, (in Japanese), NIKKAN KOGYO SHIMBUN, LTD. (1989) 335.

[5] QIN S-J, LI H-B, PENG J-G, and LI S-B: Numerical simulation and optimization of clearance in sheet shearing process, Transaction of nonferrous metals society of china, Vol.13, No.2 (2003) 407-411.

[6] Toshiya SHIRAMATSU, Kenichi KITANO, Masayoshi KAWADA and Kimiyuki MITSUI: Development of Measuring Method for Shape and Dimension of Micro-Components (Modification of the Original Measuring System, Calibration of the Probes and the Results of Dimensional Measurements), JSME International Journal, Series C, Vol.47, No.1 (2004) 369-376.

Development of Ultra Precise Gear Measureing Instrument

Second Report:Evaluation on the Measuring Accuracy

Hiroomi Ogasawara , Noritsugu Maeda , Masato Ogasawara and Teru Hayashi
OGASAWARA PRECISION LABORATORY LTD.
3819 Yamakita-cho Yamakita Ashigarakami-gun Kanagawa-pref., Japan.

1. Introduction

Gears, having sub-micron geometrical accuracy, are needed in recent industry. And that's why the Ultra Precise Gear Measuring Instrument (UPGMI) with high reliability is in demand to produce these high accurate gears. In other words, a limit of the gear measuring capability decides a limit of the technical possibility in production of such gears. Authors have been involved with study, experiment and trial production of the UPGMI with accuracy target of 0.2~0.4 microns in geometrical measurements which is one digit finer than that of Gear Inspection Instrument in the market. We have just obtained the first measurement result after the first assembling completion.

This UPGMI is composed with pure mechanical elements with no electrical feed-back assist, called open-loop system, for the purpose to pursuit the ultimate mechanical accuracy limit which can be obtained with our recent measuring and finishing techniques. As a proposal, in order to complete this project, the main indexing gears are made by repeating the following procedure. The gears are measured by this UPGI itself, and the gears being compensated / finished upon these measurement results are to be installed into this UPGMI by replacing previous gears.

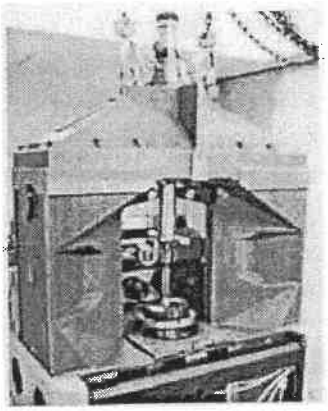

Fig.1 External View of the UPGMI

On the 1st report[1], we described that sub-micron accuracy of the main spindle (radial run-out of 25nm / axial run-out of 20nm) is obtained after trial assembling of the UPGMI. Now, on this 2nd report, based on the result of Involute-Curve measurement by means of Pin-Master, one of the practical evaluation-methods according with this instrument, and explanation of the obtained result and study to make improvement on the practical assembling of this instrument will be described.

2. The Mechanism and Specifications

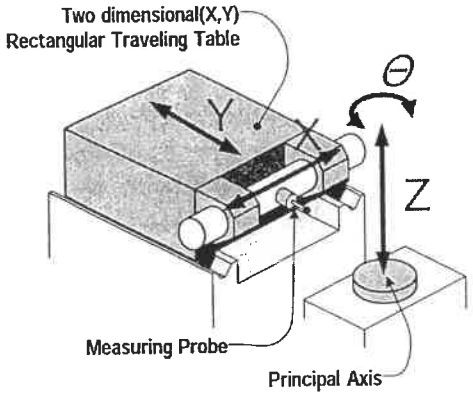

Fig.2 Systematic View of Mechanism

This Instrument is composed with the table which carries measuring probe, on double guide ways (X-Y), and with the main spindle which carries the test-gear with θ -indexing and movement of Z-axis direction. Z-axis movement and indexing guided with the one axis air bearings is the most important and significant feature of this Instrument.

- X, Y, Z travel length are, 160mm, 150mm, 130mm respectively.
- X, Y, Z positioning are made by Trapezoidal-Lead-Screw, driven by Pulse motor through Harmonic-Drive gear train.
- Indexing θ is done by means of Ultra Precise gear train and Pulse motor.

Guide-Way

- X axis linear guide. : Parallel cylinders with hydro-static air bearings.
- Y axis linear guide. : Parallel V's with oil lubricated.
- Z axis linear guide. : Cylinder with hydro-static air bearings.
- Rotary axis θ guide. : Cylinder with hydro-static air bearings.

Measuring probe has two directional measurement capabilities with 2 set of displacement to capacitance transducers coupled with oscillators. Main measuring unit, in order to measure tangential deviations of gear flank curvature, utilizes a differential capacitor system for wider linear working range. Another one, in order to measure radial deviations of the gear, uses single operational capacitor system. Each resolution is 8nm, 26nm respectively.

3. Measuring accuracy evaluation by Pin-Master measurement.

Instead of using Involute-Curve-Gauge as a master, Pin-Master is more simple and steady way to evaluate the accuracy of the Involute generating system / function. Difference between involute-curve tooth form and the equivalent radius can be calculated and used in this evaluation as known value. The measurement values / deviations are compared with this known value, and the differences in between includes geometrical deviations of this Instrument. The Pin-Master used here utilizes a precise / accurate finished cylinder as a pin.

3.1 Theory for measurement

On the measuring plane X-Y, shown in Fig.3 , we define as followings.

- R_g : Radius of Base-Circle. Distance from origin point O to center of the Pin O_p.
- P : Cross point of tangential line of Base-Circle and out-side diameter of the Pin.
- α : Pressure-angle of this Pin-Master. $\angle O_pOP$
- R_1 : Radius of Pin.
- R_2 :Radius of Feeler Ball.

α can be calculated with following formula (1).

$$\alpha = \tan^{-1}\left(R_1 / R_g\right) \qquad (1)$$

Providing that , measuring object has true-involute-curve and any value of θ is given, center point O_b of probing feeler ball moves along the line L-L which locates at the ordinate $Y = R_g$, and O_b moves by the amount of $R_g \cdot \theta$. In this case abscissa X of feeler ball center can be expressed a function of θ as Eq.(2).

$$g_i(\theta) = R_g \cdot (\theta + \tan\alpha) + R_2 \qquad (2)$$

In case of using Pin-Master, and the Pin contacts to the feeler at point C, following equation can be obtained geometrically.

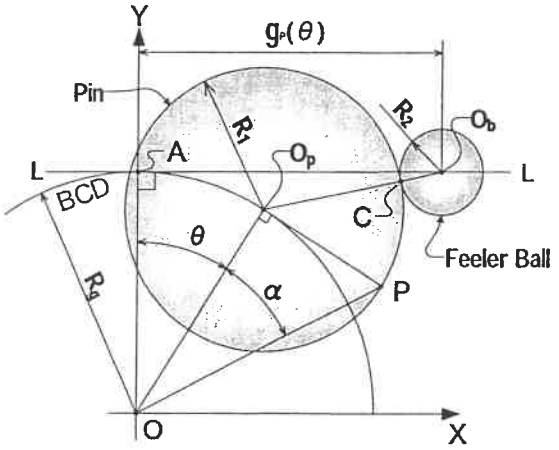

Fig.3 Definition of Pin-Master

$$g_P(\theta) = R_g \cdot \sin\theta + \sqrt{(R_1 + R_2)^2 - R_g^2 \cdot (1 - \cos\theta)^2} \qquad (3)$$

Consequently, narrow distance which can be detected with the probe is the difference between the amounts of Eq.(2) and Eq.(3).

$$f_T(\theta) = g_P(\theta) - g_i(\theta) \qquad (4)$$

We evaluated our Instrument by comparing the measured value and the theoretical value that is expressed by the above equation.

3.2 Measuring system

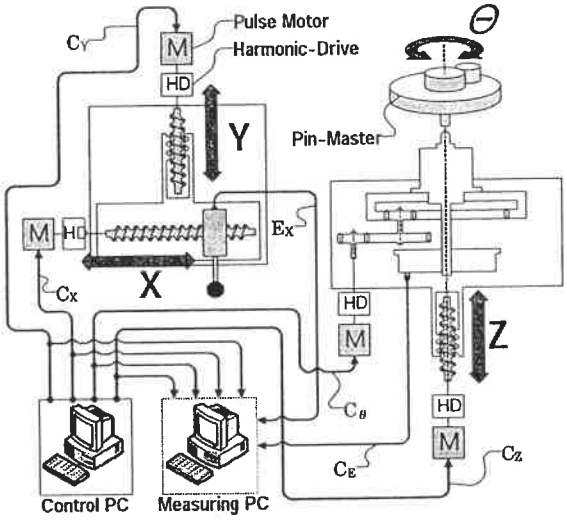

Fig.4 Measuring System

As shown in Fig 4, measurement signal from probe E_x, command pulse signals sent to the drive motor attached on every axis C_x, C_y, C_z, C_θ and angular pulse signal C_E from reference rotary-encoder attached on the main spindle, are taken by counter in computer. Linear positioning accuracy and resolution on each axis are determined by accuracy of the lead screw, accuracy and pole number of pulse motor, and accuracy and reduction ratio of HD gear unit, used here. And indexing accuracy and resolution on main spindle are governed by accuracy of the indexing gear train, accuracy and pole number of pulse motor, accuracy and reduction ratio of HD gear unit, used here.

4. Measured result and discussion

Fig 5 shows measurement result of Pin-Master. Criterion for indexing here is by gear train and for measurement along normal line is lead screw. And Fig 6 shows the deviation of the measurement to the theoretical tooth form of the Pin-Master. Fig 6 shows that system accuracy falls within 1 μm range. And it can be said that peaks in every 0.9 ° interval relate with number of main index gear of 400. This result is what we aware to occur in this first stage of improvement on spiral of the gear. Peaks in every 3 mm, chart on Fig 7, indicates excessive drunkenness amount on lead screw. Consequently, another lead screw with 1 mm pitch length is remade in order to improve accuracy.

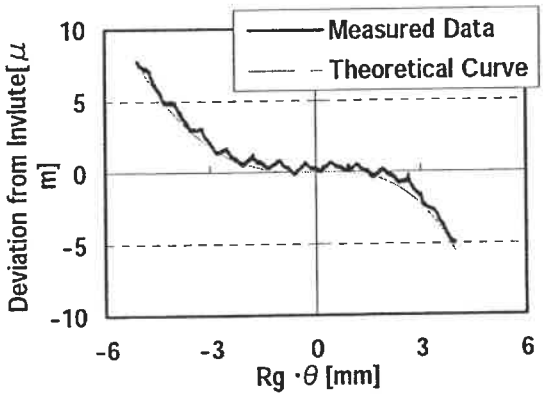

Fig.5 Measured Result / Pin-Master

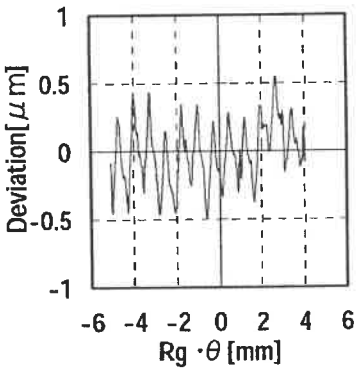

Fig.6

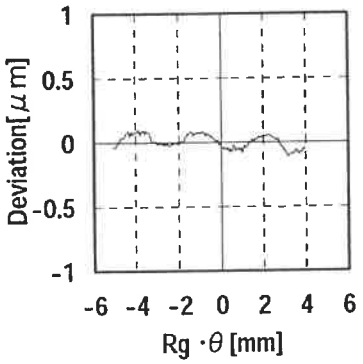

Fig.7

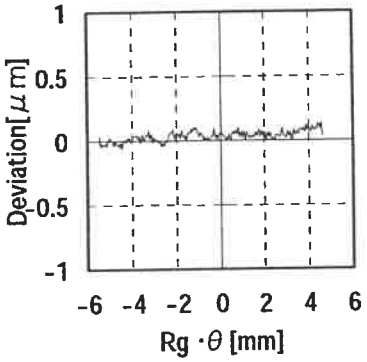

Fig.8

And as the result of this improvement, deviation including lead screw drunkenness within 0.1 μm

(R/E reference) is obtained(Fig.8).

In addition with above, Fig 9 & 10 shows the positioning accuracy measurement of X-axis, referred to laser interferometer distance measuring system. From this result, it becomes clear that improvement of lead screw accuracy and drive train, motor and HD gear reduction unit, accuracy are indispensable.

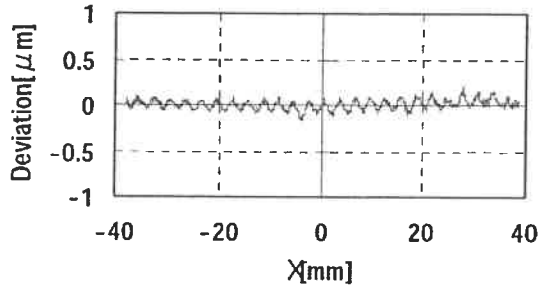

Fig.9 Positioning Accuracy/Screw Pitch 3mm

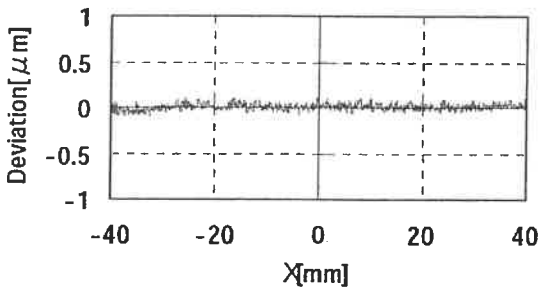

Fig.10 Positioning Accuracy/Screw Pitch 1mm

Defects with Hydro-Static Air Bearing system concerns, described on the previous report, we are now remaking them. Ball-Master method which Kondo[2)] proposed is excellent tool, especially in specifying capability in phase relationship between measuring coordinate and the Pin-Master. Because of this reason, we will be using this Ball-Master method.

5. Conclusion

Although in the pre-assemble stage, it become clear that the obtained accuracy level of this UPGMI is higher than those of Gear Measuring Instrument in the market. With specifying some deviation factors of items which are not successful in obtaining accuracy, we can see the way to complete this UPGMI.

An Index-Gear with certain indexing deviation which is already known is installed and used as measuring reference/master in this UPGMI. This development includes self improving helical with the indexing gear train accuracy, by compensating and modifying the tooth form of gears based on self measuring result and using them as a new reference.

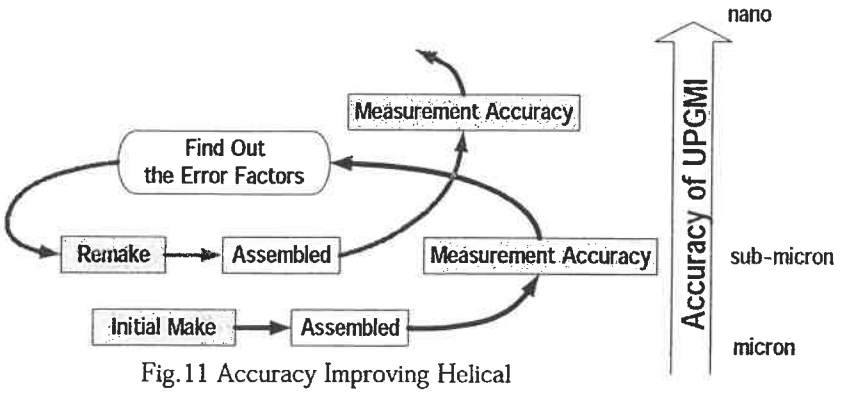

Fig.11 Accuracy Improving Helical

Reference

1)Hiroomi Ogasawara,Noritsugu Maeda, Masato Ogasawara and Yoshiharu Shibuya: Development of Ultra Precise Gear Measuring Instrument First Report: Evaluation on the Accuracy of Principal Axis, ASPE 19th Annual Meeting(2003).

2)Koshi Kondo, Hachiro Mizutani: Measurement uncertainty of tooth profile by master balls,VDI-Berichte,1665,(2002)797.

Development of micro-CMM Probe detecting contact angle

Ichiro Ogura, Yuichi Okazaki
Fine Manufacturing Systems Group
Advanced Manufacturing Research Institute
National Institute of Advanced Industrial Science and Technology (AIST),
Tsukuba 305-8564, Japan

1. Introduction

This study describes the development of a probe for a micro coordinate measuring machine (CMM). In order to guarantee the accuracy of products, a profile measurement evaluation process is indispensable. A CMM is generally used to measure product profiles. Although it can make various product measurements, such as the diameter of holes or complicated profiles, the measurement scale of a CMM is usually several tens of millimeters or more, and it is not suitable for measuring small parts of submillimeter order.

To measure micro-parts in the nanometer size range, the concepts of a nano-CMM[1] and an ultra precision CMM[2] have been proposed, and there have been many interesting studies on the development of novel probes[3]-[5].

In order to measure the 3-dimensional profiles of micro-parts, that have complex or curved shapes, it is necessary to detect not only the making of contact by the probe ball, but also the contact angle. The location of the surface can then be determined from the contact angle and the radius of the probe ball. The normal vector of the profile is described by the inclination direction ψ in the ϕ rotated x-y plane along the z-axis (z-ϕ plane). Then two angles, ϕ and ψ, are needed to determine the contact position.

Some methods exist to detect the contact angle mechanically. One such method employs a 3d-sensor based on a silicon boss-membrane with piezo resistive transducers[6]. Another uses elastic hinges made by a micro-electro-mechanical system (MEMS) technique[7].

We conducted this investigation on a two-dimensional micro probe[8]. The probe we developed could measure a contact point and a contact angle simultaneously in a two-dimensional plane, using active circular rotation. In this study, further developing the previous probe, we propose a novel probe, that detects the contact angle in three-dimensions, developed a prototype probe system, and conducted a preliminary experiment to verify the principle. The results show that accurate evaluation of profiles is possible.

2. Measurement principle

Fig. 1 shows the measurement principle of the proposed system. In this system, most contact-type probes could be used, such as the electrical touch type, optical type, or strain gauge type. However the probe must be able to detect contact from all directions in the measuring plane.

This method uses two procedures to measure the contact angle as follows.

STEP 1(Fig. 1(a)): Applying ($A \cos \omega t$) motion to the x-axis, ($A \sin \omega t$) to the y-axis, and no motion to the z-axis, the probe moves circularly with radius A in the x-y plane. When the probe contacts the profile, a periodic contact signal will be detected. The angle ϕ can be calculated by comparing the phase of rotation and the mid point of a contact signal.

STEP 2 (Fig. 1(b)) : Applying ($A \cos \phi \cos \omega t$) to the x-axis, ($A \sin \phi \cos \omega t$) to the y-axis, and ($A \sin \omega t$) to the z-axis causes the probe to rotate in the z-ϕ plane. As in STEP 1., the angle ψ can be determined.

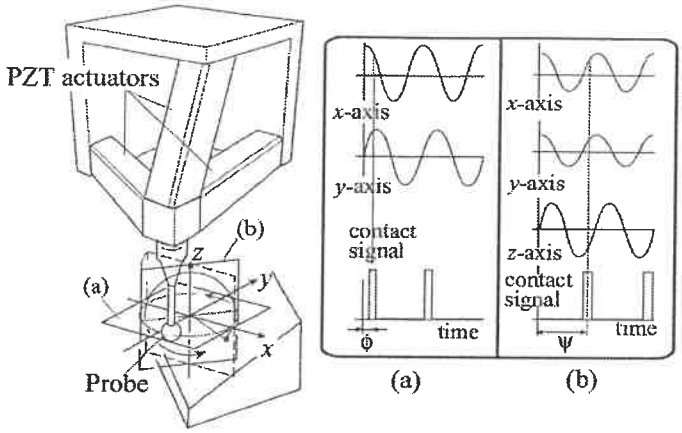

Fig. 1 Measurement principle

After determining two angles, the contact coordinate is adjusted to take into account the radius of probe the ball and the amplitude A. By applying this method to all measuring points, precise measurement is accomplished.

To obtain an equal response from all contact directions, the rotating motion should ideally be perfectly circular and the probe should have a high-precision circular profile. However, if the probe motion or probe profile have some error, measurement accuracy can be confirmed by a calibration technique.

3. Set-up of probe system

Fig.2 shows the probe system setup. This probe has four PZT actuators and three laser displacement sensors to move the probe to x, y and z direction. The feed back system moves the probe in circularly. The x and y displacement sensors are put on opposite side of actuators. The z direction needs two actuators because of symmetrical motion putting laser displacement sensors between actuators. A two-output type function generator applies sine and cosine command signals to the feedback controllers, then the probe rotates. In this study, we set that the amplitude of each axis at 3 μm and the frequency at 10 Hz.

Fig. 3 is a photograph of probe unit. This is a contact detecting type probe which uses piezoelectric gyroscope(Murata manufacturing co. ENC-03J). This gyroscope has ceramic bimorph structures to

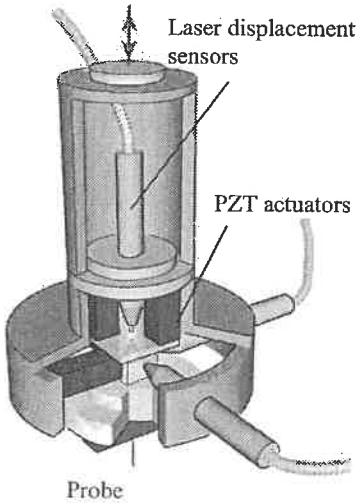

Fig. 2 Probe system setup

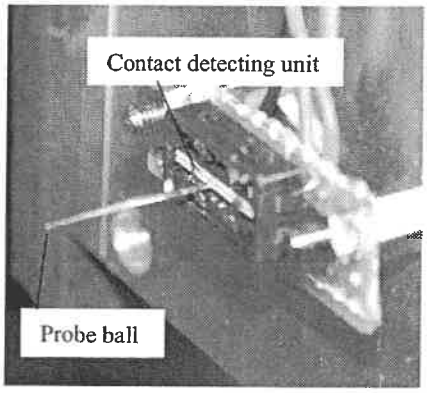

Fig. 3 Photograph of probe unit

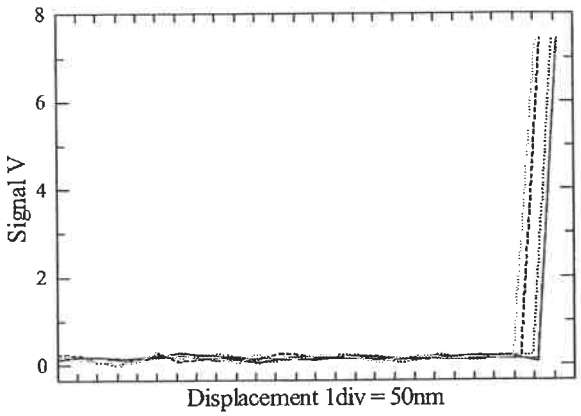

Fig. 4 Repeatability of contact detection

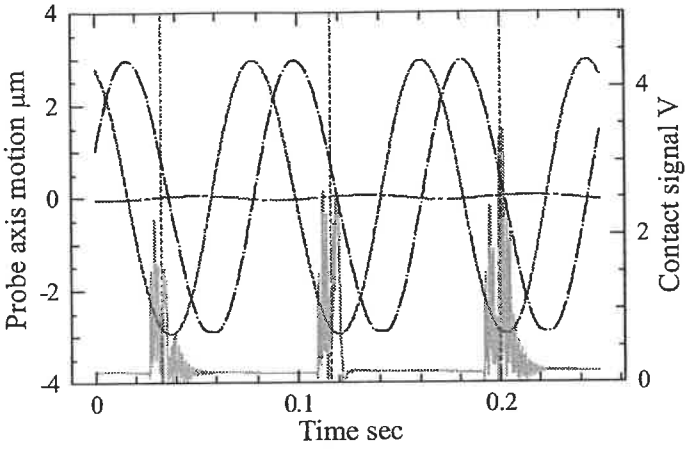

Fig. 5 Probe motion and contact points

detect Coriolis force. We used this sensors as contact detector. The glass probe is glued the middlepart of the ceramic bimorph structures. The length of glass probe is 10mm and the diameter of probe ball is 200 μm .

Fig.4 shows the repeatability of contact detection. The stage moves an optical flat to the probe in 50 nm steps. The x axis of this graph means the displacement of stage and y axis means output of probe. From these results, we can confirm that this probe has better than 50 nm contact detection repeatability. The contact signal rises up rapidly with contact from under 0.5V to over 7V.

4. Experimental results

A preliminary experiments were performed to verify our probe system.

Fig. 5 shows typical output of the contact probe. A total of 341 points were sampled in 1 cycle. The the angle resolution of this probe is about 1.05 degree. In this figure, the x and y actuators move in a sinusoidal curve without any deformation, and their phase difference is $\pi/2$. This output shows that the probe is moving circularly in x-y plane. We also confirmed same probe motion in z-ϕ plane. The contact signal of this probe includes many noise-like output. In our previous study, we made an electrical touch type probe[8]. The output of previous probe had clear rectangular signal along contact detection. Then we could set contact direction from the center point between the rising up point and setting down point. But in this time, it is hard to define the center point automatically from the signal in fig. 5. Main reason of this signal output is that the ceramic bimorph structures of piezoelectric gyroscope vibrates minutely with contact.

Therefore, we use the area moment method in Fig. 6 to detect the center point. From the series of signal output between t_1 and t_2, the area of signal output is calculated from following equation.

$$A = \int_0^{t_1} f(t)dt \qquad (1)$$

The center point of signal t_g is calculated from following equation.

$$t_g = \frac{1}{A}\int_0^{t_1} f(t)tdt \qquad (2)$$

Using discrete Fourier synthesis the contact angle is calculated. Fig. 5 shows that calculated center points in dashed vertical line. The variation of calculated angle is within plus-minus 1 sampling width.

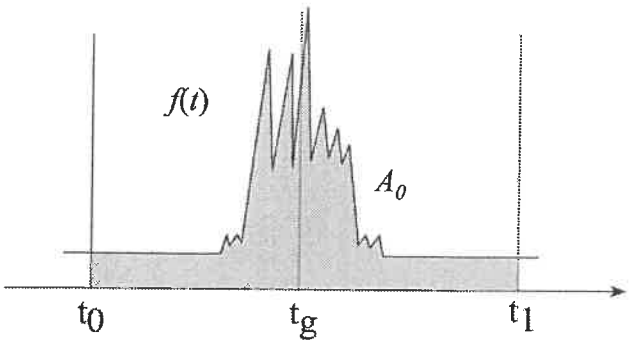

Fig. 6 Area moment method to detect center point.

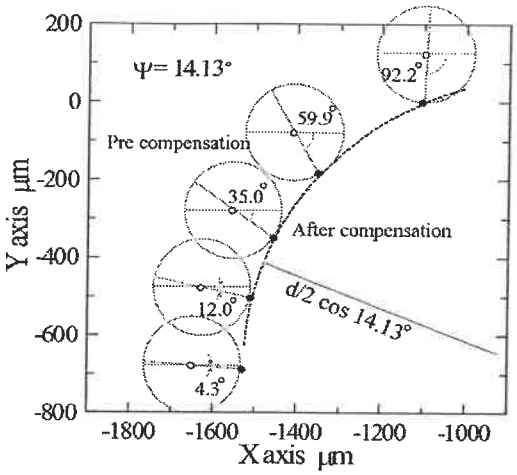

Fig. 7 Results of profile measurement

The profile measurement experiment was performed for the ball lens. The profile was measured in each *x-y* plane. The interval of z height was 200 μm. Fig.7 shows the results of the experiments. This figure plots contact detecting pints, calculated contact points in *x-y* plane and expected profiles calculated from the ψ angle. This figure also shows probe ball profiles and measured angles in each contact points. The results show good agreement with the expected profiles. The maximum error was 5 μm. The results establish the validity of the proposed method.

5 Conclusion

We have proposed a new probe for a micro CMM that can simultaneously detect the contact point and contact direction. A prototype probe system was developed and a preliminary experiment was performed. The results of the experiment confirmed the validity of our method.

References

1) K. Takamasu, et al.: Basic Concepts of Nano-CMM (Coordinate Measuring Machine with Nanometer Resolution)., Proc. of Japan-China Bilateral Symposium on Advanced Manufacturing Engineering (1996) 155.
2) T. Ruijl, et al.: Ultra Precision CMM Aiming for the Ultimate Concept., Proc. of 2nd euspen International Conference (2001) 234.
3) U. Brand, et al.: Development of a special CMM for dimensional metrology on microsystem components., Proc. of ASPE 2000 (2000) 542.
4) T. Masuzawa, et al.: Twin-Probe Vibroscannning Method for Dimensional Measurement of Microholes., Annals of the CIRP 46, 1 (1997) 437.
5) Y. Takaya, et al.: Nano-Positional Detection Using Laser Trapping Probe for Microparts, Proc. of ASPE 2000 (2000) 584.
6) U. Brand, S. Cao, W. Hoffmann et al : A Micro-Probing System for Dimensional Metrology on Microsystem Components, Proc. of 2nd euspen International Conference, (2001), 266.
7) H. Haitjema, W. O. Pril and P. H. J. Schellekens : Development of a Silicon-Based Nanoprobe System for 3-D Measurements, Annals of the CIRP, 50, 1, (2001), 361.
8) I. Ogura and Y. Okazaki : A Study for Development of Small-CMM Probe Detecting Contact Angle, Proc. of ASPE Summer topical meeting (2003) .

Traceable force metrology for micronewton level calibration

Richard M. Seugling and Jon R. Pratt
National Institute of Standards and Technology, Gaithersburg, MD 20899

Introduction

The research presented in this abstract concerns the calibration and implementation of a prototype secondary force standard to disseminate the SI (*Le Système International d'Unités*) unit of force ranging from 5.0 μN to 5000 μN. The elastic-force measuring device under consideration combines an elastic member packaged between two outer electrodes providing a capacitance-based load detection scheme. Transfer standards of this nature are primarily envisaged for use as a means of calibrating probe force apparatus such as instrumented indention machines, but may also be utilized for mechanisms like coordinate measuring machine scanning probes.

The unit of force is derived from mass (kg) and acceleration ($m \cdot s^{-2}$), generally due to gravity, which is traceable to SI units through the definitions of mass, length and time. However, SI traceability through conventional mechanical units is difficult to achieve at forces smaller than micronewtons, primarily due to the uncertainties of mass artifacts at milligram levels, among other more practical difficulties including sample preparation, contamination and handling. Alternative approaches for establishing traceable small force standards are currently under investigation at NIST [1], PTB [2] and NPL [3], though such approaches are outside the scope of methods considered here.

For this study, primary force standards were realized using deadweights ranging in mass from 0.5 mg to 500 mg. Larger artifacts are readily available with even lower relative uncertainty [4]. Such accuracy is adequate for the force range desired, and is typical of the accuracy sought in measurement standards written for instrumented indentation [ISO 14577 1,2,3]. Calibration techniques for force transducers [4] have been well established and form the basis for the methods employed throughout this work.

Issues outlined in this paper represent exploratory procedures and methods for the calibration of a specific sensor type and ***do not*** represent or replace standard practices of the ASTM or ISO. This investigation has been initiated to determine the feasibility and inherent difficulties of the dissemination of force to instruments at the micronewton level. Certain commercial equipment, instruments, or materials are identified in this article in order to specify the experimental procedure adequately. Such identification is not intended to imply recommendation or endorsement by the National Institute of Standards and Technology, nor is it intended to imply that the materials or equipment identified are necessarily the best available for the purpose.

Description of the sensor

The load cell under consideration combines an elastic member packaged between two outer electrodes providing capacitance based load detection as illustrated in Figure 1. Force may be applied along an axis perpendicular to the load button and a capacitance value measured representing the force. The device under consideration has an overall size of approximately 15.8 mm × 13.6 mm × 4.2 mm. The moving electrode is accessed from either side via a 4.0 mm diameter hole nominally at the center of the volume. The load cell was adhered to a rigid substrate and located in plane by two pins. The combined assembly acts as a mounting structure and relative datum for the calibration, creating a flat, rigid surface upon which the sensor rests during application of a force. Although the transducer can be used in a differential mode, the capacitance was measured from a single parallel plate pair using an Andeen-Hagerling AH 2700A capacitance bridge traceable to a NIST reference capacitor. The bridge and the sensor were connected in a three terminal arrangement [5] to minimize the effects of stray capacitance during the measurement.

With the basic configuration of sensor determined, initial tests were performed to establish sensitivity to the environment. A platinum resistive thermometer was used to monitor temperature throughout all measurements, while humidity and pressure variations were considered negligible at the level of the intended measurements. The elastic-force device assembly was rigidly fixed to an optical post under laboratory conditions and monitored overnight. A nominally linear drift of approximately 4.4×10^{-4} pF·°C^{-1} was observed in a 14 hour period. After removing this drift, the peak to valley (p-v) variation of the capacitance measurement under normal laboratory conditions appeared on the order of ± 0.001 pF. The measurement was repeated in an enclosure where the temperature variation was an order of magnitude lower. Removing the linear drift as done previously, the p-v capacitance variation was $\pm 3.0 \times 10^{-5}$ pF.

Force Generation and Application

Traceable force was derived using mass artifacts ranging from 0.5 mg to 500 mg to create appropriate deadweight loads. Mass values for the deadweights were determined by comparison to a Class OIML E1 weight set (1 mg to 500 mg) using a Mettler Toledo UMX2 microbalance as a comparator. A value for the 0.5 mg artifact was obtained using the direct read out of the microbalance. The deadweights were constructed from 316 stainless steel

cylindrical pins with a nominal length ranging from 7.0 mm to 35.0 mm and nominal diameters ranging from 0.038 mm to 1.65 mm based on the mass value.

The force produced by a deadweight load and the corresponding load cell response are described by,

$$F = mg\left(1 - \frac{\rho_{air}}{\rho_{wt}}\right) = k\frac{\varepsilon_D A}{C}, \tag{1}$$

where m is the mass of the deadweight (kg), g is the local acceleration due to gravity ($m \cdot s^{-1}$), ρ_{air} is the density of air (approx. 0.0012 ($Mg \cdot m^{-3}$)), ρ_{wt} is the density of the weight ($Mg \cdot m^{-3}$), k is the linear stiffness of the device, ε_D is the dielectric coefficient, A is the surface area of the capacitance sensing mechanism, and C is the capacitance.

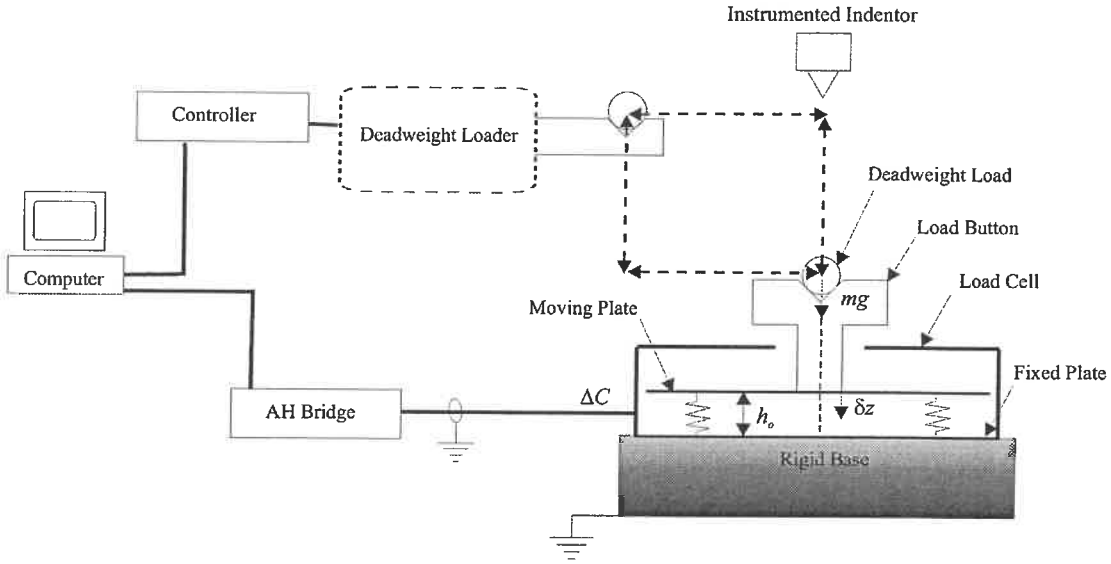

Figure 1: Schematic representation of the load cell calibration and subsequent transfer to the instrumented indentation machine. Elastic-force load cell is calibrated using deadweight loads repeatably applied by an automated loading system. The load cell is then used to disseminate force to an instrumented indentation machine.

It was the intention of the procedure to allow the instrument being calibrated to act in its normal configuration (i.e., applying a compressive force in this application). The deadweight load and the indentor force should, ideally, be done in a similar manner such that the gravitational axis, load cell travel axis and indentor axis are all nominally aligned. To accomplish this, a dual-purpose Delrin load button was created that acts as an interface between the applied load (both the deadweight and indentor) and the moving electrode of the device. Delrin was used because of its low density and insulating characteristics. The combined mass of the button, silica plate and assembly screw was 39.69 mg. It is important to note that the weight of the load button acts as a bias in the load direction to reduce possible nonlinearities in the elastic element. A schematic representation of the load cell calibration and transfer to the instrumented indentation machine is shown in Figure 1.

An automated loading system was developed to apply the deadweights to the device such that minimal disturbances were incurred. The system consists of an X-Y-Z translation stage and a single rotary stage where three of the four freedoms were automated to reduce interaction and environmental disturbances. To assess the influence of the deadweight-loading machine, the system was run without a mass in place. The null loading procedure did not show substantial influence on the measurement and was recorded to be approximately $\pm 3.0 \times 10^{-5}$ pF p-v over a time period of approximately 40 minutes. Another possible source of error was off-axis loading. Without knowing the true axis of motion of the device, an experiment was done to establish the sensitivity of off-axis loading. A 10.0 mg deadweight was placed on a mass post nominally 10.0 mm in the radial direction (r) from the post center to simulate an extreme off-axis load. This value was compared to the value of the deadweight on center and showed a maximum percent error of 0.02 %. In practice, a reasonable estimation of the center location was ±1.0 mm.

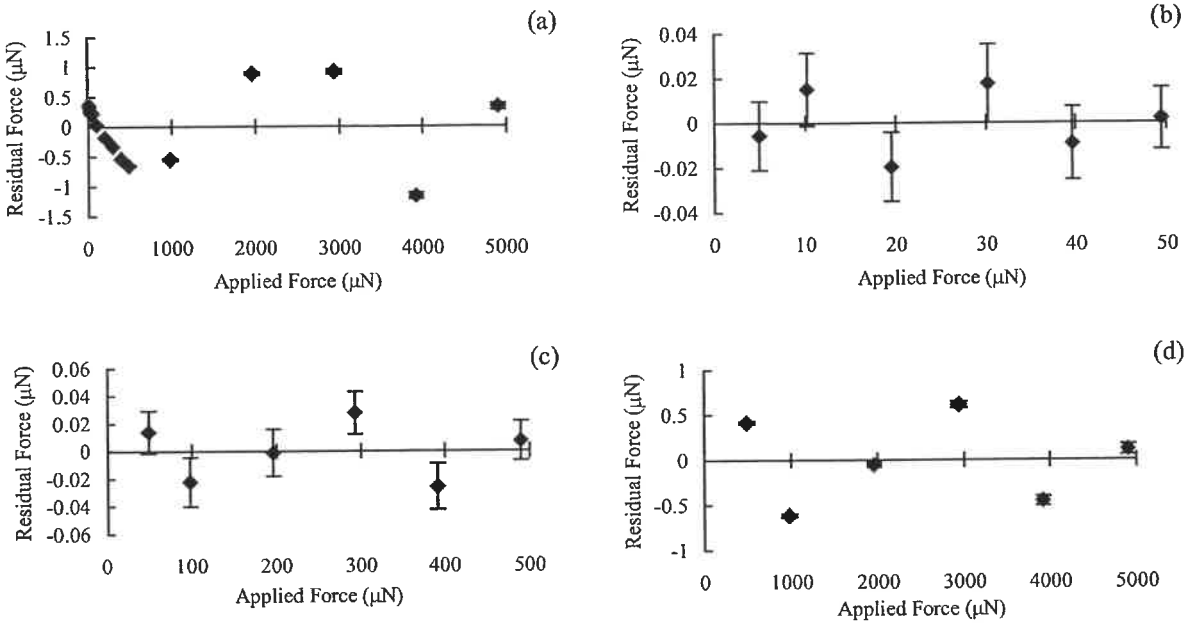

Figure 2: Plots of the residual calibration data a) Full range 5.0 to 5000 μN b) Low range 5.0 μN to 50 μN c) Mid range 50 μN to 500 μN d) High range 500 μN to 5000 μN.

Transfer Standard Calibration

Two candidate secondary force standards were tested. For each sensor, a given load was applied 10 times in succession. Upon completion of the tenth load repetition, the rotary stage moved the next deadweight into position and the process was repeated for a new load level. The data was fit to a third order polynomial given by,

$$\Delta C = A_0 + A_1 F + A_2 F^2 + A_3 F^3, \tag{2}$$

where ΔC is the change in capacitance of the device, F is the applied force and A_0 through A_3 are the polynomial coefficients. The capacitance change was calculated by,

$$\Delta C_{i,j} = \frac{1}{2}\left(\left(C_i - C_j\right) + \left(C_i - C_{j+1}\right)\right), \tag{3}$$

where C_i is the capacitance value in the loaded condition, C_j is the capacitance value in the unloaded condition and $\Delta C_{i,j}$ is the average change in capacitance due to a load between successive unloaded conditions. This technique was used to nominally remove the linear drift of the device during the calibration procedure.

Table 1: Uncertainty analysis, Type B

	Uncertainty (u) $\times 10^{-3}$
Mass (m) 1mg	2.0
Mass (m) 10mg	0.2
Mass (m) 100mg	0.05
Gravity (g)	0.001
Dielectric coefficient (ε_D)	0.1
Density ratio (ρ_{air}/ρ_{wt})	0.015
Capacitance (C)	0.01
Load position (Δr)	0.04
Combined uncertainty (u_c)	2.0

Initially, deadweight loads ranging from 0.5 mg to 500 mg were applied spanning the force range described. The standard deviation of the residual force was found to be approximately ± 0.54μN over the full range. However, it was observed that the standard deviation of successive loadings was considerably better than the full range error would imply, possibly due to the highly nonlinear characteristics of the device. Based on this observation, the procedure was repeated in decade increments (5.0 μN to 50.0 μN, 50.0 μN to 500 μN and 500 μN to 5000 μN) resulting in standard deviations of the residuals 0.02 μN, 0.04 μN and 0.44 μN over the low, medium and high ranges, respectively. Residuals of the calibrations are shown in Figure 2.

Uncertainty Analysis

Type A and B uncertainties will be discussed as described in reference [6]. The analysis is based on Eq.(1) and considers the stiffness of the device, k and the area of the capacitance mechanism, A as constant values over the range and implementation discussed above. For the procedures above, Type A uncertainty is accounted for using the standard deviations mentioned previously.

Important Type B uncertainties and their respective values are listed in Table 1. The uncertainty associated with the mass values were derived from the tolerances of the Class OIML E1 weight set and ***do not*** represent the limiting accuracy of the mass values. Combining the uncertainty values by the sum of squares method and using a coverage factor, k of 2, the combined uncertainty (U) for the low, mid and high ranges are 4×10^{-3}, 2.3×10^{-4} and 2.5×10^{-4}, respectively. It is clear that the uncertainty associated with the mass values used in this analysis dominate the error budget at small forces. However, calibrated artifacts having standard uncertainties of 2.0×10^{-4}, 2.4×10^{-5} and 2.0×10^{-5}, for 1 mg, 10 mg and 100 mg masses, respectively could have been used, which would reduce the influence of the mass value to that of the dielectric coefficient, but does not diminish the geometric and handling limitations involved in artifact based standards.

Instrumented Indentation Load Verification

As a final demonstration of the intended use of the secondary force standard, sensor assemblies were placed on the sample stage of an instrumented indentation machine and probed as if they were indentation samples. The indentor-tip was brought into contact with the load button and an indentation procedure was started. Forces generated by the indentation instrument were incremented through 10 steps over a nominal force range of 50 μN to 600 μN. The output of the instrumented indentation machine was recorded and compared to the output of the transfer standard to assess possible calibration errors. Average results of 10 loading sequences are shown in Figure 3. A discrepancy is apparent between the indentor and standard. It would appear from these tests that the indentation machine records force with an error of approximately -4.0 % as compared to the load cell.

Conclusions

The device and calibration procedure outlined in this abstract illustrates the inherent difficulties of obtaining traceable forces at the miconewton level. The elastic-force sensing device under investigation provides good repeatablity and robustness, but is highly nonlinear and very sensitive to environmental conditions. Uncertainty of the mass value at the milligram level dominates the uncertainty of the procedure and demonstrates the problems involved with artifact-based calibration procedures and implementation.

It has been shown that the dissemination of force from the elastic-force device to the instrumented indentation machine can be achieved. As mentioned earlier, this study has focused on the feasibility of providing calibration methods and artifacts at the micronewton level. More complete analysis and research is currently being undertaken to verify conclusively the accuracy and uncertainty of this device.

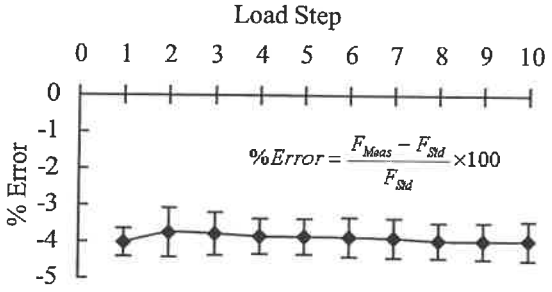

Figure 3: Plots of the average percent error of an instrumented indentation machine compared to the transfer standard. The applied load was increased from 50-600 μN in ten steps and repeated ten times where the error bars represent the standard deviation between each load step value.

Acknowledgements

The authors would like to thank David Newell and John Kramer for their input and expertise during the research outlined above as well as Dan Xiang and Doug Smith for their work and input during the design and testing of the procedures and apparatus described previously.

[1] Pratt, J.R., Smith, D.T., Newell, D.B., Kramar, H.A. and Whitenton, E., 2004, Progress toward Système International d'Unités traceable force metrology for nanomechanics, *Journal of Materials Research*, **19** (1), 366-379.

[2] Behrens, I., Doering, L. and Peiner, E., 2003, Piezoresistive cantilever as portable microforce calibration standard, *Journal of Micromechanics and Microengineering*, **13** (4), S171-S177.

[3] Cumpson, P.J. and Hedley, J., 2003, Accurate analytical measurements in the atomic force microscope: a microfabricated spring constant standard potentially traceable to the SI, *Nanotechnology*, **14** (12), 1279-1288.

[4] American Society for Testing and Materials, 2002, *Standard Practice of Calibration of Force-Measurement Instruments for Verifying the Force Indication of Testing Machines*, ASTM E 74-02.

[5] Thomas, H E and Clarke, CA, 1967, *Handbook of Electronic Instruments and Measurement Techniques*, Prentice-Hall, Englewood Cliffs, NJ.

[6] Taylor, B N and Kuyatt, C E, 1994, *Guidelines for Evaluating and Expressing the Uncertainty of NIST Measurement Results*, NIST Tech. Note 1297.

A coarse/fine motion control stage: preliminary studies

Hua Yang, Eric S. Buice, Terence Fagan, Stuart T. Smith, Robert J. Hocken, David Otten[*], *David L. Trumper*[*], and *Richard M. Seugling*[♦]
Center for Precision Metrology, UNC-Charlotte, NC 28223
[*]Massachusetts Institute of Technology, Cambridge, MA 02139
[♦]National Institute of Standards and Technology, Gaithersburg, MD 20899

Summary

We are developing a stage system, which uses a coarse/fine approach for accurate nanometer level positioning for scanning specimens over an area measuring 50 mm × 50 mm. The completed system will comprise a short-range, 6 degree-of-freedom fine-motion platform (10 μm displacement, 40 μrad rotation) carried by a long-range, two-axis *X-Y* coarse positioning system, to achieve nanometer resolution positioning. Motion of the platform relative to a measurement frame will be measured using a heterodyne laser interferometer. The complete system will be housed in a vacuum system, pumped to better than 0.10 Pa, and operated in a temperature-controlled laboratory. Prior to manufacture of the complete system, a number of concerns such as, vacuum system design, nanometer precision bearings, controller strategy and interferometer configuration must be addressed. Currently, we are developing controller algorithms and implementation strategies. As a first step to assess a cascaded controller, a considerably simpler, single-axis, coarse/fine stage has been design and manufactured. This system will be interfaced with a custom-built, DSP-based controller based around a dSPACE architecture described herein[®]. As well as some controller implementation strategies and considerations, results from preliminary tests on this system will be presented.

Introduction

Nano-scale positioning and advance control technology will be essential both for nanotechnology research instrumentation and for tools dedicated to fabrication and test of nanodevices, but few, if any, robust and reproducible solutions exist. The motivation for this project is to help facilitate the transition from nano-science to productive nanotechnology. The completed system will provide the ability to "pick and place" at nanometer levels and compare system performance with other designs at international locations such as, National Physical Laboratory (NPL) in the UK, Technical University of Eindhoven (TUE) in the Netherlands, Physikalisch-Technische Bundesanstalt (PTB) in Germany and our own sub-atomic measuring machine (SAMM) at UNC-Charlotte.

Major objectives of this project include: development of integrated position measurement system with nanometer uncertainties traceable to national standards, a translation mechanism for multi degree-of-freedom motion control, integration of fine motion controllers into long-range instrumentation for nano-scale manipulation in centimeter-sized workspaces, integration of cascaded multi degree-of-freedom control systems and carry out a combined uncertainty analyses for determination of system error budget. The paper will present details of the mechanical design, optical interferometry configuration, controller architecture and results of a simpler, single-axis, coarse/fine stage.

Mechanical system design

The choice of a particular configuration is endless, each having distinct pro's and cons, it has been decided that the coarse *XY* positioning stage will be in the form of a stacked pair of linear slides with guide ways being in an 'H' configuration. A 6 degree-of-freedom fine positioning stage[1] will be attached to the upper moving carriage of the positioning stage to compensate parasitic motion errors, thereby providing *XY* scanning over a large area with local, limited-range, and three-dimensional control at any location; see Yang, *et al.*[2]

In the development of this design, it became apparent that it would be necessary to develop and assess a number of subsystem elements to obtain a more complete knowledge of expected dynamic performance. One of the key components of this system is the slideway for long-range translation of the *X*- and *Y*-axis carriage. It was decided to base the bearing system on a previous design using PTFE thin film bearings that were successfully implemented in both the Nanostep™ profilometer and the Tetraform™ grinding machine[3]. However, it was decided to use an alternative ultra-high molecular weight polyethelene (UHMWPE) design to produce a low-cost, robust, vacuum

---

[®] Certain commercial equipment, instruments, or materials are identified in this article in order to specify the experimental procedure adequately. Such identification is not intended to imply recommendation or endorsement by the National Institute of Standards and Technology, nor is it intended to imply that the materials or equipment identified are necessarily the best available for the purpose.

compatible and modular dry rubbing bearing with sub-nanometer performance[4]. As of writing, these bearings appear to be relatively robust and appear to be capable of nanometer level repeatable motions with relatively low wear rates[5]. While further tests are being undertaken, current results are favorable for this bearing design. To assess slideway and controller performance, a simpler, single axis slideway was manufactured. The test system consisted of a collinear single axis fine motion actuator attached to a rectilinear moving carriage as shown in Figure 1.

Proposed optical interferometry configuration

Following Lawall *et al.*[6], we propose to use an iodine-stabilized laser that provides an optical signal at an absolute frequency of 473 612 324.722 MHz with a standard combined uncertainty of 11.6 kHz. This is used to lock a HeNe laser with an offset frequency of 110 MHz at an uncertainty of less than 1.0 kHz; hence, the frequency of this is 473 612 434.722 MHz corresponding to a wavelength in vacuum of 632.991 104 2 nm. To provide sufficient laser intensity for eight interferometer paths, a bank of HeNe lasers (metrology lasers) will be locked to the offset HeNe, Figure 2. Ultimately, the locked counter frequency must also be accounted for in the frequency of the laser output used for metrology.

To derive a heterodyne beam, each metrology laser is split into two beams that pass through separate Acousto-Optic Modulators (AOMs) set to a frequency difference[7] (20 MHz for example); see Figure 4. From this, the two beams pass through the interferometer configuration shown in Figure 3[8], each axis pair providing a linear displacement and an angular rotation. It is envisaged that similar pairs be stacked to provide measurement in orthogonal planes. Details of this will be presented.

System control architecture

The stage controller block diagram is shown in Figure 5. As shown, at the highest level the controller is responsible for coordinating fine and coarse motion along with taking images from probe systems associated with the stage. The fine motion stage will be implemented with a six-axis piezoelectrically actuated stage with a range of 6 μm and 0.14 mrad in each axis. Motion of this fine stage will be measured with a six-axis interferometer system. The coarse stage system provides x- and y-motion over long travel (about 50 mm) via two Rohlix/feed-screws driven with brushless DC motors with integral encoders. The controller will coordinate the motion of these two stage systems to remain within the limited travel of the fine stage while achieving nanometer-scale resolution over the full travel of the coarse stage.

In support of the high-resolution motion requirements of the stage system, we have developed novel interfaces for the A/D, D/A, and laser interferometer channels. For a more detailed description of the hardware see Yang, *et al.*[9]

Results

As a test of the performance of the single axis stage, a sinusoidal position demand was applied to the controller input. The controller has been designed using Matlab™ Simulink and resulting control codes compiled to run a dSPACE™ DS1103 control board using custom built analog to digital conversion hardware. The output of the fine motion actuator attached to the coarse stage has been monitored using a Zygo displacement measuring heterodyne interferometer monitored using their ZMI 4004 phase measurement electronics. Results from a single test during which the controller demand was a sinusoidal displacement of amplitude 50 μm over a relatively long period of 100 seconds is shown in Figure 6. The upper trace in this figure shows the demand while the middle trace is a plot of the error signal. In general, it can be seen that the error signal is maintained within a 5 nm band of the desired displacement. The lower plot shows the drive voltage to the piezoelectric actuator of the fine motion stage. Operation of the controller is apparent from the lower plot. In this trace, it can be seen that the piezo drive signal is nominally centered about the desired set-point (0 volts in this case). However, when the direction is reversed, the backlash in the feedscrew results in an inability of the coarse stage to follow the demand. During this transition, the fine stage translates to compensate this until the backlash is removed and the feedscrew is once again able to drive the piezoelectric actuator back to the desired set-point value.

In addition, using the encoder in the motor drive, it has been possible to monitor both backlash and pitch of the feedscrew. Interestingly, the pitch of the Rohlix feedscrew was found to be different when driving in the forward and reverse directions even at similar speeds. These and other results will be presented at the 19th Annual ASPE conference October 24th to 29th in Orlando, FL.

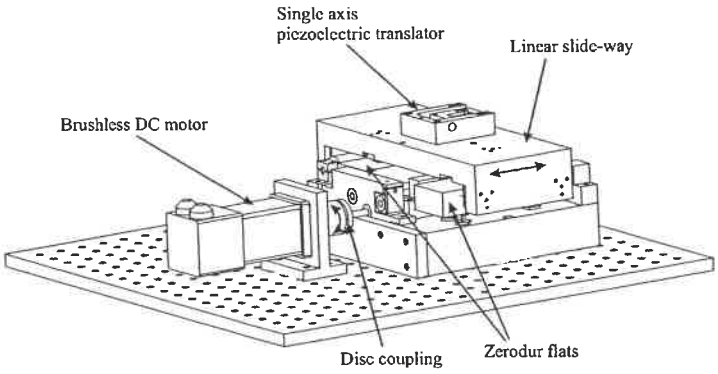

Figure 1: Single axis coarse/fine motion stage

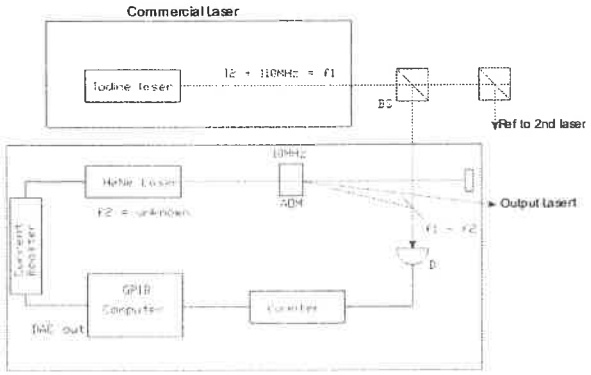

Figure 2: Iodine stabilized offset HeNe Laser.

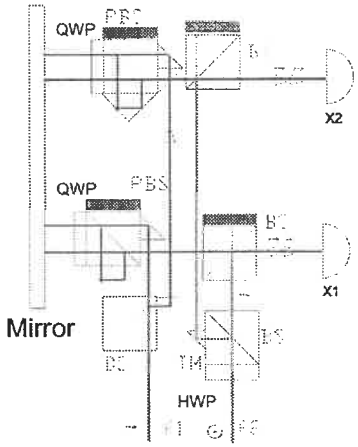

Figure 3: Proposed optical interferometer configuration

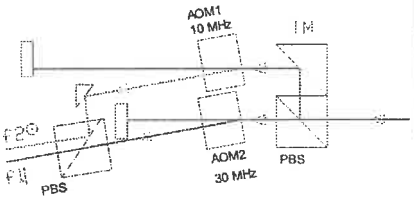

Figure 4: Heterodyne mode generation.

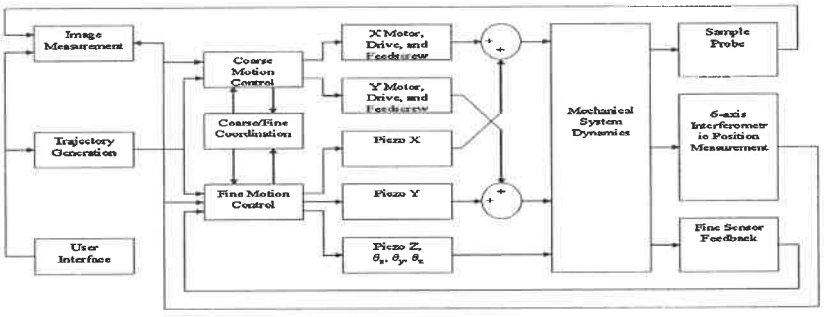

Figure 5: Block diagram of system control architecture.

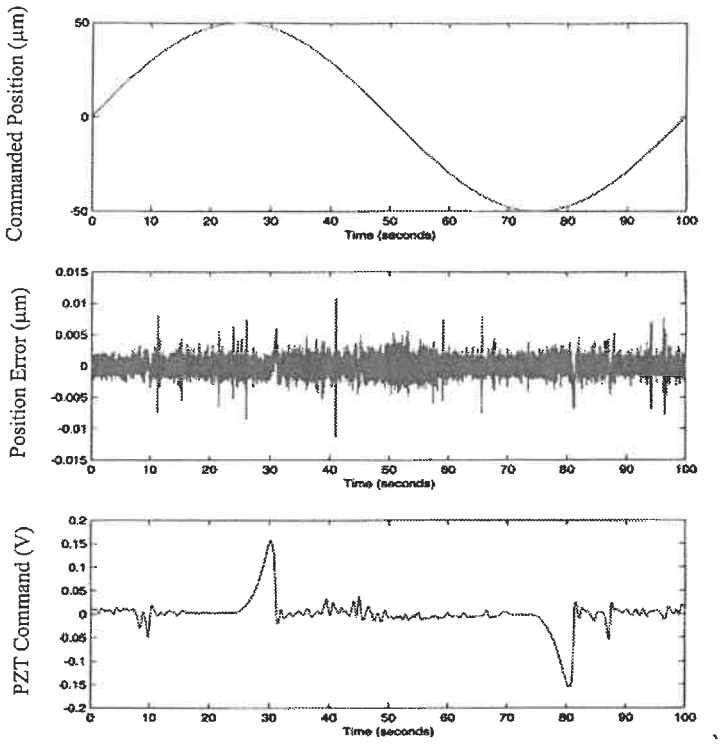

Figure 6: Control signals during a demanded sinusoidal displacement of 50 μm, upper trace is the commanded position, middle trace is the error signal to the controller, the lower trace corresponds to the voltage applied to the amplifier of the piezoelectric actuator and corresponds to the full-scale displacement of 7 μm.

---

[1] Seugling R.M., LeBrun T, Smith S.T., Howard L.P., 2002, A six degree-of-freedom precision motion stage, *Rev. Sci. Instrum.*, **73** (6), 2462 – 2468.

[2] Yang H., Seugling R.M., Jain P., Peruru H., Smith S.T., Hocken R.J, Otten D., Trumper D.L., 2004, Towards a coarse/fine approach to multi-degree-of-freedom ultra-precision motion control systems: Current status, *NSF DMII annual conference* (Dallas, TX).

[3] Lindsay K.L. Smith S.T. and Robbie C.J., 1988, Sub-nanometer surface texture and profile measurement with 'Nanosurf 2', *Annals of the CIRP*, **37**, 519-522.
-Lindsay K.L., Tetraform grinding, *SPIE*, **1573**, 129-135.

[4] Smith S.T., Yang H. and Seugling R.M., 2001, Polymeric bearings for nanotechnology applications, *Proc. ASPE*, **24**, 70-75.

[5] Hua Yang, Richard M. Seugling, Eric Buice, Stuart T. Smith, Thin film UHMWPE bearings for precision slideways *Proc. Euspen*, Glasgow, Scotland May 2004.

[6] Lawall, J., Pedulla J.M. and Coq Y.L., 2001, Ultrastable laser array at 633 nanometers for real-time dimensional metrology, *Rev Sci Instrum.*, **72**(7), 2879-2888.

[7] Wu C., Lawall J. and Deslattes R.D., 1999, Heterodyne interferometer with subatomic periodic nonlinearity, *Applied Optics*, **36** (19), 4089-4094.

[8] Holmes, M.L., Trumper D.L. and Hocken R.J., 1995, Atomic scale precision motion control stage (The Angstrom stage), *CIRP Ann.*, **44** (1), 455-460.

[9] Yang H., Seugling R.M., Jain P., Peruru H, Smith S.T., Hocken R.J., Otten D and Trumper D.L., 2004, Towards a coarse/fine approach to multi-degree-of-freedom ultra-precision motion control systems, *Proc. ASPE.*, **32**, 9 – 14.

Precision Differential Capacitor

Joe v Niekerk, Paritosh P Ambekar, Jamie G Nichol, Dave Lauben
Stanford University, CA.

Abstract

A 4-electrode multi-port precision differential capacitor to test the electronics of the Space Technology-7 (ST7) space craft has been built and tested. The differential capacitor has an intentional mismatch of 2 attofarads out of ~2 picofarads total nominal capacitance. Thus the accuracy is 1 part per million which is stable for time of order of hours.

'FastCap' computer program was used to determine the design and dimensions of the final capacitor. Required adjustability has been achieved by introducing 2 pairs of micrometers for coarse and fine adjustments. The capacitance is changed by advancing or retracting the grounded micrometer spindles in the flux path and thereby stealing more or less flux lines respectively. This mechanism of changing the capacitance in the two arms helps in achieving reproducibility and control over the change.

Change of capacitance by coarse adjustment is 30 femptofarads for each arm of the capacitor and the overlap is ~17 femptofarads. The fine adjustment had a range of 1 femptofarad with a setting resolution of 2 attofarads. The stability of capacitor was better than the Impedance Meter. All the specifications are met but some material and manufacturing improvements may be needed for future use.

2 Experimental

2.1 Design Requirements

Design and build a 4-electrode multi-port capacitance bridge having an intentional mismatch of 2 aF out of ~2 pF total nominal capacitance for the two otherwise identical primary bridge arms A-C and B-C, see Fig.1.

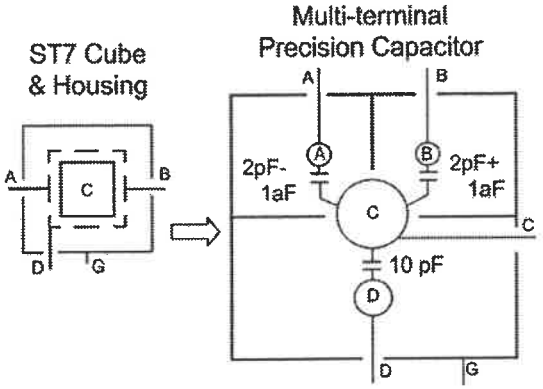

Fig.1 - Basic Concept and Requirements

The precise mismatch must be known to ± 2 aF and hold stable to 100 parts per billion. A third bridge arm C to D of ~10 pF is required for non-contact sensing of signal on C. D must be completely shielded from A and B. This requirement arose from capacitive position readout of the proof mass for the spacecraft ST7.

2.2 Design Solutions to Given Requirements

In order to achieve the stern requirements, many basic precision engineering principles were implemented while designing the capacitor. They are discussed in details in following subsections.

2.2.1 Adjustability and Required Tolerances

The required mismatch of 2 aF is 1 part per million (ppm) of the nominal bridge capacitance of 2 pF. To build a capacitance bridge with an exact mismatch of 2 aF requires manufacturing of the capacitor to a 1 ppm tolerance. For a capacitor on the scale of 100 mm this is nanometer scale tolerance. To overcome this difficulty and relax manufacturing tolerances, the capacitor is designed to be adjustable with a resolution of 2 aF.

The capacitor is constructed from a block of Macor ceramic; the conductors are created by coating holes machined into the Macor with gold. Fig. 2(a) shows cross section of the final design. It shows electrodes A, B and C in Macor, sphere D and adjustable micrometers. The assembly is covered with Aluminum shield.

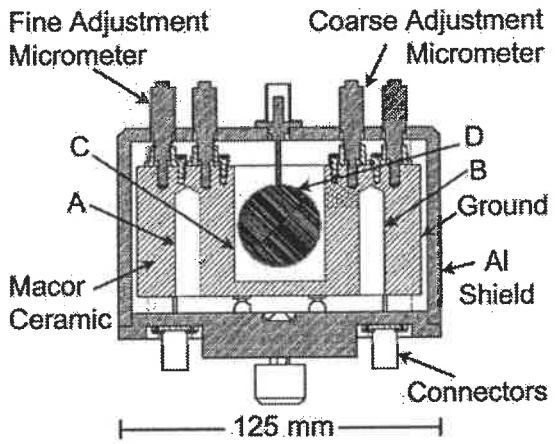

Fig 2a - Cross Section of Assembly

Fig 2(b) shows 3D cross section. Since the capacitive electrodes are rigid, adjustability of the capacitance

bridge is achieved by placing micrometer heads at ground potential in the path of the electric field between the bridge electrodes A, B and the common bridge arm C.

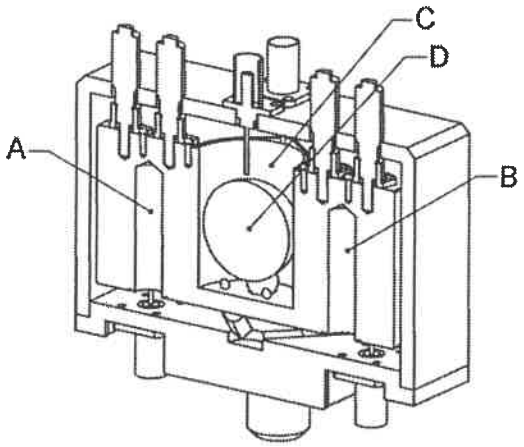

Fig 2b- 3-D Cross Section of Assembly

There are two ranges of adjustment, a coarse adjustment to match the bridge arms within 100 aF and a fine adjustment to set the exact mismatch of 2 aF. The coarse adjustment micrometers are in a direct path of the field between A, B and C and the fine adjustment micrometers in an indirect path.

The range of the coarse adjustment was chosen to allow for manufacturing tolerances on the scale of 10 μm. The limit on the range of the coarse adjustment is determined by the amount of asymmetry that is allowable. The total range of the coarse adjustment is designed to be 50 fF with 100 aF resolution. The fine adjustment was designed to have a resolution of 2 aF. The total range of the fine adjustment is 1 fF. 'FastCap', as explained later, was used to decide the positions of the micrometers.

2.2.2 Symmetric Geometry and Temperature Stability

The absolute value of the capacitances is not as important as the magnitude and stability of the mismatch between the capacitances of electrodes A to C and B to C.

On the macroscopic scale, a perfectly symmetric bridge greatly reduces the requirements on the stability of the absolute values of the bridge capacitance. If both of the bridge capacitances change by the same fraction (because of their symmetric response to a disturbance) the mismatch changes only by this same fraction, e.g. if both arms increase by 10% from 2 pF to 2.2 pF then result is the mismatch increasing by 10% from 2 aF to 2.2 aF.

The symmetry of the geometry reduces the stability requirement on the common mode capacitance of the bridge arms to 10% but for this to happen there are few symmetry requirements. First, the bridge must be symmetric in its temperature distribution. Second, the bridge should have a strict requirement on the homogeneity of the temperature. A material with a high diffusivity is favorable. Silicon is a better choice than Macor for its higher diffusivity, but Macor was chosen for its machinability and availability.

The adjustment micrometers also introduce asymmetry. The worst case is one of the coarse adjustment micrometers at full extension, the other at minimum extension. In this extreme case, it was found that the temperature difference between the arms of the capacitor must be maintained to 170 mK to ensure that the capacitance mismatch is not more than 0.1 aF.

2.2.3 Conductor Size Controlled by Insulating Block

The positions of the electrodes are very rigidly constrained in this design. There are many advantages to it. First is good vibration immunity which may have been a big problem for free conductors. Second is, using a non-porous ceramic also makes the value of the permittivity of the insulator less sensitive to changes in humidity. Third major advantage is reduced temperature sensitivity. When Macor changes its size due to temperature change, the capacitance scales with the change in dimensions. This was also verified in the FastCap computations. It is analogous to the simple parallel plate capacitor: $C = \varepsilon A / d$. For the capacitance bridge geometry, the area of the electrodes and the spacing between the electrodes scale together. The Macor block controls all these dimensions. Also it is much more rigid and controls the shape of the conductive layer.

2.2.4 Kinematic mount

It is important to keep the distance between the electrodes constant, which means, no stress should transfer from the base (e.g. stress due to temperature change) to Macor block and change its dimensions. So Macor is mounted kinematically on the base with the help of 3 spheres at the bottom of the Macor block. Also, this insures minimal transfer of heat from base to Macor block.

2.2.5 Outer shield and Stability

In order to achieve required stability, an aluminum outer shield is used. The shield is grounded and serves two purposes. Firstly, it shields the capacitor from any stray electric fields. Secondly, it helps maintain thermal homogeneity of the capacitor by providing a good heat conduction path to any heat input, thus making it less localized.

2.2.6 Shielding of D from A and B

The sensing electrode D is shielded from A and B by the design geometry. This electrode is placed inside of the electrode C. There is no path for the electric field from either electrode A or B to D. The connectors to these electrodes are located on opposite sides of the capacitor. This requirement is due to capacitive readout system employed in space craft electronics.

2.3 FastCap Field Solver

FastCap is a multi-pole accelerated capacitance extraction program for arbitrary 3-D structures, developed at MIT. It was used extensively in the design of the bridge geometry. It was used to set the nominal capacitance of 2 pF and also used to calculate the placement and size of the micrometers for the desired adjustment resolution and range. FastCap requires input files that contain the coordinates of a quadrilateral or triangular mesh. MATLAB was used to generate the meshes of the capacitor geometry. Fig. 3 shows an example of the MATLAB generated mesh that was used in the FastCap calculations.

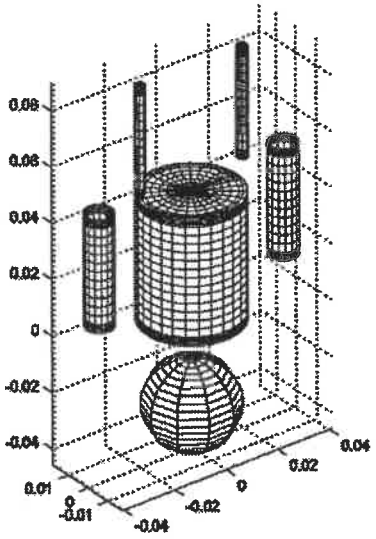

Fig. 3- MATLAB mesh

2.4 Manufacturing and Assembly

The capacitor was manufactured as per the FastCap design. Fig. 4 shows the photographs of the final capacitor which was then used for testing purposes. Spring loaded and Gold coated pogo pins were used for connecting different capacitors in the Macor block to impedance analyzer. This helped in reducing the contact impedance in the circuit.

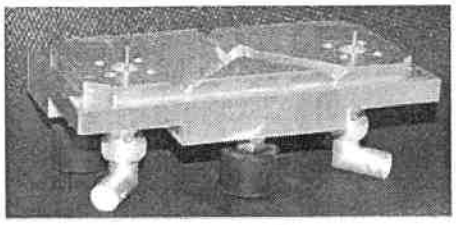

Fig 4a- Base with Connectors

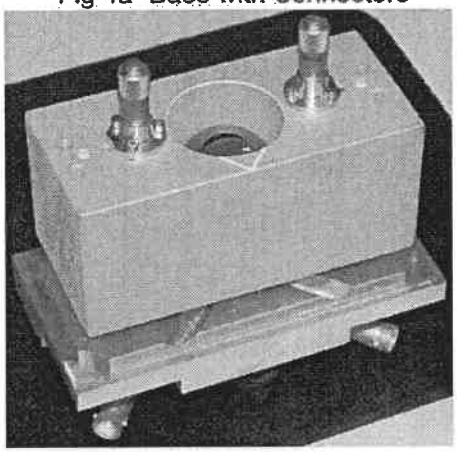

Fig 4b - Base and Macor Block

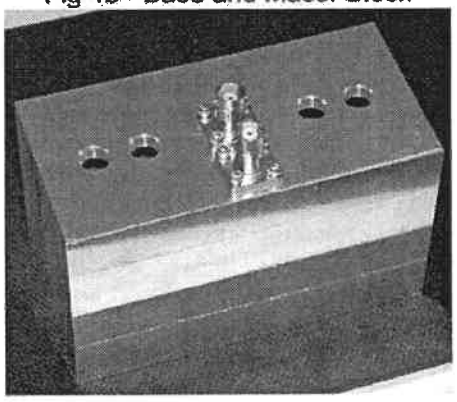

Fig 4c- Outer Aluminum Shield

2.5 Capacitance Testing

In order to check response of the capacitor to temperature changes, a known temperature change is applied, see Fig. 5(a).

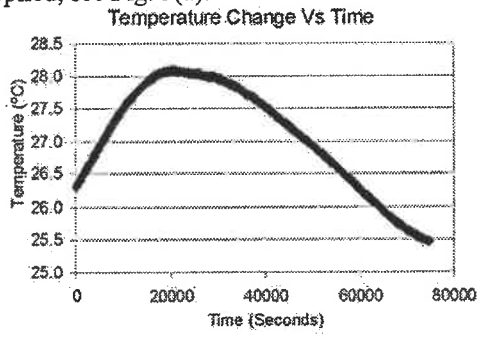

Fig 5a - Applied Temperature Change

The response of each arm was measured and plotted as shown in Fig. 5(b).

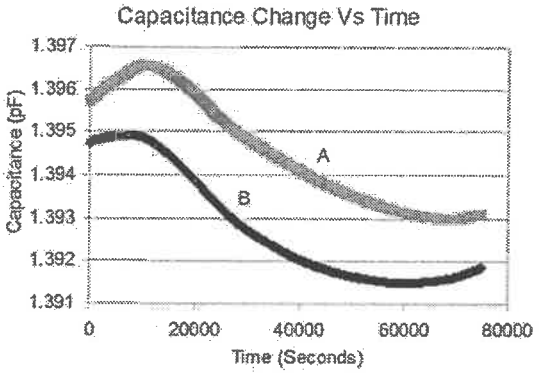

Fig 5b- Capacitance Change in Both Arms

The capacitances are changing by the same amounts with only a constant difference between them for the whole temperature change after initial settling. It shows that the employed precision engineering principles are helping in getting rid of common mode errors. It also confirms that the manufacturing errors are small and are only affecting the behavior of capacitor in linear fashion which is easy to account for.

3. Results

3.1 Primary Driven Capacitance

The final results are shown in the Fig. 6. Fig 6(a) shows variation of capacitance due to coarse adjustment micrometers.

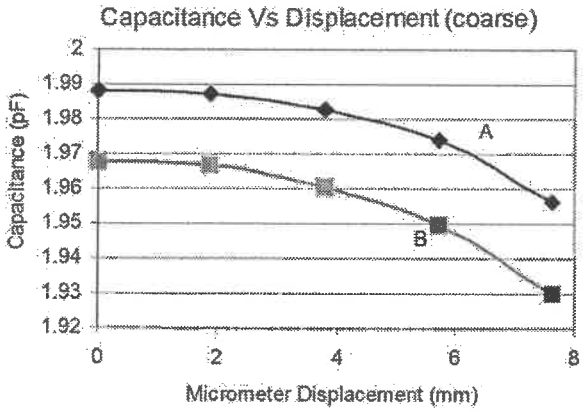

Fig 6a- Capacitance by Coarse Adjustment

The change achieved was ~30 fF for each capacitor. The slight difference between the 2 capacitances is due to the uncertainties in manufacturing as explained above. The essential part to achieve in this was the overlap of 17 fF which is actually the useful range. Fig 6(b) shows the capacitance change due to fine adjustment micrometers.

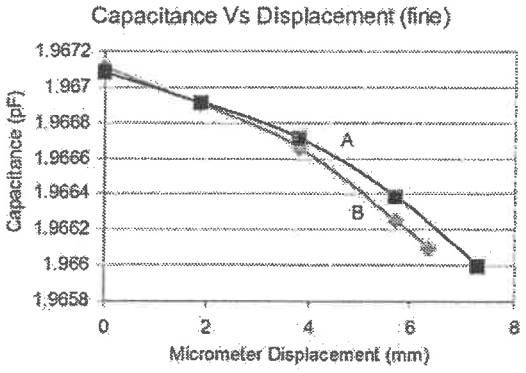

Fig 6b- Capacitance by Fine Adjustment

It can be seen that a range of 1 fF was achieved for the whole micrometer travel. On the micrometer dial, there are 500 units over the range of travel. So by changing the micrometer reading by 1 unit we can change the capacitance by 2 aF repeatably which was the requirement. There is a slight mismatch between the fine adjustments of the two arms which is due to manufacturing. For the needed change of 2 aF in capacitance, that asymmetry is tolerable. Fig. 6(c) shows a representative screen shot of the impedance analyzer.

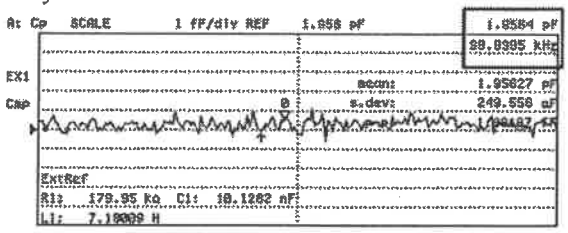

Fig 6c- Screen Shot of Impedance Meter

It shows a primary driven capacitance of 1.9564 pF at 100 kHz frequency. It also shows that the stability of the capacitor is better that 1 fF, which is the stability of the impedance analyzer. The noise in the figure is due to the impedance analyzer.

3.2 Pick-up Capacitance

The requirement for pickup capacitance was 8-12 pF. It was seen that the pickup capacitance is 11.1302 pF at 100 kHz frequency. This capacitance is also more stable than the impedance analyzer.

Summary

A 4-electrode multi-port precision differential capacitor that has an intentional mismatch of 2 attofarads out of ~2 picofarads total nominal capacitance has been successfully built and tested. Many precision design principles were used in order to achieve desired accuracy and stability. The differential capacitor has accuracy of 1 part per million and it is stable for time of order of hours.

PROGRAMMABLE RING GAGE

Faiz Warsi, Christopher Huntsinger and Robert Hocken
Center for Precision Metrology
Department of Mechanical Engineering
The University of North Carolina at Charlotte, Charlotte, NC 28223

Keywords: Ring gage, flexible ring gage, flexure, bore gage

1. Introduction

Ring gages are widely used in industries and metrology labs as masters for setting bore gages. They come in different sizes and for every different size of bore to be measured a ring gage of that particular size has to be available. These ring gages need to be maintained in a temperature controlled environment and should be used at 20° Celsius in order to maintain accuracy. The need of temperature-controlled environment to store these masters comes at a cost. Also periodic re-certification (i.e. calibration) and replacement of worn out ring gages contributes to the maintenance cost. The current process of measuring is tedious and inconvenient to personnel involved in the process. Our goal is to design, build and validate an electromechanical computer operated device for use as a sizing master to set bore gages. The aim of our research is to replace the concept of master rings (or ring gage) used currently in industry with a robust easy to use device.

2. Design Aspects

The design of this programmable ring gage was based on the following customer supplied specifications:

1. Two point measuring system.
2. Range of 1" – 3".
3. Measuring Accuracy of 10μinches.
4. Operating temperature range of 15 – 55° C

Figure 1 shows the schematic of our design. The main components of the programmable ring gage are:

a. Base
b. Ram
c. Flexure
d. Drive Mechanism
e. Anvils
f. Air Bearings

The material used for the programmable ring gage is Aluminum 6061- T6. All parts are machined out of the same material in order to minimize the effects of differential expansion and temperature gradients on the measuring accuracy of the system.

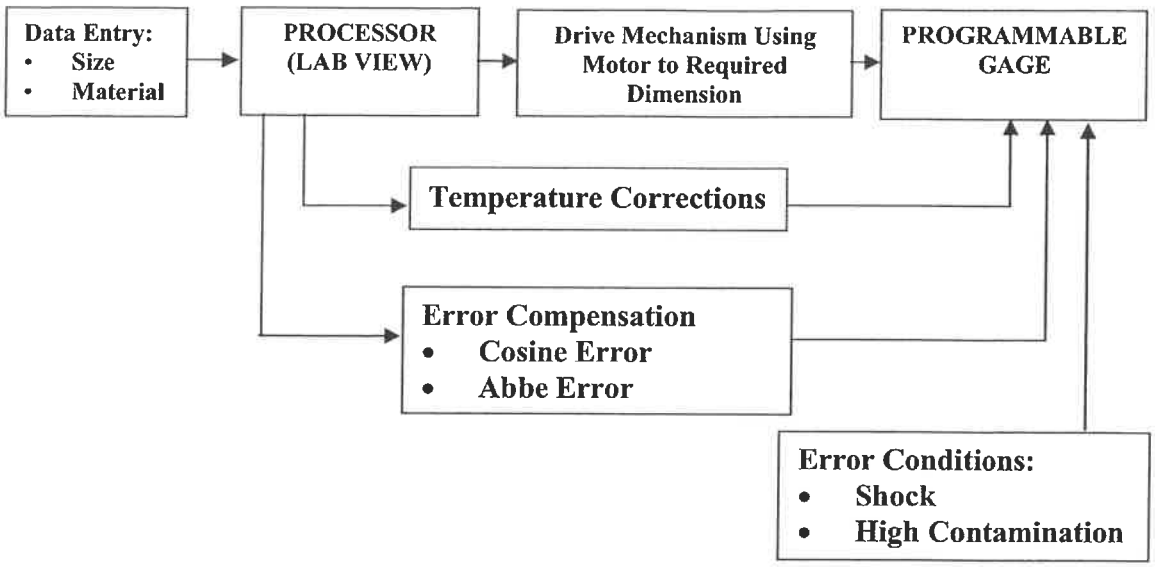

Figure 1: Schematic of our Design

A frameless, brushless DC motor provides motion to a non-influencing drive mechanism that connects to the ram. The ram slides over the base on air bearings, the surface of which is diamond turned. The ram is constrained from all the four sides by air bearings, two on either side and four each on the top and bottom of ram. A 5nm resolution glass scale tracks the movement of the ram. Refer to **figure 2** and **figure 3** which show the assembled and exploded views of the gage.

The anvils are made out of Aluminum oxide with the radius of the largest circular diameter to be measured (i.e. 3"). Aluminum oxide is a very hard (3000 HK) and wear resistant material form a better material than Aluminum for measurement purposes. The anvils are so designed so that they can be replaced with new ones in case they show signs of wear.

We know that when a force is applied to an object it deforms, similarly when the distance between the anvils is set to the required dimension and a bore gage is inserted between these anvils the ends of the bore gage in contact with the anvils will deform. This deformation is well represented by the **Hertzian** model. In order to provide force measurement to allow compensation for the deformation due to contact forces, a flexure is provided which is designed for the maximum travel of 200 microns at 5N load. A capacitor at the back of the flexure tracks the distance moved depending on the amount of force applied. A computer program will calculate the deformation based on displacement that then moves the ram accordingly to compensate for the deformation.

Temperature sensors are provided, one at the scale and other to measure the room temperature; this is done so we can compensate for the part dimensional changes due to temperature. This is done in such a way that the part when measured using this ring gage measures as it would when measured at 20°C. The system will be calibrated with zerodur masters so that the actual spacing between it anvils is know throughout the operating temperature range. When is use, the anvil spacing will be corrected for the nominal expansion of the part to be measured so as to provide temperature compensation. The uncertainty in this computation due to the uncertainty in the nominal coefficient of expansion and the uncertainty in the temperature measurement will be computed and reported to the user.

Mechanical limit switches are provided one on either end of the ram to prevent damage from over-travel. Other accessories provided are a pressure switch to prevent damage to air bearings in case of non-operating air pressure through the channels. A fault detector is provided in order to indicate the location of a problem incase of some failure in the system.

Air provided to the system is filtered through a coalescing filter and a desiccant drier before being fed into the channels. A flow meter and a regulator keep track of the air flowing through the system to maintain the proper flow for the required air gap (2 microns in our case).

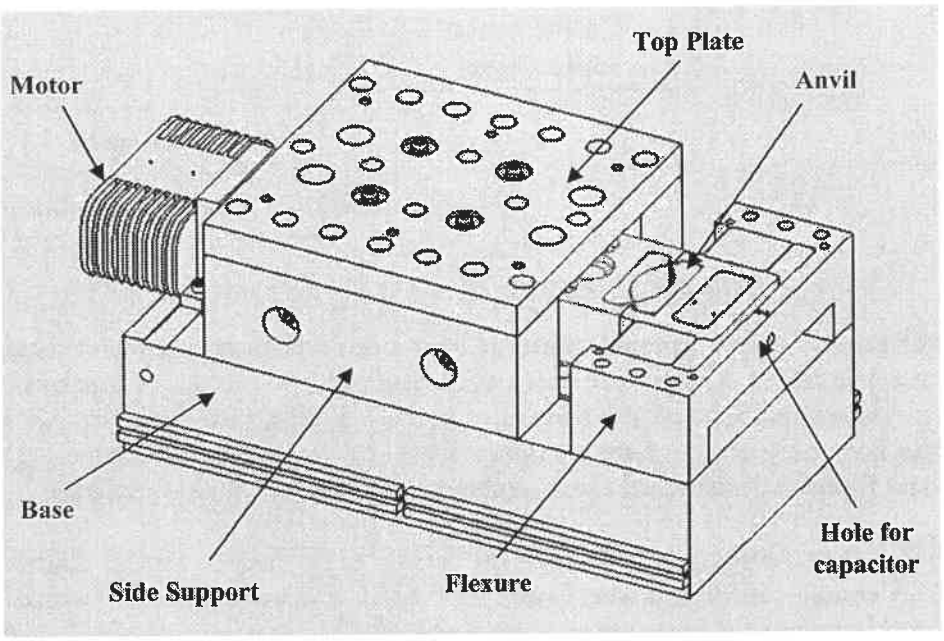

Figure 2: Assembled view

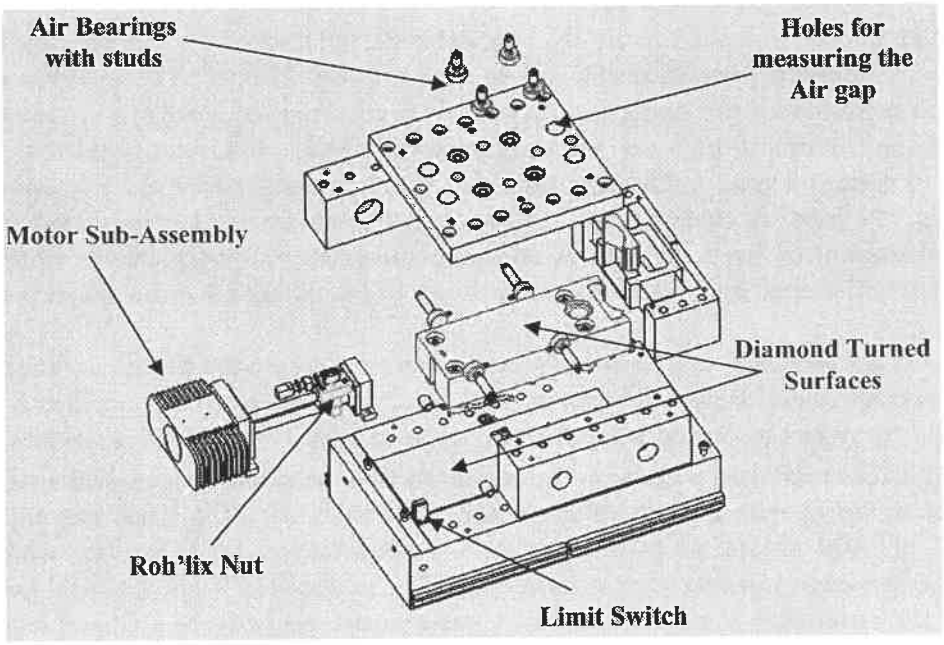

Figure 3: Exploded View

3. Conclusions and Future Work

Currently, there is no flexible instrument to set bore gages that performs temperature and force deformation compensation. The programmable ring gage will be computer-operated and will use lab-view to compute corrections for temperature difference and force behavior of different bore gages. The device will also be equipped with temperature sensors that will monitor the temperature for software correction, thus reducing the requirements for a temperature controlled environment. Contact forces will be measured by measuring the displacement of a calibrated flexure that is part of the device. This paper describes a concept, design of the instrument, and the operation. The overall goal of this project is to provide a robust easy to use measuring device, which can improve the accuracy as far as is practically possible in a workshop environment.

References

[1] Smith, S.T. Flexures: Elements of Elastic Mechanisms. Gordon and Breach, Inc. 2000.

[2] Slocum, A.H. Precision Machine Design. SME Press. Dearborn, Michigan. 1992.

[3] Smith and Chetwynd Ultraprecision Mechanism Design. Gordon and Breach 1992.

The Analysis and Compensation of Position Error in Scanning Type XY Stage from Motion Error Measurement

Jooho Hwang*, Chun-Hong Park*, Chan-Hong Lee*, Seung-Woo Kim**

* Machine Tools Group, Department of Intelligence and Precision Machine, Korea Institute of Machinery and Materials, 171, Jang-dong, Yuseong-Gu, Daejeon, 305-343, Korea
** Department of Mechanical engineering, Korea Advanced Institute of Science and Technology, 373-1, Gusung-dong, Yuseong-Gu, Daejeon, 305-751, Korea

1. Introduction

The scanning type XY stage is frequently used these days as precision positioning system in equipment for semiconductor or display element. It is requested higher velocity and more precise accuracy for higher productivity and measuring performance. The position accuracy of general stage is primarily affected by the geometric errors caused by parasitic motion of stage, misalignments such as perpendicular error, and thermal expansion of structure. In the case of scanning type stage, H type frame is usually used as base stage which is driven by two actuators such as linear motor. In the point view of scanning process, the stage is used in moving motion. Therefore, dynamic variation is added as significant position error source with other ordinary error sources. Because the scanning axis is driven by two actuators with two position detectors, 2 dimensional position errors have different characteristic compared to general tacked type XY stage.

In this study 2D position error of scanning stage is analyzed by 1D heterodyne interferometer calibrator, which can measure 1D linear position error, straightness error, yaw error and pitch error, and perpendicular error. The 2D position error is evaluated by diagonal measurement (ISO230-6). The yaw error and perpendicular error are compensated on the base stage of scanning axis. And, the horizontal straightness error is compensated by cross axis compensation.

2. Configuration of scanning type XY stage

As shown in Fig. 1, the XY stage has H type base stage which is driven by two linear motors (LM310-4, Trilogy) with 300mm strokes. The position of base stage is detected by precise optical linear scale (LIP481, HeidenHain). The step axis is moved perpendicularly to scanning axis in base stage. Y axis is driven by two linear motors simultaneously. A PC based motion control board with P-I-D filter (PMAC2, Delta Tau) is used for controlling position error.

These X and Y axes are moved on the granite bed, which is vertical guide ways of two stages, to reduce moment force in the high acceleration. The double pad type aerostatic bearing is used as constraining

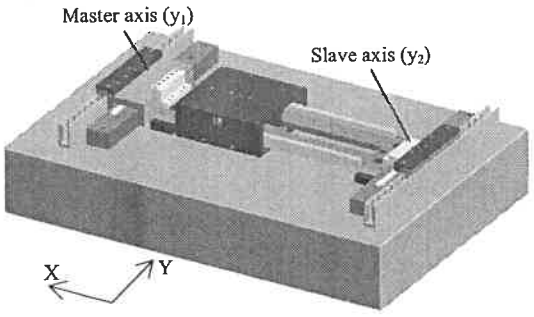

Fig. 1 Schematic diagram of Scanning type XY Stage

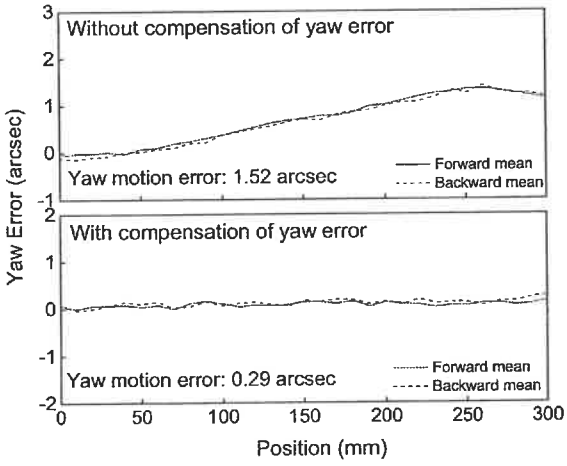

Fig. 2 Compensation of yaw error in base stage

horizontal motion. The linear motor near horizontal bearing is named as master and the other axis is slave.

3. The 2D position error models of scanning type stage

The formulation of the 2D position error for two axis cartesian machine is explained as equation (1). Where, ε is rotation motion observing right hand rule and subscript x,y,z is rotation axis. The subscript 1 means motion in the base stage and 2 means the other stage on the base stage. δ is linear motion error of the stage, one is 1D position error of the stage and the other is horizontal straightess error of the cross axis. And, θ_{12} is perpendicular error of the stage 1 and 2. The a, b, c represent amount of translation along three axis.

$$\begin{bmatrix}\delta P_x\\ \delta P_y\end{bmatrix}=\begin{bmatrix}-t_y(\varepsilon_{z1}+\varepsilon_{z2})+t_z(\varepsilon_{y1}+\varepsilon_{y2})-b_2\varepsilon_{z1}+c_2\varepsilon_{y1}-a_2(1-\cos\theta_{12})+\delta x_1+\delta x_2\\ t_x(\varepsilon_{z1}+\varepsilon_{z2})-t_z(\varepsilon_{x1}+\varepsilon_{x2})+a_2\varepsilon_{z1}-c_2\varepsilon_{x1}+a_2\sin\theta_{12}+\delta y_1+\delta y_2\end{bmatrix} \quad (1)$$

$$\begin{bmatrix}\delta P_x\\ \delta P_y\end{bmatrix}=\begin{bmatrix}-t_y(\varepsilon_{z1}+\varepsilon_{z2})+t_z\varepsilon_{y2}-a_2\varepsilon_{z1}+\delta x_1+\delta x_2\\ t_x(\varepsilon_{z1}+\varepsilon_{z2})-t_z\varepsilon_{x2}+a_2\theta_{12}+\delta y_1+\delta y_2\end{bmatrix} \quad (2)$$

In the scanning type stage, the equation (1) can be simplified to equation (2), from b_2, c_2 is 0 and geometric difference such as no effect of rolling motion of base stage on the step axis.

4. Evaluation and compensation of 2D position errors

The 2D position error is evaluated by diagonal measurement (ISO230-6), which has advantage of simple and quick measuring process, because the 2D position error is evaluated from two times of diagonal 1D positioning accuracy. However, it can't represent volumetric error, when the length of the body diagonal is caused by several source of error are cancelled out by the other sources of errors [2]. However, it is possible to evaluate accurately, if other sources of errors are measured to evaluate 2D position error. Therefore, following procedure is used for evaluation and compensation of 2D position error. 1) Yaw error of base stage is measured and compensated. 2) The linear position error of base stage is simultaneously measured and compensated in master and slave axis. 3) The 1D position error of step axis(Y) is measured and compensated according to position of X axis stage. 4) Perpendicular error is compensated in mechanical connector and slave axis. 5) Position error, which is due to straightness errors of cross axis, is compensated in cross axis. The Diagonal measurement is performed to evaluate 2D errors in middle and end of the procedure. In this research, conventional laser interferometer system (HP5529A) is used as calibrator and the

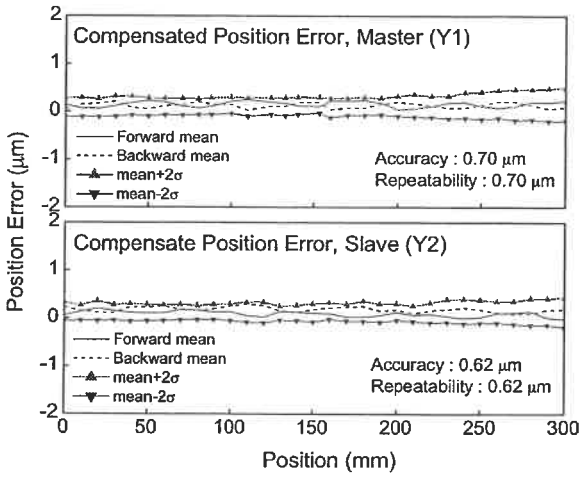

Fig. 3 Compensation of position error in base stage

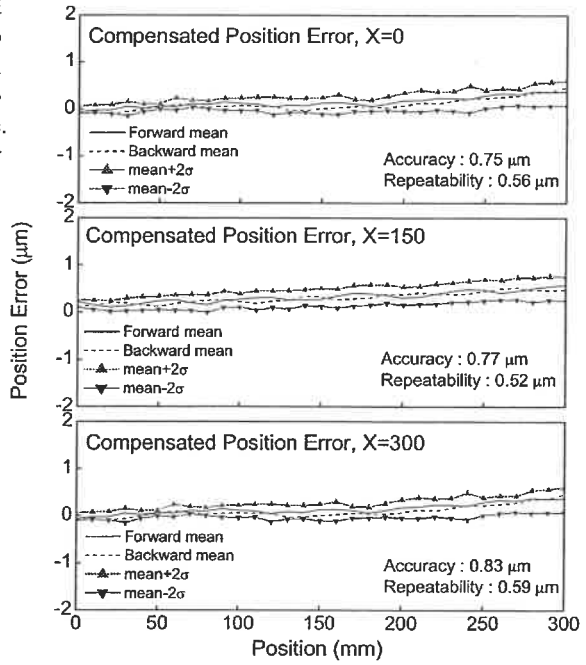

Fig. 4 Positioning accuracy of position error of moving table in scan axis(Y)

measuring point, which is explained in t in equation (1) and (2), is center of moving table.

4.1 Compensation of the scan axis(Y)

Although, the position of scanning axis is detected by two optical encoders in the base stage, the yaw error(ε_{z1}) is remained as shown in Fig. 2. From each errors of yaw along the position of scanning axis(Y) is compensated by the small adjustment of relative position of the slave axis(y_2). The small adjustment of yaw error is absorbed in gab of aerostatic bearing. For the safe of aerostatic bearing, amount of relative position is limited within 20μm in this research. The 1D position error of base stage is measured in master (y1) and slave (y2) axis. The position error of base stage is shown in Fig. 3 which is represented as equation (3). The position error can be compensated by command compensation in y1 and y2 axis as shown in Fig. 3.

$$\delta P_{y1} = t_x \varepsilon_{z1} - t_z \varepsilon_{x1} + \delta y_1 \tag{3}$$

The important error is position error of moving table on base stage, which is represented as equation (2). To obtain accurate position in the moving table, it has advantage that the pitching motion error, ε_{x1} and ε_{x2} have similar profile. If the scanning axis has different pitching motion profile, the command compensation is very difficult because the scanning axis is driven by two linear motor. The scanning type stage used in this research has similar pitching motion profile, because the surface profile of granite bed has similar profile along the y axis and the length of stage along Y axis are same. As shown in Fig. 4, the command compensation in base stage has good effect on moving table of stage along Y direction. The result of Fig. 4 is explained as compensation of left three terms and δ_{y1} in equation (2) for δp_y, because three different 1D positioning measurement of origin is resetting.

4.2 Compensation of the step axis(X)

The position error of step axis is measured and compensated 3 different Y position, Y=0, Y=150, and Y=300. This compensation table has 2D position data according as position of X and Y axis. The results are shown in Fig. 5, which represents compensating left four terms and δ_{x2} of equation (2) for δp_x.

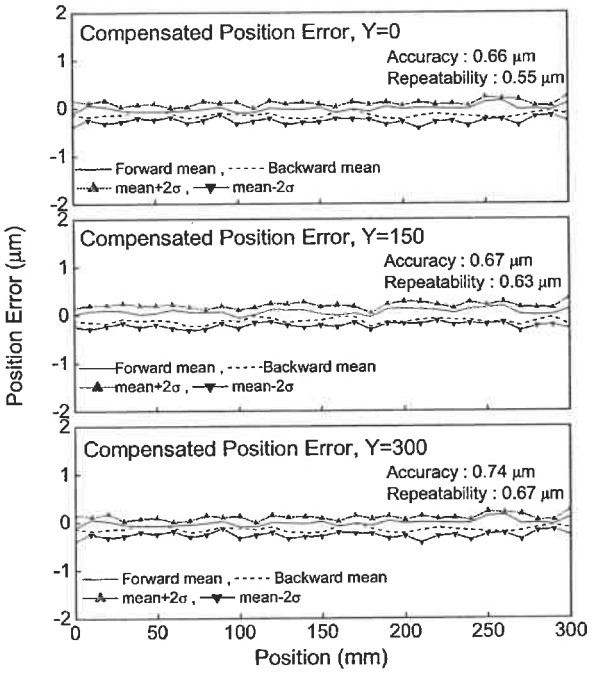

Fig. 5 Compensation of position error in step axis(X)

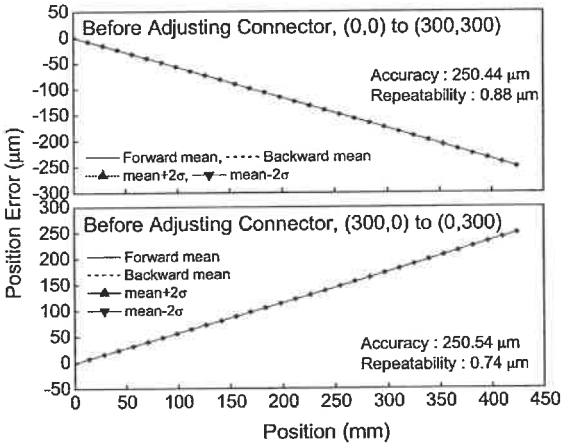

Fig. 6 Position error on diagonal measurement

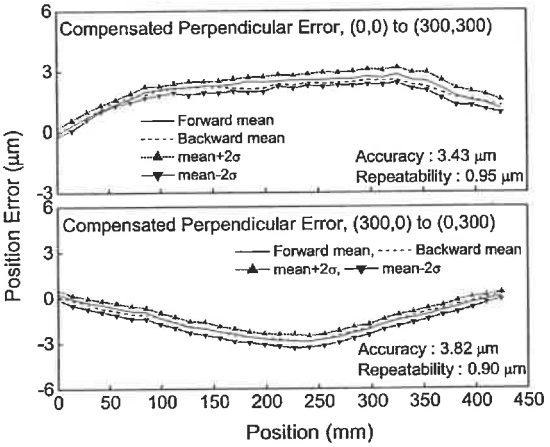

Fig. 7 Position error on diagonal measurement after compensating perpendicular error

4.3 Compensation of perpendicular and straightness error

The diagonal measurement is usually performed from one corner to the other corner of combined machine axis. Therefore, it represents all terms (error sources) of equation (2). The results of diagonal measurement shows similar amount of error and different sign in Fig. 6, which is typical error pattern of perpendicular error. The perpendicular error (θ_{12}), which has effect on position error of δp_y in equation, is obtained by diagonal measurement or squareness measurement system of interferometer, which is difficult but precise method than diagonal measurement.

The perpendicular error is adjusted in mechanical connector and finally compensated by relative position of slave axis. After compensating perpendicular error, the result of diagonal measurement is shown in Fig. 7. From the equation (2), the remained curved error in Fig. 7 is expected as horizontal straightness error of the cross axis. To compensate straightness error, measured straightness error shown in Fig. 8 is corrected by small shift of cross axis. For example, for compensating 3μm of straightness error of Y axis, the position of X axis is shifted 3μm opposite direction. The effect of compensation is shown in Fig. 9. And, the effect of straightness error on diagonal measurement is shown in Fig. 10. The curved shape error from straightness in Fig. 7 is decreased to about 1.5μm.

5. Conclusion

In this research, 2D position error of scanning type stage is modeled and analyzed. The 2D position error is evaluated by diagonal measurement and its error is corrected by compensating yaw motion error of base stage, 1D position error, perpendicular error and straightness error. From the compensation, the result of diagonal measurement is improved to 1.57μm. The considered 2D motion error this research is static error, the dynamic error in scanning motion will be analyzed in the future.

Acknowledgement

The author gratefully acknowledges the supports of Ministry of Science and Technology and Korea Institute of Machinery and Materials.

References

[1] A.H. Slocum, Precision Machine Design, Prentice Hall, 1992

[2] Mark A. V. Chapman, "Limitations of laser diagonal measurements," Precision Engineering, Vol. 27, pp. 401-406, 2003.

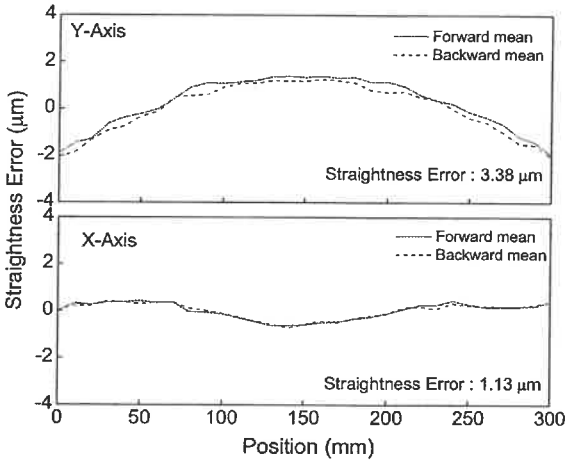

Fig. 8 Horizontal straightness errors of Y and X axis

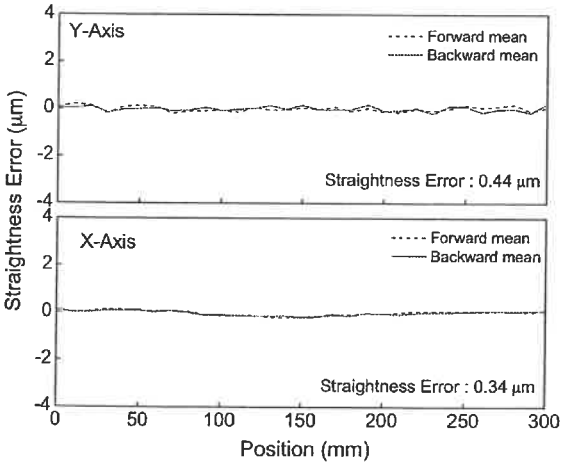

Fig. 9 Compensation effect of straightness error

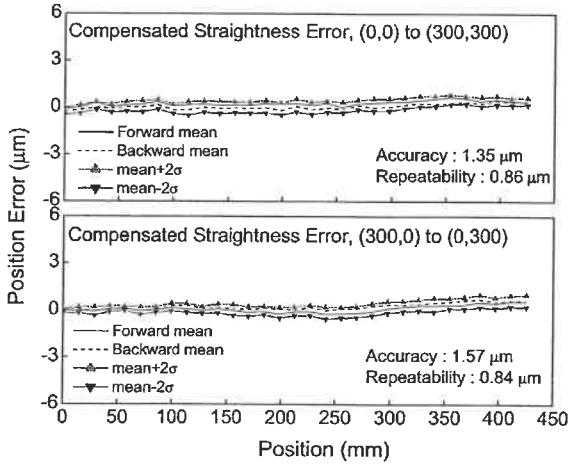

Fig. 10 Position error on diagonal measurement after compensating straightness error

Kite Square

Jimmie A. Miller, Edward P. Morse, John A. Nettles, Jeremy S. Turner
Center for Precision Metrology
The University of North Carolina at Charlotte, Charlotte, NC 28223

Introduction

Presented is a new technique for independently determining the out-of-squareness of machining centers (MCs) or coordinate measuring machines (CMMs). The method is based upon a self-calibrating scheme and related device. Various embodiments allow for measuring machines with diverse work volume dimensions and also for vision CMMs. The term "Kite Square Technique" is used to refer to the utilization of a "Kite Square" device to obtain the out-of squareness parametric term. Results from measurements taken on a CMM with touch probe, a MC, and also a CMM utilizing a visual probe are given.

The Kite Square Technique

Figure 1. Geometric Kite

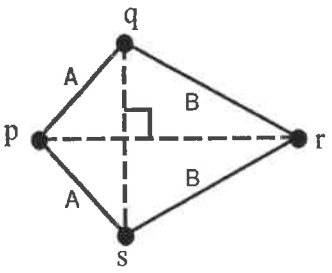

A geometric "kite" is a quadrilateral in which each side is adjacent to another side of the same length. In Figure 1, pq and ps have length A whereas qr and rs have length B. An additional advantageous property is that the two line segments between opposing vertices are perpendicular. That is, pr is perpendicular to qs.

Figure 2 shows a conceptualized gage consisting of three artifacts (1), (2), and (3) attached together via a rigid support structure (4). The three artifacts (1), (2) and (3) are at positions (5), (9) and (10), respectively. Allowing the rotation of artifacts (2) and (3) about a line of rotation (6) which passes through the positions (9) and (10) of the artifacts (2) and (3) respectively, artifact (1) thus moves from position (5) to position (7). Since the distances between position (5) and (9), and (7) and (9) are the same along with equal distances between (10) and (5), and (10) and (7), we have generated a kite with vertices at the position of our artifacts. Resultantly, positions (5) and (7) establish a reference line (11) at a right angle with respect to the line of rotation (6). Thus we have a square artifact that is self-calibrated. Rotation about the line through positions (9) and (10) can be effected through the use of kinematically seated precision spheres utilized as artifacts. In three dimensions, artifact (1) rotates in a circular motion within a plane having line (6) as a normal (perpendicular to the plane). This is useful for measuring the out-of-squareness of vertical carriages. By mounting the Kite Square on the table of a machine and subsequently measuring the initial positions of artifacts (1-3) and rotated position of artifact (1) with sensors (not shown) attached to the tool/probe location of a ram, spindle etc. of a machine, the determination of a machine's ability to move its' tool or probe in an orthogonal manner across a plane can be determined.

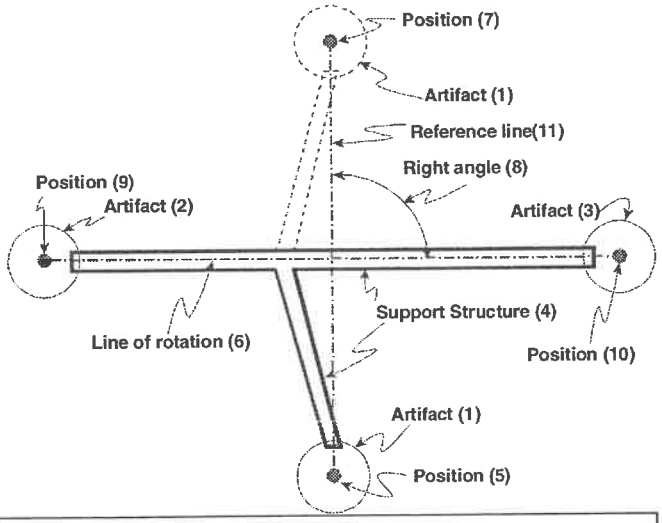

Figure 2. Conceptual Kite Square

A Kite Square

An embodiment of this concept used to measure the out-of squareness of a CMM is shown in Figure 3. The precision spheres used as the kite square artifacts have spherical deviations below one-tenth micrometer. The procedure to get data for one measurement set is simple. The locations of three spheres were measured in one orientation and subsequently in the flipped orientation. Using the X-Y positions of the spheres you can first calculate two lines between the opposite vertices of the kite and then the deviation from square. The actual equations used are given later.

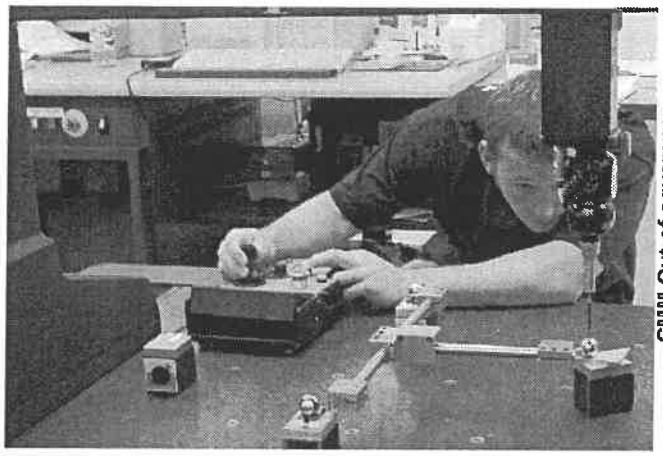

Figure 3. Kite square in use on CMM

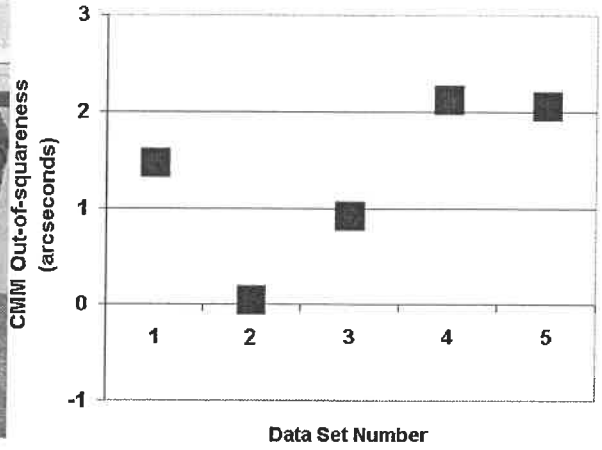

Figure 4. Out-of Squareness for CMM.

The out-of-squareness calculated from five data sets are shown in Figure 4. The average is 1.3 arcseconds. Two possible sources of variation in data are probe repeatability and kinematic seating repeatability. A source of measurement bias is deviations in position due to the beam bending of the fixture. The beam may stretch along the direction of the axis of rotation in one orientation and shrink in the other orientation if the rods connecting the two balls are bent differently depending on the orientation. This can be seen in the data. Correcting the calculations for this lowers the squareness values by 1 arcsecond. Shortening the connecting rods may eliminate this effect.

This kite square was also used to measure the out-of squareness of a machining center as shown in Figure 5. Instead of touch probe measurement as for the CMM, a capacitance sensor[1] was used to first set up the gage and then measurements. Setup was accomplished by first measuring the X,Z machine coordinates for obtaining a maximum reading against the ball that was constrained in three linear degrees of freedom, then moving the machine (Y) so that the capacitance sensor gave a nearly zero nominal displacement reading. The sensor was then moved to make measurements on the second ball constrained in two linear degrees of freedom. After finding the appropriate X-Z position and keeping the Y position as for the previous ball, the kinematic mount was tapped with a rawhide hammer to obtain a sensor scale reading near that of the

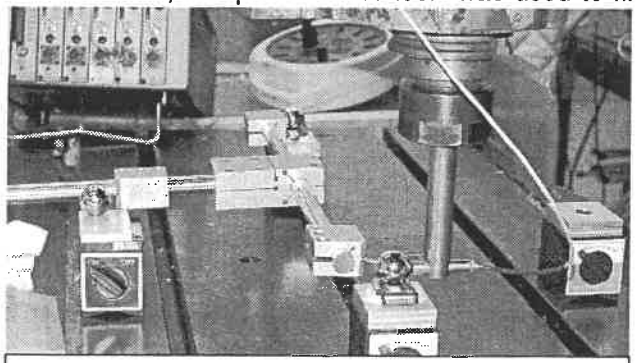

Figure 5. Setup on Vertical Machining Center

[1] Manufactured by Lion Precision, Inc.

first ball. Also, the adjustable mount of the swinging ball was moved along the mounting rod to get it within the working range of the machine. Then the nominal X,Y,Z locations for the swinging ball in both orientations were determined using the previous methods. A machine program was written to step between the two locations of the swinging ball keeping the X coordinate the same and reading the capacitance sensor displacement at each location. The readings for one data set varied by about 2 micrometers due to the servo action of the machine. Whenever the kite square was flipped, the fixture was tapped by a rawhide hammer to get a repeatable seating in the kinematic mount. Ten sets of data were obtained and the repeatability of the swinging ball location data taken from the capacitance sensors is shown in Figure 6. Position C and D are the two positions of the swinging ball. Using the average values we obtained an out-of-squareness value of 4 arcseconds for the machine. This data is in line with out-of squareness values obtained with laser diagonals measurements and other techniques. A one-to-one correspondence to other data is not expected due to the model of squareness used (discussed later) and a knowledge that this machines' out-of-squareness has been previously determined to change a few arcseconds with the ambient temperature. During these measurements the temperature was kept near 20° C.

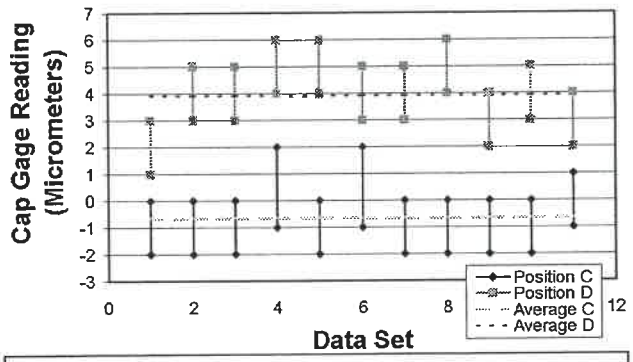

Figure 6. Repeatability of Measurements

In order to use the Kite Square Technology on a vision based CMM, a change in design was necessary since a sphere is a poor reference artifact for determining location visually. Figure 7 shows the resulting design and embodiment incorporating sphere and kinematic mounting for rotation but includes separate artifacts that can be measured using the camera and light sources of the machine. Figure 7(A) shows an isometric view taken from the drawings showing the placement of the artifacts. These recessed artifacts, produced by electro-discharge machining, each have a diameter less than 500 micrometers. Figure 7(B) shows the actual device on a visual CMM. Figure 7(C) is the visual image of one of the artifacts as viewed by the visual CMM. Notice that there is a pair of balls for allowing the swinging artifact to rotate in order to keep it viewable at all positions. This design enables the measurement of vertical as well as horizontal squareness. Actual use of the visual CMM Kite Square revealed a few flaws in the design. First, placement of one of the hole artifacts prohibited the use of backlighting to get the position in one critical orientation. Second, the artifact placement was not sufficiently near the axis of rotation resulting in a rather large uncertainty. For these reasons the resulting calculations are not given at this time.

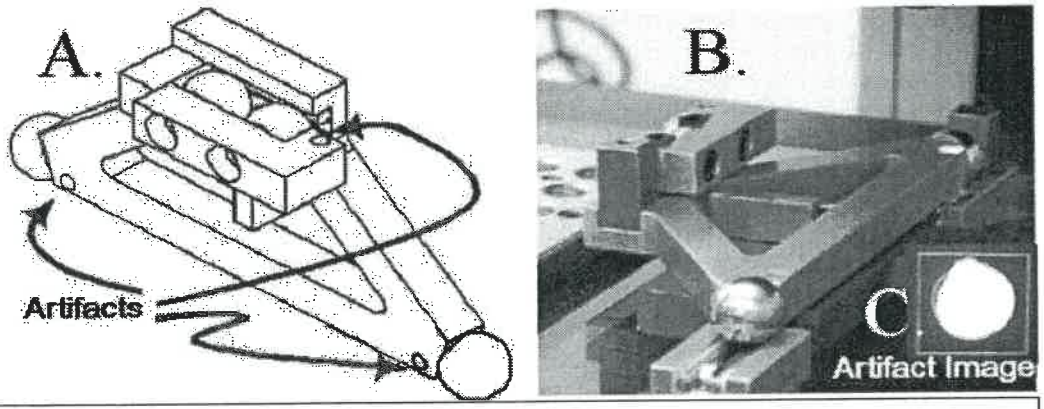

Figure 7. (A) Drawing showing artifacts, (B) on visual CMM, and (C) image of artifact on this Kite Square design.

General Mathematics:

These mathematics assume a kinematic rotation of the device while allowing, in general, artifact positions (2) and (3) to not necessarily lie along the line of rotation (6). For clarity, assume a two dimensional case. Let subscript B denote the measured position of the artifact before rotation and subscript A denote a position measured after rotation along line (6). Let $P_{1B} = (X_{1B}, Y_{1B})$, $P_{2B} = (X_{2B}, Y_{2B})$ and $P_{3B} = (X_{3B}, Y_{3B})$ etc. The squareness value α (radians) is related by the following equation:

$$\tan(\alpha) = \frac{X_{1A} - X_{1B}}{Y_{1A} - Y_{1B}} - \frac{\frac{1}{2}(Y_{3B} + Y_{3A}) - \frac{1}{2}(Y_{2B} + Y_{2A})}{\frac{1}{2}(X_{3B} + X_{3A}) - \frac{1}{2}(X_{2B} + X_{2A})} = \frac{X_{1A} - X_{1B}}{Y_{1A} - Y_{1B}} - \frac{Y_{3B} + Y_{3A} - Y_{2B} - Y_{2A}}{X_{3B} + X_{3A} - X_{2B} - X_{2A}}.$$

If the line of rotation (6) passes through positions P_{2B}, P_{2A}, P_{3B} , and P_{3A} , so that, $P_{2B}=P_{2A} = P_2$ and $P_{3B}=P_{3A} = P_3$ then $\tan(\alpha) = \frac{X_{1A} - X_{1B}}{Y_{1A} - Y_{1B}} - \frac{Y_3 - Y_2}{X_3 - X_2}$ or for small angled squareness values where α is approximately equal to the sine of α, we have $\alpha = \frac{X_{1A} - X_{1B}}{Y_{1A} - Y_{1B}} - \frac{Y_3 - Y_2}{X_3 - X_2}$.

For non-kinematic rotation, more sophisticated mathematics are required.

Machine Modeling in Light of the Kite Square

There are at least two different mathematical approaches to volumetrically model the errors of a machine. One is frame-based and the other is table-based (part-based). In the frame-based approach, the mathematics corresponds to the errors (straightness, linear positioning, angular) of each carriage being referenced to a coordinate system associated with the stationary frame or base of the carriage. In the table-based approach, the errors of a tool or probe are referenced to a coordinate system that is associated with the component of the machine on which a part or workpiece is mounted. National industrial standards for performance evaluation typically (but not consistently) follow a table-based approach to measuring the parametric errors of machine tools and CMMs with measurement lines midway in the work volume. If we use a modeling approach that is table-based and we measure errors along or near the axes of the modeling coordinate system, then the angular errors do not influence the displacement measurements. The straightness errors can be defined to be zero at two fixed points along each modeling coordinate system axis leaving the remaining lateral displacement error to be defined as squareness. This is possible because the errors due to squareness complement the straightness errors and any slope removed from the straightness finds its way in the squareness term. For example, we can choose a 10%-90% rule to define the straightness to be zero at 10% and 90% of the range of motion for each carriage.

Conclusions

We have disclosed and demonstrated novel metrology tools dubbed Kite Square for measuring the out-of-squareness of manufacturing and measuring machines having orthogonal axes. Their versatility and simplicity should enable it to replace more expensive and weightier devices in current use.

Acknowledgement:

This work was supported by the industrial affiliates of the Center for Precision Metrology, a National Science Foundation Industry / University Cooperative Research Center supported under grants #EEC9811556 and #EEC0331950. Any opinions, findings, and conclusions or recommendations expressed in this material are those of the author(s) and do not necessarily reflect the views of the National Science Foundation.

Effects of Targeting Spherical Surfaces with Capacitive Displacement Sensors

R. Ryan Vallance
Precision Systems Laboratory, The George Washington University
738 Phillips Hall, 801 22nd St., N.W., Washington, DC 20052

Eric R. Marsh
Machine Dynamics Research Laboratory, The Pennsylvania State University
21 Reber Building, University Park, PA 16802

Philip T. Smith
Mechanical Engineering, University of Kentucky
015 Ralph G. Anderson Building, Lexington, KY 40506

1 Introduction

Within the field of precision engineering, capacitive sensors are used to sense fine motion, measure positioning error (e.g., straightness, squareness, and ball bars), and inspect workpieces (e.g., roundness, cylindricity, sphericity). Capacitive sensors present a relatively inexpensive, robust, and easy-to-use solution to these and other measurement challenges.

A common realization of the capacitive sensor is a sensing electrode and guard ring enclosed within a grounded sensor body. Fig 1 shows this configuration in a commercial sensor used in precision applications. The sensor is positioned perpendicular to a target electrode formed by a conductive surface in a workpiece, machine, or instrument. In many cases the target surface is flat, but other applications common in machine and workpiece metrology require curved target surfaces. For example ASME standards for evaluating machine tools [1,2] describe several tests to measure errors with capacitive sensors targeting spherical or cylindrical surfaces. Another example is the ultra-precision measurement of spindle error motion, which is usually made with capacitive sensors and lapped spherical artifacts [3,4].

It is standard practice for commercial capacitive sensors to be factory calibrated with flat target surfaces. This paper shows how measurements taken with sensors targeting spherical surfaces lead to four sources of error if the sensors are calibrated with flat targets. First, the sensitivity of the sensor increases resulting in exaggerated displacement measurements. Furthermore, the sensing range is both decreased and shifted towards the target. Finally, the otherwise linear output of the sensor system becomes increasingly nonlinear for targets of decreasing diameter.

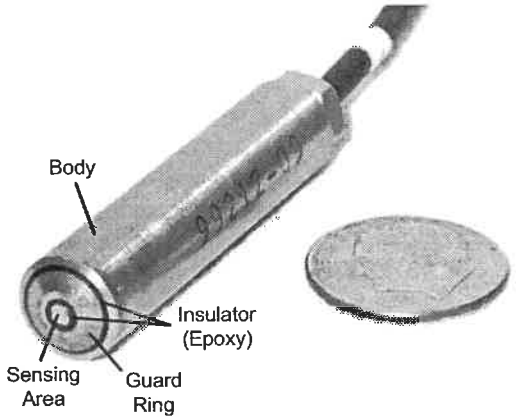

Fig. 1. Representative capacitive sensor (Lion Precision C1-C).

To investigate the severity of these effects, a capacitive sensor (Fig 1) is evaluated with spherical targets having diameters less than 25.4 mm. Complexities in this sensor preclude a simple analytical model so an approach using the finite element method is used. The results from the finite element analysis are validated experimentally by comparing the output of two capacitive sensors, one targeting a flat reference surface and another targeting a spherical surface. The excellent agreement of the finite element and experimental results suggest that either approach is valid for quantifying these effects. The output of the sensor with larger spheres is easily corrected with apparent sensitivities, but the nonlinear effects with small spheres become so significant that accurate measurements are not achieved.

2 Capacitance as a Function of Gap and Target Diameter

The dimensions, geometry, and materials of a modern capacitive sensor may not measure a

capacitance that agrees with analytical solutions. However, finite element analyses (FEA) can determine the capacitances even when sensors are constructed with multiple electrodes, complex geometry, complex boundary conditions, or multiple dielectric materials. This section therefore describes an FEA procedure for capacitive sensors; although the details of the geometry are sensor specific, the procedure is general. The results of the FEA procedure are the lumped capacitance between the sensing electrode and spherical target as a function of two variables, the gap and the target diameter.

Capacitance values for many combinations of electrode gap and target diameter are necessary to reveal nonlinearities, so the analysis was conducted in ANSYS with a set of scripts that repeatedly model the geometry and calculate capacitance [5]. The 3D geometry of the cylindrical commercial sensor targeting a spherical electrode is reduced to 2D axisymmetric geometry to significantly reduce the number of finite elements and calculation time. The axis of symmetry coincides with the centerline of the sensor and the center of the spherical target. This analysis primarily uses a 2D quadrilateral element. Special quadrilateral elements are used at the perimeter of the geometry to accurately model infinite boundary conditions. Both types of elements have one degree of freedom at their nodes, voltage, used to calculate the potential function in the non-conductive volumes of the model.

The geometry of the model includes the sensing electrode, guard ring, body, target, epoxy insulators, and the air between the sensor and target. Only the areas for the dielectric material (epoxy and air) are meshed since there is no change in potential within the conductive electrodes. The density of the mesh was evaluated and adjusted to achieve reliable convergence with acceptable solution time. The density of the mesh is highly concentrated in the regions near the sensing element, with relatively large elements at the perimeter of the axisymmetric geometry.

An exemplary result from an electrostatic finite element analysis is shown in Fig 2. This contour plot shows the electric potential within the dielectric epoxy and air when a fixed potential is applied to the sensing area and guard ring while the housing and target are grounded. It is important to observe the potential gradients in the air gap between the sensing electrode and target and also in the epoxy that separates the sensing electrode from the guard ring. These gradients indicate the fringing of the electric field beyond the sensing electrode.

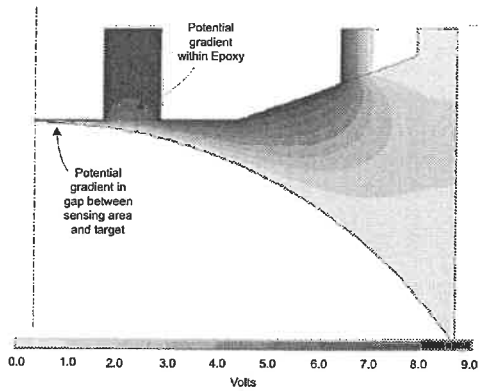

Figure 2. Voltage potential within non-conductive volumes.

Although the distribution of electric potential is of some qualitative interest, the capacitance between electrodes is more meaningful for assessing the effect of a spherical target. The three electrodes in the sensor and the single target electrode lead to four self-capacitances and six capacitances between electrodes. ANSYS provides the CMATRIX macro for determining the lumped capacitances in problems with multiple electrodes, and Smith [5] thoroughly demonstrated how this macro is used to determine the ten capacitances in the present problem. Since the electronics of the commercial sensor detect displacements by monitoring only changes in the capacitance between the sensing electrode and target, only one of these calculated values is necessary for this analysis.

The capacitance is calculated for spherical targets with diameters of 6.35, 9.53, 12.70, 15.88, 19.05, 22.23, and 25.40 mm. For comparison, the lumped capacitance is also calculated as a function of the gap for a flat target. The lumped capacitance is calculated with gap increments of 5.1 μm for the low sensitivity and 1.016 μm for the high sensitivity. Twelve to fifteen increments of the gap are analyzed for each spherical diameter. Capacitance values are not calculated for a spherical diameter of 6.35 mm and the high sensitivity since the required sensing range was unreasonably close to the target. A listing of the computed values for capacitance is available from Smith [5]. The values of capacitance for the low sensitivity range between 0.217 pF and 0.526 pF. The capacitances for the high sensitivity range between 0.593 pF and 1.822 pF.

3 Effects of Spherical Targets

The computed values for the lumped capacitance between the sensing electrode and target reveal four effects of spherical targets. As the diameter of the target is reduced, the sensing range decreases and the sensing range shifts towards the target. Furthermore, the apparent sensitivity and nonlinearity increase, which is more important to the accuracy of measurements. All of these effects become more pronounced when sensors have high sensitivity and the diameter of the target is small.

Fig 3 shows plots of the inverse of the lumped capacitance between the sensing electrode and target as a function of the gap distance and the diameter of the target. For an ideal sensor, each curve should be a straight line with positive slope; recall that the sensitivities are defined as negative values, which changes the sign of the slope. Vertical lines show the minimum, nominal, and maximum gaps for a flat target, reflecting these lines onto the ordinate gives the inverse capacitances that correspond to the minimum, nominal, and maximum gaps for a flat target.

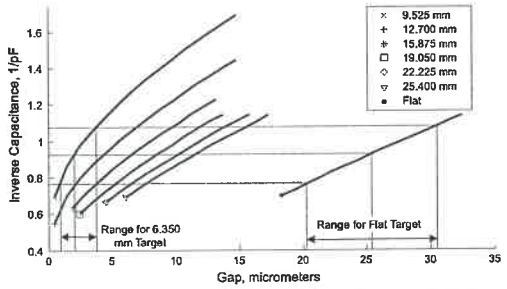

Fig. 3. Inverse capacitance for high sensitivity as a function of gap and target diameter.

The minimum, nominal, and maximum gaps for each spherical target are estimated by finding the intersection of the horizontal lines and each inverse capacitance curve. This method is illustrated for the Ø9.53 mm target at high sensitivity in Fig 4. For the high sensitivity, the nominal gap shifts from about 25 μm for a flat target to about 2 μm for a Ø9.53 mm target, and the range shifts from about 10 μm to a mere 2.8 μm.

Using the data plotted in Fig. 3, the output voltage from the sensor's electronics can be predicted. The output voltage is proportional to the difference between the inverse capacitance at the gap distance and a reference internal capacitance. Fig. 4 shows the predicted output voltage for various target diameters in the high sensitivity case. The change in slope of the curves indicates increasing values in the sensor's sensitivity S, which results in exaggerated displacement measurements.

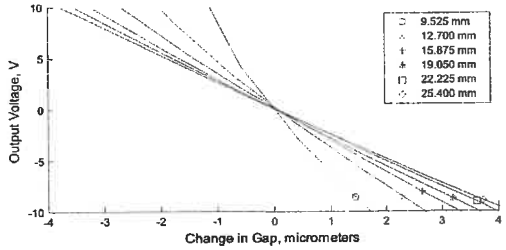

Fig. 4. Output voltage for high sensitivity as a function of changes in the gap

4 Experimental Validation

The finite element models described in the previous section can be experimentally validated using capacitive sensor systems and targets of varying diameter. The experimental hardware used for this validation allows comparison of the output from two capacitive sensors while minimizing the influence of off-axis motion and thermal gradients through thoughtful design.

Fig 5 shows the hardware used to validate the finite element models. The two sensors are held in the same bracket so that any relative motion between one sensor and its target is equal and opposite to the relative motion between the second sensor and its target. The testing is performed on a precision Moore No. 3 Universal Measuring Machine with collinear sensors in accordance with the Abbe Principle to minimize the effects of any off-axis motions. The sensor bodies are aligned to within 20 arc-seconds of the axes of travel. During testing, the machine table is moved in the direction along the sensor axes.

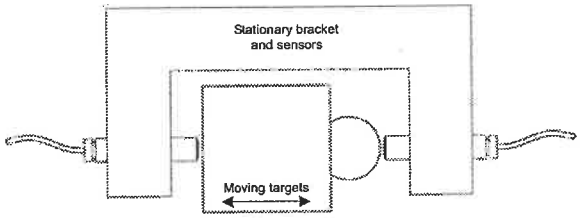

Fig. 5. Fixture used to compare output of sensors targeting spherical vs. flat surfaces.

The first (left hand) sensor always targets a precision-ground flat reference surface while the second (right hand) sensor targets either a flat surface for calibration or spheres of varying diameter. During calibration with two flat target surfaces the sensor output repeats within 20 nm and matches the manufacturer's calibration data within 0.25%, which is negligibly small compared to the effects observed due to target diameter. This result confirms the accuracy of the sensor alignment, and the insensitivity of the experimental hardware to vibration, noise, and thermal drift.

Prior to testing, the importance of sensor centering and perpendicularity to the spherical target was explored experimentally. In practice, this is equivalent to finding the "high spot" on the target sphere. This geometric effect is not included in the axisymmetric finite element model and is difficult to completely eliminate in the actual hardware. By checking the repeatability of the comparative sensor output with different amounts of deliberate decentering, it was found that the effect is negligible for sensor centering within 50 micrometers of the high spot. It is straightforward to find the high spot to within 25 micrometers or better using the three axes of the Moore measuring machine, thereby satisfying this requirement. Once the highest point on each sphere is found, both capacitive sensors are adjusted axially in the sensor bracket such that each sensor is within one micrometer of the middle of its sensing range (nominally zero Volts from the sensors' electronic output).

During each test, the machine is slowly actuated while both sensors measure several full cycles of motion over the sensing range. When the two sensors target flat surfaces, the output is linear over the range of travel. However, the relationship becomes nonlinear when a spherical target replaces the second reference flat. As predicted by the finite element results, the comparative sensor output shows a nominally linear relationship with additional higher-order behavior. The data show both the apparent sensitivity of the spherical target (the linear portion) and the nonlinear residual. The experimental results show excellent agreement with the finite element models. The maximum discrepancy between model and experiment was less than 2% for the -0.394 V/micrometer sensor system less than about 8% for the -1.969 V/micrometer sensitivity.

The experimental measurements with flat targets show residuals consistent with the manufacturer's calibration data sheet. The experimental results with spherical targets show increasing nonlinearity with decreasing sphere diameter, again consistent with theoretical results.

5 Conclusion

Capacitive displacement sensors for precision manufacturing and metrology are often used with spherical targets despite being calibrated with flat surfaces at the factory. This paper elucidates four effects of this standard practice. First, the sensitivity of the sensing system increases, which tends to exaggerate actual displacements. Second, increases in the sensitivity reduce the size of the sensing range. Third, as the diameter of the target electrode decreases, the sensing range shifts closer to the target electrode. Fourth and perhaps most important when striving for accurate measurements, the relation between the output voltage and displacement becomes increasingly nonlinear as the diameter of the spherical target decreases.

The finite element analysis and the experimental approach described in this paper prove to be equally valid techniques for quantifying these effects in a particular capacitive displacement sensing system. For a representative sensor, these approaches indicate that the error in sensitivity may be as much as 150% and that the nonlinearity may prevent accurate measurements with small diameter targets. Furthermore, the sensing range can shift so near the target that it becomes essentially impossible to even make measurements.

Since these effects lead to measurement error, precision manufacturing and metrology applications requiring the highest accuracy should correct the output of the sensor or use sensors factory calibrated with a particular spherical target. For all but the smallest targets, sufficiently accurate measurements are obtainable with corrected sensitivities. For the smallest spheres where nonlinearities are significant, a higher order correction is likely necessary. Alternatively, using a sensor with a smaller sensing area can reduce the error, and this aspect can be investigated in future work.

6 References

[1] ANSI/ASME B5.54. *Methods for Performance Evaluation of Computer Numerically Controlled Machining Centers*. American Society of Mechanical Engineers. New York. 1992.

[2] ANSI/ASME B5.57. *Methods for Performance Evaluation of Computer Numerically Controlled Lathes and Turning Centers*. American Society of Mechanical Engineers. New York. 2000.

[3] ANSI/ASME B89.3.4M. *Axes of Rotation – Methods for Specifying and Testing*. American Society of Mechanical Engineers. New York. 1985.

[4] Grejda, R.D. *Use and Calibration of Ultra Precision Axes of Rotation with Nanometer Level of Metrology*. Ph.D. Thesis. Penn State University. State College, PA. 2002.

[5] Smith, P. *Analysis and Application of Capacitive Displacement Sensors to Curved Surfaces*. Master's Thesis. University of Kentucky. 2003.

PERFORMANCE TESTING OF MULTISENSOR CMMs BASED ON SINGLE ARTIFACT MEASUREMENT

Kalyana Bhamidi, Edward P. Morse
Center for Precision Metrology
Department of Mechanical Engineering &Engineering Sciences
The University of North Carolina at Charlotte,
Charlotte, NC, USA 28223-0001

INTRODUCTION

Hybrid (or Multi-sensor) Coordinate Measuring Machines (CMMs) belong to new generation of CMMs, gaining popularity in the current world market due to the flexibility of changing the sensing device without having to re-establish the part coordinate system. The distinction we make between Hybrid and conventional CMMs – which permit multiple sensors to be swapped on and off the CMM ram – is that the different sensors in a Hybrid system have different metrology loops. There is no standard documented for the performance of such multi-sensor CMMs. The assessment of the errors or uncertainty present in the use of each probing system may be done in a manner similar to that described in the existing B89.4.1 standard (multi-tip), but the quantification of these errors has not been studied. The primary focus of our work is a better understanding of the uncertainty introduced when measuring the same work piece with different sensors, and the development of artifacts and procedures to document this uncertainty.

In this paper we report tests conducted on a Hybrid CMM at UNC Charlotte with the intent of exposing errors in the touch and vision probes and their relative offsets. We also discuss some experiments using an Opto-Mechanical hole plate, conducted for comparing machine performance with the different sensors. One series of experiments performed allows us to quantify the errors over a large fraction of the machine volume, while others examine how machine errors can change over time.

PREVIOUS WORK

Measurements on a Werth hybrid CMM at UNC Charlotte have included experiments to expose sensor offsets and reversal measurements on an "opto-mechanical hole plate" [1]. We extend this work to experiments that are designed to reveal errors in the machine volume for different sensors. This paper presents the results of drift experiments with both the sensors, and examines machine geometry errors both locally and through the whole machine volume.

DRIFT TESTS

This test is much like the one described in the existing B 89.4.1 standard [2]; it is especially pertinent for machines that use a light source for measuring with a vision probe, as self-heating of the machine can result in large geometric deformations in the metrology loop. We will discuss two long-term tests in this section. The first is a simple repeat measurement of single feature with each of the two sensors, while the second test involves tracking the apparent machine geometry errors (in this case, xy-squareness).

For these tests we use an Opto-mechanical hole plate, designed and manufactured by Centre for Geometrical Metrology at Technical University of Denmark [1]. This artifact is shown in Figure 2. In the first test, a single hole is measured alternately by touch and vision sensors, and the variation in location of the hole is tracked. As seen in Figure 1, the drift over an 8-hour test can be significant. As this experiment was conducted in a temperature controlled laboratory, the variations observed are not due to change in lab environment.

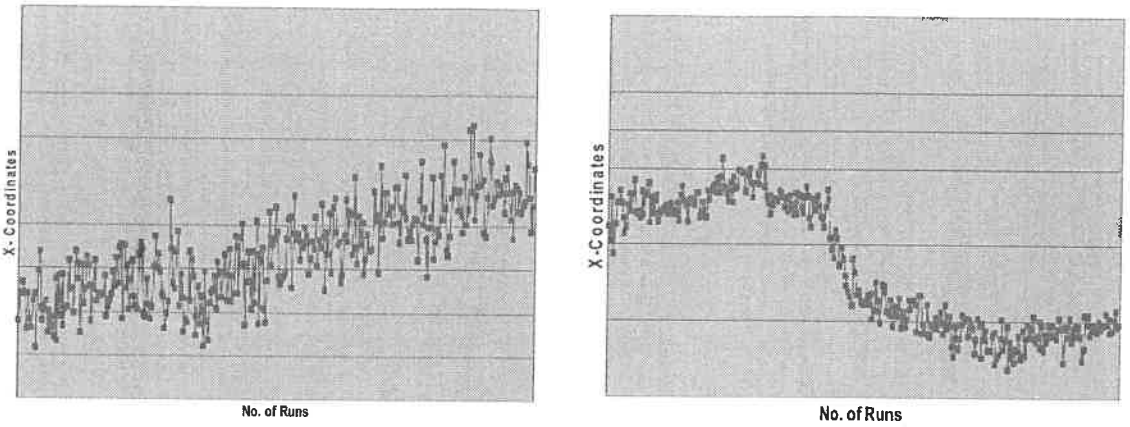

Figure 1: Vision Probe (left) and Touch Probe (right) drift in x. The horizontal line spacing is 1μm.

The second drift test used location data from all 25 of the holes on the holeplate. These locations were compared to a set of reference data obtained by measuring the holeplate on the Leitz PMM654 in several orientations. Averaging was used to eliminate the squareness errors in the data obtained from the PMM. The data obtained from the Hybrid CMM were compared to the reference values in a manner similar to that used by Hocken and Borchardt [5]. In our calculations, (x_1,y_1) are the reference coordinates, and (x_2,y_2) are the coordinates from the measuring machine under test. A shift of $(\varepsilon_x, \varepsilon_y)$ and rotation by β correspond to a rigid motion of the holeplate, while the squareness error α and scale errors γ_x and γ_y are machine errors. The machine errors calculated are those which give the minimum sum-of-squares distances between the measured and reference coordinates. Equation (1) is used to find these shifts and errors.

$$\begin{bmatrix} \sum y_2^2 & -\sum y_2^2 & -\sum x_2y_2 & 0 & -\sum y_2 & 0 \\ -\sum y_2^2 & \sum(x_2^2+y_2^2) & \sum x_2y_2 & -\sum x_2y_2 & \sum y_2 & -\sum x_2 \\ -\sum x_2y_2 & \sum x_2y_2 & \sum x_2^2 & 0 & \sum x_2 & 0 \\ 0 & -\sum x_2y_2 & 0 & \sum y_2^2 & 0 & \sum y_2 \\ -\sum y_2 & \sum y_2 & \sum x_2 & 0 & N & 0 \\ 0 & -\sum x_2 & 0 & \sum y_2 & 0 & N \end{bmatrix} \begin{bmatrix} \alpha \\ \beta \\ \gamma_x \\ \gamma_y \\ \varepsilon_x \\ \varepsilon_y \end{bmatrix} = \begin{bmatrix} \sum(x_2y_2 - x_1y_2) \\ \sum(x_1y_2 - x_2y_1) \\ \sum(x_1x_2 - x_2^2) \\ \sum(y_1y_2 - y_2^2) \\ \sum(x_1 - x_2) \\ \sum(y_1 - y_2) \end{bmatrix} \quad (1)$$

Note: In Equation (1) above, the summations are performed over the data from all 25 holes, and N in the matrix refers to the number of features being compared – in this case, 25.

This test was run for eight hours, alternately measuring the 25 holes with the touch and vision sensors. On average, a complete cycle for both sensors was started every 10 minutes. For each set of measurements, the parameters α, β, etc. were calculated. We then examined how these values changed over time, and plotted them individually. The plot in Figure 3 shows how the squareness values vary over the duration of the test for the measurements with each sensor. The original data was a bit noisy, so the plot shown here reflects the moving average of six runs over time.

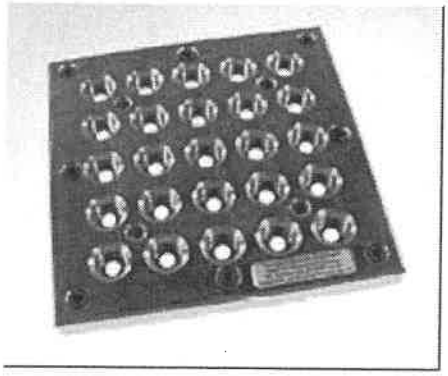

Figure 2: Opto- Mechanical Hole Plate

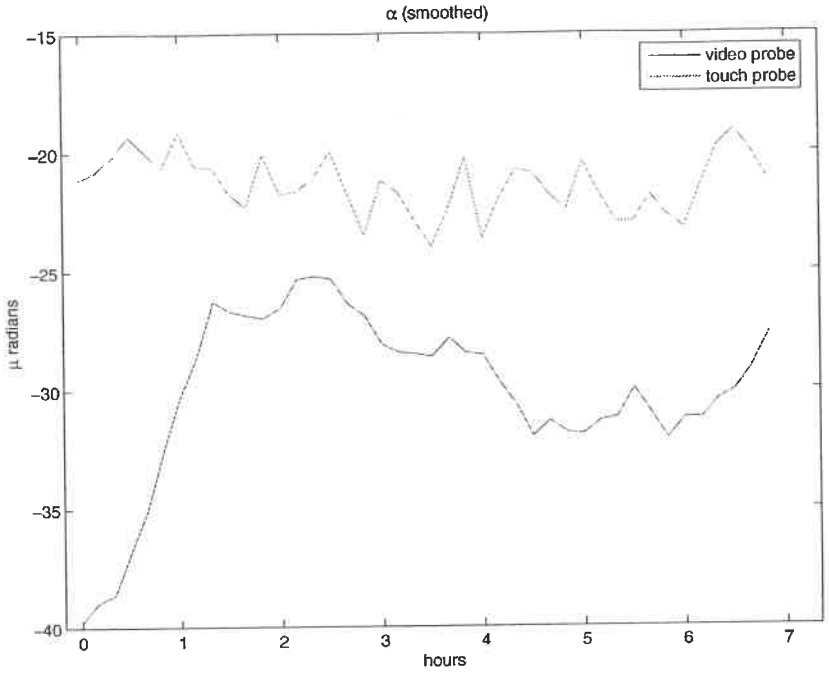

Figure 3: Apparent Squareness in XY, reported by sensor used.

GRID TEST

In the next test we again use the holeplate reference coordinates obtained by reversal measurements using our Leitz PMM. To obtain a better picture of the errors throughout the entire measuring range of the Hybrid CMM, the plate was measured in four locations which overlapped by a single row of holes [3]. The results plotted in Figures 4 and 5 show an interesting difference between the vision and touch probes. The scale of the graph is as follows: the holes are spaced on nominal 20mm centers, so the five by five grid of holes cover an 80mm by 80mm area. Since the four positions in which the hole plate artifact was measured overlap by a row of holes, the overall area spanned by these tests is 160mm by 160mm. The errors in measurement (relative to the reference values), are shown by the whiskers at each grid point and are magnified by 1000 times, so a whisker that reaches halfway across one grid spacing has a magnitude of 10μm.

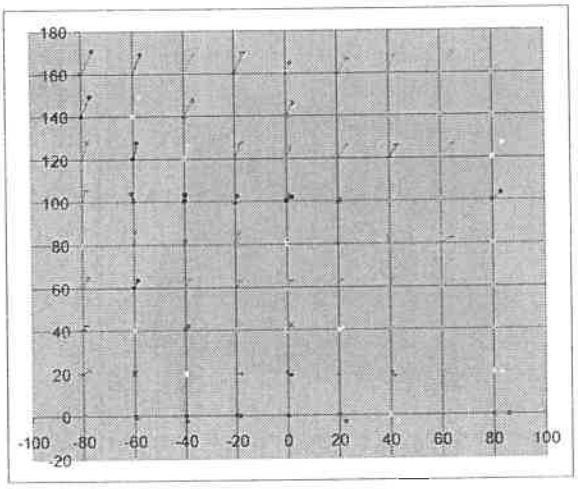

Figure 4: Vision Sensor Data in D0 position

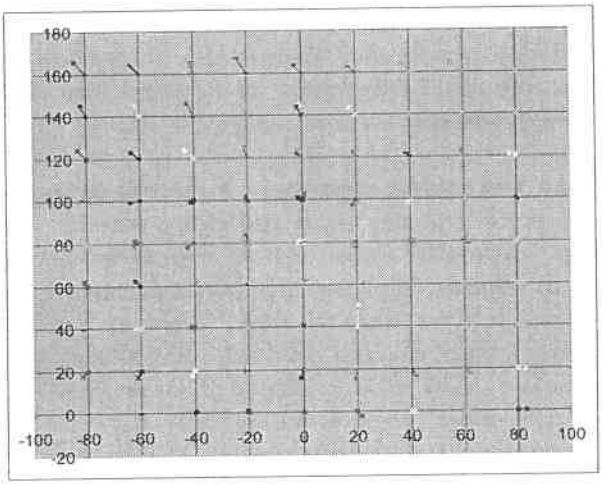

Figure 5: Touch Probe Data in D0 position

There is a systematic pattern in the errors for each sensor: as we increase in the y direction the x-error increases. For the vision data the y-increase corresponds to a positive x error, and for the touch data the y-increase corresponds to a negative x error. The conclusion we might draw from this is that the xy-squareness of the machine is different, depending on the sensor used. As a common xy-stage is used for both sets of measurements, it is possible that the geometric relationship between each of the two sensor z-axes and the plane defined by the x-y stage is different.

CONCLUSIONS

Multisensor CMMs are gaining importance in many industrial applications because of the flexibility in quickly joining the data obtained from touch and vision sensor. There are currently no standards for such CMMs. In this paper we have claimed that while standard CMM performance tests (such as a drift test or multi-tip test) described in B89.4.1 can serve as a starting point, users of this type of CMM will need additional information to fully understand the errors in their machine. A major challenge remains in incorporating the data obtained from the measurements we've described into diagnostic tools that will characterize the machine errors that occur during the tests.

FUTURE WORK

Future work will include measurements on a "Kite Square" artifact (shown in Figure 6) designed and manufactured at UNC Charlotte [4], which will help us in determining squareness between the z-axis and the xy-plane of the machine under test. It will also allow comparison with other Multi Sensor measuring machines. Ultimately, we wish to provide artifacts and procedures which will allow the estimation of the uncertainty of measurements that use both of the sensor systems. This will provide guidance for users of these Hybrid CMMs.

ACKNOWLEDGEMENTS

We gratefully acknowledge the support of the UNC Charlotte Center for Precision Metrology Affiliates and NSF support of this center through Grant #0331950. Any opinions, findings and conclusions or recommendations expressed in this material are those of the authors and do not necessarily reflect the views of the National Science Foundation (NSF). We'd also like to thank Graham Averitt for his assistance in developing Equation (1) for this paper.

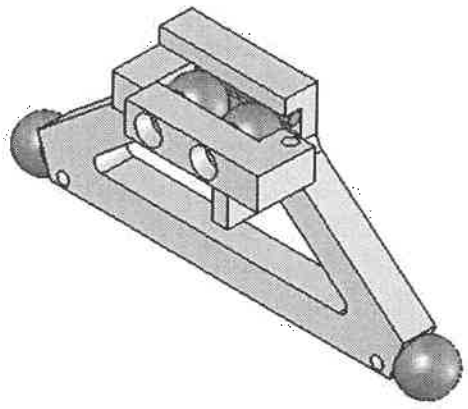

Figure 6: Model of the "Kite Square"

REFERENCES

[1] Morse, E. and Bhamidi, K., "Uncertainty of Measurements using Multisensor CMMs," ASPE *annual conference proceeding,* Portland, OR October 2003.

[2] B 89.4.1 Methods for performance Evaluation of Coordinate Measuring Machines, ASME, 1997.

[3] Morse, E. and Bhamidi, K., "Investigations in Hybrid (multi-sensor) CMM errors based on artifact Measurement," NCSL International Workshop and Symposium, 2004

[4] Miller, J., Morse, E., Nettles, J., and Turner, J., "Kite Square," *These Proceedings*, Orlando, FL, October 2004.

[5] Hocken, R. and Borchardt, B, "On Characterizing Measuring Machine Geometry", NBSIR 79-1752, National Bureau of Standards, 1979.

METROLOGY ARTIFACT DESIGN

Karalyn F. Folkert, Thomas A. Dow, Kenneth Garrard
Precision Engineering Center, NC State University, Raleigh, NC

INTRODUCTION

Coordinate Measuring Machines (CMMs) are widely used to measure the shape of machined parts. Their availability, speed, resolution and flexibility have pushed them into many new applications. Laboratories and manufacturing facilities alike use them to assess the quality of fabricated parts. However, to reap the full benefits of a CMM, there is a need to "qualify" its measuring capabilities and compare it to other CMMs available. Through the years, there have been a number of calibration artifacts developed including ball bars, ball and hole plates, ring gauges, and hole bars [1]. After considering these artifact standards, a ring gauge was chosen for further development. The overall features of the ring gauge (OD, ID, width and wall thickness) can be used to exercise multiple axes of a CMM. In addition, small features can be added to the ID and OD to assess the capability of the machine to deal with small temporal and spatial variations in surface features. The ring gauge can also be measured in different orientations and positions on the CMM to cover the entire working volume. Figure 1 shows the ring gauge geometry on the Diamond Turning Machine (DTM) during machining.

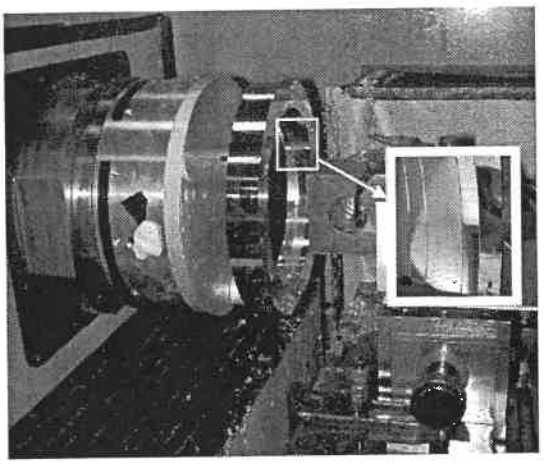

Figure 1. Ring gauge with wave feature shown in the inset.

RING GAUGE FEATURES

The first prototype of the ring gauge was created in 6061-T6 aluminum. It has a 6" (152.4mm) ID with 1" (25.4mm) square cross section and all surfaces of the gauge have been diamond turned. Reference surfaces were created on the OD and ID in the form of 0.5" (12.7 mm) wide grooves that are 30 μm deep. The OD is a smooth ring but the ID has a swept sine wave with ± 2.5 μm amplitude and spatial wavelength range from 1/80" (0.317mm) to 1/4" (6.35mm). A swept sine wave is a sine wave that continuously varies its frequency. In this case, the wave begins at the long wavelength and progresses to a short wavelength in the first 90 degrees. To produce a continuous wave, the wave is "flipped" to line up with the last wave and then the wavelength increases to the starting point as it reaches 180 degrees. From 180 to 360 degrees, the wave is a mirror image of the first 180 degrees. Figure 2 illustrates these features. The small surface features will assess the capability of the CMM to respond to small surface anomalies and to characterize the dynamic performance of the CMM as it traverses the varying wavelength features.

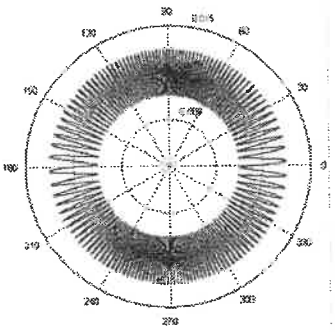

Figure 2. Swept sine wave features.

DESIGN AND FABRICATION PROCEDURE

The design of the ring was selected for a convenient size with sufficient stiffness to be usable and machinable. Significant thought went into the mounting system and machining procedure to

guarantee a cylindrical shape post-machining. Figure 1 shows the ring mounted in the diamond turning machine. It is supported on a vacuum chuck with 3 one-inch diameter posts. The procedure was to machine the back of the flat vacuum plate and mount it on the spindle. The posts are installed and machined flat. The ring was bolted to the posts and the front side was machined and then flipped over and the back side is machined. Next, the ID and OD of the ring were machined. Finally, the finished reference shapes were machined: a flat cylinder on the OD and the swept sine wave on the ID.

Fabrication of Swept Sine Wave

The wave features of the artifact were fabricated using a Fast Tool Servo (FTS) shown in Figure 3. An 18 mm long, hollow cylindrical piezoelectric actuator (25 mm OD and 12 mm ID) drives the device to a maximum displacement of 18 μm. A capacitance gage provides feedback on the position of the tool holder by looking at the back of it through the hollow actuator. A commanded position is turned into a positive input voltage and sent to a high voltage amplifier where it is amplified by 100 before being sent to the FTS.

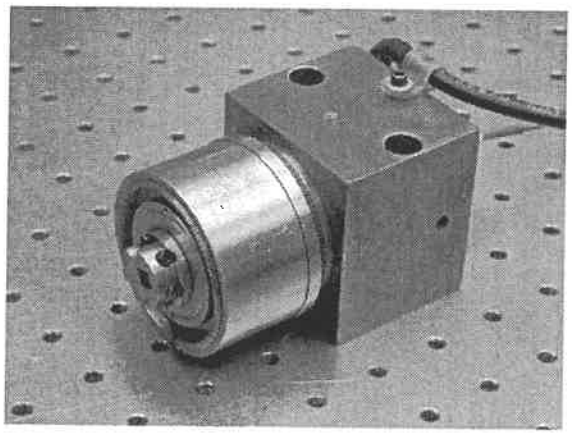

Figure 3. Fast Tool Servo.

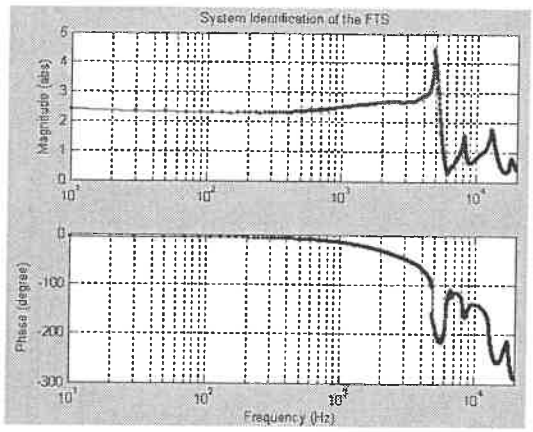

Figure 4. System dynamics of the FTS.

The open-loop dynamics of the FTS as a function of the frequency of a sine wave command is shown in Figure 4. The top graph is the amplitude ratio of the output voltage from the capacitance gage to the input voltage to the amplifier. It shows a slight decrease in amplitude with frequency up to about 400 Hz and a strong increase to the first natural frequency of 5 kHz. This frequency is a result of the first bending mode of the cylindrical plate that serves as the base for the tool holder. The phase difference between input and output shows a small offset (4°) at DC that grows to about 27° at 1000 Hz. These dynamics need to be compensated using a closed loop control system.

A dSPACE DSP control system was used to drive the actuator and compensate for the dynamics shown in Figure 4. A PI control loop was created and the results using the most appropriate gains are shown in Figure 5 up to 600 Hz. The plots of Figure 5 also compare a 1μm and 5μm input to the closed loop system to demonstrate the amplitude dependence of the FTS. The gain at low frequency has been improved (equal to approximately 1) and the phase is nearly zero from DC to 70 Hz for the 5 μm amplitude input. The step response in Figure 6 indicates the improved amplitude response and settling time using the controller.

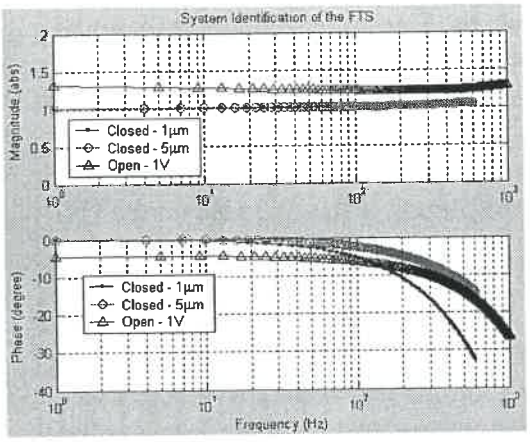

Figure 5. Closed loop dynamics.

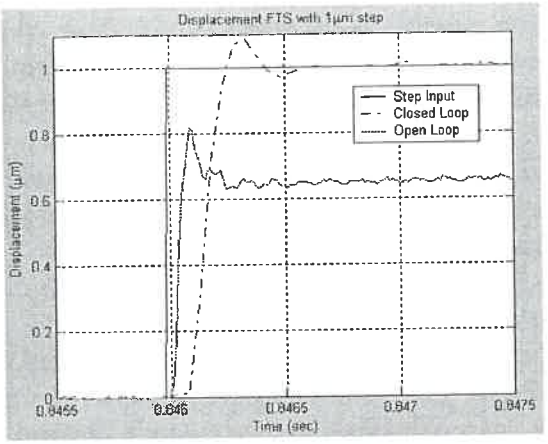

Figure 6. Closed loop step response.

To create the swept sine wave, the FTS is commanded to provide a range of sinusoidal outputs that depend on the wavelength of the feature and the spindle speed. The minimum speed for the spindle on the DTM is about 20 RPM, which makes the sinusoids of interest range from 25 to 500 Hz on the ring gauge dimensions described in Figure 1. Therefore, based on the characteristics of the FTS shown in Figure 5, the waveform at the highest frequency will be distorted in both amplitude and gain compared to the lowest frequency.

One technique that can be applied to correct the phase and gain is called Deconvolution [2]. In this technique, the dynamics of the FTS are measured, inverted and applied to the desired tool motion to create a modified input command. This command will provide the correct tool motion when applied to and distorted by the FTS dynamics. A sample swept sine wave has been fabricated on the outside of a aluminum cylinder (110 mm OD) to test the quality of the machined sine waves and the results are shown in Figure 7.

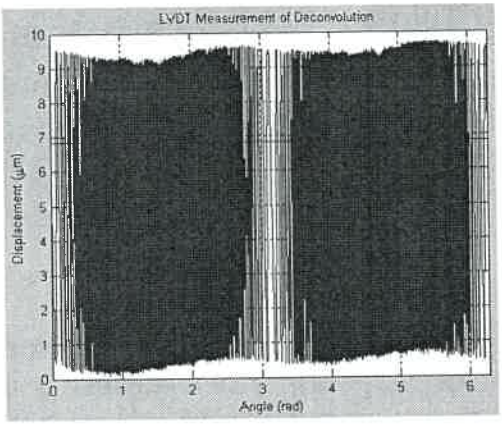

Figure 7. LVDT measurement of sine wave features on cylinder

Figure 7 was measured using an air-bearing LVDT mounted to the base of the DTM. The spindle was driven at a low speed (2 RPM) and the resulting data was modified to compensate for the 1 mm diameter of the LVDT tip. Because the tip radius is not that much smaller than the radius at the base of the shortest wavelength sine wave, the data from the LVDT will provide a distorted picture of the machined sine waves. The tip radius will appear to increase the width of the sine waves and reduce the distance between them. However, the data was corrected by finding the actual contact point between LVDT tip and sine wave (assuming the tip is a perfect sphere) and modifying the data to show the actual surface features.

MEASUREMENTS

The first prototype of the ring gauge was measured at the Precision Engineering Center (PEC) as well as at the Oak Ridge Y-12 Facility. The measurements at the PEC were performed using an LVDT on the spindle of the DTM rotating at approximately 2 RPM. Similar measurements were

made at Y-12 using a CMM as shown in Figure 8. The ring gauge was measured in a horizontal orientation mounted on a rotary table and a scanning probe. The CMM measurement showed two errors: one is reduced amplitude at the shortest wavelength (highest frequency) sine wave and the second is a lobed profile that matches the number of hold-down bolts. The former problem has been solved with a larger minimum feature size along with the deconvolution/closed loop control and the second is being addressed with a new support during machining.

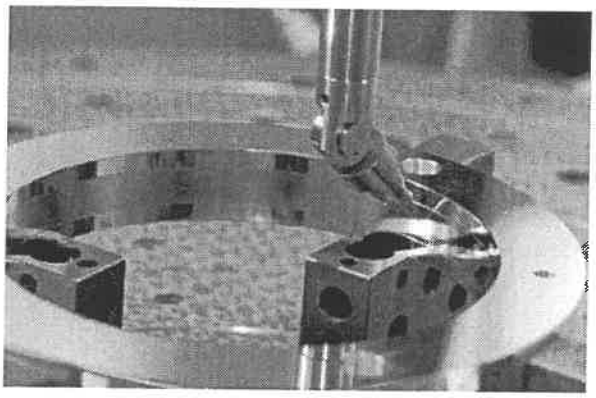

Figure 8. Measurement setup with a CMM at Y-12.

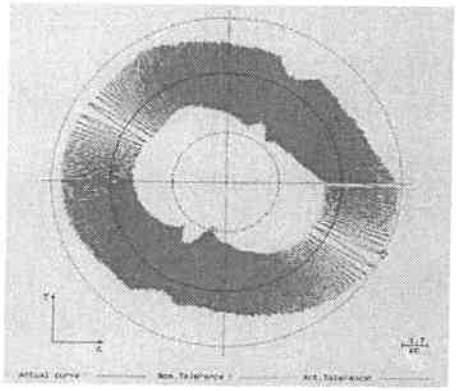

Figure 9. CMM measurement.

CONCLUSIONS

The final ring gauge design will be a useful addition to the artifacts available to calibrate CMMs. Improvements in the fabrication technique have reduced the amplitude and phase errors of the different frequency sine waves from 5 to 0.6 μm based on an amplitude input of ± 5 μm. A new design of the ring support is underway and a second prototype will be fabricated with features on both the ID and the OD of the ring. The mounting of the ring in a CMM is another issue that must be addressed to utilize the ring gauge in different orientations. The final phase of the project involves measurement and uncertainty. The accepted measurement data can then be used in the assessment process of the CMMs. The CMM will measure the artifact, and the data will be compared to the accepted measurement data through uncertainty analysis. The Guide to the Expression of Uncertainty in Measurement [3] will be the primary source for the uncertainty analysis. However, the non-linearity of the features may pose a problem with the uncertainty model. Finally, this procedure will use decision rules to make a final assessment on the uncertainty associated with a specific CMM of whether it is fit to perform measurements on real parts.

REFERENCES

1. Cauchick-Miguel, P., King, T., Davis, J., *CMM verification: a survey*. Measurement, 1996, 17 (1), p. 1-16.
2. Panusittikorn, W. *Error Compensation using Inverse Actuator Dynamics*. PhD Dissertation, NC State University, August 2004.
3. ANSI/NCSL Z540-2-1997, *US Guide to the Expression of Uncertainty in Measurement*. American National Standards Institute, 1997.

Web based Gage Management System for Quality Assurance

Abu M Mohamed Ali, Jay Raja
Center for Precision Metrology,
University of North Carolina at Charlotte, Charlotte, NC

1. Introduction:

Gage Management System (GMS) is a comprehensive database management system to maintain information about all gages in a firm efficiently and with ease. Gage Management is the process of efficiently managing and locating gages in an industrial setup in addition to generating reports and scheduling calibration dates. Calibration is a "set of operations that establish, under specified conditions, the relationship between values of quantities indicated by a measuring instrument or measuring system, or values represented by a material measure or a reference material, and the corresponding values realized by standards" [1]. In a typical industrial setup with large number of gages, tracking calibration schedules and maintaining gage information becomes a huge task. In this context, GMS are very useful and essential tools that facilitate handling this large quantity of information efficiently.

This paper introduces the novel concept of an internet based GMS that will revolutionize the way gage management system will be designed in the future. This system is designed to easily organize the maintenance of gage records such as gage history for calibration. Also, the system facilitates tracking gages within a company, maintaining calibration schedules, tracking gage supplier information and storing calibration certificates. The advantage of this system is that it allows accessing such information through a network and does not require the physical presence of an engineer at the server location itself.

The primary objective of this work is to develop the next generation Gage Management System that is flexible and user friendly. The work presented in this paper involves the development of an Internet based software system for managing the gages and securing gage information. The major task of involves developing a robust relational database system that can handle all relevant information and organize them effectively.

2. Available Packages:

There are a few gage management systems currently available but such applications have been built using two-tier architecture with Visual Basic or Visual C++ as the front end and MS Access as the backend database. These applications have to be installed on a computer where the program is supposed to run. This consumes large memory space and also the database applications have to be loaded on the system.

If it is a network based application then it overcomes physical barriers but often, only the administrator can install and make changes to the application. Also, only the administrator can deal with database design. There are other disadvantages with current GMS. In the event of a computer crash, all information involved may be lost. However, there are also many advantages with these systems. As they reside on the user's computer, there are fewer chances that the information may be misused online and there is greater security for the data. This issue can be solved to some extent by creating the database on the user's machine and then connecting to the system through the internet. There are lots of features on the two-tier architecture where many features can be included with ease.

Many of the current features supported by GMS are such that they require multiple resources to be installed and they are also not flexible compared to the web based systems. Most of the currently available software are single user versions and need a person with expert knowledge for operating and maintenance.

Such software, unlike the internet based ones, where we can have multiple user access and is also secured using a unique access for the particular system, where the login information can be shared between a few people who need to manage and access this information. The Client/Server versions available in the market now are very expensive and need extensive networking.

3. Internet Based System:

The Internet based GMS has a simple three-tier architecture system that aids in the organization and accessibility of the stored information in accordance with the industry requirements. The system is 3-tier architecture designed so that it can communicate with user and the database through the internet.

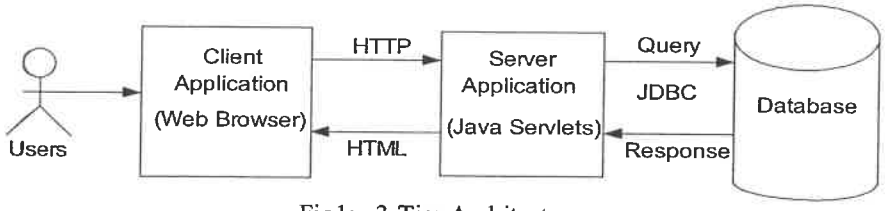

Fig1: 3-Tier Architecture

The software has been developed using Java. Oracle is the database that resides in the server and can be accessed across the Internet with the help of a Java enabled web browser. Unified Modeling Language (UML), which is a standard language for writing software blueprints, is used to design and document the software. The software also provides an insight into using XML (Extensible Markup Language) for the data transfer of calibration reports between the users and the vendors. This user friendly application is designed using object oriented programming techniques which enable easy maintenance and software upgradeability.

This system will function with minimal resources. The Internet based GMS is developed using tools such as Java JSP, Java Servlets, Oracle, HTML and XML. The front end is designed using HTML and JSP, JSP was used for implementing dynamic pages. The main database which holds all the information is created using Oracle. The main programs are written in Java and Java Servlets. The key to this system is the robust database designed to handle all the tables and entities available.

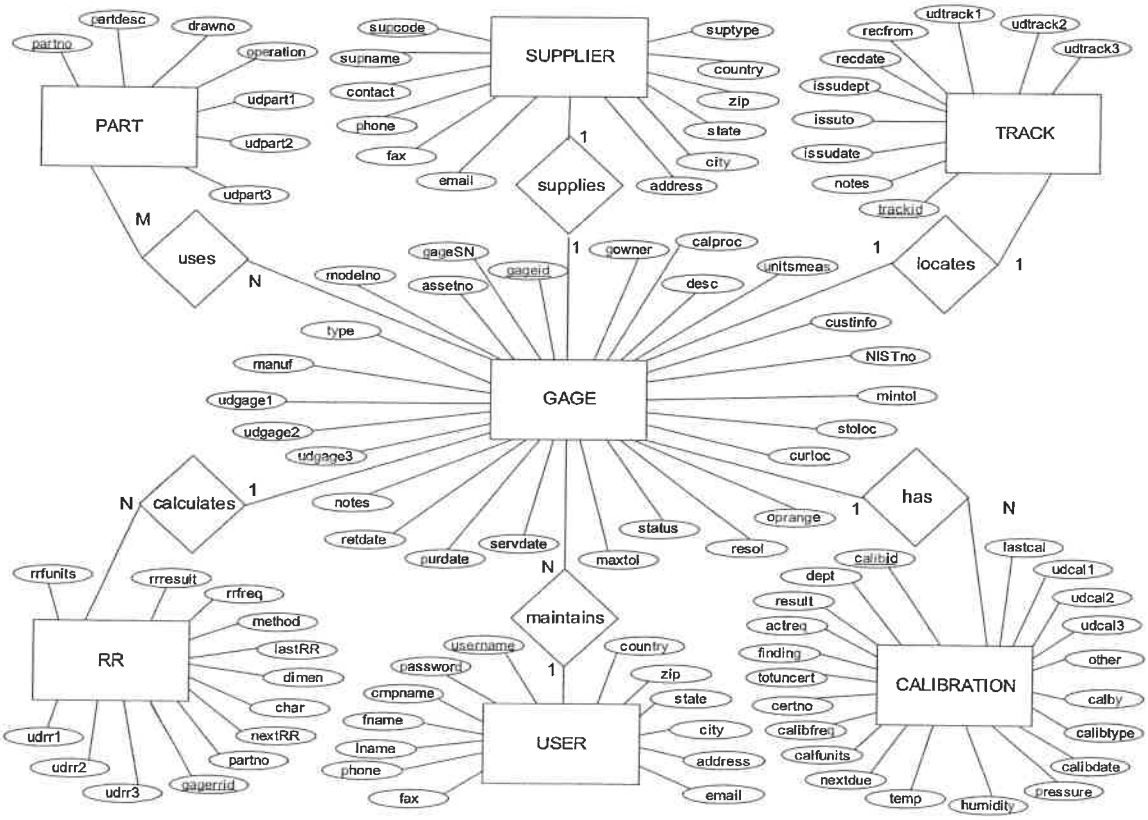

Fig 2: E-R diagram for the Gage Management System

The Entity – Relationship diagram is shown in Figure 2. Entities are real world things capable of independent existence and attributes are the properties that describe the entity. The rectangular boxes are entities and the oval boxes are the attributes. The diamond boxes are the Relationship that relates the entities.

The system is very user-friendly with help screens available for better navigation and also for guiding the first time users with better understanding of the system. Another additional feature for this system is that it uses XML (Extensible Markup Language) which is a new technology for web applications. XML is a World Wide Web Consortium standard that lets users create their own tags. It simplifies business-to-business transactions on the web. This system uses XML for the data transfer of the calibration file to and from the calibration vendors and it is fast and convenient. In the previous versions they need to wait for the calibration details to come from the vendors by mail and then they have to upload the information onto the database manually and this is avoided.

This system is aimed at reducing the effort to manage the gage records in a firm efficiently and with ease using internet. The advantage of this design is that it is easy to maintain and upgrade the software because Object Oriented programs encourage modularity and thus programs are independent of other parts of the program. The unified software development approach was used in the development of this software system. This is an iterative approach based on Unified Modeling language (UML) which is the most widely used modeling tool in the software industry. UML is divided into various phases and workflows to aid in the easy development of the software system.

4. User Interfaces:

The main feature of the system is that it is internet based and requires the minimal resources for its operation and availability at any place with a computer and an internet connection. The previously available versions had to be installed on the computer with many necessary requirements such as a computer with lot of memory and a good processor where the programs reside. It needs to be installed on many computers if they are interconnected on an intra network needing special drivers and additional cost for its maintenance. The internet based system eliminates most of the resources required compared to conventional systems. One more key feature of this system is that it lets the creation of user defined fields and the dynamic creation of user tables. This allows much of the flexibility for a versatile system. The dynamic creation of tables makes the system more advanced so that there need not be any installed programs on the user's computer to create the tables. This saves lot of cost in buying resources and adding additional hardware for running the system. Even the database account for the entire user list resides on the main server and so this becomes a very good alternative service to the currently available versions. If the user is concerned about the security of their data, the database can be setup at the user's site for confidentiality reasons. The Figure 3 on the next page shows some basic screen shots from the system. The top left is the login screen where the user can register and logon to the site; it also has the link for creating XML files for exchanging calibration information between the user and calibration vendors. The top right is the main screen the user will see after logging in, it lets the user to populate the database. During the first visit to the system, the user will be asked to create the tables and customize the fields on the tables if needed. It can also be compared to the main menu with all the functionality available in the software. The bottom left shows how the information is entered into the database. There are many Java Scripts written to validate the entered data, there is also a separate script used for date validations. The calibration information can either be loaded manually or can be imported directly from a XML file. The bottom right screen shows how the summary of the gages are reported. There are different kinds of summaries available based on the user requirements. There are reports generated for calibration information, supplier information, gage tracking etc. On the main screen there are links for creating "Add New Fields" where the user will be able to analyze all the basic available fields and then he will be able to add up to 3 user defined fields that can be either a number field or character field or even a date entry. There are functions added to access the Help function from any screen if the user is lost or if the user needs additional information on how it works. The print function is also located on all the screens to enable the user to print the information from the web browser. The user is expected to log out or sign off after using the system to add security to the system.

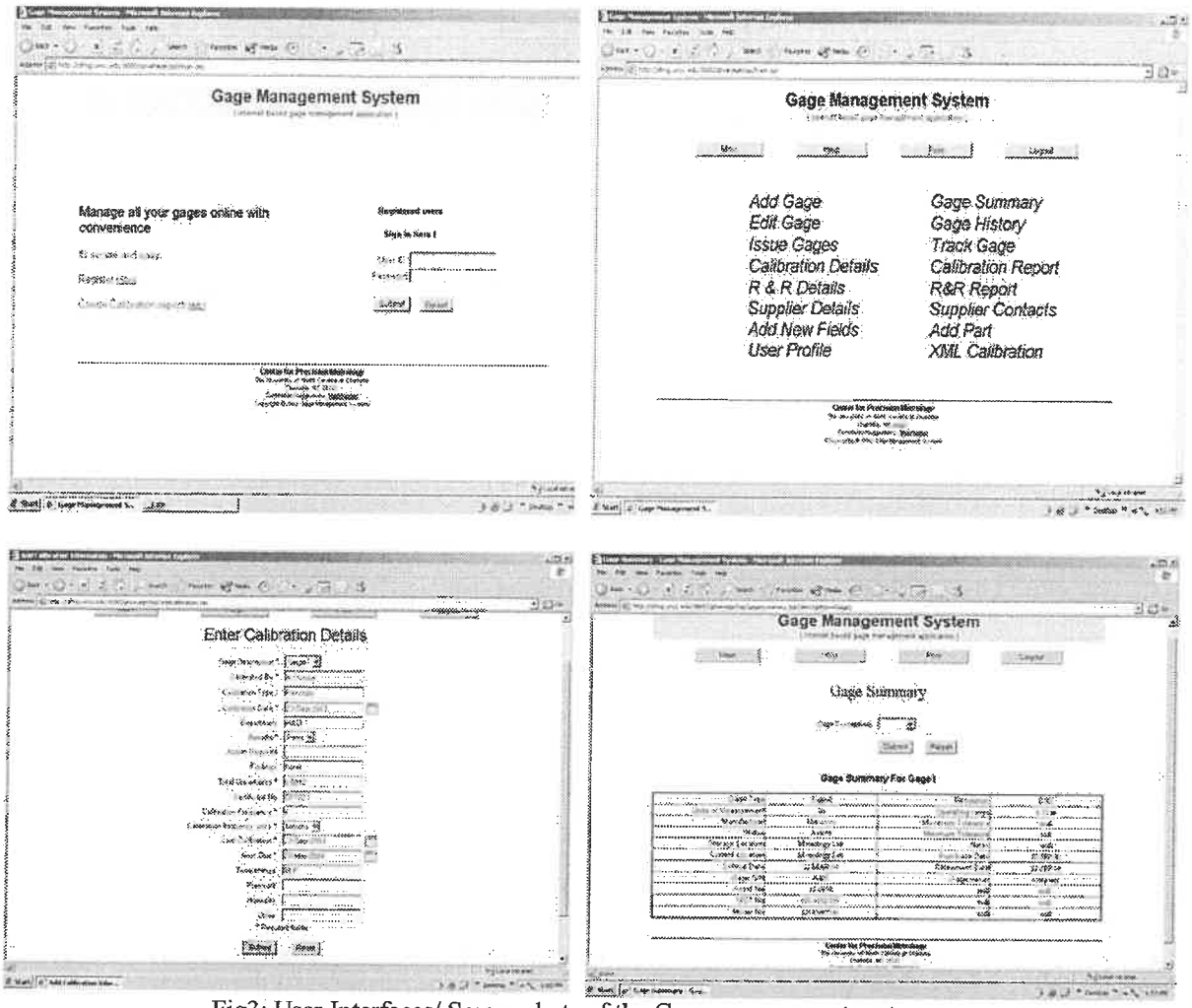

Fig3: User Interfaces/ Screen shots of the Gage management system

5. Conclusion:

In recent years, large companies have moved away from in-house manufacturing to global manufacturing. They outsource machining of parts to vendors around the world. Global manufacturing gives large companies the advantage to reduce operating costs. Thus there is a need for data to be shared over a wide geographical spread. Technology is transient and new software and new protocols for the internet are constantly being developed. This allows faster and safer access to information within and outside an organization. The Gage Management System (GMS) was successfully implemented and the output was as expected as it met all criteria of the objectives during the design of the project. This software is the first reported instance of an internet based gage management system. An updated version of this software optimized for high speed network access and with advanced features will be a task for the future. Thus web based gage management systems will help to improve the quality of the organization by better record keeping and scheduling for calibration of the available gages.

6. References:

[1]. VIM (International Vocabulary of Basic and General Terms in Metrology)
[2]. Abu M Mohamed Ali, an Internet based Gage Management System, Masters Thesis, UNC Charlotte, May 2004
[3]. S.H. Bui, Surface texture information system, Masters Thesis, UNC, Charlotte, December 1999.
[4]. R. Elmasri, S. Navathe, Fundamentals of Database System, Addison–Wesley, Meno Park, CA, 1994.
[5]. V. Gopalan, An Internet based surface texture analysis system, Masters Thesis, UNC, Charlotte, December 1999.

Highly Stable Measurements of Springs on an OCMM

Dongmei Ren, Kevin M. Lawton, Steven R. Patterson
University of North Carolina at Charlotte, Charlotte, NC 28223

Key words: measurement repeatability, optical CMM, springs

Introduction

A lot of 17-7 stainless steel springs has been measured using a View Voyager 12×12 optical coordinate measuring machine (OCMM) in the Metrology Lab of the University of North Carolina at Charlotte for a period of up to three years in order to characterize the dimensional instability [1]. The dimensional drift rates of most of these springs are smaller than 1 nm/day. Measurement of such small dimensional changes requires highly repeatable measurements. In this paper, vision probe influences on measurement repeatability, such as illumination, imaging optics, and edge detection method are discussed. These effects are analyzed, and methods are discussed for minimizing them in order to achieve the repeatability of 0.2 μm.

Uncertainty of the OCMM

The springs being investigated have a U shape with an opening of approximately 6 mm, length of 9 mm and cross section of 0.2 mm×0.9 mm. The opening dimension is measured in order to observe the dimensional variation. The View Voyager 12×12 OCMM was used to measure the springs because of its advantages in non-contact measurements.

To evaluate the underlying measurement uncertainty of the OCMM, a series of measurements of a glass plate artifact were made in which several 10 mm intervals on two perpendicular scales were measured along x and y directions, respectively. The plate was measured under back light illumination, and the pattern was magnified for 20 times by the optical system. Fourteen independent measurements over three weeks showed that the short-term repeatability, estimated by the standard deviation, was 0.05 μm in the x direction and 0.22 μm in the y direction. This test was repeated four times in two years to evaluate the long-term stability. The short-term repeatability values were stable, and no obvious drift of the machine was found. The results are shown in Fig.1.

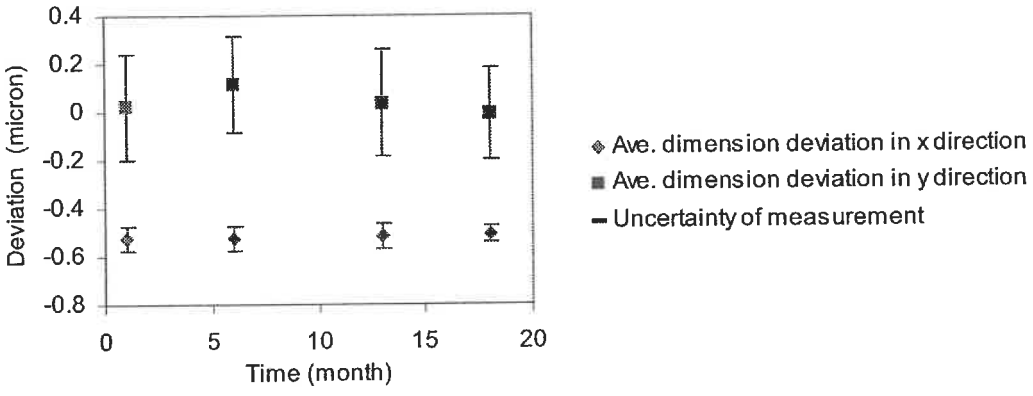

Fig.1 Uncertainty of OCMM measurement for x and y directions

Because the uncertainty of the OCMM in x direction is much smaller than that in y direction, the opening dimension of the spring is measured along x-axis of the machine. To eliminate the influence of the x-y stage motion errors to the measurement repeatability, it is necessary that springs be measured at approximately the same position on the machine each time.

Influence of the vision system to measurement

The complex spring geometry and its imperfect form make the measurement process much more complicated than glass plate measurements. The main factors related to the vision probe that may affect the spring measurement are illumination, magnification of imaging optics and edge detection method. Their interactions with the spring geometry affect the uncertainty of measurements. To investigate the influences of these factors, tests were designed and conducted in which the measurement repeatability was evaluated under different illumination, magnification, focusing methods and edge quality.

The interaction of illumination with the three-dimensional spring geometry is significantly more complicated than that with the thin pattern on the line scale. Both the illumination method and lighting intensity affect measurement repeatability and accuracy. The View Voyager 12×12 provides the backlight, through lens and ring light illuminations. The light control can be set at 0 to 255 intensity levels. To investigate the influence of the illumination, a set of experiments was made in which a spring was measured under backlight and thru lens light respectively at different intensity. The measurement results are shown in Fig. 2. It is shown in this graph that the measurement repeatability under backlight illumination improved with increasing the light intensity. But the repeatability under through light illumination showed less change. Considering the geometry of springs, backlight illumination was used for most of springs. The backlight intensity was set between 180 and 240 in the measurement to create sharp contrast without saturating the image.

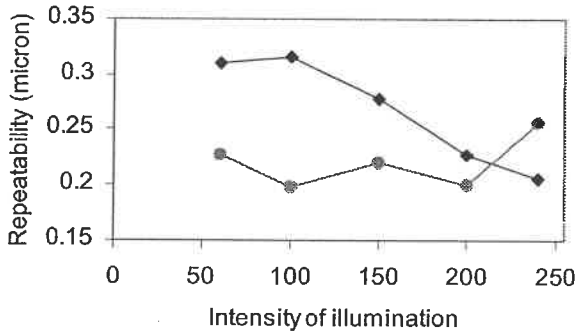

Fig.2 Influence of illumination on measurement repeatability
◆ backlight illumination, ● thru lens illumination

The magnification of the vision system influences measurements by changing the resolution and the combination of readings from the vision probe and machine scales. The repeatability of measurements using the objectives of magnification 6, 10 and 20 were tested, while other conditions were kept the same. The measurement repeatability values are 0.14, 0.19 and 0.22 μm, respectively. Lower magnification could provide improved repeatability, but it is less sensitive to the dimensional changes due to lower resolution. A magnification of 10 is used to measure the springs in order to achieve the best blend of resolution and repeatability.

The thickness and imperfect edge profile of springs make the lens focus on different planes perpendicular to the optical axis, which leads to low focusing repeatability. The edge shift caused by focusing uncertainty reduces the repeatability of edge position detection. Auto focusing was used and obtained high repeatability for springs with sharp edges. But for most springs a higher repeatability was achieved if a focus position was defined, and the machine was controlled to this position by the measurement program.

Measurement of springs

Based on above analysis and experiments, each spring was measured at a particular position on the x-y stage with its opening aligned with the x-axis. Backlight illumination with proper light intensity and objective lens with magnification of 10 were selected for most of the spring measurements. The rectangular cross sections of springs are typically not aligned to the optical axis of illumination and imaging system due to their rotations about the mean centerlines, which results in two sharpest edges at different planes of focus in backlight images. As the section mean central line lies at approximate midline between the two edges, the distance between midlines of the two spring legs is used as the measurement result. To make the most repeatable measurements, a particular measurement program was written for each spring to achieve repeatable illumination and measurement process.

A larger uncertainty than that of the glass plate measurements occurred in the spring measurements due to the complexity of spring geometry. The average measurement repeatability of fifty-one springs, that have been observed for one year or longer, is 0.23 μm, the standard deviation of which is 0.06 μm. The repeatability data of these springs are shown in Fig. 3. The spring used in the repeatability experiments was measured seventy times during the past three years. The standard deviation of these measurements is 0.20 μm, which is similar to the short-term repeatability. The variation in the repeatability data suggests that the source of the uncertainty may be the particular geometry of the edges of the springs and their interaction with the OCMM. However, with this typical repeatability and sufficient numbers of measurements, the measurement method is able to detect a dimensional variation of 1 nm/day over a period of six months.

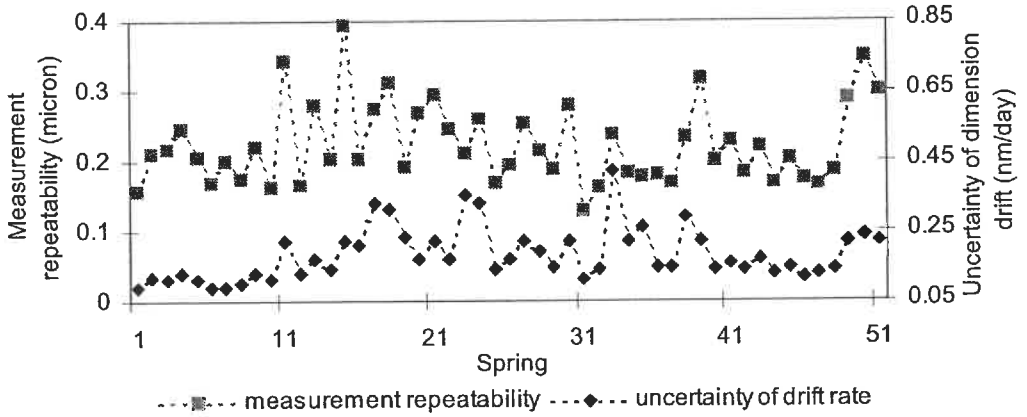

Fig.3 Measurement repeatability and the uncertainty of dimension drift

Measurements of the springs show that most of the springs have linear dimensional variations if short period dimensional fluctuations are considered to be results of measurement uncertainties. A least-squares linear model was fit to the data of each spring in order to characterize its

dimensional drift. The linear drift rates of thirty-eight springs that have been measured for one to three years are between -1.35 and 1.18 nm/day with an average of -0.14 nm/day and standard deviation of 0.60 nm/day. The distribution of drift rates is shown in Fig.4. The mean standard uncertainty of the drift rates is 0.19 nm/day. This is at the order of the measurement uncertainty over the period of observation. The uncertainties of dimensional drift rates are also shown in Fig. 3 for comparison. An obvious correlation between the measurement repeatability and uncertainty of the dimensional drift rate was observed. Twenty-five of the thirty-eight springs have shown drift rates significantly larger than their uncertainties.

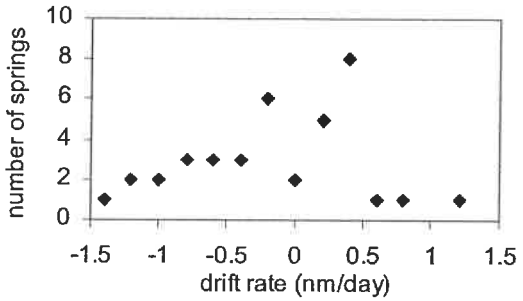

Fig.4 Distribution of dimensional drift rate

After a series of fundamental measurements, some of the springs were selected to undergo compression and heating tests, in which the springs were compressed under designed loads or/and heated to designed temperatures in a precision vacuum oven for periods of time. Consistent measurements were made after each test in order to investigate the temperature and force dependent mechanism of the dimensional instability. A steady state linear relationship was observed between the dimensional variation and the test time.

Conclusion

Measurements on a lot of 17-7 stainless steel springs have been made using the View Voyager 12×12 OCMM for up to three years. The average measurement repeatability of fifty-one springs, which have been measured for one to three years, is 0.22 micrometer (which does not include the dimensional drift with time) with standard deviation of 0.06 micrometer. An average standard uncertainty of 0.19 nm/day for measurement of linear dimensional drift was achieved. These stable measurements have provided significant information for the analysis of the dimensional instability mechanism of springs. The measurements using optical CMM have proven to be an effective method for the investigating dimensional instability with moderate accuracy.

Reference

1. S. R. Patterson, K. M. Lawton and D. Ren, Proc. 17th Annul Meeting, ASPE, 353-356, 2002.

Acknowledgement

This work has been supported by Lawrence Livermore National Laboratory.

Virtual Surface Calibration and Computational Uncertainty

Son H. Bui, T. Brian Renegar, Theodore V. Vorburger
National Institute of Standards and Technology, Gaithersburg, MD 20899, USA

1. Introduction

Surface measurement instruments, such as stylus and optical profilers, are used to characterize the roughness of surfaces. Most of these measurement instruments are microcomputer-based systems, which contain both surface analysis software and data storage. When a surface is measured, the measurement instrument generates a data file of sensor readings and stores it on a local disk. The data file is then analyzed by the analysis software provided in the measurement instrument itself. With every instrument, manufacturers or software vendors provide custom software. Hence, there can be a large variation in output results from one manufacturer to another, caused by different implementations, choice of analysis methods, the quality of software, and ambiguous surface parameters such as *RSm* parameter defined in standards leading to the possibility of different algorithms for calculating surface parameters. In 1996, the American Society of Mechanical Engineers Committee B46 (ASME B46) on the Classification and Designation of Surface Qualities conducted a surface parameter algorithm comparison to ascertain the relative agreement between various surface metrology software packages [1]. The comparison showed that results for some surface parameters do not agree with one another. Between 2002 and 2003, EUROMET (a cooperative voluntary organisation between the national metrology institutes in Europe) conducted a similar surface parameters comparison using softgauge files formatted according to ISO 5236-2 [2] [3]. The results show large differences in some height and spacing parameters. This indicates the need for a standards working group to help ensure traceability in algorithm development by providing and maintaining a set of master algorithms and data sets for companies, universities, and instrument manufacturers to compare and validate their surface analysis software. There have been recent developments in the area of surface texture algorithm verification. ISO has developed a new standard, ISO 5436-2 for verifying the software of measuring instruments. This standard defines reference topography data and reference software used to verify software under test or calibration through comparison. Physikalisch-Technische Bundesanstalt (PTB) in Germany developed reference software for roughness analysis [4]. Uchidate et al. developed a procedure to generate reference data for 3-D texture using non-causal 3-D auto-regressive (AR) Model [5].

Detailed documentation on algorithms employed within software implementations is often unavailable to the users. In those cases, it is not possible for users to know how the algorithms are implemented or how to find all coding errors in the software. So it is necessary to use black-box testing for software validation, whereby the internal workings of the analysis software being tested are not known by the users. The users are only aware of the inputs and the expected output. There are two ways for testing software using black-box testing. The first [5] is to use a data generator to generate reference data sets based on known parameters. Reference data set is then inputted into test software. The results of test software are then compared with known parameters. The other approach [1] [4] is to use reference software to generate reference results. Reference software is written to an extremely high standard and well tested. A common data set is inputted into both software under test and the reference software. The results calculated by test software are then compared with reference results. These two methods are illustrated in figure 1.

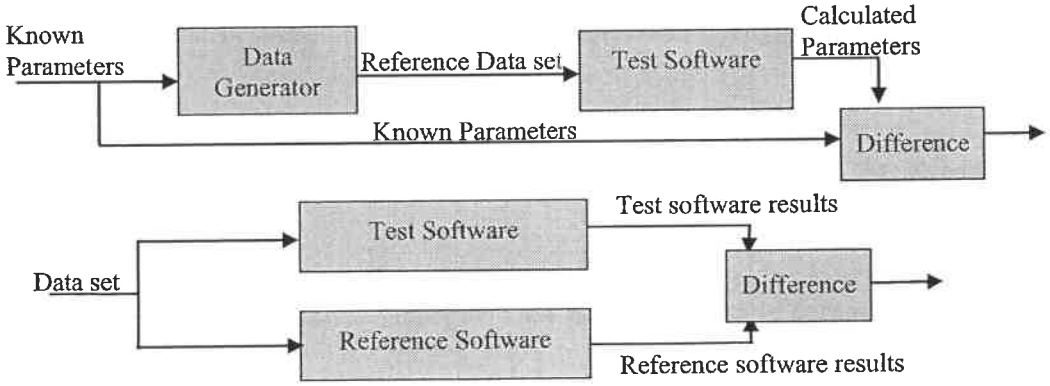

Figure 1. "Black-box" testing using Data Generator and Reference software

2. Virtual Surface Calibration

The National Institute of Standards and Technology (NIST) has developed a virtual surface calibration web site (VSC) to help users to validate or compare their surface analysis software with NIST calculations. The web site allows users to download virtual surface data files and associated information, which includes NIST generated surface analysis results, from a database. Users can then compare their surface analysis results with NIST analysis results. On the other hand, the users can upload their own surface profile or topography sensor data to the web site for analysis. After performing the analysis, they can download the NIST calculated results to their computer for comparison. The user scenario for virtual surface calibration is shown in the figure below.

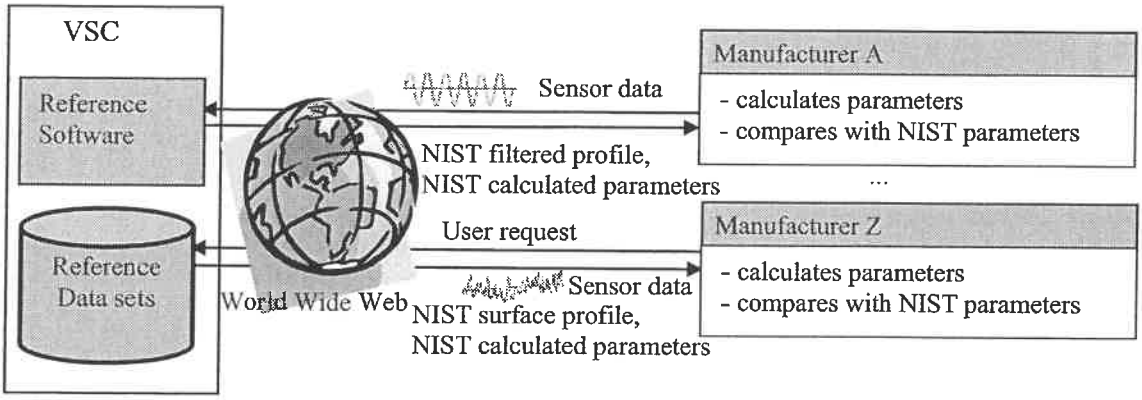

Figure 2. NIST Surface Metrology Algorithm Testing System

The web site provides users with a broad spectrum of tools to validate their surface analysis software. The web site has visualization and analysis tools for surface profiles and surface topography images. The user can upload their own data files in .txt [6], .sdf [7], and .smd [2] formats to the website and compare their calculation results with results calculated by analysis tools from the web site. These analysis tools include:

Analysis tools for surface profiles:

- slope and polynomial detrending
- Gaussian and 2RC filtering
- power spectral density, autocorrelation, and cross correlation
- surface parameters with their calculated uncertainties: *Ra, Rq, Rsk, Rku, RΔq, Rz, Rp, Rv, Rt,* and *Rsm.* These parameters can be calculated based on the American Society of Mechanical Engineers Committee B46 (ASME B46) Standards or based on the ISO 4287, and ISO 4288 standards.

Analysis tools for surface areal (3D surface topography image):

- Gaussian Filter
- least-squares surface fitting
- surface parameters with their calculated uncertainty: *Sa, Sq, Ssk, Sku, Sdq, St, Sp, Sv, S10z, Sds, Ssc*, and *Sdr*
- power spectral density, autocorrelation and cross correlation

The web site also provides a database which stores surface profiles and surface topography along with surface parameters and uncertainties calculated by NIST. With this database, the users can query information through the Internet and use the information to validate parameter calculations and the implementation of their algorithms. The database provides features for querying information based on parameters, instrument types, processes, filenames, and part names. The users are able to download surface profiles and corresponding analysis data in sdf, smd, and xml [6] format from the database using a web browser. The web site is available at http://ats.nist.gov/VSC/jsp.

For software quality assurance, the web site was tested by experts in surface metrology. Surface parameters were tested against the results of the ASME B46 surface parameters comparison [1], against commercial software packages [8], and against PTB reference software [4]. In addition to that, we generated surface profiles with known surface parameters and then used these to test our surface parameter calculations. Surface roughness filtering algorithms were tested by comparing our calculated transmission characteristics curves with theoretical curves and commercial software packages. The figure 3 shows our testing results for the 3D Gaussian filter. The maximum difference between the transmission characteristic of Gaussian filter implemented using straight convolution (figure 3b) and theoretical transmission characteristic of Gaussian filter (figure 3a) is 1.78 %.

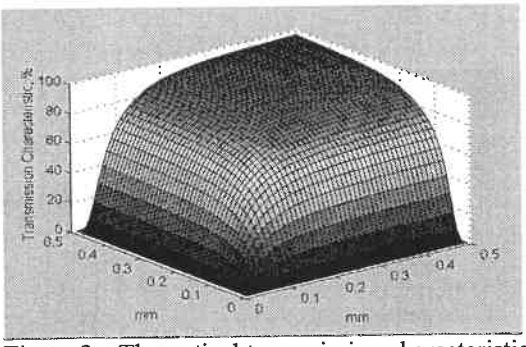

Figure 3a. Theoretical transmission characteristic curve of Gaussian filter at cutoff of 0.08 mm

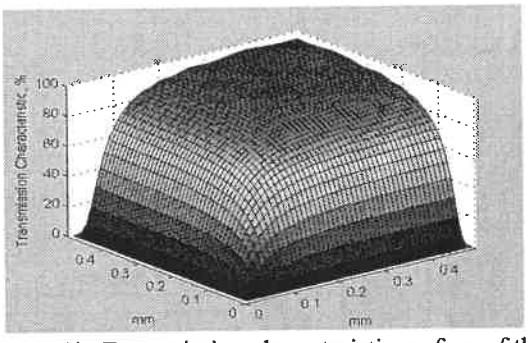

Figure 3b. Transmission characteristic surface of the Gaussian filter implemented by straight convolution

3. Computational Uncertainty

Computational metrology "refers to the study of the effects of data analysis computation on the performance of measurement systems" [9]. In engineering metrology, computations on raw data produce meaningful parameters used to verify the quality and functionality of manufactured parts or to diagnose problems in manufacturing processes. In surface metrology, raw data is normally preprocessed and filtered before computing surface parameters. This process can introduce a variety of errors such as rounding/truncation errors or errors propagated from the measurement. This is shown in figure 4. The choice of analysis method can greatly affect measurement uncertainty. Some analysis methods introduce more rounding errors due to PC precision than other methods. Equation 1 shows an example of how an rms deviation is calculated by two different formulas. The first formula introduces less rounding and truncation errors than the second formula, which is slightly faster.

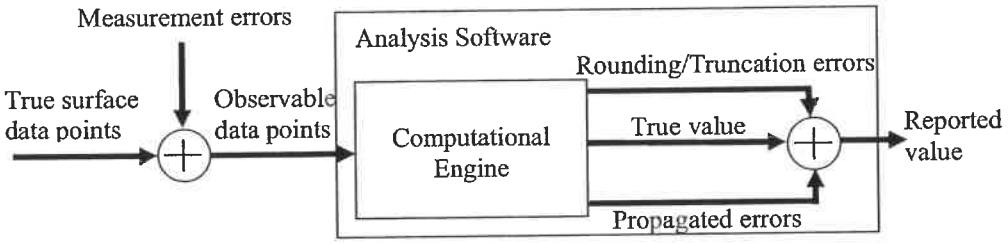

Figure 4. Propagated errors and rounding/truncation errors during analysis

$$rms = \sqrt{\frac{1}{N}\sum_{i=1}^{N}(z_i - \bar{z})^2} \qquad \text{and} \qquad rms = \sqrt{\frac{\sum_{i=1}^{N} z_i^2}{N} - \left(\frac{\sum_{i=1}^{N} z_i}{N}\right)^2} \qquad (1)$$

Where N is the number of data points and z is the value of a data point

When raw data is obtained from a measurement instrument, it always has uncertainty associated with surface profile data points. The sources of uncertainty may be from environment conditions, A/D converter resolution and

accuracy, tip geometry, etc. When surface profile data points are inputted to analysis software, the measurement uncertainty is propagated through the algorithms. An unstable algorithm, which is more sensitive to noise, will have higher propagated uncertainty. We used Monte Carlo Simulation (MCS) [10] to calculate uncertainty of the *RSm* parameter. First, we added a random noise to each data point of a sinusoidal profile that we considered as the true profile surface. The random noise had a normal distribution, mean of zero and standard deviation of 1 % *Rq* for the z-direction and 2 % spacing in the x-direction. We then calculated *RSm* parameter for a simulated sinusoidal profile based on two algorithms: one algorithm applies height and spacing discrimination on the profile peaks and other does not. In order to see the variations of the output and how their uncertainties have propagated through, we repeated the step above a large number of times. For each case we started with a true sinusoidal profile, added some noise, and calculated *RSm* parameter. The mean and standard deviation of *RSm* was then obtained based on the outputs of *RSm* from each loop. The result shows that *RSm* calculated by the algorithm with a height and spacing criteria has uncertainty of 1.97 % of mean. Without using criteria conditions, *RSm* has uncertainty of 25.7 % of mean.

4. Conclusion

In this paper, we presented the development of a virtual surface calibration web site at the National Institute of Standards and Technology. The web site helps users to validate or compare their surface analysis software with NIST calculations. We also discussed computational uncertainty and how data analysis factors affect surface measurement parameters. Software performances are affected by choice of analysis method and quality of software. Different analysis software implementations and software quality can yield significant differences in output parameters.

5. References

1) S. H. Bui, T. Brian Renegar, T. V. Vorburger, J. Raja, M. C. Malburg, Internet-based Surface Metrology Algorithm Testing System, 9th Int. Conf on Metrology and Properties Engineering Surfaces, 2003, Halmstad, Sweden, p. 122
2) ISO 5436-2, Geometrical Product Specifications (GPS) — Surface texture: Profile method; Measurement standards. Part 2: Software measurement standards
3) L. Jung, B. Spranger, R. Krüger-Sehm, L. Koenders, M. Krystek, Reference software for roughness analysis-features and results, The XI International Colloquium on Surfaces, Shaker Verlag, Germany, 2004, p. 164
4) L. Jung, R. Krüeger-Sehm, B. Spranger, L. Koenders, Reference software for Roughness Analysis, Proceedings of the EUSPEN 2001, Turin, Italy, p. 500
5) M. Uchidate, T. Shimizu, A. Iwabuchi, K. Yanagi, Generation of Reference Data of 3-D Texture Using the Non-causal 2-D AR Model, 9th Int. Conf on Metrology and Properties Engineering Surfaces, 2003, Halmstad, Sweden, p. 67
6) S. H. Bui, T. V. Vorburger, Internet-based Surface Metrology Algorithm Testing System, http://ats.nist.gov/VSC/jsp, 2004
7) K. J. Stout, P. J. Sullivan, W. P. Dong, E. Mainsah, N. Lou, T. Mathia and H. Zahouani, The Development of Methods for The Characterisation of Roughness in Three Dimensions, Report EUR 15178 EN. EC Brussels, 1993
8) S. Bui, T. V. Vorburger, B. Muralikrishnan, J. Raja, Surface Metrology Software Variability in Two-Dimensional Measurement, Proc. ASPE 2003
9) T. H. Hopp, Computational Metrology, ASME Manufacturing Review, 1993
10) M G. Cox, M. P. Dainton, P. M. Harris, Uncertainty Support for Metrology Best Practice Guide No. 6, Uncertainty and Statistical Modeling, National Physical Laboratory, UK, 2001

DETERMINATION OF APERTURE CORRECTION FACTOR OF INTEFERENCE MICROSCOPE BY DOUBLE-TILT IMAGING METHOD

Yen-Liang Chen, Chao-Jung Chen, Chen-Yu Wang
Center for Measurement Standards / Industrial Technology Research Institute, Taiwan

This paper presents a new method to determine the aperture correction factor that would adequately allow for the measurement of step heights to be established in the existing traceability chain. This method utilizes a simple methodology to measure the sample surface twice in opposite inclined angles with an interference microscope so that the error due to the leveling of the sample' position could be dismissed in the analysis. Accordingly, the name Double-Tilt Imaging Method is given for this approach. Repeated measurements for the traceable correction factor yield an average value of 1.01936 with a standard deviation of $5.6x10^{-4}$ for the 10x Mirau-type objective lens. The same method is also applied to determine the values for objective lens of 20x and 50x magnifications.

Introduction

For measurement of step heights with interference microscopes such as the Michelson, Mirau, or Linnik-type, the optical paths projected onto and reflected from the sample surface are not equal to twice of the difference in height due to light focus by objective lens[1]. In fringe pattern analysis, numerical aperture would affect the spacing of the fringes captured from the sample's surface topography. *Figure 1* illustrates the measurement between different heights of the sample surface; the height *H* is not equal to half of the optical path difference unless the incident light is perpendicular to the projected surface. Hence, a correction factor for the numerical aperture should be employed to amend the value obtained after the measurement is taken. Conventionally, the determination of the correction factor could rely on derivations from approximation equations or from numerical computation against predetermined specifications of standard specimens. Nevertheless, neither method could practically suffice the establishment of measurement traceability for the values under investigation. The need to comprehend the traceability requirement is especially significant in metrological applications. This paper presents the Double-Tilt Imaging method for determining traceable correction factor for the numerical aperture of an interference microscope.

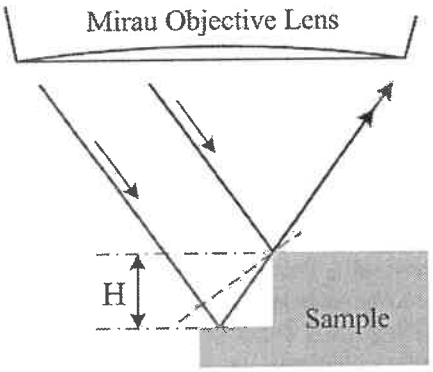

Figure 1. Optical path difference with height difference

Traceability of Step Heights

A traceable interference microscope has been established to calibrate the step height standards at the National Measurement Laboratory (NML) in Taiwan. It consists of a commercial interference microscope, a stabilized He-Ne laser and a ground glass. The light source of the microscope is replaced by a stabilized laser. To eliminate the sparkle noise during the transmission through the optical fiber, the laser passes through a rotated ground glass before interfering with the sample. By analyzing the fringe intervals in the interference image, the height value of the

standards would be calculated and traced to the definition of the meter via the stabilized laser. *Figure 2* shows the traceability of the step height standards. For stylus instruments[2], scanning probe microscopes[3], or interference microscopes[4], users usually calibrate the displacement sensors periodically by step height standards[5]. The step height standards can be calibrated by a traceable interference microscope with stabilized laser source traced to the length standards. In this study, Double-Tilt Imaging method is used to determine the correction factor for the numerical aperture. With this method, two tilted angles are measured by an autocollimator, which is calibrated by angular standards and traced to the circle closure principle.

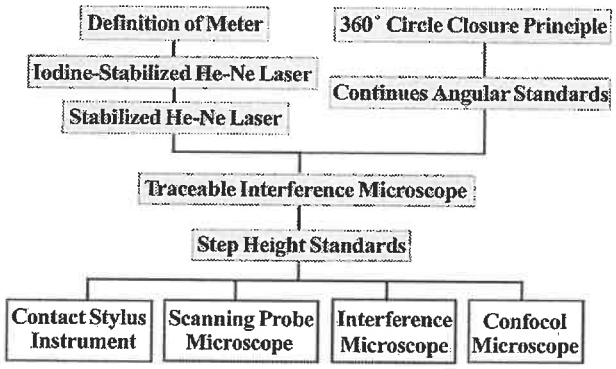

Figure 2. Traceability of step height standards

Working Principle

Figure 3 reveals the relationship between the spatial wavelength L (or pitch) of the interference fringes and the height difference. When the incident light is perpendicular to the sample surface, the height difference between single fringes interval is $\lambda/2$, where λ is the light wavelength. Due to the effect of focus by objective lens, the height difference has to be corrected by multiplying a factor k, which is the correction factor for the numerical aperture. Thus, the inclined angle $\overline{\theta}$ can be expressed by a trigonometric function as:

$$\overline{\theta} = \tan^{-1}\frac{k\cdot\lambda/2}{L} \cong \frac{k\cdot\lambda/2}{L}$$

Using the proposed method, the flat surface is measured twice at different inclined angles (θ_1 and θ_2). Simultaneously, two spatial frequencies (ω_1 and ω_2) of the fringe patterns are also calculated. The spatial wavelengths would be $L_1 = 2\pi/\omega_1$ and $L_2 = 2\pi/\omega_2$.
Thus,

$$\theta_1 \cong \frac{k\cdot\lambda/2}{L_1} = \frac{k\cdot\lambda\cdot\omega_1}{4\pi}$$

$$\theta_2 \cong \frac{k\cdot\lambda\cdot\omega_2}{4\pi}$$

Assuming that $\theta = \theta_1 + \theta_2$ and $\omega = \omega_1 + \omega_2$, the correction factor can be obtained as:

$$k = \frac{4\pi\cdot\theta}{\lambda\cdot\omega}$$

Here the values of θ and λ must be traced to the angle standards and the definition of the meter respectively, and ω can be obtained by the sine curve fitting algorithm[6].

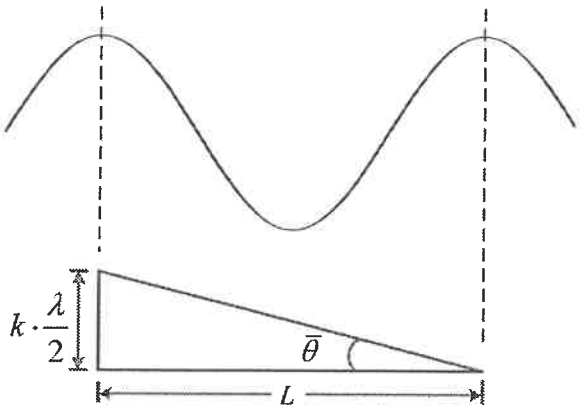

Figure 3. Fringes interval with height difference

Experimental Setup

Figure 4 illustrates the experimental setup for determining the correction factor. The stabilized laser beams (1) are separated by beam splitter (2) and then focused by Mirau-type objective lens (3). A reflected mirror with $\lambda/10$ flatness is fixed on the upper surface of square gauge block (5) positioned on the sample stage of the interference microscope. An autocollimator (6) is

positioned in adjacent to measure the inclined angle of the lateral surface of the square gauge block. After tilting the sample stage in positive (7) and negative (8) inclines separately, both images of the fringe patterns are recorded.

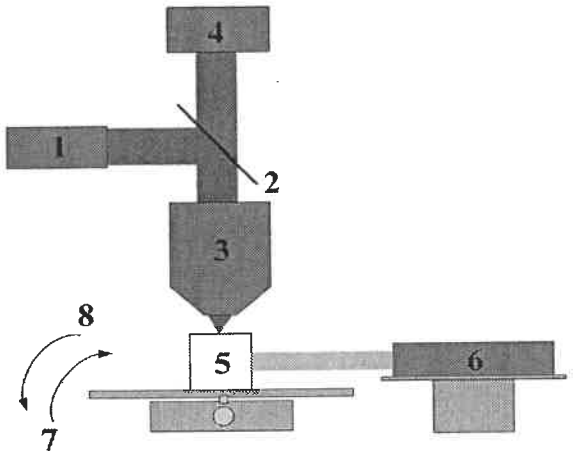

Figure 4. Setup for Double-Tile Imaging method

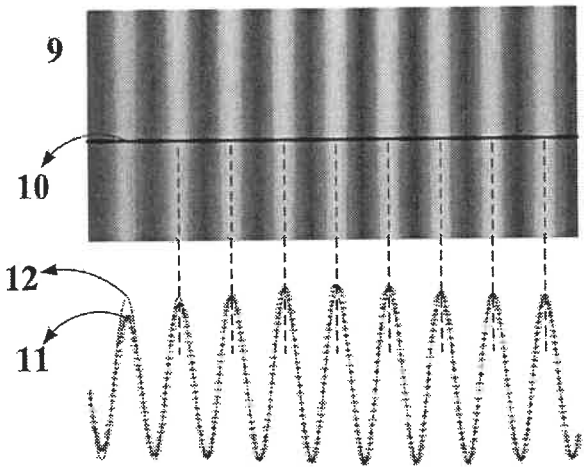

Figure 5. Sine fitting to obtain the spatial frequency from fringe pattern

Figure 5 shows the interference fringe image of the reflected mirror (9). After adjusting the focal position and the inclination of the sample stage, the image is captured by a CCD camera (4). The field of view on the camera must be calibrated by a microscale before taking the measurement. The spatial frequency of the fringe images is then calculated by the sine curve fitting algorithm (10-12). The value of the wavelength and the differences both in angle and in spatial frequencies between positive and negative tilts reveal sufficient information to allow for the determination of the correction factor for the numerical aperture directly.

Table 1 lists twenty repeated measurements of the correction factor for 10x Mirau-type objective lens by the Double-Tilt Imaging method. The average value is 1.01936 and the standard deviation is 5.6×10^{-4}. The very same method is applied to determine the correction factor for 20x and 50x Mirau-type objective lens on the traceable interference microscope. The repeated measurement data is shown in *Table 2*. For the 20x objective lens, the average value is 1.04835 with a standard deviation of 5.8×10^{-4}; and for the 50x, the average value is 1.07731 with a standard deviation of 9.1×10^{-4}.

Table 1. Measurements of the correction factor for 10x Mirau-type objective lens

10x Objective Lens							
1	1.01829	6	1.01950	11	1.01956	16	1.01985
2	1.02008	7	1.01926	12	1.01948	17	1.01977
3	1.01985	8	1.01968	13	1.01945	18	1.01896
4	1.01923	9	1.01820	14	1.01895	19	1.01912
5	1.01912	10	1.02043	15	1.01874	20	1.01971

Table 2. Measurements of the correction factor for 20x and 50x Mirau-type objective lens

20x Objective Lens				50x Objective Lens			
1	1.04784	6	1.04855	1	1.07732	6	1.07818
2	1.04893	7	1.04867	2	1.07789	7	1.07656
3	1.04792	8	1.04901	3	1.07644	8	1.07755
4	1.04773	9	1.04747	4	1.07626	9	1.07612
5	1.04903	10	1.04833	5	1.07824	10	1.07855

Evaluation of relative standard uncertainty of the correction factor

From the equation of the numerical aperture correction factor (k), the relative standard uncertainty can be expressed as

$$u_{rel}^{2}(k) = u_{rel}^{2}(\theta) + u_{rel}^{2}(\lambda) + u_{rel}^{2}(\omega)$$

Relative standard uncertainty of angle measurements by autocollimator, $u_{rel}(\theta)$: The summation of positive and negative tilted angles is $\theta = \theta_1 + \theta_2$, where θ_1 and θ_2 are measured by an autocollimator (ELCOMAT 2000/244). The error sources of angle measurement are (1) Traceability, $u(\theta')$; (2) Repeatability, $u(\theta'')$; (3) Resolution, $u(\theta''')$.

Relative standard uncertainty of laser wavelength, $u_{rel}(\lambda)$: A stabilized He-Ne laser (λ= 0.63282 μm) is used as the light source. The uncertainty of the light wavelength would not exceed 0.01 nm, which is sufficient to serve as the light source.

Relative standard uncertainty of spatial frequency, $u_{rel}(\omega)$: The spatial frequency, obtained by "Four-Parameter Fitting of Sine" algorithm, is the sum of two spatial frequencies of the fringe images ($\omega = \omega_1 + \omega_2$). The error sources that would affect sine fitting are (1) Theory limitation, $u(\omega')$; (2) Optical quality, $u(\omega'')$. *Table 3* shows the uncertainty budget of the numerical aperture correction factor for the 10x objective lens.

Table 3. Uncertainty budget of the numerical aperture correction factor for 10x objective lens

Quantity	Estimate	Type	Dist.	Std. Uncertainty	Rel. Std. Unc.	ν_i
θ	1600"	-	-	0.11"	6.9×10^{-5}	115
θ_1 Traceability		B	N	0.075"		50
θ_1 Repeatability		A	t	0.013"		249
θ_1 Resolution		B	R	0.014"		12.5
θ_2 Traceability		B	N	0.075"		50
θ_2 Repeatability		A	t	0.013"		249
θ_2 Resolution		B	R	0.014"		12.5
λ	632.82 nm	B	-	0.01 nm	1.6×10^{-5}	50
ω	0.168μm^{-1}	-	-	9.5×10^{-5}μm^{-1}	5.7×10^{-4}	60
ω1 Theory limit.		B	R	2.14×10^{-5}μm^{-1}		12.5
ω1 Optical qual.		B	R	6.4×10^{-5}μm^{-1}		12.5
ω2 Theory limit.		B	R	2.14×10^{-5}μm^{-1}		12.5
ω2 Optical qual.		B	R	6.4×10^{-5}μm^{-1}		12.5
k=1.01936 ; Rel. Std. Uncertainty of k= 5.74×10^{-4} ; υ_i = 61						

Conclusion

The Double-Tilt Imaging method is used for determining the correction factor for the numerical aperture in the phase measurement of an interference microscope with 10x, 20x, and 50x Mirau-type objective lens. The error sources such as the angle measurement, wavelength of the light source, and fitting spatial frequency are considered in the evaluation of the relative standard uncertainty. The obtained correction factor for the numerical aperture is also traceable to both the definition of the meter and the angle standards.

Reference

[1] Schulz G. and Elssner K.E., "Errors in phase-measurement interferometry with numerical apertures", Appl. Opt. 30,4500-6, 1991.

[2] Bennett, J. M., Eling, V. and Kjoller, K., "Recent developments in profiling optical surface", Appl. Opt., Vol. 32, (1993), pp. 3442-3447.

[3] Bhushan, B., Wyant, J. C. and Koliopoulos, C. L., "Measurement of surface topography of magnetic tapes by Mirau interferometry", Appl. Opt., Vol. 24, (1985), pp. 1489-1497.

[4] Brand, U. and Hillmann, W., "Calibration of step-height standards for nanometrology using interference microscopy and stylus profilometry", Prec. Eng., Vol. 17, (1995), pp. 22-33.

[5] Song, J. F. and Vorburger, T. V., "Standard reference specimens in quality control of engineering surfaces", J Res NIST, Vol. 96, (1991), pp.271-289.

[6] T.Z. Bilau, T. Megyeri, A. Sárhegyi, J. Márkus and I. Kollár, "Four-Parameter Fitting of Sine Wave Testing Results: Iteration and Convergence" Computer Standards and Interfaces 26(1), pp. 51-56, Jan. 2003.

Wavelet Analysis of Different Silicon Wafer Surfaces

Ndubuisi G. Orji and Jay Raja
Department of Mechanical Engineering,
University of North Carolina at Charlotte, Charlotte NC 28223

Introduction

We have applied wavelet analysis to a set of silicon surfaces produced by different finishing processes and previously used in a laboratory comparison of surface topography measurements [1]. Surface roughness affects the function of a wide range of engineering products. Some of the most demanding applications are in the semiconductor industry where surface roughness must be monitored and controlled. Semiconductor silicon wafer roughness affects properties such as electron channel mobility, thin-film transistors gate bias stability and thin oxide film quality [2]. Silicon wafers serve as the starting component for semiconductor devices and require surface roughness in the nanoscale regime.

A widely used roughness specification parameter is the root mean square (*rms*) roughness, a statistical parameter that characterizes the height deviation of the peaks and valleys of a rough surface. Part of the appeal of the *rms* roughness parameter comes from the ability to obtain it directly from light scattering measurements as well as profile measurements. It also has a solid statistical basis because its definition is the same as the standard deviation. However, parameters such as the *rms* roughness provide only height information, and are unable to describe other aspects of the surface. For characterizing technologically and economically important surfaces such as silicon wafers, the *rms* roughness is an important parameter but not sufficient. This fact has been recognized over the last few years by the semiconductor industry, which has conducted studies on the use of statistical functions to specify wafer surface roughness [1,3].

Experimental Approach

We measured ten different silicon wafer surfaces using an interferometric microscope. Each sample represents a step in a series of processes needed to achieve the surface finish requirements for integrated circuit substrates. Usually silicon wafers are ground, lapped, etched, rough polished, fine polished and cleaned. A list of wafers used and their final processing is shown in Table 1. The data are analyzed using two-dimensional wavelet filter banks, which partition the data into different spatial wavelengths.

Each sample represents a step in a series of processes needed to achieve the surface finish requirements for integrated circuit substrates. The measurement technique used is interferometric microscopy. A light beam is filtered for the right wavelength and split by a beam splitter. One beam goes to the sample surface and the other goes to a reference surface. The reflected beam from the sample surface is recombined with the reflected beam from the reference surface. The two beams are sent to a CCD camera. The relative phase of the reflected beam from the surface is compared with phase of the beam reflected from the reference mirror after the mirror is moved a known distance. This is the phase shift interferometry mode of the instrument, and it is used for smooth surfaces. Another mode called scanning white light interferometry, which works better for rougher surfaces was also used. The rms roughness values are averages from five locations on the wafer. In all cases a 20X objective was used.

Wavelet Analysis

In traditional surface roughness metrology, spectral techniques such as the Fourier transform methods are widely used to analyze the data. However, Fourier transform methods have some drawbacks. Fourier methods give only time averaging frequency information without indicating the location of a specific frequency event. When a signal is transformed to the frequency domain, time information is lost. It is impossible to tell when a specific frequency event took place. Only the dominant wavelengths of the signal are highlighted, while others are lost in the background noise. Fourier transform methods treat all frequencies with an equal resolution in both space and frequency domains. Little or no information about the evolution of the profile is available when roughness of different scales are involved. Wavelet transformation can be thought of as a windowing technique that allows the use of variable size windows. Large windows are used when precise low frequency information is needed and smaller windows when high frequency information is needed. In general, the time averaging feature of Fourier analysis is not a problem if the signal do not change over time (if the signal is stationary). However, surface roughness is a non-stationary signal, and contains many non-stationary and transitory characteristics such as drift, trends, spikes and other components that may be the most interesting parts of the signal.

To address these shortcomings an analysis method with the ability of analyzing the data at different scales and at resolutions that match each scale. We used the technique of wavelet transform [4] to look at the structures or signals at multiple scales. The fundamental idea is to derive a group of signals where the high frequency information in each succeeding profile is suppressed. This could also be thought of as filtering with different cutoffs. The multi-scaled view of the wavelet filter bank technique provides information about the evolution of the spectrum. An important issue to consider when analyzing surface roughness data is the choice of cut-off to use. In traditional surface roughness metrology Gaussian filters have been standardized and are widely used [5], however these standards were developed for application in the metal cutting industry where typical roughness amplitudes are several orders of magnitude larger than finished semiconductor wafers. Multi-scale analysis provides flexibility in choosing a cutoff. The wavelet transform is

$$\psi_{a,t}(x) = \frac{1}{\sqrt{a}}\psi\left(\frac{x-t}{a}\right) \tag{1}$$

where a represents scaling, and t represent translation. Hence a family of wavelets can be obtained by scaling $\psi(x)$ (the mother wavelet) by a and translating it by t. $a^{1/2}$ is a normalization factor applied across the different scales. In two dimensional wavelet function, a two dimensional scaling function denoted by

$$\phi(x,y) = \phi(x)\phi(y) \tag{2}$$

is used. $\phi(x)$ and $\phi(y)$ are one-dimensional scaling functions. The image is decomposed into vertical components, horizontal components and diagonal components based on one-dimensional wavelets $\psi(x)$ and $\psi(y)$ and one-dimensional scaling functions $\phi(x)$ and $\phi(y)$. The following equations denote the resulting components:

$$\text{Horizontal wavelet: } \psi_1(x,y) = \phi(x)\psi(y) \tag{3}$$

$$\text{Vertical wavelet: } \psi_2(x,y) = \psi(x)\phi(y) \tag{4}$$

$$\text{Diagonal wavelet: } \psi_1(x,y) = \psi(x)\psi(y) \tag{5}$$

Calculation, Results and Discussion

A description of the wafers and their rms roughness values are given in table 1. Wafers A, C, E, F and G represent starting and intermediate stages of the process, while wafers H to L represents final processes. The rms roughness could be viewed as a starting point for the analysis, however it does not give any information about the wavelength content of the images. It is interesting to note that the rms roughness values in Table 1 only start to decrease substantially from wafer H. This is expected since the later processes focus more on achieving a smooth finish. Figure 2 shows top down interferometric microscope images of the wafers. Figures 3(a) and 4(a) show the wavelet approximations, while figures 3(b) and 4(b) show the roughness after wavelet filtering.

Table 1: Wafer Description and RMS Roughness Values. Spatial frequency range: 3.38μm^{-1} x10^{-3} to 1.2 μm^{-1}

Wafer	Description	rms roughness
A	Grind only	1.59μm
C	Lap (Small grit)	1.56 μm
E	Lap (small grit)+ caustic etch	7.44 μm
F	Lap (large grit)+ acid etch	4.05 μm
G	Lap (small grit) + acid etch	1.39 μm
H	Partial polish	2.38 nm
I	Experimental polish	1.42 nm
J	Standard polish	1.29 nm
K	Epitaxial with native oxide	1.45 nm
L	H-terminated epitaxial	1.32 nm

To get a closer view of the decomposed surfaces, we look at multiresolution approximation profiles of some of the surfaces. Figure 5 shows profiles from Wafers A, C, E, F, H and K. Wafers A, C, E and F were decomposed to 7 levels and wafers H and L to eight levels. The cutoffs were from 0.709 μm to 181.55 μm, increasing by a factor of two at each level. Each image shows the wavelength content of the profiles, and all the images as a whole show how the dominant spatial wavelengths change for each polishing process.

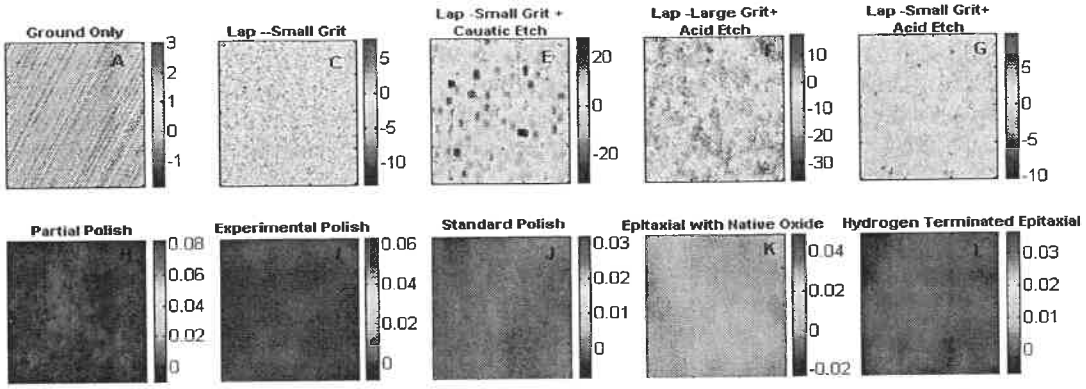

Figure 2: Top down interferometric images of the wafers. The values on the color bar are all in μm.

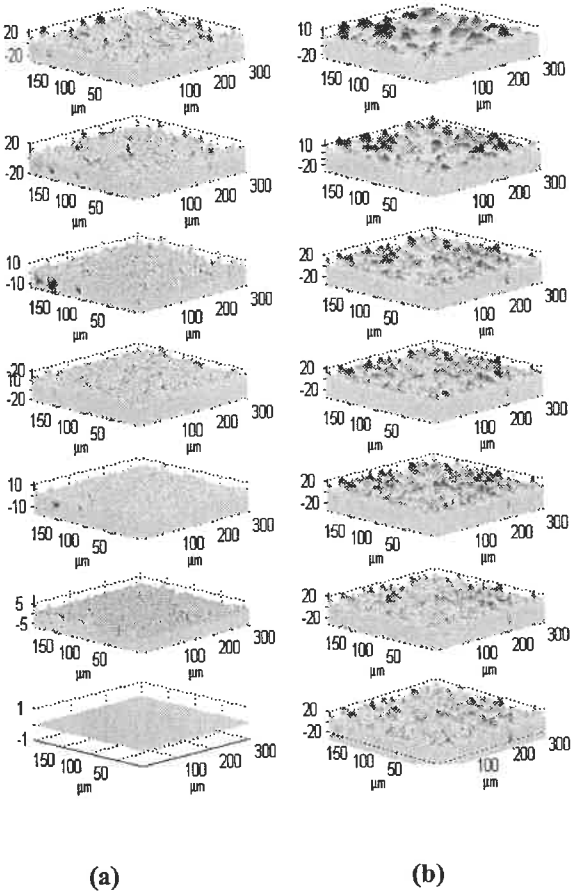

(a) (b)

Figure 3: Wafer E (a) Multiresolution approximations by wavelet transform. (b) Roughness after wavelet filtering

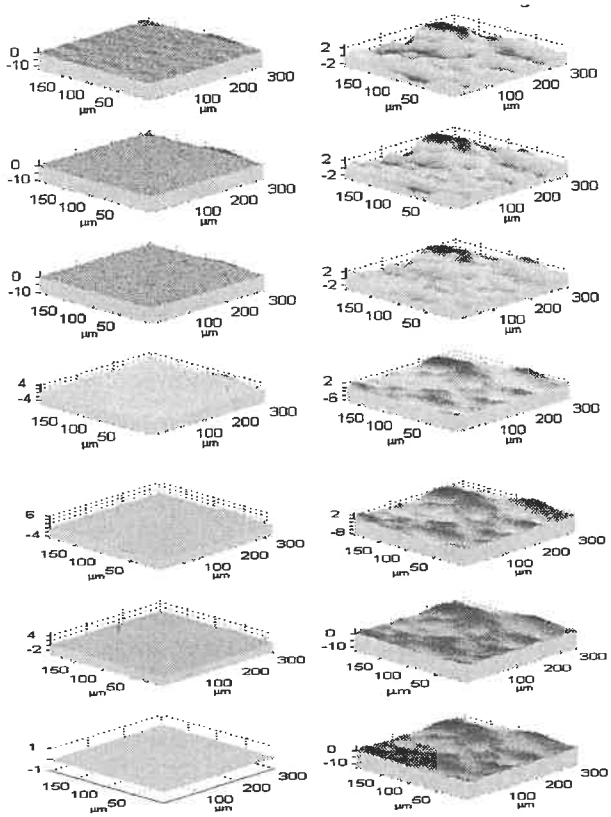

(a) (b)

Figure 4: Wafer K (a) Multiresolution approximations by wavelet transform. (b) Roughness after wavelet filtering

No claims are made as to whether a specific spatial wavelength in any of the profiles can be linked to manufacturing method from a previous process. However, using an analysis procedure like wavelets lays out the profile components and can aid in making process decisions. Table 2 shows the rms roughness *(rms)* after applying a wavelet transform filter with 11.35 μm cutoff, a length large enough to contain more than fifty 100-nm patterned lines with a one to one spacing. Comparing the values in tables 1 and 2, the biggest changes are in the values from wafers A, C, E, F and G, the values for wafers H to L stayed essentially the same, close to the vertical resolution of

the instrument. One should note that spatial wavelengths of interest will depend on the application, our purpose is to highlight how such a decomposition works. The smoother surfaces (Wafers H to L) seem to be dominated by long spatial wavelength roughness. For these surfaces, the peak to valley values are also small, but as semiconductor linewidths decrease, this could be an issue especially with the planarity of neighboring line structures.

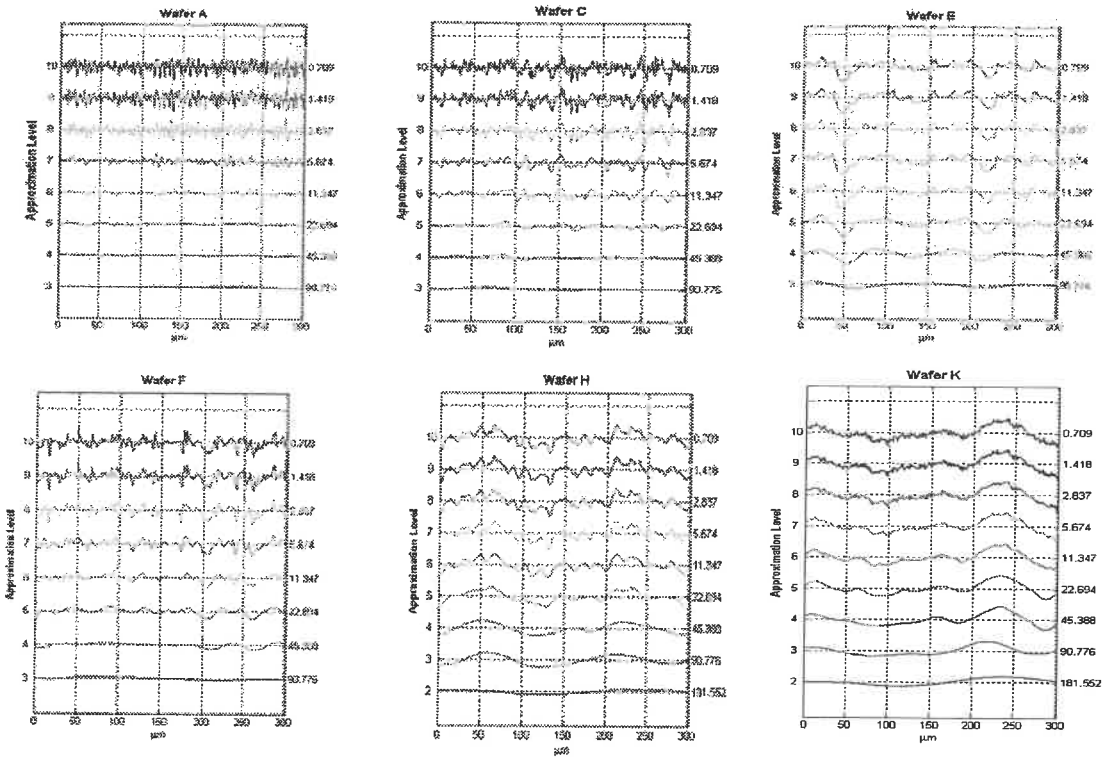

Figure 5: Multiresolution approximation by wavelet transform for profiles from wafers A, C, E, F, H and K. The values on the right side of the y-axis represent filter cuttoff in µm at different approximation levels.

Table 2: RMS Roughness Values after Wavelet Filtering (11.75 µm Cuttoff)

Wafer	rms roughness (Sq)
A	0.101 µm
C	0.452 µm
E	0.517 µm
F	0.75 µm
G	0.235 µm
H	1.73 nm
I	1.26 nm
J	1.22 nm
K	1.35 nm
L	1.38 nm

Conclusion

The above exercise illustrates one of the areas where wavelet analysis could be applied in surface topography evaluation. By looking at the multiresolution approximation one can see how the images evolve, and which levels are responsible for trends, spikes and other characteristics of the profile. Wavelet analysis can serve as a complementary technique to methods such as power spectral densities.

Reference:

1. Marx E, Malik IJ, Strausser YE, Bristow T, Poduje N, Stover JC, "*J. Vac. Sci. Technol. B* 20 (1): 31-41 (2002)
2. Ohmi, T.; Miyashita, M.; Itano, M.; Imaoka, T.; Kawanabe, I.; IEEE Trans. on Electron Devices, 39(3) p537 (1992)
3. Bullis WM *Micro* 14 (1): 47-53 (1996)
4. Raja J, Muralikrishnan B, Fu S, Prec. Eng. 26 (2): p222 (2002)
5. ASME/ANSI B46.1, Surface Texture (Surface Roughness, Waviness, and Lay), ASME, New York (2003)

Standard Deviation or Standard Deviation of the Mean - How to Report Statistical Variation in Surface Calibrations?

J. F. Song and T. V. Vorburger
National Institute of Standards and Technology (NIST)
Gaithersburg, MD 20899

Keywords: surface roughness, surface calibration, uncertainty, geometrical non-uniformity, statistical variation.

1. Introduction

Statistical variation plays an important role in the uncertainty budget of surface calibration reports. Statistical variation mainly comes from two sources: the random variation of the measurement system (the measurement repeatability) and the random variation over the calibrated surface (the geometrical non-uniformity). Geometrical non-uniformity is an important quality factor for a surface calibration specimen. It usually contributes a dominant part of the statistical variation. In a surface calibration report, statistical variation might be represented by either the standard deviation σ_x or the standard deviation of the mean $\sigma_{\bar{x}}$. Both are calculated from a set of multiple measurements distributed at different positions within the measurement area. If the standard deviation is used for representing the statistical variation, the measurement uncertainty is reported for a single measurement. Otherwise, the measurement uncertainty is reported for the mean value of multiple measurements. From the point of view of statistics, there is no difference if this information is provided sufficiently and used correctly. If not, however, an over- or under-estimated calibration uncertainty might result.

2. Uncertainty Procedure in Surface Calibrations

The measurement uncertainty in surface calibrations mainly comes from two sources: the measurement system and the measured surface. The quoted expanded uncertainty U (with a coverage factor $k = 2$) is equal to twice the combined standard uncertainty u_c calculated from the quadratic sum of the instrument (or the measurement system) standard uncertainty $u_{(i)}$ and the statistical variation of the measurements $u_{(s)}$ [1,2]. The first part, $u_{(i)}$, mainly represents the quality of the measurement system, while the second part, $u_{(s)}$, mainly represents the geometrical non-uniformity of the measured surface combined with the repeatability of the measurement system.

For the uncertainty budget of NIST surface calibrations, performed using a stylus instrument, the instrument standard uncertainty $u_{(i)}$ is a quadratic sum of six uncertainty components arising from: 1) the geometric non-uniformity and the surface finish of the step-height master calibration standard; 2) the calibration uncertainty of the step-height master standard calibrated by interferometric and stylus measurements; 3) the variation of the measured calibration constant; 4) the non-linearity of the instrument transducer; 5) the instrument noise; and 6) the tip size of the contact stylus. A detailed description of these uncertainty components may be found in Ref. 1.

The statistical variation of the measurements $u_{(s)}$ is mainly derived from the geometrical non-uniformity of the specimen under evaluation, but it also includes instrumental random variation, or measurement repeatability which usually takes a small part. The statistical variation may be represented by the standard deviation σ_x or the standard deviation of the mean $\sigma_{\bar{x}}$, and included as a Type A uncertainty [3, 4] in the uncertainty budget. Then the statistical variation $u_{(s)}$ is quadratically added with the instrument standard uncertainty $u_{(i)}$, resulting in the combined standard uncertainty u_c, from which the expanded measurement uncertainty U is calculated with a coverage factor of $k = 2$.

3. For Calibration Laboratories

How to report statistical variation in surface calibrations, standard deviation σ_x or standard deviation of the mean $\sigma_{\bar{x}}$? Currently there is not a standardized procedure. The procedure should depend on how customers use the calibrated specimen. In many cases, customers use the specimen only for a single-trace calibration, therefore, the measurement uncertainty should be reported for a single measurement. If the customer uses the specimen for a multi-trace calibration, and takes the mean value as the calibration result, then the measurement uncertainty for the mean value of the multiple measurements should be reported. The number of measurements, n, with the distribution of the measurement positions must be included in the calibration report. In either case, as long as sufficient information is shown in the calibration report, customers may convert calibration uncertainties from one approach to the other, or re-calculate uncertainties when the number of measurements is different from that shown in the calibration report.

For example, Table 1 shows a calibration result from a NIST surface calibration report for the roughness average *Ra* value of a roughness specimen. Unless the customer specifically states otherwise, it is assumed that the specimen is used for single-trace calibrations and checks. Therefore, the calibration uncertainty is reported for the single measurement. The calibration is performed at nine different positions of the roughness specimen. The calibration result, 2.958 μm ± 0.070 μm, is reported for the single measurement that includes a statistical variation of one standard deviation calculated from nine measurements at different positions. In the Appendix attached to the Calibration Report, it is useful to include the following information:

- Each *Ra* value measured at nine different positions;
- A drawing showing the distribution of the nine measurement positions;
- A detailed description of uncertainty components from the measurement system, based on which the instrument standard uncertainty $u_{(i)}$ is calculated [1];
- A measurement summary (see lower part of Table 1), which includes the average *Ra*, the statistical variation $u_{(s)}$ represented by the standard deviation σ_x, the instrument standard uncertainty $u_{(i)}$, the combined standard uncertainty u_c and/or the expanded uncertainty U ($k = 2$).

Table 1. A calibration result intended for the single measurement of *Ra*

Specimen Patch ID	Roughness Average (*Ra*) (μm)	Expanded Uncertainty ($k = 2$, μm)
3.0 μm	2.958	0.070

Appendix				
Average *Ra*	Statistical Variation (1 Standard Deviation)	Instrument Standard Uncertainty	Combined Standard Uncertainty	Expanded Uncertainty ($k = 2$)
2.958 μm	0.027 μm	0.022 μm	0.035 μm	0.070 μm

If the customer wants to report the calibration uncertainty for the mean value of nine measurements using the same data shown in Table 1, the stated measurement uncertainty for the single measurement can be easily converted to the measurement uncertainty for the mean value of nine measurements as shown below (see Table 2):

- The statistical variation $u_{(s)}$ is converted from the standard deviation σ_x to the standard deviation of the mean: $\sigma_{\bar{x}} = \sigma_x / \sqrt{n} = 0.027 / \sqrt{9} = 0.009$ μm;
- The instrument standard uncertainty $u_{(i)}$ is the same, 0.022 μm;
- The combined standard uncertainty u_c is calculated as 0.024 μm, the expanded uncertainty is $U = 0.048$ μm.

Table 2. The same data from Table 1 but showing the expanded uncertainty for the mean value of *Ra* (n = 9)

Specimen Patch ID	Roughness Average (*Ra*) (μm)	Expanded Uncertainty for the Stated Mean Value of *Ra* ($k = 2$, μm)
3.0 μm	2.958	0.048

Appendix				
Average *Ra*	Statistical Variation (1 Standard Deviation of the Mean, $n = 9$)	Instrument Standard Uncertainty	Combined Standard Uncertainty	Expanded Uncertainty ($k = 2$)
2.958 μm	0.009 μm	0.022 μm	0.024 μm	0.048 μm

From Tables 1 and 2, it can be seen that there are two uncertainty statements for the same set of measurement data. Table 1 shows the measurement uncertainty for a single measurement, which implies that when customers take any measurement within the measurement area, the measurement value may expected to lie within the range of

2.958 μm ± 0.070 μm with a confidence level approaching 95% for large n [3,4]. Table 2 shows the measurement uncertainty for the mean value of a set of nine measurements, which implies that when customers take nine measurements at different positions of the measurement area, the mean value could be expected within the range of 2.958 μm ± 0.048 μm with a confidence level approaching 95%.

4. For Users

If a customer received a calibration report showing that the measurement uncertainty was reported for a single measurement (see Table 1), and if the customer wanted to reduce the measurement uncertainty by measuring, say, three positions evenly distributed in the measurement area and taking the mean value as the result, the expanded measurement uncertainty for the mean value could be calculated by:

- Converting the standard deviation σ_x to the standard deviation of the mean $\sigma_{\bar{x}}$ for the statistical variation, $u_{(s)} = \sigma_{\bar{x}} = \sigma_x / \sqrt{n} = 0.027\ \mu m / \sqrt{3} = 0.0156\ \mu m$;
- Combining the new statistical variation, $u_{(s)} = 0.0156$ μm, with the instrument standard uncertainty, $u_{(i)} = 0.022$ μm, as the new combined standard uncertainty, $u_c = 0.027$ μm;
- Calculating the expanded uncertainty with a coverage factor $k = 2$, $U = 0.054$ μm (see Table 3).

Table 3. The same data from Table 1 but showing the expanded uncertainty for the mean value of *Ra* ($n = 3$)

Average *Ra*	Statistical Variation (1 Standard Deviation of the mean, $n = 3$)	Instrument Standard Uncertainty	Combined Standard Uncertainty	Expanded Uncertainty ($k = 2$)
2.958 μm	0.0156 μm	0.022 μm	0.027 μm	0.054 μm

5. For Standards Development Organizations

Different types of surface calibration specimens are specified in the International Standard ISO 5436 [5,6] and the U.S. National Standard ASME B46 standard [7]. In the previous version of ISO 5436 standard [5] and the current ASME B46 standard [7], tolerances and measurement uncertainties for some types of specimens are also specified. For example, for the Type D random profile roughness specimens [5-7], the specified tolerances are shown in Table 4 (originally Table 9 in Ref. 5 and Table 11-9 in Ref. 7). A wide tolerance range, ± (15 ~ 30) % (see the second column), was specified for the nominal value of *Ra*. This wide range is for the convenience of the specimen manufacturer and is usually not a problem for the user. The actual measured *Ra* value and the uncertainty are generally more important for the user. It must be noted that the standard deviation is used here for representing the statistical variation, $u_{(s)} = (3 \sim 4)$ % in the last column, mainly for the control of the geometrical non-uniformity of the calibration specimen. However, the tolerance for the uncertainty of measurement, or the expanded uncertainty, is specified for the stated mean value of *Ra*, $U = \pm (3 \sim 5)$ % (see the third column). This uncertainty includes a statistical variation represented by the standard deviation of the mean. In both the ISO and ASME standards [5,7], there is a note stating that the mean value is "taken from 12 evenly distributed readings" (see the bottom of Table 4). This information is important for

Table 4. Tolerances for type D specimens [5,7]

Nominal Value of *Ra*, μm	Tolerance on Nominal Value, %	Uncertainty of Measurement of Stated Mean Value of *Ra*[1], %	Standard Deviation from Mean Value, %
0.15	± 30	± 5	4
0.5	± 20	± 3	3
1.5	± 15	± 3	3

1) Taken from 12 evenly distributed readings.

both calibration laboratories and users. It enables one to convert the standard deviation σ_x and the standard deviation of the mean $\sigma_{\bar{x}}$ when necessary.

For example, if calibration laboratories want to know whether or not their calibration capability is qualified for the calibration shown in Table 4, they can calculate the instrument standard uncertainty, $u_{(i)}$, required for this calibration. For the specimen with nominal *Ra* of 0.5 μm, the tolerance for the expanded measurement uncertainty of the stated mean *Ra* is specified as $U = \pm 3\%$ (k =2) with the measurements taken at 12 measurement positions. That means the combined standard uncertainty for the stated mean Ra is $u_c = 1.5$ %. Because the statistical variation $u_{(s)}$ is represented by standard deviation, $\sigma_x = 3\%$ (see Table 4), it must be converted to standard deviation of the mean $\sigma_{\bar{x}} = \sigma_x / \sqrt{n} = 0.87$ % (n = 12). Then the required instrument standard uncertainty could be calculated as $u_{(i)} = [u_c^2 - u_{(s)}^2]^{1/2} = 1.22$ %. Based on this, the calibration laboratory might judge whether or not their calibration capability could be qualified for this calibration.

If the measurement uncertainty was specified for the stated mean Ra value without specifying how many readings were taken. This information was not sufficient for both calibration laboratories and users. Because the standard deviation σ_x could not be converted to the standard deviation of the mean $\sigma_{\bar{x}}$ without specifying the number of measurements n.

6. NIST Surface Calibration Reports

Most surface calibrations at NIST Surface and Microform Calibration Laboratory are performed using nine positions. However, when these calibrated specimens are used in the secondary laboratories, in many cases, only a single-trace calibration is performed. It is for this reason that the measurement uncertainty for NIST surface calibrations is reported for a single measurement except when the customer requests a report of measurement uncertainty for the mean Ra value of multiple measurements. Therefore, the standard deviation σ_x, rather than the standard deviation of the mean $\sigma_{\bar{x}}$, is used for representing the statistical variation in NIST calibration reports. As a result, a relatively conservative (large) measurement uncertainty would be introduced if customers use this specimen for multiple measurements and take the mean value as the result. However, in that case, the customer can follow the procedures illustrated in Table 3 by converting the standard deviation σ_x to the standard deviation of the mean $\sigma_{\bar{x}}$, and re-calculate the measurement uncertainty for the stated mean value of Ra.

References:

[1] Appendix A, "Measurement Conditions and Sources of Uncertainties for NIST Surface Roughness and Step Height Calibration Reports", last revised in July 2001, http://www.mel.nist.gov/div821/webdocs-13/surfcalib.htm.

[2] J. F. Song and T. V. Vorburger, Uncertainty Procedures for NIST Surface Finish and Microform Calibrations, Measurement Science Conference, CA, 1996.

[3] BIPM, IEC, IFCC, ISO, IUPAC, IUPAP, and OIML, *Guide to the Expression of Uncertainty in Measurement*, ISO, Geneva, 1993.

[4] B.N. Taylor and C.E. Kuyatt, *Guidelines for Evaluating and Expressing the Uncertainty of NIST Measurement Results*, NIST Technical Note 1297 (National Institute of Standards and Technology, Gaithersburg, MD, 1993).

[5] ISO 5436 – 1985, Calibration specimens – Stylus instruments -- Types, calibration and use of specimens, ISO, Geneva, 1985.

[6] ISO/DIS 5436-1, *Geometrical Product Specifications (GPS) – Surface Texture: Measurement Standards Part 1: Material Measures*, 18 Dec, 1998.

[7] ASME B46.1-2002, *Surface Texture*, American Society of Mechanical Engineers, New York, 2002.

Shape measurement by the grating projection technique in a microscope

[1]Hatsuzo TASHIRO, [1]Kouji KURIOKA, [2]Takashi NOMURA, [2]Kazuhide KAMIYA
[1] *Toyama University, 3190, Gofuku, Toyama, Toyama, 930-8555, Japan*
[2] *Toyama Prefectural University, 5180, Kurokawa, Kosugi-machi, Toyama, 939-0398, Japan*

1. Introduction

Many methods for measuring the three-dimensional shape of electronic components and small parts in a short time have been proposed. For nocontact measurement optical techniques, such as, confocal imaging, moire and grating projection methods, are desired [1-2]. In the moire method and the grating projection method, to illuminate the object from the oblique direction, the structure of optical systems becomes complex. We focus on the grating projection method and improve the method.

The accuracy of measurement by the grating projection method is low. To raise the accuracy, a suitable analytical method is necessary. The phase shift [3-4], the FFT [5-6], and wavelet methods [7-9] are used for the analysis of modulated gratings. The phase shift method is suitable for a static analysis because several images recorded at different times are used. The FFT method and the wavelet method are suitable for dynamic analysis because only one image is used. We use the sine-cosine transform method to analyze the modulated gratings, because the process is simple and the spatial resolving power can be suitably chosen.

In this paper, shape measurement by a grating projection technique using a microscope and the analysis by a two-dimensional sine-cosine method are proposed.

2. Optical system

In a microscope, the optical intensity of the conventional light source is irregular. The light beams with uniform intensity distribution are needed to illuminate the grating. The Koehler illumination system is used to eliminate the irregularity of optical intensity in the microscope and is adapted in this proposed system. To project a grating at a fixed illumination angle on the object, the optical axis of the objective lens should be parallel to the optical axis of the illumination lens. The optical system is shown in Fig. 1.

The light beam radiated from the light source is collimated by lens 1, and the grating is illuminated with a uniform intensity. An image of the light source is formed near objective lens 3 by lens 2 and the image is transformed to parallel light by the objective lens. The collimated light, which is sinusoidal and has high intensity, illuminates the object. The grating is projected onto the object. The optical axis of the objective lens is parallel to the axis of lenses 2 and 3, in order that the grating

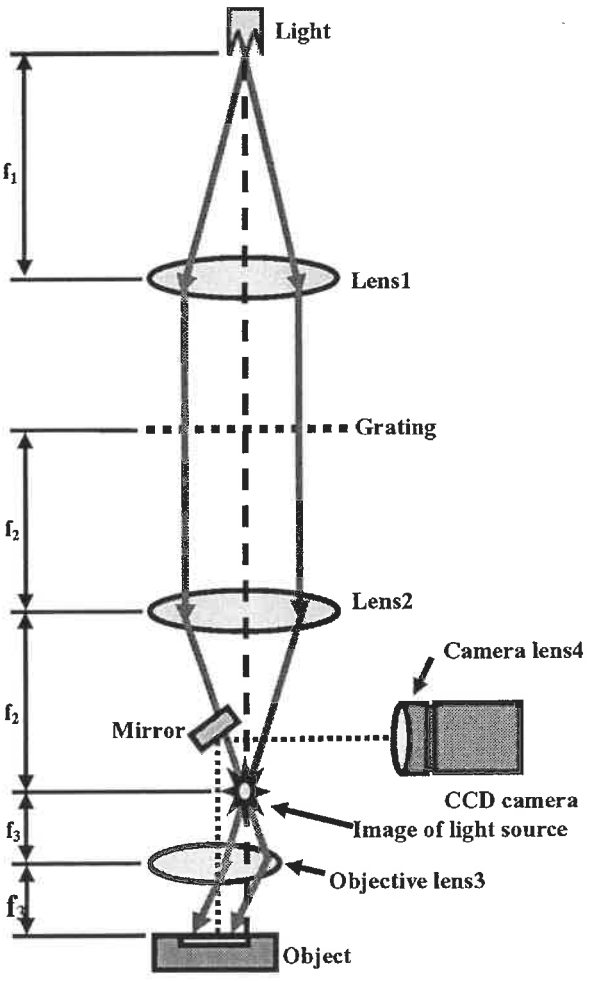

Fig.1 Optical setup

is projected at a fixed illumination angle on the object. The object and the projected grating are imaged on the charge coupled device (CCD) by lenses 3 and 4, and a grating modulated by the object shape is obtained.

3. One-dimensional sine-cosine transformation

For simplicity, the one-dimensional sine-cosine transform is explained as shown in Fig. 2. The broken line $h(x)$ in Fig. 2(a) represents the intensity distribution of the modulated grating to be analyzed, and it is phase-modulated by the shape of the object. The solid line in the figure is the product of the Gaussian window multiplied by the sine waveform, and we call the solid line a sine-packet, which is an imaginary component $s(x)$. In the figure, the frequency ν of the analyzed intensity distribution $h(x)$ agrees with the frequency of the sine-packet $s(x)$. Similarly, a cosine-packet which is a real component $c(x)$ is shown in Fig. 2(b). The sums of the products of each of the two packets multiplied by the analyzed intensity distribution, that is, *si* and *sr*, are given by the following equations.

$$si = \int h(x) \cdot s(x)\,dx \qquad (1)$$

$$sr = \int h(x) \cdot c(x)\,dx \qquad (2)$$

Spectrum S is given by the following equation.

$$S = \sqrt{si^2 + sr^2} \qquad (3)$$

The value of S is maximum when the frequency of the packet is the same as that of the analyzed intensity distribution. The phase θ of the intensity distribution when the value of S is maximum is describe by the following equation.

$$\theta = \tan^{-1}\left(\frac{si}{sr}\right) \qquad (4)$$

Using this phase, the shape of the object is calculated.

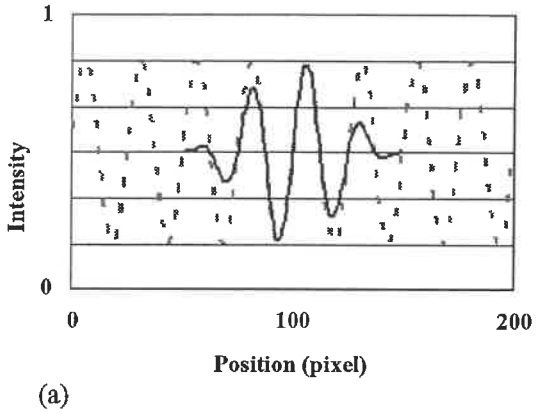

(a)

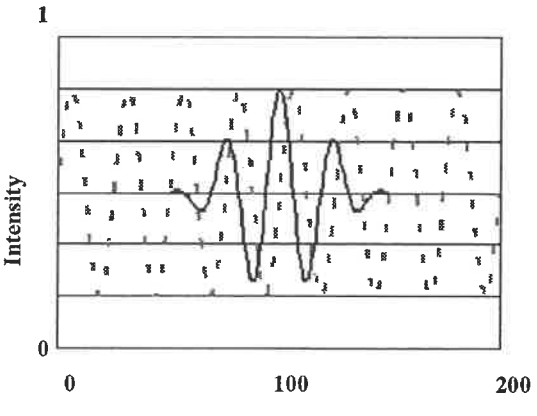

(b)

Fig.2. Schematic diagram of one-dimensional sine-cosine transformation: (a) sine-packet $s(x)$, (b) cosine-packet $c(x)$.

4.Two-dimensional sine-cosine transformation

In the two-dimensional sine-cosine transformation, two-dimensional packets are used. The analysis packets of various frequencies are considered as well as the one-dimensional sine-cosine transformation. Furthermore the rotations of the analysis packets are also varied. Figs. 3(a), 3(b) and 3(c) show analysis packets $s(x, \nu, \alpha)$ for selected frequencies and rotational angles α. The sum of the products of the two-dimensional analysis packets $s(x, \nu, \alpha)$ multiplied by analysis packet $h(x,y)$ is calculated. The frequency ν and the angle α of the analysis packet at which the spectrum becomes maximum are obtained. The phase θ of the grating on the point is obtained using Eq. (4).

5. Experimental results and discussion

In the experiments, the sensitivity of the system was obtained as follows. Some objects with known height difference were measured, and the sensitivity of the system was determined from the result. By combining multiple block gauges, height differences of 10μm units were generated, and the quantity of shear of the modulated grating was measured. The measurable range of height difference was 300μm in this system because of the depth of focus.

An example of a modulated grating image projected onto an object with a height difference of 90μm is shown in Fig. 4(a). Stripes are modulated gratings and a wide line perpendicular to the stripes is the boundary between the two block gages. Fig. 4(b) shows a phase distribution obtained by the two-dimensional sine-cosine transformation. The phase difference between the two block gages with a height difference of 90μm is 3rad. Some objects with height differences were tested, and the results are shown in Fig. 5. In the figure, the horizontal axis is the phase difference obtained by the analysis, and the vertical axis is the measured height difference Z of the object. The relation of Z=30.02α was obtained in the experiments. The error of about 5μm (2%) occurred for the measurement range of 300μm.

The shapes of some objects were measured. Fig. 6 shows a modulated grating pattern on a coin, and shows the analytical result. The results are shown as a gray-scale image and a height representation. About 40 seconds are necessary for the analysis of 300×300 pixels by two-dimensional sine-cosine transformation, where the computer had a Pentium 4 Processor 2.60C GHz with 1GB of RAM.

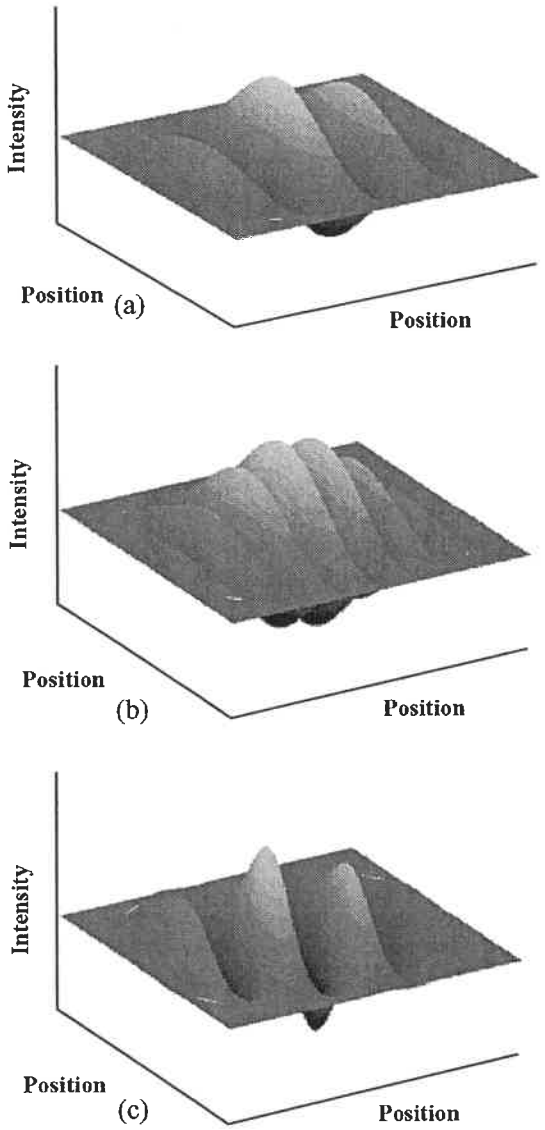

Fig. 3. Two-dimensional analysis packets: (a) ν=4, α=0 deg, (b) ν=8, α=0 deg, (c) ν=4, α=-20 deg

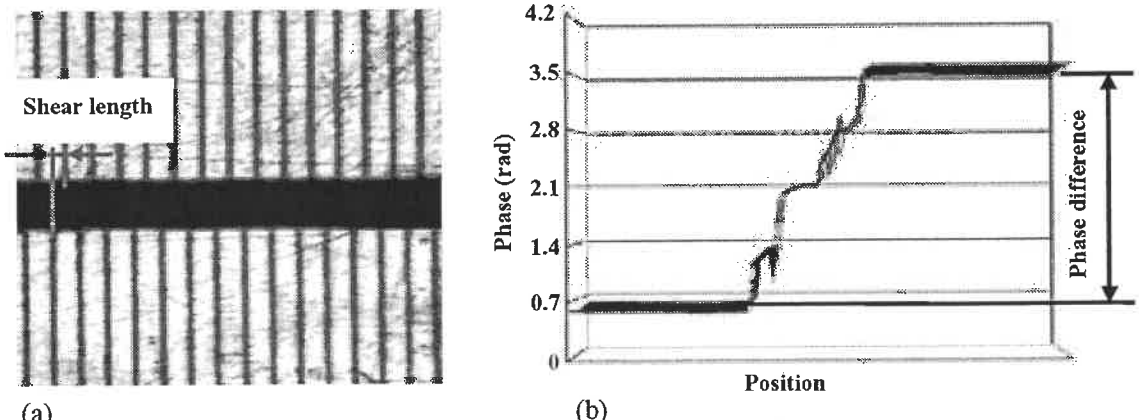

Fig. 4 (a) The image of the grating on the object and (b) the phase distribution of the grating.

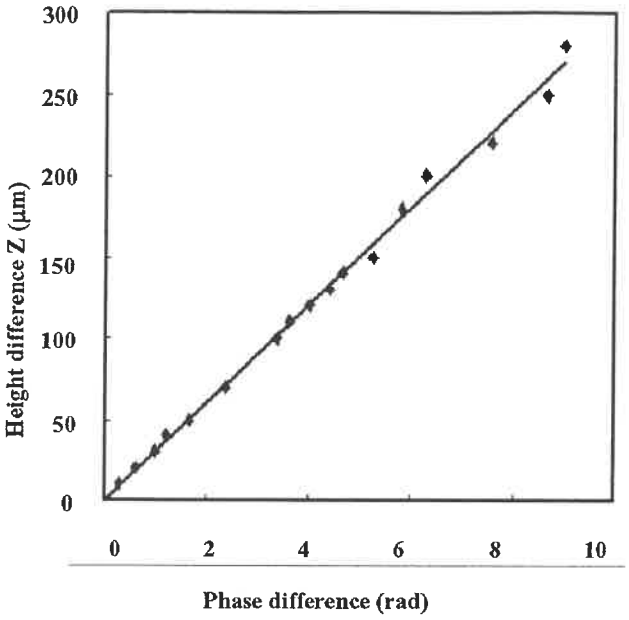

Fig. 5 The relationship between the height difference and the phase difference.

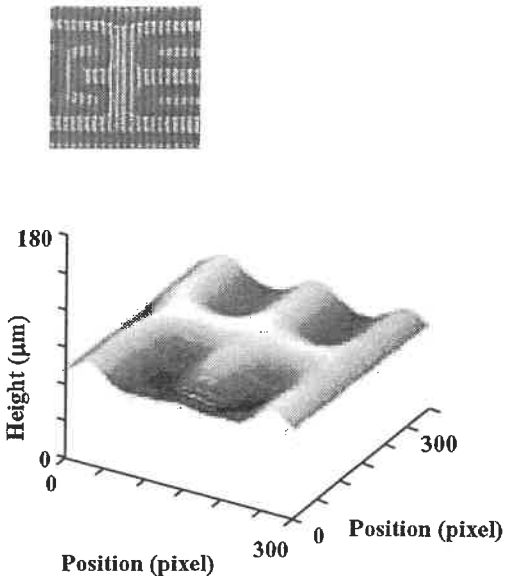

Fig. 6. Experimental results: Modulated grating on the coin, and phase distribution of analyzed image of the coin.

6. Summary

In this paper, shape measurement by a grating projection technique using a microscope and analysis using a two-dimensional sine-cosine method were proposed. In a microscope system, a grating can be projected onto an object from an oblique direction with uniform optical intensity.

For example of micro-objects, a coin was measured by the grating projection technique and the two-dimensional sine-cosine transformation. The measurement error was about 2% for the measurement range of 300μm. The frequency, the direction and the phase of the modulated grating were obtained continuously. The phase connection in the two-dimensional image analysis could be accomplished.

References

[1] W. Jaerisch, Optical Contour Mapping of Surfaces. App Opt 1973; 12: 1552-1557.

[2] M. Fujigaki, Development of Real-time Display System for Contour Line and Equal-displacement Line by Phase Shifting Scanning Moire Method. J Japan Soc Pre Eng 2000; 66: 1221-1225.

[3] K. Creath, Step height measurement using two-wavelength phase-shifting interferometry. Appl Opt 1987; 26: 2810-2816.

[4] M. Kujawinska, Use of phase-stepping automatic fringe analysis in moiré interferometry. App Opt 1987; 26: 4712-4714.

[5] M. Takeda, Fourier-transform method of fringe-pattern analysis for computer-based topography and interferometry. Opt Soc Am 1982; 72: 156-160.

[6] M. Takeda, Spetial-carrier fringe-pattern analysis and its applications to precision interferometry and profilometry. Industrial Metrology 1 1990; 79-99.

[7] H. Tashiro, Analysis of Zone-plate Interference Fringes with Wavelet Transform. J Japan Soc Pre Eng 1999; 65: 433-437.

[8] A. Federico, Evaluation of the continuous wavelet transform method for phase measurement of electronic speckle pattern interferometry fringes. Opt Eng 2002; 41: 3209-3215.

[9] L. R. Watkins, Interferometer profile extraction using continuous wavelet transform; Electronics Letters 1997; 33: 2116-2117.

Fabrication of X-ray Microscope Mirrors

Kwon Su Chon and Yoshiharu Namba
Chubu University, 1200 Matsumotocho, Kasugai, Aichi 487-8501, Japan.

Abstract

We showed the design of a Wolter type I mirror which was optimized to have a maximum effective solid angle used in X-ray microscopes, and fabricated the mirror using the replication method. Several mirrors were successfully fabricated using only one master mandrel by our replication method without destroying the master mandrel. The replicated Au focusing and imaging mirrors showed surface roughnesses and figure errors of 1.31 nm Ra and 0.19 μm, and 1.80 nm Ra and 0.2 μm, respectively.

Keywords: X-ray mirror, Wolter type I mirror, Soft X-ray microscope, Replication method.

1. Introduction

Soft X-ray microscopes can be used to investigate hydrated specimens, particularly living cells, with a high resolution about several times better than that of visible-light microscopes. Some X-ray optics, such as zone plates, multilayer mirrors, and grazing incidence mirrors, have been used successfully in X-ray microscope systems using laser-produced X-ray source and synchrotron radiation. Grazing incidence mirrors are based on the total reflection of X-rays on a very smooth surface. One of the well-known grazing incidence optics is the Wolter type I mirror [1] which consists of two axially symmetric confocal surfaces of revolution, an ellipsoid and a hyperboloid, as shown in Fig. 1.

There are two methods of fabricating such a mirror. One is the direct inner machining method of reflecting surfaces using single-point diamond turning and polishing processes [2], the other is the replication method [3] using a master mandrel. The replication method is suitable for fabricating a mirror with a high aspect ratio, a small diameter and a large length. In principle, it is possible to fabricate many replicated mirrors using only one master mandrel. However, in actual application, it is not easy to fabricate several copies.

2. Mirror design

The shape and size of the Wolter type I optic can be determined by four parameters: magnification, central grazing incidence angle, the radius of the intersection circle of two conic sections, and the length of ellipsoid. The central grazing incidence angle on the primary reflecting surface is obtained from the material and surface roughness of the reflecting surface and the wavelength of the X-ray source. Choosing an optimal central grazing incidence angle is the key to maximizing the effective solid angle in the design procedure.

We show designs with a maximum solid angle at a wavelength of 2.3 nm. The Wolter type I focusing mirror at an optimized central grazing incidence angle of 35 mrad has a

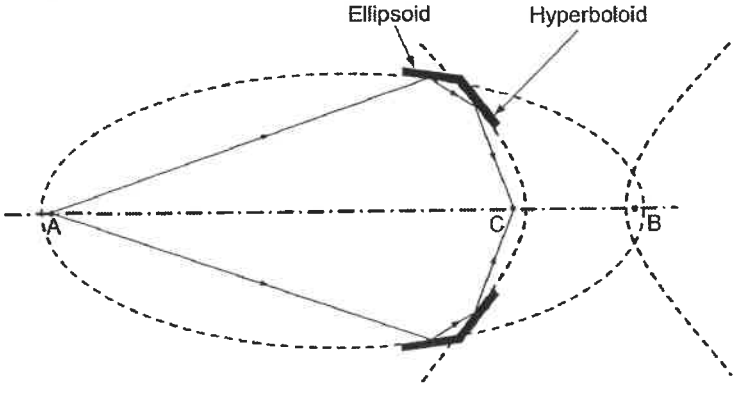

Fig. 1. Geometry of Wolter type I mirror.

central diameter of 8.875 mm, a length of 48.853 mm, and a focal length of 437.0 mm, and its geometrical and effective solid angles are 4.699 x 10^{-4} sr and 3.010 x 10^{-4} sr at the same wavelength, respectively. The specifications of the focusing mirror and imaging optic are given in Table 1.

Table 1 Specifications of focusing and imaging mirrors.

Parameter		Focusing mirror	Imaging mirror
Magnification		1/4 X	32 X
Focal length (mm)		437.0000	1640.0000
Eccentricity	Ellipsoid	0.9994115	0.9999048
	Hyperboloid	1.0023512	1.0030416
Semimajor axis (mm)	Ellipsoid	283.0810369	844.1774565
	Hyperboloid	283.0810369	24.0240261
Length (mm)	Ellipsoid	26.0000	15.9899
	Hyperboloid	22.8529	13.0851
Diameter (mm)	Front	19.2195	8.7053
	Intersection	18.8746	10.8924
	Rear	15.3433	11.6884

3. Fabrication of Wolter type I mirrors

To fabricate the Wolter type I X-ray microscope mirrors shown in Table 1 using the replication method as a primary stage, we prepared sample mandrels by two steps. First, we machined aluminum alloy samples, 7075 and 5052, to a thickness below 75 μm from the ideal surface contour using an ultraprecision lathe with a numerical controller of 1nm positional step, and then 150 μm-thick electroless Ni (NiP) was deposited on the Al alloy samples.

Generally, a surface roughness about 4-10 nm rms (root-mean-square) can be achieved for a NiP-coated master mandrel after single-point diamond turning (SPDT). The surface roughness of the master mandrel is not sufficient for fabricating soft X-ray mirrors because of the strong X-ray scattering by its rough surface. We reduced the surface roughness by polishing. The polished surface was improved approximately 2 nm rms. However there were still many spikes because of the unavailability of a systematic method for the aspherical shape, i.e., hand polishing. The shapes of the master mandrel before and after the polishing, which can destroy the shape occasionally, are almost the same, though the surface roughness is considerably improved. The figure error of the master mandrel is determined not for the polishing work but for the SPDT of the workpiece in our approach. We also found that the figure error of the master mandrel after SPDT reflects the effect of the pitch of a ball screw and the straightness error of the Z-slide table of the ultraprecision machine.

As the first step in the fabrication of a soft X-ray mirror, we prepare the master mandrel (see Fig. 2(a)). This stage is very important because the replicated mirrors strongly depend on the surface roughness and shape of the master mandrel. The next process is coating as shown in Fig. 2(b). In this step, we can introduce a multilayer to improve the throughput of the X-ray mirror. An approximately 300 nm-thick Au is deposited on the master mandrel. The Au coating plays a very important role as a reflecting surface and a separating layer between the master mandrel and the epoxy resin on the mirror substrate. Figure 2(c) shows the combination of the Au-coated master mandrel and the mirror substrate, made of steel or brass. The machining tolerance of the mirror substrate is not as tight as that of the master mandrel. The space between both objects is approximately 30-40 μm and is filled with the epoxy resin under approximately 10^{-1} Torr vacuum. The epoxy resin will compensate for the machining error of the mirror substrate. This is one of the merits of our replication method. Four days is sufficient to harden the epoxy resin, after which we can separate the two objects by cooling them down for one hour in water at 2.5°C (Fig. 3(d)). The separation is mainly based on the difference in thermal expansion coefficient between

the Al alloy and the mirror substrate, made of steel or brass. The replicated Au mirror surface is weak, so that we need to take care during the separation and cleaning.

We believe that the replication method can copy the surface of the master mandrel very accurately. Figure 3 shows the 3-dimensional surfaces of a master mandrel at one part and a replicated Au mirror at its counterpart, respectively. The surface roughnesses, measured with Zygo New View 200HR, are 1.38 and 1.31 nm Ra in the 360x270 μm^2 area. The two Ry values are different due to spikes but are close to each other. Many spikes can be found in the replicated Au reflecting surface. These spikes possibly occur randomly during the separation. On the other hand, the shape of the replicated Au mirror is associated with other factors, for example, the contraction of the epoxy resin, as well as that of the original master mandrel. Figure 4 shows the figure errors of the replicated Au mirror for the ellipsoid and hyperboloid parts, respectively; these are 0.19 μm and 0.17 μm Ry for their mirror lengths. In particular, the range from 20 mm to 26 mm in the ellipsoid part shows a behavior different from that of the master mandrel. In the plane mirror (diameter of 48 mm) case, the shapes of the replicated Au mirror and the master mandrel are almost the same. The difference between the two shapes is approximately 25 nm Ry. The imaging optic shown in Table 1 is also fabricated by the same procedure. The surface roughness and figure error are 1.8 nm Ra and 0.2 μm, respectively.

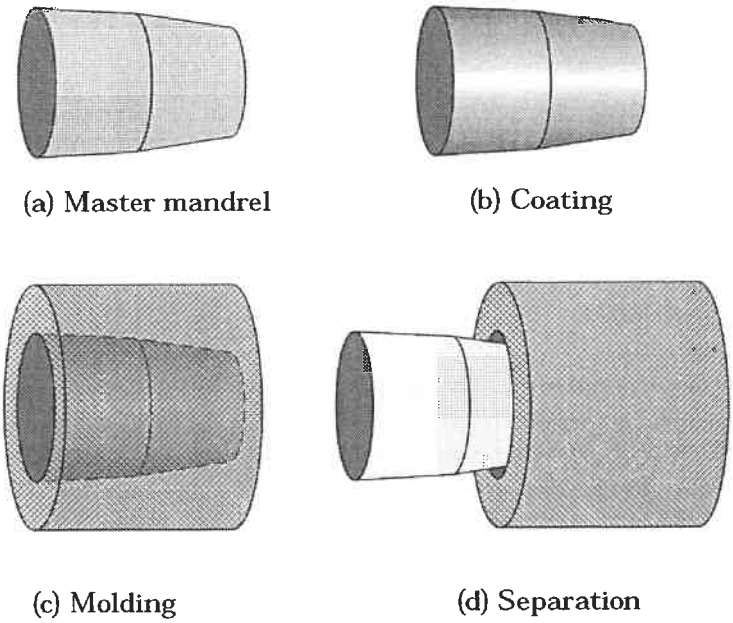

(a) Master mandrel (b) Coating

(c) Molding (d) Separation

Fig. 2. Replication procedures

The main advantage of our replication method is that only one master mandrel can make several real mirrors. The master mandrel which was already used in making a real mirror still keeps the original surface roughness and shape, and again it can be used in fabricating another mirror through the same replication procedure.

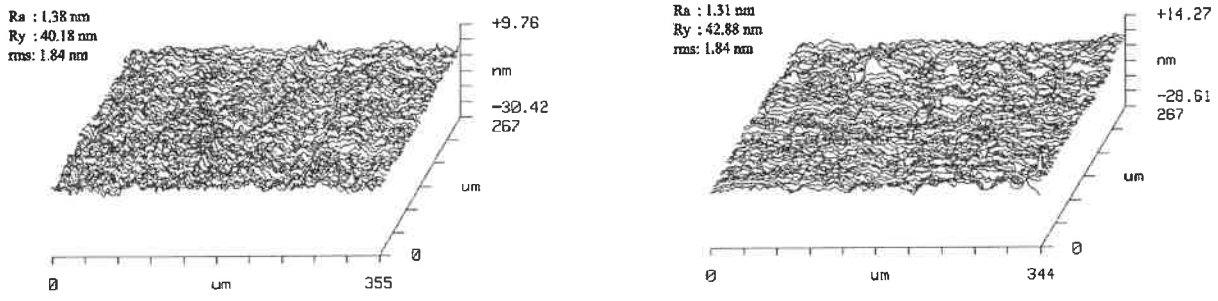

(a) Master mandrel (b) Replicated Au mirror

Fig. 3. Surface roughnesses of master mandrel and replicated Au mirror

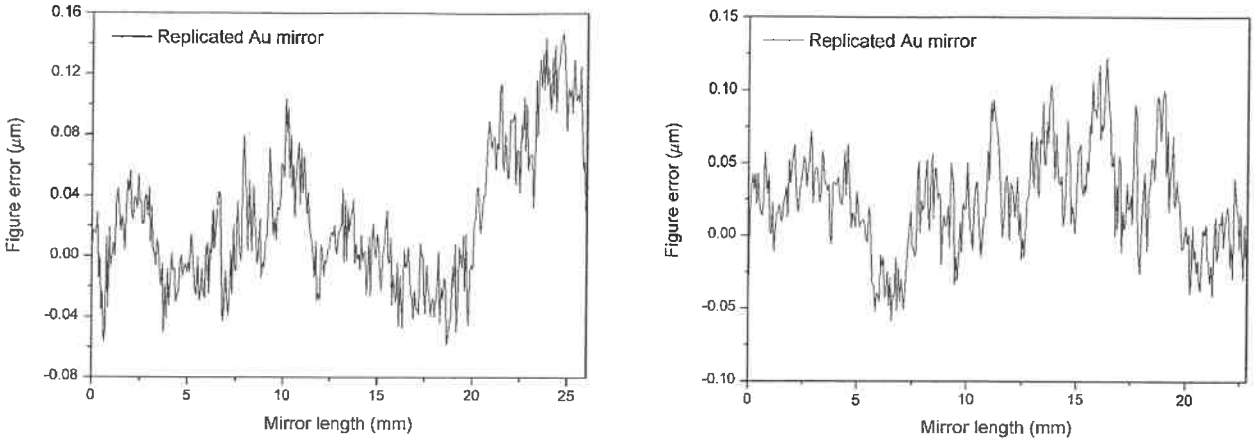

(a) Ellipsoid part (b) Hyperboloid part

Fig. 4. Figure errors of ellipsoid and hyperboloid parts of replicated Au mirror.

4. Conclusion

It is not easy to machine an inner mirror surface with a nanometer surface roughness and a good shape simultaneously. In particular, the case in which the mirror length is much larger than the mirror diameter, i.e., a high aspect ratio, may encounter serious problems during machining. The replication method can fabricate the mirror more easily than direct inner machining in this case.

First, we designed Wolter type I mirrors used in a soft X-ray microscope. These mirrors were optimized to have a maximum effective solid angle at 2.3 nm wavelength. Then we fabricated the mirrors using the replication procedure. The surface roughnesses and figure errors of the fabricated Au focusing and imaging mirrors are 1.31 nm Ra and 0.19 μm and 1.80 nm Ra and 0.2 μm, respectively. In particular, we fabricated several Au mirrors with only one master mandrel without destroying the surface roughness and shape of the master mandrel. This is the main advantage to our approach.

One of the main problems in fabricating X-ray mirrors is the separation between the master mandrel and the substrate of the mirror in the replication procedure. Thus it is important in searching for a material that can be easily separated and that has a high reflectivity in the water window (2.2~4.4 nm wavelength). There is still room to improve the surface roughness and figure of the master mandrel in order to improve replicated X-ray mirrors.

5. References

1. H. Wolter, "Spiegelsystem streifenden Einfalls als abbildende Optiken fur Rontgenstrahln", Ann. Phys. 10(6), 1952 pp.94-114.

2. M. J. Boyle and H. G. Ahlstrom, "Imaging characteristics of an axisymmetric, grazing incidence x-ray microscope designed for laser fusion research", Rev. Sci. Instrum. **49**(6), 1978 pp.746-751.

3. K. Ninomiya, K. Honda, S. Aoki, S. Nishimatsu, and K. Suzuki, "Fabrication of an Axisymmetric Wolter Type I Mirror with a Gold Deposited Reflecting Surface", Jpn. J. Appl. Phys. **26**(11), 1989 pp.2303-2308.

IMPROVE FIGURE AND FINISH OF DIAMOND TURNED SURFACES WITH MAGNETO-RHEOLOGICAL FINISHING (MRF)

Paul Dumas, Don Golini, and Marc Tricard
QED Technologies, 1040 University Avenue, Rochester, NY 14607

KEY WORDS:

Single Point Diamond Turning (SPDT), deterministic polishing, Magneto-Rheological Finishing (MRF), aspheres, free-form optics, metrology

INTRODUCTION

Aspheric optical surfaces are of increasing interest due to their ability to improve system performance and reduce overall system size and weight. There are a number of emerging technologies that are enabling the cost-effective manufacture of aspheric surfaces. Single Point Diamond Turning (SPDT) and Magneto-Rheological Finishing (MRF) are two such technologies. SPDT has been successfully applied for many years to the manufacture of infrared (IR) materials, where the final specifications and nature of the materials are compatible with the diamond turning process [1]. MRF is a relatively new technology that enables high precision aspheric manufacture of visible and IR optics [2,3,4,5]. SPDT is able to remove hundreds of microns of material, and generate surfaces with micron accuracies. Residual turning marks and machine platform accuracies are often the factors limiting performance in this process. As multi-spectral imaging systems (combining IR with near-IR and/or visible wavelengths) are driving specifications tighter, a post-SPDT smoothing and fine-figuring step is required. MRF has the inherent ability to smooth spatial frequencies on the order of microns and smaller, allowing it to efficiently remove residual diamond turning marks and produce optical finishes necessary for visible systems. At the same time, MRF's deterministic, small tool polishing process has the ability to improve figure, at and below the micron level ($\lambda/10 - \lambda/20$ PV is common). Combining SPDT and MRF technologies creates a two-step, deterministic process for manufacturing high precision aspheric surfaces.

MAGNETO-RHEOLOGICAL FINISHING

MRF is a computer controlled, sub-aperture polishing process that is based on a magneto-rheological fluid (one whose viscosity varies in the presence of a magnetic field). This process creates an extremely stable and conformable polishing tool. Since the tool is fluid-based, it conforms to any surface shape and eliminates the need for dedicated tooling. In addition, this eliminates the "tool misfit" problem in aspheric polishing.

The stable, sub-aperture nature of the MRF process enables high precision figure correction. The shear-mode of removal enables the MRF process to improve micro-roughness, remove sub-surface damage, and reduce residual stress that is typically introduced in previous manufacturing steps.

MRF is most effective at removing micron- or sub-micron-amounts of material; there are typically more efficient ways to remove many tens or hundred of microns of materials. MRF excels at improving surfaces from a few microns PV to the limits of what is "measurable" (e.g., $\lambda/20$ PV or beyond) – a regime where other commercially available technologies, such as SPDT, bottom out. When combined with the ability of SPDT to generate aspheric surfaces of hundreds of microns of departure to micron accuracies, a total high-precision aspheric manufacturing process results. Care must be taken in the SPDT process, however, not to introduce mid-spatial frequencies (e.g., grooves 50-500 μm in width due to mechanical platform inaccuracies), which can be difficult to remove afterward.

METROLOGY OF ASPHERIC SURFACES

MRF has the ability to correct both symmetric and asymmetric surface errors. Therefore, it is necessary to "feed" MRF a full aperture measurement of the surface to be corrected. This is a common practice for spheres and flats, but expensive and complicated for most aspheric surfaces. A number of technologies are available for aspheric metrology today. Each has their benefits and tradeoffs. Computer generated holograms (CGHs) are accurate and easy to use, but they are dedicated (a different hologram is required for every different aspheric design) and they are relatively expensive. 3-D profilometry tools are flexible (can measure almost any aspheric shape) but they are contact measurements, can be slow, expensive and not as accurate as interferometry. 1-D profilometry tools are less expensive, but only offer one scan of data allowing only rotationally symmetric error to be corrected. More recently,

significant progress has been made in Sub-aperture Stitching Interferometry (SSI) to provide a universal full aperture metrology tool, at least for mild aspheres [6,7]. For a given application, it is important to have the appropriate metrology, because for MRF, metrology can often be the limiting factor in performance.

RESULTS

In this section, we show two examples of MRF improving the figure and roughness of diamond turned surfaces. Figure 1 shows the figure before and after MRF for a convex single crystal silicon (Si) surface with a ~24 mm diameter and a ~22 mm radius of curvature. In this example, the MRF process was able to deterministically remove the center nib left over from diamond turning, as well as improve the 8-lobed asymmetric error. This 4.5x PV and 3.3x RMS improvement was performed in only 14 minutes of MRF polishing.

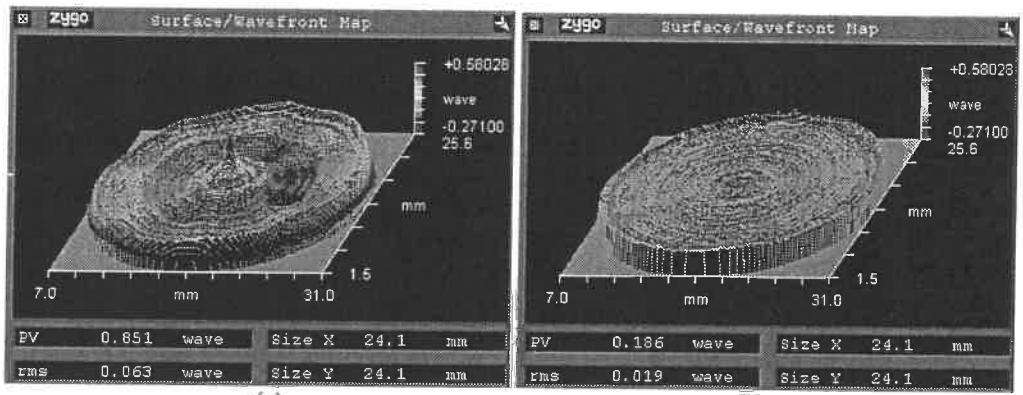

(a) (b)

Figure 1: Figure before (a) and after (b) MRF on a Si surface generated by SPDT.

Figure 2 shows the roughness before and after MRF on the same convex single crystal silicon (Si) part (Zygo NewView measurement with 20x objective and an 80 μm high-pass filter applied). The diamond turning grooves are clearly visible in the post-SPDT surface. After MRF, the grooves are eliminated. MRF consistently produces <1 nm RMS roughness on common diamond-turnable materials (e.g., Si, CaF_2, etc.), and often produces roughness <0.5 nm RMS.

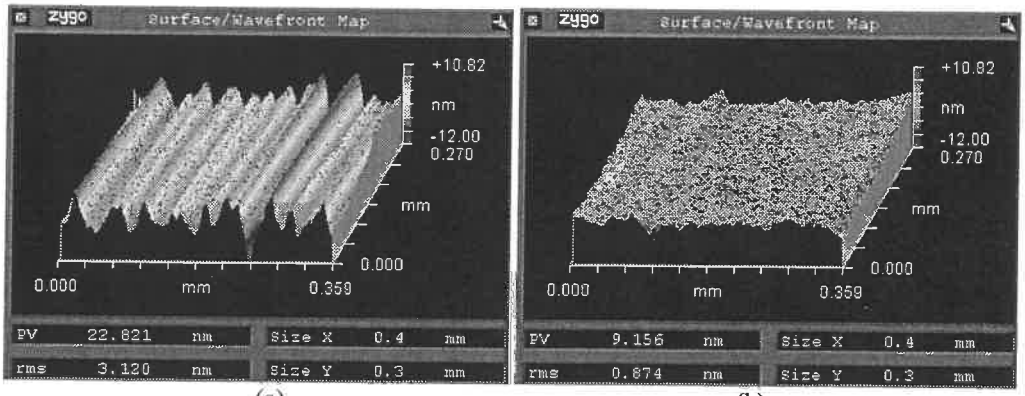

(a) (b)

Figure 2: Roughness before (a) and after (b) MRF on a Si surface generated by SPDT.

The turning marks left behind by SPDT often result in a diffraction pattern visible with the unaided eye. This results in flare that can reduce the performance of many optical systems. Figure 3 shows that this rainbow-like diffraction pattern is eliminated by applying the MRF process. The color in the visible aperture of the part (not the edge bevel) is visible before, but not after MRF.

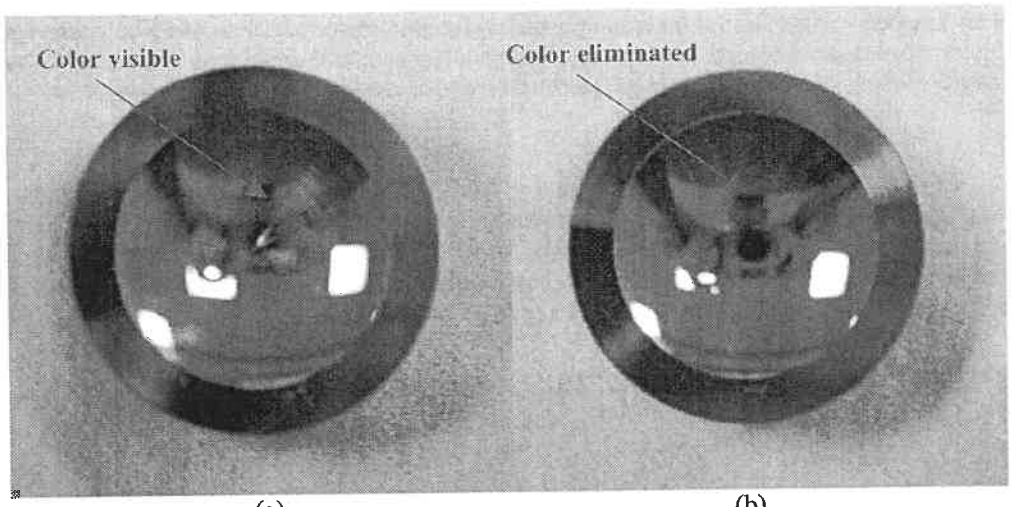

(a) (b)

Figure 3: Image of SPDT Si surface before (a) and after (b) MRF showing elimination of the color pattern caused by the turning marks.

The example above shows figure and finish improvement on a spherical surface. However, the true benefit of SPDT is realized when manufacturing aspheric surfaces. Figure 4 is an example of the MRF correction of a ~90mm diameter CaF_2 asphere with over 100 μm of aspheric departure. The diamond turning process generated the desired aspheric surface to within < 2 μm. From this point, MRF was able to reduce the error by, in this example, a factor of 10x in RMS. This example shows that MRF can be equally effective on aspheric surfaces as it is on spheres and flats.

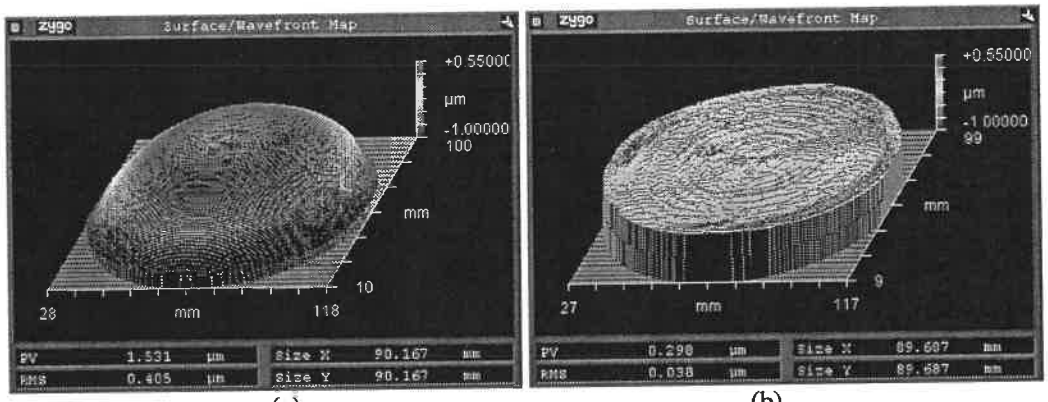

(a) (b)

Figure 4: Figure of SPDT CaF_2 aspheric surface before (a) and after (b) MRF. This surface has ~100 μm of aspheric departure.

A number of inherent properties exist that enable MRF to generate surface qualities beyond the precision level of SPDT:

- MRF is a dwell-based polishing process, not a position-based contouring process. It relies on sophisticated deconvolution algorithms rather than precision machinery to achieve high precision corrections.
- MRF does not require a temperature-controlled environment to operate. As long as the metrology is done in appropriate conditions, the polishing itself can be done at another temperature.
- MRF does not require any elaborate part mounting strategy, as it is insensitive [8] to micron-order positioning errors that compromise performance in SPDT and metrology.

As illustrated in this paper, MRF is highly effective at improving achievable geometries beyond the range of SPDT process, while improving roughness and reducing turning marks. Additionally, MRF is also very effective on materials that are not easily diamond turnable, such as Si [9]. It can also remove sub-surface damage [10,11].

CONCLUSION

The combination of Single Point Diamond Turning and Magneto-Rheological Finishing creates a completely deterministic manufacturing process for high precision aspheric surfaces. For materials compatible with the SPDT process, this two-step process can offer fewer manufacturing steps, reduced setup times, reduced overall cycle time, and reduced cost. The combination of MRF with SPDT can now enable the widespread use of aspheres in visible and near-IR systems, just as SPDT alone has already done for IR aspheric systems.

REFERENCES

1. K. Martinson, "Diamond Turning Enters a New Era," *Photonics Spectra,* pp74-81, April 2004.
2. I. A. Kozhinova, H. J. Romanofsky, S. D. Jacobs, W. I. Kordonski, Sergei R. Gorodkin, "Polishing of pre-polished CVD ZnS flats with altered magnetorheological (MR) fluids," *to be presented at OSA's Optical Fabrication and Testing 2004*, Rochester, NY, October 12-15, 2004.
3. D. Golini, W. Kordonski, P. Dumas, S. Hogan, "Magnetorheological finishing (MRF) in commercial precision optics manufacturing," Proc. SPIE Vol. 3782, p. 80-91, Optical Manufacturing and Testing III; H. Philip Stahl; Ed. Nov 1999.
4. S. Jacobs, H. Pollicove, E. Fess, and J. Schoen, "Aspheric Optics Manufacturing for Commercial and Military Systems", Proceedings of the First Symposium for Explosive Materials, Weapons and Military Technology, (Ohrid, Macedonia, Sept. 25-28, 2002) pp. 497-504.
5. S. D. Jacobs, S. R. Arrasmith, I. A. Kozhinova, L. L. Gregg, A. B. Shorey, H. J. Romanofsky, D. Golini, W. I. Kordonski, P. Dumas, and S. Hogan, "An Overview of Magnetorheological Finishing (MRF) for Precision Optics," in *Finishing of Advanced Ceramics and Glasses*, edited by R. Sabia, V. A. Greenhut, and C. G. Pantano, Ceramic Transactions, Vol. 102 (The American Ceramic Society, Westerville, OH, 1999), pp. 185–199.
6. J. Fleig, P. Dumas, P. E. Murphy, G. W. Forbes, "An automated subaperture stitching interferometer workstation for spherical and aspherical surfaces," Proceedings of SPIE Vol. 5188 (2003), San Diego, CA.
7. QED demonstrated stitching metrology on mild aspheres (25 microns of aspheric departure) live at QED Technologies booth the Optatec 2004 exhibition in Frankfurt, Germany, June 22-25, 2004.
8. M. Tricard and D. Golini, "High precision photomask polishing with magneto-rheological finishing (MRF)," Meeting of the American Society for Precision Engineering, St. Louis, Missouri, 2002, pp. 120-125.
9. E. Paul, C.J. Evans, A. Mangamelli, M. L. McGlauflin, R. S. Polvani, "Chemical Aspects of Tool Wear in Single Diamond Point Turning," Precision Engineering, 18:4-19, 1996.
10. J. Wang, R. L. Maier, "Quasi-Brewster angle technique for evaluating the quality of optical surfaces," Proc. SPIE Vol. 5375, Metrology, Inspection and Process Control, Microlithography XVIII, R. Silver, Ed., pp 1286-1294, 2004.
11. S. R. Arrasmith, S. D. Jacobs, J.C. Lambropoulos, A. Maltsev, D. Golini, W. I. Kordonski, "Use of magnetorheological finishing (MRF) to relieve residual stress and subsurface damage on lapped semiconductor silicon wafers," Proc. SPIE Vol. 4451, p. 286-294, Optical Manufacturing and Testing IV; H. Philip Stahl; Ed. Dec 2001.

Predicting Surface Figure in Diamond Turned Calcium Fluoride Using In-Process Force Measurement

Eric R. Marsh, Binu P. John, Jeremiah A. Couey
The Pennsylvania State University, University Park, PA

R. Ryan Vallance
The George Washington University, Washington, DC

Abstract

Single crystal calcium fluoride (CaF_2) shows significant variation in material properties as a function of crystallographic orientation. The surfaces generated by material removal processes such as diamond turning are influenced by this anisotropy and consequently show periodic undulations aligned with the crystal structure. This paper explores the relationship between surface figure and cutting forces measured during the diamond turning of single crystal calcium fluoride. The cutting forces, when mapped to the physical geometry of CaF_2 plano (flat) optics, show good correlation with surface figure measured by interferometry.

Introduction

Despite promising results obtained in applications such as photolithography optics, calcium fluoride is widely considered a challenging material to work with because of its high coefficient of thermal expansion (24×10^{-6} $°C^{-1}$) and relatively low hardness (one-seventh that of silicon). However, calcium fluoride is one of the few visible or ultraviolet wavelength optical materials that may be machined with single point diamond tools to obtain specular surfaces and minimal subsurface damage. A typical diamond turned workpiece might have a 3 nm R_a and 18 nm peak-to-valley micro-roughness. The subsurface damage, as measured by the quasi-Brewster angle measurement technique, ranges from 250 to 500 nanometers [1].

The surface figure and surface finish obtained in diamond turning is strongly influenced by the crystalline structure of calcium fluoride. Yan reports that the same radial spokes of damage that are well known in silicon can arise in CaF_2 with various combinations of typical diamond turning parameters [2]. Yan also reports machining parameters that may be chosen to generate damage-free surfaces in single point diamond turning for all crystal orientations [3]. This orientation-dependent behavior is further documented in the extensive literature on silicon and diamond, two other crystalline materials that show the same large variations in machinability with crystal orientation [4,5,6,7,8].

When diamond turning CaF_2 optics, the cutting tool encounters different orientations of the crystal within each rotation of the workpiece. As with diamond and silicon, the orientation-dependent material properties of calcium fluoride cause variation in the apparent material stiffness that leads to oscillatory cutting forces and undulations in the surface figure. During the course of this work, the surface figure of plano (111) CaF_2 workpieces invariably showed three-lobed (trifoil) spherical aberration with amplitudes ranging from 25 to 250 nm peak-to-valley depending on the material removal rate and the condition of the diamond tool.

Despite this lobing, single point diamond turning (SPDT), followed by magnetorheological finishing as needed, is a good alternative to traditional grinding and polishing because the material removal rate is much higher, the subsurface damage propagated into the workpiece is low (sub-micrometer) and aspheric shapes can be generated and polished directly.

An essential requirement in turning brittle materials such as CaF_2 is the selection of cutting parameters such that the material removal mechanism is in the ductile mode regardless of the crystal orientation [9]. This is achieved by keeping the effective depth of cut below the critical uncut chip thickness t_{cnb} which varies with tool geometry and crystal orientation. Yan studied this effect for (111) CaF_2 turning and found that t_{cnb} is 85 nm in the hard <112> direction with flat diamond tools and -20° rake angle [2]. In our work, we used round nosed tools and found the critical depth of cut to be somewhat larger, presumably as a result from the substantially different geometry of the chips. A micro fracture model explaining the difference between the micro fractures left by round and flat tools is found in Blake and Scattergood [10].

In summary, CaF_2 presents an interesting opportunity in optical fabrication because the material offers both favorable optical properties and the possibility of reduced manufacturing costs by replacing the traditional grinding steps with a single diamond turning setup. The remainder of this paper demonstrates the relation between crystal structure-induced spherical aberration and cutting forces that arises in diamond turning anisotropic CaF_2. A model for predicting the magnitude of these aberrations from in-process force measurement is presented and validated. The model enables the prediction of aberrations at various conditions by extrapolation from force measurements made during a single diamond turning operation.

Experimental Setup

In order to validate the cutting force model presented in the previous section, calcium fluoride turning tests were performed on a hydrostatic way, diamond turning lathe with a 10 nm programmable resolution (Moore Nanotechnology Systems AG150). An illustration of the machine and its vertical air bearing spindle (Professional Instruments Twin-Mount) is shown in Figure 1. A high resolution three-axis dynamometer (Kistler MiniDyn 9256A2) measures the three components of force on the tool.

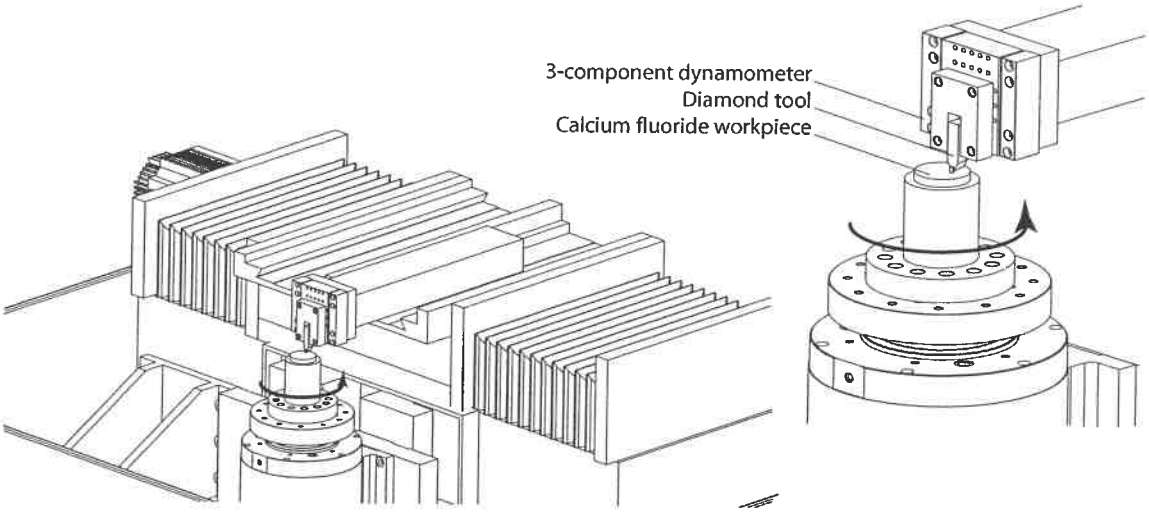

Figure 1 Hydrostatic way diamond turning lathe with air bearing spindle.

A capacitance probe (Lion Precision C1-C with DMT 10 driver) targets the rotating workholder (not shown) in order to synchronize the cutting force data with the rotation of the workpiece. This index pulse allows accurate mapping of the cutting forces to the trifoil structure of the (111) CaF_2 crystal in the presence of spindle speed variations.

When machining brittle materials such as calcium fluoride, a negative rake angle is beneficial due to its mitigating effects on fracture [11]. The synthetic, monocrystalline diamond tools used in these turning experiments achieve the negative rake angle with a chamfer, or radial rake. Most tests were run with 0° rake angle or -30° radial rake angle with a -10° clearance angle, and 1.5 mm nose radius (Edge Technologies, Inc). More negative radial rake angle tools (-45° and -60°) were also used with less favorable results. The tool edge radius, which may be measured in a low voltage SEM or by AFM, is less than 50 nm [12]. The tools are chemically faceted on the rake and nose facets to remove surface and subsurface damage from the tool edge. Mineral oil coolant was used during all cutting tests.

The three components of the diamond turning cutting forces contain useful information about the state of the material removal process. Changes in the forces reflect changes in the geometry of the tool (wear) and the surface finish of the machined surface. Figure 2 shows the three components of the average cutting force as the tool progresses from the outside to the inside of a calcium fluoride workpiece. The nominal force levels remain roughly constant, despite the fact that the cutting velocity approaches zero at the center of the workpiece. In these tests, a small hole was ground into the center of the workpieces prior to cutting so the cut ends one mm from the axis of rotation. Although not shown here, the cutting force results from subsequent passes over the workpiece are very similar to the data shown in Figure 2; however, after many facing cuts, the forces eventually increase as the tool edge begins to wear. At this point, the surface of the workpiece shows visible damage in the hard machining directions of the CaF_2 crystal and the diamond tool must be resharpened.

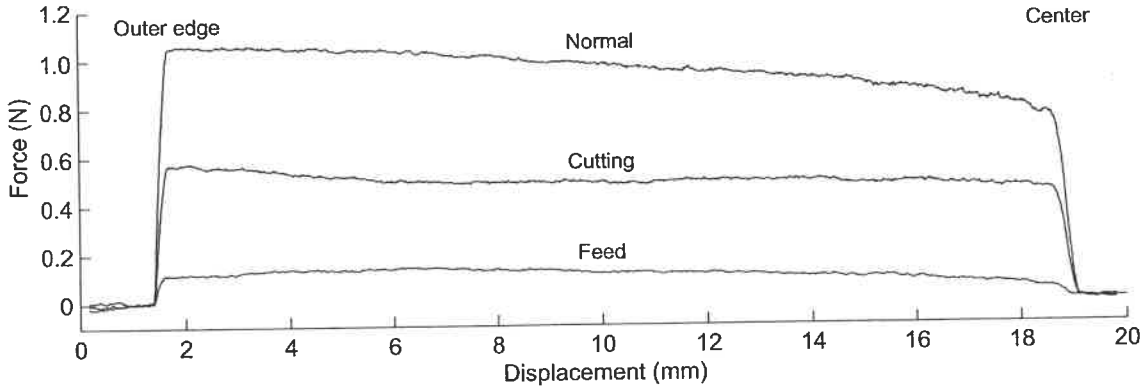

Figure 2 Calcium fluoride cutting forces after filtering to remove three-lobe fluctuations.

Figure 3 shows a close-up view of the unfiltered cutting forces with fluctuations over two revolutions of the workpiece that are due to anisotropy. The three-lobe fluctuations result from the interaction of the cutting tool and the crystalline structure of the (111) calcium fluoride workpiece. The fluctuations in forces are highly repeatable and additional similarity is seen between the subsequent revolutions (first three peaks vs. the second three peaks). The three peaks in each revolution are not identical because the crystal is not perfectly aligned with the cutting plane. As a result, the diamond tool engages the crystal at a small angular offset that leads to the slight variation between the three lobes. This effect was originally documented in diamond polishing [8].

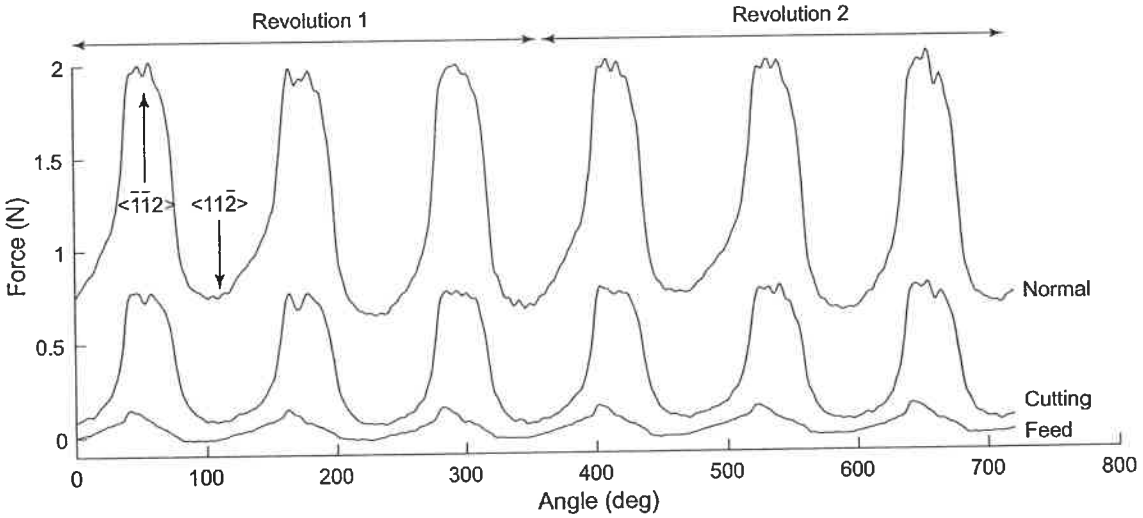

Figure 3 Two revolutions of cutting force data showing the three-lobe fluctuations on a (111) CaF_2 crystal.

Figure 4 shows the three components of cutting force mapped to the physical geometry of the round, flat workpieces. The three-lobe (trifoil) fluctuations in force resulting from the (111) symmetry of the crystal are clearly evident.

A series of calcium fluoride optics were diamond turned with -30° radial rake angle diamond tools of 1.5 mm radius with mineral oil coolant. Trial cuts were made at a depth of cut of 25 micrometers, feed rate of 4 micrometers/rev and two spindle speeds (600 and 1200 RPM). The three force components were measured during all tests. The finished workpiece surfaces were measured with a grazing incidence interferometer (Tropel FlatMaster 200) to quantify the height of the trifoil aberration. A 1.2 N PV normal force was measured when the CaF_2 workpiece was turned with a spindle speed of 600 RPM and 4 micrometers/rev feed rate. A 120 nm PV figure aberration is predicted using the measured loop stiffness of 10 N/micrometer. The actual aberration was measured to be 130 nm.

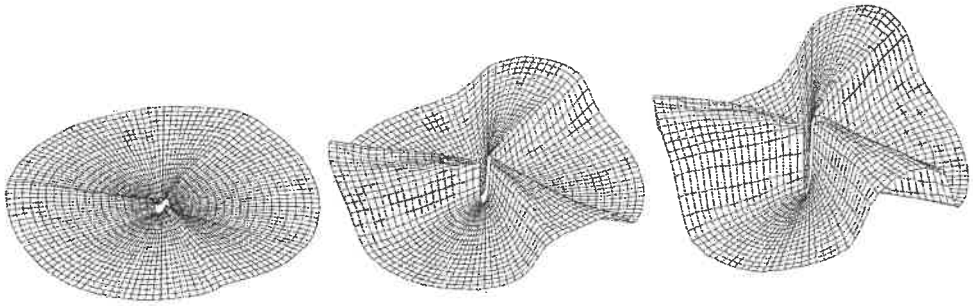

Figure 4 The cutting force components mapped to the surface of a Ø80mm plano (111) CaF_2 workpiece.

Conclusions

This paper demonstrates that trifoil aberration is predictable using in-process force measurements taken while diamond turning (111) calcium fluoride. The predictions agree with actual measurements within less than 13% error. The model also shows how the trifoil aberration can be minimized using a higher stiffness machine tool. The predictable nature of the trifoil aberration makes it possible to design a cutting process capable of generating rough-turned optics of sufficient quality for final polishing.

Acknowledgments

The authors thank Edge Technologies, Corning Tropel and QED for their assistance throughout the project.

References

1 Wang J, Maier RL, Bruning JH, "Surface characterization of optically polished CaF_2 crystal by quasi-Brewster angle technique", *Proc. SPIE* **5188**, 106-114(2003)

2 Yan J, Syoji K, Tamaki J. 2004. Crystallographic Effects in Micro/nano Machining of Single Crystal Calcium Fluoride, Journal of Vacuum Science and Technology-Series B, Vol. 22 (1), pp. 46-51.

3 Yan J, Tamaki J, Syoji K, Kuriyagawa T, (2004), Ductile Regime Machining of Single Crystal CaF2 for Aspherical Lenses, Key Engineering Materials, Vols. 257-258, pp. 95-100.

4 Syn C, Taylor J, Donaldson R, Shimada S. Ductile-brittle Transition of Cutting Behavior in Diamond Turning of Single Crystal Silicon. LLNL UCRL-98100, 1988.

5 Bifano T, Dow T, Scattergood R. Ductile-regime grinding of brittle materials: experimental results and development of a model. In: Proceedings of the SPIE: Advances in Fabrication and Metrology for Optics and Large Optics. 1988;966;108-115.

6 Blake P, Scattergood R. Ductile-regime machining of germanium and silicon. Journal of American Ceramic Society 1990;73(4);949-957.

7 Blaedel K, Taylor J, Evans C. Ductile-Regime Grinding of Brittle Materials. In: Jahanmuir S, Ramulu M, Koshy P. editors: Machining of Ceramics and Composites. New York: Marcel Dekker, Inc., 1999. 139-176.

8 Wilks J, Wilks E. Properties and Applications of Diamond. Oxford: Butterworth-Heinemann Ltd., 1991.

9 Bifano T, Dow T, and Scattergood R., "Ductile-Regime Grinding of Brittle Materials: Experimental Results and Development of a Model." *Proceedings of the SPIE: Advances in Fabrication and Metrology for Optics and Large Optics*, v 966, 1988, pp. 108-115.

10 Blake P, and Scattergood R., "Ductile-Regime Machining of Germanium and Silicon." *Journal of the American Ceramic Society*, v 73, n 4, 1990, pp. 949-957.

11 Patten JA and Gao W, (2000), Extreme Negative Rake Angle Technique for Single Point Diamond Nano-cutting of Silicon, Precision Engineering, Vol. 25, pp. 165-167.

12 Preus W, Riemer O. Single Point Diamond Machining. ASPE Annual Meeting Tutorial, 2003.

Optical Waveguide Fabricating on Lithium Niobate with UV Laser

Akira NAKANISHI, Shin'ichi WARISAWA, and Mamoru MITSUISHI

Department of Engineering Synthesis, School of Engineering, The University of Tokyo

7-3-1 Hongo, Bunkyo-ku, Tokyo, 113-8656, Japan

Abstract:

This paper presents fabrication of an optical waveguide on a lithium niobate plate using UV pulse laser of 355 nm in wavelength. The optical waveguide is composed of smooth bottom grooves with 300 μm in width and 10 μm in depth. The grooves are made by repeating a fabrication of small uniform groove. Therefore, geometry of small groove should be controllable. Some experiments were conducted to find out control methods of the geometry of a small groove. As a result, it is clarified that the width of a groove can be controlled by changing a focal position. Furthermore, it is found that there are three methods to control the depth of a groove. Finally, we tried to fabricate a smooth bottom groove with 300 μm in width and 10 μm in depth. As a result, the groove which had 300 μm in width, 9.92 μm in depth, and the bottom of 0.932 μm Rmax or 0.130 μm Ra was obtained by means of UV laser.

1.Introduction

It is required for optical components to have precise optical waveguides fabricated on a material surface. The waveguide has linear ridges as shown in Figure 1. At present they are fabricated by dicing technology while chipping may be occurred on their edges. This paper presents fabrication of an optical waveguide by means of UV laser instead of dicing. Compared with dicing technology, laser fabrication provides variety of ridge shape as well as cost and proceeding time reduction [1]. Key issues to be investigated are repeatability of fabricated geometry, control of width and depth of a groove in terms of machining conditions. The present paper provides experimental results from the viewpoint in detail.

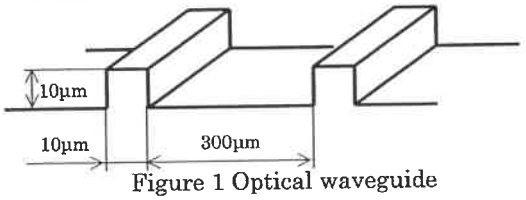

Figure 1 Optical waveguide

2.How to Make an Optical Waveguide

An optical waveguide is fabricated on a lithium niobate plate using UV pulse laser. The optical waveguide is composed of smooth bottom grooves of 300 μm in width and 10 μm in depth, called a waveguide's groove. The grooves are made by repeating a fabrication of a small uniform groove.

3.UV Laser Machining System

Small grooves are fabricated by means of pulsed UV laser of 355 nm in wavelength. The laser beam is focused to a spot with 9.02 μm in diameter by a lens. The small grooves are fabricated on a lithium niobate plate which was placed on a XY stage. The overview of the laser machining system is shown in Figure 2. Specifications of the system are shown in Table 1.

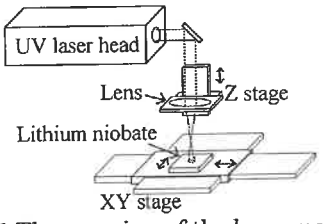

Figure 2 The overview of the laser machining system

Table 1 Specifications of the laser machining system

Wavelength	355 nm
Spot Diameter	9.02 μm
Focal Distance of Laser	42.09 mm for 355 nm wavelength
Pulse length	40 nsec
Polarization	Horizontal
Pulse Mode	TEM_{00} (M^2<1.3)

4.Geometry definitions of a small groove

In order to evaluate a small groove geometry, following factors were defined as shown in Figure 3; D(Depth of groove), W(Width of groove), H(Height of groove), and A(Area of groove). The

factors were investigated using a surface profile measurement instrument (SURFCOM 570A, TOKYO SEIMITSU).

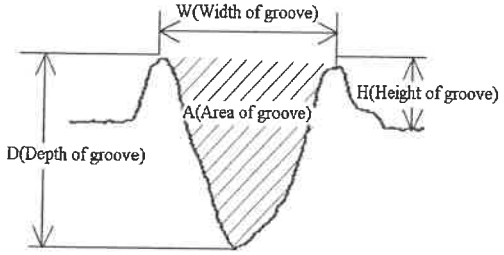

Figure 3 Geometry definitions of a small groove

5.Repeatability of geometry

Repeatability of the geometry of a small groove is very important, when an optical waveguide is fabricated. Therefore, experiments ware conducted to make relationships between focal position and the geometry of a small groove clear. Machining conditions in this experiment are shown in Table 2. The results of relationships between focal position and geometry are shown in Figure 4.

Table 2 Machining conditions

Laser energy	30 μJ/pulse
Pulse frequency	10 kHz
Feed speed	30 mm/sec
Focal position	-1400 μm～2000 μm

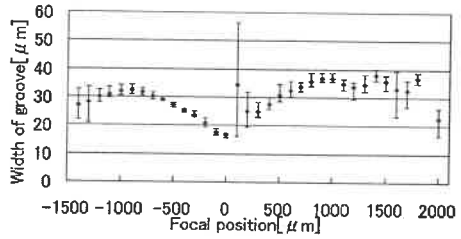

(a) Relationships between focal position and width of small groove

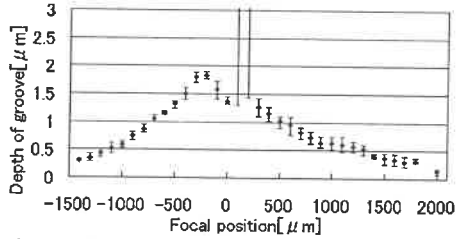

(b) Relationships between focal position and depth of small groove

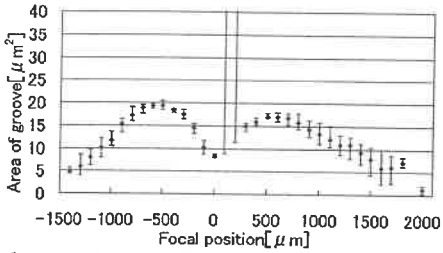

(c) Relationships between focal position and area of small groove

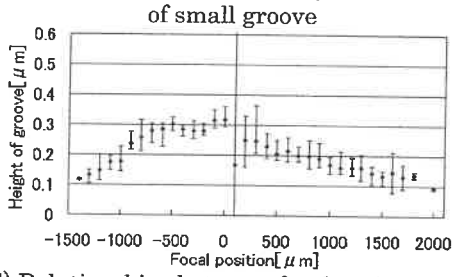

(d) Relationships between focal position and height of small groove

Figure 4 Relationships between focal position and geometry of small groove

In the results, it was found that geometrical repeatability was not good because of the crack occurrence, if the focal position from workpiece surface was less than 200 μm. It is considered that cracks are caused by high power density. Therefore, it is necessary to set the focal position to be more than 200 μm to obtain a small uniform groove.

6.Controllabirity of groove geometry

The geometry of the waveguide's groove is composed of small grooves. Therefore, it is required that a depth and width of small uniform groove should be controlled for an optical waveguide.

Machining conditions, i.e. pulse energy, pulse frequency, feed speed and focal position, which affect a geometry of a groove should be determined appropriately. Therefore, experiments were conducted to find out the relationship between the geometry of a groove and machining conditions mentioned above. Another propose of these experiments were to determine machining conditions for stable machining of a small groove that has required depth and width.

6.1 Control of the width of a small groove

From the experimental results, it is found that the width of a small groove can be easily controlled by

a focal position. It means that the range of focal position from –800 μm to 0 μm is available to control the width of a groove as shown in Figure 4(a). However, the depth of a groove is also changed as the focal position is changed as shown in Figure 4(b). Therefore, other machining conditions should be controlled to keep the depth controlled. Section 6.2 provides the control methods.

6.2 Control of the depth of a small groove

From the experimental results, we find out that there are three methods to control the depth of a small groove without changing its width.

The first method is to determine laser energy appropriately. Figure 5 shows the results of the depth and width of a groove in changing the laser energy.

Table 3 Machining conditions for the first method

Laser energy	1～200 μJ/pulse
Pulse frequency	10 kHz
Feed speed	30 mm/sec
Focal position	-600 μm

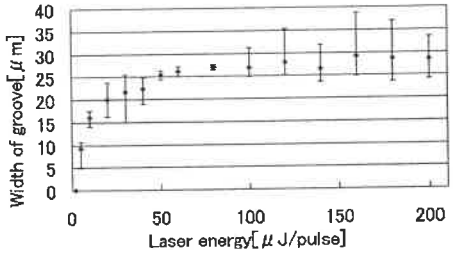

(a) Relationships between focal position and width of small groove

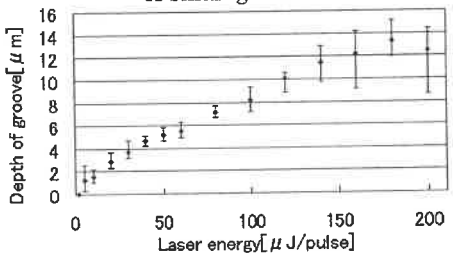

(b) Relationships between focal position and depth of small groove

Figure 5 Relationships between energy and geometry of small groove

A constant width of a groove can be obtained by the laser energy greater than 50 μJ, keeping other machining conditions constant. It means that the depth of a groove can be controlled by the laser energy greater than 50 μJ.

The second method to control the depth is to determine pulse frequency and feed speed appropriately. Figure 6 shows the results of the depth and width of a groove in changing the pulse frequency with keeping shot distance constant.

Table 4 Machining conditions for the second method

Laser energy	20 μJ/pulse
Pulse frequency	1～60 kHz
Feed speed	1～60 mm/sec
Focal position	-600 μm
Shot distance	1 μm

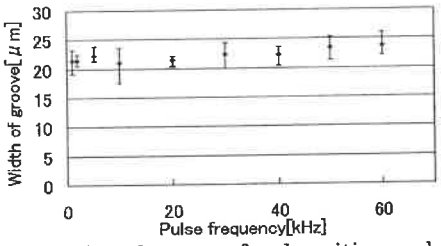

(a) Relationships between focal position and width of small groove

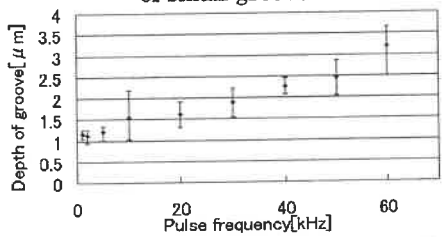

(b) Relationships between focal position and depth of small groove

Figure 6 Relationships between pulse frequency and geometry of small groove

It is observed that a constant width of a groove can be obtained when the pulse frequency and the feed speed are adjusted to realize a constant shot distance. In the case, the depth of a groove increased as the pulse frequency increased. It means that the depth of a groove can be controlled by pulse frequency and feed under the constant condition of shot distance.

The third method to control the depth is to adjust the feed speed. Figure 7 shows the results of the depth and width of a groove in changing the feed speed.

Table 5 Machining conditions for the third method

Laser energy	30 μJ/pulse
Pulse frequency	10 kHz
Feed speed	1～60 mm/sec
Focal position	-600 μm

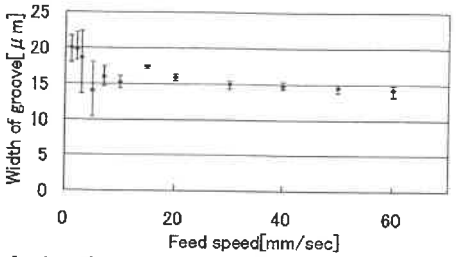

(a) Relationships between focal position and width of small groove

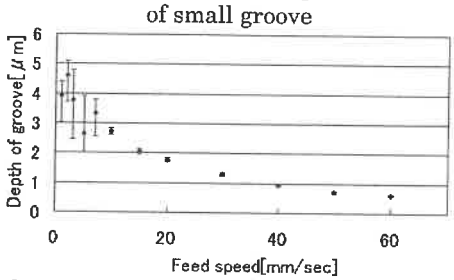

(b) Relationships between focal position and depth of small groove

Figure 7 Relationships between feed speed and geometry of small groove

It is found that the width of a groove does not change when the feed speed is changed if it is greater than 20 μm/sec. It means that the depth of a groove can be controlled by the feed speed greater than 20 μm/sec.

7.Optical Waveguide Fabrication

Finally, applying the results clarified above, we tried to fabricate an optical waveguide's groove of 300 μm in width and 10 μm in depth with a smooth bottom. In this fabrication, the machining conditions were determined as shown in Table 6, which gave the best geometry of a small groove for the optical waveguide's groove fabricating.

The fabricated optical waveguide's groove had 300 μm in width, 9.92 μm in depth, and the bottom of 0.932 μm Rmax or 0.130 μm Ra as shown in Figures 8 and 9.

Table 6 Machining conditions for an optical waveguide' groove

Laser energy	17 μJ/pulse
Pulse frequency	10 kHz
Feed speed	30 mm/sec
Focal position	-600 μm
Distance of pick-feed	6 μm
Number of small grooves	50
Number of wide grooves	5

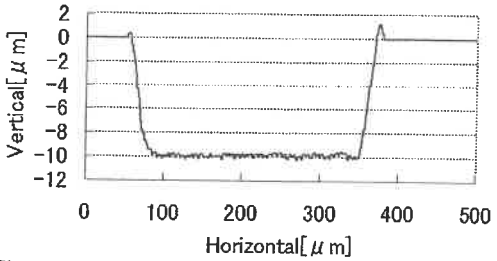

Figure 8 Cross section profile of a waveguide's groove measured by a surface roughness profile instrument

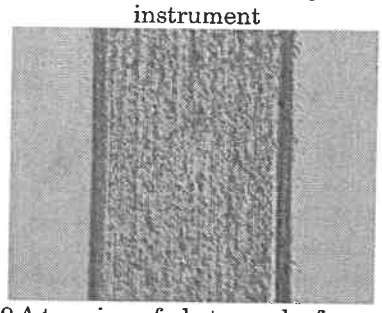

Figure 9 A top view of photograph of waveguide's groove

8.Conclusion

This paper presents fabrication of an optical waveguide on a lithium niobate plate using UV pulse laser. For the purpose, some experiments were conducted to clarify the relationships between machining conditions and a small groove geometry. As the results, it is made clear that groove geometry can be controlled by adjusting machining conditions. The details are following:

(1)The width of a small groove can be controlled by a focal position from –800 μm to 0 μm.

(2) The depth of a groove can be controlled by the laser energy greater than 50 μJ without changing its width.

(3) The depth of a groove can be controlled by pulse frequency and feed with keeping shot distance constant without changing its width.

(4) The depth of a groove can be controlled by the feed speed greater than 20 μm/sec without changing its width.

Finally, we fabricated the optical waveguide's groove, which had 300 μm in width, 9.92 μm in depth, and the bottom of 0.932 μm Rmax or 0.130 μm Ra, using the UV laser.

Reference:

1.J.Meijer,K.Do,A.Gillner,D.Hoffmann,V.S.Kovalenko,T.Masuzawa,A.Ostendorf:Laser Machining by Short and Ultrashort Pulses, State of the Art, Annals of the CIRP,51,2,pp.1-20,2002.

FABRICATION AND MICROSTRUCTURE ANALYSIS OF Pt/C MULTILAYERS FOR HARD X-RAY OPTICS

Yuji Nonomura, Naoyuki Ohnishi* and Yoshiharu Namba
Chubu University, Kasugai, Aichi 487-8501, Japan

Koujun Yamashita
Nagoya University, Nagoya, Aichi 464-8602, Japan

Abstract

Pt/C multilayers with periodic length designed for 4, 3, and 2 nm have been fabricated by an ion-beam sputtering process on float-glass or Si wafer substrates. Grazing incidence x-ray reflectivity of the first Bragg peak for the Cu-Kα radiation was significantly reduced with decreasing of the periodic length. Scanning probe microscope analysis and cross-sectional transmission electron microscopy (TEM) studies indicated that the interface roughness of the multilayers increased with decreasing of the periodic length, while density of the Pt layer lowered. Plane-view TEM observations revealed that Pt monolayer films with the thickness corresponding to the periodic length smaller than 4nm have an island structure.
Key Words : Pt/C multilayer mirror, Thin film, X-ray optics, Transmission electron microscopy, Ion beam sputtering

1. Introduction

X-ray multilayer mirror is one of the most important candidates for the optical component applied for x-ray optics such as next generation lithography techniques and x-ray microscopes. Multilayers for x-rays consist of both heavy and light element materials that are alternately deposited with periodic length in the nanometer range. Various combinations of heavy and light elements, and of the periodic length of multilayers, can be chosen depending on the x-ray wavelength and the optics design. Platinum/Carbon (Pt/C) multilayers are advantageous for the applications in a hard x-ray range up to 80 keV with relatively short wavelength, because it has a high contrast of the electron density and no absorption edge in this energy range. Especially, recent development of hard x-ray telescopes successfully demonstrated that the Pt/C multilayers are suitable for focusing optics in astronomical applications [1-3]. The current status of the astronomy regarded with the Pt/C multilayer optics is to observe x-ray with higher energy range above 40 keV. This corresponds to the development of multilayers with the periodic length d=3 – 5 nm or shorter, and improvement of the quality of multilayers in this period range is essential. Since performance of Pt/C multilayers depends heavily on the interface roughness and the errors in the layer thickness, an understanding of microstructures is important to develop multilayers with such extremely small d values. This study aims to investigate interrelations between x-ray reflectivity and microstructures of Pt/C multilayers, and to develop the multilayers with smaller d values for the higher energy x-rays. Transmission electron microscopy techniques are specifically utilized for obtaining atomic details of the microstructural information.

2. Experimental Procedure

Pt/C mulilayers with several periodic length were fabricated on float glass or Si(100) wafer substrates by an ion-beam sputtering (IBS) process. Structural parameters of the multilayers were designed as the periodic length d = 2, 3, and 4 nm, the number of layer pairs N = 10, and the thickness ratio of heavy element $\Gamma = 0.4$. The IBS system applied for the deposition has a standard arrangement with a 30 mm Kaufman-type DC ion source, a rotative target holder, and a planer substrate holder with rotating and rocking mechanism. The chamber was evacuated to ~5×10^{-5} Pa before starting the deposition, and the working pressure during the deposition was ~5×10^{-2} Pa. The substrate was kept at room temperature, and the deposition rate was ~5.33 nm/min and ~0.53 nm/min for Pt and C, respectively.

For the evaluation of the reflectivity and microstructure of the fabricated Pt/C multilayers, grazing incidence x-ray reflectivity (GIXR) analyses, scanning probe microscope (SPM) observations, and transmission electron microscope (TEM) observations were employed. The interface roughness σ_i and surface roughness σ_s of the multilayer were also evaluated by means of these three analysis methods. The GIXR analyses was made by an x-ray diffractometer (Rigaku, ATX-E) with Cu-Kα line (8.04 keV). The reflectivity profiles were measured for the incident angle range of 0-5 degree. In order to estimate the interface roughness σ_i and the other structural parameters such as d and Γ, the

*corresponding author: naoyuki@isc.chubu.ac.jp

experimental GIXR profiles were compared with calculated profiles using commercial analysis software (Rigaku, GXRR). For the SPM observations, an ordinary atomic force microscope (SII, SPA-400) was used to measure surface roughness σ_s of the Pt/C multilayers. TEM observations were performed using three electron microscopes (JEOL, JEM-ARM1250, JEM-4000EX, and JEM-2100F), of which theoretical point resolutions were 0.1 nm, 0.17 nm and 0.19 nm, respectively. A slow-scan CCD camera (Gatan SSC model-694) was utilized to quantitatively measure the electron beam intensity distributions in the TEM image.

3. Results and Discussion

Figure 1 shows a GIXR profile of the Pt/C multilayer with periodic length d=4 nm. Solid line is an experimental x-ray intensity, and dotted line indicates a profile calculated to fit to the experimental data. The reflectivity R of the first Bragg peak is 44.4 %, and the ratio of the reflectivity R to a theoretical optimum value R_0 is 62.7 %. This is relatively reasonable performance considering the periodic length of the multilayer. The R_0 value was calculated by assuming the interface roughness σ_i to zero, while the actual roughness of this specimen was estimated as 0.302 nm rms. Generally, the GIXR intensity is altered by lowering the electron density of the materials, as well as the interface roughness. Although the fitting analysis of the GIXR profile is not yet perfect, it was suggested that the density of the Pt layers of the specimen is lower than the theoretical value for the bulk Pt crystal.

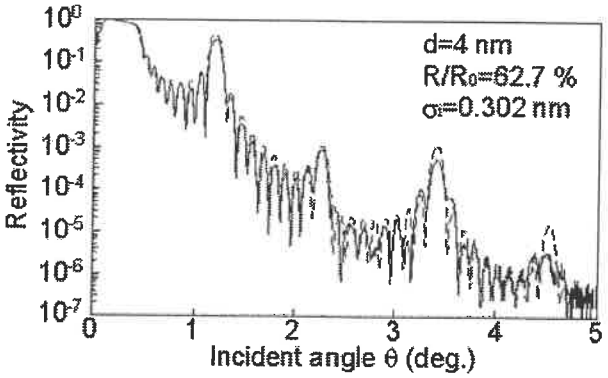

Figure 1: Grazing incidence x-ray reflectivity profile of a Pt/C multilayer with d=4 nm.

The GIXR measurements of the other multilayer samples with different design parameters indicated that the ratio of the reflectivity R/R_0 decreases significantly when the periodic length d become shorter. The obtained R/R_0 ratio for the d=3 nm was 36.5 %, and it fell down to 3.61 % for the d=2 nm sample. The interface roughness σ_i of these specimens were estimated as 0.327 nm rms and 0.418 nm rms for d=3 nm and d=2 nm, respectively. The density of the Pt layers estimated by the GIXR profile of these multilayers also indicated a tendency to become lower for the shorter periodic length. The degrading of the reflectivity ratio can be basically attributed to such changes of roughness and density.

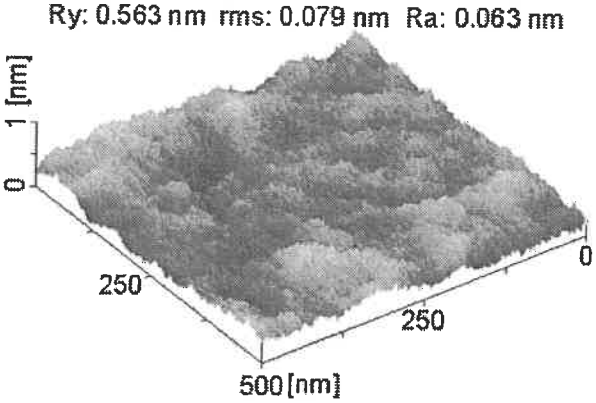

Figure 2: Surface roughness of the top Pt layer of d=4 nm multilayer measured by SPM.

Figure 2 is an SPM image of the d=4 nm multilayer sample. It shows a surface morphology of the top Pt layer. The surface rms roughness value σ_s as measured for this 500 nm x 500 nm area was 0.079 nm. Figure 3 shows a relation between the periodic length and the σ_s value measured by the SPM. The interface roughness values σ_i by the GIXR analyses are also indicated. It should be noted that the interface roughness σ_i estimated by the GIXR includes an influence of the interdiffusion of Pt and C, while the SPM measures only a morphological feature of the top surface detected by the probe tip with restricted spatial resolution. Nevertheless, both σ_s and σ_i values have the same tendency, indicating that the roughness increases for the smaller periodic length.

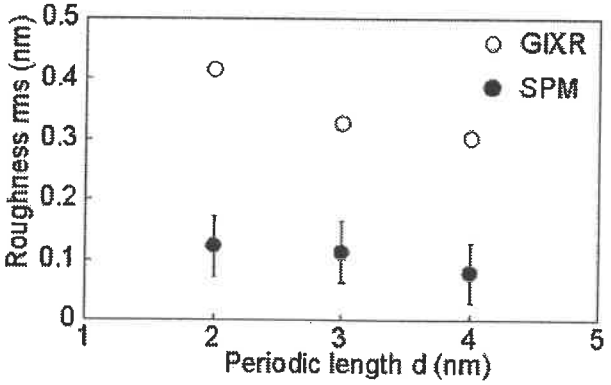

Figure 3: Relation between the periodic length d and the surface/interface roughness σ_s and σ_i.

In order to reveal detailed microstructures as origins of the GIXR and SPM results, atomic resolution TEM observations of cross-sections of the multilayers were performed. Figures 4(a) - (c) are cross-sectional TEM images of Pt/C multilayers with d=4, 3, and 2 nm. Alternating layers of Pt and C are observed as dark and blight stripes. The image contrast exhibits that the Pt layers consist of crystal phase, while the carbon layers are amorphous. Fine fringes with the spacing of about 0.3 nm observed in the Pt layers correspond to the {111} lattice planes [4]. For each TEM images with deferent d value, it seems that the grain size of the Pt crystallites in the direction across the layers is nearly equal to the layer thickness. On the other hand, the lateral size (aspect ratio) of the Pt grains changes depending on the deposition period. The image apparently indicates that the d=2nm multilayer has Pt grains with smaller aspect ratio, and the contrast at the layer interface is unclear, compared with the specimens with longer d values.

Figure 5(a) shows a TEM image of a Pt/C multilayer deposited with graded thickness. The thickness of Pt layers was designed as 9.0, 3.0, 1.0, and 0.3 nm. The image was obtained from a relatively thick area of the TEM specimen and recorded with a slow-scan CCD camera. It is to be noted that the darkness of the Pt layers in the image changes depending on the layer thickness. Figure 5(b) is a profile of the image contrast of Figure 5(a) along the direction across the multilayers. In this case, considering the experimental condition, the darkness of image contrast is basically proportional to the packing density of atoms, which is averaged along the incident electron beam. The contrast profile presents that the density of the Pt layer lowers with decreasing of the thickness.

In order to verify the above results obtained by the cross-sectional TEM observations, a plane-view observation of Pt monolayer films was carried out. Figures 6 (a) - (c) are plane-view TEM images of Pt monolayer film deposited by the IBS process on the amorphous carbon film substrate. The thickness values t of Pt films are 2 nm, 1.5 nm, and 1 nm, which correspond to the periodic length d = 4 nm, 3 nm and 2 nm, respectively. The image shows that, in the case of t=2 nm

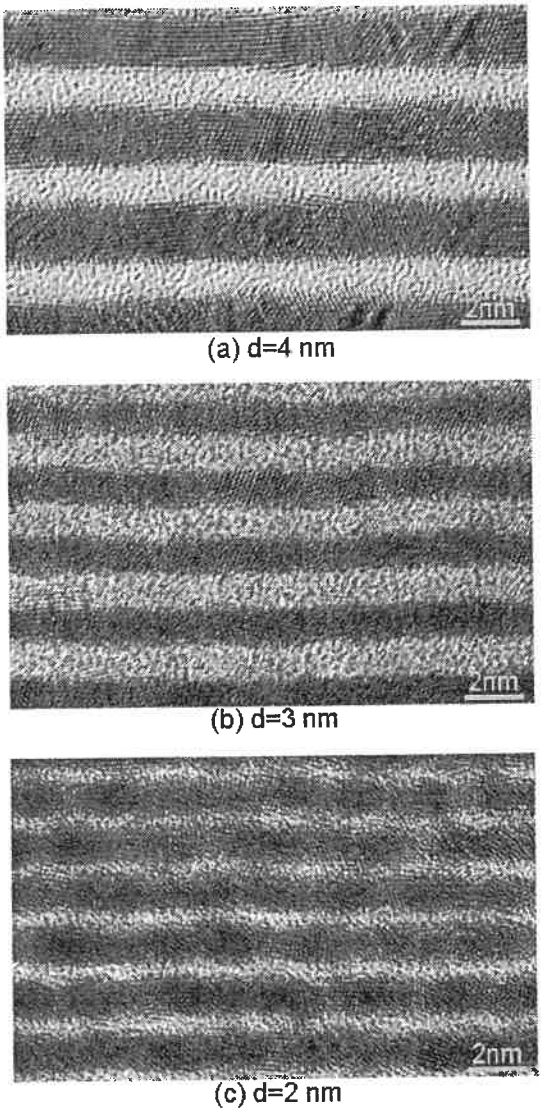

Figure 4: Cross-sectional TEM images of Pt/C multilayers with periodic length d = 4, 3, and 2 nm.

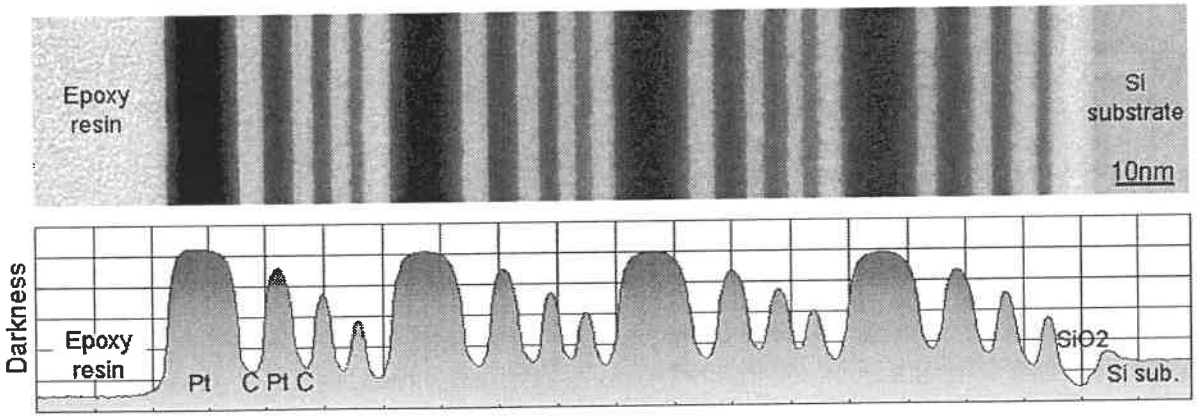

Figure 5: TEM image and its contrast profile of a Pt/C multilayer with graded thickness. The image was recorded with a slow-scan CCD camera.

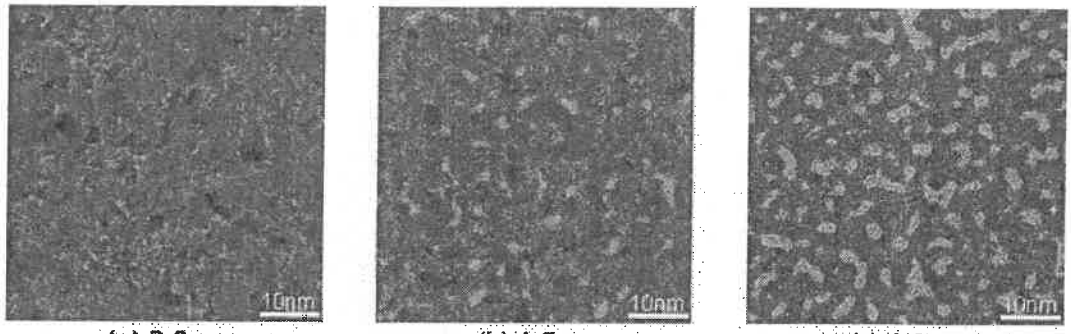

Figure 6: Plane-view TEM images of Pt monolayer films deposited on amorphous carbon films. The thickness of the Pt films is 2.0 nm(a), 1.5 nm(b), and 1.0 nm(c).

specimen, the substrate carbon film is covered nearly 100 % by the Pt crystal grains. On the other hand, a number of holes, observed as blighter contrast, exists in the Pt monolayer films with smaller thickness. The coverage of Pt grains on the substrate estimated from the image are approximately 95 % and 80 % for the t=1.5 nm and 1 nm films, respectively. This indicates that the Pt monolayers with the thickness smaller than 2 nm is in an transition stage during the growth from so called island structure to the continuous film. It is reasonably concluded that the observed characteristics of the roughness and density of the Pt/C multilayers depending on the periodic length primarily originate in the same feature.

4. Conclusions

Pt/C multilayers for the hard x-ray optics applications with periodic length d = 4, 3, and 2 nm were fabricated by an ion beam sputtering process, in order to reveal microstructures and their relations with the reflectivity. The multilayers were characterized by means of grazing incidence x-ray reflectivity (GIXR) measurement with Cu-Kα radiation, scanning probe microscopy (SPM), and transmission electron microscopy (TEM) observations. The GIXR intensity of the first Bragg peak of the d=4 nm multilayer was 62.7 % of the theoretical optimum intensity. The GIXR intensity was significantly reduced with decreasing of the periodic length. This can be mainly attributed to an increasing of the interface roughness and a lowering of the Pt layer density, which are observed by the TEM and SPM studies. Plane-view TEM observations revealed that Pt monolayer films with the thickness corresponding to the periodic length smaller than 4 nm have an island structure, which causes relatively large interface roughness and low Pt layer density.

Acknowledgements

Part of this work was supported by the Grants-in-Aid for Scientific Research (B) Nos. 14350077 and 15360075 of the Japan Society for the Promotion of Science, and the "Nanotechnology Support Project" of the Ministry of Education, Culture, Sports, Science and Technology (MEXT), Japan.

References

[1] T. Okajima, K. Tamura, Y. Ogasaka, K. Haga, S. Takahashi, S. Ichimaru, H. Kito, S. Fukuda, A. Goto, K. Nomoto, H. Satake, S. Kato, Y. Kamata, A. Furuzawa, F. Akimoto, T. Yoshioka, K. Haba, T. Tanaka, K. Wada, N. Hamada, M. Hudaverdi, Y. Tawara, K. Yamashita, P. J. Serlemitsos, Y. Soong, K.-W. Chan, S. M. Owens, F. B. Berendse, J. Tueller, K. Misaki, R. Shibata, H. Mori, K. Itoh, H. Kunieda and Y. Namba, "Characterization of the supermirror hard-x-ray telescope for the InFOCμS balloon experiment", Appl. Opt., **41** (2002) p.5417-5426.

[2] K. Yamashita, P. J. Serlemitsos, J Tueller, S. D. Barthelmy, L. M. Bartlett, K.-W. Chan, A. Furuzawa, N. Gehrels, K. Haga, H. Kunieda, P. Kurczynski, G. Lodha, N. Nakajo, N. Nakamura, Y. Namba, Y. Ogasaka, T. Okajima, D. Palmer, A. Parsons, Y. Soong, C. M. Stahl, H. Tanaka, K. Tamura and B. J. Teegarden, "Supermirror hard-x-ray telescope", Appl. Opt., **37** (1998) p.8067-8073.

[3] G. S. Lodha, K. Yamashita, T. Suzuki, I. Hatsukade, K. Tamura, T. Ishigami, S. Takahama and Y. Namba, "Platinum/carbon multilayer reflectors for soft-x-ray optics", Appl. Opt., **33** (1994) p.5869-5874.

[4] N. Ohnishi, Y. Nonomura, Y. Ogasaka, Y. Tawara, Y. Namba, and K. Yamashita, "HRTEM anarysis of Pt/C multilayers", Proc. SPIE, **5168** (2003) p.508-517.

Point diffraction interferometer using an optical saturable absorber

Hideo Furuhashi[1], Atsushi Shibata[1], Yoshiyuki Uchida[1],
Kiyofumi Matsuda[2] and Chander P. Grover[3]
[1]Department of Electrical and Electronics Engineering, Aichi Institute of Technology
1247, Yachigusa, Yakusa-cho, Toyota, 470-0392 JAPAN
[2]National Institute of Advanced Industrial Science and Technology, Japan
[3]Institute for National Measurement Standards
National Research Council Canada, Canada

The point diffraction interferometer (PDI) is a common-path interferometer that can be used to easily measure either the phase variation across the wavefront or the change in the index of refraction of a transparent phase object [1-3]. In such an interferometer, the reference beam is generated after the filter, thus providing a self-referencing system that is inherently stable and relatively insensitive to vibration. The PDI has a simple structure and is useful in the testing and evaluation of optical elements and in the analysis of phase objects and fluid flow diagnostics, for example. The filter in a PDI has either an opaque dot that is smaller than the airy disk on a transparent film or the transparent dot on an opaque film. The wavefront is focused onto the dot by a Fourier transform lens, and a spherical wave is generated by the diffraction caused by the dot. A fringe pattern is obtained at the image plane by the interference between the diffracted wave and the wavefront. However, a filter having an extremely small dot is required, and focusing the wavefront on such a small dot is difficult.

In the present paper, a point diffraction interferometer using an optical saturable absorber is proposed. In this system, the small dot is generated automatically on the film and the focal point is self-aligned.

We now consider a standard PDI consisting of a Fourier transform lens and a transparent dot filter, as shown in Fig.1. A wavefront on the object plane is focused on the filter. Here, we consider a wavefront with a complex amplitude of $u = A \cdot \exp[i\phi(x,y)]$, where A is the absolute amplitude, and x and y are the orthogonal coordinates on the object plane. We resolve the wavefront into two components: a plane wave $A \cdot \gamma$ in the direction of the z axis (orthogonal to x and y), and all other waves $v = A \cdot \exp[i\phi(x,y)] - A \cdot \gamma$, where γ is the ratio of the plane wave, referring to the ratio of the waves focused on an area smaller than the transparent dot at the focal point. If the amplitude transmittance of the filter outside the dot is α, and that of the transparent dot is α_{foc}, then the wave on the image plane is expressed as follows:

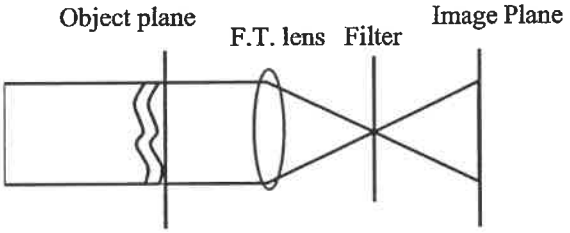

Fig. 1. Schematic diagram of a PDI system.

$$w = \alpha \cdot \left(A \cdot \exp[i\phi(x,y)] - A \cdot \gamma\right) + a_{foc} \cdot A \cdot \gamma \,. \tag{1}$$

Thus, the optical intensity is given by

$$I = A^2 \left\{\alpha^2 + \gamma^2 \cdot \left(\alpha_{foc} - \alpha\right)^2 + \cdot 2 \cdot \alpha \cdot \gamma \cdot \left(\alpha_{foc} - \alpha\right) \cos[i\phi(x,y)]\right\} \tag{2}$$

An interference fringe is then obtained, for which contrast is defined as

$$V = \left| \frac{2 \cdot \alpha \cdot \gamma \cdot \left(\alpha_{foc} - \alpha\right)}{\alpha^2 + \gamma^2 \cdot \left(\alpha_{foc} - \alpha\right)^2} \right| . \tag{3}$$

If the optical saturable absorber is used as the filter, the optical transmittance changes with the optical intensity on the Fourier transformed plane. Here, we consider a simplified model of the absorber described by the following equation:

$$\begin{aligned} \frac{dN_2}{dt} &= I' \cdot k_{12} N_1 \\ \frac{dN_1}{dt} &= -I' \cdot k_{12} N_1 \\ N_0 &= N_1 + N_2 \\ \beta_{abs} &= k_{12} \cdot N_1 + \beta_0 \end{aligned} \tag{4}$$

Here, N_1 and N_2 are the number densities of molecules in the ground state and excited state, respectively, N_0 is the initial density in the ground state, k_{12} is the absorption coefficient in the ground state, β_0 is the background absorption rate of the film, β_{abs} is the total absorption rate of the film, and I' is the optical intensity on the film. As a result, the following equation is obtained:

$$\beta_{abs} = k_{12} \cdot N_0 \cdot \exp\{-k_{12} \cdot I' \cdot t\} + \beta_0 \,. \tag{5}$$

The optical intensity at the focal point is very high; the amplitude transmittance is $\alpha_{foc} = 1 - \beta_0$.

By substituting the $\alpha = 1 - \beta_{abs}$ into equation (3), the following equation is obtained:

$$V = \left| \frac{2 \cdot \{1 - k_{12} \cdot N_0 \exp(-k_{12} \cdot I' \cdot t) - \beta_0\} \cdot \gamma \cdot k_{12} \cdot N_0 \exp(-k_{12} \cdot I' \cdot t)}{\{1 - k_{12} \cdot N_0 \exp(-k_{12} \cdot I' \cdot t) - \beta_0\}^2 + \gamma^2 \cdot \{N_0 \exp(-k_{12} \cdot I' \cdot t)\}^2} \right| . \tag{6}$$

If the intensity of the non-plane component is small, then the contrast is

$$V = \left| \frac{2 \cdot \{1 - k_{12} \cdot N_0 - \beta_0\} \cdot \gamma \cdot k_{12} \cdot N_0}{\{1 - k_{12} \cdot N_0 - \beta_0\}^2 + \gamma^2 \cdot {N_0}^2} \right| . \tag{7}$$

A photochromic bacteriorhodopsin (BR) film is used as the saturable absorber in this experiment. BR-film has very high resolution, over 5000 lines/mm, and low saturation energy. The BR-film used in this experiment is Munich Innovative Biomaterials GmbH V11S. This film has a diameter of 19 mm and a relaxation time range (RTR), after which 63% (1/e) of all excited state molecules return to the original state, of 40-80 seconds at a temperature of 22°C.

Figure 2 shows a schematic diagram for a simplified photocycle of the BR film. BR568 is the ground state, and M412 is the excited state. Ground state molecules in the BR-film absorb light of wavelengths between 500 and 700 nm. When a wavefront having a wavelength in this region is focused on the BR-film, saturation of the absorption occurs only at the focal point due to the high intensity, and the point becomes transparent with respect to this wavefront. The excited state is stable, and the thermal relaxation is slow. Therefore, the BR-film acts as a PDI filter.

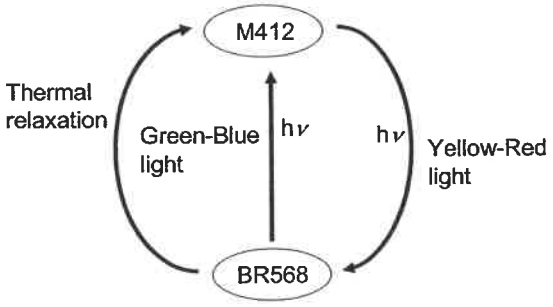

Fig. 2. Schematic diagram for a simplified photocycle of the BR film.

We have measured a wavefront passing through a transparent phase object using a collimated 633 nm He-Ne laser. Figure 3 shows the experimental set-up of the system. The Fourier transform lens has a focal length of 150 mm and a diameter of 40 mm. The fringe image was observed using a charge-coupled device (CCD) camera (resolution is 640×480 pixels). The phase object is a thin glass wedge having a refractive index of 1.5, a diameter of 2.5 mm, a thickness of 0.3 mm and a wedge angle of approximately 10^{-3} rad. The area of the wavefront, defined by the diameter of the Fourier transform lens is 1250 mm^2, corresponding to a ratio of the plane wave of 99.6%. The diameter of the Fourier transform of the non-plane component on the focal plane, as calculated from diffraction theory, is approximately 100 μm.

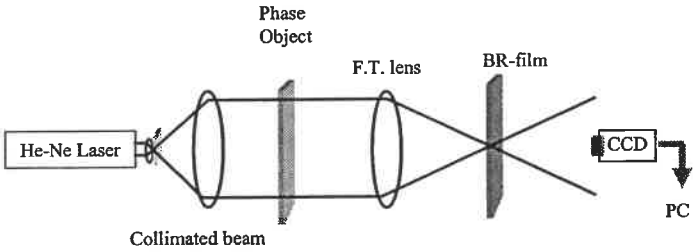

Fig. 3. Experimental set-up of the system.

Figure 4 shows the observed interference fringe image (a) without a filter and (b) with a BR-film filter. Good contrast of the interference fringe is observed for this system. Figure 4 (c) shows the fringe image with a BR-film filter after 3 minutes. Although the optical intensity on the Fourier transform plane outside the focal point is small, the fringe contrast changes as shown in equation (6).

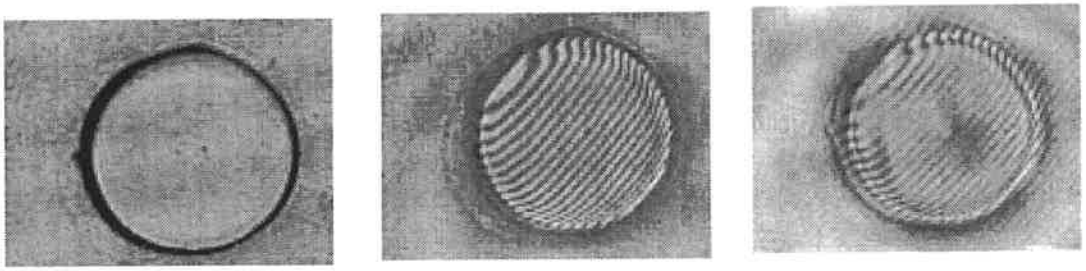

Fig. 4. Image on the image plane (a) without filter, (b) with BR-film filter after 20 seconds, (c) with BR-film filter after 3 minutes

This is because the film also becomes transparent outside the focal point. The contrast decreases and becomes 0 after a long time.

Next, we applied blue light, which de-excited the M412 state to the BR568 ground state. In this case, equation (4) changes as follows:

$$\begin{aligned}
\frac{dN_2}{dt} &= I' \cdot k_{12} N_1 - I'' \cdot k_{21} N_2 \\
\frac{dN_1}{dt} &= -I' \cdot k_{12} N_1 + I'' \cdot k_{21} N_2 \\
N_0 &= N_1 + N_2 \\
\beta_{abs} &= k_{12} \cdot N_1 + \beta_0
\end{aligned} \tag{8}$$

Here, k_{21} is the absorption coefficient in the M412 state and the excited state, and I'' is the blue light intensity on the film. As a result, the following equation is obtained:

$$\beta_{abs} = k_{12} \cdot \frac{N_0}{I' \cdot k_{12} + I'' \cdot k_{21}} \left[I'' \cdot k_{21} + I' \cdot k_{12} \cdot \exp\left\{ -\left(I' \cdot k_{12} + I'' \cdot k_{21} \right) t \right\} \right] + \beta_0 . \tag{9}$$

The absorption rate in the focal point is β_0, because the intensity I' is very high and the first term in the equation of β_{abc} is approximately 0. On the other hand, the absorption outside the focal point converges to $\beta_{abs} = k_{12} \cdot N_0 + \beta_0$, if de-excitation rate $I'' \cdot k_{21}$ is lager than the excitation rate $I' \cdot k_{12}$. Therefore, the interference fringe contrast becomes as follows after a long time:

$$V = \left| \frac{2 \cdot \left(1 - k_{12} \cdot N_0 - \beta_0 \right) \cdot \gamma \cdot k_{12} \cdot N_0}{\left(1 - k_{12} \cdot N_0 - \beta_0 \right)^2 + \gamma^2 \cdot k_{12} \cdot N_0} \right| . \tag{10}$$

Figure 5 shows the result of the interference fringe image after 10 minutes. A stable fringe image is observed for a long period of time in this method.

We have proposed a PDI system using an optical saturable absorber and have shown that good fringe contrast is obtained without alignment of the focal point.

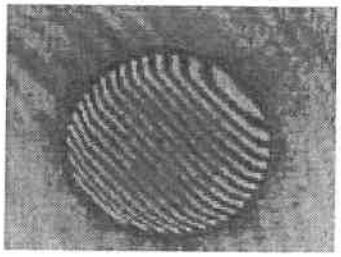

Fig. 5. Image on the image plane with BR-film filter after 10 minutes. Blue light is applied.

1. R. N. Smart, Proc. SPIE, 192, 35 (1979).
2. R. N .Smart, Jpn. J. Appl. Phys. Suppl. 14(1), 351 (1975).
3. H. Furuhashi, A. Shibata, Y. Uchida, K. Matsuda and C. P. Grover, Optics Commun. 237, 17 (2004).

Imaging by a phase grating used in displacement measurement

Yoichi Ohmura [a], Toru Oka [a], Toshiro Nakashima [a] and Kazuhiro Hane [b]

[a] Advanced Technology R & D Center, Mitsubishi Electric Corporation, Amagasaki, Japan

[b] Department of Mechanical Engineering, Tohoku University, Sendai, Japan

Abstract

Precision displacement measurement with a phase grating based on grating imaging is proposed. In this imaging system, a conventional amplitude grating as a scale is replaced by a phase grating. That generates a sinusoidal pattern, which works as an optical scale, with higher amplitude than the conventional imaging system with an amplitude grating. In this paper, analysis using an optical transfer function is described, so that optimal image contrast can be achieved. The experimental results with the image contrast of about 60 percent demonstrate good agreement with theoretical value. The results indicate the proposed method yields very good performance on displacement measurement.

Introduction

Grating imaging, used in displacement measurement, is well known [1,2]. Analyses of the grating imaging based on the optical transfer function (OTF) theory and experimental demonstration have been reported when using an amplitude grating as a pupil [3,4]. However, in amplitude grating imaging, an image contrast and received light power on an image plane, which determine accuracy and resolution in displacement measurement, were not satisfactory. In order to improve the contrast and the power, we propose using a phase grating as the pupil instead of the amplitude grating. In this paper, analysis by the OTF theory [3,4] is discussed using a phase grating with a concavo-convex shape with a 50 percent duty ratio as the pupil. To confirm theoretical results, we measured the image contrast from the intensity distribution on the image plane. Furthermore, the displacement measurement when the pupil phase grating moved was performed under high contrast imaging conditions.

Theory

The optical system of grating imaging consists of spatial incoherent light and three planes; an object plane, a pupil plane and an image plane. The optical distribution on the object plane is imaged on the image plane by the pupil. The contrast of the image, which influences measurement accuracy and resolution, depends on the wavelength, the shapes of the pupil and the distances between three planes. To study the image contrast, OTF analysis when using a phase grating as the pupil was performed.

Figure 1 is a schematic diagram of the grating imaging system. An object grating with pitch p1 is placed on the X1-axis, and illuminated by spatial incoherent light. A pupil grating with a concavo-convex shape with 50 percent duty ratio is located at a distance Z1 from the object grating. The pitch of the pupil grating is set to p. The phase-shift amount of the pupil grating is controlled by the depth of the concavo-convex shape. The image plane is placed on the X2-axis located at a distance Z2 from the pupil grating.

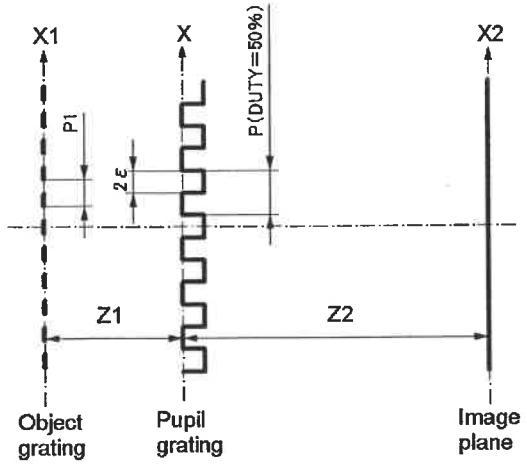

Fig.1 Schematic diagram of the optical system

The pupil function P(x) of the pupil grating is defined as

$$P(x)=1 \quad (=\exp(j0)) \qquad |x-np| \le \varepsilon$$

$$=\exp(j\theta) \qquad \left|x-\left(n+\frac{1}{2}\right)p\right| \le \frac{p}{2}-\varepsilon$$

where θ is the amount of phase-shift, 2ε is the width of its top and bottom, and n is an integer.

Generally, an OTF under incoherent illumination is defined as the Fourier transform of the square of its impulse response. In this optical system, the simplified OTF (F) in the Fresnel region can be written as

$$F(\sigma_2) = \exp\left[ika\left(\lambda^2 Z_2^2 \sigma_2^2\right)\right] \times \int P(x' - \lambda Z_2 \sigma_2) P^*(x') \exp(-2ika\lambda Z_2 \sigma_2 x') dx'$$

where $k = 2\pi/\lambda$, $a = (1/Z1+1/Z2)/2$, λ is the wavelength of the incoherent light, and σ 2(=1/P2) is the image spatial frequency [3,4].

Figures 2a and 2b show the normalized OTF calculated under the Z1 = Z2 condition at $\theta = \lambda/4$ and $\lambda/2$. The horizontal axis shows the parameter Z(=Z1, =Z2), which is normalized by T (=P^2/λ). The parameter N describes the condition of the imaging, and is defined by the following equation.

$$\left(1 + \frac{Z_2}{Z_1}\right)\sigma_2 p = N$$

When N has an integer, the optical pattern with certain spatial frequency in the object grating is imaged on the image plane. The allowable spatial frequency is determined by the OTF as shown in Fig. 2. When Z1 is equal to Z2, the allowable spatial frequency of the object and the image are the same because the magnification of this optical system is determined by the ratio of Z1 and Z2. Consequently, the imaging conditions of N = 1 and N = 2 are obtained by the following configuration. For N = 1, the pitch of the pupil grating is set to the half of that of the object grating. For N = 2, the pitch of the pupil grating is equal to that of the object grating.

When θ is $\lambda/4$, the maximum absolute value, i.e. 0.637, of the OTF is obtained under the following conditions, N = 1 and Z is equal to the product of an odd number and T. The image inverts against the object in the location where the value of the OTF is under zero.

When θ is $\lambda/2$, the maximum absolute value, i.e. 0.637, of the OTF is obtained under the following conditions, N = 2 and Z is equal to the product of an odd number and T/4. The image contrast is two times higher than when an amplitude grating is the pupil [3,4]. In Fig. 2b, the value of the OTF is always zero when N is equal to an odd number.

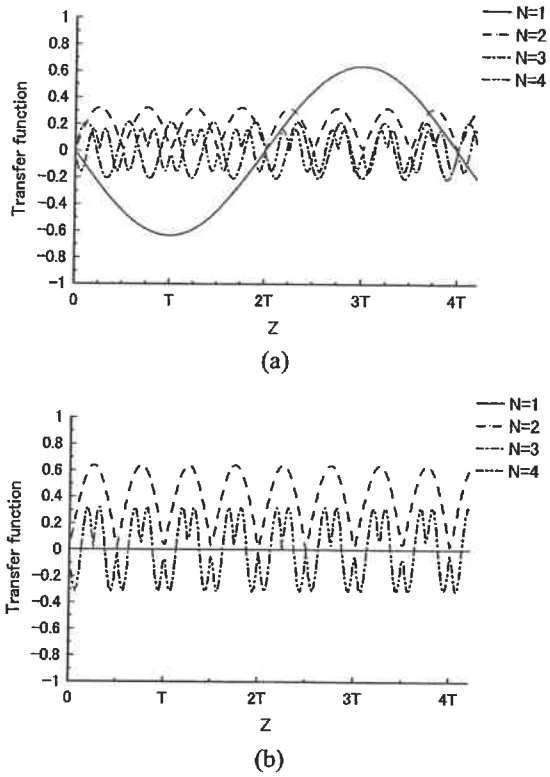

Fig. 2 Optical transfer function calculated as a function of the distance Z with allowable N, (a) $\theta = \lambda/4$ and (b) $\theta = \lambda/2$.

Experiment

Figure 3 shows the experimental setup of this optical system using the phase grating as the pupil. An infrared LED with a wavelength of 880 nm was used as the incoherent light source. The phase grating was made from a glass, and the refractive index was 1.451. The phase-shift was controlled by the depth of the concavo-convex shape. We used two phase gratings, one was 488 nm ($\lambda/4$) in depth, the other was 976 nm ($\lambda/2$) in depth. In both gratings, the duty ratios were set to 50 percent. The pitch of the phase grating when N = 1 and N = 2 were set to P = 65 μ m and P = 68 μ m, respectively. The distance Z1 between the object grating and the pupil grating was always equal to the distance Z2 between the pupil grating and the image grating.

When N = 1, the pitch of the object grating and the image grating, determined by the imaging condition, were set to 130 μ m; this was twice as much as the pitch of the pupil grating. When N = 2, the pitch of the object grating and the image grating were set to 68 μ m which was equal to the pitch of the pupil grating. The grating pattern of the object

grating and the image grating were made by evaporating chrome with a 50 percent duty ratio. A photodiode (PD) was placed close behind the image grating.

First, we observed the intensity distribution on the image plane without the image grating and the PD. The contrast of the intensity distribution was measured as a function of Z. Second, the output of the PD was measured when the pupil grating moved along the X-axis under high contrast imaging conditions.

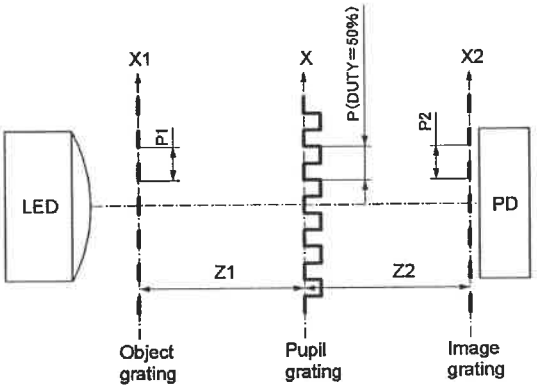

Fig. 3 Experimental setup of the optical system.

Results and discussion

Figures 4a and 4b show the experimental results of the contrast of the intensity distribution at N = 1 and N = 2. The horizontal axis shows the parameter Z normalized by T. The value of T at N = 1 and N = 2 are 4.8 mm and 5.25 mm, respectively. The solid circles and open squares show the experimental results at $\theta = \lambda/4$ and $\theta = \lambda/2$, respectively. The solid line and the broken line show the calculated results. For both N = 1 and N = 2, reasonably good agreement between the experimental results and the calculated results is apparent. When N = 1 and $\theta = \lambda/4$, the absolute value of the contrast was about 60 percent at Z = T. When N = 2 and $\theta = \lambda/2$, about 60 percent contrast was also obtained at Z = T/4, 3T/4, 5T/4 and 7T/4. Under the N = 2 condition, the contrast is two times higher than that when using an amplitude grating as the pupil.

As seen in Fig. 4a, the experimental results of $\theta = \lambda/4$ are somewhat lower than the calculated result. This is caused by the harmonics included in the object grating. Compared with the calculated results of N = 1 and N = 3 in Fig. 2a, both cases have a negative value where the experimental results are lower than the calculated results in Fig. 4a. Furthermore, the calculated results of N = 3 have a peak at same location. Since the third harmonic frequency (N = 3) and the fundamental frequency (N = 1) were imaged with same phase, the shape of the image resembled a rectangle wave.

To study the amplitude of the fundamental frequency directly, FFT analysis was performed on the experimental results of $\theta = \lambda/4$. Figure 5 shows the normalized amplitude of the fundamental frequency as a function of Z. The experimental results plotted as open circles come close to the calculated result. Although the experimental results from T/2 to T are slightly higher than the calculated results, this might be caused by the radiation characteristics of the LED.

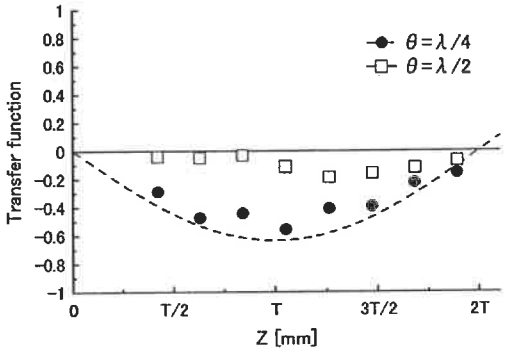

(a)

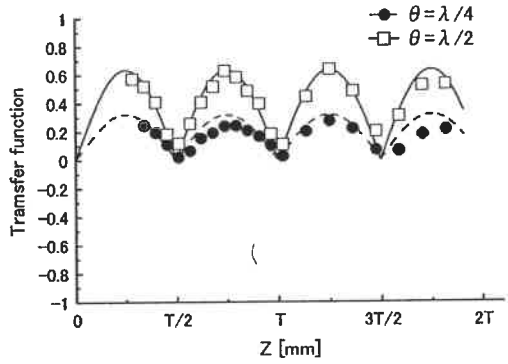

(b)

Fig. 4 Experimental results of the OTF as a function of Z. Normalized distance T is equal to p^2/ λ . (a) N = 1 and T = 4.8mm, (b) N = 2 and T = 5.25mm.

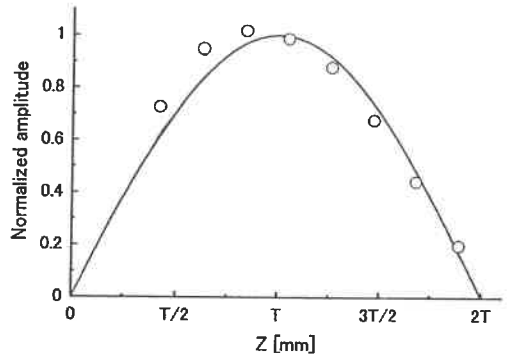

Fig. 5 The normalized amplitude of the fundamental frequency as a function of Z at N = 1 and $\theta = \lambda/4$. The open circles correspond to the experimental results and the solid line shows the calculated results.

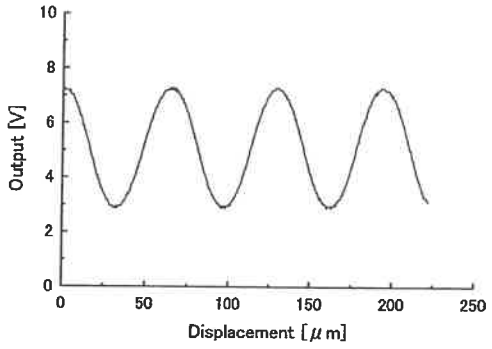

(a)

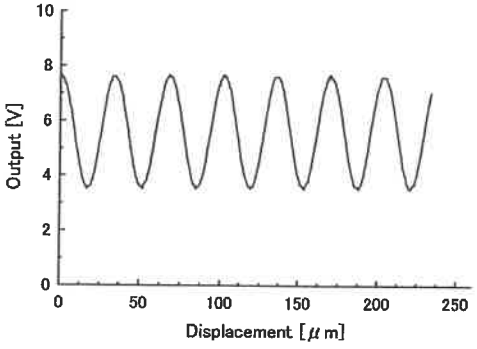

(b)

Fig. 6 Output of the PD as a function of the pupil grating displacement ; (a) N = 1, $\theta = \lambda/4$, P = 65 μ m and Z = T (= 4.8 mm) ; (b) N = 2, $\theta = \lambda/2$, P = 68 μ m and Z = 3T/4 (= 3.94 mm).

The output signal of the PD was measured as a function of the pupil grating displacement along the X-axis. Figures 6a and 6b show the displacement signal at N = 1 and N = 2. The displacement measurement of N = 1 was done under the following conditions; the distance Z was T (4.8 mm); the depth of the phase grating was set to 488 nm ($\lambda/4$). The displacement measurement of N = 2 was done under the following conditions; the Z was 3T/4 (= 3.94 mm); the depth was 976 nm ($\lambda/2$). As shown in Fig. 6b, a displacement signal having a period equal to 34 μ m, which was the half of the phase grating pitch, was measured as a function of the movement of the phase grating for N = 2. On the other hand, the pitch of displacement signal is equal to that of the phase grating for N = 1. Hence, the N = 2 condition is better than the N = 1 condition with respect to the refinement of resolution.

For both N = 1 and N = 2, AC/DC ratio of about 40 percent was obtained. This value was two times higher than that with an amplitude grating as the pupil under the N = 2 condition. The AC/DC ratio was defined by dividing the average value into the amplitude. The received light powers of both cases were also two times higher than that with an amplitude grating because the phase grating was transparent. Finally, under the N = 2 condition, the amplitude of the displacement signal was four times higher than that of an amplitude grating.

Conclusion

The OTF analysis of the grating imaging when using a phase grating as a pupil was discussed. The image contrast of about 60 percent was obtained, and the received light power was twice as much as that when using an amplitude grating. The amplitude of the displacement signal was totally four times higher than that of the conventional imaging system with an amplitude grating.

References

1. R. M. Pettigrew, "Analysis of Grating Imaging and Its Application to Displacement Metrology," Proc. Soc. Photo-Opt. Instrum. Eng. 136, 325 (1977)

2. G. J. Swanson and E. N. Leith, "Analysis of the Lau effect and generalized grating imaging" J. Opt. Soc. Am. A 2, 789 (1985)

3. K. Hane and C. P. Grover, "Imaging with rectangular transmission gratings," J. Opt. Soc. Am. A 4, pp.706-711 (1987)

4. K. Hane and C. P. Grover, "Magnified grating images used in displacement sensing," Appl. Opt. 26, pp.2355-2359 (1987)

Nonlinearity in a fiber-optic coupled heterodyne interferometer

Liang Zhang
Department of Physics, University of Florida, Gainesville, FL

Abstract

A high-accuracy (nonlinearity < 2nm) fiber-optic coupled displacement heterodyne measuring Michelson interferometer is developed. The primary limitation of accuracy encountered with this fiber-optic coupled heterodyne interferometer is the optical mixing arising from the imperfection of fiber-optic coupling system. The optical mixing results in the nonlinearity (first order and second order errors) in the displacement measurement of the interferometer. A theoretical model using Jones calculus is developed; the corresponding experiments are implemented. The theoretical results are consistent with the experimental results.

Keywords: Fiber-optic coupled interferometer; Distance measuring interferometer; Polarization-maintaining fiber; Nonlinearity;

1. Introduction

A lightweight and electrically passive interferometer is demanded by a number of applications for precision metrology such as machine tool metrology and on-machine feedback [1]. To satisfy these requirements, a fiber-optic coupled heterodyne displacement measuring Michelson interferometer [2] shown in Fig.1 is developed. In this interferometer, the laser light is coupled into the interferometer with a polarization-maintaining (PM) fiber to separate the application environment of the interferometer from the laser head.

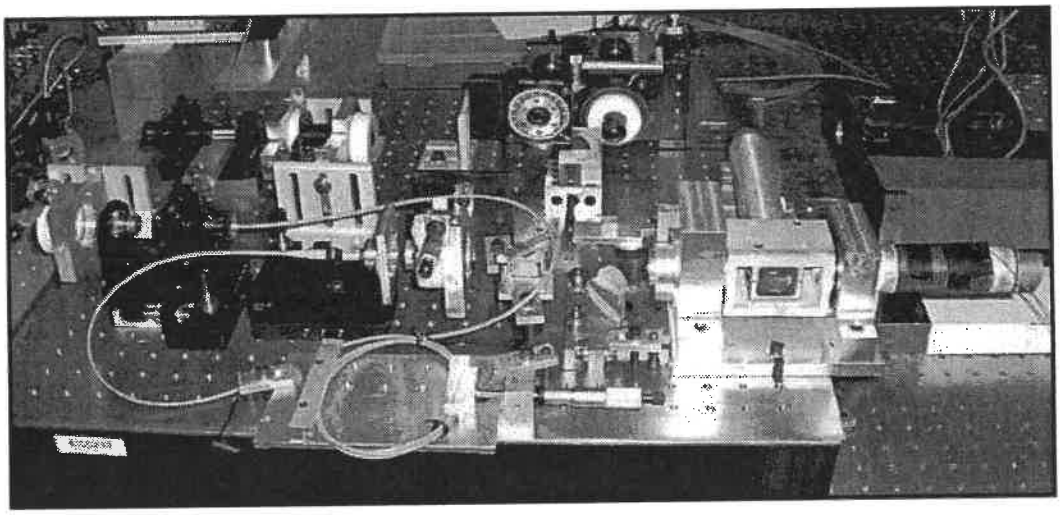

Figure 1 Fiber-Optic Coupled Displacement measuring Interferometer

2. Theory

Jones calculus [3] is used to build the theoretical model of the fiber-optic coupled interferometer. An optical fiber has a number of birefringent properties simultaneously. As the

matrices do not commute, the Jones matrix representing birefringences of the fiber is not the simple product of individual birefringence matrices. To solve this problem, the differential matrices (*N* matrices) [4] can be used for the optical fibers. Typically, the PM fiber is subjected to bending, twisting, or combination of these two external behaviors. The bending produces a linear birefringence in the fiber, and the twisting induces a rotary birefringence. These birefringent properties reduce the polarization-maintaining ability of the fiber.

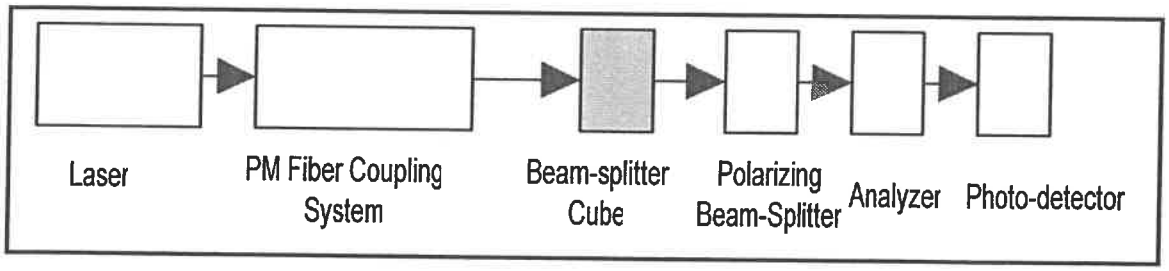

Figure 2 Block Diagram of Fiber-Optic Coupled Interferometer

The configuration of interferometer system is shown in Fig.2. The laser light transmits through the fiber-optic coupling system, a non-polarizing beam-splitter, a polarizing beam-splitter, and an analyzer in turn. The primary source of the optical mixing is fiber-optic coupling system. The fiber-optic coupling system can be represented by the following matrix [5]

$$M_{fiber-optic} = \begin{bmatrix} p & q \\ -\bar{q} & \bar{p} \end{bmatrix} \tag{1}$$

where p, q are in general complex.

The Jones matrix M_{system} of the fiber-optic coupled interferometer can be calculated from the following equation

$$M_{system} = M_{analyzer} M_{BS} M_{mirror} \left[\left(M_{PBS\parallel} M_{flip} M_{\phi_1} M_{PBS\parallel} + M_{PBS\perp} M_{flip} M_{\phi_2} M_{PBS\perp} \right) M_{fiber-optic} \right] \tag{2}$$

where $M_{analyzer}$ is the matrix of the analyzer, and M_{BS} is the matrix of non-polarizing beam-splitter, and M_{mirror} is the matrix of the turning mirror, and $M_{PBS\parallel}$ is the matrix of the polarizing beam-splitter for transmitted beam, and $M_{PBS\perp}$ is the matrix of the polarizing beam-splitter for reflected beam, and M_{flip} is transformation between the coordinate systems of the incident beam and the reflected beam, and M_{ϕ_1} is the matrix of the phase change of the light in the measurement arm, and M_{ϕ_2} is the matrix of the phase change of the light in the reference arm. According to equation (2), the first order error Γ_1 and the second order error Γ_2 can be expressed as follows

$$\Gamma_1 = \frac{K_1}{K_0} = \left({\alpha_{12}}^2 + \overline{{\alpha_{21}}^2} \right) - \frac{r}{\bar{r}} z^2 \left(\overline{{\alpha_{12}}^2} + {\alpha_{21}}^2 \right) - \frac{z}{\bar{r}} \cdot c \tan(2\theta) \left(1 + |r|^2 \right) - \frac{z}{\bar{r}} \frac{1 - |r|^2}{r \sin(2\theta)} \tag{3}$$

$$\Gamma_2 = \frac{K_2}{K_0} = {\alpha_{12}}^2 \overline{{\alpha_{21}}^2} - \frac{r}{\bar{r}} z + \frac{z}{r \sin(2\theta)} \left[\left({\alpha_{12}}^2 - \overline{{\alpha_{21}}^2} |r|^2 \right) - \cos(2\theta) \left({\alpha_{12}}^2 + \overline{{\alpha_{21}}^2} |r|^2 \right) \right]^2 \tag{4}$$

where the optical mixing term $z = \bar{q} / p$. ${\alpha_{12}}^2$, ${\alpha_{21}}^2$ are the leakage of the polarizing beam-splitter, and θ is the analyzer angle, and r is the transmission ratio of the non-polarizing beam-

splitter. The equation (3) and (4) clearly show the nonlinearity is a function of the optical mixing z, the polarizing beam-splitter's leakage and the analyzer angle θ. The optical mixing z primarily arises from the misalignment of the half-wave plates, the bending of the PM fiber in the fiber-optic coupling system.

3. Theoretical Results and Experimental Results

The theoretical results of nonlinearity vs. fiber bending change using equation (3) and (4) are show in Fig.3. The bending change refers to the length change of the minor axis of the fiber coil. Both the first harmonic error and the second harmonic error oscillate with the bending change. The experimental results shown in Fig.4 are consistent with theoretical results.

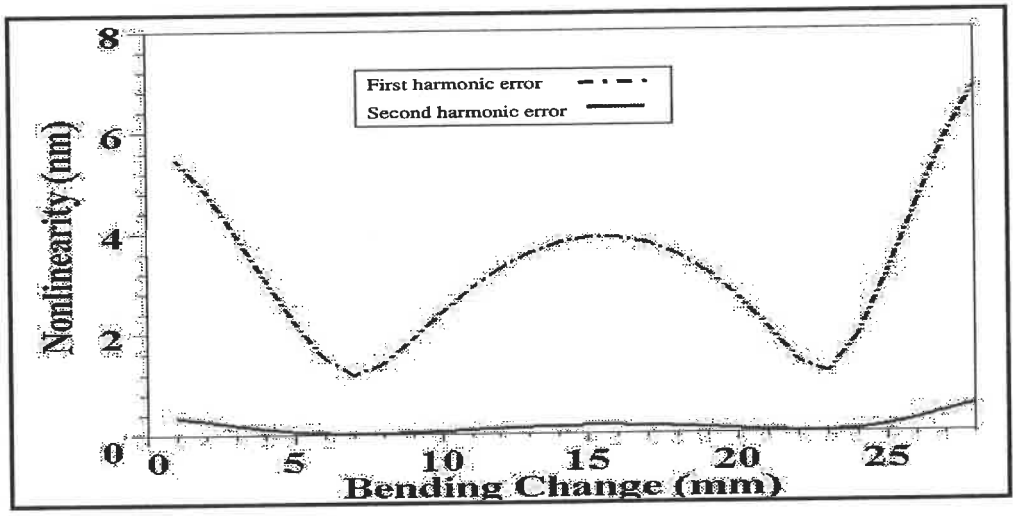

Figure 3 Theoretical Result of Nonlinearity vs. Fiber Bending Change

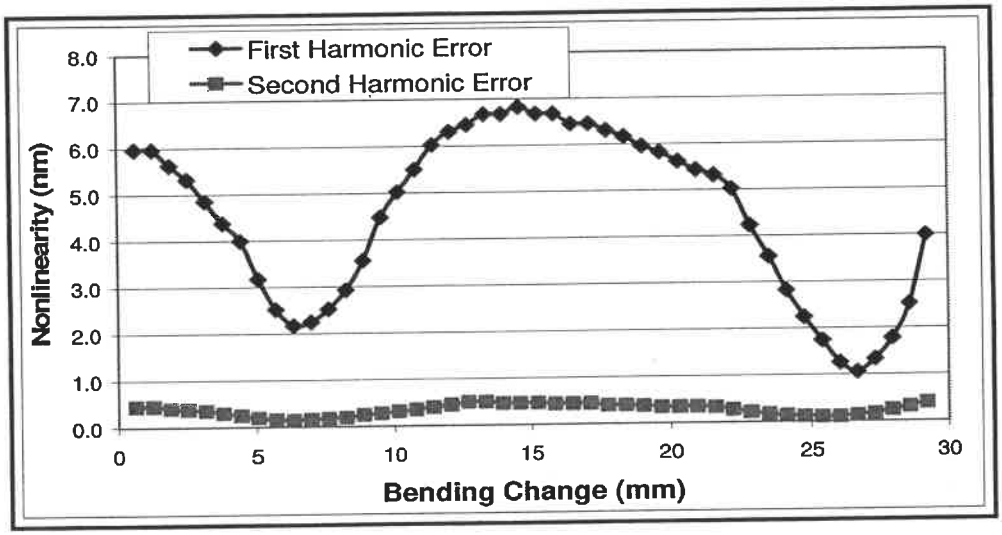

Figure 4 Experimental Results of Nonlinearity vs. Bending Change

Acknowledgements

The work repeated in this paper was done when the author was a PhD student in Center of Precision Metrology (CPM) at the University of North Carolina at Charlotte (UNCC). I would like to express my deepest gratitude to my PhD advisor, Dr. Steve Patterson, for his instruction and encouragement. The work was supported by the industrial affiliates of the CPM of UNCC.

References

1. H. Kunzmann, "Scales vs. Laser Interferometers Performance and comparison of Two Measuring Systems", *Annals of the CIRP*, Vol.42/2/1993, pp. 753-767.
2. Liang Zhang, Fiber-optic coupled heterodyne interferometer, PhD dissertation in University of North Carolina at Charlotte, 2003.
3. R. Clark Jones, "A new calculus for the treatment of optical systems I. Description and discussion of calculus", J. Opt. Soc. Am., Vol.31, July 1941, pp.488-493.
4. R. Clark Jones, "A new calculus for the treatment of optical systems. VII. Properties of the N-matrices", J. Opt. Soc. Am., Vol.38, No.8, Aug 1948, pp.671-685.
5. Vivek Gopal Badami, "Investigation and compensation of periodic nonlinearities in heterodyne interferometry.", PhD dissertation in UNCC, 1999.

High-Precision Angle Measuring Technology and High-Precision Angle Sensor

T. Kojima [a,*], Y. Kikuchi [a], S. Seki [a], H. Wakiwaka [b]

[a] Technical Management, Tamagawa Seiki, Co., Ltd, Ohyasumi 1879, Iida City, Nagano Prefecture, 395-8515 Japan
[b] Faculty of Engineering, Shinshu University, Wakasato 4-17-1, Nagano City, Nagano Prefecture, 380-8553 Japan

High-resolution and high-precision angle sensors are expected for nanotechnology control system. The technology for manufacturing high-precision disks, and the measurement evaluation technology through the angle calibration system, and the development of a high-resolution optical angle sensor with high-precision and a self-accuracy calibrating function was achieved. This was accomplished using fundamental technology such as the high-precision disk that forms the core part of the angle sensor, and a high-precision measuring instrument and the self-calibrating technology of an angle sensor. A high-precision angle calibration system and a high-precision angle sensor with a resolution of 0.001 seconds were achieved.

Keywords: 2-dimensional length measurement; High-precision disk; Angle calibration apparatus; Self-accuracy calibration; High-precision angle sensor

1. Introduction

The measurement resolution of 0.001 seconds is essential for angle sensors used in nanotechnology control systems. The component engineering for realizing the measurement of 0.001 seconds consists of six types of technology: (1) High-precision technology with disk accuracy of 0.3 seconds accuracy disk [1], (2) the CAE (Computer Added Engineering) analysis technology for the mechanism section and high-precision coupling technology, (3) the signal dividing technology developed using R/D (Resolver / Digital Conversion) technology, (4) accuracy compensation technology through the efficient use of ROM, (5) the self-accuracy calibration technology of the angle sensor by itself, and (6) the high-resolution angle calibration system technology for 0.001 seconds and self-accuracy calibrating reproducibility for 0.005 seconds. These engineered components achieved a high-resolution of 30 bits and a high accuracy angle sensor. Furthermore, a new technology that generates multi-rotation signal, speed, and angular-acceleration data within the sensor was developed and high speed bi-directional serial bus communication with a control system was achieved. An angle of 1 ms is equivalent to a resolution of one billion and a 10^9 nano-resolution. This angle is equivalent to that of the observation of the height of a person located on the moon. This high-resolution of 1 ms is equal to the length of 0.5 nm on a circle of 100 mm. A ball screw with a 10 mm pitch is equivalent to the resolution length of 0.01 nm. Thus the nanotechnology control system becomes achievable.

In order to pursue the construction of an ideal angle sensor, high-precision compositions were developed along with an evaluation measuring instrument, accuracy compensation technology, signal dividing technology for high-resolution, and less wire high-speed signal communication technology.

This paper describes high-precision angle measurement technology focusing on the high-precision (1) angle evaluation measurement system, (2) self-accuracy calibrating angle sensor, and (3) 2-dimensional length measurement technology for disks. The high-precision technology for the nanotechnology control system and the advanced features were obtained by this study.

2. Technical outline of angle measurement

2.1. Application and features and principle of angle sensors

There are two types of angle sensors, one is an optical encoder and others are electromagnetic-induction type resolver. A high-precision angle sensor has been expected for nanotechnology systems for several years. Nanotechnology systems can be applied in several areas such as the semiconductor field and scientific-optical apparatus, space observation, etc. In field applications, higher precision is expected. An encoder is an angle sensor in which high-precision can be realized. A 30-bit encoder out line is shown in Fig. 1.

2.2. Types and accuracy of angle calibration system

When developing a high-precision angle sensor, precise evaluation of accuracy is of great importance. Generally, an accuracy of 100 times is required for the resolution and that of 10 times is essential for the measured angle sensor. In order to measure the angle sensor with an accuracy of 0.1 seconds, it is necessary for the measuring device to have an accuracy of 0.01 seconds and a resolution of 0.001 seconds.

Although there are several measuring instruments such as the autocollimator, the circular dividing table, etc., the angle sensor with an accuracy of 0.1 seconds could not be evaluated because of lengthy measuring time, limited measurement points, and the error of the criteria angle sensor being included in the measurement. Further, an angle measuring device that can evaluate the angle sensor with an accuracy of 0.01 seconds has been developed by this study.

It became possible to develop a high-precision disk, high-precision coupling, and high-precision angle sensor using this measuring instrument.

Fig. 1. 30-bit encoder.

3. High-precision angle calibration system

3.1. Principle of time conversion method and equal-dividing and averaging method

This is an angle measuring technology method. The theory is a time-conversion method, which operates on the principle of high-precision angle measurement. The measured angle sensor is rotated at uniform velocity, and a clock is positioned between the pulses of the criteria angle sensor and the measured angle sensor, and rotated at fixed speed. High-precision measurement can be achieved by rotation at a speed with low variability, and at high clock frequency.

This time-conversion method can measure the angle sensor with a resolution of 0.001 seconds. However, the error of the criteria sensor will be included and the accuracy of an angle sensor and measured instrument could not be separated from the measurement result.

It is possible to carry out the separation of the accuracy of a measured angle sensor and measuring instrument by using the principle of the equal-dividing and averaging method [2]. The system can remove the error of the criteria sensor. This system arranges a criteria angle sensor and a measured angle sensor on the same axis. The relative angular position of the criteria encoder and the measured sensor change the position by about five division points of one turn. It is measured each time and the result is averaged. It can, thus, ensure the complete separation of the accuracy of the two angle sensors. The high-precision angle calibration system [3] is shown in Fig. 2 (a) and the specification is shown in Table 1.

3.2. Uniform low rotation speed motor and fixed brake

When this equal-dividing and averaging method is employed, the variability in the rotation of the speed of the main shaft motor appears in the accuracy; therefore, it is necessary that the variability in rotation should be minimal.

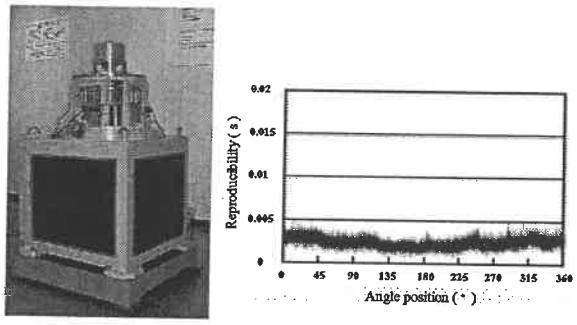

(a) Calibration system (b) Reproducibility error

• • Fig. 2. High-precision angle calibration system.

Table 1 • • Angle calibration system specification

Item	Specification
Resolution	0.001 s
Accuracy	0.01 s
Measurement uncertainty	(0.06 s (k = 2))
Rotation speed	0.01 ~ 60 min^{-1}
Starting torque	0.3 N m Max (sample)
Weight	50 Kg Max (sample)

In this study, a motor with a low variability in rotation was developed using the CAE analysis technology. The actual rotation variability data are 0.1 ratios. Moreover, it is necessary to alter the relative position of the two angle sensors arbitrarily in the equal-dividing averaging method, and once the position is decided, the precise fixation with an accuracy of 0.001 seconds was necessary. High-precision has been achieved by using an air disk brake in this study.

3.3. Measurement reproducibility and trace-ability

The method of evaluating the performance of an angle calibration apparatus consists of two parts, one is the definition of the self-accuracy function, and the other is the trace-ability to the accuracy of the angle standard. Reproducibility is shown in Fig. 2 (b). The specifications (shown in Table 1) of resolution, accuracy, reproducibility, stability, and a self-calibrating function, etc., are used to measure the performance of a measuring instrument. Moreover, the numbers that indicate these performances are required, and they should be traceable in an angle standard system. Now, a Japanese angle standard has been enacted and trace-ability is being developed. Further worldwide deployment of the angle standards is expected in the future.

4. Angle sensor with self-accuracy calibrating function

It was required to measure the accuracy of an angle sensor with high-precision, and to evaluate it when guaranteeing data. Further improvements in high-precision were realized by ROM accuracy compensation using the data. To calibrate an angle sensor in an environment where the angle calibration system cannot be used or where it cannot be removed from the equipment, it is expected to calibrate by it-self. This will be achieved by building an internal self-accuracy calibrating function [4] in the angle sensor in this study.

4.1. Basic principle of self-accuracy calibrating

The basic principle of the self-accuracy calibrating method is stated below. Two or more signal detection heads are arranged inside an angle sensor, the position data and the error component is derived from their operation, and the error of an angle sensor is automatically detected. A circuit block diagram is shown in Fig. 3. Furthermore, the secondary error separation extraction principle is shown in equation (1).

4.2. Example of error separation

Figure 4 shows the principle followed when extracting the secondary error components from the heads at 0 and 90

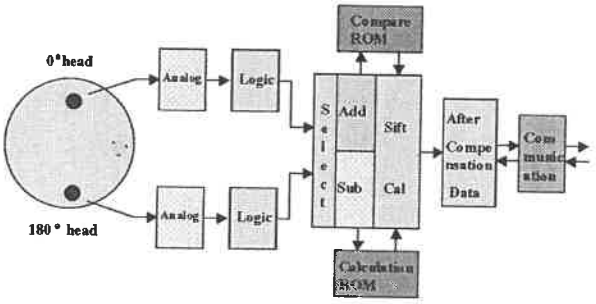

• • Fig. 3. Self-calibrating angle sensor block chart.

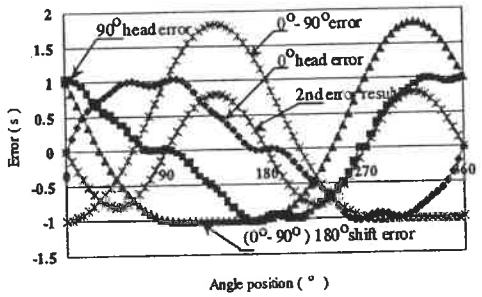

Fig. 4. Theory of secondary error separation method.

degrees. Shift 180° means to shift the error curve at 180°.

$$2^{nd}\text{error} = [(0°\text{error}-90°\text{error})-(\text{sift}180°(0°\text{error}-90°\text{error}))]/4 \quad (1)$$

The secondary error can be separated from the most of the error components using the two head signal. It is necessary to decrease the difference in each head error.

5. High-resolution and high-precision angle sensor

(1) The high-precision manufacturing technology with an accuracy of 0.3 seconds accuracy disk, (2) CAE analysis technology and high-precision coupling technology, and (3) signal dividing R/D technology were applied, (4) angle measurement technology and accuracy compensation technology was possible by efficient use of ROM. This section describes the fundamentals of high-precision angle sensor technology.

5.1. High-precision disk

In an optical encoder, the disk is an important part influencing its accuracy. The slit width of a high-precision disk is about 10 μm. But it is necessary for a high-precision disk an accuracy of less than 0.5 μm and 1 second. In order to achieve accuracy that is equivalent to that of 10 times of a conventionally disk, the measurement of the disk accuracy was evaluated by the length and angle. Therefore, the high-precision disk was achieved by eliminating the reproducibility error of the drawing equipment.

A. Error evaluation by 2-dimensional length measurement of disk

In order to evaluate the error of a disk, it is necessary to measure the disk in term of angle and length precisely. Although the accuracy of a disk is finally estimated by the angle, the length of 0.1 μm can be converted into an angle error of approximately 0.2 seconds, and it can be evaluated. In an area of 150 mm square, the length was measured with an accuracy of 0.1 μm. The recently devised high-precision 2-dimensional length measurement technology [5] can separate the error of a measuring instrument and the error of a measured disk. This principle is explained in Table 2. Similar to equation (2), the angle error $\Delta\theta$, is expressed in x-y rectangular coordinates.

$$\Delta\theta = \theta - \tan^{-1}[(G\times x)/(K\times y)] \quad (2)$$

G and K are the absolute error ratios as opposed that by the length along the x-axis and the direction of the y-axis.

Table 2 Equations of theoretical length : (La - Ld)

La = DeaA − Oea − MeA	Ld = DedA − Oed − MeA
Lb = DebB − Oeb − MeB	La = DeaB − Oea − MeB
Lc = DecC − Oec − MeC	Lb = DebC − Oeb − MeC
Ld = DedD − Oed − MeD	Lc = DecD − Oec − MeD
Lc = DecA − Oec − MeA	Lb = DebA − Oeb − MeA
Ld = DedB − Oed − MeB	Lc = DecB − Oec − MeB
La = DeaC − Oea − MeC	Ld = DedC − Oed − MeC
Lb = DebD − Oeb − MeD	La = DeaD − Oea − MeD

In addition, the scale ratio error of each axial direction and the error of the perpendicular to each axis are equivalent to the error of the measuring instrument. The measurement error of the measuring instrument of approximately 1 μm will be included. The measured encoder disk is rotated to the four directions of 0 degree, 90 degrees, 180 degrees, and 270 degrees, and measurement is carried out each time. The error of a measured encoder disk is separated from each measured value. The theoretical values of La-Ld which were solved using 16 equations are shown in Table 2, since DeaA, DebB, DecC, and DedD (error for which DeaA measured a sides of measured object using the measuring instrument A section) become constant, and it sorts eight variables Oea, Oeb, Oec, Oed, MeA (Oea is the error of a side of the measured object), and MeB, MeC, and MeD (error on measuring MeA using the A section of a measuring instrument)).

$$\Delta\theta = G_1\times\sin^{-1}(\theta) + G_2\times\sin^{-1}(2\theta+\delta_2) + G_3\times\sin^{-1}(3\theta+\delta_3) + \cdots \quad (3)$$

$$\theta = \theta + \Delta\theta \quad (4)$$

For G_1 - G_3, the error gain and θ are an angle measurement position. The error of an angle is $\Delta\theta$ and the error of a relative angle is δ_i; thus, equations (3), and (4) can be generated. The errors of the measuring instrument and the encoder disk were separated using this measurement principle. The error of the measurement tool is 1 μm and the error of the disk is 0.4 μm.

B. Disk accuracy measurement and accuracy compensation by angle

The accuracy of the disk is measured by angle using calibration system shown in session 3. These data are used as values for accuracy correction and the compensation disk is manufactured using a CAD-CAM system again. The accuracy is verified before and after the manufacture of the compensation disk, if the effect of compensation achieves the target value, the manufacture of the disk is considered completed. Figure 5 (b) shows the disk slit image figure that achieves the angle compensation (correction value δ 1, δ 2, and δ 3) of the slit arrangement angular position.

The correction value has a minimum of 0.001 seconds (0.3 nm length); high-precision compensation was attained and the manufacture of a high-precision disk was achieved. The two error results agree with the error of the length and the error from angle measurement. Both measurement results are considered appropriate. Using the error value

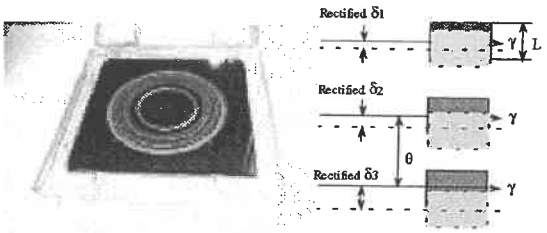

(a) High-precision disk (b) Compensation

Fig. 5. High-precision disk and compensation.

acquired from this result for the correction value, the drawing angular position of each slit was rectified, and a high-precision disk with accuracy exceeding that of the drawing equipment was achieved.

The high-precision disk after compensation is shown in Fig. 5 (a). A high-precision disk with an accuracy of 0.3 seconds can be achieved.

5.2. CAE technology for high-precision mechanical system

High precision is required in the mechanical parts of a disk and etc. The high-precision was optimized by using CAE technology focusing on coupling, as shown in Fig. 6

5.3. Signal dividing technology for high-resolution

The 16-bit signal dividing technology was achieved using a closed signal dividing method. Therefore, a high-resolution of 30 bits was achieved. Figure 7 (a) shows the minimum resolution bit of 30 bits pulse signal, and it implies an accuracy of 0.001 seconds.

5.4. ROM accuracy compensation principle for high-precision angle sensor

In the fundamental-wave accuracy of an angle sensor, an optical encoder is mostly determined by the disk pattern accuracy. However the component error is not zero and the assembling error increases, moreover, high-resolution divided signals also have dividing signal errors corresponding with the accuracy error of the sin and cos signal waves. The error is a reproducible error, and the high-precision error measurement system is achieved by the high-precision angle calibration system. So ROM compensation is achieved. ROM accuracy compensation is a method of storing the error value in ROM and removing the reproducible error by subtraction. This is shown in Fig. 7 (b). Wide accuracy 0.2 seconds was achieved using this principle.

5.5. Multi-function technology of angle sensor

A. Angular-velocity and angular-acceleration data

The resolution of angle sensor became high and it became possible to use the high-resolution position information data, which is operated to detect speed and acceleration signal data.

B. Bus communication

The sensor signal line numbers of the multi-axis robot are very large. Therefore less wire was expected. Despite using bi-directional serial communication, the 6-axis control system would require 12 wires; therefore, a bus communication system that can transmit all signals via two lines was developed.

(a) Outline of coupling (b) CAE analysis

Fig. 6. High-precision coupling and CAE analysis.

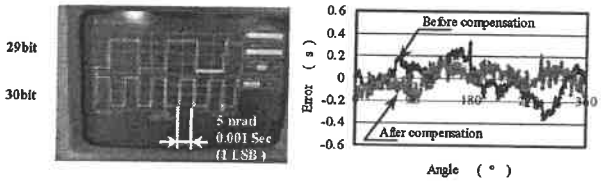

(a) Pulse signal of 30 bits (b) Wide accuracy

Fig. 7. Pulse signal of 30 bits and wide accuracy.

6. Conclusions

For technical realization of a high-precision angle measurement technical realization, development of a high-precision angle calibration system and a high-precision angle sensor was developed. (1) A high-precision angle calibration system (reproducibility 0.005 seconds, resolution 0.001 seconds) was developed using the angle calibration method. The accuracy of a disk was measured by angle using the angle calibration system. Then the error that was measured by 2-dimensional length measurement technology was equal to the error measured by angle. (2) The high-precision disk (accuracy of 0.3 seconds) was developed. The high-precision angle sensor was realized using this high-precision disk component. The accuracy of angle calibration system and the self-calibrating angle sensor, (3) The self-accuracy calibrating function automatically extracted the angle-accuracy error component. Using the detected error, the ROM accuracy compensation circuit technology resulted in the realization of further high-precision (0.2 seconds). An angle sensor with high-resolution was also studied and 30 bits (0.001 seconds) resolution were achieved. Thus, high-precision angle measurement technology was achieved in terms of both the technology of the angle sensor and the angle measurement instrument at 0.001 seconds high-resolution.

References

[1] T. Kojima, Y. Kikuchi, S. Seki, H. Wakiwaka, "Study on Angle Error Measurement and Accuracy Compensation Principle for Ultra-precise Disk Patterns", *JSPE autumn conference*, J25, pp. 438, 2003.

[2] T. Masuda, M. Kajitani, "High Accuracy Calibration System for Angular Encoders", *Journal of Robotics and Mechatronics*, 5-5, pp. 448-452, 1993.

[3] T. Kojima, Y. Kikuchi, S. Seki, T. Masuda, H. Wakiwaka, "Development of High-precise Angle Calibrating Apparatus and High-precise Angle Sensor", *The 1st ICPT2004 conference Japan*, pp. 417-422, 2004.

[4] T. Kojima, Y. Kikuchi, S. Seki, T. Masuda, H. Wakiwaka, "Study on angle calibration technology and high-precise angle sensor by self-accuracy calibration", *JSPE spring conference*, D22, pp. 356-357, 2004.

[5] T. Kojima, Y. Kikuchi, S. Seki, H. Wakiwaka, "Study on Length Error Measurement Principle for Ultra-precise Disk Patterns", *IEEJ Industrial application conference*, 2-1, pp. II 355-356, 2003.

LASER DRESSING OF METAL-BONDED DIAMOND WHEEL

Akira HOSOKAWA, Tsutomu YUNOKI, Keiji YAMADA and Takashi UEDA
Department of Mechanical Systems Engineering, Kanazawa University
2-40-20 Kodatsuno, Kanazawa 920-8667, Japan

1. Introduction

Superabrasive grinding wheels containing diamond or CBN grits are widely used in grinding hard brittle materials and hardened ferrous metals, respectively because of their high hardness, wear resistance and long tool life. Periodic truing and dressing is required in order to maintain the appropriate wheel sharp and topography for efficient grinding. It is, however, difficult to profile these superabrasive wheels precisely due to the above characteristics. Generally metal-bonded diamond truer or vitrified GC wheel are used as the truing tools and WA stick as dresser. But the truing/dressing methods mentioned above are time-consuming and cause pollution of working environment. In addition, mechanical damage of abrasive grains occurs by a direct contact between wheel and truer/dresser.

In this study, laser beam is used as a noncontact thermal dressing tool of superabrasive wheels. In previous works, vitrified bonded or resinoid-bonded wheel are mainly dealt with in dressing [1, 2], and a few experiments are done about the truing of the metal-bonded diamond wheels [3, 4]. In the present study, Nd-YAG laser is applied to dressing a metal-bonded diamond wheel and the principle of metal removal, thermal damage of wheel surface and the optimum operating parameters are investigated.

2. Principle of Laser Dressing

Figure 1 shows the schematic illustration of the basic principle of laser dressing. The bond material is removed by vaporizing and/or melting by heat input from laser irradiation. Resolidification also occurs by the rapid cooling so that air jet is supplied to the laser spot in order to blow off the molten metal. These fusion products may be easily removed by a short time initial grinding. The bond material should be removed so as to make appropriate protrusion height of abrasive grits being anchored firmly in the bond. Thermal damages of abrasive grains such as graphitization, chipping and microcracks are to be avoided. Because of noncontact process, the wheel is not deformed by dressing force.

3. Dressing of Metal-Bonded Diamond Block

3.1 Experimental setup and procedure

In the first step, a bronze block and a bronze-bond diamond block (SD120N75M) are chosen as dressing targets so as to measure 3-D profile of the dressed surface. The pulsed Nd-YAG laser operating at a wavelength of 1.064 μm with pulse duration of 2.5 ms is irradiated being focused onto the target. The specimen is mounted on the x-y stage and it is fed at a constant feed. Two types of experiments are carried out in which intermittent single-shot craters are formed and overlapped multi-shot craters are created as shown in **Fig.2**. The air jet is supplied if necessary. The dressing condition are summarized in **Table 1**.

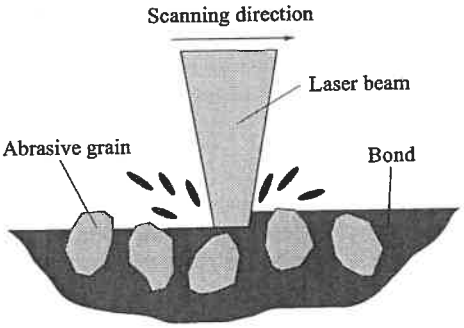

Fig.1 Principle of laser dressing

3.2 Experimental results of intermittent single-shot dressing

Figure 3 shows the close-up photograph of the cross-section of the laser irradiated bronze block without air blow. It is clear from Fig.3 that the bond material is molten by laser

heat and is resolidified including voids in it. The morphology of the crater with air blow is presented in **Fig.4**. The fused material is blown away and partially solidified around the crater edge. Both depth and diameter of the crater vary with laser peak power. The minimum dressing depth approximately 30 μm, which is appropriate amount for a #120-mesh grinding wheel, is obtained when the laser power is 104 W. The depth and diameter of the crater formed by a single-shot pulse decrease with laser power decreases. The shallower crater than a critical depth, however, cannot be formed by reducing the laser power because of the instantaneous resolidification of the material. Defocusing is also effective in controlling the dressing volume, especially minimize the dressing depth and expand the dressing region per pulse.

3.3 Experimental results of overlapped multi-shot dressing and evaluation of thermal damage

The 3-D profile of the dressed grinding block is shown in **Fig.5**, where the dressing depth is approximately 30 μm. From the figure, air spray is effective for blowing away the molten binder before it solidifies again, although it cannot be perfectly taken away due to its relatively high viscosity. An air spray has also the effect on the prevention of thermal damage and deterioration of both bond and abrasive grains. Clear damages of diamond particles such as micro-cracks or graphitization are not observed below the laser power is less than 152 W.

In order to evaluate the thermal damage of bonding material, the dressed grinding block is ground with vitrified alumina wheel (A60K7V) as shown in **Fig.6**. The testing conditions are listed in **Table 2**. **Figure 7** shows the surface morphologies before and after grinding tests. As is obvious from the figure that when the dressing peak powewr P is 104 W, almost all abrasive grits remain on the bond after grinding. In the case of P=152 W, however, some abrasive grains are dislodged by grinding force because the influence of laser heat reaches deeply in the bond. But in both cases, diamond grains are not molten or graphitized. Accordingly when the laser power is appropriate, the grains, which are left on the grinding wheel surface, are not affected in laser irradiating.

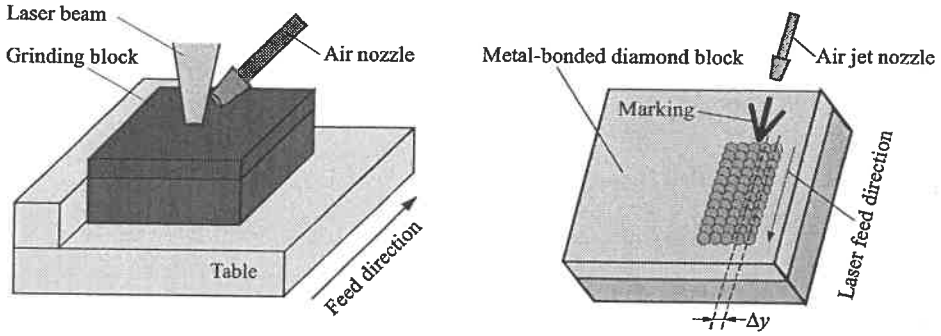

Fig.2 Procedure of laser dressing of metal-bonded grinding block

Table 1 Experimental conditions of laser dressing

Grinding block		SD120N75B (30×30×15)	
Laser			
Wavelength	λ, μm	1.064	
Peak power	P, W	104	152
Pulse duration	τ, ms	2.5	
Pulse cycle	f, Hz	10	
Beam diameter	$2a$, mm	1.26	
Operating parameters			
Table speed	v, mm9s	2	2.8
Transverse interval	Δy, mm	0.2	0.28
Air pressure	p_a, MPa	0.3	

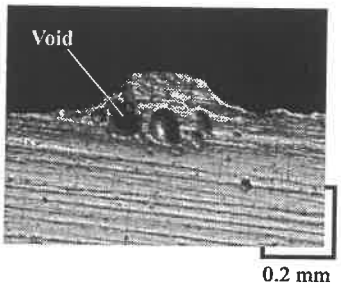

Fig.3 Thermal expansion of bond material by laser irradiation without air blow

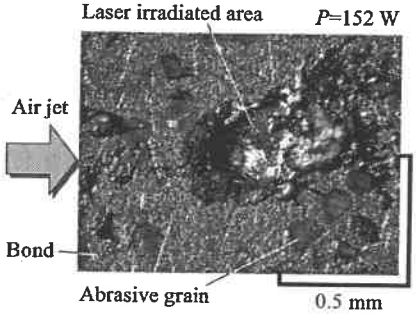

Fig.4 Crater on the grinding block by laser irradiation with air blow

4. Dressing of Segmented Bronze Wheel

4.1 Experimental procedure

Four removable bronze segments are mounted around a wheel periphery as targets because they can be easily measured with a microscope and a profilometer. The laser beam is aligned in the normal direction and focused on the wheel surface as shown in **Fig.8**. The linear stage is fed in the axial direction and this motion is coordinated with the wheel rotation, laser pulse frequency and pulse duration so as to cover the overall wheel surface by laser beam. In the present work, a crater by individual laser beam is investigated. The experimental conditions are shown in **Table 3**.

4.2 Experimental results and discussion

The groove formed by laser irradiation are shown in **Fig.9**, in which 2-D profile trace are also shown. As is obvious from the figure, resolidified bond remains in the groove even in high wheel speed without air blow. This resoridified layer cannot remove by scratching with a brass brush. The air jet is effective in blowing away the molten material as shown in Fig.9(b). The depth, length and width of the grooves are related to laser irradiation parameters. **Table 4** summarizes the dressing depth of grooves as a function of wheel revolution and laser peak power. It is noticed that the dressing can be done with high wheel speed so that the efficient dressing is expectable.

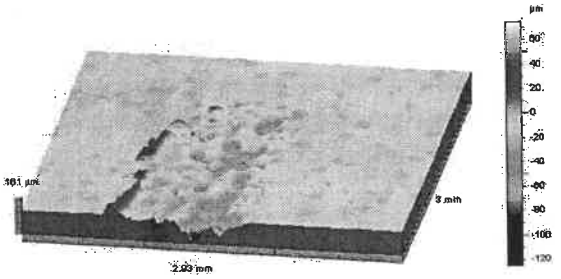

Fig.5 3-D profile of dressed metal-bonded diamond block

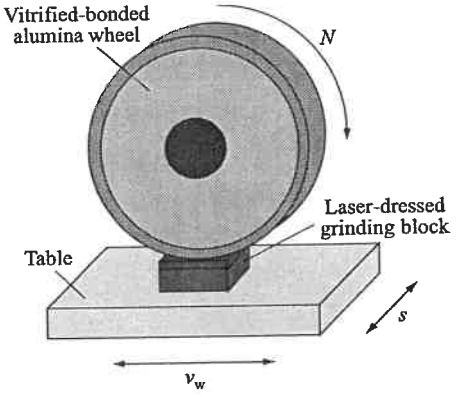

Fig.6 Evaluation of thermal damages of abrasive grains

Table 2 Grinding conditions of dressed diamond block

Grinding wheel		A60K7V
Wheel revolution	N, rpm	1800
Table speed	v_w, m9min	2
Depth of cut	a, μm	10

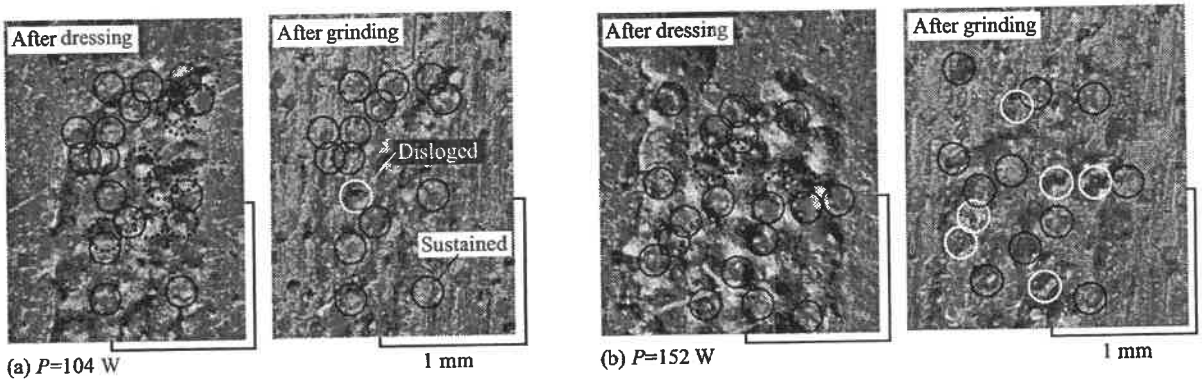

Fig.7 Change of laser-dressed grinding block surface with grinding with a vitrified-bonded alumina wheel

5. Summary

The laser dressing of a bronze bond diamond stone is investigated as a first step. Pulsed Nd:YAG laser is irradiated perpendicular to the stone surface. The bond material is partially removed by laser irradiation, in which melting and vaporizing take place. In order to efficiently remove the bond material, it is necessary to spray air on the laser irradiating spot so as to blow away the molten binder before it solidifies again. Clear damages of diamond particles such as micro-cracks or graphitization are not observed below the laser power is less than 152 W. When the laser power is less than 104 W, most diamond grains are held firmly in the bond.

Acknowledgment

The authors would like to thank Noritake Super Abrasive Co., Ltd. for providing us with the diamond wheels and blocks.

References

[1] Babu, N. R., Radhakrishnan, V. and Murti, Y. V. G. S., Investigation on Laser Dressing of Grinding Wheels Part I: Preliminary Study , J. Eng. Ind., T rans.ASME, Vol. 111, 1989, pp.244252.

[2] Nakajima, T., Ohashi, K., Sun, L. X. and Jitsumori, K., Dressing of Resinoid Bond Wheel with Moving Heat Source (1st Report) T ransformation of Wheel Surface with a Single Pulse Irradiation of YAG Laser, J. Japan Soc. Prec. Eng., (in Japanese), V ol. 59, No. 12, 1993, 19671972.

[3] Hoffmeister, H. W. and Timmer, J. H., Laser Conditioning of Superabrasive Grinding Wheels , Industrial Diamond Review. Vol. 60, No. 7, 2000, pp.209218.

[4] Kang, R. K., Yuan, J. T., Zhang, Y. P. and Ren, J. X., T ruing of Diamond Wheels by Laser, Key Engineering Materials, Vols. 202203, 2001, pp.137142.

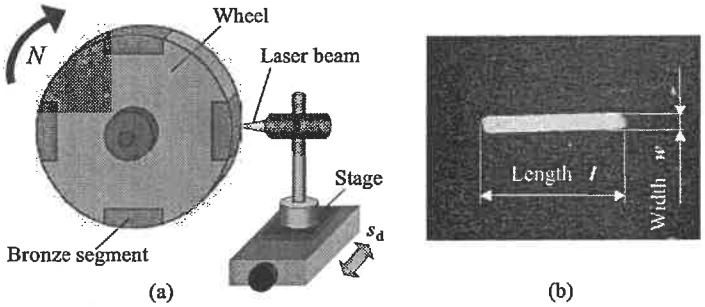

Fig.8 Experimental setup for segment wheel and heat affected region of wheek sureface by single-pulse laser

Table 3 Dressing conditions of segmented bronze wheel

Wheel revolution	N, rpm	0–1064	458
Laser perk power	P, W	1233–2403	1863
Beam diameter	$2a$, mm	1.26	
Pulse duration	τ, ms	2.5	
Air pressure	p_a, MPa	0	0.3

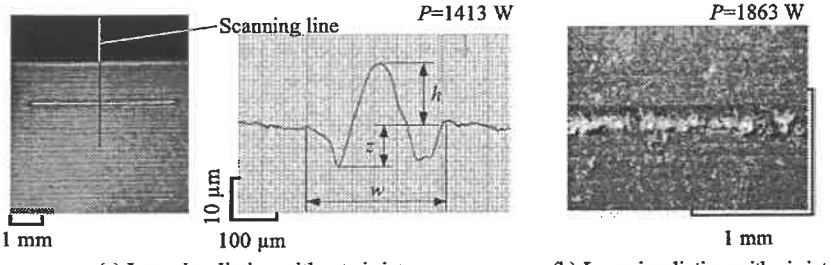

Fig.9 Photographs and profile trace of segmented bronze surface after laser irradiation with/without air jet

Table 4 Depth of groove by laser irradiation

Laser peak power P W	Crater depth z, μm	Wheel revolution N rpm 257	458	646	1063
	1233	5.2	×	×	×
	1323	9.8	4.0	×	×
	1413	12.4	4.8	×	×
	1503	15.2	6.2	2.1	×
	1593			3.1	×
	1683			5.8	×
	1773			6.2	×
	1863			6.2	×
	2313				4.0
	2403				5.0

Research on Feed Velocity Control Model of Axisymmetric Aspheric Machining

Hao Huang, Yin-biao Guo, Yi Zhang and Lin Zheng

(Dept. of Mechanical and Electrical Engineering, Xiamen Univ., Xiamen 361005, China)

0. Introduction

The factors about the occurred error are various in ultra-precision diamond grinding wheel machining. It is necessary to adopt modeling technique to analyze influence factors, in order to obtain higher accuracy based on existing equipments. Besides the effect of the form accuracy, the dimensional accuracy of the grinding wheel and the machine error to the process accuracy, the grinding linear velocity of the grinding wheel and its feed velocity are vital factors of affecting the process accuracy. Due to the characteristics of axisymmetric aspheric machining, the grinding linear velocities on different machining points of the grinding wheel, and the time for which the grinding wheel stays on different areas of the aspheric workpiece would change on the machining process. The grinding removal quantity on various machining points would be different, and the process accuracy would be worsened.

According to traditional compensation methods, when feed accuracy is 0.1 μm, machining accuracy is convergent in 3~5 μm. When 0.01 μm, machining accuracy limit is 1.5 μm[1][2]. In this paper, a new feed velocity control model is presented for higher accuracy, which can make the grinding removal quantity of different points on the process of axisymmetric aspheric grinding uniform by controlling the feed velocity of the grinding wheel.

1. Machining error analysis

1.1. *Axisymmetric aspheric surface*

The movement locus of grinding wheel machining point is generatrix locus of workpiece, and workpiece rotates around pivot axis. The generatrix formula of axisymmetric aspheric surface has different expressions. The common equation can be carried out:

$$z=-\frac{CX^2}{1+\sqrt{1-(1+K)C^2X^2}}-\sum_{i=1}^{n}\left(a_iX^i\right) \qquad (1)$$

Where $C=\frac{1}{R}$

R-- basic curvature radius of aspheric surface

a_i -- aspheric surface coefficients

In addition, the generatrix formula of axisymmetric aspheric surface also can be expressed as

$$x^2=a_1|z|+a_2z^2+a_3|z^3|+a_4z^4+a_5|z^5|+\ldots \qquad (2)$$

Where $a_1=2R$, R—basic curvature radius of aspheric surface

1.2. *Axisymmetric aspheric surface*

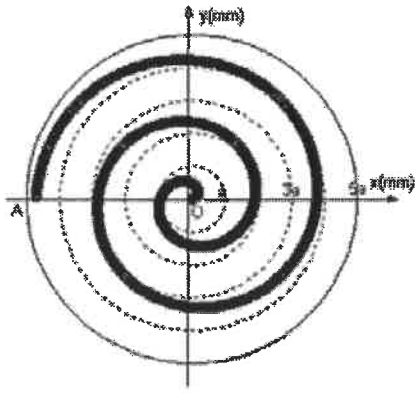

Fig.1. Vertical view of machining locus

See Fig.1. Workpiece anticlockwise rotates around pivot axis z, and meanwhile feed grinding from point A to origin O. When the feed velocity of axis x is

changeless, we name it uniform feed velocity machining. At the moment workpiece rotate angular speed and wheel feed speed are changeless, so when the workpiece rotate one round and the grinding wheel's feed distance keep invariable, and machining locus of workpiece surface is a helical line.

Because the removal quantity of the workpiece has a direct proportion to the stayed of the grinding wheel to a certain point and the grinding linear velocity of the point, a grinding principle can be attained: The grinding depth δ of a certain area has a direct proportion to the machining linear velocity GV, and has a inverse proportion to the machining square area S and the machining time t.

$$\delta = K \times \frac{GV \times t}{S} \tag{3}$$

1.3. *Error analysis of uniform feed velocity machining*

In Axisymmetric aspheric machining, if adopt the uniform feed velocity machining method, the grinding area of center part will be much smaller than the outer part at the same machining time length. According to the grinding principle, we can conclude that the grinding depth of center part is greater than other part, thereby influence the machining precision. And this theory is fit to the error form of actual machining. As figure 2 shows, using uniform feed velocity machining, regardless what accuracy is, there is a concave part at the center part of the machining error.

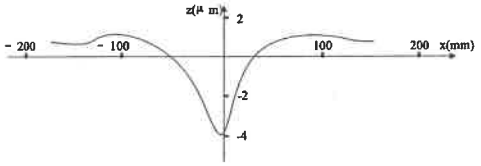

Fig.2. Error of uniform feed speed machining

2. Feed Speed Control Model

In high precision grinding machining, the rotation velocity of spindle has great influence on the tool temperature, and the control precision of spindle's rotation velocity is too bad. If we change the rotation velocity in machining, it is prone to can result in new error of machining, so the rotation velocity of wheel and workpiece must be set as invariableness. The paper presents a control method: setting the rotational velocity of the grinding wheel and the workpiece spindle as constants, the feed velocity of the grinding wheel is controlled to reach the goal of reducing the process error and improving the process accuracy.

According to formula (3), we can conclude that if we want to improve the machining precision, we must take the machining linear velocity, machining square area and machining time into account.

2.1. *Calculation Model of Machining Linear Velocity*

The machining linear speed of machining area is composed by linear speed of workpiece and grinding wheel.

In high precision grinding machining, the rotation speed of workpiece is uniform. And the linear speed orientation of workpiece and grinding wheel is vertical to the radius. So the linear speed orientation relation of workpiece's machining point and wheel's machining point only have two choice: same orientation or opposite orientation. If they are same orientation, the machining linear speed is their subtract. And if they are opposite orientation, the machining linear speed is their sum.

So when the wheel grinding in the area of generatrix between interpolation point x_{i-1} and x_i, the linear velocity of workpiece is:

$$GV_i = \omega_1 \cdot \left(\frac{|x_i| + |x_{i-1}|}{2} \right) \tag{4}$$

Where ω_1—rotation velocity of workpiece

And that adopt different wheel, the linear velocity of wheel machining point is different too. For plane wheel, the linear velocity of every machining point is uniform. For arc wheel, the linear velocity of outer part's machining point is slower than the center part's. And for spherical wheel, the linear velocity of center is zero, and the linear velocity of machining point near the center is too slower to machining. To reach the goal of improve machining precision, setting the rotational velocity as constant, and assuming it is ω_2.

The linear velocity of wheel machining point can be

obtained according to the characteristic of wheel.

Assuming the radius of plane wheel is r, the linear velocity of plane wheel's machining point can be attained. It is $\varpi_2 \cdot r$.

Assuming the radius of arc wheel's arc part is r, the radius of center part is rr. And the coordinates of a certain point of aspheric surface is $(x_i, f(x_i))$, and the normal angle θ of this point is $arctg(f'(x_i))$. Assuming the wheel inclination angle is α, and the linear velocity in the area of between the interpolation point x_{i-1} and x_i can obtained as

$$GV_i = \varpi_2 \cdot \left(rr + r \cdot \frac{Sin(arctg(f'(x_i)) - \alpha) - Sin(arctg(f'(x_{i-1})) - \alpha)}{arctg(f'(x_i)) - arctg(f'(x_{i-1}))} \right) \quad (5)$$

Assuming the radius of spherical wheel is r. Adopt equal angle rotational machining, setting the upper and lower limit of wheel's inclination angle, then the linear velocity in the area of between the interpolation point x_{i-1} and x_i can obtained as

$$GV_i = \varpi_2 \cdot r \cdot \frac{Sin(arctg(f'(x_i)) - \alpha) - Sin(arctg(f'(x_{i-1})) - \alpha)}{arctg(f'(x_i)) - arctg(f'(x_{i-1}))} \quad (6)$$

2.2. *Calculation Model of actual grinding area*

Assuming the wheel's feed velocity of axis x is v, and feed pace is dx. So the distance that wheel feed when workpiece rotate one round is $v \cdot \frac{2\pi}{\varpi_1}$. And the radian that workpiece rotate when wheel feed dx is $\varpi_1 \cdot \frac{dx}{v}$.

Use the area division pace l, the axisymmetric aspheric surface be separated into n area. And l must be the multiple of wheel feed pace dx. Assuming the sub area from center to outer is from A_1 to A_n. And the center part A_1 is a round area, its area is πl^2, and other area is cirque. Assuming the actual grinding area of A_i $(1 \leqslant i \leqslant n)$ is S_i.

Assuming the whole area can be machining in wheel's first feed. When wheel grinding in the area A_i, its actual grinding area is:

$$S_i = (2i-1)\pi l^2, 1 \leq i \leq n \quad (7)$$

2.3. *Calculation Feed Velocity Control Model*

According to the analysis of machining error, we can conclude: when the grinding linear velocity is constant, use different feed velocity in different machining point, control the machining time in a certain area and the area's actual grinding area. Then the grinding quantity difference would be reduced and the machining precision would be improved.

Assuming the axisymmetric aspheric workpiece axis x division value is l. To making the grinding depth of different machining areas equal, the product of the machining linear velocity GV, the machining square area S, and the machining time t should be constant. So we can derived:

$$\frac{GV_i \times T_i}{S_i} = \frac{GV_{i+1} \times T_{i+1}}{S_{i+1}} \quad (8)$$

For a certain workpiece, when the machining method and division value was determined, the machining linear velocity GV_i in the area A_i can be determined.

And the delay time in area A_i can be obtained as

$$T_i = \frac{l}{v_i} \quad (9)$$

Where l—axis x division value

v_i—wheel feed velocity

Then the following two equations can be obtained

$$V_i = \frac{GV_i \times S_1 \times V_1}{GV_1 \times S_i} \quad (10)$$

$$V_i = \frac{GV_i \times S_{i-1} \times V_{i-1}}{GV_{i-1} \times S_i} \quad (11)$$

3. Result Analysis

The feed velocity of tools must be in a certain range for the machining tools' feed limit. So in the feed velocity control, the upper and lower limit must be given first. And then the division number of workpiece m can be obtained. According to the formula (10) the feed velocity of every division area can be obtained.

According to the arithmetic mentioned above, the control program of feed velocity can be obtained. The program block diagram show as follow:

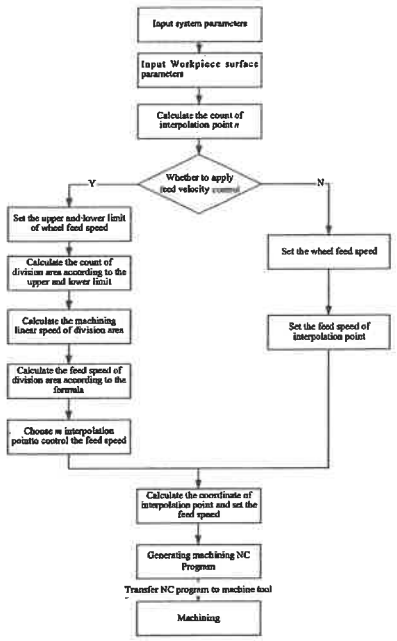
Input system parameters
Input Workpiece surface parameters
Calculate the count of interpolation point n
Whether to apply feed velocity control
Y
N
Set the upper and lower limit of wheel feed speed
Calculate the count of division area according to the upper and lower limit
Calculate the machining linear speed of division area
Calculate the feed speed of division area according to the formula
Choose m interpolation points control the feed speed
Set the wheel feed speed
Set the feed speed of interpolation point
Calculate the coordinate of interpolation point and set the feed speed
Generating machining NC Program
Transfer NC program to machine tool
Machining

Fig.3. Program block diagram

Adopt various grinding wheel in machining, the machining system parameters as table 1 shows. The generatrix formula of axisymmetric aspheric surface can be expressed as formula (2) shows, and its parameters as table 2 shows. Set the upper limit of feed velocity as 1200mm/min and lower limit as 400mm/min, and orientation of grinding wheel's machining linear speed and workpiece's machining point linear speed is same.

Table.1 Machining system parameters

System parameters	Plane wheel	Arc wheel	Spherical wheel
Arc part radius r/mm	/	60	125
Middle part radius rr/mm	125	65	/
Aspheric radius R/mm	2268.839	2268.839	2268.839
Machining pace dx/mm	1.0	1.0	1.0
Machining length xx/mm	225.0	225.0	225.0
Length of spindle L/mm	120.0	120.0	120.0
Effective width B_0/mm	18.0	/	/
Machining start point x/mm	-225.0	-225.0	-225.0
Wheel width B/mm	20.0	20.0	20.0
Machining point distance B_1/mm	10	/	/
spindle angle γ°	/	30	30

Table.2 Workpiece surface parameters

a_1	a_2	a_3	a_4	a_5
4537.6775	-0.1252	2.9830e-4	-2.3408e-5	9.8747e-7

Machining the workpiece by the parameters mentioned above, set 3mm as speed control pace, and then the feed velocity control result can be obtained as figure 4 shows.

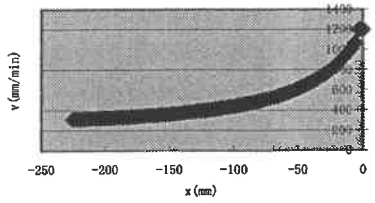

Fig.4. Feed velocity Control result

4. Conclusions

Through analyzing the affecting conditions of the grinding linear velocity and the feed velocity of the grinding wheel to the process accuracy, the machining velocity control model is presented, which can make the grinding removal quantity of different points on the process of axisymmetric aspheric grinding uniform by controlling the feed velocity of the grinding wheel. The technology avoid the defect of the differential machining removal quantity existed in the traditional grinding methods, and improve the process accuracy of the system theoretically. The research results show that:

(1). The control method is aimed at the plane grinding wheel, arc grinding wheel and spherical grinding wheel commonly used in the aspheric grinding, and achieve good control effect all.

(2). Adopting the feed velocity control method, the feed velocity would speed up while the machining is from the fringe to the center, and the change ratio would gradually increase accordingly.

1. Y. B. Guo, J. Y. Hu and X. G. Zheng, CJME, 15(4), 344(2002).
2. M. Saeki, T. Kuriyagawa, J. S. Lee, ASPE Annual, 25,433(2001)

Sizing Method Based on Grinding Ratio in Heavy Grinding

Masumi IZUMI, Akio OCHI
Hiroshima Institute of Technology, Hiroshima, Japan

1. Introduction

In this study, sizing method due to the grinding ratio in heavy grinding is discussed. When using a conventional grinding wheel to grind hardened steels, residual stock removal due to the grinding wheel wear occurs. Therefore it is difficult to finish workpieces within a given tolerance in short time. One of the best solutions to achieve an efficient grinding process is to use super-abrasive grinding wheels. However, there is a pecuniary matter to use a costly grinding wheel in rough grinding. Accordingly, sizing method to grind a workpiece more efficient has been requested.

Grinding ratio is widely known as the volume ratio of a material removed to a wheel wear. Therefore grinding wheel wear is generated by the product of grinding ratio and volume of material removed. Assuming that the grinding ratio is a constant, it can easily calculate the radial wheel wear caused by removing the grinding allowance of workpiece. To cut a grinding wheel in a workpiece according to the estimated value of the grinding wheel wear, it can finish the workpiece efficiently and in a short time. This paper deals with a new sizing method based on the grinding ratio.

2. Nomenclature

Symbols are used in this study as follows.

W : Grinding wheel wear (μm)
b : Wheel width (mm)
B : Width of workpiece (mm)
L : Length of workpiece (mm)
A_G : Area of grinding wheel surface (mm^2)
A_W : Area of workpiece surface (mm^2)
G : Grinding ratio
H : Desired grinding allowance (mm)
γ : Common ratio to produce grinding wheel wear
Z : Total setting depth of cut to remove a desired grinding allowance (mm)

3. Sizing method

Figure 1 shows a grinding wheel, a workpiece and symbols. Grinding ratio is given as equation 1 from the figure.

$$G = \frac{BL(H - W)}{\pi DbW} \qquad (1)$$

Grinding wheel wear W is derived from Equation:

$$W = \frac{BL}{\pi DbG + BL} H \qquad (2)$$

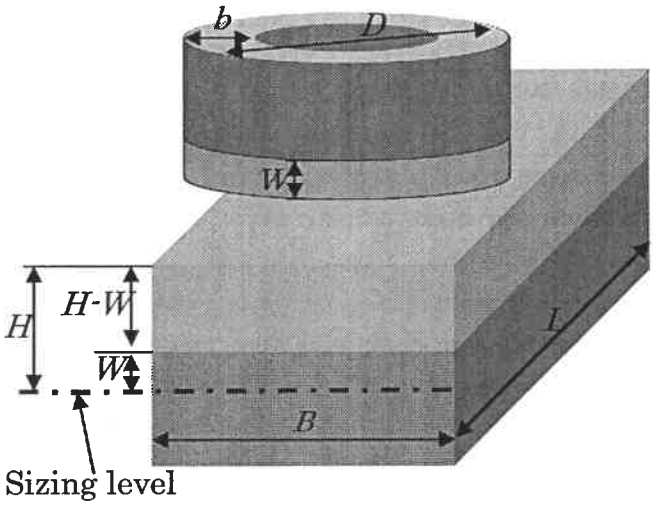

Fig.1 Schematic diagram of a workpiece and a grinding wheel

Where, common ratio γ is defined as equation (3) and assuming that the common ratio is a constant.

$$\gamma = \frac{BL}{\pi DbG + BL} \qquad (3\text{-}1)$$

$$= \frac{A_W}{A_G G + A_W} \qquad (3\text{-}2)$$

Table1 Wheel wear to be generate as the geometric series

Process	Common ratio	Setting depth of cut	Wheel wear
1	γ	H	$W_1=\gamma H$
2	γ	W_1	$W_2=\gamma^2 H$
3	γ	W_2	$W_3=\gamma^3 H$
:	:	:	:
N	γ	W_{n-1}	$W_n=\gamma^n H$
		Sum of the above $\frac{H^2}{H-W_1}$	Sum of the above $\frac{HW_1}{H-W_1}$

Grinding wheel wear W to be produced to remove a desired height H is shown equation:

$$W = \gamma H \qquad (4)$$

Where, Grinding wheel wear at the first grinding is indicated W_1 as equation (5).

$$W_1 = \gamma H \qquad (5)$$

At the second grinding operation, W_1 will be the next residual stock removal instead of the H. W_2 is generated to remove W_1. W_2 is presented by the product of common ratio γ and wheel wear W_1 as shown equation (6).

$$W_2 = \gamma^2 H \qquad (6)$$

According to these grinding processes, grinding wheel wear W_n at the n th process is shown as equation (7), and then it is able to estimate wheel wear.

$$W_n = \gamma^n H \qquad (7)$$

To finish a workpiece within a given tolerance, a residual stock removal due to the grinding wheel wear generated in every grinding processes should be removed. Therefore total setting depth of cut to finish a workpiece the tolerance Z is given as a sum of the grinding allowance H and grinding wheel wear W_i at the every process.

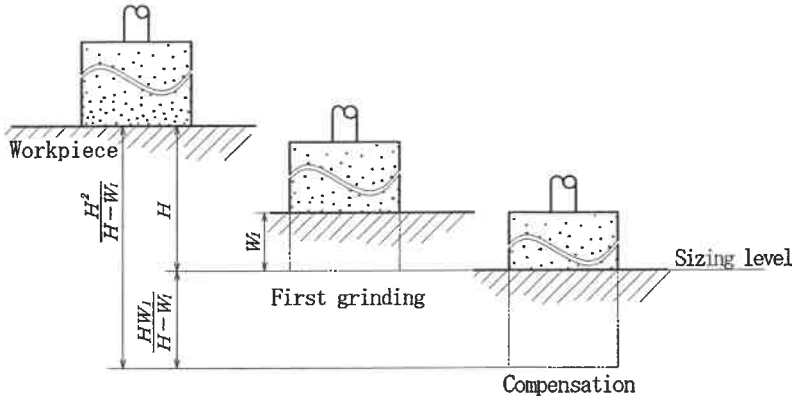

Fig. 2 The illustrated sizing method

$$Z = H + \gamma H + \gamma^2 H + \gamma^3 H + \cdots + \gamma^{n-1} H \qquad (8)$$

In the equation (8), numerical expressions after the second member show the sum of geometric series expression. And this equation is solved to the equation (9).

$$Z = H + \frac{\gamma}{1-\gamma} H \qquad (9\text{-}1)$$

$$= H + \frac{HW_1}{H - W_1} \qquad (9\text{-}2)$$

$$= \frac{H^2}{H - W_1} \qquad (9\text{-}3)$$

Table 2 Measuring conditions

Machine tool	Vertical spindle surface grinding machine with a rotary table
Grinding wheel	WA32I7V(segment grinding wheel)
Area of grinding surface	12375mm^2(49.5× 25, 10pieces)
Workpiece	Hardened dice steel SKD11 (HRC60)
Area of workpiece surface	14700mm^2, (B=147,L=100)
Wheel depth of cut	2μm /rev
Wheel speed	1300m/min
Table speed	17min^{-1}

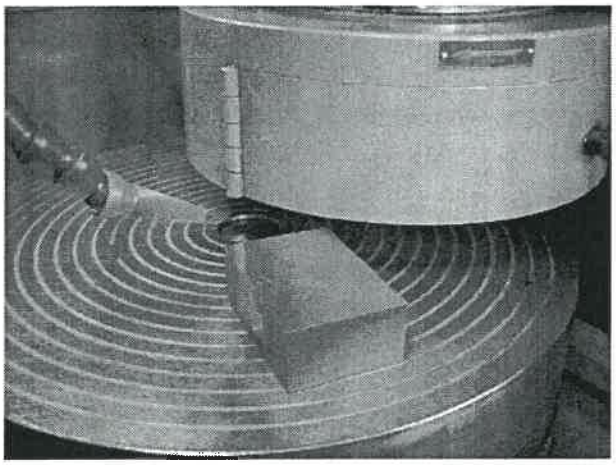

Fig.3 Grinding machine and workpiece

And these derived equations are summarized as the table 1. This table shows grinding wheel wear to be generated to grind a desired grinding allowance according to the grinding processes. In the first grinding, setting depth of cut equivalent to a derided removal height is given. Grinding wheel wear W_1 is expressed by a product of common ratio γ and a derided removal height H. In the second grinding, residual stock removal at the first grinding will be a setting depth of cut. And grinding wheel wear W_2 is presented by a product of W_1 and γ. The sum of geometric series expressing the grinding wheel wears and the setting depth of cut are shown in the table 1.

The sums of these geometric series at the infinity in the table are calculated with setting depth of cut H and grinding wheel wear W_1 at the first grinding. If the grinding ratio G is a constant, these sums will not be exerted by the kind of a grinding wheel and a workpiece. The sum of the setting depth of cut at the each grinding process is the traveling value of the wheel spindle stock to be needed to remove a desired allowance.

Figure 1 shows the preset method. At the first process grinding wheel wear W_1 will be generated to cut the grinding allowance with the setting depth of cut. W_1 will be a residual stock removal at the next operation. Setting depth of cut to grind the residual stock removal at the one compensation is obtained by the grinding wheel wear W_1 and the allowance H.

4. Change of grinding ratio

In this sizing method it is needed that grinding ratio G is a constant. Namely it can be seen that the grinding ratio doesn't change at the first operation and the compensation. Therefore the change of the grinding ratio in a grinding cycle was confirmed experimentally.

Table 2 shows the measuring conditions. Figure 3 shows the photograph of the experimental setup.

Figure 4 shows measured results of changes of grinding ratio. Plots indicated by the line segment shows the same grinding cycle. The plot indicated by the mark @ in this figure will be explained first. These two plots show grinding ratio at the removal volume 2645mm^3 and 2968mm^3. In this experiment, grinding ratio changed 6.5 to 10. Like this measurement, grinding ratios were measured within the removal volume 5500 mm^3, and then they were plotted in figure 4. From this figure, it is obviously that the grinding ratio changes widely.

Figure 5 shows frequency distribution of changes of a grinding ratio ΔG. Observed changes of grinding ratios range were -8 to 8, and changes from 0 to 4 showed the highest frequency. From this picture, grinding ratios seem to vary widely.

5. Effect of the sizing method

In order to confirm the effect of change of grinding ratio against the sizing method, grinding operation using the sizing method and that one not using the method are compared. Figure 6 shows a decrease workpiece height according the grinding process. The present sizing method was not used in this experiment. From this result, three grinding processes are needed to decrease the workpiece height within the 5 μm. On the other hand, figure 7 shows the effect of the present sizing method. At the grinding allowance of 350 μm, a workpiece which had an allowance of 350 μm was ground. After the first grinding process, residual stock removal of 49 μm due to the wheel wears remains. Sum of the setting depth of cut to remove this residual stock removal of 49 μm is calculated as 407 μm form equation (9-3). Namely the setting depth of cut 57 μm is needed to remove the residual stock of 39 μm in the compensation. This workpiece has ground within 1 μm by using the sizing method. By repeating the same grinding operation altering grinding allowance 200, 250 and 300 μm, this experiment has carried out. From this result, it is confirmed that the workpieces has ground within ±10 μm at the once compensation cycle.

6. Conclusion

In this study the sizing method based on a grinding ratio has been presented, and applied to the vertical spindle surface grinding. Results obtained in this experiment are as follows.

1) Workpieces are completely finished within the tolerance of 10 μm by the only one newly developed compensation cycle
2) This sizing method is very effective to finish the workpiece within a given tolerance especially in grinding of low Grinding ratio materials.

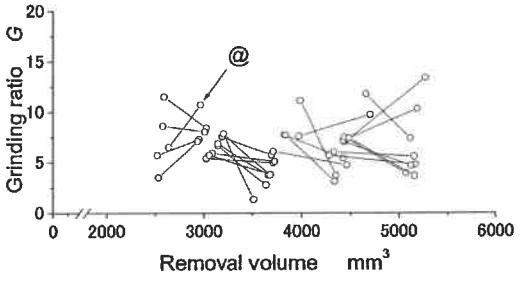

Fig.4 Change of grinding ratio

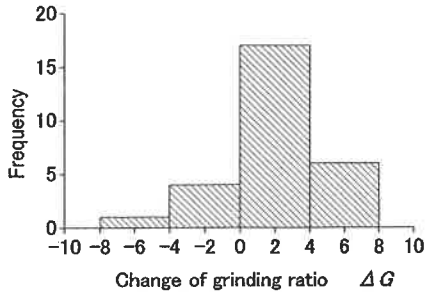

Fig.5 Frequency distribution of grinding ratio

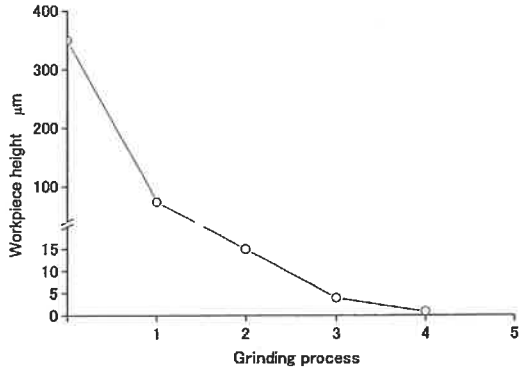

Fig.6 Results of conventional grinding operation without our newly presented sizing method

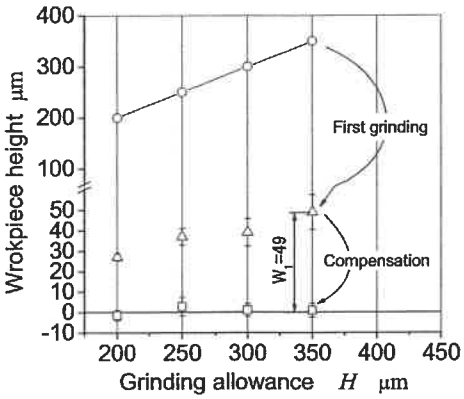

Fig. 7 Improved effect of the presented sizing method

STUDY ON THE ROUND-OFF TRUING METHOD USING CIRCULAR MOTION

– TRUING OF A SUPERABRASIVE WHEEL WITH A HOMOGENEOUS TRUING WHEEL –

Takayuki Kitajima, Shigeki Okuyama, Keishu Yamashita and Akinori Yui
National Defense Academy, Yokosuka, Kanagawa, Japan

Abstract

The round-off truing method of a grinding wheel for precision form grinding, where the circular motion of a CNC grinding machine and an abrasive stick are utilized, was previously proposed by the authors. In a former study, the compensation method of mal-distribution of wear ratio, α, for an abrasive stick was proposed and the use of this method resulted in the improvement of truing accuracy. This method, however, can not be applied to a brake truer. In this study the authors have tried to produce a homogeneous truing wheel for a brake truer, utilizing a hydraulic pressure process, and the developed wheel was applied to the round-off-truing experiment for a bronze bonded superabrasive wheel. The superabrasive wheel was trued in target accuracy in about 20 minutes when setting angle of the brake truer, θz, was at 10 degrees.

Key words: grinding wheel, round-off truing, superabrasive wheel, homogeneous truing wheel, truing accuracy, setting angle, wear ratio

1. Introduction

An envelope grinding method using a spherical wheel or a straight wheel with round-off (toroidal shape) is usually employed to fabricate non-axisymmetric aspherical lenses and their dies. In this case, the form error of the grinding wheel directly affects the form accuracy of the generated shape.

The authors previously proposed a simple round-off-truing method utilizing the circular motion of a CNC grinding machine as shown in **Figure 1** [1]. In this method, a brake truer (or an abrasive stick) was set on the machine table, and the grinding wheel was moved around the truing wheel along the circular path. In a former study [2], truing experiments for a conventional grinding wheel were performed to realize the effects of geometrical and motional error factors on the truing accuracy. As a result, the distribution of wear ratio of truing wheel, α, was realized to have a strong effect on the truing accuracy. The compensation method of the mal-distribution of α for an abrasive stick was then proposed and the use of this method resulted in the improvement in truing accuracy. This method, however, can not be applied to a truing wheel for a brake truer even though the truer is far more efficient than the abrasive stick.

In this study, the authors have tried to produce a homogeneous truing wheel for the brake truer, utilizing a hydraulic pressure process, and the developed wheel has been applied to the round-off-truing experiment of a bronze bonded superabrasive wheel.

2. Method and Conditions of the Experiment

In the truing experiment, a high-precision CNC surface grinding machine, Kuroda SPG-25, was used. Before the experiment the profile of the grinding wheel surface was transferred to a graphite plate. The edge of the plate was traced by a ultra-accurate 3-D profilometer, Panasonic UA3P-4, to evaluate the radius of the best-fit circle, Rft. In the truing experiment, Rft was set to the objective radius of grinding wheel, Rg. Circular motion radius, G, is given by the equation: $G=Rg\{(Ts/Tg)+1\}$, where Ts and Tg are thicknesses of the abrasive stick and the grinding wheel respectively [3].

In the experiment, a brake truer was set on the machine table and the grinding wheel was down-fed and moved around the truer along the circular pass. Following the first pass, the wheel was down-fed again and circularly moved in the reverse direction. After a certain number of truing passes, the profile of the wheel surface was transferred to a graphite plate, and Rft; form error, ER; and form error from the circle of the minimum square, $ERft$,

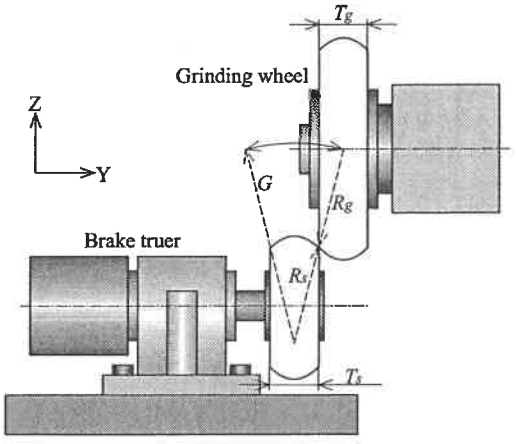

Fig.1 Schematic diagram of the round-off-truing method

were evaluated by using the UA3P-4. Experimental conditions are shown in **Table 1**.

Table 1 Conditions for the truing experiment

Grinding wheel		Conventional wheel: GC120H ($Dg180 \times Tg25.4$mm)
		Superabrasive wheel: SD1500N75MB, SD2000N75MB ($Dg150 \times Tg25$mm, Bronze bond)
Truing wheel		Newly developed wheel, Traditional wheel: C150K ($Ds100 \times Ts25.4$mm)
Wheel speed	V	1500min^{-1}
Cross feed speed	v_{cf}	300mm/min
Down feed	t	5μm
Grinding fluid		W-2 type 3, 50 times dilution

3. Results and Discussions

The production process of a conventional grinding wheel is the molding, through the press forming process of the mixed wheel materials, and the firing. Because of friction between the molding die and the wheel materials the produced wheel usually shows a mal-distribution in structure and hardness in the direction of the wheel width. In order to obtain the homogeneous wheel, the hydraulic pressure process has been applied for the molding.

3.1 Distribution of α of the newly developed truing wheel

Homogeneity of the newly developed truing wheel has been evaluated through infeed grinding tests as shown in **Figure 2(a)**. In the experiment, the free end of the truer spindle was supported by the tailstock to avoid inclination of the spindle due to a vertical truing force.

When total depth of cut, T, is at 4mm, form deviation of the trued grinding wheel becomes more than 200μm. However, this result does not show non-homogeneity of the developed truing wheel because the form deviation of the grinding wheel is also affected by the non-homogeneity of the grinding wheel itself. The truing wheel was then turned over and the infeed grinding was performed again. As shown in **Figure 2(b)**, the shape of the form deviation was not changed before or after the turning over. This result shows that the distribution of α of the developed truing wheel is homogeneous.

A similar experiment was performed using a traditional truing wheel which is available on the market. As shown in **Figure 3(a)**, form deviation was reached at about 700μm and when the truing wheel was turned over the shape of the form deviation, shown in Fig.3(b), became quite different from that in Fig.3(a). This result implies that the structure and hardness of both wheels are not homogeneous.

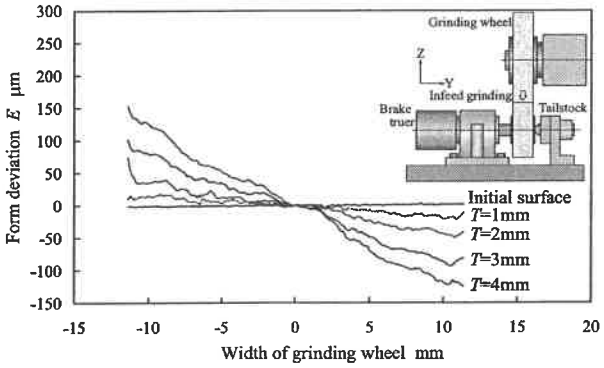

(a) Before turning over

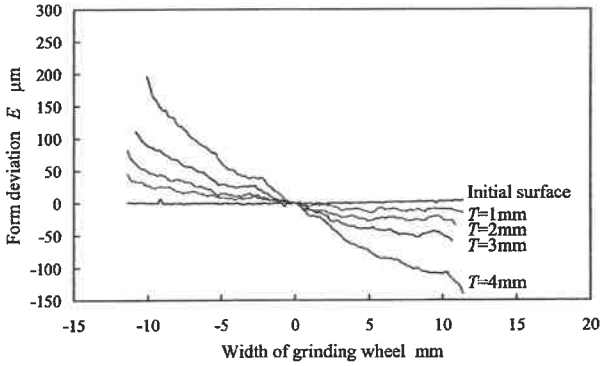

(b) After turning over

Fig.2 Form deviation of the grinding wheel when the newly developed truing wheel is used

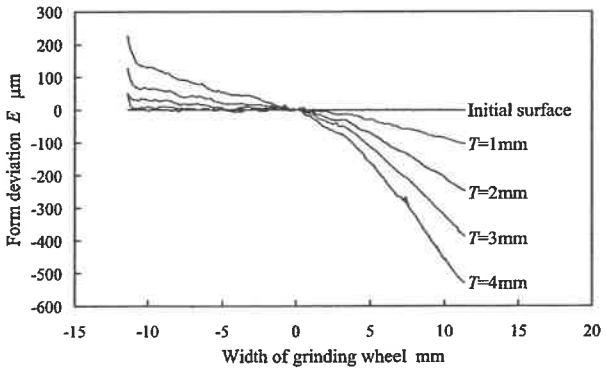

(a) Before turning over

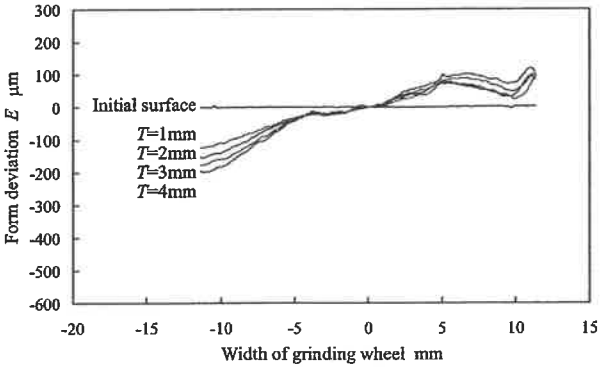

(b) After turning over

Fig.3 Form deviation of the grinding wheel when a traditional truing wheel is used

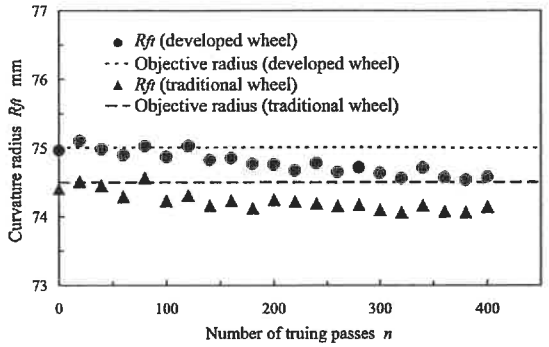
● Rft (developed wheel)
--- Objective radius (developed wheel)
▲ Rft (traditional wheel)
– – Objective radius (traditional wheel)
Curvature radius Rft mm
Number of truing passes n

Fig.4 Transition of Rft with the number of truing passes

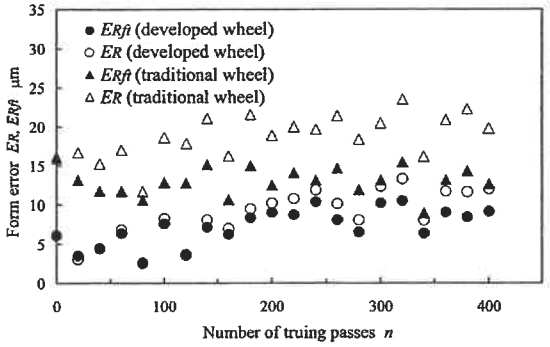
● ERft (developed wheel)
○ ER (developed wheel)
▲ ERft (traditional wheel)
△ ER (traditional wheel)
Form error ER, ERft μm
Number of truing passes n

Fig.5 Transition of ER, $ERft$ with the number of truing passes

3.2 Round-off truing of a superabrasive wheel

Figure 4 shows the transition of Rft with the number of truing passes, n, when a bronze bonded superabrasive wheel (SD1500N75MB) was trued with the homogeneous truing wheel or a traditional truing wheel. In these cases, Rft becomes less than the objective radius, Rg. **Figure 5** shows the transition of ER and $ERft$ with n. In the range of the experiment, the form error is not small and it gradually increases with n.

Figure 6 shows an example of measured form deviation of the trued wheel surface. In this case, large corner dullness can be observed at both ends of the trued wheel surface. This phenomenon occurred because both ends of the wheel surface always engaged against the truing wheel with full depth-of-cut [1]. Due to the corner dullness, Rft was estimated at less than the objective radius as shown in Fig.4. Both ends of the grinding wheel, however, are not used in free form grinding. Thus, we had to evaluate the radius and the form deviation of the wheel surface of actual use. Hereafter, we estimate the radius of the best-fit circle without considering the ranges of $Tg/8$ from both ends of the wheel surface, $RftC$; form error in the same area, ERC; and form error from the circle of the minimum square in the same area, $ERftC$.

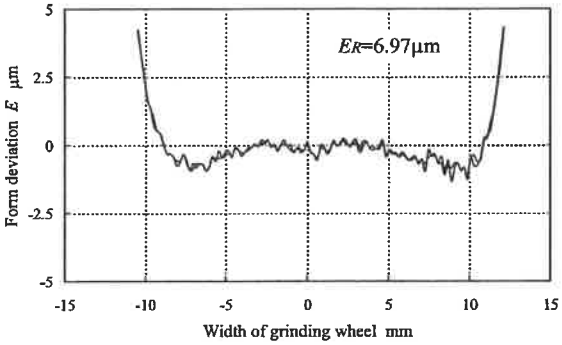

Fig.6 Form deviation of a trued wheel profile (SD1500N75MB vs. Developed wheel, n=400)

Figure 7 shows the transition of $RftC$ with n. In the case of the developed truing wheel, $RftC$ almost settled to the objective radius, where Rg=75mm. On the other hand, in the case of a traditional truing wheel, $RftC$ did not settle to the objective radius because the distribution of α was not even.

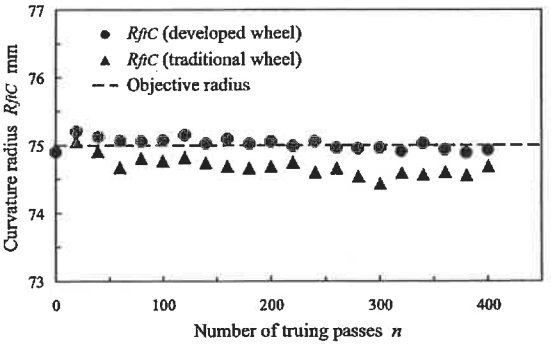

Fig.7 Transition of $RftC$ with the number of truing passes (SD1500N75MB)

Figure 8 shows the transition of ERC and $ERftC$. ERC and $ERftC$ for the developed truing wheel are about 2μm in 50-200 truing passes. Even when the developed truing wheel was used, $ERftC$ showed a slight increase with n because the wheel was not completely homogeneous. **Figure 9** shows the form deviation curve of the trued wheel surface when $ERftC$ attained the minimum value.

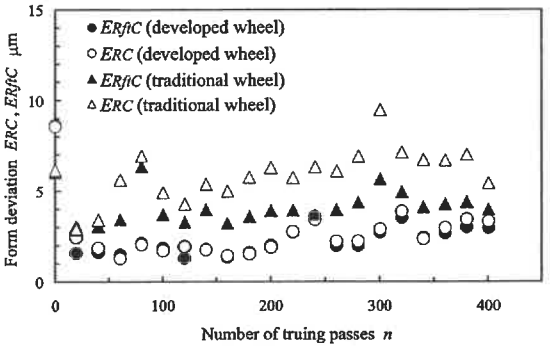
● ERftC (developed wheel)
○ ERC (developed wheel)
▲ ERftC (traditional wheel)
△ ERC (traditional wheel)
Form deviation ERC, ERftC μm
Number of truing passes n

Fig.8 Transition of $ERftC$, ERC with the number of truing passes (SD1500N75MB)

3.3 Effect of the setting angle of the brake truer

In the latest study [2], the authors investigated the effects of setting angle of brake truer, θz, using a

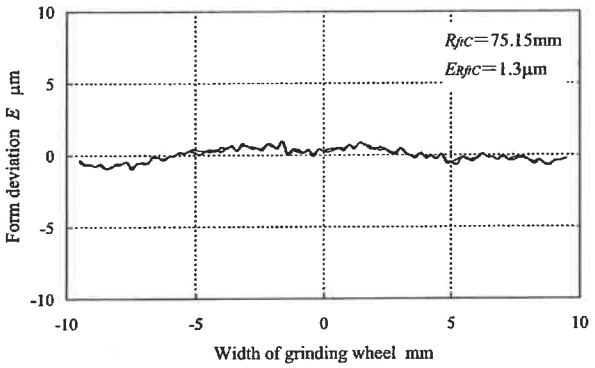

Fig.9 Form deviation of a trued wheel profile (SD1500N75MB vs. Developed wheel, n=120)

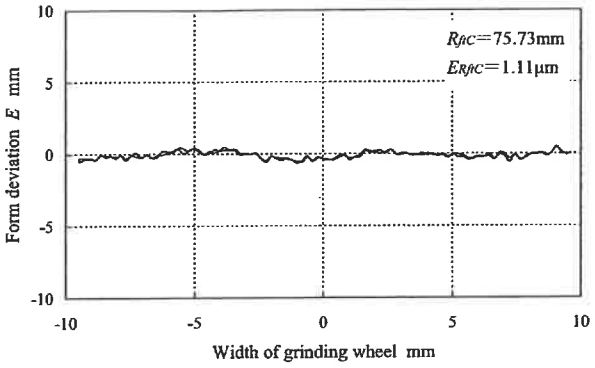

Fig.10 Form deviation of a trued wheel profile (SD2000N75MB vs. Developed wheel, θz=10°, n=80)

traditional truing wheel and experimentally confirmed that the inclination of the truing wheel resulted in improvement in form accuracy of a trued wheel when θz was set at 10-20 degrees. **Figure 10** shows the form deviation of the superabrasive wheel, SD2000N75MB, which was round-off trued with the homogeneous truing wheel when θz=10 degrees.

Since the circular motion error of the grinding machine is about ±0.7μm [4] and the range of the circular motion during the round-off truing is only a part of the full circular motion, the target accuracy of the proposed round-off-truing method was set at ±0.5μm. From Fig.10, the superabrasive wheel has been trued around the target accuracy in about 15 minutes (n_S=80 passes) by using the homogeneous truing wheel and under the condition of θz=10 degrees. In the present truing condition, the number of truing passes, n, must not exceed 150 passes because truing accuracy gradually deteriorates when n exceeds about 200 passes.

4. Conclusions

In this paper, the authors tried to produce a homogeneous truing wheel for a brake truer utilizing the hydraulic pressure process and the developed wheel was applied to the round-off-truing experiment of a bronze bonded superabrasive wheel. The main results obtained are as follows:

(1) The distribution of wear ratio, α, of the newly developed truing wheel was experimentally investigated and its homogeneity was confirmed.
(2) The use of the homogeneous truing wheel resulted in a significant improvement in truing accuracy.
(3) A superabrasive grinding wheel can be trued around the target accuracy as ±0.5μm in about 20 minutes, when setting angle of the brake truer, θz, is at 10 degrees.

Acknowledgement

The authors would like to express their heartfelt thanks to Noritake Co., Ltd. for the help of producing the homogeneous truing wheel.

References

[1] S.Okuyama, T.Iwaya, T.Kitajima, H.Suzuki and A.Une, "Theoretical investigation of a new round-off truing method" *Proc. of the 3rd Int'l ABTEC*, 243-250. (1999)
[2] T.Kitajima, S.Okuyama, T.Wakatomo, A.Yui, H.Suzuki and S.Hanasaki, "Study on the machining accuracy of round-off truing method - Experimental analysis of error factors" *Proc. of ASPE2002 Annual Meeting*, 505-508. (2002)
[3] S.Okuyama, T.Kitajima, T.Iwaya and H.Suzuki, "Experimental study on the new round-off truing method utilizing the circular motion of a CNC machine and an abrasive stick" *Proc. of the 3rd Int'l ABTEC*, 251-257. (1999)
[4] S.Okuyama, S.Watanabe and S.Kawamura, "Study on the motion errors of NC surface grinding machine – Method for measuring the motion errors under the circular interpolation" *J. of JSPE*, Vol.60, No.12, 1756-1760. (1994)

Ultra-Precision Grinding Wheels based on the Structure of Natural Whetstones

Namiko SAITO*, Takato TAKEMURA** and Jun-ichi IKENO***
*Technical Research Institute of JSPMI, Tokyo, Japan
**Research Center for Deep Geological Environments of AIST, Ibaraki, Japan
***Graduate School of Science and Engineering, Saitama University, Saitama, Japan

Introduction

Recently, polishing has become widely used in the finishing process of brittle materials such as silicon wafers in order to obtain surfaces with roughness smaller than that which can be obtained by other processing methods and a damage-less surface. However, the polishing has the disadvantages of low efficiency and a negative influence on environment from wastes. The grinding process offers the following advantages: 1) Productivity is high since the processing speed is quick; 2) it is easy to require desired form. However, the surface quality is poorer than that attained by polishing. Nevertheless, there is strong demand to change from the polishing process to the grinding process. In ultra-precision grinding, machine tools have been developed which have high stiffness and nanometer-level positioning accuracy. However, since the development of grinding stones is still inadequate, the quality of a surface has not attained to polish. On the other hand, human beings have used a geological material, called natural whetstone, as a grinding stone since ancient times. However, in recent years, natural whetstone has not been used in the industrial field.

There are various kinds of natural whetstones, and some of them are rated better than artificial grinding stones. Unfortunately, superior natural whetstones have not yet been the subject of research, and their properties as a grinding stone are still unknown.

With this background in mind, we consider that we could use findings from an examination of natural whetstones to develop a completely new grinding stone. In this paper, we report on the basic characteristics of the natural whetstones using observation and elemental analysis. Based on the internal structure of the natural whetstones, we manufactured two types of grinding stones, and their grinding performances were evaluated.

Characteristics of natural whetstones

There are many types of natural whetstones for rough grinding, semi-finishing and final polishing. Japan is a country known to produce high-quality natural whetstones, and in particular, those from Kyoto are known to be of unparalleled high quality. The geological name of the stone used is Toishi-type siliceous shale. Those who use these stones as knife grinders call the type used for final polishing *Awasedo*. The *Awasedo* includes many varieties, and thus the stones are categorized by the region they are sourced from and their color, and each has a particular name.

We note the following unique point about the usage of the *Awasedo*. We have to use this type of stone from one direction, and cannot utilize other sides as an old custom; that is to say, the *Awasedo* has directional dependability. That is, with the *Awasedo* quarried out in the rectangle, only a set of surface, which faces each other, can be used for processing. On the other hand, other types of natural whetstones do not have any directional dependability, and can be used from all directions similarly to a general artificial grinding stone. Craftsmen who make traditional Japanese swords are users of natural whetstones. According to them, artificial grinding stones have recently come to be used for rough grinding and semi-finishing, because they are better than the natural whetstones in terms of homogeneousness and removal efficiency. However, in the case of using the *Awasedo* for final polishing, the craftsmen do not substitute artificial grinding stones for the natural

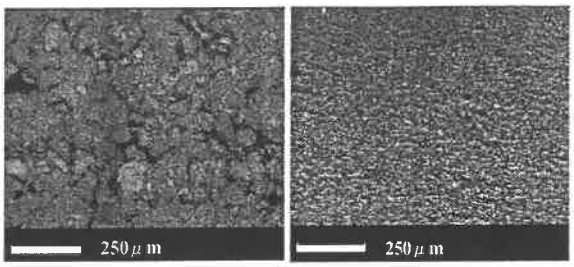

(a) Omura (b) Tomae(Awasedo)

Fig.1 SEM images of natural whetstones

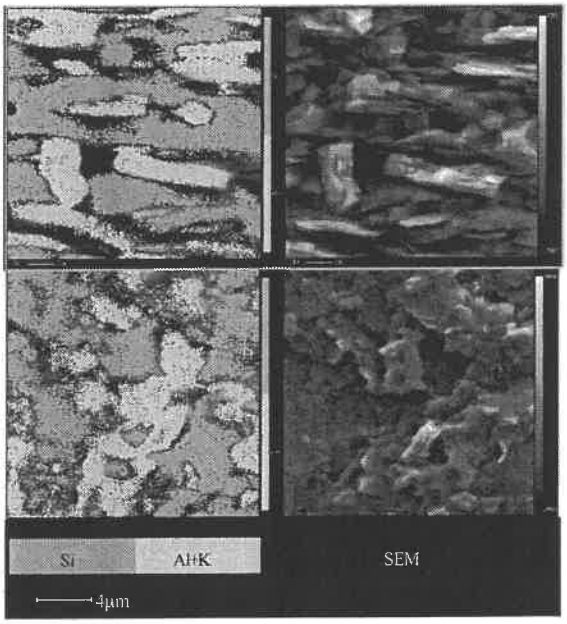

Fig.3 a result of distributive analysis

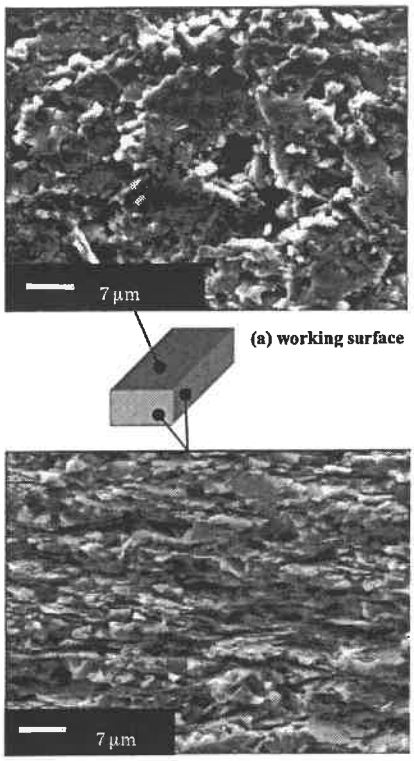

(b) side surface

Fig.2 SEM images of fine natural whetstone

whetstones, because an *Awasedo* cannot be made artificially.

Structural analysis of the natural whetstones

As the *Awasedo* has directional dependability, it is necessary to discriminate between the faces that we can use for processing and the other faces. The former is termed the working surface, and the latter is termed the side surface.

Omura, which is a natural whetstone for rough grinding, and *Tomae*, which is one used for final polishing, as well as kinds of *Awasedo*, were observed with a scanning electron microscope (SEM) to confirm their basic structures. In the case of *Omura*, a viewing screen was chosen an arbitrary side as it has no directional dependability. **Fig. 1** shows a SEM image of an *Omura* **(a)** and the side surface of a *Tomae* **(b)**. **Fig. 2(a)** shows a SEM image of the working surface, and a SEM image of the side surface of a *Tomae* under high magnification is shown in **Fig. 2(b)**. From these observation results, it is clear that the *Tomae* has a layered structure. It has a large number of thin layers, and they overlap each other in parallel with the working surface. This structural characteristic can be confirmed not only for the *Tomae* but also for other types of *Awasedo*. Artificial grinding stones now in common use are formed with an aggregate of abrasive gains. Therefore, we can say that the structure of an artificial grinding stone is similar to that of natural whetstones used for rough grinding.

The composition of an *Awasedo* was analyzed with an Electron Probe Microanalyzer (EPMA), and it was clarified that the main inclusions were Si, Al, K and O. *Awasedo* is a geological compound made up of mica and silica. As the chemical formula of *Awasedo* is as follows, mica= $K_2Al_4Si_6Al_2O_{20}(OH, F)_4$, silica= SiO_2, it does not contradict the

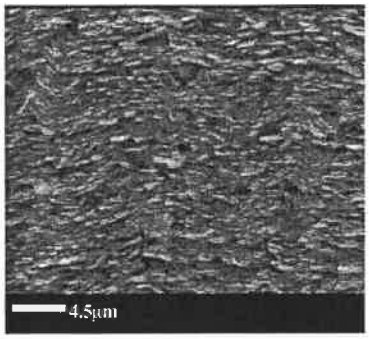

(a) Flake graphite abrasive

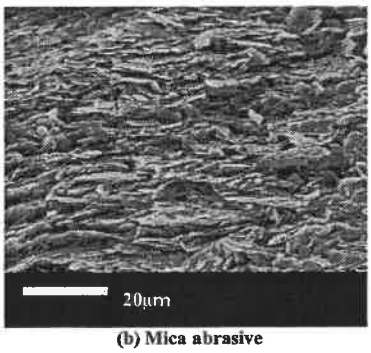

(b) Mica abrasive

Fig.4 SEM image of the developed grinding stones

Table 1 Conditions

	Flake Graphite	Mica
Wheel revolution	1000rpm	500rpm
Work revolution	30rpm	30rpm
Feed rate	3μm/min	1μm/min
Work piece	6in silicon wafer	3in silicon wafer

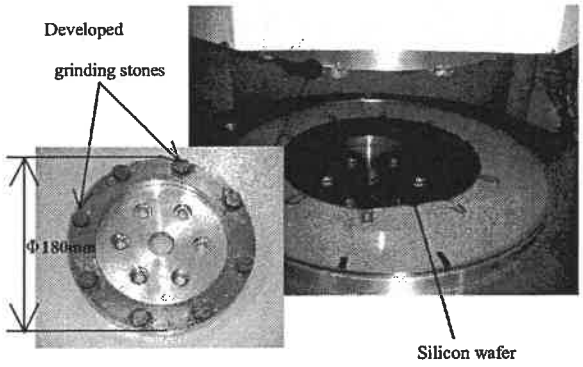

Fig.5 Setup of grinding test

findings of our analysis. Distributions of Si, K and Al were analyzed to confirm the physical relationship of mica and silica. The result is shown in **Fig. 3**. The top figure shows the result for the side surface, the bottom figure shows the result for the working surface, the right-hand images are SEM images and the left-hand images show the result of distributive analysis. They are of the same area as the SEM images. In the left-hand images, the blue(dark color) area shows a part where Si was detected abundantly and the area is thought of as silica. The yellow (bright color) area shows a part where K and Al were detected abundantly and the area is thought of as mica. Through the structural analysis, it was clarified that the *Awasedo* has two types of layers composed of mica and silica, and they overlap each other.

Structure of new grinding stone

When a layer structure like that found in the *Awasedo* is applied to an artificial grinding stone, the following behaviors are anticipated.

1) A wafer-thin step of each layer acts as a dimensionless major cutting edge height.
2) As layers break away on the machining surface, new lips are frequently created.
3) Though the major cutting edge height is dimensionless, retentively is high as each layer is held by a surface contact.

Additionally, it is thought that the mica contained in the *Awasedo* provides lubricity.

Experimental production of stratiform grinding stone

In the *Awasedo*, it would appear that silica plays the role of an abrasive and mica plays the role of the bonding, since the *Awasedo* is composed of materials with different hardnesses such as silica (Mohs hardness=6) and mica (Mohs hardness=2). However, in this study, it was expected that flaky materials would work as a lip when the flaky materials that is taken a direction and a work material take relative motion. Two types of grinding stones, which have structures like that of the *Awasedo*, were developed to confirm this behavior. One of the new grinding stones has mica as abrasive grains, and the other has flake graphite. In both of these developed

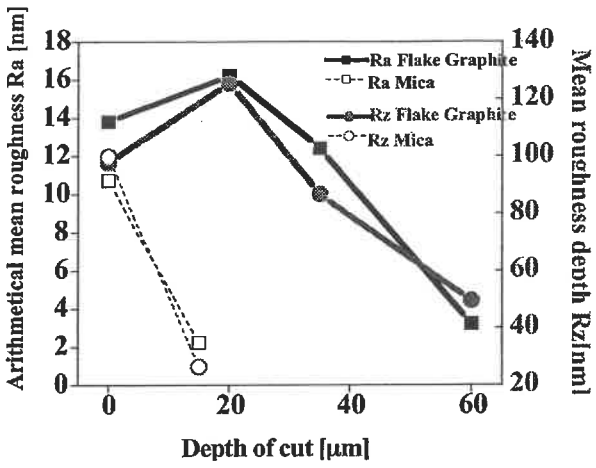

Fig.6 surface roughness

(b) flake graphite grinding stone

(b) mica grinding stone

Fig.7 Silicon wafer after grinding

grinding stones, sodium silicate is chosen as the bond.

The reason why mica is chosen as the abrasive is that it is one of the components of natural whetstones. The flake graphite offers the following advantages. It is unlikely that the flake graphite will scratch a work piece after falling off as it has a lubricating property. It is easy for the flake graphite to collocate in a layer structure the average flake radius is sufficiently large (=650μm). The flake graphite is supposed to radiate heat generated by the grinding process, as its coefficient of thermal conductivity is high.

The production procedure of a grinding stone using flake graphite is as follows. A compound of powdery sodium silicate and flake graphite is placed in a mold. Then, the flakes naturally form the layer structure. The compound is compressed at 400MPa in a direction perpendicular to the layers, and it is sintered in a furnace (770K).

The production procedure of a grinding stone using mica is as follows. A compound of sodium silicate, mica and water are placed in a mold. The consolidation and build up of the layer structure was caused by compaction[1]. The resultant grinding stone is dehydrated in a furnace.

Grinding test

Performances of the two types of developed grinding stones were measured by dry grinding tests with a surface-grinding machine. The grinding stones were used as straight cup grinding wheels. The work piece was a pre-finished silicon wafer. The setup of the grinding test is shown in **Fig. 5**. The other test conditions are listed in **Table 1**.

Fig. 6 shows changes in surface roughness. In the case of the graphite grinding stone, an arithmetical mean roughness Ra is improved from 14nm to 3nm. In the case of the mica grinding stone, Ra is improved from 10nm to 2nm. Although both grinding stones caused scratches on the surface of a silicon wafer, they could be used for mirror grinding.

Conclusions

On the basis of an analysis of the structure of natural whetstones using SEM and EPMA observation, we discussed the processing performance of grinding stones developed based on the structure of the *Awasedo* stones. The conclusions are summarized as follows:

1) It was clarified that the layer structure found in the *Awasedo* has high grindability.
2) A grinding stone with a structure like that of the *Awasedo* is applicable for mirror grinding of a silicon wafer.
3) The layer structure, as well as grain size, is an important factor in order to develop ultra-precision grinding wheels.

References[1] Takemura, T. et al. (2004) :Development of ultra-precision grinding wheels based on anisotropic structure by consolidation tests, *Jour. Japan Soc. Eng. Geol.*, submitted

Key words: ultra-precision grinding, flake graphite, mica, natural whetstone, silicon wafer

NEW DIAMOND GRINDING WHEELS WITH ELECTRICALLY CONDUCTIVE CUTTING EDGES

Kiyoshi Suzuki[1], Manabu Iwai[2], Anurag Sharma[1], Katsutoshi Tanaka[3], Tetsutaro Uematsu[2]
[1]Nippon Institute of Technology, Miyashiro, Saiitama 345-8501, Japan
[2]Toyama Prefectural University, Kosugi, Toyama 939-0398, Japan
[3]Toshiba Machine, Numazu, Shizuoka 410-8510, Japan

The application of an electrically conductive diamond material to a new type of grinding wheel whose cutting edges possess electrical conductivity has been tried in this research work. Firstly, electrical discharge machining is applied on a solid surface of an electrically conductive CVD diamond film to create protrusions like cutting edges. Secondly, it is confirmed that the EDMed surface of the diamond material has an ability of stock removing when used in the form of a small lapping wheel. Thirdly, two different types of grinding wheels for micro grinding, i.e. i) a V-shaped profile wheel and ii) a micro mounted wheel, have been manufactured. And it is found that very fine V-shaped grooves can be made on a cemented carbide workpiece by using those wheels with very small wheel wear.

Keywords: Electrically conductive CVD diamond film, Electrically conductive cutting edge diamond wheel, Electrical discharge trueing

1.Introduction

Until recent days extensive development works to improve the grinding performance of diamond grinding wheels have been carried out with respect to grinding efficiency, grinding ratio, grinding resistance, ground surface quality, etc. from the standpoints of abrasives and wheel structure. There has been a remarkable improvement in the general grinding performance as a result of these efforts. However, in the case of fine superabrasive wheels for precision grinding, the problems of limited abrasive concentration, non-uniform dispersion of abrasives and drop-off of abrasives still remain. The authors have proposed a new grinding wheel having electrically conductive cutting edges utilizing electrically conductive CVD diamond [1] in order to cope with the above-mentioned problems.

This paper describes the basic grinding performance and possible applications of the newly proposed diamond wheel with electrically conductive cutting edges by using commercially available electrically conductive CVD diamond film [2].

2. Proposed diamond grinding wheels with electrically conductive cutting edges

2.1 Manufacturing concept of electrically conductive grinding wheels

Though it is possible to perform necessary shape forming and correction operation on conventional metal bonded, electroplated or electrically conductive resin bonded superabrasive wheels by an electrical discharge trueing/dressing method [3] due to the electrical conductivity of the bonding material, no change can be made to the diamond abrasives as they do not possess electrical conductivity. Thus, new cutting edges cannot be formed directly on the individual diamond abrasives by means of electrical discharge machining (EDM). However, in the grinding wheels having electrically conductive cutting edges proposed in this paper, electrically conductive diamond films or grits, which are made conductive by doping with boron during the CVD process, are used so as to form cutting edges and it is possible to precisely make the protrusion of the cutting edges on the grinding wheel or to form fine cutting edges on the grit itself during EDM operation as shown in Figures 1(a) and (b). Moreover, the boron doped diamond [4][5] has an oxidation temperature of (750°C+_) higher than a conventional diamond and, therefore, there is a possibility of grinding materials which are difficult to be ground with existing diamond grit wheels. The proposed wheel is named electrically conductive cutting edges diamond grinding wheel (in short, EC-cutting

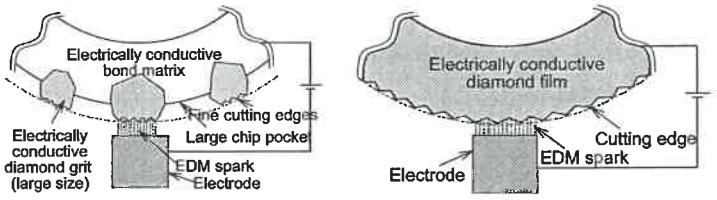

(a) Electrically conductive large diamond abrasive wheel (B-type)

(b) Electrically conductive diamond layer wheel (A-type)

Figure 1: Formation of cutting edges on new diamond wheels by EDM or ED trueing/dressing.

1. Shape forming _ Trueing and retrueing by EDM
2. Cutting edge sharpening _ Dress'g and redress'g by EDM
3. High concentration _ Bond-free _ Use of diamond film
4. Free from abrasive drop off _ Entire diamond wheel
5. Uniform cutting edge
   _ Utilization of crystal shape of diamond
6. Correspondence to both micro cutting edges and large chip pockets
   _ Fine edges by EDM on a large diamond grit
7. Application to hard-to-grind materials and ferrous alloys
   _ Diamond grits with high oxidation temperature

Table 1: Concepts of electrically conductive cutting edge diamond grinding wheel [1][2].

Wheel conformation	Bondless solid-diamond wheel		Bonded diamond-grit wheel	
Wheel classification	A-1	A-2	B-1	B-2
Diamond material for grinding wheel	CVD diamond coating on base metal	CVD diamond thick film	Grit crushed from CVD diamond film	Mono crystal grit by HPHT
Size of diamond	Large (Bulk)	Large (Bulk)	Middle	Small
Diamond content in diamond layer	100%	100%	-	-
Size of chip pocket	Small	Small	Large	Large

Table 2: Structural features of EC-cutting edges D grinding wheel.

edges diamond wheel, or EC-cutting edges D wheel) and the main concepts of the new diamond wheel are shown in Table 1.

2.2 Types of proposed EC-cutting edges D wheels

As listed in Table 2, the proposed electrically conductive cutting edges diamond grinding wheels (EC-cutting edges D wheels) are classified into two groups; "bondless solid-diamond wheel (A-type)" without bond matrix and "bonded diamond-grit wheel (B-type)" in which electrically conductive diamond grits are bonded by electrically conductive bond matrix. The former A-type wheels are further classified into a grinding wheel made by direct CVD of electrically conductive diamond film on the wheel base metal [Type A-1] and a wheel with an abrasive layer entirely composed of electrically conductive CVD diamond thick film provided with EDMed cutting edges [Type A-2]. The latter B-type wheels are classified into a grinding wheel made of diamond grits obtained by crushing of electrically conductive CVD diamond film [Type B-1] and a wheel containing electrically conductive mono-crystal diamond grits produced in a HPHT (high pressure and high temperature) synthetic process [Type B-2].

2.3 Proposed manufacturing methods for EC-cutting edges D wheels

For bondless solid-diamond wheel, Figure 2 shows a manufacturing process of the above mentioned A-2 type wheels from a boron doped electrically conductive diamond plate. At first the diamond plate is cut to desired size using laser cutting or wire EDM to make a wheel blank and then the blank is brazed onto a wheel base or, in some cases, is fastened to the base with a clamp. Then an electrically conductive wheel with desired shape and dimensions is formed by means of EDM or grinding. In the case of the A-1 type wheel, electrically conductive diamond film is directly deposited on wheel base metal to make a diamond wheel.

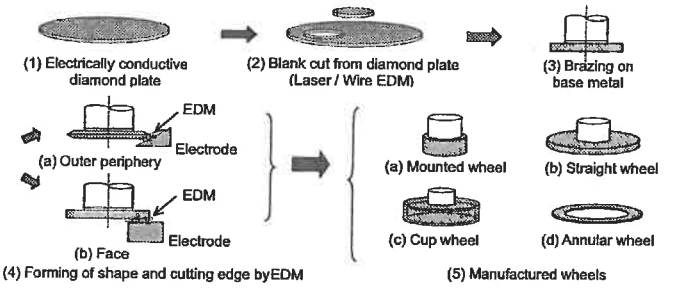

Figure 2: Manufacturing method of electrically conductive bondless diamond wheel from electrically conductive diamond film.

For bonded diamond-grit wheel, the above mentioned B-type wheels are in the form of metal bonded wheels, electroplated wheels or electrically conductive resin bonded wheels. Since the grits are electrically connected with the bonding material in all of these wheels, the formation and correction of a profile and the provision of cutting edges on the top of the grits are possible by using EDM.

3. Various EC-cutting edges diamond wheels and grinding characteristics

3.1 Experimental conditions

(1) Material for EC-cutting edges D wheel

Commercially available electrically conductive CVD diamond thick film (CVDITE-CDE, 0.5mm thick), produced by Element Six Ltd., was used to manufacture "an electrically conductive cutting edge diamond wheel". This CVD diamond film has a specific resistance of 0.4~1_10^{-3} _·m, which is adequate for performing EDM on it. An electrically conductive CVD diamond thick film blank of 5_6_0.5 mm, cut by laser, is selected as the abrasive layer. The other properties of the diamond film are given in Table 3.

(2) Experimental devices and conditions

EDM properties of the diamond film used as a workpiece were examined by die-sinking EDM in oil with a copper electrode and with the open circuit voltage of u_i=60 V and the discharge current of i_e=2 A. The experimental conditions are listed in Table 4.

CVD diamond: CVDITE-CDE (Element Six) Specific resistance: 0.4 ~ 1×10^{-3} [_·m] Specific gravity: 3.52 Young's modulus: 10 ~ 11×10^{5} [N/mm^{2}] Compressive strength: 8.69 ~ 16.53×10^{3} [N/mm^{2}] Thermal conductivity: 5 ~ 6 [W/cm·K] Thermal diffusivity: 0.27 ~ 0.33×10^{-3} [m^{2}/s] Coefficient of thermal expansion: 1.0×1 0^{-6} (Minimal level) Oxidation temperature: 750°C+_

Table 3: Properties of EC-CVD diamond thick film.

EDM machine	Die sinking EDM machine (A35R, Sodick)
Working fluid	Oil (Vitol 2, Sodick)
Diamond workpiece	Electrically conductive CVD diamond_thick film_(CVDITE-CDE, 5_6_0.5 [mm], Element Six)
Electrode	Copper
EDM conditions	u_i = 60 [V], i_e = 2 [A] t_e / t_o = 2/4, 2/10, 2/50, 6/50 [μs] Reversed polarity (Copper electrode: +) EDM time = 2 [minutes]

Table 4: Experimental devices and EDM conditions.

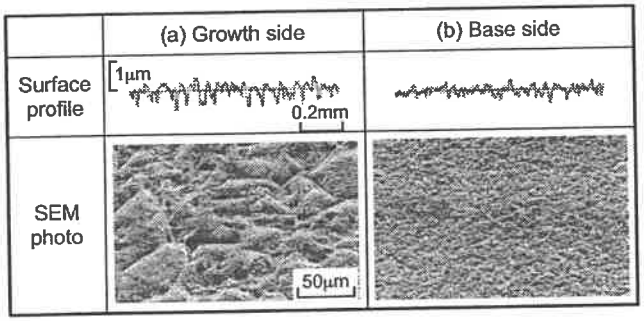

Figure 3: Difference of EDMed surface between the growth side and base side of the CVD diamond film.
(u_i=60V, i_e=2A, t_e/t_o= 6/50μs, Reversed polarity, EDM time: 2min)

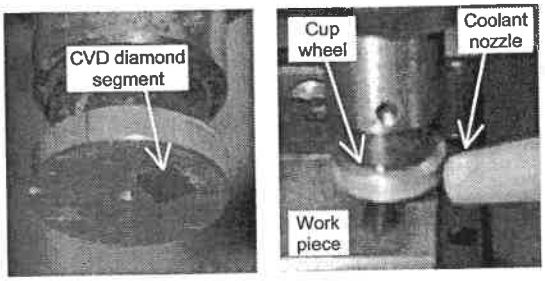

(a) Segment fixed (b) Polishing of WC

Figure 4: Grinding wheel with diamond segment.

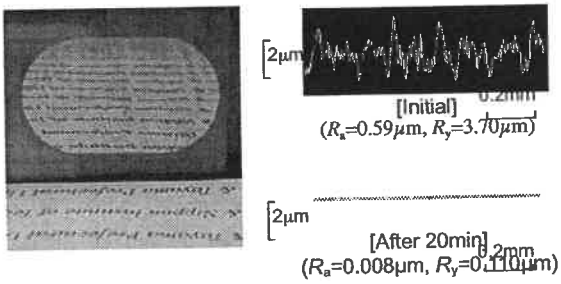

(a) Finished surface (b) Surface roughness

Figure 5: Surface of WC after finishing.

(3) Effects of surfaces of CVD diamond thick film

Figure 3 shows the results of EDM on the growth (front) side surface and the base (rear) side surface of the diamond film under the pulse conditions of t_e/t_o=6/50 μs. Though a large difference between the two EDMed surfaces is observed, the crystallites of the diamond film can be seen on both the sides.

3.2 Segment lapping wheel

A trial grinding experiment was performed to confirm the possibility of utilizing the protrusions, obtained by EDM on the CVD diamond film, as cutting edges in grinding. A small segment of the diamond film after EDM on the growth side at t_e/t_o=6/50 μs was attached to the bottom of a mounted wheel at an eccentricity of 2 mm as shown in Figure 4(a) and a cemented carbide (WC) workpiece was ground at a constant pressure of 10 N and at a grinding speed of 14 m/min for 20 minutes as shown in Figure 4(b). Figure 5(a) shows an appearance of the ground surface. As Figure 5(b) shows, the surface roughness of the cemented carbide workpiece improves from the initial values of Ry=3.70 μm and Ra=0.59 μm to Ry=0.110 μm and Ra=0.008 μm after grinding.

3.3 Disc wheel for V-groove

In order to investigate grinding ability of the edge portion of the CVD diamond thick film wheel, a small disc type wheel with a V-shaped peripheral edge was manufactured by using ED trueing. The wheel has a diameter of 20mm, a thickness of 0.5mm, a peripheral peak angle of 90 degrees and a peak radius of 6_m. Figure 6 shows a profiled disc wheel made of electrically conductive CVD diamond film. With this wheel cemented carbide material was ground by a plunge grinding method under the condition of V_s=17m/min, V_w=200mm/min, a=1_m, L=5mm, n=50passes. Figure 6(c) shows ground grooves. From the cross sectional profile shown in Figure 6(d), only a slight change in the peak radius can be observed even after grinding 50 grooves.

3.4 Small mounted wheel for grinding micro mold

A glass lens mold made of cemented carbide material requires both a mirror finished surface and an accurate profile geometry. In order to

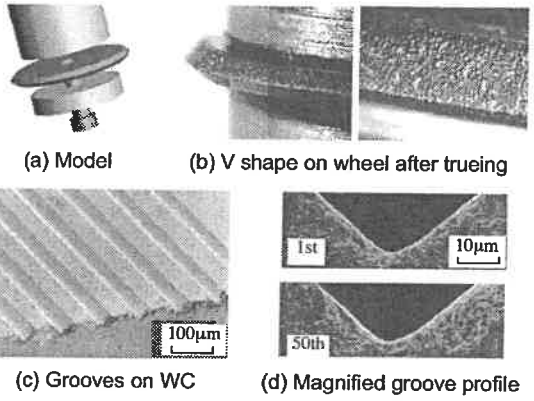

(a) Model (b) V shape on wheel after trueing

(c) Grooves on WC (d) Magnified groove profile

Figure 6: Profiled wheel made of electrically conductive CVD diamond thick film and ground grooves.
(Wheel size=ϕ20_t0.5mm, V_s=17m/min, V_w=200mm/min, a=1_m, L=5mm, n=50passes, V-shape top radius R=6μm)

meet the requirements, a diamond grinding wheel containing very small grits finer than SD1500 is usually used for manufacturing the mold. However, diamond wheels with such fine grits encounter problems of non-uniform dispersion of the grits in the binder and low fixing strength for the grits by the binder. In addition to these, the problem of reduction of abrasives acting as cutting edges arises when a small diameter wheel is used for grinding of micro lens mold. To cope with those problems, a micro mounted wheel utilizing electrically conductive CVD diamond thick film is proposed. Figure 7 shows a manufacturing procedure of such micro mounted wheels utilizing ED truing and schematic grinding of a micro lens mold with one of the wheels. Figure 8 shows a small mounted wheel made by ED truing after blazing a circular EC-CVD diamond segment on a cemented carbide rod with a diameter of 3 mm. Figure 9 shows a V-shaped groove ground with the wheel inclined at 45 degrees to the cemented carbide workpiece surface.

4. Conclusion

Three kinds of grinding wheels have been manufactured using the commercially available electrically conductive CVD diamond thick film and their grinding performances have been investigated. The followings can be concluded from these experiments:

1. A diamond segment wheel, in which cutting edges are generated by EDM on the electrically conductive CVD diamond film, has a sufficient grinding ability of obtaining a mirror surface finish of Ra=0.008μm and Ry=0.110μm on a cemented carbide surface.
2. A V-shaped profile grinding wheel with a peripheral peak angle of 90 degrees and a peak radius of 6μm can be manufactured by

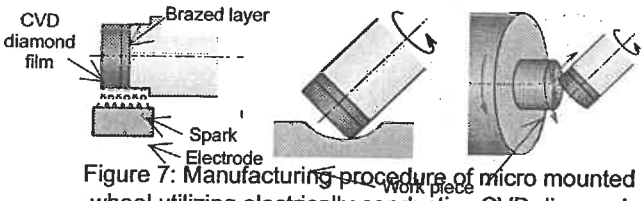

Figure 7: Manufacturing procedure of micro mounted wheel utilizing electrically conductive CVD diamond thick film and its use

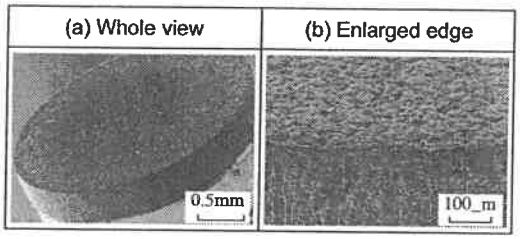

Figure 8: Micro mounted wheel and enlarged edge
(ϕ3mm, CVDITE-CDE)

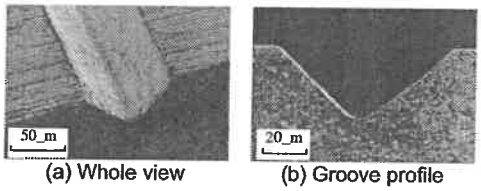

(a) Whole view (b) Groove profile

Figure 9: V-shape groove ground with micro mounted wheel
(V_s=17m/min, V_w=200mm/min, a=1μm, n=20passes)

ED trueing on a diamond film disc and grinding of V-shaped grooves on a cemented carbide workpiece is also possible using this small mounted wheel with negligible wheel wear.

The authors would like to express their heartfelt thanks to Element Six Ltd, Osawa Scientific Studies Grants Foundation and Sodick Co., Ltd. for their kind cooperation.

5. References

[1] Suzuki, K., Iwai, M., Uematsu, T., Sharma, A., 2003, Development of a Grinding Wheel with Electrically Conductive Diamond Cutting Edges, Advances in Abrasive Technology VI, Proc. of ISAAT2003, 239-244.

[2] Anon, Element Six Limited – Catalog (Element Six Limited).

[3] Suzuki, K., Uematsu. T., Nakagawa, T., 1987, On-machine trueing/dressing of metal bond grinding wheels with electro-discharge machining, Annals of the CIRP, 36:115-118.

[4] Novikov, H.B., 1993, Physicality of diamond, (Ohmsha Ltd., Japan).

[5] Inuzuka, T., 1990, Diamond film (Kyoritu Shuppan Co. Ltd., Japan).

Study on Elastic Deformations of Grinding Wheels due to Centrifugal Forces

Takazo YAMADA and Hwa-Soo LEE

Department of Mechanical Engineering, College of Science & Technology, NIHON University, Tokyo.

Abstract: Grinding wheels are deformed by the effect of centrifugal forces. In this study, applying previously proposed mathematical model of grinding wheels, the elastic deformations due to centrifugal forces are analyzed. And, the analyzed elastic results are evaluated experimentally. From these results, it is clarified that the effect of centrifugal forces on the elastic deformations of grinding wheel can be analyzed quantitatively by using the mathematical model previously proposed.

1. Introduction

In grinding operations, elastic deformations of grinding wheels are one of parameters effecting on machining accuracy. Forces affecting on grinding wheels in machining process are grinding forces, contact forces with workpieces and/or the centrifugal forces. By acting these forces, grinding wheels are deformed and they cause machining errors. Therefore, in order to realize higher machining accuracies in grinding operations, elastic deformations of grinding wheels have to be took into account quantitatively.

In the previous study, in order to analyze the dynamic phenomena of grinding wheels, a mathematical model of grinding wheels was proposed. This model consists of rigid bodies as abrasive grains and spring elements as bonds connecting successive grains. A basic unit of this model consists of nine rigid bodies and sixteen spring elements. At the first stage, spring constants of bonds connecting successive two grains in vitrified and resinoid wheels were calculated [1][2]. And the next, the contact stiffness of grinding wheels was analyzed with a mathematical model depending on the spring constant previous obtained [3]. By the evaluation of the analyzed results experimentally, it was clarified that proposed model could be applied to dynamic analysis of grinding wheels.

In this paper, in order to calculate the amounts of elastic deformations of grinding wheels due to centrifugal forces, theoretical analyses using proposed model and experiments using actual grinding wheels are carried out. From these results, it is known that grinding wheel radius expands about 2μm in vitrified wheels and about 7μm in resinoid wheels. According to the results shown above, it is clarified that the amounts of radius expansion in rotating wheels by the effect of centrifugal forces can be estimated quantitatively by applying the proposed model.

2. Analytical method

Grinding wheels consist of abrasive grains, bonds and pores as shown in figure 1(a). In this study, a mathematical model of grinding wheels as shown in figure 1(b) was proposed, and this basic unit consists of nine rigid bodies and sixteen spring elements. Arranging this basic unit, the grinding wheel as shown in figure 1(c) is modeled.

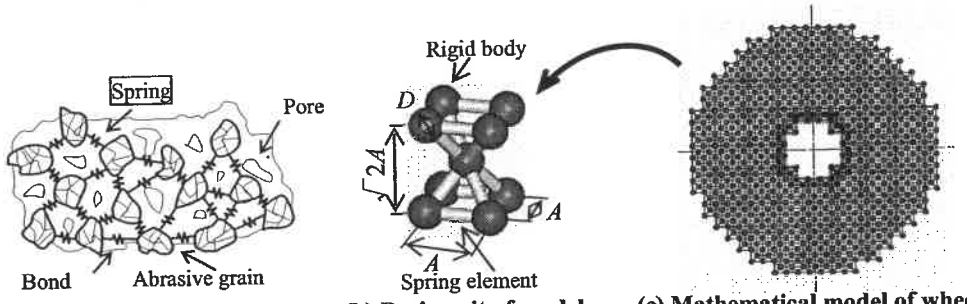

(a) Grinding wheel model **(b) Basic unit of model** **(c) Mathematical model of wheel**

Fig.1 Proposed mathematical model of grinding wheels

Figure 2 shows the condition of this analysis. Taking into account the geometrical symmetry, analyzing model can be treated in quarter. In this model, the inside boundary is restricted in the Z axis directing the wheel spindle, and symmetric condition is set in X and Y directions. The elastic deformations in radial directions are calculated under the condition that spindle rotating speed is N min^{-1}.

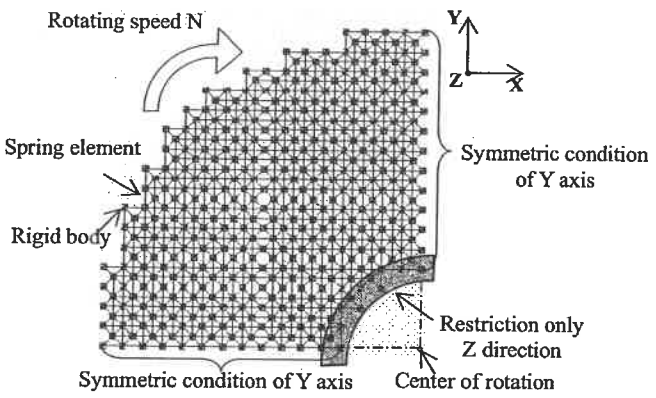

Fig.2 Condition of analysis

From previous studies, it was clarified that the spring constant k, N/μm, connecting successive two grains can be calculated from grain size # as k_v=470/# for vitrified and k_b=130/# for resinoid wheels. On the other hand, in the proposed mathematical model, the mass of bonds connecting two grains, which have effect on the centrifugal forces, cannot be considered as it is. In order to take into account this effect, it is assumed that bond masses are included in each mass of grains in this study. Table 1 shows the calculated results of mass ratios between abrasive grains and bonds corresponding to the grain size. First, the mass of abrasive sticks are measured for grain size #60, 80, 100 and 120 of resinoid wheels and #120 of vitrified wheels. Next, the numbers of abrasive grains in this model are counted. Since densities and diameters of grains had been known, using those parameters and the numbers of abrasive grains, the mass of abrasive grains for abrasive stick can be evaluated. From such a treatment, it can be known that the ratio of the mass of abrasive grains to grinding wheel is 80%, and the ratio of mass of bonds is 20%. According to the result shown above, the mass of rigid body in this analysis is set as 1.25 times that of abrasive grain.

Table 1 Calculated results of grain masses

	Resinoid wheels				Vit.
Grain size	#60	#80	#100	#120	#120
Size of abrasive stick	8.0×5.7×60.2				
Mass of grinding wheel	**6.01g**	**5.82g**	**5.82g**	**5.79g**	**5.92g**
Amount of abrasive grain	177051	483466	1389544	2258804	2258804
Diameter of grain	250μm	177μm	125μm	105μm	105μm
Density of grain	3320 kg/m^3				
Mass of a grain	0.0272mg	0.00964mg	0.00340mg	0.00201mg	0.00201mg
Mass of grains	**4.80g**	**4.72g**	**4.73g**	**4.71g**	**4.71g**
Ratio of mass of grains for grinding wheel	**80%**	**81%**	**81%**	**81%**	**80%**
Ratio of mass of bonds for grinding wheel	**20%**	**19%**	**19%**	**19%**	**20%**
Mass of rigid body	**0.0340mg**	**0.0121mg**	**0.00425mg**	**0.00251mg**	**0.00251mg**

3. Analytical results

Table 2 shows the condition used in this analysis. Used grinding wheels sizes are diameter 100, 150 and 205mm, the elastic deformations of model in radial direction in rotating speed 2800min^{-1} is analyzed. Figure 3 shows analyzed results of elastic deformations of model. Since proposed model has anisotropy itself, deformation is not uniform. And then, figure 3 shows the maximum and the minimum amounts of analyzed

Table 2 Condition and wheel sizes of analysis

Grain size	#60	#80	#100	#120
External dia.	100,150,205mm	100mm		
Internal dia.	50.8mm			
Rotating speed	2800min^{-1}			

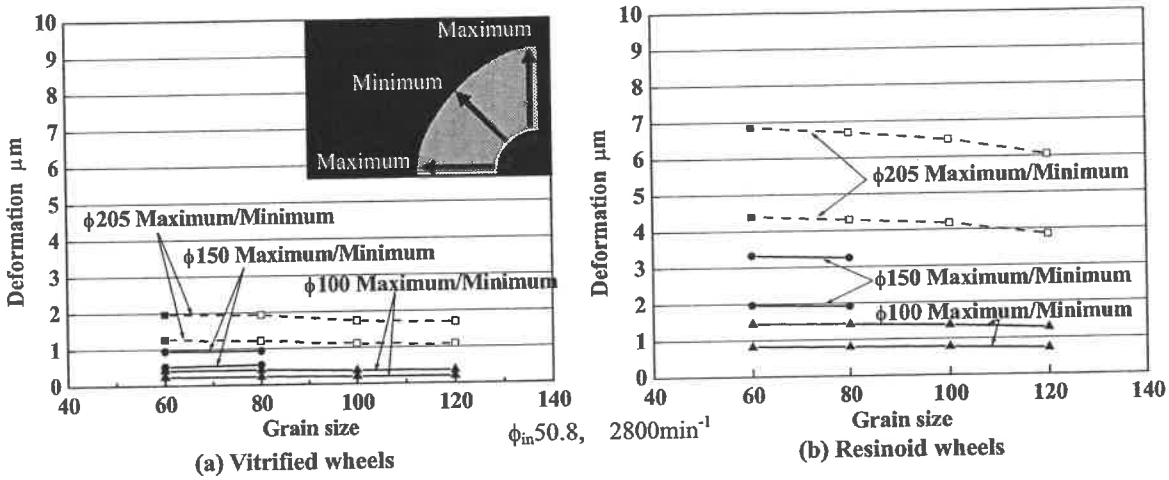

Fig.3 Results of analysis

results. In the experiments described later, grinding wheels with 205mm diameter are used. However, in case of that the grain sizes #80, #100 and 120 with diameter 205mm are not be analyzed, because of the restriction of the model size depending on the used PC. From these analyzed results, it may be known that elastic deformations due to centrifugal force are 1-2μm for vitrified wheels and 4-7μm for resinoid wheels.

4. Experimental results

Elastic deformation of the grinding wheels in radial direction is experimentally measured under the condition that diameter is 205mm and rotating speed is 2800min^{-1}. Measuring method is as follows. Using acrylic resin plate for specimen, grinding wheel shapes in low and high rotating speed are copied to the specimen surfaces. First, a flat surface is made on the specimen as shown in figure 4(a). And a groove is made under the condition that spindle rotating speed is 250min^{-1} and depth of cutting is about 5μm as shown in figure 4(b). Next, keeping the depth of cut same and increasing the spindle rotation speed to 2800min^{-1} , a new groove is made in the next to the previously made groove as shown in figure 4(c). The geometrical shapes of the section of two grooves are measured by a form measuring device. Finally comparing these measured two sections, the amounts of elastic deformations due to centrifugal force is evaluated.

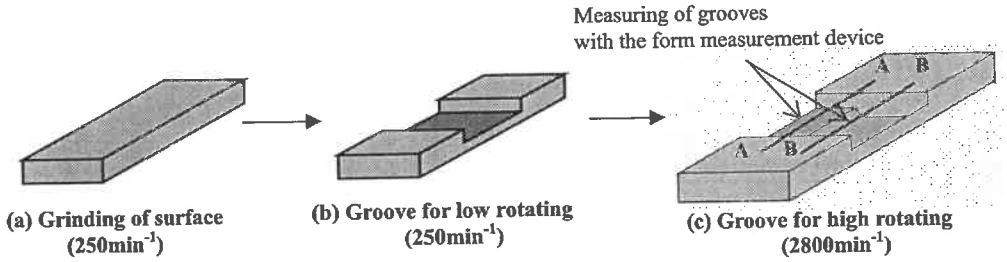

Fig.4 Method of experiment

Figure 5(a) and (b) show the measured geometrical shapes of section in rotating speed 250min^{-1} and 2800 min^{-1} with a resinoid wheel #60. A difference in level in case of rotating speed 250min^{-1} is 5.9μm and in rotating speed 2800 min^{-1} is 13.0μm. From the difference of two levels, the amount of elastic deformation due to centrifugal force can be estimated to be 7.1μm. Figure 6 shows the elastic deformations estimated in the same method for vitrified and resinoid wheels in grain size #60, 80, 100 and 120. In this figure, plots show the experimental results and lines show the analyzed result. Comparing them, it is known that experimental results are almost same amounts with the maximum amounts of analyzed results. These maximum amounts of analyzed results indicate the elastic deformation in lowest stiffness directions in proposed model as shown figure 3. Since, as well known, actual

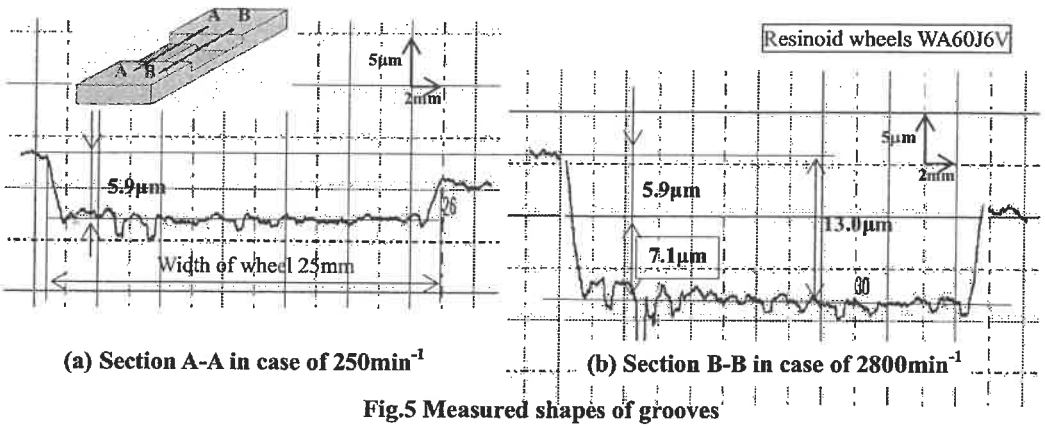

(a) Section A-A in case of 250min^{-1} (b) Section B-B in case of 2800min^{-1}

Fig.5 Measured shapes of grooves

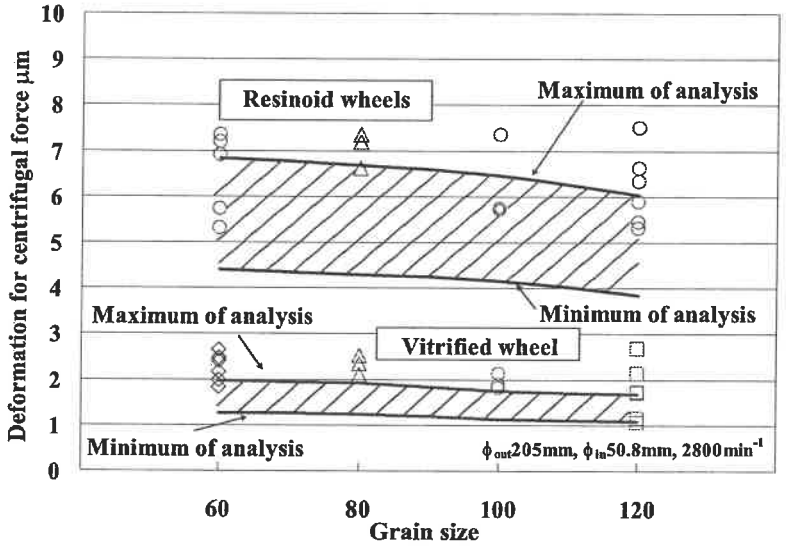

Fig.6 Results of deformations for analyses and experiments

grinding wheel is not isotropic body, it can be considered that the elastic deformation due to centrifugal force may not be uniform in any directions. On the other hand, since the most external shapes of grinding wheel are copied to the surface of acrylic resin, experimental results shown in figure 6 are almost same amounts of the maximum analyzed results.

5. Conclusions

Using proposed mathematical model of grinding wheels, it is known that the maximum amounts of analyzed results agree with experimental results. And, it is clarified that the elastic deformation of grinding wheels due to centrifugal force can be analyzed quantitatively.

References

[1] Hwa-Soo Lee, Kojiro SADASUE, Yujiro ITO and Tadashi WAKABAYASHI, Static Modeling of Grinding Wheel, Proceedings from ASPE2000 Annual Meeting, ASPE(2000-10)99.

[2] Takazo YAMADA, Hwa-Soo LEE, T. SHIKAUCHI and H. MATSUSHITA, Identification of the Static Stiffness of Grinding Wheels with Resin Bond, Proceedings from ASPE2002 Annual Meeting, ASPE(2002-10)521.

[3] Takazo YAMADA, Hwa-Soo Lee and Hiroyuki MATSUSHITA, A Study on the Contact Stiffness of Grinding Wheels, Advances in Abrasive Technology VI, ISSAT(2003)263.

Ultra Precision Grinding of Micro Aspherical Surface
– Development of a Three-Axes Controlled Single Point Inclined Grinding Method –

Yuji Yamamoto, Hirofumi Suzuki, Tadashi Okino, Yoshio Hijikata and Toshimichi Moriwaki
Kobe University, Rokkoh, Nada, Kobe, 657-8501, Japan

Masahiko Fukuta, Masahiko Nishioka and Yoichi Kojima
Toshiba Machine Co. Ltd., Ohoka, Numadu, Shizuoka, 410-8510, Japan

1. Introduction

Needs of digital devices increase rapidly in recent years, and the demand for a micro axis-symmetric aspherical glass lens of large NA (numerical aperture) is expanding rapidly especially in the device for digital camera, camera-equipped mobile phone, DVD pick-up and the optical transmission [1][2]. Moreover blue lasers have been increasingly used to make wavelengths short and the maximum tangent angle of the lens reaches to 70 degrees. In addition, demand of glass lenses is high because glass lenses are superior to plastic lenses in optical characteristics. The glass lenses are manufactured by glass molding method by using ceramics dies such as WC (tungsten carbide) or SiC (silicon carbide) [3]. Therefore ultra-precision grinding technology of ceramic dies is gaining importance.

Authors have successfully to develop inclined grinding method, and micro aspherical shape has been obtained. In previous researches the grinding system shown in Figure 1 was developed. The grinding wheel axis was 45 degrees inclined from workpiece rotational axis. The grinding spindle was an air bearing and the maximum rotational rate of grinding wheel was $15\times10^4 min^{-1}$. The grinding head was actuated by two-axes (X, Z) drives, the wheel center point was calculated numerically by using Newton-Raphson method. This system was suitable for grinding micro aspherical surfaces and a form accuracy of less than 0.1 μmP-V was obtained. The improvement of the form accuracy will be required because the specifications of micro lenses become more and more strict in future. However, the shape correction cannot be done satisfactorily, because the wheel wear is not even and the grinding point on the wheel moves as shown in Figure 2. In this case, wheel truing is necessary and it will increase the non-processing time. In this paper, a new grinding method is proposed to solve the above problems. In this method, three-axes (X, Y, Z) are controlled simultaneously so that the position of the grinding point on the diamond wheel is fixed. Then the grinding system was developed and grinding experiments of using tungsten carbide micro dies were carried out.

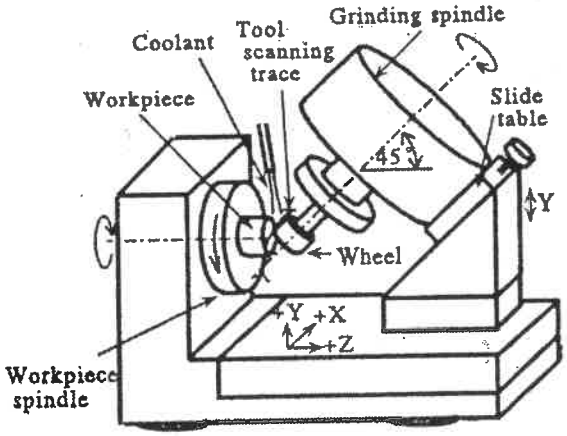

Fig.1 Micro axis-symmetric aspherical grinding system

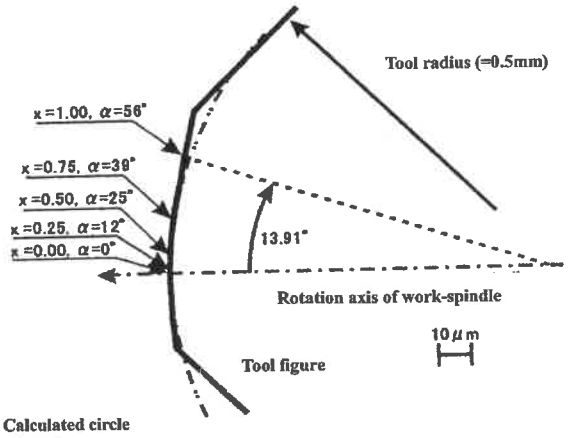

Fig.2 Changes of grinding point and unequal wheel wear (conventional micro aspherical grinding method)

2. Wheel path of grinding point fixation method

The rotation axis of wheel-spindle inclines by 45 degrees. The wheel center point O (X_o, Y_o, Z_o), grinding point G (X_g, Y_g, Z_g), and the normal vector $\vec{n}(a,b,c)$ at the grinding point are shown in Figure 3. An axis-symmetric aspherical function is given by $Z=f((X^2+Y^2)^{0.5})$, and a normal vector in grinding point G (X_g, Y_g, Z_g) is given by Eq.(1).

$$\vec{n}(a,b,c)=(-\frac{\partial f}{\partial X},-\frac{\partial f}{\partial Y},1) \tag{1}$$

And the relationship between the wheel center point O and the grinding point G is obtained Eq.(2).

$$\left.\begin{aligned} X_o &= X_g+\frac{a}{l}\cdot R_1+\frac{a}{L}R_2 \\ Y_o &= Y_g+\frac{b}{l}\cdot R_1+\frac{b-c}{2\cdot L}R_2 \\ Z_o &= Z_g+\frac{c}{l}\cdot R_1+\frac{c-b}{2\cdot L}R_2 \end{aligned}\right\} \tag{2}$$

Where, $|\overrightarrow{GP}|=R_1$, $|\overrightarrow{PO}|=R_2$, $l=\sqrt{a^2+b^2+c^2}$ and $L=\sqrt{a^2+0.5\cdot(b-c)^2}$.
To let the grinding point in radial position $r=(X^2+Y^2)^{0.5}$, an aspherical function is expressed as follows:

$$Z=f(r),\ X=r\cdot\cos\theta,\ Y=r\cdot\sin\theta \tag{3}$$

The normal vector is expressed as follows:

$$\begin{aligned} \vec{n}(a,b,c) &= (-\partial r/\partial X,\ -\partial r/\partial Y,\ 1) \\ &= (-\partial r/\partial X\cdot df/dr,\ -\partial r/\partial Y\cdot df/dr,\ 1) \\ &= (-f'(r)\cdot\cos\theta,\ -f'(r)\cdot\sin\theta,\ 1) \end{aligned} \tag{4}$$

In the conventional method, $\angle QPO$ becomes 45 degrees in case of r=0. On the other hand, $\angle QPO$ always becomes 45 degrees in the proposed method as shown in Figure 4. Therefore, the next relationship is obtained.

$$\overrightarrow{PQ}\cdot\overrightarrow{PO}=|\overrightarrow{PQ}|\cdot|\overrightarrow{PO}|\cos 45° \tag{5}$$

From Eq.(5) of the following relationship is obtained

$$a^2=2bc \tag{6}$$

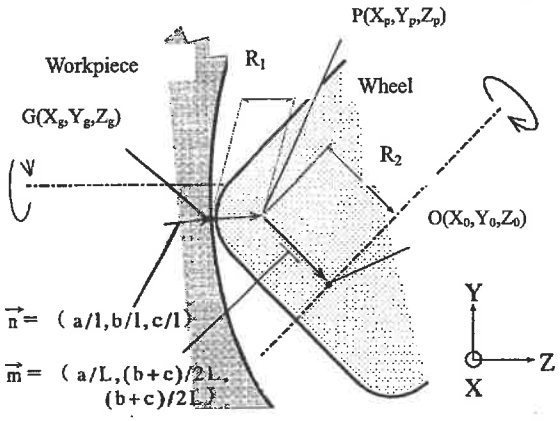

Fig.3 Calculation of tool path in the inclined grinding method

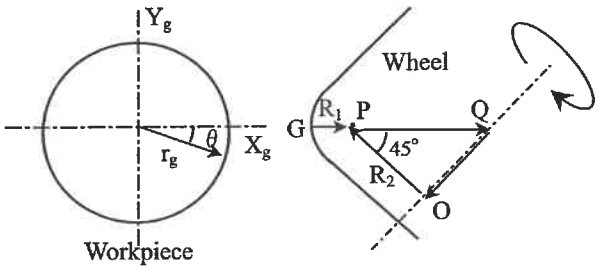

Fig.4 Calculation of tool path

The next expression is obtained from Eqs.(4) and (6).

$$\sin\theta = \frac{1}{f'(r)} - \sqrt{\frac{1}{f'(r)^2}+1} \quad \text{(Concave surface)} \qquad (7a)$$

$$\sin\theta = \frac{1}{f'(r)} + \sqrt{\frac{1}{f'(r)^2}+1} \quad \text{(Convex surface)} \qquad (7b)$$

When a radial position of the grinding point on the ground workpiece surface is assumed to be r_g, the relationship of the next expression is obtained from Eq.(3).

$$X_g = r_g \cdot \cos\theta \,,\; Y_g = r_g \cdot \sin\theta \,,\; Z_g = f(r_g) \qquad (8)$$

Therefore, in this method the angle θ in the grinding point on the workpiece is calculated from Eq.(7a), (7b), the coordinates G (X_g, Y_g, Z_g) of the grinding point is calculated from Eq.(8), and finally the coordinates of wheel center point O (X_o, Y_o, Z_o) is obtained by Eq.(2).

3. Grinding experiments

A view of the simultaneous 4-axis (X, Y, Z, C) controlled grinding machine (Toshiba Machine Co. Ltd. ULG-100D(SH3)) is shown in Figure 5. The grinding wheel actuated in X, Y and Z-axes by the linear scale feedback system of 1 nm positioning resolutions. In the grinding test, the aspherical workpiece was vacuum chucked to the workpiece spindle (C-axis). The diamond wheel was adjusted to grinding spindle with collet chuck on the Y-axis table. Table 1 shows the grinding conditions. As a wheel, a resinoid bonded diamond wheel of # 1200 was used and diameter was about ϕ 2 mm. The wheel shape was columnar shape and the tip end was trued to radius of 0.2 mm. As the workpiece, molding die of about 1.5 mm in radius curvature and radius was tested and the material was tungsten carbide (Figure 6). Micro aspherical surface was measured with contact type of surface measurement instrument (Form Talysurf) with a 2 μm radius stylus.

Table 1 grinding conditions

Grinding wheel	Resinoid bonded diamond
Grain size	#1200
Diameter	ϕ2 mm
Rotational rate	4×10^4 rpm
Workpiece	Tungsten carbide
Rotational rate	3×10^2 rpm
Depth of cut	0.5 μm/pass
Feed rate	0.3 mm/min
Coolant	Solution type

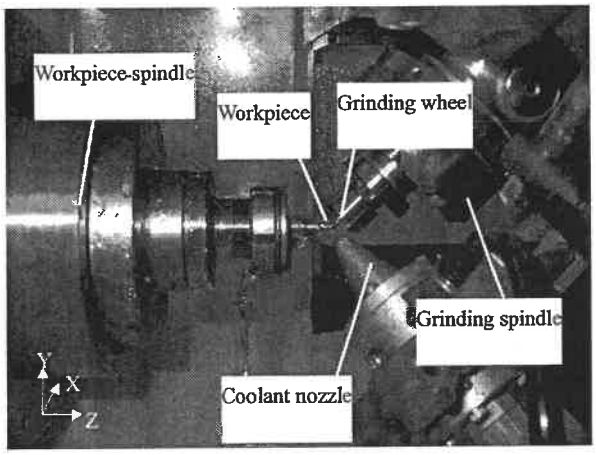

Fig.5 A view of the simultaneous 4-axes controlled grinding machine

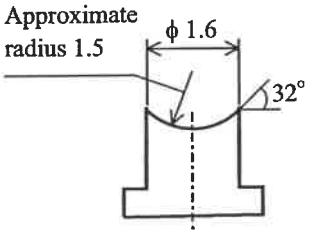

Fig.6 Shape of target aspherical molding die

4. Experimental results

Figure 7 shows the form deviation profile of first workpiece in the proposed grinding method. The form accuracy was about 0.09 μmP-V. Figure 8 shows the change of form accuracy to the number of grinding passes in case of the conventional and the proposed method. The initial form accuracy was 0.09 μmP-V. After 200 grinding passes (correspond to the finish grinding of 20 dies), the form accuracy was about 0.2 μmP-V in the proposed method and about 1.3 μmP-V in the conventional method. Moreover, wheel tip shape after 200 passes finish grinding is shown in Figure 9. It can be seen that there is a flat area in the wheel tip in the proposed method.

5. Conclusions

The micro aspherical grinding by the grinding point fixation diagonal axis grinding method of three axis control simultaneously was proposed, and examined in this research, therefore it was clarified that this proposed method was effective.

References

1) Hirofumi Suzuki, et al., Precision Grinding of Aspherical CVD-SiC Molding Die, Int. JSPE,1998, 32(1):25-30.
2) Hirofumi Suzuki, et al., Precision Grinding of Micro Aspherical Surface, Proc. of ASPE98, 1998:149-152.
3) Hirofumi Suzuki, et al., Ultra Precision Grinding of Micro Fresnel Shape, Proc. of ABTEC'99, 1999:59-65.

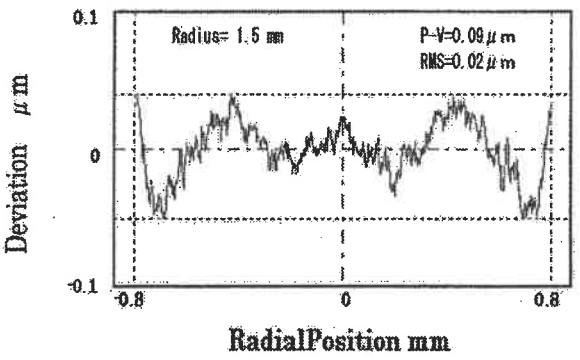

Fig.7 Form deviation profile after grinding

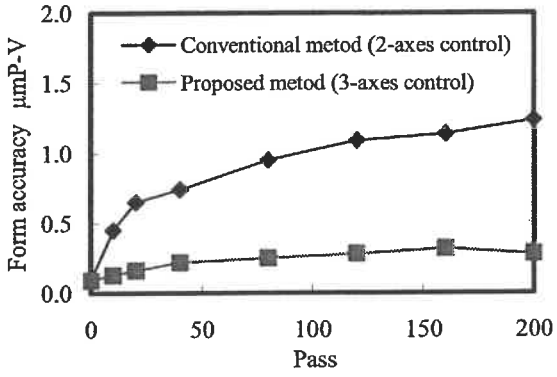

Fig.8 Changes in form accuracy of conventional and proposed method

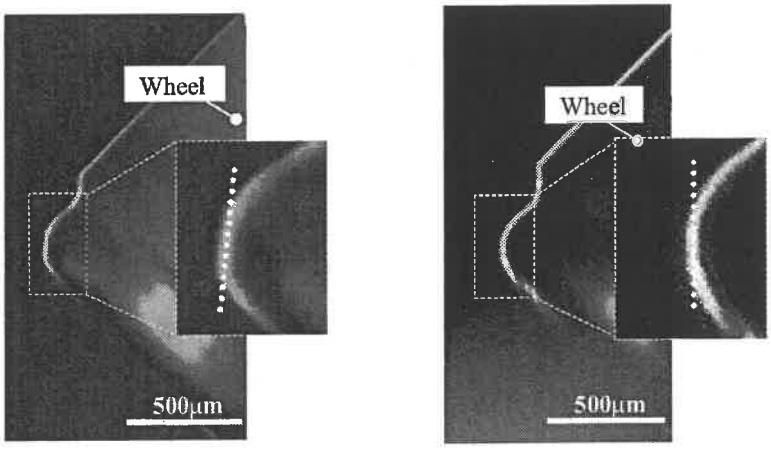

(a) Conventional method (2-axes control) (b) Proposed method (3-axes control)

Fig.9 Wheel tip shape after 200 passes of finish grinding

Quantitative Investigation of Relation between CBN Wheel Life and Loading Using Automatic Image Processing System for Wheel Surface

Heiji YASUI*, Takahito KAMIYA* and Kenji MARUO*

*:Dept. of Mechanical Engineerring & Materials Science, Kumamoto University
2-39-1 Kurokami , Kumamoto 860-8555, JAPAN

1. Introduction

The grinding wheel surface condition characterized by the distribution and shape of cutting edges and loadings has strong influence on grinding results such as surface roughness, grinding force and temperature, and so on. There are a great number of cutting edges on a wheel surface, which are more than several thousands and one distributed irregularly. To evaluate quantitatively the surface condition, in our previous researches[1),2)], the automatic image processing system attached to a surface grinder is newly developed. In the system, the evaluation is automatically done by means of quick digital handling technique of numerous microscopic images of cutting edges taken precisely from the wheel surface through a video-capture system.

By applying the system to several grinding experiments, the system is ascertained to be useful for pursuing and evaluating quantitatively the behavior of numerous cutting edges. The loading generated by grinding of workpiece, however, can not be evaluated adequately because the loading can not be extracted, in the high accuracy, from the original photo by the developed image processing software program.

In the research, the new software program for the separation of loadings and cutting edges from the original photo is additionally developed. By using the new program, the change of loading and cutting edge on metal bond CBN wheel surface with plunge grinding of a die steel (SKD11) is pursued precisely and quantitatively until wheel life. On the basis of the results, the relation between the CBN wheel life and loading is discussed.

2. Image processing for loading

Figure 1 shows the schematic view of the automatic image processing system developed in the previous research[2)]. The original photo image is taken into the computer through the microscope, CCD camera and video-capture-board. The displacement of the wheel surface taken successively to the computer is automatically controlled precisely with the servo-motor driving the wheel spindle. In the research, the encorder of servo-motor moving the microscope is changed from the incremental type to the absolute type. It is ascertained useful for the precise controll of wheel surface displacement.

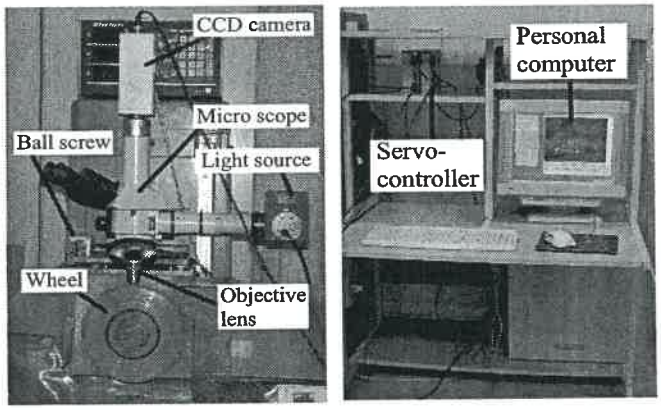

(a) Surface grinding with micro-scope and CCD camera (b) servo-controller and personal computer

Fig. 1 Appearance of the automatic image processing system

Figure 2 shows the two types of original wheel surface of the G type and the L type, on which loading is observed little and big, respectively. In the image processing developed previously for the G type, the brilliant image is decided firstly by extracting lighter pixels than the brilliance of threshold. Secondly, the outline image between the bond and cutting edge is obtained by calculating the difference of the neighborhood pixels. Finally the images of the cutting edges are extracted by overlapping the brilliant image and the outline.

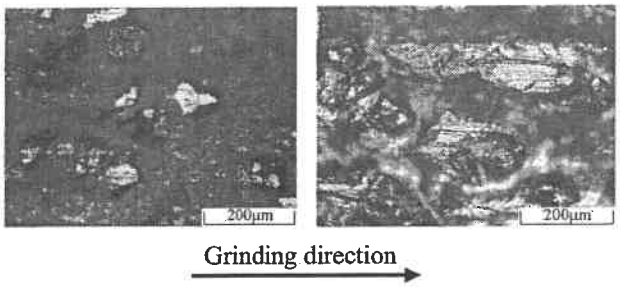

(a) G type (b) L type

Fig.2 Comparison of wheel surface having little loading with big loading
[CBN140Q100M,SKD11(Hv=800),Vg=30m/s, vw=1.8m/min,t_f=5μm/pass,Soluble(1/50)]

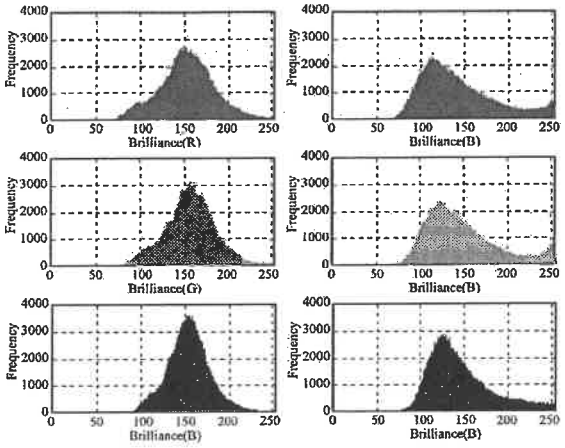

(a) G type (b) L type

Fig.3 Histogram of RGB color for the original image

If such an image processing for the G type is applied to that for the L type, a lot of loading images are extracted at the same time together with cutting edge image because the brilliance of threshold for loading is lighter than that of flat cutting edge formed by grinding the workpiece. Therefore it is necessary to build the separation technique of cutting edge and loading from the original photo.

To make the new program for the separation, the following handling is added newly to the previous image processing software program. The histograms of RGB color for the original surfaces of G type and L type are shown in **Fig.3**. As compared with the G type, the brilliance curve for all the colors of red, green and blue in the L type shows higher frequency in the region of high brilliance. Especially the brilliance curves of L type for the colors of red and green have two peaks. Thus, the brilliance of RGB color is used for the distinction between loading and cutting edge. Namely after the brilliant image is decided firstly due to the previous image processing for the G type, the stronger brilliance part of RGB colors than a given threshold in the image as decided above is selected as loading.

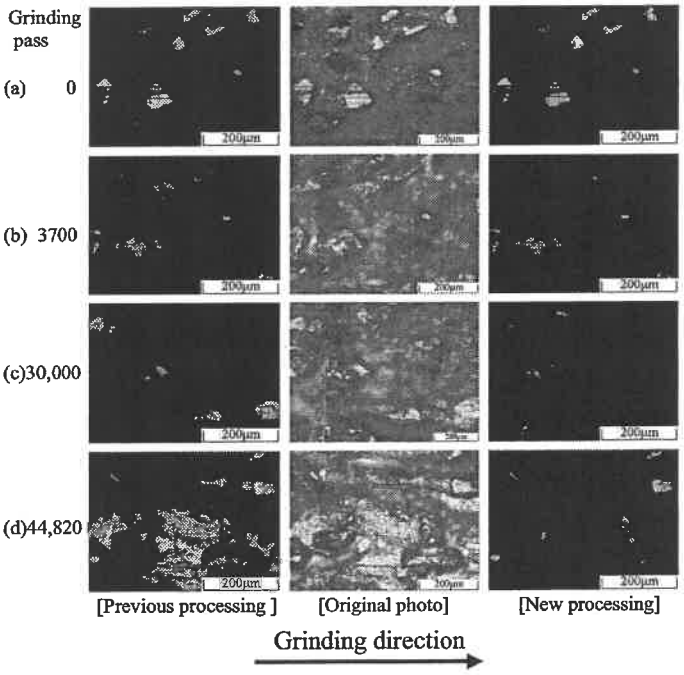

Fig.4 Change of wheel surface condition with grinding process
[CBN140Q100M,SKD11(Hv=800),Vg=30m/s, vw=1.8m/min,t_f=5μm/pass,Soluble(1/50)]

Figure 4 shows the change of the original photos of wheel surface with grinding process and those extracted images after the previous and new image processing. From the original photos, it is found that loading occurs little until numerous grinding passes of 30,000. Loading begins to be generated a little at 30,000 passes and to be observed big at 44,820 passes on the wheel surface. The images after the previous and new image processing are almost the same until 30,000 passes. At 44,820 passes, however, the image after the previous processing is much bigger than those after the new processing because it includes both images of cutting edge and loading. Comparing with the extracted image after the new processing at 44,820 passes, the cutting edges on the original photo are found to be overlapped on the extracted image in the relatively high accuracy. Accordingly it is referred

that the loading image is excluded in the extracted image after the new processing. From the results as mentioned above, the extracted loading image is considered to equal approximately the image obtained from the difference between the previous and the new image processing.

3. Experiments

3.1 Evaluation of wheel surface conditions

In order to evaluate the wheel surface conditions precisely, the wheel surface is divided, as shown in **Fig.5**, into 25 tracks to axial direction of wheel spindle and 938 locations along the circumferential direction of wheel. One photograph image has the dimensions of 600μm in axial direction and 480μm in circumferential direction. The whole wheel surface of ϕ200mmx12mm used in the experiment consists of 23,450 images. The evaluation of wheel surface condition is done using the parameters such as cutting edge density n_p, cutting edge ratio η and successive cutting edge spacing a.

3.2 Experimental procedure

The experiments are carried out by plunge grinding method with a surface grinder. The experimental conditions are summarized in **Table 1.** One grinding pass corresponds to grinding once the workpiece of 100mm long.

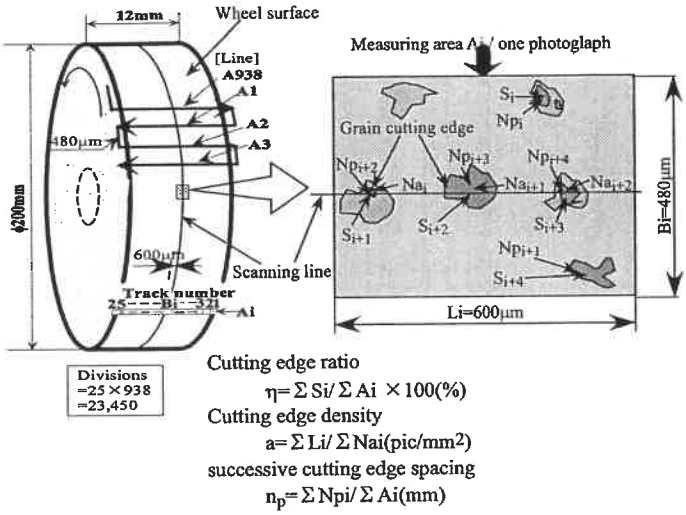

Fig.5 Division of the wheel surface and parameters for the evaluation of wheel surface condition

Table 1 Experimental conditions

Wheel	CBN140Q100M Do×B×Di:ϕ200×12×ϕ50mm
Workpiece	SKD11(Hv≒800) Lw×Bw:100mm×10mm
Wheel speed	Vg=30m/s
Table speed	v_w=1.8m/min
Depth of cut	t_i=5μm/pass
Coolant	Soluble(1/50),Flow rate:12*l*/min

4. Results and discussions

Figure 6 shows the quantitative variation of cutting edge ratio, cutting edge density and successive cutting edge spacing after the previous and new image processing in grinding process. The data is average over the whole wheel surface. Generally the cutting edge ratio and cutting edge density are within the range of 3 to 0.5 % and 30 to 10 pic/mm^2, respectively. From the results, the number of cutting edges on the whole grinding surface is over twenty thousands. The average area of a cutting edge is about 525 μm^2, which equals to the area of about 23μmx23μm in square shape. In the initial grinding of 0 to about 3000 passes, the cutting edge ratio and cutting edge density decrease rapidly. On the other hand, the successive cutting edge spacing increases steeply. From the decrease of cutting edge density, it is considered that the numerous cutting edges are largely fractured and/or removed from the bond because the flat area of cutting edge after dressing is large and , as the result, the grinding force to cutting edge becomes big. Until 30,000 passes after the initial process, the wheel surface conditions of cutting edge ratio, cutting edge density and successive cutting edge spacing is kept steadily at almost the same situation. In the steady state, the wheel surface image after the previous and new image processing is almost the same.

Over 30,000 passes, however, the cutting edge ratio and cutting edge density after the previous image processing increase steeply and the successive cutting edge spacing decreases largely. On the other hand, the cutting edge ratio and cutting edge density after the new image processing do not change largely and the

successive cutting edge spacing increases somewhat. The difference between the wheel surface image after the previous and new image processing depends on the difference between the image processing for loading.

Over 30,000 passes, as shown in **Fig.7,** the step in wheel radial direction between cutting edge and bond tail is considered to be run away by wearing of cutting edge and, as the results, the loading increases rapidly. The occurrence of a lot of loading has bad influence on grinding results[2]. Accordingly the metal bond CBN wheel life is referred to be related to the generation of a large quantity of loading

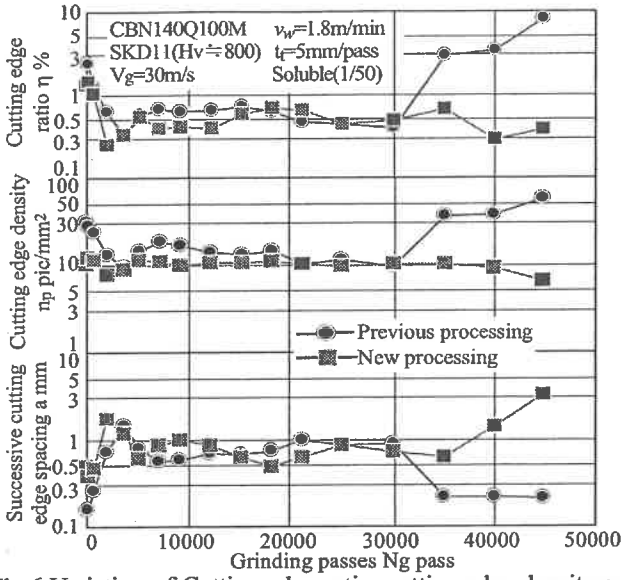

Fig.6 Variation of Cutting edge ratio, cutting edge density and successive cutting edge spacing with grinding process [CBN140Q100M,SKD11(Hv=800),Vg=30m/s, vw=1.8m/min,t_t=5μm/pass,Soluble(1/50)]

5. Summary

The main results obtained are as follows:

(1) The new software program is available for separating loading and cutting edges from original photo.

(2) The improved automatic image processing system is useful evaluating the change of wheel surface conditions characterized by the distribution and shape of numerous cutting edges and loadings with grinding process

(3) Loading begins to increase steeply just after the step in radial wheel direction between the cutting edge and bond tail is run away by wearing of cutting edge.

(4) The occurrence of metal bond CBN wheel life is related to the generation of a large quantity of loading.

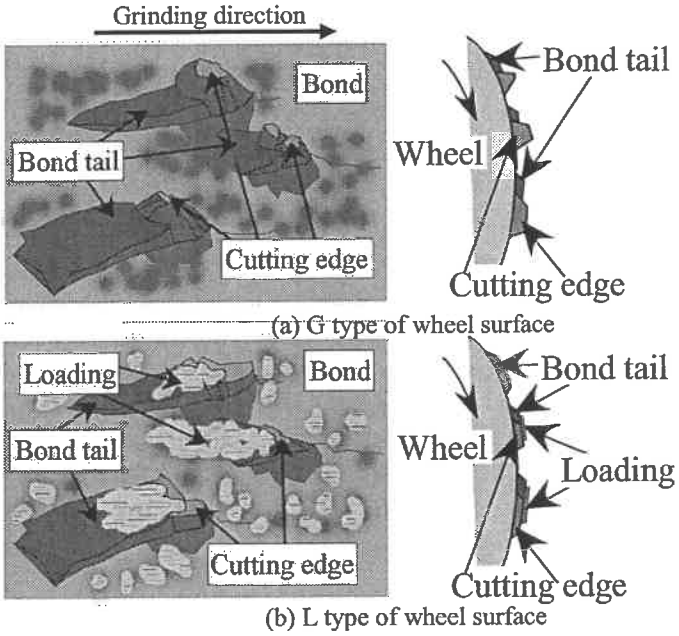

Fig.7 Estimated models for wheels of G type and L type

Acknowledgement

The authors would like to thank Noritake Super Abrasive Co. Ltd., Yushiro Chemical Industry Co. Ltd., and Okamoto Machine Tool Works Co. Ltd. for providing grinding wheels, grinding fluids and grinder.

References

[1] H. Yasui *et al.*: Development of automatic image processing system for evaluation of wheel surface condition x in ultra-smoothness grinding., Proc. 2001 ASPE Annual Meeting, Vol.25 (2001) 62

[2] H. Yasui *et al.*: Quantitative Analysis of the Cutting Edge Behavior on Wheel Surfacein Long Grinding Process., Proc. 2003 ASPE Annual Meeting,

Influence of Fluid Supply on Ultra-smoothness Grinding of Silicon Nitride Ceramic with #140 Metal Bond Diamond Wheel

Heiji YASUI* , Takekazu SAWA* and Yuki YAMAMOTO*
***Dept. of Mechanical Engineering & Materials Science, Kumamoto University**
2-39-1 Kurokami , Kumamoto 860-8555, JAPAN

1. Introduction

Grinding operation is one of the most effective manners for high smoothness machining of fine ceramics. However, it is difficult to form crack-free high smoothness surface by ductile-mode grinding because of their mechanical properties of high brittleness. To machine the ceramic component of high quality by low productive cost, the high productive ultra-smoothness grinding technique for the fine ceramics has been strongly required. In our previous researches[1),2)], the new ultra-smoothness grinding method is developed and ascertained to be useful for finishing to near the ultra-smoothness surface. The surface roughness of silicon carbide ceramic and cemented carbide tool formed by the ultra-smoothness grinding method using the #140 diamond wheel is found to attain below 25nm(*Rz*) or 4nm(*Ra*), and below 30nm(*Rz*) or 5nm(*Ra*), respectively.

This is one of a series of the researches on ultra-smoothness grinding of fine ceramics. In this report, the influence of grinding fluid supply on ultra-smoothness grinding of silicon nitride ceramic (HIPSN) is examined.

2. Ultra-smoothness grinding method

In the previous research[1)], the possibility of the high removal rate ultra-smoothness grinding method which can finish to almost the same smoothness formed by polishing is examined using traverse grinding. It is found from the results that the smoothness, which can be attained by traverse grinding, is limited roughly over the critical surface roughness because of the occurrence of rough grinding groove parallel to grinding direction formed by grinding.

To diminish the groove, the newly devised ultra-smoothness grinding method[1)] is proposed as shown in **Fig.1** and ascertained to be useful for finishing near the ultra-smoothness surface. First of all, in the new method, the workpiece-wheel contact width is ground by feeding the workpiece toward the direction normal to grinding direction. As shown in **Fig.2**, in the grinding process, the feed per a wheel revolution f_{Gn}, is smaller than the wear width of cutting edge w_n, normal to grinding direction. In the second step, the workpiece is slightly step-fed the length of f_p parallel to grinding direction so that the geometrical surface roughness, H_p, formed by overlapping cross-sections of two wheel circles before and after the step-feed becomes smoother than the required surface roughness. Then the workpiece-wheel contact width is ground again by feeding reversibly the workpiece toward the direction normal to grinding direction. By repeating such a grinding procedure, the whole surface of workpiece is finished.

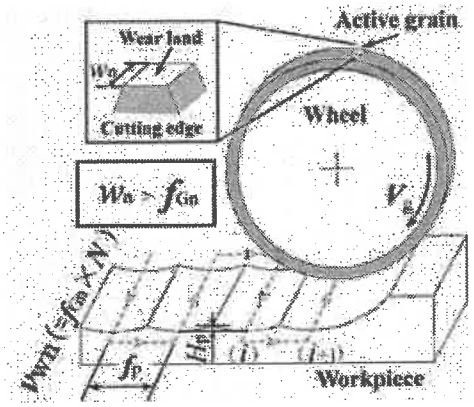

Fig.1 Ultra-smoothness grinding method

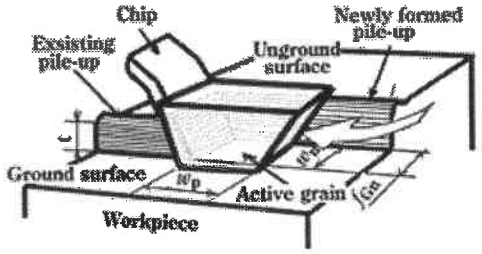

Fig.2 Mechanism of ultra-smoothness grinding

3. Experiments

The experiments are carried out with the NC grinder as shown photographically in **Fig.3.** The grinder having air spindle has the accuracy of 0.1μm for each movement of the X, Y and Z direction. The experimental conditions are summarized in **Table 1**. The grain size and concentration of the wheel used are #140 and 50,

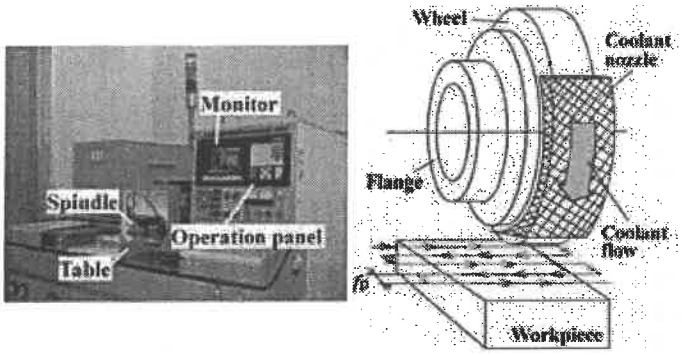

Fig.3 Appearance of experimental system

respectively. The hot isostatic pressed silicon nitride (HIPSN) is used as the workpiece of fine ceramic. All the grinding fluids are soluble type. Type T1 includes a plenty of anionic surfactant. Type T2 includes a plenty of fatty acid and a little ester and glycol. Type T3 includes a plenty of glycerin. The observation and roughness measurement of the ground workpiece surface are done with Nomarski microscope and SEM, and with the surface interferometer (WYKO TOPO-3D), respectively.

4. Results and discussions

4.1 Influence of grinding fluid type on ductile-mode plunge grinding

Figure 4 shows the micrographs and SEM photographs of the HIPSN surface formed by plunge grinding with the #140 diamond wheel at v_{wp}=0.01mm/s under the wheel speed of V_g=20m/s in dry grinding and wet grinding. In wet grinding, three types of grinding fluids are used. The grinding condition is shown in the figure. In case of dry grinding, from the figure, grinding grooves together with a plenty of large cracks formed by brittle-mode grinding are observed on the workpiece surface. And also, the surface topography like melted surface layer is observed on the workpiece surface. In case of wet grinding, on the other hand, the grinding grooves are observed similar to dry grinding. But the grooves are less and smoother than dry grinding. And also, most of the ground surface is formed by ductile-mode grinding. In wet grinding, however, the surface smoothness depends on grinding fluid type. When using fluid type T1, the smooth ductile-mode surface is found all over the workpiece surface. When using fluid type T2 and T3, on the other hand, the ductile-mode surfaces with some grinding cracks are observed on the workpiece surface. It is considered from these results that grinding fluid type has strong influence on ductile-mode grinding of fine ceramics. As the grinding grooves parallel to grinding direction in the

Table1 Experimental conditions

Work piece		HIPSN
Wheel		SD140Q50M Do×B×Di ; ϕ100×6×40
Wheel speed : V_g		20m/s
Depth of cut : t		5μm
Grinding fluid	Type	Soluble type
	Dilution	1/10, 1/50, 1/100
	Flow late	12 l/min
	Temperature	20℃
[Plunge grinding]		
Table speed : v_{wp}		0.01~1mm/s
[Ultra-smoothness grinding]		
Vertical feed : f_{Gn}		10μm/rev
Table speed : v_{ws}		0.63mm/s
Parallel feed : f_p		10μm

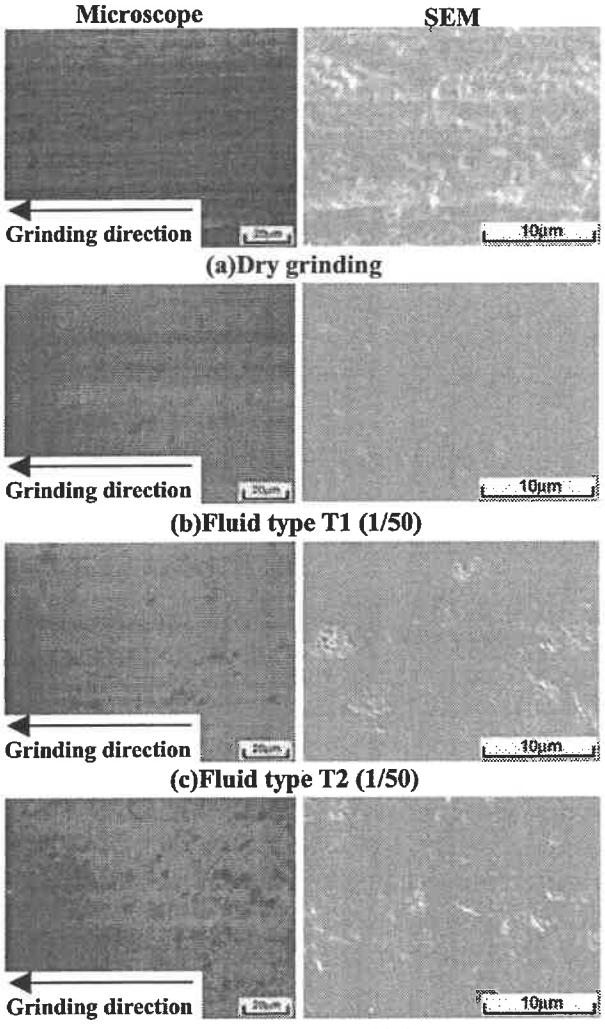

Fig.4 Micrographs and SEM photographs of HIPSN surface ground using three types in the case of plunge grinding
[V_g =20m/s, v_{wp}=0.01mm/s, t=5μm
Soluble type(1/50) 12 l/min]

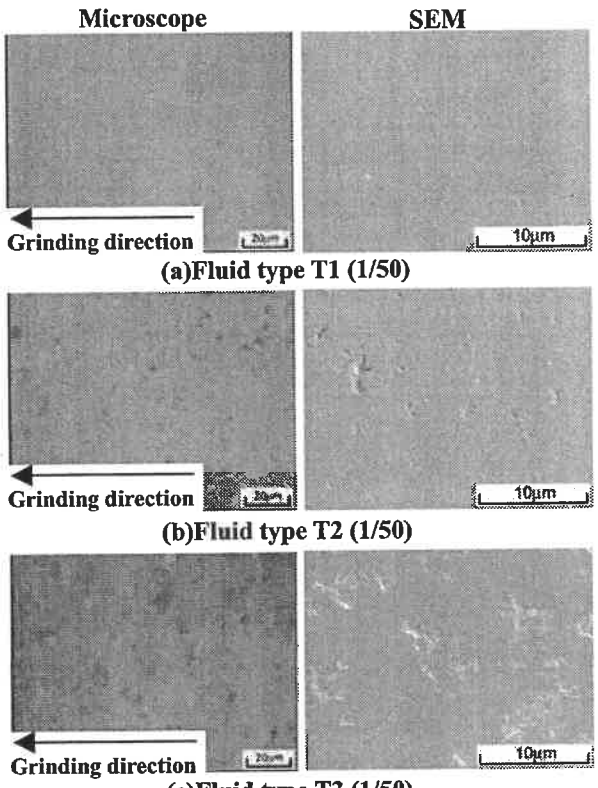

Fig.5 Micrographs and SEM photographs of HIPSN surface ground using three types of grinding fluid in the case of ultra-smoothness grinding [Vg =20m/s, fGn =10μm/rev ($v$wn=0.63mm/s) fp =30μm, t=5μm, Soluble type(1/50) 12 l/min]

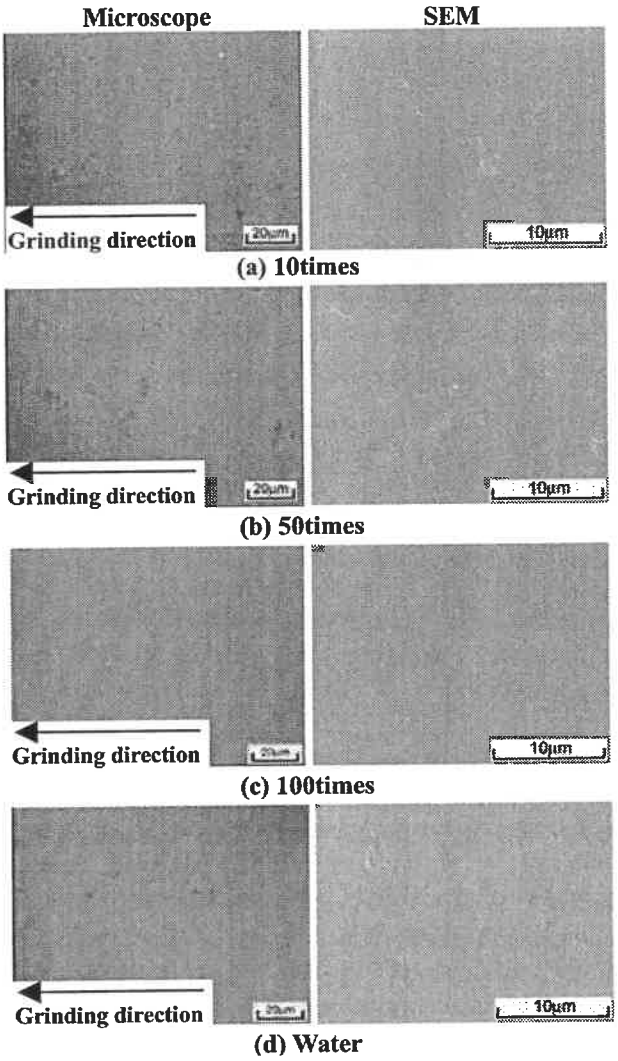

Fig.6 Micrographs and SEM photographs of HIPSN surfaces ground using grinding fluid of T1 and water in the case of ultra-smoothness grinding [Vg=20m/s, fGn=10μm/rev ($v$wn=0.63mm/s), fp=10μm, t=5μm, Soluble type T1 12 l/min]

plunge grinding method are formed roughly on the surface, it is difficult to finish to the ultra-smoothness surface[1].

4.2 Influence of grinding fluid type on ultra-smoothness grinding

Figure 5 shows the micrographs and SEM photographs of the HIPSN surface formed by ultra-smoothness grinding method using three types of grinding fluids. It is found from the figure that, for all the fluid type, the smooth ductile-mode surface without grinding grooves is obtained on the workpiece. Especially, when using fluid type T1, the ultra-smoothness surface without grinding cracks is observed as well as the result of HPSC as reported previously[2]. When using fluid type T2 and T3, however, the some grinding crack are formed on the ground workpiece surface. From the results, it is referred that the suitable grinding fluid is important to be selected for the ultra-smoothness surface of HIPSN.

4.3 Influence of grinding fluid dilution on ultra-smoothness grinding

Figure 6 shows the comparison of HIPSN surfaces ground by ultra-smoothness grinding using the grinding fluid diluted at 10 times, 50times, 100 times and only water. Grinding fluid used is the type T1, which gives the best result in Fig.5. In case of 10 times and 50 times, as seen from the figure, some grinding cracks are observed on the ground workpiece surface. In cases of 100 times, on the other hand, the grinding cracks are hardly observed. In case of only water, the generated grinding cracks are a little.

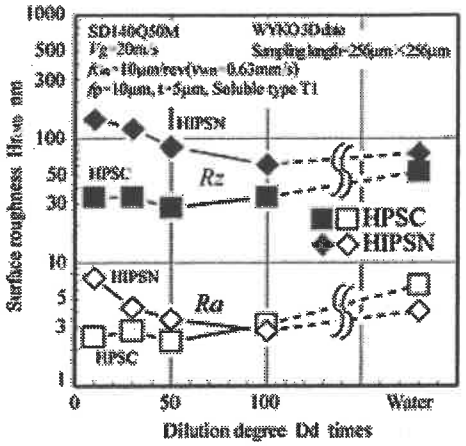

Fig.7 Relationship between HIPSN surface roughness and dilution degree in the case of ultra-smoothness grinding

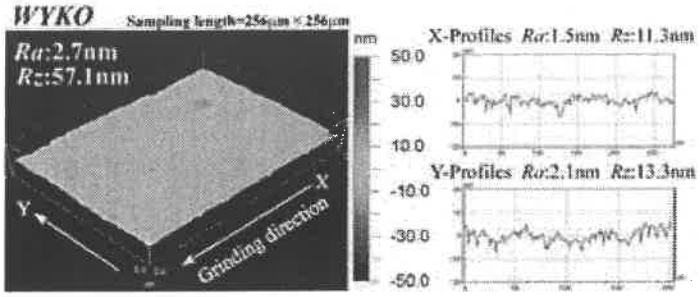

Fig.8 Surface image of HIPSN surface ground by ultra-smoothness grinding, measured with WYKO [Vg=20m/s, fGn=10μm/rev ($v$wn=0.63mm/s), fp=10μm t=5μm, Soluble type T1(1/100) 12 l/min]

Figure 7 shows the relationship between HIPSN surface roughness and dilution degree of grinding fluid. For the reference, the same relationship for HPSC[2] is also shown in the figure. In case of HIPSN, the surface roughness is the worst at dilution degree of 10 times. And, the surface roughness becomes smoother as grinding fluid is diluted higher to 100 times. In case of only water, however, the surface roughness becomes somewhat rougher than that in case of 100 times. From the results, the dilution of grinding fluid is considered to have strong influence on the surface roughness in ultra-smoothness grinding.

Figure 8 shows a WYKO 3D image and 2D profiles of 256μm square of HIPSN surface formed by ultra-smoothness grinding using the grinding fluid type T1 diluted at 100 times. It is found from the figure that the 3D surface roughness is about 57nm(Rz) or 2.7nm(Ra) and the 2D surface roughness parallel and normal to grinding direction is about 11nm(Rz) or 1.5nm(Ra) and about 13nm(Rz) or 2.1nm(Ra), respectively. Such a high smooth surface roughness is near the surface roughness formed by lapping or polishing.

5. Summary

Using the newly developed ultra-smoothness grinding method, the influence of the grinding fluid supply on the ultra-smoothness grinding of silicon nitride ceramic (HIPSN) is examined. The main results obtained are as follows:

(1) Grinding fluid supply is necessary for the ultra-smoothness grinding of silicon nitride ceramic. In case of dry grinding, the surface topography like melted surface layer is observed on the workpiece surface.

(2) The type and dilution of grinding fluid have the strong influence on the surface roughness in ultra-smoothness grinding of silicon nitride ceramic.

(3) The 3D and 2D surface roughnesses of silicon nitride ceramic formed by the newly developed ultra-smoothness grinding method with the suitable grinding condition attain about 57nm(Rz) or 2.7nm(Ra), and about 12nm(Rz) or 2.0nm(Ra), respectively.

Acknowledgement

The authors would like to thank Mr. Y.Oyama, Y.Tanaka and K.Sonomura for the assistance to experiments and Noritake Super Abrasive Industries Co. Ltd., Yushiro Chemical Industry Co. Ltd., and Nippon Tungsten Co. Ltd. for providing grinding wheels, grinding fluids and workpiece materials.

References

1)H.YASUI: Development of Polishingless Ultra-Smoothness Grinding Method (1st Report) -Theory and Some Experimental Investigations-, J.JSPE, vol. 69, No.12 (2003) pp1713-1717.

2)H.YASUI and T.SAWA: Effect of Grinding Fluid Supply on Ultra-Smoothness Grinding of Fine Ceramics, Proc.2003 ASPE Annual Meeting. Process Grinding No.5.

INVESTIGATION OF WHEEL LOADING BASED ON ADHESION THEORIES AND TEMPERATURE

Ping Zhang, Michele H. Miller
Michigan Technological University, Houghton, MI

INTRODUCTION

Wheel loading is one of the main factors limiting the capability of the grinding wheel. It results in an increase in grinding forces and temperature. As a consequence, the rate of abrasive wear increases and the surface finish of the workpiece deteriorates. The literature[1] indicates that the main cause of chip (or wheel) loading is adhesion between the active grits and the workpiece material deformed in the form of chips. There are six primary theories explaining adhesion:[2] physical adsorption, chemical bonding, diffusion, electrostatic, mechanical interlocking and weak boundary layer. The underlying mechanisms of each adhesion event may involve one or several adhesion theories. This paper investigates the applicability of three of the adhesion theories to chip loading including physical absorption, mechanical interlocking and diffusion theories. We try to explain why some materials tend to load more than others. Also, the effect of temperature on wheel loading is investigated here.

PHYSICAL ADSORPTION THEORY

I. Derivation of Equations

Physical adsorption involves van der Waals forces across the interface. These involve attractions between permanent dipoles and induced dipoles, and are of three types. Contact angle measurements are the most sensitive of surface characterization tools,[3] capable of probing short-range van der Waals forces. In a contact angle measurement, a drop of liquid is placed upon the surface of a solid, and the contact angle is measured. A diagram of the contact angle measurement is shown in Figure 1.

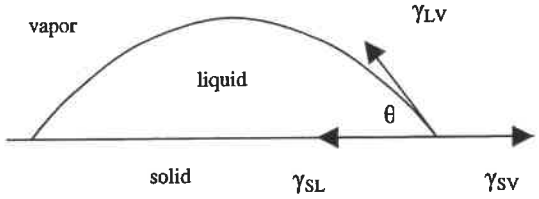

Figure 1 Contact angle meausement

Original analysis of contact angle measurement was established by Young. Referring to Figure 1, γ_{ij} are the appropriate interfacial tensions between the "S" solid, the "L" liquid, and the "V" vapor. The Young equation describes the equilibrium condition:

$$\gamma_{LV}\cos\theta = \gamma_{SV} - \gamma_{SL} \qquad (1)$$

where θ is the contact angle. The Dupre equation for the contact angle situation relates the work of adhesion to the interfacial tensions.

$$W_A = \gamma_{LV} + \gamma_{SV} - \gamma_{SL} \qquad (2)$$

Combining Eq. 1 with Eq. 2 results in the Young-Dupre equation

$$W_A = \gamma_L(1+\cos\theta) \qquad (3)$$

where $\gamma_L = \gamma_{LV}$ = surface tension of the liquid. Therefore, work of adhesion, a thermodynamic parameter, is related to two quantities: the contact angle θ and the surface tension of the liquid. Another form of the Young-Dupre equation is[4][5]

$$\gamma_L(1+\cos\theta) = -\Delta G_{SL} \qquad (4)$$

where ΔG_{SL} is the free energy of adhesion between two polar substances: "S" solid and "L" liquid.

The free energy of adhesion has two components: ΔG_{SL}^{LW}, the energy due to apolar electrodynamic Lifshita-van der Waals (LW) interaction, and ΔG_{SL}^{AB}, the energy due to polar (AB) interaction. The LW component is expressed as

$$\Delta G_{SL}^{LW} = -2\sqrt{\gamma_S^{LW}\gamma_L^{LW}} \qquad (5)$$

where γ_S^{LW} is the LW component of surface tension of "S" solid, γ_L^{LW} is the LW component

of surface tension of "L" liquid. Selecting the symbols γ^+ for the electron-acceptor and γ^- for the electron-donor parameter of the surface tension, the AB component is

$$\Delta G_{SL}^{AB} = -2\sqrt{\gamma_S^+\gamma_L^-} - 2\sqrt{\gamma_S^-\gamma_L^+} \qquad (6)$$

From Eq. 4, 5, and 6, a complete version of the Young-Dupre equation for a polar material (by van Oss-Chaudhury-Good approach) is derived as

$$(1+\cos\theta)\gamma_L = 2\sqrt{\gamma_S^{LW}\gamma_L^{LW}} + 2\sqrt{\gamma_S^+\gamma_L^-} + 2\sqrt{\gamma_S^-\gamma_L^+} \qquad (7)$$

Values for γ_L, γ_L^{LW}, γ_L^-, and γ_L^+ have been determined for a number of liquids. The θ value can be measured. Three independent unknowns, (γ_S^{LW}, γ_S^+, and γ_S^-), remain. To solve for three unknowns requires three equations. Therefore, the contact angle measurement must be made with three different liquids, and the Young-Dupre equation must be used three times.

After inferring γ_S^{LW}, γ_S^+, and γ_S^- from three contact angle measurements, the work of adhesion between liquid and solid material can be calculated from:

$$W_A = 2\sqrt{\gamma_S^{LW}\gamma_L^{LW}} + 2\sqrt{\gamma_S^+\gamma_L^-} + 2\sqrt{\gamma_S^-\gamma_L^+} \qquad (8)$$

Similarly, for two adhering solids:

$$W_A = 2\sqrt{\gamma_{S1}^{LW}\gamma_{S2}^{LW}} + 2\sqrt{\gamma_{S1}^+\gamma_{S2}^-} + 2\sqrt{\gamma_{S1}^-\gamma_{S2}^+} \qquad (9)$$

II. Experimental Results and Analysis

Four samples were prepared for the contact angle measurement: aluminum oxide (wheel grit material), glass (wheel bonding material), 1018 steel and 6061 aluminum. Measurements were taken in a goniometer, which is just a protractor mounted inside a telescope. Dropshape software was used to process the images and calculate the contact angle values. The advancing contact angles were measured under room temperature. The three liquids were water, diiodomethane (DIM), and ethylene glycol (E.G.). For each sample, ten contact angles were recorded under each liquid. Then the average values were calculated. Table 1 shows the average contact angles for each sample under each liquid.

For each solid material, Eq. 7 was used three times to calculate γ_S^{LW}, γ_S^+, and γ_S^-. Results are listed in Table 2.

	Water	DIM	E.G.
Glass	13.34	35.17	15.18
Alumina	25.51	34.87	15.16
6061 Al	6.76	23.61	9.09
1018 Steel	5.55	39.41	14.45

Table 1: Contact angle measurements (unit: degree)

	γ_S^{LW} (mN/m)	γ_S^+ (mN/m)	γ_S^- (mN/m)
Glass	42.0	0.02559	65.1823
Alumina	42.1	0.07909	55.2675
6061 Al	46.6	0.00184	65.5301
1018 Steel	39.9	0.06421	68.6998

Table 2: Calculated γ_S^{LW}, γ_S^+, and γ_S^-

Finally, Eq. 9 was used to calculate the work of adhesion between combinations of two materials, as shown in Table 3.

	Work of Adhesion (mN/m)
glass + 1018 steel	88.62
glass + 6061 Al	91.76
alumina + 1018 steel	90.40
alumina + 6061 Al	93.78
1018 steel + 1018 steel	88.20
6061 Al + 6061 Al	94.59

Table 3: Calculated work of adhesion

The values in Table 3 are all very similar. The work of adhesion due to physical adsorption is almost the same at room temperature for grinding wheel and 1018 steel, and grinding wheel and 6061 aluminum.

For most liquids, the surface tension decreases with increasing temperature. A semi empirical equation for predicting the temperature dependence of the surface tension is:[3]

$$\gamma = \gamma^0\left(1-\frac{T}{T_c}\right)^n \qquad (10)$$

where T_c is the critical temperature and $\gamma^0 = \gamma$ at T=0°K. The critical temperature is defined as

the temperature at which the interface of two surfaces vanishes. Therefore, work of adhesion should become zero at the critical temperature. Equation (10) indicates that work of adhesion decreases with increasing temperature.

Typically, grinding temperatures are several hundreds of degrees, which is far above room temperature. If adhesion decreased at such high temperature, there would be no chip loading. But in the following part of the paper, we show that loading actually increases with increasing temperature. Also aluminum chips load much more than steel chips experimentally, which can not be explained from Table 3. Therefore, the physical adsorption theory cannot explain the difference of wheel loading by various materials. Van der Waals forces are not the major reason for the adhesion between the wheel and different types of chips.

MECHANICAL INTERLOCKING THEORY

If a substrate has an irregular surface, then the adhesive may enter the irregularities prior to hardening. This is the mechanical interlocking theory of adhesion. For evidence of mechanical interlocking in wheel loading, sections on an alumina grinding wheel with 1018 steel chips loaded on it were examined by scanning electron microscopy (SEM). Figure 2 shows a typical interaction between wheel and chips. For 1018 steel, grinding chips are mostly located in the spaces between aluminum oxide grits. These long, curled chips may be deformed under high grinding temperature and pressed by grinding forces to fit into the area between wheel grits. This indicates that mechanical interlocking theory is a possible reason for wheel loading.

Our previous research[6] shows that vibration assisted grinding reduces wheel loading compared to regular grinding processes. 1018 steel chips were collected under the same working condition during regular grinding and vibration assisted grinding processes, and examined by SEM. Figure 3 and Figure 4 are typical chip images from each process. There is no significant difference in size or curvature. They are both long, curled and have machining marks. This suggests that another factor (such as temperature) may be more important than chip shape in explaining wheel loading.

It seems reasonable that chip shape would be an important factor in mechanical interlocking. However, we have not yet observed a correlation between chip shape and high loading rates.

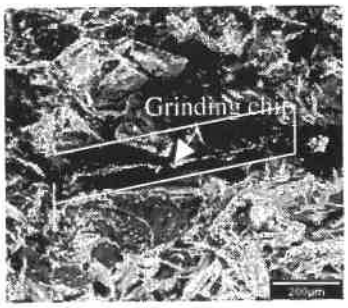

Figure 2 Chip embedded between wheel grits

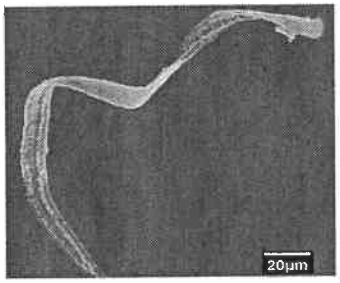

Figure 3 Chip from regular grinding processes

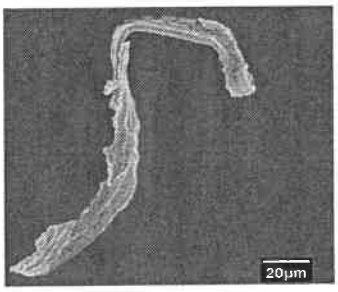

Figure 4 Chip from vibration assisted grinding processes

DIFFUSION THEORY

Diffusion[7] is the net relative movement of atoms in a solid, liquid, or gas. We use phase diagrams, which are plots of the equilibrium phase(s) for various chemical compositions as a function of temperature, to investigate the applicability of diffusion to loading. When an aluminum oxide wheel grinds steel, an Aluminum-Iron-Oxygen[8] phase diagram is utilized. Figure 5 is a typical phase diagram of Al-Fe-O at 900°C. Along Al-O line, Al_2O_3 forms when component percents of Al and O arrive at some point. It is a straight line that connects Al_2O_3 and Fe, which means that at such temperature and pressure, an equilibrium state is reached. Similar condition also can be found at other temperature and pressure. With an equilibrium state, no diffusion can occur between grinding wheel and workpiece materials. Therefore, diffusion theory cannot be applied to explain wheel loading.

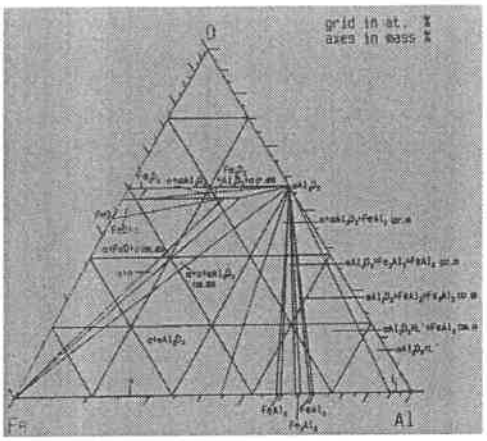

Figure 5 Isothermal section at 900°C (Numbers in tie triangles are of $-\log p_{O_2}(bar)$)[8]

EFFECTS OF TEMPERATURE

When different kinds of materials are ground, a difference in grinding temperature is observed. Vibration assisted grinding reduces loading compared to grinding without vibration assistance. Both higher vibration amplitude and frequency result in less loading. Vibration assisted grinding also results in a large temperature reduction. When vibration frequency up to 2.5kHz, the maximum temperature reduction is almost 40%.[9] Based on these findings, surface grinding tests were done at different workpiece temperatures to investigate the effect of temperature on wheel loading. A 1018 steel workpiece was mounted on a disk heater and heated 204°C. Grinding was done with and without preheating, and wheel loading was measured after 100 passes. Tests were repeated ten times. Figure 6 summarizes the results. The middle point of each bar represents the average of the ten tests; the error bars span ± 3×standard deviation. Figure 6 shows that loading nearly doubles when the workpiece is pre-heated. While it is still unclear whether the higher temperatures are affecting the mechanical interlocking, electrostatic, or some other mechanisms, grinding temperature is a key factor in wheel loading.

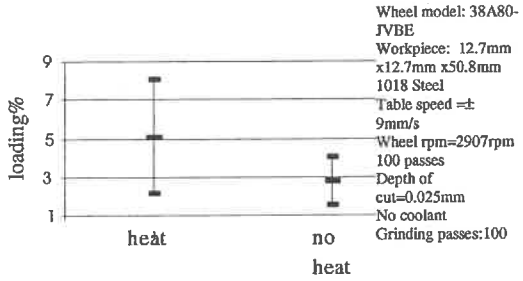

Figure 6 Temperature Effect

CONCLUSION

By contact angle measurement experiments, the theory of physical adsorption was found to contribute little to wheel loading. As for the mechanical interlocking theory, positions of deformed chips on the grinding wheel indicate the possible relation of this theory to loading. We continue to investigate the correlation between chip shape and loading. By analyzing phase diagrams, the diffusion theory is eliminated as an explanation for loading. Finally, experiment shows the importance of temperature to wheel loading. Future work will investigate the relationships between materials, temperature, pressure, particle size and surface texture on loading.

REFERENCES

[1]Nagaraj, A.P. and A.K. Chattopadhyay, "On some aspects of wheel loading," *Wear*, Vol. 135, pp. 41-52, 1989.

[2]Pocius, A.V., *Adhesion and adhesives technology : an introduction*, Munich , New York : Hanser Publishers , Cincinnati : Hanser/Gardner Publications, 1997.

[3]Parker, Robert Sydney Richard, *Adhesion and adhesives*, Oxford, New York, Pergamon Press, 1966.

[4]Van Oss, C.J., "Use of the combined Lifshitz van der Waals and Lewis acid-base approaches in determining the apolar and polar contributions to surface and interfacial tensions and free energies", *Journal of Adhesion Science and Technology*, Vol. 16, No. 6, pp. 669-677, 2002.

[5] Van Oss, C.J., "Addictive and non-addictive surface tension components and the interpretation of contact angles", *Langmuir*, Vol. 4, pp.884-891, 1988.

[6]Zhang, P. and M. H., Miller, "Grinding wheel loading with and without vibration assistance," *Proc. of the ASPE Annual Meeting*, pp. 529-533, 2003.

[7]Carter, G.F, *Materials science & engineering*, ASM International, US, 1993.

[8]Petzow G. and G. Effenberg, *Ternary Alloys*, VCH Verlag, Weinheim, Vol. 5, pp. 335-353, 1992.

[9]Mahaddalkar, P.M., *Force and Temperature Reduction in Vibration Assisted Grinding*, MS thesis, Michigan Technological University, 2002.

CUTTING FORCE PREDICTION USING A MOLECULAR DYNAMIC ASSISTED FINITE ELEMENT SIMULATION MODEL

Mohamed F. Aly, Eugene Ng and Stephen C. Veldhuis
McMaster University
Hamilton, Ontario, Canada L8S 4L7

Abstract

Linking material property acquisition and modeling in the nanometric scale with those on the macro-scale is currently one of the most challenging fields of research in material science in general and in micromachining in particular. Due to computational limitations it is presently impossible to inflate atomic level models and simulations to the macro sized components we work with daily. This knowledge of material behaviour will provide insight into process development, modeling and the optimization of critical ultra-precision machining processes.

Key words

Ultra-precision machining, Cutting Force Prediction, Molecular Dynamic Simulation, Material Properties, Finite Element Model.

Introduction

The investigation of ultra-precision machining is vital for developing new materials, tooling and processes. In the past extensive cutting tests were carried out to understand and optimize critical process parameters. This procedure is often costly and time consuming [Komanduri, 1993]. An alternate approach is to make use of detailed physics based models like Finite Element Analysis (FEA), Finite Difference Method (FDM), and Molecular Dynamic (MD) techniques. Through the use of FEA and FDM techniques, a wide range of problems in traditional machining applications have been investigated, such as determining the temperature and stress distribution in the cutting zone, residual stress and chip formation [Li et al, 1995]. FEA and FDM use continuum mechanics approaches to address metal cutting problems. In these techniques the workpiece material is looked at as a continuous structure where the micro-constituents such as crystal structure, grain sizes, and inter-atomic distances are neglected. In MD simulations the nodes, which define the resolution of the model, are selected based on the atomic structure of the material where the inter-nodal spacing relates to inter-atomic distances [Komanduri and Raff, 2001]. In this case detailed information related to material behavior is captured. Unfortunately the depths of cut and cutting speed, which can be investigated using MD, are not currently at levels commonly practiced in ultra-precision machining.

Calibrating the required material properties necessary to run the FEA models with experimental data is a significant challenge. As the size of the sample under study decreases the challenge increases due to the complexity of handling the workpieces and measuring the parameters under the required conditions of workpiece size, high stress and high strain rate. However, atomic based simulations like MD provide a means of acquiring new data that can assist in calibrating the material properties for use in an FEA model.

Thus this paper presents a new methodology to provide an FEA model with relevant material properties for ultra-precision machining. The approach used is based on the MD simulation of a uniaxial tension test configuration from which key material properties are extracted. In this way the nanometric scale information required for two dimensional FEA simulations evaluating the cutting force can be obtained. Ultra precision single point turning operations were performed and the cutting forces were measured using a high frequency, high resolution dynamometer. This was done to validate the forces obtained from the FEA model and to demonstrate the effectiveness and usefulness of the proposed technique.

Molecular Dynamic Simulation Model

Extensive experimental work has been carried out in metal cutting to develop, describe, and optimize cutting conditions and processes. This procedure is typically costly and time consuming. This has motivated the search for alternatives to expand our understanding of these processes while minimizing the experimental effort required. The molecular dynamic simulation approach was introduced in the early 1990's to model nanometric cutting processes [Stowers et al, 1991; Belak et al, 1993; Li et al, 1995].

In this work, MD is used to acquire material properties at the nanometric level by conducting simulations of tension tests under nanometric scales as shown in figure 1.

The potential function used to describe the interatomic relations between the silicon atoms in this work is the Tersoff potential energy in the form:

$$V = \sum_{i \neq j} \phi(r_{ij})$$

Where:
$$\phi(r_{ij}) = F_r(r_{ij}) + b_{ij} F_a(r_{ij})$$

Where b_{ij} is a function of the cut-off radius and the angles between the atomic bonds. $F_r(r_{ij})$ & $F_a(r_{ij})$ are the repulsive and attractive forces between atoms *i* and *j* and can be represented as:

$$F_r(r_{ij}) = Ae^{(-\lambda r_{ij})} \qquad F_a(r_{ij}) = -Be^{(-\mu r_{ij})}$$

Some of the silicon properties and the computational parameters used in the MD model are listed in Table 1. MD simulations were carried out at different loading rates (20-500 m/s) to investigate the effect of strain rate on the material behaviour and mechanical properties. It was concluded that atomic rearrangements were slightly different with no obvious change in material behaviour. Figures (2-3) show the formation of the necking phenomena with 100 atoms at $0.5r_0$ tensile load.

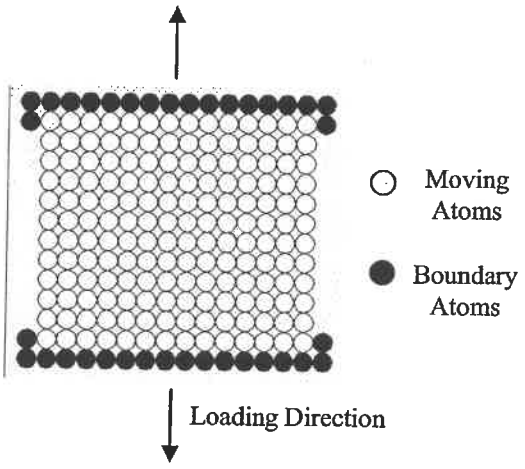

Fig.1: Test specimen used in MD simulations

Table 1: Parametric values and Silicon properties used in MD simulation

Potential Energy function	Tersoff potential
Configuration	2D
A	1830 eV
B	471 eV
μ	1.7322 $Å^{-1}$
λ	2.48 $Å^{-1}$
Tension test	Uniaxial
Lattice structure	Diamond cubic
Lattice constant (r_0)	5.43 Å
WP dimensions	$16r_0$ x $4r_0$
Crystal orientation	[001]
Density	2328 kg/m^3
Temperature	300 K
Melting temperature	1410 ^0C

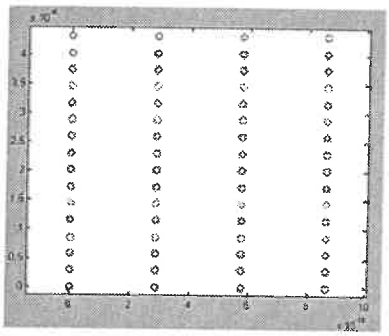

Fig.2: Initial atomic position for the tension test specimen

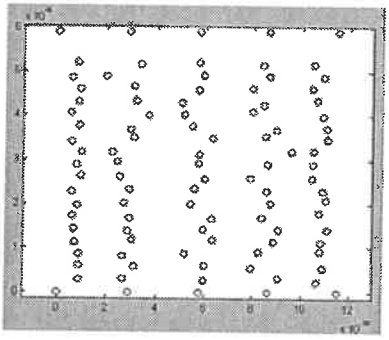

Fig.3: Simulation test for 100 atoms structure with $0.5r_0$ stretch

MD simulation results

A different set of parameters was used to test and validate the proposed techniques performance under variable loading rates. Table 2 presents the corresponding values of the simulation results of key material properties. The stress-strain relation curves at

different loading rates for silicon are provided in figure 4.

Table 2: MD simulation results for Si

σ_{ut} (GPa)	$\varepsilon_{max.Stress}$	E (GPa)
24	0.25	165

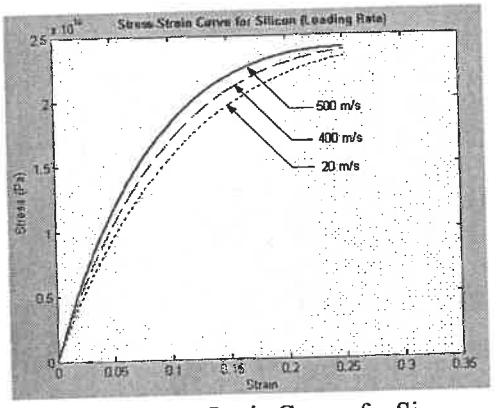

Fig.4: Stress-Strain Curves for Si

Finite Element Model

Finite element analysis (FEA) is a simulation technique that can provide useful information and address a wide range of machining problems. It uses continuum mechanics approaches to address metal cutting problems where the workpiece material is considered a continuous structure where the micro-constituents such as crystal structure, grain sizes, inter-atomic distances...etc. are neglected. In this method, distances between nodes and number of nodes are selected based on the level of detail expected from the simulation. An orthogonal cutting test was then simulated using FEA. The model is developed using ABAQUS/Explicit Finite element solver (v.6.4). The workpiece and tool are constructed as 2D deformable shell structures. The cutting is performed using a diamond tool at 5 m/s constant cutting speed with a 10 micrometer depth of cut. The rake and clearance angles are both set to be of 10 degrees. The cutting was simulated under dry conditions. Figure 5 shows the simulation setup with the tool/workpiece arrangement.

The linear elastic as well as the nonlinear plastic behaviour of the workpiece material is introduced to the FEA model from the data acquired through the MD simulation model. The crack propagation criterion is based on the plastic strain failure inequality described as follows:

$$\varepsilon_{pl} \succ \varepsilon_{pl}^{f}$$

Where ε_{pl} is the current plastic strain on each element of the model and ε_{pl}^{f} is the maximum allowable plastic strain before failure.

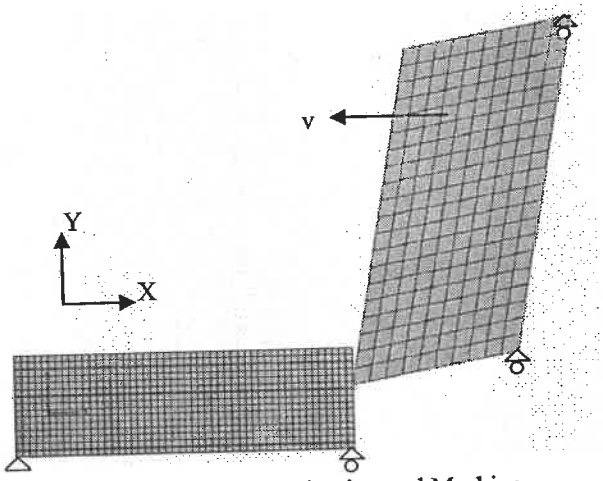

Fig.5: Tool/Workpiece Fixation and Meshing

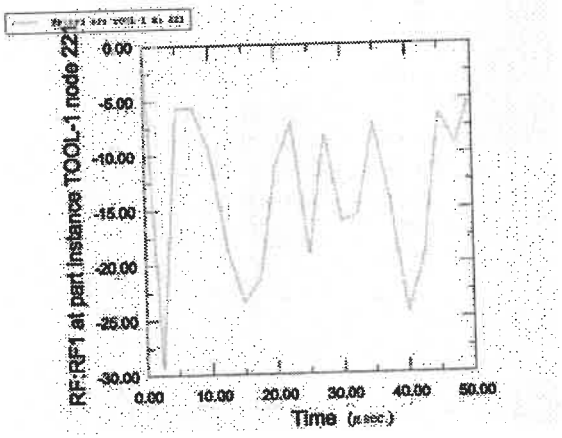

Fig.6: Cutting force from FEA model

The FEA model presented provides the necessary link between the MD simulation model and the experimental work. It gives the means required to validate both the MD and the FEA models by comparing their combined results (figure 6) to the experimental ones obtained in the lab for the prediction of the forces during the cutting process.

Experimental Setup

Experimental validation of the MD simulation model and FEA model were conducted on a Precitech machine with nanometric position accuracy using a

diamond tool for a 10 micron depth of cut and a 10μm/rev feed rate. Figure 8 shows the arrangement setup between the silicon wafer on the vacuum chuck and the tool holder setting on the Kistler Mini-Dynamometer for the force measurement using Lab view software.

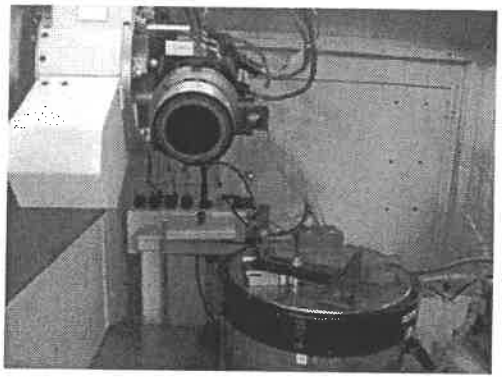

Fig.7: Experimental setup on the Precitech machine

Experimental Results

Cutting forces were measured with the Kistler MiniDyn through Lab view software. Figure 8 shows the variation of the cutting forces with time. Comparing figure 6 and 8, we can conclude that there is a good agreement between the theoretical values calculated using the hybrid MD-FEA model and the experimental values measured in the micro-cutting lab. Cutting forces were found to be in the order of 15-20 Newton for a 10μm depth of cut.

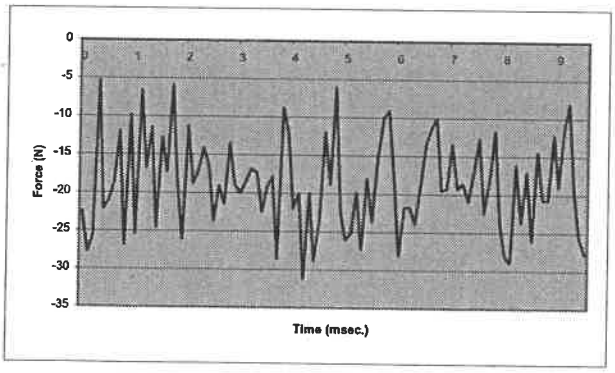

Fig.8: Cutting forces from experimental test

Conclusion

In this work, we introduced the use of molecular dynamics and dislocation theory as a link between nano-scale and meso-scale modules with the finite element method calculations serving as a bridge between the modules. The purpose of this work is to fill the void between the nanometric scale information required to model micro-cutting and the known macro-scale mechanical behaviour of materials in metal cutting. The proposed study suggests several future perspectives for the use of alternative modules aiming to further our knowledge of material behaviour modeling related to manufacturing processes.

References

Belak, J. and Stowers, I., "A molecular dynamics model of the orthogonal cutting process", In proceedings of ASPE annual conference, p. 76, New York, 1990.

Komanduri, R. and Raff, L., "A review on the molecular dynamics simulation of machining at the atomic scale", Proc. Instn. Mech. Engrs., Vol. 215, Part B, p.1639-1672, (2001).

Komanduri, R., "Machining and grinding: a historical review of the classical papers", Transactions of the ASME, Applied Mechanics Review, Vol.46, No.3, p. 80-132, (1993).

Li, X, Kopalinsky, E. and Oxley, P., "A numerical method for determining temperature distributions in machining with coolant. Part 1: modeling the process", Proc. Instn Mech. Engrs., Vol. 209, Part B, p.33-43, (1995).

Stowers, I. F., Belak, J., Lucca, D., Komanduri, R., Rhorer, R., Moriwaki, T., Okuda, K., Ikawa, N., Shimada, S., Tanaka, H., Dow, T. and Drescher, J., "Molecular dynamics simulation of the chip forming process in single crystal copper and comparison with experimental data", In proceedings of ASPE annual conference, p. 100-103, 1991.

FABRICATION AND METROLOGY OF MICRO-SCALE SINUSOIDAL SURFACES IN POLYMER WORKPIECE MATERIALS

Matthew J. Bono, Robin L. Hibbard
Lawrence Livermore National Laboratory, Livermore, California 94550

Introduction

This study investigates the fabrication of precision, micro-scale sinusoidal surfaces in polymer workpiece materials and discusses methods to quantitatively characterize these surfaces. These precision sinusoidal surfaces are an important feature in a meso-scale assembly that will be used as part of a physics experiment. The experiment will study the formation of Rayleigh Taylor instabilities and requires a sinusoidal surface with an amplitude of 2.5 μm and a wavelength of 70.7 μm in both the x- and y-directions. The sinusoids must have sub-μm form accuracy with a surface finish on the order of 100 nm, and they must be produced in a workpiece consisting of adjacent pieces of polyimide and iodine-doped polystyrene, a portion of which is illustrated in Figure 1.

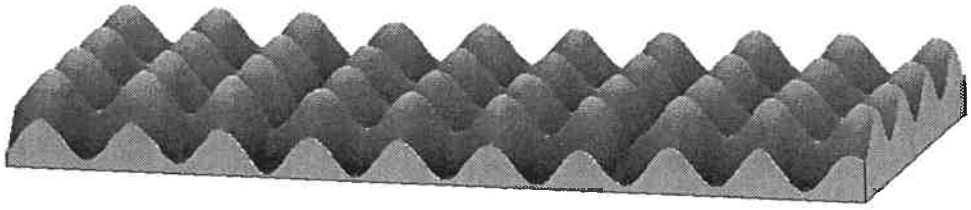

Figure 1. Machined sinusoidal surface

The fabrication of micro-scale sinusoidal surfaces is a recurrent problem relevant to many different scientific applications. The most common use for precision sinusoidal surfaces is the optics field, for which sinusoidal optical components are commonly produced using lithography processes. However, lithography can only be used with limited types of workpiece materials, and they cannot be used to make precision parts from iodine-doped polystyrene or polyimide. Other applications for micro-scale sinusoidal surfaces involve more traditional engineering materials, such as metals [1,2].

In the current study, sinusoidal surfaces are machined using a single point diamond tool with a commercial fast tool servo on a diamond turning machine. Producing acceptable surfaces requires the programming of the fast tool servo, the selection of the proper diamond tool geometry, and the selection of appropriate cutting conditions.

Fabrication Method

Machining is performed with a Precitech Nanoform 200 diamond turning machine. The workpiece is mounted on the spindle of the machine tool and rotates clockwise with a constant angular velocity, as shown in Figure 2. A Precitech Fast Tool Servo Ultra Precision Machining System with a stroke of 35 μm is mounted on the tool slide and is oriented so that its stroke is parallel to the z-axis, perpendicular to the face of the workpiece. The stroke of this fast tool servo is driven by a piezoelectric actuator, and a capacitance probe in-line with the stroke provides closed-loop control. A single point diamond cutting tool is mounted in the fast tool servo, and the height of the cutting edge is carefully set so that it cuts to the center of the workpiece. To machine the face of the workpiece, the machine spindle (the C-axis) rotates the workpiece clockwise, and the motion of the x-axis moves the workpiece relative to the diamond tool such that the tool travels from right to left relative to the workpiece, from the outer edge toward the center of rotation. The stroke of the fast tool servo is slaved to the C-axis and the x-axis, both of which contain high resolution encoders that constantly read the angular orientation of the machine spindle, θ, and the distance of the diamond tool tip from the axis of rotation of the machine spindle, r. In other words, the fast tool servo is programmed so that its stroke is a function of the encoder readings, θ and r.

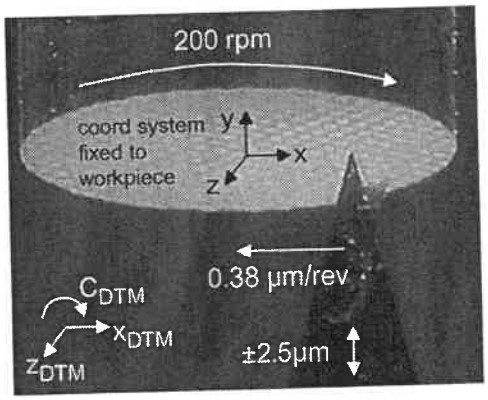

Figure 2. Machining setup

Programming the Fast Tool Servo

The desired form of the surface machined by the fast tool servo is given by Eq. (1), where the amplitude, A, is 2.5 μm, and the wavelength, λ, is 70.7 μm. In Eq. (1), x and y lie in the workpiece coordinate system. r and θ lie in the machine tool coordinate system, where r corresponds to the x-axis of the machine tool and θ corresponds to the C-axis of the machine tool.

$$z = A\sin\left(\frac{2\pi x}{\lambda}\right)\sin\left(\frac{2\pi y}{\lambda}\right) = A\sin\left(\frac{2\pi r\cos\theta}{\lambda}\right)\sin\left(\frac{2\pi r\sin\theta}{\lambda}\right) \tag{1}$$

To produce the desired form of the machined workpiece surface, the fast tool servo must be programmed to account for the finite nose radius of the cutting tool. Note that because the cutting edge of the tool always lies along the x-axis, compensation for the tool nose radius must only be performed in the radial direction. The importance of this compensation is apparent from Figure 3. This figure illustrates a radial trace of the workpiece surface at some angle $\theta=\theta_0$, and it shows that to machine the surface correctly, the stroke of the fast tool servo must be such that when the center of the tool is at $r=r_0$, the nose of the tool is tangent to the desired workpiece surface.

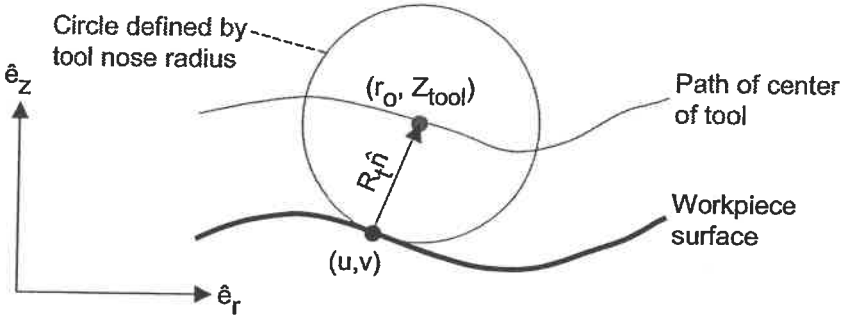

Figure 3. Tool nose radius compensation for a tool of nose radius R_t

The problem is to find the z-coordinate of the center of the tool, z_{tool}, at which the tool is tangent to this radial trace of the workpiece surface. The point of tangency is denoted as ($r = u$, $z = v$). Thus, the problem reduces to finding the value of u that satisfies the relation in Eq. (2).

$$u + \left(R_t\hat{n}\right)\bullet\hat{e}_r = r_o \tag{2}$$

R_t is the nose radius of the tool. $\hat{n}$ is the unit vector that is normal to the trace of the workpiece surface in the plane $\theta=\theta_0$, and it can be found by taking the gradient of the equation of the machined workpiece surface. To facilitate calculating the gradient, a function $m(r, \theta_0, z)$ is defined in Eq. (3).

$$m\left(r,\phi_0,z\right) = 0 = z - A\sin\left(\frac{2\pi r\cos\theta_0}{\lambda}\right)\sin\left(\frac{2\pi r\sin\theta_0}{\lambda}\right) \tag{3}$$

The unit normal vector to the trace of the workpiece surface is simply the normalized gradient, which is given by Eq. (4).

$$\hat{n} = \frac{\bar{\nabla}m}{\left|\bar{\nabla}m\right|} = \frac{\frac{\partial m}{\partial r}\hat{e}_r + \frac{\partial m}{\partial z}\hat{e}_z}{\sqrt{\left(\frac{\partial m}{\partial r}\right)^2 + \left(\frac{\partial m}{\partial z}\right)^2}} = \frac{\frac{\partial m}{\partial r}\hat{e}_r + \hat{e}_z}{\sqrt{\left(\frac{\partial m}{\partial r}\right)^2 + 1}} \tag{4}$$

Eq. (4) can be substituted into Eq. (2) to solve for the value of u. After finding u, the value of v can be calculated from Eq. (5).

$$v = A\sin\left(\frac{2\pi\cdot u\cos\theta_0}{\lambda}\right)\sin\left(\frac{2\pi\cdot u\sin\theta_0}{\lambda}\right) \tag{5}$$

The z-coordinate of the center of the tool can now be calculated from Eq. (6) and can be used to calculate the stroke of the fast tool servo for the point ($r=r_0$, $\theta=\theta_0$).

$$z_{tool} = v + R_t\hat{n}\bullet\hat{e}_z \tag{6}$$

different loading rates for silicon are provided in figure 4.

Table 2: MD simulation results for Si

σ_{ut} (GPa)	$\varepsilon_{max.Stress}$	E (GPa)
24	0.25	165

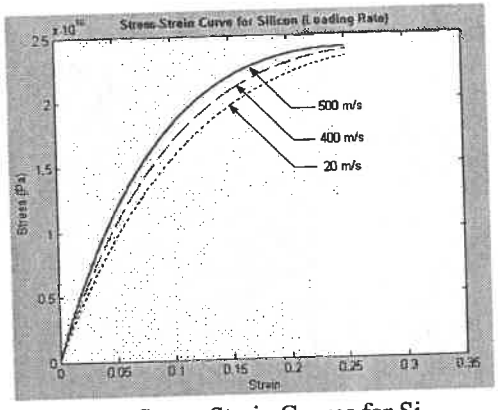

Fig.4: Stress-Strain Curves for Si

Finite Element Model

Finite element analysis (FEA) is a simulation technique that can provide useful information and address a wide range of machining problems. It uses continuum mechanics approaches to address metal cutting problems where the workpiece material is considered a continuous structure where the micro-constituents such as crystal structure, grain sizes, inter-atomic distances...etc. are neglected. In this method, distances between nodes and number of nodes are selected based on the level of detail expected from the simulation. An orthogonal cutting test was then simulated using FEA. The model is developed using ABAQUS/Explicit Finite element solver (v.6.4). The workpiece and tool are constructed as 2D deformable shell structures. The cutting is performed using a diamond tool at 5 m/s constant cutting speed with a 10 micrometer depth of cut. The rake and clearance angles are both set to be of 10 degrees. The cutting was simulated under dry conditions. Figure 5 shows the simulation setup with the tool/workpiece arrangement.

The linear elastic as well as the nonlinear plastic behaviour of the workpiece material is introduced to the FEA model from the data acquired through the MD simulation model. The crack propagation criterion is based on the plastic strain failure inequality described as follows:

$$\varepsilon_{pl} \succ \varepsilon_{pl}^{f}$$

Where ε_{pl} is the current plastic strain on each element of the model and ε_{pl}^{f} is the maximum allowable plastic strain before failure.

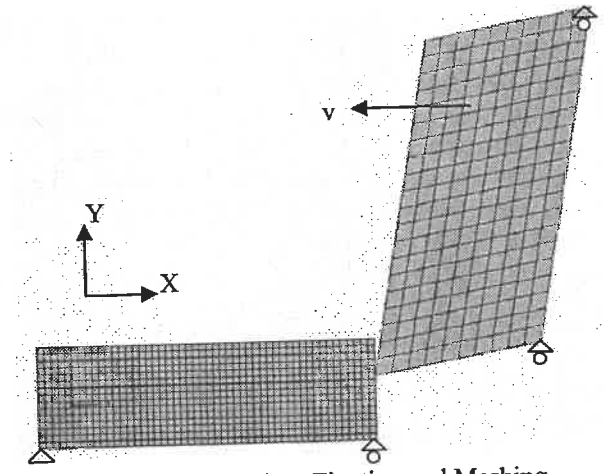

Fig.5: Tool/Workpiece Fixation and Meshing

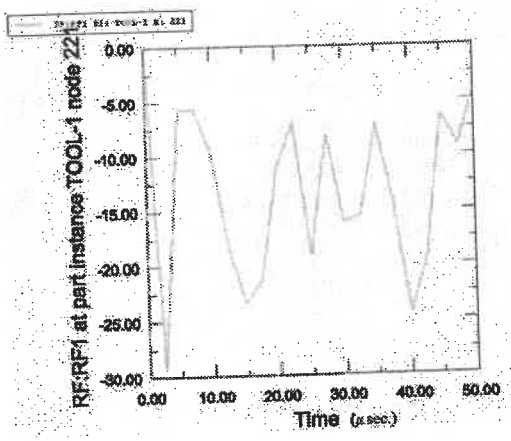

Fig.6: Cutting force from FEA model

The FEA model presented provides the necessary link between the MD simulation model and the experimental work. It gives the means required to validate both the MD and the FEA models by comparing their combined results (figure 6) to the experimental ones obtained in the lab for the prediction of the forces during the cutting process.

Experimental Setup

Experimental validation of the MD simulation model and FEA model were conducted on a Precitech machine with nanometric position accuracy using a

probe with a radius of 2 μm to measure the specimen surface with an accuracy of 0.1 μm in the displacement direction and a lateral accuracy of 50 nm. A dataset collected by this device with a lateral point spacing of 2 μm is plotted in Figure 5.

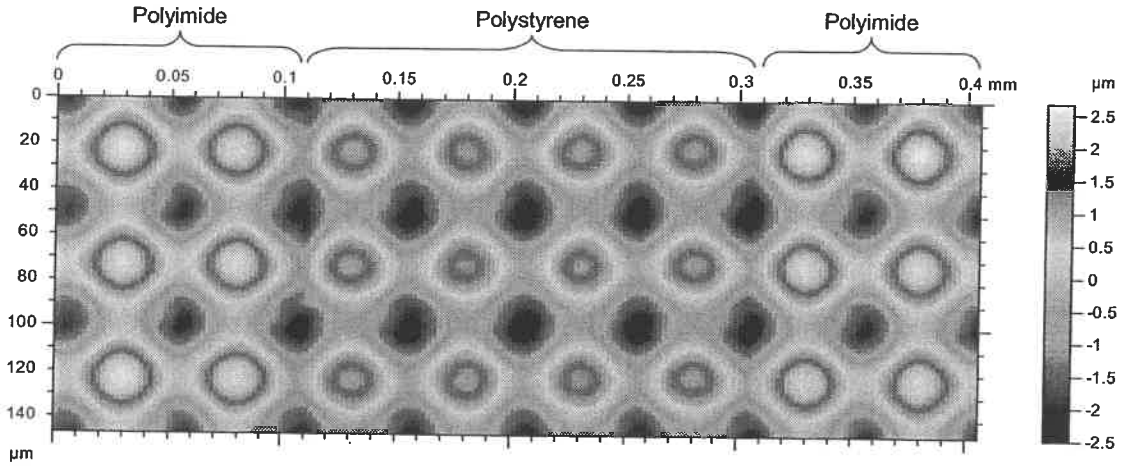

Figure 5. Surface profile data measured by the CMM

The data clearly shows the interfaces between the polyimide and the 200 μm wide strip of iodine-doped polystyrene. Several profile traces were taken through this dataset to measure the magnitude of the step discontinuity at the interface between the dissimilar materials, and the measured values ranged from 0.3 to 0.6 μm.

The form of the machined surfaces can also be determined from this dataset. Profile traces of the dataset in the iodine-doped polystyrene region reveal sinusoids with an amplitude of 2.5 μm and a wavelength of 70.7 μm. Profile traces in the polyimide material reveal an amplitude of 2.4 μm and a wavelength of 70.7 μm. The 0.1 μm error in the magnitude of the sinusoids in the polyimide could be a result of the poor machining characteristics of this material [3]. The depth of cut of only 1.25 μm combined with a rake angle that varies from +13° to -13° may result in significant ploughing or workpiece deflection that cause an error in amplitude. Conversely, the iodine-doped polystyrene is known to machine well with this type of depth of cut when using a diamond tool.

To determine the surface finish of the machined sinusoids, the specimen is measured in several places using an atomic force microscope (AFM). The AFM measures a 65 μm × 65 μm area with a lateral point spacing of 0.13 μm, and the environment is estimated to cause a noise floor in the displacement direction of approximately 2 nm. To separate the form of the surface from the roughness profile, the dataset collected with the AFM is filtered with a 10 μm Gaussian filter to reveal an RMS roughness of $S_q = 50$ nm.

Conclusions

This study investigates the fabrication of precision, micro-scale sinusoidal surfaces in a workpiece consisting of adjacent pieces of polyimide and iodine-doped polystyrene. A diamond tool in a commercial fast tool servo machines a sinusoidal surface with an amplitude of 2.5 μm and a wavelength of 70.7 μm. Because of the large slope of the machined surface and the optical properties of the workpiece material, the surface cannot be adequately characterized with a white light interferometer. Measurements with a precision touch-probe CMM indicate that the sinusoids have sub-μm form accuracy, and AFM measurements indicate a surface finish on the order of $S_q = 50$ nm.

Acknowledgement

This work was performed under the U.S. Department of Energy by the University of California, Lawrence Livermore National Laboratory under Contract No. W-7405-Eng-48.

References

1. E.C. Teague, F.E. Scire, and T.V. Vorburger, "Sinusoidal profile precision roughness specimens," *Wear* (v83, 1982) pp 61-73.
2. W. Gao, T. Araki, S. Kiyono, Y. Okazaki, and M. Yamanaka, "Precision nano-fabrication and evaluation of a large area sinusoidal grid surface for a surface encoder," *Precision Engineering* (v27, 2003) pp 289-298.
3. J. Carr, and C. Feger, "Ultraprecision machining of polymers," *Precision Engineering* (v15, 1993) pp 221-237.

DESIGN AND MANUFACTURE OF ASPHERIC LENSES FOR NOVEL HIGH EFFICIENT PHOTOVOLTAIC CONCENTRATOR MODULES

Ekkard Brinksmeier (1), Alexander Gessenharter (1), Daniel Pérez (2), José Blen (2), Pablo Benítez (2), Vicente Díaz (3), Jesús Alonso (3)
(1)Laboratory for Precision Machining LFM, University of Bremen, Germany
(2)Instituto de Energía Solar, Universidad Politécnica de Madrid, Spain
(3)ISOFOTON S.A., Málaga, Spain

Abstract

Within this project novel high efficient photovoltaic concentrator modules composed of a TIR-R (total internal reflection - refraction) lens system and small GaAs solar cells were designed and manufactured. Main objective was the development of a photovoltaic system with an efficiency of 21% and production costs not exceeding those of conventional silicon solar cells. This paper reports on the design and simulation of the concentrator, diamond machining of the ultraprecision molds for injection molding of the PMMA lenses and first functional tests of the lens system. Finally, a prototype of a photovoltaic panel consisting of 138 individual concentrator modules is presented.

Introduction

The main objective of this project is the development of a photovoltaic system with an efficiency of about 21% and production costs not exceeding those of conventional silicon solar cells [1], [2]. For this low cost and high efficient photovoltaic system a novel concentrator module was designed and manufactured basically composed of a total internal reflection (TIR) - refraction (R) lens system and a small GaAs solar cell. The lens system was designed for a 1000X light concentration (module surface: 1000 mm^2, solar cell surface: 1 mm^2) leading to a significant reduction of solar cell costs. Moreover, the system was designed for an acceptance angle of 1.1° of the incident radiation in order to reduce the costs of the tracking system, and a uniformity of the solar cell illumination better than 2:1. The optical efficiency of the designed lens system was 82.4% (i.e. 17.6% absorption and scattering losses).

Concentrator design and simulation

The concentrator design solution consists of a primary aspheric TIR Fresnel lens and a secondary aspheric lens located between the primary lens and the solar cell. The optical path through the lens system is shown schematically in figure 1. The incident radiation is not focused on the surface of the solar cell but inside the secondary lens yielding a more uniform

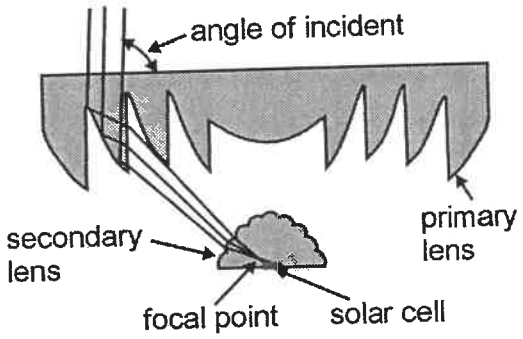

Fig. 1: Principle of photovoltaic concentrator module.

illumination of the cell. A cross-section and a 3D model of the lens system is shown in figure 2. The primary lens has a square size of 32 mm x 32 mm and a total thickness of 18 mm. It consists of eight "giant" aspheric facets with depths up to several millimeters and included angles of about 30°. The secondary lens is about 6 mm thick and exhibits an aspheric front surface and a spherical rear side.

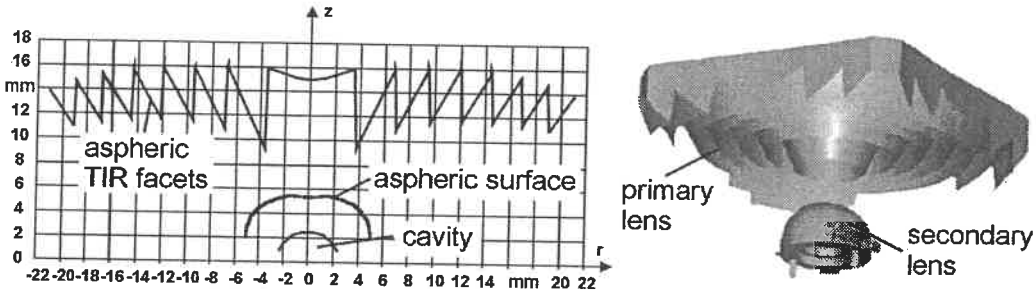

Fig. 2: Cross-section and 3D model of the TIR-R lens system.

The optical efficiency of the TIR-R lens system was calculated for PMMA and for wavelengths between 350 nm and 1800 nm (left side of figure 3). An efficiency > 80% is achieved between 400 nm and 800 nm. This calculation includes absorption of the glass plate that covers the module as well as the absorption of the silicone used for encapsulating the GaAs solar cell. The optical efficiency decreases with an increase of the angle of incidence (right side of figure 3). The decrease is < 10% for angles of incidence < 1.1°.

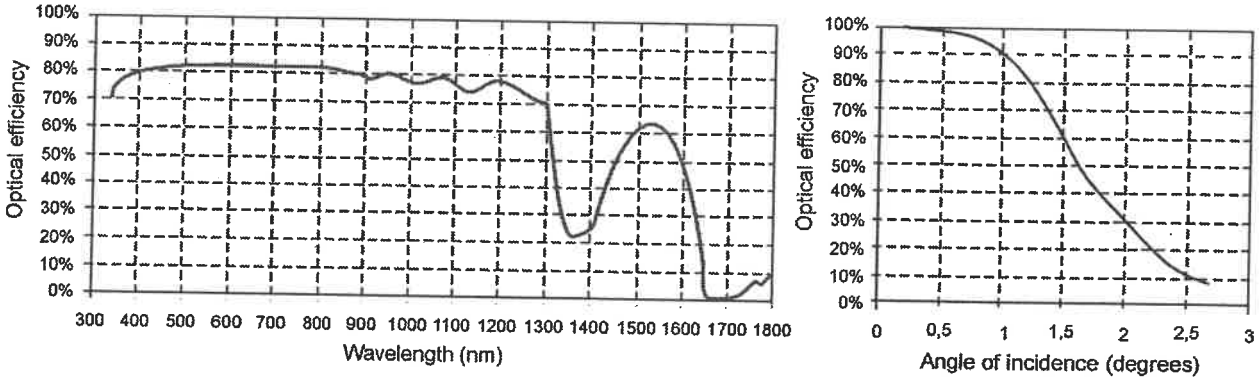

Fig. 3: Spectral dependence of the optical efficiency of the TIR-R lens system (left) and its decrease with increasing angle of incidence (right).

Mold design and manufacture of concentrator

For injection molding of both primary and secondary lenses two complex molds were needed which were realized by diamond machining at the LFM. The design of the molds is shown in figure 4 and 5. Since diamond tools for diamond turning of very deep and narrow Fresnel grooves as required by the optical design of the TIR lens are not

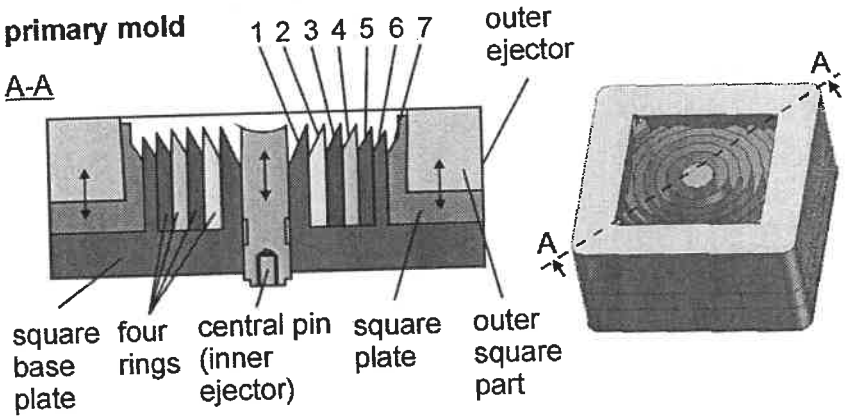

Fig. 4: Design of primary mold.

available, the mold of the primary lens had to be divided into eight pieces: a square base plate with two rings for facets 1 and 6, four rings for facets 2, 3, 4 and 5, resp., a central pin exhibiting the central asphere (which is also used as inner ejector), a square plate for facet 7, and an outer square part. The outer ejector is formed by the square plate and the outer square part.

The eight pieces of the primary mold, made of aluminum AlZnMgCu1.5, were pre-machined on a Moore M18 Aspheric Generator, electroless nickel plated and diamond turned using a diamond tool with a special shank design. All cylindrical surfaces were diamond turned in order to secure a fitting tolerance of ± 5 µm. After diamond machining, the square shape of the Fresnel lens was generated by electrical discharge machining.

The mold for the secondary lens was divided into three parts (cf. figure 5): an upper part exhibiting the aspherical cavity, a cylindrical plate containing the sprue, and a base plate with the central spherical pin. The machining sequence was similar to the primary mold.

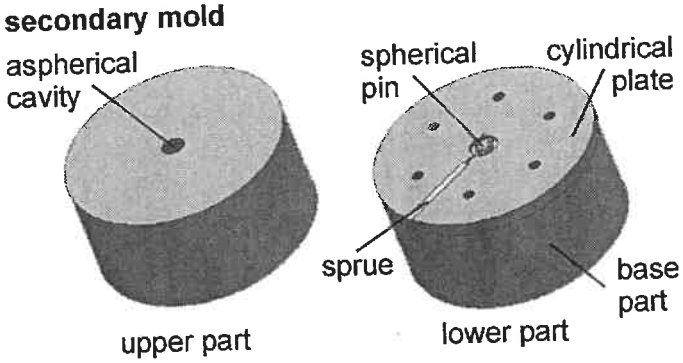

Fig. 5: Design of secondary mold.

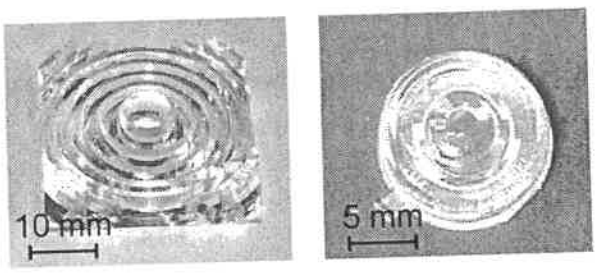

Fig. 6: Injection molded primary (left) and secondary (right) lens.

The geometry of the completed primary mold was measured with a Moore M18 Universal Coordinate Measuring Machine. A peak-to-valley form deviation better than 2 µm could be achieved. The figure accuracy of the molded PMMA primary lens (figure 6, left) was 60 µm to 80 µm due to inhomogeneous shrinkage. The figure accuracy of the secondary PMMA lens (figure 6, right) was well within specifications.

Prototype of photovoltaic system

Although the geometry of the giant Fresnel facets of the primary lens could not be replicated very well by injection molding, a prototype photovoltaic system consisting of 138 concentrator modules was assembled, figure 7. The GaAs solar cells were mounted on an insulated metal substrate and encapsulated by the secondary lenses. The primary lenses were positioned with respect to the secondary lenses by use of special plastic holders. Finally, a glass plate was glued on top of the primary lenses for sealing the panel.

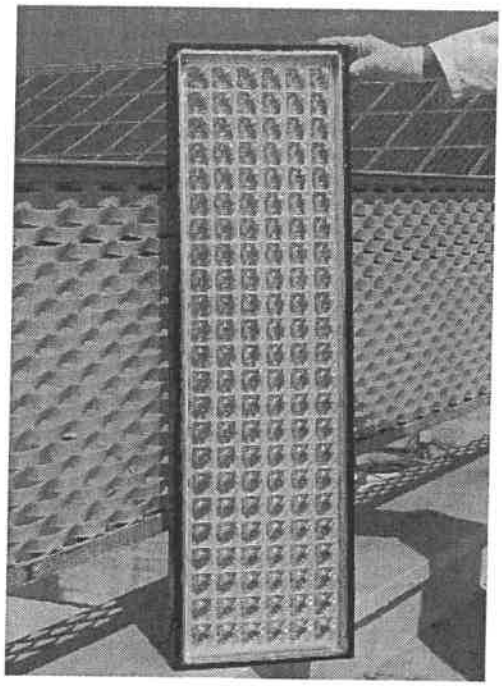

Fig. 7: Prototype of photo-voltaic panel.

Summary

A novel type of solar cell concentrator module, consisting of a primary TIR lens with seven giant Fresnel grooves and an aspheric secondary lens, was realized by diamond machining of electroless nickel plated aluminum molds and injection molding of PMMA lenses. The new concentrator concept could be verified. Due to the inhomogeneous shrinkage of the primary lens in the injection molding process an optical efficiency of only 55% (compared to the theoretical value of 82.4%) could be achieved. The next important step of the development will be the improvement of the injection molding process.

Acknowledgement

This work was funded by the European Community within the Fifth Framework Program under the contract number ENK5-CT2001-00548 (HAMLET).

References

[1] Díaz, V. et al.: Progress in the Manufacture of Ultra Flat Optics for Very High Concentration Flat Panels. 29th IEEE Photovoltaic Specialists Conference, New Orleans, Louisiana, USA, May 20th-24th, 2002.

[2] Alonso, J. et al.: Industrialization of Ultra-Flat Concentrator Module of High Efficiency. PV in Europe - From PV Technology to Energy Solutions, Rome, Italy, October 7th - 11th, 2002, pp. 530-533.

A Framework of a Model-based Simulation System for Predicting Surface Generation in Ultra-precision Raster Milling of Freeform Surfaces

C.F. Cheung, W.B. Lee and S. To

Advanced Optics Manufacturing Centre, Department of Industrial and Systems Engineering, The Hong Kong Polytechnic University, Hung Hom, Kowloon, Hong Kong.

Abstract: The fabrication of high quality freeform surfaces used in many photonics and telecommunication products is based on ultra-precision raster milling which allows direct machining of the freeform surfaces with sub-micrometric form accuracy and nanometric surface finish. However, the achievement of a superior mirror finish still depends largely on the experience and skills of the machine operators through an expensive trial-and-error approach when new materials, new surface design or new machine tools are used. As a result, this paper presents a framework of a model-based simulation system is proposed for the prediction of the surface generation in ultra-precision multi-axis raster milling of freeform surface. The potential benefits for the use of the system for the optimization of cutting parameters and cutting strategies are also discussed.

Keywords: Ultra-precision Raster Milling, Freeform Surfaces, Surface Generation, Model-based Simulation, Optimization

1. Introduction

Freeform surfaces give designers freedom to design products with functional, aesthetic, and ergonomic surfaces. However, it is difficult to generate complex freeform surface [1] to high degree of accuracy. It is usually time consuming, information intensive, and prone to errors. Limited research has been conducted toward the use of multi-axis freeform surface machining. Most of the research work is focused mainly on the improvement of tool path uniformly and the reduction of the computational complexity at the same time [2]. Ho et al. [3] has conducted real-time analysis between a tool and an environment. Some research work has been found on which studies a collision-free tool path for freeform machining [4]. Recent review can be found in Jensen and Anderson [5] and Austin et al [6]. Tseng and Sue [7] summarize four main approaches which are: the parametric method [8], the Cartesian method [9], the offset surface method [10] and the cubic approximation method [11, 7]. However, most of them focus on the tool path generation for freeform end-milling or ball milling processes. Relative little research has been found in the study of the surface generation in freeform raster milling making use of single crystal diamond tool.

Due to the geometrical complexities, the simulation of surface generation in ultra-precision raster milling of freeform surfaces is more difficult than conventional machining. The challenges include the detection and avoidance of local tool gouges [12] and global tool interference as well as meeting the specified surface roughness and form accuracy at minimal cost and machining time. In ultra-precision multi-axis raster milling, the surface quality depends largely on the selection of cutting conditions and cutting strategies such as whether to cut in only one direction, or both, or, whether to perform raster cuts or spiral cuts, etc. The spiral method and the zigzag method are commonly used cutting strategies for freeform machining [13]. However, most of the work to date has been based on empirical studies. On the other hands, the machining time can not be minimized effectively since optimal cutting parameters are not easy to find manually using a trial and error approach [14]. Relatively little quantitative work has been reported. Although some attempts have been made in the development of geometric models to simulate surface topography of a workpiece, most of them focused on the synthesis of surface topography from a number of limit points generated from CAD/CAM system [15]. The effect of cutting mechanics and the materials factors on surface roughness have been overlooked in most of the studies of surface generation in freeform machining. There is a need for the development of deterministic models which take into account both the process and materials factors in the generation of the surface. In this paper, a framework of a model-based simulation system is presented for predicting the cutting performance and the optimal cutting strategies for the ultra-precision raster milling of freeform surfaces.

2. Surface Generation in Ultra-precision Raster Milling

Fig. 1 shows the ultra-precision raster milling of freeform surface using a Five-axis Freeform 705G from Precitech Inc. As shown in Fig. 2, honeycomb-shaped surface topography is found on the raster milled surface. The surface generation in ultra-precision raster milling is affected by a number of factors which include: feed rate, spindle speed, swing distance, depth of cut, step distance, tool nose radius, relative vibration between the tool and

the workpiece, etc. It is interesting to note that cusp height is minimized by well matching the feed rate and the step distance.

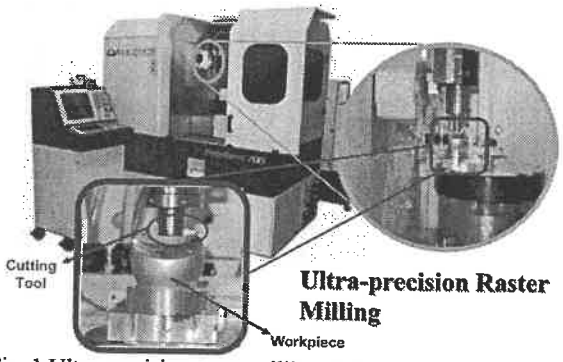

Fig. 1 Ultra-precision raster milling of freeform surface

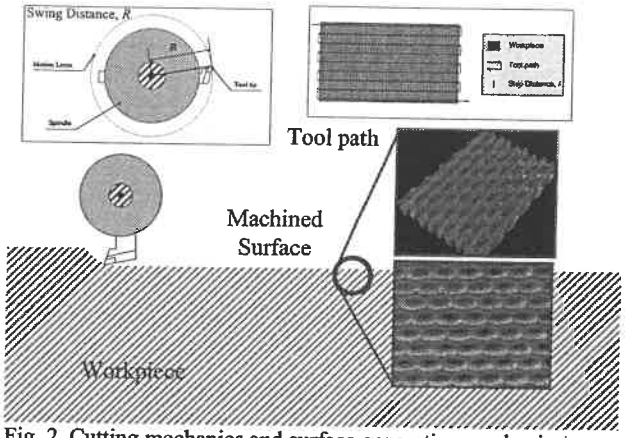

Fig. 2 Cutting mechanics and surface generation mechanisms in Ultra-precision raster milling

3. Framework of the Model-based Simulation System

As shown in Fig. 3, the model-based simulation system is composed of a freeform tool path simulator, a surface topography simulation model and an optimization module, respectively. The freeform tool path simulator is capable of integrating the optical design system with the CAD/CAM software so that the tool path can be generated directly from optical design without the need for any data post-processing. The conceptual freeform tool path generator is composed of several elements which include the ZEMAX optical design software, a data conversion program, and a numerical mathematical algorithm for tool path construction and a NC program translator [16]. The surface topography simulation module is a core module which is used to predict the technological aspects in ultra-precision raster milling. Fig. 4 shows a proposed architecture of the surface topography simulation model. It performs several functions which include the simulation of the motion of the cutting tool based on the kinematics and dynamics of the cutting processes, the simulation of a 3D surface topography and hence the prediction of the surface quality in freeform raster milling. For the optimization module as shown in Fig. 5, the optimization of surface quality is undertaken by an iterative algorithm which will be developed based on a surface topography simulation model [17]. The iterative algorithm will search for the optimal cutting condition with an incremental step size within a pre-defined range of process parameters for different cutting strategies based on the minimum surface roughness criteria. The outputs of the optimization module are the suggested optimum cutting conditions, recommended cutting strategy and the projected performance characteristic diagrams which depicts the variation of surface roughness with the process parameters and cutting strategy being investigated.

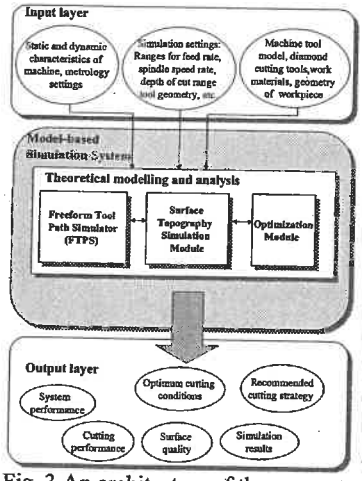
Input layer
Static and dynamic characteristics of machine, metrology settings
Simulation settings: Ranges for feed rate, spindle speed rate, depth of cut range
Machine tool model, diamond cutting tools, work materials, geometry of workpiece
Model-based Simulation System
Theoretical modelling and analysis
Freeform Tool Path Simulator (FTPS)
Surface Topography Simulation Module
Optimization Module
Output layer
System performance
Optimum cutting conditions
Recommended cutting strategy
Cutting performance
Surface quality
Simulation results

Fig. 3 An architecture of the conceptual model-based surface simulation system

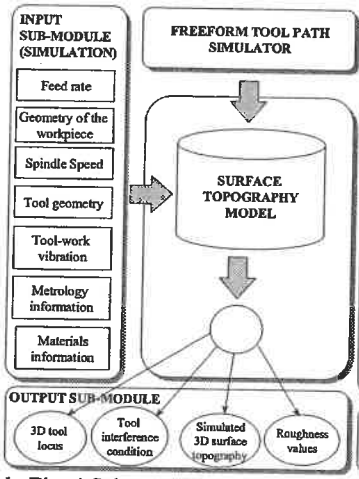

Fig. 4 Schematic diagram for the topography simulation model

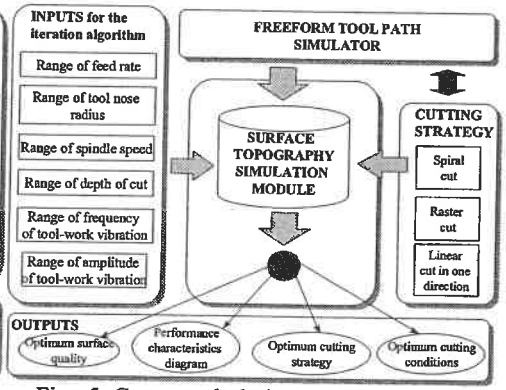

Fig. 5 Conceptual design of the optimization module

4. Preliminary Experimental

The tool path generator of the model-based simulation system has been experimentally verified through preliminary cutting test conducted on a Precitech 705G five-axis ultra-precision freeform machining system and encouraging results are obtained. The surface roughness of raster milled surface was measured by a WYKO NT8000 optical profiler system. Snapshots of the simulation of the tool path generation are shown in Fig. 6. Figs. 7 to 10 show the effect of feed rate, depth of cut, spindle rotational speed and step distance on the surface generation, respectively. It is interesting to note that the surface roughness appears to be more susceptible to the change of spindle rotation speed, step distance and feed rate while the depth of cut has less significant effect on surface roughness.

The successful development of the model-based simulation system allows the optimization of cutting parameters and cutting strategies to be determined prior to the actual production. It also helps to find the best surface quality that can be achieved under a given cutting condition. This avoids the need to conduct massive and costly trial-and-error cutting tests.

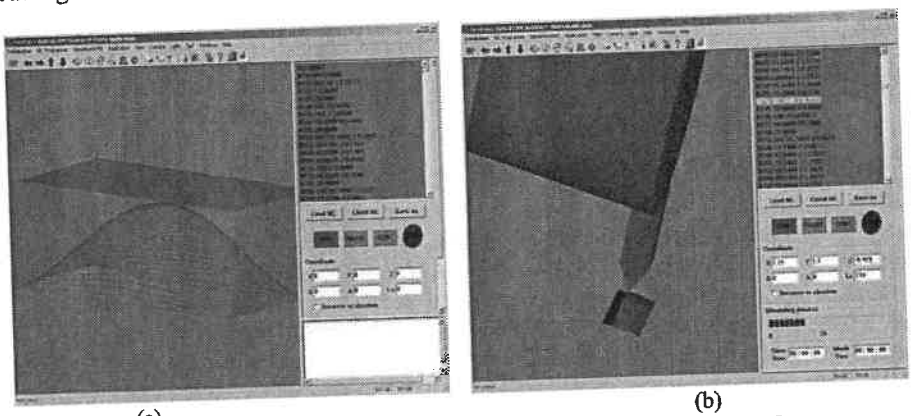

(a) (b)

Fig. 6 Simulation of (a) tool path and (b) raster milling of a F-theta surface

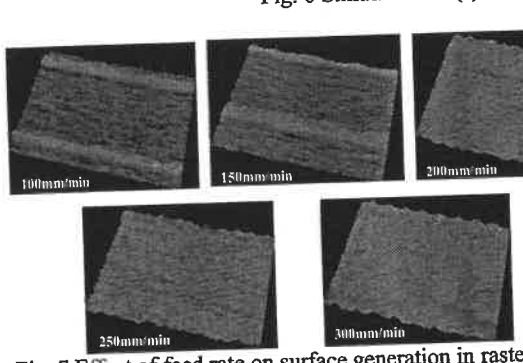

Fig. 7 Effect of feed rate on surface generation in raster milling

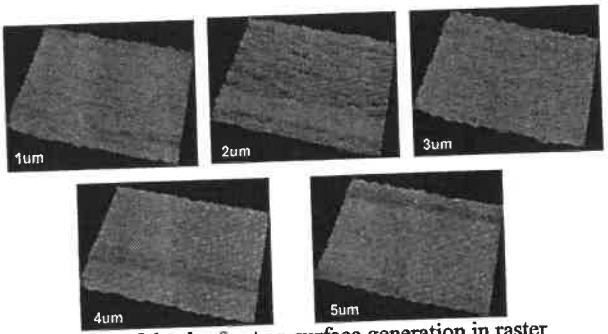

Fig. 8 Effect of depth of cut on surface generation in raster milling

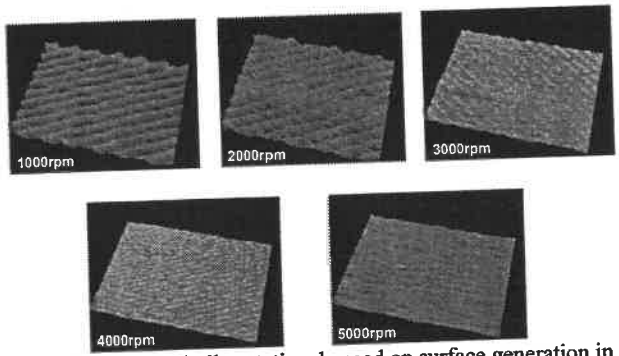

Fig. 9 Effect of spindle rotational speed on surface generation in raster generation raster milling

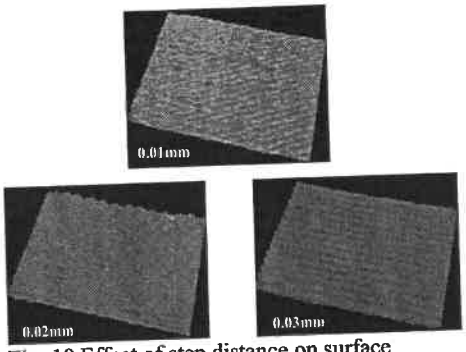

Fig. 10 Effect of step distance on surface milling

5. Conclusion

Ultra-precision raster milling is an expensive process. Nowadays, the achievement of a super mirror finish in many current industrial applications still depends much on the experience and skills of the machine operator through an expensive trial and error cutting test. In this paper, a framework of a model-based simulation system is proposed for the prediction of surface generation in ultra-precision raster milling. The successful development of the system can help to identify the optimal cutting conditions and cutting strategy for different work materials without the need for costly trial and error cutting tests. It also helps to find the best surface quality that can be achieved under a given cutting condition for a specific machine. This will contribute significantly to the knowledge of ultra-precision freeform machining and to the further improvement of the performance of ultra-precision freeform machines.

Acknowledgements

The authors would like to express their sincere thanks to the Research Grants Council of the Hong Kong Special Administrative Region of the People's Republic of China for financial support of the research work under the project no. PolyU 5264/03E. Many thanks are also due to Precitech Inc. for the support of the research work.

References

1. Kurgano, J. et al., (2002) 'Generation of NC Tool Path for Subdivision Surface' CAD/Graphics' 2002, 22-24 August, Kumming, International Academic Publisher, 1-7.
2. Dragomatz, D. and Mann, S. (1997) 'A Classified Bibliography of Literature on NC Milling Path Generation' *Computer-Aided Design*, 29(3), 239-247.
3. Ho, S., et al., (2001) 'Real-time Interference Analysis between a Tool and an Environment', *Computer-Aided Design*, 33, 935-947.
4. Balasubramaniam, M., et al., (2002) 'Generation of Collision-free 5-axis Tool Path Using Haptic Surface' Computer-Aided Design, 34, 267-279.
5. Jensen, C.G. and Anderson, D.C. (1996) 'A Review of Numerically Controlled Methods for Finish-sculptured-surface Machining' IIE Transactions, 28, 30-39.
6. Austin, S.P. et al. (1997) 'Comparison of Discretization Algorithms for NURBS Surfaces with Application to Numerically Controlled Machining' *Computer-Aided Design*, 29(1), 71-83.
7. Tseng, Y.J. and Sue, Y.R. (1999) 'Machining of Free-form Solids Using an Octree Volume Decomposition Approach' *Int. J. of Production Research*, 37(1), 49-72.
8. Loney, G.C. and Ozsoy, T.M. (1987) 'Machining of Free Form Surfaces' *Computer-Aided Design*, 19(2), 85-90.
9. Huang, Y. and Oliver, J.H. (1994) 'Non-constant Parameter NC Tool Path Generation on Sculptured Surfaces' *Int. J. of Advanced Manufacturing Technology*, 9, 281-290.
10. Kim, K.I. and Kim, K. (1995) 'A New Machine Strategy for Sculptured Surfaces Using Offset Surface' *Int. J. of Production Research*, 33(6), 1683-1697.
11. Lee, K., et al. (1994) 'Generation of Toolpath with Selection of Proper Tools for Rough Cutting Processes' *Computer-aided Design*, 26(11), 823-831.
12. Choi, B.K. and Jerard, R.B. "Sculptured Surface Machining," Kluwer Academic Publisher (1998).
13. Chen, Y.H., Lee, Y.S. and Fan, S.C. "Optimal Cutter Selection and Machining Plane Determination for Process Planning and NC Machining of Complex Surfaces," *J. of Manufacturing Systems*, Vol. 17, No.5, p.371-388 (1998).
14. Sun, G., Wang, F.C., Wright, P. and Sequin, C. "Operation Decomposition for Freeform Surface Features in Process Planning," *Proceedings of the 1999 ASME Design Engineering Technical Conferences*, 12-15, September, Las Vegas, Nevada, p.1-12 (1999).
15. Tseng, Y.J., Chen, Y.D. and Liu, C.C. "Numerically Controlled Machining of Freeform Curves Using Biarc Approximation," *Int. J. of Advanced Manufacturing Technology*, Vol. 17, p.783-790 (2001).
16. Lee, W.B., et al. (2003) 'A NC Tool Path Translator for Virtual Machining of Precision Optical Products' *J. of Materials Processing Technology*, 140(1-3), 211-216.
17. Cheung, C.F. and Lee, W.B. (2003) 'Surface Generation in Ultra-Precision Diamond Turning: Modelling and Practice' Engineering Research Series, Professional Engineering Publishing Limited of Northgate Avenue, Bury St Edmunds, Suffolk, IP32 6BW, UK.

Machining characteristics with nanometer-cutting machine equipped parallel mechanism

Katsushi Furutani* and Michio Suzuki**
* Toyota Technological Institute
12-1, Hisakata 2-chome, Tempaku-ku, Nagoya 468-8511 Japan
E-mail: furutani@toyota-ti.ac.jp
** NSK Warner K. K. at present

1. Introduction

Today, fabrication of nanometer-scale structures using scanning probe microscope (SPM) instruments are actively investigated [1]-[3]. The authors have proposed a SPM type machine tool equipped a parallel mechanism with 6 degrees of freedom [4][5] for free form surface generation.

In this paper, the machining characteristics are investigated by using the nanometer-cutting machine. At first, a structure of the fine motion device employing the parallel mechanism is introduced. Then the dependence of machining direction to a cantilever is discussed.

2. Fine motion stage for nanometer-cutting machine

Fig. 1 shows an overview of a fine motion stage for a nanotemer cutting machine [5]. The stage supported with 6 links with an elevation angle of 35° stands on a base platform. The machine measures 170 mm × 170 mm × 108 mm. A table weighs 103 g. The movable range of the table is 30 μm × 40 μm in the x- and y-directions and 100 μm in the z-direction. Stacked piezoelectric actuators with dimensions of 5 mm × 5 mm ×20 mm are used to change the link length. Displacement of the piezoelectric actuator is magnified over 8.6 times (approximately 100 μm) with a lever mechanism with flexure hinges made of ASTM S30400 stainless steel. Both ends of the links are connected with the base platform and the table by flexure joins.

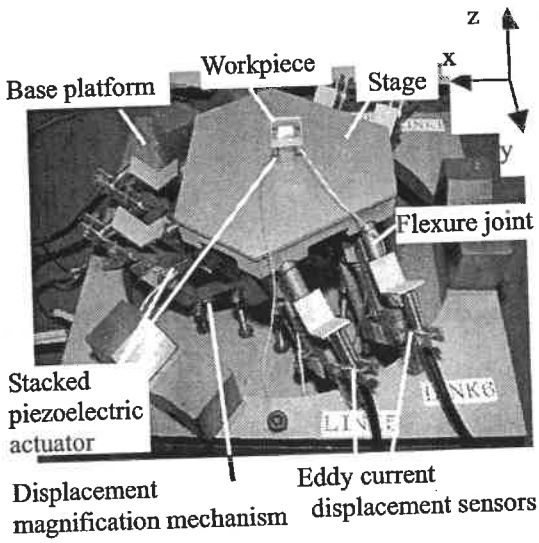

Fig. 1 Appearance of fine motion stage

The motion of the stage is controlled by a feedback of link displacements. A given posture of the table is resolved into the link lengths by inverse kinematics. Then, the link lengths are given as references in each servo systems with a proportional-integral (PI) controller. The controller is installed in a personal computer (80586, 100 MHz). The manipulation signal through a 12-bit D/A converter is given to the piezoelectric actuator through a voltage amplifier. The feedback signal is obtained with a 12-bit A/D converter. The displacement of each link is measured with an eddy current sensor with a resolution of 0.4 μm.

The displacement of the stage was calibrated by the least square fit with measured displacement in all directions. The repeatability (3σ) is 0.1 μm in translation and 10 μrad in inclination.

3. Machining characteristics

3.1 Machining conditions

Fig. 2 shows an experimental setup. The fine motion stage works as a part of an atomic force microscope (AFM) used as the nanometer-cutting machine in which the probe tip was used as a cutting tool. Table 1 shows the machining conditions. The probe is designed for a lateral force microscope.

Acrylic resin was scratched with the probe. At the beginning of the machining process, an inclination of a workpiece was measured by scanning with a smaller contact force and a rough measurement pitch. Then the stage was moved in parallel to the inclined surface of the workpiece and the probe scratches it with a larger contact force on the same machine. Finally, the scratched area was observed with a commercial AFM.

3.2 Machining characteristics without vibration

Fig. 3 shows a result of machining in the case of

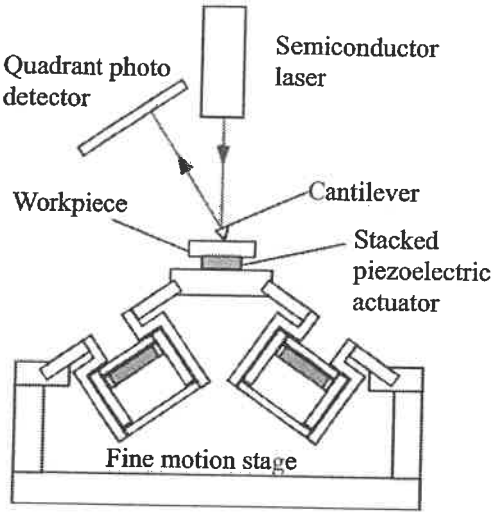

Fig. 2 Experimental setup

Table 1 Machining conditions

Pre-scan area	10 μm × 10 μm
Machined area	5 μm × 5 μm
Scanning frequencies	2 Hz in scratching direction, 0.05 Hz in another direction
Number of scratches	100
Cantilever	100 μm × 40 μm × 800 nm (L×W×T), 0.73 N/m, 71 kHz Si_3N_4 (tip and lever)
Pressing force	400 nN
Workpiece	Acrylic resin $(C_5H_8O_2)_x$

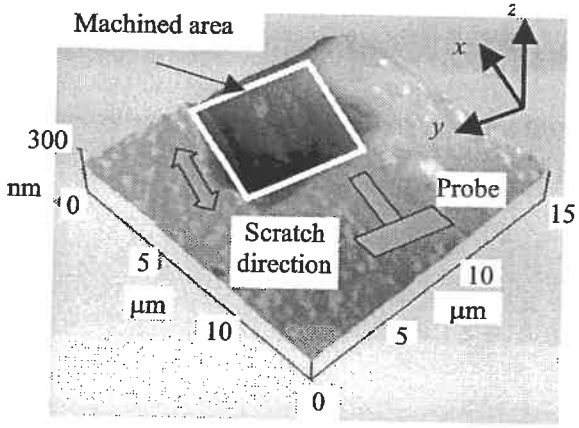

Fig. 3 Result of machining in x-direction

scratch in the x-direction. The shape error corresponded with the motion error of the stage. Because the cantilever is a strip, it was buckled in the

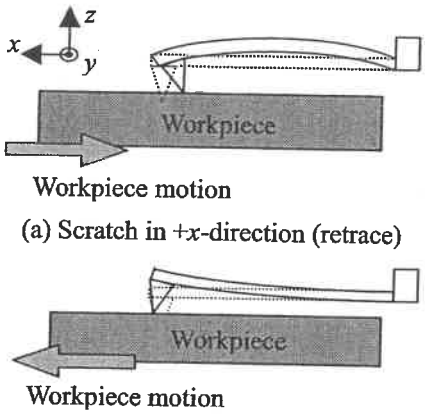

Fig. 4 Scratch in x-direction

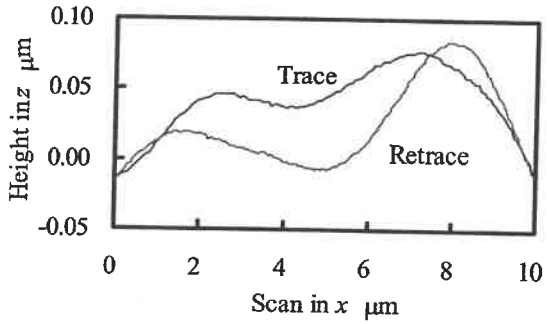

(a) Cantilever height in trace and retrace motions

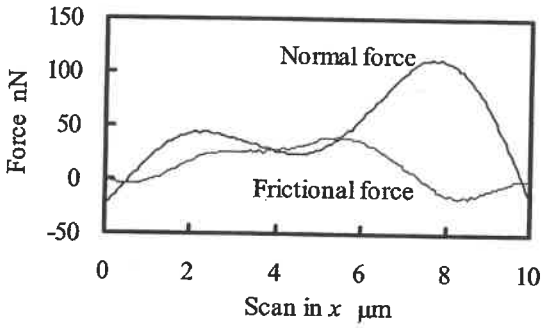

(b) Resolved forces

Fig. 5 Forces acting during scratch in

x-scanning by the frictional force between the tip and the surface of the workpiece as shown in Fig. 4. The normal and frictional forces shown in Fig. 5 (b) can be calculated by using the forces in both trace and retrace motions shown in Fig. 5 (a). Because the normal force was small at both ends and the frictional force was almost flat, no ridge was observed on the boundary of the machined area. Fig. 6 shows a contour map of 10 μm × 10 μm area when the number of scratches was changed from 25 to 100. Although non-machined area

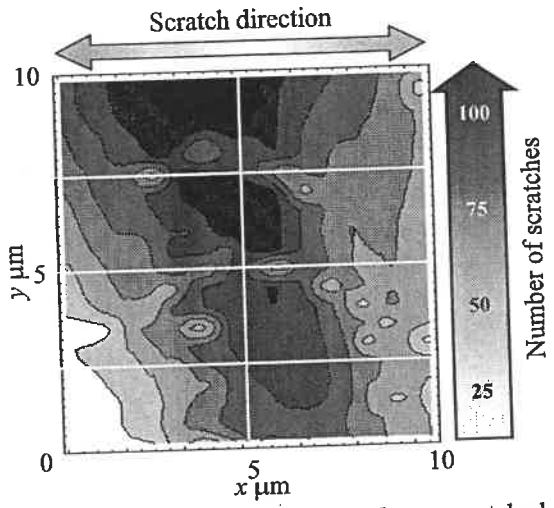

Fig. 6 Contour map of machined area scratched in x-direction (machined area: 10×10 μm)

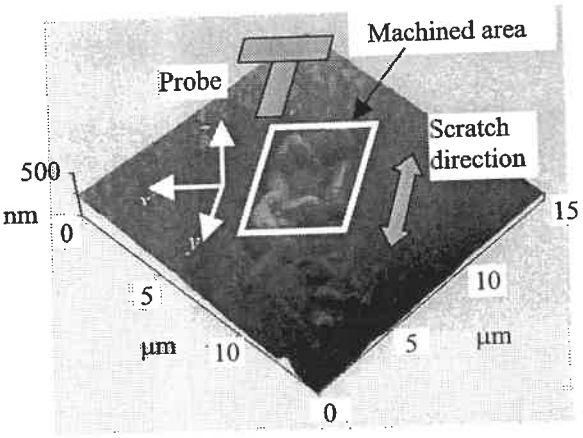

Fig. 7 Result of machining in y-direction

was decreased with an increase of the number of scratches, the bottom of the machined area was not flat. The non-machined area causes the viscoelasity of the acrylic resin put to an end with the probe tip.

Fig. 7 shows a result of machining in the case of scratch in the y-direction. Some ridges with a height of 180 nm because of the viscoelasticity were observed on the boundary of the scratched area. The cantilever distorted during the y-scanning by the frictional force between the tip and the surface of the workpiece. Because the cantilever is stiffer in the y-direction than the x-direction, the normal force was not decreased at both ends which are the turning points of the scratches as shown in Fig. 8. Fig. 9 shows a contour map in the case of scratch in the y-direction. Although some ridges were observed, non-machined area was decreased and the bottom of the machined area was flat.

The error of the tip position in the y-scanning was

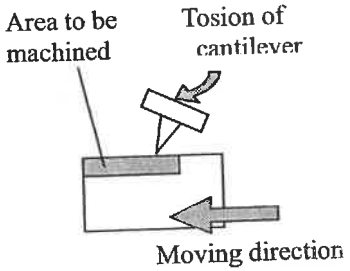

(a) Feeding workpiece

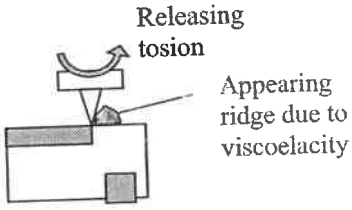

(b) Reach to workpiece end

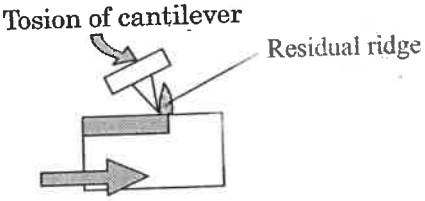

(c) Switch moving direction in reverse

Fig. 8 Mechanism of ridge generation

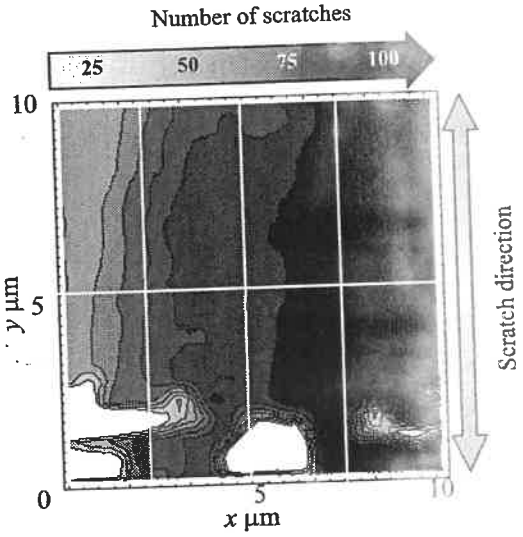

Fig. 9 Contour map of machined are scratched in y-direction (machined area: 10×10 μm)

smaller than that in the x-direction. Because the stiffness affected the scanning, machined shapes were

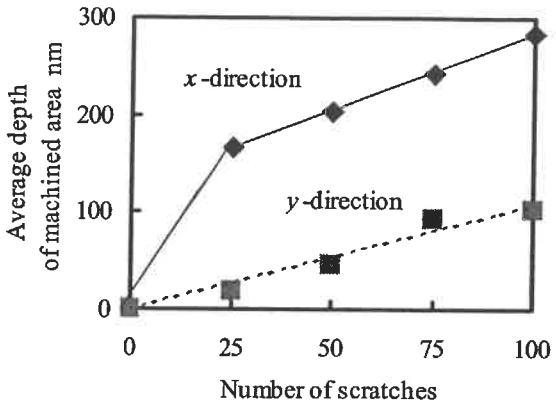

Fig. 10 Relationship between depth of machined area and number of scratches against scratch direction

different between the scanning directions.

Fig. 10 shows the relationship between the machined depth and the number of scratches against the machining direction. In the x-direction, the machining speed decreases when the number of scratches exceeds 25. However, the depth of the pocket increases linearly for numbers higher than 25. Although the machined depth per scratch in the y-direction was smaller than that in the x-direction, it was proportional to the number of scratches. The machining error was small in the case of scratching in the y-direction. Therefore, scratching in the y-direction is preferable for the machining because of the anisotropic stiffness of the probe.

3.3 Machining characteristics with vibration

Then the vertical vibration with an amplitude of 59 nm and a frequency of 9.4 kHz was added to the stage motion with a piezoelectric actuator mounted on the stage to increase the relative velocity between the cantilever and the specimen. The piezoelectric actuator measures 5 mm × 5mm × 10 mm. Fig. 11 shows a result of machining. Although the scratched area was 5 μm × 5 μm, the machined area measured 4 μm × 4 μm. The positioning accuracy of the stage and the distotion of the cantilever affects the decrease of the machined area. The depth of the pocket measured 20 nm after 100 scratches. No ridge was observed though the depth was decreased.

4. Conclusions

In this paper, the machining characteristics of the nanometer-cutting was discribed. The conclusions can be drawn as follows.

(1) Pockets were machined by scratching acrylic resin with an AFM probe.

(2) Because the stiffness of the probe is anisotropic, the machining accuracy depended on the scratch direction.

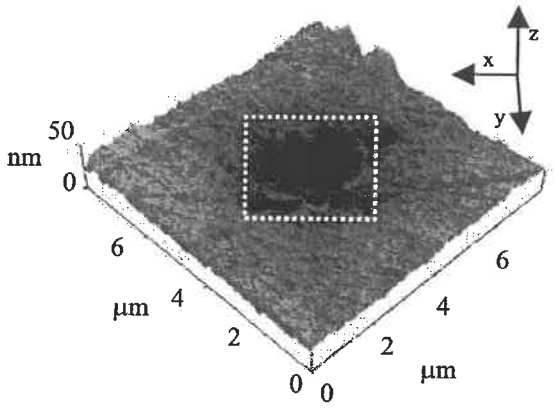

Fig. 11 Experimental result of machining

(3) The additional vibration helps to decrease the ridges on the boundary of the machined area.

Acknowledgement

The authors wish to thank Prof. Kazuyoshi Kondo of Toyota Technological Institute for his valuable advice. This study was financially supported by the Sasakawa Scientific Research Grant from the Japan Science Society and the Grant-in-Aid for High-tech Research Center for "Space Robotics" and for Scientific Research (C)(2)(13650289) of the Ministry of Education, Science, Sports and Culture of Japan.

References

[1] D. M. Eigler, E. K. Schweizer: Positioning Single Atoms with Scanning Tunneling Microscope, Nature, 334, p. 524 (1990).

[2] B. Bhushan, V. N. Koinkar: Tribological Studies of Silicon for Magnetic Recording Applications, J. Appl. Phys., 75, pp. 5741-5746 (1994).

[3] K. Asamoto, K. Furutani, N. Mohri: A Basic Study on Nanometer Cutting of Brittle Materials, Proc. 12th ASPE, Norfolk, VA, USA, pp. 466-469 (1997).

[4] K. Furutani, R. Kudoh, N. Mohri: Nanometer Cutting Machine Employing Parallel Mechanism, Proc. 16th Ann. Meet. Am. Soc. Precis. Eng., Arlington, VA, USA, pp. 164-167 (2001).

[5] K. Furutani, M. Suzuki, R. Kudoh: Nanometer-cutting Machine Using Stewart-platform Parallel Mechanism, Meas. Sci. Technol., 15, 2, pp. 467-474 (2004).

Mechanical Machining of Thin Polycrystalline Diamond Films

Hans H. Gatzen, Christos Kourouklis
Institute for Microtechnology, Hanover University, Germany

Key Words: Diamond films, CVD, Nanogrinding
Abstract: Polycrystalline diamond films can be deposited on a variety of materials by chemical vapor deposition (CVD). Due to its rough surface, such a material is unsuited for many applications. This paper describes a mechanical machining process which allows to reduce the average roughness R_a of a polycrystalline diamond film from 350 nm as deposited to a couple of nanometers. This is done with a three step process, starting out with lapping plates made of composite cast iron/copper to remove the protruding grains, followed by machining on a copper and a tin plate.

1. Introduction

Diamond films are used for coating tools, for diaphragm coating, heat sinks for large scale integrated circuits, or as x-ray windows [1, 2]. In micro electro-mechanical systems (MEMS) they are used as coatings to improve the mechanical and tribological properties [3]. A typical deposition technique is the hot filament CVD method which can produce thin diamond films of a few micron thickness. Because of their polycrystalline structure, these films are rather rough, due to crystallites protruding from the surface. However, a smooth surface is mandatory for many applications. One approach to smoothen the surface is to subject it to mechanical machining. Since the diamond films are extremely hard, eliminating the roughness through a machining process is challenging [4]. Several polishing technologies have been investigated for smoothening: mechanical polishing, chemical polishing, chemical-mechanical polishing, high energy beam (ion, electron, laser) polishing, and electrical discharge machining (EDM) [5]. So far, known mechanical polishing techniques achieve a maximal surface roughness R_{max} of as much as 1 µm [5], far to rough for many applications.
The work described in this paper is aimed at achieving an average roughness two to three orders of magnitude better, i.e. achieving a roughness in the nanometer range through mechanical machining. The challenges of mechanical machining are an inefficient material removal rate at one end of the machining spectrum, as well as damage and crushing of the film due to its weak adhesion to the substrate on the other. To overcome these challenges, a multi step process using a combination of lapping and nanogrinding processes has been chosen. While lapping uses a loose grain, nanogrinding employs a tool with imbedded grain. The commonality with lapping is the use of a lapping kinematic.[6]. Nanogrinding was developed at the Institute for Microtechnology (imt) at the Hanover University in Hanover, Germany and is capable of machining planes on micro parts made of brittle materials with an average surface roughness R_a of less then 1 nm [7].

2. Experimental Setup and Procedure

The polycrystalline diamond films were provided by the Institute of Microstructure Technology and Analytics at the University of Kassel in Kassel, Germany [8]. The diamond films were deposited on 500 µm thick silicon substrates. The deposition was done with the hot filament method at 50 mbar by using a methane hydrogen mixture. By heating up tungsten wires located above the substrate to 2,250°C, diamond was deposited on the silicon surface. The resulting film had a thickness of about 5 µm and a polycrystalline structure. The substrate was subsequently cut in 5 mm x 5 mm pieces for the machining experiments.

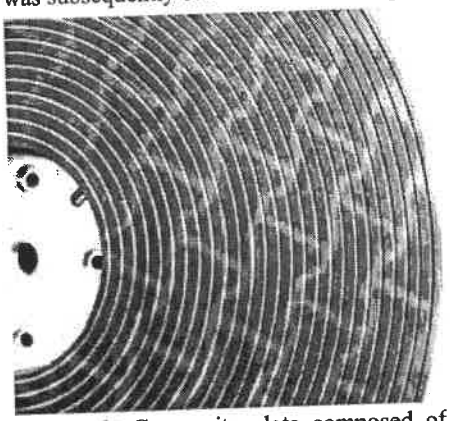

Figure 1: Composite plate composed of cast iron and copper

To investigate the mechanical machining of the diamond films, Peter Wolters 3R40 polishing machines were used. The plate diameter was 400 mm and the load was applied through weights. A three step process was developed, using three different plates, and a combination of lapping, polishing, and nanogrinding. Table 1 provides an overview of the process steps as well as over the key process parameters.
For the first lapping process, a lapping plate made of composite cast iron/copper was used as depicted in figure 1. This type of plate has been designed specifically for the machining of natural and synthetic diamonds and diamond films. The plate chosen consists to 90 % of cast iron and 10% of copper. The purpose of the cast iron is to achieving a high removal rate while the copper is responsible for the surface finish.
For the second process step, a pure copper plate was used. Two machining alternatives were investigated: lapping and nanogrinding.
The third and final step is aimed at achieving the final finish. For it, a tin plate was used. As before, this process was run in two versions: with lapping and with nanogrinding.

As abrasive material in all process steps, diamond grain in different sizes was used. For lapping, the diamond grains were dispersed in either a water or an oil based fluid, while for the nanogrinding, the diamond grain was embedded in the respective plate and the fluid did not contain any cutting grit.

TABLE 1
PROCESSING PARAMETERS FOR THE MACHINING OF THE DIAMOND FILMS

Process	Plate	Diamond grain	Fluid
First step: lapping on composite plate	Composite (90% cast iron, 10% copper)	4 – 6 µm, 1.5 – 3 µm, 0.5 – 1 µm	Water- and oil-based
Second step: lapping	Copper	1.5 – 3 µm	Water- and oil-based
Alternative second step: nanogrinding	Copper	1.5 – 3 µm	Water-based
Finishing step: lapping	Tin	0.5 – 1 µm	Water-based
Alternative finishing step: nanogrinding	Tin	0.5 – 1 µm	Water-based

3. Process Experiments and Results

In order to select the influencing process parameters, preliminary investigations were conducted. It was found that a pressure of 3.3 MPa and a cutting speed of 0.5 m/s are appropriate to machine the film on the different plates without creating any optically observable fractures. This pressure was then used in all processing steps. For the determination of the machining result the machined surfaces were analyzed with atomic force microscopy (AFM) and optical microscopy.

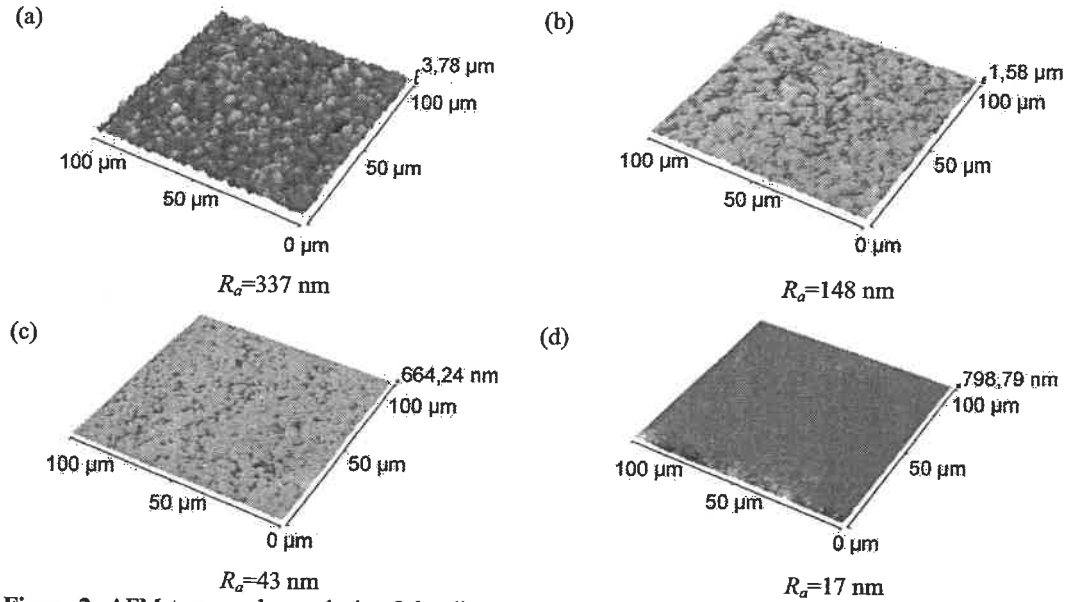

Figure 2: AFM topography analysis of the diamond film (a) as deposited and after lapping with a composite plate (b) for 10 minutes (top right), (c) 40 minutes (bottom left), and (d) 100 minutes (bottom right)

The challenge of the first process step was to develop a technology allowing to cut the protruding peaks of the single diamond grains of the diamond film at a reasonable rate without jeopardizing the film integrity. As it is shown in figure 2, the deposited film had a rough surface with sharp peaks. Using a soft plate resulted in a grazing of the plate, combined with a fracture or delamination of the film. Such a damage was observed in first investigations with a soft tin plate to machine the films. By using a relatively hard plate, this issue could be resolved. Three sizes of diamond grain were used: 4-6 µm, 1,5-3 µm, and 0.5-1 µm. To ensure that a transition to smaller grain was not compromised by larger grain embedded in the lapping plate, the plate surface was lapped by using pumice grain.

An investigation using 4-6 µm diamond grain for lapping showed no better result regarding the removal rate than for the 1,5-3 µm grain. Figure 2 shows the surface before the test and for three different machining times with 1,5-3 µm diamond grain. The surface roughness of R_a of 337 nm before machining was reduced to a value of 17 nm after 100 minutes of lapping. Longer machining time did not result in any further roughness reduction. The surfaces did show any fractures anywhere at the film surface.

To investigate if an even smaller grain results in a further improved roughness, diamond grain with a size of 0.5-1 µm was used during an additional test run. By using the smaller diamond abrasives, the roughness of the probes did not change at the same speed as it did before with the bigger grain. After a machining time of 120 min with 0.5-1 µm abrasives, the roughness was lowered from a R_a of 17 nm to 10 nm. Also, further machining did not smoothen the surface any further. The use of oil instead of water based fluids resulted in a surface waviness with a wavelength of 60 µm and a amplitude of 40 nm. The reason for the waviness could not yet be determined. This showed that the use of oil on the composite plate will not enhance the machining result as it should because of the higher viscosity of the oil and the resulting lower penetration of the abrasive in the film. The higher viscosity leads to a higher gap between workpiece and plate and this should have led to a smoother removal process. Figure 3 depicts the results of the finer grain and the usage of oil as fluid.

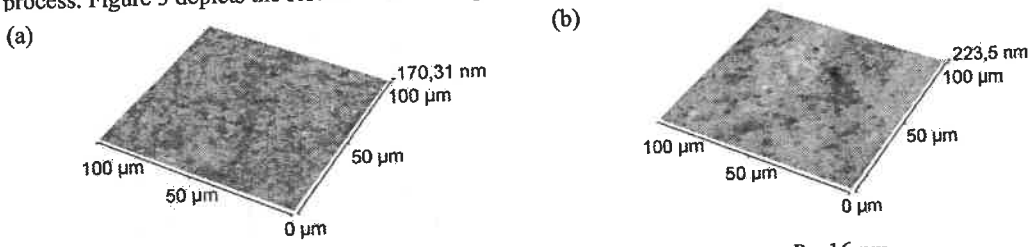

R_a=10 nm R_a=16 nm

Figure 3: AFM topography analysis of the diamond film after lapping with a composite plate with 0.5-1 µm diamond grain for 120 minutes and (a) with water based fluid and with (b) oil based fluid

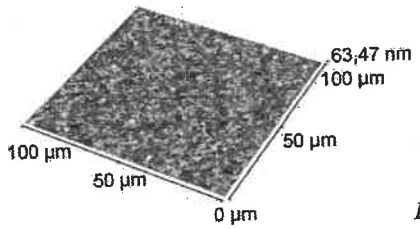

R_a=8 nm

Figure 4: AFM topography analysis of the diamond film after lapping on a copper plate with 1.5-3 µm diamond grain for 60 minutes

While the first process step accomplishes the brunt of the cutting by removing the protruding grains, step two and three are aiming at further smoothening the diamond film, ultimately aiming at an average roughness R_a in the nanometer range. To do so, for each consecutive step a softer plate than used for the previous one is used. As previously mentioned, process step 2 is executed on a copper plate. Two process versions are investigated: using a water-based and an oil-based lapping slurry. Figure 4 depicts the resulting surface after lapping for 60 minutes with 1.5-3 µm diamond grain. The roughness is further reduced when using a water-based slurry, while an oil-based one doesn't result in further roughness improvements. What may also be noticed is a fine texture pattern which the authors expect to be caused by the variation in crystal orientation in the polycrystalline diamond film. A similar effect may be observed when surface machining multiphase ceramics where the different orientation of the single crystals leads to different elastically behavior and removal rates [7]. By conditioning a copper plate with diamond grain in a slurry, diamond grains were embedded in the copper. Combining it with a machining process using a water based fluid without diamond grain results in a process similar to nanogrinding. This approach did not yield any improvements over lapping: the machining time was up to two times longer than for lapping, while the surface roughness achieved was always in the same range as the one accomplished with lapping.

In order to reduce the roughness further, a third step using a tin plate which is very soft was executed. When machining ceramics, the use of a tin plate substantially decreases the cut rate. This could also be observed for the diamond film. A reduction of the roughness occurred much slower than when machining the film on a copper plate. Both lapping and nanogrinding using a water based slurry or nanogrinding fluid, respectviely. Figure 5 shows a surface of a nanoground diamond film. The roughness could be further reduced to a R_a of 6 nm after 120 minutes of machining. Lapping and nanogrinding achieved similar roughness results. The surface also shows the same texture as it did after machining on the copper plate.

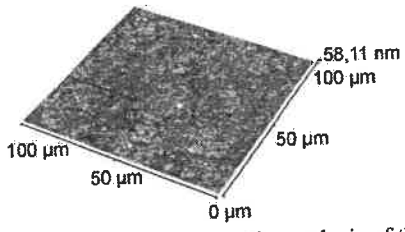

R_a=6 nm

Figure 5: AFM topography analysis of the diamond film after nanogrinding with a tin plate with 0.5-1 µm diamond grain for 120 minutes

After showing that mechanical machining techniques could be used to smoothen the diamond film to an average roughness R_a in the nanometer range, additional tests were done to investigate the machining of discontinuous diamond surfaces. Such a discontinuous surface was

created by depositing the polycrystalline diamond film on a silicon wafer with surface waffle pattern created by anisotropic etching. As previously, the film thickness was 5 µm. A mechanical machining results in a cutting of the film at the surface while the film on the side walls and bottom of the pits remained. The process sequence developed was applied to this film. Figure 6 shows a series of optical micrographs made at different times while the diamond film was run through the different process steps. Figure 6(a) shows the film as deposited. In figure 6(b) and 6(c) the crystallites protruding from the surface were cut away. In figure 6(d) the diamond film was partially machined off and only at the edges some diamond film remained. By applying nanogrinding, the remainder of the film originally 5 µm thick was totally machined off the wafer surface, with film material remaining only at the pit sidewalls and bottom (Figure 6(e)). As previously in the case of the continuous film, no cracks or delaminations occurred.

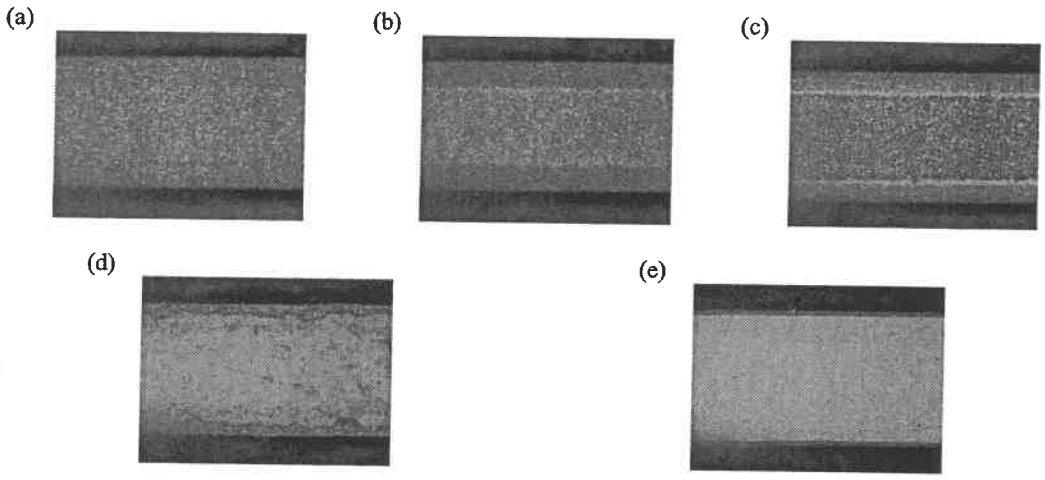

Figure 6: Microscope images of the diamond film removal. (a) starting point, (b) lapping on the composite plate, (c) lapping on the copper plate, (d) nanogrinding (e), width of the machined bar: 300 µm

4. Conclusion

The investigations showed that mechanical machining of polycrystalline diamond films created by HFCVD yields excellent roughness results. Thin diamond films on silicon substrates are machinable and with the three step process presented a smooth surface with an average roughness R_a of as little as 6 nm can be achieved. A three step process using plates with staggered hardness yielded excellent results. For the first step, a composite plate composed of cast iron an copper is employed. For the second step, a copper plate and for the third a tin plate is used. The experiments further proved the feasibility of machining a polycrystalline diamond film with a diamond grit.

Acknowledgement

This work was sponsored in part by the Center of Competence for Ultra Precise Surface Treatment in Braunschweig, Germany. The authors would like to thank the Institute for Microstucture Technology and Analysis at the University of Kassel in Kassel, Germany for the fabrication of the polycrystalline diamond films.

References

[1] Chung, H.K. et al.: "The rapid growth of thin transparent films of diamond", Materials Chemistry and Physics, 72 (2), 2001, pp. 130-132

[2] Shen, C.-H.: "Performance and applications of CVD thin film diamond coated tools", Key Engineering Materials, 138-140, 1998, pp. 25-55

[3] Krauss, A.R. et al.: "Ultrananocrystalline diamond thin films for MEMS and moving mechanical assembly devices", Diamond and Related Materials, 10 (11), 2001, pp. 1952-1961

[4] Kant, A. et al.: "Microstructural effects on the hardness, elastic modulus and fracture toughness of CVD diamond films", Proc., Materials Research Society Symposium, 505, 1998, pp. 611-616

[5] Guo, Z.N. et al.: "Polishing of CVD films", Key Engineering Materials, 202-203, 2001, pp. 165-170

[6] Gatzen, H.H.; Maetzig, J.C.: "Nanogrinding", Precision Engineering, 21 (2-3), Elsevier Science 1997, pp 134-139

[7] Siekmann, H.: "Optimization of the tool plate in nanogrinding", Dissertation, Fortschritt-Berichte VDI, Reihe 2, Nr. 574, VDI Verlag, Düsseldorf 2000

[8] Oesterschulze, E. et al.: "Diamond cantilever with integrated tip for nanomachining", Diamond and Related Materials, 11, 2002, pp. 667-671

HIGH-EFFICIENT WIRE SAWING OF GAAS-WAFERS BY UTILIZATION OF CRACK NUCLEATION MECHANISMS

R. Hammer[1)], M. Jurisch[1)], A. Kleinwechter[1)], M. Schaper[2)], F. Bergner

[1)] *Freiberger Compound Materials GmbH, Am Junger Löwe Schacht 5, D-09599 Freiberg, Germany*
[2)] *Technische Universität Dresden, Institut für Werkstoffwissenschaften, Helmholtzstraße 7, D-01069 Dresden, Germany*

1. Introduction

An issue of high relevance in the production of semiconductor wafers is the enhancement of the crystal cutting efficiency and reduction of bow of the cut wafers as an important quality parameter. One of the main reasons for bow is the appearance of a deflection a_x of the wire across its movement during the sawing process. This transverse deflection a_x is controlled by cutting forces acting perpendicular to a plane (cutting plane) defined by feed direction and wire direction. These forces are influenced by process conditions as the cross section of wires and the distribution of slurry in the cutting slit [1]. In addition, as shown recently for a compound semiconductor like GaAs, the forces acting on the wire in the cutting slit are significantly determined by the material properties of the ingot to be cut. A close relationship between fundamental material parameters such as Vickers hardness and scratching behaviour and the complex mechanisms of material removal during wire sawing has been found.

2. Cutting forces during wire sawing

The basic mechanism which underlies material removal during wire sawing is nucleation of micro cracks and their cross linking by the impact of abrasive grains in the lapping slurry. The threshold for the transition from a plastic to a brittle removal mechanism mentioned above is characterized by a critical penetration depth h_c and a corresponding critical stress of the grains according to [2]:

$$h_c = \Theta_1 \cdot \left(\frac{E}{H}\right) \cdot \left(\frac{K_{IC}}{H}\right)^2 \qquad (1)$$

with the Young´s modulus E, the Vickers hardness H and the stress intensity factor K_{Ic}. The parameter Θ_1 depends on tool geometry and details of the complex deformation mechanism. To reach this threshold a well defined load P_c must be transferred from the cutting tool (grain) to the material to be cut. So, a counterforce of the same amount acts on the grains and consequently on the wire. The relationship between h_c and P_c simply follows from the hardness formula and is given by [4]:

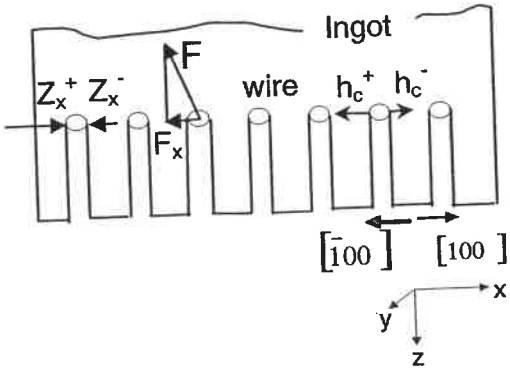

Fig. 1 Forces in the cutting slit during wire sawing

$$h_c(P) \propto P_c^{\frac{1}{2}}. \qquad (2)$$

Depending on their causes, the forces acting on the cutting tool in the cutting slit are divided in external, impressed forces F and constraint forces Z (see fig.1). Their components Z_x and F_x perpendicular to the cutting plane will be in equilibrium under quasi-stationary conditions:

$$Z_x^+ + Z_x^- + F_x = 0 \qquad (3)$$

The external forces F on the wires are determined by technological conditions of the cutting process as for example by the

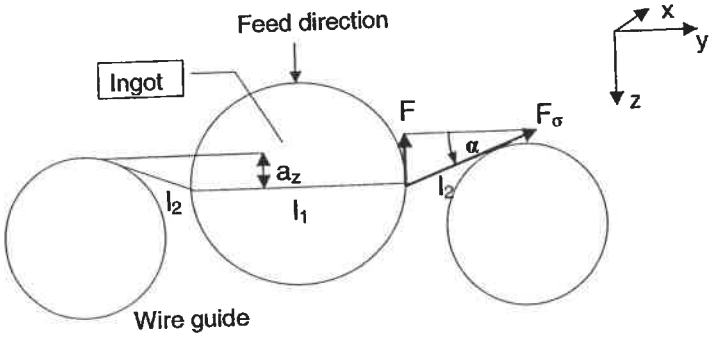

Fig. 2 Forces and geometrical situation during wire sawing

wire tension σ in combination with the wire deflection in the cutting plane. The constraint forces Z^+_x and Z^-_x perpendicular to the uncovered planes results from the counterforces to the critical loads necessary for setting in the brittle material removal mechanism on this surfaces. They are controlled by the critical penetration depths h^+_x and h^-_x for the ductile to brittle transition for the (100) and $(\bar{1}00)$, respectively, according to eqs. (1) and (2) [3]:

$$\left[\frac{h_c^+}{h_c^-}\right]^2 = \left|\frac{Z_x^+}{Z_x^-}\right| \qquad (4)$$

For $\alpha << 1$ (see fig. 2) the deflection of wires a_x perpendicular to the cutting plane is given by [3]:

$$a_x \approx \frac{p_x^+ + p_x^-}{F_\sigma} l_1 l_2 = C f(z) \qquad (5)$$

with $f(z) = l_1 l_2$; $C = \frac{p_x^+ + p_x^-}{F_\sigma}$; $p_x^+ = \frac{Z_x^+}{l_1}$ and $p_x^- = \frac{Z_x^-}{l_1}$

(see fig.1 and fig.2). F_σ acts in the wire direction and is determined by the wire tension σ. The bow of the cut wafers is mainly caused by the lateral deflection a_x which according to eq. (5) is composed of a shaping factor $f(z) = l_1 l_2$ related to geometrical parameters (distance between the wire guides, contour of ingot, contact length l_1) of the sawing process and a factor C which is controlled by the constraint forces Z^+_x and Z^-_x, i. e. by material properties according to eq. (4).

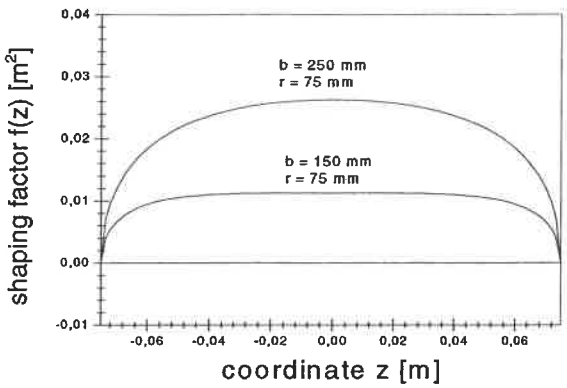

Fig. 3 Shaping factor f(z) for ingot diameter 2r = 6" and different distances between wire guides 2b

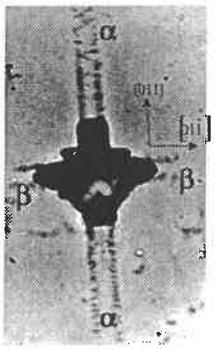

Fig. 4 Paths of α- and β-dislocations in the stress field of a Vickers indenter after heat treatment and etching

3. Crack nucleation at Vickers indentations

The ductile to brittle transition in brittle-hard materials can be characterized by a critical penetration depth of an indenter for initiation of cracks [7]. For a Vickers indenter the critical diagonal length for initiation of a radial-median crack system is given by [4]:

$$d_C = \Theta\left(\frac{K_{IC}}{H}\right)^2 \qquad (6)$$

with K_{IC} as the stress intensity factor, H the Vickers hardness and a factor Θ depending on the geometry of the indenter and the complex deformation mechanism beneath the indenter. Around the indentation a system of radial-median cracks is formed the initiation of which is associated with local plastic deformation and a corresponding network of dislocations even for brittle materials [4]. For GaAs two sets of dislocations with different core structure and PEIERLS potential are involved in crack nucleation, the α- and β-dislocations which exhibit different mobilities under identical conditions. This can be revealed by DSL-etching of a (001)-oriented specimen with Vickers indentations after heat treatment for stress relaxation at 300°C as represented in fig. 4. The rows of etch pits indicating the displaced dislocations are longer for α- than β-dislocations. It could be shown experimentally, that there also exist two types of cracks propagating parallel to the rows of the α- and β-dislocations, called A- and B-cracks. As determined experimentally, the A-cracks are formed at loads of about 0.1N.The B-cracks and the complete radial-median crack system are formed at loads which are roughly an order of magnitude

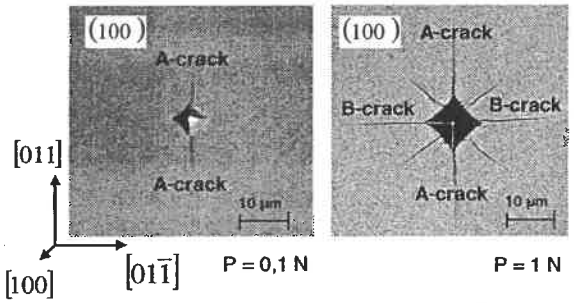

Fig. 5 Vickers-indentations at {100} GaAs surfaces

greater (see fig. 5). The A- and B-cracks are preferentially formed in {110} cleavage planes. This further means that instead of one condition for the ductile-to-brittle transition two conditions must be formulated for GaAs [3]: For Vickers indentations in undoped (100) GaAs the critical lengths of diagonals d_A and d_B for crack nucleation in surfaces according to eq. 6 is given by:

$$d_{A,B} = \Theta_{A,B}\left(\frac{K_{IC}^{A,B}}{H}\right)^2 \quad (7a,b)$$

for A and B-cracks.

At a critical load $P_A \leq P_B$ characterized by $d_A \leq d_B$ the A- and B- cracks are formed (see fig. 6). It has been shown by corresponding measurements that for the stress intensity factors in eqn. (7a,b) determining the resistance for crack propagation holds $K^A_{IC} = K^B_{IC}$ [3]. Therefore, the crack length c_o after their nucleation is given by $c_o(P) \propto P^{3/2}$ with the fracture toughness as the relevant material parameter. Thus, the observed difference in crack formation is assumed to be caused by differences of the dislocation assisted crack nucleation due to the existence of α- and β-dislocations.

4. Results of single grain scratching tests

The modified criterion for ductile-to-brittle transition implies a dependence of the critical penetration depth of a tool (see eq. 1) on the angle γ of its direction of movement relative to the propagation directions of cracks of type A and B, i. e.

$$h_c = h_c(\gamma) \quad (8)$$

This finding was verified by single grain scratching tests on polished (100)-oriented GaAs-surfaces results of which are represented in fig. 7. In addition it was found that h(γ) depends on the geometry of the cutting tool. For roof-shaped diamonds which describe the situation in the slit during wire sawing best, tension forces act parallel to the moving direction creating cracks which propagate perpendicular to this movement [3]. Therefore, the critical penetration depth is high if B-cracks are initiated and low for A-cracks resulting in a two-fold symmetry (see fig. 7). As the scratching angle γ corresponds to the feeding direction ω, the balance of forces (eqs. 2 and 3) on the wires depends on the feed direction ω as well.

5. Consequenzes for the wire sawing technology

GaAs crystallizes in the $\bar{4}3m$ crystal class. This means that the $(\bar{1}00)$ and (100) planes in fig. 1 are not identical, i. e. B-cracks on $(\bar{1}00)$ are par-

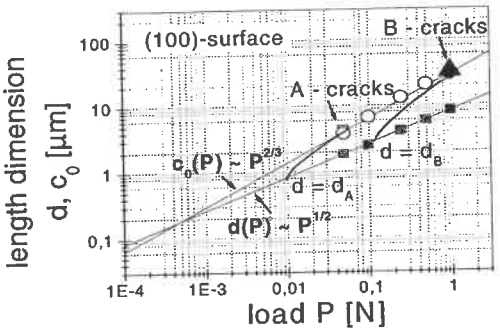

Fig. 6 Diagonal length of Vickers indentation and crack length depending on indenter load at undoped {100} GaAs

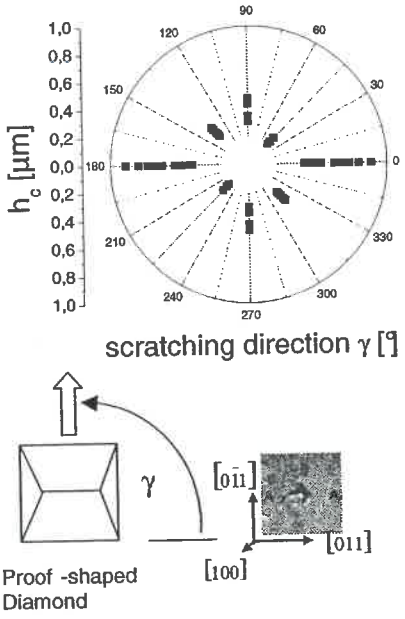

Fig. 7 Results of scratch tests on polished {100}-GaAs surface undoped: critical depth of cut depending on cutting direction

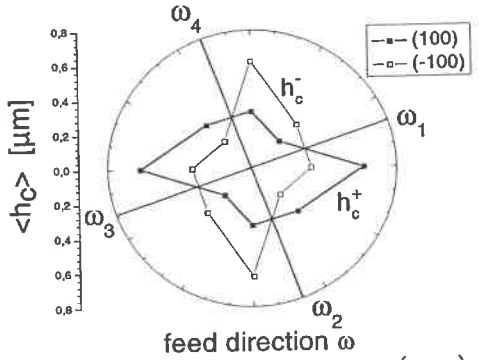

Fig. 8 Critical penetration depth on $(\bar{1}00)$- and (100)- surface planes

allel to A-cracks on (100) and vice versa. To match the crack pattern on these two planes an inversion and rotation is necessary. With other words: if the critical penetration depths for both planes h_c^+ und h_c^- are reassigned to the feeding direction ω, the graphs of h_c^+ for $(\bar{1}00)$ and h_c^- for (100)-plane are not congruent with each other but have to be rotated by an angle of 90° (fig. 8). Thi s finding offers the opportunity to create well defined ratios h_c^+/h_c^- by choosing different feeding directions ω. Consequently, according to eq. 3 the ratio of constraint forces, wire deflection and finally the bow (eq. 4) can be directly controlled.

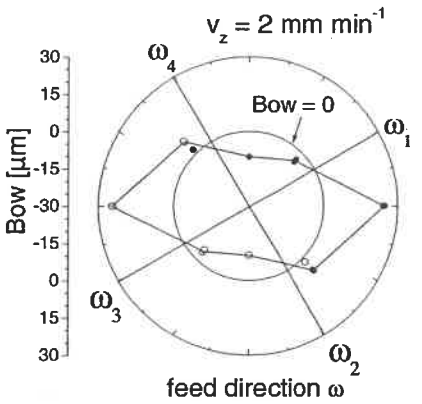

Fig. 9 Dependence of wafer parameter bow on feed direction ω

This is illustrated in fig. 9. The bow is given in dependence on the feeding direction. ω is measured after wire sawing and removal of a damage layer by wet chemical etching. It is obvious that absolute value and sign of bow of the sliced wafer can be defined very precisely by the ratio of the critical penetration depths h_c^+ and h_c^- (fig. 8). Interferometrically measured shapes of wafers for different feeding directions are represented in fig. 10. The general profile in the feed direction corresponds to the shape factor f(z) in fig. 3., but is quantitatively determined by the factor $C \approx \frac{p_x^+ + p_x^-}{F_\sigma}$.

From eq. (4) and (5) follows

$h_c^+ < h_c^- \Rightarrow C < 0$ fig.10a

$h_c^+ = h_c^- \Rightarrow C = 0$ fig.10b

$h_c^+ > h_c^- \Rightarrow C > 0$ fig.10c

Fig. 10a

Fig. 10b

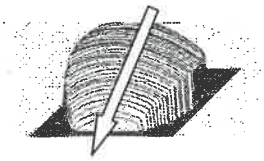

Fig. 10c

Topographic shape of GaAs wafers after wire sawing under different feeding directions (arrow) and etching for damage layer removal, (TROPEL-Flatmaster)

6. Conclusions

The mechanisms of micro-crack nucleation in GaAs and the respective symmetric properties allow a defined adjustment of the force balance in the cutting slit by using wire direction relative to crystallographic direction of the crystal as a control parameter. Setting the condition $h_c^+ = h_c^- \Rightarrow C = 0$ allows to produce wafers with very small bow. As a side effect of these findings, feed velocity of more than 2mm min^{-1} can be applied. This technology requires single direction of wire movement.

References

[1] H. Uishi, K. Asawaka, J.Matsusaki, Proc of ASPE Spring Topical Meeting, Carmel-by-the-Sea (1998) 109-112
[2] R. O. Scattergood, Proc. of ASPE Spring Topical Meeting (1993) 17- 20
[3] R. Hammer, PhD Thesis, Erlangen 2002
[4] B. Lawn, "Fracture of Brittle Solids", Cambridge University Press, 1995
[5] J.L. Weyher, C. Frigeri, K. Schohe, S. K. Krawczyk, T. Wosinski, R. Fornari, Inst. Phys. Conf. Ser. No. 135 (1993) Chapter 6,
[6] P. D. Warren, P. Pirouz, S. G. Roberts, Philosophical magazine A (1984) Vol. 50, No 5, 23-28
[7] B. Lawn, Journal of materials science 11(1976) 573 – 575

Acknowledgement

The authors would like to thank Dr. Hendrik Engel and Clemens Paesler from Technical University Berlin for carrying out the single grain scratching test.

FABRICATION OF MICROCYLINDER PARTS: A STUDY ON MICROMANUFACTURING

Masahiko JIN, Yota HIRAGA and Masao MURAKAWA
Nippon Institute of Technology, Saitama, Japan

Introduction: Recently, many studies on the fabrication of micro-machine elements and micro-machine tools have been carried out worldwide [1][2]. These achievements are expected to have many applications, such as in medical microdevices (for example, catheter), various microrobots, micro-machine tools for saving energy and factory space, and microfactories. However, these studies are still at an early trial stage. Therefore, we have not found many studies on manufacturing technologies for the efficient production of micro-machine elements. In this paper, we discuss a micromanufacturing method that includes microcutting and microassembly processes, for producing micro-machine elements accurately and efficiently.

Proposal of micromanufacturing method and experiment: In particular, we focus on a microcylinder as a subject for this study as shown in **Fig. 1**, and investigate the techniques for manufacturing the elements of the microcylinder, such as the micropiston rod with a high aspect ratio and the microcylinder tube with a small-diameter deep hole. Several techniques investigated in this study are as follows: a multipurpose machine tool is used as the base for micromanufacturing as shown in **Fig. 2** because the repeat of rechucking of microproducts is minimized during the cutting and assembly operations. To realize high-accuracy chucking, an ultraprecise diaphragm chuck and a workpiece which has the standardized arbor for chucking are used. Regarding the cutting operation, as shown in **Fig. 3**, we investigated the use of the cutting pass schedule in which a minimal cutting force acts on microproducts during the cutting operation [3].

In the experiment, we used an ultraprecision grinding center (Toshiba Machine Tools Co., Ltd.) as the base machine tool, which has three linear axes and one rotary axis with positioning accuracies of 10nm and 0.0001 deg, respectively. We used cemented carbide single point tools and microdrills as tools, and used annealed die steel (SKD11-JIS) with a hardness of 45HRC as the workpiece. Main experimental conditions are listed in **Table 1**.

Experimental results: The results of the experiments are as follows. Concerning the cylindrical turning of the micropiston rod, first, we found that the cutting force acting on the micropiston rod during operation can be minimized using the proposed cutting pass schedule in which the objective dimensions of the micropiston rod are produced by just a single feed. Thus, as shown in **Fig. 4**, we showed that a small-diameter long micropiston rod with a diameter of 150μm, an approximate length of 6mm and an aspect ratio of 40, can be fabricated accurately and

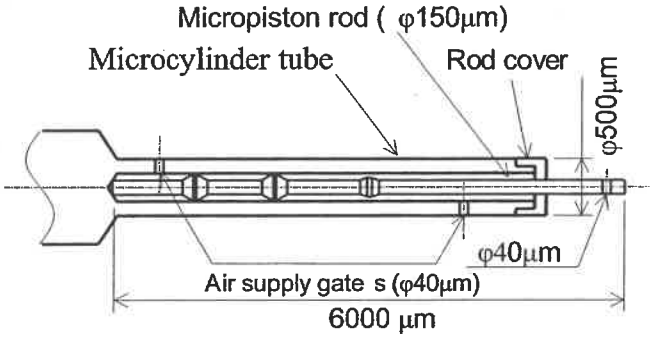

Figure 1 Investigated microcylinder

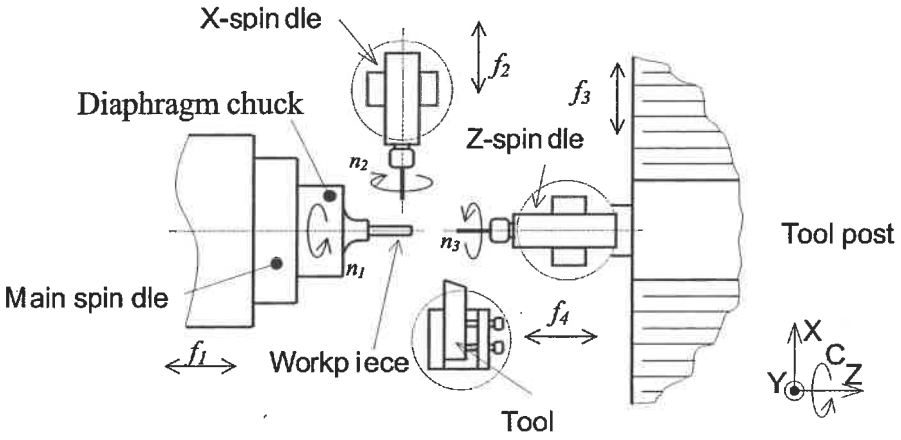

Figure 2 Experimental setup for manufacturing microcylinder

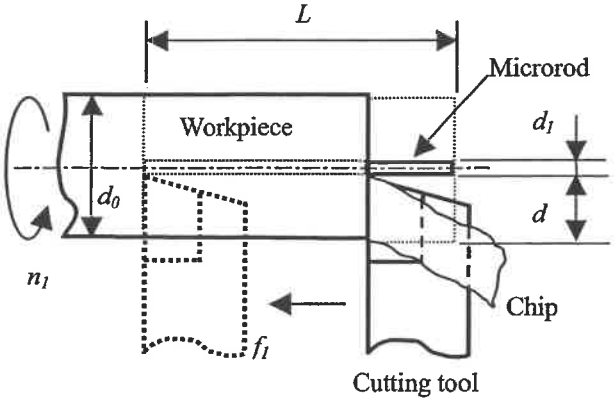

Figure 3 Proposed cutting-path and cutting method of microrod

Table 1 Experimental conditions

Cutting tool	Cemented carbide K10
Work material	SKD61 (45HRC) Diameter: 3 mm
Cutting speed n_1	1,000 min^{-1} (0.2-9.4 m/min)
Feed rate f_1	0.5μm/rev
Drilling speed $n_{2,3}$	35,000 min^{-1}
Feed rate f_2	57nm/rev
Cutting fluid	Oil-mist

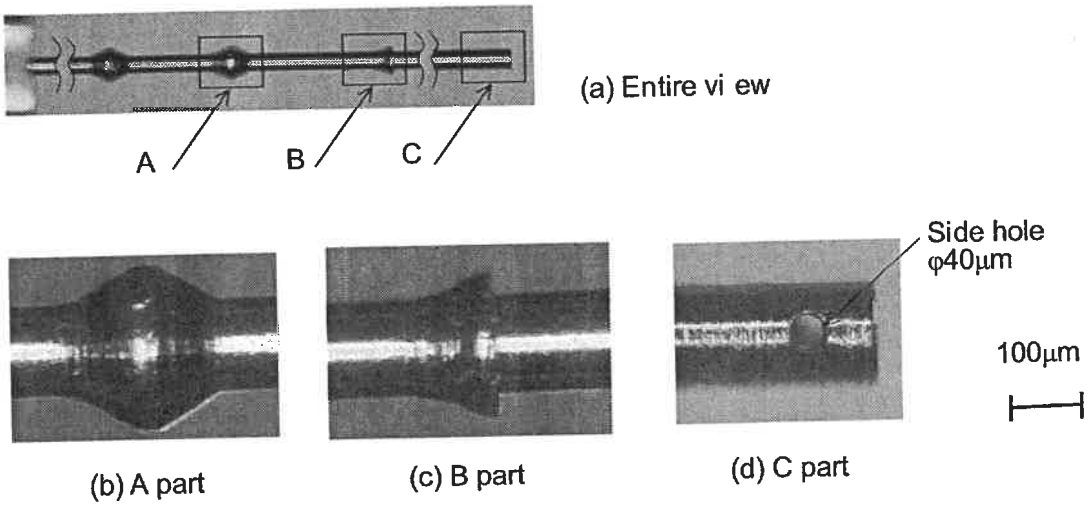

Figure 4 Entire and magnified views of manufactured microrod

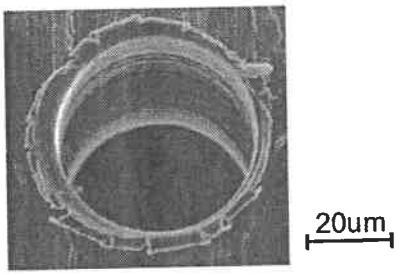

Figure 5 Drilled φ40μm hole on the microrod

effectively. Secondly, we investigated the drilling technique for the microhole on the side of the micropiston rod. As a result, we clarified that the small-diameter deep hole with a diameter of 40μm and a depth of 150μm can be accurately drilled as shown in **Fig. 5**. The reason why the micropiston rod does not receive a harmful influence from the deflection by the drilling force is that the micropiston rod is held in the diaphragm chuck with a minimum overhang.

Conclusion: In conclusion, we clarified that the objective microcylinder elements can be fabricated accurately and efficiently using the proposed micromanufacturing method.

References:

[1] Masuzawa, T., 2000, "State of the Art of Micromachining", Annals of the CIRP, 49, 2, pp. 473-488.

[2] Saotome, Y. and Inoue, A., 2000, "New Amorphous Alloys as Micromaterials and the Processing Technologies", Prof. IEEE 13th Int. Conf. on Micro Electro Mechanical Systems, MEMS 2000, pp. 288-292.

[3] Jin, M., Kobinata, T. and Murakawa, M., 2002, "Study on Fabrication of Microrods by Cutting Process", Prof. of IMECE' 02 (ASME), CD-ROM.

Near Dry Machining Utilizing Lubricant Applying Effect -Required Minimal Quantity of Oil Mist-

Toshiaki Kaneeda[1], Yoshikazu Okada[1], Seiichi Yokomizo[2], Shoichi Shimada[3], and Masahiro Higuchi[4]
[1]Okayama University of Science, 1-1 Ridai-cho, Okayama city, Okayama 700-0005, Japan
[2]Industrial Technology Center of Okayama Prefecture, 5301 Haga, Okayama 701-1296, Japan
[3]Osaka Electro-Comunication University, 18-8 Hatsu-cho, Neyagawa city, Osaka 572-8530, Japan
[4]Kansai University, 3-3-35 Yamate-cho, Suita city, Osaka 564-8680, Japan

Keywords: lubricant applying effect, near dry machining, oil mist, lubrication, pre-cut surface, pure aluminum, oleic acid, spray gun, AFM, ellipsometer

1. Introduction

This paper dealt with the minimal quantity of the cutting fluids in the lubricant applying effect cutting, which leads to the highest efficiency in lubrication. Applying materials on the pre-cut surface in ductile metal cuttings can dramatically improve the machinability, due to a reduction in friction between the lamellas of the chip. This effect we define as the lubricant applying effect (called LAE hereafter) [1]. The authors have already established that the improving machinability phenomenon is quite different from Rebinder effect. The authors have also reported the mechanism of the LAE. The LAE has been already recognized in such ductile metals as pure aluminum, pure copper and mild steel [2]. Under optimal conditions the LAE can reduce the cutting forces by more than 90% [3]. The LAE plays a major role in lubrication in most cutting conditions, therefore, near dry machining could be performed by using the LAE [4]. Considering the ecological problems and costs for the waste disposal, the minimal quantity of the applied material to apply on the pre-cut surface should be determined. That is to say, the minimal thickness of the applied material film has yet to be determined. In order to conduct near dry machining using the LAE with the minimal quantity of applied material, we have developed the oil mist supply method using a spray gun. The thickness of applied material film, that is film adhered to the pre-cut surface was measured with an ellipsometer. Detailed analysis of adhered film was done by an AFM.

2. Experimental Procedures

2.1 Experimental apparatus and work material

Two types of cutting experiments, as described in 2.3 and 2.4, were conducted on an NC orthogonal precision cutting apparatus. A large-work hardening-capacity ductile metal, pure aluminum (A1050, 1/2) was used as the work material. Dimensions of the work was 300 •35 •3 mm. Cemented carbide (WC+Co) K10 was selected as the tool material. The rake angle was a constant 0 ^. Depth of cut in the last-pre cutting t_L, being able to control the rate of work hardening in the region to be cut, was 10 m. Depth of cut t_1 was 10 m. Cutting on these conditions can present the maximum LAE definitely. Cutting speed is a constant 25.7 m/min. A quartz force transducer (Kistler Co. type 9251A) was employed to measure the cutting forces.

Table 1 summarizes the cutting conditions.

Table 1 Cutting conditions

	Lubricant applying effect by spray gun	Normal lubricant applying effect
Work material	Pure aluminum (Al050-H24)	
Tool material	Cemented carbide K10	
Rake angle ^	0	
Relief angle ^	7	
Cutting form	Orthogonal	
Cutting speed V m/min	25.7	
Last pre-cutting tL μm	10	
Depth of cut t1 μm	10	
Lubricant	Oleic acid	
Injection time sec	30	
Accumulation time sec	10,15,30,60,90,120,300,600	

2.2 Pre-cutting

Extent of LAE and lubrication increases with a decrease in thickness of the work hardened layer of pre-cut surface at the same depth of cut [2], therefore pre-cuttings, i.e. arranging the work hardening in the cutting zone before the cutting experiment, should be done. Surface layers usually have work hardened layer associated with manufacturing at plants and sectioning at laboratories. In order to avoid or control the effects of the work hardened layer, first pre-cuttings were done more than ten times at every depth of cut such as t_1 = 30, 20, 10 m with conventional cutting fluids. Then, after recognizing alternative change in the cutting forces[5], featuring large-work hardening-capacity ductile metal cutting, the last pre-cutting was performed at a depth of cut t_L =10 m without any cutting fluids.

2.3 Cutting experiment with oil mist supply

It is very important to supply misted oil as fine as possible. After last pre-cutting, a box shape capsule was prepared. The capsule size is 570 •385 •200, which can contain the work completely. The spray gun injected oil mist toward a shield plate in the capsule for 30 sec as shown in Fig.1(a). Then, the capsule was filled with the oil mist, however oil particles larger than 50 m diameter were adhered to the shield plate surface [5]. That is to say, the particles smaller than 50 m were filled in the capsule. After 60 sec, larger diameter particles, whose size were smaller than 50 m, in the capsule settled down by the gravity, then only minute particles were suspending inside the capsule eventually (Fig.1 (b)).

The capsule was put on the work, then, suspending particles accumulated on the work surface for a given time. This time is called as an accumulation time hereafter. The amount of particle adhered to the work surface could be controlled by altering the accumulation time ranged from 10 sec to 600 sec.

At the same time the first half of the work was covered by an aluminum foil to avoid the accumulation on the work surface (Fig.1(c)). After the particles accumulated on the applied part, the aluminum foil was removed. Then, the cutting experiments were conducted as shown in Fig.1(d).

2.4 Lubricant applying effect cutting

After last pre-cutting, the first 270mm of a 300mm work was cleaned without any grease, while the last 30 mm part was applied with oleic acid as an applied material. The clean part was much longer than the applied part, because ductile metals, in particular the work materials having large-work hardening-capacity, usually require a longer cutting length before reaching a steady state in the cutting forces compared with other kinds of metals. The applied material on the applied part appears to be less than 1 m thickness, which led to lusterless pre-cut surfaces. After that, the cutting expriments were done.

2.5 Measurement of adhered oil film thickness

Oil particles accumulated on the work surface as shown in Fig.1 (c), then adhered oil film thickness was

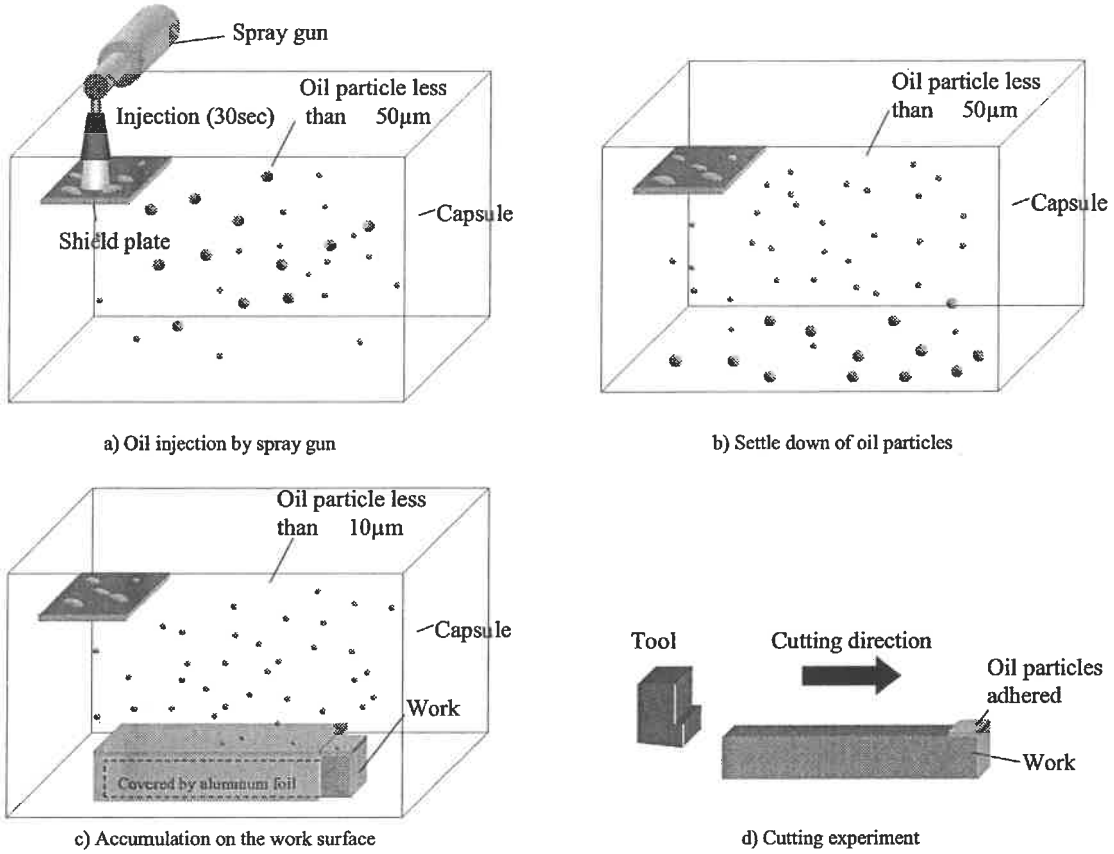

Fig. 1 Cutting experiment with oil mist supply

measured by an ellipsometer. Detailed analysis, distribution of adhered point and size of oil particles, was done by an AFM.

3. Experimental results and discussion

It is reported before by the authors that LAE has a major role in lubrication during ductile metal cuttings [4]. In most cutting conditions extent of LAE is nearly the same as of lubrication. It is easily recognized that the former could be controlled by the amount of adhered oil particles. The extent of lubrication by the adhered oil particles can be evaluated by comparing the extent of LAE. It is essential to determine the minimal thickness of adhered film, that is to say applied material, offers the top performance in lubrication.

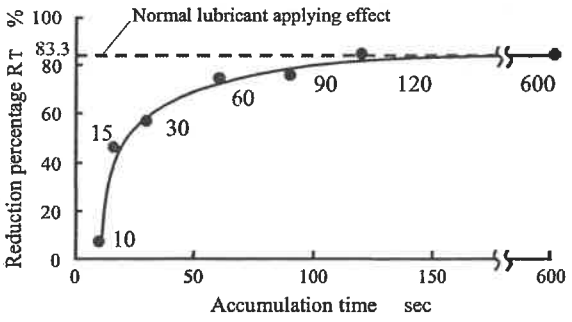

Fig. 2 Relationship between reduction percentage and accumulation time

Fig.2 shows relationship between reduction percentage with oil mist supply and accumulation time. The reduction percentage in the cutting forces is the amount of cutting force reduction divided by cutting force in dry cut. The reduction percentage increased gradually with an increase of the accumulation time, then reach the maximum value, which was 83.3% equivalent to the paper presented before [4], at longer than 120 sec.

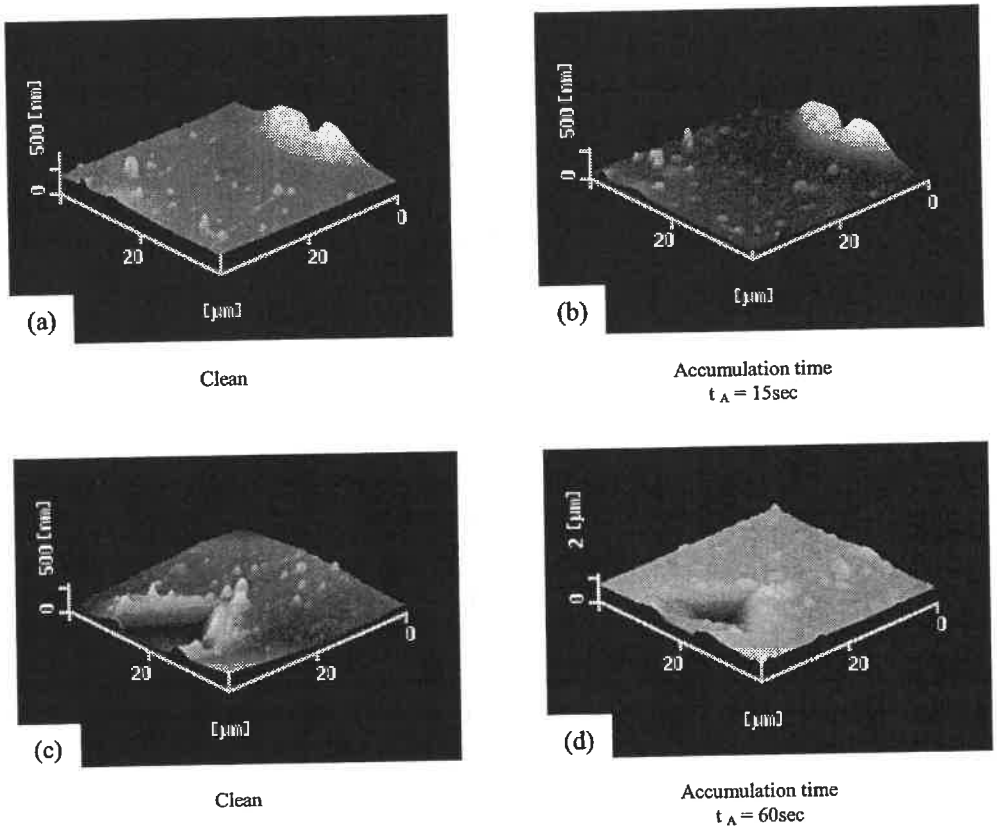

Fig. 3 AFM observation result

Fig.3 shows AFM images of clean and oil adhered surface (accumulation time; 15 sec and 60 sec). A large dimple on each surface was made by a Vicker's indentater to identify the part of the surface before the AFM analysis. On the work surface of 15 sec accumulation, very small particles were spotted with the surface as shown in Fig.3(b). On the other hand, oil adhered film was recognized on the work surface of 60 sec accumulation.

The ellipsometer analysis provided that this film had 2nm-thickness. These analysis suggested that oil adhered film more than 2nm-thickness would produce almost maximum reduction percentage, which means almost top performance in lubrication.

References

[1] T. Kaneeda, Advancement of Intelligent Production, Elsevier Science B.V. (1994) 385.

[2] T. Kaneeda, et al., J. of Japan Soc. Prec. Engng. 61, 5 (1995) 702.

[3] T. Kaneeda, et al., J. of Japan Soc. Prec. Engng. 66, 1 (2000) 74.

[4] T. Kaneeda,. Proceedings of 10th ICPE (2001) 107.

[5] S. Zaima, et al., Trans. Japan Soc. Mech. Engineers, Ser.3, 35, 277 (1969) 1940.

[6] H. Nakajima,. Air pressure technology book for users (in Japanese), Ohm-sha (1974) 140.

HIGH PRECISION AND HIGH EFFICIENCY MACHINING OF POLYBENZIMIDAZOLE USING THE FINE CRYSTALLINE DIAMOND COATED TOOL WITH THE SHARP EDGE

Hideharu KATO*, Kazuhiro SHINTANI*, Kyougo MIYAHARA* and Hiroyuki HANYU**
* Department of Mechanical Engineering, Kanazawa Institute of Technology,
7-1 Ohgigaoka, Nonoichi, Ishikawa 921-8501 Japan
** OSG Corporation, 1-15 Honnogahara Toyokawa, Aichi, 442-8544 Japan

1.Introduction

Recently, the application of engineering plastic materials in machine parts has been increasing. Especially among engineering plastic materials, the polybenzimidazole (P.B.I.) is expected to increase in demand due to its excellent tensile strength and heat resistance compared with that of other engineering plastics. P.B.I. is supplied in simple forms, such as boards and pipes, for molding using a hot press. It is effective to use a cutting method for final shaping of machine parts. However, P.B.I. is a difficult-to-cut material [1]. When a cemented carbide tool is used for face milling of this material tool life is shortened and the cutting speed needs to be as low as 1.67m/s. In addition, it is difficult to attain a certain accuracy in the finished surface of P.B.I. using of the cemented carbide tool [2]. Thus the face milling of P.B.I. has a lot of problems that need to be solved. It is effective to use a diamond coated cemented carbide tool, because P.B.I. undergoes chip formation like ceramic materials. However, even when using this tool for finishing, the improvement in the surface accuracy of P.B.I. by face milling is not sufficient.

In this study, the effects of tool geometry and edge sharpening of a fine crystalline diamond coated tool on the finished surface of P.B.I. are investigated in high-speed face milling.

2. Experimental procedure

The workpiece material is P.B.I. This material is supplied in the form of a plate shape in order to mold the precursor powder by hot pressing. **Figure. 1** shows the molecular structure and characteristics of P.B.I. The deformation temperature of this material is 708K, which is the highest deformation temperature among all thermoplastic resins. The tensile strength is 160MPa which is equivalent to that of pure aluminum. The workpiece after layer removal has a rectangular parallel-pipe shape of 100 •200 •30mm.

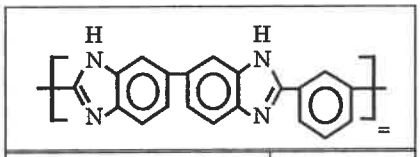

Tensile strength	160MPa
Bending strength	240MPa
Rockwell hardness (R.T.)	50 HRA
Deformation temperature	708K

Fig. 1 The molecular structure and characteristics of the polybenzimidazole.

Table 1 shows the fine crystalline diamond coated tools used in this experiment. The fine crystalline diamond coating was synthesized by using hot-filament chemical vapor deposition (CVD) [3]. All of the fine crystalline diamond coated tools used cemented carbide (K10) as the substrate material. As shown in this table, DKF10 is a coated tool without edge sharpening. The radius of roundness of the cutting edge is 30μm. In order to improve the sharpness of the cutting edge, the cutting edge of the other tools is sharpened using a chemical polishing method. **Figure 2** shows tool geometry. Four kinds of tools, in which the rake angle of the end cutting edge changed, were used (FDK-10P, FDK0P, FDK10P and FDK20P).

Table 1 Cutting tools

Tool	Rake angle of end cutting edge [deg.]	Roundness radius of cutting edge [μm]	Cutting edge treatment
FDK 10	5	30	As coating
FDK-10P	-15	<1	Polishing*
FDK 0P	-5		
FDK 10P	5		
FDK 20P	15		

* chemical polishing method

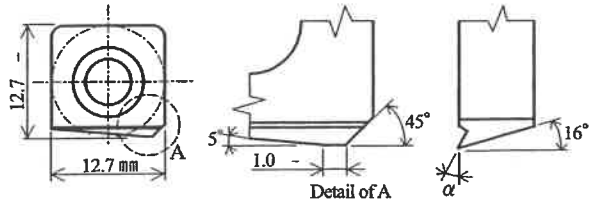

Fig. 2 Schematic illustration of tool geometry

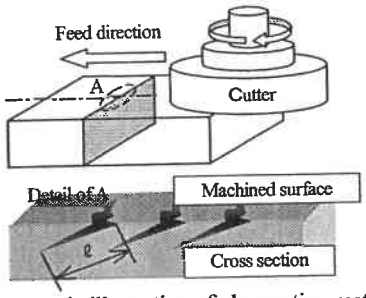

Fig.3 Schematic illustration of observation method of crack

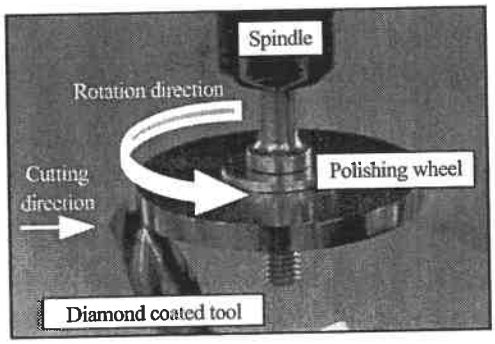

Fig. 4 Equipment for sharply polishing the cutting edge of diamond coated tool

Table 2 Polishing condition

Polishing wheel	
Material	Austenitic stainless steels
Diameter	45 [mm]
Polishing condition	
Spindle rotational number	25,000 [min^{-1}]
Polishing speed	60 [m/s]

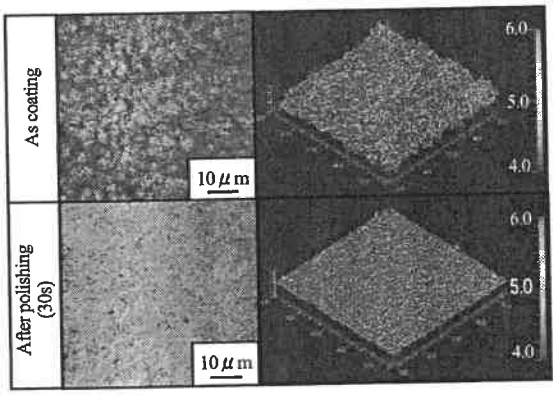

Fig. 5 Comparison of the 3D image with microscopic photograph of diamond coated film; (a) as coating and (b) after polishing (30 seconds).

In milling experiments, the fine cutting conditions were as follows: feed rate (Sz): 0.04mm/tooth, axial depth of cut (dA) : 0.2mm, offset : 0mm and cutting speed (V) : 6.7 40.0m/s. The cutting point was supplied with dry air at a pressure of 0.68MPa. The evaluation of the machined surface is carried out on the basis of the number and length of cracks on the surface. **Figure 3** shows the observation method for cracks. The cross section shown in this figure was broached, and the crack length per unit cutting distance and number of cracks were observed.

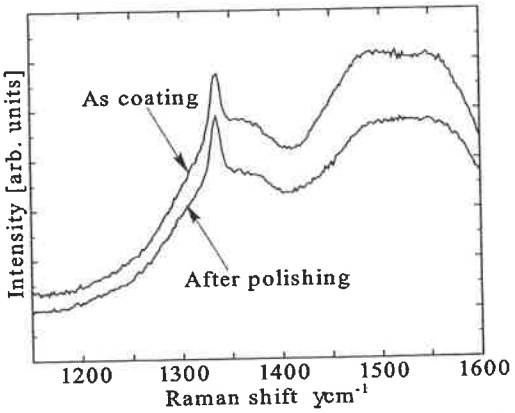

Fig. 6 Raman spectra of the fine crystalline diamond coated film before and after polishing

3. Experimental results and discussion

3.1 Sharpening of edge using chemical polishing method and observation of polished surface

The radius of roundness of the end cutting edge of the fine crystalline diamond coated tool was thought to have a major effect on the maximum height of the machined surface [2]. **Figure 4** shows the polishing equipment [4]. The chemical polishing method utilized the dynamic friction between the stainless steel disk and tool in high-speed rotation [5], and the diamond film is smoothed in a short time. **Table 2** shows the polishing conditions. **Figure 5** shows the surfaces of the fine crystalline diamond film before and after polishing. As seen in this figure, it is clarified that the ruggedness of the fine crystalline diamond film is removed and is smoothed after polishing. The measurement results of Raman spectroscopy for the cases before and after polishing are shown in **Fig. 6**. There was no significant difference in the Raman spectra between the case before polishing and that after polishing. **Figure 7** shows SEM images of the end cutting edge for the cases before and after polishing using the chemical polishing method. It is confirmed that the cutting edge of FDK10P is sharply polished in comparison with that of FDK10. It is confirmed that the radius of roundness of the cutting edge of FDK10P is less than 1.0μm.

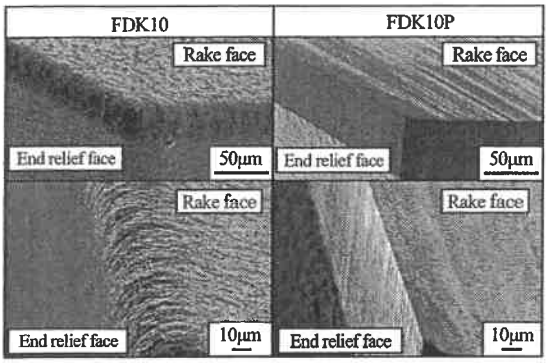

Fig. 7 Comparison of cutting edge; (a) FDK10 (before polishing) and (b) FDK10P (after polishing)

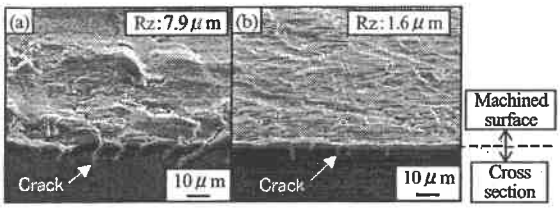

Fig. 8 Comparison of machined surface and cross section at cutting length of 1km(V:13.3m/s); (a) FDK10 and (b) FDK10P

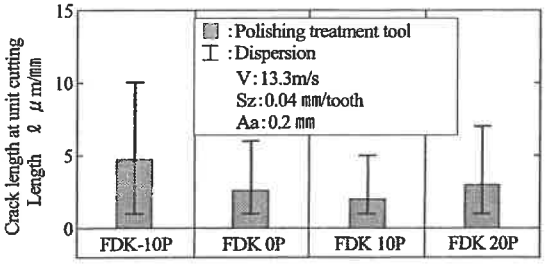

Fig. 9 Comparison of the crack length and dispersion using several axial rake angle (Ln:1km)

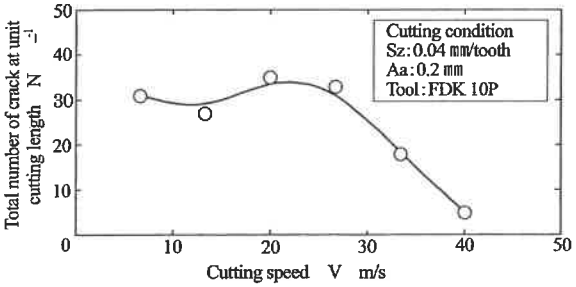

Fig. 10 Relation between cutting speed and total number of crack using FDK10P (Ln:1km)

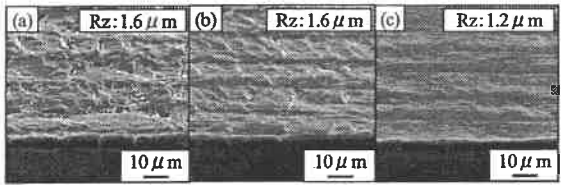

Fig. 11 Comparison of machined surface and cross section at several cutting speed using FDK10P (Ln:1km); (a) 20.0 m/s ,(b) 33.3 m/s and (c) 40.0 m/s

3.2 Effect of improvement in sharpness of cutting edge on finished surface.

The effect of the radius of roundness of the cutting edge on the finished surface was investigated. **Figure 8** shows a comparison between the finished surface damage with the FDK10 (as coating) and FDK10P (polishing). In the case of using FDK10, large cracks occur in great numbers, and these cracks seem to influence the concavity of the finished surface. On the other hand, it is clear that the number of cracks is reduced and the crack length is also shortened using FDK10P. The effect of A.R. on number of cracks in the finished surface was examined. As seen in **Fig. 9**, the crack length of the finished surface can be shortened using FDK10P.

3. 3 Effect of cutting speed on number of cracks in finished surface

As mentioned in the previous section, it was clarified that a fine crystalline diamond coated tool with a sharp edge is effective in decreasing the number of cracks. In this section, the effect of high-speed cutting conditions on the number of cracks in the finished surface was investigated using FDK10P. **Figure 10** shows the change in crack number with increasing cutting speed. Although the number of cracks was 30/mm at a cutting speed of 6.7 to 27.0m/s, this number decreased at speeds over 27.0m/s. Under a high-speed cutting condition of 40m/s, the number of cracks was only 5/mm. **Figure 11** shows comparisons of the finished surface and cross section between the cutting conditions used. It is confirmed that the number of cracks decreases with increasing cutting speed. In addition, as seen in Fig.11 (c), a thin fluid bed on the finished surface can be also observed. As shown in **Fig.12**, the glass transition temperature of this material is near 700K. With the increasing cutting speed, it seems that the cutting temperature approaches to the glass transition temperature. The cracks formed by the machining of P.B.I. are thought to have a major effect on the mechanical strength of the product. A three-point bending test was carried out on the test piece produced under following machining conditions. Type A : lap treatment [crack less], Type B : 13.3m/s using FDK10 (as coating) and Type C :

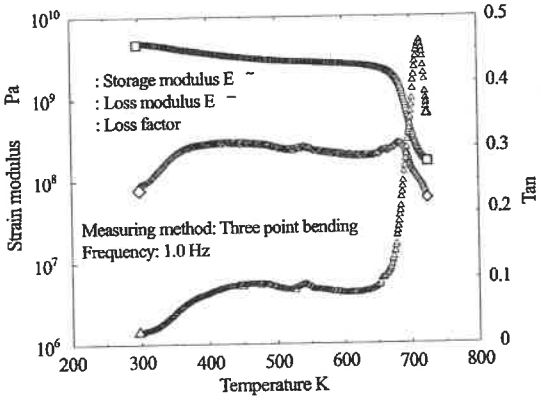

Fig. 12 The dynamic viscoelasticity behavior of Polybenzimidazole

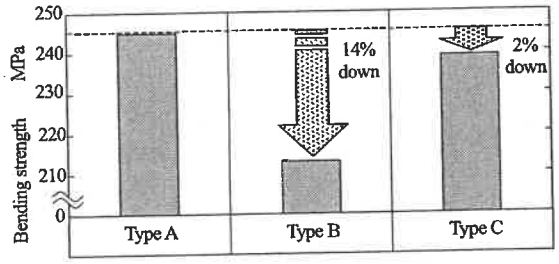

Fig. 13 Comparison of bending strength at three cutting conditions; Type A : lap treatment, Type B : 13.3m/s using FDK10 and Type C : 40.0m/s using FDK10P

40.0m/s using FDK10P (polishing). **Figure 13** shows a comparison of bending strength between the conditions used. Each condition also shows the mean value of 4 results. From the figure, the bending strength of Type B with many cracks which occur during processing is approximately 14% lower than the that of the original P.B.I. material (Type A). In Type C which has an optimized edge shape and optimized cutting conditions, the decrease in bending strength is very small, approximately 2 %.

From these tests and observations, in order to suppress cracking during processing of P.B.I. material, it is effective to use a fine crystalline diamond coated tool with a sharp cutting edge under a high-speed machining condition of 40.0 m/s.

4. Conclusion

In the high-speed milling of polybenzimidazole using a fine crystalline diamond coated face mill tool, the effects of tool geometry and edge sharpening of the fine crystalline diamond coated tool on the finished surface are investigated. The following conclusions were obtained.

(1) By sharply reshaping the edge of the fine crystalline diamond coated tool using a chemical polishing method, it is possible to reduce the number of cracks in the finished surface.

(2) In the case of using FDK10P, the mean value of the length of cracks decreases by 2.0μm, and the dispersion is also reduced.

(3) The number of cracks per unit cutting distance is small at cutting speed over 27.0m/s, and under a high-speed cutting condition of 40m/s, the number of cracks was only 5/mm.

(4) For a fine crystalline diamond coated tool with an optimized edge shape under optimized cutting condition, the decrease in bending strength is very small, approximately 2%.

References

[1] T.Nakamura: Super Engineering Plastic, PBI Resin Serazol, Synthetic Resin Vol.37, No.7 (1991) 21. (in Japanese)

[2] H.Kato, K. Shintani, T.Fujita, H.Hanyu and O.Yamazaki: High-speed Milling of Polybenzimidazole (PBI) Using Diamond Coated Tool, J.Jpn.Soc.Abra.Tech.,Vol.47, No.9 (2003) 501. (in Japanese)

[3] H.Hanyu, Y.Murakami, S.Kamiya and M.Saka, New Diamond Coating with Finely Crystallized Smooth Surface for the Tools to Achieve Fine Surface Finish of Non-ferrous Metals, Surface and Coating Technology, Vol.169-170, 2 June (2003) 258.

[4] Kato H, Shintani K, Fujita T, Hanyuu H and Yamazaki O: High-Precision Cutting Technology with Diamond Coated Tool in High-speed Milling of Polybenzimidazole, International Conference on Leading Edge Manufacturing in 21st Century, Niigata, Japan (2003) 577.

[5] M.Iwai, K.Suzuki, T.Uematsu and N.Yasunaga, A Study on Dynamic Friction Polishing of Diamond. 1st Report: Application to Polishing of Single Crystal Diamond, J.Jpn.Soc.Abra.Tech., Vol.46, No.2 (2002), 82. (in Japanese)

Development of Surface Texturing System by Mechanical Machining

Y. Kobayashi*, K. Shirai*, S. Masaaki* and K.Tozawa**
*Nihon University, Koriyama, Fukushima, 963-8642, Japan
**Nissan Motor Co.,Ltd, Atsugi, Kanagawa, 243-0126, Japan

1. Introduction

Surface texture is an important function in enhancing aesthetic and tactile qualities and mechanical properties of products. The roughness of the product surface is generally textured by etching or sand-blasting. The amplitude of roughness is usually about several hundred μm. However these manufacturing techniques have problems related to repeatability of manufacturing and environment pollution. To resolve theses problems, we developed an exclusive system for generating surface texture by machining.

2.Generation process of surface texture

Fig. 1 shows the generation process of surface texture. This process consists of the following steps.

1) Measure the shape, waviness and surface trend of the specimen using a laser displacement meter.
2) Design the surface texture using the developed CAD system and map the designed texture to macroscopic data obtained in step 1) or designed geometrical shapes.
3) Generate the CAM data from CAD data.
4) Machine the specimen to generate the texture on the surface.
5) Measure the textured surface of the specimen using a confocal microscope system.
6) Assess the textured surface.
7) End.

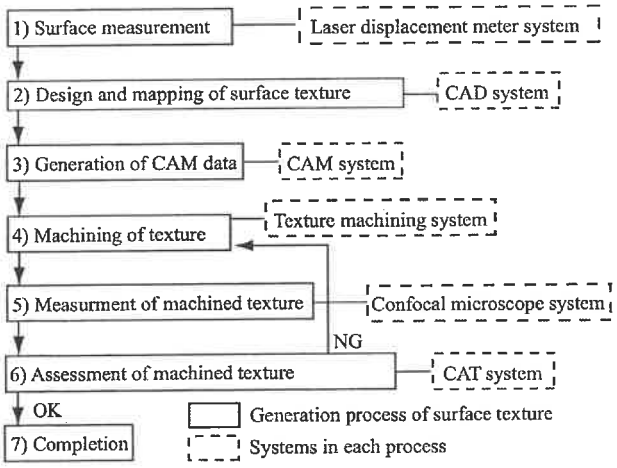

Fig. 1 Process flow of surface texture generation

Fig. 2 shows a systematic diagram of the surface texturing system. This system consists of a 3-axis milling machine with two spindles, control units, measurement instruments, laser displacement meter and confocal microscope, and CAD/CAM/CAT systems

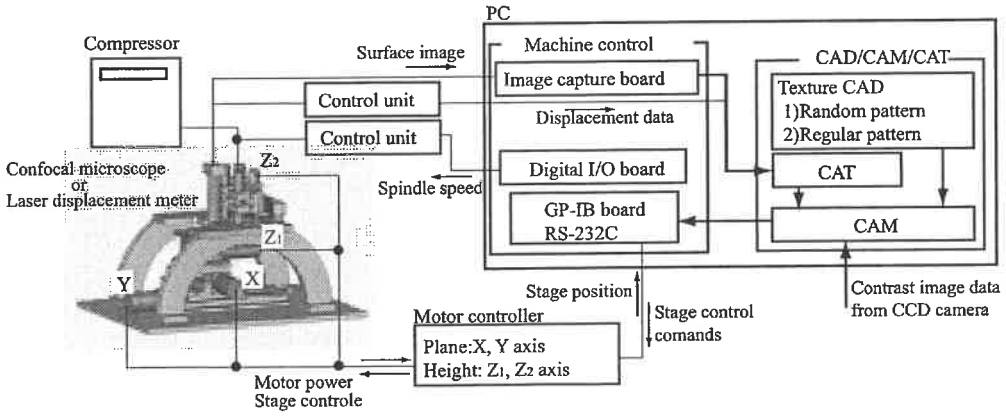

Fig. 2 Systematic diagram of surface texturing system

running on a PC.

3. Surface texturing systems

CAD/CAM system

It is very difficult to design the surface texture using a commercial CAD system applying geometrical shapes. The developed CAD system can design random texture patterns such as human skin pattern and regular patterns such as fabric pattern like knitwear. The algorithm for designing random texture pattern is based on the arithmetic theory of 2D auto-regressive models [1]. When users want to design random texture, they must input the values of six parameters related to surface topography to the system, i.e. correlation length in the X and Y directions, multiplier of auto-correlation function, root mean square, skew, and kurtosis. The created random texture satisfies the statistical information defined by the six parameters. The user can also redesign the random texture pictured on the screen interactively by changing the parameters or using certain commands. On the other hand, a new algorithm for regular patterns was developed at our laboratory based on the theory of shape pattern recognition and self-assembly system, L-system, proposed by Lindenmayer [2]. The designed surface texture can be mapped to geometrical shapes designed on a commercial CAD system or surface data measured by step 1) of Fig. 1. Fig. 3 shows the texture image designed on the developed CAD system. Fig. 3(a) shows the designed texture pattern and Fig. 3(b) shows the texture pattern to mapped to geometrical shape such as cylinder.

The developed CAM system can handle the CAD data mentioned above and contrast image data obtained from CCD cameras shown in Fig. 2. CAM data is generated to control the plane axis, X and Y, and height axis, Z, for the developed three-axis milling machine.

Milling machine

Fig. 4 shows the overview of the milling machine. This machine is controlled by 3 axis, X, Y, Z , and has two

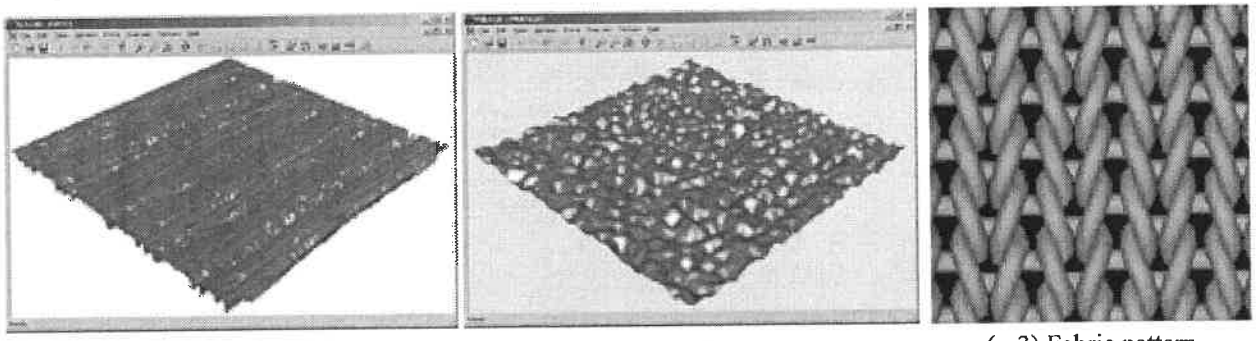

(a-1) Anisotropic pattern (a-2) Isotropic pattern (a-3) Fabric pattern

(a) Texture pattern design

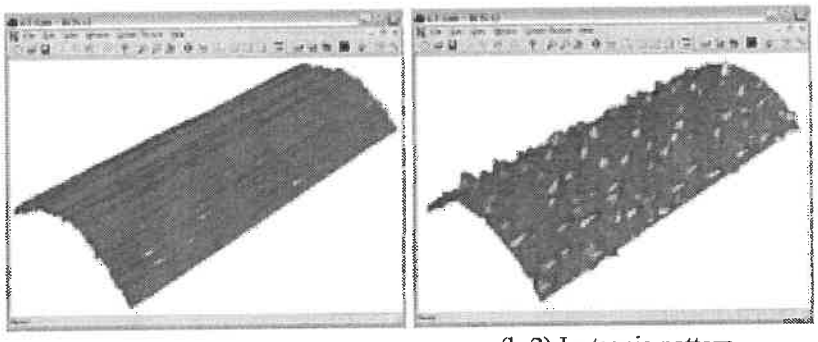

(b-1) Anisotropic pattern (b-2) Isotropic pattern

(b) Mapping to designed geometrical shapes

Fig. 3 Texture image designed by developed CAD system

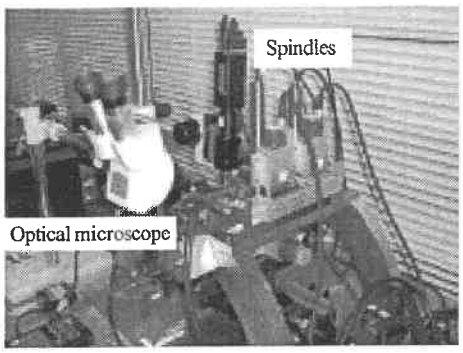

Fig. 4 Overview of milling machine

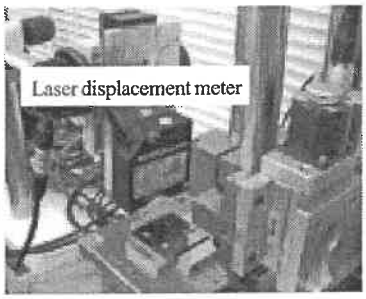

(a) Overview

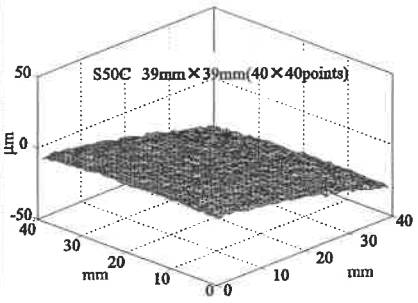

(b) Measurement result

Fig. 5 Laser displacement meter system

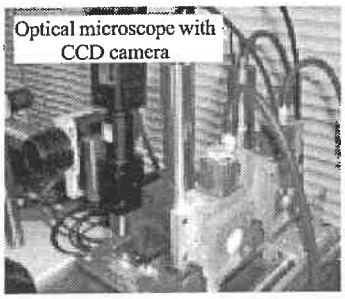

(a) Overview

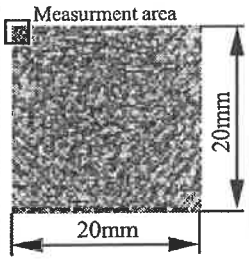

(b-1) CAM data

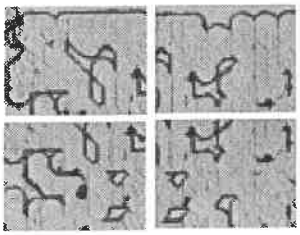

(b-2) Microscope images

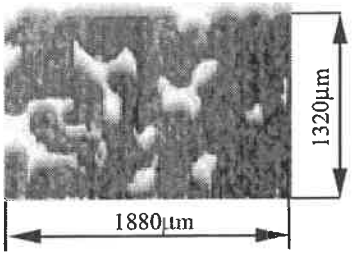

(b-3) Result of stiching

(b) Measurement of texture pattern

Fig. 6 Confocal microscope system

spindles. The specifications of the milling machine are as follows: Minimum X and Y axis travel is 10μm, Z axis is 1μm, and maximum spindles speed are 40,000 and 80,000 rpm respectively. The size of this machine is about 500mm(W)×400mm(D)×350mm(H).

Measurement system

A laser displacement mater system and confocal microscope system can be set up on the milling machine to measure the sample surface before and after milling. The laser displacement meter system is used to measure macroscopic surface information, shape, waviness and surface trend before milling. The measured macroscopic surface data is incorporated in the CAM data to mill the constant depth. Fig. 5 shows the overview of the laser displacement meter system and measured surface data. Fig. 5(b) shows that the surface trend of the specimen have been measured.

The confocal microscope system is used to measure the microscopic texture pattern after milling. As the image area taken by the confocal microscope system is small, the stitching technique is applied to broaden the area of surface texture. Fig. 6 shows the overview of the confocal microscope system and measured texture data. This system enables measurement of the machined surface by using the built-in optical microscope with CCD camera positioned in front of the spindles as shown in Fig. 6(a). The texture images are photographed continuously while changing the surface height. This microscope system allows selection of the focus pixels from these images by software to create the confocal image. Fig. 6(b) shows the measured texture pattern. Fig. 6(b-1) shows the cutter pass image of a human skin sample. Metal surface is machined based on its data. Fig. 6(b-2) shows the images taken by the confocal microscope system. As the image area of one shot is too small for assessing the machined texture patterns, macroscopic image is made by the stitching technique which can consist of many measured images. The result of stitching composed of the four images shown in Fig. 6(b-2) is shown in Fig. 6(b-3).

Finally the results of measuring the textured surface were compared with the CAD data and if there were inadequacies in milling, disagreement of surface height, etc., these flaws on the textured sample surface were milled again according to the CAD data shown in step 6) of Fig. 1. As a result, the textured surface and CAD data showed good

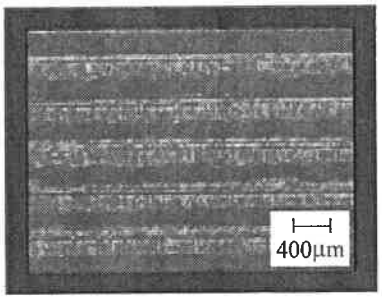

(a-1) Machined steps

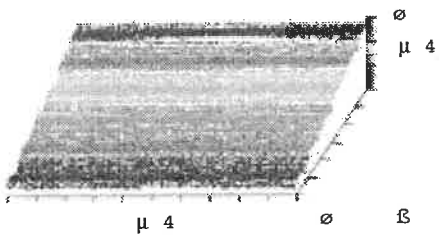

(a-2) Measurment result

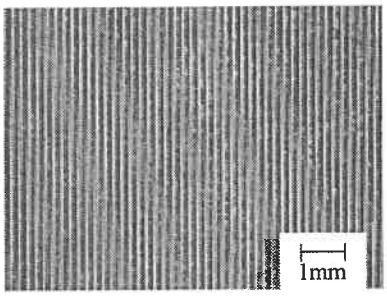

(b) Machined grooves

Fig. 7 Basic experiments

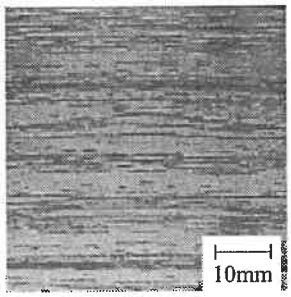

(a) Machined anisotropic texture
(Based on Fig. 3(a-1))

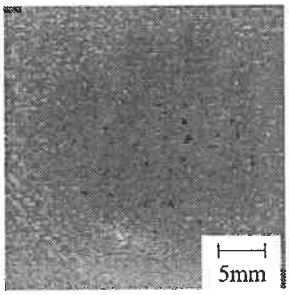

(b) Machined isotropic texture
(Based on Fig.6(b-1))

(c) Experimental conditions

	Fig.8(a)	Fig.8(b)
Spindle speed, rpm	35,000	
Feed rate, μm/s	1000	500
Diameter of end-mill, μm	500	300
Material	Aluminum	
Cutting depth, μm/Z Step	50	30

Fig.8 Results of surface texture generation

agreement.

4. Experimental work

Basic experiments

Fig. 7 shows the basic experiments of milling. Fig. 7(a-1) shows the stage configuration produced by a flat-end mill. Fig. 7(a-2) shows the 3-D image measured by scanning white-light interferometer. The height of each stage is 3 μm. The figure on the right shows grooves of 50 μm in depth at the intervals of 200 μm. Both are well machined.

Results of surface texture generation

Fig. 8 shows the generation results of surface texture. Fig. 8(a) shows the anisotropic texture based on the CAD data of Fig. 3(a-1). Fig. 8(b) shows the isotropic texture of human skin photographed by the CCD camera. The table on the right shows each experimental condition. As shown in these examples, it is possible to produce extremely fine textures in the order of μm from various data. The developed milling machine can be said to be an efficient processing system for the generation of surface texture.

5. Conclution

An exclusive system to generate the surface texture by machining has been developed. The system can design surface texture, perform milling in the μm level, and set up two measurement instruments to assess the surface topography of specimen. The technique applied in this system also allows generation of precision surface texture better than usual generation processes such as etching or sand-blasting.

References

[1] M. Uchidate, T. Shimizu and A. Iwabuchi, Proceedings of International Tribology Conference Nagasaki 2000, 223 (2001).

[2] A. Lindenmayer, P. Prusinkiewicz, Artificial Life, Addison-Wesley, 221(1990).

SIMULTANEOUS OPTIMIZATION OF REMOVAL RATE AND PART ACCURACY IN HIGH-SPEED MILLING

Mohammad H. Kurdi, Tony L. Schmitz, Raphael T. Haftka, Brian P. Mann
University of Florida, Department of Mechanical and Aerospace Engineering, Gainesville, FL 32611

1 INTRODUCTION

Intense competition in manufacturing places a continuous demand on developing cost-effective manufacturing processes with acceptable dimensional accuracy. High-speed milling offers these benefits provided appropriate operating parameters are selected. Some typical applications include, but are not limited to, end milling (pocketing) of airframe panels and ball end milling of stamping dies in automotive manufacturing.

However, the selection of these preferred operating parameters is not trivial. Existing barriers to the full realization of the potential productivity gains in manufacturing environments include: 1) the requirement for multiple tool point dynamic measurements; 2) sensitivity of part quality to small changes in process variables; and 3) the difficulty in concurrently considering stability, accuracy, and surface finish in an analytical framework. Therefore, balancing the multiple requirements, including high material removal rate, f_{MRR}, minimum surface location error $|f_{SLE}|$, sufficient tool life, chatter avoidance, and adequate surface finish, to arrive at an optimum solution is difficult without the aid of optimization techniques.

Multi-objective optimization addresses the issue of competing objectives using concepts developed by Pareto [1], the French-Italian economist who established an optimality concept in the field of economics based on multiple objectives. A Pareto front [2] is generated that allows designers to trade off one objective against others. However, generating a Pareto front is typically much more expensive than optimization of a single objective. The Temporal Finite Element Analysis (TFEA) [3-7] approach is used here to obtain rapid process performance calculations of surface location error, f_{SLE}, and stability. The computational efficiency of TFEA compared to conventional time-domain simulation methods makes it the most attractive candidate for use in the optimization algorithm. Additionally, TFEA provides a clear and distinct definition of stability boundaries (i.e., eigenvalues of the milling equation with an absolute value greater than one identify unstable conditions, see Section 2).

In this paper, an initial effort to apply analytical tools that find optimum cutting parameters (spindle speed, Ω and axial depth of cut, b, for peripheral end milling operations are considered at this stage) is attempted. Two objectives are simultaneously addressed, f_{MRR} and $|f_{SLE}|$, where only stability and side constraints of the design variables are considered. At this stage, no consideration is given to limitations of spindle power, torque or tool strength. The tradeoff method [8] is used to generate the Pareto front of f_{MRR} and $|f_{SLE}|$. Here, the two-objective problem is transformed into a series of single objective problems by establishing a set of different limits on the second objective. Solution of the optimization problem is performed using Matlab's Sequential Quadratic Programming algorithm (SQP) and Particle Swarm Optimization (PSO) [9].

The paper is organized as follows: Section 2 gives the milling model description and solution technique; Section 3 defines the optimization problem standard form and optimization methods used; Section 4 summarizes the main conclusions of the paper.

2 MILLING MODEL

The schematic for a two-degree of freedom (2-DOF) milling process is shown in *Figure 1*. With the assumption of either a compliant tool or structure, a summation of forces gives the following equation of motion:

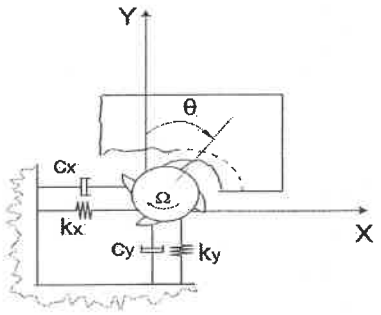

Figure 1. Schematic of 2-DOF milling tool.

$$\begin{bmatrix} m_x & 0 \\ 0 & m_y \end{bmatrix}\begin{Bmatrix} \ddot{x}(t) \\ \ddot{y}(t) \end{Bmatrix}+\begin{bmatrix} c_x & 0 \\ 0 & c_y \end{bmatrix}\begin{Bmatrix} \dot{x}(t) \\ \dot{y}(t) \end{Bmatrix} +\begin{bmatrix} k_x & 0 \\ 0 & k_y \end{bmatrix}\begin{Bmatrix} x(t) \\ y(t) \end{Bmatrix}=\begin{Bmatrix} F_x(t) \\ F_y(t) \end{Bmatrix}, \quad (1)$$

where the terms $m_{x,y}$, $c_{x,y}$, and $k_{x,y}$ are the modal mass, viscous damping, and stiffness terms and $F_{x,y}$ are the cutting forces in the x and y directions, respectively. A compact form of the milling process can be found by considering the chip thickness variation and forces on each tooth (a detailed derivation is provided in references [3-7]):

$$M\ddot{\vec{X}}(t)+C\dot{\vec{X}}(t)+K\vec{X}(t)=K_c(t)b\left(\vec{X}(t)-\vec{X}(t-\tau)\right)+\vec{f}_o(t)b\,, \quad (2)$$

where $\vec{X}(t)=\left[x(t)\;\; y(t)\right]^T$ is the two-element position vector and **M**, **C**, and **K** are the 2x2 modal mass, damping, and stiffness matrices, K_c and $\vec{f}_0$ are defined in references [3-7], $\tau = 60/(N\Omega)$ is the tooth passing period, Ω is given in rev/min (rpm), and N is the number of teeth on the cutting tool.

TFEA [3-7] is used here to transform Eq. (2) into a discrete linear map. Stability of the milling process can be determined using eigenvalues of the dynamic map, while surface location error (see *Figure 2*) is found from the fixed points of the dynamic map. Details can be found in references [3-7].

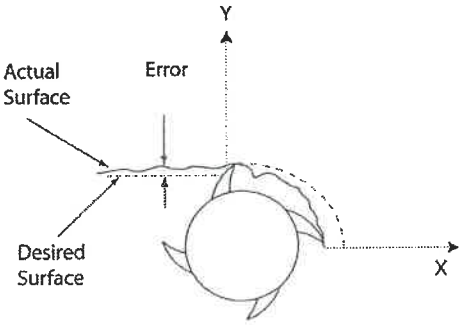

Figure 2. Up-milling schematic showing surface location error in milling as a result of cutting tool vibrations.

3 OPTIMIZATION PROBLEM STATEMENT

The problem of minimizing surface location error $|f_{SLE}|$ and maximizing material removal rate f_{MRR} is stated as follows:

$$min\left[\left|f_{SLE}(b,\Omega)\right|,-f_{MRR}(b,\Omega)\right] \quad (3)$$

Subject to: $g_\lambda(b,\Omega): max\left|\vec{\lambda}(b,\Omega)\right| \le 1$ (4)

where g_λ is the stability constraint obtained from the dynamic map eigenvalues, f_{SLE} is found from the fixed points, and f_{MRR} is given as:

$$f_{MRR}(b,\Omega)=Cb\Omega \quad (5)$$

where C depends on the feed per tooth, number of teeth, and radial depth of cut.

3.1 Tradeoff method

As shown in *Figure 3*, the Pareto front (line connecting A to B) is comprised of a set of optimal points, also called non-dominated points, in the function space consisting of all possible values of the objectives for feasible design points. In that space, the Pareto front is part of the boundary of the feasible function space, such that in moving from one point to another in the set, any improvement in one of the objective functions comes at the expense of at least one of the other objective functions [10]. Based on this definition, point C is not on the Pareto front (i.e., it is a dominated point), while points A and B belong to the non-dominated set (Pareto optimal set). In essence, the front defines a limit beyond which the objectives cannot be further improved simultaneously [10].

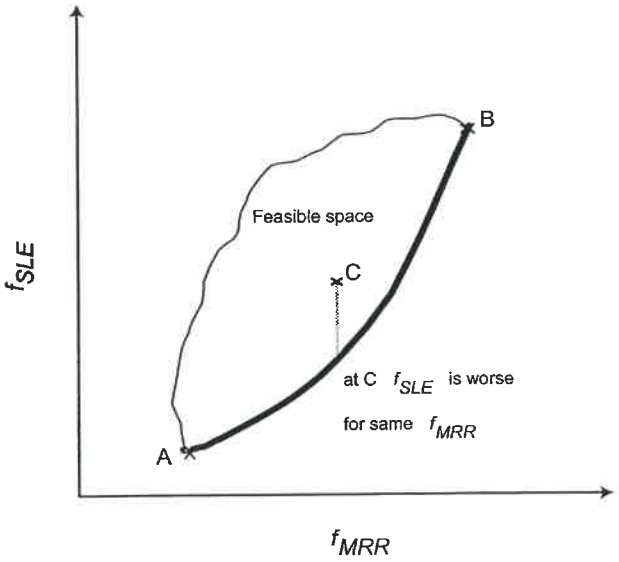

Figure 3. Typical Pareto front as per [10].

As noted, to address the multi-objective problem the constraint method is used, where the two-objective problem is transformed into a single objective problem of minimizing one objective with a set of different limits on the second objective. Each time the single objective problem is solved, the second objective is constrained to a specific value until a sufficient set of optimum points are found that are used to generate the Pareto front [2] of the two objectives. The constrained form of the problem becomes:

$$min\left|f_{SLE}(b,\Omega)\right| \quad (6)$$

Subject to: $-f_{MRR}(b,\Omega) \le \varepsilon_i\,,\; i=1,\ldots,k$ (7)

$$g_\lambda(b,\Omega): \max\left|\vec{\lambda}(b,\Omega)\right| \le 1 \quad (8)$$

for a series of selected limits (ε) on f_{MRR}.

3.2 Robust optimization: SQP vs. PSO

Two optimization algorithms were used to solve the two-objective problem, namely Sequential Quadratic Programming (SQP) using Matlab and Particle Swarm Optimization (PSO). The former is a local, gradient-based search method, while the latter is a global, non-gradient-based approach. SQP was implemented by using a number of initial guesses along the constraint objective, where the number of initial guesses was

chosen with the goal of finding a global optimum; therefore the spindle speed design range was divided into 20 and 40 points. The finer division provided better Pareto optimal set. In generating the Pareto front for this problem using the SQP algorithm, the minimum $|f_{SLE}|$ points were found to favor spindle speeds where the tooth passing frequency is equal to an integer fraction of the system natural frequency which corresponds to the most flexible mode (these are the traditionally-selected 'best' speeds which are located near the lobe peaks in stability lobe diagrams). *Figure 4* shows a stability lobe diagram, which describes the allowable axial depth of cut as a function of the spindle speed. Any (Ω, b) combination which lies above the boundary, represented by a heavy dashed line, gives chatter, or unstable cutting conditions. The diagram also gives the values of the objective functions: constant material removal rate is seen along the dotted f_{MRR} lines and the surface location error magnitude is given by the thin $|f_{SLE}|$ lines. The optimum points obtained using SQP are superimposed on the plot (circles).

Because f_{SLE} can undergo large changes in value for small perturbations in Ω at the optimum points, the formulation provided in Eqs. (6)-(8) leads to optima which are highly sensitive to spindle speed variation. Therefore, the optimization problem was redefined in order to avoid convergence to these points. Two approaches were applied: 1) an additional constraint was added to the $|f_{SLE}|$ slope; and 2) the f_{SLE} objective was redefined as the average of three perturbed spindle speeds. The latter proved to be more robust than the former. Therefore, Eq.(6) was redefined as:

$$min\left[\frac{\left|f_{SLE}\left(b,\Omega+\delta\right)\right|+\left|f_{SLE}\left(b,\Omega\right)\right|+\left|f_{SLE}\left(b,\Omega-\delta\right)\right|}{3}\right], \quad (9)$$

where δ is the spindle speed perturbation selected by the designer (a typical value for our analyses was 50 rpm).

The optimization problem can be expressed in a reverse manner as well. That is, the objective function can be defined as $-f_{\_MRR}$ and the optimization problem can be solved for a different set of constraints on average f_{SLE} as:

$$\left[\frac{\left|f_{SLE}\left(b,\Omega+\delta\right)\right|+\left|f_{SLE}\left(b,\Omega\right)\right|+\left|f_{SLE}\left(b,\Omega-\delta\right)\right|}{3}\right]\le\varepsilon_i \text{ for } i=1..k, \quad (10)$$

In comparison, when using the PSO method the objective function - f_{MRR} was minimized for a set of different constraints on $|f_{SLE}|$, rather than its perturbed average as shown in Eq. (6), where the swarm population was 60. In the PSO method, the optimum points did not converge to the highly f_{SLE} sensitive points.

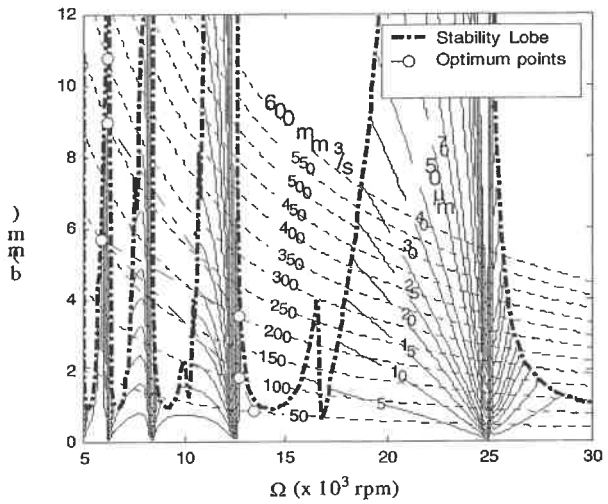

Figure 4. Stability, $|f_{SLE}|$ and f_{MRR} contours with optimum points found using optimization statement in Eqs. 6-8. The figure shows that optimum points occur in regions sensitive to spindle speed variation.

A comparison of the three optimization schemes is shown in Figure *5* and *6*. Figure *5* shows the optima for each approach superimposed on the corresponding stability lobe diagram. In Figure *6*, the Pareto fronts for the three methods are shown. The optimum points found using the two SQP formulations closely agree.

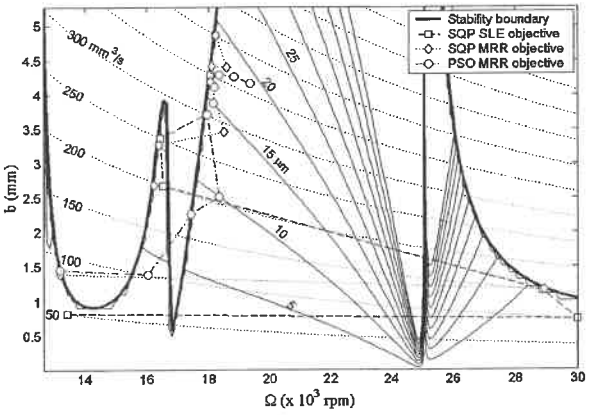

Figure 5. Stability, f_{SLE}, and f_{MRR} contours with optimum Pareto front points found using PSO and SQP with average perturbed f_{SLE}. The figure shows that optimum points are not in regions sensitive to spindle speed.

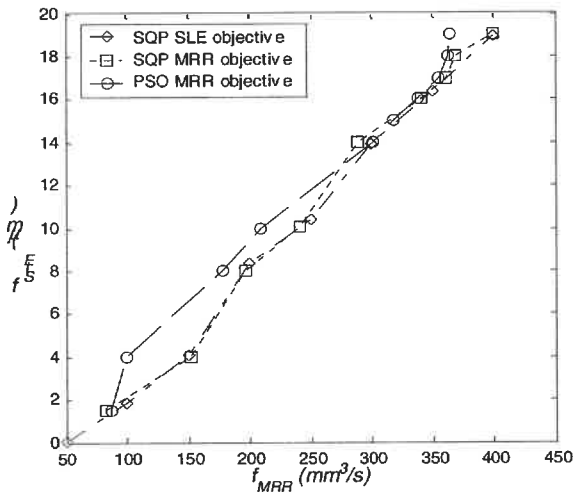

Figure 6. Pareto front showing optimum points found using three optimization algorithms/formulations. The same trends are apparent; however, the SQP methods required additional computational time.

Although the PSO points show the same trend, some improvement in the fitness is still possible relative to the SQP results. Because the PSO search avoided optimum points that are spindle speed sensitive, there is no need to use average perturbed f_{SLE} as SQP, which leads to a decreased number of f_{SLE} evaluations. This makes PSO less computationally intensive than SQP. However, narrow optimum points may go undetected when using PSO.

Although SQP in both variations of the objective function and constraint converged to approximately the same optima, the one with the average perturbed $|f_{SLE}|$ constraint required a larger number of initial guesses in order to converge to the same optimum as the SQP with the f_{MRR} constraint approach. This can be attributed to the low damping in the dynamic system used in this study which makes the $|f_{SLE}|$ contours (constraint) quite steep.

Table 1: Modal parameters for 19.05 mm diameter tool used in optimization simulations.

M (kg)		**C** (N-s/m)		**K** (N/m)	
0.061	0	3.86	0	1.67×10^6	0
0	0.056	0	3.94	0	1.52×10^6

4 CONCLUSIONS

This paper describes initial efforts toward the multi-objective optimization of high-speed milling. Material removal rate and surface location error were considered to arrive at a set of optimum operating conditions, referred to as the Pareto front. Consideration was given to the practical issue of convergence to optima near regions of high sensitivity of surface location error to spindle speed variations.

ACKNOWLEDGMENTS

The authors acknowledge financial support from the National Science Foundation (DMI-0238019 and CMS-0348288) and Office of Naval Research (2003 Young Investigator Program).

REFERENCES

1. Schwier, A.S., *Manual of Political Economy, Translation of the French Edition (1927)*. 1971, London-Basingslohe: McMillan Press Ltd.
2. Kalyanmoy, D., *Multi-Objective Optimization Using Evolutionary Algorithms*. 2001, West Sussex, England: John Wiley.
3. Mann, B.P., *Dynamics of Milling Process*. 2003, Washington University: Saint Louis, Mo.
4. Mann, B.P., P.V. Bayly, M.A. Davies and J.E. Halley, *Limit Cycles, Bifurcations, and Accuracy of the Milling Process*. Journal of Sound and Vibration, 2004: p. in press.
5. Mann, B.P., T. Insperger, P.V. Bayly and G. Stepan, *Stability of up-milling and down-milling, Part 2: Experimental verification*. International Journal of Machine Tools and Manufacture, 2003. **43**: p. 35-40.
6. Insperger, T., B.P. Mann, G. Stepan and P.V. Bayly, *Stability of up-milling and down-milling, Part1: Alternative analytical methods*. International Journal of Machine Tools and Manufacture, 2003. **43**: p. 25-34.
7. Halley, J.E., *Stability of Low Radial Immersion Milling*. 1999, Washington University: St. Louis, Mo.
8. Eschenauer, H.A., J. Koski and A. Osyczka, *Multicriteria Design Optimization: Procedures and Applications*. 1986, NY: Springer-Verlag.
9. Hu, X. and R. Eberhart. *Solving constrained nonlinear optimization problems with particle swarm optimization*. in *6th World Multiconference on Systemics, Cybernetics and Informatics*. 2002. Orlando, USA.
10. Wu, J. and S. Azarm, *Metrics for Quality Assessment of a Multiobjective Design Optimization Solution Set*. Journal of Mechanical Design, 2001. **123**: p. 18-25.

Ultraprecision Cutting of Molybdenum By Ultrasonic Elliptical Vibration Cutting

Toshimichi Moriwaki[1)], Hirohumi Suzuki[1)], Junji Mizugaki[1)], Yoshito Maeyasu[1)],
Yasuo Higashi[2)] and Eiji Shamoto[3)]
1) University of Kobe, Hyogo, Japan, 2) KEK, Ibaraki, Japan,
3) University of Nagoya, Aichi, Japan

Abstract

The present research aims to carry out ultraprecision diamond cutting of hard and brittle materials by using ultrasonic elliptical vibration cutting method, and to demonstrate the feasibility of the technique. In this research, molybdenum test pieces were cut by both conventional diamond cutting and ultrasonic elliptical vibration cutting. It was confirmed that the cutting force was reduced significantly as compared with the conventional ultraprecision diamond cutting. Moreover, continuous chips were formed in ductile mode cutting and a mirror surface finish of 72nmRy was obtained by ultrasonic elliptical vibration cutting.

1. Introduction

The accelerating tube cell of linear accelerators is currently made of copper. However, it is found that the electrical discharge phenomenon causes damages in the central part of the accelerating tube cell. It is examined to substitute copper with molybdenum for next-generation linear accelerators because the melting point of molybdenum is much higher than that of copper, and it can withstand prolonged exposure to high temperature. However, molybdenum is difficult to cut by conventional ultraprecision diamond cutting due to brittleness at the grain boundary, which results in poor surface finish.

The authors have developed a new cutting technology named elliptical vibration cutting [1-3] and have clarified that ultraprecision diamond cutting of hardened die steel can be realized by the technology [4-5]. In this research, elliptical vibration cutting is applied to cut molybdenum.

2. Ultrasonic Elliptical Vibration Cutting

2.1 Elliptical Vibration Cutting Process

Figure 1 shows a schematic illustration of elliptical vibration cutting process. The tool is vibrated elliptically and fed in the nominal cutting direction relatively to the workpiece at the same time, so that the chip is formed intermittently and pulled out in each vibration cycle. Since the friction between the chip and the tool rake face is reversed, the shear angle is increased and consequently the cutting force and cutting energy are reduced significantly.

2.2 Vibrator and Control System

Figure 2 shows schematic illustration of the ultrasonic elliptical vibrator and the control system. It was originally developed in the previous research [4]. The vibrator has four large piezoelectric plates as actuators and two small plates as sensors. It is vibrated in the cutting direction in the third resonant mode by applying sinusoidal voltage to the upper and lower actuator with a phase shift of 180 degrees. It is also vibrated in the normal direction to the cutting

direction and the vibrator axis, so that the end of the vibrator, where the cutting tool is attached, is vibrated in an elliptical vibration locus. The two directional vibrators are detected by the two PZT sensors.

A vibration control system is developed to keep the vibration amplitudes, their phase shift and their resonant frequencies to desired values in the system. The vibration signals detected by the piezoelectric sensors are input to the controller and the cross talk remover as feedback signals as shown in Fig.2.

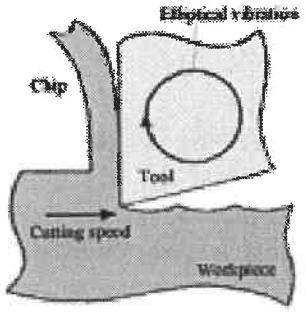

Fig.1 Elliptical vibration cutting process

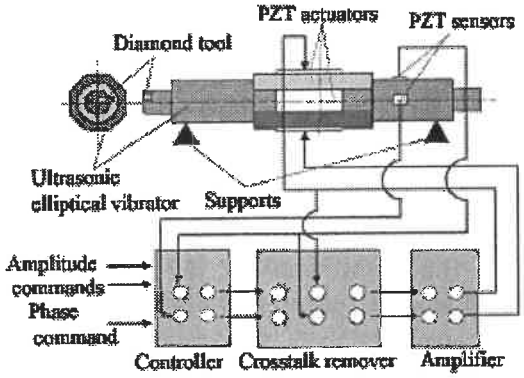

Fig.2 Vibrator and control system

3. Experiment

3.1 Experimental setup

The ultrasonic elliptical vibration cutting is applied to ultraprecision cutting of molybdenum in order to demonstrate the feasibility of the technique.

The experimental setup is shown in Fig.3 and Fig.4. The elliptical vibration tool with the diamond tool tip is mounted on an ultraprecision lathe, and circular workpiece is face turned. The tool tip is made of single crystal diamond, whose nose radius is 1mm and rake and relief angles are 0 and 15 degrees, respectively. The sintered molybdenum workpiece has with grain size of 3-5 μm. The feed rate is 12 μm/rev and the spindle rotation is 2 min^{-1}. The initial vibration locus is set to be circular with a radius of 4 μm and its frequency is 20 kHz. The angle of elliptical vibration shown in the Fig.4 is 40 degrees in the present experiments.

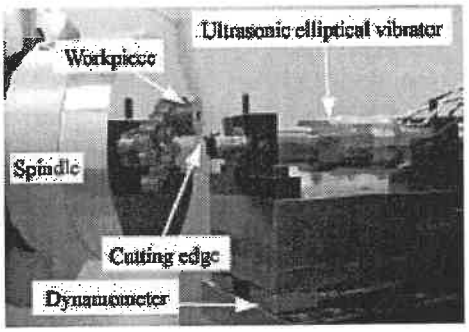

Fig.3 Ultraprecision machine tool equipped with vibration cutting tool

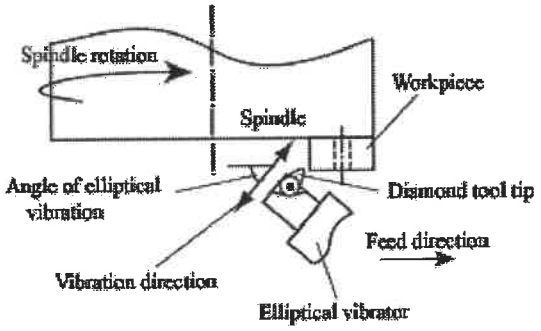

Fig.4 Experimental setup

3.2 Results

The experimental results are shown in Fig.5, Fig.6 and Fig.7. Figure 5 shows a photograph of the finished surfaces obtained in the present experiment. The surface finished by the conventional cutting appears cloudy. In contrast, the whole area of the surface finished by the ultrasonic elliptical vibration cutting is a clear mirror. An example of measured cutting force in each direction is shown in Table 1. The cutting force is reduced significantly as compared with conventional cutting

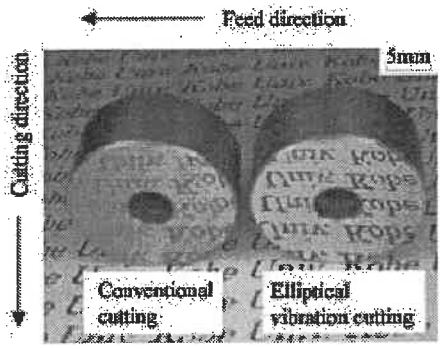

Fig.5 Photographs of finished surface

Table 1 An example of cutting force

	Principal force (N)	Thrust force (N)
Conventional cutting	2.29	4.14
Elliptical vibration cutting	0.34	1.21

Figure 6 and Figure 7 shows microphotographs of the finished surfaces and chips obtained in the present experiment. In the case of conventional diamond cutting, the surface is filled with asperities due to micro fractures at the grain boundaries caused by the brittleness of the material. The chips are discontinuous and formed in brittle mode. The maximum surface roughness is about 0.158 μ mRy. On the other hand, a mirror surface and continuous chips can be obtained by the ultrasonic elliptical vibration cutting. The maximum surface roughness is about 0.072 μ mRy.

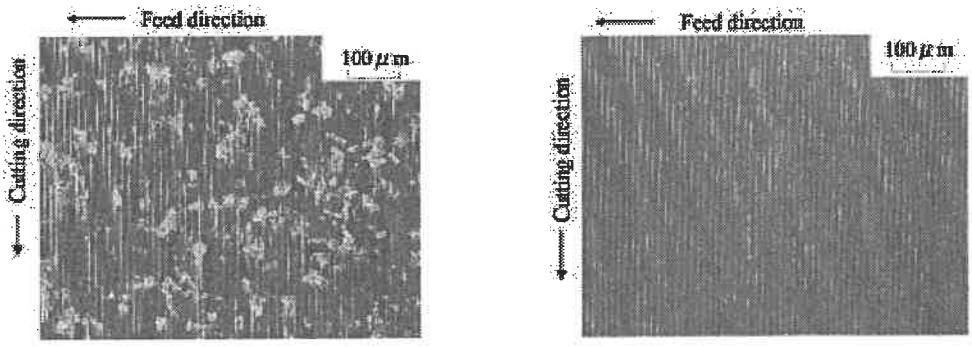

(a) Conventional cutting (b) Elliptical vibration cutting

Fig.6 Microphotographs of finished surfaces

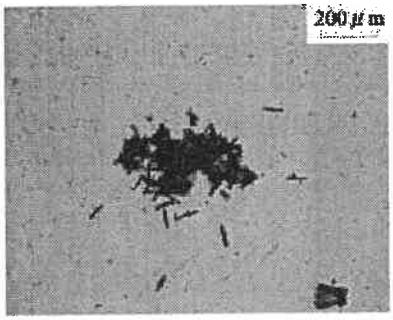

(a) Conventional cutting

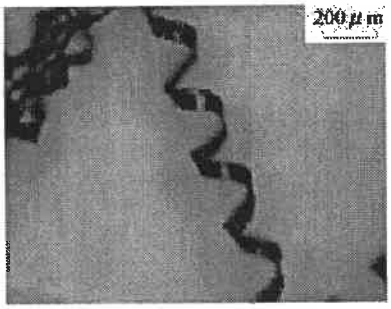

(b) Elliptical vibration cutting

Fig.7 Microphotographs of chips

4. Conclusion

Molybdenum test pieces were cut by both conventional diamond cutting and ultrasonic elliptical vibration cutting. The experimental results show that continuous chips are formed in ductile mode cutting and a mirror surface finish of 72nmRz is obtained by ultrasonic elliptical vibration cutting.

5. References

[1] E. Shamoto, T. Moriwaki: Study on Elliptical Vibration Cutting, Annals of the CIRP, (1994), 43/1, 35-38.

[2] T. Moriwaki E. Shamoto,: Ultrasonic Elliptical Vibration Cutting, Annals of the CIRP, (1995), 44/1, 31-34.

[3] E. Shamoto, T. Moriwaki: Ultraprecision Diamond Cutting of Hardened Steel by Applying Elliptical Vibration Cutting, Annals of the CIRP, (1999), 48/1, 441-444.

[4] E. Shamoto, N. Suzuki, T. Moriwaki, Y. Naoi: Development of Ultrasonic Elliptical Vibration Controller for Elliptical Vibration Cutting, Annals of the CIRP, (2002), 51/1, 327-330.

[5] E. Shamoto, N. Suzuki, S. Matsuda: Ultra precision Machining of Sintered Tungsten Carbide by Applying Ultrasonic elliptical vibration cutting, Proc of euspen 4th Int. Conf (2004) 187-188

FLUCTUATIONS IN CHIP FLOW VELOCITY WITH TIME

Masataka Nomura
Kobe University

Abstract

Fluctuations in chip flow velocity on the tool with time significantly affect heat generation on the rake face of the tool, tool temperature, tool wear, tool life and surface quality of workpiece as the cutting forces do. There has been no study that tried to observe the chip flow velocity with time, although a considerable number of studies on the cutting force have been made over the past decades. The paucity of reports on the chip flow velocity and the wide use of a high-speed camera system in public prompted us to investigate this. The chip flow velocity is evaluated by measuring the displacement of a point on the chip between successive two pictures taken by a high-speed camera system. This paper points out that the chip flow velocity in a very short time is not constant even under the steady cutting conditions and that the oscillation of this may causes great effects on the fluctuation in heat generated on the rake of the tool, which is considered to have significant effects on the tool wear.

1 Introduction

In the conventional cutting theory, it is assumed that after a certain period of time, chip flow velocity is constant with respect to time during cutting in a steady state maintaining the same cutting condition. The process of chip formation and destruction, however, is repeated continuously for a brief period during the cutting operation and the chip thickness in practice is not constant even in continuous chips generated. We can calculate the chip flow velocity by multiplying the cutting speed by the cutting ratio, which can be expressed as the ratio of the depth of cut to the chip thickness, but it is technically quite difficult to measure directly the chip thickness because of changes in chip formation process which take place in a very short time. Thus, the chip formation process is a high-speed phenomenon and an instrument for the actual measurements is necessary in order to obtain a satisfactory result.

Cutting forces on the tool in turning can be directly measured by using dynamometers mounted on the machine tool and a large number of studies have been made on the cutting forces, the oscillation of them and the change in the chip formation. It has been reported that cutting forces are subject to small fluctuation with time even in a steady state in machining.

Although the careful examination of the fluctuation in the chip flow velocity is of great importance, there has been no study that investigates the chip flow velocity in a very short time because of the lack of devices for measuring it. Recently high-speed camera systems have developed rapidly and they are suitable for direct observation of the chip formation. The purpose of this study is to examine the fluctuation in the chip flow velocity in millisecond time-scale in turning using a high-speed camera system.

2 Experimental setup

Cutting experiments were carried out in a turning operation on a lathe. The workpiece material was a carbon steel for machine structural use, S45C. The experiments were performed in changing cutting speed, feed rate and depth of cut using an uncoated P20 grade carbide tool. All tests were conducted without coolant. The cutting conditions are show in **Table 1.**

The experimental setup is shown in **Fig. 1.** The workpiece was chucked on a lathe and was supported at the end with a centre held in the tailstock. The straight turning was conducted without cutting fluids. High-speed camera was fixed on right upper side in order to observe the chip during machining and took some consecutive pictures of the phenomenon of turning over several seconds at a rate of 1000 images per sec.

Table 1 Cutting conditions

Cutting speed	43.3, 77.5, 108.2 m/min
Feed rate	0.1, 0.12 mm/rev
Depth of cut	0.65, 1.5, 3.0 mm
Work material	S45C
Tool material	P20 grade carbide tool
Tool geometry	(0°, 0°, 10°, 10°, 15°, 15°, 0.75mm)
Cutting method	Dry

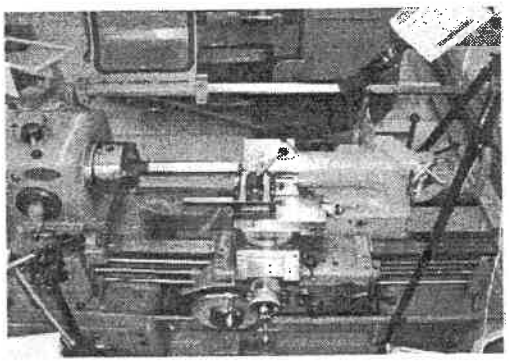

Figure 1 Experimental setup for taking successive pictures of chip formation with high-speed camera

Pictorial images taken were stored on personal computer. As an example successive photographic images taken are shown in **Fig. 2**. Successive photographs in this figure shows that the chip flowing on the rake of the tool and the rotating workpiece. Symbol t means the elapsed time from a certain time during turning.

The chip flow velocity values were calculated by measuring the change of the position at the same spot between the two successive images. In order to observe the change of the radius of curvature of the chip, the change of the chip flow velocity was measured at both the outside and the inside edges in curled chip.

3 Results and discussion

3.1 Observation of Chip formation

We find the various types of chips produced in turning under different cutting conditions. Resulting photographs of some types of chips observed in practice are shown in **Fig. 3** together with data about cutting speed, feed rate and depth of cut. This figure shows that various chips can be produced by changing cutting conditions as in turning operations. This paper observes the chip flow velocity in these three types of chips shown in this figure.

We refer the chip on the left side in the figure as continuous curled chip, on the middle as continuous irregular shaped chip and on the right as side curled chip. Continuous curled chip has a certain radius of curvature and does not break off during observation. Continuous irregular shaped chip also does not break off but is different from continuous curled chip without constant radius of chip curvature in the geometry. Side curled chip hits tool flank and breaks off short. The length of the chip in practice is almost 7 mm.

We discuss a few points about the relationship between the types of chips and the chip flow velocity.

3.2 Chip flow velocity with time

The relationship between the chip flow velocity measured and the elapsed cutting time under producing continuous curled chip is shown **Fig. 4**. The cutting condition is that cutting speed is 108.2 m/min, feed rate is 0.12 mm/rev and

$t = 0.509$ s $t = 0.510$ s $t = 0.511$ s

Figure 2 The sequential photographs of chip movements: cutting speed : 43.3m/min, feed rate : 0.1mm/rev, depth of cut : 1.5mm

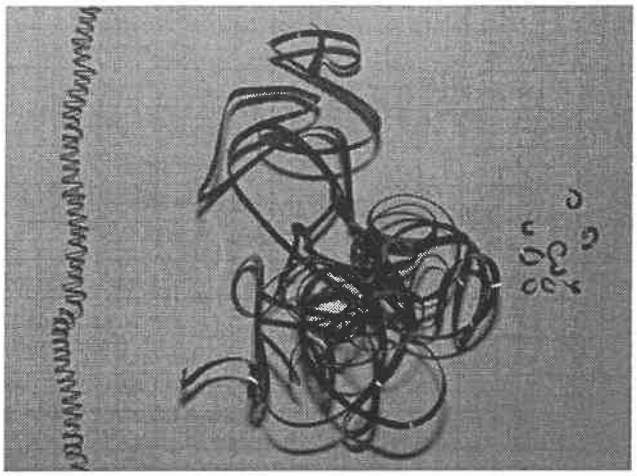

		(a)	(b)	(c)
Cutting speed	m/min	108.2	77.5	43.3
Feed rate	mm/rev	0.12	0.1	0.1
Depth of cut	mm	0.65	3.0	1.5

Figure 3 Typical types of chips and its cutting condition: (a) Continuous curled chip; (b) Continuous irregular shaped chip; (c) Side curled chip

depth of cut is 0.65 mm. The chip flow velocity is measured at an interval of 1 millisecond. The ordinate is the axis of the chip flow velocity and the abscissa is the axis of the elapsed time from a certain point during turning.

In this cutting condition, the chip observed is generating continuously without breaking off and is flowing in the same direction instead of the slight change of the radius of chip curvature during turning operation. The cyclical length of chip spiral is about 16 mm, which corresponds to 0.05 seconds on this figure. We can find that the chip flow velocity varies with amplitude correspondingly to the time. The average velocity in chip flow is 18 m/min at the edge of outer curled chip, 20 m/min at the edge of inner and shows 15% fluctuations in amplitude with time. This implies that chip does not flow steady even in a steady state maintaining the cutting condition.

Figure 5 shows the chip flow velocity calculated using photo images taken under the cutting condition, cutting speed is 77.5 m/min, feed rate is 0.1 mm/rev and depth of cut is 3.0 mm.

In this chip geometry although the average velocities in chip flow at the edge of outer curled chip, 19.5 m/min is slightly greater than that at the edge of inner curled chip, 19 m/min there is not a marked difference in them. Thus the chip flows in the direction nearly perpendicular to the cutting edge of the tool.

It is noticeable that fluctuating amplitude in the chip flow velocity is superimposed on a certain uniform rate of chip and that after 0.03 seconds the chip flow velocity fluctuates considerably. It is possible that the large oscillation

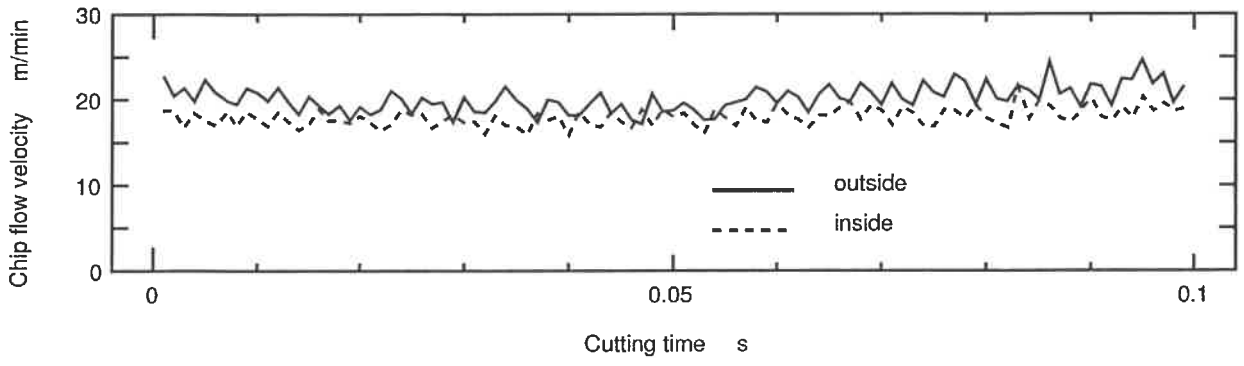

Figure 4 Chip flow velocity in generating continuous curled chip

in chip flow velocity is attributed to the effect of the chip already generated.

The chip flow velocity is significantly affected by the existence of the chip generated, although the chip flow direction seems to be almost steady. And that explains the continuous irregular shaped chip type shown in Fig. 3

The chip flow velocity with respect to time is shown in **Fig. 6** under the cutting condition, cutting speed is 43.3 m/min, feed rate is 0.1 mm/rev and depth of cut is 1.5 mm. The average chip flow velocity may be read from this figure as 5.2 m/min and 9.0 m/min at the inner side and outer side of curled chip respectively. The difference in chip flow velocity between at both sides is the greatest of three results in this paper, and explains the chip geometry with the small radius of curvature displayed in Fig. 3

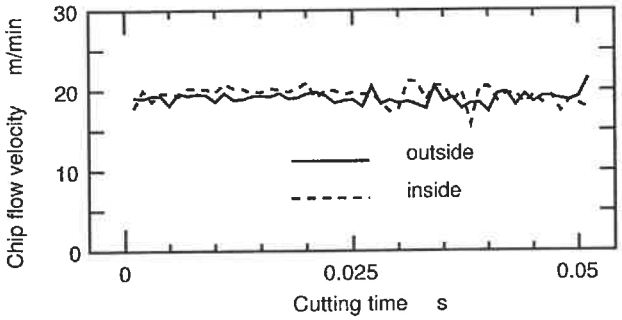

Figure 5 Chip flow velocity in generating continuous irregular shaped chip

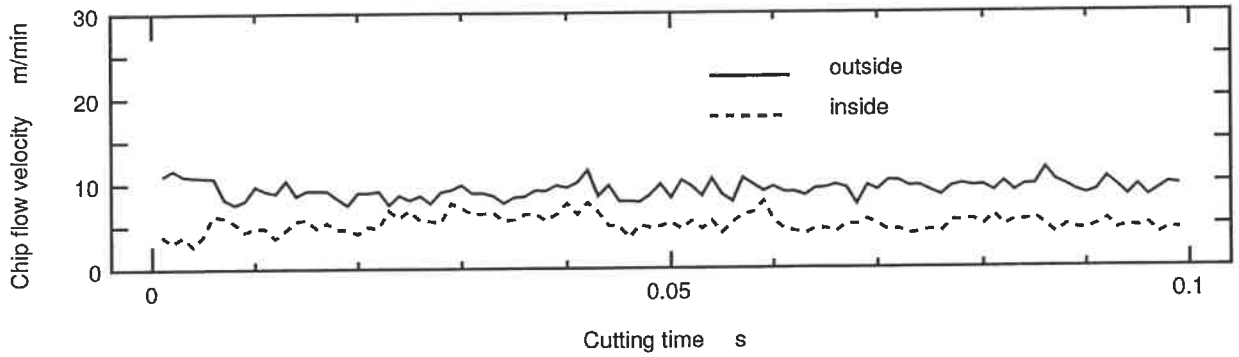

Figure 6 Chip flow velocity in generating side curled chip

This study makes it clear that the chip flow velocity oscillates in a very short time period. We, however, feel there is still room for further investigation on the relationship between chip flow velocity and cutting forces or chip geometry under the various cutting conditions and on the effects of the fluctuation in the chip flow velocity on the tool temperature.

4 Conclusions

The results of this study can be summarized as follows:

(1) Accurate measurements of the chip flow velocity are made with a high-speed camera system.

(2) High fluctuations in chip flow velocity with time are observed in an ordinary turning operation.

(3) The chip flow velocity oscillates regardless of the cutting conditions such as cutting speed, feed rate or depth of cut and affects the chip geometry.

(4) Continuous irregular shaped chip is generated by the deformation at a certain distance from the edge of the tool and the shape of that is affected by the chip generated.

(5) The oscillation of the chip flow velocity may causes effects on the fluctuation of the cutting temperature on the tool.

EXPERIMENTAL OBSERVATIONS OF TOOL WEAR IN MULTILAYER COATED INSERTS

Jorge A. Olortegui-Yume and Patrick Y. Kwon
Department of Mechanical Engineering, Michigan State University, East Lansing, MI

ABSTRACT

This paper deals with understanding the evolution of tool wear of multilayer coated inserts using Confocal Laser Scanning Microscopy (CLSM). Steady-state turning experiments were carried out on 1045 steel bars with commercially available multi-layer coated inserts consisting of TiN /Al_2O_3 /TiCN deposited on a C6 carbide substrate provided by Kennametal, Inc.. Topographical images of the crater wear as well as orthogonal sections of the flank and crater wears as functions of machining time are obtained. A humped island of TiN coating material next to a growing crater of Al_2O_3 and steel traces were found. The maximum crater depth value and location respect to the edges of the insert are gathered for all machining times. The maximum crater depth location was observed to move across the rake face as machining time increased. These unexpected features of crater wear are suspected to have their origin in the competition of the abrasive and dissolution mechanisms, and the difference in wear-resistant properties between the TiN and Al_2O_3 coatings. Validations of the confocal results are also performed using the Scanning Electron Microscope (SEM) and the Atomic force microscope (AFM).

1. INTRODUCTION

Up to date many efforts have been made to understand the nature of tool wear, however, it continues to have unsolved problems. Solutions to these problems would bring a great economical impact in machining industry. However, a thorough understanding of the micro-mechanisms involved in tool wear and a meaningful method to measure it must precede such solutions. So far, the traditional methods used to measure tool wear have included reflected light interference microscopy, scanning electron microscopy, and stereo microscopy [1, 2]. However, due to the limitation on the depth of field, the difficulty while obtaining and interpreting images and the high cost involved, these methods have proven to be burdensome and time-consuming.[3,4] .Traditional methods of surface measurement have also involved stylus profilometers. However, this method has a number of disadvantages such as the limitations on the detail they can resolve, the slow scanning rate, and the potential damage to the surface investigated. Also, severe difficulties arise when 3D information of surfaces is required [4]

The main advantages of Confocal laser scanning microscopy (CLSM) include the fast and convenient means of obtaining surface features and the determination and analysis of the true surface topography. These capabilities provide the unique characteristics of the CLSM such as the versatile depth of field, the minimal sample preparation, the adequate image quality for engineering purposes, and the savings in costs relative to SEM technology [4]. Even though CLSM has been established as a powerful tool in biological and medical sciences since the early 80's, only in the past few years some comparative studies on the performance of traditional methods versus CLSM have been carried out in wear measurement, tribology, fractography, and biomedical sciences [3, 4, 5, 6]. A superior performance of CLSM surface profiles compared to those of a profilometer was always found. Further, CLSM measurements were in good agreement with Atomic Force Microscope (AFM) values.

2. BACKGROUND

The confocal principle

The power of the CLSM resides in its ability to get an image only from the light in the focal plane. This means that all the out-of-focus light is blocked from the final image allowing a sharper image compared to the conventional light microscope. This feature is achieved by positioning a pinhole in the light path. Light that is exclusively coming from the focal plane is focused at a point right in the position of the pinhole (Figure 1). The pinhole is positioned so that it passes light from the focal plane to a detector. Light rays originally coming from out-of-focus regions have a focal point either in front

or behind the pinhole, therefore, few of these rays make their way through the pinhole. As a consequence, the image is formed mostly by rays coming from the region of the sample located in the focal plane. This process is the main concept of optical section. An optical section can be better understood as an electronical slice of the sample coinciding with the focal plane level. The advantage is that an actual sectioning is not necessary to perform, the sample remains intact and repetition of the process can be done. Once light of the region not in focus has been discarded in the final image, resolution and contrast are drastically improved respect to the conventional light microscopes.

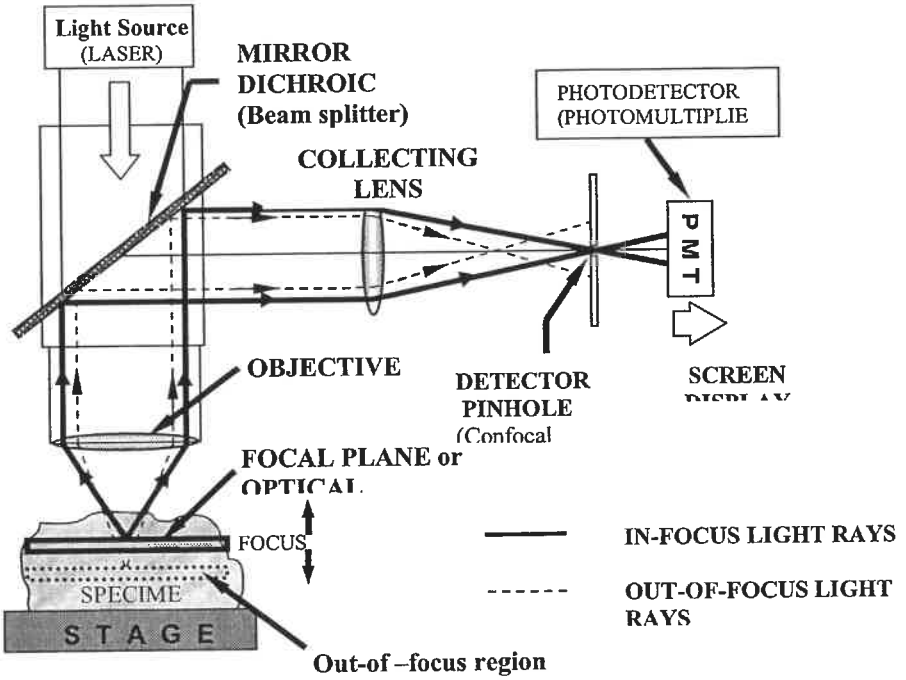

Figure 1 The confocal principle

The CLSM can perform operations such as the gathering of a series of optical slices called a z-stack which could be overlaid to give sharp 2D image. Also, the 3D reconstruction feature allocates for the acquisition of a height value (z) that identifies the surface position and stores it a matrix , z(x,y), that can be manilpulated to obtain different types of rendering including surface topography, isolines (contour lines), and roughness parameters .

3 EXPERIMENTAL PROCEDURE

3.1 Machining tests

Dry turning tests were carried out in 8033 Clausing/Colchester lathe with the control for infinitely variable speed. The experiments are carried out at the constant feed of 0.3175 mm/ rev, depth of cut of 1.905 mm and constant cutting speed of 250 m/min (820 sfpm). These conditions are used based on the following criteria: the range of optimal speeds provided by the insert manufacturer's, the need for obtaining as much measurable wear as possible in the shortest time, and the torque limits of the lathe while obtaining minimal chattering, good surface finishing and optimal area size for imaging. After few trial runs the approach angle was set to 5 degrees and the toolholder shank was machined to provide a back rake angle of 2°. These angles set a compromise between minimal chattering and proximity to orthogonal cutting conditions. Machining times were interrupted at: 60 s, 120 s, 180 s, 240 s, 300 s, 480 s and 720 s. in order to obtain a cutting edge at each of these times. Thus, allowing for the wear evolution to be observed as function of time. Steel rounded bars of 1045 steel, 6" diameter and 18" length, were used as work material.

3.2 Inserts and Work material

The square inserts are provided by Kennametal, Inc., Latrobe, PA , having a SNMA 190612 ISO designation The multi-layer insert is designated as a KC9315 grade insert, which corresponded to a top layer made of TiN, an intermediate layer of Al_2O_3, and a bottom layer of TiCN deposited

on a C6 cemented carbide substrate. TiN thickness is found to be 2.5 μm, Al_2O_3 7.1 μm, and TiCN 7.8 μm.

3.3 Confocal microscopy data acquisition

A Zeiss LSM 210 confocal microscope is used in reflection mode to obtain 2D images and 3D data sets z(x,y) matrices of all the corners with the different machining times. Then a Zeisss LSM 310 software was used to manipulate the z(x,y) matrices for measurement , analysis and topographical rendering. Finally Adobe photoshop 7.0 is employed to post-processs the images and give the final pictures.

3.4.SEM data acquisition

A JEOL JSM-6400 Scanning microscope is used to obtain BSE images and X-ray spectroscopy chemical analysis are performed in all the corners to identify the evolution of the wear associated to the limits of the two first layers (TiN and Al_2O_3). In addition, four SE (secondary electrons) images are merged to validate the shape of the crater for the corner with 300s machining time.

3.5 AFM data acquisition

This is the main validation for the depth values obtained with the confocal microscope. Nanoscope III Scanning probe microscope manufactured by Digital Instruments Inc. was used to perform this part.

3. RESULTS AND DISCUSSIONS

The confocal pictures reveal an unexpected hump starting approximately at 190 μm from the edge, a growing crater next to the hump and a thin depression that run along with the edge-side limit of the crater (Figures 2 (a) and (b)). The BSE images and X-ray spectroscopy showed the hump composed of TiN (bright zone), the growing crater composed of Al_2O_3 (black zone) and some traces of steel (very bright zones). It turned out that the thin depression was coinciding with a strip of Al_2O_3 running along with the edge limit of the crater (Figure 3). In addition, the maximum crater depth locations and its values are obtained out of the z(x,y) confocal matrices (Figure 4). An increasing trend of the maximum crater depth with machining time and constant tendency between 300 and 720s is observed (Figure 5). This location moved across the tool face as the machining process continues (Figure 6), suggesting that the peak temperature location, which occurs in the vicinity of maximum crater depth, is also moving [7]. It is believed that this behavior is the result of the competition between the dissolution and diffusion mechanisms, which are greatly influenced by the temperature [8]. Regarding flank wear, phi-z sections are obtained in the locations correspondent to the maximum crater depth for all machining times. Although gradual flank wear is observed, no clear trend is observed when measuring the slopes in different parts of the flank profiles. The secondary electrons image corroborated the shape of the worn tool face obtained in the topography view of the confocal pictures. A good agreement with the AFM depth values was found during the validation.

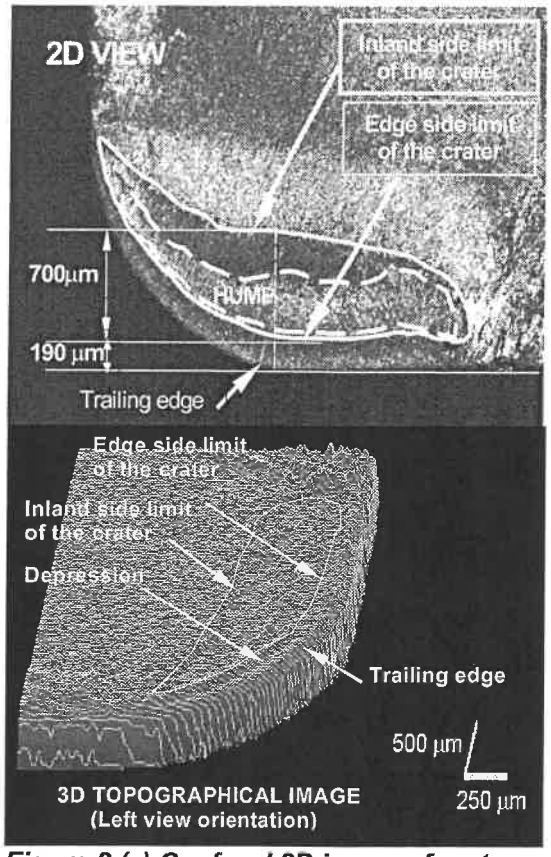

Figure 2 (a) Confocal 2D image of crater wear , (b) Confocal 3D image of crater wear

4. CONCLUSIONS

The usefulness of confocal microscopy to obtain reliable surface profiles and topography was confirmed. SEM and AFM microscopes aid was relevant as validation tools for the CLSM information. Also, the optical properties of steel are found to have a distorting influence in the results of the topography rendering. The particular behavior of coated tools wear was also verify [9, 10] and in particular the wear of

multi-layered coated has unexpected features in the tool face and maximum crater depth behavior. However, extended work and analysis are currently being carried out to interpret these results in terms of wear mechanisms.

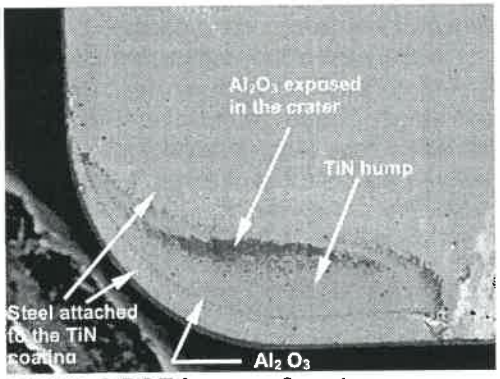

Figure 3 BSE image of crater wear

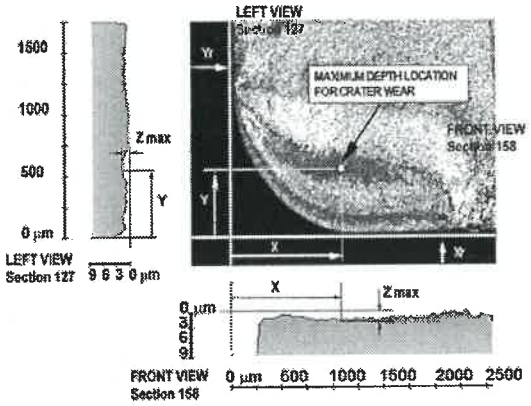

Figure 4 Maximum crater depth location

REFERENCES

[1] Devillez, A. , Lesko, S. and Mozer, W., "Cutting tool crater wear measurement with white-light interferometry", Wear, 256, pp. 56–65, 2004

[2] Dawson, T.J. and Kurfess, T.I., "Wear trends of PCBN cutting tools in hard turning", http://www.hardinge.com/hardium/PDF/Dawson_NAMRC_2002.pdf

[3] Gee, M.G. and McCormick, N.J., " The application of confocal scanning microscopy to the examination of ceramic wear surfaces", Journal of Applied Physics, 25 , A230-A235, 1992

[4] Anamalay, R.V., Kirk, T.B. and Panzera, D., "Numerical descriptors for the analysis of wear surfaces using laser scanning confocal microscopy", Wear, 181-183, pp. 771-776, 1995

[5] Hanlon, D.N., Todd, I., Peekstok, E., Rainforth, W.M., Van der Zwaag, S., "The application of laser scanning confocal microscopy to tribological research", Wear 251, pp. 1159-1168, 2001

[6] Wessel, S., Pagel, S., Ritter, M., Hohenberg, H., and Wepf, R., "Topographic measurements of real structures in reflection confocal laser scanning microscope (CLSM)", Microscope Microanalysis, 9, suppl. 3, p. 162, 2003.

[7] Childs,T.H.C., Maekawa , K. ,Obikawa, T.,and Yamane, Y., "Metal Machining", Arnold Publishers, pp.76-132,

[8] Kim, W.S., "A new methodology for predictive tool wear", PhD dissertation, Michigan State University, p. 15, 2000

[9] Chubb, J.P. and Billingham, J., "Coated cutting tools- A study of wear mechanisms in high speed machining", Wear, 61, pp. 283-293

[10] Kountanya, R.K., "Predictive Tool wear of coated tools systems", M.S. Thesis, Michigan State University, 1998

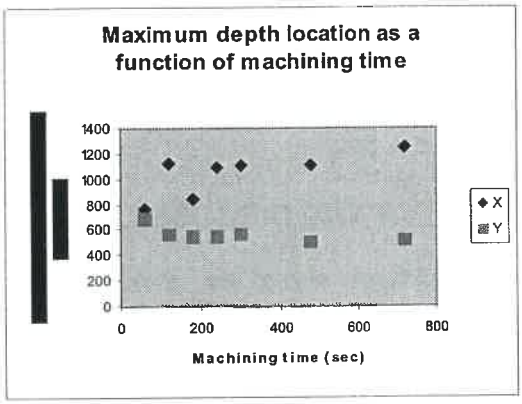

Figure 5 Maximum depth locations

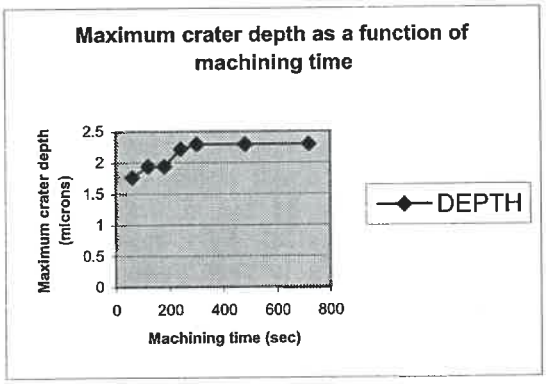

Figure 6 Evolution of crater depth

Assessing the Sharpness of Hand Plane Cutter Blades

Richard L. Rhorer
Gaithersburg, MD -- prhorer@starpower.net

The modern hand plane used in numerous wood working shops around the world has a history dating back at least a couple of millennia. One can argue that the development of the hand plane in general is rather obvious: a wood cutting chisel was probably first developed from stone or metal, and some type of guide was developed to hold the chisel at a consent angle with the wood surface being cut, which then evolved into the more complicated planes of today. By the 18th Century, specialized and rather sophisticated hand planes for cutting wood were being used by most carpenters, furniture makers, and production shops. As power machines became common during the 19th Century, hand planes became less important and they pretty much disappeared in production manufacturing of wood items. And yet, in the small or custom shop, and the toolbox of the fine wood worker, you will still find a selection of hand planes even now as we enter the 21st Century. The technical aspect of the hand plane that is of interest from the precision engineering perspective is the geometry and sharpness of the cutter, and how one measures these parameters. For a manufacturer of hand plane cutters (called plane irons in the trade) any of the standard measurement methods used in any machine shops—coordinate measuring machines, shadow graphs, stylus instrument, etc—would be appropriate. However, for the very small wood shop or hobby shop, how can one measure the sharpness of a hand plane iron without investing in a lot of measuring equipment? The answer presented here is to use items common in most homes: digital cameras, scanners, and computers all available at the corner drug store for a few hundred dollars. This paper presents some of the history of hand planes, some examples of cutter geometry and sharpness, and how the cutting wood differs from cutting common metals.

Development of Precision Coated-Cemented-Carbide Tools for Ultra-Precision Cutting of Titanium and Titanium Alloys

Shigehiko Sakamoto*, Heiji Yasui*, Akira Shinozaki*, Takafumi Shingai* and Tatsuya Furuno*

* Dept. of Mechanical Engineering & Materials Science,
Kumamoto University,
2-39-1, Kurokami, Kumamoto, 860-8555, Japan
Phone: +81-96-342-3758
Fax: +81-96-342-3764
E-mail: sak@mech.kumamoto-u.ac.jp

Key words: ultra-precision cutting, titanium alloys, cutting tool, surface roughness

1. Introduction

The precision cutting techniques for titanium metals are strongly required to finish high accuracy dimensions and ultra-smoothness surface. In our previous researches, it has been found that the coated-cemented-carbide tool is very effective for the ultra-precision cutting of pure titanium, titanium alloys and stainless steels [1, 2]. In this paper, it is proposed that newly precision coated tool is more effective for the ultra-precision cutting of pure titanium and titanium metals.

2. Experimental procedure

The experiments are executed by face-turning the beta type of titanium alloy Ti-22V-4Al and alpha-beta type of titanium alloy Ti-6Al-4V with TiCNO-coated-cemented-carbide tools set on the ultra-precision turning lathe. Water-immiscible type cutting fluid is directly supplied to area of cutting point with compressed air. Principal experimental cutting conditions are summarized in **Table 1**. The face-turned surface of titanium alloys are examined by observing with a Nomarski differential interference microscope and measuring with surface interferometer WYKO. Cutting tools are also observed with Scanning Electron Microscope (SEM).

Table 1 Experimental conditions

Machine tool:	Ultra-precision lathe ULC-100A, Toshiba Machine CO., LTD
Cutting tools:	Coated cemented carbide tool (Commercial, Formed coated) Nose radius: 0.4 mm, Rake angle: 0 deg, Relief angle: 7 deg
Workpiece materials:	β titanium alloy (Ti-22V-4Al) α-β titanium alloy (Ti-6Al-4V)
Cutting fluid:	Water-immiscible type cutting fluid
Cutting conditions	Cutting speed: V = 31-65 m/min
	Depth of cut: d = 5 μm
	Feed rate: f = 2 μm/rev

3. Experimental Results

Formed coated cutting tool

Two kinds of coated-cemented-carbide tools for ultra-precision cutting are prepared in these experiments. One of the coated tools is commercial tool for hard-metal cutting. On the other hand, shape-formed coated tool is made for ultra-precision cutting of difficult-to-cut materials in

our researches. The formed coated tool is based on cemented-carbide which has been formed by tool shape forming machine as shown in **Fig. 1**. The cutting edge of base material for ultra-precision cutting tool which has a radius of about 1 μm is formed sharply. Then, the base material has been covered with TiCNO thin coating layers by use of physical vapor deposition processes (PVD) techniques. **Figure 2** shows cutting edge and shape of formed coated tool which are newly produced for ultra-precision cutting of difficult-to-metals. Formed coated tool has sharper cutting edge than commercial coated cutting tool. The cutting edge of formed tool has radius of 2 μm and smoother rake and flank faces.

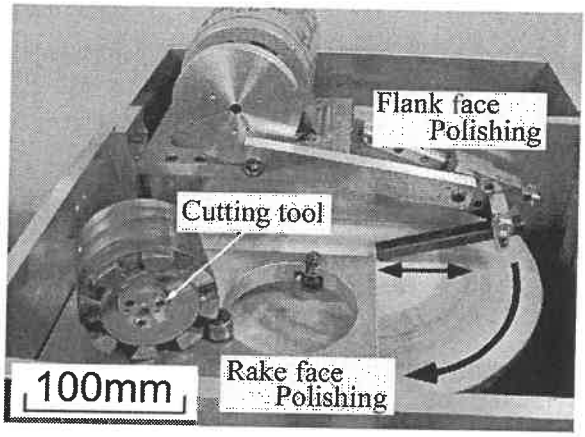

Fig. 1 Tool shape forming machine

Finished surfaces of beta titanium alloy

Ultra-precision face-turned surface of beta titanium alloy Ti-22V-4Al is obtained as shown workpiece on the left with **Fig. 3**. The surface roughness of finished area is 80 nm(P-V) *Rz*. Microphotographs and WYKO images of finished surface with commercial and formed tool are shown in **Fig. 4** respectively. Crystal grain boundaries on the microphotograph of finished surface with commercial tool are clear compared with the surface in case of formed tool. The appearance of crystal grains on the WYKO 3D image of finished surface with formed tool is also obscure. The 3D surface roughness of finished surface with formed tool which is below 100nm(P-V) $Rz_{(3D)}$ as shown WYKO image on the right with **Fig. 4** (b) is a great improvement on that with commercial tool. In addition, the 2D surface roughnesses of feed and cutting direction are 89 nm(P-V) *Rz* and 23 nm(P-V) *Rz* respectively. The crystal grain

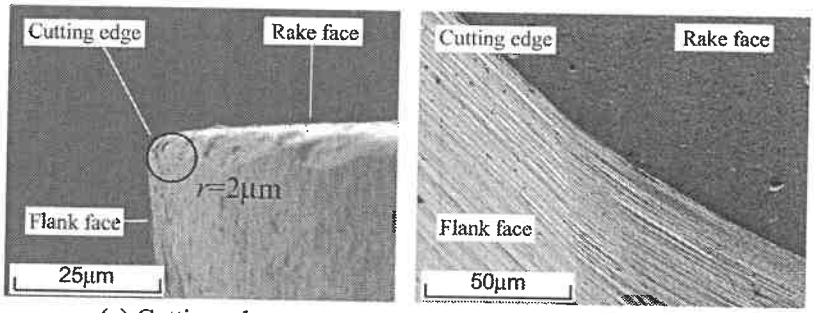

(a) Cutting edge (b) Tool shape

Fig. 2 SEM photographs of formed coated tool

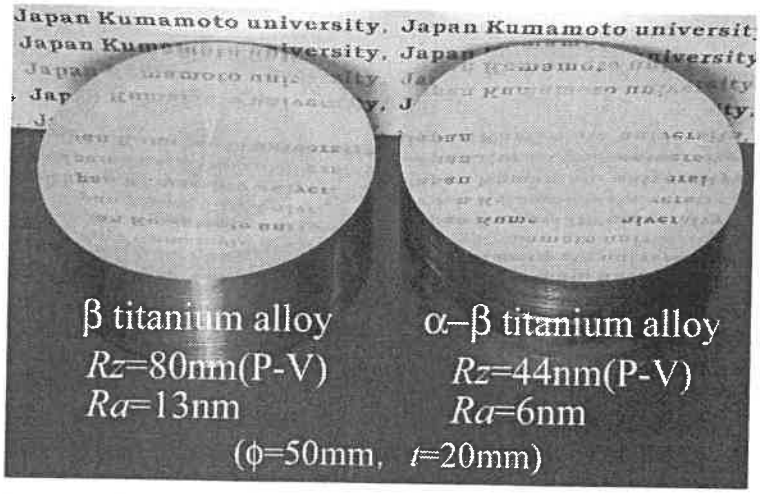

Fig. 3 Finished surface of beta and alpha-beta titanium alloys

boundary steps in the cutting direction of finished surface are reduced from 114 nm(P-V) *Rz* to 23 nm(P-V) *Rz* as shown in **Fig. 4** (d). Reduction in surface roughness by use of formed tool may be a useful technique in some conditions. **Figure 5** shows a family of curves for the surface roughness of finished surfaces with two kinds of tool. The either tool life of them is approximately cutting length of 2,000 m in the separate experiments. The performance of finished surface is more greatly influenced by the shape of cutting edge.

Finished surfaces of alpha-beta titanium alloy with formed coated tool

The surface roughness of alpha-beta titanium alloy is already obtained below 100 nm(P-V) *Rz* in our previous researches[1]. Because the crystal grains of alpha-beta titanium alloy Ti-6Al-4V which is grain size 1 μm in diameter is smaller than beta titanium alloy Ti-22V-4Al, the surface roughness of Ti-6Al-4V is not mainly influenced by the crystal grain boundary steps. The finished surface of alpha-beta titanium alloy is obtained as shown workpiece on the right with **Fig. 3**. The surface roughness of finished area is 44 nm(P-V) *Rz*. **Figure 6** shows the microphotograph and WYKO images of face-turned alpha-beta titanium alloy surface. Surface roughness of alpha-beta titanium alloy finished surface exceeds that of beta titanium alloy by 50 nm. The surface roughness of feed and cutting direction is 44 nm(P-V) *Rz* and 24 nm(P-V) *Rz* respectively. There are not any effects of crystal grain boundary steps on the finished surface in

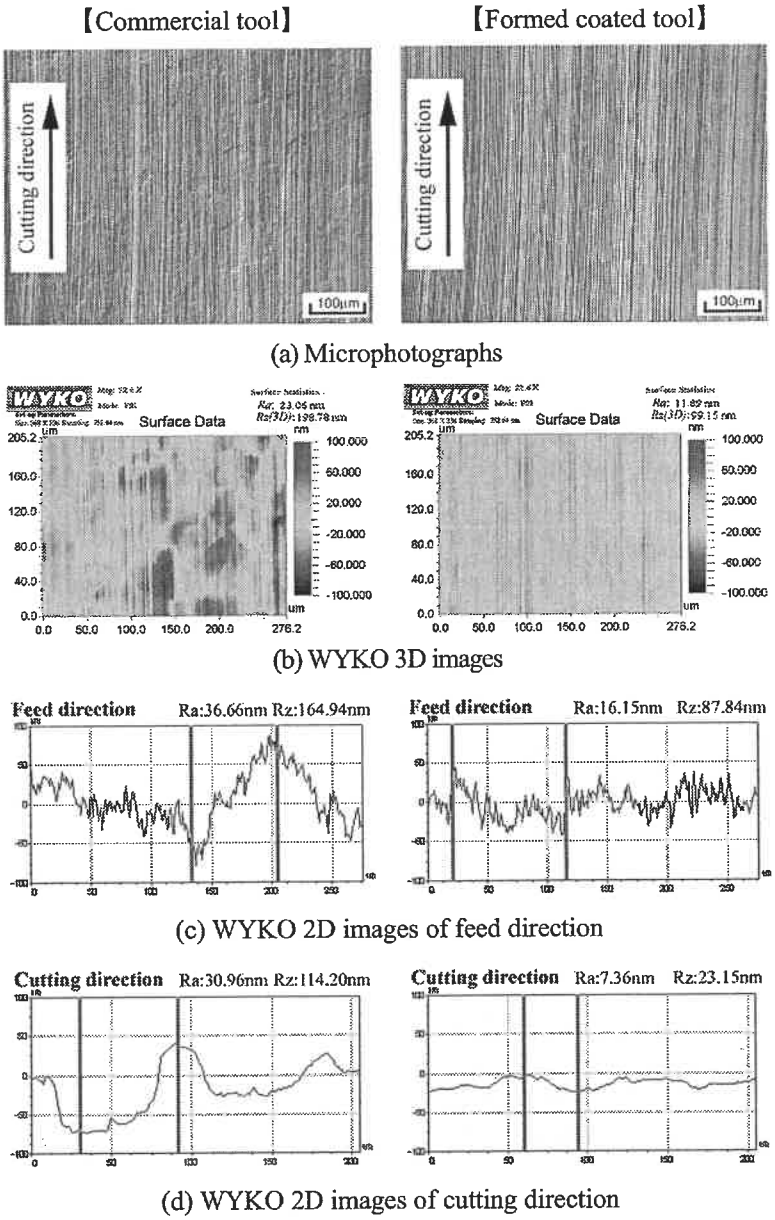

(a) Microphotographs

(b) WYKO 3D images

(c) WYKO 2D images of feed direction

(d) WYKO 2D images of cutting direction

〔*V*=60m/min, *f*=2μm/rev, *d*=5μm, Water-immiscible type cutting fluid〕

Fig. 4 Face-turned beta titanium alloy surfaces

case of alpha-beta titanium alloys. Surface textures of alpha-beta titanium alloy are smoother than those of beta titanium alloy. The surface texture along the cutting direction is only 4 nm(P-V) Ra. The newly formed coated cutting tool has major advantage for ultra-precision cutting of titanium alloys.

4. Summary

The formed coated tool is newly developed for ultra-precision cutting of difficult-to-cut metals in this paper. The sharpness of cutting edge is much influenced on surface roughness of titanium alloys. The surface roughness of alpha-beta titanium alloy is improved to below 50 nm(P-V) by using the formed coated tool. The desired effect of formed coated tool is continued until the cutting length of 2,000 m.

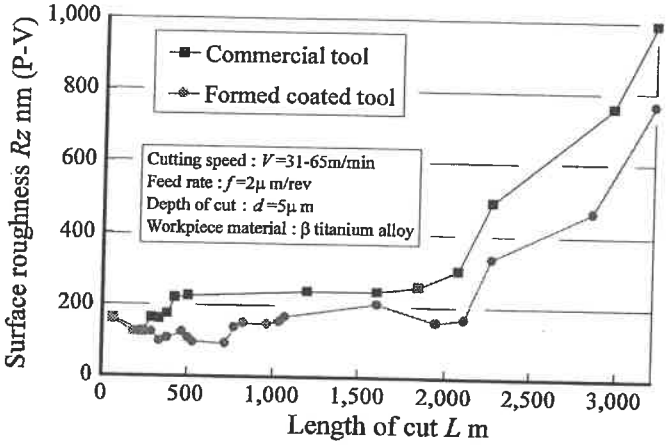

Fig.5 Relationship between surface roughness of beta titanium alloy and cutting length

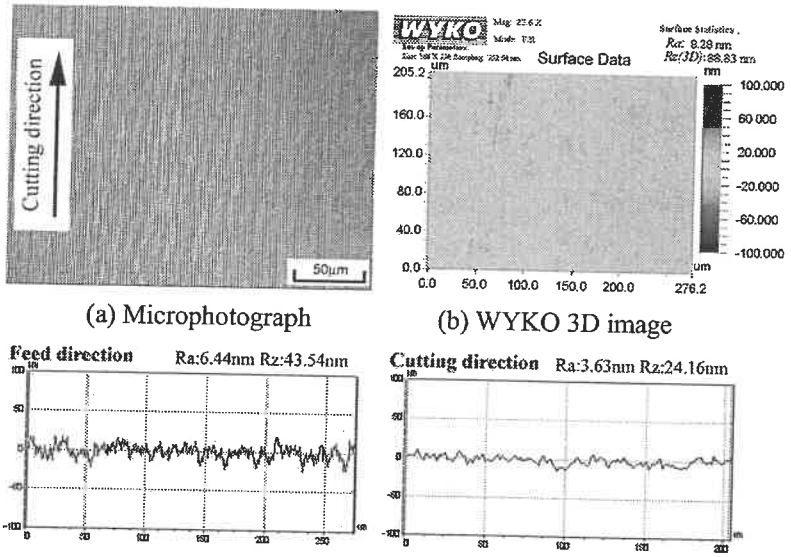

(a) Microphotograph (b) WYKO 3D image

(c) WYKO 2D images of feed and cutting directions

[V=60m/min, f=2μm/rev, d=5μm, Water-immiscible type cutting fluid]

Fig.6 Face-turned alpha-beta titanium alloy surface

Acknowledgement

The authors would like to thank Yushiro Chemical Industry Co., Ltd., Daido Steel Co., UEX Co., Ltd. and Tungaloy Co., Ltd. for providing cutting fluids, workpiece materials and cutting tools. A part of this research is supported by Grant-In-Aid for Scientific Research, 2003, in Japan.

References

[1] Yasui H., Sakamoto S. and Kawada M., "Ultra-precision Cutting of Titanium Alloys by Using Coated Carbide Bite", Journal of the JSPE, vol. 68, no. 7, 928-932(2002).

[2] Sakamoto S. and Yasui H., "Ultra-precision Cutting of Titanium Alloy with the Formed Coated-Cemented-Carbide Cutting Tool", Proceedings of the euspen International Topical Conference, 257-260(2003).

Work Affected Layer of Machined Surface in Ultra-Precision Cutting of Austenitic Stainless Steel

Shigehiko Sakamoto*, Heiji Yasui*, Shunsaku Hanaoka* and Hirofumi Hayashi*

*: Dept. of Mechanical Engineering & Materials Science,
Kumamoto University,
2-39-1, Kurokami, Kumamoto,860-8555, Japan
Phone : +81-96-342-3758
Fax : +81-96-342-3764
E-mail : sak@mech.kumamoto-u.ac.jp

Key words: ultra-precision cutting, stainless steel, work affected layer, surface roughness

1. Introduction

The technique of ultra-precision cutting for difficult-to-cut materials is not still established up to the present because tool life is very short and finished surface is not enough smooth for ultra-precision cutting. In our previous researches, the coated-cemented-carbide tool is very useful and convenient for ultra-precision cutting of difficult-to-cut materials which are stainless steels and titanium metals. The surface roughness of stainless steel SUS316 is obtained below 100 nm(P-V) with a coated-cemented-carbide tool [1, 2]. In case of SUS304, on the other hand, the surface roughness is beyond 100 nm(P-V) with the same conditions. The differences of ultra-precision cutting of SUS316 and SUS304 are reported by explaining the effect of work affected layer on the finished surface of austenitic stainless steels.

2. Experimental procedure

The experiments are executed by face-turning the stainless steels which are SUS316 and SUS304 with a commercial coated-cemented-carbide tool set on the ultra-precision lathe with the conditions as shown in **Table 1**. The cutting fluids used are water-immiscible type of cutting fluids. The face-turned stainless steel surfaces are examined by observing with a Nomarski differential interference microscope, measuring with surface interferometer (WYKO) and scanning with X-ray diffractometer. Used cutting tools are also observed with scanning electron microscope (SEM).

Table 1 Experimental conditions

Machine tool:	Ultra-precision Lathe ULC-100A, Toshiba Machine CO., LTD.
Cutting tool:	Coated cemented carbide tool Nose radius: 0.4 mm Rake angle: 0 deg Relief angle: 7 deg
Workpiece materials:	SUS316(18Cr-12Ni-2Mo) SUS304(18Cr-8Ni)
Cutting fluid:	Water-immiscible type cutting fluid
Cutting conditions:	Cutting speed: V = 0-153 m/min Depth of cut: d = 5μm Feed rate: f = 2μm/rev

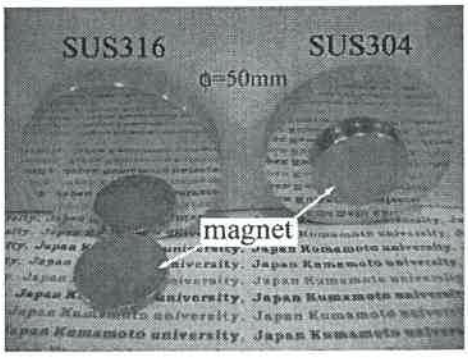

Fig. 1 Reactions of magnet on the surface

3. Results and Discussions

Ultra-precision face-turned surfaces of SUS316 and SUS304 have a magnetic permeability. Especially, as shown in **Fig. 1**, magnetic permeability of mirror

finished SUS304 is much stronger than that of SUS316. **Figure 2** shows the microphotographs and WYKO images of face-turned SUS316 and SUS304 surfaces. Surface roughnesses of SUS316 and SUS304 surfaces are 46 nm(P-V) *Rz* and 134 nm(P-V) *Rz* respectively. Quality of finished SUS316 surface is much smoother than that of SUS304. There are deep cutting graves on the finished surface of SUS304. Coated tools after face-turning stainless steel are also observed as shown in **Fig. 3**. Tool wear after cutting SUS304 is larger than the case of SUS316. Therefore, hardness tests of finished SUS316 and SUS304 surfaces are carried out by Vickers hardness tester as shown in **Fig. 4**. Vickers hardness of the finished SUS304 surface which is 490 Hv is much higher than that of SUS316. Due to observe microstructures on the finished surface, the surfaces are corroded as shown in **Fig. 5**. There are no austenitic structures on the finished surfaces of SUS316 and SUS304. The surfaces are also scanned by X-ray diffractometer for analyzing microstructure of surfaces as shown in **Fig. 6**. There are more martensitic structures α(110) exist more than austenitic structures γ(111) on the finished surface of SUS304. In the case of SUS316, on the other hand, those martensitic structures are less than austenitic structure. It is confirmed by observing finished surface with microscope that a part of

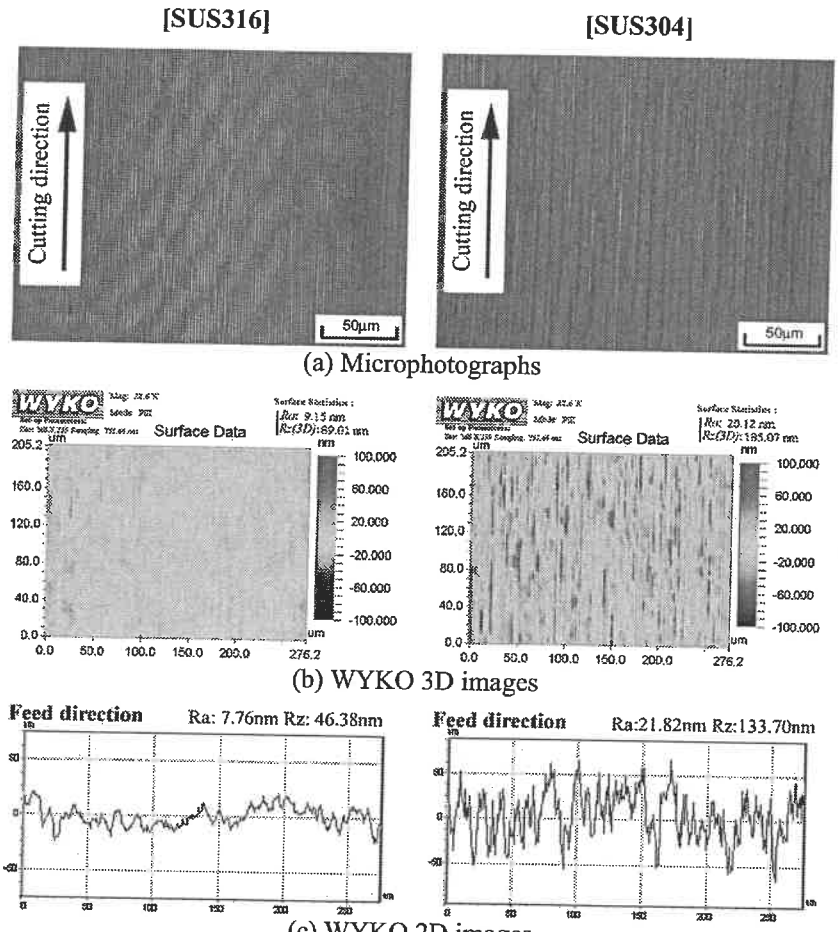

(*V*=100m/min, *f*=2μm/rev, *d*=5μm, *L*=270m,
Water-immiscible type cutting fluid)

Fig. 2 Face-turned SUS316 and SUS304 surfaces

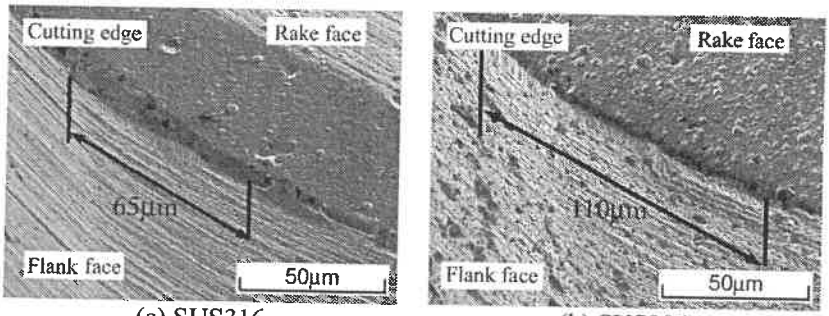

(a) SUS316 (b) SUS304

(*V*=100m/min, *f*=2μm/rev, *d*=5μm, *L*=270m,
Water-immiscible type cutting fluid)

Fig. 3 SEM photographs of coated tool

the work affected layer on the finished surface is transformed from austenitic stricture to martensitic structure.

Finally, the characteristics of original SUS316 and SUS304 before any cutting are confirmed by same methods. Vickers hardnesses of original SUS316 and SUS304 which are not so hard are below 200 Hv as shown in **Fig.7**. Both austenitic stainless steels SUS316 and SUS304 fundamentally have only austenitic microstructures as shown in **Fig. 8** and **9**. Ultra-precision face-turned surface of austenitic stainless steel always has been influenced by work affected layer together with martensitic transformation.

4. Summary

The characteristics of ultra-precision face-turned SUS316 and SUS304 surfaces are compared in this paper. The main conclusions obtained are as follows;

1) A part of the work affected layer on the finished surface of austenitic stainless steels which are SUS316 and SUS304 by ultra-precision cutting is transformed from austenitic structure to martensitic structure. Both of them have a magnetic permeability which is not as a characteristic of original austenitic stainless steels.

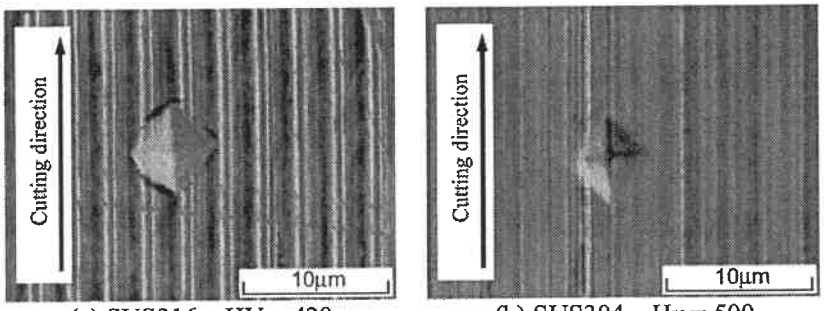

(a) SUS316 HV = 420 (b) SUS304 Hv = 500

(V=100m/min, f=2μm/rev, d=5μm, L=270m, Water-immiscible type cutting fluid)

Fig. 4 Vickers marks on face-turned surfaces of SUS316 and SUS304

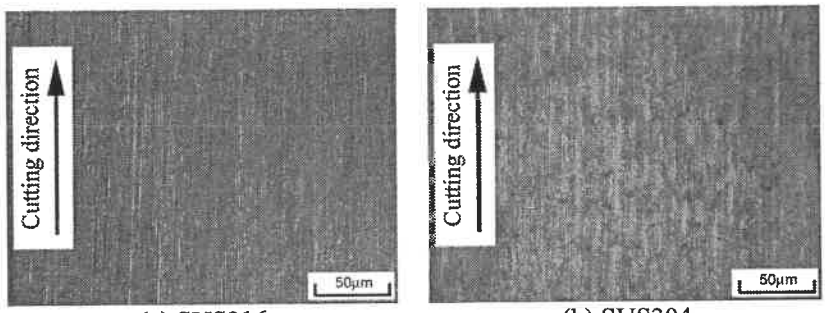

(a) SUS316 (b) SUS304

(V=100m/min, f=2μm/rev, d=5μm, L=270m, Water-immiscible type cutting fluid)

Fig. 5 Corroded surfaces of face-turned SUS316 and SUS304

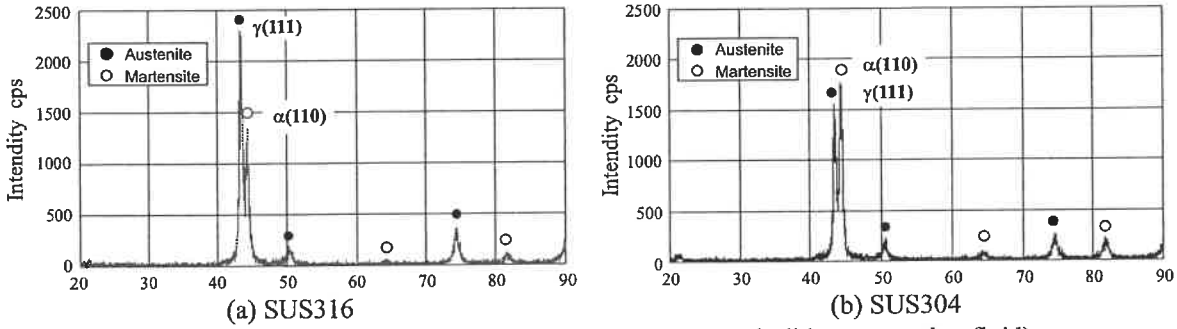

(a) SUS316 (b) SUS304

(V=100m/min, f=2μm/rev, d=5μm, L=270m, Water-immiscible type cutting fluid)

Fig. 6 X-ray diffractions on face-turned surfaces of SUS316 and SUS304

2) The finished surface roughness is affected by the transformation of face-turned austenitic stainless steel. Because the face-turned SUS304 on the finished surface has much more martensitic structures than SUS316, the surface roughness of SUS304 is rougher beyond 100 nm(P-V).

3) The surface roughness of ultra-precision face-turned stainless steels also depends considerably on the wear of coated-cemented-carbide tool. In case of SUS304, cutting tool wear is large because the finished surface of SUS304 is much harder than that of SUS316.

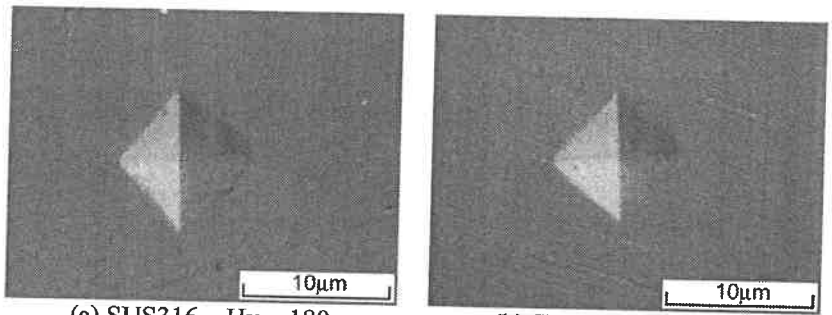

(a) SUS316 Hv = 180 (b) SUS304 Hv = 190

Fig. 7 Vickers marks on the original SUS316 and SUS304

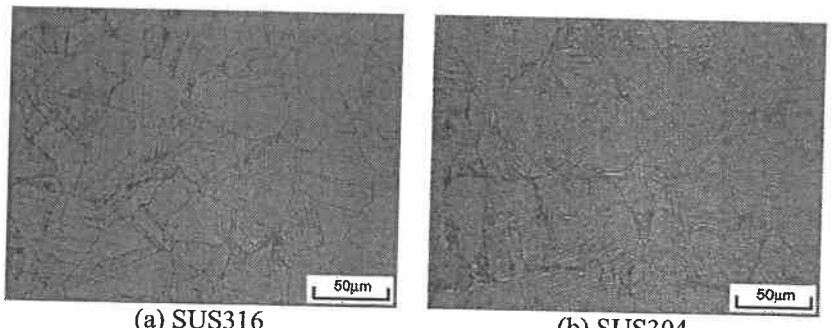

(a) SUS316 (b) SUS304

Fig. 8 Microphotographs of austenitic microstructure

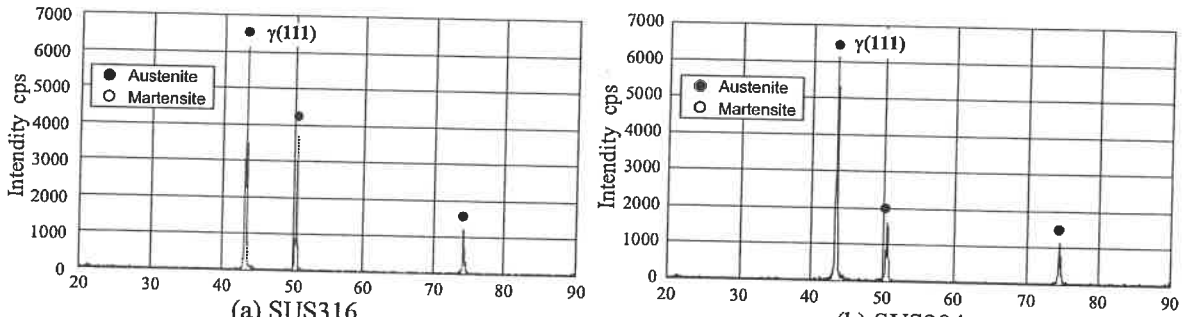

(a) SUS316 (b) SUS304

Fig. 9 X-ray diffractions on original surfaces of SUS316 and SUS304

Acknowledgement

The authors would like to thank Yushiro Chemical Industry Co., Ltd., Daido Steel Co., UEX Co., Ltd. and Tungaloy Co., Ltd. for providing cutting fluids, workpiece materials and cutting tools. A part of this research is supported by Grant-In-Aid for Scientific Research, 2003, in Japan.

References

[1] Sakamoto S., Yasui H., Shinozaki A. and Fujimori A.: "Ultra-precision Cutting of Stainless Steel SUS316 with Coated Cemented Carbide Tool", Journal of the JSPE, vol. 70, no. 3, 397-401(2004).

[2] Sakamoto S., Yasui H., Fujimori A. and Kondo S.: "Ultra-Precision Cutting of Stainless Steel by Using Coated Carbide Bite", Proceedings of the ASPE 2002 Annual Meeting, 597-600(2002).

High Pressure Phase Transformation and Ductility in Diamond Turned Single Crystal Silicon

T. Randall, J. J. H. Walter, R. Scattergood, R. Nemanich
North Carolina State University
Raleigh, NC 27695-7918

1.0 Introduction

It has been well documented that single crystal silicon and germanium undergo phase transformation with the generation of high pressure on the surface by contact processes such as micro-indentation, scribing, and single point diamond turning. Investigations of the transformation region created report phase transformation from diamond cubic (dc) structure to the amorphous structure. The transformation to the metallic beta-tin phase is thought be responsible for anomalous plastic flow behavior without fracture seen in contact loading processes. The beta-tin phase is not generally seen at room temperature or pressure but is rather identified by an amorphous phase or R8/BC8 crystal structure seen after material unloading, depending on experimental conditions. [1]

The implication of the ductile behavior is, that using careful machining conditions, single crystal silicon may be ground or diamond turned in the ductile regime. Ductile machining will reduce cracks and dislocations generated by machining on the surface and subsurface regions that can reduce the mechanical integrity and lower the operation lifetime of the components. The mechanisms governing the material removal (a combination of microcracking, dislocation motion, and structure change- HPPT) in ductile-regime turning are not well understood. The work presented here is mainly focused on the appearance of amorphization (structure change) in a ductile-turned region. Secondary focus is placed on the characterization of surface finish and cutting behavior as a function of crystallographic orientation and cutting direction, feed rate, and rake angle.

2.0 Experimental

A Rank Pneumo ASG 2500 Diamond Turning Machine is used to turn various orientations of single crystal silicon wafers at room temperature as a function of feed rate (1-15 um/rev) and tool rake angle (-30° and -45°) with a large radius (3mm) round-nosed tool.

Characterization of the machined surface was accomplished with Macro-Raman spectroscopy done at room temperature using an ISA U-1000 scanning monochromator. Raman excitation was done with the 514.5 nm line of an Argon-ion laser, with a spot size of approximately 1mm in diameter. Raman spectra were taken in the 200-600 cm^{-1} range which contains the characteristic peaks normally associated with crystalline, amorphous, and various metastable crystalline phases seen in other research. A spectral resolution of ≈ 4 cm^{-1} was utilized, and the laser power was ≈ 5 mW.

Surface finishes of the ductile-turned regions were measured using a Zygo New View 5600 white light interferometer. MetroPro, the software suite used to analyze the interferometer data, reports a measure of surface roughness by the root mean square (RMS) parameter and peak to valley (PV) values. Measurements were taken for from the center outward in regions within and outside the predicted fracture pattern area (further explained in Results section.)

3.0 Results and Discussion

Optical quality, low RMS surfaces (1-10 nm) were created by single point diamond turning single crystal Si wafers in the ductile regime. Ductile regime material removal was evident by the absence of fracture damage and repeated feed marks in the surface as well as generation of continuous chips. Increasing feed rate seemed to create an increase in surface roughness as shown in Figure 1.

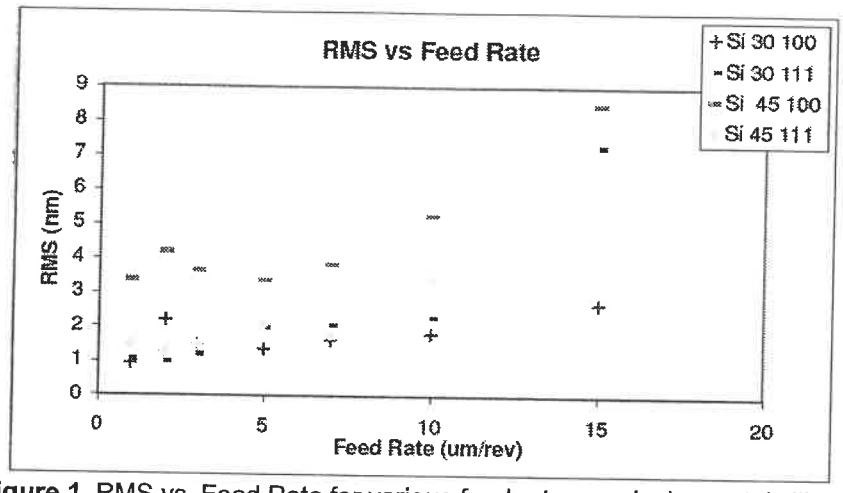

Figure 1. RMS vs. Feed Rate for various feed rates on single crystal silicon.

Feed rate seemed to be the limiting factor for generating a damage free surface. At increasing feed rates, certain directions on a wafer face initiated fracture at before others, creating symmetric damage patterns on the surface. The more negative rake angle tool tended to suppress the onset of fracture in the favored direction allowing machining at higher feed rates. The damage patterns for the wafer orientations tested ((100), and (111)) were very similar to those found in previously and were explained qualitatively by an orientation stress model used in that research. [2] These are shown in Figure 2. For surfaces that were ductile turned with similar parameters of tool rake and low feed rate, there appeared to be no difference in surface roughness and profile shape with changing cutting directions.

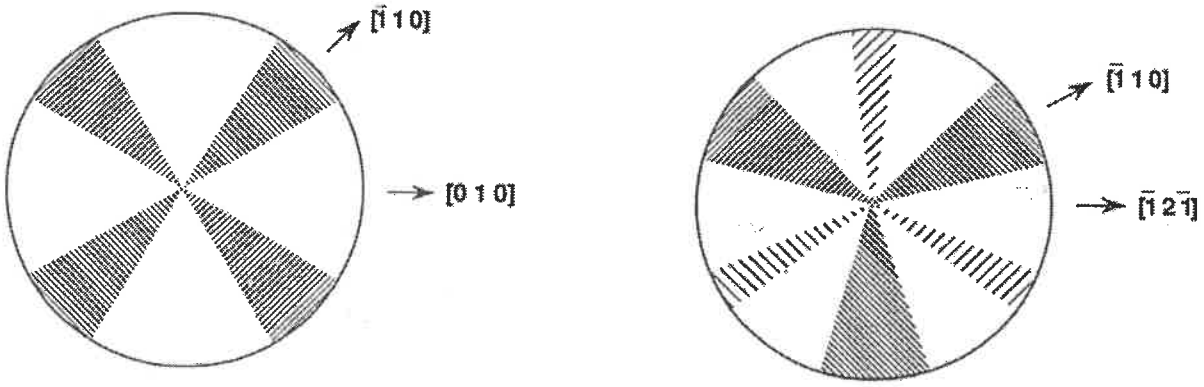

Figure 2. Damage patterns for (100) and (111) wafers resultant from machining at sufficiently high feed rates. [2]

The RMS (and PV) value of ductile turned surfaces was limited by the effect of the condition of the tool tip. While tips were freshly sharpened, experimental preparation (i.e. part touch off and preliminary facing cuts) perhaps dulled the tips enough to result in non-ideal material removal (deformation under the tool and elastic spring back.) This was evident by higher-than-theorized PV values, and machining profiles that did not fit theoretical shape (but were similar to realistic expectations) as measured by interferometery techniques. Additionally, machining runs on Si were subject to tip wear and damage considerations as evident by the repeated patterns of tip damage features into the part surface. Despite these various problems, surfaces turned within the ductile regime had RMS values in the range of <1 nm to 10 nm increasing with feed rate.

Raman measurements of the ductile turned surfaces for various machining conditions indicated what is thought to be the presence of a near-surface amorphous layer. The presence of this layer is thought to be a remnant of a rapid back transformation from the beta-tin metallic phase. The most

noticeable trend for each of the parameters tested is the drastic decrease in amorphous intensity coupled with an increase in dc peak intensity when switching feed rates from 1 to 5um/rev. While the Raman measurements did not always clearly indicate the existence of this layer for samples machined at 5 um/rev, closer direct evident difference in amorphous signal intensity between crystal orientations, cutting direction, or rake angle as seen in Figure 3.

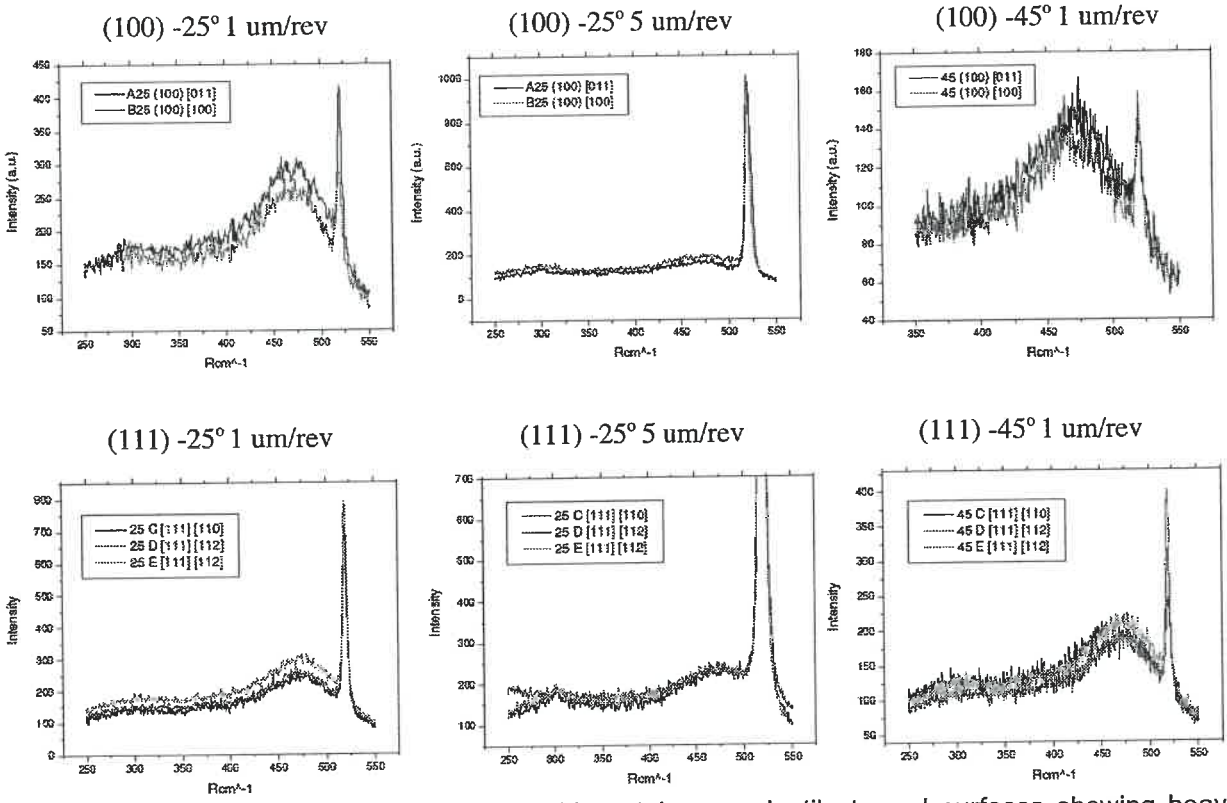

Figures 3. Raman spectra for various conditions taken on ductile turned surfaces showing heavy dependence of amorphous/dc intensity ratio on feed rate but little else.

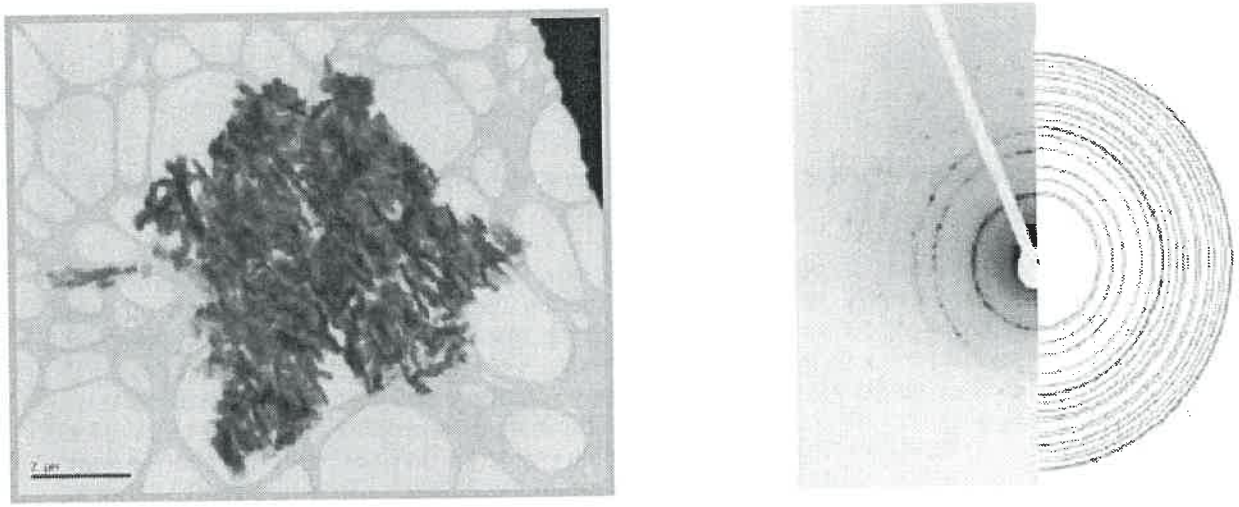

Figure 4. TEM image of Silicon chip generated during ductile regime turning and corresponding electron diffraction pattern showing crystalline structure of chip.

TEM results shown in Figure 4 indicated that the chips have the Si dc crystal structure. Si chips displayed a morphology of smaller (1-2 um) clustered chips. Despite the amorphous nature of the near surface machine regions, TEM failed to show any direct evidence for amorphization within the chips. It is thought that intense local heating during machining may cause recrystallization of the amorphized material as the thin chips lack cannot dissipate heat quickly.

4.0 Conclusions

Low RMS surfaces were achieved by ductile regime turning with high negative rake, large radius round nosed tools for various crystallographic orientations of single crystal silicon. Symmetric fracture patterns resulting from high feed rate machining were the limiting factor for ductile regime machining. Surface characteristics such as roughness and profile seemed to show little dependence on cutting direction within the ductile regime. Raman measurements indicated the presence of a near surface amorphized layer for regions where ductile turning occurred. Based on the relative intensity of the amorphous peak, the Raman scans indicated that lower feed rates produce more amorphous phase, ie., a thicker surface layer. This layer thought to be the remnant of a back transformation from the metallic beta-tin phase, which could be responsible for the ductile behavior during machining. TEM analysis of the chips showed them to be crystalline in nature, indicating rapid recrystallization of the chips during machining.

References

1. V. Domnich and Y. Gogotsi. "Phase Transformations In Silicon Under Contact Loading", Rev.Adv.Mater.Sci. 3 (2002) 1-36
2. W.S. Blackley and R.O. Scattergood. "Crystal Orientation and Dependence of Machining Damage- A Stress Model." J. Am. Ceram. Soc., 73[10], 3113 (1990).

An Improved RCSA Model for Tool Point Frequency Response Prediction

Tony L. Schmitz, G. Scott Duncan, Michael F. Tummond
Department of Mechanical and Aerospace Engineering, University of Florida, Gainesville, FL 32611

Introduction

One area of manufacturing research that has made significant technological advancements in recent years is high-speed machining. A primary obstacle to the successful implementation of high-speed machining and full utilization of the available technology is chatter, or unstable machining. Many research efforts geared toward the understanding and avoidance of chatter have been carried out [e.g., 1,2]. This work has led to the development of stability lobe diagrams that identify stable and unstable cutting zones as a function of the chip width and spindle speed. However, the methods used to produce these diagrams, whether analytic or time-domain, require knowledge of the tool point dynamics. The required dynamic model is typically obtained using impact testing, where an instrumented hammer is used to excite the tool at its free end (i.e., the tool point) and the resulting vibration measured using an appropriate transducer, typically a low mass accelerometer. However, due to the large number of spindle, holder, and tool combinations, the required testing time can be significant. Therefore, a model which is able to predict the tool point response based on minimum input data is the preferred alternative.

The purpose of this paper is to build on the previous work of Schmitz *et al.* [3-5], which describes tool point frequency response function, or receptance, prediction using the Receptance Coupling Substructure Analysis (RCSA) method. In order to enable RCSA predictions for a wider variety of machine-spindle-holder-tool combinations, an improved three-component model is presented here. In this model, the machine-spindle-holder substructure is separated into two parts: 1) the machine, spindle, holder taper, and portion of the holder nearest the spindle with standard geometry from one holder to another (hereafter referred to as the spindle-holder base subassembly); and 2) the remaining portion of the holder from the base to the free end (hereafter referred to as the extended holder subassembly). A technique for determining the rotation-to-force/moment and displacement-to-moment receptances for the free end of the spindle-holder base subassembly using only displacement-to-force measurements is also described. The experimental procedure involves direct and cross displacement-to-force measurements of a simple geometry 'standard' holder clamped in the spindle to be modeled. The portion of the standard holder beyond the section with consistent geometry from holder-to-holder is then removed in simulation using an inverse receptance coupling approach (i.e., decomposition) to identify the four spindle-holder base subassembly receptances. These receptances are then rigidly coupled to models of the actual holder and tool (no stiffness or damping coupling parameters between the tool and holder are applied). In this way, the tool point response for any holder and tool combination can be predicted from a single set of measurements completed on the desired machine-spindle. In the following sections, the method is described and experimental validation is presented.

Background and notation

Substructure analysis, or component mode synthesis, methods have been used for several decades to predict the dynamic response of complicated assemblies using measurements and/or models of the individual components, or substructures. These components can be represented by spatial mass, stiffness, and damping data, modal data, or receptances [e.g., 6-9]. The latter representation is preferred in situations where the assembly receptances are the desired analysis output, as is the case in this research. For an assembly consisting of two rigidly connected substructures, as shown in Fig. 1, the assembly receptance, $G_{jk}(\omega)$, can be expressed as shown in Eq. (1), where ω is the frequency, X_j and Θ_j are the assembly displacement and rotation at coordinate j, and F_k and M_k are the force and moment applied to the assembly at coordinate k. If coordinate j is coincident with coordinate k, the receptance is referred to as a direct receptance; otherwise, it is a cross receptance. For the purposes of this paper, the nomenclature $G_{jk}(\omega)$ is used to describe the receptances that are produced when two substructures (or subassemblies) are coupled to produce the final assembly. The nomenclature $GS_{jk}(\omega)$ will replace $G_{jk}(\omega)$ in all relevant equations when two substructures (or subassemblies) are coupled that do

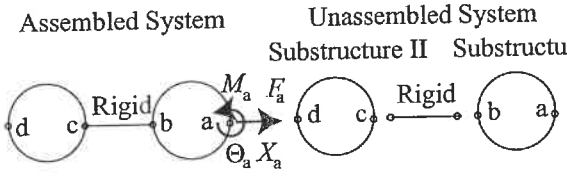

Figure 1: RCSA System Description

not form the final assembly.

The substructure receptances, $R_{jk}(\omega)$, are defined in Eq. (2), where x_j and θ_j are the substructure displacement and rotation at coordinate j, and f_k and m_k are the force and moment applied to the substructure at coordinate k [10].

$$G_{jk}(\omega)=\begin{bmatrix}\frac{X_j}{F_k} & \frac{X_j}{M_k}\\ \frac{\Theta_j}{F_k} & \frac{\Theta_j}{M_k}\end{bmatrix}=\begin{bmatrix}H_{jk} & L_{jk}\\ N_{jk} & P_{jk}\end{bmatrix} \quad (1)$$

Bishop and Johnson [11] presented closed-form receptance functions for the analysis of flexural vibrations of uniform Euler-Bernoulli beams with free, fixed, sliding, and pinned boundary conditions. In this work we apply the Bishop and Johnson expressions for free-free beam receptances to model the holder and tool substructures.

$$R_{jk}(\omega)=\begin{bmatrix}\frac{x_j}{f_k} & \frac{x_j}{m_k}\\ \frac{\theta_j}{f_k} & \frac{\theta_j}{m_k}\end{bmatrix}=\begin{bmatrix}h_{jk} & l_{jk}\\ n_{jk} & p_{jk}\end{bmatrix} \quad (2)$$

Spindle-holder base subassembly identification

The experimental procedure used to determine the receptances at the free end of the spindle-holder base subassembly, $GS_{jk}(\omega)$, is described in this section. It is composed of three primary steps. First, the standard holder displacement-to-force direct and cross receptances are determined by impact testing. The standard holder geometry, which was selected to approximate a broad range of potential holders, is shown in Fig. 2 (a CAT 40 spindle-holder interface is shown as an example). Second, these results are used to determine the three other direct receptances at the free end of the standard holder. Third, the section of the standard holder which is not common to other holders (see Fig. 3) is removed using inverse receptance coupling to determine all four spindle-holder base subassembly receptances.

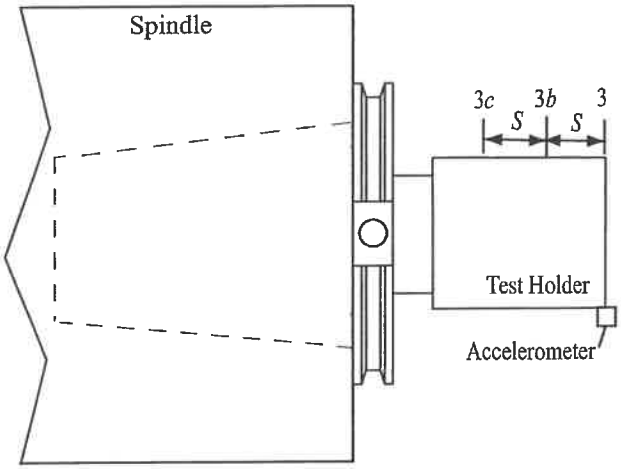

Figure 2: Standard holder for spindle-holder base subassembly receptance identification

The standard holder was mounted in a 36000 rpm/36 kW rolling element bearing spindle as shown in Fig. 2. The four subassembly receptances were determined by measuring the direct, H_{33}, and cross, H_{33b}, and H_{33c}, displacement-to-force receptances on the standard holder, applying a 2nd-order backward finite difference method to find L_{33} (and, equivalently, N_{33}) [12], and then synthesizing P_{33}. For the cross displacement-to-force measurements, the distance S should be selected to increase the difference in relative amplitudes between H_{33}, H_{33b}, and H_{33c} without leading to a poor signal-to-noise ratio for the H_{33c} measurement (i.e., many of the lower frequency spindle-holder modes resemble a fixed-free fundamental mode shape and have very small amplitudes near the spindle face). Practically, we have observed that the finite difference results improve as S is increased ; however, for large values, error is introduced into the calculated finite-difference slope. The receptance L_{33} is determined from the measured displacement-to-force receptances using Eq. (3).

$$L_{33}=\frac{3H_{33}-4H_{33b}+H_{33c}}{2S} \quad (3)$$

By reciprocity, N_{33} can be set equal to L_{33}. The remaining receptance, P_{33}, is synthesized from H_{33}, L_{33}, and N_{33}, as shown in Eq. (4)[8].

$$P_{33}=\frac{\Theta_3}{M_3}=\frac{F_3}{X_3}\frac{X_3}{M_3}\frac{\Theta_3}{F_3}=\frac{1}{H_{33}}L_{33}N_{33}=\frac{{L_{33}}^2}{H_{33}} \quad (4)$$

Due to the subtraction of the similarly scaled H_{33}, H_{33b}, and H_{33c} receptances, noise in the measurement data can reduce the quality of L_{33} and N_{33} (produced by the finite-difference method) and, therefore, P_{33}. To reduce the noise effect, the measured receptance data was smoothed using a Savitzky-Golay filter, which performs a local polynomial regression to determine the smoothed value for each data point [13], prior to the application of Eq. (3). For this study, a filter with a polynomial order of two was applied over a window of 31 data points.

The extended holder subassembly for the steel standard holder consisted of solid, cylindrical substructures I and II as shown in Fig. 3. Equations (5-8) provide the direct and cross extended holder subassembly receptance matrices, where rigid coupling has been applied.The receptances for substructures I and II, $R_{jk}(\omega)$, in Eqs. (5-8) were produced using the Bishop and Johnson free-free beam receptances.

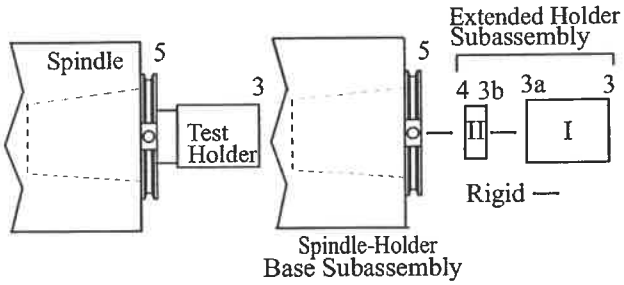

Figure 3: Standard holder for spindle-holder base subassembly receptance identification

The spindle-holder subassembly receptance matrix, $G_{33}(\omega)$, can be expressed as shown in Eq. (9). The left hand side of this equation is known once the finite difference procedure has been completed. Also, the extended holder subassembly receptances, GS_{33}, GS_{44}, GS_{34}, and GS_{43}, have been determined in Eqs. (5-8). Therefore, Eq. (9) can be rewritten to solve for the spindle-holder base subassembly receptances, $GS_{55}(\omega)$. See Eq.(10).

$$GS_{33}(\omega) = R_{33}(\omega) - R_{33a}(\omega)[R_{3a3a}(\omega) + R_{3b3b}(\omega)]^{-1} R_{3a3}(\omega) \quad (5)$$

$$GS_{44}(\omega) = R_{44}(\omega) - R_{43b}(\omega)[R_{3b3b}(\omega) + R_{3a3a}(\omega)]^{-1} R_{3b4}(\omega) \quad (6)$$

$$GS_{34}(\omega) = R_{33a}(\omega)[R_{3a3a}(\omega) + R_{3b3b}(\omega)]^{-1} R_{3b4}(\omega) \quad (7)$$

$$GS_{43}(\omega) = R_{43b}(\omega)[R_{3a3a}(\omega) + R_{3b3b}(\omega)]^{-1} R_{3a3}(\omega) \quad (8)$$

Tool point response prediction

To predict the tool point dynamics, the modeling procedure was applied to a 36000 rpm/36 kW spindle (CAT 40 interface) using a collet holder and four flute, 19.1 mm diameter carbide tool with a flute length of 84.2 mm, as shown in Fig. 4. The overhang length of the tool was 101.6 mm. The assembly was divided into the spindle-holder base subassembly and four cylindrical substructures of differing diameters.

$$G_{33}(\omega) = \begin{bmatrix} H_{33} & L_{33} \\ N_{33} & P_{33} \end{bmatrix} = GS_{33}(\omega) - GS_{34}(\omega)[GS_{44}(\omega) + GS_{55}(\omega)]^{-1} GS_{43}(\omega) \quad (9)$$

$$GS_{55}(\omega) = \begin{bmatrix} \frac{x_5}{f_5} & \frac{x_5}{m_5} \\ \frac{\theta_5}{f_5} & \frac{\theta_5}{m_5} \end{bmatrix} = GS_{34}(\omega)[GS_{33}(\omega) - G_{33}(\omega)]^{-1} GS_{43}(\omega) - GS_{44}(\omega) \quad (10)$$

Each substructure was assumed to be a hollow or solid steel beam according to the substructure geometry. All substructures were modeled using the Bishop and Johnson receptances; however, a composite modulus and mass were substituted for substructures II and III to account for the material differences between the steel holder and the carbide tool [14]. Finally, an effective diameter was used for substructure I to account for the flute geometry [14].

The next step was to rigidly couple substructures I through IV to produce the direct and cross extended holder-tool subassembly receptances at coordinates 1 and 4. The final step in the procedure was to predict the tool point dynamics by rigidly coupling the extended holder-tool subassembly to the spindle-holder base subassembly. The tool point receptance, $G_{11}(\omega)$, was determined according to Eq. (11), where the receptances associated with coordinates 1 and 4 are the extended holder-tool subassembly direct and cross receptances. The predicted and measured assembly tool point displacement-to-force receptances, H_{11}, are displayed in Fig. 5, showing reasonable agreement between the measured and predicted receptances, although the 600 Hz spindle mode amplitude is underpredicted.

To further validate the procedure, the method was repeated for a 24000 rpm/40 kW spindle, a tapered heat shrink holder with a 19.1 mm bore, and a carbide tool blank with 101.6 mm tool overhang.[14].

$$G_{11}(\omega) = \begin{bmatrix} H_{11} & L_{11} \\ N_{11} & P_{11} \end{bmatrix} = GS_{11}(\omega) - GS_{14}(\omega)[GS_{44}(\omega) + GS_{55}(\omega)]^{-1} GS_{41}(\omega) \quad (11)$$

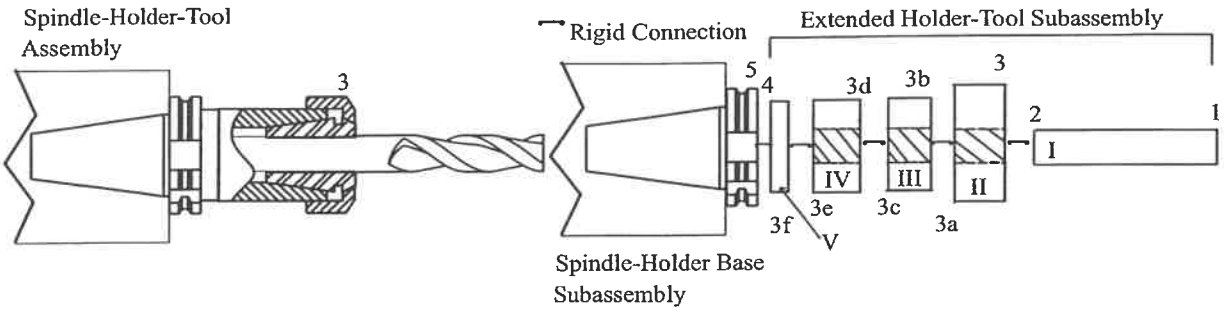

Figure 4: Collet holder and four flute tool substructure model

Conclusions

Tool point dynamics prediction using the second generation Receptance Coupling Substructure Analysis (RCSA) method was demonstrated. The improved method includes the following features: 1) separation of the spindle-holder-tool assembly into three substructures- the spindle-holder base, extended holder, and tool; 2) experimental identification of the spindle-holder base subassembly translational and rotational receptances using a finite difference approach; 3) analytical determination of the holder and tool substructure receptances; and 4) rigid coupling of the spindle-holder base subassembly, extended holder, and tool to determine the tool point response. The proposed method eliminates the need to measure the spindle-holder-tool dynamics for each tool and holder substructure combination and, therefore, significantly reduces the number of impact tests required for stability lobe diagram generation.

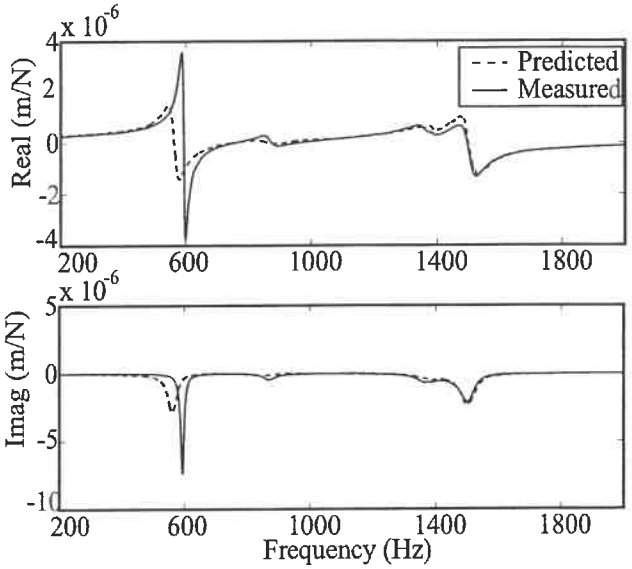

Figure 5: Collet holder and four flute tool H_{11} predicted and measured results

References

[1] Tobias, S. A. and Fishwick, W., 1958, "The Chatter of Lathe Tools under Orthogonal Cutting Conditions", Transactions of the ASME, **80**, p. 1079.

[2] Tlusty, J. and Polocek, M., 1963, "The Stability of the Machine-Tool against Self-Excited Vibration in Machining", Proc. of the International Research in Production Engineering Conference, Pittsburgh, PA, ASME, New York, pp. 465.

[3] Schmitz, T. and Donaldson, R. 2000, "Predicting High-Speed Machining Dynamics by Substructure Analysis", Annals of the CIRP, **49**(1), pp. 303-308.

[4] Schmitz, T., Davies, M., and Kennedy, M., 2001, "Tool Point Frequency Response Prediction for High-Speed Machining by RCSA", Journal of Manufacturing Science and Engineering, **123**, pp. 700-707.

[5] Schmitz, T., Davies, M., Medicus, K., and Snyder, J., 2001, "Improving High-Speed Machining Material Removal Rates by Rapid Dynamic Analysis", Annals of the CIRP, **50**(1), pp. 263-268.

[6] Ren, Y., Beards, C.F., 1993, "A Generalized Receptance Coupling Technique", Proc. of the 11th International Modal Analysis Conference (IMAC-1993), Kissimmee, FL, pp. 868-871.

[7] Ren, Y., Beards, C.F., 1995, "On Substructure Synthesis with FRF Data", Jour. of Sound and Vibration, **185**, pp. 845-866.

[8] Ewins, D.J., 2000, Modal Testing: Theory, Practice and Application, 2nd Ed., Research Studies Press, Philadelphia, PA.

[9] Park, S., Altintas, Y., Movahhedy, M., 2003, "Receptance Coupling for End Mills", Journal of Machine Tools and Manufacture, **43**, pp. 889-896.

[10] Ferreira, J., and Ewins, D., 1995, "Nonlinear Receptance Coupling Approach Based on Describing Functions", Proc. of the 14th International Modal Analysis Conference, Dearborn, Michigan, pp. 1034-1040.

[11] Bishop, R., 1955, "The Analysis of Vibrating Systems which Embody Beams in Flexure", Proc. Institution of Mechanical Engineers (British), **169**, pp. 1031-1050.

[12] Sattinger, S., 1980, "A Method for Experimentally Determining Rotational Mobilities of Structures", Shock and Vibration Bulletin, **50**, pp. 17-27.

[13] Mathworks, 2002, Matlab 6.5.0 Release 13: High-Performance Numeric Computation and Visualization Software, Natick, Massachusetts.

[14] Schmitz, T., Duncan, G., Tummond, F., 2004, "Three-component receptance coupling substructure analysis for tool point dynamics prediction", ASME Journal of Manufacturing Science and Engineering, under review.

MECHANISM OF CUTTING EDGE CHIPPING AND ITS SUPPRESSION IN DIAMOND TURNING OF COPPER

Shoichi Shimada, Hiroaki Tanaka
Osaka Electro-Communication University, Neyagawa, Osaka, Japan
Masahiro Higuchi, Tomomi Yamaguchi
Kansai University, Suita, Osaka, Japan
Toshiaki Kaneeda
Okayama University of Science, Okayama, Japan
Seiichi Yokomizo
Industrial Technology Center of Okayama, Okayama, Japan

Background

Diamond is well known as an ideal tool material for single point metal cutting because of its extremely high strength and hardness. According to a stress analysis in cutting edge, effective stress to fracture diamond tools does not exceed the fracture strength of diamond even in turning of hardened steel [1]. However, cutting edge chipping sometimes takes place, as experienced in practice, in turning of highly machinable materials such as copper which is much softer than hardened steel. This fact may suggest that the strength of diamond decreases due to some thermo-chemical ambient in turning.

In this paper, to understand the mechanism of cutting edge chipping in diamond turning of copper, change in Hertzian strength is investigated on diamond specimens in contact with copper powder under various thermal hysteresis which simulates the atmosphere in cutting process. Furthermore, based on the investigation, the cutting under reduced oxygen atmosphere, which can suppress the decrease of strength on diamond specimen, is proposed for the useful technique to suppress the cutting edge chipping in diamond turning of copper.

Effect of thermal hysteresis on Hertzian strength of diamond

The thermo-chemical effect on strength of diamond has been overlooked so far. A cutting edge under attritious contact with work material is inevitably subject to elevated temperature in metal cutting process. Therefore, the durability of diamond cutting edge may be affected by thermo-chemical reaction, because diamond is known to be easily oxidized and/or graphitized under high temperature conditions.

Figure 1 shows the change in Hertzian strength on (100) polished diamond specimens under various thermal hysteresis measured by the

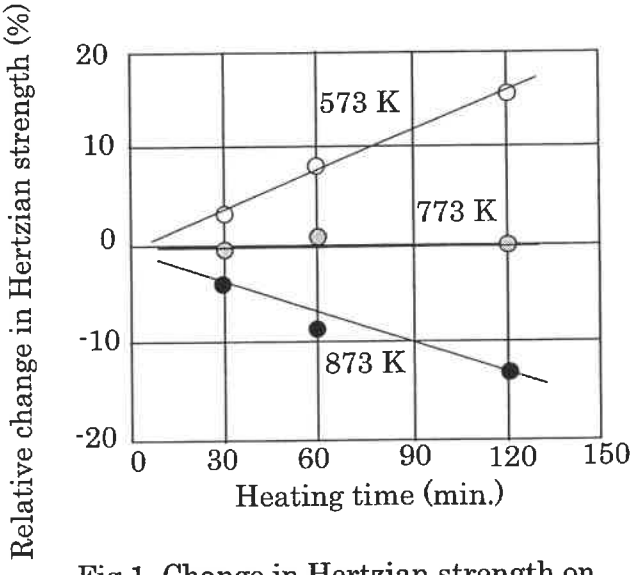

Fig.1. Change in Hertzian strength on polished diamond surface by thermal

indenter of 50 μm tip radius. The values of strength data on diamond specimen statistically distribute following a Weibull distribution. The average contact pressure of the indenter on specimen surface, p_0, at the fracture probability of 50% is used as a characteristic strength value. The specimen subjected to elevated temperature higher than 800K deteriorates in strength. On the other hand, the specimens heated at the temperature lower than 600K do not show any deterioration but rather some improvement in strength.

Possible mechanism of change in strength

Fracture on diamond surface takes place when the tensile stress exceeds the critical level for the sudden extension of pre-existing surface microcracks which may be induced in polishing process. The strength is controlled by the length of the weakest microclack to be extended. Therefore, the change in strength can be described as the result of the change in the length of surface microcracks due to thermal hysteresis as shown in Fig.2. On a solid surface at a finite temperature, thermally activated atoms frequently jump out from and return to the surface. The both probabilities of jumping out and returning are in equilibrium on a flat surface. However, the probability of jumping out from the surface of the atom at crack tip is higher than that of returning due to the resultant force of interatomic attractive force from the neighboring atoms toward the inside of the crack. Therefore, the atoms at crack tip tend to emit toward the inside of the crack. The emission rate exponentially increases as the ambient temperature rises.

At the temperatures lower than 630K, the surface of diamond is reported to be covered by a stable layer of adsorbed oxygen molecules [2]. In this case, by the successive emission of atoms at the crack tip, the length of the crack is gradually decreases (clack healing), hence, the Hertzian strength increases as shown in Fig.1. On the other hand, at the temperature higher than 800K, the carbon atoms those jumped out at the crack tip are oxidized by the thermally activated oxygen and removed as CO or CO_2. In place of the removed atoms, vacancies are induced at the crack tip on diamond surface. As the result of the phenomenon, the pre-existing microcracks extend and they deteriorate the fracture strength. In the range of temperature between 650K and 800K, the rate of crack healing and the oxidization of emitted carbon atoms can be in equilibrium.

The temperature of cutting edge in diamond turning of copper is predicted to be about 500 to 550 K [4]. In this temperature range, strength of diamond rather increases by the thermal hysteresis in air as shown in Fig.1. If the strength of diamond decreases in turning process of copper, its catalytic reaction may play an important role for the extension of microcracks. To examine the effect of catalytic reaction of copper on crack

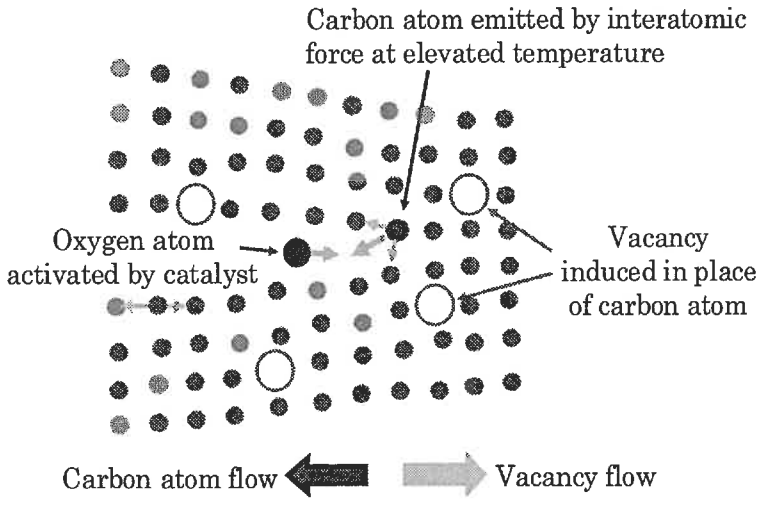
Carbon atom emitted by interatomic force at elevated temperature
Oxygen atom activated by catalyst
Vacancy induced in place of carbon atom
Carbon atom flow
Vacancy flow

Fig.2. Possible mechanism of strength change

extension, change in Hertzian strength of diamond specimens is investigated in contact with copper powder heated at 523K as shown in Fig.3. The strength of diamond specimens obviously decreases as the heating time increases.

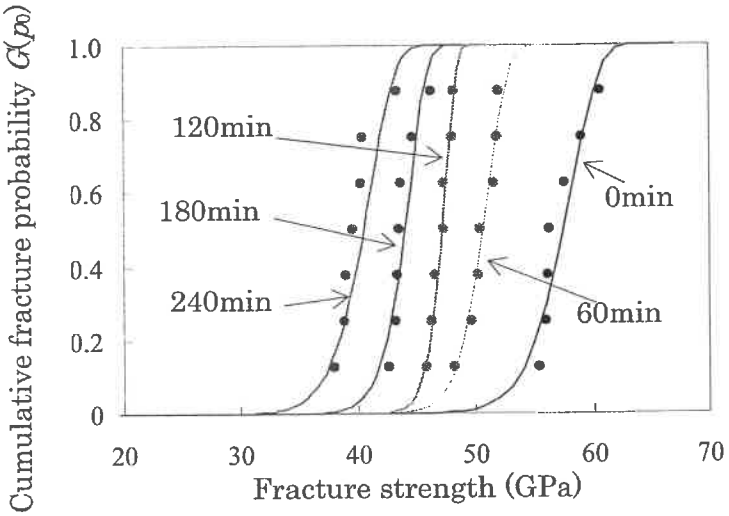

Fig.3. Effect of heating time on Hertzian strength of diamond in contact with copper powder heated at 523 K in air

On the other hand, the mechanism of gradual crater wear on rake face of cutting tool in diamond turning of copper has been investigated by the authors. The carbon atoms on rake face are removed due to oxidization of diamond accompanied with deoxidization of copper oxide [3]. The results in Fig.3 suggest that the decrease of fracture strength of diamond is attributed to the crack extension due to the same thermo-chemical erosion as that of crater wear at crack tip and that a catalytic reaction of copper accelerates the crack extension. Hence, cutting edge chipping or fracture may suddenly occur in turning of copper even at lower cutting temperature tan 600K.

Suppression of chipping under low oxygen partial pressure

As atmospheric oxygen obviously plays an important role in the thermo-chemical wear mechanism of diamond in turning of copper [3], effect of oxygen on the change in Hertzian strength is investigated. The deterioration in strength is reduced when the specimens are heated in nitrogen-rich atmosphere as shown in Fig.4.

The result suggests that the suppression of thermo-chemical reaction to remove the carbon atoms at crack tip by reduced oxygen atmosphere can be a useful method to suppress cutting edge chipping. Therefore, the cutting experiments under reduced oxygen atmosphere are carried out. By blowing of nitrogen gas, the oxygen partial pressure at cutting point is reduced to be one fourth of that in the normal atmosphere. Figure 5 shows the comparison of tool life in

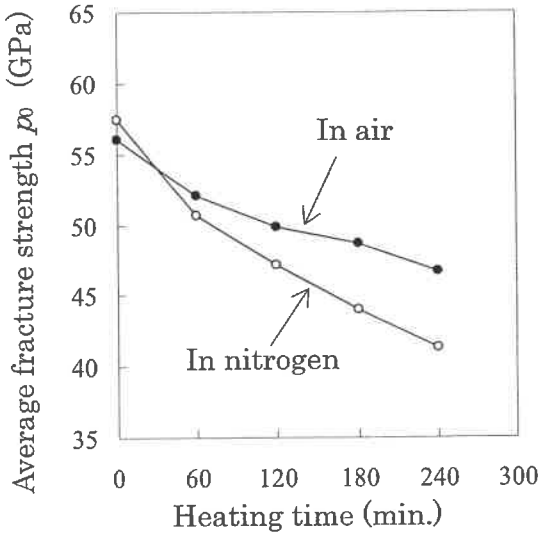

Fig.4. Effect of atmosphere on Hertzian strength of diamond in contact with copper powder heated at 523 K

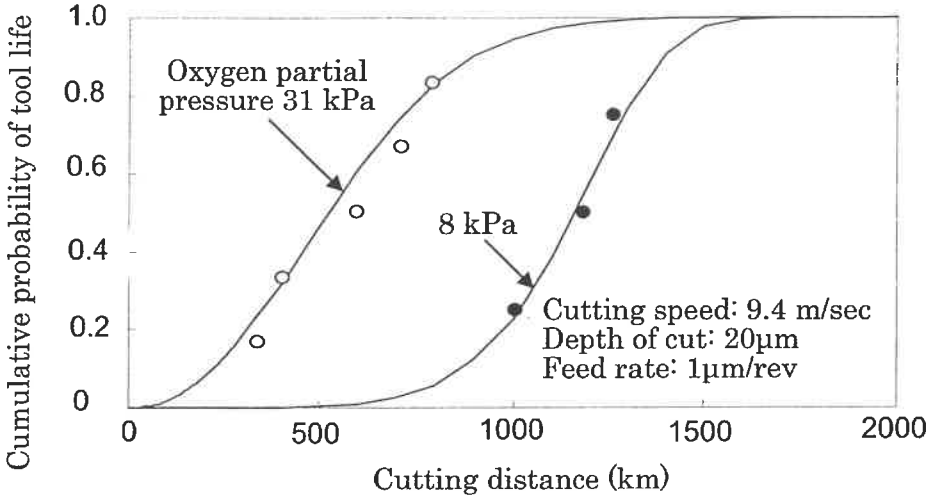

Fig.5. Effect of oxygen partial pressure on tool life in turning of copper

turning of copper under reduced oxygen atmosphere with that in normal one. The tool life is defined as the cutting length until the occurrence of large fatal chipping by which the feed mark is disturbed and scratches are produced on work surface. In general, tool life of diamond cutting tool has wide scattering. Therefore, cutting experiments are carried out using five different diamond tools and the life is evaluated by cumulative probability curve of tool life as a function of cutting distance until fatal chipping. The results shown in Fig.5 suggest that the use of reduced oxygen atmosphere is an effective method to suppress chipping in diamond turning of copper. The method can be a useful technique for large quantity production of diamond-turned copper components such as those to-be-encountered in construction of a high energy linear collider in the next generation.

Conclusions

To understand the mechanism of cutting edge chipping in diamond turning of copper, change in Hertzian strength on diamond specimens heated in contact with copper powder is investigated. The results suggest that the strength of diamond decreases by thermal hysteresis in contact with copper due to atomistic thermo-chemical erosion at crack tip with a catalytic reaction of copper and ambient oxygen. Furthermore, based on the investigation, the cutting under reduced oxygen atmosphere, which suppresses the decrease of strength on diamond specimen, is proposed for the useful technique to suppress the cutting edge chipping in diamond turning of copper.

References

[1] N. Ikawa, S. Shimada: Annals of the CIRP, 31, 1 (1982) 71.
[2] Y. Sato, M. Kamo: Surface, 19 (1981) 197.
[3] S. Shimada, T. Inamura, M. Higuchi, H. Tanaka, N. Ikawa: Annals of the CIRP, 49, 1 (2000) 21.
[4] T. Moriwaki, N. Sugimura, S. Luan,: Annals of the CIRP, 42, 1 (1993) 75.

Analysis and improvement of machining stability in noncircular turning

Dan Wu Xiankui Wang Ken Chen Wangmin Yi

Department of Precision Instrument and Mechanology
Tsinghua University, Beijing, 100084, P.R.China

Abstract

Noncircular turning process (NCTP) has been demonstrated to be effective in machining workpieces with noncircular cross-sections. To further improve noncircular profile precision, this paper applies variable spindle speed machining (VSM) to NCTP and attempts to investigate machining stability in NCTP. The noncircular turning system with continuous spindle speed variation is described. And, an adaptive repetitive controller at fixed sampling rate is designed for the fast tool servo (FTS) to track variable periodical signals in the discrete system. By computing the work done by the regenerative cutting force and the electromagnetic force provided by the FTS during spindle speed variation, the energy either delivering to or dissipating from the machining system is obtained to analyze machining stability. Experimental results demonstrate the tracking performance of the adaptive repetitive controller and the ability to improve machining stability using VSM.

Keywords: Noncircular turning; Repetitive control; Variable spindle speed machining; Stability

1. Introduction

In the field of precision engineering as well as optics, simple geometries are rapidly disappearing in favor of complex surfaces such as noncircular cross sections and free-form surfaces. This allows the integration of additional functions and improved performances into components. Noncircular turning process (NCTP) has been demonstrated to be effective in machining workpieces with noncircular cross sections such as the engine piston and camshaft, characterized by high productivity, flexibility and quality. In NCTP, a fast tool servo (FTS) carrying the cutting tool must follow a specially designed profile in synchronization with the spindle angular position and subject to variable cutting force disturbance.

NCTP concept was first applied to elliptical piston turning. Many researchers focus on the design of the linear actuator and control of the FTS. Various kinds of actuators, such as electromagnetic, piezoelectric and electro-hydraulic actuators, or their combinations were employed to achieve dynamic tool oscillations [1]. On the other hand, different control algorithms, such as repetitive control, fuzzy PID and zero-phase tracking control [2~4] are applied in the FTS to obtain high bandwidth, stiffness and low tracking error.

One of the most significant factors adversely affecting the machining precision and productivity is machining instability, also called chatter. Likewise, machining instability has adverse effects on NCTP. However, such a machining instability can be inhibited through improved FTS controller or other innovative concepts such as variable spindle speed machining (VSM) which refers to machining operation that the tool performs precision motion while the spindle carrying the workpiece rotates in a speed that varies in a periodic fashion with certain frequency and amplitude over some nominal constant speed [5-6].

In this paper, a newly developed noncircular turning system is firstly described. Then, an adaptive controller for the FTS is designed and analyzed for its stability. Finally, VSM's improvement in NCTP stability is analyzed and experimentally demonstrated.

2. Noncircular turning system

The hardware architecture of noncircular turning system is shown in Fig.1. The noncircular turning machine tool employs a conventional horizontal lathe structure but is specially designed in its bed and spindle structure to achieve high structural stiffness and spindle revolution accuracy. The universal NC servo unit is developed to provide open-loop servo motions in both X and Z directions, which are respectively driven by two AC servo motors and controlled by the DSP-based programmable multi-axis controller.

The FTS with a voice-coil motor actuator is a closed-loop position tracking system that carries the tool to reciprocate to achieve desired noncircular cross section profile. For low friction tool actuation and easy-available tool zero position, the tool slide is mounted on the combination of roll and spring bearing. A raster linear sensor is employed for the position feedback. A special controller is designed for the FTS with low tracking errors and high robustness.

The spindle unit involves the asynchronous AC motor and the varying frequency speed modulation based driver, which facilitates continuous spindle speed variable. A rotary encoder is mounted at the back of the spindle to feedback the workpiece angular positions to the FTS and programmable multi-axis controller to obtain synchronization between the tool actuation and workpiece rotation.

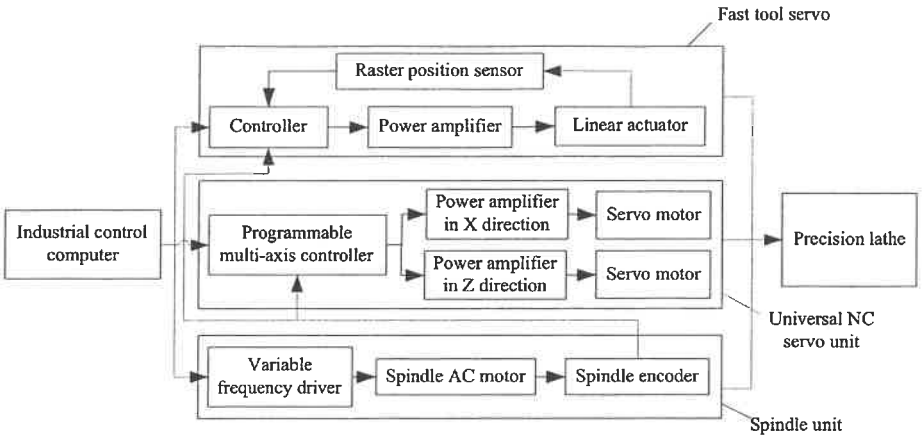

Fig.1. Hardware architecture of the noncircular turning system

3. Design of an adaptive repetitive controller

3.1. Modeling of the linear actuator

The dynamic equation of the voice-coil motor actuator can be expressed as:

$$m\frac{\mathrm{d}^2x}{\mathrm{d}t^2}+C\frac{\mathrm{d}x}{\mathrm{d}t}+K_sx=F_e-F_c \tag{1}$$

Where m=mass, C=coefficient of damp, K_s=spring stiffness, F_e=electromagnetic force, F_c=cutting force, and x=tool position. Since the cutting force in NCTP is dynamically variable and difficult to be analytically described, it can be eliminated from the equation and regarded as an external disturbance in modeling and control of the actuator. Therefore, after considering computation of the electromagnetic force, the transfer function of the actuator is derived:

$$G(s)=\frac{K_0/m}{s^2+\frac{C}{m}s+\frac{K_s}{m}}=\frac{K\omega_n^{\ 2}}{s^2+2\xi\omega_n s+\omega_n^{\ 2}} \tag{2}$$

where $\zeta=\dfrac{C}{2\sqrt{mK_s}}$, $\omega_n=\sqrt{\dfrac{K_s}{m}}$, $K=\dfrac{K_0}{K_s}$, and K_0 is a coefficient relating to the electromagnetic force. Therefore, the actuator is modeled as a two order system. With the aid of the model identification method of LEVY, the parameters in Eq.(2) can be obtained.

3.2. Design of an adaptive repetitive controller

Since the desired tool trajectories are approximately periodic signals in NCTP, repetitive control that can achieve asymptotic tracking and disturbance rejection of periodic signals is employed. However, while VSM is applied to NCTP, the application problem requires a periodic sampling rate. Hence, an adaptive repetitive control algorithm is specially developed to track variable periodic signals with a fixed sampling rate in the discrete system. The block diagram of the proposed repetitive control system is shown in Fig.2.

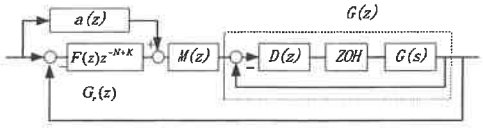

Fig.2. Block diagram of the adaptive repetitive control

In Fig.2, $G_r(z)$ is the repetitive controller consisting of a signal generator and a low-passed filter. Generally a low-passed filter is incorporated in the signal generator because of high frequencies contained in the reference decreasing the tracking performance.

Let the transfer function for the control plant $G(z)$ be described as:

$$G(z)=\frac{z^{-d}B(z^{-1})}{A(z^{-1})},$$

$$A(z^{-1})=1+a_0z^{-1}+\cdots+a_nz^{-n}$$

$$B(z^{-1})=b_0+b_1z^{-1}+\cdots+b_mz^{-m}N \tag{3}$$

where d is the plant delay and adjusted so that b_0 is nonzero. The order of the compensation phase K is chosen as:

$$K=d+m \tag{4}$$

It is very important in stabilizing the system and tracking variable periodic signals for the compensator $M(z)$ that is one order low-passed filter. The stabilizing controller $D(z)$ is designed by the method of minimum step control and utilized to improve the rejecting ability to the disturbance.

When the spindle speed is 1200rpm, the uniform sampling rate T_s is about 49μs. If a zero order holder is incorporated, the transfer function of the controlled object in discrete time is:

$$G(z)=\frac{0.0006398z+0.0006389}{z^2-1.995z+0.9955} \tag{5}$$

So the stabilizing controller $D(z)$ is designed as:

$$D(z)=\frac{-1948.107z^{-1}+1116.561}{0.7487z^{-1}+1} \quad (6)$$

Then the controlled block $G(z)$ is described as:

$$G(z)=-0.7453z^{-3}+0.4872z^{-2}+1.247z^{-1} \quad (7)$$

and K=3 according to Eq.(4) and (7).

For convenience of realization, both the low-pass filter $F(z)$ and the compensator $M(z)$ are described as:

$$F(z)=\frac{a_1}{a_2z+a_3},\quad M(z)=\frac{b_1z+b_2}{b_3z+b_4} \quad (8)$$

3.3. Stability analysis

Based on the small gain theorem, the discrete repetitive control system is stabilized with the following sufficient and necessary condition[2]:

$$\left|F(e^{\omega j})(1-M(e^{\omega j})G(e^{\omega j})\right|<1 \quad (9)$$

To simplify Eq.(10), Euro theorem is employed to compute and analyze the stability. After simulation using MATLAB software, the controller parameters are derived. The amplitude value in the left of Eq.(9) is less than 1 in the range of work frequency, indicating the system is stable.

4. VSM's improvement in NCTP stability

4.1. VSM and its investigation

VSM has been applied to processes involving turning, boring, milling and grinding. It is shown through simulations and experiments that the vibration of the tool and workpiece can be significantly reduced by moving from constant to variable spindle speed [5]. Tsao applied VSM to NCTP and designed a repetitive controller for a periodically time-varying system [2]. The success of VSM has been attributed to its ability to break-up the regenerative and forced vibration excitation frequencies that develop during conventional constant spindle speed machining.

4.2. Analysis of stability improvement

In NCTP, the actual trajectories of the tool are the combinations of desired vibration with low frequency and chatter vibration with high frequency. The former is a forced vibration driven by the electromagnetic force and identified by the noncircular profile. The latter is a self-excited vibration arising in machining. In fact, to improve NCTP stability is to reduce the chatter.

The self-excited vibration is produced by dynamic electromagnetic force and cutting force, resulting from the interaction between the FTS and cutting process dynamics. Since maintaining a self-excited vibration relies on the machining system, energy is not only delivered to but also dissipated from the system [6]. The effect of VSM on NCTP stability can be investigated by considering the balance between the work done by the electromagnetic force and cutting force and the energy absorbed by the system damping. The NCTP system is stable as long as the total energy variation being negative over one cycle of vibration.

Considering the case of an elliptical piston turning, the desired vibration of the FTS can be approximately expressed as:

$$R(t)=\frac{a-b}{2}(1-\cos(2\omega_m t)) \quad (10)$$

Let the chatter vibration of the FTS is described as:

$$x(t)=X\cos(\omega t+\phi) \quad (11)$$

Then the work done by the cutting force $F_c(t)$ and electromagnetic force $F_e(t)$ over n integer cycles of vibration can be computed from the relation:

$$\Delta W=\int_0^{2\pi n/\omega}-F_c(t)\dot{x}(t)\mathrm{d}t+\int_0^{2\pi n/\omega}F_e(t)\left(\dot{R}(t)-\dot{x}(t)\right)\mathrm{d}t \quad (12)$$

In Eq.(13), $F(t)$ and $F_e(t)$ can be respectively written as:

$$F(t)=K_c b\left(x(t)-x(t-\tau)+h_0\right) \quad (13)$$

$$F_E(t)=2K_s x(t)+F(t)+m\ddot{R}(t) \quad (14)$$

where K_c is the static cutting stiffness, b is the axial cutting depth, $x(t)$ and $x(t-\tau)$ are the inner and outer modulated chatter vibrations of the tool on two consecutive cuts.

It has been shown that a sinusoidal function is the most feasible speed trajectory for VSM since it is more convenient for the spindle drive system to track and easier for CNC realization. Typical sinusoidal spindle speed trajectory is represented as:

$$S(t)=S_0(1+\mathrm{RVA}\sin(2\pi f_s t)) \quad (15)$$

where S_0 is the mean spindle speed in rpm; RVA is the amplitude ratio; f_s is the signal frequency in Hz. So the number of vibration cycles is expressed by:

$$n=\frac{\omega}{(2\pi)^2 f_s} \quad (16)$$

The average work $\overline{\Delta W}$ done by the cutting force and electromagnetic force over one vibration cycle is computed by dividing Eq.(12) by the number of cycles (n) Eq.(16). While VSM is applied to NCTP, the phase angle ϕ between the current and previous chatter vibration is variable and can be expressed as:

$$\phi=2\pi M_m+\varepsilon_m \quad (17)$$

Where $M_m=0,1,2\cdots$, $0\le\varepsilon_m<2\pi$. After substitution and arrangement, $\overline{\Delta W}$ can be solved analytically:

$$\frac{\overline{\Delta W}}{K_c b X^2}=-2\sin(\varepsilon_m) \quad (18)$$

To investigate the effect of VSM amplitude ratio

RVA and ε_m on the stability, the work done by the electromagnetic force and cutting force is computed for the amplitude ratio in the range $0 < RVA < 0.6$. Fig.3 shows the effects at the cases of $M_m = 2$ and $M_m = 8$.

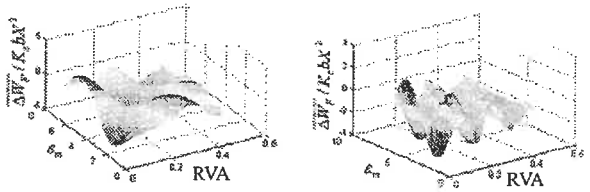

$M_m = 2$ $M_m = 8$

Fig.3. Effect of RVA and ε_m on the work done by the electromagnetic force and cutting force

It is indicated that applying VSM to NCTP changes the work done by the electromagnetic force and cutting force, resulting in variation of stability performance. Although VSM has potential to improve NCTP stability, it is necessary to select appropriate VSM parameters.

5. Experiments

A prototype NCTP machine tool with variable spindle speed has been built and shown in Fig.4. A VSM software module generates sinusoidal signals to the varying frequency modulator, which control the AC motor driving the lathe spindle through the belt and gear group transmission. A Googol programmable multi-axis controller is employed to control the AC servo motors in both X and Z directions as well as the spindle unit. In addition, a TMS2407-DSP-based special controller is developed to control the voice-coil actuator. And an accelerometer is mounted on the end of the actuator slide bar to provide the acceleration signals. The windows-based NCTP software system has been developed to implement universal NC and noncircular NC turning with both constant and variable spindle speed.

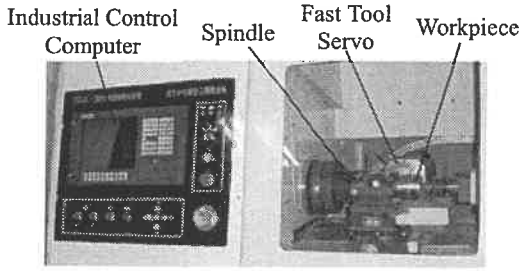

Fig.4. Photograph of the noncircular turning machine tool

Extensive experiments are carried to focus on the tracking performances of the FTS and the effect of VSM parameters on NCTP stability. Fig.5. shows the tracking performance of the FTS with the adaptive repetitive controller under variable spindle speed.

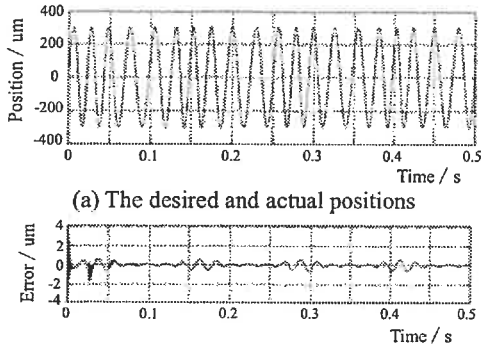

(a) The desired and actual positions

(b) Tracking error

Fig.5. Tracking performance of the FTS under VSM

6. Conclusions

VSM is applied to improve NCTP stability that relates to the FTS and cutting process dynamics. The adaptive repetitive control algorithm with fixed sampling rate is designed to adapt the periodical sampling rate and maintain stable cutting process. Stability improvement in NCTP results from VSM's potential to break up regenerative chatter effect. However, only under appropriate VSM parameters, NCTP stability can be improved significantly.

Acknowledgements

The authors gratefully acknowledge the financial support of this research by the National Natural Science Foundation of China (No. 50105009).

References

[1] T. Higuchi, T. Yamaguchi, etc. Development of a high speed noncircular machining NC-lathe by electrohydraulic servo mechanism. JSPE 1990; 56: 293–7.

[2] Hanson RD, Tsao TC. Periodic sampling interval repetitive control and its application to variable spindle speed noncircular turning process. Journal of Dynamic systems, Measurement, and control 2000; 122(3): 560-6.

[3] Hwang CL, Shi YD. Noncircular cutting on a lathe using tool position and differential motor current. International Journal of Machine Tools & Manufacture 1999; 39(2): 209-27.

[4] Liu JL, Wang XK, Wu D. Fuzzy-reasoning based self-tuning control for servo drive in linear motor. Journal of Tsinghua University 1998; 38(2): 44-6.

[5] Radulescu R, Kapoor SG, Devor RE. An investigation of variable spindle speed face milling for tool-work structures with complex dynamics, part 1: simulation results. Journal of Manufacturing Science and Engineering 1997; 119(3): 266-72.

[6] Al-Regib E, Ni J, Lee SH. Programming spindle speed variation for machine tool chatter suppression. International Journal of Machine Tools & Manufacture 2003; 43(12): 1229-40.

Bonding Quartz Glass at Room Temperature

Tetsuya Hamaguchi, Natsuki Yamamoto, Takeshi Ooi, Kensuke Tsuchiya, Masayuki Nakao
The University of Tokyo, Graduate School of Engineering
7-3-1 Hongo, Bunkyo-ku, 113-8656 Tokyo, Japan

1. Introduction

The authors are developing a method for directly bonding two pieces of quartz glass at room temperature. The conventional way of bonding glass with additives, like soda glass or borosilicate glass, is anodic bonding. For bonding pure quartz glass, ways exist by softening the surface with high temperature, melting the surface with hydrogen fluoride acid (HF)[1], and using glue. Applying these methods, however, for bonding micro Total Analysis System (μ-TAS) chips (Fig. 1), causes surface deformation or glue entering the micro grooves and destroys the micro-features on the chip surfaces. Also, optical parts that pass ultraviolet ray are made of quartz glass and gluing them together causes drops in transmissivity of the ultraviolet ray.

We thus want to develop a technology to directly bond two pieces of quartz glass together. For direct bonding of metal, a known technique[2] bonds metal surfaces activated by inert gas ion beam or fast atom beam (FAB) irradiation cleaning under vacuum. We applied FAB irradiation and succeeded in bonding quartz glass. This paper reports the relations of bonding strength versus quartz glass surface roughness, FAB irradiation time, FAB source gas type and bonding pressure.

2. Test equipment and procedure

Fig. 2 sketches our test equipment, with a vacuum chamber, 2 FAB guns, 2 samples fixtures, and a pressing mechanism. The FAB guns are oriented to irradiate FAB on two samples both at angles of 45 degrees. The pressing mechanism has a load cell to measure the bonding pressure.

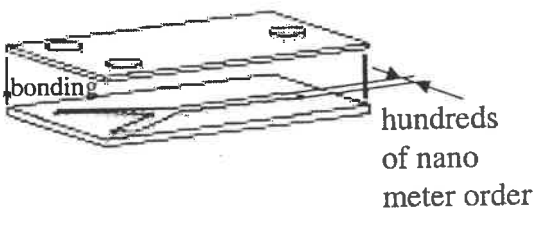

Fig. 1 Example of μ–TAS Chip

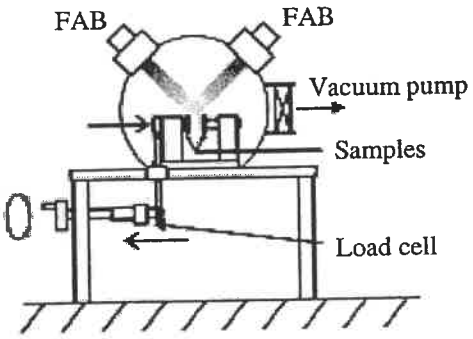

Fig. 2 Test equipment

The test proceeds as follows: First the sample surfaces are cleaned with organic solvent, a mixture of H_2SO_4+H_2O_2 and then with NH_4F. The cleaning process then takes the samples through boiling in a H_2SO_4+H_2O_2 mixture, and ends with pure water rinsing and drying. The two samples fixtures hold the sample to thoroughly dry them. The fixtures are then set inside the vacuum chamber which we vacuum down to 7.5×10^{-4}Pa. We then fill the chamber with the source gas at a pressure of 1.3×10^{-2}Pa and irradiate FAB on the sample surface. After the set irradiation time, with the FAB irradiation running, the pressing mechanism presses the two samples together to bond them.

We then take the bonded sample out from the vacuum chamber and set it on the tensile test machine with the fixtures holding it in place. The load cell measures the force when the bonded surface separate to give the bonding strength value.

The samples were quartz glass plates of 6 x 6mm with a thickness of 0.2mm. We prepared two types of sample with different surface roughness values of 0.17 and 3.2nmRa. We used an atomic force microscope (AFM) for measuring the surface roughness. For FAB source gas, we readied Ar gas, an inert gas commonly used for diffusion bonding, and CHF_3 gas expecting some chemical reaction with quartz glass.

3. Test results and discussion

3-1. FAB irradiation time and surface roughness

We expected that the sample surface roughness should strongly affect the bonding strength. Cleaning the sample surface requires FAB irradiation for its activation and we were concerned that the irradiation may degrade the surface roughness. We thus tested how the FAB irradiation time affects the surface roughness. We applied CHF_3 gas FAB irradiation to the sample with an original surface roughness of 3.2nmRa, and both the CHF_3 gas and Ar gas FAB irradiation to ones with 0.17nmRa. Fig. 3 shows the test results, and Fig. 4, the AFM images of the sample surface before and after 300 seconds of CHF_3 gas FAB irradiation. The figures show

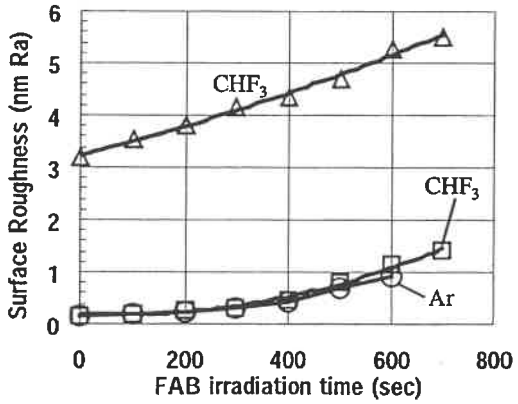

Fig.3 Relation between FAB irradiation time and surface roughness

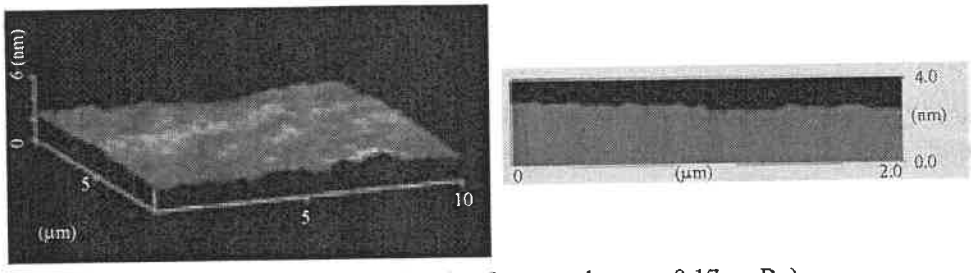

(a) Before FAB irradiation (surface roughness = 0.17 nmRa)

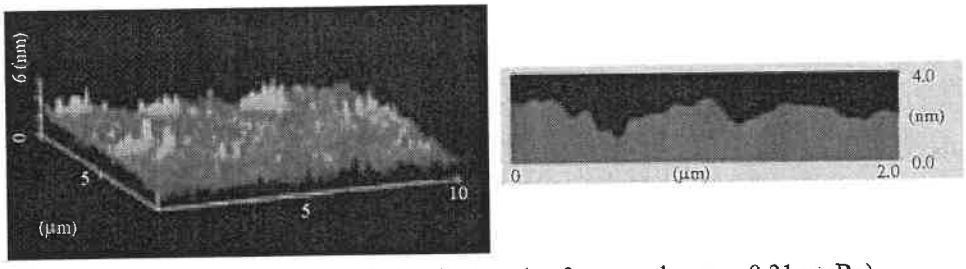

(b) After 300 seconds of FAB irradiation (surface roughness = 0.31 nmRa)
Source gas: CHF_3

Fig.4 Change of surface roughness with FAB irradiation

that FAB irradiation degrades surface roughness.

Longer irradiation worsens the surface roughness with both Ar and CHF_3 gas. When neutral atoms hit the sample surface, they clean the surface by removing molecules and contamination, but at the same time, roughs the glass surface by hitting it.

3-2. Bonding strength and FAB source gas

Fig. 5 shows the test results. The horizontal axis gives the surface roughness after FAB irradiation, and the vertical axis the bonding strength. Ar gas failed bonding the glass plates with both surface roughness values. CHF_3 gas, on the other hand, succeeded in bonding the two pieces. A component of the CHF_3 gas must have caused some chemical reaction on the quartz glass, however, the detail of this process has not been clarified.

With CHF_3 gas, the bonding strength maximized when the surface roughness was about 0.25nmRa. Samples with smoother surfaces had shorter FAB irradiation time. The results indicate that smoother surfaces produce larger contact area and thus stronger bonding strength, however, if the FAB irradiation time is too short for smoothness, the process loses the cleaning effect and the bonding strength drops.

3-3. Bonding strength and bonding pressure

Once FAB irradiation is complete, the two samples are pushed together to make the bonding and Fig. 6 shows the bonding pressure in the horizontal axis and the bonding strength in

the vertical. We compared the results with samples made of gold and quartz glass. The quartz glass samples had surface roughness of 0.31nmRa after FAB irradiation with CHF_3 gas. Larger bonding pressure generated stronger bonding strength for gold. The smaller Young's modulus of gold produced greater contact area with larger bonding pressure. In contrast, quartz glass has a large Young's modulus and increasing the bonding pressure does not affect the contact area. The bonding strength did not increase with the bonding pressure.

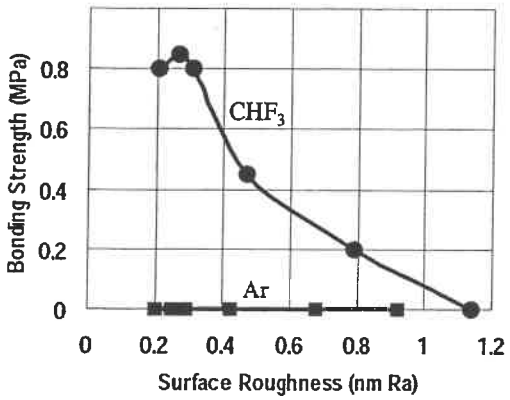

Fig.5 Relation between surface roughness and bonding strength

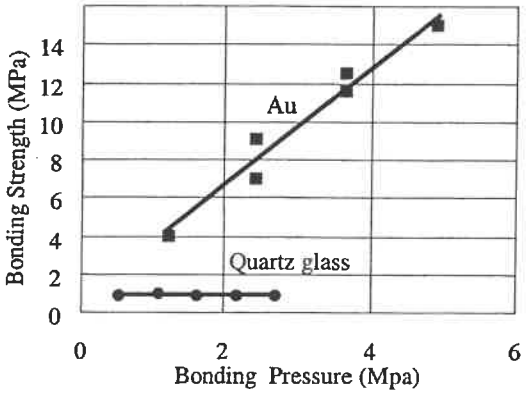

Fig.6 Relation between bonding pressure and bonding strength (CHF3, 0.31nmRa)

4. Conclusions

We confirmed that we can directly bond two pieces of quartz glass at room temperature by using FAB. The following conditions are important for stronger bonding strength:

- CHF_3 gas is effective for the FAB source gas.
- Surface roughness of 0.25nmRa after FAB irradiation produces the best results .
- The bonding pressure, when it is 3MPa or less, does not affect the bonding strength.
- The bonding strength will improve if we can clean the surface without affecting the surface roughness.

References

[1]Akihide Hibara, et al.: Nanochannels on a Fused-Silica Microchip and Liquid Properties Investigation by Time-Resolved Fluorescence Measurements, ANALYTICAL CHEMISTRY, Vol.74, pp.6170-6176, 2002.

[2]Yuzo Matsuzawa, Toshihiro Itoh, and Tadatomo Suga: Room-temperture Interconnection of Electroplated Au Microbump by means of Surface Activated Bonding Method, Electronic Components and Technology Conference, pp.384-387, 2001.

EFFECTS OF DIFFUSION BRAZING PARAMETERS ON DIMENSIONAL VARIATION OF NICKEL ALUMINIDE MICROCHANNELS

Kannachai Kanlayasiri
Department of Industrial Engineering, Faculty of Engineering
King Mongkut's Institute of Technology-Ladkrabang, Bangkok 10520, Thailand

Abstract

Nickel aluminide (NiAl) foil is a novel structural material for high-temperature micro-scale fluidic devices. NiAl foils can be used to fabricate micro-scale fluidic devices through a microlamination process. For the micro-scale fluidic devices, dimensional variation of flow conduits is very critical to fluid flow behavior and heat transfer performance. It is found that the variation usually occurs during the joining stage of the microlamination process. In this study, diffusion brazing was used as the joining technique of NiAl foils. However, information on the relationship between brazing parameters and dimensional variation of flow passages is not available. An investigation of brazing parameter effects on the dimensional variation of flow conduits was performed in this study. Analysis of variance technique was employed to analyze the effects of each brazing parameter. The results showed that the minimum deviation would appear to obtained when the temperature and the time are at the high level and the pressure is at the low level.

Key words: Diffusion brazing, Nickel aluminide foil, Micro-scale fluidic devices, Analysis of variance

Introduction

Microtechnology-based Energy and Chemical Systems (MECS) have been under development with the goal to decentralize and make portable micro- and meso-scale fluidic systems such as heat pumps, chemical reactors, and bio-sensors. The miniaturization of MECS devices is made possible by the use of microchannel arrays to increase the ratio of surface area to volume of the conduits within the devices resulting in an improvement in the heat and mass transfer performance of the flow conduits in the devices (Wang et al., 1991; Peng et al., 1995; Brooks et al., 1999). In building MECS devices, conventional materials that have been used are stainless steel, copper, and brass. However, the devices made by these conventional materials are not functional at high temperatures, which are required of many applications such as steam reforming, flue gas desulphurization, and mobile engine heat recovery (Jovanovic, 2001; Paul et al., 2002). New material systems for high-temperature microchannel array devices are required to fulfill these applications.

Nickel aluminide (NiAl) possesses high potential to be used as structural material for high-temperature microchannel array devices. This intermetallic compound is attractive to high-temperature applications because of its high melting temperature and good high-temperature corrosion resistance. This is because of the inherent property of the aluminum (Al) contained in the aluminides to form protective oxide layers (Al_2O_3).

NiAl foils can be used to fabricate MECS devices by microlamination techniques. These techniques have been used to produce MECS devices that typically possess complex arrays of internal micro-scale features. Three steps are involved in microlamination: lamina patterning, laminae registration, and laminae bonding. With the development of micromachining methods, many techniques can be used for lamina patterning including micromilling, laser micromachining, photochemical etching, and electrochemical machining (Wegeng et al., 1996; Martin et al., 1999; Paul et al., 1999). For intermetallic materials, electro discharge machining (EDM) has been widely used for patterning purposes (Nakao et al., 1991; Lutfullin et al., 1995; Glatz and Clemens, 1997). After the lamina patterning step, laminae are registered and then consolidated into a solid block of material by a joining process.

Joining of intermetallic compounds has been studied by many researchers. Joining techniques, such as diffusion bonding, diffusion brazing, and transient liquid phase bonding, were found promising for bonding intermetallic compounds (Nakao et al., 1991; Glatz and Clemens, 1997; Uenishi et al., 1995; Moore and Kalinowski, 1993; Strum and Henshall, 1994; Wu and Huang, 2001). It is found from these reports that joining intermetallic compounds is successful when performed under high temperatures and/or high pressures. However, results from the literature cannot be applied directly to the case of joining intermetallic microchannels because the previous research efforts were performed on simple bulk specimens, but microchannel devices are complex structure. Applications of

heat and pressure affect not only joining the foils, but also causing dimensional variation of the devices. In the case of fabricating the microchannel devices, dimensional variation (warpage) of microchannels or fins is very critical to the fluid flow behavior and heat transfer performance of the devices as reported in research of Alman et al. (2001) and Paul et al. (2001; 2002). Joining under high temperature and pressure can lead to warpage of microchannel fins in the devices. In this study, NiAl foils were laminated by a diffusion brazing process, and effects of the brazing parameters on warpage of the foils were investigated.

Experimental Approach

The foil used in this study was NiAl foil with nominal thickness of 127 μm. Diffusion brazing was employed as the joining technique. Commercially pure (99.99%) Ni foil with nominal thickness of 7.5 μm was used as the filler metal to promote joining of the NiAl foils. Test article was intentionally designed to emulate the fin of microchannel devices. Geometry and cross section of the patterned foils and filler metal are shown in Figure 1. The dimensions of the bridge structure are 5.08 mm wide and 10.16 mm long.

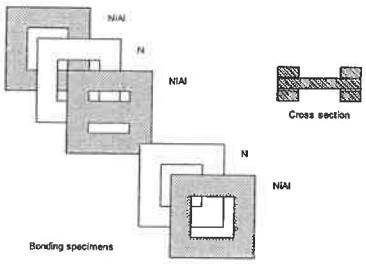

Figure 1. Test sample configuration and cross section

The laminae were then registered to the designed sequence. In this experiment, a graphite fixture with edge alignment was employed to register all specimens during bonding. Finally, the foils were diffusion brazed at various conditions in a vacuum environment. For every bonding cycle, the specimens were heated up from and cooled down to room temperature. Deflection of the fin structure was measured by a profiler. The profiler's stylus was traced along the length of the bridge to measure magnitude of the warpage. The measurement was performed at three different locations on the bridge, near the left and right edges and at the center line of the bridge, to obtain an average value of the warpage.

Process parameters investigated in this study were bonding temperature, pressure, and time. The process response was the magnitude of the fin warpage. Each process parameter was run at two levels. A 2×2^3 full factorial design was created to study brazing parameter effects on warpage of the foils. There were totally 16 runs performed in this experiment. The experiments were run in a random order to average out the effects of confounding factors that may be present. It is assumed that three-way interaction has negligible effect on the warpage. The experimental conditions are shown Table 1.

Table 1. Experimental Factors Levels

	Factor	Lower Level	Higher Level
A	Pressure	1500 psi	3000 psi
B	Temperature	600 °C	800 °C
C	Time	2 hr	8 hr

Results and Discussion

Analysis of variance was performed on the data sets as shown in Table 2. Based on the analysis, brazing temperature had significant effect on warpage of the fin (*p-value* < 0.05). From Figure 3, the magnitude of warpage increases with the increase of brazing temperature. It was suggestive, but inconclusive, that the brazing pressure also had effect on the warpage (0.05 < *p-value* < 0.10). The warpage of the fin seems to increase as the brazing

pressure increases as shown in Figure 2. From the analysis, the brazing time did not show influence to the deformation of the fins. Note from the AB interaction as shown in Figure 4 that the pressure (A) has a large positive effect when the temperature (B) is at the high level, but the pressure has fairly large negative effect at low temperature, with the best results obtained with either the pressure is at the low level and the temperature is at the high level, or the pressure is at the high level and the temperature is at the low level. From Figure 5, the AC interaction indicates that the pressure effect is very small when the time (C) is at the low level and very large when the time is at the high level, with the best results obtained with the low level of the pressure and the high level of the time. Therefore, the minimum warpage would appear to obtained when the temperature and the time are at the high level and the pressure is at the low level.

Table 2. Analysis of Variance Table

Analysis of Variance for Deviation - Type III Sums of Squares

Source	Sum of Squares	Df	Mean Square	F-Ratio	P-Value
MAIN EFFECTS					
A:ExpPressure	271.083	1	271.083	4.78	0.0566
B:Temp	370.685	1	370.685	6.54	0.0308
C:Time	29.941	1	29.941	0.53	0.4859
INTERACTIONS					
AB	1034.44	1	1034.44	18.24	0.0021
AC	247.112	1	247.112	4.36	0.0664
BC	157.506	1	157.506	2.78	0.1299
RESIDUAL	510.319	9	56.7021		
TOTAL (CORRECTED)	4238.38	15			

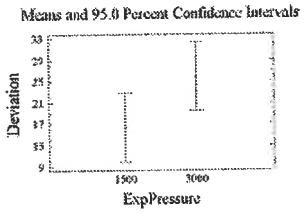

Figure 2. Plot of pressure and deviation

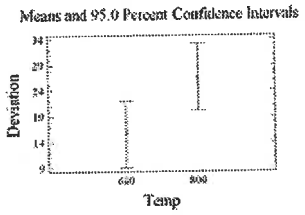

Figure 3. Plot of temperature and deviation

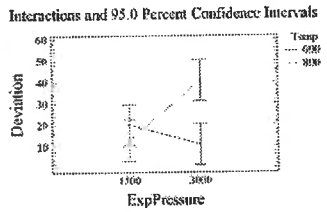

Figure 4. Interaction of pressure-temperature

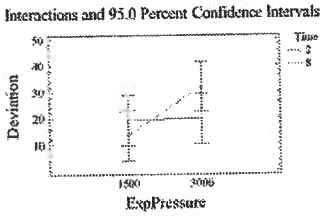

Figure 5. Interaction of pressure-time

Conclusions

This study investigated effects of brazing parameters on warpage of nickel aluminide foils. The results showed that brazing temperature had significant effect on warpage of the fin. The warpage of the fin increased with the increase of brazing temperature. It was suggestive, but inconclusive, that the brazing pressure also had significant effect on the warpage. After considering interactions of brazing parameters, nickel aluminide foils

should be brazed at the high level of temperature and time and low level of pressure to obtain minimum warpage. Future research could be performed on optimization of these brazing parameters.

References

Alman, D. E., Wilson, R. D., and Paul, B. K., 2001, "Fabrication of NiAl Intermetallic Reactors for Microtechnology-Based Energy Chemical Systems (MECS)," *Transactions of NAMRI/SME*, Vol.XXIX, pp.453-459.

Brooks, K. P., Martin, P. M., Drost, M. K., and Call, C. J., 1999, "Mesoscale Combustor/Evaporator Development," *ASME IMECE Conference*, pp.37-43.

Glatz, W., and Clemens, H., 1997, "Diffusion bonding of intermetallic Ti-47Al-2Cr-0.2Si sheet material and mechanical properties of joints at room temperature and elevated temperatures," *Intermetallics*, Vol.5, pp.415-423.

Jovanovic, G. N., Drost, M. K., Paul, B. K., Warnes, W. H., and Watson, P. R., 2001, "Intermetallic/catalyst technology development for high temperature catalytic micro reactors," *Proposal to the National Science Foundation*.

Lutfullin, R. Y., Imayev, R. M., and Kaibyshev, O. A., 1995, "Superplasticity and solid state bonding of the TiAl intermetallic compound with micro- and submicrocrytalline structure," *Scripta Metallurgica et Materialia*, Vol.33, No.9, pp.1445-1449.

Martin, P. M., Matson, D.W., and Bennett, W. D., 1999, "Microfabrication Methods for Microchannel Reactors and Separations Systems," *Chem. Eng. Comm.*, V.173, pp.245-254.

Moore, T. J., and Kalinowski, J. M., 1993, "Diffusion brazing NiAl with self-generated filler metal," *Mat. Res. Soc. Symp. Proc.*, Vol.288, pp.1173-1178.

Nakao, Y., Shinozaki, K., and Hamada, M., 1991, "Diffusion bonding of intermetallic compound TiAl," *ISIJ International*, Vol.31, No.10, pp.1260-1266.

Paul, B. K., Peterson, R. B., and Wattanutchariya, W., 1999, "The Effect of Shape Variation on the Performance of High-Aspect-Ratio Metal Microchannel Arrays," *IMRET 3: Proceedings of the Third International Conference on Microreaction Technology*, pp.53-61.

Paul, B.K., Hasan, H., Thomas, J., Wilson, R. D., and Alman, D., 2001, "Limits on Aspect Ratio in Two-Fluid Micro-Scale Heat Exchangers," *Transactions of NAMRI/SME*, Vol. 29.

Paul, B. K., Hasan, H., Dewey, T., Alman, D., and Wilson, R., 2002, "An evaluation of two methods for producing intermetallic microchannels," *ASME International Mechanical Engineering Congress and Exposition*, New Orleans, LA.

Peng, X. F., Wang, B. X., Peterson, G. P., and Ma, H. B., 1995, "Experimental Investigation of Heat transfer in Flat Plates with Rectangular Microchannels," *International Journal of Heat and Mass Transfer*, Vol.38, No.1, pp.127-137.

Pope, D. P., and Darolia, R., 1996, "High-temperature applications of intermetallic compounds," *Journal of Materials Education*, Vol.18, No.4-5, pp.205-219.

Strum, M. J., and Henshall, G. A., 1994, "Liquid-assisted diffusion bonding of NiAl," in *Advanced Joining Technologies for New Materials II*, editors Flore, N. F., and Stiegler, J. O., pp.76-88.

Uenishi, K., Sumi, H., and Kobayashi, K. F., 1995, "Joining of intermetallic compound TiAl by using Al filler metal," *Z. Metallkd.*, Vol.86, No.4, pp. 270-274.

Wang, J. H., Yeh, H. Y., and Shyu, R. J., 1991, "Thermal-Hydraulic Characteristic of Micro Heat Exchangers," *ASME Dynamic Systems and Control Division*, DSC Vol.32, pp.331-339.

Wegeng, R. S., Call, C. J., and Drost, M. K., 1996, "Chemical System Miniaturization," *Proceedings of the 1996 Spring National Meeting of AIChE*, New Orleans, LA, February, pp.25-29.

Wu, G. Q., and Huang, Z., 2001, "Superplastic forming/diffusion bonding of laser surface melted TiAl intermetallic alloy," *Scripta Materialia*, Vol.45, pp.895-899.

Development of Automated Machining of Precision Inertial Instrument Components
Extended Abstract
by

Anthony Kondoleon
Robert Faiz
Richard Walker
Draper Laboratory
555 Technology Square
Cambridge, Ma. 02139
617-258-1537
kondo@draper.com

Overview

High performance inertial instruments require ultra high precision in their manufacturing processes in order to achieve their desired performance. While these precision processes are possible, they usually rely on the skill of one or two operators and are expensive to maintain. With the decline in the support base for precision inertial instruments, due to contractions and mergers, maintaining these skills is continuous challenge to both the government and contractors. One solution is the use of state of the art machining systems developed for the optics industry for use on precision inertial instrument components. While these machines have been used traditionally for manufacturing of visual and infrared optics, their micro-inch resolution and repeatability make them ideal for high performance inertial instrument component manufacturing. This paper describes the work being carried out by Draper Laboratory to determine the suitability of utilizing these machines for machining and finishing precision gas bearing wheels assemblies. Examples of wheel machining experiments will be described as well as the results obtained from a number of different systems on two different gas bearing wheel designs.

Introduction

Draper Laboratory has a program for the investigation into the worth of developing an automated finishing system for precision gas bearing wheel components. This paper documents the work to date on the finish machining experiments being carried out both in-house and by suppliers of precision machining equipment. The work in-house is being carried out on a Precitech Nanoform 200, which we have in our machine shop. This is a diamond turning machine that was purchased to be used as a precision grinding machining. Draper Laboratory also has provided support to two machine suppliers, which produce precision machining and finishing machines. They are Precitech of Keene, New Hampshire and OptiPro from Ontario, New York. A third machine tool supplier, Moore Machine Tools of Keene, New Hampshire, declined to support our effort. This paper documents the results obtained from the three systems used to obtain a finish on wheel parts without the use of manual (hand lapping) labor.

Wheel Parts

Two gas bearing wheel designs are the focus of this investigation. The first wheel design is a spool wheel, which has a pyroceram rotor, and an aluminum oxide bearing material, which requires finishing operations. Figure 1 shows this wheel design. The second wheel design, called a hemispherical wheel, has a concave and convex aluminum oxide coated bearing surface, which requires finishing operations. Figure 2 shows this wheel design. Both require the surface to be better than 1 micro inch surface finish and a form tolerance of less than 10 micro inches after the finishing

operations are completed. These specifications can presently be met, but only after a lengthy and expensive series of manual operations.

Experimental Results

Precitech was provided with some spool rotors to experiment on as well as some aluminum oxide coated hemispherical parts. The spool rotors were measured to have in excess of a 40 micro inch finish prior to any work being performed on them by Precitech. Precitech only worked on the face of two spool rotors in order to get a feel for the tolerances and precision that the wheel parts are required to attain. With spindle speeds of 30,000 rpm, a part speed of 359 rpm, and two grit size wheels were used. The 1,200 grit wheels produced a finish of 7 nano meters (.28 micro inches) while the 3,000 grit wheels produced a finish of 5.5 nano meters (.22 micro inches). After these two rotors were worked on, the effort was redirected to working on the hemispherical parts. No results have been obtained from Precitech at this time on these parts.

The work OptiPro carried out was on hemispherical parts, both rotors and bearings and some roughed up spool rotors. The initial male bearing parts had a plasma spray coating, which was not as consistent as the rotor coatings. The ground bearing surfaces had a finish that ranged from 10 micro inches to 7.5 micro inches. When the male bearing parts were polished on OptiPro's polishing machine, the finish went down to 2.5 micro inches. The dummy hemispherical rotors parts were ground to a surface finish of 8 to 9 micro inches with a polished surface finish of 1.5 to 3.5 micro inches.

Draper Laboratory followed the path that we gave to Precitech, which was to machine the spool wheel parts first to get a feel for the machine and then precede on to the hemispherical parts. Using a 1200 grit wheel, we were able to attain a surface finish of .4 micro inches on the pyroceram rotors, which duplicated the results of Precitech. Draper Laboratory next worked on aluminum oxide coated thrust plates to see what could be learned when machining this material. Using grinding wheels with grit up to 2200, the best surface finish, which we attain, was 4.5 micro inches. The geometry of the male hemispherical bearing, Figure 3, allowed for only a grinding wheel grit size of 600 to be used. With this wheel, Draper Laboratory was able to get surface finishes of 7.5 to 9 micro inches.

Discussion

The purpose of the paper was to show a path for success for precision finishing of gas bearing wheel parts with out manual labor involved. Figure 4 shows the plot of surface finish of the aluminum oxide coated surfaces versus diamond grit size. The plot shows, as the diamond grit size gets smaller, a higher wheel grit number, the surface finish improves, goes down. The trend line is very linear. It also indicates that pure grinding alone may not meet the 1 micro inch surface finish currently called out for the aluminum oxide coated wheel components. A secondary operation of polishing might be required. The 1 micro finish has been obtained on the spool rotors both at Draper Laboratory and Precitech. Draper Laboratory has ordered and received additional sets of finer grit grinding wheels that we plan to use for work in-house in the near future.

Conclusions

Both Draper Laboratory and Precitech obtained a surface finish of better than 1 micro inch on face grinding of the spool rotor. Since this was used only for set up tests, no further work has been performed on these parts. Grinding alone does not appear able to get to a 1 micro inch finish on the aluminum oxide coated surfaces both for the thrust plates, used for set up, and the dummy hemispherical bearing parts. There is potential for the automated polishing system, developed by OptiPro, being able to meet this goal, based on the limited, but promising, results so far.

Figure 1
Spool Gas Bearing Wheel Assembly

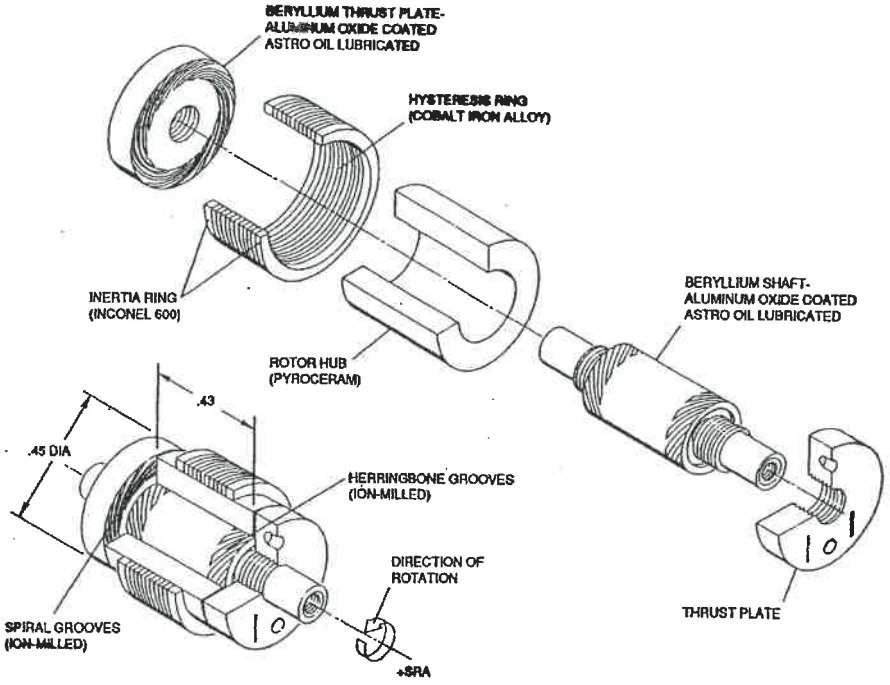

Figure 2
.375 Hemispherical Gas Bearing Wheel

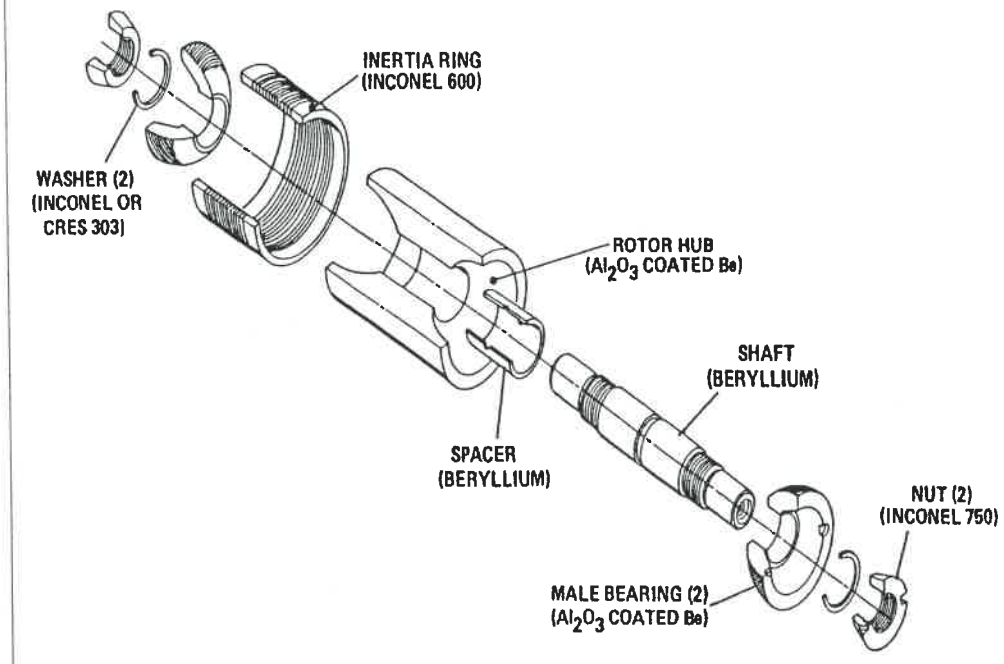

Figure 3
Dummy .375 Diameter Hemispherical Bearing Mounted on In-House Precitech Nanoform 200

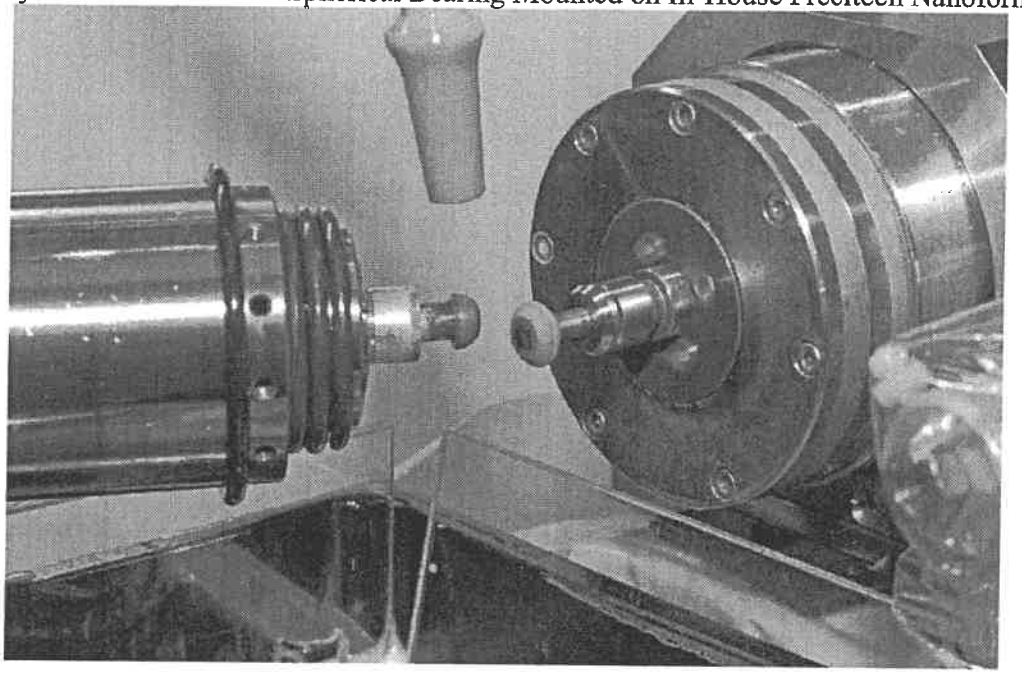

Figure 4
Surface Finish to Grit Size Trend Line

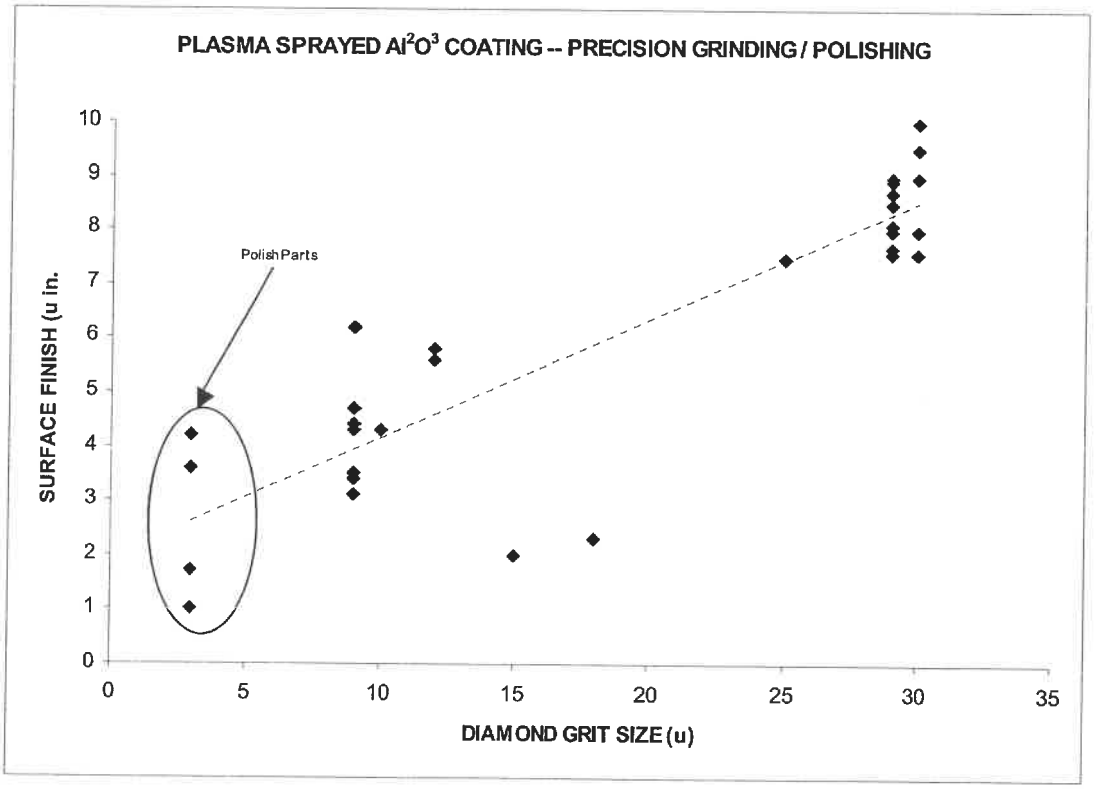

Pushing The Precision Level of Mechanical Alignment System Into The Nano Meter Region

Neville K. S. Lee, Z. Q. Li
Dept. of IEEM, Hong Kong University of Science and Technology
Clear Water Bay, Kowloon, Hong Kong

Abstract With the advance of MEMS and NEMS technology, assembly of micro device may some day become important. The quality of the assembled micro device would depend on the accuracy of the alignment process. Optical Alignment System (OSA) for semiconductor industry has very high level of precision. But the system is too expensive, and the size of the marker is too big for practical application in the area of micro assembly. On the other hand, the alignment resolution of typical vision type of optical alignment system, limited by the wavelength of the light, is difficult to push too much beyond the um range. Therefore it is the objective of this presentation to discuss the finding of our investigation for an alternative low cost method that can operate in the tens of Nano Meter (nm) Range, and have the potential extending further into nm range.

Mechanical alignment system (MAS) is widely used in industry because of its simplicity, low cost and easy to use. However, there is a fairly common notion in the industry that MAS is relatively crude, and is not suitable for precision manufacturing. To certain extend, there are some reasons leading to that kind of erroneous conclusion. Some of the MAS used in the industry may indeed perform rather poorly with resolution merely in the tens of micron meter (um). The level of precision of MAS depends strongly on the design of the MAS and the operating condition of the MAS.

One of the difficulties in the understanding of the level of precision achievable in MAS is due to the lack of a multi-dimensional position monitoring device with high enough resolution. In this paper, we will discuss the development and the performance characteristics of a new multi-dimensional positioning monitoring system with resolution better than 10nm. Using this multi-dimensional ultra-high resolution positioning monitoring system, the performance of two different types of MAS commonly used in industry has been studied. For our preliminary study, only alignment of macroscopic parts has been studied due to their availability. But in fact, smaller system should perform better. Even with our present macroscopic system, performance level at 60-70nm has already been demonstrated.

In the presentation, we will discuss the key design issues and key operation factors that can significantly affect the accuracy of the MAS as well as some of the detail of our investigation.

Key Word: Precision Alignment System, Mechanical Alignment System, Ultra-Precision Multi-dimensional Position Monitoring System.

1. INTRODUCTION

Manufacturing precision is important since it affects the product quality and production yield. With global competitions, manufacturers are increasingly facing the challenge of producing high precision products while keeping the production costs low. Therefore, precision manufacturing can no longer be an expensive, luxury item. In fact, low cost manufacturing processes are a fundamental requirement for participating in design and manufacturing hi-tech products.

Assembly processes in contemporary manufacturing have the workpiece assembled together and subject to certain inspection activities to assure the quality of the final product. Therefore, how good the assembly task is performed in assembly process is one of the important factors that will greatly affect the assembly quality. Considerable research effort has been done in the past to deal with the problem. Xie et al.[1] have proposed to determine the reasonable alignment position before the real starting of the whole assembly work by using robot's functions and measurement on a small amount of practical run with the assembly line and then teach the right alignment position to the robot. Derby [2] developed an end-effector that dramatically improved the accuracy and repeatability of the robot to which it was attached.

Slocum and Weber [3] developed a passive mechanical wafer alignment technique that is based on the principle of elastic averaging and uses mating pyramid and groove elements to passively align wafers to each other as they are stacked. By their approach, an alignment accuracy of 0.47μm was observed for kinematic couplings. Lee et al. [5-7] investigated the effect of how a datum is secured in a mechanical alignment system with the aid of a high-resolution multidimensional optical position monitoring system, an alignment accuracy of 0.246μm was achieved for fixed cylindrical datum system by their approach. They also studied the performance of different MAS in terms of assembly accuracy in the presence of the form error, surface waviness and surface roughness of the references surface, and analysed the effect of imperfections of the workpiece on the manufacturing precision.

In manufacturing industry, there was some common belief that the low cast mechanical alignment method, in which the mechanical datum are used to align the reference surfaces of the workpiece for each setup, is cheap but not precise. In this respect, the aim of this study is to understand the ultimate level of the performance of a well-performing assembly with mechanical alignment system. Furthermore, the factors that adversely affect precision, and the means to counteract these effects, have been investigated.

2. CAPACITIVE MEASUREMENT SYSTEM

The shape of a capacitive sensor used in our test is the rectangular with area of $3.18\times8mm^2$. To reduce the noise and improve the stability of the sensor, the area of sensor is surrounding by a guard-rectangle which is separated from the sensor by a narrow gap and grounded. In this way the noise will be virtually eliminated and the ideal situation may be approached very closely [8].

To identify the relationship between output voltage V_o and the resolution of the system, the sensor with an area of $3.18\times8mm^2$ is tested. The experiment condition as follow:

1. Signal: square wave, $V_i = 10.75V$, frequency $f = 40KHz$
2. Noise of the system: $\Delta V_{noise} = \pm 0.1mV$
3. Observed resolution of the meter: $\Delta V_o = 0.1mV$

For a small space between sensor and workpiece, the sensitivity and the resolution of the system may be defined as

$$senstivity = \frac{dV_o}{dD}, \qquad res = \frac{\Delta V_o}{sensitivity} \tag{2.1}$$

Figure 1(a) shows the measured relationship of output voltage and the space between the sensor and workpiece. At a gap of $\delta = 0.05mm$, which was used to measure the position of workpiece in our test, a quite high resolution of $7.16nm$ will be achieved (Fig. 1(b)).

3. EXPERIMENTAL SET UP

The experiment setup for measuring displacement in x direction is shown in Fig. 1(c). The idea for this situation is that, after calibration of the system, the workpiece can be removed and then restored to the same position for each test. In this respect, two kinds of mechanical alignment datums are designed for repeatability experiment.

1. Three steel balls with diameter of 8mm were embedded into the platform and formed a three semi-ball datum system. These three semi-balls act as a reference and are used to located the L shape workpiece with two crossed V-grooves as shown in Fig. 1(d). A screw locates at the centroid of the triangle formed by the three semi-balls and is used to exert a contact force between the balls and the grooves.
2. In this procedure, three stainless dowel pins with diameter of 12mm were fixed on the platform by pressing them into the bored holes whose diameters were slight smaller than that of the pins. The L shape workpiece is located on the platform via a 3-2-1 scheme of cylindrical datum system formed by the pins as shown in Fig. 1(e). Two screws are used to fasten the workpiece to prevent any displacement after it is alignment.

A sensor frame is mounted on a *xyz* stage and can be moved freely in x direction to calibrate the system. Three sensors s_1, s_2 and s_3 with an area of $3.18 \times 8mm^2$ are located on the frame (Fig. 1(c)).

4. EXPERIMENTAL RESULTS

A series of repeatability experiments for two datum systems were conducted at room temperature (23°C). Our study shows that, for a good design, the high alignment precision can be achieved by a low cost mechanical alignment system. The average errors for cylindrical datum and three-ball kinematic coupling are 143nm and 67nm, respectively.

The three-ball kinematic coupling datum system exhibits a better alignment accuracy than that of the cylindrical datum system. The mechanism for this difference is not fully understood since many factors, such as surface roughness of the workpiece and datum, the elastic indentation, magnitude of the holding force, etc. will affect the precision of the alignment. It also implies that what kind datum is chosen in mechanical alignment system is a significant factor contributing to the accuracy of workpiece alignment in MAS.

7. CONCLUSION

Statistical experiment and data analysis have been performed to study the alignment precision of the mechanical alignment system with two alignment setups. The following major conclusions could be drawn on the displacement of workpiece under different alignment conditions:

1. A real-time multidimensional capacitive position monitoring system (CPMS) with a high resolution up to 7.16nm has been developed as the tool for characterizing the alignment precision.
2. Our data shows that the high alignment precision can be achieved by a low cost mechanical alignment system. The average errors for cylindrical datum and three-ball kinematic coupling are 143nm and 67nm, respectively.
3. The three-ball kinematic coupling datum system exhibits a better alignment accuracy than that of the cylindrical datum system. The results suggest that what kind datum is chosen in mechanical alignment system is indeed a significant factor contributing to the accuracy of workpiece alignment in MAS.

Acknowledgement

This work has been supported by an RGC Grant from the Government of the HKSAR (Project No. HKUST 6224/01E).

Reference

1. Xie, C., Guo, Z., and Chen, X., (1994), "A new approach to improvement assembly accuracy on robot automatic assembly line", *Proc. 2nd Asian Conf. On Robotics and Its Applications*, Int. Acad. Publishers, pp. 121-125
2. Derby, Stephen., "Closed loop assembly micro-positioner (CLAMP) end effector for high precision robotic assembly", Sme Technical Paper (Series) Ms. Var paging
3. Slocum, A. H., and Weber, A. C., (2003), "Precision passive mechanical alignment of wafers", J. Microelectromechanical Systems, Vol. 12, pp. 826-834
4. Lecarpentier, G., Mottet, J. S., Dumas, J. and Cooper, K., (2000) "High accuracy machine automated assembly for opto electronics", *50th Electronic Components and Technology Conference, Las Vegas, NV, USA,* pp. 1-4
5. Lee, N. and Joneja, A., (1997), "A methodology to improve manufacturing precision in the presence of workpiece imperfections", *J. of Manufacturing Science and Technology*, Vol. 119, pp. 616-622
6. Lee, N., Hon, K., Cheung, V. and Joneja, A., (2000) "Effect of datum securing method on precision of mechanical alignment system", *J. of Manufacturing Science and Technology*, Vol. 122, pp. 350-359
7. Lee, N., Yu, G. H., Chen, J. Y., and Joneja, A., (2003) "Effect of mechanical alignment system on assembly accuracy", *J. of Manufacturing Science and Engineering*, Vol. 125, pp. 595-608
8. Baxter, L. K., (1997), "Capacitive Sensors", *IEEE Press*, NY
9. Slocum, A. H., "Precision Machine Design", Prentice-Hall, New Jersey

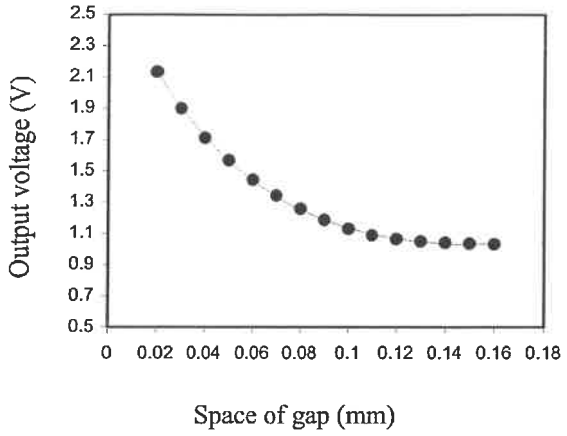

(a)

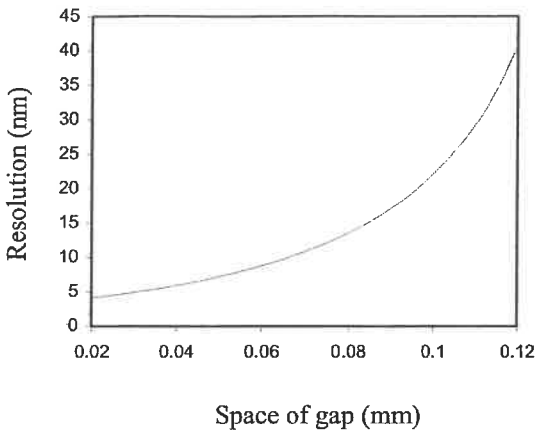

(b)

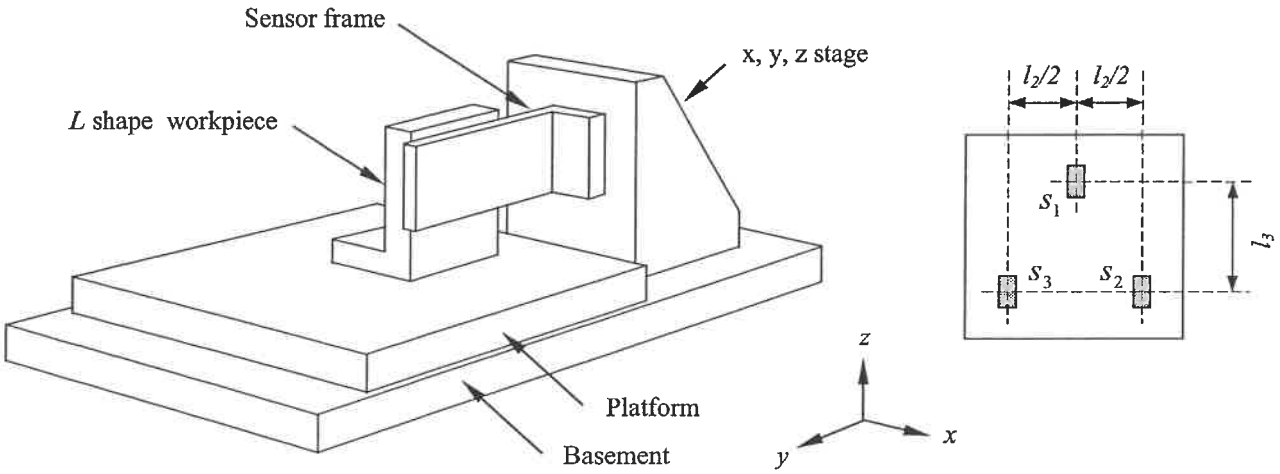

(c)

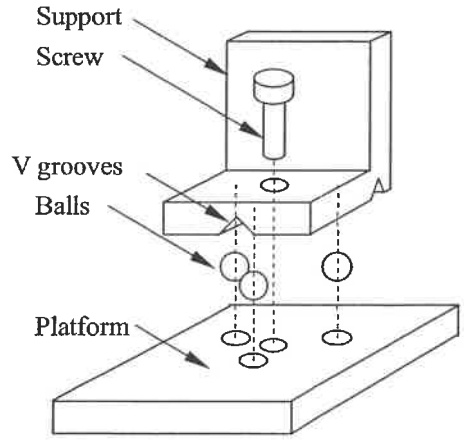

(d)

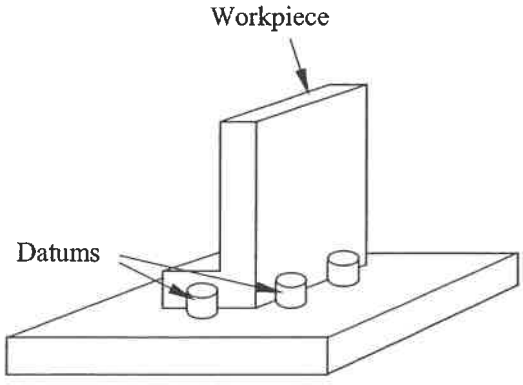

(e)

Fig. 1. (a) The relationship of output voltage and the gap; (b) The variation of resolution of system at different gaps; (c) Experiment setup; (d) Three-balls datum system; (e) cylindrical datum system.

Effect of Securing Processes on Precision Assembly

Neville K. S. Lee, Z. Q. Li
Dept. of IEEM, Hong Kong University of Science and Technology
Clear Water Bay, Kowloon, Hong Kong

Abstract Assembly precision is important since it affects the product quality and production yield. One of the key steps in the assembly process is the fastening process. However, little research has been conducted in this area in terms of the effect of the securing process on the assembly accuracy. One of the difficulties to carry out the research in this area is the lack of proper instrument with high enough resolution to perform the study. Using an inhouse developed ultra-high resolution multi-dimensional position monitoring system, the effect of screw-fastening process and glue-bonding process on the final assembly precision in a controlled environment has been studied.

In our study of the screw-fastening process, the effects of different parameters such as number of screws, applying torques, holding force, external datum pins and washer have been investigated. Our analysis shows that these parameters would interact with each other in the contribution to the lateral and rotational displacement in the screw-fastening process. Number of screws and washer are the most significant factors for the translation displacement induced by the screwing process. As for the rotational displacement, the presence of the external pins, and the joint effect of holding force and number of screws are the more important factors. Our study shows that proper design and operating condition of the screwing process have a very significant effect on the level of displacement introduced by the screw fastening process. An order of magnitude difference (range from about a um to over 10um) in the assembly accuracy may result using different screw-fastening conditions.

In the glue-bonding process, the effect of different types of glues, and different type of glue-bonding configuration have been studied. For the side joint where glue is applied on the sides of the work piece, there is significant difference in performance when glue is applied on all sides versus just applied only on one side. UV glue and AAA bond work better in terms of accuracy than the epoxy. There is again close to an order of magnitude difference in performance of between the best glue-bonding application method and the worst application glue-bonding method. In the lap joint configuration where glue is applied to the backside of the parts, the displacement is mainly due to shrinkage of glue, and the shrinkage depends on glue thickness and glue shrinkage rate.

As a whole, the glue-bonding process can provide an order of magnitude better accuracy than the screwing process. The best glue-bonding process we have observed would only cause about 0.1um of displacement of the parts. In other words, our study shows that there are a two order of magnitude of difference in accuracy between an optimized and a non-optimized fastening process.

Key Word: Precision Assembly System, Fastening Process, Screw-fastening Process, Glue-fastening Process, Ultra-Precision Multi-dimensional Position Monitoring System

1. INTRODUCTION

Industry assembly is very important in production. As the final step in the manufacturing process, it directly influences the product quality and life cycle. Assembly is finished by a serial of assembly activities, such as alignment, jointing, insertion, fastening and bonding, that have the workpieces assembled together. Therefore, how good the assembly task is performed in assembly process is one of the important factors that will greatly affect the assembly quality.

In the assembly process, there are two basic categories of assembly task involved: parts mating and parts joining. In parts mating, two or more parts are brought into contact or aligned with each other. After parts are mated, fastening is applied to hold them together. A great deal of research efforts has been done in the past to deal with the problem of assembly inaccuracy in parts mating [1-3]. Although these progress, little research has been done in parts joining or fastening.

For assembly with bonding, it appears that relatively little systematic research and study has been done in this area. In industry, the level of precision achievable by bonding assembly is not well understood. This research tries to answer following questions; 1. What level of assembly accuracy will be achieved with glues at different joint conditions. 2. What factors will strongly affect the accuracy of assembly process by glues and how to prevent it. 3. What is the best way to reduce the effects of these factors to improve the level of precision.

There are many factors that may affect the precision of the bonding process. In the course of this investigation, the effects of whether the glue permeates into gap or not was found to have a strong effect than the other factors for side joint. For example, the AA glue exhibits a better accuracy than epoxy although the volume shrinkage of AA glue is much larger than that of epoxy.

Among all the factors that affect the precision of the assembly with bonding, how the workpiece is bonded is a factor in a class of its own deserving special attention. In this respect, a systematic study of the effect of joint conditions on the assembly precision has been conducted. Specially, it is aim of this study to understand the ultimate level of the performance of a well-performing assembly with bonding.

2. EXPERIMENT PROCEDURE

2.1 Experiment of screw-fastening process

Two workpieces with aluminum had been milled for the study. One was $100\times130\times6.35mm^3$ for the top piece and the other was $98\times128\times12.7mm^3$ for the bottom piece. A multi-dimensional high-resolution optical monitoring system [4] will be used to measure the displacement of the workpiece during the screw-fastening process. In our experiment, effects of several factors such as torque, washer, holding force, number of screws and mechanical constraint on the displacement of the piece during the screw-fastening process are to be studied. The impacts of these factors were also investigated via factorial experiments that can exam several factorial effects simultaneously.

2.2 Experiment of glue-bonding process

2.2.1 Glue selection and characterization

Three kinds of commercially available glues with room temperature curing are chosen as bonding materials in our tests; 1. U-V glue (UV 82025, Electro-lite Corp.); 2. A-A glue (Aron Alpha, Toagosei co., Ltd); 3. Epoxy (Epoxy 5 minutes, Bostik, Australia Pty Ltd).

Two approaches are used to measure the volume shrinkage of the glues; i). To measure the shrinkage of the glues in a long glass tube. ii) To measure the shrinkage of a block of the glue in z direction. The volume shrinkage for UV and epoxy will be taken as the average of the values obtained by two ways. Table 1 shows the measured volume shrinkage by our approach.

Table 1. The measured volume shrinkage of glues

UV glue	AA glue	Epoxy
k_{uv}= -7.69%	k_{AA}= -60.38%	k_{EP}= -3.28%

2.2.2 Experiment setup for glue-bonding process

Two types of glue-bonding configuration were studied; i) side joint; ii) lap joint. Two kinds of work pieces of aluminum had been milled for side joint. One was $46\times46\times20mm^3$ for the top piece (piece1) and the other was $110\times70\times12mm^3$ for the bottom piece (piece2). For lap joint, the sizes were $40\times40\times20mm^3$ for piece1 and $50\times50\times20mm^3$ for piece2, respectively. Two experiment setups were designed for different joint conditions.

1. Setup for measurement of displacement components in xy plane for side joint
2. Setup for measurement of displacement components in z direction for lap joint

A developed multi-dimensional ultra-high resolution positioning monitoring system [5] is used to measure the displacement of the workpiece.

3. EXPERIMENT RESULT

For screwing process, the main effect plot in Fig. 1(a) suggests that number of screws and washer are the most significant factors for the translation inaccuracy induced by the screwing process. As for the rotational displacement, Fig. 1(b) indicates that the most important factors are the pins.

The results of glue bonding process for side joint show that, i) for all side joint conditions and glues used in test, the displacements are sub-micron. The four sides joint shows the best assembly accuracy and the one side joint condition exhibits a largest displacement among five conditions. ii) it is interesting that, for all conditions, the displacements for epoxy which exhibits a smallest volume shrinkage (-3.28%) among three kinds of glues are larger than that for UV and AA while the joints with AA glue show the displacement in almost same scale as that with UV glue although AA glue exhibits a significant volume shrinkage (-60.38%) among three glues (Fig. 1(c)).

For lap joint with nearly parallel gap, it can be seen that the displacement u_z for all gaps is in scale of microns and increases with an increase of the gap (Fig. 1(d)).

For lap joint with an inclined and a constant average gap, the results shown that, i) the average displacement u_z shows only about 5.4% different when the initial inclined angle varieties from $\beta_x = 0$ to $\beta_x = 7.5\times10^{-3} Rad$. For the applications with small inclined angle, we may regard that the average displacement u_z is independent on the initial inclined angle; ii) the magnitude of the rotation angle of the piece1 increases with an increase of the initial inclined angle as shown in Fig. 1(e).

4. CONCLUSION

1. The experiment results shown that number of screws, datum pins, washer and holding force are the important factors that affect assembly accuracy. That the order of magnitude difference in the assembly accuracy may result using difference screw-fastning conditions is also observed.
2. For all side joint conditions of bonding process, the displacements are sub-micron. The four sides joint shows the best assembly accuracy. The one side joint condition exhibits a largest displacement among five conditions. The results suggest that how the two pieces are jointed by glue is a major affecting factor of MAS precision.
3. For all side joint conditions, the displacements for epoxy that exhibits a smallest shrinkage among three kinds of glues are larger than that for UV and AA. The joints with AA glue show the displacement in almost same scale as that with UV glue while AA glue exhibits a much large shrinkage than that of epoxy.
4. For lap joint, the displacement u_z is close to proportional to the magnitude of the initial gap. The rotation angle is close to linear dependent on the initial inclined angle.

Acknowledgement

This work has been supported by an RGC Grant from the Government of the HKSAR (Project No. HKUST 6224/01E).

Referance

1. Xie, C., Guo, Z., and Chen, X., (1994), "A new approach to improvement assembly accuracy on robot automatic assembly line", *Proc. 2nd Asian Conf. On Robotics and Its Applications*, Int. Acad. Publishers, pp. 121-125
2. Lee, N., Hon, K., Cheung, V. and Joneja, A., (2000) "Effect of datum securing method on precision of mechanical alignment system", *J. of Manufacturing Science and Technology*, Vol. 122, pp. 350-359
3. Lee, N., Yu, G. H., Chen, J. Y., and Joneja, A., (2003) "Effect of mechanical alignment system on assembly accuracy", *J. of Manufacturing Science and Engineering*, Vol. 125, pp. 595-608
4. Lee, N., Cai, Y. and Joneja, A., (1997) "A high resolution multu-dimensional displacement monitoring system", J. of Optical Engineer, Vol. 36, pp. 2287-2293
5. Lee, N and Z. Q. Li, "Pushing the precision level of mechanical alignment system into nano meter region", This conference

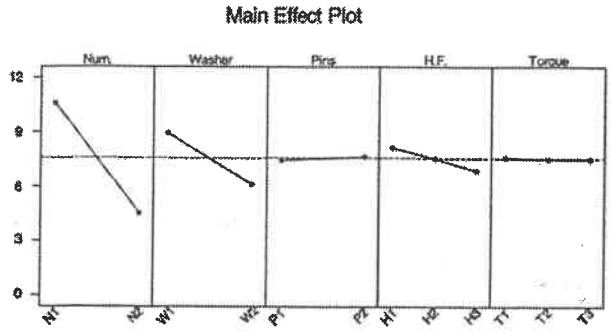

(a)

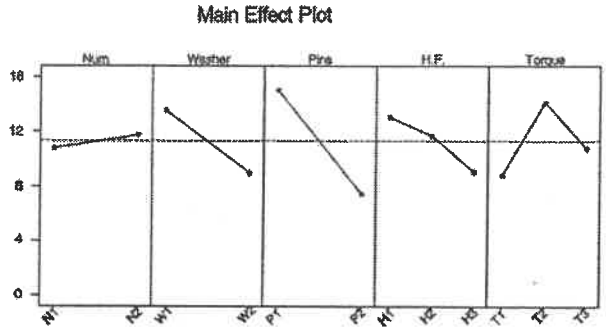

(b)

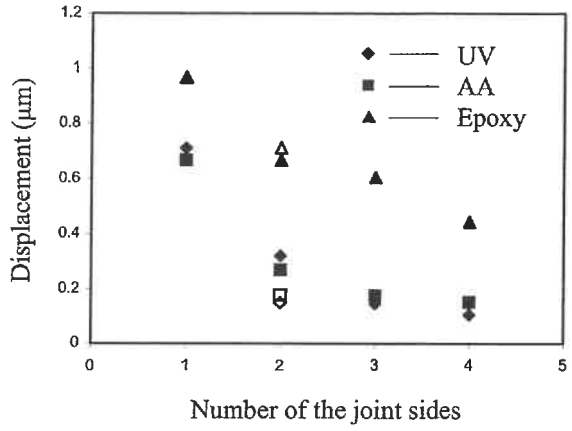

(c)

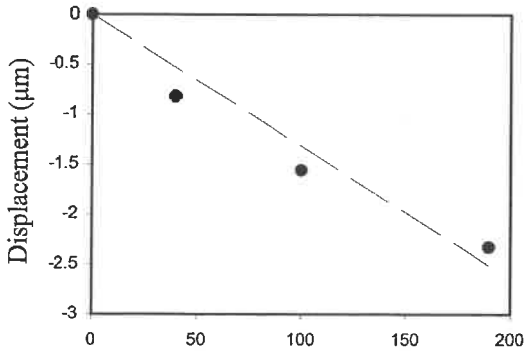

(d)

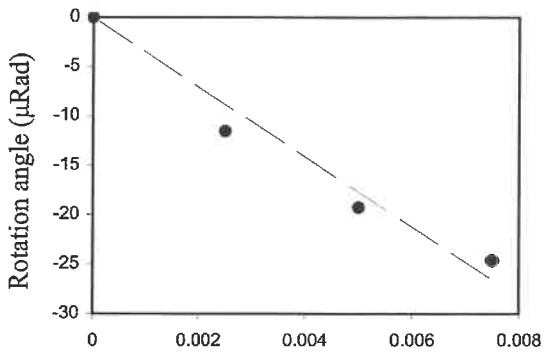

(e)

Fig. 1. (a) Main effect plot for $\overline{\Delta l_0}$; (b) Main effect plot for $\overline{\Delta \theta_0}$; (c) The displacement of side joint for different joint sides, the hollow markers present the displacement of two-symmetry side joint corresponding to different glues; (d) The variation of the displacement of piece 1 at z direction for lap joint at different gaps; (e) The relationship of the rotation angle of piece1 and initial inclined angles with constant average distance between two pieces.

Multilayered metal micro-reactor integrated for chemical synthesis processes

Kensuke Tsuchiya, Junichi Yamazaki, Takeshi Ooi,
Tetsuya Hamaguchi and Masayuki Nakao
Graduate School of Engineering, The University of Tokyo
7-3-1 Hongo, Bunkyo-ku, 113-8656 Tokyo, JAPAN

1. Introduction

Recently, the use of micro-channels is catching much attention for miniaturizing and integrating chemical reaction systems.

In industrial chemical synthesis, large amount of source chemicals are mixed in a huge reaction chamber. However, it has distributions of temperature or density inside, delaying the reaction and producing unexpected by-products. Also, exothermic reaction and explosive reactions require feed control of source and effective cooling. In addition, toxic chemical reactions need mechanically strong chambers with reliable sealing.

A micro-reactor is highly efficient for thermally controlling reagents and is suitable for exothermic reaction, which requires cooling, and other reactions that need tight thermal control for putting a reagent into a specific temperature range for producing a target chemical. The large surface area, per volume, gives high thermal conductivity to a micro-channel allowing quick and accurate temperature control of the chemicals inside[1].

In addition, its small size shortens the molecule diffusion time for fast and efficient reaction[2], and reduces distributions of temperature or density.

There are a lot of chemical systems using micro-channels. Many of them are made of transparent material, such as glass, plastics, or silicone rubber, so the researchers can visually observe the reactions[3][4]. Plastics and silicon rubber, however, do not stand high temperature, and corrode when exposed to acid, alkali and organic solvents. These liquids are often used for chemical synthesis. The other choice glass can easily break with shock or stress, and is difficult to put into desired shapes. Glass is not suitable material for a micro-reactor either. In contrast, metal generally resists high temperature and pressure, and has excellent thermal conductivity. In addition, it is easy to form and is shock resistant. Some metal even resist acid, alkali, and organic solvent. However, not many metal made micro-reactors have been reported and there is a strong need for new processing methods for their production.

Miniaturizing chemical reaction systems poses another problem; the reaction only produces a small quantity of the product made, although the reaction speed may be fast. Arranging multiple channels for running reactions in parallel can defeat this problem, e.g., like a multilayered micro-reactor. Another benefit of arranging the channels in multilayer is the 3-dimensional layout that can realize complex reaction processes, for example, starting with four different inputs into two different reagents and ending with one final product.

To counter these problems, we invented a multilayered metal micro-reactor for chemical synthesis.

2. Design of micro-reactor

A micro-reactor are manufactured by cutting grooves on the surface of a flat substrate, placing another plate over the grooves and bonding the two, and connecting with pipes. In this method, the most difficult process is bonding, and the second is pipe connecting.

The micro-reactor material has to resist both high and low temperature, pressure, or stress. It also has to remain unaffected by such reagents as acid, alkali or organic solvent. As a material meeting these requirements, we chose stainless steel for its ease of forming and low cost.

We then cut micro-channels on the surface of the stainless substrate using a fine end mill. The micro-channel size usually determines the method for machining them on stainless substrates. The channel size we needed was in the range of 200-1,000 micro-meters in both width and depth. When larger, we can neglect the scale effect, however, for smaller channels, viscosity of the fluid causes flow resistance that cannot be neglected. Ferric chloride or aqua regia wet etching is also popular in cutting channels but only when the channels are 100 micro-meters deep or shallower.

For the next process of covering the channels machined on the substrate, we laser welded a stainless steel plate.

Metal is not popular for micro-reactor material because of difficulty to bond the whole substrate.

We overcome the problem by welding substrate locally along the micro channels by laser.

The specific machine we used was a Compact YAG Laser (ML-2030, MIYACHI Co., Ltd.), with a wavelength of 1064nm and a focus diameter of 500 micrometers. Laser welding, which is used for automobile body industrially, can make high bonding strength without high surface flatness. However, the micro laser welding has the same problem as the automobile welding, that air gap between the plates and lack of power cause incomplete welding. For finding the optimum welding conditions, we ran a preliminary test varying the laser power, irradiation time and plate thickness.

As the result we found the optimum condition of laser output at 9.8W and irradiation time of 10msec for welding 300-micrometer cover to a substrate.

We produced a single layer micro-reactor with this processes. Specifically, we cut 1,000 micro-meters wide and 800 micro-meters deep T-shaped micro-channel, using an end mill, on a 1mm thick SUS316L substrate. We then welded 300 micro-meters thick SUS316L plate with the condition above on the substrate to cover the channels. A thermocouple was attached to the junction for measuring the reaction temperature. Fig. 1 shows a photo of the micro-reactor we produced and Fig. 2 shows the cross-sectional view. We tested the welding quality by pressurizing the micro-reactor to 5MPa, a pressure high enough pressure for general reaction, and holding the pressure for 20 minutes. No pressure drop was observed during this time demonstrating that the YAG laser successfully welded the micro-reactor.

Next, we produced multiple layers of micro-channels by a sequential process. Fig. 3 shows the multilayering process. We first machined the first layer of micro-channels on the substrate surface. We then laser welded the second layer that covers the channels in the first layer. Next, we ground this cover plate, just welded, to flatten its surface that served as the substrate for the second layer of micro-channels. Repeating these processes of cutting, welding, and flattening produced multiple layers for the micro-reactor.

We applied the processes described above to prototype a triple-layered micro-reactor shown in Fig. 4. Channel size was same as single layer micro-reactor, and to cut 800 micro-meters deep micro-channel with 300-micrometer plate, we welded two plates penetrated by micro channels.

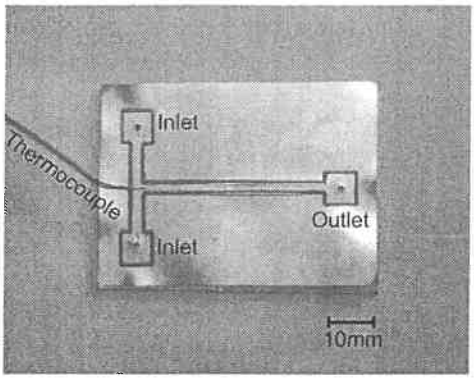

Fig. 1 Photo of the single layer metal micro-reactor.

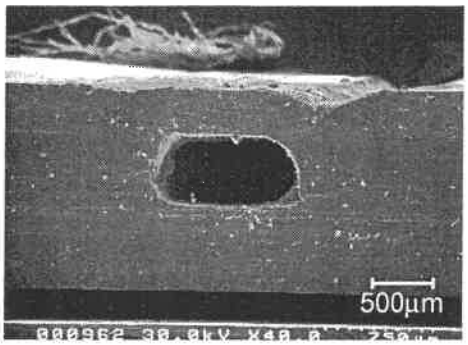

Fig. 2 Cross-sectional view of the substrate welded with the YAG laser.

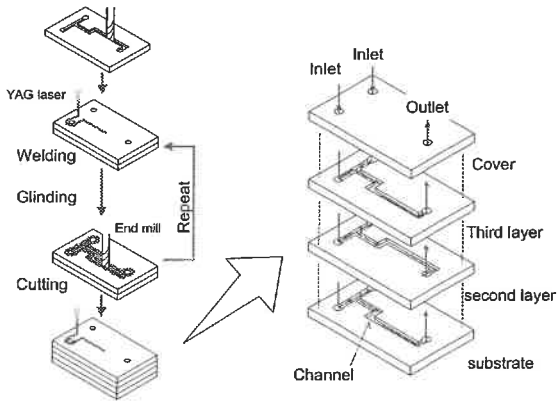

Fig. 3 Configuration of the multilayering process of the micro-reactor repeating cutting, welding and grinding and triple layered micro-reactor.

Furthermore, laser welding can joint 3-dimensional structure. For connection with pipes most micro-reactor use some packings in between, e.g. O-ring or gasket, decreasing the reliability of micro-reactor both mechanically and chemically. For highly reliable connection, we laser welded pipes to our micro-reactor, as like shown in Fig. 5.

3. Experiment

We tested the micro-reactors constructed in the former section by a temperature controlled reaction that mixed the chemicals. The test demonstrated an exothermic reaction with acid, which is nitration of benzene. The reaction progressed mixing 7.5ml of benzene with 15ml of mixed acid (7.5ml of sulfuric acid and 7.5ml of nitric acid). This reaction produces not only the target product nitrobenzene but also by-product dinitrobenzene at over 90 degrees.

We carried out this reaction in different reaction times 10, 30, 120 minutes, with the single layer micro-micro reactor. The micro-reactor was cooled by thermostatic water at 0, 20, 40 degrees Celsius. We also took a reference measurement of the same reaction inside a much larger beaker.

Fig. 6 shows the temperature transition during a 30 minutes reaction at 20 degree Celsius. The graph show that the reaction temperature values were kept at 20 degrees Celsius or less inside the micro-reactor, whereas it went up to 60 degrees in the reference system.

We next analyzed the composition of the products from the micro-reactor and the reference system using gas chromatography. Fig. 7 shows the reactivity and the selectivity of the 30 minutes reaction with different reaction temperature. Reactivity is the proportion of the reacted benzene (nitrobenzene + dinitrobenzene) in the source benzene, and selectivity is that of nitrobenzene in the reacted benzene (nitrobenzene + dinitrobenzene). The graph shows that the micro-reactor produces nitrobenzene only and kept 100% of selectivity while the reference system produced dinitrobenzene with higher temperature. This result means the micro-reactor, performing efficient heat transfer, hampered the temperature rise.

Fig. 8 shows the reactivity and the selectivity at 20 degrees reaction in different time. The graph shows almost the same result as above. These results show that the micro-reactor is effective at keeping reaction temperature or inhabiting the by-product compared with a conventional large beaker, nevertheless the reactivity was inferior.

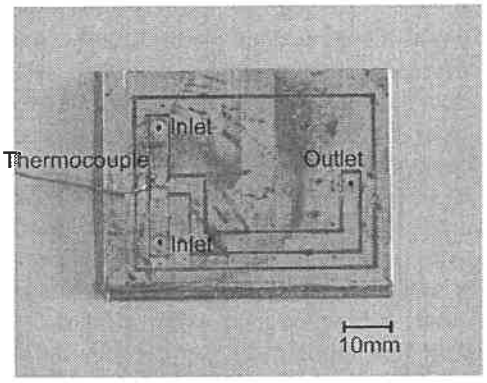

Fig. 4 Photo of the triple-layered metal micro-reactor

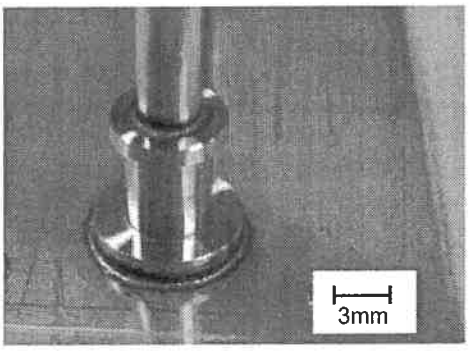

Fig. 5 Laser welded joint between the micro-reactor and the pipe.

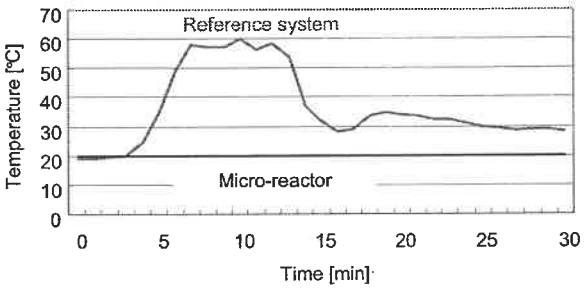

Fig. 6 Temperature transition during 30 minutes reaction, in 20°C thermostatic water.

At last, we executed the same reaction with triple benzene and mixed acid by the triple-layered micro-reactor. Fig. 9 shows the reactivity and the selectivity of the 30 minutes reaction with different reaction temperature. The graph shows both the reactivity and the selectivity decrease, compared with single layer micro-reactor. The low selectivity could be caused by accumulation of heat in the internal channel. Also, the low reactivity derived from unequal distributions of the benzene and mixed acid to each micro-channel, causing the reaction to be out of balance.

In order to improve the multilayered micro-reactor performance, a better branch channel which allows equal distribution of reagents, have to be create, and coolant channels have to be integrated to the micro-reactor for more effective heat exchange, in future.

4. Conclusions

We developed a multilayered metal micro-reactor, for mechanical reliability of the structure and highly efficient for thermally controlling reagents in chemical synthesis.

We found the optimum laser welding condition of laser output at 9.8W and irradiation time of 10msec for multiple layers of 300-micrometer stainless steel, and prototyped a triple-layered micro-reactor

To test the micro-reactors we executed an experiment of nitration of benzene demonstrating an exothermic reaction with acid. The result shows that the micro-reactor has an excellent selectivity with no by-product, nevertheless the reactivity was inferior compared with a conventional beaker system.

References

[1] K. Kusakabe, J. of Chem. Eng. of Jpn, Vol. 35, No. 9, pp. 914-917, (2002).

[2] Y. Murakami, Eelectrochemistry, Vol. 68, No4, 294 (2000).

[3] M. Fujinami, Micro Total Analysis Systems 98, pp. 339-342 (1998).

[4] T. Ooi, Micro Total Analysis Systems 2002, pp. 121-123 (2002).

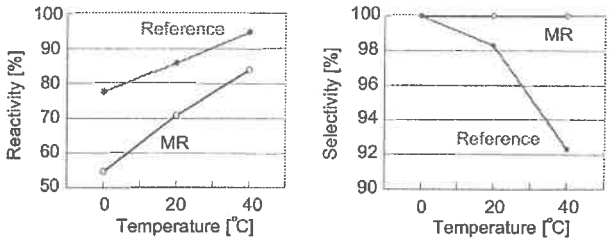

Fig. 7 Reactivity and selectivity of the 30 minutes reaction by the micro-reactor (MR) and the reference system at different temperatures.

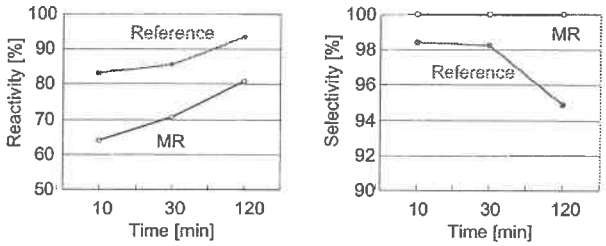

Fig. 8 Reactivity and selectivity of the 20°C reaction by the micro-reactor (MR) and the reference system in different reaction times.

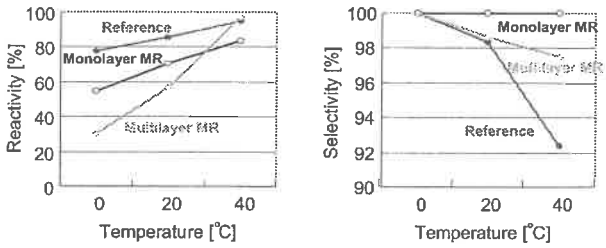

Fig. 9 Reactivity and selectivity of the 30 minutes reaction by the single layer MR, the multilayered MR and the reference system at different temperatures.

Influence of the Electrical Conductivity of Dielectric Fluid on WEDM Machinability

Chang-Ho Kim
Dept. of Mechanical Engineering, Dong-Eui University, Gaya-2 Dong, Pusanjin-Gu, Pusan, 614-714,Korea URL: *www.deu.ac.kr* e-mail : *chkim21@deu.ac.kr*

ABSTRACT: In wire-electrical discharge machining (WEDM), The dielectric plays an important role as the working fluid. During machining, the melted material by heat is dispersed into dielectric. The presence of minute metal particles (gap debris) contaminates dielectric fluid. It affects the material removal rate and properties of the machined surface because it exists in the spark gap between work and electrode. This work deals with the effect of the electrical conductivity of a dielectric fluid on the metal removal rate and surface quality by WEDM. The specimens are three types of sintered carbides and a low-carbon steel. Experimental results show that increasing the fraction of cobalt in carbides improves the metal removal rate, but the surface quality is degraded as a greater quantity of solidified metal deposits on the eroded surface. Lower electrical conductivity of the dielectric results in a higher metal removal rate as spark gap reduced. The debris, the surface characteristics of material and wire electrode were also analyzed through scanning electron microscopy (SEM) and surface roughness tester.

Key words: electrical conductivity of dielectric, cobalt fraction of sintered carbide, wire electrical discharge machining, offset

1 INTRODUCTION

Wire EDM(WEDM) has been an important nontraditional machining process, and regarded as a reliable and flexible machining method, due to its capability of machining any material with electrical conductivity more than 0.01μS/cm.

WEDM is a numerically controlled, modified EDM technique where the work geometry is generated by a NC-controlled traveling wire. A CNC WEDM machine can generate almost any 3-D intricate parts at a considerable cutting speed with a new wire electrode and generator. Further, the method is applicable to an extensive variety of work materials including hard alloys, PCD, CBN and silicon wafers.

In WEDM, the erosion mechanism has been described as melting and/or evaporation of the surface material by the heat generated in the plasma channel.

S. Banerjee et al proposed three dimensional transient temperature distribution and crater formation of the wire during a single discharge period in the electrical discharge machining process by an explicit finite-difference model.

Usually some extra repetitive finish cuts along the contour of a previous rough cut are necessary, done by offsetting the wire by a small amount, to obtain the specified accuracy and a good surface quality. The finish cut is a side-cutting process, which uses a smaller offset value and lower electrical energy.

The surface eroded by EDM is of random nature. Therefore, the study of the surface is to be done not only from metallurgical aspects but also from the point of view of its topography. In EDM process, the thermal expansion is generated intensively in the vicinity of discharge point.

2 DIELECTRIC

The dielectric has several functions including insulation, ionization, cooling, and removal of waste metal particles. As the voltage builds up, the water ionizes and becomes a conductor. After the spark, which develops tremendous heat, the water becomes coolant, and flushes away the eroded material. Wire EDM uses high-pressure flow of the water dielectric to wash away the debris. The water exits a nozzle at pressure up to 300 psi to surround the cutting wire and flush away the eroded material.

When dielectric oil breaks down, electrons move towards the anode under the electric fields from the no-load potential. These electrons collide with neutral atoms producing many positive ions and electrons that move across the channel toward the cathode and anode respectively. The plasma channel is short about 10 ㎛. If kerosene is used, the number of sparks is initially small, but is increased as the metal debris diffuses into the channel. Since deionized water does not have free electrons, this phenomenon does not occur in the same manner as above.

The electrical conductivity of water is expressed to measure its current value and is related with specific

resistance of its own(Ω cm). The water used is collected into dirty tank and metal particles of it are filtered out through filter cartridge unit. The conductivity of the filtered water is controlled automatically through ionic exchanger unit according to the conductivity designated by operator.

The electric field is now given by the quotient of the applied voltage divided by the electrical gap. The electrical gap is defined, by opposition to the mechanical one, by the part-electrode distance(μm) minus the local mean debris diameter[3]. These debris are due to the contamination.

$$E(x,y)=\frac{U}{Gap(1-contamination(x,y))}$$

where, U is the applied voltage.

This paper deals with the results of a series of WEDM tests carried out on various cemented carbides having different percentage of cobalt present in tungsten carbides(GT10, GT20, GT30), and a low-carbon steel(S25C). The aim of these tests is to evaluate the machinability and other characteristics of those materials due to the variation of the electrical conductivity of dielectric.

3 EXPERIMENT

3.1 Machine

The experiments were conducted using a Robofil 220 CNC wire cutting machine from the Charmilles Co.(Swiss). As listed in table 1, the wire electrode used was zinc-coated brass(Cu: 65, Zn: 35%) wire, 0.25mm diameter.

Table 1 Chemical composition of sintered carbides

Items / Carbide	Chemical composition (%)		
	Co	TiC + TaC	WC
GT 10	6	-	94
GT 20	12	3	85
GT 30	15	3	82

Table 2 Chemical composition of low-carbon steel (S25C)

Chemical composition(%)								
C	Si	Mn	P	S	Ni	Cr	Mo	Fe
0.28	0.26	0.66	0.05	0.06	0.10	0.12	0.04	remants

3.2 Experimental procedure

The WEDM process consists of one rough cut and four successive finish cut operations, varying machining conditions according to machine-manufacturer's operating manual. Cutting conditions for the experimental procedures are shown in table 3.

Table 3 Cutting conditions

Items		Kinds
Workpiece (thickness = 5mm)		3 sintered carbides (Co 6, 12, 15%)
		Low-carbon steel(S25C)
Wire	material	Zn coated CuZn35 brass
	feedrate	60 mm/sec
	diameter	0.25 mm
Cutting regime		A) Rough cut B) As A+ fine shaping C) As A + surface semi-finishing D) As A + surface finishing E) As A + surface micro finishing
WEDM machine		Robofil 220 (Charmilles Co., Swiss)
Dielectric		Deionized water, Electrical conductivity : 5, 10, 15,20μS/cm

4 EXPERIMENTAL RESULTS AND DISCUSSION

We analyzed the machinability and surface characteristics of workpieces used in the WEDM test. Data were gathered on each material relative to the electrical conductivity, removal rate and surface roughness parameters. To analyze the machined surface characteristics of workpieces, they were molded into epoxy, ground with diamond wheels and polished with diamond paste.

Roughness and topography were measured by the aid of surface roughness tester(Tallysurf-120L, Tallyhobson Co.) on a measuring length of 4.0mm and a cutoff length of 0.8mm.

4.1 Material removal rate and surface roughness

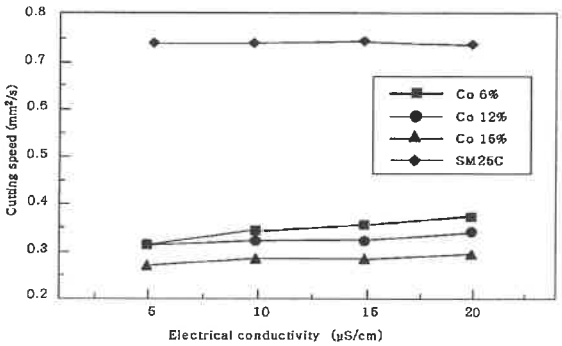

Fig. 1 Electrical conductivity and cutting speed

Fig. 1 shows the average cutting speed for rough

cutting as a function of electrical conductivity of dielectric. Higher electrical conductivity of dielectric yields a higher removal rate. The reason for this is that finely dispersed waste particles make it possible for ionization channels to build up more rapidly. When the spark progresses through the water towards the workpiece, it may encounter pieces of ejected material. This debris can improve process stability, probably by the reduction of arcing frequency, but too much debris in a spark gap is generally believed to be the cause of arcing.

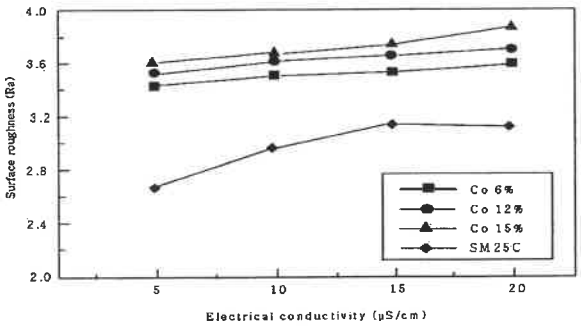

(a) Rough cutting

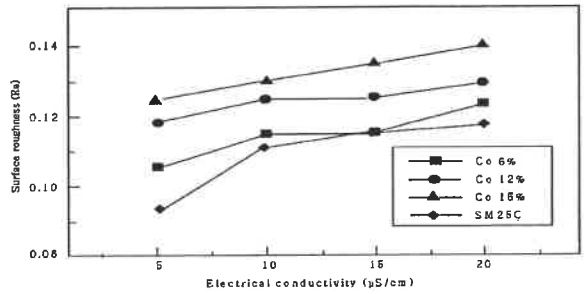

(b) Finish cutting

Fig. 2 Relationship between electrical conductivity and surface roughness

Fig.2 shows the surface roughness for rough cutting and four finish cuts for workpieces. In case of sintered carbides, these graphs show that lower cobalt content decreases the surface roughness. They also show that the surface roughness after roughing and three or four finish cuts is independent of cobalt content. With a high Co-content, the final surface quality is worse because a greater quantity of solidified metal deposits on the eroded surface.

4.2 Surface Characteristics

The rough-cut surface of a workpiece, GT-10 (WC 90%, Co 10%) was analyzed with EDS as shown Fig.3. This figure suggests that a certain amount of wire material gets deposited on the workpiece surface. There 2.18 % of copper can be seen, coming from the wire material. This means that the transfer of wire material (Cu, Zn) to the workpiece occurs during normal sparking.

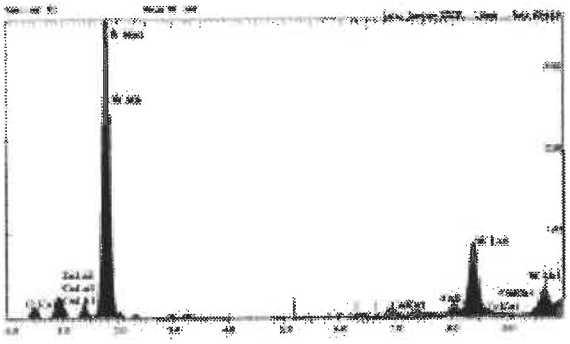

Fig. 3 X-ray diffraction pattern from rough-cut surface of sintered carbide(WC 90%, Co 10%, electrical conductivity of dielectric 20μS/cm)

And it is considered that the cutting surface consists of cleavage planes sometimes contaminated with Cu and Zn.

The surface eroded by EDM is of random nature. Therefore, the study of surface is to be done not only from metallurgical aspects but also from the point of view of its topography. The surface of material generated using WEDM is composed of many microscopic craters associated with the random spark discharge.

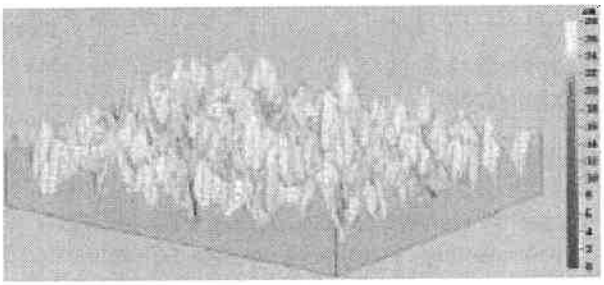

(a) by rough cutting

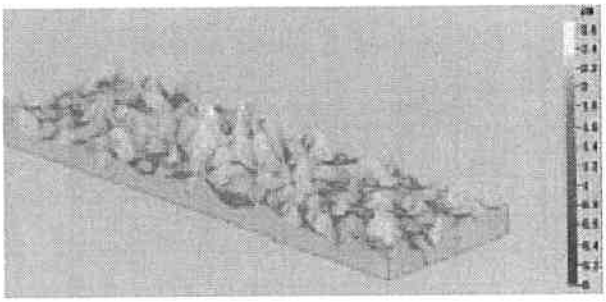

(b) by finish cutting (6th cutting)

Fig. 4 Surface topography of WEDMed sintered carbide (Co 16%, electrical conductivity of dielectric 20μS/cm)

WEDM topographies are presented in Fig 4 by surface roughness tester (measuring length of 4.0 ㎜, interval of 0.05 ㎜ and a cutoff length of 0.8 ㎜), the crater structure with their high peaks adjacent to valleys of removed material is clearly evident. Fig 4(a) shows that the rough

cutting leaves a large crater having large diameter and depth in random location. The size of the craters produced on the workpiece surface depends mainly upon the energy of the discharge. When successive fine cutting of five times are imposed over the rough surface, many high peaks on rough-cut surface were removed. The height of peak, 4～6 ㎛ was lowered to 0.8～2.4 ㎛ as shown Fig 4(b).

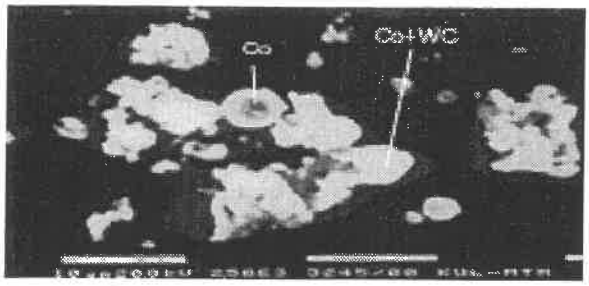

Fig. 5 SEM photograph for debris during rough cutting (WC 88%, Co 12%)

Fig. 5 shows the analyzed debris from the polluted dielectric with EDS. Molten mixture of WC-Co and Co of Sintered Carbide are detected. Cu and Zn can be found, which means some part of wire electrode material with workpiece are also melted and dispersed into the dielectric during machining.

The presence of minute particles in insulating liquids drastically lowers the breakdown strength of dielectric. Evidently, gap debris facilitates ignition process and increase gap size. According to these observations and knowledge, debris can improve process stability probably by the reduction of arcing frequency. Small gap size (approximately 5-30 ㎛)is often considered a cause for the instability since debris evacuation could be blocked. In accordance with a traditional strategy to avoid arcing, the main cause for an unstable process, gap size should always be increased to evacuate more debris.

5 Conclusions

The following conclusions were drawn from the experimental results of WEDM performed on a low-carbon steel and 3 different sintered carbides under variation of electrical conductivity of dielectric fluid.

1) The grade of the cemented carbide has an influence on the machining results. Low cobalt concentration yields a higher removal rate, however the microcracks will be somewhat longer.

2) It is important to have good quality water in the work tank. Higher electrical conductivity of water yields a higher removal rate but poorer surface smoothness. It is recommended that the ideal conductivity vary from 5 to 10 μS/cm to prevent from corrosion and electrolytic wash for fine surface and precision machining.

3) The presence of mixed carbides (TiC, TaC) has no influence on the erosive process. Cobalt wash along edge is present in all alloys.

4) EDS reveals that some of the wire electrode material from the WEDM gets deposited onto the workpiece surface. Some elements of workpiece material can also be seen on the wire electrode surface during EDM.

Acknowledgement

The research described in this paper was supported by the BK-21 Program of Dong-Eui University, Korea.

References

S.Banerjee, B.V.S.S.S. Prasad, and P.K. Mishra, 1997, "Analysis of Three-dimensional Transient Heat Conduction for Predicting Wire Erosion in the Electrical Discharge Machining Process", J. of Material Processing Technology, Vol.75, pp.134-142.

Ajit Singh and Amitabha Ghosh, 1999, "A Thermo-electro Model of Material Removal during Electrical Discharge Machining Process", Int. J. of Machine Tools and Manufacture, Vol.39, pp.669-682.

G. N. Levy and R. Wertheim, 1988, "EDM Machining of Sintered Carbide Compacting Dies," Annals of the CIRP, Vol.37, No.1, pp.59-62.

T. Magara, K. Kobayashi, T. Yatomi and K.K.B. Hon, 1989, "Micro-Finishing by High Frequency AC Source in Wire EDM," Proc. of the 9th Inter. Symp. Electromachining (ISEM-9), pp. 76-79.

A. M. Gadalla and W. Tsai, 1989, "Electrical Discharge Machining of Tungsten Carbide-Cobalt Composites," J. American Ceramic Society, Vol. 72, No. 8, pp. 1396-1401.

R.E. Williams and K.P. Rajurkar, 1991, "Study of Wire Electrical Discharge Machined Surface Characteristics," J. of Material Processing Technology, Vol. 28, pp.127-138.

F. Maggi, 1991, "Wire Cut Electro-Erosion of Hard Metals," Agie Erosion Technology, April.

M. Storr, 1992, "New Dielectric Medium IONOPLUS IME-MM," Proc. of the 10th Inter. Symp. for Electromachining (ISEM-X), pp. 161-169.

Dunnebacke, George, 1992, "High Performance Electrical Discharge Machining using Water-based Dielectic," Proc. of the 10th Inter. Symp. for Electromachining (ISEM-X), pp. 161-169.

Y. F. Luo, 1997, "The dependence of interface discharge transitivity upon the gap debris in precision electrodischarge machining," J. of Material Processing Technology, Vol.68, pp.121-131.

Chang-Ho Kim and Jean Pirre Kruth, 2001," Influence of the Electrical Conductivity of Dielectric Fluid of Sintered Carbide, KSME International Journal Vol. 15, No. 12, pp. 1676-1682.

Manufacture of a spatial light modulator integrated directly on CMOS: Development of a planarized CMOS-MEMS interface

Jin Hong Kim and Thomas Bifano
Boston University College of Engineering

Technological feasibility of a new kind of spatial light modulator (SLM) is demonstrated. The core innovation is the use of a multi-segment, micromachined mirror array fabricated on a complementary metal-oxide semiconductor (CMOS) electronic array. A low-temperature microfabrication process was developed to permit fabrication of the microelectromechanical system (MEMS) on the CMOS electronics wafer. Key aspects of this work – planarization of the interface and interconnection between the MEMS to CMOS – are presented here.

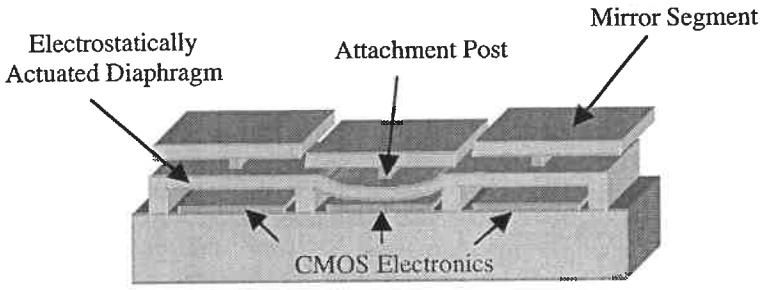

Figure 1: Cross-sectional schematic of three elements in a micro-machined spatial light modulator (μSLM). Electrostatic actuators provide high precision gray scale piston motion to an array of segmented micromirrors

In the proposed low temperature MEMS fabrication process, patterned thin layers of structural and sacrificial materials are be built up on a substrate through sequential deposition and lithography. Ultimately, the sacrificial layers are etched away, leaving a self-assembled, integrated opto-electromechanical device. Each individual pixel (phase modulator) in the device can be controlled using an underlying array of CMOS electronics. Electrostatic actuation holds considerable promise for SLM shape control because it offers nearly reversible (i.e. low power) actuation, no hysteresis, several micrometers of stroke, and nanometer-scale precision and repeatability.

The principal objective of our research was to demonstrate feasibility of a new class of spatial light modulator based on surface micromachining. Challenges associated with the proposed work included using advanced modeling tools for the design of mechanical structures and electronic drivers, integration of a thin-film metal micromachining process with a commercially available CMOS fabrication process, and development of process technology to relieve residual stresses in the fabricated device.

Highlights of this work include:

- A low temperature fabrication technology for μSLM structures was developed using polyimide sacrificial layers and aluminum alloy structural layers.
- Actuator arrays were manufactured with acceptable electromechanical performance in array sizes of up to 150 x 150.
- A CMOS electronics driver array was manufactured using commercially available foundry fabrication
- Successful process integration included overcoating CMOS chips with silicon nitride, planarizing and polishing the overcoat layer, etching and filling via holes in the overcoat layer.

The baseline design for the metal SLM is illustrated in Figure 1. Each pixel is made up of three main components: 1) electrodes, 2) actuator, and 3) mirror, shown in Figure 1. As illustrated in Figure 2b, the electrodes consist of four concentric pads, each of which has double the area of the neighboring interior electrode. Therefore, if the smallest center electrode, E1, has area A1, then electrode E2 has a total area of 2A1, electrode E3 has an area of 2A2=4A1, and electrode E4 has an area of 2A3 = 4A2=8A1. This electrode layout will allow the 16-level control of the actuators. Small vias connect individual electrodes with the underlying CMOS driver.

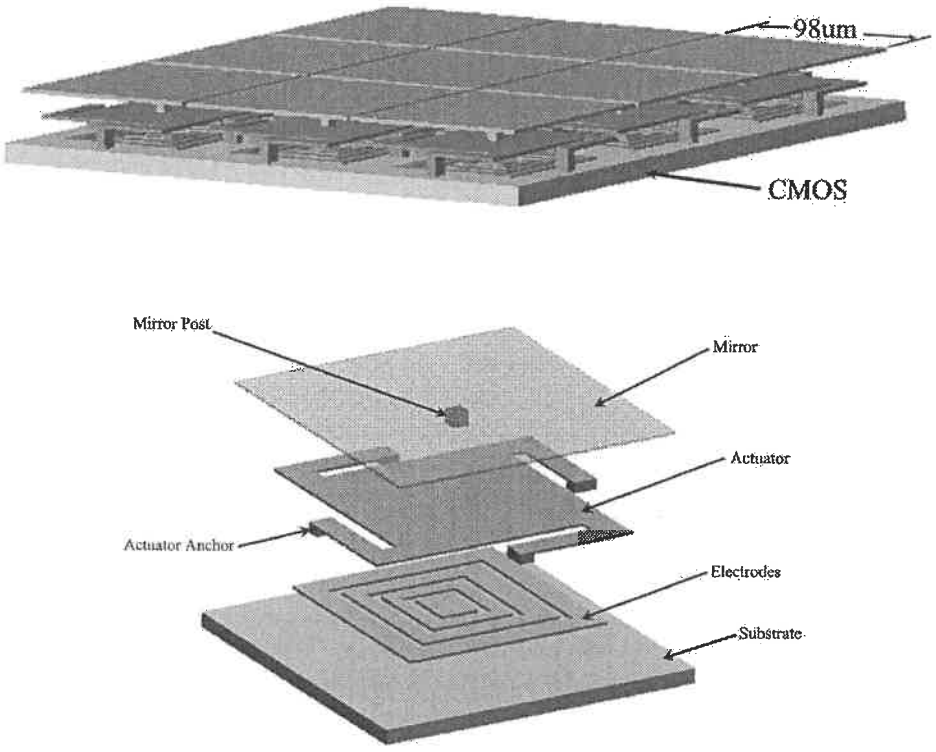

Figure 1. Top - Schematic of 3 x 3 micro-fabricated spatial light modulator. Bottom - Single μSLM pixel illustrating the three main components of the device.

Centered directly over the electrodes is an actuator made up of a square membrane supported by four flexures on each side. The membrane area is the equal to the total area available for

the four underlying electrodes to maximize the electrostatic force exerted by the electrodes on the actuator – the effective area is reduced from the maximum available area by the lateral gaps between the electrodes. The membrane perimeter corresponds with the outer perimeter of the largest electrode to maximize the electrostatic force.

The μSLM is made up of an array of identical pixels, placed on a pitch of 100μm. The pitch determines the maximum pixel size and constrains the maximum size of the CMOS drive electronics, the available electrode area, the actuator layout, and the mirror size. The segments are manufactured on top of the actuator and each segment is attached to an actuator by a small post located in the center of the actuator membrane and the mirror surface.

Due to the existence of multi-layer repetitive deposition and etching processes during CMOS electronics fabrication, the surface of the CMOS electronics is not flat. This surface topography limits the usefulness of CMOS substrates for direct integration with MEMS structures for the μSLM. To meet the requirements of uSLM, the array should have RMS flatness of each segment area of ~30nm. To flatten this surface, a layer of silicon nidride (Si_3N_4) was deposited by Plasma Enhanced Chemical Vapor Deposition (PECVD) on the CMOS surface. The layer is polished, and then vias are etched through it to interconnect the MEMS electrodes and CMOS electronics. Using RF sputtering, vias are filled with aluminum, and then aluminum electrodes are patterned with lift-off process. Figure 2 illustrates the schematic of overall planarization process.

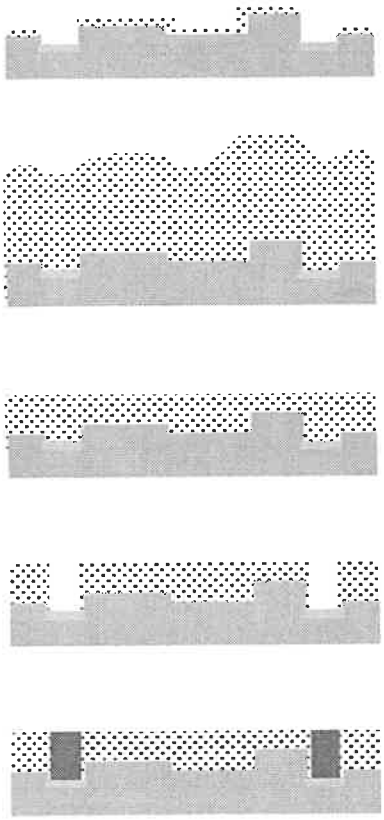

Foundry-delivered CMOS chip exhibiting severe topography.

Dielectric layer (Si_3N_4) is deposited up to 4um thick using Plasma Enhanced Chemical Vapor Deposition (PECVD)

Dielectric layer is planarized using Chemical-Mechanical Polishing

Dielectric layer is patterned and etched to expose metal vias

Etched vias are filled with metal (aluminum) to prevent Print-through during further fabrication process

Figure 2: Schematic of planarization and via-fill processes

Layers of 4um thick Si_3N_4 were deposited on CMOS chips using PECVD by Surmet Corporation. Process temperature was less than 100°C, and thickness variation was measured at ±10%. No visible pinholes and cracks are appeared after planarization process (Figure 3).

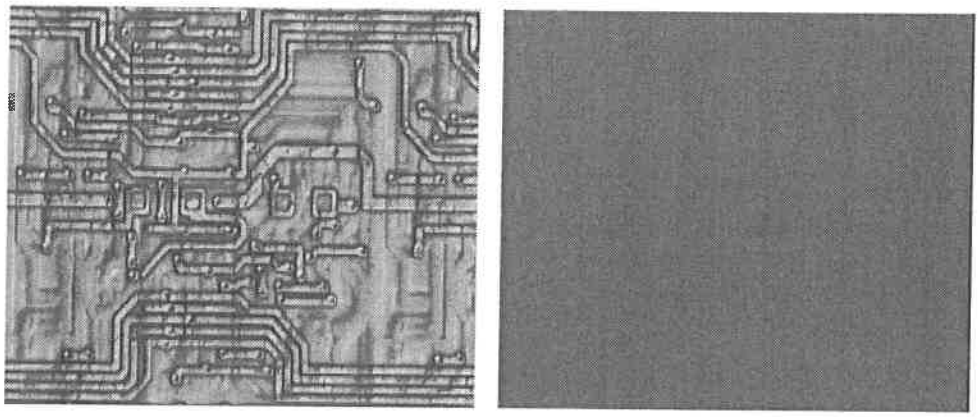

(a) (b)

Figure 3: Planarized CMOS electronics. (a) Chip with 4um thick PECVD Si_3N_4 coating (b) Planarized CMOS surface, free of pinholes or cracks.

Nitride-coated CMOS chips were subsequently planarized with conventional CMP techniques. CMOS chips were bonded onto a 3.5inch (89mm) diameter, 0.25inch (6.4mm) thick glass substrate. Double-sided coated PSA (Pressure Sensitive Adhesive) tape was used for mounting. To distribute downward pressure during polishing, eight balancing pieces (5 x 5mm silicon pieces) were mounted onto the glass polishing block. Each balancing piece was coated with Si_3N_4 film to match the surface composition and polishing properties of the CMOS chip that was mounted centrally on the glass polishing plate. During the planarization on a commercial polishing apparatus, the glass plate was preloaded by a pneumatic actuator. Slurry was delivered on top of the pad surface with automatic feeder system.

Samples were polished with 30nm grain size colloidal silica slurries (Levasil 45/100, Universal Photonics, INC.) until the desired surface topography was achieved. The polishing pad (ESM-U, Universal Photonics INC.) is covered on top of the cast iron plate during polishing. There are five dominant adjustable parameters to the polishing process; downward pressure on holder, rotating speed of the pad, frequency of the reciprocating arm, amount of offset from the pad's center, and holder's travel distance. Parameter optimization was performed using a fractional factorial experimentation approach.

Polishing is performed for about 60min until the desired surface topography (30nm overall) was achieved. Initial flatness of >500nm RMS before planarization and polishing was reduced to <20nm RMS after planarization and polishing.

A Study on the Material Removal Mechanism in EDM
- Single Discharge Experiments with Low Melting Temperature Alloy -

Hirotaka KOKUBO*, Hideki TAKEZAWA**, Ken'ichiro HORIO*, Naotake MOHRI***, Tsugio YAMAZAKI*
* Saitama University, 255 Shimo-okubo, Sakura, Saitama, 3388570, Japan
** Kogakuin University, 2665-1 Nakano, Hachioji, Tokyo, 1920015, Japan
*** The University of Tokyo, 7-3-1 Hongo, Bunkyo, Tokyo, 1138656, Japan

1. Introduction

EDM (electrical discharge machining) is one of advantageous methods to shape very hard materials into complicated form. In EDM, material is removed due to accumulation of a very small crater generated on surface by heat energy of single discharge. In order to fundamentally elucidate mechanism of material removal in EDM, it is necessary to clarify mechanism of the single discharge. It has been reported that craters formed on carbon steel (AISI-1049) or brass by the single discharge are small and they have complicated shapes [1]. It is considered that melting point of these test materials are so high that few volume is removed from test piece in the single discharge. Because the heat energy of the single discharge is very small. Therefore, it was difficult to directly investigate the mechanism of the material removal from these small craters. In this paper, we use low melting temperature alloy (LMTA, melting point 47 degrees Celsius). It is expected that large amount of volume is removed by the single discharge to the LMTA. We observe craters on the LMTA and investigate its removed volume, changing pulse duration, polarity of electrode, dielectric fluid and electrode diameter. We also investigate debris of the LMTA. Based on these experimental results, we discuss the mechanism of material removal in EDM.

2. Single Discharge Experiments on the LMTA

Table1 shows experimental conditions. We developed power circuit to achieve the single discharge. Fig.1 shows typical SEM images of craters and cross sections under the condition using kerosene oil. The shape of the crater formed on the LMTA is close to a part of sphere as shown in Fig.1 (a). On the other hand, the shape of the crater formed on the carbon steel (AISI-1049) has complicated shape as shown in Fig.1 (b). Fig.2 shows relationship between the pulse duration and diameter (D in Fig.1 (a)) of the craters formed on the LMTA. Fig.3 shows relationship between the pulse duration and depth (H in Fig.1 (a)). Fig.4 shows relationship between the pulse duration and the removed volume calculated from the diameter and the depth. The diameter increases according to the pulse duration under all conditions. Although it is considered that molten volume by heat energy of discharge increases according to the pulse duration, the removed volume decrease over 200μs pulse duration due to the shallow depth under the condition using negative polarity of electrode and the kerosene oil. In the conventional studies, it was estimated that a part of molten material is blown off by movement of a bubble generated in the dielectric fluid and the rest of them leaves as the resolidified layer [1]. Therefore, in regard to the results of the LMTA, we can estimate that the resolidified layer remains under the craters.

3. The Cross Sections of the Craters on the LMTA

In order to make sure of existence of the resolidified layer, we conduct experiments to observe the cross sections of the craters on the LMTA. Fig.5 shows experimental procedure. In the first step, two workpieces are adhered into together. In the second step, single discharge is carried out on the adhesive line between the two workpieces. After that, we divide the adhered workipiece into two parts again and observe the cross sections. Fig.6 shows typical SEM images of the cross sections under the condition using the kerosene oil. The resolidified layer remains under the craters when the pulse duration is 200μs or 400μs. Fig.7 shows relationship between the pulse duration and

Table.1 Single discharge conditions

Electrode	W (ϕ 0.1mm), polarity : (-), (+)
Work piece	Low melting temperature alloy (LMTA) Carbon steel (AISI-1049)
Open voltage	100V
Current	20A
Pulse duration	25, 50, 100, 200, 400μs
Dielectric fluid	Kerosene oil, De-ionized water

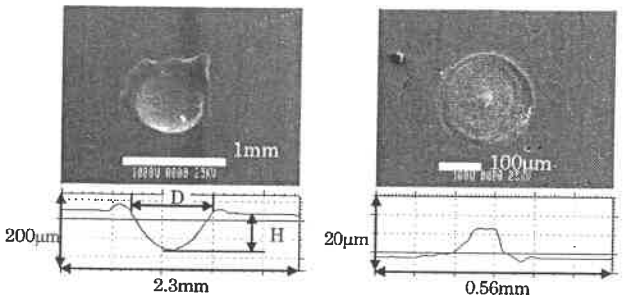

(a) LMTA (b) AISI-1049

(Kerosene oil, Electrode:−, I_e:20A, t_i:200μs)

Fig.1 SEM images of the craters and cross section profile

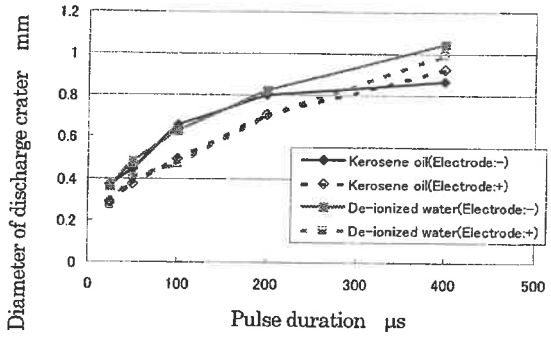

Fig.2 Relationship between pulse duration and diameter of discharge crater

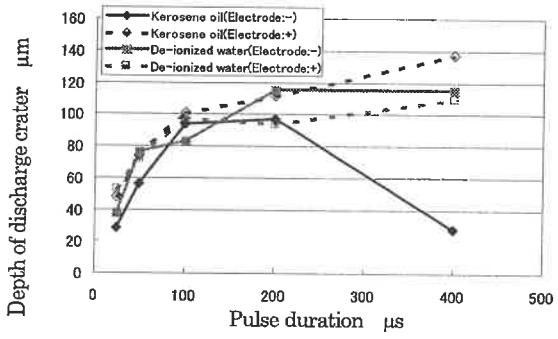

Fig.3 Relationship between pulse duration and depth of discharge crater

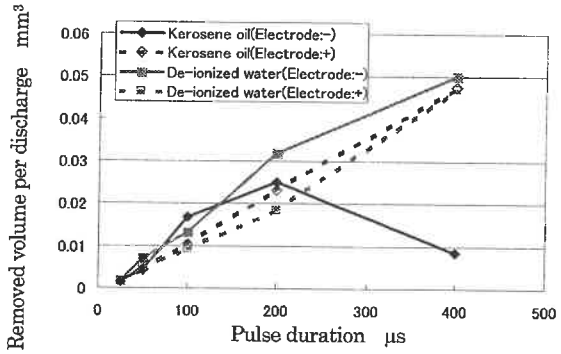

Fig.4 Relationship between pulse duration and removed volume per discharge

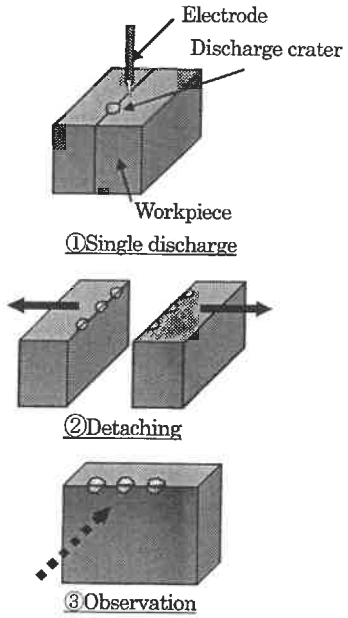

Fig.5 The observation method of cross sections of craters

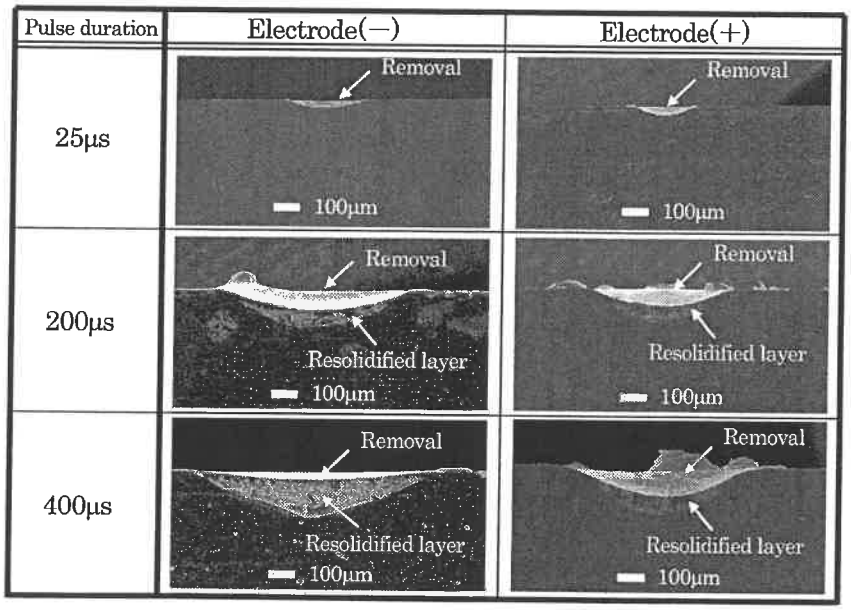

(Kerosene oil, I_e : 20A)

Fig.6 Cross sections of the craters

the removed or molten volume under the negative polarity in the kerosene oil. Under this condition, the volume of the resolidified layer increases according to the pulse duration as shown in Fig.7. Fig.8 shows relationship between the pulse duration and the removed or the molten volume under the positive polarity in the kerosene oil. The volume of the resolidified layer does not increase extremely. In de-ionized water, the volume of the resolidified layer shows the same tendency as Fig.8. If the time required for all molten part to be resolidified is same under the all conditions, we can estimate that timing of the material removal is late only under the positive polarity in the kerosene oil.

3. The Debris of the LMTA

The debris of the LMTA is expected to involve information regarding the timing of the material removal and molten state at that time. So, we conduct the experiments to observe of the debris. Fig.9 shows SEM images of the debris of the LMTA under the condition using the kerosene oil. Fig.10 shows shapes of the each debris. The debris consists of a lot of spherical debris and some non-spherical ones over 100μm long. It is considered that the debris become spherical when the temperature of the molten part is high at the moment of removal, on the contrary, the debris become non-spherical when the temperature of the molten part is low at the moment of removal. Fig.11 shows relationship between the pulse duration and number of the non-spherical debris per unit removal volume. Under the negative polarity in the kerosene oil, the number of the non-spherical debris increases extremely at 400μs pulse duration. Considering increase of both the resolidified layer and the non-spherical debris under the negative polarity in the kerosene oil, we can estimate that the material is removed after the temperature of the molten part drops around melting point, and most of the molten part is resolidified. The reason that the number of the non-spherical debris is much more under the positive polarity in de-ionized water than the other conditions has not been cleared yet.

4. Effect of Electrode Diameter

The maximum diameter of the bubble generated in the dielectric fluid by single discharge is a few millimeters [2]. It is considered that electrode of 0.1mm in diameter is so thin that effect of the bubble on the material removal decrease. In order to investigate the effect of the electrode diameter, we conduct single discharge experiments using tungsten electrode of 3mm in diameter under the negative polarity in the kerosene oil. Fig.12 shows the effect of the electrode diameter on the depth of the craters. Fig.13 shows the effect on the removed volume. In the case of using the thick tungsten electrode, the removed volume does not decrease over 200μs pulse duration. We can estimate that the timing of the material removal is fast, or the effect of the bubble on the material removal increases because of large area of the electrode facing workpiece.

5. Conclusions

From the single discharge experiments with LMTA, following results are obtained.

(1) The craters on the LMTA are close to a part of sphere regardless of the polarity of electrode or a kind of the dielectric fluid.
(2) The removed volume generally increases according to the pulse duration. It decreases over 200μs pulse duration only under the negative polarity of electrode in kerosene oil.
(3) The number of non-spherical debris increases when the resolidified layer increases.
(4) It seems that the timing of the material removal is fast, or the effect of the bubble on the material removal increases when the electrode diameter is larger than the bubble diameter.

Acknowledgements

This study is financially supported by the Grant-in-Aid for Young Scientists (B) (14750080) of the Ministry of Education, Science, Sports, and Culture, Japan.

References

[1] E.Capello, L.Filice, F.Micari, M.Vedani:Surface Integrity and Quality Induced by EDM Processes, 13th International Symposium for Electromachining ISEM XIII, (2001) 701.
[2] Takezawa, H., Ito, Y., Mohri, N., "The Behavior of Thin Electrode Wear in Electrical Discharge Machining", 13th International Symposium for Electromachining ISEM XIII, (2001) 727.

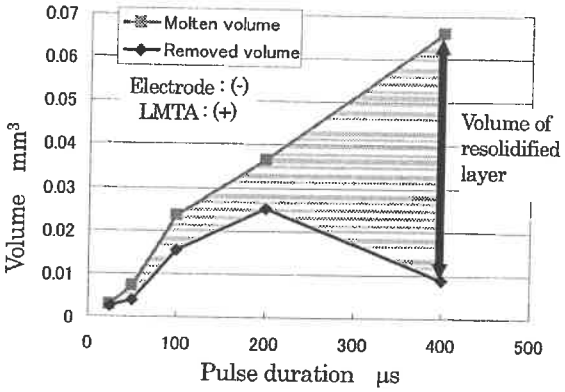

Fig.7 Relationship between pulse duration and removed or molten volume (Kerosene oil, Electrode:—)

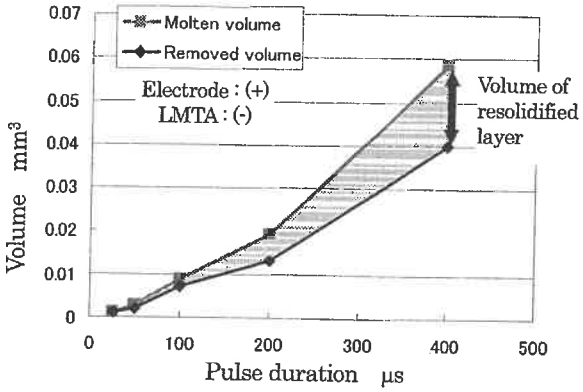

Fig.8 Relationship between pulse duration and removed or molten volume (Kerosene oil, Electrode:+)

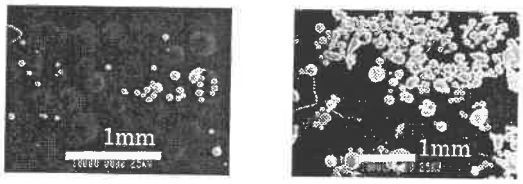

(a) 25μs (b) 400μs

(Kerosene oil, Electrode:—, I_e :20A)

Fig.9 Wide SEM images of debris of LMTA

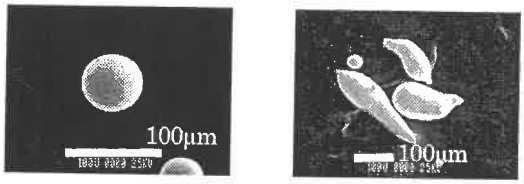

(a) Spherical debris (b) Non-spherical debris

Fig.10 Shape of debris of LMTA

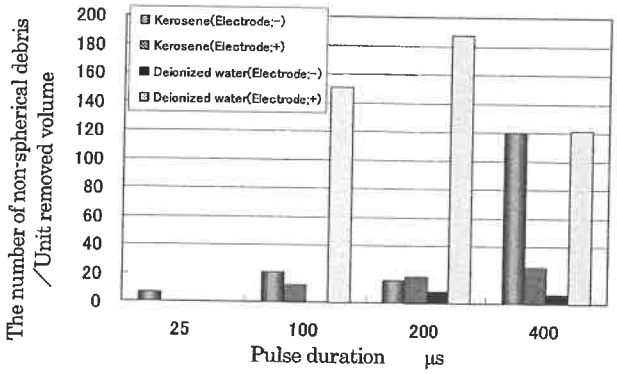

Fig.11 Relationship between pulse durations and the number of non-spherical debris

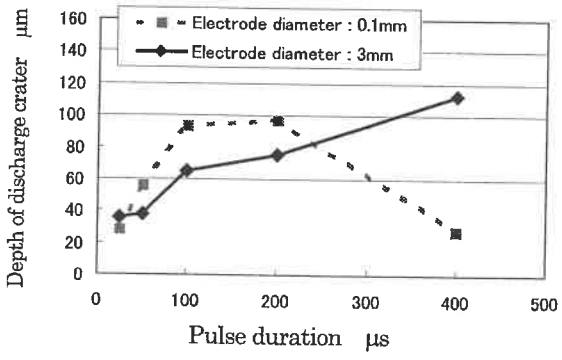

Fig.12 The effect of the electrode diameter on the depth of discharge crater (Kerosene oil, Electrode:—)

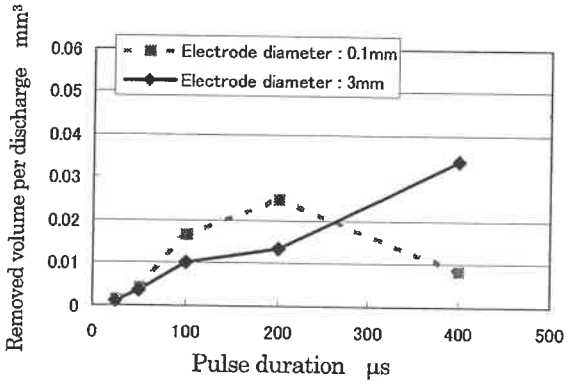

Fig.13 The effect of the electrode diameter on the removed volume per discharge (Kerosene oil, Electrode:—)

MONITORING OF ULTRASONIC VIBRATION MICROMACHINING PROCESS

Nobuyuki Moronuki, Satoshi Saneshima and Yasunori Saito
Tokyo Metropolitan University, 1-1 Minami-Ohsawa, Hachioji, Tokyo 192-0397, JAPAN

1. Introduction

Glasses are preferred as the structural materials for bio/chemical analysis because of its superior stability. However, it is difficult to obtain smooth surface except etching processes. Abrasive jet machining can provide three-dimensional profiles, however, the geometrical accuracy is limited and random factor is introduced because of the fluctuation of the flow of the jet [1, 2]. Ultrasonic vibration machining can also provide deterministic three-dimensional profiles with smooth surface [3]. When the vibration machining is applied to micromachining, the monitoring of the process is essential because not only dose a tiny tool easily break due to slight collision against the workpiece but large chippings deteriorate the finished roughness and generate sub-surface damages. One of the authors has already demonstrated the importance of monitoring using an acoustic emission (AE) sensor [4] and a force sensor [3] as well as the multi-axes tool vibration [5]. Applying appropriate control based on the sensor signal, a tiny tool as small as ϕ40μm can be used without breakage and also tool wear can be compensated [4]. However, the vibration frequency was limited to 20kHz. This paper extends this limitation up to 40kHz and the monitoring of the process during micromachining of glass is discussed to improve the quality.

2. Experimental setup

Figure 1 shows the schematic illustration of the experimental system. A tiny tool, just a cylinder made of sintered carbide, was set at the tip of an ultrasonic resonator (40kHz). The workpiece was set on a three-axis table that was numerically controlled by a PC. A force sensor set beneath the worktable measured the force that acted between a tool and a workpiece. The sensor signal was conditioned with an AC/DC converter or a spectrum analyzer to monitor the machining condition. This configuration enables the detection of tool-workpiece engagement (touch-sense for the reference of the depth of cut) and the process monitoring. Table 1 summarizes the specifications and the typical machining conditions.

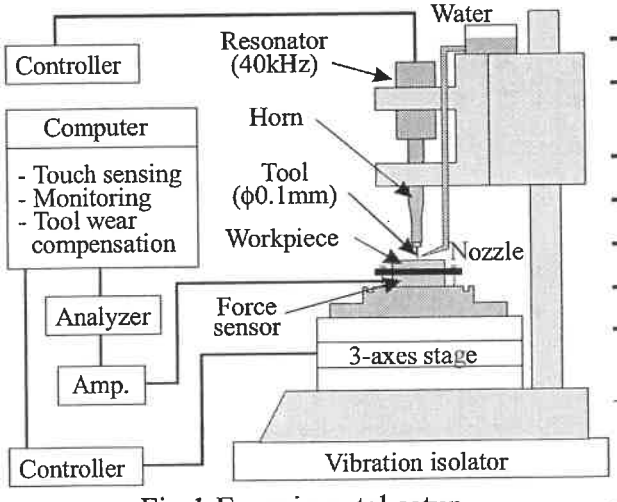

Fig.1 Experimental setup

Table 1 Specifications and conditions

Tool vibration	40kHz, 20μmp-p		
Positioning resolution	X,Y: 0.1μm, Z: 0.05μm		
Tool	Sintered carbide, φ100μm		
Depth of cut (infeed)	5μm		
Feed rate, length	50μm/s, 1mm		
Machining fluid	Pure water		
Workpiece	*E* [GPa]	Hardness [Knoop]	Softening temp.[°C]
Low-melting-temp. glass (Super Vidron®, Sumita)	64.2	352	285 (*Tg*)

Low-melting-temperature glass was used for the workpiece because smooth surface can be obtained with ultrasonic machining [3]. The overall size was 400mm in width, 400mm in depth, and 680mm in height. The experiments were carried out in a clean room (class 10000) where the temperature was controlled at 20°C.

3. Detection of tool engagement

Figure 2 shows the typical force measured during machining. To eliminate the effect of the noise due to electromagnetic interference (EMI), the background signal before machining was subtracted from the monitored signal. It was found that the distortion of sinusoidal waveform could be well observed. However, the first resonant frequency was 5kHz though the bandwidth of the amplifier and other processing equipments were high up to 100kHz, and thus it is difficult to discuss the quantitative value of the force due to the difficulty of calibration.

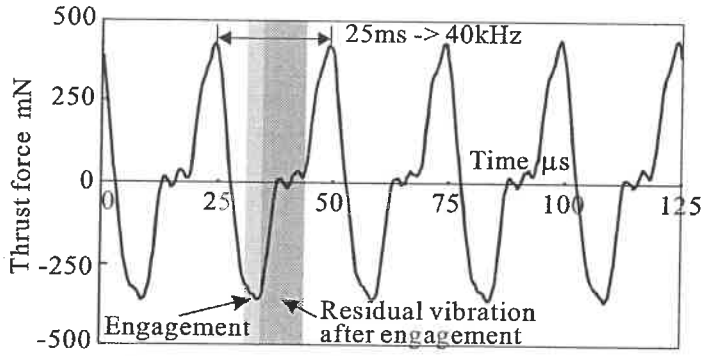

Fig.2 Original waveform of the force sensor

Figure 3 shows the time history of the measured force and the frequency components before and after the machining of 1μm depth of cut. It was found that the amplitude increased when the tool engaged in the workpiece. In addition, the waveform distorted because of the engagement during the partial period of each cycle. The distortion was well monitored with the power spectrum. It was found from Fig.3 (right) that the harmonics components, especially the first harmonics 80kHz, rapidly increased with the engagement. Both of these signals can be used for monitoring during the touch-sensing, the detection of engagement between the tool and workpiece.

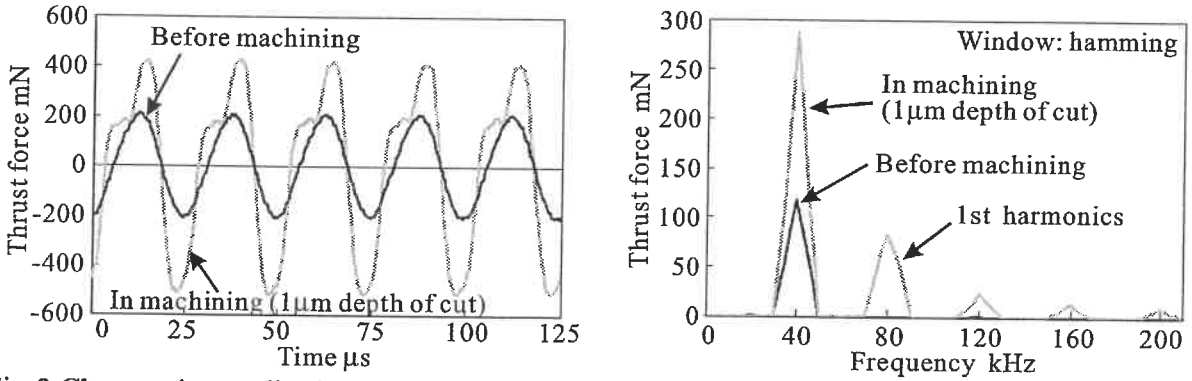

Fig.3 Changes in amplitude (left) and frequency components (right) before and after machining

Figure 4 shows the monitoring signals during the touch sensing process. This process is important to ensure the machining accuracy. The horizontal axis shows the stepwise feed of the

Z-stage and the vertical axis shows the changes in peak-to-peak (P-P) value and RMS of 80kHz components. In this case, at 0.9μm, the tool engaged in the workpiece. At this point, the P-P value rapidly increased with the increase in position Z. Also, the RMS value rapidly increased from zero to 4mV in this case. It is not easy to determine which of these is suitable for the detection of tool engagement because the signal to noise ratio (S/N ratio) has not been evaluated. However, it was confirmed that the repeatability was good as less than 0.1μm.

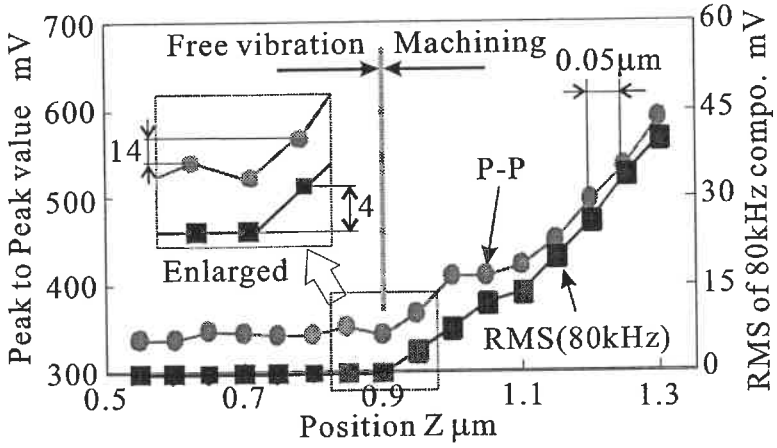

Fig.4 Touch sensing between tool and workpiece

4. Monitoring of the machining process

Figure 5 shows the correspondence between the monitoring results during the grooving process and the microscopic observation. The nominal depth of cut was 5μm, however, the actual depth of cut varied from 5μm (left edge) to 6.8μm (right edge) because of the inclination of the worktable. Due to this inclination, the process changed from mild (left) to severe (right) condition and the effectiveness of the monitoring could be well examined.

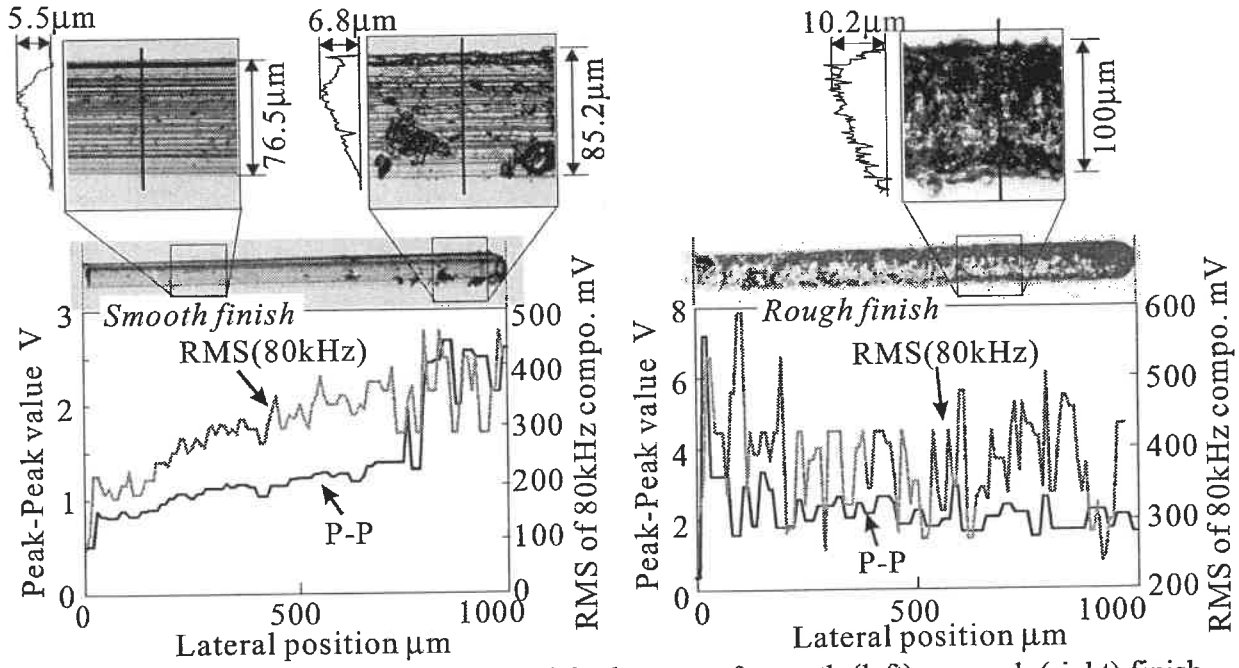

Fig.5 Changes in P-P and RMS (80kHz) in the case of smooth (left) or rough (right) finish

The left side of Fig.5 shows the results of smooth finish and it was found that the fluctuation of both of the P-P value and the RMS value were small, however, at the last part of machining (right end), the fluctuation became large due to the generation of chippings. The right side of Fig.5 shows the severe case in chippings. It was found that the fluctuation of RMS value was larger than that of P-P value of the force. These results suggest the possibility of the detection of chippings through the analysis of RMS value of 80kHz component. Such signal can be used for the adaptive control to prevent the generation of chippings. Actually, in the specific conditions using low-melting-temperature glass as a workpiece, smooth surface as shown in Fig.5 (left) can be obtained and thus the prevention of chipping is crucial [3].

5. Discussion

It was found from the above results that both of the P-P and RMS of the machining force could be used not only for the detection of the tool engagement but also for the monitoring of the process. However, before the actual application, the following items should be considered.

In this paper, the P-P value and RMS value are treated independently. However, any combination of these signals may give further valuable information. For example, any algorithm in sensor fusion should give a hint. In addition, another source such as an acoustic emission (AE) sensor will give additional information and other types of signal processing are also possible such as wavelet analysis.

In the above experiments, the FFT analysis was done with an optional function of the digital oscilloscope and the transmission to the PC was carried out through the GPIB interface. The transmission rate was limited up to 8 samples/s and it was not sufficient for practical use. If the frequency of the importance is fixed, another method can be possible such as the combination of band-pass filter, an AC/DC converter and an A/D converter.

6. Conclusions

A monitoring procedure was proposed for micromachining of glass with ultrasonic vibration tool. The force between the tool and the workpiece was measured and analyzed. The results are summarized as follows:

- Both of the peak-to-peak value and the RMS of harmonics of the thrust force well indicated the condition of the process.
- These signals can be used not only for the detection of the tool engagement but also for the monitoring of chip generation during the process.

References

[1] Belloy, E. et al., Microfabrication of High-Aspect Ratio and Complex Monolithic Structures in Glass, J. of MEMS, 11, 5, 2002, pp.521-527.

[2] Kuriyagawa, T., Syoji, K., Shirosawa, T., Saitoh, O., Development of Micro Ultrasonic Abrasive Machining System. 1st report, JSME Int. Journal. Ser C. Mech. Systems, Mach Elem. Manuf., 45, 2, 2002, pp.593-600.

[3] Moronuki, N. et al., Vibration Micromachining of Low-Melting-Temperature Glass, 7th International Symposium on Advances in Abrasive Technology, 2004, pp.489-494.

[4] Moronuki, N., Brinksmeier, E., Proc. 3rd euspen, 2002.

[5] Moronuki, N., Yoshida, F., Sato, Y., and Kaneko, A., Key Engineering Materials, Vol.257-258, 2004, pp.447-452.

Design and Fabrication of Three Dimensional MEMS Actuators using Diamond Turning and Electroplating Processes

Greg Reimann and Thomas Bifano
Boston University College of Engineering

Diamond turning and electroplating processes have been used to fabricate MEMS structures. This new combination of processes frees MEMS design from the traditional stacks of two-dimensional layers that have constrained the geometry of devices. The devices described in this work consist of a thin film of metal suspended across a trench 500 microns wide and 20 microns deep. Actuation occurs when a voltage is supplied to the membrane while the trench is held at ground. The bottom of the trench is an asphere diamond turned into the substrate and designed to maximize the deflection to voltage ratio of the device without sacrificing stroke. Manufacturing a device with an asphere like this using exclusively traditional photolithography technology is not possible, but the hybrid process illustrated here allows for true three-dimensional structures to be fabricated.

Conventional micromachining consists of additive CVD and PVD processes, lithographic patterning, and chemical etching. Using these processes iteratively generates "extruded" shapes and can approximate three dimensional structures. However, these structures are really only stacks of two dimensional components. As 3D approximations get better and features get higher, the number of steps in the process increases dramatically.

An alternative to this method is to use electroplating for material addition and traditional mechanical machining for material patterning and removal, thereby allowing true 3D structures and reducing the number of process steps needed. This research focuses on using copper electroplating and diamond turning to create MEMS electrostatic actuators with a greater deflection per unit voltage than is achieved by their 2D counterparts.

The process described herein does not entirely eliminate conventional micromachining methods. It is a hybrid of traditional micromachining methods and traditional mechanical machining methods, each used where most appropriate. Future work will aim toward eliminating photolithography entirely, simplifying the process to a series of plating and machining steps. The actuators described in this paper are a first step toward that goal.

The process designed to fabricate this actuator requires four materials. The cross section of an unreleased device is shown below.

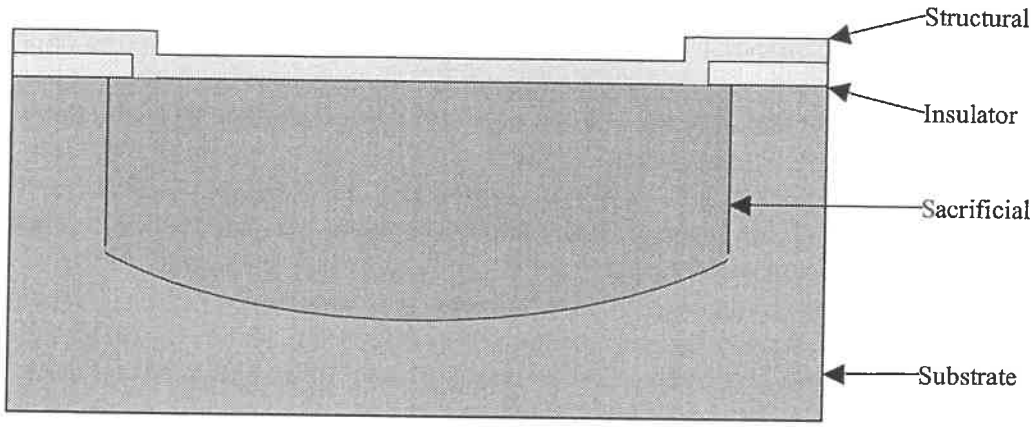

Figure 1 Material Cross-section

The process involves diamond turning the substrate, electroplating the sacrificial layer to fill the trench, turning the sacrificial material back, depositing the insulator and structural materials through PVD, patterning those layers with lithography and chemical etching, and finally, isotropically etching the sacrificial material to release the device.

The substrate material must be diamond turned and then plated. Aluminum was selected because of its machinability. Aluminum is somewhat difficult to electroplate because of the native oxide that forms upon its surface. However, this problem has been overcome by the electroplating industry by first displacing the oxide with a coating of zinc and then displacing the zinc with the plating material. A relatively pure alloy (1100) was chosen because silicon impurities impair the turning process and magnesium impurities complicate the zincating process.

Copper was selected as the sacrificial plating material because it is relatively easy and common material to plate, it is very easily diamond turned, and it does not require a cyanide plating solution. Many of the traditional copper etches, such as Ferric Chloride and Ammonia/Hydrogen Peroxide attack aluminum also. Transene APS-100 and some dilutions of nitric acid have selectivity of copper over aluminum of more than 1000:1.

Silicon Oxide was chosen as an insulating material. Its adhesion to other oxides (ie. Native aluminum oxide) is good, and it is easily sputtered or evaporated. It can be anisotropically etched in a reactive ion etcher and is resistant to all other chemical etches in the process. Aluminum was chosen as a structural layer because it is easily sputtered. Its thin film properties are well understood, and the release chemistry and adhesion properties have already been verified in the process since it is the substrate material.

The structural material choice of thin-film aluminum fixes the modulus of elasticity. Previous work has been done to successfully deposit one micron thick aluminum layers to form MEMS actuators, so one micron was chosen as a thickness to capitalize on that experience.

The diamond turning tool used to cut the trenches in the aluminum substrate rotates in a circular fashion, so the trenches were cut in a circular fashion. This leaves a curved trench on which to put the actuator. Therefore, the actuator size was chosen to be small enough to minimize effects of this curvature, yet large enough to be able to see elements and time etches with the naked eye. A value of 500 microns emerged as both length and width.

A maximum gap (g_0) of 20 microns was selected because it is a reasonable depth to diamond turn, yields reasonable a snap-through voltage of 103 volts, and will allow 6.6 microns of stroke.

With all of these parameters selected, the shape of the fully deflected actuator was modeled. The final shape looks like the following graph.

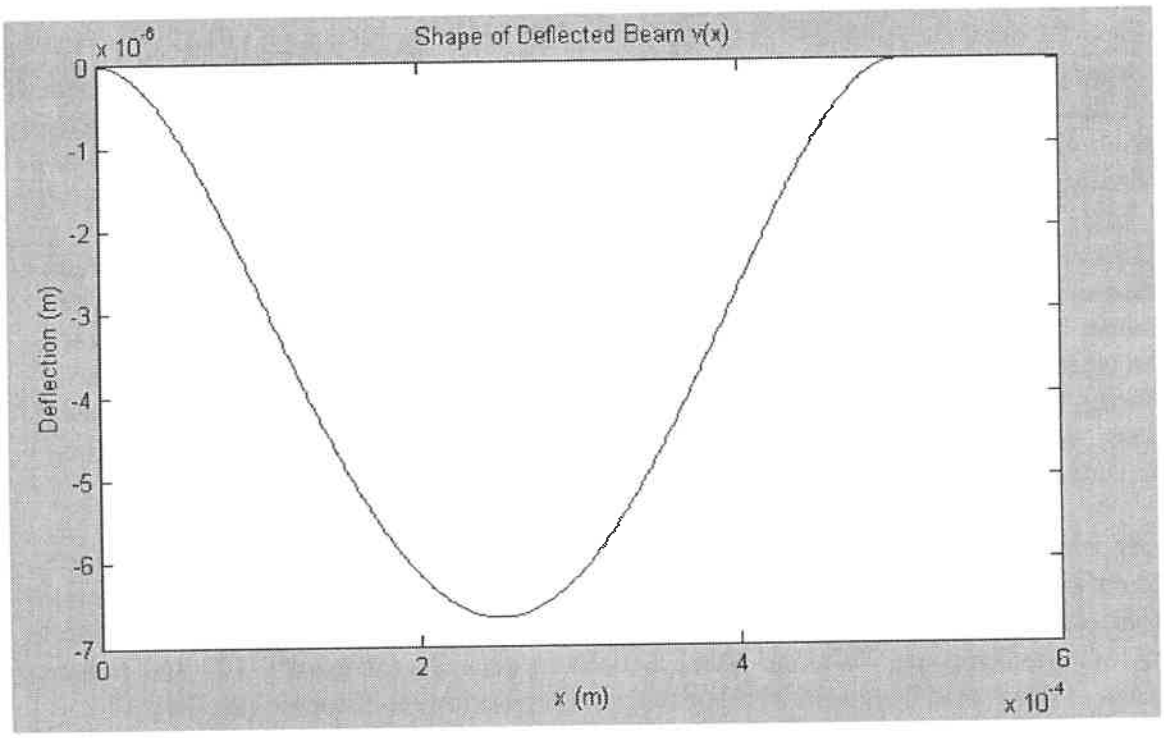

Figure 2: Curve of trench bottom to match maximum deflection

The final circular trench made in the aluminum substrate has 13.3 micron high vertical sidewalls, with a cross section matching Figure 2 at the base.

The multi-step manufacturing process outlined above will permit a new class of ultraprecision machined MEMS structures with improved electromechanical performance. Process integration is currently underway, and test devices should be produced soon.

PERFORMANCE OF ELECTRICALLY CONDUCTIVE CVD DIAMOND AS AN ELECTRODE FOR EDM

Anurag Sharma[1], Manabu Iwai[2], Sadao Sano[3], Tetsutaro Uematsu[2], Kiyoshi Suzuki[1]
[1]Nippon Institute of Technology, Miyashiro, Saitama 345-8501, Japan
[2]Toyama Prefectural University, Kosugi, Toyama 939-0398, Japan
[3]Sodick Co. Ltd, Yokohama, Kanagawa, 224-8522

Abstract
The reduction of electrode wear is very important for high finish and high accuracy machining in micro-EDM. Electrically conductive CVD diamond has shown almost zero electrode wear, even at short pulse duration of 3μs, which is extremely important for maintaining the desired shape. This research involves an investigation into the EDM performance of the electrically conductive CVD diamond with respect to electrode polarity, electrode wear and efficiency. An investigation into the factors responsible for the low wear of the electrically conductive CVD diamond electrode leads us to deduce that an accelerated deposition of heat resolved carbon along with the high thermal stability of the diamond are mainly responsible.

Keywords: EDM, Electrically conductive CVD diamond, Low-wear electrode

1. Introduction

In the case of micro machining using EDM, it is extremely important not only to provide a good surface finish to the workpiece but also to reduce the electrode wear in order to increase the shape accuracy of the machined part. Although EDM with very low electrode wear can be achieved due to the adhesion of heat resolved carbon from the dielectric fluid, which protects the electrode from thermal wear, this phenomenon takes place only at sufficiently long pulse durations. To obtain a good EDMed surface finish it is necessary to lower the EDM current and make the pulse durations extremely short. However, presently at very short pulse durations, the wear rate of the electrode increases rapidly as a result of which the desired shape accuracy of the workpiece cannot be achieved.

Suzuki et al., demonstrated for the very first time the ability of the electrically conductive CVD diamond (EC-CVD diamond) electrode to perform no wear EDM not only at the no wear EDM condition of conventional copper and graphite electrode materials i.e. long pulse duration, but also at the short pulse duration of 3 μs [1]. The present research work deals with further investigation on the performance of the EC-CVD diamond for EDM of die steels as well as the factors responsible for the low wear of the diamond electrode. The effect of various EDM conditions on the performance of the EC-CVD diamond electrode is investigated. The results of the experiments indicate almost zero wear on the EC-CVD diamond electrode compared to conventional electrode materials, when EDM is performed in oil. This is thought to be due to an accelerated adhesion of heat resolved carbon from the dielectric oil onto the electrode surface as well as the high thermal stability of the EC-CVD diamond.

2. Characteristics of EC-CVD diamond

The physical properties of EC-CVD diamond (CVDITE-CDE, Element Six Ltd.) along with copper, graphite and Cu-W are given in Table 1. The important properties of a material for use as an electrode in EDM are its specific resistance, thermal conductivity and thermal diffusivity. As can be seen from Table 1, the specific resistance of EC-CVD diamond is suitable for its use in EDM. The thermal diffusivity of the EC-CVD diamond is

Material	EC-CVD diamond*	Copper	Graphite	Cu-W
Specific resistance (Ω·m)	$\approx 0.4 \sim 1\times10^{-3}$	17×10^{-9}	14×10^{-6}	6.8×10^{-9}
Specific gravity	≈ 3.5	9.0	1.8	14
Young's modulus (N/m^2)	$\approx 1000 \sim 1100\times10^{9}$	130×10^{9}	-	255×10^{9}
Thermal conductivity (W/m·K)	≈ 500 ~ 600	400	75	≈188-295
Coefficient of thermal expansion	$\approx 1\times10^{-6}$	17×10^{-6}	-	6.5×10^{-6}
Thermal diffusivity (m^2/s)	$\approx 0.27 \sim 0.33\times10^{-3}$	0.12×10^{-3}	0.15×10^{-3}	-

* CVDITE-CDE from Element Six Co., Ltd

Table 1: Properties of EC-CVD diamond thick film.

the highest among the conventionally used electrode materials, which helps in a faster dissipation of heat from the machining point and is quite advantageous with respect to EDM.

The oxidation tests for EC-CVD diamond (CVDITE-CDE, which is made conductive by doping with boron during the CVD process) and electrically non-conducting CVD diamond (CVDITE-CDM) were performed. The tests consisted of heating the CVD diamond thick film segments, each weighing 38 milligrams, at different temperatures in air for 30 minutes. Figure 1 shows the appearance of the diamond surface after oxidation test at 850 °C and Fig.2 shows the relation between the oxidation temperature and the percentage of weight loss due to oxidation. There is no change in the appearance of the EC-CVD diamond surfaces after heating for 30mins at 850°C, whereas, in the case of the electrically non-conductive CVD diamond thick film, the surface appears to be deteriorating along with a reduction in weight by 8~10%. Furthermore, the electrically conductive CVD diamond thick film (CDE) does not show a significant loss in weight even at the temperature of 900°C. These results indicate that the resistance to oxidation of the CVD diamond increases by the addition of boron during the CVD process.

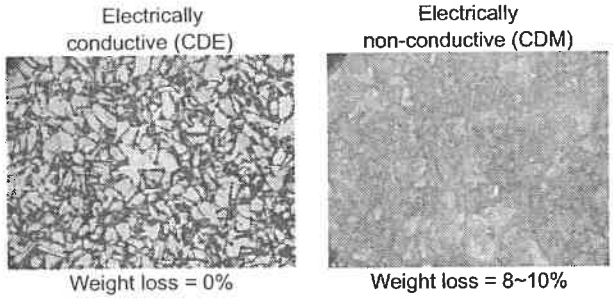

Figure 1: Comparison of oxidation of EC-CVD diamond (CVDITE-CDE) with normal CVD diamond (CVDITE-CDM) by heating for 30 mins at 850°C in air.
(Diamond segment: 5×6×0.5mm, initial weight=38mg, in air)

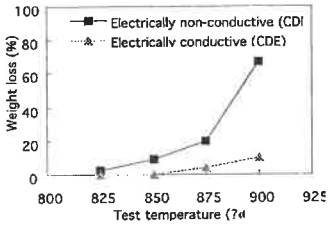

Figure 2. Comparison of resistance to oxidation of electrically conductive and non-conductive CVD diamond

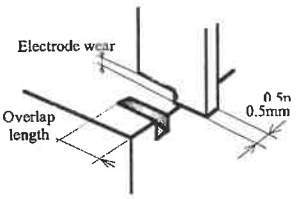

Figure 3. Experimental setup on EDM machine.

3. EDM experiments using EC-CVD diamond

3.1 Experimental setup and conditions

Die sinking EDM was performed as shown in Fig.3 by overlapping a length of 3mm of the electrode on the workpiece. The experimental conditions are listed in Table 2. An EC-CVD diamond segment (6×5×0.5mm) along with copper, graphite, and Cu-W segments of approximately the same size was used for the electrode. Die steel SKD11 (HRC 61) was used as the workpiece material. Kerosene (vitol 2) and de-ionized water were used as the working fluid.

EDM machine	Die sinking EDM machine (AQ35L, Sodick)
Dielectric working fluid	1. Oil (Vitol 2, Sodick) 2. De-ionized water
Electrodes	1. Electrically conductive CVD diamond film (CVDITE-CDE, 5×6×0.5mm, Element Six) 2. Copper (10×5×0.5mm) 3. Graphite (5×6×0.5mm) 4. Cu-W (5×6×0.5mm)
Workpiece	Die steel (SKD11, Hardness HRC61)
EDM conditions	u_i= 90V, i_e =3, 6A, t_e = 3,7,15,30,50μs, t_o=10,50μs, EDM depth=0.5,1mm

Table 2: Experimental devices and conditions.

3.2 Effects of electrode polarity and pulse duration

The effect of polarity on the EC-CVD diamond electrode was investigated and compared with a copper electrode under the same EDM conditions.

The results of this experiment are shown in Fig. 4. In the case of the copper electrode, at reversed polarity (electrode +), no wear EDM could be performed at the long pulse duration of 50μs, whereas, at the short pulse duration of 3μs, there was a large wear of about 340μm. In comparison, the diamond electrode showed no wear not only at the long pulse duration but also at the short pulse duration.

Further, at straight polarity (electrode -), both the copper and the diamond electrodes showed a very high wear.

3.3 Comparison of electrode wear and EDM efficiency

Experiments to compare the wear depths and EDM efficiency of the EC-CVD diamond electrode with copper, graphite and Cu-W electrodes were performed in oil and de-ionized water as the working fluid.

The results of the electrode wear depths and EDM efficiencies are shown in Fig. 5(a) and (b). It is well known that the electrode wear is reduced at sufficiently long pulse durations when EDM is performed in oil at reversed polarity, and this phenomenon is mainly due to the adhesion of carbon, resulting from dielectric breakdown, onto the electrode surface. However, this phenomenon is not observed at short pulse durations due to a reduction in the amount of carbon adhesion with a decrease in the pulse duration. The electrode wear depth in the case of the EC-CVD diamond electrode is almost zero even for the short pulse duration of 3μs, whereas, the electrode wear depths are about 255, 150 and 105μm for copper, graphite and Cu-W electrodes respectively. Therefore, no wear EDM condition may be achieved in the case of the EC-CVD diamond electrode under finish EDM conditions, which is impossible in the case of presently used electrode materials.

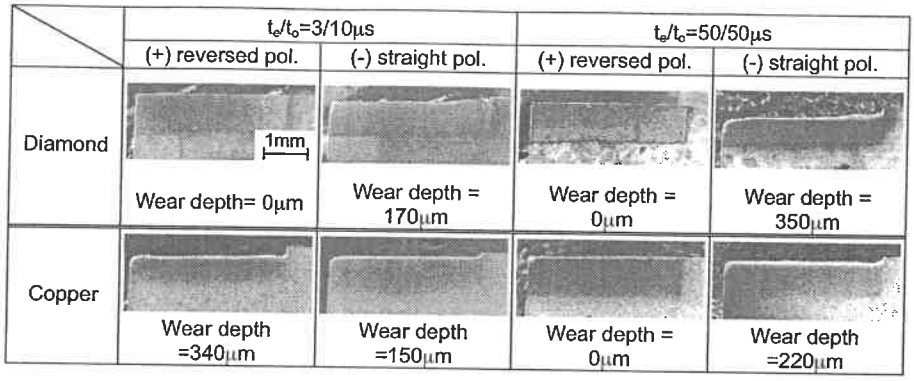

Figure 4. Effect of electrode polarity on electrode wear.
(u_i=90V, i_e=3A, work=SKD11, EDMed depth=0.5mm)

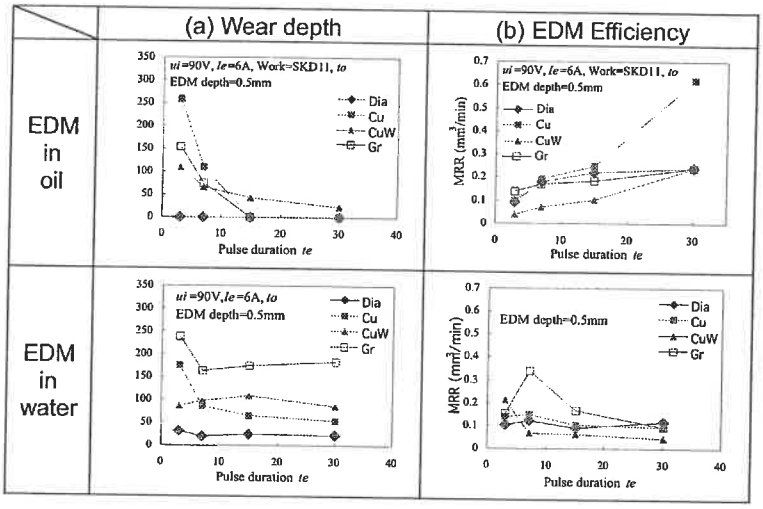

Figure 5. Comparison of wear and efficiency among electrode materials.

(u_i=90V, i_e=6A, t_o=50μs, Work=SKD11, EDM depth=0.5mm, Reversed polarity (electrode +))

In the case of EDM in water, although a maximum wear depth of about 30μm is observed for the EC-CVD diamond electrode at the pulse duration of 3μs, it is significantly low compared to the wear depths of 174, 239 and 87μm for the copper, graphite and Cu-W electrodes respectively. The wear of the EC-CVD diamond during EDM in water may be due to the oxidation of diamond by oxygen ions produced as a result of the ionization of water. On the other hand, the significantly low wear, compared to the other electrode materials, is thought to be due to the high thermal stability as well as the high thermal diffusivity of the EC-CVD diamond. This EDM characteristic of the EC-CVD diamond electrode is particularly important for the die sinking EDM of micro sized parts at finish EDM conditions without damaging the shape accuracy.

As shown in Fig 5(b), in oil, the EDM efficiency of the EC-CVD diamond is significantly low compared to the copper electrode at pulse durations of more than 15μs. The efficiency of the diamond and graphite electrodes is found to be same for the various pulse durations. The efficiency of the Cu-W electrode is the lowest among the electrode materials.

In the case of EDM in de-ionized water, the EDM efficiency of the graphite electrode is the highest followed by the copper, diamond and Cu-W electrodes at the pulse duration of 7μs. For the pulse durations of 3, 15 and 30μs much difference in the EDM efficiencies are not observed.

4. Surface characteristics of EC-CVD diamond electrode after EDM

In order to investigate the surface characteristics of the EC-CVD diamond electrode surface, Raman spectrum measurements of the surface of the diamond used for EDM were performed. Figure 6(a) shows the Raman spectrum of copper electrode surface after EDM in oil at a long pulse duration of t_e=50μs. Figure 6(b) and (c) show the Raman spectra of the EC-CVD diamond electrode surface after EDM in oil at a short pulse duration of t_e=3μs and in water at pulse duration of t_e=20μs respectively. The Raman spectrum of the EC-CVD diamond electrode surface after EDM in oil is similar to that of the copper electrode surface, which indicates the presence of heat-resolved graphitic carbon from the dielectric oil. The Raman spectrum in Figure 6(c) shows that when EDM is performed in water, a damaged crystal structure of the EC-CVD diamond is observed. However, there is no presence of graphite or graphitic carbon on the surface, which indicates that the EC-CVD diamond may be oxidized by the oxygen ions during the discharge process.

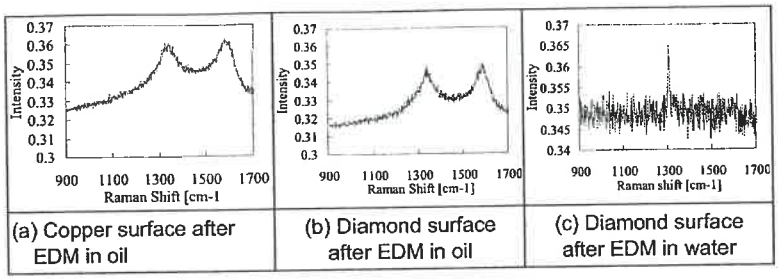

(a) Copper surface after EDM in oil | (b) Diamond surface after EDM in oil | (c) Diamond surface after EDM in water

Figure 6. Raman spectra of diamond surface after EDM.

5. Mechanism of low wear of the EC-CVD diamond electrode

5.1 Accelerated adhesion of carbon

One of the most important reasons for the low wear of the EC-CVD diamond electrode at reversed polarity, when oil is used as the dielectric medium, is the accelerated adhesion of carbon compared to other electrode materials. This is believed to be mainly due to the fact that at reversed polarity (electrode positive) the EC-CVD diamond electrode shows an almost zero wear even at the short pulse duration of 3μs compared to a large amount of wear in the case of copper, graphite and Cu-W electrodes, as shown in Fig. 4 and Fig. 5. However, the wear depth of the EC-CVD diamond electrode increases drastically at straight polarity (electrode negative) because the heat resolved carbon generated during the EDM goes towards the positive side only.

5.2 Thermal stability

In the absence of oxygen, diamond is thermally stable up to 1000°C after which conversion to graphite starts [2]. From the results of EDM using the diamond electrode in water in Figure 5(a), a very low wear of the diamond electrode compared to copper, graphite and Cu-W can be observed. This can be attributed to the high thermal stability of diamond in the absence of oxygen. This property of diamond may also be useful in the case of EDM using the EC-CVD diamond in oil.

6. Conclusion

In conclusion the following can be pointed out.

1. The electrode polarity in the case of EDM in oil using the EC-CVD diamond electrode plays a very important part i.e. at straight polarity (electrode -), a rapid electrode wear is observed at short as well as long pulse durations and at reversed polarity (electrode +), almost zero wear of the EC-CVD diamond electrode is observed even at the short pulse duration of 3μs which is presently not possible with conventional electrode materials.
2. The EDMing ability of the EC-CVD diamond electrode without any wear even at very short pulse durations gives it a great advantage to become an important electrode material for the machining of micro-parts.
3. The extremely low wear of the EC-CVD diamond electrode even at short pulse duration is thought to be due to the acceleration in the rate of carbon adhesion onto the EC-CVD diamond electrode surface as well as the high thermal stability of the EC-CVD diamond.

The authors would like to thank Element Six Co., Ltd. for providing the EC-CVD diamond thick films. The authors are very thankful for the support received from Osawa Scientific Studies Grants Foundation. The authors would like to express their heartfelt thanks to Prof. M. Kunieda and Mr. K. Shoda for their valuable advice.

7. References

1) K.Suzuki, A.Sharma, M.Iwai, T.Uematsu, K.Shoda, M.Kunieda: Electrical Discharge Machining Using Electrically Conductive CVD Diamond as an Electrode, NDFCT 443, Vol. 14, No.1 2004, p35-44

2) Hugh O. Pierson: Handbook of Carbon, Graphite, Diamond and Fullerenes, Noyes Publications, New Jersey (1993)

Laser Planarization Process Assisted by Chemical Mechanical Polishing for Copper Surface

Yasuhiro TAKAYA[1], Keiichi KIMURA[2], Takashi MIYOSHI[1], Toshiki MIYAMOTO[1], Keisuke SUZUKI[3]

[1] Osaka University, 2-1 Yamadaoka, Suita,Osaka, 565-0871 JAPAN
[2] Kyushu Institute of Technology, 680-4, Kawazu, Iizuka, Fukuoka, 820-8502 JAPAN
[3] Rodel Nitta Company, 6-5-6, Sakyo, Nara-shi, Nara, 631-0801 JAPAN

1. INTRODUCTION

ULSI have been developed constantly followed by Moore's law [1], and improvement of ULSI's performances and supply with low price have made ULSI spread over every human activities and every people's life on foundations. This evolution was realized by ULSI process innovation in respect of lithography and planarization process for multi-layers interconnects. Particularly, in planarization process, planarization technique has been advanced by development of CMP (Chemical Mechanical Polishing) technique [2] and by application for planarization process in ULSI manufacturing process. In recent years, CMP technology encountered turning for new direction such as planarization for new material of Cu interconnects and Low-k dielectrics, and Cu Dual-Damascene process which is based on CMP technology is introduced. However, some difficulties as Cu layer delaminating and damages generation on Low-k films [3] are coming up seriously in the process. Low down force and high rotation speed CMP machine [4] was developed to solve these problems, but performances are not sufficient yet. As an essential solution for the problem, material removal with no contact between a polishing pad and a surface of silicon wafer is one of the basic ideas. Based on the idea, ECMP (Electro chemical mechanical planarization) [5] has been tried, but geometrical selectivity for planarization is insufficient because of its properties of material removal mechanism, and further, material removal speed is necessary for increasing.

On the research, the new material removal method is attempted for a development of no-contact planarization process with high geometrical selectivity on Cu film's asperity. On this method, laser light irradiates onto the surface of Cu film on the silicon wafer in reactive liquid environments. Material removal with the depth of nanometer order can be obtained by localized activation of laser- material interaction or laser-induced chemical reaction at just the microscopic region where tightly focused laser light irradiates. As a first step of the research, the fundamental experiments were carried out and possibilities to control material removal rate are investigated.

2. LASER PLANARIZATION PROCESS

We propose the new laser planarization method that is based on the control of local material removal process using laser-material interactions. The process is performed without using a polishing pad to avoid the serious problems such as dishing, erosion and delaminating on copper layer and inter-layer dielectrics (ILD), as seen in the conventional CMP technologies with using a polishing pad.

Fig.1 shows the basic concept of the laser planarization process. Copper interconnect requires damascene processes because copper cannot be easily plasma etched. In the damascene process, copper is deposited into an etched ILD trench pattern, typically by electroplating over barrier and seed layer. Then the excessive copper should be removed and the copper film's asperity is finished to be perfectly flat ideally. In the laser planarization process, copper surface is irradiated by tightly focused laser light in reactive liquid environment such as slurry used for CMP. The planarization process is performed by scanning the laser light in the radial direction on copper surface of a rotating wafer as shown

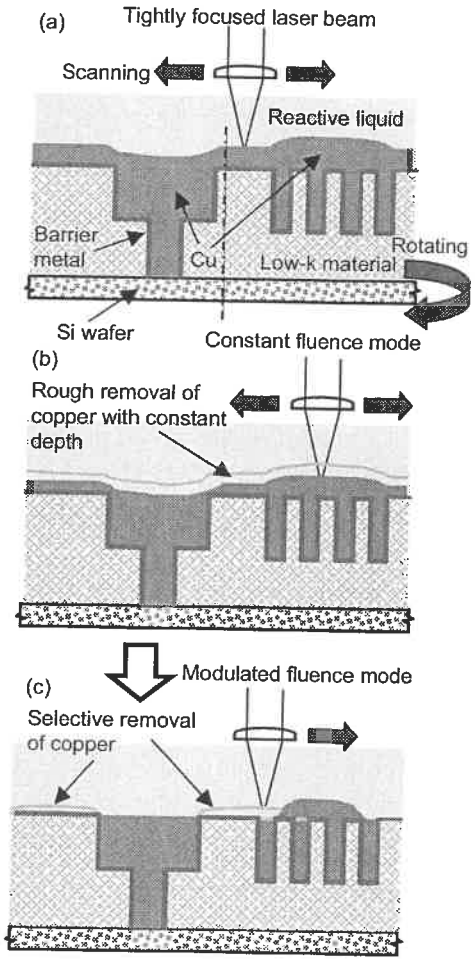

Fig.1 Basic concept of the laser planarization process.

in Fig.1 (a). Depending on a fluence, material removal is considered to be occurred by laser-material interactions in reactive liquid environment such as laser-induced evaporation, laser-induced wet chemical etching, laser ablation or a combination of them. So, it is expected that the material removal rate can be controlled by changing the laser irradiating conditions, and moreover the control is localized in the laser spot size. As the initial phase of the laser planarization process, rough removal process with constant rate in depth is needed to decrease the excessive copper quickly. In this process, large constant fluence is employed to remove copper with high rate as indicated in Fig.1 (b). However most of the excessive copper is eliminated by this process, there exists irregularities such as the humps on the deposited copper layer, which reflects the trench patterns. At this phase, selective removal process is required to remove the humps. In this process, removal rate for each hump, which can be estimated from the trench patterns, is controlled by modulating fluence as indicated in Fig.1 (c). Therefore, the laser planarization method makes it possible to attain no-contact planarization of copper film's asperity with high geometrical selectivity.

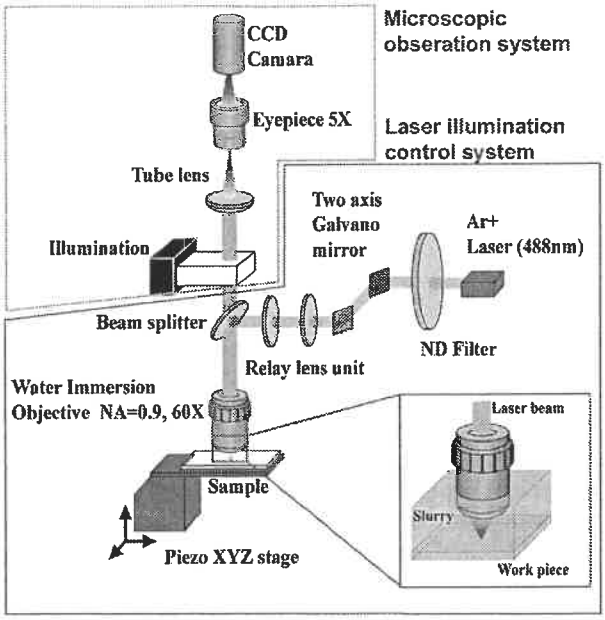

(a) Schematic diagram of the optical system.

(b) Layer construction of a copper wafer.

Fig.2 Experimental setup and workpiece.

3. EXPERIMENTAL SETUP

Schematic diagram of the optical system is illustrated in Fig.2 (a). The optical system is composed of a microscopic optical system and a laser irradiation optical system for controlling the laser light illumination conditions such as beam spot position, scanning frequency and laser power. The light with wavelength of 488 nm is emitted from a Ar^+ laser and is deflected by a pair of computer-controlled galvano-mirrors with axes perpendicular to each other for scanning the beam.

The laser beam is deflected by a beam splitter, after through a pair of relay lens unit to adjust maximum scan length within the aperture size of an objective, then focused by a water immersion objective with N.A. of 0.9. The focused laser spot of about 0.35 μm (theoretical) in diameter is scanned on a copper surface of a workpiece which consists of Cu layer with 1000 nm thickness, Cu seed layer with 100 nm, TaN barrier layer with 50 nm and silicon substrate as shown in Fig.2 (b). The workpiece is dipped in the Cu-CMP slurry containing copper etchant. Positioning of the workpiece is performed using a xyz-stage with positioning accuracy of 5 nm, which is driven using PZT actuators. The experimental conditions are listed in Table 1.

Table 1 Experimental condition.

Laser	Ar^+Laser Wave length: 488 nm Theoretical spot size: 0.35 μm (using an objective of NA0.9)
Work	Copper filmed silicon wafer Surface roughness: Rq 3 nm
Working fluid	Cu-CMP slurry PLANERLITE-7101 (Fujimi)
Laser beam scanning condition	Linear scan Scanning direction: back and forth Scanning length: 28 μm Frequency: 1 Hz

4. FUNDAMENTAL EXPERIMENT

In order to investigate the material removal properties in working fluid and in the laser irradiation conditions as process control parameters, fundamental experiments to produce fine grooves on a copper surface. The tightly focused laser beam is scanned repeatedly on the surface with the scan speed of 56 μm/sec and scan rate of 1 Hz. Veeco NanoScope IIIa AFM is used to examine the processed surface in detail.

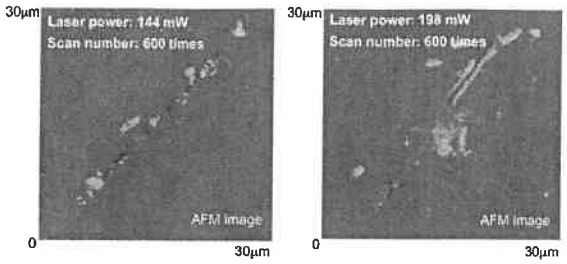

(a) AFM images of grooves processed in ultra-pure water.

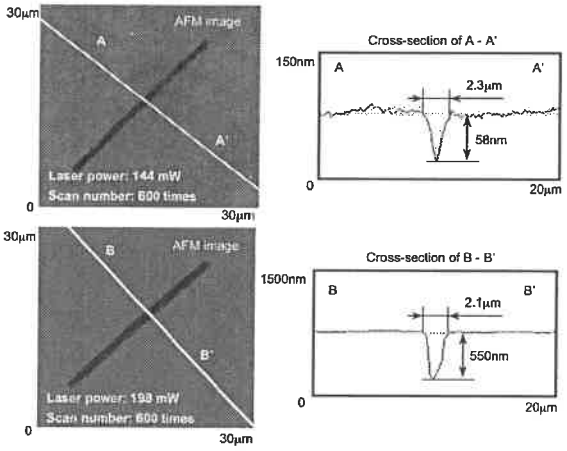

(b) AFM images of grooves processed in Cu-CMP slurry.

Fig.3 Difference in material removal property for working fluid.

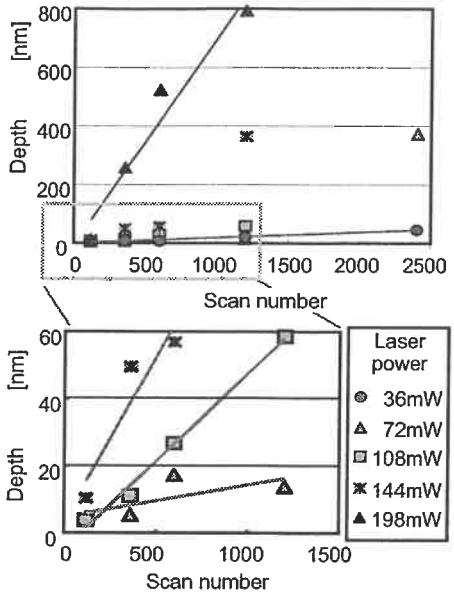

Fig.4 Relationship between depth of groove and laser beam scan number for each laser power.

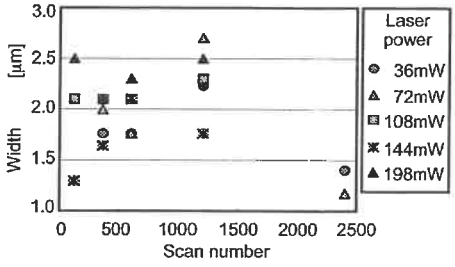

Fig.5 Relationship between width of groove and laser beam scan number for each laser power.

4.1 Material removal properties

Machining of a fine groove on a copper surface for two types of working fluids is performed to investigate material removal property for the process in reactive liquid environment and in not reactive. Fig.3 shows the difference in material removal property for each working fluid. The copper surfaces were treated at the laser scan number of 600 times in linear motion for a range of laser power and analyzed by AFM. According to the AFM observations shown in Fig.3 (a), the grooves produced for ultra-pure water become unacceptable from the point of view of controlled material removal. At the laser power of 144 mW, a small amount of sputtered debris appeared around the extremely discontinuous groove. The groove edge is not clearly recognizable and irregular. At 198 mW, remarkable ejected debris was present possibly due to the melted material being pushed to the sides of the deep groove or vaporization of the removed material. The depth and the width of the groove are not measurable. On the other hand, material removal property for Cu-CMP slurry is drastically different from that for ultra-pure water. Fig.3 (b) shows the AFM images of the grooves produced for Cu-CMP slurry and examples of the cross sections. At both 144 mW and 198 mW, not only was the fine groove with smooth and sharp edge produced, but ejected and sputtered debris did not appear around the groove. According to the cross sections, the grooves are confirmed to be V-shape. The groove produced at the laser power of 198 mW is deeper than 144 mW, but both of the grooves have almost same width. Depth of a produced groove in Cu-CMP slurry is found to be related to irradiated laser power.

4.2 Laser power and material removal rate

In order to examine the relationship between laser power and material removal rate, machining of the grooves for Cu-CMP slurry was achieved over a range of laser scan number for each laser power. Depth and width of the grooves are estimated by the cross sections obtained from the AFM images.

Fig.4 shows the relationship between the depth of the produced groove and the laser scan number for each laser power. At the laser power of 198 mW, the depth of about 250 nm to 800 nm is directly proportional to the laser scan number of about 300 to 1200 times. The depth changing from several nm to nearly 100 nm at 36 mW shows almost same tendency as 198 mW for the laser scan number up to 2500 times. But the depth ranging from several nm to about 400 nm shows different change at the laser power of 72 mW, 108 mW and 144 mW. The linearity of the depth and the laser scan number is not approved from the

depth more than 60 nm.

Fig.5 shows the relationship between the width of the produced groove and the laser scan number for each laser power. Although the measurement results show fluctuation between nearly 1.5 μm to 2.5 μm, the width is independent of laser scan number and laser power. Consequently, material removal rate in depth is potentially controllable by laser power and scan number, but not in width.

4.3 Results and Discussion

Controllability of material removal in depth is considered from the point of view of material removal rate per one laser scan for laser irradiation power. Fig.6 shows the material removal rate per one laser scan in depth for each laser power. The material removal rate is almost directly proportional to the laser power ranging from 36 to 144 mW for the depth less than about 60 nm, but rapidly jumps to 0.7 nm/scan at the laser power of 198 mW for the depth more than about 200 nm. Since material removal rate is supposed to linearly change with laser power, a copper layer in Cu-CMP slurry is assumed not to be bulky structure with uniform material but covered with a thin film of different material. The thickness of the thin film can be estimated nearly 60 nm. Taking account of reactive liquid environment of Cu-CMP slurry, the experimental results suggest the material removal process model as shown in Fig.7. Being covered in oxide film by the oxidizer included in Cu-CMP slurry where the copper surface is suitable, it becomes the passive state. It is supposed that the material removal rate of this Cu passive state film for laser irradiation is lower than that of Cu. Because the Cu passive state film is removed initially for low laser power the material removal rate is low as suggested in Fig.7 (a). Reaching at Cu layer, the material removal rate increases suddenly as shown in Fig.4. When Cu passive state film is irradiated by high power laser, the depth of removed material reaches into Cu layer in an instant. The Cu layer irradiated by high power laser is dug much deeper as indicated in Fig.7 (b). Meanwhile, since Cu passive state film is not generated significantly in ultra pure water, the uncontrollable material removal properties shown in Fig.3 result from the different material removal process of direct laser-copper interaction.

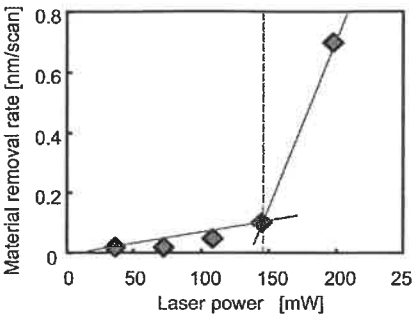

Laser power [mW]	Material removal rate [nm/scan]
36	0.02
72	0.01
108	0.05
144	0.1
198	0.7

Fig.6 Material removal rate per one laser scan in depth for each laser power.

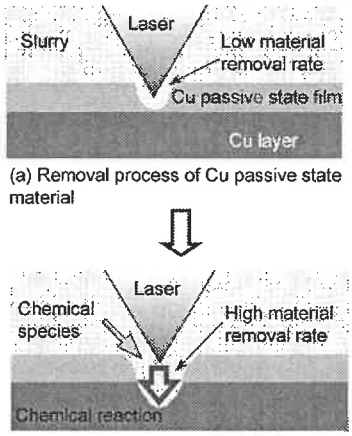

(a) Removal process of Cu passive state material

(b) Removal process of Cu

Fig.7 Material removal process by laser-material interaction.

5. CONCLUSIONS

The new laser planarization method which is based on the control of local material removal process using laser-material interactions are proposed. Using Cu-CMP slurry, the fine groove with smooth and sharp edge produced without ejected and sputtered debris. Considering material removal rate per one laser scan for laser irradiation power, the material removal process model is suggested. The experimental results can be explained by the assumption that the material removal rate of this Cu passive state film for laser irradiation is lower than that of Cu. Nanometer order material removal rate in depth is potentially controllable by laser power and scan number.

REFERENCES

[1] G. E. Moore : IEDM Technical Digest, 11 (1975).

[2] B. Davari et al : "A new planarization technique, using a combination of RIE and Chemical Mechanical Polishing (CMP) ", IEDM89, (1989) 61.

[3] M. Miyajima : "Cu/Low-k CMP technology for 65nm generation", Proceeding on 37th meeting of planarization CMP Committee (2004) 9-13.

[4] S. Hoshino et al: "Development of Next-Generation CMP System (Technical Development of Ultra-Low Pressure Polishing and Local Polishing) ", J. JSPE, 70, 06(2004) 742-745.

[5] Shuzo Sato et al: "Newly developed Electro-Chemical Polishing of Copper as Replacement of CMP Suitable for Damascene Copper Inlaid in Fragile Low-k Dielectrics", IEDM2001, 12 #4.4(2001).

CHARACTERIZING FORM, WAVINESS, AND ROUGHNESS OF MICRO EDM ELECTRODES

R. Ryan Vallance[*], Chris J. Morgan[†], Shelby M. Shreve[†], and Eric R. Marsh[‡]

[*]Precision Systems Laboratory, The George Washington University
738 Phillips Hall, 801 22nd St., N.W., Washington, DC, 20052, USA
Tel: +1-202-994-9830; Fax: +1-202-994-0238. Email: vallance@gwu.edu
[†]Mechanical Engineering, University of Kentucky
015 Ralph G. Anderson Building, Lexington, KY, 40506, USA
[‡]Machine Dynamics Research Laboratory, The Pennsylvania State University
21 Reber Building, University Park, PA, 16802, USA

Introduction

High precision micro tools are necessary for a variety of 3D micro machining processes [1,2,3]. Micro tools, such as the cylindrical tool in Figure 1, are made by micro electro discharge machining (μEDM), and they are used in several processes including secondary μEDM (to produce holes, slots, or pockets) [4,5], ductile-regime drilling of brittle materials like silicon [6], micro ultrasonic machining [7], and micro ultrasonic vibration lapping [8]. To achieve deep holes or pockets and compensate for tool wear [9,10], these tools require high aspect ratios, with the length of the tool up to fifty times the diameter. Micro tools produced by μEDM range between three and a few hundred micrometers in diameter and up to a few millimeters in length.

During μEDM, a workpiece is submerged with a sacrificial electrode in dielectric fluid and shaped by high frequency electrical discharges. Micro tools are made from any electrically conductive material, including refractory metals with high melting temperatures (e.g. tungsten), hard materials that are difficult to cut (e.g. tungsten carbide), or brittle materials (e.g. doped silicon). The Ø50 μm × 1.5 mm tool shown in Figure 1was produced from a drawn tungsten wire.

High aspect ratios and small diameters are realizable because the μEDM process is non-contact, and the machining forces are insignificant. However, material removal with electrical discharges has two undesirable effects. First, the thermal nature of the process produces a layer of recast material and weakens the region below the surface known as the heat affected zone (HAZ). Surfaces machined by electrical discharges exhibit overlapping spherical craters with resolidified protrusions and cracks produced during rapid cooling [11]. The recast layer degrades surface integrity and affects the geometry of the tool at the micro scale. Craters and cracks are observable on the surface of the tool shown in Figure 1. Second, the electrical discharges also remove material from the sacrificial electrode, which propagates into the waviness and form of micro tool.

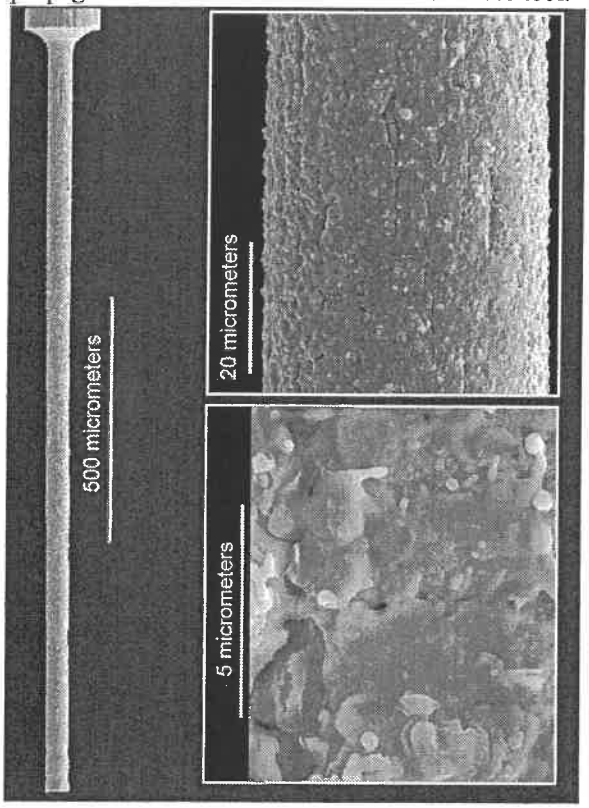

Figure 1. High aspect ratio micro tool with 50 μm diameter and 1.5 mm length that was produced by μEDM.

This paper describes a metrology technique for characterizing high aspect ratio tools for use in micro machining. The technique uses commercially available instruments and complies with standard metrology practice. In this technique, the 3D topography along the length of micro tools is measured with a scanning white light interferometer. 2D profiles from the crest of the micro tool are extracted from the 3D data and separated into form, waviness, and roughness using frequency domain filtering techniques. Height and shape parameters

computed from the roughness, waviness, and form profiles enable quantitative comparison of tool geometry in a reproducible manner. The utility of the technique is demonstrated by characterizing the precision of a micro tool produced by wire electro discharge grinding.

Profiles from Scanning White Light Interferometry

The 3D surface topography along the length of a micro tool is measured using scanning white light interferometry. The measurements are conducted with a commercially available white light interferometer (Zygo NewView 5000). Positioning and orienting stages are used to set the tool's centerline perpendicular to the optical axis and to move the micro tool during measurements. The field of view with a 10× Mirau parfocal objective and a 2× camera lens is approximately 360 μm × 280 μm. Interference fringes are detected with a 640 × 480 pixel CCD camera that yields a lateral resolution of about 0.56 μm/pixel. Since the field of view cannot include tools up to a few millimeters in length, sequential measurements are collected and stitched together with an automated routine provided by the instrument manufacturer.

Figure 2 illustrates typical results from the scanning white light interferometry of a micro tool. This micro tool is 500 μm long and 50 μm in diameter. Periodicity of wavelength about 30 μm, along the length of the tool is evident. Such periodicity has not been previously reported on micro tools made by WEDG, but it is readily detected and quantified with the techniques described in this paper.

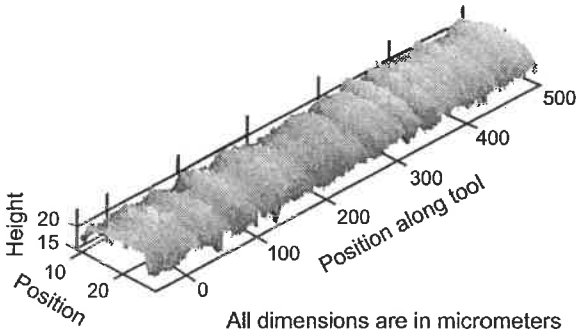

Figure 2. 3D surface topography of a micro tool as measured with scanning white light interferometry.

2D height profiles $h(x)$ with n data points are extracted from the 3D surface along the length of the tool (x direction) and along the crest of the topography. The height profiles exhibit an arbitrary offset that depends upon the datum during the measurements. As shown in Eq (1), this offset is removed to yield a measured profile $z(x)$ by calculating the difference between the measured heights $h(x)$ and the mean of the measured heights $\bar{h}$. This ensures that the mean of the measured profile $z(x)$ is zero.

$$z(x_i) = h(x_i) - \bar{h} \text{ for } 1 \le i \le n \qquad (1)$$

A least-squares polynomial $\zeta(x)$ that best fits the measured profile $z(x)$ is next determined. We use a second order polynomial such that the best-fit heights ζ_i at discrete points x_i along the tool are computed with Eq (2). A modified profile $Z(x)$ is computed as the difference between measured points z_i and the best-fit polynomial ζ_i as shown in Eq (3). This removes spectral content with wavelengths exceeding the length of the tool, which reduces leakage when the profiles are later transferred into the frequency domain.

$$\zeta_i(x_i) = C_2 x_i^2 + C_1 x_i + C_0 \text{ for } 1 \le i \le n \qquad (2)$$

$$Z_i(x_i) = z_i(x_i) - \zeta_i(x_i) \text{ for } 1 \le i \le n \qquad (3)$$

Figure 3 shows the steps of this procedure for the height measurements extracted from the surface shown in Figure 2. The first chart in Figure 3 shows the original height profile $h(x)$ and the second chart in shows the measured profile $z(x)$ obtained after removing the offset and the least-squares second order polynomial $\zeta(x)$. The third chart in Figure 3 shows the final modified profile $Z(x)$ after the removal of the second order polynomial.

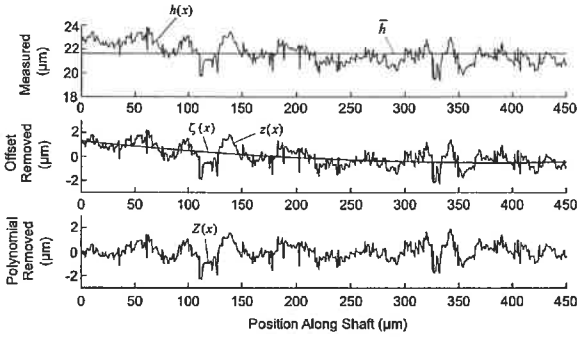

Figure 3. Processing of 2D profiles to remove offset and a second order polynomial.

Processing Profiles

The modified profiles Z(x) are transformed into the frequency domain with a discrete fast Fourier transform (FFT). Figure 4 shows a plot of the magnitude spectrum obtained after performing the discrete FFT on the modified profile (after removing offset and polynomial) shown in Figure 3. The sampling frequency for this profile was $f_s = 1.79\ \mu m^{-1}$, and the quantity of data points in the profile is $N = 822$. Therefore, the frequency ranges from 0 to 0.894 μm^{-1}, and the frequency resolution is $\Delta f = 2.18 \times 10^{-3}\ \mu m^{-1}$. The spectrum has its maximum magnitude of

0.327 μm at a frequency of 2.39×10^{-2} μm^{-1} (wavelength of 41.8 μm). The spectrum decays to magnitudes less than 0.1 μm for high frequencies exceeding 0.1 μm^{-1}.

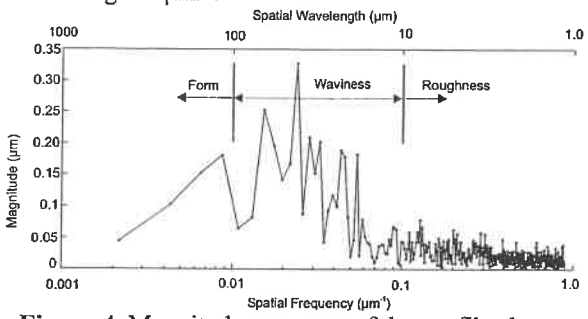

Figure 4. Magnitude spectrum of the profile shown in Figure 3.

The measured profile shows that the spectra are separable into three regimes based on spatial frequency (or its inverse, spatial wavelength). The profile exhibits distinct low frequency content below 0.01 μm^{-1} (wavelengths exceeding 100 μm). Also, the spectra levels off to a flatter region above around 0.1 μm^{-1} (wavelengths below 10 μm). Therefore these cutoff frequencies (or wavelengths) define the separation between form, waviness, and roughness. Spectral content below the waviness cutoff frequency $f_1 = 0.01$ μm^{-1} (wavelengths longer than $\lambda_1 = 100$ μm) is classified as form. Spectral content above the roughness cutoff frequency $f_2 = 0.1$ μm^{-1} (wavelengths shorter than $\lambda_2 = 10$ μm) is classified as roughness. Spectral content between $f_1 = 0.01$ μm^{-1} and $f_2 = 0.1$ μm^{-1} is classified as waviness. These classifications are consistent with standard surface characterization techniques but based on different cutoff frequencies [12].

The roughness, waviness, and form profiles are computed with Eq (4), Eq (5), and Eq (6), respectively. Figure 5 shows the form, waviness, and roughness profiles determined with the spectrum of the modified profile plotted in Figure 4.

$$Z_R(x_i) = real\left[\frac{1}{N}\sum_{k=1}^{N} R_k \exp\left(\frac{2\pi(k-1)(i-1)}{N} j\right)\right] \quad (4)$$

where $1 \le i \le N$

$$Z_W(x_i) = real\left[\frac{1}{N}\sum_{k=1}^{N} W_k \exp\left(\frac{2\pi(k-1)(i-1)}{N} j\right)\right] \quad (5)$$

where $1 \le i \le N$

$$Z_F(x_i) = real\left[\frac{1}{N}\sum_{k=1}^{N} F_k \exp\left(\frac{2\pi(k-1)(n-1)}{N} j\right)\right] \quad (6)$$

where $1 \le i \le N$

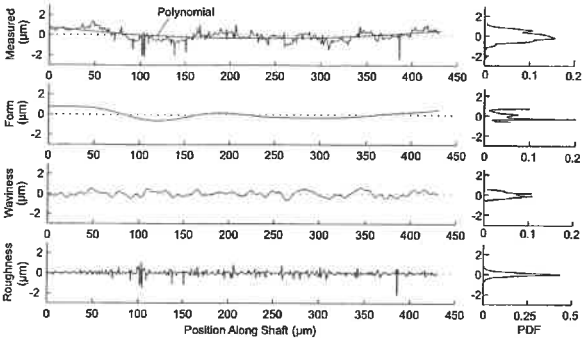

Figure 5. Separation of the modified profile $Z(x)$ shown in Figure 3 into form $Z_F(x)$, waviness $Z_W(x)$, and roughness $Z_R(x)$ profiles.

Characterizing Micro Tools

The technique described in the previous sections was evaluated with a study of the micro tool shown in Figure 6. The tool was ultrasonically cleaned after machining and before inspection. The 500 μm long tool is made from Ø150 μm drawn tungsten wire that was reduced to Ø50 μm by WEDG. Scanning electron microscopy (SEM) at low and high magnifications is used for inspecting the entire tool and its surface topography.

The tool shown in Figure 6 was produced with a feed rate $F_r = 5$ μm/s, voltage of $V_s = 70$ V, and a capacitance of $C = 10$ pF. In the SEM micrograph, the diameter of the tool appears uniform along its length. The surface of this tool exhibits a terrace structure with sub micrometer craters. Valleys are present in between the terraces, and their dimensions are a few micrometers in width but exceed 20 μm in length.

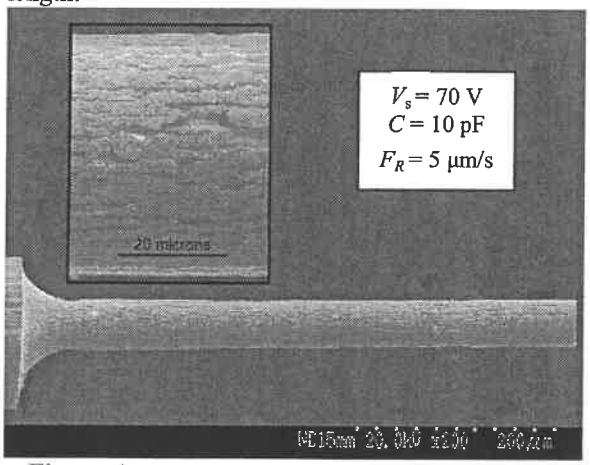

Figure 6. Scanning electron micrographs a micro tool produced with $F_r = 5$ μm/s, voltage of $V_s = 70$ V, and a capacitance of $C = 10$ pF. The tool is 500 μm in length and 50 μm in diameter.

The subjective observations using the SEM images are conveniently quantified by the metrology techniques described in this paper. Results from opposite sides of the tool were consistent with one

another, suggesting that the form, waviness, and roughness are typically independent of tool orientation. One of the two measured profiles from each tool is separated into its form, waviness, and roughness profiles in Figure 5, Also included in these figures are the PDFs for each profile. The height and shape parameters, computed as the average of the two values measured from opposite sides of each shaft, are listed in Table 1.

Profiles of the tool confirm the high precision of this tool. The peaks and valleys within its roughness profile are shallow, falling mostly within +/- 0.5 μm. Therefore, the roughness PDF exhibits a very sharp peak with R_{ku}=19. The roughness profile has a negative skewness of R_{sk} = -1.9, suggesting that most of the roughness height values are above the mean height. The waviness profile of the tool has peaks and valleys that are mostly within +/- 0.5 μm of the mean. The form error is only slightly greater than the waviness and roughness, with a peak-to-valley measurement of $F_{p\text{-}v}$ = 1.45 μm.

Table 1. Height and shape parameters of the micro tool.

Roughness				Waviness				Form
R_a (nm)	R_q (nm)	R_{sk}	R_{ku}	W_a (nm)	W_q (nm)	W_{sk}	W_{ku}	$F_{p\text{-}v}$ (nm)
150	250	-1.9	19	210	260	-0.1	3.0	1450

Conclusions

Micro tools produced by μEDM processes such as WEDG have small diameters and long lengths. In prior work, these tools were characterized by either diameter measurements or scanning probe microscopy over small surface areas on the tools. In this paper, we describe a new metrology technique useful in characterizing the entire length of these high aspect ratio tools using scanning white light interferometry and 2D profiles. These profiles indicate variation in the surface height with sub-nanometer resolution along the entire length of the tool, which may be a few millimeters in length.

The profiles are separated into form, waviness, and roughness profiles using frequency domain filtering. Based on spectral analysis, wavelengths of 10 μm and 100 μm were found to reasonably separate roughness from waviness and waviness from form. The computation of height parameters, like R_a and R_q, and shape parameters, like R_{sk} and R_{ku}, are quantitative metrics useful in comparing the precision of micro tools.

References

[1] Dario, P., M.C. Carrozza, N. Croce, M.C. Montesi, and M. Cocco. "Non-traditional Technologies for Microfabrication". *Journal of Micromechanics and Microengineering*. V. 5. 1995. p. 64-71.

[2] Masuzawa, T, and H.K. Tönshoff. "ThreeDimensional Micromachining by Machine Tools". *Annals of the CIRP*. International Institution for Production Engineering Research. Vol. 46, No. 2. 1997. p. 621-628.

[3] Masuzawa, T. "State of the Art of Micromachining". *Annals of the CIRP*. International Institution for Production Engineering Research. V. 49. p. 473.

[4] Allen, D.M., H.J.A. Almond, J.S. Bhogal, A.E. Green, P.M. Logan, and X.X. Huang. "Typical Metrology of Micro-Hole Arrays Made in Stainless Steel Foils by Two-Stage Micro-EDM". *Annals of the CIRP*. International Institution for Production Engineering Research. V. 48, No. 1. 1999. p. 127-130.

[5] Li, H. and T. Masaki. "Micro-EDM". SME Technical Paper MS91-485. Electrical Discharge Machining Conference. Society of Manufacturing Engineers. Grand Rapids, MI. September 17-18, 1991.

[6] Egashira, K and K. Mizutani. "MicroDrilling of Monocrystalline Silicon using a Cutting Tool". *Precision Engineering*. V. 26. 2002. p. 263-268.

[7] Sun, X-Q., T. Masuzawa, and M. Fujino. "Micro Ultrasonic Machining and Its Applications in MEMS". *Sensors and Actuators A*. V. 57. 1996. p. 159-164.

[8] Wang, A.C., B.H. Yan, X.T. Li, and F.Y. Huang. "Use of Micro Ultrasonic Vibration Lapping to Enhance the Precision of Microholes Drilled by Micro ElectroDischarge Machining". *International Journal of Machine Tools and Manufacture*. V. 42. 2002. p. 915-923.

[9] Yu, Z., T. Masuza, and M. Fujino. "3D Micro-EDM with Simple Shape Electrode, Part 1: Machining of Cavities with Sharp Corners and Electrode Wear Compensation". *International Journal of Electrical Machining*. V. 3. p. 7-12.

[10] Yu, Z., T. Masuzawa, and M. Fujino. "3D Micro-EDM with Simple Shape Electrode, Part 2: Machining and Error Analysis of Conical and Spherical Cavities". *International Journal of Electrical Machining*. V. 3. p. 71-78.

[11] Wong, Y.S., M. Rahman, H.S. Lim, H. Han, and N. Ravi. "Investigation of Micro-EDM Material Removal Characteristics Using Single RC-Pulse Discharges". *Journal of Materials Processing Technology*. V. 140. 2003. p. 303-307.

[12] ASME/ANSI B46.1. *Surface Texture (Surface Roughness, Waviness, and Lay)*. American Society of Mechanical Engineers. New York. 1996.

Investigating Different Methods of Bonding Glass Substrates

Jaime B. Werkmeister
Alexander H. Slocum
Precision Engineering Research Group
Massachusetts Institute of Technology
Cambridge, Massachusetts, U.S.A.

For many years, different methods for bonding glass borofloat substrates have been investigated[1], including fusion and various adhesives like cyanoacrylate [1]- **[6]**. This paper investigates the properties of different bonding processes available and presents solutions for bonding plain glass wafers, with investigation into using the same process for bonding glass with microfluidic channels etched in them.

The bonding process must satisfy three requirements to preserve the channels. The first requirement is that the bond has to preserve the colorlessness and transparency of the wafers. No particles may form between the bond and cause the wafers to become opaque. A second requirement is that the material must be non-toxic as the device application will require contact with human tissue or fluids. Lastly, the seal between the wafers has to be sufficient to prevent leakage while still preserving the depth of the microfluidic channels. Given these requirements, three main categories for bonding glass borofloat substrates are considered: adhesive, anodic, and fusion:

Adhesive

Several different adhesives were investigated, including cyanoacrylate, Sylgard 184 (PDMS), Sylgard 839, Duco Cement, Epoxy, and Industrial Strength E600. To successfully bond, each adhesive required a specific application process. For cyanoacrylate, application required rotating the wafer at a speed of 1500 rpm and applying a quarter sized daub at the center of the wafer. Within 20 seconds, the rotation was stopped and the mating glass substrate was pressed onto the drying cyanoacrylate. Acetone was used to remove any unwanted cyanoacrylate.

The second method, required for Duco Cement, Epoxy, and Industrial Strength E600, entailed spreading the adhesive evenly on top one glass substrate with a knife, then pressing the mating glass substrate on top of the drying adhesive. Extra adhesive material was removed with isoproponal.

The third method, used only for the Sylgard compounds, required that the adhesive be cured in a separate mold, then transferred to the glass substrate. Since the layer was only 100 um thick, the material was difficult to remove from the mold. The adhesive would tear in small pieces and proved difficult to mend. If the adhesive was removed properly, it held the two glass substrates well and it was difficult to pull the two bonded wafers apart. More than 10 – 20N hand force was required to break the seal.

With each of the different adhesives used, a good seal was created, but a potential difficulty is for the liquid adhesive to run into the etched channels.

---

[1] **Alfi, Oren and Brandon Choi, Glass to Glass Bonding, UCI Symposium**
http://www.urop.uci.edu/symposium/past_symposia/03/abstracts_groups.html

Anodic

Anodic bonding is an electrical and thermal process that typically bonds a silicon wafer to a glass substrate. The wafer and glass substrate are placed between two metal electrodes and heated to 400°C. By applying a DC potential up to 1kV, an electric field is created causing sodium ions to deplete the surface of the glass and to diffuse into the Silicon. In this state, the glass becomes highly reactive with silicon surface and forms a solid chemical bond.

While this process is well established for silicon-glass bonding, the requirement of this project is to bond two glass substrates. To anodic bond glass, a series of three layers was sputtered onto one glass borofloat substrate: a 100 angstroms layer of Indium-Tin-Oxide, followed by a 100 angstroms of silicon dioxide, and 250 angstroms of silicon [7]. This substrate was then brought into contact with a virgin glass substrate under 10 kPa of pressure and a potential of 100V applied at 55°C. While this bond worked well because it could not be pealed apart by tweezers nor with the hand, the glass substrates did not remain transparent due to the silver color of the Silicon layer. However, this research shows that anodic bonding can conserve channels in a glass substrate and create a good seal.

Fusion

Fusion bonding the two glass substrates proved to be successful without the issues associated with adhesives or sputtering. The basic fusion bonding process entails pressing two virgin glass substrates together and applying heat for a long duration. 700 μm thick glass borofloat substrates were pressed together by hand until the substrates were fixed by Van der Waals forces. The substrates were transferred to a furnace at atmospheric pressure and placed on top of an unpolished nitride wafer. The nitride wafer prevents the glass from fusing and deforming over the small diameter ceramic base. Silicon and quartz wafers were also tried as the holding base, but were unsuccessful because the borofloat would fuse with them. Glass substrates can be heated up to 600 °C to allow the material to partially slump and fuse with the opposite substrate, but without melting. Therefore, the borofloat wafers were heated in the furnace for 6 hours at 600°C.

In several experiments, trapped air bubbles appeared between the two glass substrates. Therefore, additional substrates were bonded under vacuum in an attempt to reduce the number of bubbles. The above process was altered to allow the two borofloat wafers to be pressed together in a vacuum chamber of 1e-2 bars for 2.5 minutes. Once the borofloat wafers were fixed under Van der Waals forces during initial contact, they were transferred to a furnace at atmospheric pressure and heated to 600 °C for 6 hours.

Once cooled, the wafers were removed from the furnace and investigated under a microscope. The bond was solid with few impurities trapped between the surfaces for the glass substrates as shown in Figure 1 and Figure 2. To decrease impurities on the substrate, it is recommended that a preliminary clean be done in a 1 part hydrogen peroxide to 3 parts Sulfuric acid bath (termed piranha).

In conclusion, bonding glass substrates is possible by the three methods: adhesives, anodic bonding, and fusion bonding. As a result of this research, the only method to meet the above

requirements is fusion bonding. Additional experiments on the fusion bonding of glass substrates with etched channels are currently underway and look promising.

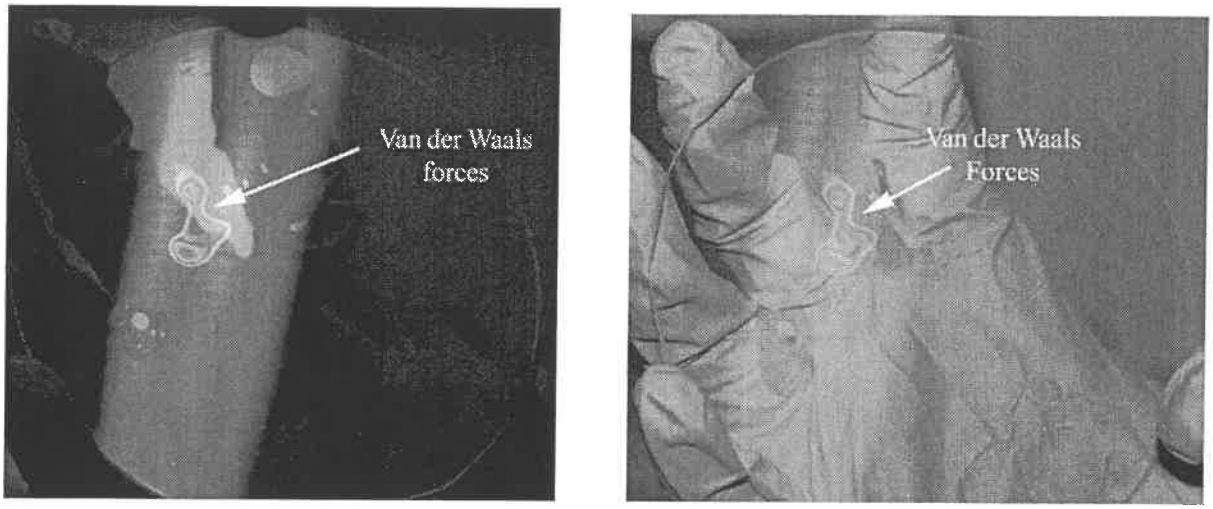

Figure 1: Van der Waals forces shown in fused glass substrates (left and right picture) that were pressed together without vacuum.

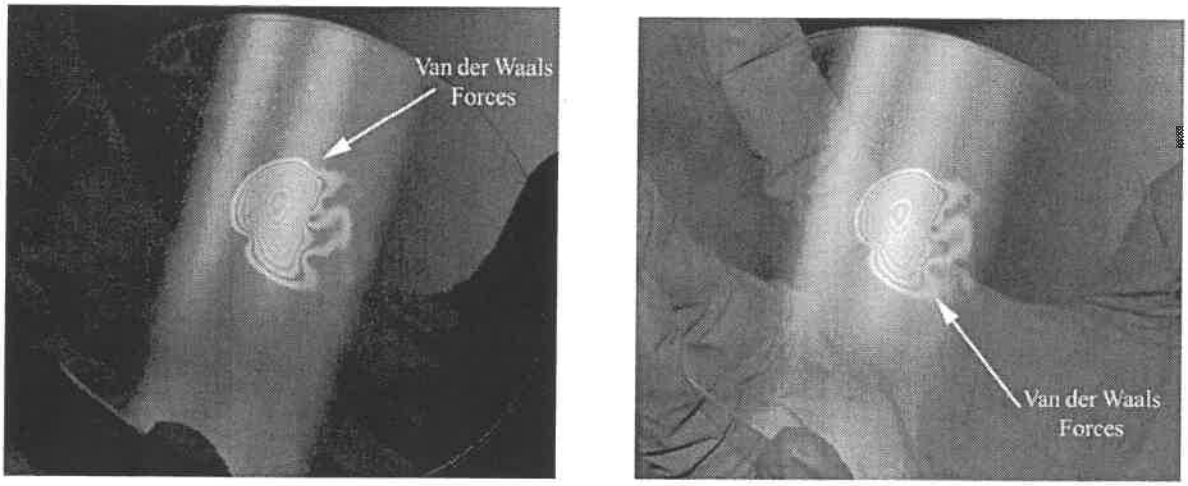

Figure 2: Van der Waals forces shown in fused glass substrates (left and right picture) that were prebonded in 1e-2 vacuum.

Keywords: Bonding, Glass, fusion

References:

[1] Jackman, R. J., D. C. Duffy, et al. (1999). *Using elastomeric membranes as dry resists and for dry lift-off.* Langmuir 15(8): 2973-2984.

[2] Xia, Y. N. and G. M. Whitesides (1998). *Soft lithography.* Annual Review of Materials Science 28: 153-184.

[3] Li, H. W., B. V. O. Muir, et al. (2003). *Nanocontact printing: A route to sub-50-nm-scale chemical and biological patterning.* Langmuir 19(6): 1963-1965.

[4] Efimenko, Kirill, W. E. Wallace, and J. Genzer, *Surface Modification of Sylgard -184 Poly(dimethyl siloxane) Networksby Ultraviolet and Ultraviolet/Ozone Treatment.* Journal of Colloid and Interface Science 254, pp 306 – 315 (2002).

[5] Wallis, George and Daniel I. Pomerantz, *Field Assisted Glass-Metal Sealing.* Journal of applied physics Vol. 40, Number 10, Sept 1969 pp. 3946 -3949.

[6] Lee, D-J, Ju, B., Lee, Y., Jang, J., and Oh, M., *Glass-to-Glass Anodic Bonding For High Vacuum Packaging of Microelectronics and its Stability.* Journal of IEEE, 2000 pp. 253-258.

[7] Choi, W. B., B.K. Ju, et al. *Silicon-to-indium Tin Oxide Coated Glass Bonding For Packaging of Field Emission Arrays Fabricated on Silicon Wafer.* J. Materials Science Vol. 34 (1999) pp. 4711-4717.

Fabrication of high aspect ratio metal shadow mask for OTFTs

Sang Min Yi[1], Sung Hun Jin[2], Hae Sung Lee[1], Jong Duk Lee[2], and Chong Nam Chu[1]

[1] *School of Mechanical and Aerospace Engineering, Seoul National University, Seoul 151-742, Korea*

[2] *Inter-University Semiconductor Research Center (ISRC), and School of Electrical Engineering, Seoul National University, Seoul 151-742, Korea*

1. Introduction

Recently organic thin-film transistors (OTFTs) have attracted much attention for a variety of electronic applications, including information display, electronic paper, and radio frequency identification [1]. Even though OTFTs can be implemented in one of two configurations-top contact and bottom contact, the best performances of OTFTs in the literature have always been in the top contact configuration [2]. However, the top contact mode is incompatible with conventional photolithography for the definition of source and drain (S/D) electrodes on organic semiconductors due to the intolerance of organic material to the exposure of solvents and other liquids [3]. Therefore, metal shadow masks can be a good technique for defining the S/D electrodes in the fabrication of OTFTs because they can guarantee simple, robust, and low cost source-drain definition process without damage to the organic materials.

Current drivability of OTFTs is proportional to the physical dimensions of an OTFT, i.e. the ratio of the channel width (W_c) to the channel length (L_c) [4]. Therefore, the current drivability of OTFTs with the same areal density can be improved by reducing the spacing of S/D electrodes (L_c) for a fixed width of the channel (W_c). Consequently, we need to control the spacing of S/D electrodes, which is equal to the width of the wall (L_b) after machining the S/D holes in the shadow mask, as shown in Fig. 1.

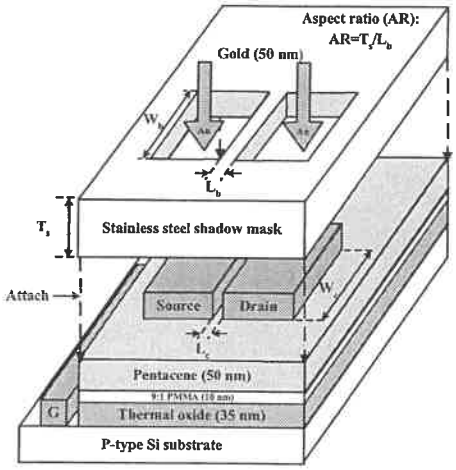

Fig. 1 Schematic illustration of process steps for pentacene TFTs fabricated using a shadow mask.

The thickness of the shadow mask is an important factor for achieving structural robustness, re-usage, and easy handling of the shadow mask. The aspect ratio ($AR= T_s/ L_b$) is defined as the ratio of the thickness of the shadow mask (T_s) to the width of the wall (L_b). However, conventional metal shadow masks fabricated by photochemical machining or laser beam machining are inappropriate to the fabrication of OTFTs due to the inherent limit of the process resolution and aspect ratio [5].

In order to fabricate a high-aspect-ratio and high-resolution stainless steel shadow mask, we proposed a new method by a combination of micro-electro-discharge machining (micro-EDM) and electro-chemical etching (ECE) and investigated the machining characteristics of micro-EDM and ECE.

After S/D electrodes of OTFTs were defined on pentacene active layer through the fabricated shadow mask, the electrical characteristics of pentacene TFTs were investigated.

2. Micro-EDM in the new process

Micro-EDM is an attractive micro-fabrication technique that can be used to machine any electrically conductive material [6]. Figure 2 shows a schematic diagram of the experimental setup for the micro-EDM. This setup has the Z stage for feeding the tool electrode and the X-Y stage for positioning the workpiece to control the spacing of the S/D holes. The positioning resolution is 0.02 μm. A resistance-capacitance (RC) circuit pulse generator with 500 pF and 1 kΩ is used and the applied voltage is 100 V. The workpiece for shadow mask is 100-μm thick 304 stainless steel.

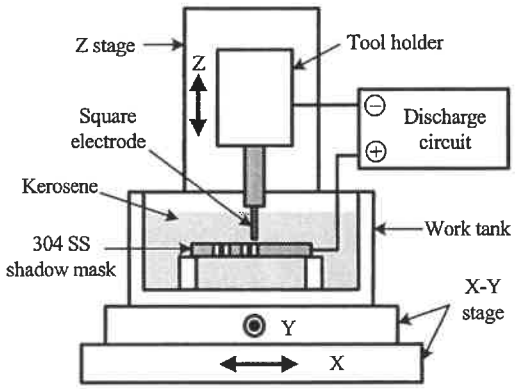

Fig. 2 Experimental setup for micro-EDM process

In order to drill S/D holes, first a square copper electrode with one side length of 130 μm is fabricated by WEDM [6], and then using the fabricated tool electrode, square holes are serially machined by micro-EDM. When drilling holes by micro-EDM, the machined hole is not straight but tapered, as shown in Fig. 3. The taper of the hole is caused by secondary discharges between debris and workpiece. Consequently, the bottom width (L_b) of the wall is wider than the top width (L_t). To reduce the bottom width of the wall, the finishing was conducted after perforating by moving the tool electrode 7 μm toward the wall. Figure 3 shows the micro-EDM process flow and the scanning electron microscopy (SEM) images of the micro-EDMed holes after finishing is shown in Fig. 4. The difference between the top and bottom walls is only 1.2 μm in width.

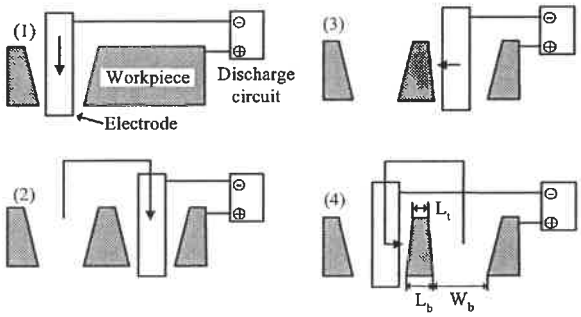

Fig. 3 Flow of micro-EDM process

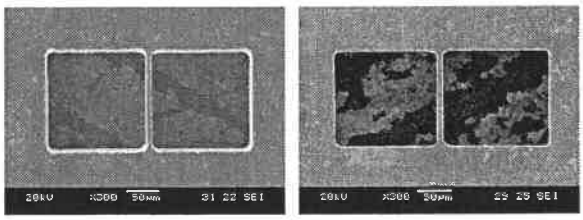

(a) (b)

Fig. 4 SEM images of shadow mask after micro-EDM process: (a) top view, L_t = 8.8 μm and (b) bottom view, L_b = 10 μm

The wall width (L_b) can be controlled by positioning the tool electrode considering the lateral discharge gap. However, there is a limit to how much the wall width can be produced. Figure 5 shows the distortion of the wall according to the spacing of machined holes. During machining, the local temperature in the workpiece approaches the vaporization temperature of

the material [7]. As the wall becomes thin, the wall tends to be bent due to thermal expansion and collapses locally due to heat and pressure generated during machining. Consequently, the dimension of the wall and material influence the allowable minimum width of the wall. For 150-μm long, 100-μm thick, 304 stainless steel, the minimum width of the wall is about 10 μm.

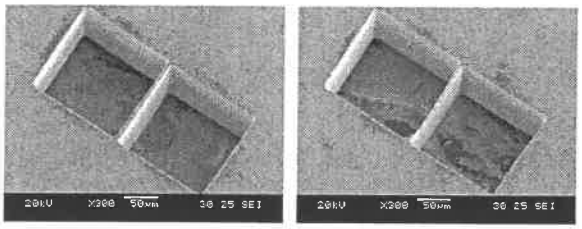

(a) (b)

Fig. 5 Distortion of wall shape according to the spacing of machined holes: (a) L_b = 10 μm and (b) L_b = 8 μm.

3. Electro-chemical etching in the new process

Electro-chemical etching (ECE) is basically an isotropic machining process [8]. This characteristic of ECE might be a fatal drawback, which prevents the production of a straight wall and high aspect ratio, whereas it can be effectively used to uniformly decrease the dimension of the structure already perforated. Therefore, ECE was used to decrease the width of the wall after micro-EDM. The experimental system used for the ECE is shown schematically in Fig. 6. A saturated calomel electrode (SCE) was used as the reference electrode, a platinum wire as the counter electrode, and H_2SO_4 solution as the electrolyte. In ECE process, the width of the wall can be controlled by the etching time. At the applied voltage of 1.2 V (vs. SCE) and with 0.1 M H_2SO_4 solution, the etching rate was 19 nm/min.

Figure 7 (a) shows a SEM image of the shadow mask after micro-EDM process and before ECE process. The width of the wall was 10 μm. The final shadow mask after micro-EDM and ECE process is shown in Fig. 7 (b). The etching time was 150 min and the width of the wall was reduced to 3.6 μm.

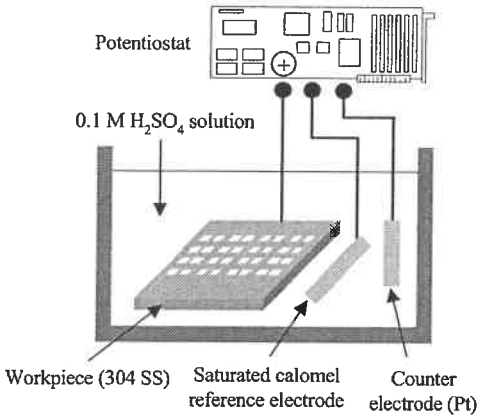

Fig. 6 Schematic diagram of ECE system

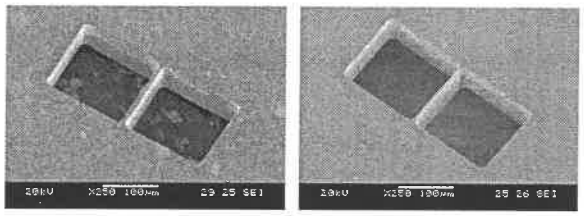

(a) (b)

Fig. 7 SEM images of shadow mask: (a) after micro-EDM process, L_b = 10 μm and (b) after ECE process, L_b = 3.6 μm.

4. Fabrication and electrical characteristics of pentacene TFTs

Figure 1 shows a schematic diagram of the fabrication of pentacene TFTs. 50 nm of gold was e-beam evaporated on pentacene active layer through the fabricated shadow mask to define S/D contacts as well as the gate contact. S/D electrodes with L_c = 3.6 μm and W_c = 150 μm were successfully patterned through the fabricated shadow mask as shown in Fig. 8.

Figure 9 (a) shows the SEM image of the stainless

steel shadow mask for pentacene TFTs. The dimension of S/D holes was 150 μm × 150 μm and the spacing of S/D holes (L_b) was 5 μm. Figure 9 (b) shows the output characteristics of pentacene TFTs with channel length (L_c) of 5 μm in the saturation region. For the pentacene TFTs with L_c = 5 μm at V_{GS} = -20 V and V_{DS} = -20 V, the saturated drain current was -104 μA.

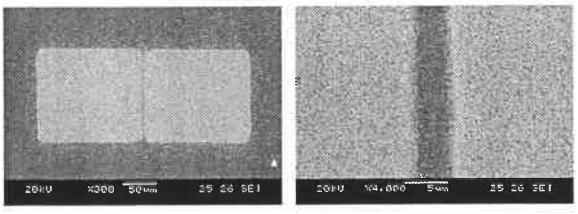

(a) (b)

Fig. 8 SEM images of the defined source and drain electrodes through the fabricated shadow mask: (a) the dimension of S/D electrodes is 150 μm × 150 μm and (b) an enlarged view of the spacing between source and drain electrode. The spacing of S/D electrodes is 3.6 μm.

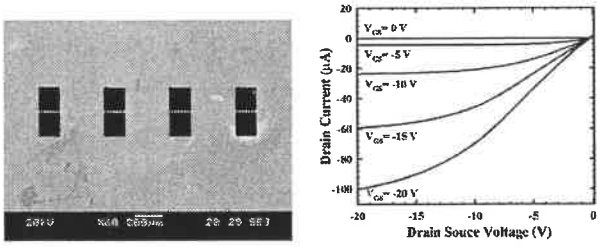

(a) (b)

Fig. 9 (a) SEM image of stainless steel shadow mask with walls of 5 μm (b) output characteristics of a pentacene TFT with a channel length of 5 μm

5. Conclusion

In this paper, a new micro-fabrication process which combines with micro-EDM and ECE was developed, and stainless steel shadow mask with a high aspect ratio and high resolution was fabricated through the proposed process. The fabricated stainless steel shadow mask has 95 μm thickness and 3.6 μm resolution and the aspect ratio of the shadow mask is about 26. Source and drain electrodes with the channel length of 3.6 μm were defined on pentacene active layer by the use of the shadow mask.

Source and drain electrodes with the channel length of 5 μm were routinely defined on pentacene active layer by the use of the shadow mask, and for the fabricated pentacene TFTs with the channel width of 150 μm, the current drivability at V_{GS} = V_{DS} = -20 V was 104 μA. The obtained electrical characteristics confirmed that stainless steel shadow mask deposition method can be used to fabricate pentacene TFTs as a high-resolution source and drain patterning method.

References

[1] Baude P F, Ender D A, Haase M A, Kelley T W, Muyres D V and Theiss S D 2003 *Appl. Phys. Lett.* **82** 3964–3966

[2] Kymissis I, Dimitrakopoulos C D and Purushothaman S 2001 *IEEE Trans. Electron Devices* **48** 1060–1064

[3] Gundlach D J and Jackson T N 1999 *Appl. Phys. Lett.* **74** 3302–3304

[4] Dimitrakopoulos C D and Mascaro D J 2001 *IBM J. RES.& DEV.* **45** 11–27

[5] Sommer C 2000 Advanced Publishing Inc. Houston

[6] Masuzawa T, Fujino M and Kobayashi K 1985 *Annals of the CIRP* **34** 431–434

[7] DiBitonto D D, Eubank P T, Patel M R and Barrufet M A 1989 *J. Appl. Phys.* **66** 4095–4103

[8] Datta M 1998 *IBM J. RES.&DEV.* **42** 655–669

A NEW INTERNAL MAGNETIC ASSISTED MACHINING PROCESS FOR NON-FERROMAGNETIC THICK TUBING USING MAGNETIC MACHINING JIG

Yanhua Zou*[1] and Takeo Shinmura*[1]
*[1] Graduate School of Engineering, Utsunomiya University, Tochigi, Japan

Abstract

This paper describes a new magnetic field assisted machining process using a magnetic machining jig to finish the internal surface of thick tubing (10~30mm in the thickness). Because the magnetic machining jig consists of permanent magnets, it can generate a higher magnetic force than conventional magnetic abrasives, and makes the internal finishing of thick non-ferromagnetic tubing possible. Moreover, in order to obtain a high-quality surface, this process method was developed using magnetic particles abstracted on magnet surface of the magnetic machining jig and offering the abrasive slurry. First, this paper characterizes the processing principle of this process. Next, the certificated experiment was carried out. It was clarified that not only the surface roughness, but also the roundness of inside tubing can be improved. The results showed that the initial surface roughness of 6.5μm*Ra* can be improved to 0.06μm*Ra*, and the roundness of inside tubing can be improved from 187μm to 89μm.

Keywords: Magnetic field assisted machining, Internal finishing, Magnetic machining jig, Thick tubing, Finishing characteristics, Surface roughness, Roundness.

1.Introduction

Most of the previous research on the internal finishing, the magnetic abrasive was used as a machining tool, and it was clarified that the internal finishing of thin tubing (about 1~3mm in thickness) is very effective [1] [2]. However, when the thickness of the tube becomes thicker, finishing becomes impossible, because the magnetic force (finishing force) weakens. In this study, a new magnetic field assisted machining process using magnetic machining jig was proposed [3]. Because it consists of permanent magnets, the magnetic machining jig can generate high magnetic force compared with the case to use the magnetic abrasives, due to higher material susceptibility, and makes the internal finishing of thick non-ferromagnetic tubing (10~30mm in the thickness) possible. Moreover, this new process was developed using magnetic particles and abrasive slurry, these particles are magnetically attracted to the surface of a permanent magnet of a magnetic machining jig. While the magnetic machining jig follows the rotation of the pole through the magnetic particles, the relative motion against the inner surface of tube is generated, the abrasive behavior is indirectly given from magnetic particles to abrasive grains, and the precise finishing can be achieved. The realizability of this processing method was confirmed [4] [5].

In this paper, the processing principle and advantages of this new process are described. The applicability of improving the internal surface roughness and roundness of inside tubing of the thick SUS304 tubing were examined. The magnetic machining jig and the experimental setup applied to the internal finishing of thick tubing were manufactured, and an experiment was carried out. In this study, a multiple-stage

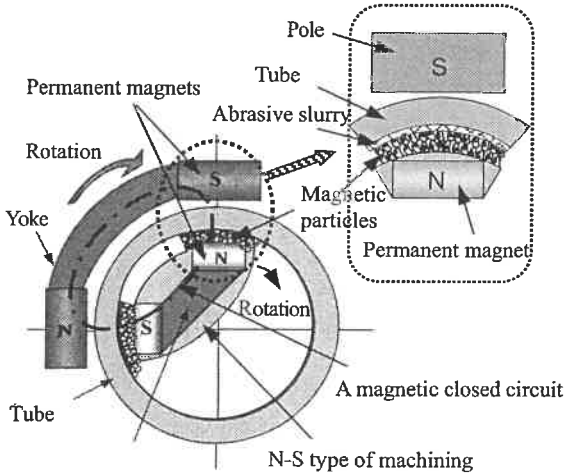

Fig.1 Schematic of internal machining process using a magnetic machining jig

finishing was carried out to obtain a high-quality surface. The results of the experiment showed that precise internal finishing of a thick SUS304 stainless steel tube (10mm in the thickness) could be achieved, and the surface roughness and the roundness of inside tubing can be improved at the same time. In this study, it was clarified that this processing method using magnetic machining jig is very effective in improving the roundness of the inside tubing, although the conventional magnetic field assisted finishing process using magnetic abrasives was ineffective [6].

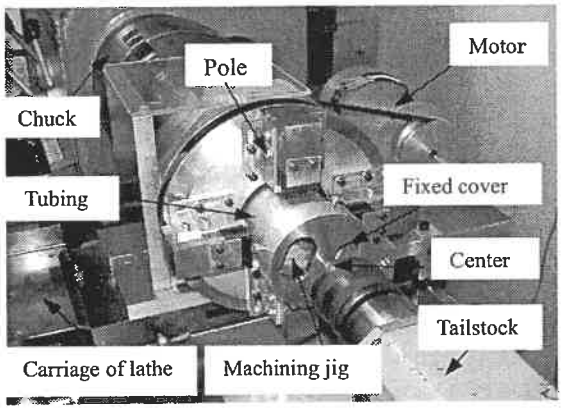

Figure 2. External view of the experimental setup

2. Processing principle

Figure 1 shows a schematic of the internal machining process using a magnetic machining jig by the use of a pole rotation system [1,2]. The magnetic machining jig placed in the tube is magnetically attracted by the poles placed outside the tube, pushing the inner surface of the tube by the generation of magnetic force. When the poles are rotated around the tube, the machining jig follow rotate along the inner surface of the tube by magnetic force (finishing force) together with the rotating poles, resulting in the occurrence of relative movement between the magnetic machining jig and the tube surface.

If the rotating poles are driven in the direction of the tube axis, the magnetic machining jig is also driven by the magnetic force in the direction of the tube axis while rotating along the inner surface of the tube. As a result, finishing of the entire inner surface of the tube is achieved. While the magnetic machining jig follows the rotation of the pole through the magnetic particles, the relative motion against the inner surface of tube is generated, the abrasive behavior is indirectly given from magnetic particles to abrasive grains, and the precise finishing is achieved. Because the problem of the abrasive paper longevity was solved and the size of magnetic particles and abrasive grains can be selected freely by this technique, high-precision process could be achieved.

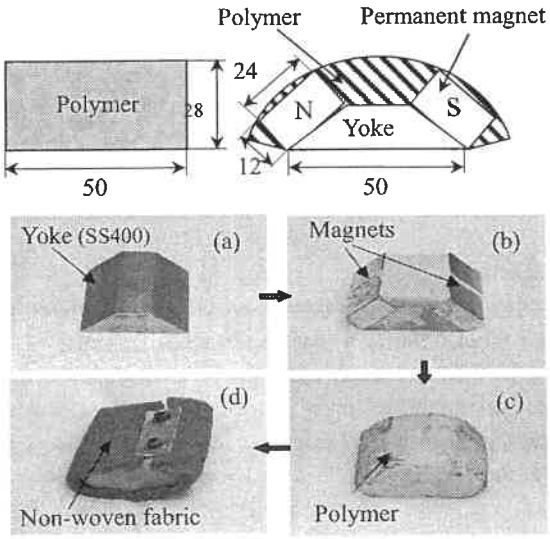

Figure 3.Composition and the external view of a magnetic machining jig

3. Experimental setup and conditions

Figure 2 shows an external view of the experimental setup for the internal machining process using a magnetic machining jig. A finishing unit, consisting of magnet poles attached inside a yoke (SS400 steel), is set on the reciprocating table of a lathe, and a stainless steel tube as a workpiece is fixed between the chuck and the tail stock center of the lathe. Ferrite magnets were used as poles for safety of processing environment, and the poles are big (50×35×26mm) for the increase of the finishing zone in this experiment, but sufficient magnetic force (finishing force) can be obtained by using a magnetic machining jig. The poles were set symmetrically toward the tube center in an N-S-S-N pole arrangement, and the pole arrangement is flexible for various tube diameters. Figure 3 shows the composition and the external view of a magnetic machining jig. First, two magnets are installed on a yoke (SS400 steel), as shown in Fig.3 (b). Next, polymer is put on the magnetic machining jig surface to make the surface shape consistent with the internal

surface of the tube, as shown in Fig.3 (c). Finally, the surface is rolled with non-woven fabric, the magnetic particles are added and magnetically attracted strongly to the machining jig surface through the non-woven fabric, as shown in Fig.3 (d). The experimental conditions are shown in Table 1.

In order to obtain a high-quality surface and high-efficiency finishing, a multiple-stage finishing process was performed in this experiment. Because of a SUS304 stainless steel tubing barefacedly was used, the pre-processing surface is very rough, and the surface roughness is not uniform in the entire surface of tubing. Therefore, the large iron particles and coarse abrasives are used for coarse finishing at the first stage processing, and then decreases the size of iron particle and abrasive grain little by little for the medium finishing and fine finishing in the following three stage processing as shows in table 1. The tubing rotation was set to 34min^{-1}, and the pole rotation was set to 150min^{-1}.

Table 1 Experimental conditions

Workpiece	SUS304 stainless steel tube Ø89.1×Ø79.1×500mm, Initial surface roughness: 6.5μmR_a, Revolution: 34min^{-1}	
Magnetic machining jig	Magnet: Nd-Fe-B rare earth permanent magnet, Yoke: SS400 steel, Molding material: Polymer	
Pole	Magnet: Ferrite magnet, 50×35×26mm; Yoke: SS400 steel, Pole revolution: 150min^{-1}	
Processing	1st-stage processing	Magnetic particles: Electrolytic iron particles (1680μm in mean dia.) Abrasive: WA #1000, Finishing time: 40min
	2nd-stage processing	Magnetic particles: mixing magnetic abrasives (500μm in mean dia.), Abrasive: WA #4000, Finishing time: 40min
	3rd-stage processing	Magnetic particles: Electrolytic iron particles (330μm in mean dia.), Abrasive: WA #6000, Finishing time: 20min
	4th-stage processing	Magnetic particles: Electrolytic iron particles (75μm in mean dia.), Abrasive: 0~1μm diamond particles, finishing time: 20min

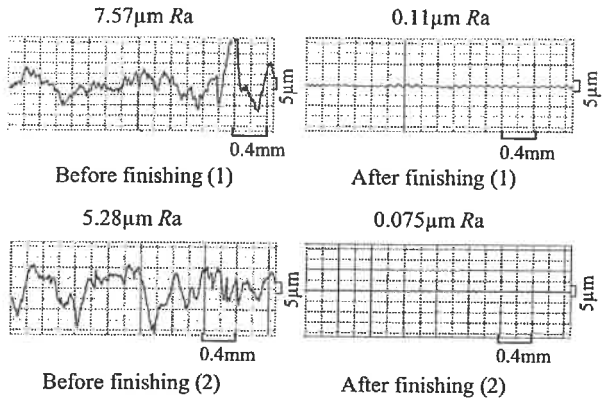

(a) Change in surface roughness profiles before and after finishing

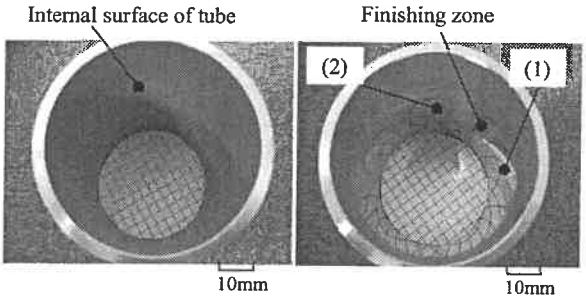

(b) Photos of internal surface of tubing

Fig.4 Photos of inside tubing and surface roughness profiles before and after finishing

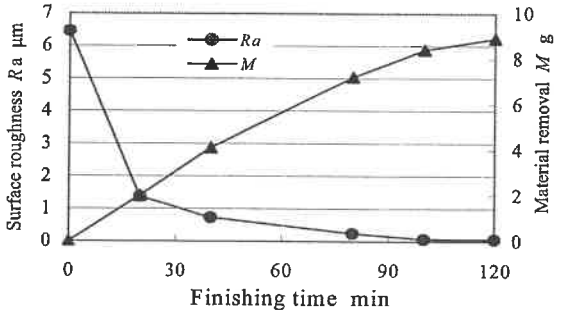

Fig.5 Relationships between surface roughness *Ra*, material removal *M* and finishing time

In order to confirm that a tube of 10 mm in thickness can be finished, a tube of 5 mm in thickness was used as a workpiece, and the clearance between the pole tip and the tube was set at 7 mm in this experiment. It is thought that the same result is obtained when a tube of 10 mm in thickness was used, and the distance was set at 2 mm.

4. Experimental results and discussion

4.1 Improvement of surface roughness

The finishing experiments were halted every 20min to measure the roughness surface and material

removal and roundness. Because the pre-processing surface is very rough and the surface roughness is not uniform in the entire surface of tubing, the surface roughness was measured four times at intervals of 90°, and the arithmetic mean of measurement value was defined as surface roughness in this study. Figure 4 shows the photos of internal surface of tubing and the change of the surface roughness profiles for two points before and after finishing. Figure 4 (a) shows, 1 point's initial surface roughness of 7.57 μmR_a was improved to 0.11 μmR_a, 2 point's initial surface roughness of 5.28 μmR_a was improved to 0.075 μmR_a. While nothing shows on the rough surface before finishing, the reflection appears on the smoothly finished surface as shown in Fig. 4 (b).

Figure 5 shows relationships between surface roughness R_a, material removal M and finishing time. The result shows that the initial surface roughness of 6.5μmR_a can be improved to 0.06μmR_a. It was confirmed that the process enables precise internal finishing of a thick SUS304 stainless steel tube (10 mm in thickness).

4.2 Improvement of roundness of inside tube

The roundness of the inside tubing was measured three times at an interval of 10mm in the direction of the tubing axis. Figure 6 shows the changes in roundness of tubing by measuring it 3 times and the average roundness value with the finishing times. The result shows that the average roundness value was improved from 187μm to 89μm.

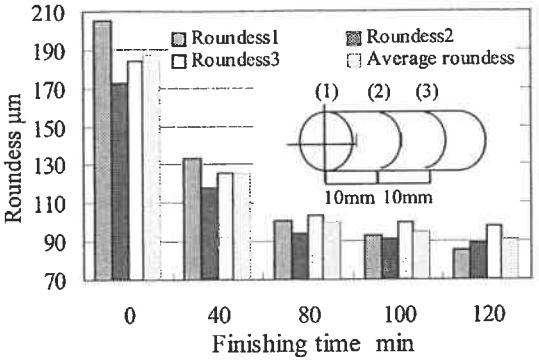

Fig.6 Changes in roundness with finishing time

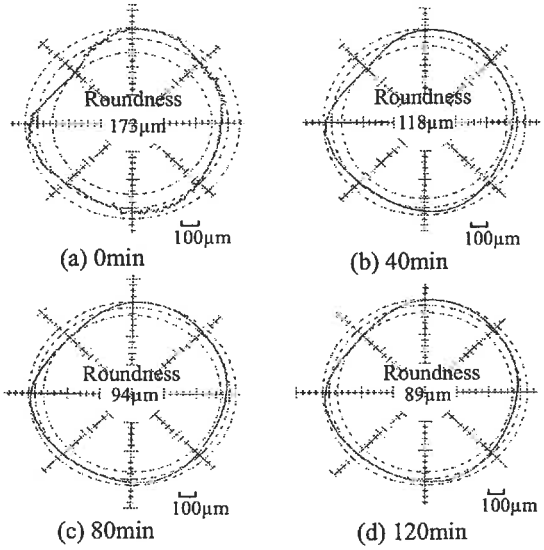

Fig.7 Changes in roundness profiles with finishing time

Figure 7 shows changes in roundness profiles of the second measurement with finishing time at every 40 min. It is apparent that the form profile became rounder with more finishing time, and the roundness was improved from 173μm to 89μm. It was clarified that this processing method was an effective processing method to improve the roundness of inside tubing, and it was difficultly for the conventional magnetic field assisted finishing process using magnetic abrasives [6]. It is thought that a grinding action was obtained in case of using magnetic machining jig.

5. Conclusions

In this study, it was clarified that this processing method enables the improvement of the roundness of inside tubing while improving the surface roughness, and the initial surface roughness of 6.5μmR_a can be improved to 0.06μmR_a, and the roundness of inside tubing can be improved from 187μm to 89μm.

Acknowledgement

This topic of research is supported by Cooperation of Innovative Technology and Advanced Research in Evolutional Area of MEXT, JAPAN.

Reference

[1]. T. Shinmura and H. Yamaguchi, Trans. Jpn Soc. Mech. Eng.(C), 38(4), 798 (1995).
[2]. H. Yamaguchi, T. Shinmura and T. Kaneko, J. Jpn Soc. Prec. Eng., 30(4), 317 (1996).
[3]. Yanhua Zou and T. Shinmura, Trans. Jpn Soc. Mech. Eng.(C), 68(669), 1575 (2002). [in Japanese]
[4]. Yanhua Zou and T. Shinmura, Key Engineering Material, 257-258, 2004:505-510.
[5]. Yanhua Zou and T. Shinmura, J. of Japan for Abrasive Technology, Vol. 48, No.8 (2004), pp. 444-449. [in Japanese]
[6]. H. Yamaguchi, T. Shinmura, J. Jpn Soc. Prec. Eng., 62(11), 1617 (1996). [in Japanese]

The method of finishing the inside of a minute hole

Masakazu Mitsuhashi, Ken'ichiro Horio, Tsugio Yamazaki
Saitama University
255 Shimo-okubo, Sakura, Saitama, 3388570, JAPAN

1. Introduction

In recent years, various technologies for improving fuel consumption are developed in an engine system. Nozzles that supply fuel in those technologies play an important role. From now on, it is expected as diameter of the nozzle become small in order to realize high pressure in fuel injection system. In case of processing hole down to 0.2mm, a drilling process is generally used. The flow of the fuel in a nozzle depends on smoothness of the hole inside. Now, the polishing method corresponding to such the minute hole is not developed. The purpose of this research is improving the surface roughness of inside of the hole after the drilling process.

2. Electrolytic polishing

There are some ways for improving the surface roughness of the hole inside. For example fixed abrasive method or loose abrasive method is used. However these methods need tool rigidity, it is hard to respond to a small hole. Besides these are not suitable for polishing of hard material for nozzles. We adopted the electrolytic polishing method without necessity of considering the rigidity. It is easy to apply the process to high hardness alloy used for the high-pressure fuel injection technology. It is also suitable for finishing of a slanting hole.

3. Experimental procedure

Setup of experiments is shown in Fig.1. We smoothed side surfaces of the workpiece of stainless steel by grinding. Two smooth surfaces was stuck together by vice. We drilled the hole along the border of two surfaces in order to evaluate the inside wall easily. Electrolytic polishing (EP) was performed, after evaluating a hole inside and making the samples stuck together again. Power supply for EP is done by direct-current power supply equipment, which is used for constant current mode. Both scanning electron microscope (SEM) and stylus method surface profiling machine were used for evaluation

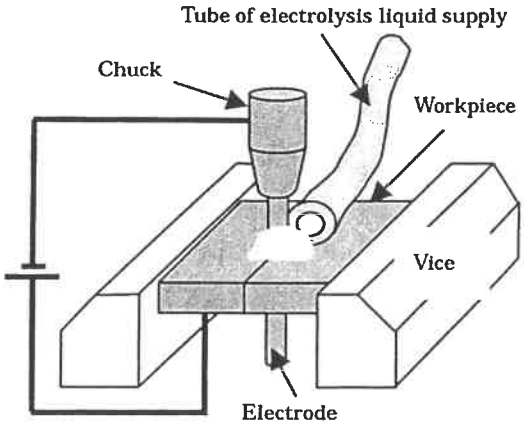

Fig. 1 Experimental setup

4. Effect of electrolysis products

1) The flow of electrolysis liquid

First, in order to investigate the characteristic of fundamental electrolysis polish, the electrode was soaked in electrolysis liquid and the hole inside was polished. Fig.2 is a SEM image of the polished hole of 0.5mm diameter. Electrolysis liquid evaporated with heat, and the electrolysis products adhered to the inner wall. As a result it did not become the good surface. Thus we made the micro tube pump system to inhale the electrolytic liquid. Experimental conditions are shown in Table 1. In fig.3, both the surface of 100 milliamperes current supply and that of 200mA are better than fig.2. However, there is a slight difference between them. In 200mA, getting electrolysis products blocked with the hole inside, the surface turned into a spots polishing, and on the contrary it was not well polished in 100mA. We think the balance of the current of electricity and the amount of inhalation is required in order to acquire a good surface.

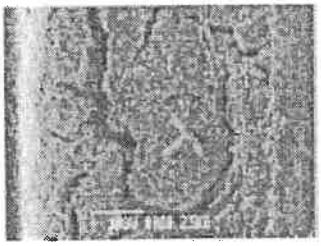

Fig.2 Inside wall of a hole adhered electrolysis products

Table 1. Electrolysis polish conditions

Sample	Stainless steel
Path of a hole	0.8(mm)
Path of a electerode	0.5(mm)
Electrolysis liquid	NaNO3
Concentration	4(wt%)
Inhalation speed	2 ¢m3/min)
Voltage	4~5(V)
Electric current	100,200(mA)
Polishing time	2(min)

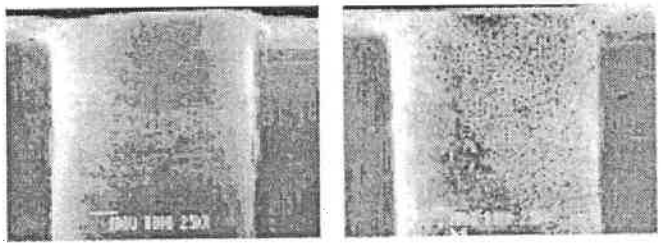

(a) 100mA (b) 200mA

Fig.3 Inside wall after polishing

2) Rubbing action

As mentioned above electrolysis product prevents the surface from improvement in the surface roughness. Thus we tried to introduce a rubbing action during electrolytic process in order to remove the electrolysis generation compulsorily. We designed and tried various type of the electrode for working a rubbing action well. We tried what wound around the copper wire, thread, sponge, and the resin with slit (Fig.4). Most excellent electrode was resin by factors, such as durability.

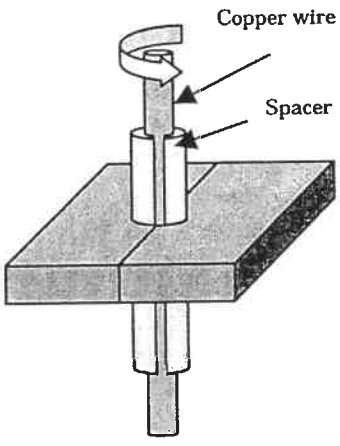

Fig.4 Newly developped electrode

5. Process parameters

1) Current

In electrolysis polishing, the electric current is the important element. So we investigated influence of the electric current value. Experimental condition is shown in Table 2. The results are shown in Fig.5 and 6. If the surface coarseness before and after polishing is compared, surface roughness became the best on 200mA by 100mA. We found existence of an optimum electric current value.

Table 2. Electrolysis polish conditions

Sample	Stainless steel
Diameter of a hole	0.8(mm)
Diameter of a electrode	0.8 (mm)
Rotation	4000(rpm)
Electrolysis liquid	NaNO3
Concentration	20(wt%)
Voltage	5~8(V)
Electric current	100,200,300(mA)
polishing time	2(min)

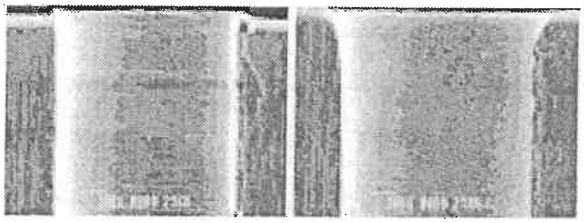

(a) (b)

Fig.5 The minute hole before polishing (a) the minute hole after polishing (b)

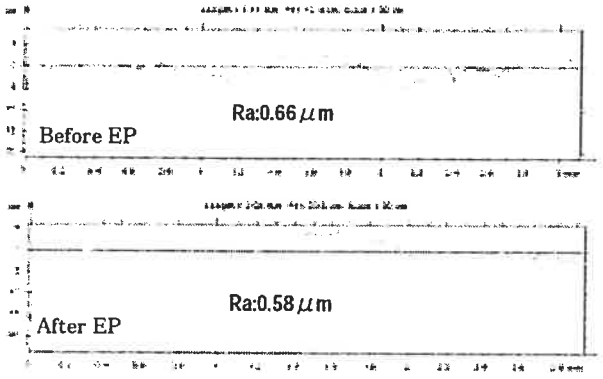

(a)100mA

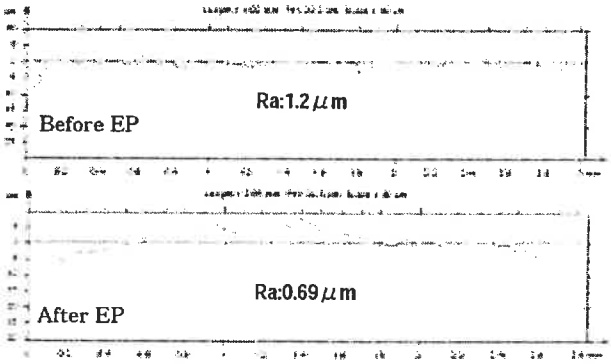

(b)200mA

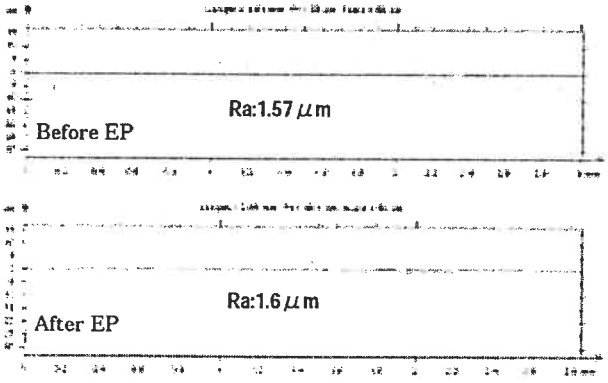

(c) 300mA

Fig.6 Comparison of the cross-sectional form polishing before and after polishing

2) The electrode rotation speed

In order to investigate influence of the electrode rotations speed, the experiments by 1000, 4000 and 7000rpm were done. Results are shown in fig.7. In 1000rpm, the electrolysis action is so

strong that the form has deteriorated. Especially the diameter at the inlet increases remarkably. Among them the best result is obtained in 4000rpm. In 7000rpm, the amount of polishing is small. Since the rotation speed is too fast we suggest that an electrolysis action does not work well.

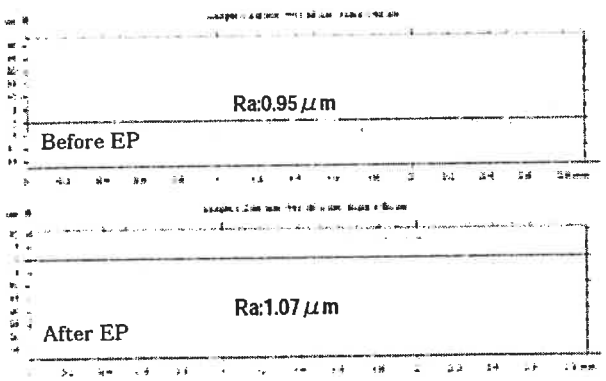

(a)1000rpm

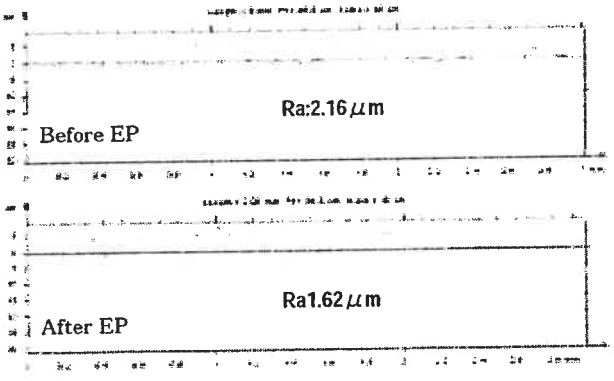

(b)4000rpm

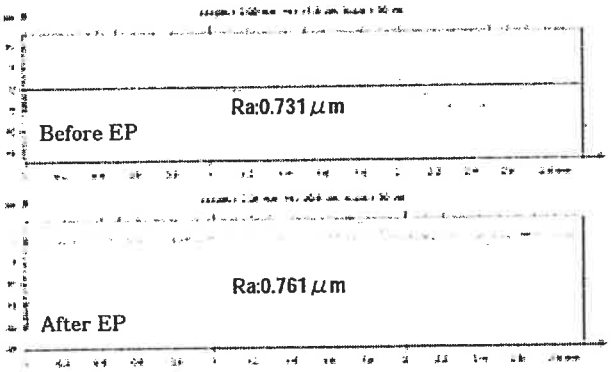

(c)7000rpm

Fig.7 Comparison of the cross-sectional form polishing before and after polishing

6. Conclusions

1) We proposed the new polishing method of a minute hole inside by electrolysis polish.
2) Electrolysis liquid needed to be pouring compulsorily in order to prevent electrolysis products from adhering on the inside of a hole.
3) In order to remove electrolysis products positively, it is necessary to add a rubbing action by the electrode during the electrolytic polishing process.
4) We were able to acquire the better surface by the electrolytic polishing process using the newly developed electrode with a spacer.
5) There are optimum values on rotation speed of the electrode or on the current value of the current supply.

FLEXIBLE SUPER FINISHING PROCESS FOR INTRICATE SHAPES

K.Narayanasamy[#], H.P.Raju[##], Y.G.Srinivasa[#], and R.Krishnamurthy[#]
[#] Indian Institute of Technology Madras, Chennai-600 036, INDIA
E-mail: kns@iitm.ac.in
[##] Department of Mechanical Engineering,
P.E.S. College of Engineering, Mandya-571401, INDIA,
E-mail: rajuhp@hotmail.com

1.0 INTRODUCTION

The removal of superfluous material plays a key role in materials processing and hence abrasive as well as cutting processes are of vital importance in this regard. Product performance that are usually sensitive to surface quality are fatigue strength, corrosion rate, stress corrosion cracking, tribological properties such as lubrication, friction and wear, magnetic properties(memory discs). Hence the surface quality assumes greater importance for proper functioning of any product with due importance to aesthetic aspect also. This necessitates production of required surface texture to perform a specific function. Surface topography influences both mechanical and physical properties, apart from affecting functional applications of contacting parts. Improved product performance, minimum running in period, and enhanced product life all are highly surface dependent, since most of the failures are surface originated; achieving high surface finish is a challenging task with the development of high strength and hard to machine materials. In order to overcome the limitations of traditional finishing processes in meeting the surface finish of internal passages of high end technological products, some new approaches are called for. The process should employ some new form of "tool" that can assume the shape of the passage/hole and flows over the surface(1-2).

Extrusion honing (EH) is one such approach; a flexible honing process that can address these problems to greater extent with consistent results. It may be used for removing internal and external burrs, smoothing flow paths and surface enhancement. It is an unconventional finishing process that removes small quantities of material by flowing semi solid, abrasive impregnated putty, under pressure through or across work piece. It can finish, deburr, polish, or radius and induce compressive residual stress on the surface (3-5). Inaccessible, intricate, complex shapes, and difficult to machine internal or external surfaces can be finished with this process.The abrasion occurs only where medium flow is restricted. The other areas remain unaffected. Any product with a passage to flow could be a candidate to this process. It can process a selected passage or many passages of a component or more. Multiple holes, stepped passages, tapered holes can be finished with this process. Removal of sharp corners enhances the edge quality. It is a proven, reliable and accurate method that provides consistent results. Aerospace components, I.C. engine manifolds, hydraulic components, electronic and biomedical parts are some areas of application of the candidate process. Improvement in air flow and fluid flow characteristics for injector nozzles of cast automotive engine components is one of the new applications

Traditional methods of finishing of manifolds involve cutting the manifolds, polishing it, and then rewelding. Extrusion honing eliminates these, by forcing flowable abrasive medium through the entire manifold. Besides providing a polished surface it produces a surface lay that is parallel to air flow which results in increase in air flow velocity that contributes directly to significant power gains. This process is not limited to engine manifolds alone. Carburetors, water pumps all are suitable as they all have internal passages.

2.0 EXPERIMENTAL

The work material considered in the current investigation is AISI 4419 steel which is used for manufacturing highly stressed components used in construction of engine and vehicles as well as gears and pumps etc. The carrier medium, apart from rheological properties has to possess properties of better grit retention, bond uniformity, and higher abrasive exposure for satisfactory performance. A select grade silicone polymeric medium is thoroughly mixed with a volume fraction of 25% SiC abrasives of 36 grit size using a polymer mixing device. An experimental set-up was designed and developed to implement extrusion honing process(Fig.1). Details of work material, carrier medium, process parameter used in the trials are presented in Table1.

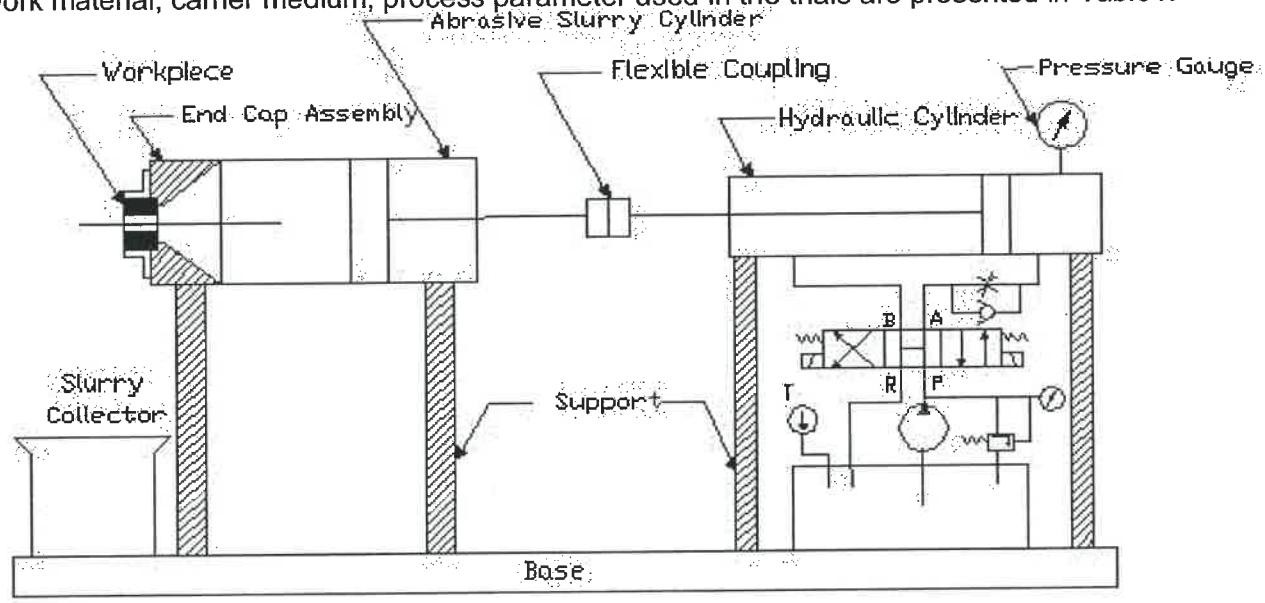

Fig. 1 Schematic Diagram of the Extrusion Honing Machine

Table1. Details of work material, carrier medium, process parameter

Work material		Carrier medium		Process parameter	
AISI 4419 steel		Silicone polymer			
Carbon (%)	0.18-.0.23	Appearance	Transluce nt	Temperature	Ambient
Tensile Strength (MPa)	431	Density (kg/m^3)	$1.13X10^3$	Volume fraction	0.25
Machinability (%)	65	Viscosity(Pa.s)	20250	Velocity (m/min)	0.4-1.2

3.0 RESULTS AND DISCUSSION

3.1 Surface roughness

Typical observed parametric influence of surface characteristics of extrusion honed AISI 4419 steel bored specimen is illustrated in Fig.2. It is seen that there is a visible / drastic reduction in R_t, R_a values during early phase of honing, followed by progressive reduction with number of

passes. Removal of waviness/dominant asperities present over the bored surface during early phase of extrusion honing results in appreciable reduction in R_t, R_a values.

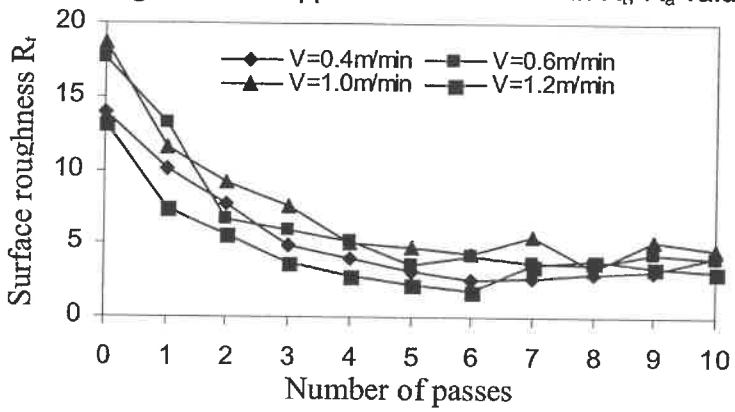

(a)

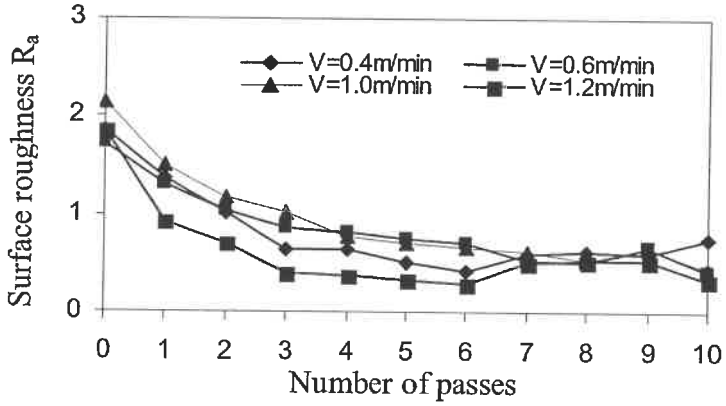

(b)

Fig, 2 Parametrical influence on surface roughness characteristics of AISI 4419 steel (a) R_t and (b) R_a

Typical observed variation of R_t/R_a with number of passes is illustrated in Fig. 3. In general it is seen that up to 6 passes, there is steady reduction in R_t/R_a followed by a rise, indicating that the workpiece attains a core roughness by 6 passes, after that deterioration sets in.

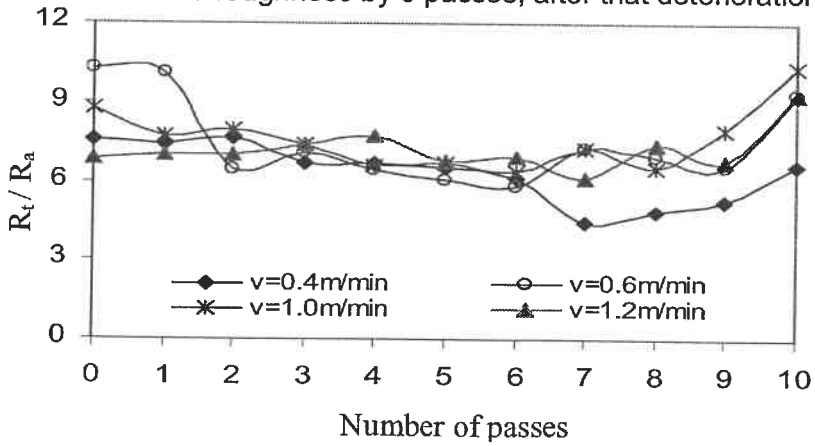

Fig. 3 Typical observed variation of R_t/R_a with number of passes

With the velocity of 0.4 m/min , there exists a steady reduction in R_t/R_a up to 6 passes, and during the seventh pass the ratio drops down to minimum and thereafter it shoots to maximum. After attainment of core roughness by the surface, the spalling of material will increase the R_t value that results in sudden rise of R_t/R_a values. Irrespective of the velocity, over a range of 3-6 passes most of these ratios are in closed range. This can be attributed to core roughness attainment during the process over this range and material spall out thereafter.

3.2 Scanning electron macrographs

For better understanding of the nature of texture produced by extrusion honing, surfaces as bored and as honed were observed (Fig.4) through scanning electron microscope.

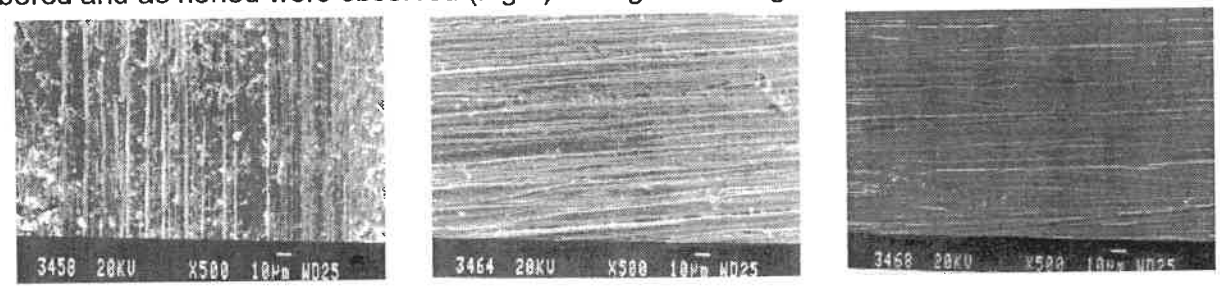

(a) as bored (b) after 5 passes (c) after 10 passes

Fig.4 Scanning electron macrographs of surface at different stages of extrusion honing

After extrusion honing fairly uniform lay pattern with localised folding of asperity can be seen. Further, due to continuous honing, surface has experienced localised discrete glazed texture.

4.0 CONCLUSION

The major conclusions drawn based on the trials conducted are as follows.

1. A progressive improvement in surface roughness parameter is seen till eighth pass, beyond which the surface starts deteriorating.

2. It is seen that up to 6 passes, there is steady reduction in R_t/R_a followed by a rise, indicating that the workpiece attains a core roughness by 6 passes, after that deterioration sets in.

3. Extrusion honing producesfairly uniform lay pattern.

5.0 REFERENCES

1. Chris J. Evans., James B. Bryan., "Structured", "Textured" or "Engineered" Surfaces Annals of the CIRP, Vol. 48/2/1999 541-556
2. A.R.Jones., J.B.Hull., "Ultrasonic flow polishing", Ultrasonics , 36 (1998) 97-101
3. L J.Rhoades., H. A.Clouser., "Abrasive Flow Machining", ASM Metals Handbook,16 (1989) 514-519
4. R.E. Williams, K.P.Rajurkar, "Stochastic Modeling and of Analysis of Abrasive Flow Machining", Trans.ASME. Journal of Engineering for Industry 144 (1992) 74-81
5. J. Matechen, John., "Advantages of abrasive flow machining", Abrasives, (1995) 20-21

ATOMIC STRUCTURE OF FLOAT POLISHED SURFACES OF CALCIUM FLUORIDE SINGLE CRYSTALS FOR ULTRA VIOLET APPLICATIONS

Naoyuki Ohnishi*, Yoshiharu Namba, Shinji Yoshida, Tomohiro Yoshida and Yasuhiro Kanda
Chubu University, Kasugai, Aichi 487-8501, Japan

Kunio Yoshida
Osaka Institute of Technology, Osaka 535-8585, Japan

Abstract

Calcium fluoride (111) single crystals for ultra violet applications have been finished to flat by the float polishing process with 7nm-diameter silicon dioxide powder, pure water and a tin lap. The flatness of 32nm P-V on 90-mm-diameter samples that had a surface roughness of 0.72 nm Ry, and 0.077 nm rms were obtained. High-resolution transmission electron microscopy study of the cross-sectioned crystal surface showed that the float-polished surface had (111) plane with small atomic steps, and no subsurface defect. The polished surface roughness depends on the mismatch between the sample surface and the (111) plane. This result was also verified by scanning probe microscope observation.
Key Words: Calcium fluoride, Ultra-precision polishing, Atomic surface structure, Transmission electron microscopy

1. Introduction

High purity calcium fluoride (CaF_2) single crystal is the only candidate for materials of micro-lithography optics using excimer lasers of Deep Ultra Violet (DUV) and Vacuum Ultra Violet (VUV) region. The requirements for the CaF_2 optical components surface are to have a high precision figure and an ultra-smooth surface, even though the CaF_2 crystal is difficult to polish because it is soft and has a relatively high thermal expansion coefficient. The major problem of commercially polishing CaF_2 crystals is producing surface sleeks or fine scratches which introduce subsurface damage and scattering. In order to increase the laser-induced damage threshold, the polished surface must be extremely smooth and without subsurface damage caused by finishing. Float polishing has been used to polish various single crystals and optical glasses to an ultra-smooth finish without a deformed subsurface layer. [1-3] From previous report [4], the smoothest surface of CaF_2 single crystals is expected to be achieved by float polishing, even though the material is fairly soft. In this study, we performed the float polishing of CaF_2 single crystals to obtain DUV lithography-grade surfaces, and an analysis of the finished surface structure mainly focused on detailed atomic structures of the polished surfaces by means of high-resolution transmission electron microscopy (TEM) .

2. Experimental Procedure

High purity, DUV-grade CaF_2 single crystals were sawed into 100-mm-diameter, 40-mm-thick discs and 10 mm x 10 mm x 5 mm rectangular plates. The large flat area of the samples was aligned parallel to the (111) plane that is used for optical applications. The samples were mounted on a stainless steel holder and precisely ground by the ultra-precision surface grinder using an SD3000-75-B wheel. The samples were float polished on a tin lap with 7-nm-diameter SiO_2 powder in a water solution on the ultra-precision float polishing machine [3]. The polishing fluid was a mixture of pure water and 3 wt% SiO_2 powder, and was controlled within a temperature range of 0.01 K. Polishing pressure was only applied by the weight of the sample and sample holder. The flatness of a 100-mm-diameter, float-polished CaF_2 sample was measured with a phase measuring interferometer system.

All machined or etched surfaces were observed under a Nomarski differential interference contrast microscope. Surface microtopography of polished samples was measured with a scanning probe microscope as well as with two three-dimensional optical surface profilers. In order to investigate the microstructure and nanostructure of both the surface and subsurface of the polished CaF_2 crystals, two transmission electron microscopes (TEM) were used to observe cross sections of crystals. For the TEM specimen preparation, the float-polished crystal samples were sectioned oriented normal to the polished surface. The samples were then ground and polished with a water slurry of ~ 50-nm-diameter Al_2O_3 powder. They were finally ion polished with a 3 keV argon ion beam oriented at 15 deg to the sample surface. The TEM observations were made using either the microscope with a 200 kV accelerating

*corresponding author: naoyuki@isc.chubu.ac.jp

voltage or the other with a 400 kV accelerating voltage. The theoretical resolutions of the 200 kV and 400 kV accelerating voltages are 0.23 nm and 0.17 nm, respectively.

3. Results and Discussion

Figure 1 shows the flatness of a float-polished 100-mm-diameter, 40-mm-thick CaF_2 sample, as measured with a laser interferometer on a 90-mm-diameter area. After 80 min of float polishing, we obtained a flatness of 31.9 nm p-v and 6.03 nm rms. This is excellent flatness for such a high thermal expansion material. Figure 2 shows the surface roughness of a float-polished CaF_2 sample measured with an optical profiler. The surface roughness values are 0.120 nm Ra, 1.25 nm Ry, and 0.151 nm rms in the measurement area of 250 x 250 μm^2.

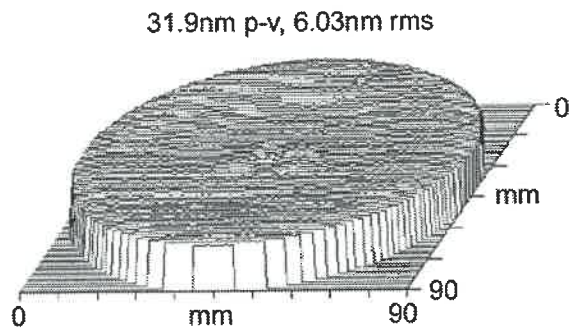

Figure 1: Surface flatness of a float-polished CaF_2 sample measured on a 90-mm-diameter area.

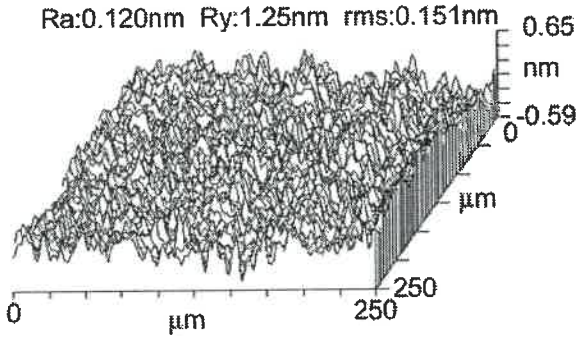

Figure 2: Surface roughness of a float-polished surface as measured on a 250 x 250 µm area with an optical profiler.

Figures 3(a) and 3(b) are cross-sectional TEM images of CaF_2 single crystal surfaces after the ultra-precision grinding and the float polishing, respectively. The images were obtained by using the 200 kV accelerating voltage TEM. In Figure 3(a), the image clearly shows subsurface damage due to the grinding process. The thickness of damaged layer observed in the TEM image is of about 200-300 nm. The image contrast also shows that the damaged area consists of a severely deformed upper layer with fine strain contrast, and an elastic strain field with broad contrast beneath the upper layer. This can be a typical example of subsurface damage structure of brittle ionic crystals induced by the machining. However, the thickness of damaged layer in this case is much smaller than those predicted for ordinary grinding processes. After float polishing process following the ultra-precision grinding, the subsurface damage was completely removed as shown in Figure 2(b). In this image, none of strain field contrast is observed, indicating that the float-polished CaF_2 has dislocation-free subsurface structure. This is consistent with the result obtained by Nomarski differential interference contrast microscope observations of surface etch-pits.

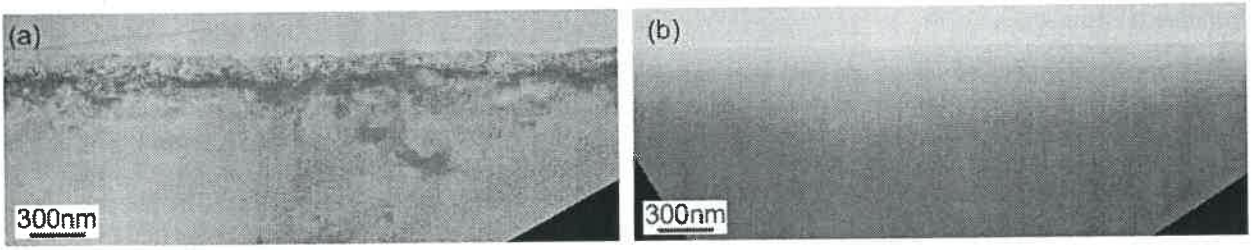

Figure 3: Low magnification cross-sectional TEM images of CaF_2 single crystal samples after ultra-precision grinding (a), and float polishing (b).

Figures 4(a) and 4(b) show high-magnification TEM images of a float-polished CaF_2 crystal surface obtained with the 400 kV accelerating voltage TEM. Although the float-polished crystal showed a damage-free subsurface structure, the roughness of the surface imaged in the TEM was not always excellent compared with the ideal roughness expected from the theoretical analysis [5]. Specifically, the TEM images often indicated a characteristic "ridged" shape surface roughness on the profiles, depending on the specimens, as shown in Figure 4(a). Figure 4(b) is a high-resolution TEM image of a part of the region in Figure 4(a). It shows the (111) crystal lattice fringes with a spacing of 0.32 nm. It should be noted that the profiles of terraced part of the surface are aligned exactly parallel to the (111) lattice fringes, as marked on the images.

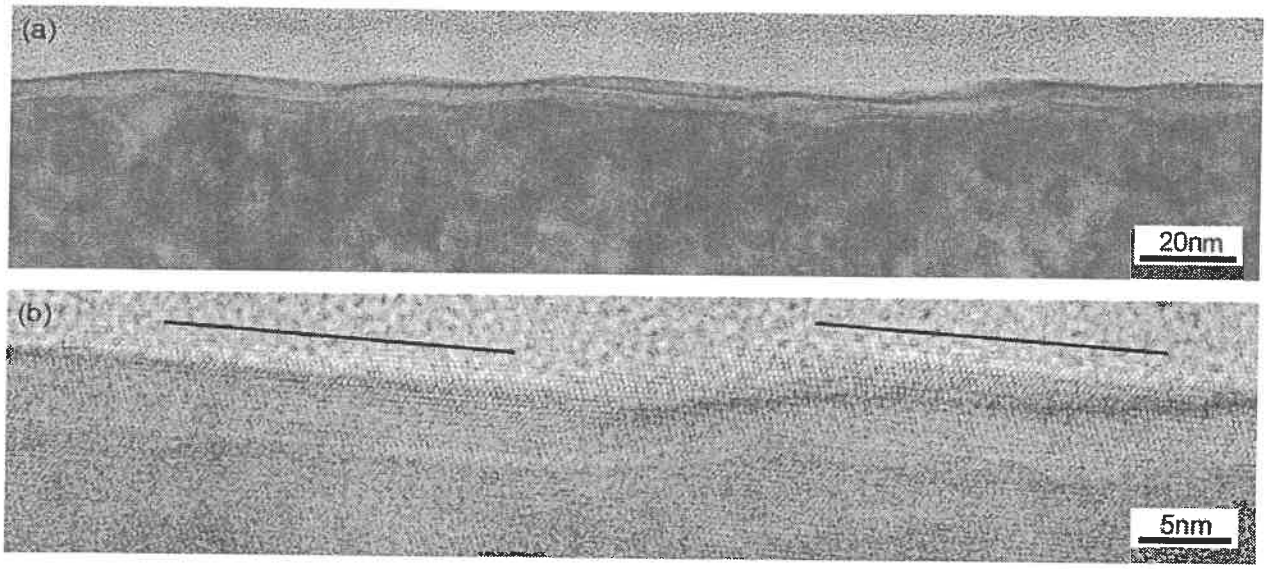

Figure 4: TEM images of a float-polished CaF_2 surface, indicating the (111) lattice fringes.

Figure 5 is an atomic structure model of the ridged shape surface derived from the observed TEM image and the atomic arrangement of the CaF_2-type crystal structure. The surface is composed of the flat (111) plane terraces and the nanometer height steps in between. This implies that the chemical-mechanical reactions during the float polishing process preferentially remove surface atoms of the CaF_2 crystal along the (111) planes. This also suggests that the roughness of the surface mainly arises from the mismatch between the macroscopic surface orientation and the (111) crystal planes. In fact, the average orientation of the specimen surface in Figure 4 is mismatched by about 5 deg from the (111) plane. This causes a relatively large surface roughness.

The above results suggest that an atomically smooth CaF_2 surface can be obtained by the precise alignment of the crystal surface to the (111) planes. Figures 6(a) and 6(b) show the roughness of float-polished surfaces as measured on a 1 x 1 μm areas with an SPM. Before the samples were float polished, they were precisely oriented with the (111) lattice plane. The misfit angles θ of the surface from the (111) plane are 0.18 deg and 0.02 deg, respectively, for the specimens of Figures 6(a) and 6(b). Both the SPM images clearly show that the surface has the characteristic ridged shape with a step height of a few nanometers. This is quite consistent with the results of TEM observations. Further, the smallest roughness for 1 x 1 mm area, which is of 0.059 nm Ra, 0.077 nm rms, and 0.72 nm Ry, was obtained, as shown in Figure 6(b).

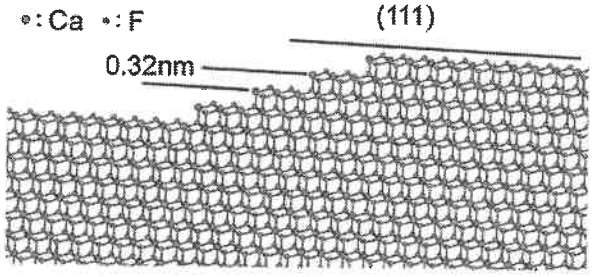

Figure 5: An atomic structure model of a float-polished CaF_2 surface.

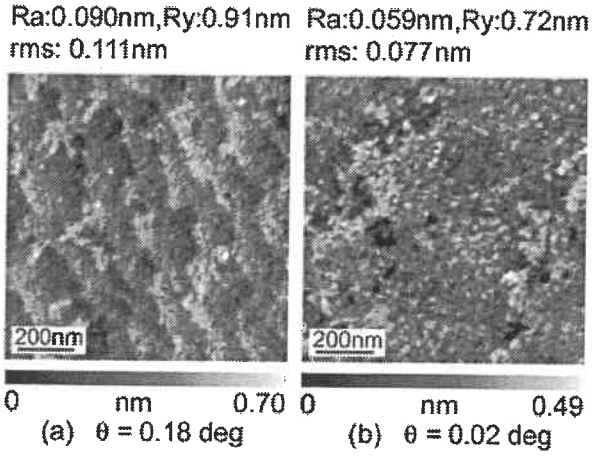

Figure 6: Surface roughness of float-polished surfaces near the (111) planes, as measured on 1 x 1 μm areas with an SPM.

Figure 7 is a high-resolution TEM image of a float-polished CaF_2 surface obtained with the 400 kV TEM. Before starting the ultra-precision grinding prior to the float polishing process, the sample was precisely aligned and carefully sawed so that the mismatch angle of the crystal surface from the (111) plane become as small as possible. The mismatch angle roughly estimated by the SPM measurement was of the order of 1/100 deg, which makes the interval between the surface steps over several hundred nanometers. The image clearly demonstrates that an atomically smooth surface with a p-v roughness smaller than the (111) single crystal lattice spacing (*i.e.*, 0.32 nm) can be achieved. The image also proves that no subsurface crystal defects, shown as a deformation of the lattice fringes, are introduced by the machining. This TEM result suggests that it is possible to obtain an atomically perfect, flat surface on a CaF_2 crystal by using the float polishing technique. From above-mentioned results, in addition to float polishing, the nanoaligning technology necessary to obtain a sample exactly oriented to the (111) plane is essential for making atomically-flat, real surfaces.

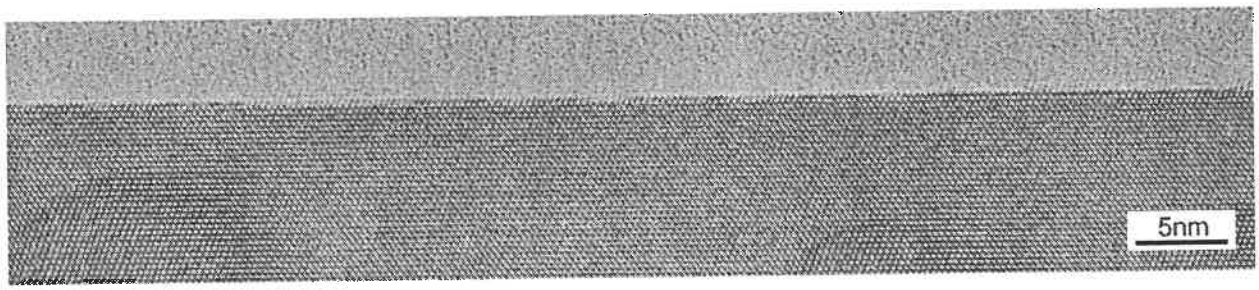

Figure 7: High resolution TEM image of a float-polished CaF_2 crystal surface of which the orientation precisely aligned parallel to the (111) plane.

4. Conclusions

High purity DUV grade calcium fluoride (111) single crystals have been float polished in order to obtain the highest quality surfaces. The finished surfaces were observed with a Nomarski differential interference contrast microscope, optical profilers, a scanning probe microscope and transmission electron microscopes. A flatness of 31.9 nm p-v and 6.03 nm rms were obtained on 90-mm-diameter area samples by 80 min of float polishing after optical polishing. It is clear from high resolution transmission electron microscope images, scanning probe microscope and Nomarski differential interference contrast microscope observations that there is no subsurface damage in the float-polished CaF_2 single crystal sample. The float-polished surface is formed from a perfect (111) lattice with small atomic steps, so that the polished surface roughness depends on the mismatch between the sample surface and the (111) planes. A surface roughness of 0.059 nm Ra, 0.077 nm rms, and 0.72 nm Ry was obtained by the float polishing process, as measured on a 1 x 1 μm area with an SPM.

Acknowledgements

Part of this work was supported by the Grants-in-Aid for Scientific Research (B) Nos. 11450063, 12450063, 14350077 and 15360075 of the Japan Society for the Promotion of Science, and the "Nanotechnology Support Project" of the Ministry of Education, Culture, Sports, Science and Technology (MEXT), Japan.

References

[1] Y. Namba and H. Tsuwa, "Ultra-Fine Finishing of Sapphire Single Crystal", Annals of the CIRP, **26/1** (1977) p.325-329.

[2] J. M. Bennett, J. J. Shaffer, Y. Shibano, and Y. Namba, "Float Polishing of Optical Materials", Appl. Opt., **26/4** (1987) p.696-703.

[3] Y. Namba, H. Tsuwa, and R. Wada, "Ultra-Precision Float Polishing Machine", Annals of the CIRP, **36/1** (1987) p.211-214.

[4] Y. Namba, N. Ohnishi, K. Harada, and K. Yoshida, "Float Polishing of Calcium Fluoride Single Crystals for Ultra Violet Applications" Proc. 17th Annl. Mtg. of ASPE, (2002) p.450-453.

[5] Y. Namba, J. Yu, J. M. Bennett, and K. Yamashita, "Modeling and Measurements of Atomic Surface Roughness", Appl. Opt., **39/16** (2000) p.2705-2718.

Polisher Life in High Speed Ultra-Smoothness Polishing of NiP Plated Aluminum Magnetic Disk Substrate

Heiji YASUI*, Shoji KURIBAYASHI*, Seiji MATSUKAWA*,
Yutaka YAMASAKI* and Kanta YAMAGUCHI*
***:Dept. of Mechanical Engineering & Materials Science, Kumamoto University**
2-39-1 Kurokami , Kumamoto 860-8555, JAPAN

1. Introduction

In manufacturing of the compact magnetic disk, reducing its cost together with realizing higher storage capacity has been steadily required. One of the methods for filling the requirement is to build the high productive ultra-smoothness polishing technique of the magnetic disk substrate. In our previous researches[1),2)] high speed polishing in excess of 5 times the usual polishing speed is attempted for getting high removal in polishing of electroless nickel phosphorus (NiP) plated aluminum magnetic disk substrate. From the result, high speed polishing is useful for getting high removal rate with ultra-smoothness substrate surface. Polisher life, however, is not examined yet although it is one of the most important factors from the standpoint of the manufacturing cost.

The research deals with the polisher life in the polishing of NiP plated aluminum magnetic disk substrate. In the report, the polisher life in the high speed polishing is examined.

2. Experiments

The appearance of the polishing machine is shown in **Fig. 1**. The machine is available for polishing speed up to 9m/s which is in excess of 5 times the maximum polishing speed executed by the conventional polishing machine. The main experimental conditions are listed in **Table 1**. The aluminum substrate used is 3.5inch type. Polishing speed is 9m/s. The polisher and abrasives used are suede type and colloidal silica, respectively. The polisher surface is observed with a differential interference microscope and SEM. The substrate smoothness is evaluated from the standpoint of the slight undulation *H*wa(Ra), and the surface roughness *H*ra(Ra), which are obtained from the surface profiles of 4mm length and 256μm length measured with a interferometric surface profiler (WYKO), respectively. The data of slight undulation and surface roughness are obtained by averaging the values of two-dimensional profiles at five random positions on the three-dimensional WYKO images measured at four substrate surface locations. AFM is also used to examine ultra-precisely the substrate surface roughness.

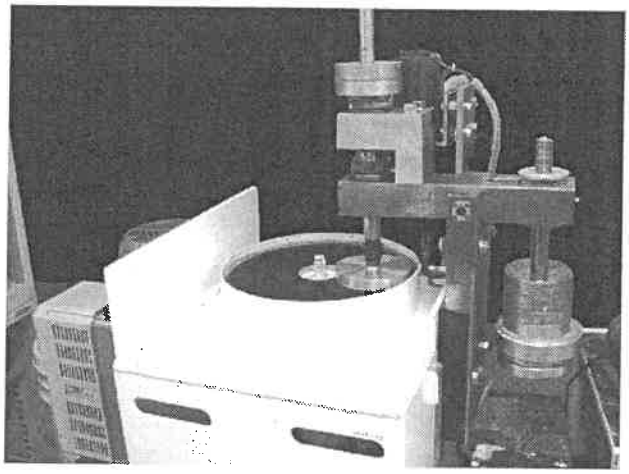

Fig.1 Appearance of the polishing machine

Table1 Main experimental conditions

Workpiece	NiP plated aluminum magnetic disk (3.5inch-type)
Polisher	Suede type
Polishing fluid	Abrasives : Colloidal silica Supply flux : 6, 14 g/min
Polishing conditions	Polishing speed *V*a : 9.0 m/s Polishing pressure *P* : 3.7, 11.1 kPa

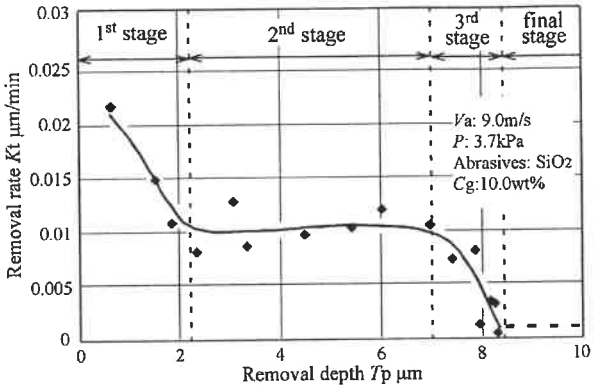

Fig.2 Change of removal rate with removal depth

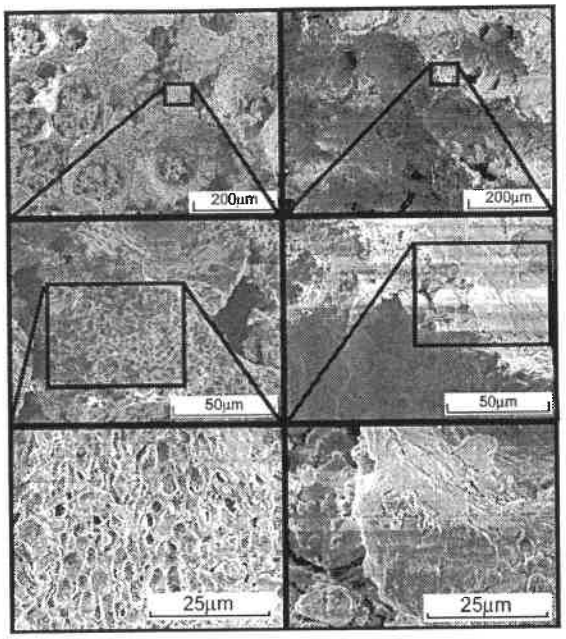

(a)Before polishing (b)Polisher life

Fig.3 Change of polisher surface due to polishing

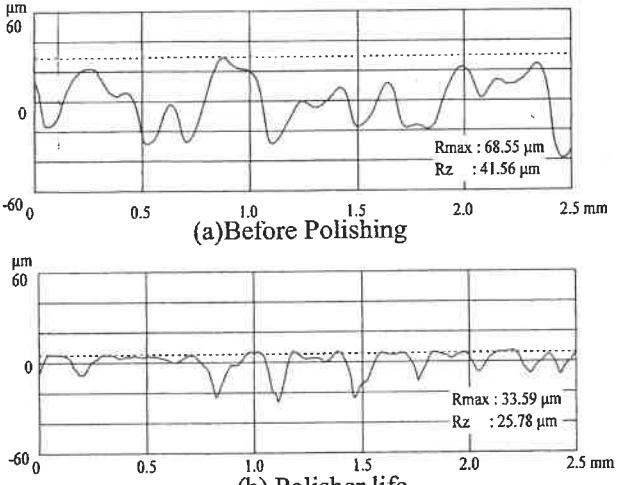

(a)Before Polishing

(b) Polisher life

Fig.4 Change of polisher cross-section profile due to polishing
[Abrasive:SiO_2 Polisher:Suede-type Cg:10.0wt% *Va*:9.0m/s *P*:11.1kPa]

4. Results and discussions

4.1 Change of removal rate with polishing process

Figure 2 shows the change of removal rate with removal depth. Polishing speed and pressure are 9m/s and 3.7kPa, respectively. The removal rate is high at the beginning of polishing. In the initial polishing process, however, the removal rate steeply decreases transiently with the increase of removal depth (1st stage). After the initial polishing process, the removal rate is kept steadily a constant value in the range of removal depth of about 8μm (2nd stage). Over the range of steady state, the removal rate steeply decreases again (3rd stage). Finally the removal rate converges to extremely small values near zero (Final stage). The polisher life is defined when the removal rate comes to the final stage level.

4.2 Change of polisher surface due to polishing

The change of removal rate due to polishing is considered to depend on the state of the polisher surface. **Figure 3** shows the polisher surfaces before polishing and after coming to polisher life. Polishing speed and pressure are 9m/s and 11.1kPa, respectively. The new polisher surface before polishing consists of large holes and wall layers having a lot of micro-pores. After coming to life, however, the micro-pore is vanished and observed little on the polisher surface. In addition, the large hole is filled up with the chip of polisher formed by polishing. As the result, the polisher surface becomes nearly flat. The colloidal silica abrasives are difficult to stay on such a flat polisher surface. Thus the removal rate in polisher life is considered to become extremely small value near zero.

Figure 4 shows the change of polisher cross-section profile due to polishing. The cross-section profile before polishing is rough. The roughness is about 70μm. After coming to the final stage, however, the roughness becomes small and about 30μm.

Figure 5 shows the change of polisher surface roughness with polishing time. From the figure, the surface roughness decreases steeply from about 70μm to about 30μm in the short polishing time. Thus the polisher used is considered soft for high polishing speed and pressure. It is referred important to select the suitable polisher for effective polishing of long life though dressing technique is additionally one of the most important subjects.

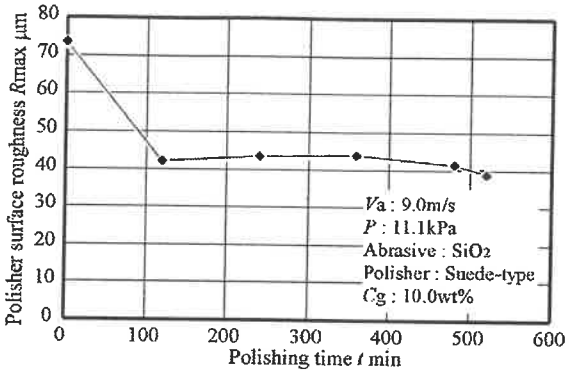

Fig.5 Change of polisher surface roughness with polishing time

4.3 Effect of flow rate of polishing fluid

The effect of flow rate of polishing fluid on polisher life time is shown in **Fig.6**. The experiments are carried out in two supplying methods in which the flow rates are 6g/min with one nozzle and 14g/min with two nozzles. From the result, the change of removal rate with removal depth is almost the same curve for both those methods. For high flow rate of 14g/min, however, the removal depth in the region of the steady polishing state is larger than low flow rate of 6g/min. In high speed polishing with high polishing pressure, large heat generation occurs. Accordingly it is considered important to remove effectively the generated heat.

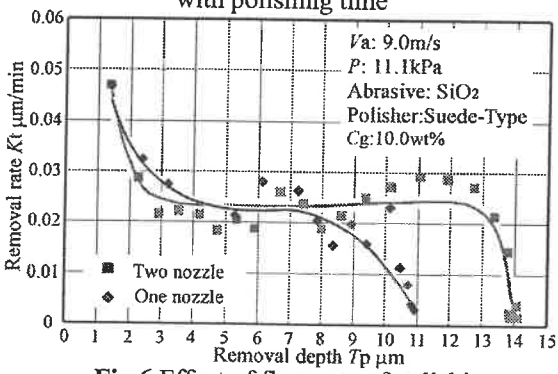

Fig.6 Effect of flow rate of polishing fluid on polisher life time

4.4 Influence of polisher surface condition on substrate surface smoothness

In **Fig.7**, the change of substrate surface smoothness with polishing time is shown for polishing pressures of 11.1kPa and 3.7kPa under polishing speed of 9m/s. It is found from the figure that both of slight undulation and surface roughness are almost the same values through whole polishing process from the beginning of polishing to final stage, which are about *H*wa=0.4nm(Ra) and *H*ra=0.3nm(Ra), respectively. The polishing pressure has little influence on slight undulation and surface roughness. Accordingly the polisher surface condition is referred to influence little on polished substrate surface smoothness measured with WYKO.

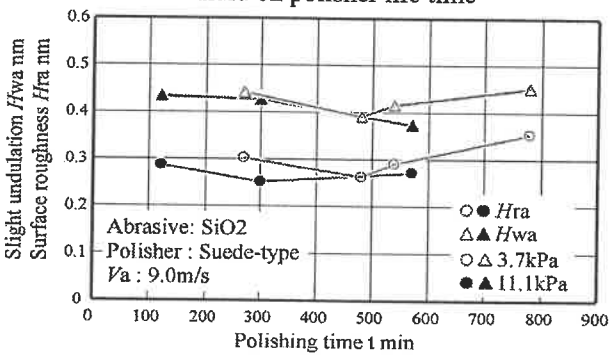

Fig.7 Influence of polisher surface topography on surface smoothness

Figure 8 shows the three dimensional WYKO image for two polishing times. It is clear that the surface roughness in both of polishing time of 300min in the range of steady state and 510min in polisher life are almost the same.

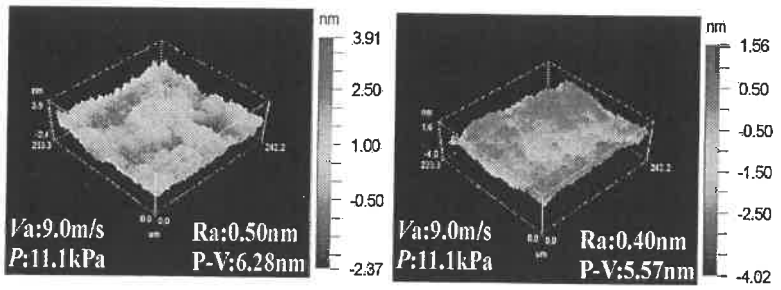

(a) 300min (a) 510min

Fig.8 Comparison of WYKO image after polishing in two polishing time [Abrasive:SiO2 Polisher:Suede-type *Cg*:10.0wt% *Va*:9.0m/s *P*:11.1kPa]

Figure 9 shows an example of AFM image of substrate surface formed in the final polishing process. From the figure, some grooves with small particles are found on the polished substrate surface. As the surface roughness excluding the grooves is about 0.2nm(Ra), the surface is referred to be polished relatively smooth. When including the height of grooves, however, the surface roughness can not use as a product. Accordingly, it is considered important to exchange new polisher before coming to polisher life.

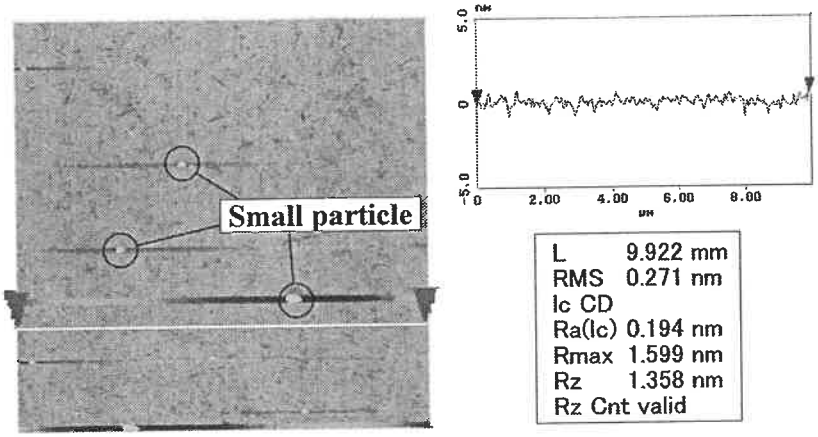

Fig.9 An example of AFM image of substrate surface formed with the polisher in the life process
[Abrasive:SiO_2 Polisher:Suede-type *C*g:10.0wt% *V*a:9.0m/s *P*:11.1kPa]

5. Summary

The main results obtained are as follows:

(1) The removal rate is high at the beginning of polishing. However, it decreases steeply in the initial polishing process transiently. In the second process after the initial process, the removal rate is kept a constant value. In the third process, the removal rate transiently decreases steeply and finally converges to a life value near the removal rate of zero.

(2) The polisher life occurs when the small hole with wall layer having micro-pores is mostly filled up with the chip of polisher , as the result , polisher surface becomes flat.

(3) The flow rate of polishing fluid influences on polishing life time.

(4) Both of slight undulation and surface roughness is almost the same values through whole polishing process from the beginning of polishing to final stage defined as polisher life, which are about *H*wa=0.4nm(Ra) and *H*ra=0.3nm(Ra), respectively

(5) In the polisher life, some grooves with small particles are found on the polished substrate surface measured with AFM.

Acknowledgement

The authors would like to thank TOYO KOHAN Co. Ltd and FUJIBO EHIME Co. Ltd for providing magnetic disk substrate and polisher.

References

[1] H. Yasui *et al.*: High Removal Rate Ultra-Smoothness Polishing of NiP Plated Aluminum Magnetic Disk Substrate, Proc. ASPE 2001 Annual Meeting, Vol.25 (2001) p. 545-548.

[2] H. Yasui *et al.*: High Removal Rate Ultra-Smoothness Polishing of NiP Plated Aluminum Magnetic Disk Substrate by Means High Polishing Speed with High Polishing Pressure, Proc. ASPE 2002 Annual Meeting, Vol.27 (2002) p. 689-692.

Authors Index

Abiko, Daichi 313
Abu Ibrahim, Fadi 205
Aigeldinger, Georg 153, 366, 378, 386
Aizawa, Yoshiaki 261
Aketagawa, Masato 313
Akilian, Mireille 209
Alonso, Jesús 582
Aly, Mohamed Fawzy 574
Ambekar, Paritosh P. 438
Angelis, Georgo Z. 60
Aoyama, Hisayuki 253, 273
Ariga, Yukinori 321
Arora, Will 141
Autschbach, Lutz 88
Awtar, Shorya 205
Barbastathis, George 141
Bauza, Marcin 28
Benítez, Pablo 582
Bergner, F. 598
Bertram, Torsten 185
Bhamidi, Kalyana P. 458
Bifano, Thomas G. 20, 117, 686, 698
Bikshapathi, Manupati 169
Blair, Robert 229
Blen, José 582
Bono, Matthew J. 578
Brinksmeier, Ekkard 88, 582
Brocato, Brett Chandler 80
Brodziak Jr., John E. 101
Büchner, Hans-Joachim 145
Buchner, Tilman 141
Buescher, Nathan P. 213
Bui, Son Hoang 474
Buice, Eric S. 217, 434
Burton, David 221
Carnevale, Sharon 101
Ceremuga, Joseph T. 366, 378, 386
Chaney, Marcus A. 101
Chen, Chao-Jung 478
Chen, Ken 654
Chen, Shih-Chi 293, 329, 333, 337
Chen, Yen-Liang 478
Cheung, Chi-Fai 586
Chiba, Naoto 273
Chon, Kwon Su 494
Chu, Chong Nam 717
Chu, David 92
Chun, Keyoung-Jin 289, 390
Chung, Sung-Chong 189, 289, 352
Couey, Jeremiah A. 105, 502
Culpepper, Martin L. 113, 293, 297, 329, 333, 337, 345, 362
Cuttino, James F. 76, 374
Dalrymple, Timothy M. 40
Davies, Angela D. 101
Davies, Matthew A. 349
de Klerk, Angelo 60
Díaz, Vicente 582
Dong, Lei 137
Dow, Thomas A. 48, 80, 201, 213, 462
Dumas, Paul R. 498
Duncan, G. Scott 221, 646
Eikenberry, Stephen . . . . . *
Eom, TaeBong 394, 414
Esashi, Masayoshi 157
Fagan, Terence J. 434
Faiz, Robert 666
Fan, Xiaorui 84
Farooqui, Sami A. 398
Folkert, Karalyn F. 462
Forest, Craig R. 209
Frank, Thomas 245
Freitag, Karl 48
Fricke, Liesel 101
Fuchiwaki, Ohmi 253, 273
Fujiwara, Takanori 249
Fukuta, Masahiko 558
Furuhashi, Hideo 514
Furuno, Tatsuya 634
Furutani, Katsushi 590
Füßl, Roland 145
Gamo, Yoshihiro 309
Gao, Yongsheng 370
Garrard, Kenneth P. 201, 462
Gatzen, Hans H. 594
Geraghty, Paul 36
Gessenharter, Alexander 582
Golda, Dariusz 297
Golini, Donald 498
Gopal, Krishnakumar 374
Goto, Satoshi 157
Grover, Chander P. 514
Grünwald, Rainer 145
Guo, Yin-biao 534
Hackel, Tobias 245
Haftka, Raphael T. 617
Hamaguchi, Tetsuya 121, 658, 678
Hammer, Ralf 598
Han, Jin Wan 394
Han, Y. 68

*Abstract unavailable at press time.

Hanaoka, Shunsaku 638
Hane, Kazuhiro 518
Hanyu, Hiroyuki 609
Hashizume, Hitoshi 64, 177
Hausotte, Tino 145
Hayashi, Hirofumi 638
Hayashi, Teru 422
Hayashi, Toshiki 177
Heilmann, Ralf K. 382
Hibbard, Robin L. 578
Higashi, Yasuo 621
Higuchi, Masahiro 605, 650
Hijikata, Yoshio 558
Hikichi, Kousuke 157
Hiraga, Yota 602
Hirao, Masatoshi 197
Hocken, Robert J. 28, 217, 434, 442
Höhne, G. 245
Hollis, Ralph L. 32
Honda, Satoshi 225, 233, 301
Hong, Jae Soo 390
Hopkins, David J. 36
Horie, Mikio 309
Horio, Ken'ichiro 690, 725
Hoshino, Shoichi 325
Hosokawa, Akira 530
Hsieh, Chen 193
Hsin, Yi-Ping 249
Huang, Hao 534
Huntsinger, Christopher 442
Hwang, Jooho 446
Ikeno, Jun-ichi 546
Imai, Hidetaka 197
In, Hyun Jin 141
Inami, Yusuke 177
Inamura, Toyoshiro 197
Inazuki, Yuichi 149
Ishikawa, Ken-ichi 129
Isomura, Kousuke 157
Iwai, Manabu 550, 701
Iwata, Futoshi 305
Iwata, Tomoyuki 225
Izumi, Masumi 538
Jäger, Gerd 145
Jain, Anurag 133
Jain, Pavan 28
Jin, Masahiko 602
Jin, Sung Hun 717
John, Binu P. 502
Jones, James F. 153
Jurisch, Manfred 598
Kajihara, Yusuke 149
Kallenbach, Eberhard K. 185
Kamiya, Daiki 309
Kamiya, Kazuhide 341, 490
Kamiya, Nagayuki 341
Kamiya, Takahito 562
Kanda, Yasuhiro 733
Kane, Nathan R. 229
Kaneeda, Toshiaki 605, 650
Kaneko, Arata 317
Kang, Seong-Ho 109
Kanlayasiri, Kannachai 662
Kato, Hideharu 609
Kato, Mitsuhiro 257
Kato, Norihiko 281
Kato, Shigeo 165, 257, 261, 281, 285
Kawaguchi, Kazuki 402
Kawara, Hiroyuki 197
Kikuchi, Yoshimi 526
Kim, Chang-Ho 682
Kim, Gyung-Bum 265
Kim, Jin Hong 117, 686
Kim, Jong-Ahn 414
Kim, Min-Seok 189
Kim, Myong-Zoo 189
Kim, Seung-Woo 446
Kimura, Keiichi 705
Kireev, Vladimir 185
Kitajima, Takayuki 542
Kleinwechter, Andre 598
Knapp, Byron R. 105
Kobayashi, Fumiyuki 241
Kobayashi, Shintaro 325
Kobayashi, Yoshikazu 613
Kojima, Takaomi 526
Kojima, Yoichi 558
Kokubo, Hirotaka 690
Komatsu, Kou 64
Kondoleon, Anthony S. 666
Koning, Robert J. 229
Korb, Samuel 333
Kourouklis, Christos 594
Kramar, John A. 16
Krenz, Kevin D. 366, 378, 386
Krishnamurthy, R. 729
Kumar, S. G. 169
Kuramoto, Kouichi 125
Kurdi, Mohammad H. 617
Kuribayashi, Shoji 737
Kurioka, Kouji 490
Kwon, Patrick Y. 181, 629
Lai, B. 68
Landsiedel, Nathan 345
Larsen, Eric R. 349
Lauben, David 438
Lawton, Kevin M. 470
Lee, Chan-Hong 446
Lee, Hae Sung 717
Lee, Hwa-Soo 402, 554

Lee, JaeYun 414
Lee, Jinmo 313
Lee, Jong Duk 717
Lee, Neville K. S. 670, 674
Lee, Sun-Kyu 313
Lee, William 93
Lee, Wing-Bun 586
Li, Zhi Qi 670, 674
Lim, Kyoung-Soo 313
Liu, Bong-Yu 193
Lo, C. 370
Lotz, Markus 245
Lu, Xiaodong 269
Maeda, Noritsugu 422
Maeyasu, Yoshito 621
Magara, Kenji 313
Mann, Brian P. 617
Manske, Eberhard 145
Marsh, Eric R. 105, 454, 502, 709
Maruo, Kenji 562
Masaaki, S. 613
Maser, J. 68
Masuya, Yu 233
Matsuda, Kiyofumi 514
Matsukawa, Seiji 737
Medicus, Kate M. 101
Miller, Jimmie A. 137, 450
Miller, Michele H. 84, 570
Misaki, Daigo 253, 273
Mishima, Nozomu 237
Mitsuhashi, Masakazu 725
Mitsui, Kimiyuki 418
Mitsuishi, Mamoru 125, 506
Miyahara, Kyogo 609
Miyamoto, Toshiki 705
Miyazawa, Hajime 321
Miyoshi, Takashi 705
Mizugaki, Junji 621
Mohamed Ali, Abu M. 466
Mohri, Naotake 690
Montesanti, Richard C. 44
Montoya, Juan 382
Moore, Rochelle 406
Morgan, Christopher J. 709
Moriwaki, Toshimichi 558, 621
Moronuki, Nobuyuki 317, 694
Morse, Edward P. 374, 398, 450, 458
Munakata, Yutaka 313
Murakawa, Masao 321, 602
Muraki, Takashi 313
Muralikrishnan, Bala 24
Nagami, Shin-ichirou 305
Nagarajan, T. 169
Nagato, Keisuke 121
Naito, Takayuki 285
Nakamura, Hisashi 165
Nakanishi, Akira 506
Nakao, Masayuki 121, 658, 678
Nakao, Yohichi 241
Nakashima, Toshiro 518
Nakayabu, Toshihiro 197
Nakazato, Yuichi 321
Namba, Yoshiharu 72, 494, 510, 733
Narayanasamy, K. 729
Nemanich, Robert J. 642
Nettles, John A. 450
Newell, David B. 16
Ng, Eugene 574
Nichol, Jamie G. 438
Nimmakayala, Pawan Kumar 56
Nishioka, Masahiko 558
Nomura, Masataka 625
Nomura, Takashi 341, 490
Nonomura, Yuji 510
Norlund, Bruce K. 213
Novak, Erik L. 97
Novak, W. Thomas 249
Nuttall, Melissa M. 349
Ochi, Akio 538
Ogasawara, Hiroomi 422
Ogasawara, Masato 422
Ogawa, Sinnosuke 257
Ogura, Ichiro 426
Ohmura, Yoichi 518
Ohnishi, Naoyuki 510, 733
Ohsige, Kouhei 121
Oka, Toru 518
Okada, Yoshikazu 605
Okada, Yusuke 418
Okaji, Masahiro 197
Okazaki, Yuichi 277, 426
Okino, Tadashi 558
Okuyama, Shigeki 542
Olortegui-Yume, Jorge 629
Ono, Manabu 165, 257, 261, 281, 285
Ono, Masashi 313
Ooi, Takeshi 121, 658, 678
Ooide, Takahito 321
Orji, Ndubuisi George 482
Osada, Tsubasa 261
Otsuki, Manabu 281
Otten, David 434
Overcash, Jerald L. 76
Panusittikorn, Witoon 201
Park, Chang-Woo 289
Park, Chun-Hong 446
Patten, John A. 137
Patterson, Steven R. 470
Pérez, Daniel 582
Potluri, Anil 24

Pratt, Jon R. 16, 430
Raasch, Thomas W. 161
Raja, Jayaraman 466, 482
Raju, H. P. 466, 729
Randall, Travis 642
Reimann, Greg 698
Ren, Dongmei 470
Renegar, T. Brian 474
Rhorer, Richard L. 633
Rizzi, Alfred A. 32
Roblee, Jeffrey W. 161, 213, 229
Roehrig, C. 68
Ryu, Kentaro 317
Sagesaka, Yuji 241
Sahay, Chittaranjan 24
Saile, Volker 52
Saito, Namiko 546
Saito, Norio 165
Saito, Teruaki 410
Saito, Yasunori 694
Sakamoto, Shigehiko 634, 638
Saneshima, Satoshi 694
Sano, Sadao 701
Sasaki, Akira 305
Sasazaki, Tomoya 281
Sato, Kaiji 64, 177, 325
Sawa, Takekazu. 566
Sawano, Hiroshi 125
Scattergood, Ronald O. 642
Schaper, M. 598
Schattenburg, Mark L. 209, 382
Schmit, Joanna 97
Schmitz, Tony L. 173, 221, 617, 646
Schott, Walter 145
Seki, Shigeo 526
Seugling, Richard M. 16, 217, 430, 434
Shamoto, Eiji 621
Sharma, Anurag 550, 701
Shibata, Atsushi 514
Shimada, Shoichi 605, 650
Shimokohbe, Akira 177
Shingai, Takafumi 634
Shinmura, Takeo 721
Shinno, Hidenori 64
Shinozaki, Akira. 634
Shinshi, Tadahiko 64, 177
Shintani, Kazuhiro 609
Shirai, Kenji 613
Shreve, Shelby M. 709
Shu, Deming 68
Sihler, Joachim 229
Slocum, Alexander H. . . . 205, 209, 229, 356, 359, 713
Smith, Henry I. 141
Smith, K. Scott. 349
Smith, Philip T. 454
Smith, Stuart T. 28,
Smolyanitskiy, A. . . . . .
Sohn, Alex 80,
Soma, Takeshi 24
Song, In-Ho 352
Song, Jun-Feng. 486
Sprunt, Alexander D. 356
Sreenivasan, S. V. 56
Srinivasa, Y. G. 169, 729
Stephenson, G. B. 68
Stone, Jack A. 24
Stoup, John R. 24
Subramanian, Ramkumar 181
Sugaya, Isao 249
Sumiya, Yosuke 305
Sutin, Jason. 205
Suwabe, Hitoshi 129
Suzuki, Hirofumi 558, 621
Suzuki, Keisuke. 705
Suzuki, Kiyoshi 550, 701
Suzuki, Michio 590
Takada, Koji. 313
Takahashi, Satoru 149
Takamasu, Kiyoshi 149
Takaya, Yasuhiro 705
Takemura, Takato 546
Takeuchi, Sadao 321
Takezawa, Hideki. 690
Tanaka, Hiroaki 650
Tanaka, Katsutoshi 550
Tanaka, Shuji. 157
Tashiro, Hatsuzo 341, 490
Terao, Kohsei. 313
Tesar, Delbert 109
Theska, R. 245
Tieman, B. 68
To, Suet Sandy 586
Togo, Shin-ichi. 157
Tozawa, K. 613
Tricard, Marc 498
Trumper, David L. 44, 209, 269, 434
Tse, Shuet Fung 370
Tsuchiya, Kensuke 121, 658, 678
Tummond, Michael F. 646
Turner, Jeremy S. 450
Uchida, Yoshiyuki. 514
Uda, Yutaka 249
Ueda, Takashi 530
Uematsu, Tetsutaro 550, 701
Uneda, Michio 129
Usuda, Takashi 273
Vallance, R. Ryan 105, 454, 502, 709
van Eijk, Jan 60
van Niekerk, Johannes B. 438
Varadarajan, Kartik Mangudi. 113, 337

Veldhuis, Stephen C. 574
Vemuri, Srinivas C. 24
Vogt, S. 68
Volkert, Ralf 185
Vorburger, Theodore V. 474, 486
Wakiwaka, Hiroyuki 526
Walker, Richard 666
Walter, J. J. H. 642
Walter, Mark M. 229
Wang, Chen-Yu 478
Wang, Xiankui 654
Warisawa, Shin'ichi 125, 506
Warsi, Faiz Mohammad 442
Watson, Douglas C. 249
Werkmeister, Jaime Brooke 713
Willoughby, Patrick J. 359
Winarski, R. 68
Winter, Amos G. 362
Wolff, Rachel 101
Woody, Shane C. 28
Wu, Dan. 654
Yamada, Keiji 530
Yamada, Takazo 402, 554
Yamaguchi, Kanta 737
Yamaguchi, Tomomi 650
Yamamoto, Natsuki 658
Yamamoto, Yuji 558
Yamamoto, Yuki 566
Yamasaki, Yutaka. 737
Yamashita, Keishu 542
Yamashita, Koujun. 510
Yamazaki, Junichi 678
Yamazaki, Tsuguo 690, 725
Yanagi, Kazuhisa. 410
Yang, Hua 217, 434
Yasui, Heiji. 562, 566, 634, 638, 737
Yasui, Takeshi 197
Yeon, Kwang-Heum. 352
Yi, Allen Y. 133, 161
Yi, Sang Min 717
Yi, Wangmin 654
Yokomizo, Seiichi. 605, 650
Yoshida, Kunio. 733
Yoshida, Satoshi 418
Yoshida, Shinji 733
Yoshida, Tomohiro 733
Yoshioka, Hayato. 64
Yuan, Bausan 249
Yui, Akinori. 542
Yunoki, Tsutomu 530
Zavislan, James M. 15
Zentner, Johannes 185
Zhang, Liang 522
Zhang, Ping. 570
Zhang, Yi 534
Zheng, Lin 534
Zhou, Yaopeng. 20
Ziegert, John C. 221
Zou, Yanhua. 721